NANOSTRUCTURES:
PHYSICS AND TECHNOLOGY

15th International Symposium

Novosibirsk, Russia, June 25–29, 2007

Co-Chairs
Zh. Alferov
L. Esaki

PROCEEDINGS

Ioffe Institute
St Petersburg, 2007

Published by
Ioffe Physico-Technical Institute
26 Politekhnicheskaya, St Petersburg 194021, Russia
http://www.ioffe.ru/

Publishing license ΛP No 040971 of June 16, 1999.

ISBN 5-93634-022-8

The International Symposium "Nanostructures: Physics and Technology" is held annually since 1993. The first Symposium was initiated by Prof. Zh. Alferov and Prof. L. Esaki who are its permanent co-chairs. More detailed information on the Symposium is presented on the World Wide Web **http://www.ioffe.ru/NANO2007/**

The Proceedings include extended abstracts of invited talks and contributed papers to be presented at the Symposium. By tradition this book is published before the beginning of the meeting.

The volume was composed at the Information Services and Publishing Department of St Petersburg Physics and Technology Center for Research and Education from electronic files submitted by the authors. When necessary these files were converted into the Symposium style without any text revisions. Only minor technical corrections were made by the composers.

Design and layout: N. Vsesvetskii
Desk editor: L. Solovyova

Information Services and Publishing Department
St Petersburg Physics and Technology Center for Research and Education of RAS
8, bld. 3 Khlopina, St Petersburg 195220, Russia
Phones: (812) 534-58-58
Fax: (812) 534-58-50
E-mail: nano@mail.ioffe.ru

Printed in Russian Federation

The Symposium is held under the auspices of
the Russian Academy of Sciences

Organizers

Institute of Semiconductor Physics Siberian Branch of RAS
Scientific Engineering Center for Microelectronics at the Ioffe Institute
Ioffe Physico-Technical Institute
St Petersburg Physics and Technology Center for Research and Education of RAS

in association with

the institutions of the Russian Academy of Sciences
Siberian Branch of Russian Academy of Sciences
Division of Physical Sciences
St Petersburg Scientific Center

Acknowledgments

The Organizers gratefully acknowledge the following
for their contribution to the success of the Symposium:

Russian Academy of Sciences

Russian Foundation for Basic Research

AIXTRON AG, Germany

Intel Corporation, USA

RIBER, France

NT-MDT, Russia

Intech Electronics, Russia

RTI Ltd. Cryomagnetic Systems, Russia

ATC—Semiconductor Technologies & Equipment, Russia

Location and Date

Symposium is held in Novosibirsk, June 25–29, 2007.

Advisory Committee

G. Abstreiter (*Germany*)
Zh. Alferov (*Russia*)
Y. Arakawa (*Japan*)
A. Aseev (*Russia*)
G. Bastard (*France*)
D. Bimberg (*Germany*)
L. Eaves (*United Kingdom*)
L. Esaki (*Japan*)
S. Gaponov (*Russia*)
E. Gornik (*Austria*)
Yu. Gulyaev (*Russia*)
N. Holonyak Jr. (*USA*)
L. Keldysh (*Russia*)
G. Landwehr (*Germany*)
J. Merz (*USA*)
M. Shur (*USA*)
M. Skolnick (*United Kingdom*)
R. Suris (*Russia*)

Programme Committee

R. Suris, Chair (*St Petersburg, Russia*)
V. Evtikhiev, Secretary (*St Petersburg, Russia*)
A. Andronov (*Nizhny Novgorod, Russia*)
N. Bert (*St Petersburg, Russia*)
C. Chang-Hasnain (*Berkeley, USA*)
A. Chaplik (*Novosibirsk, Russia*)
V. Dneprovskii (*Moscow, Russia*)
V. Dubrovskii (*St Petersburg, Russia*)
A. Gippius (*Moscow, Russia*)
S. Gurevich (*St Petersburg, Russia*)
S. Ivanov (*St Petersburg, Russia*)
P. Kop'ev (*St Petersburg, Russia*)
Z. Krasil'nik (*Nizhny Novgorod, Russia*)
V. Kulakovskii (*Chernogolovka, Russia*)
M. Kupriyanov (*Moscow, Russia*)
X. Marie (*Toulouse, France*)
I. Merkulov (*St Petersburg, Russia*)
V. Panov (*Moscow, Russia*)
O. Pchelyakov (*Novosibirsk, Russia*)
E. Poltoratskii (*Moscow, Russia*)
H. Sakaki (*Tokyo, Japan*)
N. Sibel'din (*Moscow, Russia*)
M. Stutzmann (*Garching, Germany*)
V. Timofeev (*Chernogolovka, Russia*)
V. Volkov (*Moscow, Russia*)
L. Vorobjev (*St Petersburg, Russia*)

Organizing Committee

A. Aseev, Chair (*Institute of Semiconductor Physics*)
A. Dvurechenskii (*Institute of Semiconductor Physics*)
M. Mizerov (*Center for Microelectronics*)
E. Efremov (*Institute of Semiconductor Physics*)
L. Il'ina (*Institute of Semiconductor Physics*)
A. Latyshev (*Institute of Semiconductor Physics*)
O. Pchelyakov (*Institute of Semiconductor Physics*)
N. Sibeldin (*Lebedev Physical Institute*)
E. Solovyova (*Ioffe Physico-Technical Institute*)
V. Zayats (*Division of Physical Sciences*)

Award Committee

Zh. Alferov, Chair (*Russia*)
A. Aseev (*Russia*)
L. Asryan (*USA*)
D. Bimberg (*Germany*)
D. Heitmann (*Germany*)
W. Knap (*France*)
J. Merz (*USA*)
I. Neizvestnyi (*Russia*)
J.-C. Portal (*France*)
Yu. Požela (*Lithuania*)
F. Schulte (*Germany*)
R. Suris (*Russia*)

Contents

Metal Nanostructures

Microcavity and Photonic Crystals

Nanostructure Characterization

Nanostructure Devices

Nanostructures and Life Sciences

Nanostructure Technology

Quantum Wells and Quantum Dots

Si-Ge Based Nanostructures

Spin Related Phenomena in Nanostructures

Transport in Nanostructures

Tunnelling Phenomena

2D Electron Gas

Wide Band Gap Nanostructures

Closing Plenary Session

Author Index

Unprinted Papers

The papers listed below are included in the Symposium Programme, but not printed in the Proceedings, as the authors had not submitted electronic files in due time.

AIXTRON Young Scientist Award

In 1999, the Symposium Programme Committee and the Board of AIXTRON AG (Germany) established a special award to honour a young scientist who will present at the Symposium the best paper in the field of solid state nanostructures. The award comprises a diploma and since 2004 a $1000 reward sponsored by AIXTRON.

The AIXTRON Young Scientist Award recipients are:

1999 **Alexey R. Kovsh**, Ioffe Institute, St Petersburg, Russia
2000 **Thomas Gruber**, Physikalisches Institut, Universität Würzburg, Würzburg, Germany
2001 **Ivan Shorubalko**, Department of Solid State Physics, Lund University, Lund, Sweden
2002 **Scott Kennedy**, Department of Electrical and Computer Engineering, University of Alberta, Edmonton, Canada
2003 **Sergey A. Tarasenko**, Ioffe Institute, St Petersburg, Russia
2004 **Ivan A. Dmitriev**, Ioffe Institute, St Petersburg, Russia
2005 **Matthias Kuntz**, Institut für Festkörperphysik, Technische Universität Berlin, Germany
2006 **Dmitry S. Sizov**, Ioffe Institute, St Petersburg, Russia

Dr. D. Sizov
became the recipient of AIXTRON Award for the presentation of the paper:

Nonequilibrium carrier statistics in deep InGaN quantum dots

Co-author: *W. V. Lundin, E. E. Zavarin, V. S. Sizov, A. F. Tsatsul'nikov, A. M. Mintairov, R. A. Suris, N. N. Ledentsov and J. Merz* .

15th Int. Symp. "Nanostructures: Physics and Technology"
Novosibirsk, Russia, June 25–29, 2007

Effect of incoherent scattering on dynamics of stimulated polariton–polariton scattering in planar GaAs microcavities

A. A. Shchekin, A. A. Demenev, A. V. Larionov and V. D. Kulakovskii
Solid State Physics Institute, RAS, Chernogolovka, 142432, Russia

Abstract. Effect of an additional above band gap cw excitation on dynamics of the cavity transmission and photoluminescence has been investigated for GaAs planar microcavities (MCs) excited into the low polariton (LP) branch near an inflection point of its dispersion. It was found that a weak (10 W/cm^2) cw excitation with a HeNe laser leads to a well pronounced acceleration of the development of the stimulated parametric polariton scattering and a strong, more than 20%, lowering of its threshold ($\sim$ 7 kW/cm^2 under the only resonant excitation). Thus an incoherent scattering of LPs with photoexcited carriers and excitons has a strong influence on a condensation in highly excited system of LPs and should be taken into account for a quantitative description of the stimulated parametric polariton scattering.

Introduction

Quasi 2D excitonic polaritons in a semiconductor microcavity (MC) have attracted the attention just after a pioneering work by Weisbuch *et al* [1]. A lot of exciting physics has been established connected to bosonic nature of polaritons and their unique dispersion with an extremely small effective mass. One of the most striking features is a giant polariton–polariton scattering under the excitation at wavevector $\mathbf{k}_p$ close to the inflection point of the low polariton (LP) branch that has an unusually low threshold [2,3]. It has been found that the scattering does not follow the key prediction of a standard four wave mixing (FWM) theory: the signal and idler appear always at $\mathbf{k} = 0$ and $2\mathbf{k}_p$, respectively, and locate above the LP dispersion curve. Such a behavior was ascribed to a competition between two instabilities, namely, bistability of the pumped polariton mode response and multiple polariton–polariton scatterings developing just after the bistable transition [4,6]. To take these effects into account Gippius *et al* [5] have suggested the model considering the coupling of the electric field on the QW $\mathcal{E}_{\mathrm{QW}}(k,t)$ and exciton polarization in the QW $\mathcal{P}(k,t)$ in the active range of the MC. The model allows for the only LP-LP scatterings in the system and neglects any scatterings with phonons, high excitons and free carriers.

The calculations have shown that the exciton-exciton interactions cause the renormalization in the LP energies and result in an abrupt jump of the inner field $\mathcal{E}_{\mathrm{QW}}$ at the excitation slightly above the LP mode energy. It occurs when the excitation density exceeds a threshold one for a bistable transition in the LP system. The jump in $\mathcal{E}_{\mathrm{QW}}$, in its turn, causes a hard excitation of LP-LP scattering that leads first to the high occupation of LP states in a wide range of $\mathbf{k}$ near the LP band bottom. According to this model, the scattering into the modes with $\mathbf{k} = 0$ and $2\mathbf{k}_p$ develops with the time as a result of a selforganization in a highly excited LP system. Comparison of this model to the experiment has shown that the model describes qualitatively the main feature of the stimulated parametric scattering in the LP system, namely, the constancy of the signal and idler $\mathbf{k}$-vectors ($\mathbf{k}_{\mathrm{signal}} = 0$ and $\mathbf{k}_{\mathrm{idler}} = 2\mathbf{k}_p$) and their location above the LP dispersion curve for a wide range of excitation wavevectors and frequencies [7]. Nevertheless, there is a problem in the description of the threshold excitation density for the stimulated LP scattering.

So far as the considered model does not take into account any incoherent scatterings of LPs it is natural to suppose that these scatterings have a marked influence on the selforganization process in the highly excited LP system. The present paper is devoted to the investigation of incoherent scatterings with free carriers on the dynamics of the stimulated polariton–polariton scattering in GaAs based planar MC with InGaAs QWs in the active range.

1. Experimental

We have investigated a microcavity structure grown by a metal organic vapor phase epitaxy. It consisted of two Bragg reflectors with 17(20) repeats of $\lambda/4$ $Al_{0.13}$ $Ga_{0.87}$ As/AlAs layers in the top(rear) mirrors and $3/2\lambda$ active layer between them. The active layer contained six 10-nm thick $In_{0.06}Ga_{0.94}As$/GaAs QWs. Rabi splitting of coupled exciton — cavity modes was $\Omega \approx 6$ meV. The sample was placed into the optical cryostat at temperature of 7 K. It was resonantly excited by the laser pulse with the duration 1 ns, linewidth 1 meV and the repetition rate 5 kHz. The output mean power could be varied from 0 to 10 μW.

The pump beam excited the sample under an angle 14° relative to the cavity normal (lateral wavevector $k = 1.96 \times 10^4$ cm^{-1}). Both the kinetics of the transmission signal and the time dependence of MC luminescence at $\mathbf{k} = 0$ from the opposite to the pump side of the cavity have been measured. The signal from the microcavity was detected by the streak camera with spectral resolution 0.28 meV and time resolution 100 ps. To study the influence of incoherent processes we have organized additional excitation of the sample by a cw He-Ne laser with the power 1 mW. Focusing was produced onto the spot on the sample, having a diameter 100 μm. The detuning between photon and exciton modes of the cavity was $\delta = -2$ meV.

2. Experimental results

Figure 1(a) illustrates the effect of a weak above band gap excitation on the stimulated parametric scattering of excitonic polaritons in a planar MC. It shows a comparison of time dynamics of the MC luminescence at $\mathbf{k} = 0$ recorded at the same strong resonant pulse excitation into the inflection point of the LP dispersion with and without extra above band gap excitation with a weak cw HeNe laser.

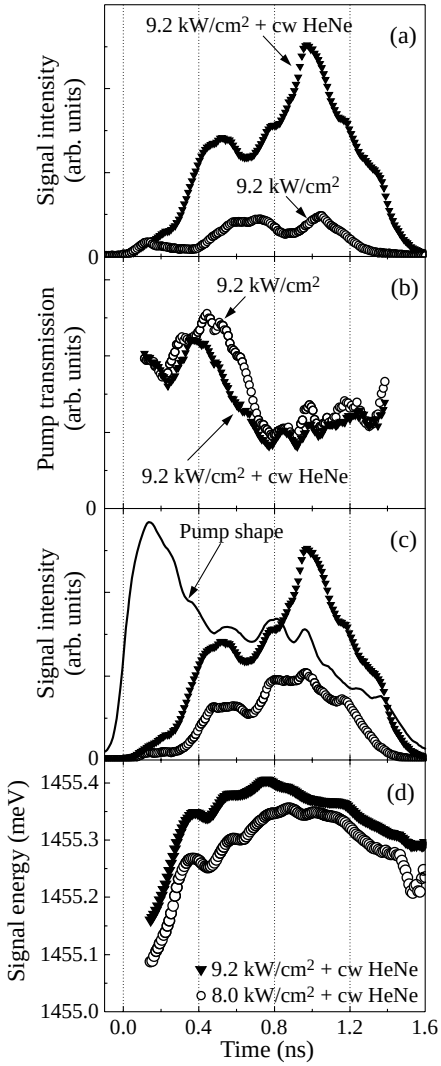

Fig. 1. Time profiles of: (a), (b) the luminescence at $\mathbf{k} = 0$ and the pump transmission for resonant excitation density of 9.2 kW/cm^2 with ▼ and without ○ extra cw HeNe excitation, respectively; (c), (d) — the luminescence at $\mathbf{k} = 0$ and its spectral position for two resonant excitation densities ○ 8.0 kW/cm^2 and ▼ 9.2 kW/cm^2 with the additional excitation by HeNe laser. Thin line shows the time profile of the resonant laser pulse.

The density of the resonant excitation is 9.2 kW/cm^2 whereas that of the HeNe laser is 3 orders of magnitude smaller. Nevertheless one can see a dramatic effect of the above band gap excitation. The resultant luminescence signal in the presence of HeNe excitation is several times bigger and it develops, evidently, about 100 ps earlier than that with only pulsed excitation.

Figure 1(b) displays analogous time profiles of the pulse laser transmission T reflecting a magnitude of the electric field on the quantum well, $T \sim |\mathcal{E}_{\rm QW}|^2$. An abrupt increase of T at $t_d \sim 0.3$ ns reflects the jump of $\mathcal{E}_{\rm QW}$ when it reaches the bistability threshold connected with nonlinearity of the excitonic oscillator [6]. The decrease of the inner field at ~ 0.5 ns for the case of the only pulse excitation is due to a FWM instability with respect to LP-LP scattering [6,8,9] resulting in the appearance of a strong stimulated parametric scattering (c.f. Fig. 1(a)) One can see that with extra cw HeNe excitation the fall of the transmission caused by the LP-LP scatterings occurs about 100 ps earlier in accordance with an earlier appearance of the scattering signal in Fig. 1(a).

Figures 1(c), (d) compare time profiles of the signal at $\mathbf{k} = 0$ and its spectral position for two resonant excitation densities with extra excitation by HeNe laser. One can see a big (more than 300 ps) time delay of the luminescence relative to the laser pulse that can be caused by mentioned above processes of selforganization in LP system [5,6,8]. The magnitude of the time delay decreases with the increasing of excitation density. It means the acceleration of the selforganization in LP system. Also one can see a typical "blue shift" of the signal due to the renormalization of the LPs energy in a highly excited polariton system [5,8]. This shift increases with excitation density and its time dynamics is strongly constrained with that of the signal intensity.

So incoherent scatterings of LPs generated by the pulse excitation with nonequilibrium phonons, high excitons, free carriers generated by additional HeNe pumping strongly affect the process of their condensation onto the LP band bottom. The most striking feature is that the instantaneous power density of the HeNe laser causing the incoherent processes is 10^{-3} times smaller than that of the pulsed pumping. Thus, even very small excitation in the system of phonons and free carriers could strongly influence on the dynamics of polariton–polariton scattering in MC.

3. Conclusions

In present paper we have explored time dynamics of polariton–polariton scattering in MC with extra nonresonant above band gap excitation. The dynamics of the luminescence at $\mathbf{k} = 0$ and transmission is qualitatively explained in framework of the model [5,8]. The comparison of the two regimes of polariton–polariton scattering (with extra HeNe pumping and without it) have shown that even a small excitation in the system of phonons, high excitons and free carriers affect dramatically the dynamics of polariton–polariton scattering. We suggest that incoherent processes can accelerate the processes of LP condensation onto the LP band bottom.

Acknowledgements

We thank S. S. Gavrilov, N. A. Gippius, S. G. Tikhodeev for valuable remarks and fruitful discussions, M. S. Skolnick for rendered samples, and M. N. Makhonin for help in the experiment and discussions.

References

[1] C. Weisbuch *et al*, *Phys. Rev. Lett.* **69**, 3314 (1992).
[2] P. G. Savvidis *et al*, *Phys. Rev. Lett.* **84**, 1547 (2000).
[3] C. Ciuti *et al*, *Phys. Rev. B* **62**, R4825 (2000).
[4] V. D. Kulakovskii *et al*, *Nanotechnology* **12**, 475 (2001).
[5] N. A. Gippius *et al*, *Europhys Lett.* **67**, 997 (2004).
[6] N. A. Gippius *et al*, *UFN* **175** (3), 327 (2005).
[7] V. D. Kulakovskii *et al*, *UFN* **175** (3), 334 (2005).
[8] S. S. Gavrilov *et al*, to be published in *JETP* (2007).
[9] A. A. Demenev *et al*, *Nanotechnology* (2007).

15th Int. Symp. "Nanostructures: Physics and Technology"
Novosibirsk, Russia, June 25–29, 2007

Quantum-sized excitonic states observed in photoluminescence spectra of thick GaAs layers in high magnetic fields

E. V. Ubyivovk[1,2], I. Ya. Gerlovin[1], Yu. K. Dolgikh[1], S. A. Eliseev[1], G. E. Lachinova[1], D. K. Loginov[1], V. V. Petrov[1], D. R. Yakovlev[2,3] and M. Bayer[2]

[1] Institute of Physics, St Petersburg State University, 198504, St Petersburg, Russia
[2] Fachbereich Physik, Universität Dortmund, 44221 Dortmund, Germany
[3] Ioffe Physico-Technical Institute, St Petersburg, Russia

Abstract. Photoluminescence spectra of the 330 nm thick GaAs quantum well have been investigated at magnetic field up to 9.5 T in Faraday configuration. The oscillations in the high-energy part of the spectra resulted from quantum-size effect have been found. Specific modification of oscillations in high magnetic field was observed. The obtained data are compared with theoretical and experimental results published earlier.

Introduction

Excitonic quantum size effect results in quasi-periodic oscillations appeared in reflectivity spectra of high-quality heterostructures with thick epitaxial layers of GaAs sandwiched between two AlGaAs barrier layers [1]. Energy structure and number of band parameters of those layers have been determined by the theoretical analysis of experimental spectra. The further studies have shown that the oscillations in reflectivity spectra are strongly modified at longitudinal magnetic fields (Faraday configuration). This fact has been treated as the result of strong g-factor dependence on size quantization energy [2,3].

Deficiency of reflectivity spectra formed by both of really and imaginary parts of dielectric function is the difficulty of extracting of an unambiguous information about energy structure of investigated quantized states from experimental data. Photoluminescence (PL) and photoluminescence excitation (PLE) spectra have more advantages for this application. At the same time, there is no information in literature about revealing of high-energy size-quantized excitonic states in such spectra. In this report we present the results of experimental study of PL and PLE spectra of thick quantum well (QW) GaAs in strong magnetic field.

1. Experiment and Discussion

The sample has been grown by molecular beam epitaxy on (001) GaAs substrate. Structure contains 330 nm thickness GaAs layer (QW) sandwiched by two $Al_{0.3}Ga_{0.7}As$ barrier layers. Luminescence measurements have been performed at a temperature 2 K under the linearly and circularly (σ^+ and σ^-) polarized excitation. Energy of the exciting radiation was varied by tuning a Ti:sapphire laser. Typical PL spectrum excited near the free exciton peak and measured in linear polarization is present in Fig. 1.

In the spectrum, two luminescence peaks dominate, one is at energy $E_{Dx} = 1.51314$ eV and another one at $E_x = 1.51415$ eV. We attribute peak E_x to the ground state of the heavy-hole exciton. Its intensity is smaller than that of peak E_{Dx} which we attribute to the exciton bound at an impurity. One can see the damped quasi-periodic peaks at the high-energy tail of the main excitonic peak. In the inset of Fig. 1, the part of the reflectivity spectrum of the structure in the same

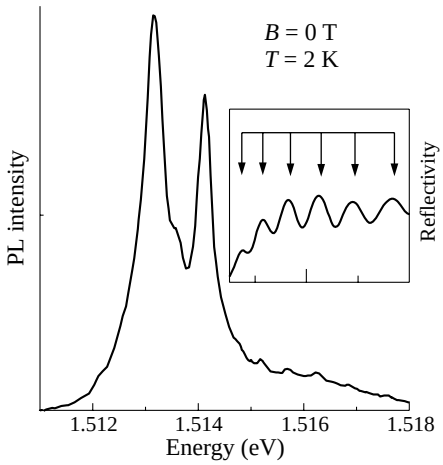

Fig. 1. PL spectrum of the $GaAs/Al_{0.3}Ga_{0.7}$ heterostructure at the linearly polarized excitation. Insert: reflectivity spectrum.

energy range is present. It is seen that the spectral positions of PL peaks well coincide with positions of the reflectivity oscillations. Because the oscillations in reflectivity spectra correspond, according to Ref. [1], to the size quantization levels, this coincidence allows us to conclude that the luminescence peaks have the same nature.

In Fig. 2, the PL spectra measured at $B = 8.5$ T in the circular and linear polarizations at the excitation energies $h\nu = 1.52466$ eV and $h\nu = 1.52891$ eV are shown. Peaks corresponding to size quantization levels are clearly seen in the PL spectrum measured under the excitation with a small energy ($h\nu = 1.52466$ eV) and disappear for the excitation energy exceeding 1.526 eV.

The reason of difference of two spectra is that the laser radiation at $h\nu = 1.52466$ eV can be absorbed directly by the exciton transition while the high-frequency excitation results in the interband absorption. In the first case, the energy relaxation follows through the excitonic size-quantized levels, and the hot luminescence from these levels can be observed. At the high-energy excitation, the electron-hole pairs are created and each carrier can independently relax to the ground state in which they bound in an exciton.

The analysis of experimental data obtained under the low-

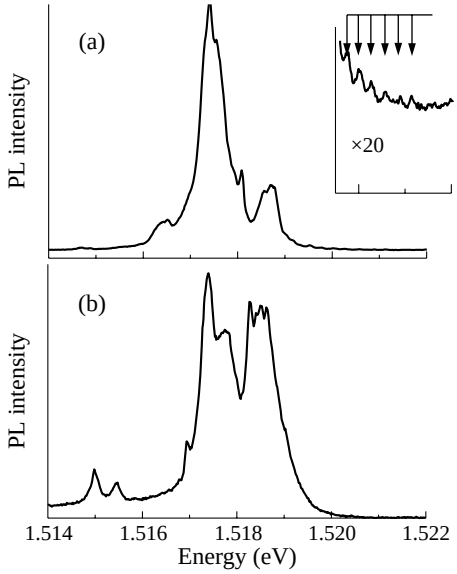

Fig. 2. PL spectra of the 330 nm GaAs layer in Faraday configuration at $B = 8.5$ T. (a) PL spectrum measured in the linear polarization at the excitation energy 1.5247 eV. Insert: the same PL spectrum with the 20-fold zoomed intensity. (b) PL spectrum measured in σ^+ polarization at the excitation energy 1.5289 eV.

energy excitation has shown that the behavior of high-energy levels of the exciton size quantization in the longitudinal magnetic field is significantly different from that of the ground state. In particular, at non-zero magnetic field, these levels run out in the high-energy side of the spectrum slower than in the spectrum measured with no magnetic field. Such behavior qualitatively correlates with that of the reflectivity spectra at high magnetic field described in Refs. [2,3].

Figure 3 shows the PL spectra measured at different angles between the magnetic field direction and the growth axis of the sample. As seen, spectral oscillations become observable at the high energy side of the spectra with the angle increase. Spectral behavior of the oscillations allows us to conclude that they are related to the size quantization of the exciton. Physical origin of the angular dependence should be further studied.

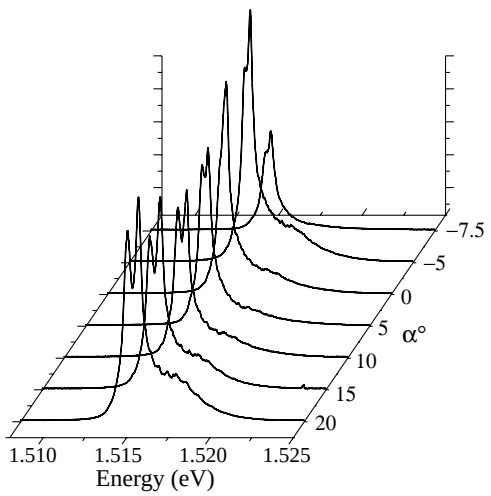

Fig. 3. Angular dependence of PL spectrum of the GaAs/$Al_{0.3}Ga_{0.7}$ heterostructure. Excitation energy $E = 1.527$ eV.

Acknowledgements

This work was supported by the BMBF "nanoquit" program, by the Deutsche Forschungsgemeinschaft through (grant 436 RUS 17/144/05), by DAAD (PKZ: A/05/56896 / Ref.: 325), by RFBR, and by ISTC (grant 2679).

References

[1] D. R. Loginov *et al*, *Fizika Tverdogo Tela* **48**, 1979 (2006).
[2] V. P. Kochereshko *et al*, *Proc. 13th NANO*, St Petersburg, 2005.
[3] J. J. Davies *et al*, *Phys. Rev. Lett.* **97**, 187403 (2006).

15th Int. Symp. "Nanostructures: Physics and Technology"
Novosibirsk, Russia, June 25–29, 2007

Magneto-optics of excitons in motion

A. Litvinov[1], D. Loginov[1], V. Kochereshko[1], R. Cox[2], L. Besombes[2], H. Mariette[2], H. Boukari [2], Yu. Efimov [3], S. Eliseev [3], Yu. Dolgikh [3], J. Davies [4], L. Smith [4] and D. Wolverson [4]

[1] Ioffe Physico-Technical Institute, St Petersburg, Russia
[2] Laboratoire de Spectrométrie Physique, Université Joseph Fourier de Grenoble, France
[3] Institute of Physics, St Petersburg State University, St Petersburg, Russia
[4] Department of Physics, University of Bath, Bath BA2 7AY, UK

Abstract. We studied the excitonic magneto-reflectivity spectra in Faraday and Voigt geometries for structures containing a wide quantum well in three cases: (a) in the case when, due to mechanical strain, the heavy exciton state was at lower energy than the light exciton, (b) when the light exciton state was lower than the heavy exciton, and (c) when the two excitons were degenerate. We found the following phenomena: (1) in Faraday geometry an effect of Motional Enhancement of the Exciton Magnetic Moment was observed both for light and heavy hole excitons; (2) in both magnetic field geometries we observed an enhancement of the exciton effective mass with increasing kinetic energy; (3) in Voigt geometry we observed a "magnetic field inversion" effect in the range of the light exciton.

Introduction

In exciton magneto-optics studies, the exciton's center of mass motion is usually neglected. This is due to, first of all, to the fact that generally only excitons with very small wave-vector $K = \frac{\omega}{c} n \propto 10^5$ cm^{-1} and small kinetic energy, or even localized exciton states (e.g. in photoluminescence spectra) participate in optical experiments. Spectroscopy of moving excitons is difficult because moving excitons can not interact with light.

The magnetic moment of the immobile exciton is determined by the sum of the hole and electron magnetic moments as well as the orbital momentum in some cases. Motion of the exciton center of mass can significantly change this, or even give rise to new magnetic properties of the exciton. The exciton center of mass motion can entangle with the internal motion and this will result in specific magnetic properties. The first experimental observations of the mutual effects of magnetic field and exciton motion was reported in classic papers [1,2]. In these papers, exciton motion perpendicular to a magnetic field leads to emergence of a quasi-electric field in the system of the exciton center of mass. Theoretical paper [3] also predicts an increase of the exciton effective mass due to its motion perpendicular to a magnetic field. The effect of magnetic field induced spatial dispersion was observed in thin CdSe and GaAs crystals [4,5]. Detailed analysis of mutual magnetic field and wave vector effects on the exciton reflectivity spectra in zinc-blende crystals were published in [6]. Recently, a new effect *"Motional Enhancement of the Exciton Magnetic Momentum"* (MEM) has been observed. This means that for the moving exciton the exciton magnetic moment (the exciton g-factor) increases as a function of its kinetic energy [7].

An excellent opportunity for studying exciton states with large kinetic energy is provided by quantum well (QW) structures. In such structures the quantized exciton states correspond to states with different kinetic energies. The higher the quantum number of the state, the higher is the kinetic energy of the exciton in this state [10].

Experimental

In the present paper we have studied reflectivity spectra from QW structures in magnetic fields in Faraday $H \parallel K \parallel [100]$ and Voigt $H \perp K \parallel [100]$ geometries. In this study we used quantum wells, but it is obvious that the observed phenomena are general and relate to bulk zinc-blende type crystals. The use of quantum wells in this research just allowed us to visualize the states with high kinetic energies.

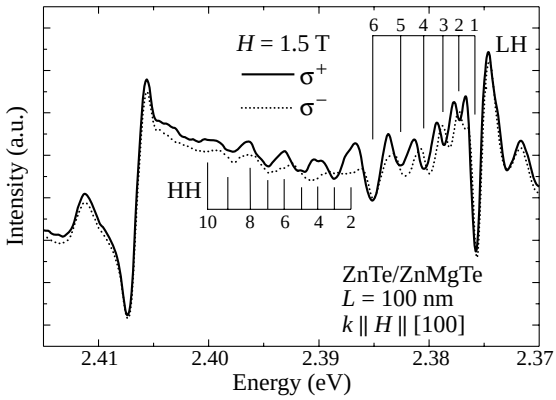

Fig. 1. Reflectivity spectra taken from a ZnTe/ZnMgTe structure with a 100 nm quantum well in 1.5 T magnetic field in Faraday geometry $K \parallel H$. The numbers indicate the sequence numbers of the light LH and heavy HH excitons center of mass quantization levels.

We studied GaAs, CdTe and ZnTe based semiconductor structures containing wide quantum wells (the well width was much bigger than the exciton Bohr radius). In such structures exciton center of mass quantization occurs [10]. A distinctive feature of these structures is that different kinds of mechanical strains, caused by barrier and well lattice constant mismatch, can be obtained. GaAs/AlGaAs-based structures are not strained and the states of light and heavy excitons are degenerate at $K = 0$. The CdTe/CdZnTe structures are strained, so that the heavy exciton forms the ground state while the light exciton state lies 10–30 meV higher in energy. In the ZnTe/ZnMgTe structures the light exciton is, on the contrary, 15 meV lower than the heavy exciton.

We observed the MEM effect in every structure in the presence of the magnetic field in Faraday geometry both for heavy hole excitons [7] and light hole excitons. Fig. 1 shows reflectivity spectra taken from ZnTe/$Zn_{0,95}Mg_{0.05}$Te quantum well structure with a 100 nm well in 1.5 T magnetic field in Faraday geometry in σ^+ and σ^- circular polarizations. The spectra

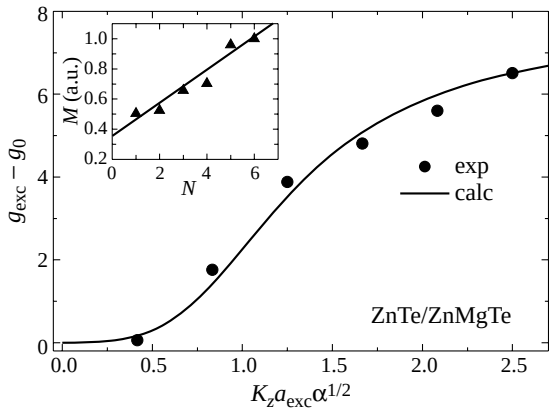

Fig. 2. Dependence of the value of light exciton magnetic momentum in ZnTe/ZnMgTe quantum well versus dimensionless wavevector K_z. Dots represent experimental values, the solid line represents calculation according to the formula:
$g_{exc} - g_0 = \frac{1}{2} G\left(1 - \frac{1}{\sqrt{1+\alpha^2 (a_{exc} K_z)^4}}\right)$ [7],
where $a_{exc} = 41$ Å is the exciton Bohr radius, $G = 15.5$, $\alpha = 2.64$ are fitting parameters. The inset shows modifications of the exciton reduced mass with increasing quantization level index.

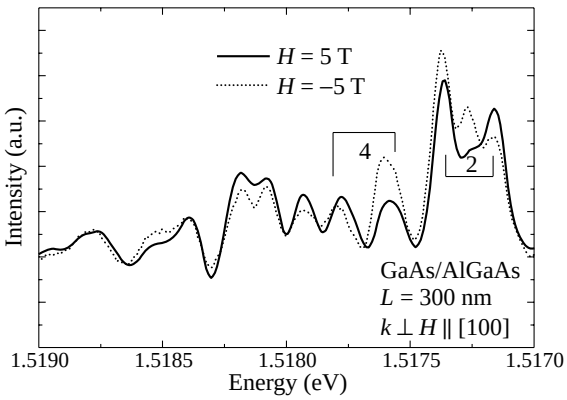

Fig. 3. Reflectivity spectra of GaAs/AlGaAs 300 nm quantum well in $+5$ T and -5 T magnetic field in Voight geometry $K \perp H$.

contain three distinctive regions: in the energy range between 2.370 and 2.385 eV, the spectral signature of light exciton quantization is observed, between 2.385 and 2.400 eV the signature of heavy exciton quantization is observed, and at 2.45 eV the energy signature of ZnMgTe barrier exciton states is observed. Index numbers N of the quantization levels are shown above the spectra. In order to determine the indexing of the quantization levels we performed a reflectivity spectrum calculation [8] with parameters taken from [9]. Considering the spectra presented, it is obvious that the magnitude of the Zeeman splitting increases with increasing quantization number, both for light and heavy exciton states. Fig. 2 shows the dependence of the light exciton magnetic moment on its wave-vector. This dependence is qualitatively similar to the previously published heavy exciton dependence [7]. However, the dependence is "steeper" for light excitons. This is reflected in the magnitude of the α constant, which turned out to be significantly larger (almost by an order of magnitude) than the typical constants for heavy excitons. This could be caused by two reasons: first by the fact that $\alpha \sim m^{-3/2}$, second by mutual influence of strain and cubic-in-wavevector terms in the valence band [11].

The inset to Fig. 2 shows the increase of the reduced mass with quantization level index. The modification of the exciton mass was determined from the value of the diamagnetic shift for each quantization level. The reasons for the exciton mass increase were analyzed in [3]. But additionally to [3] we have observed the effective mass increase both in Faraday and Voigt geometry.

In Voight geometry Fig. 3 we observed an effect of *"Magnetic field inversion"* [1,2] that consisted of a difference between reflectivity spectra for opposite magnetic field $+H$ and $-H$. This effect was strongest in the spectrum region where heavy and light excitons co-exist and was evidently caused by mixing of light and heavy excitons by the magnetic field.

Conclusion

We studied wide GaAs/AlGaAs, CdTe/CdZnTe, and ZnTe/ZnMgTe wide semiconductor quantum well structures (the well width far exceeding the exciton Bohr radius) with different magnitudes and sign of the built-in strain. In CdTe/CdZnTe-based structures, due to mechanical strain, the heavy exciton state was energetically lower than the light exciton, in ZnTe/ZnMgTe the light exciton state was lower than the heavy exciton, and in GaAs/AlGaAs the two excitons were degenerate. Reflectivity spectra were studied in magnetic field both in Faraday and Voigt geometries. We observed the following phenomena: 1) in Faraday geometry an effect of *"Motional Enhancement of the Exciton Magnetic Momentum"* was observed both for light and heavy hole excitons; 2) in both magnetic field geometries we observed an enhancement of the exciton effective mass with increase of its kinetic energy; 3) in Voigt geometry we observed a *"Magnetic field inversion"* effect in the range of the light exciton.

References

[1] D. G. Thomas and J. J. Hopfield, *Phys. Rev.* **124**, 667 (1961).
[2] E. F. Gross *et al*, *Soviet Physics. Solid State* **3**, 305 (1961).
[3] L. P. Gorkov, I. E. Dzyaloshinsky *et al*, *JETP* **53**, 717 (1967).
[4] E. L. Ivchenko *et al*, *JETP Lett* **37**, 137 (1983).
[5] O. V. Gogolin *et al*, *JETP* **87**, 1038 (1984).
[6] K. Cho *et al*, *Phys. Rev. B* **11**, 1512 (1975).
[7] J. J. Davies *et al*, *Phys. Rev. Lett.* **97**, 187403 (2006).
[8] D. K. Loginov *et al*, *FTT* **48**, 1979 (2006).
[9] *Numerical Data and Functional Relationships in Science and Technology*, edited by Landolt-Bournstein, New Series, Group III, (Springer-Verlag, Berlin, 1987).
[10] V. A. Kiselev *et al*, *Phys. Status Solidi* **72**, 161 (1975) and H. Tuffigo *et al*, *Phys. Rev. B* **37**, 4310 (1988).
[11] G. E. Pikus *et al*, *Sov. Phys. Semicond.* **22**, 185 (1988).

15th Int. Symp. "Nanostructures: Physics and Technology"
Novosibirsk, Russia, June 25–29, 2007

Binding energies of 2D laterally-confined trions

M. A. Semina, R. A. Sergeev and R. A. Suris
Ioffe Physico-Technical Institute, St Petersburg, Russia

Abstract. The localization of two-dimensional (2D) election-hole complexes on the attractive potential of an arbitrary shape is studied theoretically. General method of a simple and descriptive trial function construction for calculation of the ground state binding energy for such complexes is suggested. The limiting cases corresponding to different relations between characteristic parameters are analyzed. Binding energy of 2D trions, localized on parabolic potential is calculated in wide range of values of its parameters.

Introduction

Low-dimensional semiconductor heterostructures are widely used in different branches of semiconductor electronics, thus their optical properties are extensively studied theoretically and experimentally. The bound states of electron-hole complexes with small number of particles (excitons, X^+ and X^- trions, etc.) that determine the spectral features in the vicinity of the fundamental absorption band edge are of special interest. An in-plane localization on the quantum well heterogeneities causes a substantial effect on the bound states of electron-hole complexes [1, 2]. For example, it can lead to nearly twofold increase of the binding energy of a trion in a narrow quantum well as compared with an ideal system [2]. Usually the variational methods with up to thousands trial parameters are used for the computation of the binding energies of such systems [3]. These methods possess a very high accuracy, but because of the complexity they are not capable to give a clear qualitative description of the electron-hole complex structure and to explain its dependence on the system parameters.

In this context, it would be important to construct a trial wave function that would allow us to calculate the binding energy of an electron-hole complex localized in the plane of the QW but in a simple descriptive manner applicable to the most general case, even though with a lower accuracy. Such an approach allows us to understand the structure of the complex and to estimate its binding energy for arbitrary parameters of the localizing potential without cumbersome calculations. The developed method is applied to the case of a 2D X^+ and X^- trion localized in the parabolic potential.

1. Trial function for electron-hole complex

We consider deep narrow QWs, where the motion of charge carriers can be considered as two-dimensional. We characterize the interaction of electrons and holes with a defect by independent single-particle attractive 2D potentials of arbitrary shape $U_{\rm e}(\mathbf{r}_{\rm e})$, ($U_{\rm h}(\mathbf{r}_{\rm h})$) for electrons (holes), where $\mathbf{r}_{\rm e}$ and $\mathbf{r}_{\rm h}$ are the 2D coordinates of an electron and a hole. In this way, it is possible to describe, e.g., fluctuations in the QW width or its composition, see [4] and references therein.

The total Hamiltonian consists of the kinetic energy part and the potential energy. The latter can be represented as a sum of the Coulomb interaction terms,

$$\hat{V}_{\rm c} = \sum_{i\neq j} \frac{e^2}{\varepsilon|\mathbf{r}_{{\rm e}_i} - \mathbf{r}_{{\rm e}_j}|} + \sum_{i\neq j} \frac{e^2}{\varepsilon|\mathbf{r}_{{\rm h}_i} - \mathbf{r}_{{\rm h}_j}|} - \frac{1}{2}\sum_{i,j} \frac{e^2}{\varepsilon|\mathbf{r}_{{\rm e}_i} - \mathbf{r}_{{\rm h}_j}|}. \quad (1)$$

Here the first and the second terms are repulsion of carriers with the same charge, and the third sum is attractive interaction between carriers with opposite charges (e is the elementary charge, ε is the static dielectric constant). The contribution to the potential energy arising due to the interaction of charge carriers with the external lateral potential is:

$$\hat{V} = \hat{V}_{\rm e} + \hat{V}_{\rm h}, \quad (2)$$

$$\hat{V}_{\rm e}\left(\mathbf{r}_{{\rm e}_1},\ldots,\mathbf{r}_{{\rm e}_{N_{\rm e}}}\right) = \sum_{i=1}^{N_{\rm e}} U_{\rm e}\left(\mathbf{r}_{{\rm e}_i}\right),\ \hat{V}_{\rm h}\left(\mathbf{r}_{{\rm h}_1},\ldots,\mathbf{r}_{{\rm h}_{N_{\rm h}}}\right) = \sum_{j=1}^{N_{\rm h}} U_{\rm h}\left(\mathbf{r}_{{\rm h}_j}\right).$$

Here $N_{\rm e,h}$ is number of electrons or holes consequently.

We introduce three characteristic parameters: the typical value of the electron-hole Coulomb interaction energy $E_{\rm c}$, and the interlevel separations for non-interacting electrons (holes) $\Delta E_{\rm e}$ ($\Delta E_{\rm h}$). The ratios between these quantities define the basic structure of the complex. Let us denote

$$W_{\rm e} = \frac{\Delta E_{\rm e}}{E_{\rm c}}, \qquad W_{\rm h} = \frac{\Delta E_{\rm h}}{E_{\rm c}}. \quad (3)$$

There are only two qualitatively different limiting cases, where the Schroedinger equation can be simplified and reduced to several independent equations for a smaller number of particles. In the first case both $W_{\rm e}$, $W_{\rm h} \ll 1$ and the wavefunction reduces to the product of the center-of-mass function and the wavefunction depending on the relative coordinates. In the other limit, where $W_{\rm e} \gg 1$ or $W_{\rm h} \gg 1$, the motion of different type of the carriers can be separated. In such a case the wavefunction can be recast as a product of wavefunctions of electrons and holes.

The general form of trial function which interpolates between these limiting cases is given in [4]. In the case of trions, it can be represented as

$$\Psi(\mathbf{r}_{{\rm e}_1}, \mathbf{r}_{{\rm e}_2}, \mathbf{r}_{{\rm h}_1}) = \left[\Psi^{\rm C.M.}(\mathbf{R})\right]^{\alpha_{\rm R}} \left[\Psi^{\rm int}(\boldsymbol{\rho}_1, \boldsymbol{\rho}_2)\right]^{\alpha_\rho} \times \left[\Phi^{\rm e(h)}(\mathbf{r}_{{\rm e(h)}_1}, \mathbf{r}_{{\rm e(h)}_2})\right]^{\alpha_{\rm e(h)}} \left[\Phi^{\rm h(e)}(\mathbf{r}_{\rm h(e)})\right]^{\alpha_{\rm h(e)}}. \quad (4)$$

Here $\Psi^{\rm C.M.}(\mathbf{R})$ is the wavefunctions of trion center of mass, $\Psi^{\rm int}(\boldsymbol{\rho}_1, \boldsymbol{\rho}_2)$ is the function describing relative motion of electrons and holes in a free 2D trion, $\Phi^{\rm e(h)}(\mathbf{r}_{{\rm e(h)}_1}, \mathbf{r}_{{\rm e(h)}_2})$ is the wavefunction of the ground state of electrons (holes) in the sum of the inhomogeneity potential and the averaged effective Coulomb potential of the hole (electron) and $\Phi^{\rm h}(\mathbf{r}_{\rm h(e)})$

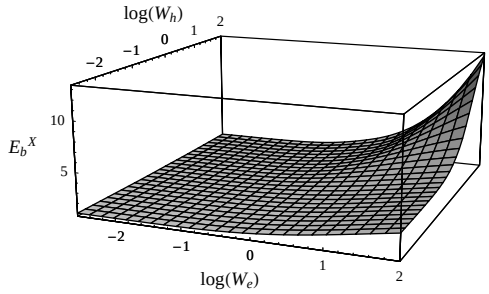

Fig. 1. Exciton binding energy as a function of electron and hole potential parameters (W_e and W_h), calculated for $\sigma = 0.3$.

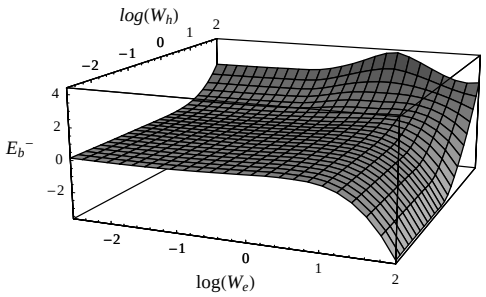

Fig. 2. X^- trion binding energy as a function of electron and hole potential parameters (W_e and W_h), calculated for $\sigma = 0.3$.

is the similar wavefunctions for the hole (electron) in case of $X^-(X^+)$ trion. Values α_R, α_ρ, α_e, α_h are the trial parameters. We note that all the wavefunctions in Eq. (4) can be found independently from the solution of the simplified Schrödinger equations with smaller number of variables.

2. Results and discussion

In order to illustrate our approach,we consider the case of X^+ and X^- trions localized by the parabolic lateral potential. We assume the co-axial parabolic attractive potentials for electrons and holes written as (the validity of our approach for the different types of potential is discussed in [4])

$$U_\mathrm{e}(\mathbf{r}_\mathrm{e}) = 4\,(1+\sigma)\,W_\mathrm{e}^2 r_\mathrm{e}^2,\; U_\mathrm{h}(\mathbf{r}_\mathrm{h}) = 4\left(1+\frac{1}{\sigma}\right) W_\mathrm{h}^2 r_\mathrm{h}^2. \quad (5)$$

Here we use the 2D Rydberg as a unit of energy and 2D exciton Bohr radius as a unit of length, $\sigma = m_\mathrm{e}/m_\mathrm{h}$ with m_e (m_h) being electron (hole) mass. In this paper we calculate the binding energy of the singlet state of the trions, so our trial function is symmetric. We assume electron to hole mass ratio being $\sigma = 0.3$.

We define the trion binding energy as a difference between the trion energy (obtained by the minimization of the total Hamiltonian) and the sum of exciton energy and the energy of extra particle (electron for X^- and hole for X^+ trion). Therefore, the knowledge of the exciton binding energy E_b^X is needed in order to calculate trion's binding energy.

Figure 1 shows the exciton binding energy as a function of W_e and W_h, calculated in [4]. One can see an increase of the binding energy with an increase of W_e and W_h due to increasing of efficiency of the electron-hole interaction [4].

Figs. 2 and 3 show the X^- (E_b^-) and X^+ (E_b^+) trions binding energies as functions of W_e and W_h. Comparison of Figs. 2 and 3 shows that for fixed W_e X^- and X^+ binding energies behave differently as the functions of W_h. In the case of X^-

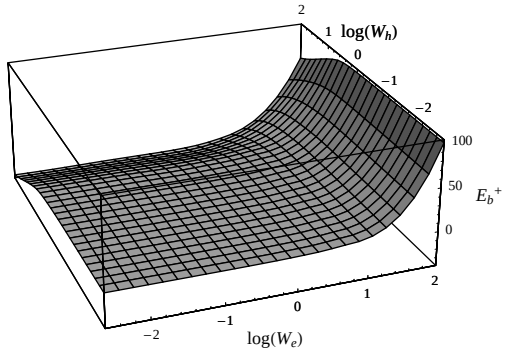

Fig. 3. X^+ trion binding energy as a function of electron and hole potential parameters (W_e and W_h), calculated for $\sigma = 0.3$.

trion the single hole becomes more localized with the increase of W_h and its attraction to the electrons becomes stronger, thus, the binding energy increases. On the other hand, for X^+ trion two holes are pressed to each other and they repel stronger. It leads to the decrease of X^+ trion binding energy. In case of weak potentials (W_e, $W_\mathrm{h} \ll 1$) binding energies of both trions tend to those of free 2D trions. It can be seen that depending on the ratio between W_e and W_h the ratio between E_b^+ and E_b^- can be different, e.g. if $W_\mathrm{e} \gg W_\mathrm{h}$, E_b^+ is larger than E_b^-; in the opposite limit $W_\mathrm{h} \gg W_\mathrm{e}$, X^- trion has a larger binding energy.

The non-monotonous dependence of the E_b^- on W_e at fixed W_h is due the fact that the X^- trion binding energy is determined by an interplay of exchange interaction and Coulomb repulsion of electrons. Increase of W_e results in increasing of the exchange interactions, while for larger W_e Coulomb repulsion dominates. There is no similar non-monotonicity in E_b^+ because of that holes are heavier than electrons.

Our calculation shows that for the certain parameter range the binding energy of a trion can be negative. It takes place for $W_\mathrm{e} \gg W_\mathrm{h}$ for the X^- trion and $W_\mathrm{e} \ll W_\mathrm{h}$ for X^+, respectively. Physically, an increase of the localizing potential for one type of carriers leads an increase of their repulsion for fixed potential for other type of carrier. Despite the fact that the binding energy for such a trion is negative (and its emission line lies above that of an exciton), all three carriers are still localized due to the confinement potential. One can surmise that in this case the triplet state has a lower energy that the singlet.

To conclude, we have applied a general formalism which allows to build a simple and physically reliable trial functions for electron-hole complexes to the problem of trion, localized on the quantum well inhomogeneity potential. The binding energies of X^+ and X^- trions were obtained in a whole range of the potential strengths for electron and hole.

Acknowledgements

The work is supported by RFBR, grant 05-02-16679, Federal Program on Support of Leading Scientific Schools and SCOPES, grant 110986. Binding energy of trions was calculated on St Petersburg branch of Interdepartmental Supercomputer Center (http://scc.ioffe.ru/).

References

[1] G. Bastard *et al*, *Phys. Rev. B* **29**, 7042 (1984).
[2] R. A. Sergeev *et al*, *Eur. Phys. J. B* **47**, 541 (2005).
[3] A. V. Filinov *et al*, *Phys. Rev. B* **70**, 035323 (2004).
[4] M. A. Semina *et al*, *Semiconductors* **40** (11), 1338 (2006).

15th Int. Symp. "Nanostructures: Physics and Technology"
Novosibirsk, Russia, June 25–29, 2007

Ground state of excitons, charged excitons and biexcitons in double quantum well structure with spatial separation of carriers

R. A. Sergeev and R. A. Suris
Ioffe Physico-Technical Institute, St Petersburg, Russia

Abstract. The ground states of exciton, X^- and X^+ trions, and biexciton in the system of two quantum wells with spatial separation of electrons and holes are studied theoretically. The simple vivid trial functions for the binding energy calculations of such spatially indirect excitonic complexes are proposed. The qualitative structure of the complexes in such a system is discussed. For the trions and the biexciton the critical values of the distance between the wells, where the corresponding complexes become unbound, are estimated. The mass ratio dependence of the binding energy of these complexes is analyzed.

Introduction

Since Lampert predicted the existence of trions in bulk semiconductors in 1958 [1], bound states of the electron-hole complexes with more than two particles attract the attention of researches. This interest has vastly risen in last few decades due to considerable progress in semiconductor heterostructure fabrication. The theoretical calculations performed in the 1980s [2] predicted a strong sensitivity of parameters of electron-hole complexes (such as transition energies and corresponding oscillator strengths) to configuration of the heterostructure, if a characteristic scale of the latter becomes comparable to Bohr radius. Thus, X^- and X^+ binding energies are up to tenfold larger in tight quantum well as against their bulk values [3]. Stochastic potential fluctuations, causing an additional localization of the complexes in plane of quantum wells, generally lead to further increasing of the binding energy [4].

Recently a considerable interest was risen to double quantum well heterostructures due to the possibility of spatial separation of the carriers [5]. Such separation decreases electron and hole wavefunction overlapping, leading to a drastic increase of their lifetimes, enabling to hold a high concentration of electron-hole plasma. That is of particular interest due to the possibility of realization of many exciton Bose-condensate [6]. Variation of the distance between QWs also gives us an additional handle to control the system parameters.

In the present paper simple variational approach is used to estimate the ground state energy dependencies of spatially indirect exciton, X^+ and X^- trions, and biexciton (X_2) versus the distance between the wells (d) and to define a range of the existence of these complexes.

1. Models and trial functions

We consider the heterostructure with spatially separated electrons and holes using an oversimplified model of two 2D quantum wells: one — for the holes, and the other — for the electrons. In order to obtain the binding energy of trions or biexciton we have to find their full energy and subtract it from the exciton energy (double exciton energy for X_2). Therefore, if we intend to calculate the trion or biexciton binding energy with reasonable accuracy, we should take their trial function based on the exciton function, transforming to the latter if the distance between the exciton and the electron/hole/second exciton tends to the infinity. The simplest trial exciton wave function with the minimum number of variational parameters, which gives plausible results for the binding energy and the shape of wave function in the whole range of the distances between the wells, is the follows [7]:

$$\Psi_X\left(a_X, \rho\right) = \exp\left(-a_X\sqrt{\rho^2 + d^2}\right). \qquad (1)$$

Here a_X is the only variational parameter, nontrivially corresponding to the length scale of the exciton wavefunction, ρ — in-plane distance between the carriers.

The X^+ trion in coupled 2D quantum wells can be represented as two heavy holes in the same quantum well bound together by an electron in adjacent one. The holes are supposed to be much heavier than the electron and considered in adiabatic approximation. The simplest electron in-plane wave function is proposed to be a symmetrical sum of two exciton-like wave functions (1) matched to each of the holes and shifted toward each other due to the polarization effect [8]:

$$\Psi_{X^+}(\boldsymbol{\rho}) = \Psi_X\left(a_{X^+}, \rho^+\right) + \Psi_X\left(a_{X^+}, \rho^-\right), \qquad (2)$$

$$\rho^{\pm} = \left|\boldsymbol{\rho} \pm \frac{1-c}{2}\mathbf{R}\right|. \qquad (3)$$

Here $\boldsymbol{\rho}$ is a 2D projection of the vector from a center of mass of the holes to the electron, $\mathbf{R}$ is a 2D vector from one hole to the other; a_{X^+} controls the scale of electron wavefunction, and c is a polarization factor. $R = |\mathbf{R}|$, a_{X^+} and c we consider as fitting parameters.

The exciton and electron bonding into X^- trion is mainly provided by an exchange interaction between the electrons and a low-distance polarization of the exciton by farther electron. The simplest trial function taking this into account can be constructed by analogy with functions (1–3) and Chandrasekhars function [9]:

$$\Psi_{X^-}\left(\boldsymbol{\rho}_1, \boldsymbol{\rho}_2\right) = \Psi_X\left(a_{X^-}, \rho_1\right)\,\Psi_X\left(b_{X^-}, \rho_2\right) + \Psi_X\left(a_{X^-}, \rho_2\right)\,\Psi_X\left(b_{X^-}, \rho_1\right)\left(1 + c\left|\boldsymbol{\rho}_1 - \boldsymbol{\rho}_2\right|\right). \qquad (4)$$

Here $\boldsymbol{\rho}_1$, $\boldsymbol{\rho}_2$ are 2D projections of the vectors between the hole and the electrons; a_{X^-}, b_{X^-} are the parameters controlling the scale of wavefunctions of adjacent and farther electrons, and c is a polarization factor. a_{X^-}, b_{X^-} and c are considered as fitting parameters.

The bond between the excitons in biexciton is provided by an exchange interaction between the electrons. As for X^+ trion, the holes are supposed to be much heavier than the electrons and considered in adiabatic approximation. By analogy with function (2–3), we can take the trial function for the electrons in biexciton as follows:

$$\Psi_{X_2}\left(\boldsymbol{\rho}_1, \boldsymbol{\rho}_2\right) = \Psi_X\left(a_{X_2}, \rho_1^+\right)\Psi_X\left(a_{X_2}, \rho_2^-\right) + \Psi_X\left(a_{X_2}, \rho_2^+\right)\Psi_X\left(a_{X_2}, \rho_1^-\right). \quad (5)$$

Here are 3 variational parameters: a_{X_2}, R and c. Parameters R and c are introduced through $\rho_{1,2}^{\pm}$ (3). The calculations of the biexciton even with the simple function (5) are quite complex. Thus, for practical reason, we took:

$$\Psi_X\left(a_X, \rho\right) = \exp\left(-a_X\rho\right) \quad \text{and}$$
$$\Psi_X\left(a_X, \rho\right) = \exp\left(-a_X\rho^2\right) \quad (6)$$

for the biexciton energy calculations and the same for subtracted double exciton energy. A reasonable agreement between the results, obtained with different functions (6), confirms the applicability of the approach. Hereinafter we settle on the results of the first function (6).

2. Results and discussion

The calculated dependencies of the binding energy versus the distance between the wells for exciton, X^- and X^+ trions, and biexciton are shown on the figure. Hereinafter we use atomic units for the energy scale (bulk exciton Bohr energy, $\mu e^4/2\varepsilon^2\hbar^2$) and the length (Bohr radius, $\hbar^2\varepsilon/\mu e^2$), where μ is a reduced in-plane mass of the electron and the hole, ε is a dielectric constant. The curves on the figure are plotted for zero electron to hole mass ratio: $\sigma = m_e/m_h = 0$.

The binding energy of all considered complexes sharply decreases with the distance between the wells due to reduction of the electron-hole attraction in comparison with the electron-electron and the hole-hole repulsions. However, the exciton is bound at any value of the distance between the wells in the absence of repulsion potentials in the system. Nevertheless, for complexes with more particles, such as X^- and X^+ trions, and biexciton, the repulsion of the same charges overpowers the attraction of opposites. Thus, an asymptotic potential between the exciton and remaining hole in X^+ trion is:

$$V_{X^+}(R) \approx \frac{1}{R^3}\left[d^2 - \frac{1}{2}\frac{1-\sigma}{1+\sigma}\left\langle\Psi_X\left|\rho^2\right|\Psi_X\right\rangle\right]. \quad (7)$$

The expression for X^- trion can be obtained from (7) by substitution $\sigma' = 1/\sigma$. At $d > 1.87$ the potential (7) becomes positive for all σ, and the bonding is provided only by short-range effects. Also, it is worth to note that for X^- trion potential (7) is positive even in the limit of a single quantum well ($d \to 0$). For biexciton the asymptotic potential between the excitons is positive at any $d > 0$ and in the first order does not depend on σ:

$$V_{X_2}(R) \approx 2\,d^2/R^3. \quad (8)$$

The potentials (7–8) grow without limit with increasing of d, and for each complex there must be a critical value of the distance d_{cr}, at which its binding energy becomes zero, and corresponding bound state disappears. The estimated values of d_{cr} are also shown on the figure. The more complicated complex is, the higher is the asymptotic repulsion, and the lower is the value of d_{cr}. It allows us to conclude that for $d > 0.5$ there are no bound electron-hole complexes with the number of particles more than three.

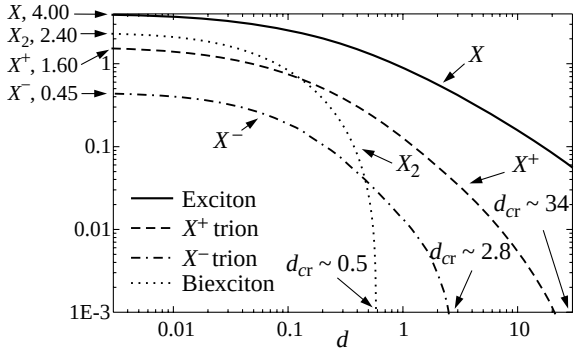

Fig. 1. Binding energies of excitonic complexes versus the distance between the wells. The bulk excitonic units are used for the energy and the distance. $m_e/m_h = 0$.

Let us finally discuss the influence of mass ratio σ on the curves shown on the figure. It is easy to show that the binding energy in reduced units does not depend on σ for the exciton, and only slowly increases with σ growth for X^- trion:

$$E_X^B(\sigma) = E_X^B(0), \quad E_{X^-}^B(\sigma) \approx E_{X^-}^B(0). \quad (9)$$

On the contrary, for X^+ trion and biexciton situation is completely different. The presence of two heavy particles introduces their zero-point oscillation energy, with very sharp dependence on σ, to the binding energy of the complex:

$$E_{X^+,X_2}^B(0) - E_{X^+,X_2}^B(\sigma) \sim \sqrt{\sigma}\,. \quad (10)$$

Thus the energy curves and the estimated values of d_{cr} for X^+ trion and biexciton should be considered as an upper bound for their real values.

To conclude, the binding energies of exciton, X^- and X^+ trions, and biexciton in double quantum well heterostructure with spatial separation of the carriers are calculated versus the distance between the wells. The critical distances, where the corresponding complexes become unbound, are estimated, and mass ratio dependence of binding energies and critical distances is discussed.

Acknowledgements

This work is supported by RFBR, grant 05-02-16679, Federal Program on Support of Leading Scientific Schools and SCOPES, grant 110986.

References

[1] M. A. Lampert, *Phys. Rev. Lett.* **1**, 450 (1958).
[2] B. Stebe *et al*, *Superlatt. Microstruct.* **5**, 545 (1989).
[3] R. A. Sergeev *et al*, *Eur. Phys. J.* **47**, 541 (2005).
[4] M. A. Semina *et al*, *Proc. of 15th Nanostructures* (2007).
[5] V. B. Timofeev *et al*, *Phys. Rev. B* **60**, 8897 (1999).
[6] O. L. Berman *et al*, *Phys. Rev. B* **73**, 235352 (2006).
[7] R. A. Sergeev *et al*, *NATO Sc. Series II* **119**, 279 (2003).
[8] R. A. Sergeev *et al*, *Semiconductors* **37**, 1205 (2003).
[9] S. Chandrasekhar, *Astrophys. J.* **100**, 176 (1944).

15th Int. Symp. "Nanostructures: Physics and Technology"
Novosibirsk, Russia, June 25–29, 2007

Novel terahertz devices based on carbon nanotubes

O. V. Kibis[1], M. Rosenau da Costa[2] and *M. E. Portnoi*[3]

[1] Dept. of Applied and Theoretical Physics, Novosibirsk State Technical University, Novosibirsk 630092, Russia
[2] International Center for Condensed Matter Physics, University of Brasilia, 70904-970 Brasilia DF, Brazil
[3] School of Physics, University of Exeter, Exeter EX4 4QL, United Kingdom

Abstract. We propose and justify two schemes utilizing the unique electronic properties of carbon nanotubes for novel THz applications including tunable THz generation by hot electrons in quasi-metallic nanotubes and THz radiation detection by armchair nanotubes in strong magnetic fields.

Creating compact reliable sources and detectors of terahertz (THz) radiation is one of the most formidable tasks of the contemporary applied physics [1]. One of the latest trends in THz technology [2] is to use carbon nanotubes — cylindrical molecules with nanometer diameter and micrometer length [3] — as building blocks of novel high-frequency devices. Below we discuss several novel schemes to utilize physical properties of single-wall carbon nanotubes (SWNTs) for generation and detection of THz radiation.

THz emitters

The first proposed scheme of THz generation is based on the electric-field induced heating of electron gas resulting in the inversion of population of optically active states, with the energy difference within the THz spectrum range. The electron energy spectrum of metallic SWNTs, $\varepsilon(k)$, linearly depends on the electron wave vector k close to the Fermi energy [3]. In the Fig. 1 the zero of energy is defined as the Fermi energy position in the absence of an external field.

When the voltage is applied along the SWNT axis, the electron distribution is shifted in the way shown by the heavy lines in Fig. 1(a) corresponding to the filled electron states in the presence of the applied voltage. It results in the inversion of population and, correspondingly, in optical transitions between filled states in the conduction band and empty states in the valence band (Fig. 1(b)). It is well-known that the major scattering mechanism in SWNTs is due to electron-phonon interaction [3].

Since the scattering processes erode the inversion of electron population, an optimal condition for observing the discussed optical transitions takes place when the length of the SWNT $L < l_{ac}$, where $l_{ac} \approx 2.4\ \mu$m is the electron mean-free path for acoustic phonon scattering. Below we consider such short SWNTs only. If the electron heating energy $\Delta\varepsilon$ is less than the value $\hbar\Omega \approx 0.16$ eV, at which the fast emission of

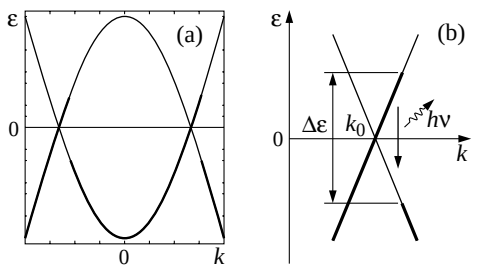

Fig. 1. (a) The filling of electron states (heavy lines) in the first Brillouin zone of SWNT in the presence of the bias voltage; (b) The scheme of electron radiation transitions resulting in terahertz emission from SWNT.

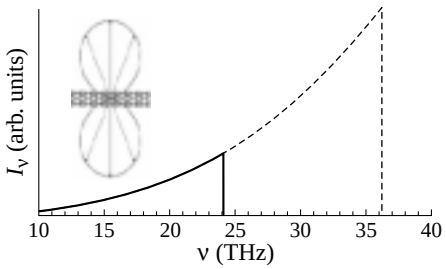

Fig. 2. The spectral density of spontaneous emission as a function of frequency for two values of applied voltage: solid line for $V = 0.1$ V; dashed line for $V = 0.15$ V. The inset shows the directional radiation pattern of the THz emission with respect to the nanotube axis.

high-energy optical/zone-edge phonons begins, the electronic transport is ballistic and $\Delta\varepsilon = eV$, where V is the potential difference between the SWNT's ends. At higher applied voltages, $V \geq \hbar\Omega/e$, the heating energy is $\Delta\varepsilon \approx \hbar\Omega$. The heating results in the spontaneous photon emission with the peak frequency $\nu \approx \Delta\varepsilon/h$ controlled by applied voltage and restricted by the SWNT optical/zone-edge phonon energy corresponding to the frequency of about 40 THz. Let us select a SWNT with the crystal structure most suitable for observation of the discussed effect. Firstly, the required nanotube should have metallic conductivity and, secondly, the optical transitions between the lowest conduction subband and the top valence subband should be allowed. It is well-known that he crystal structure of SWNTs is described by two integers (n, m), which completely define their physical properties [3]. The SWNTs with true metallic energy band structure, for which the energy gap is absent for any SWNT radius, are the armchair (n, n) SWNTs only [4]. However, for armchair SWNTs the optical transitions between the lowest conduction and top valence subbands are forbidden [5]. So we propose to use for the observation of THz generation the so-called quasi-metallic (n, m) SWNTs with $n - m = 3p$, where p is an integer. These nanotubes, which are gapless within the frame of a simple zone folding model of the π-electron graphene spectrum [3], are in fact narrow gap semiconductors due to curvature effects. However, their band gap is decreasing rapidly with increasing the nanotube radius [4]. Therefore for large values of R this gap can be neglected even in the case of moderate applied voltages due to the Zener tunneling of electrons across the gap. For example, for a zigzag (30,0) SWNT the gap is $\varepsilon_g \approx 6$ meV and the Zener breakdown takes place for the electric field $E \sim 10^{-1}$ V/μm. Since almost the whole voltage drop in the ballistic regime occurs within the few-nanometer regions near the contacts, a typical bias voltage of 0.1 V corresponds to an electric field, which is more than sufficient to achieve a complete breakdown. In

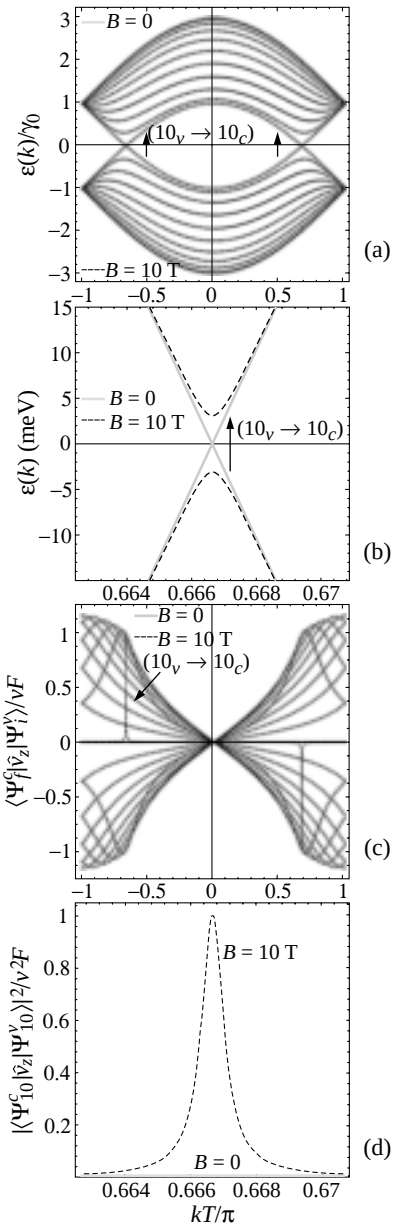

Fig. 3. (a) Band structure of a (10,10) SWNT, with and without an external magnetic field along the nanotube axis; (b) Detailed view of the gap, which is opened between the top valence subband and the lowest conduction subband in an external field $B = 10$ T; (c) The change in the dipole optical transitions matrix elements, for the light polarized along the SWNT axis, due to the introduction of the external magnetic field. The only appreciable change is in the appearance of a high narrow peak associated with the transition $(10v \rightarrow 10c)$, which is not allowed in the absence of the magnetic field; (d) Dependence of the squared dipole matrix element for the transition $(10v \rightarrow 10c)$ on the 1D wave vector k, with and without an external magnetic field.

Fig. 2 the spectral density of emission from the quasi-metallic SWNTs is shown for two values of the bias voltage. It is clearly seen that the maximum of the spectral density of emission has strong voltage dependence and lies in the THz frequency range for experimentally attainable voltages. The directional radiation pattern, shown in the inset of Fig. 2, reflects the fact that the emission of light polarized normally to the nanotube axis is forbidden by the selection rules for the optical transitions between the lowest conduction subband and the top valence subband. The discussed effect can be used for creating a THz source with the frequency controlled by the applied voltage.

THz detectors

The problem of detecting THz radiation is known to be at least as challenging as creating reliable THz sources. Our proposal of a novel detector is based on several features of the truly gapless (armchair) SWNTs shown in Fig. 3. The main property to be utilized is the opening of the gap in these SWNTs in a magnetic field along the nanotube axis [3]. For a (10, 10) SWNT this gap is approximately 1 THz in the field of 6 T. The gap grows linearly with increasing both magnetic field and the nanotube radius. It can be shown that the same magnetic field also allows dipole optical transitions between the top valence subband and the lowest conduction subband, which are strictly forbidden in armchair SWNTs without the field [5]. The electronic (hole) energy spectrum near the bottom (top) of the gap produced by magnetic field is parabolic as a function of a carrier momentum along the nanotube axis. This dispersion results in the van-Hove singularity in the reduced density of states, which in turn leads to a very sharp absorption maximum near the band edge and, correspondingly, to a very high sensitivity of the photocurrent to the photon frequency. Notably, the same effect can be used for the generation of a very narrow emission line having the peak frequency tunable by the applied magnetic field. A population inversion can be achieved, for example, by optical pumping with the light polarized normally to the nanotube axis.

Conclusion

We have demonstrated that a quasi-metallic carbon nanotube can emit the THz radiation when the potential difference is applied to its ends. The typical required voltages and nanotube parameters are similar to those available in the state-of-the-art transport experiments. The maximum of the spectral density of emission is shown to have the strong voltage dependence, which is universal for all quasi-metallic carbon nanotubes in the ballistic regime. Therefore, the discussed effect can be used for creating a THz source with the frequency controlled by the applied voltage. Appropriately arranged arrays of the nanotubes should be considered as promising candidates for active elements of amplifiers and generators of the coherent THz radiation. Finally, we have discussed the feasibility of using the effect of the magnetic field, which opens the energy gaps and allows optical transitions in armchair nanotubes, for tunable THz detectors and emitters.

Acknowledgements

This work is supported by the INTAS Foundation (Grants 03-50-4409 and 05-1000008-7801), the Royal Society (UK), the Russian Foundation for Basic Research (Grants 06-02-16005 and 06-02-81012), the Russian Ministry for Education and Science (Grant RNP.2.1.1.1604), and MCT and FINEP (Brazil).

References

[1] B. Ferguson and X. C. Zhang, *Nature Materials* **1**, 26 (2002).
[2] D. Dragoman and M. Dragoman, *Prog. Quantum Electronics* **28**, 1 (2004).
[3] R. Saito, G. Dresselhaus and M. S. Dresselhaus, *Physical Properties of Carbon Nanotubes*, (London: Imperial College Press), 1998.
[4] C. L. Kane and E. J. Mele, *Phys. Rev. Lett.* **78**, 1932 (1997).
[5] I. Milošević, *et al*, *Phys. Rev. B* **67**, 165418 (2003).

15th Int. Symp. "Nanostructures: Physics and Technology"
Novosibirsk, Russia, June 25–29, 2007

Amplification and generation of THz radiation in semiconductor superlattice devices: Progress in theory

K. N. Alekseev[1], T. Hyart[1], A. V. Shorokhov[2], N. V. Alexeeva[1], J. Isohätälä[1] and F. V. Kusmartsev[3]

[1] Department of Physical Sciences, FI-90014 University of Oulu, Finland
[2] Institute of Physics and Chemistry, Mordovian State University, 430000 Saransk, Russia
[3] Department of Physics, Loughborough University, Loughborough, LE11 3TU, UK

Abstract. We consider a feasibility of amplification and generation of THz radiation in semiconductor superlattices in the absence of space-charge instability. We mainly focus on the physical principles and basic schemes of parametric amplification and generation in superlattices.

There exists a strong demand for miniature, coherent, monochromatic, solid-state, room temperature operating sources of THz radiation. Currently there are two main directions in this active area of research: Quantum cascade lasers [1] and frequency multipliers [2]. In spite of great progress in the development of these two types of coherent THz sources, both of them have some fundamental limitation in their operation. For example, it is very difficult to establish a population inversion at room temperature in quantum cascade lasers for frequencies below 2 THz [3]. On the other hand, it is still unclear how to realize an intermediate amplification of (sub-)THz field in the chain of multipliers. Development of a reliable THz amplifier is important but very difficult task.

Semiconductor superlattices, operating in the miniband transport regime, are interesting electronic devices demonstrating properties of both nonlinear [4] and active media [5]. Superlattice devices can potentially be a supplement and alternative to the quantum cascade lasers and "traditional" frequency mixers because they can in principle provide a reasonable THz gain at room temperature [6] (superlattice Bloch oscillator [5, 6]) and amplify a THz signal in the presence of additional ac pump [7, 8]. The main obstacle in an experimental observation of these interesting effects is a formation of high-field electric domains inside superlattice [9].

Here we briefly review the progress in a resolution of main dilemma in the realization of THz superlattice devices: Finding operational conditions which allow simultaneously to achieve gain at high frequencies and to avoid destructive space-charge instabilities [10]. We consider devices with dc bias (Bloch amplifier/oscillator) and with ac pump (parametric amplifier/generator). For the case of Bloch oscillator we are extending and developing a recent suggestion for the generalized Limited Space-Charge Accumulation scheme [11]. For the case of superlattice with microwave or terahertz pump, we investigate an effective frequency conversion and a parametric amplification in domainsless mode of operation. Our report is mainly based on the original results [12–16], with particular focus on recent findings [14, 15].

Acknowledgements

This work was partially supported by Academy of Finland (grant 109758), Emil Aaltonen Foundation, Grant of President for Russian Young Scientists (MK-4804.2006.2) and AQDJJ Programme of ESF.

References

[1] R. Köhler, A. Tredicucci, F. Beltram, H. E. Beere, E. H. Linfield, A. G. Davies, D. A. Ritchie, R. C. Iotti and F. Rossi, *Nature* **417**, 156 (2002).

[2] T. W. Crowe, W. L. Bishop and D. W. Porterfield, *IEEE J. Solid-State Circuits* **40**, 2104 (2005).

[3] J. M. Chamberlain, *Phil. Trans. Roy. Soc. London A* **362**, 199 (2004).

[4] R. Tsu and L. Esaki, *Appl. Phys. Lett* **19**, 246 (1971).

[5] L. Esaki and R. Tsu, *IBM J. Res. Dev.* **14**, 61 (1970).

[6] S. A. Ktitorov, G. S. Simin and V. Ya. Sindalovskii, *Sov. Phys. Solid State* **13**, 1872 (1972).

[7] V. V. Pavlovich, *Sov. Phys. Solid State* **19**, 54 (1977).

[8] L. K. Orlov and Yu. A. Romanov, *Sov. Phys. Solid State* **19**, 421 (1977).

[9] P. G. Savvidis, B. Kolasa, G. Lee and S. J. Allen, *Phys. Rev. Lett.* **92**, 196802 (2004).

[10] K. N. Alekseev, *Proc. 12th International Conference on Terahertz Electronics (Karlsruhe, Germany, 2004)*, edited by M. Thumm and W. Wiesbeck, p. 163, 2004. Online IEEE: doi: 10.1109/ICIMW.2004.1422004

[11] H. Kroemer, *Eprint cond-mat/0009311*.

[12] K. N. Alekseev, E. H. Cannon, J. C. McKinney, F. V. Kusmartsev and D. K. Cambell, *Phys. Rev. Lett.* **80**, 2669 (1998).

[13] K. N. Alekseev, M. V. Gorkunov, N. V. Demarina, T. Hyart, N. V. Alexeeva and A. V. Shorokhov, *Europhys. Lett.* **73**, 934 (2006).

[14] T. Hyart, N. V. Alexeeva, A. Leppanen and K. N. Alekseev, *Appl. Phys. Lett.* **89**, 132105 (2006).

[15] T. Hyart, A. V. Shorokhov and K. N. Alekseev, *Eprint cond-mat/0612461*.

[16] A. V. Shorokhov and K. N. Alekseev, *Physica E* **33**, 284 (2006).

15th Int. Symp. "Nanostructures: Physics and Technology"
Novosibirsk, Russia, June 25–29, 2007

"Ratchet" effect in Galton-board-like 2DES with broken spatial inversion symmetry

S. Sassine[1,2], Yu. Krupko[1], Z. D. Kvon[3], V. T. Renard[1], J.-C. Portal[1,2,4], R. Murali[5], K. P. Martin[5], G. Hill[6] and A. D. Wieck[7]

[1] GHMFL, CNRS, 25 avenue des Martyrs, BP 166, F-38042, Grenoble Cedex 9, France
[2] INSA, 135 Avenue de Rangueil, F-31077, Toulouse Cedex 4, France
[3] Institute of Semiconductor Physics, 630090 Novosibirsk, Russia
[4] Institut Universitaire de France, 103 Bd. St. Michel, F-75005, Paris, France
[5] Microelectronics Research Center — Georgia Institute of Technology,
791 Atlantic Dr NW, Atlanta GA 30332, USA
[6] Department of Electronic and Electrical Engineering — University of Sheffield, S13JD Sheffield, UK
[7] Lehrstuhl für Angewandte Festkörperphysik, Ruhr-Universität Bochum D-44780, Bochum, Germany

Abstract. The directed electron transport, driven by external linear-polarized microwave irradiation, in a two-dimensional spatially-periodic asymmetrical system called "ratchet" has been studied experimentally. The broken spatial symmetry was introduced in a high mobility two-dimensional electron system based on AlGaAs/GaAs heterojunction by patterning an array of artificial semi-discs-shaped scatterers (antidots). A directed electric current of few μA was observed in the "ratchet" antidot lattice under microwave irradiation (of few μWatts) in absence of any external current applied to the sample. The signal was recorded as a function of magnetic field, temperature, microwave power and polarization.

Introduction

In condensed matter physics, the directed transport in externally driven systems with naturally broken spatial inversion symmetry called "ratchet" effect, has been studied extensively for many years. A number of phenomena, including mesoscopic photovoltaic effect [1], photogalvanic effect [2] and many others [3] have been investigated. Also, this effect has proved to be of great importance in biological applications [4]. As for artificially broken symmetry, such phenomena hasn't been studied enough in the widely investigated semiconductor based two-dimensional electron system (2DES), where the charged particles (electrons or holes) could be scattered by an artificial scatterers (antidots). Nowadays technology allows fabricating a periodic array of antidots in 2DES, based on high mobility semiconductor heterojunction, so, that the period of the lattice will be much shorter than the mean free path in the initial heterostructure. In this case one could consider 2D-motion of electrons as a set of ballistic trajectories between the antidots boundaries. Symmetry breaking can be obtained by choosing a specific shape for the antidots, for example semi-disc. Such systems could be considered as slightly modified case of the Galton board [5]. In the present work we report on the experimental study of the directed electron transport induced by linear-polarized microwave (MW) irradiation in such system and compare our experimental results with recent theoretical investigations of this problem [6,7].

1. Samples

The samples for this work are based on MBE-grown AlGaAs/GaAs modulation-doped heterojunction, having 2DES at depth of 117 nm below the surface. A Hall bar geometry with two consecutive parts of lateral sizes 250×50 μm^2 was fabricated on the top of every sample, using conventional photolithography technique. A periodic array of semidisc-shaped antidots (hexagonal lattice), with period $d = 1.5$ μm and semi-disc's radius $r = 0.5$ μm (see inset to Fig. 1), has been fabricated in one of these two parts of the Hall bar by means of electron beam lithography and subsequent plasma etching. The second part was left intact in order to perform the check of pure 2DES parameters: it demonstrates the electron mobility $\mu = (2-3) \times 10^2$ m^2/V s and density $n_s = (2-3) \times 10^{15}$ m^{-2} at 1.5 K. This corresponds to an electron mean free path of $(15-30)$ μm which is much larger than the antidot spacing. In order to show the key role of the system symmetry in the origin of the "ratchet" effect, lattices with the same parameters but with symmetrical circular antidots were also fabricated in some of the same samples.

2. Experimental

Magnetotransport and photovoltage measurements were performed: the magnetotransport was measured by standard low frequency ac technique with low current (13 Hz, 10^{-7} A) to identify the 2DES parameters and to study the transport in the "ratchet" lattice; the dc photovoltage measurements were carried out with a sensitive voltmeter to measure the signal directly from the "ratchet" (see inset to Fig. 1). The measurements were performed in low magnetic fields at temperatures 1.4–100 K, using linear-polarized MW irradiation from a "carcinotron" generator tunable in the 33–50 GHz frequency range. A cylindrical brass tube with rectangular input and output profiles has been used as waveguide. The sample was placed very close to the waveguide output in a Variable Temperature Cryostat.

3. Results

The standard magnetotransport measurements in the antidot lattice and intact 2DES have demonstrated that the lattice resistivity (at zero magnetic field) is much larger than that of intact part. This means that the scattering on antidots is playing the major role and control the transport in the lattice at low temperatures.

Fig. 1 presents the key results of the rectification experiments: the magnetic field dependence of the dc-current mea-

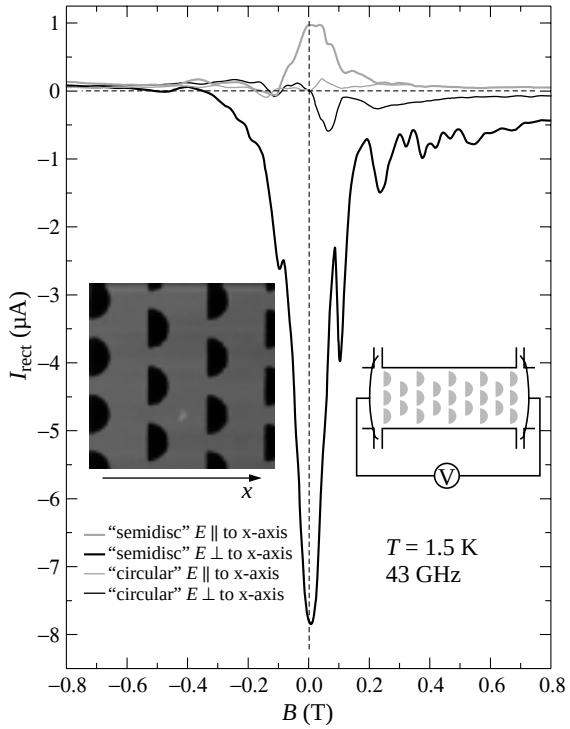

Fig. 1. Magnetic field dependence of the dc-current measured in the "ratchet" lattice (gray: polarization along x-axis and black: perpendicular to it) and in a lattice of circular antidots (thin curves). An AFM image of the "ratchet" lattice and the measurement configuration are shown in the insets.

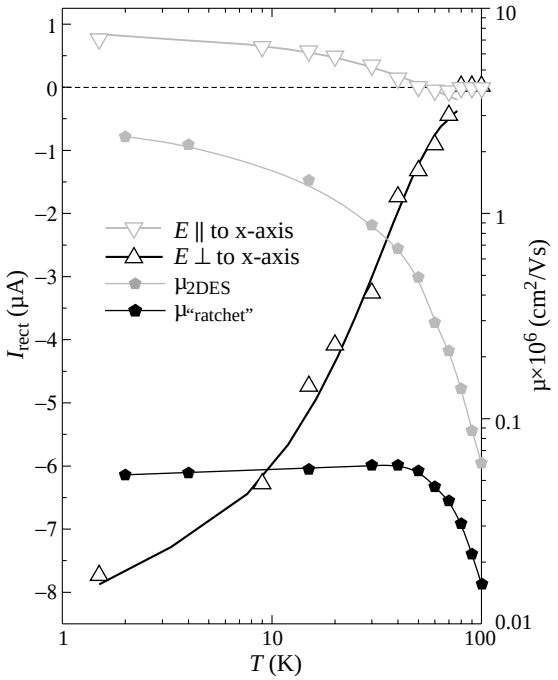

Fig. 2. Temperature dependence of the rectification current plotted together with temperature dependencies of the mobility in "ratchet" and intact 2DES. Temperature and mobility axes are presented in logarithmical scales.

sured in the "ratchet" antidot lattice under MW irradiation of frequency 43 GHz and few μW power. The vector of linear polarization (driving electric field) was oriented along the x-axis (gray curve) or perpendicular to it (black curve). In both cases a dc-current of few μA induced by the linear-polarized MW irradiation was measured (there was no external bias or current applied to the sample). Importantly the sign of the signal is opposite for the two orientations of polarization. When the direction of linear-polarization coincides with the x-axis, the plane side of the antidots dominates scattering. This forces electrons to move to the left. However, when the electric field component of the MW is rotated by 90°, the total scattering is dominated by the semicircular side of antidots and electrons move to the right. In other words the signal changes sign! This is in good qualitative agreement with theory [6,7]. It demonstrates that it is possible to control the direction of the transport in the "ratchet" lattice using the direction of the MW polarization. The signal shows a linear dependence on MW power for both directions of polarization. At magnetic field of about 0.2 T, the effect vanishes for any angle of MW polarization, when the classical Landau orbits become smaller than the antidot spacing. This accords to theoretical expectations too. The absence of the rectification current in a lattice of circular antidots (thin curves) further confirms that symmetry breaking is a necessary ingredient to the "ratchet" effect.

Fig. 2 presents the temperature dependence of the dc-current plotted together with the mobility of the "ratchet" lattice and intact 2DES. The mobility of the 2DES has behaviour comparable to high mobility samples [8] while the mobility in the antidot part is almost constant below 70 K. This means that the antidot scattering controls entirely the transport until 70 K and then phonon scattering becomes dominant, as can be seen in the rectification current that vanishes at $T \approx 70$ K (at 70 K the electron mean free path becomes equal to 1.7 μm which is comparable to the period of the antidot lattice).

Having obtained this first result we believe that making such a MW polarization detector work at higher temperatures should be possible. It is just necessary to fabricate a "ratchet" lattice with smaller period (0.1−0.2 μm), that is not beyond the nowadays technical possibilities.

Acknowledgement

This work was financially supported by ANR PNANO MICONANO project.

References

[1] A. A. Bykov *et al*, *JETP Lett.* **49**, 13 (1989).
[2] V. I. Belinicher *et al*, *Sov. Phys. Usp* **23**, 199 (1980).
[3] P. Reimann, *Phys. Rep.* **361**, 57 (2002).
[4] R. D. Astumian *et al*, *Phys. Today* **55**, 33 (2002).
[5] F. Galton, *Natural Inheritance*, (London: Macmillan) 1889.
[6] A. D. Chepelianskii *et al*, *Phys. Rev. B* **71**, 052508 (2005).
[7] A. D. Chepelianskii, *Eur. Phys. J. B* **52**, 389 (2006).
[8] L. Pfeiffer *et al*, *Appl. Phys. Lett.* **55**, 1888 (1989).

15th Int. Symp. "Nanostructures: Physics and Technology"
Novosibirsk, Russia, June 25–29, 2007

Experimental study of the microwave-induced resistance oscillations in high mobility 2DEG at mK temperatures

S. A. Studenikin[1], O. M. Fedorych[2], D. K. Maude[2], M. Potemski[2], A. S. Sachrajda[1], J. A. Gupta[1], Z. R. Wasilewski[1] and L. I. Magarill[3]

[1] Institute for Microstructural Sciences, NRC, Ottawa, Canada
[2] Grenoble High Magnetic Field Laboratory, CNRS, Grenoble, France
[3] Institute of Physics of Semiconductor, Russian Academy of Sciences, Novosibirsk, Russia

Abstract. In this work we investigate microwave induced resistance oscillations (MIROs) in a GaAs/AlGaAs heterostructure containing a high mobility 2DEG at milli-Kelvin temperatures. We find that MIRO persist to much lower magnetic fields than expected from the quantum relaxation time as determined from Shubnikov–de Hass oscillations. A possible quasi-classical origin of MIROs is discussed based on earlier predictions of MIROs in [Magarill *et al*, *Condens. Matter.* **7**, 1101 (1995)].

Introduction

The Microwave Induced Resistance Oscillations (MIROs) were discovered experimentally by Zudov *et al* [1] who were unaware of the much earlier theoretical prediction of the effect by Ryzhii [2]. A great deal of interest has arisen in this phenomenon after the observation of the so-called MIRO zero-resistance states on the highest mobility samples [3, 4]. The term MIRO is a very general one and any kind of oscillations induced by microwaves would suite to this definition. The absence of a specific name is due in part to the fact that the final origin of this phenomenon is not yet fully understood. There are several theoretical approaches published in the literature to explain MIROs, e.g. envolving scattering due to disorder [5, 6], a non-equilibrium distribution function [7], and a quasi-classical drift of electronic orbits [8]. All these models correctly describe the period and phase of MIROs but none of them are able to explain other well established experimental observations such as the independence of MIROs on the direction of the circular polarization [9] and the quenching of MIROs at higher MW frequencies [10]. It should also be stressed that electrodynamics, in particular magnetoplasmons, need to be taken into account in low temperature MIRO experiments, as was pointed out by Mikhailov [11], discussed in more detail by Volkov [12], and addressed experimentally in ref. [13]. In this work we continue our study of MIRO, in particular we examine the importance of modulation in the density of states (Landau levels) and a possible quasi-classical origin of MIROs by simultaneous mesurements and a careful comparison of MIROs with Shubnikov–de Haas (SdH) oscillations at milli-Kelvin temperatures where SdH oscillations do not depend on temperature and are only limited by quantum scattering time. In this respect, one earlier paper should be mentioned (ref. [14]) on this topic where the dynamic conductivity of 2DEG was calculated using a purely classical approach based on the Boltzmann kinetic equation. In that paper, in addition to the expected commensurability oscillations due to a weak lateral superlattice potential, another type of oscillations appeared in the conductivity simulations, whose period coincided with harmonics of the cyclotron resonance but which were phase shifted — very much resembling MIROs.

Experimental

The experiments were conducted on a 2DEG in GaAs/AlGaAs heterostructure placed in He_3/He_4 top-loaded dilution refrigerator allowing temperatures down to 50 mK. After brief illumination with a red LED the electron concentration attained a value of 1.9×10^{11} cm^{-2} and mobility reached a value of about 5.0×10^6 cm^2/V s. An Agilent generator was used as the microwave source providing frequencies in the range between 0.01 and 70 GHz and MW power up to 100 mW at the output. The microwave radiation was introduced into the dilution refrigerator by means of an approximately 3 m long silver plated copper-beryllium semi-rigid coaxial cable with a 6 dB broad band attenuator inserted in series to reduce rf noise and heating. An estimated maximum MW power emitted by the antenna was about 1 mW due to the frequency dependent attenuation of the coaxial cable and the antenna efficiency.

Results

Figure 1(a) shows two magnetoresistance R_{xx} curves measured at 50 mK — the solid line is R_{xx} without microwaves, and the dash one is Rxx in the presence of MWs. The electron temperature was verified by measurements of the spin-split peaks seen in SdH oscillations at higher magnetic fields $B > 0.22$ T in Fig. 1(a). Under irradiation with MWs the electron temperature increases and MIROs become evident in the low magnetic field region bellow 0.2 T (dash curve). Figure 1(b) shows a zoom of the low-field region. It is interesting to point out that MIROs extend to almost three times lower magnetic field (dash arrow) than the onset field (solid arrow pointing down) of the SdH oscillations limited by the quantum relaxation time. A similar result was obtained in Ref. [15], where the relaxation time obtained from MIROs was three times larger than the one obtained SdH oscillations. This result suggests a possible quasi-classical origin of MIROs [14] and will be analyzed in more detail. In this presentation we will also discuss a new kind of MW induced resistance oscillation, the origin of which is very similar to discussed above MIRO and can be interpreted in a simple way as due to MW-induced electron transitions between Landau levels near the Fermi level in a strongly degenerated 2DEG. These oscillations have same periodicity as the SdH ones, but differ by phase. The phase of this oscillations changes by π every time when crossing $\omega = N\omega_c$ nodes

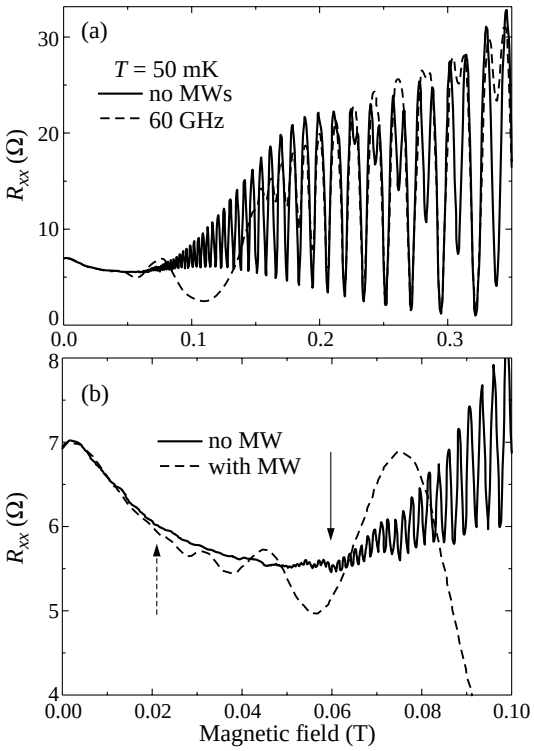

Fig. 1. Magnetoresistance traces of a high-mobility 2DEG without and in a presence of MW radiation ($f = 60$ GHz) at $T = 50$ mK (a), and a close up view of low field part (b) with the arrows showing onset fields for SdH oscillations (solid arrow) and MIROs (dash arrow).

during the magnetic field sweep, where ω and ω_c are the MW and cyclotron cyclic frequencies correspondingly.

References

[1] M. A. Zudov, R. R. Du, J. A. Simmons, and J. L. Reno, *Phys. Rev. B* **64**, 201311 (2001).

[2] V. I. Ryzhii, *Fiz. Tverd. Tela* **11**, 2577 (1969); (*Sov. Phys.: Solid State* **11**, 2078 (1970).

[3] R. G. Mani *et al*, Nature **420**, 646 (2002).

[4] M. A. Zudov, R. R. Du, L. N. Pfeiffer, and K. W. West, *Phys. Rev. Lett.* **90**, 046807 (2003).

[5] A. C. Durst, S. Sachdev, N. Read, and S. M. Girvin, *Phys. Rev. Lett.* **91**, 86803 (2003).

[6] V. Ryzhii, *Phys. Rev. B* **68**, 193402 (2003).

[7] A. Dmitriev, M. G. Vavilov, I. L. Aleiner, A. D. Mirlin, and D. G. Polyakov, *Phys. Rev. B* **71**, 115316 (2005).

[8] J. Inarrea, and G. Platero, *Phys. Rev. Lett.* **94**, 016806 (2005).

[9] J. H. Smet, B. Gorshunov, C. Jiang, L. Pfeiffer, K. West, V. Umanksy, M. Dressel, R. Meisels, F. Kuchar, and K. v. Klitzing, *Phys. Rev. Lett.* **95**, 11680 (2005).

[10] S. A. Studenikin *et al*, *Physica E* **34**, 73 (2006).

[11] S. A. Mikhailov, cond-mat/0303130 (2003); *Phys. Rev. B* **70**, 165311 (2004).

[12] V. A. Volkov, E. E. Tahtamirov, cond-mat/0506727; *Soviet Physics JETP* **104**, 602 (2007).

[13] S. A. Studenikin *et al*, *IEEE Transactions on Nanotechnology* **4**, 124 (2005).

[14] L. I. Magarill, I. A. Panaev, and S. A. Studenikin, *J. Phys.: Condens. Matter* **7**, 1101 (1995).

[15] S. A. Studenikin, M. Potemski, A. Sachrajda, M. Hilke, L. N. Pfeiffer, and K. W. West, *Phys. Rev. B* **71**, 245313 (2005).

15th Int. Symp. "Nanostructures: Physics and Technology"
Novosibirsk, Russia, June 25–29, 2007

Terahertz emission and absorption at lateral electric field in p-GaAsN/GaAs and n-GaAs/AlGaAs heterostructures

V. A. Shalygin[1], D. A. Firsov[1], L. E. Vorobjev[1], *A. N. Sofronov*[1], V. Yu. Panevin[1], D. V. Kozlov[2], S. D. Ganichev[3], S. N. Danilov[3], A. V. Andrianov[4], A. O. Zakhar'in[4], N. N. Zinov'ev[4], A. Yu. Egorov[4], O. V. Bondarenko[4], A. G. Gladyshev[4] and V. M. Ustinov[4]

[1] St Petersburg State Polytechnic University, 195251 St Petersburg, Russia
[2] Institute for Physics of Microstructures, 603950 Nizhny Novgorod, Russia
[3] University of Regensburg, 93040 Regensburg, Germany
[4] Ioffe Physico-Technical Institute, St Petersburg, Russia

Abstract. Optical phenomena in terahertz spectral range in strained p-GaAsN/GaAs microstructures and n-GaAs/AlGaAs quantum well structures are experimentally studied under lateral electric field at liquid helium temperatures. At high electric fields impurity breakdown conditions are realized and spontaneous terahertz emission is observed. Modulation of terahertz absorption related to electron heating in electric field was observed in quantum well structures. Theoretical consideration of acceptor energy levels in strained GaAsN layers was carried out and the major lines in the observed terahertz emission spectrum in GaAsN/GaAs structures are attributed to intracenter optical transitions between the resonant and localized acceptor states.

Introduction

Compact solid-state sources of THz radiation can be developed using shallow-impurity-doped semiconductors. Stimulated emission in THz range have been observed from uniaxially stressed p-Ge crystals in strong electric fields. Altukhov *et al* [1] experimentally showed that it is related to the inverted population of acceptor levels split by compressive strain. A mechanism of the intracenter population inversion (PI) between resonant state and localized acceptor state (related to the light hole (lh) subband) under electrical breakdown of acceptor was considered in [2]. A strong electric field empties the localized state due to impact ionization process. Hot free holes are captured at the resonant level and accumulated there as well as in the lh subband states with close energies. The uniaxial strain can be created also in thin alternating semiconductor layers with different crystal lattice periods. In [3] it was reported about a THz laser structure of this type based on a boron-doped $Si/Si_{1-x}Ge_x/Si$ quantum well (QW) nanostructure.

The population inversion between resonant and localized acceptor states can be also realized in strained p-GaAsN/GaAs microstructures with small nitrogen content [4]. In the present paper we report on the experimental studies of THz emission spectra in strained GaAsN:Be layers under strong electric fields, present results of calculations of the acceptor energy levels, and determine dominating optical transitions. At the same time resonant impurity states can also arise in doped QW structures where band and impurity states are split due to confinement. Such systems also can be suitable for achieving the intracenter PI in THz spectral range. We present spectra of THz emission from n-GaAs/AlGaAs QWs under lateral electric field and results on the modulation of THz absorption in QW structures related to electron heating in electric field. The latter studies allow to evaluate the temperature of 2D electron gas.

1. Experimental technique

The strained p-GaAsN/GaAs microstructures and n-GaAs/AlGaAs QW structures were grown by MBE on GaAs substrates. Strained microstructures comprised 10 periods of alternating 0.1 μm thick GaAsN layers and 0.5 μm thick GaAs layers. The nitrogen concentration in GaAsN layers was 1.8%. In this microstructure, GaAsN layers are subject to mechanical stresses equivalent to uniaxial compressive strain in the growth direction. The splitting of the hh and lh subbands is 21 meV. The GaAsN layers were doped with an acceptor (Be) to a concentration of 3×10^{17} cm^{-3}. Emission spectra were also measured in nanostructures contained 200 periods of $GaAs/Al_{0.3}Ga_{0.7}As$ quantum wells. Barrier width was 7 nm. Central 10 nm part of each well was doped with Si, so electron sheet concentration was 10^{11} cm^{-2}. Well width was 30 nm, energy distance between the ground and first subband was 15 meV. Modulation experiments were made on tunnel-coupled QW structures containing 100 periods of $GaAs/Al_{0.36}Ga_{0.64}As$ quantum wells (energy distance between the first subbands is about 38 meV).

Current-voltage characteristics (CVC) and dependencies of integral THz luminescence intensity upon electric field were experimentally studied in pulse regime at the temperature of 4.2 K on the samples immersed in liquid helium. Integral luminescence intensity was measured in the range of 60 ... 110 μm using a system of Ge:Ga photodetector and a black polyethylene filter. Spectra of spontaneous THz electroluminescence (EL) were recorded with a spectral resolution of 0.6 meV using a Fourier spectrometer operating in step-scan mode described elsewhere [5]. A voltage was applied to the samples with a shape of pulse "bundles". THz emission signal was detected using a liquid-helium-cooled silicon bolometer by means of lock-in amplifier. Molecular cw THz laser with radiation wavelength of 118 μm and output power of 10 mW was used as a source of THz radiation for modulation experiments, the sample was placed in helium flow cryostat.

2. Experimental results and discussion

Measurements of CVC for the p-GaAsN/GaAs structure showed that the processes of impurity impact ionization and avalanche breakdown start from the electric fields of 200 V/cm. The dependence of integral THz luminescence intensity upon elec-

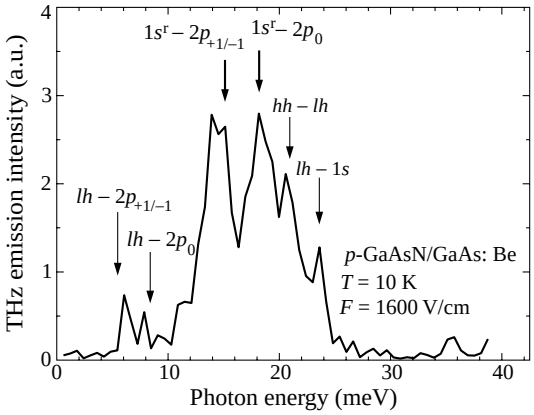

Fig. 1. The THz electroluminescence spectrum of strained p-GaAsN/GaAs structure at strong lateral electric field. Arrows show the possible optical transitions corresponding to calculated energy spectrum.

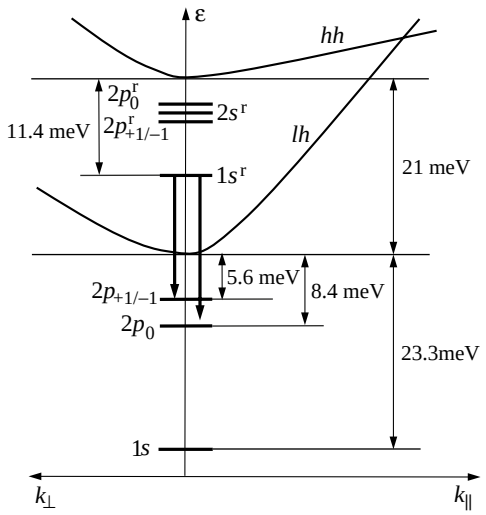

Fig. 2. Calculated positions of resonant and localized Be states in strained $GaAs_{0.972}N_{0.018}$/GaAs layers. Heavy hole (hh) and light hole (lh) subbands are shown schematically.

tric field demonstrates the sharp threshold at $E \sim 1300$ V/cm, consequently the emission of a THz radiation was observed in conditions of impurity avalanche breakdown only.

The typical THz EL spectrum detected in the conditions of impurity avalanche breakdown represents a series of narrow lines close together (Fig. 1). To recognize their nature, the spectra of shallow acceptors in strained GaAsN layers have been theoretically calculated in the envelope function approximation. The acceptor Hamiltonian used is a 4×4 matrix operator including the Luttinger Hamiltonian, the deformation term, and the Coulomb potential. Similarly to [6] the axial approximation has been used and the problem has been reduced to diagonalization of the finite symmetric matrix. Then we have to take into account the chemical shift of the binding energy, the necessary fitting parameter was determined from comparison of the calculated value and experimental data for the ground state of Be in the bulk GaAs. The results of the calculations of Be energy levels in strained GaAsN layers are shown in Fig. 2.

Arrows in the Fig. 1 show the photon energies for possible optical transitions corresponding to calculated energy spectrum for strained GaAsN:Be layers. It is possible to see that the

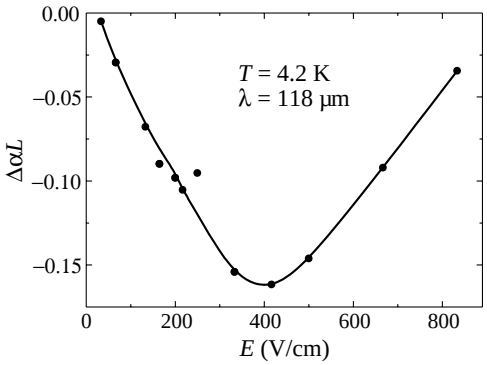

Fig. 3. The change of absorption (α is absorption coefficient, L is optical path) in lateral electric field in structures with GaAs/AlGaAs tunnel-coupled quantum wells.

major lines of THz emission lie quite close to the calculated transition energies. It allows us to conclude that intracenter optical transitions of holes from resonant acceptor level $1s^r$ to localized levels $2p_{+1/-1}$ and $2p_0$ predominate in the observed spectrum. As was mentioned above, this is precisely the emission mechanism which is proposed for use in lasers emitting in the THz frequency range. Intersubband transitions of holes (hh–lh) and the band-acceptor level transitions (lh–$2p_{+1/-1}$, lh–$2p_0$, lh–1s) give less significant contributions. As for thermal oscillations of the crystal lattice their contribution into EL is negligible.

The EL spectra of THz spontaneous emission were also obtained in GaAs/AlGaAs QW nanostructures. In this case impurity bounding energy is not so high, so emission spectra were observed at lower electric fields. Features in the spectra can be associated with the electron transitions with participation of impurity and band states.

Results of modulation experiments are presented in Fig. 3. Lateral electric field leads to electron gas heating. This process changes the probabilities of electron scattering with participation of impurities and phonons. As a result, absorption coefficient also changes. Experimentally, the decrease of absorption was found at relatively low electric field, at higher fields absorption begin to increase. These results correlate well with the data on temperature dependence of equilibrium light absorption and can be explained by the change of scattering mechanism with electron heating. The electron temperature can be evaluated from comparing these data to the data on equilibrium absorption.

Acknowledgements

This research was supported by the Russian Foundation for Basic Research (projects No. 05-02-17341, 05-02-17225, 05-02-17770), Russian President's program for support of young candidates of science (project 1860.2005.2), Russian Ministry of Education and Science and Russian Science Support Foundation.

References

[1] I. V. Altukhov *et al*, *JETP Lett.* **59**, 476 (1994).
[2] M. A. Odnoblyudov *et al*, *Phys. Rev. Lett.* **83**, 644 (1999).
[3] V. I. Altukhov *et al*, *Appl. Phys. Lett.* **79**, 3909 (2001).
[4] L. E. Vorob'ev *et al*, *Technical Physics Letters* **32**, 384 (2006).
[5] A. V. Andrianov *et al*, *JETP Letters* **79**, 365 (2004).
[6] V. Ya. Aleshkin *et al*, *Nanotechnology* **11**, 348 (2000).

15th Int. Symp. "Nanostructures: Physics and Technology"
Novosibirsk, Russia, June 25–29, 2007

Interplay between a coherent electron ensemble and terahertz radiation in a semiconductor superlattice

N. V. Demarina[1], A. Lisauskas[2], E. Mohler[2] and H. G. Roskos[2]

[1] Radiophysics Department, Nizhny Novgorod State University, 603950 Nizhny Novgorod, Russia
[2] Physikalisches Institut, J.W. Goethe-Universität, Frankfurt/Main D-60054, Germany

Abstract. We present a theoretical study of interplay between terahertz radiation and an electron ensemble in a GaAs/AlGaAs superlattice after ultra-short optical excitation. The simulation was performed by means of a single-particle Monte Carlo method. We found that interaction between the optically excited electron ensemble and the high-frequency field may lead either to terahertz field amplification or damping depending on an initial phase of the field. The time, the electron ensemble needs to reach the state ensuring the stationary terahertz gain, is determined by the electron intraminiband relaxation time. However, the net terahertz gain, i.e. the gain averaged over all possible initial phases of the incident field, is present in a superlattice right after the optical excitation. The study delivers criteria for experimental observation of the terahertz gain in a superlattice.

Introduction

The property of a biased superlattice to amplify terahertz (THz) radiation [1] remains barely experimentally explored owing to inhomogeneous electric field distribution in a superlattice if an applied static electric field is larger than a critical field. Domains of a strong electric field suppress the superlattice ability to serve as a gain medium. One of the possible ways to avoid domain formation is using an un-doped superlattice with charge carriers excited in it by means of an optical pulse [2]. Matching a time of carrier drift in a superlattice with a time of domain formation in a way that the latter is larger, one may achieve homogeneous field distribution within the time frame while charge carriers are still present in the superlattice. If the superlattice is additionally exposed to a terahertz (THz) field then the latter might be amplified. In our paper we present a three-dimensional Monte Carlo analysis of charge carrier dynamics in a superlattice after optical excitation and show that the net stationary gain sets in in a superlattice right after the optical excitation.

1. Object of the study and method

We describe the electron-hole transport in a superlattice along the superlattice axis (Oz) after optical excitation within a semiclassical theory. We assume that charge carriers are introduced into a superlattice at a time instant $t = 0$ and the concentration of the excited electrons, n, and holes, p, is $n = p = 10^{15}\,\mathrm{cm}^{-3}$. The relatively large electron-hole density justifies the applicability of the semiclassical theory and also enables us to estimate an achievable value of a THz amplification coefficient. After the excitation, the holes and electrons in the superlattice grow separated by the applied static electric field which induces an intrinsic electric field affecting the total electric field distribution. In our study we focus on the evolution of the electron-hole ensemble from the optically prepared to the stationary state determined by applied electric field. This process may last not longer than several intraminiband relaxation times thus we restrict our consideration to the first 10 ps after the optical excitation. The pump-probe photocurrent measurements and the calculation performed by making use of an ensemble Monte Carlo technique showed that during first ten picoseconds and for n and p smaller than 5×10^{15} cm^{-3} the electric field remains almost homogeneous and is determined by the applied static voltage. The holes due to their large effective mass are almost immovable after the excitation and do not contribute into the superlattice response on a THz field. Thus, we simulate only the electron transport in a superlattice with the homogeneous electric field by means of a single-particle Monte Carlo technique.

We consider a GaAs/$Al_{0.3}Ga_{0.7}$As superlattice with the period (d) of 8.4 nm and the width of the first miniband of 38 meV. Electrons in the miniband scatter at acoustic and optical phonons (for details of the scattering description see Ref. [3]) at a lattice temperature of 10 K.

We also assume that all electrons are initially distributed in k-space in at the miniband bottom, in accordance with the Gaussian intensity of the optical pulse with the pulse spectral band width of 15 meV.

2. Results

In order to explore the property of optically excited electrons in a superlattice to amplify a high-frequency field we calculate a response of the biased superlattice ($\upsilon_{\mathrm{stat+sin}}(t)$) on a THz field ($E_{\mathrm{THz}}(t) = E_\omega \sin(\omega t + \varphi)$) beginning at $t = 0$, i.e. in the instant of the superlattice excitation (Fig. 1 (inset)). The superlattice response caused by the THz field should exclude the superlattice reaction on the applied static field (E_0). Thus, we calculate the time-dependent drift velocity of the optically excited electrons in the biased superlattice ($\upsilon_{\mathrm{stat}}(t)$) and subtract it from the total drift velocity $\upsilon_{\mathrm{stat+sin}}(t)$. The final result reads $\upsilon_{\mathrm{sin}}(t) = \upsilon_{\mathrm{stat+sin}}(t) - \upsilon_{stat}(t)$.

We describe the interaction between the electron ensemble and high-frequency field by an average power absorbed by the electron ensemble over a period of the terahertz field, $T = 2\pi/\omega$. In fact, it implies that a period of the THz field is a shortest time one needs to make conclusion about whether the THz field can be amplified or not. The average power depends on the time instant, τ, we begin to calculate it at and is given by

$$P_{\mathrm{sin}}(\tau) = (qn/T)\int_{\tau}^{\tau+T} \upsilon_{\mathrm{sin}}(t)\, E_\omega \sin(\omega t + \varphi)\, dt = \frac{c\sqrt{\varepsilon}E_\omega^2}{8\pi}\alpha(\tau),$$

where $\alpha(\tau) = 4\pi qn\left(\upsilon_{\sin\omega}(\tau)/E_\omega\right)/c\sqrt{\varepsilon}$ is the time dependent amplification coefficient

$$\upsilon_{\sin\omega}(\tau) = \frac{1}{T}\int_{\tau}^{\tau+T} \upsilon_{\sin}(t)\sin(\omega t+\varphi)\,dt,$$

ε is the dielectric constant of GaAs, q is the elementary charge, and c is the light velocity. The positive value of the average power or of the amplification coefficient indicates damping of the terahertz field over the period while its negative value corresponds to the field amplification. Fig. 1 shows the time-dependent amplification coefficient for the superlattice subject to the static electric field and high-frequency fields ($\varphi = 0$). As the frequency of the terahertz field is smaller than the Bloch frequency (4.1 THz for $E_0 = 20$ kV/cm) the amplification coefficient should be negative for a time long after the excitation. The amplification coefficient decreases in time and after about 2.5 ps changes from positive to negative value. The latter indicates that the ensemble is capable to amplify external terahertz radiation when it reaches the state with high-frequency field stimulated coherence. We fitted the time-dependent amplification coefficient with the exponential function $\alpha(\tau) = \alpha_0\exp(-\tau/\tau_\alpha) + \alpha_\infty$ where α_∞ is the amplification coefficient in the stationary state and we denote the time of the amplification buildup as τ_α.

At this stage we like to point out that the analysis of the interaction between electrons and continuous-wave high-frequency field in a biased superlattice might be carried out using simplified semiclassical model based on velocity and energy relaxation times [5]. The calculation in this case is based on the assumption that behavior of electrons optically introduced in the vicinity of the miniband bottom at $t = 0$ in a superlattice with an electric field E_0 is similar to the case when the superlattice with the equilibrium electron population is subject to electric field increasing abruptly from 0 to E_0 at $t = 0$. Then the solution for the average velocity, which we obtained from this model, yielded $\upsilon(t) \propto \exp(-t/\tau_{ib})$ where τ_{ib} is the electron intraband relaxation time ($\tau_{ib} = 2\tau_\upsilon\tau_\varepsilon/(\tau_\upsilon+\tau_\varepsilon)$, τ_υ and τ_ε is the velocity and energy relaxation time correspondingly). Averaging of $\upsilon(t)$ over a period of the applied high-frequency electric field gives us the amplification coefficient exponentially dieing out in time with the intraband relaxation time. This agrees well with the results obtained by the Monte Carlo method.

The non-monotonous behavior of the time-dependent amplification coefficient displayed in Fig. 1 is manifestation of interplay between the optically-coherent electron ensemble and the high-frequency field. The center of the electron ensemble within first two picoseconds periodically traverses the Brillouin zone with the Bloch frequency and the phase of this oscillation is imposed by the initial condition. For the external electric field with the zero initial phase the electron motion is so that the electron ensemble gains energy from the high-frequency field. It takes a while before the electrons in the ensemble redistribute over the Brillouin zone and the ensemble reaches the state which favors the THz gain. Vice versa, if the electric field with the initial phase equal to π is incident on the superlattice (Fig. 1) then the electron ensemble pumps its energy into the THz field and $\alpha(\tau)$ is negative over the whole time interval. Let us now assume that the superlattice is exposed to THz

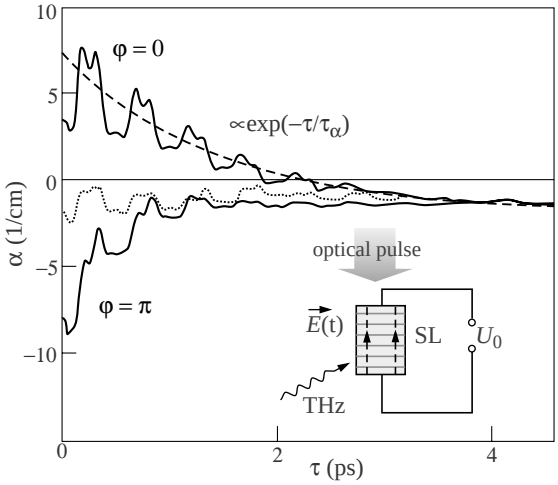

Fig. 1. Amplification coefficient for a THz electric field ($E_0 = 20$ kV/cm, $E_\omega = 5$ kV/cm, $\omega/2\pi = 2$ THz) with different initial phases, $\varphi = 0$ and π (thin solid lines) and the amplification coefficient averaged over all initial phases (thick dotted line) in the superlattice; the exponential fit of the superlattice response (dashed line); Inset: Sketch of the principle of the experiment on a biased superlattice (SL).

fields with a whole variety of the initial phases. This enables us to eliminate transient interplay of optically coherent ensemble with a THz field within first picoseconds. Experimentally this might be realized by continuous excitation of electrons within the certain time and averaging over all phases corresponds to the measurement of the average response of the entire electron ensemble. The averaged response is also presented in Fig. 1. Negative sign of the amplification coefficient implies that for this choice of the THz field majority of the electrons in the ensemble favors gain immediately after optical excitation and the net gain for THz radiation does not need time to settle in. It is worth noting that in our description we conclude about possible amplification at least after one period of applied THz field.

Acknowledgements

Support by the Russian Agency of Education and CRDF (grant BF5M01), the Federal Agency of Science and Innovations (contract No. 02.444.11.7093), and RFBR is acknowledged.

References

[1] S. A. Ktitorov *et al*, *Sov. Phys. Solid State* **13**, 1872 (1972).
[2] A. Lisauskas *et al*, *Appl. Phys. Lett.* **86**, 102103 (2005).
[3] N. V. Demarina and K. F. Renk, *Phys. Rev. B* **71**, 035341 (2005).
[4] M. Dignam, J. E. Sipe, and J. Shah, *Phys. Rev. B* **49**, 10502 (1994).
[5] A. A. Ignatov and Y. A. Romanov, *Phys. Status Solidi B* **73**, 327 (1976); A. A. Ignatov, E. P. Dodin, and V. I. Shashkin, *Mod. Phys. Lett. B* **5**, 1087 (1991).

15th Int. Symp. "Nanostructures: Physics and Technology"
Novosibirsk, Russia, June 25–29, 2007

The generation of the difference frequency radiation by subpico- and picosecond semiconductor lasers

A. A. Dubinov and V. Ya. Aleshkin
Institute for Physics of Microstructures RAS, 603950, Nizhny Novgorod, Russia

Abstract. The parametric generation of the difference frequency arising by propagation of two or one near-infrared mode pulses with a wavelength of about 1 μm in a pulse semiconductor lasers are studied theoretically. It is shown that the pulse power of the difference frequency in the wavelengths range 5–9 μm can be about 1 mW and in the wavelengths range longer 60 μm can be about 0.2 mW generated by pump of CW 10 W near-infrared laser and 100 W near-infrared pulse laser in a 100 μm-wide waveguide at room temperature.

Introduction

Semiconductor lasers operating in the middle and far-infrared (IR) regions attract considerable interest in view of their high potential for different applications. The quantum cascade medium-IR lasers capable of room-temperature operation have been successfully implemented [1], whereas with far-IR lasers based on cascade structures generation has been achieved only at cryogenic temperatures [2]. However, an extremely complicated band diagram of cascade structures and high requirements for control of parameters restrict their application.

An alternative way is development of noninversion generation schemes. One such approach might be that where far- or middle-IR radiation is generated in a quadratically nonlinear semiconductor structure by extracting difference frequency $\omega = \omega_2 - \omega_1$ resulting from mixing two near-IR fields at frequencies ω_1 and ω_2. Of III–V semiconductors, GaAs and GaP seem to be the best candidates for nonlinear elements, because its exhibit a sufficiently high second-order lattice nonlinearity [3]. Note that highest power semiconductor lasers currently available radiate exactly in the 1 μm range [4].

The highest power semiconductor lasers are the most efficient for nonlinear conversion, because the difference frequency power is proportional to near-IR mode powers. One of the ways for achievement of the large generation power is pulse generation in picosecond GaAs based lasers with saturable absorber, where pulse power can to achieve some hundred watts [5]. Moreover, in order to attain effective parametric generation, the three conditions should be satisfied:

1. the phase-matching condition, which means that the phase velocities of the polarization wave, produced by nonlinearity-induced interaction between near-IR modes, and the difference frequency propagating mode must be the same;
2. the high second-order nonlinearity;
3. the low losses of difference frequency radiation.

Our investigations show that optimal ways of parametric generation depend on difference frequency radiation wavelength. In this work, we propose two schemes for difference frequency generation using subpico-and picosecond lasers, which optimized for two wavelength ranges.

1. The results of calculations

For generation of radiation with wavelengths shorter 10 μm, we propose to use the scheme of the two-chip laser with compound resonator, which consist snap-together two lasers on common heat sink (Fig. 1). The first laser generates picosecond pulses in the 1 μm wavelength range, the second laser is a CW laser generating other near-IR frequency. It was shown that the phase matching condition can be satisfied by using transverse modes of a different order for pumping [6]. In the suggested scheme picosecond laser generates the fundamental mode, and it radiation be put in the CW laser, which generated the first excited mode. The difference frequency generation will take place in CW laser cavity. Our recent experiments have demonstrated a possibility to introduce about one half laser radiation inside the cavity of an other laser diode [7]. For the third condition execution we suppose, that the laser for the difference frequency generation must be grow on semiinsulating GaAs substrate.

For difference frequency generation with wavelengths longer than 60 μm we propose to use an one near-IR pulse generating laser and an external waveguide. The first condition is satisfied for pump with wavelengths near 1 μm by the use of the external GaP based waveguide [8]. Moreover, the second-order nonlinearity of GaP is 2–10 times more than that in GaAs [3] for the generation of far-IR radiation. So we propose to use the similar scheme as indicated above for the radiation generation in this wavelengths range. The first part of this scheme is a subpicosecond GaAs based laser and the second part is a GaP based waveguide. For the third condition execution in this wavelengths range very important to avoid the free carrier absorption of the difference frequency radiation. This condition can be satisfied in a semiinsulating GaP waveguide. In this case laser is used for pumping only, and waveguide is a nonlinear element.

The calculated difference frequency power spectra for some

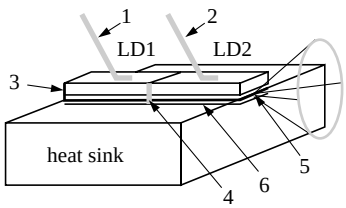

Fig. 1. The disposition of laser chips on the common heat sink. LD1 — the pulse laser; LD2 — the CW laser; 1 — the upper contact from substrate side of the LD1; 2 — the upper contact from substrate side of the LD2; 3 — the reflecting crystal face of the LD1; 4 — the splice of the antireflection lasing crystal face of the LD1 and reflecting crystal face of the LD2; 5 — the lasing crystal face of the LD2; 6 — the waveguide area.

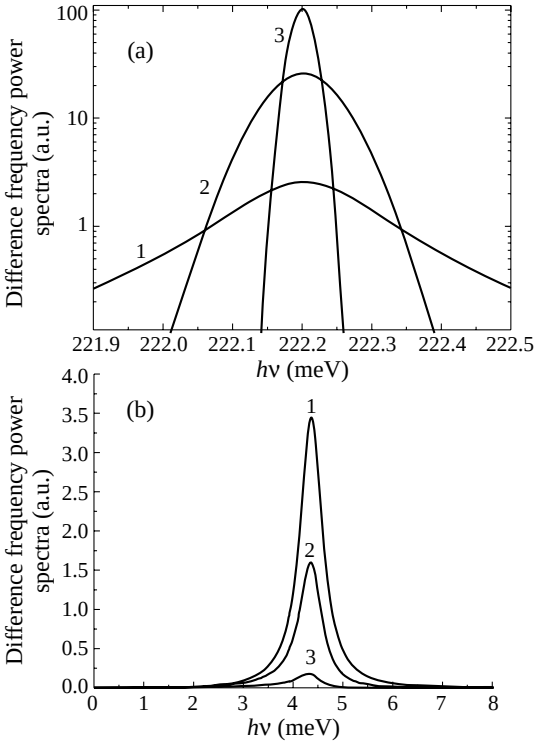

Fig. 2. The difference frequency power spectra for some duration of near-IR pulse ((a): 1 — 1 ps, 2 — 10 ps, 3 — 40 ps; (b): 1 — 0.3 ps, 2 — 0.4 ps, 3 — 0.6 ps) in the two-laser scheme with common resonator ((a), the long-waviest laser wavelength is 1.135 μm) and in the scheme of snap-together laser and waveguide ((b), the laser wavelength is 1.015 μm).

duration of near-IR pulse and two discussed schemes are shown in Fig. 2. In the case when the semiconductor structure is grown on the (001)-plane substrate and the near-IR modes have TE polarization and propagate along the [110] direction, the nonlinear polarization in GaAs or GaP is normal to the plane of layers and the TM mode is generated at the difference frequency [6]. We suppose that near-IR laser pulses are Gauss pulses.

The time dependence of the magnetic field of the difference frequency radiation is shown in Fig. 3. The time dependence of the amplitudes of the near-IR pulses is shown there too. In spite of the fact that the phase-matching condition is satisfied, the shape of the difference frequency pulse changes during propagation along waveguide due the distinction of the group velocities of the near-IR and difference frequency radiations.

For the estimation of the power of the difference frequency radiation we suppose that the CW pump power is 10 W and the amplitude of the pump pulse is 100 W. In this case for the 100-μm-wide planar waveguide the pulse power is 1 mW in the wavelengths range 5–9 μm and 0.2 mW in the wavelengths range longer than 60 μm at room temperature.

Acknowledgements

This work has been supported by CRDF (RUE1-2657-NN-05), RFBR (06-02-81020, 07-02-00486), the RAS "Coherent optical emission of semiconductor materials and structures" and "Electromagnetic waves of the terahertz range" Programs, the Russian President (MK-3344.2007.2), the Council for Support of the Leading Scientific Schools of the Russian Federation (4582.2006.2).

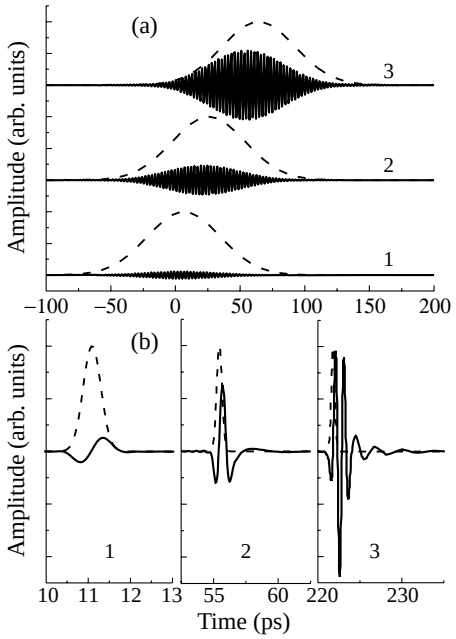

Fig. 3. The time dependences of the magnetic field of the difference frequency radiation (solid curves) and the amplitudes of the near-IR pulses (dashed curves) for the first scheme and propagation of pulses on 1 — 0.1 mm, 2 — 2 mm, 3 — 5 mm (a), and for the second scheme and propagation of pulses on 1 — 0.5 mm, 2 — 0.5 cm, 3 — 2 cm (b).

References

[1] J. Faist *et al*, *IEEE J. of Quantum Electron.* **38**, 533 (2002).
[2] M. Rochat *et al*, *Appl. Phys. Lett.* **81**, 1381 (2002).
[3] C. Flytzanis, *Phys. Rev. B* **6**, 1264 (1972).
[4] S. O. Slipchenko *et al*, *Semiconductors* **38**, 1430 (2004).
[5] G. B. Venus *et al*, *Pis'ma v ZhTF* **23**(4), 11 (1997).
[6] V. Ya. Aleshkin *et al*, *Semiconductors* **35**, 1203 (2001).
[7] A. A. Biryukov *et al*, *J. Modern Optics* **52**, 2323 (2005).
[8] V. Ya. Aleshkin *et al*, *Technical Physics* **51**, 1207 (2006).

15th Int. Symp. "Nanostructures: Physics and Technology"
Novosibirsk, Russia, June 25–29, 2007

Plasmon enhanced electrostriction and terahertz photoconductivity in a spatially periodic two-dimensional electron system

G. R. Aizin[1], V. V. Popov[2], *D. V. Fateev*[2] and G. M. Tsymbalov[2]

[1] Department of Physical Sciences, Kingsborough College of the City University of New York, 2001 Oriental Blvd., Brooklyn, NY 11235
[2] Saratov Branch of the Institute of Radio Engineering and Electronics of the Russian Academy of Sciences, 410019 Saratov, Russia

Abstract. A theory of dc photoresponse in a spatially periodic two-dimensional (2D) electron channel of the grating-gated field-effect transistor irradiated by an electromagnetic wave of terahertz frequency is developed. It is shown that the photoresponse in 2D electron channel with spatially modulated electron density is due to two different mechanisms: electron drag and electrostriction. Both electrostriction and electron drag contributions exhibit resonant peaks when the frequency of an external radiation coincides with 2D plasmon frequencies. In a strongly spatially modulated 2D electron channel, the electrostriction contribution to the photoresponse exceeds the electron drag contribution bythe order of magnitude. The results explain qualitatively some important features of the photoresponse observed in recent experiments.

Introduction

Recently, resonant detection of the terahertz (THz) electromagnetic (EM) radiations by plasma oscillations in the two-dimensional (2D) electron channel of the field-effect transistor (2D-FET) has been a subject of intensive experimental studies [1–3]. Such type of the detector can be tuned in frequency by gate voltage. Detection can be associated with the photovoltaic response of the submicron-size-gate GaAs-HEMT with asymmetric boundary conditions at the source and the drain sides of the 2D channel [1] as well as with the effect of the THz photoconductivity in the grid-gated GaAs/AlGaAs 2D-FET [2,3]. In both devices the photoresponse resonantly increases at the plasma resonance conditions in the 2D-FET irradiated by the EM wave of THz frequency. The theory of the photovoltaic response in the 2D-FET is given in Refs. [4,5]. The theory of the THz photoconductivity in the grating-gated 2D-FET with a homogeneous 2D electron channel is developed in Ref. [6]. The THz photoconductance in the homogeneous 2D electron channel results from the drag of 2D electrons by the plasma waves excited in 2D-FET by an external THz radiation. When a finite direct bias current is applied between the source and drain contacts, the non-zero dc drag current flows in the channel, manifesting itself as a change of the effective dc resistance of the channel [6].

In this paper, we present a theory of photoconductance in an inhomogeneous 2D electron channel (with a spatially periodic electron density) of the grating-gated 2D-FET interacting with an external THz field.

Results and discussion

We describe the dynamics of 2D electrons in the inhomogeneous 2D-FET channel by the hydrodynamic equations (Euler equation and equation of continuity) and consider the interaction of the 2D electron fluid with normally incident external EM wave of frequency ω which is polarized in a direction perpendicular to the grating fingers (x axis). This wave is modulated in the x direction by the grating gate fingers to give the total (self-consistent) electric field in the 2D plane, $E_0 + E(x,t)$. Here E_0 is the constant bias field and $E(x,t) = E(x+l,t)$ is the spatially periodic THz correction, l is the grating period. The local density and velocity in the 2D electron fluid can be written as $n(x,t) = n_0(x) + \delta n(x,t)$ and $v(x,t) = v_0(x) + \delta v(x,t)$, where $\delta n(x,t)$ and $\delta v(x,t)$ are THz corrections to the spatially periodic equilibrium 2D electron density $n_0(x)$ and stationary drift velocity $v_0(x) = -j_0/en_0(x)$ with j_0 being a spatially homogeneous direct bias current in the channel and e is the electron charge ($e > 0$). The total current is $j(x,t) = j_0 + \delta j(x,t)$, where $\delta j(x,t)$ is local spatially periodic THz current correction. Then the dc photocurrent correction is given by the time and space average of the THz current, δj_{00}.

The Fourier-harmonics of the density and velocity corrections $\delta n_{\omega q}$ and $\delta v_{\omega q}$ can be obtained directly from the Fourier-transformed hydrodynamic equations for the 2D el-ectron fluid once the Fourier-harmonics of the total THz electric field $\delta E_{\omega q}$, in the plane of the 2D electron channel are determined. We assume that the amplitude of an external THz wave is relatively small and consider photoresponse linear in the THz power. (This type of photoresponse was reported in Refs. 2 and 3.) Then, in the second order with respect to the THz electric field amplitude, the photocurrent can be calculated as

$$\begin{aligned}\delta j_{00} &= -e\sum_{q\neq 0}\left[n_q^{(0)}\delta v_{0,q}^{(2)} + v_q^{(0)}\delta n_{0,q}^{(2)}\right] \\ &\quad -2e\sum_{q\neq 0} q\sum_{q'q''} A_{qq'}^{-1}(\omega) N_{qq'}\delta v_{\omega q''}^{(1)}\left[\delta v_{\omega q}^{(1)}\right]^*, \quad (1)\end{aligned}$$

where $\delta n_{\omega q}^{(1)}$, $\delta v_{\omega q}^{(1)}$ and $\delta n_{\omega q}^{(2)}$, $\delta v_{\omega q}^{(2)}$ are the Fourier-harmonics of the electron density and velocity corrections that are linear and quadratic in the THz electric field amplitude, respectively, $n_q^{(0)}$ and $v_q^{(0)}$ are the Fourier-harmonics of the (spatially periodic) equilibrium 2D electron density and stationary drift velocity, $A_{qq'}(\omega) = \omega\delta_{qq'} - q\,v_{q-q'}^{(0)}$, and $N_{qq'} = n_{q-q'}^{(0)}$. The second term in Eq. (1), describes the plasmon-driven dc electron drag in the 2D electron channel, while the first term in Eq. (1), which appears only in a spatially periodic 2D electron channel(i.e., when $n_q^{(0)} \neq 0$, $v_q^{(0)} \neq 0$), describes the electrostriction

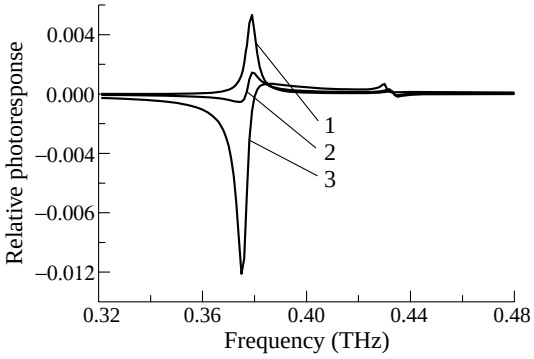

Fig. 1. Photoresponse versus frequency for $n_0^{(\max)} = 2.57 \times 10^{11}$ cm^{-2} and three different values of $n_0^{(\min)}$: 2.57×10^{11} cm^{-2} (homogeneous channel, curve 1), 2.55×10^{11} cm^{-2} (curve 2) and 2.5×10^{11} cm^{-2} (curve 3). The photoresponse is normalized to the dc bias voltage drop across the 2D-FET channel.

contribution.

We calculate the Fourier-harmonics of the total electric field, $\delta E_{\omega q}$, in the plane of 2D electron channel of the 2D-FET numerically using a self-consistent electrodynamic approach [7]. The ac response of the inhomogeneous 2D electron channel is described by the Ohm's law in the form

$$\delta j_{\omega q} = \sum_{q'} \sigma_{qq'} \delta E_{\omega q'}, \qquad (2)$$

where

$$\sigma_{qq'}(\omega) = -i\omega \frac{e}{m^*} \sum_{q''q'''} A^{-1}_{qq''}(\omega) N_{q''q'''} A^{-1}_{q'''q'}(\omega + i\gamma) \quad (3)$$

is the high-frequency conductivity tensor, which accounts for the spatial dispersion in the drifting 2D fluid with spatially periodic electron density. Here $\gamma = 1/\tau$ with τ is a phenomenological 2D electron relaxation time. Then, we use the Fourier-harmonics of the total electric field, $\delta E_{\omega q}$, to calculate the oscillating electron density and velocity corrections, $\delta n^{(1)}_{\omega q}$, $\delta v^{(1)}_{\omega q}$ and $\delta n^{(2)}_{\omega q}$ and $\delta v^{(2)}_{\omega q}$, and finally we calculate the photocurrent by Eq. (1).

In the regime of a constant direct bias current, THz illumination of the grating-gated 2D-FET results in an additional source-drain dc photovoltage $\delta U_0 = -\delta j_{00} L/\sigma_0$, where L is the channel length and σ_0 is the spatially averaged dc conductivity of the channel. This photovoltage is measured as a photoresponse [2,3]. We calculate the photoresponse δU_0 of the grating-gated GaAs/AlGaAs 2D-FET with the following parameters: $L = 2$ mm, $l = 4$ μm, the width of the grating gate finger is 2 μm, the distance between the grating gate and the 2D channel is 0.4 μm, and input THz radiation intensity is 1 W/cm^2, $j_0 = 0.05$ A/m, $\tau = 6.67 \times 10^{-11}$ s. We assume the sinusoidal profile of the equilibrium electron density in 2D electron channel with $n_0^{(\max)}$ and $n_0^{(\min)}$ as the maximal (under the center of the grating-gate opening) and minimal (under the center of the grating-gate finger) values of the electron density, respectively.

The dc photoresponse as a function of the THz frequency near the fundamental plasmon resonance is presented in Fig. 1. At the plasmon resonance frequency, the total electric field in the plane of 2D channel increases resonantly giving rise to the

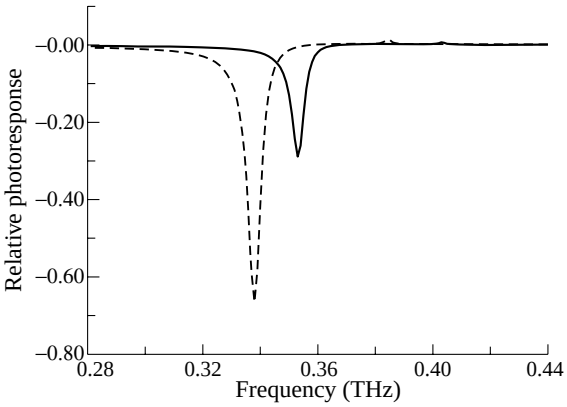

Fig. 2. The same as in Fig. 1 for $n_0^{(\min)} = 2 \times 10^{11}$ cm^{-2} (solid curve) and $n_0^{(\min)} = 1.7 \times 10^{11}$ cm^{-2} (dashed curve).

photoresponse resonance. It follows from Fig. 1 that with increasing spatial modulation of the equilibrium electron density in the channel the sign of the photoresponse is changing from the positive to the negative one. The positive photoresponse in a weakly density modulated (including homogeneous) 2D electron channel is due to the dc electron drag [the second term in Eq. (1)], while at an increased modulation the electrostriction mechanism [the first term in Eq. (1)] dominates, giving rise to the negative photoresponse. Figure 2 demonstrates that the THz photoresponse in the 2D-FET channel with large spatial modulation of the equilibrium electron density, which is almost entirely due to the electrostriction mechanism, might exceed the electron drag photoresponse in a spatially homogeneous 2D electron channel by an order of magnitude. This fact qualitatively explains the sharp increase of the height of the photoresponse resonant peaks with increasing spatial modulation of the electron density in the grating-gated 2D-FET channel reported in Refs. [2,3].

Acknowledgements

This work has been supported by the Russian Academy of Sciences through Program "Quantum Nanostructures", the Russian Foundation for Basic Research (Grant 06-02-16155), and the U.S. Army Research Office (Grant # W911NF-05-1-0031).

References

[1] D. Veksler, F. Teppe, A. P. Dmitriev, V. Yu. Kachorovskii, W. Knap, and M. S. Shur, *Phys. Rev. B* **73**, 125328 (2006) and references therein.

[2] X. G. Peralta, S. J. Allen, M. C. Wanke *et al*, *Appl. Phys. Lett.* **81**, 1627 (2002).

[3] E. A. Shaner, M. Lee, M. C. Wanke *et al*, *Appl. Phys. Lett.* **87**, 193507 (2005).

[4] M. Dyakonov and M. Shur, *IEEE Trans. Electron Devices* **43**, 380 (1996).

[5] M. Shur, J.-Q. Lu, *IEEE Trans. Microwave Theory and Technique* **48**, 750 (2002).

[6] G. R. Aizin, V. V. Popov, O. V. Polischuk, *Appl. Phys. Lett.* **89**, 143512 (2006).

[7] V. V. Popov, O. V. Polischuk, T. V. Teperik *et al*, *J. Appl. Phys.* **94**, 3556 (2003).

15th Int. Symp. "Nanostructures: Physics and Technology"
Novosibirsk, Russia, June 25–29, 2007

THz gain in semiconductor superlattices due to oscillations of effective mass

T. Hyart and K. N. Alekseev
Department of Physical Sciences, University of Oulu, Finland

Abstract. Semiconductor superlattices, operating in the single-miniband transport regime, are interesting nanodevices demonstrating properties of both nonlinear and active media. Although the average effective mass of the miniband electrons can be negative during some time-interval, this is not a necessary condition for gain. More precisely, the gain in superlattices can occur due to the oscillations of the effective mass. An important consequence of this fundamental difference to the negative mass amplifiers is that negative dynamical conductivity and negative dc differential conductivity can occur separately. This enables amplification without formation of high-field domains inside the superlattice. Here we consider theoretically a dc biased superlattice under an action of bichromatic electric field. The bichromatic field consists a large amplitude external pump ac field and a weak probe field. The probe field stimulates its amplification by inducing oscillations of the effective mass at certain frequencies, which are combinations of the pump and probe frequencies. In this kind of amplification scheme the frequencies of the pump and probe fields can be incommensurable and the gain does not depend on the phase difference between pump and probe fields. The amplification occurs typically at the technologically and scientifically important terahertz frequencies.

Introduction

Terahertz (THz) spectral range (0.2–10 THz) of electromagnetic radiation is located between optical and microwave frequencies. It is the borderline between quantum transition-based photonics and transport-based electronics, and there still exists a technological gap in construction of good, compact and reliable sources, amplifiers and detectors. It is known that a superlattice subject to dc electric field can demonstrate properties of active media due to Bloch oscillations [1]. However, the realization of Bloch amplifier is complicated by formation of destructive high-field electric domains inside the superlattice. Therefore, a search of other schemes for amplification in semiconductor superlattice devices is a very actual task.

Recently, we have predicted a parametric resonance phenomenon in a single miniband of superlattice subject to dc and ac electric field [2, 3]. The parametric resonance is based on oscillations of effective mass of miniband electrons and, at least in theory, it can result in amplification of a probe ac field without operation in conditions of negative differential conductivity. Thus it is possible to prevent the formation of high-field domains inside the superlattice.

On the other hand, it has been experimentally verified that alternating field at THz frequency opens up new transport channels leading to distinct photon-assisted peaks in the voltage-current characteristic [4]. By fixing the dc bias close to a value corresponding to one of the peaks in the current, an ac field can be amplified [5] in conditions where the formation of electric domains is suppressed [6]. However, there exists a threshold value for the ac field amplitude in order that the dc differential conductivity close to the photon-assisted peak is positive and the accumulation of space-charges is suppressed.

We extend the analysis of Kroemer [6] by introducing an additional ac pump field, which can suppress the electric instability even for a weak probe signal. We present a general method to use the photon-assisted peaks in the voltage-current characteristic for generation of THz radiation in conditions, where formation of electric domains is suppressed. We interpret these results in terms of oscillations of the effective mass, which is stimulated by the probe field.

1. Miniband transport under action of electric field

We assume a tight-binding miniband dispersion relation

$$\varepsilon(p) = -(\Delta/2)\cos(pd/\hbar). \tag{1}$$

Here Δ is the miniband width, d is the superlattice period and p is the quasimomentum. The effective mass of an electron with quasimomentum p is given by $m^{-1}(p) = \partial^2\varepsilon(p)/\partial p^2$. In this particular case the average of the inverse masses of the miniband electrons is

$$M^{-1}(t) = -\left(d^2/\hbar^2\right) W(t), \tag{2}$$

where $W(t)$ is the average miniband energy of the electrons. In single relaxation time (τ) approximation, the electron transport in homogeneous sample can be described in terms of balance equations

$$\begin{aligned} \dot{V} &= eM^{-1}E - V/\tau, \\ \dot{W} &= eEV - \left(W - W_{\mathrm{eq}}\right)/\tau. \end{aligned} \tag{3}$$

Here $V(t)$ is the average velocity of the miniband electrons, W_{eq} is the average miniband energy of the electrons in thermal equilibrium and $E(t)$ is the electric field. From the first equation we see, that miniband electrons behave like free electrons with time-dependent mass under the action of electric field. The second equation describes the competition between heating due to electric field and relaxation towards the thermal equilibrium. For static field $E(t) = E_{\mathrm{dc}}$ one finds the Esaki–Tsu characteristic, which in units of Esaki–Tsu peak velocity V_{peak} can be expressed as

$$V/V_{\mathrm{peak}} = V_0(E_{\mathrm{dc}}) = \frac{2E_{\mathrm{dc}}/E_{\mathrm{c}}}{1 + (E_{\mathrm{dc}}/E_{\mathrm{c}})^2}. \tag{4}$$

Here $E_{\mathrm{c}} = \hbar/ed\tau$ is the critical field.
In order to study the amplification of a probe signal $E_{\mathrm{ac}}\cos\omega t$, we define a dimensionless absorption

$$\mathcal{A} = \left\langle (V(t)/V_{\mathrm{peak}})\cos\omega t \right\rangle, \tag{5}$$

where $\langle \ldots \rangle$ denotes the time average. If $\mathcal{A} < 0$, it is possible to amplify the probe field.

2. The amplification scheme

We consider miniband electrons under an action of electric field

$$E(t) = E_{\mathrm{dc}} + E_{\mathrm{p}} \cos \Omega t + E_{\mathrm{ac}} \cos \omega t. \tag{6}$$

Here $E_{\mathrm{ac}} \cos \omega t$ is a probe field, which can be a mode of oscillator's resonator and $E_{\mathrm{dc}} + E_{\mathrm{p}} \cos \Omega t$ is an external pump field. We assume that frequencies ω and Ω are incommensurable. Because the results are independent on the phase difference between pump and probe fields, we do not introduce phases to the alternating signals.

In the small probe field limit ($E_{\mathrm{ac}} \ll E_{\mathrm{c}}$) the dc current is determined by the pump field (photon replicas of the Esaki–Tsu characteristic)

$$\frac{V_{\mathrm{dc}}}{V_{\mathrm{peak}}} = V_0^{\Omega}\left(E_{\mathrm{dc}}\right) = \sum_{l=-\infty}^{\infty} J_l^2\left(eE_{\mathrm{p}}d/\hbar\Omega\right) V_0\left(E_{\mathrm{dc}} + l\hbar\Omega/ed\right) \tag{7}$$

and the small-signal absorption at the frequency ω can be expressed as

$$\mathcal{A} = \frac{eE_{\mathrm{ac}}d}{2} \frac{V_0^{\Omega}\left(E_{\mathrm{dc}} + \hbar\omega/ed\right) - V_0^{\Omega}\left(E_{\mathrm{dc}} - \hbar\omega/ed\right)}{2\hbar\omega}. \tag{8}$$

From equation (7) one obtains, that dc differential conductivity can be positive if the applied dc bias is small or it is fixed close to a value corresponding to a photon-assisted peak in the voltage-current characteristic. Thus, in order that the formation of electric domains is suppressed, dc bias E_{dc} and pump frequency Ω should satisfy condition $|\hbar\omega_{\mathrm{B}} - n\hbar\Omega| < \hbar/\tau$ ($n = 0, 1, 2, 3\ldots$), where $\omega_{\mathrm{B}} = eE_{\mathrm{dc}}d/\hbar$ is the Bloch frequency. Importantly, gain resonances close to frequencies $\hbar\omega \approx m\hbar\Omega - \hbar/\tau$ ($m = 1, 2, 3\ldots$) [equation (8)] can still lead to an amplification of the probe field in these conditions, where the formation of electric domains is suppressed. Surprisingly, gain can exist also without dc bias.

We interpret these results in terms of oscillations of the effective mass stimulated by the probe field. Due to dc bias and ac pump field the stimulated oscillations of mass at frequencies $|\Omega \pm \omega|$ and ω effectively contribute to the accelerating force at frequency ω. At certain amplitudes and frequencies of the electric fields, the contribution of mass oscillations in the effective accelerating force makes the dynamical conductivity at frequency ω negative, although dc differential conductivity is positive.

Since the amplification mechanism is not based on population inversion, the gain does not depend strongly on temperature. This kind of generalization of Bloch oscillator can be considered as a candidate for room-temperature THz radiation source.

Acknowledgements

This work was supported by Academy of Finland, Emil Aaltonen Foundation and AQDJJ Programme of European Science Foundation.

References

[1] L. Esaki *et al*, *IBM J. Res. Dev.* **14**, 61 (1970).
[2] T. Hyart *et al*, *Appl. Phys. Lett.* **89**, 132105 (2006).
[3] T. Hyart *et al*, cond-mat/0612461.
[4] K. Unterrainer *et al*, *Phys. Rev. Lett.* **76**, 2973 (1996).
[5] Y. Romanov *et al*, *Sov. Phys. Semicond.* **12**, 987 (1978).
[6] H. Kroemer, cond-mat/0009311.

15th Int. Symp. "Nanostructures: Physics and Technology"
Novosibirsk, Russia, June 25–29, 2007

Cyclotron resonance of holes in strained InGaAs/GaAs QW heterostructures in high magnetic fields

D. V. Kozlov[1], A. V. Ikonnikov[1], K. E. Spirin[1], B. N. Zvonkov[2], V. I. Gavrilenko[1], W. Knap[3] and M. Goiran[4]

[1] Institute for Physics of Microstructures RAS,
603950 Nizhniy Novgorod, Russia
[2] Physico-Technical Research Institute of the Lobachevskii N. Novgorod State University, 603950 N. Novgorod, Russia
[3] GES–UMR, CNRS — Université Montpellier 2, Place E. Bataillon 34950 Montpellier, France
[4] Institut d'Electronique, de Microelectronique et de Nanotechnologie, 59652 Villeneuve d'Ascq, France

Abstract. Hole cyclotron resonance in strained InGaAs/GaAs QW heterostructures was studied in pulsed magnetic fields up to 30 T at $\lambda = 118$ μm. Numerical calculations of hole Landau levels using 4×4 Luttinger Hamiltonian were carried out to interpret the experimental results. The observed CR absorption line at $B = 12.5$ T is shown to result from in the optical transition between two lowest Landau levels with spin $J = +3/2$ while the earlier observed absorption line at $\lambda = 10.6$ μm, $B = 80$ T (Proc. 14th. Int. Symp. "Nanostructures: physics and technology", St Petersburg, 2006, p. 166) to the *intersubband* cyclotron resonance (transition from the 1^{st} hole subband into the 3^{rd} one).

Introduction

Cyclotron resonance (CR) is known to be a powerful mean to measure the effective masses and to probe a band structure at the scale of the cyclotron energy. In p-type InGaAs/GaAs quantum well (QW) heterostructures the CR studies were restricted to the present by measurements of the cyclotron mass m_c at the Fermi energy in the magnetic fields up to 6 T at $\lambda = 393 - 513$ μm [1–2]. The value of $0.12m_0$ was obtained from the extrapolation of the m_0 value down to the bottom of the valence band in strained $In_xGa_{1-x}As$ QW ($x = 0.2$) [2]. At the same time at $\lambda = 10.6$ μm in a similar structure (♯ 4722, see below) a CR absorption line was observed in the magnetic field 80 T that formally corresponds to the cyclotron mass as low as $0.08m_0$ [3]. To make the situation clear in the present work we studied the hole CR in InGaAs/GaAs QW heterostructures at the intermediate wavelength $\lambda = 118$ μm in magnetic fields up to 30 T.

1. Experimental

n-GaAs/GaAs heterostructures under study were grown by MOCVD method on s emiinsulating GaAs(100) substrates. $In_{21}Ga_{79}As$/GaAs structure ♯ 2229 contained 20 $In_{21}Ga_{79}As$ QWs with nominal width 100 A separated by GaAs barriers 100 A thick. Zn δ-layers were introduced in the barrier centers. $In_{15}Ga_{85}As$/GaAs heterostructure ♯ 4722 containing 50 $In_{15}Ga_{85}As$ QWs nominally 70 A wide, the GaAs barriers being 500 A thick. Two carbon δ-layers were introduced in the barriers from both sides of each QW 15 nm apart. The hole sheet concentrations in the above samples determined from the Hall effect measurement at room temperatures were 1.7×10^{11} cm^{-2} and 4.5×10^{11} cm^{-2} per QW correspondingly. CR measurements were carried out at National Laboratory of Pulsed Magnetic Fields (LNCMP) in Toulouse. The pulsed magnetic solenoid was placed in the liquid nitrogen cryostat. The pulse duration and energy were 800 ms and 1.2 MJ respectively. CH_3OH gas laser operating at $\lambda = 118$ μm optically pumped with CO_2 laser was used as a radiation source. The radiation was guided by a polished stainless steel light pipe into liquid helium cryostat inserted in the bore of the pulsed solenoid. The sample under study was placed in the liquid helium in the center of the solenoid. All measurements were carried out at $T = 4.2$ K in Faraday configuration $\mathbf{E}_\omega \perp \mathbf{B}$. The transmitted radiation was detected by a Ge:Ga impurity photodetector. The measurements of the signal versus magnetic field were carried out at both the up and down sweep of the magnetic field.

2. Calculation method

To calculate hole Landau levels (LLs) in GaAs/InGaAs QW heterostructures we used 4×4 Hamiltonian taken as the sum of the Luttinger Hamiltonian, the potential describing deformation effects and the potential of a rectangular QW. The eigenfunctions of this Hamiltonian are computed in the vector potential gauge specified by $\mathbf{A} = 1/2[\mathbf{H} \times \mathbf{r}]$ using the axial approximation in which the nondiagonal terms proportional to $(\gamma_2 - \gamma_3)$ related to the anisotropy in the plane of the QW are neglected. In this case, the projection of the hole angular momentum on OZ axis, J_z, is an integral of motion and the w ave functions of the holes states have the form:

$$\Psi_{n,M}(z, \rho, \phi) = \begin{pmatrix} f_n^4 u_{n-3,M-3}(\rho, \phi) \\ f_n^3 u_{n-2,M-2}(\rho, \phi) \\ f_n^2 u_{n-1,M-1}(\rho, \phi) \\ f_n^1 u_{n,M}(\rho, \phi) \end{pmatrix} \qquad (1)$$

Each state is characterized by the quantum number $n (n = r + (M + |M|)/2$, $r = 0, 1, \ldots \infty$ with $M = J_z/\hbar + 3/2)$, $u_{n,M}$ is the normalized Landau wave function. The Landau states are infinitely degenerate with respect to M, namely $M = -\infty, \ldots, -1, 0, \ldots, n$. After substitution the expression (1) into effective mass equation we obtain the linear differential equations for functions $f_n^i(z)$. These equations were solved using the transfer-matrix technique.

3. Results and discussion

The results of the hole CR measurements in two strained InGaAs/GaAs QW samples at $\lambda = 118$ μm are given in Fig. 1. One can see that prominent absorption lines at $B = 12.5$ T for

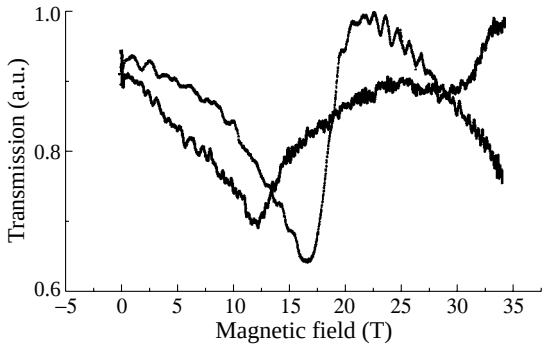

Fig. 1. The measured transmission of illumination at $\lambda = 118$ μm for two strained InGaAs/GaAs QW samples ♯ 2229 (solid curve) and ♯ 4722 (dotted curve).

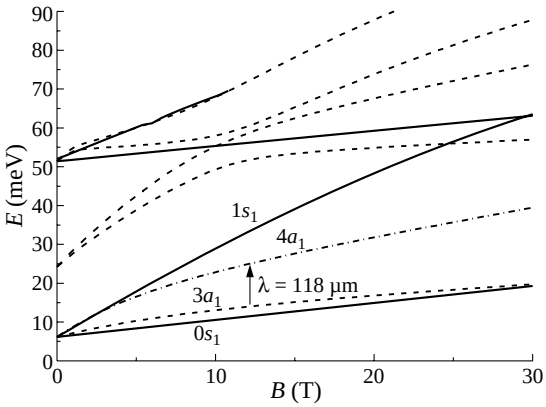

Fig. 2. Calculated hole LLs in GaAs/InGaAs sample ♯ 2229. The solid curves presented the $0s_{1-3}$ and $1s_{1-3}$ levels, dashed curves give the $3a_{1-3}$ and $4a_{1-3}$ levels.

the sample ♯ 2229 and at $B = 17$ T for ♯ 4722 one. The calculated LLs in these samples are presented in Figs. 2,3. LLs are characterized by a quantum number n (a kind of Landau level number), by a wave function parity (with respect to the XOY plane: a — antisymmetric, s — symmetric) and by the index i which labels the subband of size quantization (cf. [4]). Symmetric and antisymmetric LLs are plotted in Figs. 2,3 with solid and dashed lines respectively. In high enough magnetic fields only two lowest LLs $0s_1$ and $3a_1$ are populated by holes and one should observe two (rather than one) CR lines in quantizing magnetic fields (cf. [4]). The calculated energy of $3a_1 \to 4a_1$ transition for the sample ♯ 2229 at $B = 12.5$ T is 11 meV, which is in a reasonable agreement with the photon energy ($\hbar\omega = 10.5$ meV at $\lambda = 118$ μm). The calculated energy of $3a_1 \to 4a_1$ transition for the sample ♯ 4722 at $B = 17$ T is about 12.2 meV that again exceeds a little bit the photon energy $\hbar\omega = 10.5$ meV. At this photon energy the second CR transition, $0s_1 \to 1s_1$, should be observed in both samples at $B = 5.5 - 6$ T. However this resonance could be smeared at the magnetic field (rather than frequency) sweeping because of high broadening of the dominant $3a_1 \to 4a_1$ transition resulting from the valence band nonparabolicity and highly nonlinear dependence of $3a_1$ and $4a_1$ LL energies on the magnetic field. As has been already mentioned in the sample ♯ 4722 a sharp resonance has been observed in the magnetic field 80 T at $\lambda = 10,6$ μm [3]. As one can see from Fig. 3 this energy is much more than a typical CR energy. According to our calculation results (Fig. 3) this resonance is attributed to the

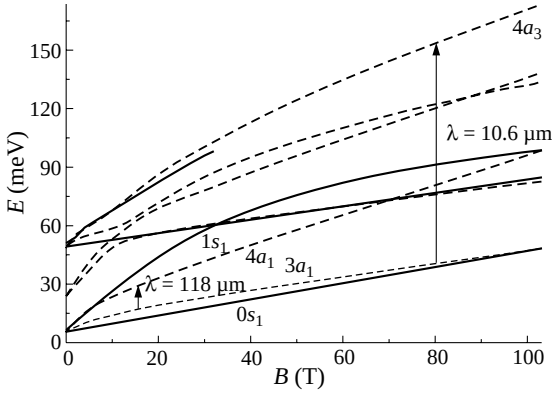

Fig. 3. Calculated hole LLs in GaAs/InGaAs sample ♯ 4722 in the 3 subbands of size quantization. The solid curves presented the $0s_{1-3}$ and $1s_{1-3}$ levels, dashed curves give the $3a_{1-3}$ and $4a_{1-3}$ levels. For actual InGaAs QW width is supposed to be 100 A to fit the results on intersubband CR [3].

intersubband hole CR, namely from the transition from $3a_1$ LL into $4a_3$ one pertained to the 3rd subband of size quantization. Such a transition (forbidden in a simple band) becomes observable due to a mixing of the hole wavefunctions in different subbands of size quantization (cf. [4]).

Acknowledgements

The work has been financially supported by RFBR (grant 05-02-17341, 07-02-01382), INTAS (YS Fellowship 04-83-3169), BRHE (Fellow ♯ Y2-P-01-08), Russian Science Support Foundation and by Russian Academy of Sciences. Measurements at LNCMP are supported by the contract FP6 "Structuring the European Research Area, Research Infrastructure Action" contract R113-CT2004-506239. (TSE7-206).

References

[1] S. Y. Lin *et al*, *Appl. Phys. Lett.* **55**, 666 (1989).
[2] S. Y. Lin *et al*, *Appl. Phys. Lett.*, **67**, 2170 (1995).
[3] V. I. Gavrilenko *et al*, *Proc. 14th Int. Symp. "Nanostructures: physics and technology"* 166 (2006).
[4] V. Ya. Aleshkin *et al*, *Physics of the Solid State* **46**, 130 (2004).

15th Int. Symp. "Nanostructures: Physics and Technology"
Novosibirsk, Russia, June 25–29, 2007

Terahertz absorption bands in scaled plasmonic crystals

T. V. Teperik[1,2], F. J. García de Abajo[1,3], *V. V. Popov*[2] and M. S. Shur[4]

[1] Donostia International Physics Center, Aptdo. 1072, 20080 San Sebastian, Spain
[2] Institute of Radio Engineering and Electronics (Saratov Division), RAS, Zelyonaya 38, 410019 Saratov, Russia
[3] Instituto de Óptica — CSIC, Serrano 121, 20006 Madrid, Spain
[4] Department of Electrical, Computer, and System Engineering, Rensselaer Polytechnic Institute, Troy, New York 12180, USA and RPI/IBM Center for Broadband Data Transfer, CII 9015, Rensselaer Polytechnic Institute, Troy, New York 12180, USA

Abstract. We show the existence of total-absorption bands in scaled plasmonic crystals composed of periodic arrangements of spherical two-dimensional free-electron-like open shells at terahetz frequencies. These absorption bands appear as a result of the coupling between plasmon modes of different shells in the crystal and can be tuned throughout the entire terahetz frequency domain by varying the electron density in the shells.

Introduction

Dielectric, metallo-dielectric and semiconductor photonic crystals have been extensively studied for nearly three decades. These crystals exhibit the photonic band gaps in visible. The photonic band gaps is a consequence of the either Bragg scattering of photons in the photonic crystal or the polaritonic interaction between photons and an inner resonance localized in an individual unit cell of the photonic crystal that can be, for example, the localized plasmons [1] or excitons [2]. In the terahertz (THz) domain, Bragg scattering cannot play a role on the electromagnetic response of nanoscale photonic crystals, since the dimension of the nanocrystal unit cell is much less than the wavelength of the THz radiation. However, localized inner resonances might affect significantly the THz response of the nanocrystal if the frequency of these resonances falls into the THz spectral region. Similar to visible plasmon resonances in metals, low-dimensional semiconductor nanostructures exhibit plasmon resonances at THz frequencies, thus offering natural candidates to realize the THz plasmonic crystal.

While the plasmons in planar two-dimensional (2D) electron systems have been broadly investigated, a live interest to the electron kinetics in curvilinear quantum wells has arisen quite recently [3,4]. Curvilinear quantum wells can be formed in granular pyroelectric-semiconductor structures [4]. As a result of the spontaneous polarization inherent in pyroelectric spherical inclusions, a 2D electron (hole) gas can be formed in spherical shells. Such electron-gas shells, when arranged in a three-dimensional (3D) periodical lattice, form a scaled plasmonic crystal that should exhibit the complex electromagnetic response associated with collective plasmon excitations.

In this paper, we show that broad THz absorption bands can be formed in a scaled plasmonic crystal composed of 2D electron-gas shells due to the interaction between plasmons excited in different shells of the crystal.

Results and discussion

In order to reveal the basic physics of plasmon excitations in a scaled plasmonic crystal, let us first consider a single spherical 2D electron-gas shell. It is well known that a conductive sphere can support Mie plasmon modes [5]. In a conductive shell, each of these modes splits into a doublet of sphere-like and void-like modes with in-phase and out-of-phase charge oscillations at opposite (outer and inner) surfaces of the shell wall, respectively [6,7].

The frequencies of electromagnetic multipole modes of electrical character in a conductive shell (only modes of this type can couple to plasmon excitations in such particles) can be estimated by setting the denominator of a corresponding scattering matrix element [5] equal to zero. In the quasi-electrostatic limit, this yields the following equation for the eigen-frequencies of these modes:

$$\frac{l\varepsilon_1 + l\varepsilon_2(\omega) + \varepsilon_2(\omega)}{\varepsilon_1 - \varepsilon_2(\omega)} = fl(l+1)\frac{\varepsilon_3 - \varepsilon_2(\omega)}{l\varepsilon_2(\omega) + l\varepsilon_3 + \varepsilon_3}, \quad (1)$$

where l is the orbital momentum quantum number, ε_1 and ε_3 are the dielectric constants of materials in the core and outside the shell, respectively, $\varepsilon_2(\omega)$ is the frequency-dependent dielectric function of the material forming the shell, $f = a^{2l+1}/(a+h)^{2l+1}$, a is the shell inner radius and h is the wall thickness. For $l = 1$, these dipolar modes are known as the Fröhlich modes [5]. We describe the electromagnetic response of the electrons inside the shell wall in the local Drude model as

$$\varepsilon_2(\omega) = \varepsilon_\mathrm{b}\left(1 + i\omega_\mathrm{p}^2/\omega(\nu - i\omega)\right), \quad (2)$$

where $\omega_\mathrm{p} = 4\pi e^2 N_\mathrm{s}/(\varepsilon_\mathrm{b} m^* h)$ is the bulk plasmon frequency, N_s is the areal electron density in the shell wall, e and m^* are the electron charge and effective mass, respectively, and ν is a phenomenological free electron scattering rate. If $\nu = 0$ and $\varepsilon_1 = \varepsilon_3 = \varepsilon$, the frequencies of Fröhlich ($l = 1$) modes are given by

$$\omega_\pm^2 = \frac{4\omega_\mathrm{p}^2(1-f)}{4\varepsilon_\mathrm{b}(1-f) + \varepsilon(5 + 4f \mp 3\sqrt{1+8f})}, \quad (3)$$

where lower and upper signs refer to sphere-like and void-like modes, respectively. For a 2D electron shell with $N_\mathrm{s} = 2.5 \times 10^{12}\mathrm{cm}^{-2}$, $m^* = 0.242 m_e$ (m_e is the free electron mass), $\varepsilon = \varepsilon_\mathrm{b} = 9$, inner shell radius $a = 45$ nm, and wall thickness $h = 5$ nm, the frequencies of sphere-like and void-like plasmons are $\omega_- = 3.43$ THz and $\omega_+ = 13.1$ THz, respectively. These parameters are characteristic for granular plasmonic crystals based on GaN [4].

Figure 1 shows the THz absorption cross section of a shell with different angular openings to external radiation calculated in the framework of a rigorous electromagnetic Boundary Element Method (BEM) [8] assuming $\nu = 4.4 \times 10^{13}\mathrm{s}^{-1}$ in

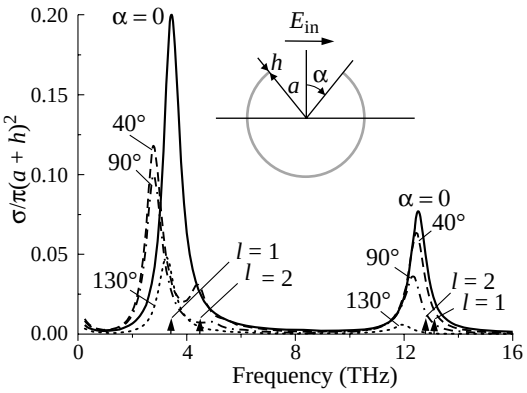

Fig. 1. Terahertz absorption cross section, σ, versus frequency for 2D spherical shells with areal electron-gas density $N_s = 2.5 \times 10^{12}\text{cm}^{-2}$ and different angular openings (see inset). The arrows mark the frequencies of the sphere-like and void-like multipole modes of a full shell, as calculated in the quasi-electrostatic limit for $l = 1, 2$. The cross section is normalized to the projected area of the shell, $\pi(a+h)^2$. The polarization of the electric field E_{in} in the incident THz radiation is shown in the inset.

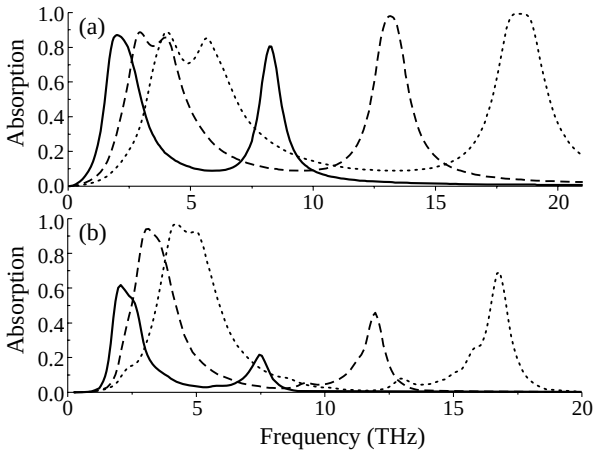

Fig. 2. Terahertz absorption spectra of a plasmonic crystal slab composed of 256 [111]-layers of 2D electron shells with $a = 45$ nm and $h = 5$ nm arranged in a fcc lattice for (a) full shells and (b) open shells with angular opening $\alpha = 130^\circ$ for different values of the surface electron density: $N_s = 10^{12}\text{cm}^{-2}$ (solid curves), $2.5 \times 10^{12}\text{cm}^{-2}$ (dashed curves), and $5 \times 10^{12}\text{cm}^{-2}$ (dotted curves).

Eq. (2). Using the BEM, the exact solution of Maxwell's equations is reduced to self-consistent integral equations for the interface oscillating charges and currents, which are solved through linear algebra upon discretization of the integrals. In the spectra of a full shell the resonances are exhibited at frequencies, which are in good agreement with the frequencies of sphere-like and void-like Fröhlich modes calculated above for $\nu = 0$. In this case of full shells, higher-order multipole plasmons are not observed because the shells are too small compared to the wavelength, so that higher multipoles beyond the dipole have negligible coupling strength to an incident plane wave. However, a quadrupolar ($l = 2$) sphere-like plasmon-mode resonance is excited in open shells due to the spherical symmetry breaking, which presumably provides a coupling mechanism between quadrupolar and dipolar modes, and through the latter also between the former and external light.

Our plasmonic crystals will consist of 2D electron-gas shells arranged into a 3D lattice. Figure 2 shows THz absorption spectra of multilayered plasmonic crystal slabs composed of 256 [111]-layers of shells arranged in a face-centered cubic (fcc) lattice (the [111] plane of the lattice is parallel to the slab surface) for both full shells [Fig. 2(a)] and open shells with angular opening $\alpha = 130^\circ$ [Fig. 2(b)]. The fcc lattice constant is 212 nm. The optical spectra of the plasmonic crystals have been calculated using a self-consistent electromagnetic multiple-scattering layer-Korringa–Kohn–Rostoker (KKR) approach [9], into which we have introduced scattering matrices of non-spherical shells obtained using the BEM [8].

One can see from Fig. 2 that broad low- and high-frequency absorption bands emerge in the vicinity of sphere-like and void-like plasmon resonances, respectively. These bands appear as a result of strong coupling between plasmons excited in different [111]-layers of shells and they signal of the presence of plasmonic bands of the crystal. The plasmonic absorption bands considered here are drastically different from conventional photonic band gaps of a photonic crystal, where photon transmission is forbidden. While a single full shell does not support plasmon modes of higher multipolar order beyond dipolar due to its perfect spherical symmetry, their interaction in the crystal produce a sizeable contribution of quadrupolar components, apparent through the fine structure of the low-frequency absorption band. Absorption bands can be tuned in frequency throughout the entire THz range by changing the surface electron density in the shell, which can be realized in turn by applying external electric and/or magnetic fields or through light irradiation of the plasmonic crystal slab. Such plasmonic crystals may find various applications as tunable THz filters, absorbers and thermally-activated sources.

Acknowledgements

This work has been supported in part by the Russian Academy of Sciences, Russian Foundation for Basic Research (Grants 05-02-17513, 07-02-91011, and 06-02-81007). F.J.G.A. acknowledges support from the Spanish MEC (contract No. FIS 2004-06490-C03-02 and No. NAN2004-08843-C05-05). The work at PRI was supported by ONR (Project Monitor, Dr. Colin Wood).

References

[1] A. Christ *et al*, *Phys. Rev. Lett.* **91**, 183901 (2003).
[2] S. Nojima, *Phys. Rev. B* **59**, 5662 (1999).
[3] A. I. Vedernikov and A. V. Chaplik, *JETP* **90**, 397 (2000).
[4] V. Yu. Kachorovskii and M. S. Shur, *Appl. Phys. Lett.* **86**, 012101 (2005).
[5] C. Bohren and D. Hufmann, *Absorption and Scattering of Light by Small Particles*, New York: J.Wiley, 1998.
[6] E. M. Prodan *et al*, *Science* **302**, 419 (2003).
[7] T. V. Teperik *et al*, *Phys. Rev. B* **69**, 155402 (2004).
[8] F. J. Garcia de Abajo and A. Howie, *Phys. Rev. B* **65**, 115418 (2002).
[9] N. Stefanou *et al*, *Comput. Phys. Commun.* **113** 49 (1998); **132** 189 (2000).

15th Int. Symp. "Nanostructures: Physics and Technology"
Novosibirsk, Russia, June 25–29, 2007

Dynamic localization and electromagnetic transparency in superlattices of various dimensionalities under multi-frequency electric fields

J. Y. Romanova and Y. A. Romanov
Institute for Physics of Microstructures RAS, Nizhny Novgorod, 603950, Russia

Abstract. We consider dynamics of electrons in semiconductor superlattices of various dimensionality (1D, 2D, 3D SLs) with nonharmonic and non-additive dispersion laws. We examine the conditions for electron dynamic localization and electromagnetic transparency in intense multi-frequency electric fields. We show that they differ essentially from commonly used harmonic approximation. We investigate processes of formation and destruction of electromagnetic transparency in biharmonic field.

It is well-known that in the semiconductor superlattices (SL) electrons perform complex Bloch oscillations (BO) in the presence of strong electric field. BOs are periodic in the dc electric field in the nearest-neighbor tight-binding (NNTB) approximation. For specific ratio of amplitude and frequency of applied harmonic field average electron velocity (no scattering) vanishes independently of its initial momentum. This effect is called dynamic localization (DL) in literature [1]. One of macroscopic manifestation of complex Bloch oscillations is nonmonotonic dependence of high-frequency conductivity on amplitudes and frequencies of fields. In particular the effect of electromagnetic self-induced transparency (SIT) arises in a SL; that is, all the current harmonics simultaneously vanish under conditions of rare collisions ($\omega\tau \gg 1$, τ is the characteristic relaxation time of the electron distribution function).

At the present time the electron dynamics in 1D SL within the nearest-neighbor tight-binding (NNTB) approximation (the idealized harmonic dispersion law) is well-studied for both harmonic and dc electric field. The BOs in ideal quantum dot superlattices of various dimensionality and with arbitrary dispersion laws under dc field were studied in paper [2]. 1D SL within the next nearest-neighbor tight-binding approximation were analyzed by Dignam *et al* [3] for dc-ac electric fields. But the electron dynamics in a SL with an arbitrary dispersion law under an arbitrary electric field remains to be explored. Taking into account next "nearest-neighbors" may be necessary for SLs with thin barrier layer. It leads to appearance of non-additive item in dispersion law of 2D and 3D SLs. Besides, namely SLs with a nonharmonic dispersion law are the most perspective for practical applications, for example, for creation of the Bloch oscillator (see, e.g. [4]).

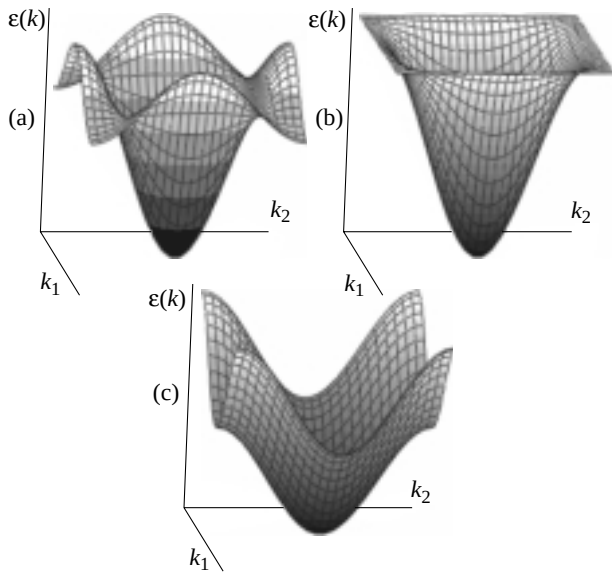

Fig. 1. Non-additive dispersion law (3) for various relationship $\Delta_2/\Delta_1 =$ (a) $= 0$; (b) $= 0.5$; (c) $= 1$.

In this study we investigated effects of DL and SIT in the SLs of various dimensionality in the presence of the multifrequency field:

$$\begin{aligned} E(t) &= E_c + \sum_{\alpha=1}^{M} E_\alpha \cos(\omega_\alpha t - \delta_\alpha), \\ n_\alpha \omega_\alpha &= n_\beta \omega_\beta, \quad n_{\alpha,\beta} = 1, 2, \ldots \end{aligned} \tag{1}$$

We considered such dispersion laws:

$$\varepsilon_3(k_3) = \sum_{n=1}^{N} \varepsilon_n(k_3) = \sum_{n=1}^{N} \Delta_n [1 - \cos(nk_3 d)] \tag{2}$$

for 1D SL (Δ_n is width of n-th partial sine-like miniband);

$$\begin{aligned} \varepsilon_3(k_1, k_2) &= \Delta_1 \left\{ 1 - \frac{1}{2} [\cos(nk_1 d) + \cos(nk_2 d)] \right\} \\ &\quad + \Delta_2 \{1 - \cos(nk_1 d)\, \cos(nk_2 d)\} \end{aligned} \tag{3}$$

for 2D SL [4], and

$$\begin{aligned} \varepsilon_3(\mathbf{k}) = \Delta_1 \left\{ 1 - \frac{1}{2} [\cos(nk_1 d) + \cos(nk_2 d) + \cos(nk_3 d)] \right\} \\ + \Delta_3 \left\{ 1 - \cos\left(\frac{nk_1 d}{2}\right) \cos\left(\frac{nk_2 d}{2}\right) \cos\left(\frac{nk_3 d}{2}\right) \right\}. \end{aligned} \tag{4}$$

for 3D SL. Here k_i is a component of the quasi-wave vector along x_i-axis of SL, d is SL period, Δ_i is the width of the sine-like minizone along the crystal axis x_i. It is determined by coupling between nearest neighbors along this direction. The non-additive item takes into account the coupling effect between diagonal nearest neighbors. The energy $\Delta_{2,3}$ characterizes its intensity. Such structure can be fabricated from regularly spaced quantum dots or quantum wires. Fig. 1. represents non-additive dispersion law (3) for various relationship Δ_2/Δ_1.

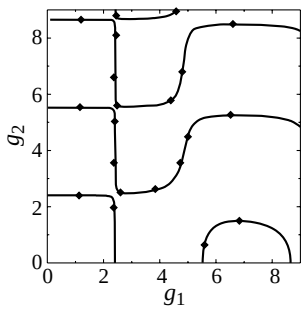

Fig. 2. The conditions of DL and SIT for 1D SL in biharmonic field (1) ($M = 2$, $\delta_1 = \delta_2 = 0$) and various dispersion law (2): curves — $N = 1$, marks — $N = 2$. $g_i = eE_i d/\hbar\omega$ is dimensionless field component.

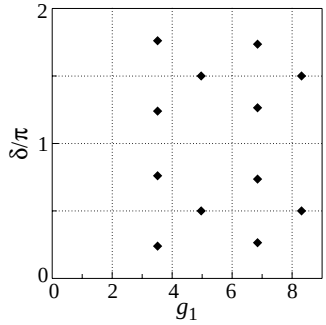

Fig. 3. Loci for DL and SIT in 2D SL under harmonic electric field $\mathbf{E}(t) = \mathbf{x}_1 E_1 \cos(\omega t) + \mathbf{x}_2 E_2 \cos(\omega t - \delta)$.

We showed:

1. In general in 1D SL with the N-harmonic dispersion law (2) DL and SIT arise only under fields which contains N or more harmonics. If all harmonics are odd, SL dispersion law can contain $(2N - 1)$ partial minizones. Fig. 2 illustrates conditions of DL and SIT for 1D SL in biharmonic field (1).

2. There is only one-dimensional DL (along one of the crystal axes) in the 2D(3D) superlattice with nonadditive dispersion law in a pure harmonic field. This field has to be oriented strictly along the crystal axes or to have elliptical polarization (Fig. 3)

3. Complete DL and SIT arise in 2D (3D) SL only:

— in biharmonic (or multi-frequency) fields;

— in dc-ac fields.

The field direction must be irrational ($E_1/E_2/E_3 = l/m/n$, l, m, n are irrational numbers.)

4. The states of self-induced transparency are not stable with respect to the generation of static or hf fields. Usually the static field generation is dominated. Fig. 4 illustrates process of apperance and destruction of SIT for SLs with the various dispersion laws. It can be seen that the SL is transferred to a state of the self-induced transparency, where all the current harmonics are small, fairly rapidly within a few periods of the field ($\sim \tau$). Then, slowly (over approximately 200 periods), accelerating appreciably for $g_c(t) \to 1$ in accordance with the resonant increase in energy exchange between the static and harmonic fields, the SIT is destroyed (aperiodic instability), and the superlattice is transferred to the state with $| g_c | \approx 1$ and relatively large current and a significantly different spectral composition. A rate of SIT destruction depends on a dispersion law.

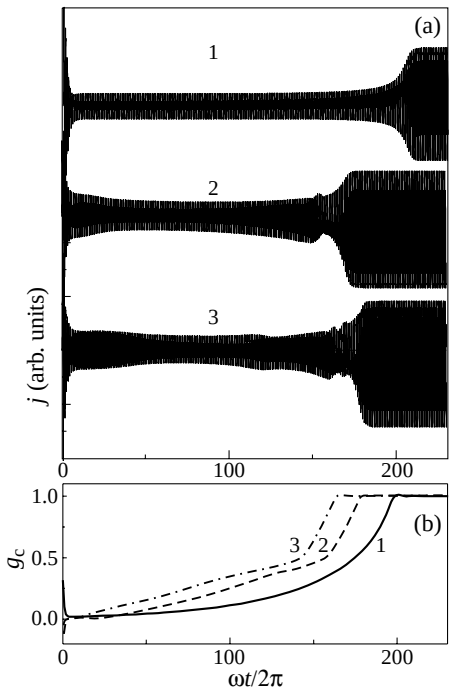

Fig. 4. Time evolution of current (a) and average field (b) in biharmonic field. Superlattice dispersion law involves one (1), two (2) and three (3) partial minizones accordingly. $g_1 = 2.39$, $g_2 = 1.9$, $\omega_2 = 3\omega_1$, $\delta = 0$.

Acknowledgements

The work is supported by the Russian Foundation for Basis Research (Grant No. 05-02-17319a) and by the Program "Quantum nanostructures" of RAS.

References

[1] O. N. Dunlap, V. M. Kenkre, *Phys. Rev. B* **34**, 3625 (1986).
[2] I. A. Dmitriev, R. A. Suris, *Semiconductors* **35**, 212 (2001).
[3] M. M. Dignam *et al*, *Phys. Rev. Lett.* **88**, 046806 (2002); J. Wan *et al*, *Phys. Rev. B* **70**, 125311 (2004).
[4] Yu. A. Romanov, J. Yu. Romanova, *Semiconductors* **39**, 147 (2005).
[5] M. L. Orlov, Yu. A. Romanov, L. K. Orlov, *Microelectronics Journal* **36**, 396 (2005).

15th Int. Symp. "Nanostructures: Physics and Technology"
Novosibirsk, Russia, June 25–29, 2007

Generalized Bloch oscillator and instability of space-charge waves in semiconductor superlattice

A. V. Shorokhov[1], N. N. Khvastunov[1] and K. N. Alekseev[2]

[1] Institute of Physics and Chemistry, Mordovian State University, 430000 Saransk, Russia
[2] Department of Physical Sciences, P.O. Box 3000, FI-90014 University of Oulu, Finland

Abstract. We investigated the instability of space-charge waves in SSL in the conditions of the schemes of generation based on the the generalized LSA scheme. We demonstrate that in general case the condition for space-charge instability depends on the wave vector of perturbation k. This effect can change conditions for the operation in generalized limited space-charge accumulation mode of Bloch oscillator.

1. Introduction

Semiconductor superlattices (SSL) can be potentially used for amplification and detection of a high-frequency electromagnetic radiation (0.3–10 THz) as supplement and alternative to the quantum cascade lasers and traditional frequency mixers [1]. The need of these devices is caused by a rapid progress of THz science and technology ranging from the astronomy to the biosecurity [2].

It was shown in the classical work [3] that static VI-characteristic of SSL has a part demonstrating negative differential conductance (NDC) due to Bloch oscillations of electrons within a miniband. Ktitorov *et al* [4] predicted that NDC should be accompanied by a small-signal gain for ac fields of very broad frequency range, from zero up to several THz. These works stimulated enormous theoretical activity devoted to the non-linear interaction of a high-frequency electric field with miniband electrons of SSL.

However, the progress in realization of this idea has been elusive during several decades. The main obstacle in a realization of these high-frequency devices is a formation of high- and low- field electric domains inside superlattice [5]. These domains are believed to be destructive for the Bloch gain. Therefore the main dilemma in the realization of SSL devices is finding operational conditions which allow simultaneously to achieve gain at THz frequencies and to avoid destructive space-charge instabilities.

Recently, modifications of this canonic scheme of generation were suggested [6,7]. The main idea of these papers based on the Limited Space-Charge Accumulation scheme. H. Kroemer reconsidered the problem for the case of high-frequency currents of a large enough amplitude [6]. He found that the dc part of NDC becomes positive (PDC), while the high-frequency NDC still can be negative. The PDC should be considered as one of the conditions for electric stability of the system. Another possibility in a realization of the generalized Bloch oscillator consists in an application of ac bias (instead of dc bias) to SSL and a consideration of amplification at harmonics of the pump [7,8]. The strong ac field in this system suppresses the space-charge instabilities inside SSL under certain conditions and simultaneously pumps an energy for generation and amplification of harmonics. This scheme can be quite realistic and allow a suppression of domains. However, to verify these scheme we need to know the kinetic properties of the formation and annihilation od domains. In particular, we need to consider perturbations of the internal field inside of SSL.

In this paper we study the instability of space-charge waves in SSL in the conditions of the schemes of generation [6,7]. Namely, we consider SSL under action of the strong pump field $E = E_0 + E_1 \cos(\omega_1 t)$ (E_0 is dc-bias, E_1 is the amplitude of the pump field, ω_1 is the frequency of the pump field). Then we need consider a stability of the system to a small perturbation $E_2(x,t) = E_2 \cos(\omega_2 t - k_2 x)$ taking into account spatial-dispersion effects.

To solve this problem we use the kinetic approach based on the Boltzman equation with energy spectrum of electrons in the tight-banding approximation. This approach to the calculation of the high-frequency conductivity with allowance for spatial-dispersion effects was formulated by Ignatov and Shashkin [5] for the case dc biased SSL. This approach permits adequate account of the influence exerted on the space charge wave spectrum both by resonance effects due to the Bloch oscillation of the electrons and by effects connected with carrier drift and diffusion under condition of strong spatial dispersion. It becomes possible as a result to determine the condition under which either low-frequency instability or high-frequency oscillation are produces in the system.

2. Complex conductivity

We have investigated in the present study the small-signal complex conductivity $\sigma(\omega_2, k_2)$ of a semiconductor SSL under conditions of a sufficiently strong field and a weak perturbation $E_2(x,t)$ taking into account a strong space dispersion. To describe the response of the electrons to external fields we use the Boltzmann transport equation with BGK (Bhatnagar–Gross–Krook) collision integral, which permits adequate allowance for the particle-number conversation law for scattering in inhomogeneous field.

We used the standard tight-banding approximation for diapertion relation of the electron belonging to a single miniband

$$\varepsilon(p) = \frac{\Delta}{2}\left[1 - \cos\left(\frac{pd}{\hbar}\right)\right], \qquad (1)$$

where Δ is the miniband width, d is the superlattice period, p is the quasimomentum.

We supplement the Boltzman equation with the Poisson equation

$$\frac{\partial E(x,t)}{\partial x} = \frac{4\pi e}{\varepsilon}\left[n(x) - n_0\right], \qquad (2)$$

where ε is the lattice dielectric constant. This formulates completely the electrodynamics of the problem.

The Boltzman equation in the approach of the constant relaxation time τ is

$$\frac{\partial f}{\partial t} + v(p)\frac{\partial f}{\partial x} + eE(x,t)\frac{\partial f}{\partial p} = -\nu\left(f - \frac{n(x)}{n_0} f^{\mathrm{eq}}\right), \quad (3)$$

where $f^{\mathrm{eq}} = (n_0 d)/(2\pi\hbar I_0)\exp\left[(\Delta/T)\cos(pd/\hbar)\right]$ is the equilibrium distribution function normalized to the electron density n_0, $v(p) = v_0 \sin(pd/\hbar)$, $v_0 = \Delta d/2\hbar$ is the maximum electron velocity in the miniband, I_m is the modified Bessel function of argument $(\Delta/2T)$, T is the lattice temperature. The BGK collision integral makes it possible, by virtue of the conservation of the number of scattered particles, to take into account the influence of the carrier drift and diffusion effects on the space-charge wave spectrum.

Solving (2) and (3) we get the following formula for the complex conductivity

$$\sigma(\omega_2, k_2) = \sigma_0 + ik_2 V_d + k_2^2 D. \quad (4)$$

Here

$$\begin{aligned}\sigma_0 &= -\frac{i\omega_0^2}{8\pi\omega_2}\sum_{l_1=-\infty}^{\infty} J_{l_1}^2(\beta_1)\left(\frac{1}{1+i(l_1\omega_1+\Omega_0)\tau}\right.\\ &+ \frac{1}{1+i(l_1\omega_1-\Omega_0)\tau} - \frac{1}{1+i(l_1\omega_1+\omega_2+\Omega_0)\tau}\\ &- \left.\frac{1}{1+i(l_1\omega_1+\omega_2-\Omega_0)\tau}\right) \quad (5)\end{aligned}$$

is the conductivity of SSL without spatial dispersion ($k = 0$). In the limit $E_0 = 0$, σ_0 goes to the Romanov's formula [9]

$$\begin{aligned}V_D &= \frac{\varepsilon V_0 I_1}{8\pi I_0}\sum_{l_1=-\infty}^{\infty} J_{l_1}^2(\beta_1)\left[\frac{1}{1+i(l_1\omega_1+\omega_2+\Omega_0)\tau}\right.\\ &- \left.\frac{1}{1+i(l_1\omega_1+\omega_2-\Omega_0)\tau}\right] \quad (6)\end{aligned}$$

and

$$\begin{aligned}D = -\frac{\varepsilon V_0^2\tau}{16\pi}&\left\{\frac{I_2}{I_0}\sum_{l_1=-\infty}^{\infty} J_{l_1}^2(2\beta_1)\right.\\ &\times\left[\frac{1}{(1+i(l_1\omega_1+\omega_2+2\Omega_0)\tau)^2}\right.\\ &+ \left.\left.\frac{1}{(1+i(l_1\omega_1+\omega_2-2\Omega_0)\tau)^2}\right] - \frac{2}{(1+i\omega_2\tau)^2}\right\}. \quad (7)\end{aligned}$$

Here $\Omega_i = edE_i/\hbar$ $(i = 0, 1, 2)$, $\beta_i = \Omega_i/\omega_i$ $(i = 1, 2)$, $\omega_0^2 = 4\pi e^2 d n_0 V_0 I_1/\hbar I_0$ is the square of the plasma frequency. Note that $V_d = 0$ in the limit $E_0 = 0$.

The temporal evolution of the initial perturbation in active medium is determined by the solution of the dispersion equation

$$\varepsilon(\omega_2, k_2) = 0, \quad (8)$$

where

$$\varepsilon(\omega_2, k_2) = \varepsilon + i\frac{4\pi\sigma(\omega_2, k_2)}{\omega_2} \quad (9)$$

is the dielectric constant of the SSL.

3. Conclusion

Solving the dispersion equation (8), we can find the space-charge wave spectrum in SSL and to determine a stable of the system to the small perturbations. The analyze of the Eq. (8) shows that the regions of instability strongly depends on the plasma frequency ω_0. However if the plasma frequency is small $\omega_0\tau < 3$ the regions of instability coincide with regions of absolute negative conductance (ANC) (for the case $E_0 = 0$). Note that in the quasistatic limit there are no ANC and the system is stable in scheme [7] at low electron concentration. Note also that in the dynamic limit regions of amplification is wider than regions of ANC. In the case of scheme [6], the regions of instabilities coincide with regions of NDC. However, if we take into account the partial dispersion of perturbation, the regions of instabilities can expand depending of k_2.

In the limit of low frequencies $\omega_2\tau \ll 1$ (using the method developed in [10]) when the density of free carriers is low so $\omega_p\tau < 2$, and the spatial dispersion is weak $kv_0 \ll 1$, the dispersion equation becomes

$$\omega_2 = k_2 V_D - i\left(\omega_0^2\tau + Dk^2\right). \quad (10)$$

In this case V_D makes sense of the drift velocity of particles, and D makes sense of the diffusion coefficient.

Acknowledgements

This work has been supported by Academy of Finland, and grant of President of Russia (MK-4804.2006.2).

References

[1] A. Wacker, *Phys. Rep.* **357**, 1 (2002).
[2] B. Ferguson, X. C. Zhang *Nature Materials* **1**, 26 (2002).
[3] L. Esaki, R. Tsu, *IBM J. Res. Dev.* **14**, 61 (1970).
[4] S. A. Ktitorov *et al*, *Sov. Phys. Solid State* **13**, 1872 (1995).
[5] A. A. Ignatov, V. I. Shashkin, *Sov. Phys. JETP* **66**, 526 (1987).
[6] H. Kroemer *et al*, *cond-mat/0009311* **73**, 934 (2006).
[7] K. N. Alekseev *et al*, *Europhys. Lett.* **73**, 934 (2006).
[8] V. V. Pavlovich, *Sov. Phys. Solid State.* **19**, 54 (1977).
[9] Yu. A. Romanov, *Sov. Phys. Solid State* **21**, 513 (1979).
[10] A. V. Shorokhov, K. N. Alekseev, *Physica E* **33**, 284 (2006).

15th Int. Symp. "Nanostructures: Physics and Technology"
Novosibirsk, Russia, June 25–29, 2007

Quantum dot based mode locked lasers and applications

A. Martinez[1], K. Merghem[1], C. Gosset[1], G. Moreau[1], F. Lelarge[2] and *A. Ramdane*[1]

[1] CNRS Laboratory for Photonics and Nanostructures (CNRS LPN), Route de Nozay, 91460 Marcoussis, France
[2] ALCATEL THALES III-V Lab, route de Nozay, 91460 Marcoussis, France

Abstract. The unique properties of Quantum Dot (QD) based active layers such as broad gain optical spectrum, high saturation output power, ultrafast gain dynamics and low loss are very attractive for the realization of mode-locked lasers (MLLs).
The aim of this talk is to discuss recent results in the field of long wavelength monolithic QD based MLLs. During the last decade or so the InAs/GaAs material system has experienced significant progress both in the growth and quality but also in the understanding of the physics of directly modulated lasers, with the demonstration of superior performance to that of their quantum well counterparts. This also led to the investigation of MLLs for which many properties have readily been demonstrated in the $1-1.3$ μm wavelength range.
On the other hand no report on QD based MLLs emitting in the 1.5 μm window has been made until very recently, illustrating the less mature state of QD gain medium at these wavelengths. The reported results are obtained using the so-called Quantum Dash active layers which demonstrate remarkable properties related to enhanced non-linear effects. Applications such as very high bit rate clock recovery, based on ultra-low noise, or optical interconnects and clock distribution are finally discussed.

Introduction

Self-assembled semiconductor quantum dot based lasers are attracting considerable interest owing to their unique optoelectronic properties that result from the three dimensional carrier confinement. They are indeed expected to exhibit much improved performance than that of quantum well devices [1]. Extremely low threshold currents [2] as well as high temperature stability [3–4] have readily been demonstrated in the InAs/GaAs material system with temperature-independent transmission experiments already carried out at 10 Gbit/s [5].

QD based active layers have hence recently been used in the fabrication of mode locked lasers. Inhomogeneous broadening of the gain spectrum due QD size distribution is indeed an asset for mode mocked lasers as this should result in pulse shortening. Ultrafast carrier dynamics [6] is also a major advantage in the short pulse generation process. Small jitter of the generated pulses is further expected owing to the theoretically predicted low enhancement factor (Henry factor) of low dimensional active layer based lasers.

InAs/GaAs mode locked lasers for 1.3 µm applications

The first demonstration of passive MLLs using QD based active layer was reported by X. Huang *et al* [7]. The authors showed stable mode locking at 1278 nm (ground state laser emission) at a repetition rate of 7.4 GHz in a two-section device (a gain section isolated from an absorber section) based on a 2 Dot-in-a-Well (DWELL) layer stack. Relatively broad pulses (17 ps width) were observed, under appropriate bias conditions, in this low modal gain structure. This first report pointed out that significant performance improvement, in terms in particular of pulse width, was achievable through the use of high modal gain (multi-stack active layers) QD lasers.

Indeed short pulses of a few ps or less are readily obtained by avoiding ground state gain saturation by stacking several QD layers up to 10 [8–10].

Simultaneous high peak power up to 3W and sub-picosecond pulse generation have been demonstrated at 21 GHz repetition rates [9]. The availability of an intrinsic wide band gain spectrum with a FWHM of 14 nm led to pulses as short as 390 fs, the lowest pulse width ever reported in the InAs/GaAs QD material system even if the time bandwidth product of ~ 1 indicated residual chirping of the pulses. Similar results are reported for a two-section device incorporating a flared waveguide [10], in this latter close to transform limited pulses are demonstrated. In both cases high reverse biases are applied to the absorber section for ultra-fast carrier dynamics [6].

Of particular importance is the potential of QD based material to achieve low noise properties owing to a small ASE rate [11] and low waveguide propagation losses. This has resulted in low timing jitter in these passively mode locked two-section devices [12–13]. The first demonstration of subpicosecond timing jitter was reported in [12]. Compared to the standard timing jitter of Quantum Well based MLLs these QD ML lasers exhibit $\sim$ more than one order of magnitude improvement.

The highest repetition rate reported for QD lasers grown on GaAs has been limited to $\sim$ 40 GHz corresponding to a cavity length of $\sim$ 1 mm, even though the active region comprises 10 QD layer stacks. A record 80 GHz repetition rate has very recently been demonstrated through optimized active layer made of 15 stacks which allowed laser emission for cavity lengths of ~ 500 μm [14].

InAs/InP mode locked lasers for 1.5 µm applications

Growth of quantum dots on InP(100) substrates generally leads to quantum 'dash' nanostructures (elongated dots) and the litterature has been less fertile in device results related to 3D confinement of the carriers. InAs/InP quantum dash based lasers have recently demonstrated subpicosecond pulse generation (800 fs) at a very high repetition rate of 134 GHz [15–16]. The laser active layer consists of a stack of 6 QDash layers which results in high modal gain [17] thus allowing laser emission for very short cavity lengths.

Passive mode locking is achieved in one-section Fabry–Perot lasers without resorting to an absorber section (Fig. 1), attributed to an enhancement of four wave mixing interactions in the laser cavity. A time-bandwidth product of $\sim$ 0.46 is

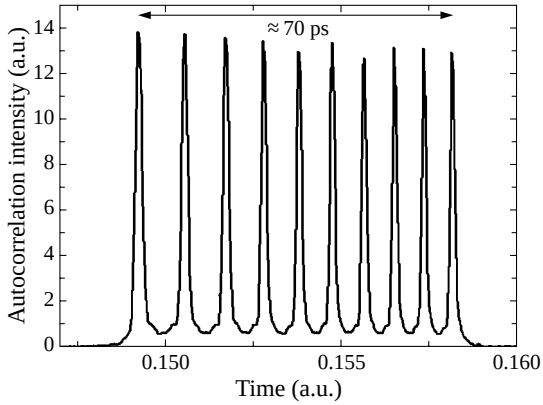

Fig. 1. Pulse train at 130 GHz with ∼ 800 fs pulse width, obtained with a 340 μm-long one section InAs/InP Fabry–Perot laser.

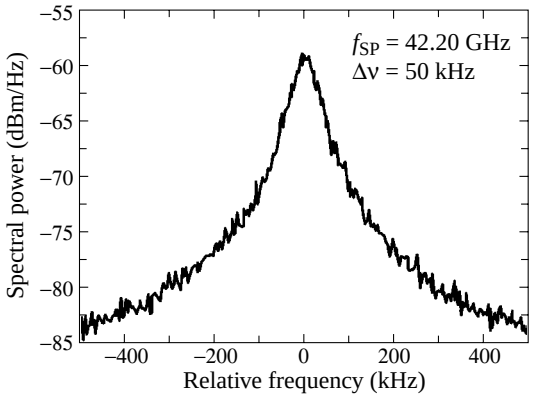

Fig. 2. Record free-running spectral linewidth of 50 kHz.

reported for these self-pulsating devices indicating close to transform-limited pulses.

Analysis of the radio frequency photocurrent spectrum has shown a record low linewidth of 50 kHz (Fig. 2). With such a low linewidth, the high frequency timing jitter can be estimated to be less than ∼ 200 fs.

Applications

Practical applications of mode locked lasers rely on short pulse duration and low timing jitter in such diverse areas as high bit rate optical communications (OTDM optical sources, clock recovery), microwave signal generation, optical sampling, optical interconnects. . .

Two specific applications will be highlighted, namely pulse generation for optical interconnect and clock distribution in ICs and clock recovery at 40 Gbit/s.

In the former application [12] advantage may be taken of the temperature stability of QD based lasers for which extremely high T_0 coefficients have been reported. Mode locked lasers operating up to 80 °C have hence been reported [18]. Improvement in the temperature behaviour is however still needed as a main requirement for these applications is the capability to operate the devices above at least 100 °C.

Of particular significance is the recent demonstration of 40 Gbit/s all-optical clock recovery [19], compliant with ITU-T recommendation. This used a one-section self-pulsating QDash laser which realizes high frequency jitter suppression owing to its inherently narrow free running spectral linewidth. This result paves the way to all-optical clock recovery at 160 Gbit/s.

References

[1] D. Bimberg, N. Kirstaedter, N. N. Ledentsov, Zh. I. Alferov, P. S. Kop'ev, V. M. Ustinov, *IEEE J. Sel. Topics in Quantum Electronics* **3**, 196 (1997).

[2] G. T. Liu, A. Stintz, H. Li, K. J. Malloy, and L. F. Lester, *Electron. Lett.* **35**, 1163–1165, (1999).

[3] O. B. Shchekin and D. G. Deppe, *IEEE Photon. Technol. Lett.* **3714**, 1231 (2002).

[4] I. I. Novikov, N. Yu. Gordeev, L. Ya. Karachinski, M. V. Maksimov, Yu. M. Shernyakov, A. R. Kovsh, I. L. Krestnikov, A. V. Kozhukhov, S. S. Mikhrin, and N. N. Ledentsov, *Semiconductors* **39**, 477 (2005).

[5] M. Ishida, N. Hatori, K. Otsubo, T. Yamamoto, Y. Nakata, H. Ebe, M. Sugawara, and Y. Arakawa, *IEE Electron. Lett.* **43**, 219 (2006).

[6] T. Akiyama, H. Kuwatsuka, T. Simoyama, Y. Nakata, K. Mukai, M. Sugawara, O. Wada, and H. Ishikawa *IEEE J. Quantum. Electron.* **37**, 1059 (2001).

D. B. Malins, A. Gomez-Iglesias, S. J. White, W. Sibbett, A. Miller, E. U. Rafailov, *Appl. Phys. Lett.* **89**, 171111 (2006).

[7] X. Huang, A. Stintz, H. Li, L. F. Lester, J. Cheng and K. J. Malloy, *Appl. Phys. Letters* **78**, 2825 (2001).

[8] M. Kuntz, G. Fiol, M. Lämmlin, D. Bimberg, M. G. Thompson, K. T. Tan, C. Marinelli, R. V. Penty, I. H. White, V. M. Ustinov, A. E. Zhukov, Y. M. Shernyakov, and A. R. Kovsh, *Appl. Phys. Lett.* **85**, 843 (2004).

[9] E. U. Rafailov, M. A. Cataluna, and W. Sibbett, N. D. Il'inskaya, Yu. M. Zadiranov, A. E. Zhukov, and V. M. Ustinov, D. A. Livshits, A. R. Kovsh, and N. N. Ledentsov, *Appl. Phys. Lett.* **87**, 081107 (2005).

[10] M. G. Thompson, A. Rae, R. L. Sellin, C. Marinelli, R. V. Penty, I. H. White, A. R. Kovsh, S. S. Mikhrin, D. A. Livshits, and I. L. Krestnikov, *Appl. Phys. Lett.* **88**, 133119 (2006).

[11] T. W. Berg and J. Mork, *Appl. Phys. Lett* **82**, 3083 (2003).

[12] L. Zhang, L. Cheng, A. L. Gray, S. Luong, J. Nagyvary, F. Nabulsi, L. Olona, K. Sun, T. Tumolillo, R. Wang, C. Wiggins, J. Zilko, Z. Zou, and P. M. Varangis, *Techn. Digest of OFC 2005*, paper OWM4 (2005).

[13] D. Larson, A. R. Rae, K. Yvind, R. V. Penty, I. H. White, J. Hvam, A. R. Kovsh, S. S. Mikhrin, D. A. Livshits, I. L. Krestnikov, *Techn. Digest of ECOC'06*, paper We4.6.3 (2006).

[14] M. Laemmlin, G. Fiol, C. Meuer, M. Kuntz, F. Hopfer, A. R. Kovsh, N. N. Ledentsov and D. Bimberg, *IEE Electron. Lett.* **42**, 697 (2006).

[15] C. Gosset, K. Merghem, A. Martinez, G. Moreau, G. Patriarche, G. Aubin, J. Landreau, F. Lelarge and A. Ramdane, *Electron. Lett.* **42**, 91 (2006).

[16] C. Gosset, K. Merghem, A. Martinez, G. Moreau, G. Patriarche, G. Aubin, and A. Ramdane, J. Landreau and F. Lelarge, *Appl. Phys. Lett* **88**, 1 (2006).

[17] G. Moreau, K. Merghem, D. Cong, G. Patriarche, F. Lelarge, B. Rousseau, B. Dagens, F. Poingt, A. Accard, F. Pommereau and A. Ramdane, in *Proc IEEE. Int. Conf. Indium Phosphide Related Mater.* 411 (2006).

[18] M. A. Cataluna, E. U. Rafailov, A. D. McRobbie, W. Sibbett, D. A. Livshits and A. R. Kovsh, *IEEE Photon. Tech. Lett.* **18**, 1500 (2006).

[19] J. Renaudier, B. Lavigne, F. Lelarge, M. Jourdan, B. Dagens, O. Legouezigou, P. Gallion and G.-H. Duan, *IEEE Photon. Tech. Lett.* **18**, 1249 (2006).

15th Int. Symp. "Nanostructures: Physics and Technology"
Novosibirsk, Russia, June 25–29, 2007

Indirect capture and ground-state lasing in quantum dot structures

Li Jiang and *Levon V. Asryan*
Virginia Polytechnic Institute and State University, Blacksburg, Virginia 24061, USA

Abstract. Excited-state-mediated capture into the ground state in quantum dots (QDs) is studied and conditions for ground-state lasing are formulated. No *separate* bottleneck problem (problem of slow carrier supply to the lasing state) is shown to exist — the longest, cut-off transition time from the excited- to ground-state, at which ground-state lasing becomes unattainable, is inherently controlled by the structure parameters. In a properly optimized (highly uniform or dense QD ensemble) or long-cavity device, ground-state lasing is attainable even if the transition time is of the order of a nanosecond; otherwise, when any of the parameters is close to its critical tolerable value, there can be no ground-state lasing even if the carrier transfer to the ground state is instant.

Introduction

Quantum dot (QD) lasers have attracted considerable attention in view of the interesting physics involved and potential for wide range of applications [1,2]. Operating characteristics of QD lasers are controlled by a number of factors. Among them are excited states, which are present in QDs in addition to the ground-state. Excited states can affect the capture of carriers from the waveguide [optical confinement layer (OCL)] into the lasing ground state (Fig. 1). Also carriers can recombine through the excited states rather than contribute to ground-state lasing. For direct capture from the OCL into single-state QDs, the output optical power was calculated in [3]. In this work, indirect capture into the QD ground-state, which occurs via the QD excited-state, is discussed and the conditions for ground-state lasing are formulated in terms of the structure parameters. In [4], such a capture was shown to place a fundamental limitation on ground-state lasing — the output power saturates at high injection currents. The saturation power $P_1^{\max}$ was shown to be controlled by the transition time τ_{21} between the excited- and ground-state in a QD. The longest, cut-off transition time $\tau_{21}^{\max}$ was shown to exist, beyond which no ground-state lasing is possible. Here, the shortest cavity length and the critical tolerable values of the parameters controlling the ground-state gain (the maximum QD size dispersion and the minimum surface density of QDs) are calculated versus the transition time τ_{21}.

1. Results and discussion

The normalized saturation power of ground-state lasing can be presented as the following universal function of the normalized transition time (Fig. 2):

$$\frac{\dfrac{1}{N_S S}\dfrac{P_1^{\max}}{\hbar\omega_1}}{\dfrac{f_{n1}^2}{\tau_{QD1}}} = \frac{1}{\dfrac{\tau_{21}}{\tau_{21}^{\max}}} - 1\,, \qquad (1)$$

where N_S is the surface density of QDs, S is the QD layer area, $\hbar\omega_1$ is the energy of photons emitted via the ground-state transitions, and τ_{QD} is the spontaneous radiative recombination lifetime via the ground-state.

In (1), f_{n1} is the ground-state occupancy (averaged over the QD ensemble); it is pinned above lasing threshold,

$$f_{n1} = \frac{1}{2}\left(1 + \frac{\beta_1}{g_1^{\max}}\right), \qquad (2)$$

where $\beta_1 = (1/L)\ln(1/R_1)$ is the mirror loss and R_1 is the mirror reflectivity for ground-state lasing, and L is the cavity length. The maximum (saturation) modal gain for the ground-state transitions $g_1^{\max} \propto N_S/\delta$, where δ is the RMS of QD size fluctuations [5].

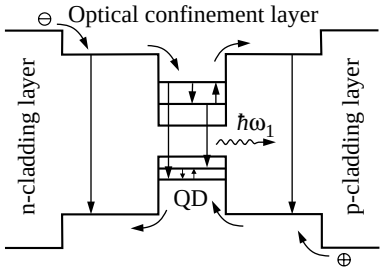

Fig. 1. Energy band diagram of a QD laser.

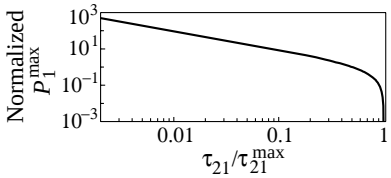

Fig. 2. Normalized saturation power of ground-state lasing versus normalized transition time.

The numerator in the left-hand side in (1) is the saturation stimulated recombination rate per QD and the denominator is the spontaneous recombination rate per QD.

In the right-hand side in (1), $\tau_{21}^{\max}$ is the longest, cut-off value of τ_{21}, above which no ground-state lasing is possible: at $\tau_{21} = \tau_{21}^{\max}$, the ground-state saturation power vanishes, $P_1^{\max} = 0$ (Fig. 2). $\tau_{21}^{\max}$ is given by

$$\tau_{21}^{\max} = \tau_{QD1}\frac{1 - f_{n1}}{f_{n1}^2}\,. \qquad (3)$$

The condition for the ground-state lasing is

$$\tau_{21} < \tau_{21}^{\max}\,. \qquad (4)$$

Since the maximum gain $g_1^{\max}$ and the ground-state occupancy f_{n1} [see (2)] are controlled by the structure parameters,

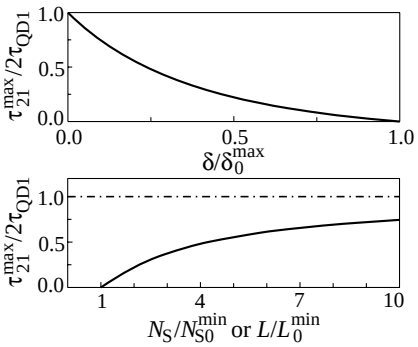

Fig. 3. Normalized cut-off transition time versus normalized structure parameters.

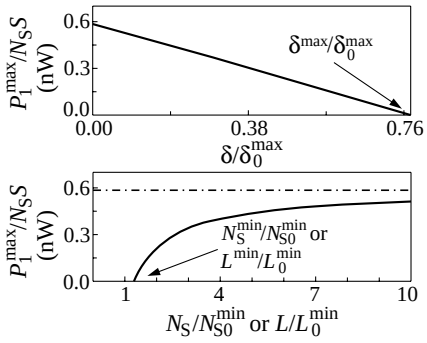

Fig. 4. Saturation power per QD versus normalized structure parameters. $\tau_{21} = 100$ ps. The horizontal dashed line shows the value given by eq. (8).

the cut-off time is also a function of the structure parameters. As seen from (2), the lowest value of f_{n1} is 1/2. Hence it follows from (3) that τ_{21}^{max} can not exceed $2\tau_{QD1}$; the latter is the absolute upper limit for τ_{21} (see below).

The above condition (4) can be written in the form of one of the following equivalent conditions:

$$\delta < \delta^{max}, \qquad N_S > N_S^{min}, \qquad L > L^{min}, \tag{5}$$

where δ^{max} is the maximum RMS of QD size fluctuations, N_S^{min} is the minimum surface density of QDs, and L^{min} is the minimum allowed cavity length. These critical tolerable parameters are

$$\delta^{max} = \delta_0^{max} Z, \quad N_S^{min} = N_{S0}^{min}/Z, \quad L^{min} = L_0^{min}/Z, \tag{6}$$

where δ_0^{max}, N_{S0}^{min}, and L_0^{min} are the critical tolerable parameters for the case of a direct capture into the lasing ground-state [5,6] and the factor Z is given by

$$Z = \left(\frac{1}{4} + \sqrt{\frac{1}{16} + \frac{1}{4}\frac{\tau_{21}}{\tau_{QD1}}} \right)^{-1} - 1. \tag{7}$$

The factor Z is less than unity: as τ_{21} varies from 0 to $2\tau_{QD1}$, Z changes from 1 to 0. Hence, in the case of indirect capture into the lasing ground state, more strict requirements apply to the structure design as compared to the case of a direct capture: $\delta^{max} \le \delta_0^{max}$, $N_S^{min} \ge N_{S0}^{min}$, $L^{min} \ge L_0^{min}$.

Figure 3 shows the cut-off time normalized to twice the spontaneous recombination time via the ground state versus the normalized structure parameters. As the figure suggests, τ_{21}^{max} can be as long as $2\tau_{QD1}$ if $\delta \to 0$, $N_S \to \infty$, or $L \to \infty$. When $\delta \to \delta^{max}$, $N_S \to N_S^{min}$, or $L \to L^{min}$, the cut-off time for the ground-state lasing is zero. What is meant by this is *there is no separate, isolated bottleneck problem (problem of slow carrier transfer to the lasing ground state) — the cut-off time τ_{21}^{max} is inherently determined by the structure parameters.* In an ideally uniform or infinitely dense QD ensemble ($\delta = 0$, or $N_S \to \infty$), or infinitely long cavity ($L = \infty$), ground-state lasing is attainable even if τ_{21} is as long as $2\tau_{QD1}$ (≈ 1.4 ns). Otherwise, when $\delta \to \delta^{max}$, $N_S \to N_S^{min}$, or $L \to L^{min}$, there can be no ground-state lasing even if the carrier transfer to the ground state is instant ($\tau_{21} = 0$).

The saturation power per QD is shown versus the normalized structure parameters in Fig. 4. For an ideally uniform or infinitely dense QD ensemble, or infinitely long cavity, the saturation power per QD is

$$\frac{\hbar\omega_1}{2\tau_{21}} \left(1 - \frac{\tau_{21}}{2\tau_{QD1}} \right). \tag{8}$$

2. Conclusion

Under conditions of indirect capture into the QD ground state, *no separate bottleneck problem* for ground-state lasing has been shown to exist — the longest, cut-off transition time from the excited- to ground-state, at which ground-state lasing becomes unattainable, is inherently controlled by the structure parameters. In a properly optimized device (highly uniform or dense QD ensemble, or long cavity), ground-state lasing is attainable even if the transition time is of the order of a nanosecond. Otherwise, when any of the structure parameters is close to its critical tolerable value, there can be no ground-state lasing even if the carrier transfer to the ground state is instant.

Acknowledgements

This work was supported by the U.S. Army Research Office under Grant No. W911-NF-05-1-0308.

References

[1] D. Bimberg, *J. Phys. D.* **38**, 2055 (2005).
[2] S. Fathpour, Z. Mi and P. Bhattacharya, *J. Phys. D.* **38**, 2103 (2005).
[3] L. V. Asryan, S. Luryi and R. A. Suris, *IEEE J. Quantum Electron.* **39**, 404 (2003).
[4] L. Jiang and L. V. Asryan, *IEEE Photon. Technol. Lett.* **18**, 2611 (2006).
[5] L. V. Asryan and R. A. Suris, *Semicond. Sci. Technol.* **11**, 554 (1996).
[6] L. V. Asryan and R. A. Suris, *IEEE J. Quantum Electron.* **36**, 1151 (2000).

15th Int. Symp. "Nanostructures: Physics and Technology"
Novosibirsk, Russia, June 25–29, 2007

ZnSe/ZnMgSSe nanostructures and a longitudinal e-beam pumped blue (458 nm) laser based on them

V. I. Kozlovsky[1], V. P. Martovizky[1], Ya. K. Skasyrsky[1], *P. I. Kuznetsov*[2], V. A. Jitov[2], L. Yu. Zakharov[2], B. S. Shchamkhalova[2] and M. D. Tiberi[3]

[1] P. N. Lebedev Physical Institute of RAS, 53 Leninsky pr., 119991 Moscow, Russia
[2] Institute of Radioengineering and Electronics of RAS, 1 Vvedenskogo, 141190 Fryazino, Russia
[3] Principia LightWorks Inc., CA, USA

Abstract. ZnMgSSe layers and ZnSe/ZnMgSSe nanostructures were grown by metal-organic vapor phase epitaxy on GaAs substrates. Their structural and luminescence properties are studied. The decay of epilayers with high Mg and S contents into two ore more phases was observed while in periodic ZnSe/ZnMgSSe nanostructures grown at temperatures higher than 430 °C the stabilization of the ZnMgSSe layers occurs. A longitudinal e-beam pumped blue (wavelength 458 nm) laser with output of 1.5 W at pumping electron energy 42 keV and temperature 300 K is realized on these structures.

Introduction

For realizing a blue laser on a low-dimensional structure with ZnSe quantum well (QW) a wide bandgap solid solution of ZnMgSSe with $E_g = 3$ eV may be used as a barrier. This compound is now in use as cladding layers in green injection lasers [1,2], but the problem of p-type doping of ZnMgSSe remains unsolved yet. For longitudinal optical or e-beam pumping lasers required for projection TV [3] the doping of the active layers is not needed. The main problem here becomes to get the uniform solid solution of ZnMgSSe having a wide bandgap $E_g = 3$ eV and lattice matched with the GaAs substrate, because the suitable compound comes over metastable phase region and is close to the boundary of the immiscibility and spinodal decomposition [4]. Decay of ZnMgSSe into two or more phases was observed experimentally [5,6,7].

Uncontrolled decay of the solid solution results in a considerable deterioration of characteristics of the longitudinal e-beam pumping lasers with generation of electron-hole pairs in thick ZnMgSSe barrier layers mostly. On the one hand there appear structural defects which cause nonradiative recombination of the carriers, on the other hand nonuniform potential relief is formed which prevents the carrier transport into the QW. In this work ZnMgSSe epilayers and ZnSSe/ZnMgSSe structures with QWs grown by the metal-organic vapor phase epitaxy (MOVPE) are studied. It is found that ZnMgSSe epilayers with high Mg and S contents decay, but we managed to grow stable ZnMgSSe epilayers with E_g up to 3.1 eV in the periodic ZnSe/ZnMgSSe multiquntum well (MQW) structures. On the base of these structures we realized longitudinal e-beam pumping lasers, lasing at 300 K with characteristics better than in the paper [8].

1. Experimental

ZnMgSSe epilayers and MQW structures with the number of 8 nm QWs up to 65 and period of λ/N and $\lambda/2N$ (λ is the desired laser wavelength and N is the average refractive index along the period) were grown by the MOVPE utilizing Me_2Se, Et_2S, $ZnEt_2$ and $(MeCp)_2Mg$ as precursors. The growth runs were carried out at 430–470 °C on GaAs substrates with misorientation 10 degrees from (001) plane to (111) plane. As-grown structures were studied using cathodoluminescence (CL), photoreflection, x-ray diffraction, optical and atomic force microscopy methods. The CL spectra were recorded at $T \leq 14$ K and 300 K, pumping electron energy $E_e = 3$, 10, 30 keV and current $I_e = 1$ μA and an electron beam diameter $d_e = 1$ mm. When preparing the laser target, first the dielectric mirror with the reflectance $R = 0.984$ was deposited on the structure, then the sample was glued by epoxy to a sapphire holder and the GaAs substrate was removed by selective etching. A second closed mirror containing dielectric layers and thin Al layer was deposited on the etched surface. The microcavity length was about ~ 5 μm. Active element was excited by scanning electron beam with $E_e = 30-50$ keV, $I_e = 0-2$ mA and $d_e = 25-50$ μm increasing with increasing pumping current and deceasing electron energy. The scanning rate was 4×10^5 cm/s.

2. Results and discussion

Figure 2 shows the CL spectra at $E_e = 10$ keV and $T \simeq 14$ K for a set of ZnMgSSe epilayers with various Mg and S contents and lattice period close to that of GaAs. One sees that with increasing E_g the emission spectra become broader and at $E_g > 2.9$ meV one can discriminate two or more lines. We relate this to the solid solution decay into two or more phases. The decay of solid solution into two phases is confirmed by study of the profiles of diffraction reflexes (444) and (551) recorded in the regime of $\phi - 2\theta$ scanning. In periodic ZnSe/ZnMgSSe structures with thickness ~ 5 μm neither CL spectra (Fig. 1(b)), no x-ray diffraction do not point to any decay of the solid solution. The intensity of the QW emission is of orders of magnitude higher than that of ZnMgSSe barrier what evidences the effective transport of non-equilibrium carriers into the QW. The emission lines of the ZnMgSSe barriers are about five times narrower than those of the ZnMgSSe epilayers with the same composition. We suppose that the stabilization of ZnMgSSe crystal lattice in periodic structures is a result of intrinsic strains in the plane of the substrate caused by the QWs. Another reason of the stabilization is the high growth temperature, T_g. At higher T_g the lower number of defects is formed and the defects are passivated more effectively.

The positions of the QW emission lines presented in Fig. 1(b) differ from those of calculated for the pure ZnSe QW, the QW emission wavelength being shorter for the structure with the higher Mg content in barriers. This is caused by uncontrolled

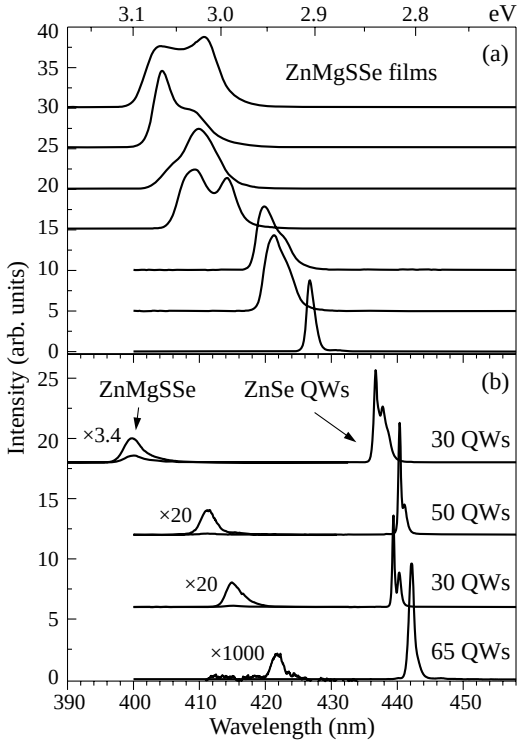

Fig. 1. CL spectra at $T = 14$ K and $E_e = 10$ keV of: (a) ZnMgSSe epilayer with thickness of ~ 2 μm; (b) 5 μm periodic ZnSe:Mg/ZnMgSSe structure with QW.

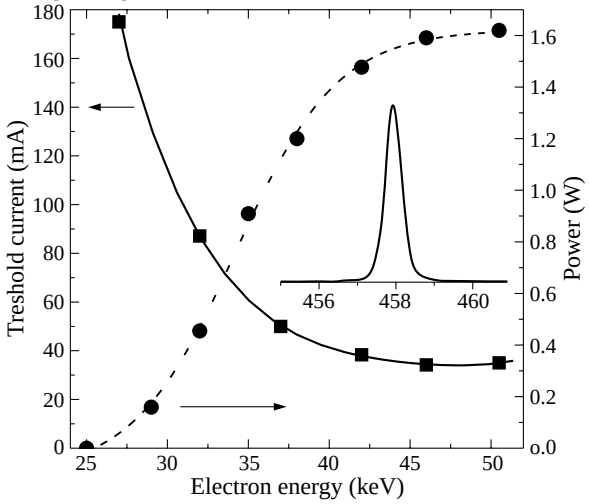

Fig. 2. Lasing threshold current and output power at pumping current $I_e = 1.8$ mA vs. pumping electron energy, E_e. Insert shows lasing spectra at $E_e = 42$ keV, $T = 300$ K and $I_e = 1.8$ mA.

Mg penetration into the QW. In spite of 15 s interruption of the growth run before and after growing of the QWs, when the QW is growing some amount of Mg goes on to enter the reactor due to desorption of the low volatile $(MeCp)_2Mg$ from cold walls of the reactor and pipelines. The larger observed shift of the QW emission was about 35 meV which corresponds to 3% of Mg in ZnSe. It is also noteworthy that the QW emission consists of two lines mostly. We relate the short wavelength line to the free exciton emission while the long wavelength one is related to exciton localized in the potential well fluctuation along the layers caused by nonuniformity of the width or composition of the QW.

3. Blue laser on periodic ZnSe/ZnMgSSe structure

Figure 2 shows the dependence of a threshold current and an output power of a laser with 30 QW on a pumping electron energy. The lasing power as much as 1.6 W was achieved at temperature 300 K (pumping power is 83 W, $E_e = 46$ keV and $I_e = 1.8$ mA) which corresponds to laser efficiency of 2%. The latter can be increased using the more transparent output mirror. The lowest threshold current was 35 μA that is current density 7 A/cm^2. Insert in Fig. 2 shows the lasing spectra consisting of one longitudinal mode at wavelength 458 nm. In some structures lasing was observed at two close mode separated by 5–6 nm. In this case the maximum of an optical gain is located between the lasing modes. A far-field pattern of the laser is circular symmetric with a central spot with a total divergence angle of about 10 degrees and one ring at angle of 150 degrees containing about 10% of the whole output power.

Acknowledgements

This work was supported by RFBR(grants 05-02-16390, 07-02-01139) Program "Scientific Schools", Grant 6055.2006.2, by RAS Programs "Coherent optical radiation of semiconductor compounds and lasers", "New materials and structures" and Principia LightWorks Inc., CA.

References

[1] S. Itoch *et al*, *J. Crystal Growth* **214/215**, 1029 (2000).
[2] D. C. Grillo *et al*, *Electron. Lett.* **30**, 2131 (1994).
[3] M. D. Tiberi and V. I. Kozlovsky, *Proceedings of SPIE* **5740**, 60 (2005).
[4] V. S. Sorokin *et al*, *J. Crystal Growth* **214/215**, 130 (2000).
[5] B. J. Wu *et al*, *Appl. Phys. Lett.* **66**, 3462 (1995).
[6] G. C. Hua *et al*, *J. Crystal Growth* **138**, 367 (1994).
[7] I. P. Kazakov *et al*, *Proc. 13th Int. Symp. Nanostr.: Physics and Technology* St Petersburg, Russia, 114 (2005).
[8] V. Yu. Bondarev *et al*, *Phys. Stat. Sol. (c)* **2/2**, 935 (2005).

15th Int. Symp. "Nanostructures: Physics and Technology"
Novosibirsk, Russia, June 25–29, 2007

The multi-wavelength interband two-cascade laser with tunnel junction

A. A. Dubinov[1], V. Ya. Aleshkin[1], A. A. Belyanin[2], A. A. Biryukov[3], P. B. Demina[3], V. I. Gavrilenko[1], V. V. Kocharovsky[2,4], Vl. V. Kocharovsky[4], K. V. Maremyanin[1], S. V. Morozov[1], S. M. Nekorkin[3], N. N. Semenov[3] and B. N. Zvonkov[3]

[1] Institute for Physics of Microstructures RAS, 603950, Nizhny Novgorod, Russia
[2] Department of Physics, Texas A&M University, College Station, TX 77843-4242, USA
[3] Research Physical-Technical Institute of the Nizhny Novgorod State University, 603950, Nizhny Novgorod, Russia
[4] Institute of Applied Physics RAS, 603950, Nizhny Novgorod, Russia

Abstract. The multi-wavelength generation in a new class of injection heterolasers — interband two-cascade laser with a tunnel junction, which separates two active regions of quantum wells in one waveguide, is fabricated and investigated. The fabricated laser oscillator with pulsed injection demonstrates simultaneous generation of a couple of the first-order modes at wavelengths 1.063 μm and 0.98 μm, and a couple of the third-order modes at wavelengths 0.951 μm and 0.894 μm. The second and sum frequency generation is observed due to nonlinear mode mixing in the laser cavity.

Introduction

Recently there has been growing interest in the development of multi-wavelength semiconductor lasers, with potential applications including multi-wavelength spectroscopy, broadly tunable sources, ultrashort pulse generation, and intracavity nonlinear frequency up- and down-conversion [1]. The simplest approach to a multi-wavelength laser diode would be to place two quantum-well (QW) stacks with different energies of ground-state interband transitions into the two active region. Unfortunately, multi-wavelength lasing can be unstable in this case because lasing processes in two active regions compete for the same carriers and higher-frequency radiation gets absorbed in the QWs with narrower band gap. One promising way to solve these problems is to insert a narrow, strongly doped tunnel-junction layer between the two active regions. As a result, we have essentially a cascade laser, in which current flows through each active region in series [1], similarly to mid/far-infrared intersubband quantum cascade lasers and type-II interband cascade lasers. Each injected carrier undergoes some optical interband transitions: in the first and then in the second active region, emitting a some photons at different energies. Note that tunnel-junction based cascade lasers and LEDs of this type emitting one frequency [2] or two frequencies [3] into a fundamental waveguide mode were proposed and demonstrated before, with the goal of improving the laser output power and current efficiency. The tunnel-junction design eliminates electric competition between two active regions but the problem of the optical cross-absorption remains. When two active regions have different interband transition energies, generation of the fundamental mode for some frequencies is suppressed because a higher-frequency modes experience strong resonant absorption in the active region for a lower-frequency radiation. Therefore, the waveguide should be designed to accommodate a low-loss higher-order transverse mode at a higher frequencies. Such a mode will have a node at the position of the narrow-gap active region. Next, to reduce absorption it is desirable to minimize the overlap of both modes with a strongly doped tunnel junction. In this work we report demonstration of such a tunnel junction multi-wavelength cascade laser implemented in the InGaP/GaAs/InGaAs material system following the above design guidelines. The goal was to demonstrate multi-wavelength generation of the different order modes and nonlinear mixing of this modes due the quadratic nonlinearity of GaAs.

1. The laser structure

The structures are grown by MOCVD on n-GaAs substrates with doping concentration of 10^{18} cm^{-3}. A compound active region of total thickness of 1.5 μm consists of two $p-n$ junctions separated by thin tunnel $p-n$ junction. Waveguide cladding is formed by a 0.78 μm n-InGaP bottom layer and 0.78 μm p-InGaP top layer. Layer sequence from the top of the substrate includes n-InGaP cladding layer 0.78 μm, i-GaAs 300 nm, $In_{0.28}Ga_{0.72}As$ 10 nm QW for a long-wavelength laser, i-GaAs 115 nm, p^+-GaAs 300 nm, p^{++}-GaAs 40 nm, n^{++}-GaAs 55 nm, n^+-GaAs 300 nm, i-GaAs 300 nm, $In_{0.14}Ga_{0.86}As$ 10 nm QW for a short-wavelength laser, i-GaAs 90 nm, n-InGaP cladding 0.78 μm, p^{++}-GaAs 300 nm, and Au contact. For lateral current confinement in the growth plane the structure is implanted by 80 keV hydrogen ions to form 100 μm wide strips. Cavities were cleaved to lengths of 0.4–1.5 mm. Waveguide design and the positions of QWs and the tunnel junction were chosen to support generation of the first order TE_1 mode at the lower frequencies and the third order TE_3 mode at the higher frequencies.

2. The measuring results

We have measured IV characteristics, spectra, and radiation patterns of the devices pumped by 350 ns pulses of current varying from several to several tens of A with 1.6 kHz repetition rate at room temperature. Typical spectra for two different currents are shown in Fig. 1(a). We observed lasing at two wavelengths $\lambda_1 = 0.951$ μm and $\lambda_2 = 1.063$ μm, corresponding to interband transitions between ground states in two active regions, and the components at $\lambda_3 = 0.894$ μm and $\lambda_4 = 0.98$ μm, which corresponds to the transitions between first excited states in smaller and deeper QWs with smaller and higher In fraction correspondingly. Relative strengths of these

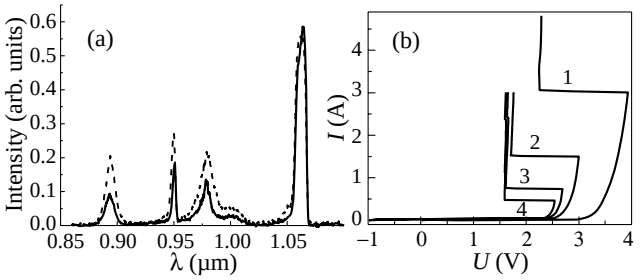

Fig. 1. (a) Laser generation spectra at 45 A (solid curve) and 60 A (dashed curve) currents under the pulsed pumping. The cavity length is 1 mm. Threshold current for lasing at wavelengths (μm) 0.951, 1.063, 0.894, 0.98 is 25, 10, 30, 15 A, correspondingly. (b) Typical IV characteristics of the laser for some temperatures, K: 1 — 77, 2 — 233, 3 — 273, 4 — 303.

lines depend on the cavity length. For example, in 1.5-mm cavity the lasing at λ_2 dominated, while in a 0.4-mm cavity the line at wavelength λ_1 was the strongest one.

IV characteristics (Fig. 1(b)) obtained in the continuous-wave regime show current switching and the appearance of the S-shaped negative differential resistance region at a voltage corresponding to the double band gap energy in GaAs. This is an indication of injection of the minority carriers into the tunnel junction, which sharply reduces the voltage drop across the junction and leads to the decline of laser radiation intensity. The instability does not show up when the pumping is pulsed. One probable reason for that is that capacitors formed by $p-n$ junctions do not have time to recharge during the current pulse, so the instability cannot develop.

To identify the transverse modes involved in generation we measured radiation patterns for all wavelengths. Fig. 2 illustrates radiation pattern for the short-wavelength radiation at $\lambda_1 = 0.951$ μm. The position and relative strengths of the four maxima observed in the plane perpendicular to the growth plane agree well with calculated far-field distribution for the third-order TE_3 mode. In Fig. 2 the far-field pattern for the longer-wavelength radiation at $\lambda_2 = 1.063$ μm is shown too. The two-peaked distribution is in agreement with the first order TE_1 mode. Similar far-field distribution is observed for the modes at $\lambda_3 = 0.894$ μm and $\lambda_4 = 0.98$ μm, also indicating the TE_3 and TE_1 modes correspondingly. Lateral far-field distributions in the growth plane are the same as in standard broad-area diode lasers of 100 μm width [4]. They have one maximum with approximately 10 degree half-width for all wavelengths.

We may conclude that there is an excellent agreement between the designed and observed device parameters, which proves that a high degree of control can be achieved for these rather sophisticated devices by standard growth and fabrication technique.

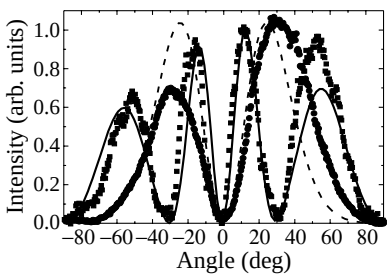

Fig. 2. Calculated (solid curve for 0.951 μm, dashed curve for 1.063 μm) and measured (squares for 0.951 μm, circle for 1.063 μm) far field patterns of radiation in the plane transverse to the growth plane.

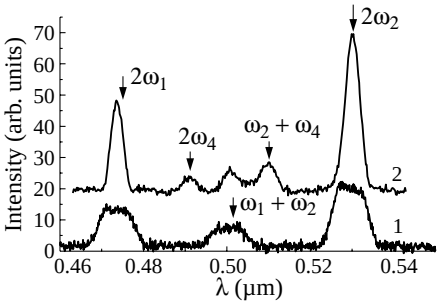

Fig. 3. Measured spectra of second-harmonic and sum-frequency radiation at two currents of 20 and 35 A. Frequencies ω_i correspond to wavelengths λ_i.

To check the feasibility of the nonlinear mode mixing we measured radiation at sum frequencies and second harmonics. The results are presented in Fig. 3. In agreement with the fundamental laser spectra shown in Fig. 1(a), at lower currents we observe second harmonics and the sum frequency radiation of laser modes at wavelengths λ_1 and λ_2. At higher currents two additional lines appear that correspond to the second harmonic of laser mode at wavelength λ_4 and sum-frequency radiation of modes at λ_2 and λ_4. Note that radiation at wavelength λ_2 and λ_4 is generated by the same QW. Our observations demonstrate feasibility of intracavity mixing of several wavelengths generated by the common active region in the diode lasers.

In conclusion, we demonstrated for the first time the multi-wavelength generation and intracavity nonlinear mode mixing in the new type of diode lasers: a cascade laser with the tunnel junction separating two different QW active regions integrated within the same waveguide. Our waveguide design eliminates or greatly reduces electrical and optical competition between laser modes at different frequencies and supports low-loss modes at all wavelengths.

Acknowledgements

This work has been supported by CRDF (RUE1-2657-NN-05), AFOSR, NSF, the Research Corporation, RFBR (06-02-81020, 07-02-00486), the RAS "Coherent optical emission of semiconductor materials and structures" Program, the Russian President (MK-3344.2007.2), the Russian Ministry of Education (BRHE, REC-NN-001, #Y1-P-01-06), NATO (SfP-973799 Semiconductors).

References

[1] A. A. Belyanin *et al*, *Physics-Uspekhi* **46**, 986 (2003).
[2] K. Kim *et al*, *Appl. Phys. Lett.* **74**, 3251 (1999).
[3] Ch. Garcia *et al*, *Appl. Phys. Lett.* **71**, 3752 (1997).
[4] H. C. Casey and M. B. Panish, *Heterostructures Lasers*, (Academic Press, New York) 95 (1978).

15th Int. Symp. "Nanostructures: Physics and Technology"
Novosibirsk, Russia, June 25–29, 2007

New effective scheme for frequency down conversion to mid IR in optically pumped heterolasers

A. A. Andronov[1], Yu. N. Nozdrin[1], A. V. Okomel'kov[1], A. A. Babenko[2], D. G. Ikusov[2], R. N. Smirnov[2] and V. S. Varavin[2]

[1] Institute for Physics of Microstructures, RAS, Nizhny Novgorod GSP-105 603600, Russia
[2] Institute for Physics of Semiconductors, Siberian Division of RAS, Novosibirsk, Russia

Abstract. New approach for effective generation of tunable mid IR radiation via down conversion in optically pumped heterolaser structures is put forward and demonstrated. In the approach both difference frequency $\Omega_D = \omega_p - \omega_L$ and combination frequency $\Omega_C = 2\omega_L - \omega_p$ (ω_p is the pump frequency while ω_L is the laser frequency) can be generated with close efficiency. The heterolaser transition serve as resonant (at the transition) quadratic nonlinear medium while phase matching conditions can be easily fulfilled due to 2-d nature of the harmonic generation of the traveling wave antenna type. All inversion symmetry less zinc-blende heterolaser systems: double heterostructure, quantum well and quantum dot based could be used in the approach. We demonstrate the approach with a set of HgCdTe double heterostructure laser structures under Nd: YAG laser pump at 1.06 microns. We consider this approach as promising universal way to fabricate wide band tunable room temperature source of mid IR and THz radiation.

Introduction

Simple and cheap wide band tunable sources of mid IR and THz radiation working at room temperature are needed for a number of applications. In recent years substantial progress was made in this direction as a result of development in the Quantum Cascade Lasers. However the lasers are still quite expensive and have other drawback (e.g. narrow band tunability). And the problem is still unresolved. Another approach to fabricate the sources is based on parametric generation with down-conversion from optical or IR laser to mid IR. But in this approach one should find out a medium which has low losses, high non linearity and phase matching condition. Here only systems based on powerful pulsed solid state lasers are eventually available now [1]. Seems we came across [2] a way for parametric generation which permit to produce combination frequency generation in standard semiconductor heterolaser structures.

1. Outline of the approach

To simplify discussion consider equivalent inversion symmetry free (nonsymmetrical) two level system. In this case main contribution to the quadric nonlinear coefficient α of polarization $P_N = \alpha E^2$, E is electric field consisting of the fields with frequencies ω_B and ω_A, can be written as:

$$\alpha = \frac{e^3(N1 - N2)x_{12}^2\delta_{12}}{\varepsilon_0\hbar^2(\omega_A - \omega_{12} - i\nu)(\omega_B - \omega_A - \omega_{12} - i\nu)}.$$

Here $\delta_{12} = x_{22} - x_{11}$, $N_{1,2}$ are the level populations, ν is the transition width, x_{ij} are coordinate matrix elements; $\delta_{12} \neq 0$ if the system has no inversion symmetry.

In our approach we propose [2]:

1. To use resonant condition: $\omega_A = \omega_L = \omega_{12}$. In this case $\alpha^R = \alpha_0(\omega_A/\nu) \approx (10{-}50{-}100)\alpha_0$, α_0 is the non resonant coefficient. Usually resonant conditions are accompanied by losses. But in our case there is resonant laser field produced by pump and there is no such problem.

2. The second important feature in our approach is easiness to fulfill phase-matching conditions. Simplified picture of fields both lasing mode and pump is shown in Fig. 1(b). Because the pump is an exponent, phase matching along z-axis is absent. Now we immediately have the condition for effective emission at difference frequency by the P_N: phase velocity of the polarization wave V_P should be higher than phase velocity at difference frequency V_{ph}: $V_P > V_{ph}$. This condition can be easily fulfilled.

3. The third feature of our approach is employment of *cascade cubic* nonlinearity (originated from quadratic nonlinearity) to get effective emission at combination frequency Ω_C. As a result for the cubic nonlinearity when $P_N = \beta E^3$ coefficient $\beta \propto \alpha^2$ and under resonant conditions is high. Cascade nonlinearity is well known in nonlinear optics. But to the best of our knowledge none propose to employ it for down conversion in semiconductor.

For combination frequency down conversion the phase matching condition discussed above are even more easily satisfied than the one for difference frequency conversion because of two laser fields involved. For example for two contra propagating laser fields (standing wave) vertical pump can give vertical combination frequency emission.

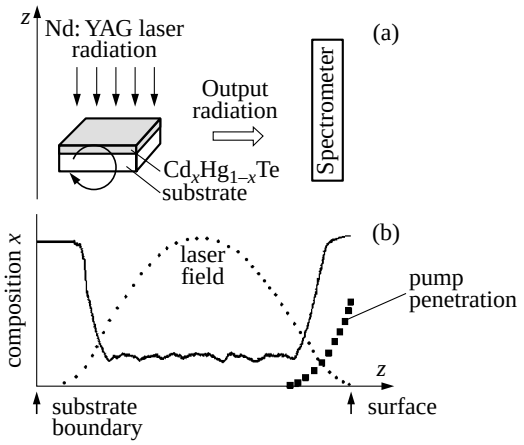

Fig. 1. (a) Observation set up. (b) Composition x across a structure and scheme of lasing mode and pump field.

2. Difference and combination frequencies generation in HgCdTe optically pumped double heterostructure laser structures

Double $HgCd_xTe_{1-x}$ (MCT) heterostructures were grown by MBE on GaAs and Si substrates (for details see [3]). Initially they there grown for mid IR detector fabrication. The heterostructures are waveguides for emerging laser and harmonic radiation. Fig. 1 give the experimental scheme for stimulated emission and harmonics observation and qualitative picture of composition x variation across the structure. Low x gives low bandgap. Photoluminescence from un-patterned (as grown) structures under pulsed excitation by Nd: YAG laser was studied. There is some overlapping of the laser mode and the pump in low x (narrow bandgap) region that provide harmonics generation. At pump perpendicular to the structure surface and emission observation in the structure plane (only results found in this case are discussed here) we observe spontaneous emission and above the threshold stimulated emission (super-luminescence). In this geometry only the combination harmonics are observed. Both the stimulated and spontaneous emission produce the combination harmonics radiation proving efficiency of the down conversion in the scheme. Figures 2–4 give example of observed emissions spectra for different heterostructures with stimulated emissions (MCT) and combination harmonics shown. All observed features can be qualitatively explained by the discussed above picture.

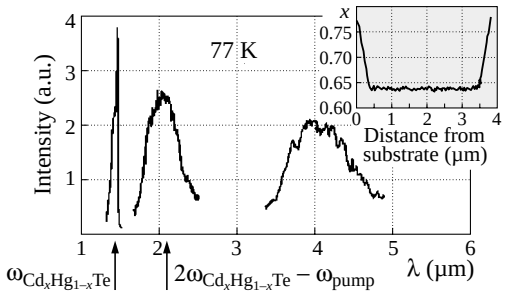

Fig. 2.

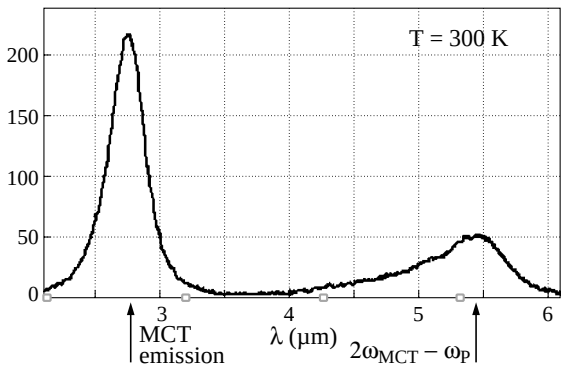

Fig. 3.

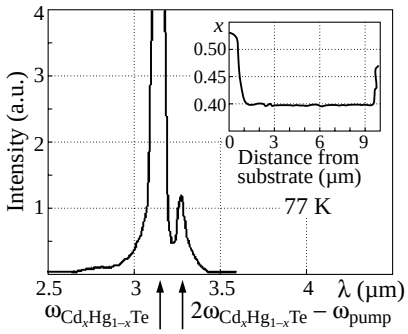

Fig. 4.

3. Conclusions

We propose and demonstrate new approach for down conversion from IR laser radiation to mid IR. It seems likely that the most promising is the combination frequency conversion which can easily provide high efficiency of the conversion with vertical narrow output beam.

We also started investigation of similar conversion effects in heterostructures based on other material system including ones with quantum wells and quantum dots.

Also a lot of questions emerge. That is final (limiting) efficiency of the conversion? Does the Manly–Row condition holds in this, active, scheme? That are selection rules of the quadratic nonlinear coefficient in quantum structures? Is HgCdTe material of choice for the conversion? In that heterostructure the highest conversion efficiency should occur? How the above discussion is changed due to saturation effect in the laser system?

Acknowledgements

The authors are indebted to V. V. Kurin and M. A. Novikov for stimulating discussion of cascade cubic nonlinearity. The work was supported by the Russian Foundation of Basic Research (Grants 06-02-16685 and 07-02-00935) and the Russian Academy of Sciences Program “Problems of Radiophysics”.

References

[1] T. Tanabe, K. Suto, J. Nishizawa, K. Saito and T. Kimuta, *Appl. Phys. Letters* **83**, (2), 237–239 (2003).

[2] A. A. Andronov, Yu. N. Nozdrin, A. V. Okomel’kov, A. A. Babenko, D. G. Ikusov, R. N. Smirnov and V. S. Varavin, *Vestnik NNSU “Radiophysics”* **1**, 39 (2007).

[3] A. A. Andronov, Yu. N. Nozdrin, A. V. Okomel’kov, A. A. Babenko, D. G. Ikusov, R. N. Smirnov and V. S. Varavin, *Fiz. i Tech. Polupr*, **40**, (11) 1300–1309 (2006).

15th Int. Symp. “Nanostructures: Physics and Technology”
Novosibirsk, Russia, June 25–29, 2007

Pulsed difference-frequency generation in two-color nonlinear mixing heterolasers

V. A. Kukushkin[1], V. Ya. Aleshkin[2], A. A. Belyanin[3], A. A. Dubinov[2], V. V. Kocharovsky[1,3], Vl. V. Kocharovsky[1] and M. O. Scully[3,4]

[1] Institute of Applied Physics of RAS, 46 Ulyanov st., 603950 Nizhny Novgorod, Russia
[2] Institute for Physics of Microstructures of RAS, GSP-105, 603950 Nizhny Novgorod, Russia
[3] Physics Department and Institute for Quantum Studies, Texas A&M University, College Station, TX 77843, USA
[4] Applied Physics Group, Dept. of Mech. & Aerospace Eng. and PRISM, Princeton Univ., Princeton, NJ 08544, USA

Abstract. Mid/far infrared (IR) and terahertz (THz) pulse generation in quantum-well (QW) mode-locked dual-wavelength heterolasers is proposed. The long-wavelength field is produced in the process of intracavity difference-frequency mixing of two lasing near infrared fields due to both the resonant intersubband nonlinearity in QWs and the non-resonant second-order bulk nonlinearity. Estimates show that this method of IR or THz generation at room temperature is capable of producing picosecond pulses at $\sim$1 GHz repetition rate with a peak power $\sim$1 W and $\lesssim$0.2 mW at 10 μm and at 50 μm wavelengths, respectively.

Introduction

The generation of mid- to far-infrared (IR) and terahertz (THz) powerful short pulses poses now a field of intensive research due to increasing need of intense coherent emission in this frequency range both for fundamental science and various applications. There are many different techniques to produce IR or THz radiation, but a well-known nonlinear optical process of difference-frequency mixing of strong driving fields remains one of the most efficient and promising ways for obtaining coherent pulsed radiation in this wavelength domain. The corresponding schemes are divided roughly into two categories.

The first of them involves difference-frequency mixing of Fourier components of an external near-infrared laser pulse (optical rectification) in second-order nonlinear media [1] and quantum well (QW) heterostructures [2] or nonlinear interaction of two external laser fields in QWs [3]. Unfortunately, these methods as a rule have a rather low down conversion efficiency, in particular because of strong pump depletion via one or multi-photon absorption.

The second is based on intracavity mixing of laser modes in semiconductor lasers [4]. Such devices do not suffer from the above mentioned pump depletion since it is mitigated by laser gain, have excellent and controllable modal overlap and can work at room temperature in CW regime, as opposed to THz quantumm cascade lasers that require cryogenic cooling. In addition, intracavity mixing devices can be pumped by current injection, which makes corresponding IR and THz sources much cheaper and more compact than those with external beam pumping. Current pumping, however, has also a negative outcome as it leads to a high free-carrier density in the active region and, as a consequence, strong IR and THz field absorption which rapidly increases with growing wavelength. Being added to diffraction leakage and modal overlap which both deteriorate with increasing wavelength, this circumstance makes the typical nonlinear conversion efficiency in such devices rather low.

In the present paper we consider pulsed intracavity difference-frequency generation (DFG), when one or both near-infrared lasing fields are generated in the mode-locking regime. This obviously enhances all nonlinear effects and can potentially provide higher peak output power of the IR or THz radiation as compared to the CW regime (for the latter see, e.g., [5]). Moreover, in the case of both near-infrared fields being generated in the mode-locking regime, this can enhance an average DFG power as well.

1. Model of a quantum well heterolaser

As an example, let us consider a $Al_xGa_{1-x}As$ QW heterostructure consisting of two adjacent wells made of two 5–8 nm thin layers separated by a thin spacer ($\sim$30 nm) and incorporated into a core of an AlGaAs and plasmon waveguide [6]. We shall consider a simple structure with one heavy-hole (1) and two electron (2 and 3) states in the left asymmetric QW and one hole (4) and one electron (5) state in the right one so that the transition $3 \to 1$ is resonant to $5 \to 4$ one (Fig. 1). Of course, all the following consideration can be easily suited for the situation when two hole and one electron levels in the left QW are used. The interband transitions correspond to $\lambda_{1,2} \sim 1$ μm whereas intersubband transitions lie at $\lambda_3 \sim 10-70$ μm for electronic states and even at higher wavelengths $\lambda_3 \gtrsim 70$ μm

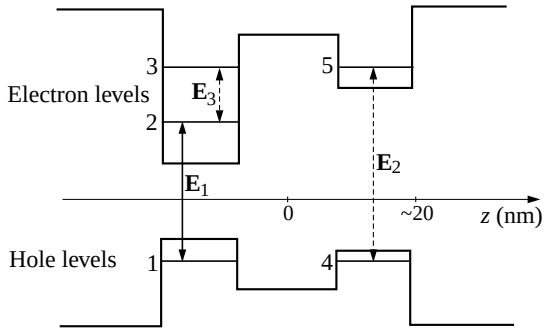

Fig. 1. The scheme of electron (hole) levels and transitions involved in the IR or THz pulse generation in a QW heterolaser. In the process of the nonlinear difference-frequency mixing, strong CW or pulsed $\mathbf{E}_1$ and pulsed $\mathbf{E}_2$ near-infrared fields (typically TE modes) generated in the left and right QW respectively produce a weak pulsed IR or THz field $\mathbf{E}_3$ (typically TM mode), which is in resonance with the intraband transition $3 \to 2$.

for hole ones [4]. It is well-known that for asymmetric QWs all four transitions $2 \to 1$, $3 \to 2$, $3 \to 1$, $5 \to 4$ can have large matrix elements of $\sim 0.3-1$ nm in the near-IR range and $\sim 1-5$ nm in the IR and THz one [3].

Two near-infrared fields $\mathbf{E}_1$, $\mathbf{E}_2$ with central frequencies ω_1, ω_2 and longitudinal wavenumbers k_1, k_2 are generated in the left and right QWs at $2 \to 1$ and $5 \to 4$ transitions in the CW or mode-locking and mode-locking regimes, respectively, with injection current pumping providing the necessary inversion. Due to resonant coupling on the $3 \to 2$ transition in the left QW and non-resonant interaction through second-order semiconductor bulk nonlinearity these fields create pulses of long-wavelength (IR or THz) polarization with the central longitudinal wavenumber $k_3 = k_2 - k_1$ and frequency $\omega_3 = \omega_2 - \omega_1$. This polarization, in turn, produces an IR or THz electromagnetic pulsed field $\mathbf{E}_3$ via excitation of corresponding cavity modes. The efficiency of this process depends on the closeness of ω_3 to the real part, ω'_k, of the cavity mode frequency with longitudinal wavenumber $k = k_3$. Such phase-matching requires a special waveguide design [6] which can be implemented both by adjusting its geometrical parameters and changing the long-wavelength refractive index by slight additional doping.

2. Power estimates and methods for further increase of the IR or THz signal power

For power estimates of the output long-wavelength radiation we consider a particular example of an IR or THz signal excited by two near-infrared fields both generated in the mode-locking regime [5] and having wavelengths ~ 1 μm typical for $Al_xGa_{1-x}As$ heterostructures. We assume the non-resonant long-wavelength losses to be ~ 100 cm^{-1}, the homogeneous line width $\sim 10^{13}$ s^{-1}, the matrix element for the $3 \to 2$ transition ~ 2 nm, and the output mirror transmission coefficients nearly the same and equal to 0.4. Taking for the output peak powers of the near-infrared fields a value of ~ 24 W for a waveguiding structure with ~ 10 μm width and ~ 0.2 μm confining layer height, we obtain for the output long-wavelength peak power an estimate of 2.6 W (an average power of 13 mW at 1 GHz repetition rate) at $\lambda_3 = 10$ μm, 0.2 mW (an average power of 1 μW) at $\lambda_3 = 50$ μ and ~ 7.4 μW (an average power of 37 nW) at $\lambda_3 = 120$ μm. These values comprise the contributions from both resonant intersubband nonlinearity and non-resonant second-order bulk nonlinearity with the second being, however, much smaller than the first.

The IR or THz pulse duration under strong absorption conditions is obviously determined by the lasting of the near-infrared pulses and is of the order of several ps [5]. The slight difference in group velocities of the driving pulses (which corresponds to their relative shift by approximately half the pulse duration after their trip from one mirror to another) can be compensated by employing at one end of the cavity a Bragg mirror with varying period or a Bragg mirror for just one near-infrared frequency so that the signal with a larger group velocity should be reflected from its deeper layers or from the crystal facet and therefore pass a longer distance.

It is interesting to note that though the linear absorption of the long-wavelength field is greatly enhanced near the transverse optical phonon frequency (which corresponds to $\simeq 35$ μm for GaAs), the second-order nonlinear coefficient also rises rapidly near this point [7]. As a result, the power of the generated difference-frequency field may substantially increase near the phonon resonance frequency.

Finally, let us mention that there are two possible ways for the produced IR or THz field to be radiated from a heterostructure. First of them is a traditional method employing edge-emitting geometry and transmitting mirrors. In this case IR/THz signal is radiated only during short periods of time when the long-wavelength field pulse is near one of the mirrors. For all the other time IR or THz energy is confined in the waveguiding structure and does not give any contribution to the output radiation.

Another method employs Surface-Emitting Grating-Outcoupled Lasers (SEGOLs) [7, 8] which use a metallic or dielectric diffraction grating placed on top of the heterostructure waveguide. This grating changes the IR or THz radiation modes from edge-emitting to surface-emitting in a certain direction, i.e. provides phase-matching of a nonlinear driving polarization (that is coupled to an IR or THz mode inside a heterostructure, whose phase velocity is determined by the grating period) and an IR or THz mode in vacuum (air). Namely, if IR or THz radiation pattern with an anglewidth $\delta\phi$ is directed by grating almost perpendicular to the surface of a heterostructure, then the regime is CW, and if there is a large enough angle $\phi > \delta\phi$ between the IR or THz radiation beam and vertical axis, then during one half of the round-trip time the driving near-infrared pulses generate IR or THz radiation at the angle ϕ and during the other half of the round-trip, on the way back, they generate IR or THz radiation at the angle $-\phi$. Such SEGOLs seem to be rather promising and efficient for IR or THz generation since strong absorption and small nonlinear mode overlap are not the problems anymore in this scheme.

Acknowledgements

This research was supported by awards from AFOSR (FA-9550-05-1-0360, FA-9550-06-1-0338), NSF (ECS-0501537, EEC-0540832, OISE 0530220, ECS-0547019), the Research Corporation (RI0986), CRDF (RUE1-2657-NN-05), ISTC (2293), Presidium RAS (Programs "Low-dimensional quantum structures", "Electromagnetic waves of the THz range"), Department of Physical Sciences of RAS (Programs "Semiconductor Lasers", "Coherent Optical Emission of Semiconductor Materials and Structures"), RFBR (05-02-17525, 07-02-00486, 06-02-81020b), the Council for support of the leading scientific schools in Russia (4588.2006.2) and the President of Russia (MC-3344.2007.2).

References

[1] Y. R. Shen, *The principles of Nonlinear Optics*, J. Wiley & Sons, New York, Toronto 1984.
[2] A. A. Belyanin *et al*, *J. Modern Optics* **51**, 2523 (2004).
[3] E. Kapon, ed., *Semiconductor Lasers*, Academic Press, San Diego, USA 1999.
[4] A. A. Belyanin *et al*, *Phys. Rev. A* **63**, 053803 (2001).
[5] P. J. Delfyett, *Ultrafast Single- and Multiwavelength Mode-locked Semiconductor Lasers: Physics and Applications* in *Ultrafast lasers: Technology and Applications*, ed. by M. Fermann *et al*, Marcel Dekker, Inc, New York, USA 2001.
[6] V. Berger *et al*, *Semicond. Sci. Technol.* **19**, 964 (2004).
[7] A. A. Afonenko *et al*, *Semicond. Sci. Technol.* **20**, 357 (2005).
[8] A. A. Aleshkin *et al*, *Proc. SPIE (ICONO 2005)* **6257**, 6257OI-1-8, Bellingham, WA, USA 2006.

15th Int. Symp. "Nanostructures: Physics and Technology"
Novosibirsk, Russia, June 25–29, 2007

Difference frequency radiation from dual-wavelength vertical external-cavity surface-emitting laser

Yu. A. Morozov[1], T. Leinonen[2], M. Pessa[2], V. V. Popov[1] and M. Yu. Morozov[3]

[1] Institute of RadioEngineering and Electronics of Russian Academy of Sciences,
38, Zelyonaya Str., Saratov, 410019, Russia
[2] Optoelectronics Research Center, Tampere University of Technology, P.O. Box 692, 33101 Tampere, Finland
[3] Saratov State University, 83, Astrakhanskaya Str., Saratov, 410026, Russia

Abstract. Nonlinear optical interaction accompanied by difference frequency generation in the mid-infrared range (~ 17.7 μm) is simulated for the two-color vertical external-cavity surface-emitting laser (VECSEL). The nonlinear isotropic crystal is placed inside of the microcavity tuned to the difference frequency. The efficiency of frequency down conversion is shown to have a multi-resonance-like behavior. The peak values of optical mid-infrared power are in the order of milliwatt for pump and laser parameters which may be easily available in the experiments.

Introduction

Today, quantum-cascade lasers (QCLs) are considered to be at the leading position among semiconductor mid- and far-infrared lasers [1]. However, a wide application of QCLs is restricted by certain of their features. Among those features one could pick out both the fundamental ones preventing the room-temperature continuous-wave operation at long wavelengths ($\lambda > 10$ μm) and the technical ones because of active region complexity.

Therefore, an analysis of alternative approaches to mid- and far-infrared wave generation is indeed of great importance [2]. Three-wave nonlinear interaction accompanied by difference frequency radiation within above mentioned ranges is one of these attractive approaches. To achieve a frequency down conversion, it is desirable to have a laser emitting at two wavelengths simultaneously. Most optimal device would emit both coaxial beams with high enough power and have an external cavity to put a nonlinear crystal.

Recently, the two-color optically pumped VECSEL with near optimal operation characteristics was demonstrated by our group for the first time [3]. We obtained single transverse mode continuous-wave (CW) operation at the wavelength of 984 and 1042 nm with an efficiency of 10 percents. The external cavity of the device admits to a nonlinear crystal to be placed. The wavelength corresponding to the difference frequency generation is about 17 μm for our VECSEL. Since most of the usual nonlinear materials (KDP, ADP, lithium niobate, etc.) absorb strongly above 5 μm, they could not be applied to nonlinear conversion in that range [4]. On the other hand, semiconductor of the main technological stream (GaAs, InP) are excellent candidates for the optical frequency conversion because of their high nonlinear susceptibility and superior transparency over 1–18 μm. However, these materials are isotropic so that the ordinary methods based on birefringence to achieve phase-matching are not available.

An efficiency of nonlinear interaction in isotropic crystals could be enhanced with an application of so-called quasiphase matching technique. One of the idea's variety initially proposed in the pioneer paper [5] and developed in [6] consists in using of a nonlinear microcavity tuned to a difference frequency.

This paper is devoted to the analysis of three-wave interaction in the nonlinear microcavity located in the external cavity of novel dual-wavelength VECSEL [3].

1. Design of laser structure

Fig. 1 shows the band diagram for the laser structure which is designed for dual-wavelength operation [3,7]. The active region is divided into three sections by 15 nm blocking layers. Sections I and III contain two 8 nm quantum wells, each made of $In_{0.17}Ga_{0.83}As$ (QW_S) emitting at the wavelength of λ_S. Four 8 nm quantum wells of $In_{0.23}Ga_{0.77}As$ (QW_L) with maximal gain at $\lambda_L > \lambda_S$ are located in Section II. To enhance the achievable gain coefficient, all the quantum wells are placed at the antinodes of their own standing waves, i.e., $QW_{L,S}$ location corresponds to the standing wave at $\lambda_{L,S}$. On the other hand, QW_L's are near the nodes of the cavity mode of λ_S to minimize optical absorption of short-wavelength emission in the deeper quantum wells. It should be particularly noted that the stationary dual-wavelength oscillation is achievable only if interaction of optical fields at both wavelengths is minimal [7].

The blocking layers, made of wide bandgap AlAs, are transparent to the pump light and laser emission, but impenetrable for charge carriers. Therefore, nearly equal pumping of the QWs is possible. The blocking layers are really of great importance. Without the blocking layers the deeper quantum wells

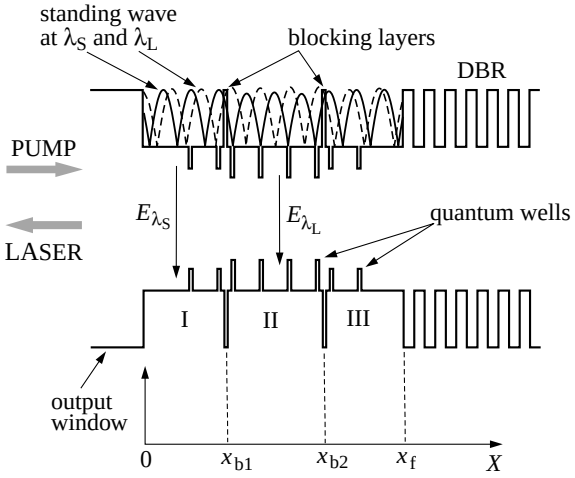

Fig. 1. Band diagram and the standing waves λ_S and λ_L for a dual-wavelength VECSEL.

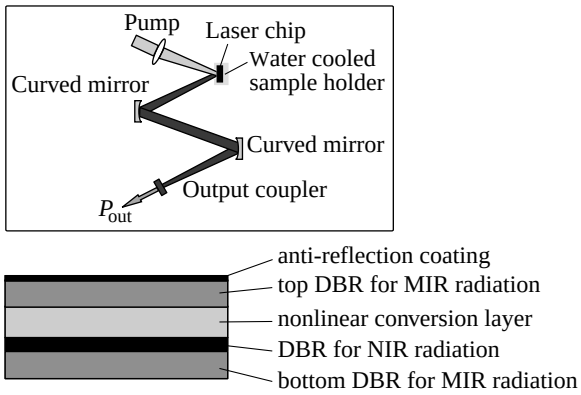

Fig. 2. Nonlinear microcavity with the output coupler. Inset: the schematic view of the VECSEL.

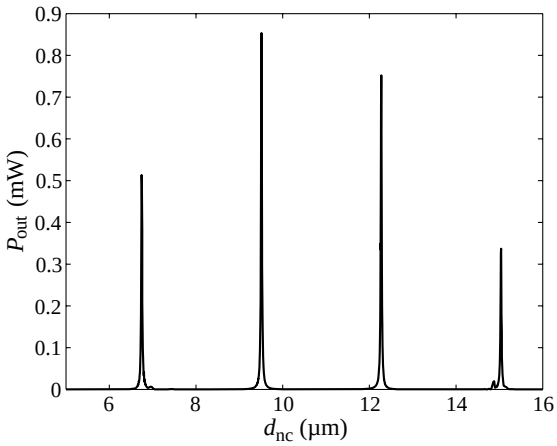

Fig. 3. Output power at the difference frequency vs. the width of nonlinear conversion layer.

would become more densely populated than the shallow QWs because of their longer carrier escape time and shorter capture time [8]. This would ultimately lead to lasing only at the longer wavelength.

The distributed Bragg reflector (DBR), made of alternating GaAs and AlAs layers, and the output window layer of $Al_{0.3}Ga_{0.7}As$ are actually the same as those of conventional VECSEL at these wavelengths.

2. Analysis of nonlinear interaction

To calculate the field distribution and the geometry of the device, we have solved the boundary eigenvalue problem for the Helmholtz equation within the one-dimensional transfer matrix approach (see [7] for more detail).

Schematic view of the nonlinear microcavity combined with the output coupler is shown in Fig. 2. (The inset displays the scheme of the VECSEL with Z-configured external cavity). The nonlinear conversion layer made of (311)-oriented GaAs is sandwiched between two highly reflecting Bragg mirrors (top (bottom) DBR for mid-infrared radiation (MIR-DBR)). The DBR for near-infrared radiation (NIR-DBR) being the output coupler for corresponding optical fields is placed inside of said microcavity. Of course, top MIR-DBR should be highly transparent for NIR radiation. Besides, an antireflection coating is applied on the top side of the structure in order to possibly diminish a NIR-fields reflection.

To obtain the electrical field E_r at the difference frequency, the inhomogeneous one-dimensional wave equation was solved:

$$\left(\nabla^2 + \gamma^2\right) E_r = -\frac{\gamma^2}{\varepsilon\varepsilon_0}\wp, \qquad (1)$$

where $\nabla^2 = d^2/dz^2$ is the Laplace operator, $\gamma = k_0\sqrt{\varepsilon}$ is the wave number, ε is the relative permittivity, ε_0 is the permittivity of free space, $k_0 = 2\pi/\lambda_r$, λ_r is the wavelength corresponding to the difference frequency, $\wp = 2\chi\varepsilon_0 d_{14} E_1(z) E_2(z)$ is the second-order nonlinear polarization, d_{14} is the component of nonlinear susceptibility tensor, $\chi = 27/(11\sqrt{22})$ is the coefficient related to the rotation from plane (100) to (311), $E_{1,2}(z)$ is the electric field at the wavelengths $\lambda_{S,L}$. The rigorous approach [9] combining the Green-function method and the transfer-matrix method was used for the solution of the equation (1).

Fig. 3 shows the output power P_{out} at the difference frequency versus width d_{nc} of the nonlinear conversion layer. The simulation has been performed for the following laser's parameters: the intra-cavity power of NIR radiation $P_{1,2} = 200$ W, the beam radius $r_b = 50$ μm, $d_{14}(\text{GaAs}) = 170$ pm/V, $\lambda_r = 17.7$ μm, the loss factor of MIR radiation $\alpha_r = 1$ cm^{-1} [10], the number of periods for NIR-DBR $N_{NIR} = 30$. Note that indicated value of the intra-cavity power $P_{1,2}$ is readily available for the pump power about of 10 W and the output coupler reflection of 0.99. The top and the bottom MIR-DBRs including in 10 pairs of GaAs/AlAs alternating layers have the reflection factor of 0.93.

One can see from Fig. 3 that the dependence of MIR-power on width of the nonlinear conversion layer has a multi-resonance-like behavior. The peaks of unequal height follow one after another with the free-space interval corresponding to the half-wavelength of λ_r in the material. The maximal peak is observed at $d_{nc} = 9.51$ μm. This value being summed up with the NIR-DBR width corresponds approximately to the coherence length $L_{coh} = \pi/\Delta k \approx 10.5$ μm. Here Δk is the wave number mismatch. The subsequent peaks of maximal amplitude should likely be seen at the resonance values of d_{nc} which are nearly coincided with an odd number of L_{coh}. It is seen from Fig. 3 that the maximal value of output power is about 1 mW for given parameters.

Acknowledgement

This work was supported in part by The Academy of Finland within the projects 115810 and 109080.

References

[1] M. Beck *et al*, *Science* **295**, 301 (2002).
[2] A. A. Belyanin *et al*, *Usp. Phys. Nauk* **173**, 1015 (2003).
[3] T. Leinonen *et al*, *IEEE Phot. Techn. Lett.* **17**, 2508 (2005).
[4] R. Haidar *et al*, *IEEE JQE* **39**, 569 (2003).
[5] J. Armstrong *et al*, *Phys. Rev.* **127**, 1918 (1962).
[6] E. Rosencher *et al*, *Opt. Lett.* **23**, 1010 (1998).
[7] Yu. A. Morozov *et al*, *IEEE JQE* **42**, 1055 (2006).
[8] C.-Y. Tsai *et al*, *IEEE Journ. of Sel. Top. in QE* **1**, 316 (1995).
[9] Yu. A. Morozov *et al*, *Semiconductors* **39**, 113 (2005).
[10] D. Zheng *et al*, *Opt. Lett.* **23**, 1010 (1998).

15th Int. Symp. "Nanostructures: Physics and Technology"
Novosibirsk, Russia, June 25–29, 2007

High efficiency LED with optoelectrically optimized p-contact

S. Shapoval[1], M. Barabanenkov[1], V. Sirotkin[1], L. Saptsova[1], A. Kovalchuk[1], V. Zemlyakov[2], N. Antonova[2], A. Tsatsulnikov[3], W. Lundin[3], E. Zavarin[3], A. Sakharov[3] and V. Ustinov[3]

[1] Institute of Microelectronics Technology RAS, 142432 Chernogolovka, Moscow region, Russia
[2] R&D Corporation "Istok", Fryazino, Moscow region, Russia
[3] Ioffe Physico-Technical Institute, St Petersburg, Russia

Abstract. Electro-optical characteristics of LED with an optimized p-contact are presented. The LED structure consists of a GaN buffer layer, a thick n-GaN:Si layer, an InGaN/GaN active region, a p-AlGaN:Mg blocking layer and a p-GaN:Mg contact layer. The p-contact which is produced as orthogonal grating with strip-like metal rulings, obeys two requirements. It creates spatially homogeneous distribution of current density in a $p-n$ junction area and is resonantly transparent for LED generated electromagnetic radiation.

Introduction

The device studied in the present paper is a LED structure grown by MOCVD on a sapphire substrate. The LED structure consists of a GaN buffer layer, a thick n-GaN:Si layer, an InGaN/GaN active region, a p-AlGaN:Mg blocking layer and a p-GaN:Mg contact layer. The structure is processed in order to obtain circuit devices, 10 μm in diameter, including ECR-plasma mesa-etching, passivation by silicon nitride film, e-beam lithography and precision etching to produce a p-contact. To increase light emission, the p-contact was optimized by shaping it as an orthogonal grating with strip-like metal rulings. This p-contact shape allows meeting two requirements. The 2D grating creates spatially homogeneous distribution of current density in the $p-n$ junction area and is resonantly transparent for LED generated electro-magnetic radiation.

1. p-contact optimization

As it is known [1] optical properties of 2D orthogonal grating can be modeled by spectra of 1D grating in some special directions which are parallel to the grating rulings. Therefore, we calculate the reflection spectra of 1D grating (Fig. 1) with strip-like rulings on the basis of the Riccati equation method [2]. We describe quantitatively a resonant suppression of the reflection of plane monochromatic electromagnetic waves from the grating as a function of the grating gap (or inter-rulings spacer $d\ell$), rulings thickness (h) and wave incidence angle (α). Fig. 2 shows two minima on the solid curve and local minima on the

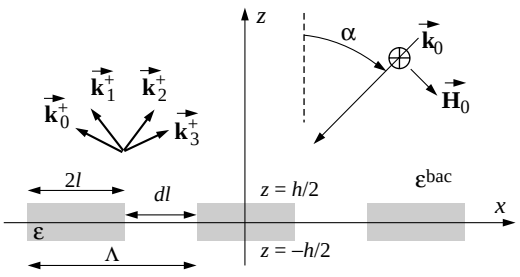

Fig. 1. The schematic showing an z-x plane of a p-contact (1D grating with strip-like metal rulings). The wave vector $\mathbf{k}_0$ and the magnetic vector $\mathbf{H}_0$ are perpendicular and the electric vector $\mathbf{E}_0$ is parallel to the y axis (TE polarization), i.e. to the rulings, respectively. The vector $\mathbf{H}_0$ is replaced with the vector $\mathbf{E}_0$ in the case of TH polarization.

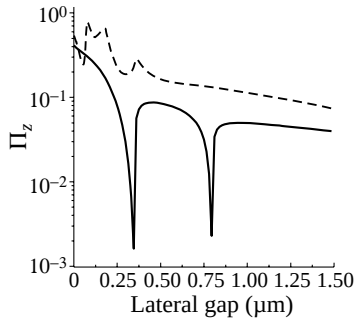

Fig. 2. Calculated power reflection spectra for TE (solid curve) and TH (dashed curve) polarized wave ($\lambda = 0.45$ μm) incident along the normal ($\alpha = 0$) from the medium ($\epsilon^{\rm bac} = 1$) from Au ($\epsilon = -1.76 + i5.28$) grating with rulings ($2\ell = 0.1$ μm) versus grating lateral gap $d\ell$.

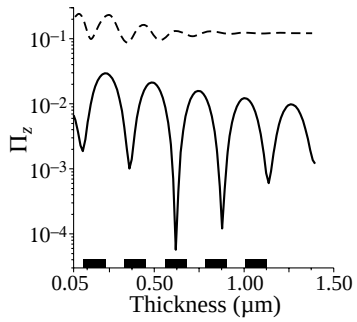

Fig. 3. Calculated power reflection spectra (see details in Fig. 2) from the grating ($d\ell = 0.35$ μm; see the first minimum in Fig. 2) versus grating thickness h. The dark rectangles on the abscissa axis represent the experimental results [3].

dashed curve at $d\ell = 0.35$ μm which indicate partial suppression of specular reflection (Rayleigh type of Wood anomalies). Let us fix this lateral gap value and find an optimal grating thickness. Fig. 3 shows some minima on the curves which are known as Palmer type of Wood anomalies. The minima on the curves coincide with the experimental results [3]. Varying the incidence angle, we found that reflection power rises sharply from 10^{-3} ($\alpha = 0$) to 0.1 ($\alpha = 70^\circ$) for TE polarized waves (see Fig. 4).

On the basis of presented calculations we fabricate a p-contact as a grating with the lateral gap 0.35 μm and ruling thickness equal to 0.35 and 0.65 μm, respectively.

Fig. 6 shows that an angular distribution of light emission

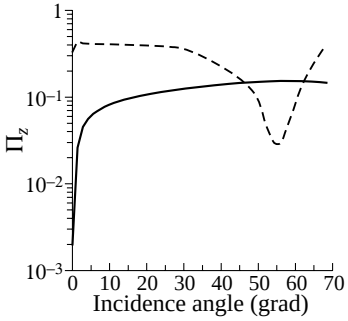

Fig. 4. Calculated power reflection spectra (see details in Fig. 3) from the grating versus incidence angle of waves.

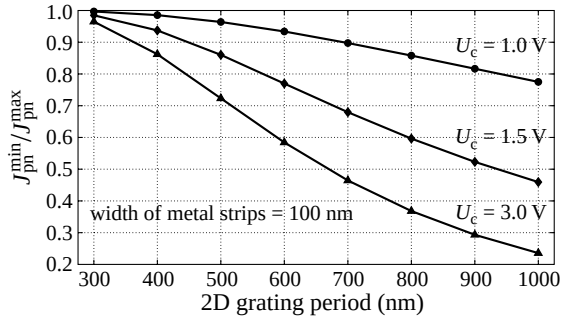

Fig. 5. Calculated ratio between minimum and maximum values of the current density in the $p-n$ junction area as a function of the 2D grating period and voltage across the LED (U_c).

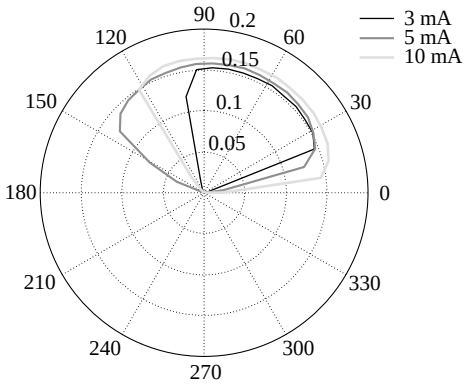

Fig. 6. Light emission distribution at different diode currents.

becomes narrower with the voltage applied to p-contact. It may be intuitively explained in terms of light power distribution among grating spectral orders with low (close to the normal direction) and high numbers. The higher the voltage, the closer the potential distribution to line-like light sources, i.e. to the p-contact grating shape. The geometric optics approach defines only low index orders to be energy filled. In the opposite case of low voltage, the potential distribution is homogeneous and a critical angle has to be defined from the wave optics approach which takes near fields of a plate source into account. Diffraction of near field evanescent waves contributes to the high index spectral orders.

To evaluate the effect of 2D grating design on the homogeneity of current density in the $p-n$ junction area we use the 3D numerical simulation (see Fig. 5).

In conclusion, the presented optimized p-contact increases LED light emission efficiency by 26% in comparison with 18% for LED with a conventional p-contact.

References

[1] S. A. Akhmanov, S. Y. Nikitin, *Physical Optics*, Moscow University Publ. 252 (1998).

[2] Yu. N. Barabanenkov, M. Yu. Barabanenkov, *JETP* **96**, 674 (2003).

[3] C. H. Palmer, *J. Opt. Soc. Am.* **42**, 269 (1952).

15th Int. Symp. "Nanostructures: Physics and Technology"
Novosibirsk, Russia, June 25–29, 2007

Fundamental reason for limitation of the maximum output optical power in semiconductor lasers at superhigh excitation levels

M. A. Khomylev[1], N. A. Pikhtin[1], Z. N. Sokolova[1], *S. O. Slipchenko*[1], V. V. Shamakhov[1], D. A. Vinokurov[1], K. S. Borschev[2] and I. S. Tarasov[1]

[1] Ioffe Physico-Technical Institute, St Petersburg, Russia
[2] Voronezh State University, 394006, Russia

Abstract. Processes of stimulated radiation recombination have been investigated in semiconductor lasers ($\lambda = 980-1900$ nm) at superhigh excitation level (up to 0.1 MA/cm^2 pump pulse current density). It is established that the fundamental reason limiting maximal attainable output optical power of semiconductor laser under pulse excitation is the finite energy scattering time of carriers in quantum well, which characterizes the delivery velocity of injected carriers on energy levels in active region

Introduction

Investigation results of stimulated radiative recombination processes and reasons of output optical power saturation at superhigh pump levels of semiconductor lasers ($\lambda = 980-1900$ nm) based on wide variety of quantum well (QW) separate confinement heterostructures (AlGaAs/GaAs [1], InGaAsP/GaAs [2], InGaAsP/InP [3], AlInGaAs/InP [4]) are presented for the first time.

It is well known that the saturation of output optical power in semiconductor lasers operating in continuous wave (CW) regime is completely defined by active region overheating thus limiting maximum allowable excitation levels. To eliminate the overheating effect we have used pulse current source which drives semiconductor lasers with pulses of 100 ns duration, 1 kHz repetition frequency and 0–200 A amplitude.

1. Experimental results

Fig. 1 demonstrates that turning from the CW to the pulse regime allows increasing sufficiently pump current densities of semiconductor lasers. However, it is seen that the maximum value of output optical power is still limited by external differential quantum efficiency decrease. Such behavior of light-current pulse characteristics has been observed in all types of investigated samples.

Measured pulsed lasing spectra (Fig. 2) show that the active region overheating remains inessential (less than 20 °C) in the whole range of pump currents. At the same time two peculiarities in the dependencies of lasing spectra on pulsed pump current are seen: (i) saturation of the peak intensity in the lasing spectrum and (ii) considerable broadening of the lasing spectrum due to the blue shift of its short-wavelength edge. The broadening of the lasing spectrum to 50–60 nm is possible only if the threshold conditions are satisfied for energy levels lying higher than those already involved in lasing. To meet this condition, the carrier density on high-energy levels must increase to the threshold value.

Investigations of spontaneous emission spectra reveal the carrier concentration growth in the active region with excitation level increase. This results in enhancing of carriers escape from the active region into the waveguide layers, carrier concentration increasing in the waveguide, fulfillment of the threshold conditions in the waveguide and its lasing, consequently. Comparison of the dependencies of output optical power and emission intensity from the waveguide layer on excitation level show, that accumulation of carriers in the active layer and their escape into the waveguide layer is the reason lim-

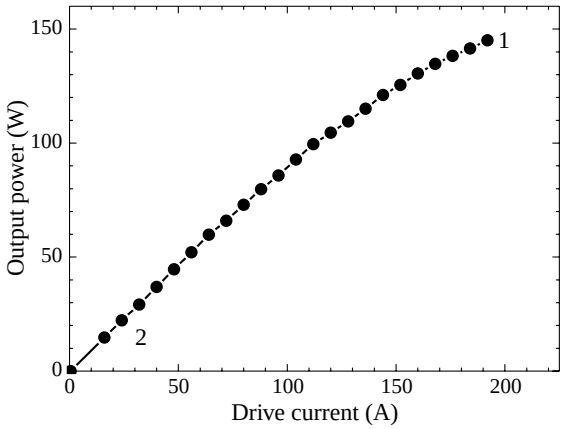

Fig. 1. Room temperature light-current characteristics in pulse (1) and CW (2) regimes for a 100 μm aperture semiconductor laser with 3 mm cavity length and antireflecting 5% highreflecting 95% front rare facets.

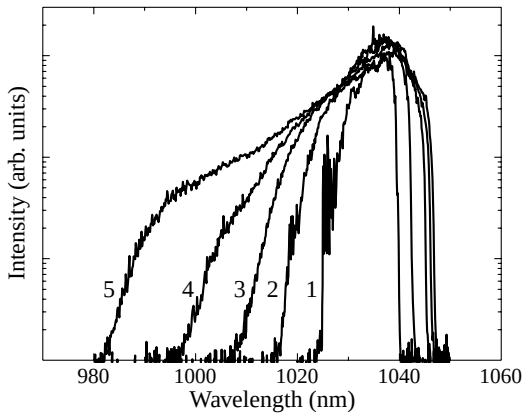

Fig. 2. Lasing spectra at different pulse pump current densities for a 100 μm-aperture semiconductor laser with 1.5 mm cavity length: 1 — 13 kA/cm^2, 2 — 40 kA/cm^2, 3 — 67 kA/cm^2, 4 — 73 kA/cm^2, 5 — 80 kA/cm^2.

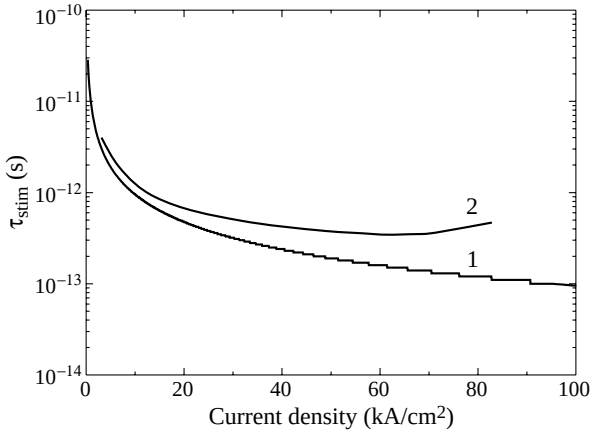

Fig. 3. Averaged carrier lifetime associated with stimulated recombination in the QW active region vs. the drive current density in a 100 μm-aperture semiconductor laser with 1.5 mm cavity length 1 — the threshold density of carriers in the active region increases with the drive current, 2 — the threshold density and the material gain are stable in all the range of the drive currents $n_{\text{th}} = 5 \times 10^{17}$ cm^{-3}, $G = 2180$ cm^{-1}.

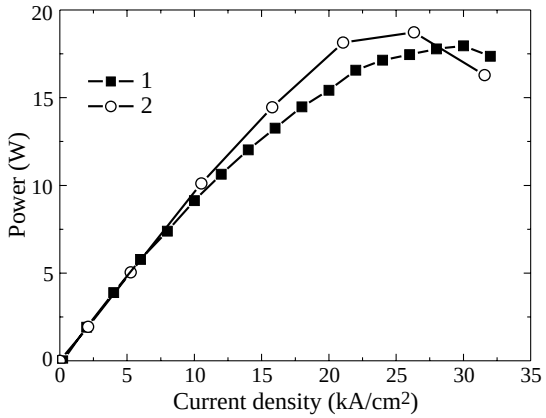

Fig. 4. Light-current characteristics for InP-based semiconductor lasers $\lambda = 1800$ nm: (1) — experiment; (2) — calculation, with taking into account threshold concentration increase.

iting maximum optical output power in semiconductor laser.

Carrier lifetime associated with stimulated recombination decreases above threshold as the excitation level increase. However our calculations based on the experimental data have shown that as stimulated radiative recombination lifetime reaches the value of energy relaxation time, it stabilizes (Fig. 3). Exactly this phenomenon accounts for the saturation of the peak intensity in the lasing spectrum. Further increase of the pump current results in carriers accumulation on the high energy levels and their involvement into the stimulated recombination processes.

In order to determine the contribution of carrier concentration increase in the active region above threshold to the saturation effect the dependencies of output optical power on the pump current have been calculated (Fig. 4). Experimental dependencies of carrier concentration in the active region on the excitation level have been used in the calculation. Carrier concentration increase above threshold has been taken into account using experimental values of threshold current. Internal optical loss and internal quantum efficiency are considered to be constant in the used assumption. Good agreement of the calculated curve with the experimental results (Fig. 4) indicates on the dominant role of threshold concentration increase in the processes of light-current characteristics saturation and limitation of maximum optical output power of semiconductor lasers at superhigh excitation levels.

Acknowledgements

This work has been supported in part by the Russian Foundation for Basic Research (project No. 06-02-08095-ofi, 07-02-00714-a). S. O. Slipchenko acknowledges the financial support from the Russian Science Support Foundation and grant of President of Russian Federation.

References

[1] N. A. Pikhtin *et al*, *Electron. Lett.* **40**, 1413 (2004).
[2] D. A. Vinokurov *et al*, *Semiconductors* **40**, 745 (2006).
[3] E. G. Golikova *et al*, *Semiconductors* **34**, 853 (2000).
[4] S. O. Slipchenko *et al*, *Tech. Phys. Lett.* **29**, 290 (2003).

15th Int. Symp. "Nanostructures: Physics and Technology"
Novosibirsk, Russia, June 25–29, 2007

New design of nanophotonic silicon waveguide structures and its application for multi-reflector filtering technology

A. Tsarev

[1] Institute of Semiconductor Physics, Siberian Branch of Russian Academy of Science, Novosibirsk, Russia

Abstract. Paper present the first description and simulation by FDTD and BMP methods of novel nano-photonic silicon-on-insulator (SOI) waveguide structures and reconfigurable optical add/drop multiplexers (ROADMs) that utilizes multi-reflector beam expanders. New structure design includes p^+ side-doping of SOI ridge waveguide with 220 nm×20 μm silicon core. It provides mono-mode behavior due to artificial strongly mode-dependent optical losses (by the free charge absorption). These heterogeneous waveguides are used to build ROADM that also utilize photonic crystal as 2D-grating for fiber coupling and polarization diversity, nano-grooves or p^+ doping reflector strips for multi-reflector beam expanders, and local heaters for wide-band thermo-optic tuning.

Introduction

Reconfigurable optical add/drop multiplexers (ROADMs) are among the most demanded devices that can increase flexibility and capacity of wavelength-division-multiplexing (WDM) fiber optic networks. Although a great progress has been achieved in recent years, none of actual technologies could be regarded as ideal to substitute all the others in the near future.

In order to reduce the cost per channel needed for the commercialization of WDM systems, tunable optical filters and ROADMs based on integrated optics and patented multi-reflector (MR) filtering technology have been already proposed [1–5]. This technology combines physical phenomena of wave-guiding, reflection and constructive interference in a novel way. The MR filtering technology accomplishes filtering operation by spatially expanding the optical beam through a patented MR-beam expander (BE) [5], then tuning and filtering the desired wavelength by a set of tunable channel waveguides (see Fig. 1) (or by acousto-optic Bragg sell) and by constructive interference of multiple sub-beams, combined at the output channel waveguide by another beam expander [3]. Multi-reflector technology provides the possibility of developing tunable devices (TOF and ROADM) on different materials (silicon, polymer, lithium niobate) [1–3], allowing partial reflector manufacturing, optical phase tunability and low optical losses in single-mode waveguides. Nowadays, MR-filtering technology has not yet been studied experimentally and its theoretical study is not completed, containing a lot of unresolved aspects.

This paper described the new design of heterogeneous optical waveguides with p^+ side-doping based on wide nano-wires in Silicon-on-Insulator and its application for novel types of ROADM. New structure design is accompanied by a number of numerical simulations performed by beam propagation method (BPM) and finite difference time domain (FDTD) method by commercial software tools from RSoft Design Group, Inc. [6]. To fasten simulations 3D structure has been replaced by 2D analogy using the effective index method (EIM) that decomposes 3D strip waveguide into two 2D slab waveguides.

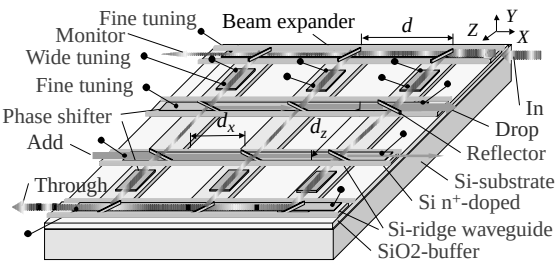

Fig. 1. General view of thermo-optic MR-ROADM.

1. Multi-reflection technology in thin SOI

Recently, photonic crystals as two-dimensional grating [7] etched in thin silicon-on-insulator waveguide had been used as a fiber-to-ridge waveguide coupler. This 2D grating is also perspective for multi-reflector technology as it provides additional possibility of polarization diversity without polarization rotators. This device is very compact and couples orthogonal modes from a single-mode optical fiber into two quasi-TE modes of two ridge waveguides that could be connected to the input/output of the photonic integrated circuit. The problem is that ridge waveguide has dimension 10 μm by 220 nm that provides (due to high index contrast) a multi-mode behavior which strongly disturbs device performances.

We propose new heterogeneous device architecture that is very suitable for SOI devices. From the well-known paper by Soref *et al* [8] one could derive simple relation between obtained changes in refractive index (Δn) and absorption ($\Delta\alpha$) at the wavelength of interest ($\lambda_0 = 1.55$ μm) due to presence of free electron (N_e) and hole concentration (N_h) in silicon:

$$\begin{aligned} \Delta\alpha_e &= 0.12 \times |\Delta n_e|\ [\mathrm{cm}^{-1}], \\ \Delta N_e &= 1.14 \times 10^{21} \times |\Delta n_e|\ [\mathrm{cm}^{-3}], \\ \Delta\alpha_h &= 0.16 \times |\Delta n_h|^{5/4}\ [\mathrm{cm}^{-1}], \\ \Delta N_h &= 2.18 \times 10^{21} \times |\Delta n_h|^{5/4}\ [\mathrm{cm}^{-3}]. \end{aligned} \quad (1)$$

Thus total change of complex refractive index due to the charge effect is:

$$\Delta n = \Delta n + jn', \quad (2)$$

where $n' = \Delta\alpha\lambda_0/(4\pi)$, $\Delta n = \Delta n_h + \Delta n_e$, $\Delta\alpha = \Delta\alpha_h + \Delta\alpha_e$.

From equation (1) one can see that if $\Delta n < 0.3$ then the hole doping is more preferable as it provides smaller optical losses at the same index change with quality factor $|\Delta n_h|^{1/4}$. Thus we propose to use p^+-doping for all structures discussed below.

Multi-mode behavior of wide thin ridge waveguides could be compressed by manufacturing additional heavily doped p^+-Si regions of width W_g on both sides of the Si-ridge of initial width W. Total width is $W + 2 \times Wg$. One can see from data of Fig. 2 that fundamental mode of this heterogeneous waveguide has negligible losses related to losses of the high order modes. Heavily doped p^+-regions could be also used for manufacturing slanted reflectors of MR-ROADM. Dependence of reflected and transmitted power for the incident angle 75° is shown in Fig. 3. Although the additional absorption losses are noticeable but they provides possibility to manufacture device with suitable performances.

Alternative method to manufacture partial reflectors for MR-ROADM design is based on the deep groove technology. For the case if quasi-TE mode incidents the reflector at close to the Brewster angle then reflective coefficient could be sufficiently small that will make possible to eliminate complex back filling of the groove by

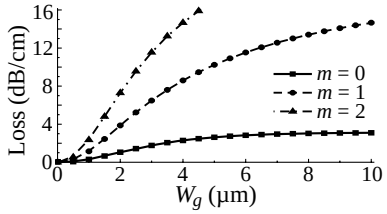

Fig. 2. Optical losses for different modes of heterogeneous ridge waveguide ($W = 10$ μm) as a function of width Wg of p^+-doped regions. BPM simulation.

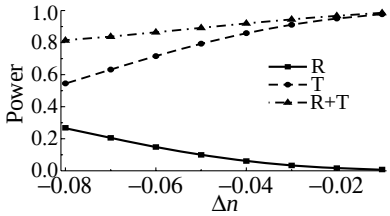

Fig. 3. Dependence of the power reflection and transmitting coefficients as a function of $\Delta n = \Delta n_h$. 2D FDTD simulation [6].

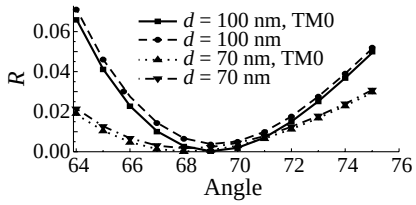

Fig. 4. Dependence of the power reflection as a function of the incident on the deep groove. Waveguide width $W = 10$ μm. Solid dots corresponds to the reflection to the fundamental TM_0 mode. 2D FDTD simulation [6].

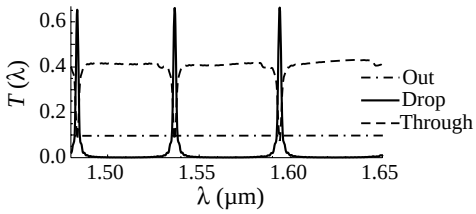

Fig. 5. Simulated frequency response of MR-OADM with 32 slanted reflectors ($\varphi = 45^\circ$). FWHM = 1.6 nm. 2D FDTD simulation [6].

the material with appropriate refractive index [3]. Results presented in Fig. 4 shows for the case of nano-width groove the reflection coefficient could be variable by changing the width and angle of the groove. One must mention that at Brewster angle the reflected filed is distorted and energy of fundamental mode is less than the total reflected power (due to the presence of high order modes). As it was mention before these modes decay due to the presence of heavy dopes sides of heterogeneous ridge waveguide.

The typical simulation of MR-ROADM is shown in Fig. 5. It proves that device could realize Drop/Through function. Better performances provides by the device with the larger number of reflectors with variable reflector coefficients [3]. New MR-ROADM design needs implementation of small area bends. Deep grooves in the heterogeneous waveguide with heavy dopes sides provides very small optical losses for the large area of bend angles (see Fig. 6). All these provide the new designs of MR-ROADM that also utilize 2D-grating, heavy p^+-doping and nono-scale grooves. The part of this design is presented in Fig. 7. It also describes the way to provide polarization diversity of the device. Different polarization will be coupled by 2D-grating in different direction and will be filtered by two simultaneously tuned identical ROADMs (initial part shown on the Fig. 7). The partial nano-reflectors of MR-beam expander could

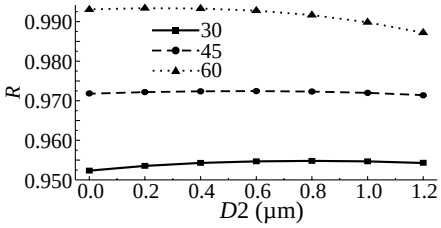

Fig. 6. Dependence of the corner reflection as a function of the waveguide shift ($D2$) at different incident angle. 2D FDTD simulation [6].

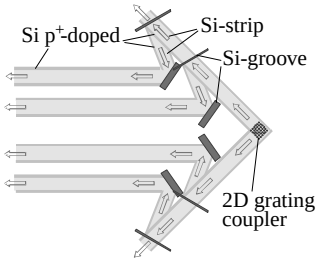

Fig. 7. General design of nono-scale SOI MR-ROADM.

be etched in silicon core simultaneously with deep reflector grooves for corner bends.

2. Conclusions

This paper present the first description and simulation by FDTD and BMP methods of novel nano-photonic SOI waveguide structures that provides better performance and manufacturability of multi-reflector reconfigurable optical add/drop multiplexers (RO
ADMs) that utilises multi-reflector beam expanders [5]. New structure design includes p^+-doping on both sides of SOI ridge waveguide with 220 nm$\times$10 μm silicon cross section surrounded by the silica cladding. It provides small optical losses for fundamental quasi-TE mode and large losses for high-order modes due to different free charge absorption depending on the modes field distribution. Nono-grooves etched at Brewster angle with respect to SOI ridge waveguide with p^+-regions provide small reflection coefficients of quasi-TE mode that has a principal role for simplifying manufacturing of novel multi-reflector ROADMs. Incorporation of these novel heterogeneous structures with 2D nono-grating couplers [7] provides new opportunity for polarization diversity of ROADM. These new SOI design will be also interesting for implementation in other multiple nano-photonic optical element.

Acknowledgements

The author thanks Prof. Vittorio M. N. Passaro from the Politecnico di Bari, Italy for the fruitful cooperation concerning muli-reflector filtering technology. The author thanks Company RSoft Design Group, Inc. [6] that provides user licence and technical support for powerful Rsoft Photonic CAD Suite 6.0 including BPM and FDTD software. This work is done under support by Grant No. 05-02-08118-ofi-a from Russian Fund for Basic Research.

References

[1] A. V. Tsarev *et al*, *Proc. ECIO*, 394 (2005).
[2] V. M. N. Passaro *et al*, *Optics Express* **13**, 3429 (2005).
[3] A. V. Tsarev *et al*, *in Silicon Photonics*, Editor: Vittorio M. N. Passaro, Research Signpost, Trivandrum, Kerala, India, ch. 3, p. 47–77 (2006).
[4] A. V. Tsarev, USA Patent No. 6,999,639 (2006).
[5] A. V. Tsarev, USA Patent No. 6,836,601 (2004).
[6] www.rsoftdesign.com.
[7] D. Taillaert *et al*, *IEEE Photon. Technol. Lett.* **15**, 1249 (2003).
[8] R. A. Soref *et al*, *IEEE J. Quantum Electron.* **23**, 123 (1987).

15th Int. Symp. "Nanostructures: Physics and Technology"
Novosibirsk, Russia, June 25–29, 2007

Acoustoelectron and acoustooptic interactions in the IR nanodimentional heterolasers

L. A. Kulakova[1], I. S. Tarasov[1], V. V. Sherstnev[1], A. N. Baranov[2] and *Yu. P. Yakovlev*[1]

[1] Ioffe Physico-Technical Institute, St Petersburg, Russia
[2] Université Montpellier II-Sciences, 34095 Montpellier, France

Frequency modulation of diode laser radiation is the basis of the most of interferometric measurement systems. Modulation of the radiation frequency in multisectional diode lasers with the help of an operating current change and also by heat effects have a main defect arising from rather inaccurate reproducibility of the frequency and intensity of radiation at the tuning. On the other hand, it is known, that the elastic strain results in the change of both permittivities and properties of the electronic subsystem.

So the experimental and theoretical study of deformation influence on the laser radiation change have been spent. The techniques of effective excitation of an alternating strain in the InGaAsP/InP laser heterostructures has been devised and implemented by excitation of bulk and surface acoustic waves (SAW). Dynamic and static spectral analysis of the laser radiation at the presence of an ultrasonic strain were carried out.

The experimental data of the dynamic analysis are qualitatively and quantitatively close for bulk and surface acoustic waves. It is unambiguously shown, that the introduction of an ultrasonic wave in the laser heterostructure results in the modulation of the radiation frequency with the period a sound wave (Fig. 1).

With the purpose of revealing of the interaction mechanisms the experimental study of the spectral distribution change (static analysis) of the laser radiation under alternating strain has been carried out. The experimental data on the spectral distribution of the radiation intensity of the heterolaser are presented in Fig. 2 (1), where as a variable the deviation $\Delta\lambda = \lambda - \lambda_{\rm m}^0$ (where $\lambda_{\rm m}^0 = 1.48$ mcm — maximum intensity wavelength) is used. The introduction of SAW ((Fig. 2 (2)) results in redistribution of the radiation intensity between laser resonator lines.

We have developed the theoretical model of such analysis. From the comparison of experimental data with the theoretical calculation the deviation value $F = 60$ GHz is obtained (accordingly 120 GHz — full range of the frequency tuning for the acoustic period).These results agree well with the data of the dynamic spectrum analysis. From all of the data the predominant role of the acoustoelectron interaction in the InGaAsP/InP laser heterostructures has been found out and effective value of the deformation potential constant ($\sim$ 4.2 eV) of it active layer (stressed quantum well of width 65 Angstroem) has been calculated.

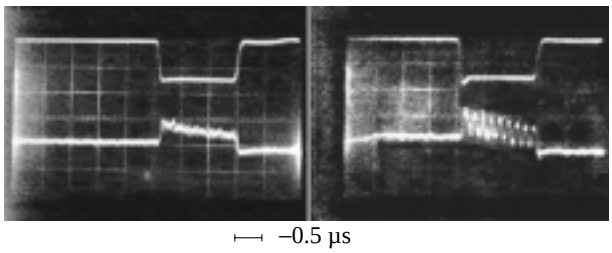

Fig. 1. Oscillograms showing the operating current $I_{\rm op}$ pulse (top, 33 mA/div, $I_{\rm op}/I_{\rm th} = 1.5$) and the laser radiation pulses (bottom) measured with the acoustic wave (a) switched off and (b) switched on, for the ultrasound frequency $f = 6.5$ MHz; the radiation pulse was detected after the Fabry–Perot etalon (FPE) (dynamic dispersion range 18.25 Å).

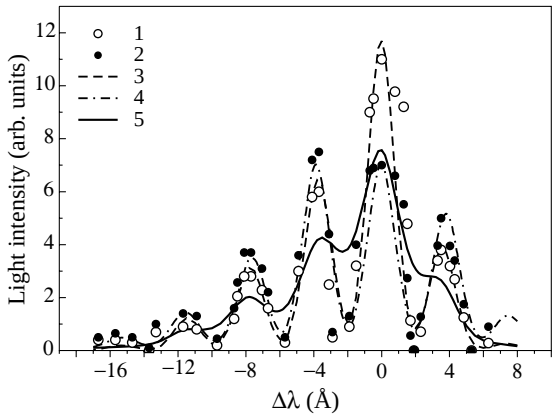

Fig. 2. The spectral distribution of the laser radiation. Points — experiment, with the SAW switched (1) off and (2) on; lines — the theoretical calculation of the spectral structure at the sound off (3) and arising from acousto-electron (4) and acousto-optic (5) interactions.

To find the ways of the interaction efficiency increasing and of the band enhancement into the IR region we have fabricated new types of nanodimentional laser heterostructures AlGaAsSb/IGaSb (on the basis of more efficient acoustooptic materials), emitting at room temperature in the middle IR-range (1.8–2.5 μm). Quantum-size laser heterostructure for Mid-IR spectral range consists of the wide gap cladding AlGaAsSb layers (with 90% of Al content) and the narrow-gap active layer. Active layer contents from undoped p-GaSb layer with two GaInAsSb quantum wells inside it and divided by 25 nm GaSb barriers. Emission wavelength is determined by quantum well width and can be tuned in the range of 1.8–2.5 μm by changing the quantum well width from 1.5 up to 2.7 nm. Laser structure was grown by molecular beam epitaxy on the GaSb substrate. Heavy doped p-GaSb with thickness of 5 μm was used as on contact layer. For fabrication of the laser chip with stripe width of 5–10 μm from the laser structure under study, a standard photolithography method was used. Isolating $Si_{1-x}N_x$ layer was utilized to provide a current limitation through laser structure. Laser chips (length in the range of 500–1000 nm) were installed on polished Cu holder to provide good heat sink in the process of coherent emission generation.

The effective excitation of bulk elastic waves (with frequency of 10 MHz) has been implemented and significant frequency modulation under ultrasonic deformation in the structures is detected. The researches on optimization and the efficiency increase of processes continue.

Acknowledgements

The authors are grateful to Presidium of RAS and the Russian Foundation for Basic Research (project no. 04-02-16205) for financial support.

15th Int. Symp. "Nanostructures: Physics and Technology"
Novosibirsk, Russia, June 25–29, 2007

Diode lasers with ultra-broad emission spectra

A. E. Zhukov[1], V. M. Ustinov[1] and A. R. Kovsh[2]

[1] St Petersburg Physics and Technology Center for Research and Education of RAS, Khlopina 8/3, 194021, St Petersburg, Russia
[2] Innolume GmbH, 44263, Dortmund, Germany

Abstract. We report on ridge-waveguide diode lasers with multiply-stacked arrays of self-organized InGaAs/GaAs quantum dots having intentional inhomogeneous broadening of energy levels. The lasers demonstrate room temperature lasing spectra as broad as 70–75 nm in the $\sim$1.2$-$1.28 μm wavelength interval with an average spectral power density of $>$10 mW/nm. This combination of parameters makes such a laser useful as an optical source for various applications in sensing, optical communication, imaging, and diagnostic systems compatible with silica fibers and silicon-based planar waveguides.

Introduction

An optical source having broad emission spectrum and high spectral power density is needed for various purposes, such as optical spectroscopy and optical coherence tomography. In this respect a broadband laser is evidently preferable to a superluminescent LED because of a higher efficiency. Although a diode laser is usually characterized by a narrow spectrum of emission, Sugawara *et al* have reported on an emission over a range of 50–60 meV at 80 K in a laser with self-organized quantum dots (QDs) [1]. Recently, a possibility of achieving unusually broad (15–21 nm) spectra has been demonstrated in QD lasers at room temperature [2,3]. However the bandwidth and/or the spectral power density were insufficient for a practical use. In this work, we report on a QD laser capable of emitting an extremely broadband (75 nm) spectrum at a very high-power level of 750 mW. This combination of parameters, as well as sufficiently long wavelengths ($>$1.2 μm), makes such lasers potentially useful as an optical source for various applications being compatible with silica fibers and SiGe/Si planar waveguides.

1. Experiment

Two AlGaAs laser structures were grown by molecular-beam epitaxy on n^+-doped GaAs (100) substrates. A laser active region represents several planes of InAs/InGaAs QDs formed using a method described in [4]. Laser structure A comprises seven equivalent planes of QDs. Laser structure B comprises three groups each comprising three QD planes whereas the thickness of the InGaAs covering layers was slightly different between the groups (1.5, 3 and 4 nm), such that the QD optical transitions were additionally broadened. A ridge-waveguide structure was fabricated using a standard process. Few-mm-long Fabry–Perot lasers defined by as-cleaved facets were p-side up mounted on heatsinks and tested at 25 °C under pulsed excitation. A threshold current of 34–50 mA and a slope efficiency of 0.24–0.4 W/A (both facets) were revealed depending on the resonator length. Far-field patterns confirmed a single-spatial-mode operation.

2. Results

Fig. 1(a) shows experimental lasing spectra taken from the laser structure A at different currents. The corresponding spectral full width at half maximum (FWHM) is shown in Fig. 2 as a function of current (open circles). An average spectral power

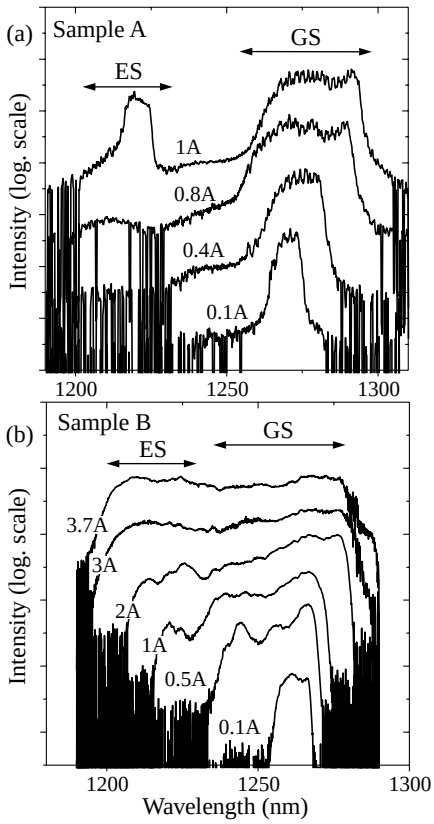

Fig. 1. Lasing spectra in a semi-logarithmic scale taken 25 °C at under various current levels for laser structure A (a) and B (b).

density, ρ, estimated as a ratio of the total output power of the laser to the FWHM is shown as well with open squares. At the lowest curren,t the spectrum is centered at 1.27 μm which corresponds to the peak wavelength of the ground-state (GS) optical transition as determined from the low-excitation electroluminescence spectroscopy. As the current increases, the FWHM becomes progressively broader reaching 26.5 nm for the spectrum taken at 0.8 A. The lasing spectrum mainly occupies the GS spectral band (marked as "GS" in Fig. 1). However, an additional shorter-wavelength band appears around $\sim$1.22 μm, which corresponds to the excited state ("ES") QD transition. As the current increases further, the ES band predominantly increases, whereas the GS band (its intensity and FWHM) remains essentially unchanged. Because the ES band is well separated from the GS band in the laser structure A, the spectrum has two distinguished maxima with pronounced

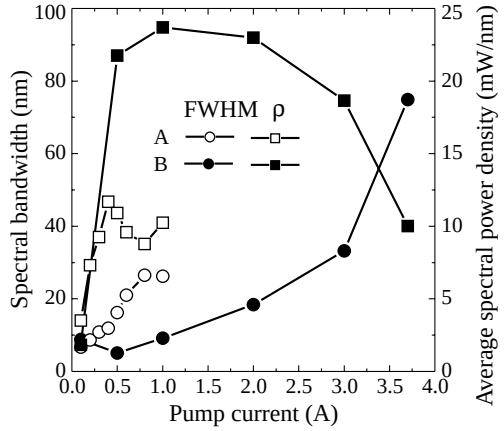

Fig. 2. The spectral bandwidth (FWHM) of the lasing spectra (circles) and the average spectral power density (squares) as a function of pump current for the laser structure A (open symbols) and B (solid symbols).

intensity suppression between them. Such a spectrum is very inconvenient in practical use.

Fig. 1(b) shows an evolution of the laser spectrum taken from the laser structure B. The corresponding spectral bandwidths (FWHM) and average spectral power density (ρ) are shown in Fig. 2 against pump current (solid symbols). Similar to the previously discussed structure, increase of the pump current to 0.5 A results in spectral expansion of the GS band. Starting from the pump current of 1 A a contribution of the ES optical transition at $\sim$1.22 μm becomes apparent. Further broadening of the spectrum with increasing current is due mainly to progressive increase of intensity of the ES spectral band and its expansion to shorter wavelength.

A peculiarity of the laser structure B in that the GS band and the ES bands appreciably overlap. The FWHM demonstrate progressive broadening with increasing current. The average spectral power density exceeds 10 mW/nm in a wide range of operation conditions ($I > 0.1$ A). The lasing spectrum reaches its largest bandwidth, with the FWHM of 74.9 nm at current of 3.7 A. Under such condition, the laser's emission spectrum fills a wavelength interval of 1.2–1.28 μm. To our best knowledge, this is the broadest spectrum of laser emission ever reported for a semiconductor diode laser of any kind. The corresponding optical power is 750 mW (both facets). As it is seen in Fig. 2, the spectrum is nearly flat-topped; variation of the spectral power density within the central part of the spectrum is less than 4.5 dB.

3. Discussion and conclusion

The reason of a spectrum broadening effect in a QD laser is a relatively low rate of QD states refilling process resulting in a lack of carriers at the electronic states involved in lasing. As a result, more modes are excited at elevated pump levels. At still higher currents, simultaneous lasing at two energy levels of QDs becomes apparent [5,6]. However in most cases a significant separation between the GS and ES bands prevents further broadening of lasing spectra. In particular case of the laser structure B the broadening of the GS lasing band was intentionally enhanced such that the GS and the ES bands noticeably overlap. This was achieved by means of properly chosen difference in growth conditions of the three QD groups in the laser active region. Moreover, the intensities of these spectral bands becomes well comparable at certain pump current (3.7 A). This results in nearly flat-topped and widely spread spectrum.

In conclusion, we demonstrated the room temperature operation of the QD laser in the 1.2–1.28 μm wavelength interval with a broadband spectrum (FWHM as larger as 74.9 nm) and a high spectral power density ($>$10 mW/nm). With further optimization of intentional inhomogeneous broadening and overlap of the optical transitions, more uniform spectral distribution of the laser's power over a broad emission band is feasible.

Acknowledgements

The work was supported by ZODIAC and SANDiE projects of EC, the Russian Science Support Foundation and the RFBR. A.E.Z. acknowledges grant MD-3858.2007.2 of the president of Russian Federation.

References

[1] M. Sugawara *et al*, *Appl. Phys. Lett.* **74**, 1561 (1999).
[2] A. E. Zhukov *et al*, *Semiconductors*, in print (2007).
[3] H. S. Djie *et al*, *Optics Letters* **32**, 44 (2007).
[4] A. E. Zhukov *et al*, *Photon. Technol. Lett.* **11**, 1345 (1999).
[5] A. E. Zhukov *et al*, *Semicond. Sci. Technol.* **18**, 774 (2003).
[6] A. Markus *et al*, *Appl. Phys. Lett.* **82**, 1818 (2003).

15th Int. Symp. "Nanostructures: Physics and Technology"
Novosibirsk, Russia, June 25–29, 2007

Can a dc voltage proportional to the persistent current be observed on segment of asymmetric mesoscopic loop?

S. V. Dubonos, V. L. Gurtovoi, A. V. Nikulov, and V. A. Tulin

Institute of Microelectronics Technology and High Purity Materials, Russian Academy of Sciences,
142432 Chernogolovka, Moscow District, Russia

Abstract. In order to clear up a question on possibility of a dc voltage proportional to the persistent current in normal metal and semiconductor mesoscopic loops conjectural causes of this phenomenon observed in superconductor loops is investigated.

Introduction

I. O. Kulik had shown in theory 1970 that the persistent current can be observed both in normal state of superconductor at $T > T_c$ [1] and in non-superconductor mesoscopic structures [2]. An experimental evidence of the persistent current in the fluctuation region of superconductor at $T \geq T_c$ was obtained as far back as 1962 [3], before the theory [1]. According to the universally recognized explanation [4] the resistance oscillation in magnetic field $\Delta R(\Phi/\Phi_0) \propto \Delta T_c(\Phi/\Phi_0)$ of superconducting cylinder [3] or loop [5] is a consequence of the persistent current oscillations $I_p(\Phi/\Phi_0)$. The Little–Parks oscillations of the loop critical temperature $\Delta T_c(\Phi/\Phi_0)$ [3–6] are observed since the velocity circulation $\oint_l dl v_s = (1/m)(n2\pi\hbar + 2e\Phi) = (2\pi\hbar/m)(n + \Phi/\Phi_0)$ can not be equal zero at the magnetic flux Φ inside the loop (or cylinder) not divisible by the flux quantum $\Phi_0 = \pi\hbar/2e$, $\Phi \neq n\Phi_0$, because of the quantization $\oint_l dlp = \oint_l dl(mv_s + 2eA) = m\oint_l dlv_s + 2e\Phi = n2\pi\hbar$.

The persistent current has measurable value in real superconducting loop even at $T \geq T_c$. For example, according to the experimental data presented in [5] the amplitude of the persistent current, $I_{p,A} = |I_p|$ at $\Phi = (n + 0.5)\Phi_0$, of a square loop with a size 1×1 μm and wire section $s = w \times d = 0.15 \times 0.025$ μm ≈ 0.004 μm^2 is equal approximately $I_{p,A} \approx 0.2$ μA at the midpoint of the resistive superconducting transition $T \approx T_c$. This value is much larger than a current of two electrons $I_{2e} = 2ev_s/l \approx 10^{-11}$ A at the velocity $|v_s| = (2\pi\hbar/ml)(0.5) \approx 100$ m/c permitted in this loop with the perimeter $l = 4$ μm at $\Phi = (n + 0.5)\Phi_0$ since superconducting pairs, as condensed bosons, have the same velocity and therefore $I_p = sj_p = s2e\overline{n_s}v_s$. The average fluctuation density of superconducting pairs $\overline{n_s} = I_p/s2ev_s = I_p/s2ev_s \approx 3 \times 10^{24}$ m^{-3} in the Al loop [5] at $T \approx T_c$ corresponds to $\approx 10^{-5}$ of the total density of electron pairs in aluminum. The great number of pairs in the loop, $N_s = sl\overline{n_s} \approx 10^5$ at $T \approx T_c$, explains why the persistent current can be observed even in the fluctuation region, in spite of the great size l in comparison with the one of atom orbit: the energy difference between adjacent permitted states $E_{n+1} - E_n \approx N_s 2\pi^2\hbar^2/ml^2 \approx k_B 1000$ K $\gg k_B T_c$ whereas for single electron $E_{n+1} - E_n \approx 2\pi^2\hbar^2/ml^2 < k_B 0.1$ K [7].

The persistent current is much weaker and it can be observed only at very low temperature in non-superconductor loop since $2\pi^2\hbar^2/ml^2 < k_B 0.1$ K for a real size l. Therefore first attempts to observe this quantum phenomenon in normal metal [8] and semiconductor [9] loops were made 20 years later its prediction [2] and 28 years later its observation in superconductor at $T \geq T_c$ [3]. The typical amplitude of the persistent current oscillations measured on Cu [8], Au [10,11], GaAlAs/GaAs [9,12–14], Ag [15] mesoscopic loops estimated to be of the order of 10^{-10} A. In order to increase the magnetic response from this weak current systems with great number of loops, 10^5 [12,14,15] and even 10^7 [8] were used. Quite enough response could be observed in a system with such number of asymmetric loops if an analogy with conventional circular current is valid.

1. Analogy with conventional circular current

It is well known that a potential difference $V = (R_{ls} - R_l l_s/l)I$ is observed on a segment l_s (with a resistance R_{ls}) of an asymmetric conventional metal loop l (with a resistance R_l) when a circular current $I = \oint_l dlE/R_l$ is induced by the Faraday's voltage $\oint_l dlE = -d\Phi/dt$. It was found experimentally [16,17] that there is an analogy between this conventional current and the persisent current in superconductor loop in spite of the Faraday's voltage absence $d\Phi/dt = 0$ in the second case. The observations of the quantum oscillations of the dc potential difference $V_{dc}(\Phi/\Phi_0) \propto I_p(\Phi/\Phi_0)$ on asymmetric aluminum rings at $T \approx T_c$ [16] and $T < T_c$ [17] raise a question about possibility of like phenomenon in asymmetric normal metal and semiconductor mesoscopic loops with $I_p(\Phi/\Phi_0)$. It was proved experimentally [17] that the $V_{dc}(\Phi/\Phi_0)$ amplitude increases with number of asymmetric superconductor loops connected in series. The measurable $V_{dc}(\Phi/\Phi_0)$ oscillations with the amplitude up to 1 μV could be expected on a system of 10^5 loops with $I_{p,A} \approx 10^{-10}$ A and resistance asymmetry $(R_{ls} - R_l l_s/l) \approx 0.1$ Ω if the analogy with conventional circular current is valid.

Possibility of this analogy for the persistent current in normal metal and semiconductor loops seems paradoxical. But the observations [3–6, 8–17] of the dc circular current $I_p \neq 0$ in loops with non-zero resistance $R > 0$ and without the Faraday's voltage $d\Phi/dt = 0$ is already incomprehensible paradox. The statement [18] that the existence of a finite Ohmic resistance for a phase coherence sample is not paradoxical when one properly takes into account the influence of the measuring leads is disproved with simultaneous observations $I_p \neq 0$ and $R > 0$ of loops with leads made in numerous works [3–6,16,17]. The $V_{dc}(\Phi/\Phi_0)$ oscillations were already observed in superconductor loops [16,17]. In order to clear up a question on possibility this phenomenon in normal metal and semiconductor loops its cause in superconductor loops should be investigated comprehensively.

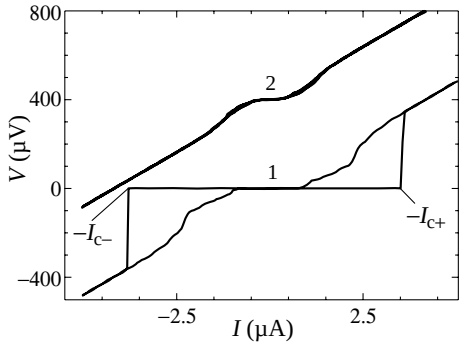

Fig. 1. The current-voltage curves of system of 18 asymmetric Al loops connected in series measured at different temperature 1) $T \approx 0.984T_c$ and 2) $T \approx 0.995T_c$.

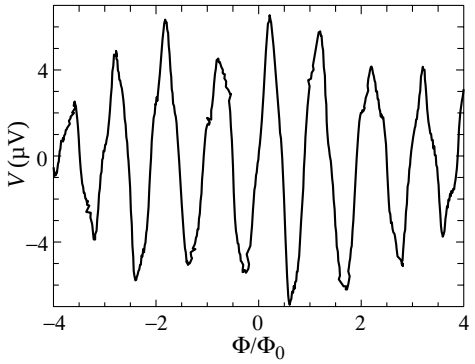

Fig. 2. The quantum oscillations of the dc potential difference $V(\Phi/\Phi_0)$ induced by the ac current with frequency $f = 40$ kHz and amplitude $I_0 = 3\ \mu$A on system of 18 asymmetric Al loops near superconducting transition $T \approx 0.996T_c$ where the hysteresis of the current-voltage curves is absent, see Fig. 1.

2. Conjectural causes of the quantum oscillations $V_{dc}(\Phi/\Phi_0)$ observed in superconducting loops

We have shown in [19] that the rectification of ac current observed at $T < 0.99T_c$ is consequence of the critical current anisotropy of asymmetric superconducting loops. The current-voltage curves (CVC) in this temperature region have a hysteresis and sharp transition in the resistance state at I_{c+} or I_{c-}, Fig. 1. We have found that the value of the critical current depends on direction of its measurement $I_{c+} \neq I_{c-}$ and that the sign and value of this anisotropy $I_{c,an} = I_{c+} - I_{c-}$ are periodical function of magnetic flux $I_{c,an}(\Phi/\Phi_0)$ [19]. Although the cause of the anisotropy $I_{c,an}(\Phi/\Phi_0)$ is very strange [20] the CVC and the proportionality $V_{dc}(\Phi/\Phi_0) \propto -I_{c,an}(\Phi/\Phi_0)$ [19] allow to explain the dc voltage $V_{dc}(\Phi/\Phi_0)$ observed at $T < 0.99T_c$ as a result of the transition in the normal state of the whole loop at different values I_{c+} and I_{c-}. This case is not useful for the clearing up of the question on the $V_{dc}(\Phi/\Phi_0)$ possibility in normal metal and semiconductor mesoscopic loops.

More useful may be our results obtained at $T > 0.99\,T_c$ where the CVC are smooth and reversible, Fig. 1. The voltage observed at $I_p \neq 0$ and $R < R_n$ can be reversible only if the loop is switched between superconducting states with different connectivity of wave function. Because of such switching induced by thermal fluctuations the persistent current $I_p \neq 0$ can be observed at $R > 0$ [7]. The break of the wave function describing superconducting state in loop segments is similar to electron scattering in mesoscopic loop with the persistent current. Therefore the observation of the quantum oscillations $V_{dc}(\Phi/\Phi_0)$ in superconducting loop at $T > 0.99\,T_c$, Fig. 2, allow to expect that such quantum oscillations can be observed also in normal metal and semiconductor mesoscopic loops. It is no coincidence that I. O. Kulik made the works [1,2] on superconductor and non-superconductor mesoscopic structures in the same year. The persistent current has the same cause in the both cases. Therefore the results of the investigations of the $V_{dc}(\Phi/\Phi_0)$ oscillations in superconductor loop can give an information about possibility this phenomenon in normal metal and semiconductor loops.

Acknowledgements

This work has been supported by a grant of the Program "Quantum Nanostructures" of the Presidium of RAS, grant "Quantum bit on base of micro- and nano-structures with metal conductivity" of the Program "Technology Basis of New Computing Methods" of ITCS department of RAS and a grant 04-02-17068 of the Russian Foundation of Basic Research.

References

[1] I. O. Kulik, *Zh. Eksp. Teor. Fiz.* **58**, 2171 (1970).
[2] I. O. Kulik, *Pisma Zh. Eksp. Teor. Fiz.* **11**, 407 (1970) (*JETP Lett.* **11**, 275 (1970)).
[3] W. A. Little and R. D. Parks, *Phys. Rev. Lett.* **9**, 9 (1962).
[4] M. Tinkham, *Introduction to Superconductivity*, McGraw-Hill Book Company (1975).
[5] H. Vloeberghs *et al*, *Phys. Rev. Lett.* **69**, 1268 (1992).
[6] M. Morelle *et al*, *Phys. Rev. B* **64**, 064516 (2001).
[7] A. V. Nikulov, *Phys. Rev. B* **64**, 012505, (2001).
[8] L. P. Levy *et al*. *Phys. Rev. Lett.* **64**, 2074 (1990).
[9] D. Mailly, C. Chapelier, and A. Benoit, *Phys. Rev. Lett.* **70**, 2020 (1993).
[10] V. Chandrasekhar *et al*, *Phys. Rev. Lett.* **67**, 3578 (1991).
[11] E. M. Q. Jariwala *et al*, *Phys. Rev. Lett.* **86**, 1594 (2001).
[12] B. Reulet *et al*, *Phys. Rev. Lett.* **75**, 124 (1995).
[13] W. Rabaud *et al*, *Phys. Rev. Lett.* **86**, 3124 (2001).
[14] R. Deblock *et al*, *Phys. Rev. B* **65**, 075301 (2002).
[15] R. Deblock *et al*, *Phys. Rev. Lett.* **89**, 206803 (2002).
[16] S. V. Dubonos, V. I. Kuznetsov and A. V. Nikulov, *Proc. of 10th International Symposium "Nanostructures: Physics and Technology"*, St Petersburg: Ioffe Institute, p. 350 (2002).
[17] S. V. Dubonos *et al*, *Pisma Zh. Eksp. Teor. Fiz.* **77**, 439 (2003) (*JETP Lett.* **77**, 371 (2003)).
[18] R. Landauer, *Phys. Scr.* **42**, 110 (1992).
[19] V. L. Gurtovoi *et al*, *Proc. of 14th International Symposium "Nanostructures: Physics and Technology"*, St Petersburg: Ioffe Institute, p. 216 (2006).
[20] A. A. Burlakov *et al*, *Proc. of 14th International Symposium "Nanostructures: Physics and Technology"*, St Petersburg: Ioffe Institute, p. 240 (2006).

15th Int. Symp. "Nanostructures: Physics and Technology"
Novosibirsk, Russia, June 25–29, 2007

The quantum challenge on mesoscopic level

A. V. Nikulov

Institute of Microelectronics Technology, Russian Academy of Sciences,
142432 Chernogolovka, Moscow region, Russia

Abstract. Most experts reject the quantum potential introduced by David Bohm in 1952. But it is impossible to describe some quantum mesoscopic phenomena observed in nanostructures without a quantum force.

Introduction

The Lecture by one of the Nobel Prize winners presented at the Eighth International Symposium "Frontiers of Fundamental Physics" [1] called "What is Quantum Mechanics?" This question may seem strange for many scientists who studied and used formalism of quantum mechanics. We can describe numerous phenomena of atomic physics, solid state physics, mesoscopic physics and many others using the so-called Copenhagen formalism. But experts understand that quantum mechanics *not yet based on a generally accepted conceptual foundation* [2]. Albert Einstein has always regarded the Copenhagen interpretation of the quantum theory as incomplete and has always believed that, even at the quantum level, there must exist precisely definable variables determining the actual behavior of each individual system. This point of view known as "realism" is the basis of hidden-variable theories [3]. Bell's theorem [5], and the experiments [6] based on it, have provided convincing evidence that a local hidden-variable theory will never be able to account for the full rang of quantum phenomena. But the very first hidden-variable theory proposed by David Bohm in 1952 [4] was radically nonlocal. In order to save the principle of realism he must conclude that nonlocality can be real. The assumption on a real nonlocality seems so strange that most experts prefer to renounce realism [3]. Nevertheless one should not reject without hesitation the nonlocal quantum potential introduced by Bohm [4]. The well known Aharonov–Bohm effect [7] can bear a relation to this problem [8]. The nonlocal momentum transfer [9] observed in the Aharonov–Bohm double-slit experiment can be interpreted in terms of complementarity [3]. But such interpretation can be not possible in some cases of the Aharonov–Bohm effect observed in nanostructures. This problem is urgent because of numerous Aharonov–Bohm phenomena observed in semiconductor [10], normal metal [11] and superconductor [12] mesoscopic systems.

1. Quantum force

The Bohm's theory is based on the Schrodinger equation. Bohm has divided it into two, one for the amplitude $|\Psi|$ of wave function $\Psi = |\Psi| \exp i\varphi$ and the other for the phase φ [4]. When the wave function describes a probability, as for example in the double-slit experiment, it is enough easy to reject the Bohm's quantum potential, inadmissible for most experts, and to repudiate realism. But this renunciation of realism can be impossible when the wave function describing a density, for example superconducting pairs. There is an experimental challenge to the Copenhagen interpretation connected with observations of the persistent current $I_p \neq 0$ in semiconductor [13], normal metal [11] and superconductor [14]

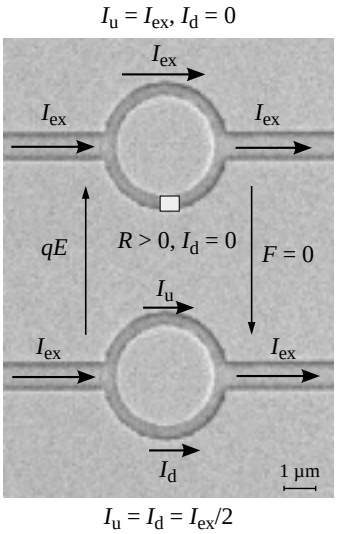

Fig. 1. Example of momentum change induced by switching between states with different connectivity of the wave function.

rings with non-zero resistance $R_l > 0$. According to classical physics a circular direct current I is possible at $R_l > 0$ only at a non-zero Faraday's voltage $d\Phi/dt \neq 0$ when the force balance $I R_l = -d\Phi/dt$ takes place. The observations $I_p \neq 0$ at $R_l > 0$ and $d\Phi/dt = 0$ violate this balance. In order to restore it a quantum force was introduced in [15].

The quantum force introduced in [15] describes a change of momentum p and velocity v_s of superconducting pairs because of the Bohr's quantization $\oint_l dlp = \oint_l dl\overline{h} \bigtriangledown \varphi = \oint_l dl(mv_s + qA) = m\oint_l dlv + q\Phi = n2\pi\overline{h}$ at closing of wave function: $v_s = 0$ and $\oint_l dlp = q\Phi$ at unclosed wave function whereas $\oint_l dlp = n2\pi\overline{h}$ and $\oint_l dlv = (1/m)(n2\pi\overline{h} - q\Phi) = (2\pi\overline{h}/m)(n - \Phi/\Phi_0)$ at closed wave function. $\Phi_0 = 2\pi\overline{h}/q = \pi\overline{h}/e$ is the flux quantum; $q = 2e$ is the charge of superconducting pair. The necessity of the quantum force is obvious from the example shown on Fig. 1. The external current I_{ex} flows on the top semi-ring of the superconducting loop, $I_u = I_{ex}$, $I_d = 0$, when a segment of the lower one in the normal state with a resistance $R > 0$. But the currents should be equal in the both semi-rings, $I_u = I_{ex}/2$, $I_d = I_{ex}/2$, because of the Bohr's quantization $\oint_l dlv = l_u v_u - l_d v_d \propto (n - \Phi/\Phi_0) = 0$ after switching of this segment into superconducting state. This change of the current values occurs without any electric field and it could not occur in an ideal conductor at switching from $R > 0$ to $R = 0$.

2. Intrinsic breach of symmetry

There is an important difference between atomic and mesoscopic levels [16]: it is impossible to realize the switching

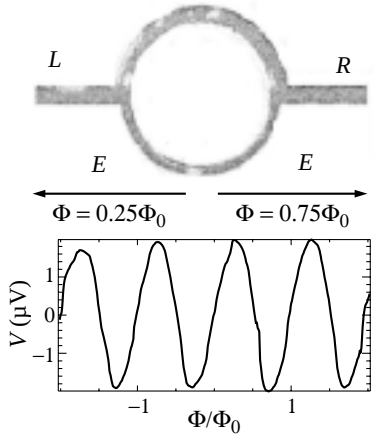

Fig. 2. Aluminum asymmetric loop with radius 2 μm and the quantum oscillations of the dc potential difference $V(\Phi/\Phi_0)$ observed on such loop.

between states with different connectivity of the wave function on the atomic level whereas it is possible in real mesoscopic structures. A potential difference with a dc component $V_{\rm dc} = L\omega I_{\rm ex}/2$ should be observed both on top and lower semi-rings when a segment only in the lower semi-ring, Fig. 1, is switched with a frequency $\omega < R/L$ between superconducting and normal state with $R > 0$. L is the semi-ring inductance. The dc potential difference $V_{\rm dc} = L\omega I_{\rm p}(\Phi/\Phi_0)$ can be observed [17] also without any dc external current because of the persistent current $I_{\rm p}$, the value and sign of which is periodical function of magnetic flux Φ inside the ring with period equal the flux quantum Φ_0. Such quantum oscillations of the dc voltage $V_{\rm dc}(\Phi/\Phi_0) \propto I_{\rm p}(\Phi/\Phi_0)$ were observed on segments of asymmetric aluminum ring [12]. The periodical change of the dc electric field $E(\Phi/\Phi_0) = -\bigtriangledown V(\Phi/\Phi_0)$ direction with the scalar value Φ observed in this experiment gives experimental evidence of intrinsic breach of right-left symmetry [18].

This result has fundamental importance and should be connected with the necessity of the quantum force. There was a logical difficulty in the Bohr's model until electron considered as a particle having a velocity since it was impossible to answer on the question: "What direction has this velocity?" The uncertainty relation and the wave quantum mechanics have overcame this difficulty. Albert Einstein considered it as weakness: *The weakness of the theory lies … in the fact, that it leaves time and direction of the elementary process to "chance"* (the citation from [2]). Thanks to this "weakness" the Bohr's quantization does not violate symmetry between opposite directions on the atomic level. But we see experimental evidence of the intrinsic breach of symmetry because of the Bohr's quantization in nanostructures.

Acknowledgement

This work has been supported by a grant 04-02-17068 of the Russian Foundation of Basic Research.

References

[1] G t' Hooft, the Lecture at the FFP8, Madrid, October, 2006.
[2] A. Zeilinger, *Foundations of Physics* **29**, 631 (1999).
[3] G. Greenstein and A. G. Zajonc, *The Quantum Challenge. Modern Research on the Foundation of Quantum Mechanics*. Second Edition. Jones and Bartlett Publishers, Sudbury, Massachusetts, 2005.
[4] David Bohm, *Phys. Rev.* **47**, 166 (1952).
[5] J. S. Bell, *Physics* **1**, 195, (1964).
[6] A. Aspect *et al*, *Phys. Rev. Lett.* **47** 460 (1981); P. G. Kwiat *et al*, *idid* **75**, 4337 (1995); G. Weihs *et al*, *idid* **81**, 5039 (1998); W. Tittel *et al*, *Phys. Rev. A* **57**, 3229 (1998).
[7] Y. Aharonov and D. Bohm, *Phys. Rev.* **115**, 485 (1959).
[8] Y. Aharonov and D. Bohm, *Phys. Rev.* **123**, 1511 (1961).
[9] H. M. Wiseman *et al*, *Phys. Rev. A* **56**, 55 (1997).
[10] O. A. Tkachenko *et al*, *in Proceedings of 14th International Symposium "Nanostructures: Physics and Technology"* St Petersburg: Ioffe Institute, 2006, p. 250; D. V. Nomokonov *et al*, *in Proceedings of 13th International Symposium "Nanostructures: Physics and Technology"* St Petersburg: Ioffe Institute, 2005, p. 197; B. Szafral and N. M. Peeters, *idid*, p. 203; O. A. Tkachenko *et al*, *idid*, p. 205.
[11] L. P. Levy *et al*, *Phys. Rev. Lett.* **64**, 2074 (1990); V. Chandrasekhar *et al*, *idid* **67**, 3578 (1991); E. M. Q. Jariwala *et al*, *idid* **86**, 1594 (2001).
[12] V. L. Gurtovoi *et al*, *in Proceedings of 14th International Symposium "Nanostructures: Physics and Technology"* St Petersburg: Ioffe Institute, 2006, p. 216; S. V. Dubonos *et al*, *in Proceedings of 10th International Symposium "Nanostructures: Physics and Technology"* St Petersburg: Ioffe Institute, 2002, p. 350.
[13] D. Mailly, C. Chapelier, and A. Benoit, *Phys. Rev. Lett.* **70**, 2020 (1993); B. Reulet *et al*, *idid* **75**, 124 (1995); W. Rabaud *et al*, *idid* **86**, 3124 (2001).
[14] M. Tinkham, *Introduction to Superconductivity*. McGraw-Hill Book Company, 1975.
[15] A. V. Nikulov, *Phys. Rev. B* **64**, 012505 (2001).
[16] A. V. Nikulov, the talk at the FFP8, Madrid, October, 2006.
[17] A. V. Nikulov, I. N. Zhilyaev, *J. Low Tem. Phys.* **112**, 227 (1998).
[18] A. V. Nikulov, the talk at the 13th General Meeting of the European Physical Society "Beyond Einstein — Physics for the 21th Century", Bern, Switzerland, July 2005.

15th Int. Symp. "Nanostructures: Physics and Technology"
Novosibirsk, Russia, June 25–29, 2007

Plasmon-assisted magnetophotonic crystals

A. G. Zhdanov[1], A. A. Fedyanin[1], A. V. Baryshev[2], A. B. Khanikaev[2], H. Uchida[2] and M. Inoue[2]

[1] Dept. of Physics, M. V. Lomonosov Moscow State University, Moscow 119992, Russia
[2] Dept. of Electrical and Electronic Eng., Toyohashi University of Technology, Toyohashi, Japan

Abstract. Magneto-optical Kerr effect in 2D magnetophotonic crystals (slabs) formed from the array of nickel nanorods is considered. It is shown that Kerr angle increase is achieved at the certain wavelength and angle of incidence corresponding to the Wood's anomaly when first order of diffraction lies close to the surface of nickel array. This enhancement is shown to be accompanied by weakening of reflected light intensity in the zeroth order of diffraction. It is observed at p-polarization of incident light which indicates on the plasmonic nature of the effect. The experimental results are proved by numerical calculations.

Introduction

Periodically structured dielectric elements with magnetic properties at the nanometer scale, called magnetophotonic crystals, have been in the focus of attention within the latest few years due to the unique abilities of light propagation control they provide. One-dimensional magnetophotonic crystals have been studied thoroughly and the results have been reported in several works [1, 2]. In such structures significant Faraday angles are achieved practically without weakening of the transmitted light.

In dielectric structures magneto-optical effects are limited by low magneto-optical response of dielectrics in comparison with metals, at the same time, metals possess large absorption. However magneto-optical response can be efficiently enhanced in metal structures by taking into consideration periodic structures [3]. In such structures due to modified dispersion properties for surface plasmon-polaritons (SPP) on the periodic surface, they can be excited by the incident wave. It occurs due to lateral wave-vector matching conditions on the metallic surface of incident wave-vector, SPP wave-vector and vector of reciprocal lattice.

In the present work, enhancement in Kerr spectra of 2D array of nickel nanorods is studied. Nickel demonstrates significant magneto-optical response and it seems to be rather attractive for such studies. At the same time it possesses huge absorption at optical frequencies that is why magneto-optical effects dealing with transmitted light are expected to be practically vanished. Summing it all up one can conclude that Kerr geometry is the most efficient in this case.

1. Experiment

Studied sample represents itself a 2D array of nickel discs placed on 500-micron-thick nickel foil. Such array has hexagonal spatial arrangement, the hight of each disc is $h \simeq 50$ nm, diameter is $d \simeq 200$ nm and the distance between centers of neighbor discs is $l \simeq 400$ nm. The FESEM image of the surface of experimental sample is shown in Fig. 1. Such structure is called plasmon assisted magnetophotonic crystal.

In specular reflection spectra (zeroth order of diffraction) the reflected intensity is one-half weakened in the case of k-matching conditions. It can be called Wood's anomaly and corresponds to SPP excitation: a part of radiation is reradiated in specular peak and another part is needed for SPP excitation which leads to reflected intensity weakening. Experimental spectra for various angles of incidence are shown in Fig. 2. Calculations show that in the presence of magnetic field applied in longitudinal Kerr effect configuration makes right and left circular polarized waves be unequal and leads to polarization plane rotation [4]. It was proved experimentally by measuring Kerr angle in the specular reflected diffraction maximum. Saturation magnetic field applied to the sample was 4 kOe. The peak of Kerr angle being correlated with peculiarity in reflectance spectrum corresponds to the SPP excitation conditions (Fig. 3a). Experimental results show nearly 2 times enhancement of Kerr angle for various angles of incidence (Fig. 3b).

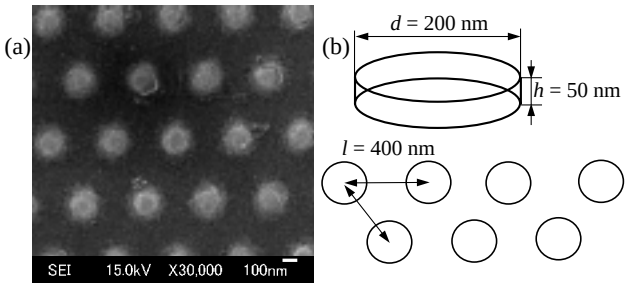

Fig. 1. (a) FESEM image of experimantal sample, (b) Sketch of experimental sample.

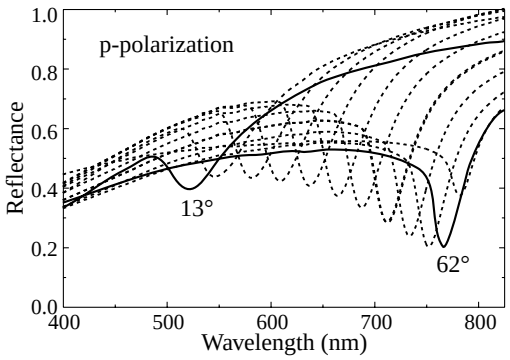

Fig. 2. Experimental results of spectral dependencies of reflected intensity at various angles of incidence.

2. Discussion

The experimental results described above vividly prove the ability of SPP excitation on nanostructured nickel surface, forming 2D magnetophotonic crystal. Due to significant absorption in nickel SPP excited on its surface can be called *induced* SPP. Despite large optical absorption of nickel the effects studied in

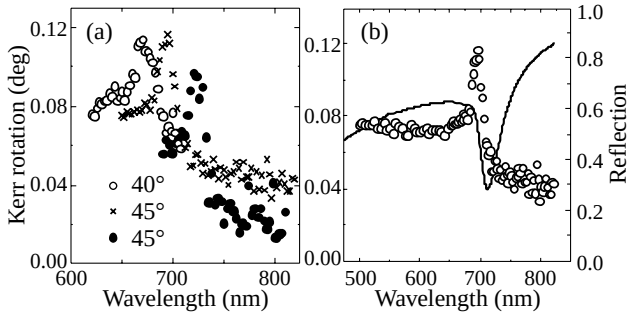

Fig. 3. (a) MOK at various angles of incidence, (b) correlation in spectrum between Kerr angle (circles, left axis) and reflected light intensity (solid line, right axis) in zeroth order of diffraction (specular reflection).

the present work are undoubtedly connected with SPP.

Firstly, dramatic difference between *s*- and *p*-polarization is observed. Only in the case of *p*-polarization nearly 2 times weakening in specular reflection is experimentally demonstrated. Some part of electromagnetic energy of incident radiation is needed for inducing SPP, it leads to weakening of reflected light intensity. In the case of *s*-polarized incident light no peculiarities in reflectance spectrum is observed. It is connected with *s*-polarization restriction for SPP occurred due to boundary conditions on the metallic surface. No SPP is excited in this case and no weakening in reflected light intensity is observed.

Secondly, the effects described above take place at every angle of incidence at the corresponding wavelength. Wavelength and angle of incidence are connected by k-matching conditions of lateral component of incident wave vector, SPP wave-vector and vector of reciprocal lattice. Such behavior indicates on plasmon excitation due to SPP dispersion properties modified by periodic conditions.

Phenomenological description of Kerr effect enhancement can be given in the following way. Due to *s*-polarization restriction for SPP *s*-component appeared due to traditional Kerr effect is immediately radiated, in contrast, some part of *p*-component is transformed in SPP. It leads to Kerr effect enhancement as Kerr angle can be approximately assumed to be equal to ratio of amplitudes of *s*- and *p*-component reflected light.

3. Conclusion

Wood's anomaly is experimentally observed in 2D plasmon-assisted nickel magnetophotonic crystals. It is shown to be polarization-dependent and appears at any angle of incidence in the range between 10° and 70°. Wavelength corresponding to this spectrum peculiarity satisfies k-matching conditions for lateral component of incident wave, SPP wave vector and vector of reciprocal lattice. All it vividly indicates SPP inducing on the metal surface of the sample. Magneto-optical Kerr effect measurements also prove SPP excitation. Experimental results are in good agreement with numerical calculations.

Acknowledgements

This work was supported by Russian Foundation of Basic Research and by Grant-in-Aid from Ministry of Education, Culture, Sport and Technology of Japan.

References

[1] A. A. Fedyanin, O. A. Aktsipetrov, D. Kobayashi, K. Nishimura, H. Uchida, M. Inoue, *J. Magn. Magn. Mater.* **282**, 256 (2004).
[2] V. I. Belotelov and A. K. Zvezdin, *J. Opt. Soc. Am. B* **22**, 286 (2005).
[3] L. Martin-Moreno *et al*, *Phys. Rev. Lett.* **86**, 1114 (2001).
[4] V. I. Belotelov, A. K. Zvezdin, *J. Magn. Magn. Mater.* **300**, e260 (2006).

15th Int. Symp. "Nanostructures: Physics and Technology"
Novosibirsk, Russia, June 25–29, 2007

Optical modes in semiconductor microtube ring resonators

Detlef Heitmann, Tobias Kipp and Christian Strelow
Institut für Angewandte Physik und Zentrum für Mikrostrukturforschung, Universität Hamburg, Germany

Using sophisticated MBE growth and etching technique it is possible to fabricate microoptical resonators with semiconductors, like Bragg reflector based microcavities, microdisk or photonic-crystal microcavities, which are interesting systems for lasers, quantum computing or cavity quantum electrodynamics. We have fabricated self-supporting microtubes starting from MBE grown strained bilayers. By underetching a sacrificial layer the bilayer rolls up producing a 5 μm diameter microroll with 200 nm walls. These walls guide light and act as an optical ring resonator. We probe the optical modes by the photoluminescence of self assembled InAs quantum dots imbedded in the tube wall. We find a series of sharp modes indicating Q-factors up to 3000.

I will further address arrays of semiconductor microdisks which have been prepared by holographic lithography and which support whispering gallery modes.

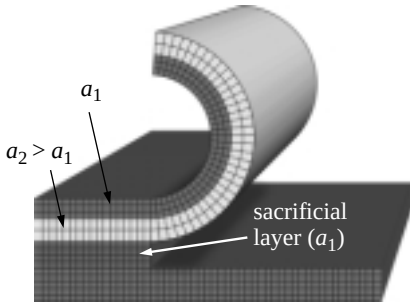

Fig. 1.

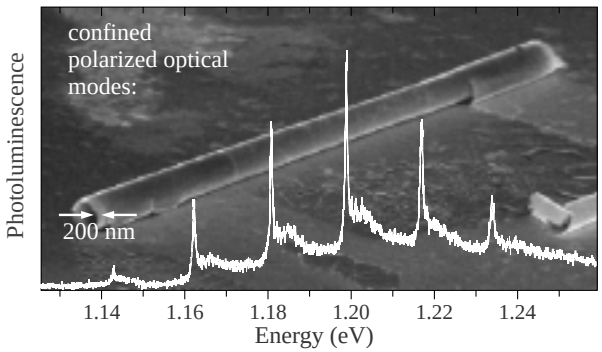

Fig. 2.

References

[1] Tobias Kipp *et al*, *PRL* **96**, 077403 (2006).

15th Int. Symp. "Nanostructures: Physics and Technology"
Novosibirsk, Russia, June 25–29, 2007

Opals versus Langmuir–Blodgett colloidal crystals — three-dimensional ensembles with different photonic bandgap dimensionality

S. G. Romanov[1], M. Bardosova[2], I. Povey[2], C. M. Sotomayor Torres[2] and M. Pemble[2]

[1] Ioffe Physico-Technical Institute, St Petersburg, Russia
[2] Tyndall National Institute, University College Cork, Cork, Ireland

Abstract. The optical transmission of self-assembled opals and Langmuir–Blodgett assembled colloidal crystals has been compared. Elimination of zero order diffraction resonances from all but growth planes, and broadening and deepening of the remaining resonance have been observed. The transmission minima in LB crystals at shorter wavelengths have been identified as losses due to excitation of eigenmodes in a sphere monolayer. Similar minima in transmission of thin opal films have been explained as the surface effect.

Introduction

Colloidal crystals are proved to be suitable model materials to study the photonic energy band structure (PBG) in three-dimensional (3D) lattices. The energetically favorable face-centered cubic (fcc) symmetry dominates the self-assembled colloidal crystal lattices leading to the opal formation. Among alternative techniques, the Langmuir–Blodgett (LB) method [1,2] is arguably the one, which possesses a prospect for large-scale implementation. LB crystals are stacks of monolayers of pre-packed 2D colloidal crystals. The LB approach has a distinct advantage over other methods of assembly, where either only few monolayers are required or a low symmetry of PBG is needed.

In order toevaluate the pros and contras of LB colloidal ensembles as potential photonic crystals (PhCs), it is instructive to compare their optical properties with that of opals. Recently we demonstrated that LB crystals can be described as (2+1)D PhCs [3]. This approach allows the separation of the PBG spectral range into two parts, $\lambda \leq 2D$, where D is the diameter of spheres, and $\lambda \approx D$. Here we report the comparative analysis of the anisotropy of light propagation in opals and LB crystals.

1. Experimental

Silica spheres of $D = 250$ and 519 nm were made hydrophobic using 3-(trimethoxysilyl)propyl methacrylate. Opals were prepared from these spheres by controlled evaporation of an ethanol solution on a glass substrate. LB crystals were deposited on a glass substrate from doubly distilled deionized water subphase [4]. First, monolayers of hexagonally packed spheres were compressed on a water surface and, then, they were transferred onto a glass substrate. The LB film studied was 10 and 20 monolayer thick and the thickness of opal film was made nearly equal to this in order to facilitate the comparison.

Angle-resolved transmission spectra were acquired at different angles of incidence, θ, with respect to the film normal. A 1 mm in diameter beam of linearly polarised white light from a tungsten halogen lamp was used. The transmitted light was collected from a solid angle of 2° and passed through a quarter-wavelength plate before detecting.

2. Results and discussion

Transmission spectra of opal and LB crystals (Fig. 1) show (i) similar transparency, (ii) different structure of diffraction resonances, (iii) the same angle dispersion of similar minima branches, (iv) broader and deeper transmission minima in LB crystals, (v) similarity of polarisation anisotropy, (vi) stronger transmission decay with decreasing wavelength in LB crystals.

In the LB crystal only one branch of the diffraction resonance was observed. This occurs due to random lateral displacement of monolayers in a stack. The interplane spacing in LB crystal exceeds that of opal assembled from the same beads (Figs. 2,3). Thus, LB crystal properties in the wavelength range $\lambda \leq 2D$ are those of the Bragg mirror. The polarisation anisotropy in LB crystal approaches its maximum at the Brewster angle ($\theta_B \approx 53$ °), whereas in the opal it occurs at the wavelength of the multiple-wave diffraction ($\theta \approx 45$ °).

The width of the transmission minimum in the LB crystal exceeds that in opal in both polarizations due to smaller

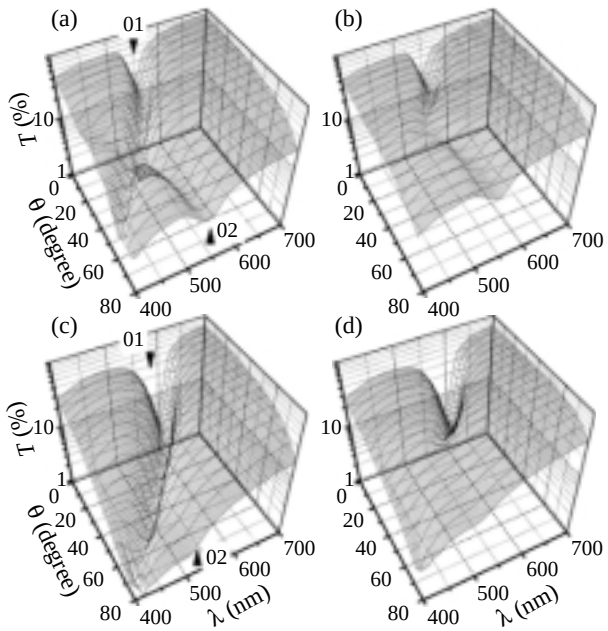

Fig. 1. Transmission spectra of the opal (a), (b) and the LB crystal (c), (d) in s- (a), (c) and p- (b), (d) polarised light in the range $\lambda \leq 2D$. $D = 250$ nm.

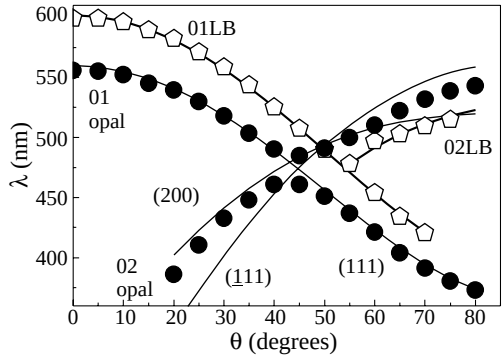

Fig. 2. Dispersion of transmission minima in opal (solid symbols) and LB crystal (open symbols). Lines show fitting of dispersion with Bragg–Snell law.

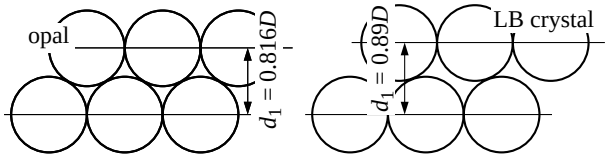

Fig. 3. Schematics of opal and LB crystal lattice.

volume fraction of dielectric in its lattice (Fig. 4). Whether this broadening is enhanced by stronger light localization in partly disordered lattice, similar to the quasi-crystals, remains a matter of modeling.

Transmission spectra in the range $\lambda \approx D$ (Fig. 5) bear similar motif in opals and LB crystals. The transparency of the samples and the angle dispersion of main minima suggest the similar mechanism behind this behaviour. The transmission spectra of a single monolayer are similar to that of LB stack of 10 sphere monolayers. This suggests that in the range $\lambda \approx D$ the transmission minima occur due to excitation of TE and TM modes propagating in a monolayer, which is effectively a 2D PhC [5]. In the first approximation, these modes in each monolayer are independent from that in other monolayers, since the total attenuation in the transmission minimum increases linearly with the number of monolayers. Surprisingly, the same features survive in an opal. This is a boundary effect, which should be taken into account, when opal spectra are interpreted on a basis of calculations made for infinitely large structure. Thus TE and TM type modes, which propagate along the surface of the opal film, contribute strongly to the transmission of a 3D PhC. The 3D ordering leads to splitting of 2D modes by the interplane interaction.

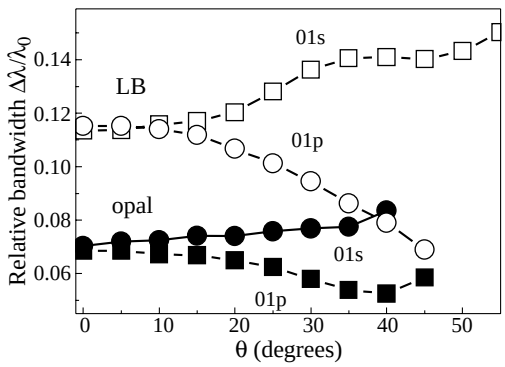

Fig. 4. Angle dispersion of the relative minimum width, which is the FWHM divided on the central wavelength of the minimum.

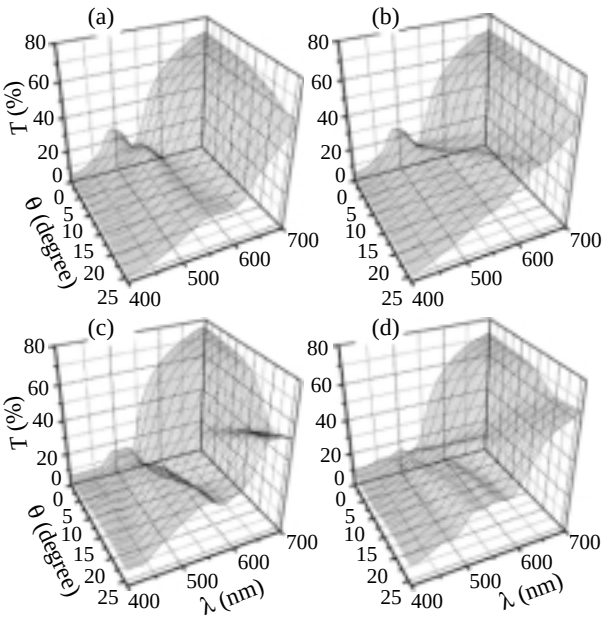

Fig. 5. Transmission spectra of the LB crystal (a), (b) and the opal (c), (d) in *s*- (a), (c) and *p*- (b), (d) polarised light in the range $\lambda \approx D$. $D = 519$ nm.

3. Summary

Comparative studies of optical transmission in 3D colloidal ensembles of different topology revealed the essential difference of related PBG structures. Eliminating the correlation between sphere monolayers in LB crystals reduces the total PBG dimensionality due to separation of the 1D and 2D components. In the case of PhCs based on thin opal films, the 2D component is also present that generates more spectral features then expected for opal of infinitely large size.

Acknowledgements

This work was supported in part by the NoE Phoremost, the Science Foundation Ireland and the RFBR 05-02-16975 grant.

References

[1] B. van Duffel *et al*, *J. Mat. Chem.* 3333 (2001).
[2] M. Bardosova *et al*, *Thin Sol. Films* **437**, 276 (2003).
[3] S. G. Romanov *et al*, *Appl. Phys. Letters* **89**, 43105 (2006).
[4] M. Bardosova *et al*, *Acta Phys. Slovaca* **54**, 1 (2004).
[5] H. T. Miyazaki *et al*, *J. Appl. Phys.* **87**, 7152 (2000).

15th Int. Symp. “Nanostructures: Physics and Technology”
Novosibirsk, Russia, June 25–29, 2007

Controlling super- and subradiant modes in a plasmonic lattice

A. Christ[1], Y. Ekinci[2], H. H. Solak[3], N. A. Gippius[4,5], S. G. Tikhodeev[4] and O. J. F. Martin[1]

[1] Nanophotonics and Metrology Laboratory, Swiss Federal Institute of Technology, 1015 Lausanne, Switzerland
[2] Laboratory of Metal Physics and Technology, Swiss Federal Institute of Technology, 8093 Zürich, Switzerland
[3] Laboratory for Micro- and Nanotechnology, Paul Scherrer Institut, 5232 Villigen, Switzerland
[4] A. M. Prokhorov General Physics Institute RAS, Moscow 119991, Russia
[5] LASMEA, UMR 6602 CNRS, Université Blaise Pascal, 63177 Aubière, France

Abstract. We study radiation damping of localized surface plasmon modes in a plasmonic lattice. It is shown that the spectral interference between the supported super- and subradiant modes results in characteristic line shape modifications which are directly controlled by the chosen lattice geometry. Metallic structures with symmetrical as well as asymmetrical unit cells are analyzed. The presented fundamental physical effects allow a broad range of applications including the design of novel metamaterials, filters and sensors.

Introduction

Metal nanostructures supporting localized surface plasmon polariton modes (i.e., so-called particle plasmons) play a crucial role in several emerging fields of nanoscience, where their remarkable optical properties are currently the subject of considerable research efforts. When illuminated at their resonance frequency, such nanostructures produce extremely strong and confined optical fields, which can be used to alter light-matter interactions on the nanoscale. Prominent phenomena such as surface-enhanced Raman scattering [1], waveguide-plasmon polariton formation [2], or magnetic activity at optical frequencies [3] have been widely discussed. Furthermore, the design of so-called nanometer-scale dipole antennas has attracted recent interest. Their specific design, which is generally based on particle dimers, allows efficient interconversion of propagating light and localized, enhanced fields [4]. However, whereas the near-field coupling [5] and the induced local field enhancement [6] of various dimer structures has been extensively analyzed, only few studies on radiation damping phenomena in such structures can be found [7]. In general, radiation damping can be controlled by coherent coupling of the bare dimer modes. Similar to their well-known semiconductor equivalents [8, 9], radiative coupling in a well designed plasmonic system should result in the formation of super- and subradiant states [10].

The aim of the work is to investigate the formation of collective states in a suitable plasmonic model system. In particular, it is shown how the interplay between super- and subradiant modes in a plasmonic lattice is controlled by simply tuning the geometrical properties of the ensemble. Integration of such plasmonic nanostructures will allow a broad range of applications including novel metamaterials, filters, and sensors.

1. One-dimensional plasmonic lattice

The numerically analyzed one-dimensional plasmonic model system is schematically displayed in Fig. 1. The bare plasmonic crystal in panel (a) consist of a regular gold nanowire array with an individual wire cross-section of $100 \times 15\,\mathrm{nm}^2$. The considered structure can be interpreted in terms of a so-called plasmonic superlattice [11]. In contrast to a simple grating with a single wire per unit cell, the superlattice unit cell is now composed of a set of 2 wires. The supercell period is specified by d_x, while d_s describes the lateral wire displacement within the individual supercell. In a first step [see panel (b) of Fig. 1], periodic defects are introduced by shifting vertically one of the supercell wires (i.e., each second wire of the lattice). In a second step [see panel (c) of Fig. 1], a modification of the lateral wire separation within the individual supercells is also considered. A plasmonic lattice with asymmetrical unit cell is hence obtained. For the calculation of the optical response (transmission, reflection, absorption) and of the characteristic electromagnetic field distributions, a scattering-matrix formalism has been employed [12]. This numerical method is generally well-suited for the study of a periodically structured multilayer medium and works without any fit parameters.

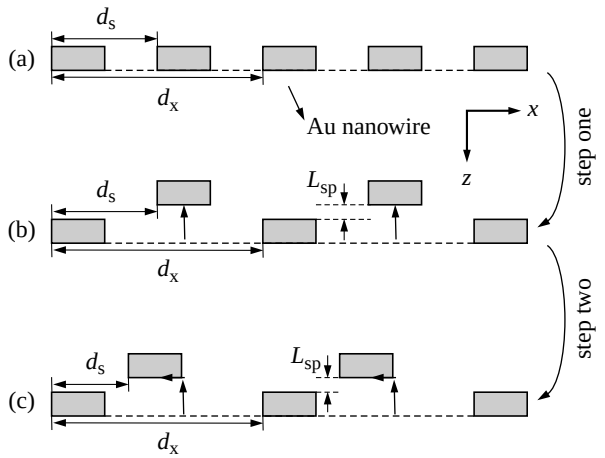

Fig. 1. Sketch of the investigated gold nanowire structure. In a first step, the perfect grating structure (a) is modified by shifting each second wire of the array (b). The obtained vertical wire separation is specified by L_{sp}. In a second step, an additional lateral displacement of the upward shifted wires is introduced (c) to implement a lattice with asymmetrical unit cell.

2. Fano-type interference

The induced modifications of the reflection and absorption spectra are highlighted in Fig. 2. Exemplary, numerical results are shown for three fundamental wire arrangements. The spectra of a regular lattice ($d_x = 400$ nm, $d_s = 200$ nm) are shown in panel (a). The corresponding spectra for lattice geometries with $L_{sp} = 10$ nm and $L_{sp} = 30$ nm ($d_x = 400$ nm, $d_s = 200$ nm) are displayed in panels (b) and (c). In contrast to

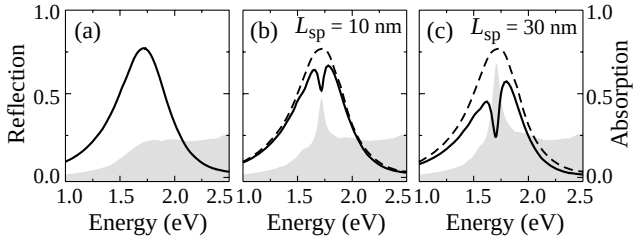

Fig. 2. Calculated reflection (solid lines) and absorption spectra (shaded areas) for TM polarization and normal light incidence. The spectra of a regular grating ($d_x = 400$ nm, $d_s = 200$ nm) are shown in panel (a). The corresponding spectra for lattice geometries with $L_{sp} = 10$ nm and $L_{sp} = 30$ nm ($d_x = 400$ nm, $d_s = 200$ nm) are displayed in panels (b) and (c). Additionally, the reflection spectrum of the perfect lattice is plotted as a reference (dashed lines).

the single localized surface plasmon resonance of a bare grating layer, the vertical shift results in the excitation of two collective surface plasmon modes. Compared to the recently discussed optical response of grating-film structures [13], antisymmetric (subradiant, spectrally narrow) and symmetric (superradiant, spectrally broad) surface plasmon modes can be excited simultaneously. Their spectral interference leads to a characteristic Fano-type line shape in the reflection spectra of the interacting wire ensemble [14].

The situation changes dramatically when the lateral wire separation within the supercell is also modified. The influence of an asymmetrical unit cell on the optical response is illustrated in Fig. 3. The calculated reflection and absorption spectra are shown for structures with a constant period of $d_x = 400$ nm and a constant spacer thickness of $L_{sp} = 30$ nm. Only the vertical wire separation is changed and structures with $d_s = 100$ nm, $d_s = 50$ nm, and $d_s = 0$ nm are compared. The displayed spectra directly reflect the influence of an increased near-field coupling between the wires of the supercell. The spectral position of the collective surface plasmon modes is altered due to the modification of the effective restoring forces of the optically induced surface charges. The subradiant plasmon mode of the wire ensemble is lowered in energy, while the superradiant mode is blueshifted. Note that the considered asymmetrical supercells changes the structure factor of the lattice. As important result, a Wood anomaly appears as additional feature of the reflection and absorption spectra [15].

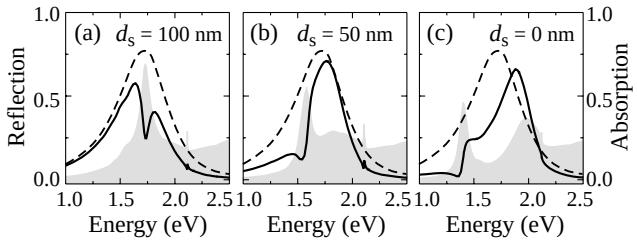

Fig. 3. Calculated reflection (solid lines) and absorption spectra (shaded areas) for TM polarization and normal light incidence. While the period $d_x = 400$ nm and the spacer thickness $L_{sp} = 30$ nm are kept constant, only the parameter d_s is modified. Spectra for grating structures with $d_s = 100$ nm (a), $d_s = 50$ nm (b), and $d_s = 0$ nm (c) are compared. Additionally, the reflection spectrum of the perfect lattice ($d_x = 400$ nm, $d_s = 200$ nm) is plotted as a reference (dashed lines).

Acknowledgements

Financial support by the European Commission (Grant No. FP 6-2002-IST-1-507879), the Russian Academy of Sciences, and the Russian Foundation for Basic Research (Grant No. 06-02-17211) is acknowledged.

References

[1] M. Moskovits *et al*, *Rev. Mod. Phys.* **57**, 783 (1985).
[2] A. Christ *et al*, *Phys. Rev. Lett* **91**, 183901 (2003).
[3] S. Linden *et al*, *J. Science* **306**, 1351 (2004).
[4] P. Mühlschlegel *et al*, *Science* **308**, 1607 (2001).
[5] W. Rechenberger *et al*, *Opt. Commun.* **220**, 137 (2003).
[6] J. P. Kottmann *et al*, *Opt. Express* **8**, 655 (2001).
[7] C. Dahmen *et al*, *accepted Nano Lett.* (2007).
[8] E. L. Ivchenko *et al*, *Phys. Solid State* **36**, 1156 (1994).
[9] M. Hübner *et al*, *Phys. Rev. Lett.* **76**, 4199 (1996).
[10] R. H. Dicke *et al*, *Phys. Rev.* **93**, 99 (1954).
[11] T. Zentgraf *et al*, *Phys. Rev. B* **73**, 115103 (2006).
[12] S. G. Tikhodeev *et al*, *Phys. Rev. B* **66**, 045102 (2002).
[13] A. Christ *et al*, *Phys. Rev. B* **74**, 155435 (2006).
[14] A. Christ *et al*, *submitted* (2007).
[15] A. Christ *et al*, *Phys. Rev. B* **70**, 125113 (2004).

15th Int. Symp. "Nanostructures: Physics and Technology"
Novosibirsk, Russia, June 25–29, 2007

Hard excitation regime of polariton scattering in microcavities

S. S. Gavrilov[1,2,3], *N. A. Gippius*[2,3], S. G. Tikhodeev[3] and V. D. Kulakovskii[1]

[1] Institute of Solid State Physics, RAS, Chernogolovka, Moscow District 142432, Russia
[2] LASMEA, CNRS, Université Blaise Pascal, 24 av. des Landais, 63177 Aubière, France
[3] General Physics Institute, RAS, 38 Vavilov Street, Moscow, 119991, Russia

Abstract. We report a theoretical analysis of the polariton parametric scattering in semiconductor microcavities. The abrupt jump of a driven cavity mode amplitude with a graduate increase of the laser pump intensity is shown to result in a drastic redistribution of the parametric scattering pattern.

Introduction

Light-matter coupling in semiconductor nanostructures is a quickly developing field of modern physics that has already proved its high potential for both the fundamental science and practical applications. A prominent example are semiconductor microcavities with a strong resonant amplification of the intra-cavity electromagnetic field. The coupling of this electromagnetic resonance with, e.g., exciton resonance in the cavity-embedded quantum well results in the formation of cavity polaritons, provided the overall dephasing is smaller than the coupling between the exciton and photon modes (so called strong coupling regime).

The nonlinearities of the polariton system are mainly due to the exciton-exciton interaction that is strongly increased at frequencies close to the exciton resonance. The resulting nonlinear interaction of polaritons has been studied intensively in the last decade and lot of interesting nonlinear phenomena have been observed, including the blue shift of the lower polariton branch and the stimulated scattering of cavity polaritons [1–3]. The latter is usually treated in a way similar to hyper-Raman scattering in bulk semiconductors and an analog of the optical parametrical oscillator model is often used for interpretation of the experimental results [4–6].

In this contribution we address the important feature of nonlinear scattering in a driven 2D microcavity system that makes it essentially different from the bulk parametric scattering. This feature is the possibility of drastic changes of intra-cavity field under negligibly small variations of the external laser intensity, as has been shown recently in [8,9,7]. As a result, the stimulated parametric scattering in a planar microcavity arises through a hard excitation regime. An indirect consequence of this drastic change — the fact that the scattered polariton signal above the threshold of parametric scattering is always directed perpendicular to the cavity plane — has been experimentally discovered in [10] (see also in [8]) and later confirmed in [11].

Hard excitation of the parameric scattering

To illustrate the difference between the parametric scattering in the bulk and in a planar microcavity, let us compare the excitation by infinite external plane wave (this corresponds to a broad enough laser beam). As it is well known, the plane wave excited in a bulk semiconductor by external laser incident on a flat surface is characterized by the same frequency and in-plane quasimomentum as the external wave. The third quasimomentum component (normal to the surface) depends on the semiconductor refractive index nonlinearity and changes smoothly with the amplitude of the internal field, that, in turn, is a smooth function of the external power except of a narrow frequency range around the sharp exciton resonance [12].

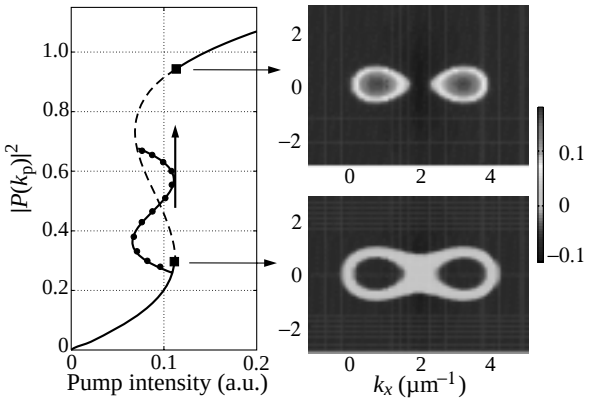

Fig. 1. Hard excitation regime of polariton scattering. See explanation in the text.

On the other hand, in the case of a planar cavity, the wavevector component normal to the surface is fixed by the mirrors. This means that the field inside the cavity is increased near the specific resonance frequency for a given in-plane quasimomentum. This resonant frequency also depends on the intensity of the field *inside* the cavity and is usually blue shifted for larger intensities. As a result the field *inside* the cavity is a sharp function of both the frequency and external pump power.

In this work we extend our previous semi-classical approach [8,9,7] to account for the two polarization states of the cavity modes (TE and TM) and for the two spin states of the quantum well excitons that can optically couple with the cavity modes.

The main results are summarized in the Figure.

Left panel shows the driven polariton density as a function of linearly polarized external pump intensity. The solid lines display the trajectory of a stable system under the slowly growing pump at quasimomentum $\mathbf{k}_\mathrm{p} = (k_x, k_y)$, $k_x \approx 2\ \mu\mathrm{m}^{-1}$, $k_y = 0$. The two points of discontinuity are shown by square markers. These points correspond to the high intensity boundary of the polariton bi-stability area. The line marked by dots shows the other possible stable driven states with predominant circular polarization (either positive or negative) of the driven polariton mode.

Right panel shows the distribution of the polariton increment, $\Gamma(k_x, k_y)$ in the quasimomentum $\mathbf{k}$-space, calculated at two driven polariton densities shown by the square markers in the left panel. The color-map of the plot is shown on the right. Whereas in the low-density regime the scattered polariton increment is maximum on an eight-shaped region (bottom right

sub-panel), in the high-density regime it is centered around $\mathbf{k}_{\rm signal} \gtrsim 0$ for the signal and $\mathbf{k}_{\rm idler} \lesssim 2\mathbf{k}_{\rm p}$ for the idler (top right sub-panel).

The predominant scattering pattern in the system should reveal these distributions of increments. For the high-density regime it was established experimentally in [10,11], and for the low-density regime — in [13]. The transition from the low-density to the high-density regime has been recently demonstrated experimentally [14].

Acknowledgements

This work was supported by the Russian Foundation for Basic Research (Grant No. 06-02-17211), the Russian Academy of Sciences (Programs "Quantum Nanostructures" and "Strongly correlated electrons") and the ANR Chair of Excellence Program.

References

[1] R. M. Stevenson, V. N. Astratov, M. S. Skolnick, D. M. Whittaker, M. Emam-Ismail, A. I. Tartakovskii, P. G. Savvidis, J. J. Baumberg, and J. S. Roberts, *Phys. Rev. Lett.* **85**, 3680 (2000).

[2] A. I. Tartakovskii, D. N. Krizhanovskii, and V. D. Kulakovskii, *Phys. Rev. B* **62**, R13298 (2000).

[3] J. J. Baumberg, P. G. Savvidis, R. M. Stevenson, A. I. Tartakovskii, M. S. Skolnick, D. M. Whittaker, and J. S. Roberts, *Phys. Rev. B* **62**, R16247 (2000).

[4] C. Ciuti, P. Schwendimann, and A. Quattropani, *Phys. Rev. B* **63**, 041303 (2001).

[5] D. M. Whittaker, *Phys. Rev. B* **63**, 193305 (2001).

[6] P. G. Savvidis, C. Ciuti, J. J. Baumberg, D. M. Whittaker, M. S. Skolnick, and J. S. Roberts, *Phys. Rev. B* **64**, 075311 (2001).

[7] S. S. Gavrilov, N. A. Gippius, V. D. Kulakovskii, and S. G. Tikhodeev, *JETP* (2007), to be published.

[8] N. A. Gippius, S. G. Tikhodeev, V. D. Kulakovskii, D. N. Krizhanovskii, and A. I. Tartakovskii, *Europhys. Lett.* **67**, 997 (2004).

[9] N. A. Gippius and S. G. Tikhodeev, *J. Phys.: Condens. Matter* **16**, S3653 (2004).

[10] V. D. Kulakovskii, A. I. Tartakovskii, D. N. Krizhanovskii, N. A. Gippius, M. S. Skolnick, and J. S. Roberts, *Nanotechnology* **12**, 475 (2001).

[11] R. Butte, D. M. Skolnick, M. S. Whittaker, D. Bajoni, and J. S. Roberts, *Phys. Rev. B* **68** 115325 (2003).

[12] V. F. Elesin and Y. V. Kopaev, *Sov. Phys. JETP* **36**, 767 (1973).

[13] W. Langbein, *Phys. Rev. B* **70**, 205301 (2004).

[14] D. N. Krizhanovskii, S. S. Gavrilov, A. Love, N. A. Gippius, S. G. Tikhodeev, V. D. Kulakovskii, D. Sanvitto, D. Whittaker, M. S. Skolnick, and J. S. Roberts, (2007), to be published.

15th Int. Symp. "Nanostructures: Physics and Technology"
Novosibirsk, Russia, June 25–29, 2007

Whispering-gallery modes in micro-disk cavities with InAs quantum dots: near-field photoluminescence spectroscopy imaging

A. Mintairov[1,2], Y. Chu[1], Y. He[1], J. Merz[1], V. Tokranov[2], S. Oktyabrsky[2], S Blokhin[3], A. Kuzmenkov[3], E. Tanklevskaya[3], M. Maximov[3] and V. Ustinov[3]

[1] Department of Electrical Engineering, University of Notre Dame, IN 46556, USA
[2] Institute for Materials, SUNY Albany, NY 12203, USA
[3] Ioffe Physico-Technical Institute, St Petersburg, Russia

Abstract. The images of whispering-gallery modes (WGM) in high quality factor ($\sim 10^4$) AlGaAs micro-disks (radii 1–3 μm) with InAs quantum dots have been resolved using near-field scanning photoluminescence spectroscopy technique. The technique, allowing direct measurements of the azimuthal numbers (m) of WGMs, reveals anomaly spectral dependence of m.

Introduction

Few micrometer diameter semiconductor discs are represent whispering-gallery mode (WGM) [1] resonators. They can provide quality factors (Q) up to $\sim 10^5$ [2] and are promising for low threshold micro-lasers [3]. Embedding of quantum dots (QDs) in such high-Q micro-disks (MDs) cavities is promising for single photon sources [4] and for studying cavity quantum electrodynamics effects [5]. During last decade optical properties of such cavities were studied intensively. However, using of high spatial resolution optical techniques, such as near-field optical scanning microscopy (NSOM), which allows imaging of optical field distributions in MDs is limited by few publications [6, 7], which however did not provide enough resolution to analyze WGM structures. The probing of the optical fields in such small size cavities except interesting fundamental problem can be very important for designing of the devices based on MDs.

In the present paper we studied the possibilities of detecting optical fields related to WGM in 2–6 μm GaAs/AlGaAs MDs with self-organized QDs emitting in 1.2–1.3 μm using the combination of NSOM and photoluminescence spectroscopy.

Experimental and calculation details

MDs studied in this work were prepared from two structures, further denoted as A and B, with embedded self-organized InAs quantum dots. For A(B) structures single QD layers with density $8(5)\times10^{10}$ cm^{-2} were inserted in the waveguide consisting of 170(195) nm thick GaAs($Al_{0.3}Ga_{0.7}As$) layer and 20(40) nm thick $Al_{0.3}Ga_{0.7}As$($Al_{0.56}Ga_{0.44}As$) high-refractive index layers. The waveguide layer was grown on the top of the high Al content (90–98%) AlGaAs layer having thickness 500 nm. The emission spectra of the A(B) structures at intermediate excitation level consist of the band with halfwidth ~60 nm centered at ~1.3 (~1.2) μm, related to the ground state transition of QDs. Weaker bands separated by ~100 nm and related to the exited states transitions were also observed at shorter wavelengths.
From structure A MDs were prepared by optical lithography, reactive ion etching (RIE) and by the oxidation of $Al_{0.98}Ga_{0.02}As$ layer. Here we studied MDs having radii 2.7 and 3 μm. We will denote them further as MDA.

The structures B was first wafer bonded to Si or GaN wafer using spin-on-glass. Then after removal of GaAs substrate and $Al_{0.90}Ga_{0.10}As$ layer MDs, further denoted as MDB, were fabricated using e-beam lithography and RIE.

Near-field photoluminescence (NPL) spectra were excited using 488 nm emission from Ar laser and measured in collection-illumination mode with a 270 mm focal length spectrometer and liquid nitrogen cooled InGaAs multi-channel detector. The spectral resolution was 0.3–0.6 nm. For measuring emission patterns we used the same spectrometer with nitrogen cooled Ge-detector attached to second exit slit port. The spatial resolution was ~300 nm. Micro-PL spectra reveal quality factors of the cavities up to $\sim 10^4$.

For evaluation of mode parameters for ideal disks we used the analytical method using conformal transformation and Wentzel–Kramers–Brillouin approximation [8] with boundary condition of first kind (field is equal zero at disc edge). Numerical finite-difference-time-domain method, available commercially, was used to account for effect of surface roughness on WGM. The roughness was generated by dividing disk on 14 sections with small (2%) random deviations of radius, centre and ellipticity. We found that MDA cavities can support only TE modes, while MDB can support both TE and TM modes.

Results and discussion

Fig. 1 shows azimuthal numbers (m) versus resonance wavelength ($\lambda_{m,n}$, where subscript n denotes radial number) and selected magnetic field patterns for WGM predicted for our MDA ($R = 2$ and 3 μm) and MDB ($R = 1$ and 2 μm) cavities by analytical model for spectral range corresponding to QD emission (1150–1400 nm for MDA and 1100–1300 nm for MDB). The optical field for (m, n)-WGM has m maxima along the circumference and n maxima along the radius. Fig. 1 demonstrates trends expecting for ideal disk: decreasing m with of the increase of $1/R$, λ and n, together with the decreasing of mode splitting ($\Delta\lambda_{m,n}$) with R increase. The increasing of the refractive index (on ~ 0.03), for MDA cavity increases $\lambda_{m,n}$ on $\sim$ 40 nm. The TM modes have smaller $\lambda_{m,n}$ then TE modes. For $R = 1$ μm the shift is $\sim$ 90 nm and for $R = 2$ μm it is $\sim$ 30 nm. For TE modes and $R = 1$, 2 and 3 μm one can expect have $m \sim 10$, 25 and 37 for $n = 1$, and $m \sim 7$, 20 and 34 for $n = 2$, respectively; the mode splitting between the modes with the same n is expected to be $\sim$ 60, 30 and 20 nm, and between $n = 1$ and $n = 2$ modes $\sim$ 20, 10, 5 nm, respec-

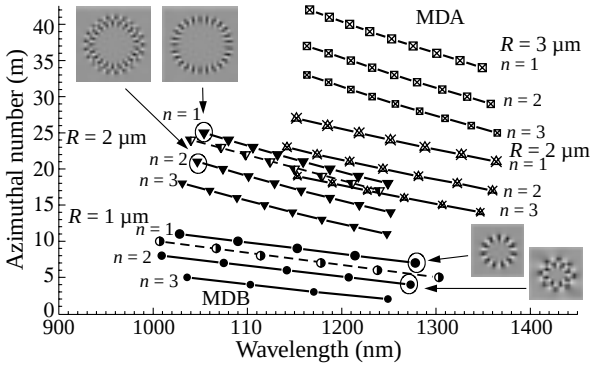

Fig. 1. Azimuthal numbers (m) versus resonance wavelength $\lambda_{m,n}$ ($n = 1, 2, 3$) for TE WGM for MDA with $R = 2$ (crossed triangle) and $R = 3$ μm (crossed square) and MDB with $R = 1$ (solid circles) and $R = 2$ μm (solid triangles). The m numbers for TM modes with $n = 1$ are shown for $R = 1$ (half-filled circles) and 2 (half-filled triangles) μm. Inserts show magnetic field amplitudes for four selected TE modes.

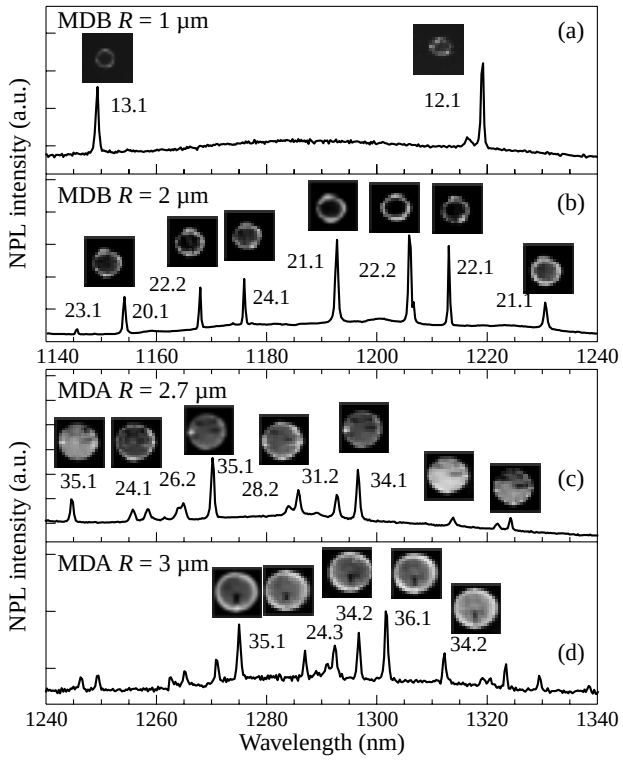

Fig. 2. NPL spectra and $8 \times 8\,\mu$m mode images of micro-disk cavities: (a) MDB $R = 1\,\mu$m, (b) MDB $R = 2\,\mu$m, (c) MDA $R = 2.7\,\mu$m and (d) MDA $R = 3\,\mu$m.

tively. Neglecting the higher order radial modes one can expect for 100 nm spectral range ~ 4, ~ 6 and ~ 10 TE modes for $R = 1$, 2 and 3 μm respectively. For MDB cavities number of modes can be twice higher due to contribution of TM modes.

In Fig. 2 we present the 100 nm range NPL spectra and selected mode images for $R = 1$, 2, 2.7 and 3 μm. Fig. 3 shows comparison of NPL spectra of 1 μm MDB with the FDTD calculations together with experimental images and theoretical mode patterns for three main WGMs observed in spectral range 1050–1300 nm. The images in Fig. 2 and 3 show clear bright maxima near the cavity circumference. Maxima with very weak intensities located ~ 700 nm from the edge are also observed for some modes. The maxima are elongated along radial direction and have size $\sim 500 \times 200$ nm. The shape, intensities and spacing of the maxima are strongly varying. Counting the number of maxima or measuring the angle between them allows approximate determining the azumithal numbers, which are shown in Fig. 2 near each line.

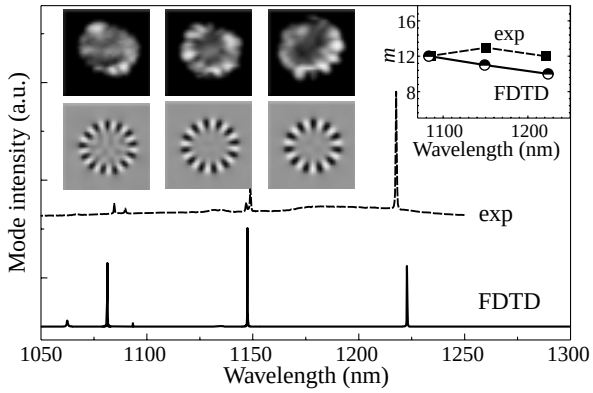

Fig. 3. NPL spectra (exp), calculated mode intensity (FDTD) response together with 3.5×3.5 μm images and field patterns for $R = 1$ μm MDB. Right insert shows experimental and calculated azimuthal numbers.

Analysis of Fig. 2 shows that that the number of lines, the mode splitting (accounting for TM mode contribution for $R = 2$ μm) and average azimuthal numbers follow well cavity size. However dependence of the m on wavelength shows anomaly behavior: for some modes, it can increase at longer wavelength. This effect can be seen in Fig. 3 for $R = 1$ μm, for modes (23.1) and (24.1) for $R = 2$ μm, and for modes (35.1) and (36.1) for $R = 3$ μm. The possible sources of such anomaly can be contribution of QD ground and excited states transition to the dielectric function of the cavity as well as mixing of the WGM by surface roughness. The FDTD calculations for accounting of these effects are in progress.

Conclusions

The images of whispering-gallery modes (WGM) in high quality factor ($\sim 10^4$) AlGaAs micro-disks (radii $R = 1$–3 μm) with InAs quantum dots have been resolved using near-field scanning photoluminescence spectroscopy technique. The technique, allowing direct measurements of the azimuthl numbers (m) of WGMs, reveals anomaly spectral dependence of the m.

Acknowledgements

The support of Program of the fundamental studies of the Physical Department of RAS "Novel materials and structures", Program of the physical department of RAS, Program of St Petersburg scientific center are acknowledged.

References

[1] Lord Reylrigh, *Scientific papers* (Cambridge University, Cambridge, U.K., 1912) 5, 617 (1912).
[2] K. Srinivasan *et al*, *Appl. Phys. Lett.* **86** 151106 (2005).
[3] S. L. McCall *et al*, *Appl. Phys. Lett.* **60** 289 (1992).
[4] P. Michler *et al*, *Science*, **290** 2282 (2000).
[5] J. M. Gerard *et al*, *Phus. Rev. Lett.* **81**, 1110 (1998); J. P. Reithmaier *et al*, *Nature* **432**, 197 (2004).
[6] X. Zhu *et al*, *J. Microscopy* **194**, 439 (1999).
[7] D. J. Shin *et al*, *Lasers and Electro-Optics Society*, 2001. LEOS 2001. The 14th Annual Meeting of the IEEE, Vol. 2, 661 (2001).
[8] M. K. Chin *et al*, *Appl. Phys. Lett.* **75**, 3302 (1992).

15th Int. Symp. "Nanostructures: Physics and Technology"
Novosibirsk, Russia, June 25–29, 2007

Light propagation in imperfect photonic crystals

L. Braginsky[1] and V. Shklover[2]

[1] Institute of Semiconductor Physics, 630090 Novosibirsk, Russia
[2] Laboratory of Crystallography, ETH Zürich, 8093 Zürich, Switzerland

Abstract. The envelope function approach for the electric and magnetic fields of the light wave in the photonic crystals has been used to investigate the propagation of light in disordered photonic crystals and its reflection/refraction at the boundary. We showed that small long-range distortion of the crystal lattice can explain peculiarities of the transmittance spectrum of the polystyrene colloid film we have grown.

1. Introduction

Photonic crystals provide a powerful tool for manipulating and controlling photons in three dimensions of space. Photonic crystals of spherical nanoparticles are produced by the self-assembly or lithography techniques. Self-assembly usually results in 3D close packing (fcc or hcp structures), whereas more complicated structures also can be grown. It is important that lattice constants of all photonic crystals are comparable with the size of the particles their comprising. At the same time, dispersion of the particles sizes, which is inevitable for the artificial "atoms", leads to imperfection of the photonic crystals. This is the main point that distinguishes the photonic and common crystals. The latter comprise of identical atoms that occupy rather small part of the lattice volume.

The problem of the light propagation in the perfect photonic crystals can be solved numerically. Translation symmetry of crystals considerably simplifies the problem, because in this case the Bloch theorem holds [1]. Solution of the Maxwell equations for the light fields in the crystal lattice yields the photonic band structure, which has been calculated for the perfect photonic crystals of different symmetries. This allows one to estimate the transmission spectra of the finite photonic crystal layers and compare the results with experiments [2, 3]. It has been established that positions of dips in these spectra are usually in accordance with the contemporary theory; however, the dips are essentially wider and their depth is a few orders of value less than that predicted by the theory.

The problem of light propagation in imperfect photonic crystals is much more complicated, because even small disorder disturbs the translation symmetry; this violates the Bloch theorem making difficulties for numerical consideration. To cope with this problem, we employ the envelope function approach [4], which is commonly used in the solid state theory for investigation of the electron properties. The approach permits dividing the problem into two parts: (1) determination of the photonic band spectrum of the perfect crystal, and (2) investigation of the influence of imperfection or small disorder on the photon transport. The first problem should be considered numerically [1]; the results of such calculations can be expressed in terms of gap values and effective speeds of light in the appropriate photonic bands. These values can be used then as the phenomenological parameters for solution of the second problem; this considerably simplifies the numerical consideration of the problem and permits its analytical analyzing for the small or smooth imperfections.

To study the reflection or refraction of light at the crystal boundary, we have to apply the boundary conditions to the effective electric and magnetic fields. In the optics of common crystals this procedure leads to the well known Fresnel equations. Derivation of these equations assumes the dielectric permittivity as the smooth function on a scale of the wavelength. This is possible, if the wavelength of light much exceeds the lattice constant of the crystal. This is the case of the common crystals, but not the photonic crystals, the lattice constant of which is comparable with the photon wavelength. To avoid this difficulty, some authors use the dynamic scattering theory that has been developed for investigation of the X-ray scattering at the crystal surface. This theory supposes that electric field does not change essentially on a scale of an atom. This is the case of the common crystals, but not the photonic crystals, which "atoms" are of the size comparable with the light wavelength.

In this report we obtain the generalized boundary conditions for the envelopes of light wave fields at the boundaries of the photonic crystal/photonic crystal and photonic crystal/vacuum. The approach is used to investigate the transmittance of the photonic crystal film.

2. Results

The shear-flow crystallization method has been used for fabrication of the polymer photonic crystals. Typical examples of fabricated crystals are presented in Fig. 1.

Choosing the photonic gap value from the experiment (Fig. 2), we can estimate transparency of the perfect film. The result of this estimation is also presented in Fig. 2 (solid curve); it is of four orders less than the measured value of transparency. Similar results have been obtained also in Refs. [2, 3], where the measured values of transparency of the colloid structures have been compared with that obtained after calculating of the photonic band structures from the fist principles.

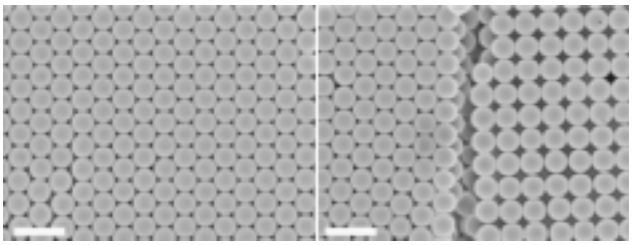

Fig. 1. Photonic crystals, fabricated from colloidal polystyrene spheres. Left: homogeneous crystal with top (111) surface parallel to the substrate. Right: non-homogeneous crystal build of two kinds of domains with top surfaces (111) and (100) parallel to the substrate. Scale bar is 1 μm.

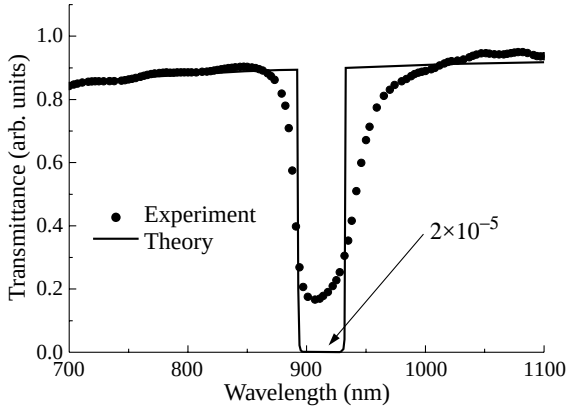

Fig. 2. Transparency of a photonic crystal. Theoretical curve corresponds to the model of the perfect crystal.

2.1. *Sort-range irregularities in pseudo-PBG crystals*

Photonic crystals of the small-index materials are pseudo-PBG. The gap in such materials is narrow and is not absolute; its position is determined by the edge of the Brillouin zone and, therefore, depends on direction in the crystal. If the frequency of light ω belongs to the photonic gap in the direction of the normal **n** to the crystal boundary, then the light propagation in this direction is prohibited. However, mid-gap position depends on direction in the crystal, and if the gap value is small, then the same ω can be outside the gap in some direction close to **n**. If so, then elastic scattering of the light can increase the in-gap transparency.

Figure 3 presents results of estimations using this model for the specimen from Fig. 1. We see that short-range irregularity increases the mid-gap transparency, but does not lead to widening of the dip. The reason is clear. Short-range scattering changes the wave vector of the in-gap photon and, consequently, makes it out-gap. Inverse process, i.e. scattering that changes the wave vector of the out-gap photon and makes it in-gap is improbable for the narrow-gap photonic crystals.

2.2. *Long-range irregularities*

Consider an imperfect photonic crystal, whose irregularities are due to the smooth structure distortion. Such distortion effectively changes the lattice constant and, therefore, shifts the mid-gap frequency, which becomes position dependent. As a result, the photon that frequency belong to the gap in the perfect crystal can propagate without attenuation in some regions of the imperfect crystal where the gap position is different. On the other hand, the photon that frequency is outside the gap, but close to it in the perfect crystal propagates with attenuation in some regions of the imperfect crystal where its frequency corresponds to the local gap. Thus, long-range irregularities should lead to widening of the dip in the transparency spectra and increase the mid-gap transparency.

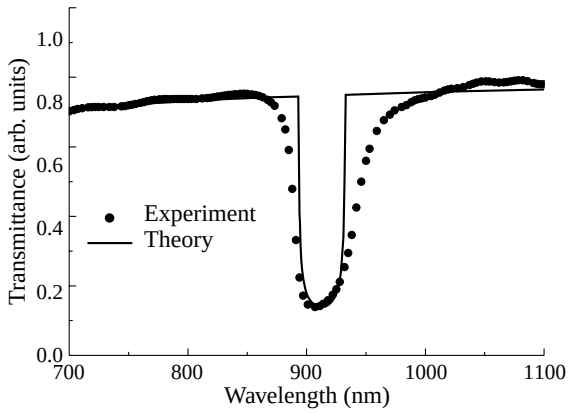

Fig. 3. Transparency of a photonic crystal. Theoretical curve corresponds to the model of the short-range irregularity.

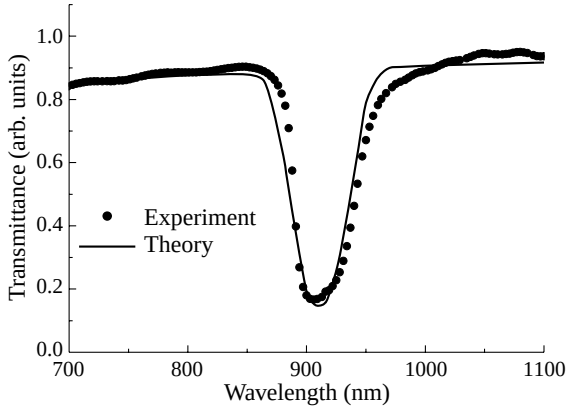

Fig. 4. Transparency of a photonic crystal. Theoretical curve corresponds to the model of the long-range irregularity.

The light propagation in the structure with long-range irregularities can be described by wave equation with the position dependent effective speed of light. The results of such simulations for the specimen of Fig. 1 are presented in Fig. 4. In our structure this can be resulted from the 4–6% deviation of the polystyrene spheres size.

References

[1] S. G. Johnson and J. D. Joannopoulos, *Optics Express* **8**, 173 (2001).
[2] Yu. A. Vlasov, M. A. Kaliteevski, and V. V. Nikolaev, *Phys. Rev. B* **60**, 1555 (1999).
[3] V. N. Astratov, A. M. Adawi, S. Fricker, M. S. Skolnick, D. M. Whittaker, and P. N. Pusey, *Phys. Rev. B* **66**, 165215 (2002).
[4] L. Braginsky and V. Shklover, *Phys. Rev. B* **73**, 085107 (2006).

15th Int. Symp. "Nanostructures: Physics and Technology"
Novosibirsk, Russia, June 25–29, 2007

Ultrafast photoinduced shifts of microcavity modes frequencies in ZnSe films on metal substrates under excitation by femtosecond laser pulse

S. V. Chekalin, *V. O. Kompanets*, Yu. E. Lozovik, Yu. A. Matveets and E. A. Vinogradov
Institute of Spectroscopy, Russian Academy of Sciences, Troitsk, Moscow region, 142190, Russia

Abstract. Red or blue ultrafast photoinduced shifts of interference modes frequencies in ZnSe films on metal substrates were observed at subgap and overgap excitation of ZnSe. These shifts and peculiarities in the relaxation times are explained through photoinduced changes of the boundary conditions and optical thickness of the microcavity.

It was shown that the measurements of interference (cavity) modes frequencies are very sensitive instrument for investigation of ultrafast photoinduced processes on "semiconductor film–metal" interface with the time resolution up to several femtoseconds due to ultrafast evolution of the cavity modes. The excitation of the structure under investigation by laser pulse induces a hierarchy of ultrafast processes which in turn produces a photoinduced change of the dielectric function of both the semiconductor film and the metal substrate. The change of the dielectric function of the film gives rise to change their optical thickness. The change of the dielectric function of the metal gives rise to change the boundary conditions for interference modes of the film. Both of these phenomena lead to change the frequencies and the shape of the interference modes which are measured by RA spectra [1–5].

Ultrafast changes of photoinduced reflection at frequencies of optical microcavity (thin ZnSe films on different metal substrates) eigenmodes were studied by femtosecond pump-supercontinuum probe method. Two types of the samples excitation were studied: *"overgap" excitation*, when the photon energy of the excitation pulse $\hbar\omega_{\rm pu}$ is higher than ZnSe semiconductor energy gap $E_{\rm g}$ (2.7 eV) and *"subgap" excitation*, when $\hbar\omega_{\rm pu}$ is smaller than $E_{\rm g}$. The excitation was accomplished by laser pulses of 50 fs duration at intensities of $(1-4)\,10^{11}$ W/cm^2 for $\hbar\omega_{\rm pu1} = 1.57$ eV and $(1-4)\,10^{10}$ W/cm^2 for $\hbar\omega_{\rm pu2} = 3.14$ eV.

Derivative-like feature centered at the microcavity eigenmode wavelength was observed in differential reflection spectra of ZnSe films with 160-nm and 250-nm thickness on a thick Cr substrate (Fig. 1). This feature arose due to ultrafast (in femtosecond scales) photoinduced shift of the cavity mode frequencies and changed its sign for pump quanta greater or smaller than semiconductor ZnSe forbidden gap (blue or red shift, respectively, see Fig. 1).

As can be seen from Fig. 1 a pulsewidth-limited blue shift with a decay time of ∼200 fs and absorption increase with a decay time of ∼20 ps was observed at the cavity mode frequency in the case of overgap excitation. In the case of subgap excitation a pulsewidth-limited red shift with a decay time of more than 20 ps was observed.

Such a behavior can be attributed to the interplay of different processes. The permittivity change arising from these processes has the effect that the microcavity modes shift and adopt new spectral positions upon the excitation of the structure by femtosecond laser pulses. The frequency shift of the interference mode of a plane-parallel dielectric layer on a metal

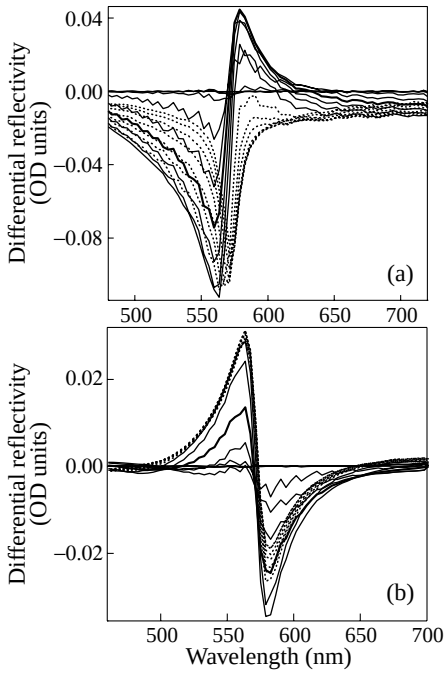

Fig. 1. Differential reflection spectra of 160 nm ZnSe-Cr microcavity at overgap (a) and subgap (b) excitation. Solid lines correspond to signal increase, dotted lines to signal decrease (later times). Zero time delay assigned by thick solid line. Increment of the time delay — 250 fs.

can be explained by the competition of excitonic and Drude contributions (the last is connected with excited electrons in conduction band) to dielectric function of the semiconductor or metal.

Overgap excitation, $\hbar\omega_{\rm pu} > E_{\rm g}$. In this case the laser pulse is absorbed in a thin semiconductor surface layer and generates a nonuniform distribution of hot carriers in the semiconductor. The appearance of nonequilibrium charge carriers in the semiconductor layer changes the semiconductor permittivity due to occupation of states in the conduction band and emptying of states in the valence band (screening of excitonic transitions and even photoinduced disappearance of exciton states as well). A change in the permittivity near the absorption edge $\hbar\omega \approx E_{\rm g}$ gives negative change of the refractive index in the subgap energy range (Fig. 1(a)). Photoinduced changes of the dielectric function transform the optical thickness of the cavity. Increase of free carriers density on absorption depth of ZnSe results in increase of corresponding plasma frequency $\omega_{\rm p}^2$. This

leads to decreasing of $\varepsilon_s(\omega)$ of semiconductor where

$$\varepsilon_s(\omega) = \varepsilon_{s\infty} + \frac{S\omega_{\rm ex}^2}{\omega_{\rm ex}^2 - \omega^2 - i\gamma_{\rm ex}\omega} - \frac{\omega_{\rm p}^2}{\omega^2 - i\gamma_{\rm p}\omega}$$

and to instant blue shift of ZnSe-Cr cavity modes due to change optical thickness of the cavity (nd).

Subgap excitation, $\hbar\omega_{\rm pu} < E_{\rm g}$. For an excitation energy smaller than the semiconductor energy gap, the laser pulse primarily excites electrons in a thin surface metal layer at the boundary with the semiconductor. Metal heating under subgap excitation results in increase of damping $\gamma_{{\rm p}m}$ of dielectric function $\varepsilon_m(\omega)$ of the metal:

$$\varepsilon_m(\omega) = \varepsilon_{m\infty} - \frac{\omega_{{\rm p}m}^2}{\omega^2 - i\gamma_{{\rm p}m}\omega}$$

and red shift due to the photoinduced change of phase of reflected light at the interface. This lead to the observable shift of cavity modes frequencies to the red region of spectrum (Fig. 1(b)).

The slow relaxation stage (∼20 ps and longer) of the photoinduced change in spectra for the structures under investigation is due to lattice cooling and heat diffusion from the excitation region.

Resuming we can conclude that at $\hbar\omega_{\rm pu} > E_{\rm g}$ we observed instant *blue* shift of ZnSe-Cr cavity modes due to change optical thickness of the cavity (nd) with decay time of ∼200 fs. For $\hbar\omega_{\rm pu} < E_{\rm g}$ instant *red* shift of cavity modes due to photoinduced change of boundary conditions of the cavity (metal excitation) and change the dielectric function of the metal was observed with a decay time of longer than 20 ps. It should be noted that ultrafast shift of cavity modes can be used for femtosecond scale optical switching.

Acknowledgements

This work was supported in part by Grants from the Russian Foundation for Basic Research 05-02-17338 and 06-02-16186.

References

[1] E. A. Vinogradov, *Physics-Uspekhi*, **45** (12), 1213 (2002).
[2] E. A. Vinogradov, V. M. Farztdinov, A. L. Dobryakov, S. A. Kovalenko, Yu. E. Lozovik and Yu. A. Matveets, *Laser Physics*, **8** (1), 316 (1998).
[3] E. A. Vinogradov, V. M. Farztdinov, S. A. Kovalenko, A. L. Dobryakov, Yu. E. Lozovik, Yu. A. Matveets, *Laser Physics*, **9** (1), 215 (1999).
[4] E. A. Vinogradov, C. C. Davis, A. L. Dobryakov, Yu. E. Lozovik, I. I. Smolyaninov, *Laser Physics*, **10** (1), 76 (2000).
[5] E. A. Vinogradov, Yu. E. Lozovik, *Izv. Ross. Akad. Nauk, Ser. Fiz.*, **68** (1), 25 (2004).

15th Int. Symp. "Nanostructures: Physics and Technology"
Novosibirsk, Russia, June 25–29, 2007

Kinetics of stimulated polariton–polariton scattering in planar GaAs microcavities under a resonant nanosecond excitation

A. A. Demenev[1], A. A. Shchekin[1], A. V. Larionov[1], S. S. Gavrilov[1,2], N. A. Gippius[2] and V. D. Kulakovskii[1]

[1] Institute of Solid State Physics RAS, Chernogolovka, 142432 Russia
[2] General Physics Institute RAS, Vavilova 38, Moscow, 119991 Russia

Abstract. We investigate the nature of an unusual behavior of stimulated polariton scattering in planar microcavities (MCs) under a resonant excitation of the lower polariton (LP) branch. The time dependencies of the cavity transmission and photoluminescence were investigated for GaAs-based planar MCs with InGaAs quantum wells (QW) in the active layer, under a long (∼1 ns) pulse excitation at $T = 7$ K. The signal of stimulated scattering is found to appear at zero in-plane wave-vector $\mathbf{k} = 0$ with the delay of a few hundred picoseconds. Appearance of the signal is preceded by a strong increase of the pumped harmonic of intra-cavity field (due to the bistability of excitonic oscillator) and its consequent decrease (due to development of its break-up instability). Such a behavior is in a qualitative agreement with results of numerical modelling and proves the hard regime of excitation of the giant signal of stimulated scattering.

Introduction

A giant stimulated polariton–polariton scattering is one of the most striking features in GaAs-based planar microcavities. The phenomenon was firstly observed under a *cw* excitation at wave-vector $\mathbf{k}_\mathrm{p}$ close to the inflection point of lower polariton branch, when the scattering exhibits an unusually low (smaller than 100 W/cm^2) threshold [1]. It was described in the framework of a four wave mixing (FWM) model used earlier for explanation of the hyper-Raman effect in bulk semiconductors. Nevertheless the stimulated scattering in MCs seems to be breaking the key statement of a standard FWM theory: the conservation of energy and momentum within the LP branch. Namely, the signal and idler appear always at $\mathbf{k} = 0$ and $\mathbf{k} = 2\mathbf{k}_\mathrm{p}$, for a wide range of pump energies and wave-vectors. In order to explain that, one should account for an interplay between the two types of nonlinear behavior: the bistability of the pumped polariton mode, on the one hand, and its instability with respect to break-up onto 'signal' and 'idler', on the other hand [4]. The suggested model concerned the system of coupled equations for the intra-cavity optical field $\mathcal{E}_\mathrm{QW}$ and excitonic polarization $\mathcal{P}$:

$$\left[i\frac{d}{dt} - E_\mathrm{C}(\mathbf{k})\right]\mathcal{E}_\mathrm{QW}(\mathbf{k},t) = \alpha(\mathbf{k})\mathcal{E}_\mathrm{ext}(\mathbf{k},t) + \beta(\mathbf{k})\mathcal{P}(\mathbf{k},t), \quad (1)$$

$$\left[i\frac{d}{dt} - E_\mathrm{X}\right]\mathcal{P}(\mathbf{k},t) = A(\mathbf{k})\mathcal{E}_\mathrm{QW}(\mathbf{k},t) + F\sum_{\mathbf{q},\mathbf{q}'}\mathcal{P}(\mathbf{q}',t)\mathcal{P}^*(\mathbf{q}+\mathbf{q}'-\mathbf{k},t)\mathcal{P}(\mathbf{q},t) + \xi(\mathbf{k},t). \quad (2)$$

These equations account for exciton-exciton contact interaction (that leads to the *cubic* nonlinearity) and external pumping $\mathcal{E}_\mathrm{ext}$.

Numerical simulations based on Eq. (1,2) reveal the crucial role of the bistability of the pumped polariton mode. The bistability can lead to sharp rising of intra-cavity field with a slowly increasing pump density. Above the the certain threshold pump power, abrupt jump of the inner field results in a hard excitation of polariton scattering [4], that means an explosion-like populating of LP modes in a wide range of k-space around the bottom of LP branch. According to this model, eventual macrooccupation of the states with $\mathbf{k} = 0$ and $\mathbf{k} = 2\mathbf{k}_\mathrm{p}$ should develop as a result of a self-organization [5] in a highly excited LP system.

To investigate this scenario, we have performed time-resolved measurements of the pump transmission and magnitude of the stimulated polariton scattering under a ns pulse excitation near the inflection point of the LP dispersion.

1. Experimental details

We investigated MC structure grown by metal organic vapor phase epitaxy. It was consisted of two Bragg reflectors with 17(20) repeats of $\lambda/4$ $Al_{0.13}Ga_{0.87}As$/AlAs layers in the top (rear) mirrors and $(3/2)\lambda$ active layer between them. The active layer contained six 10-nm thick $In_{0.06}Ga_{0.94}As$/GaAs QWs. The Rabi splitting of coupled exciton and cavity modes was $\Omega \approx 6$ meV. The detuning between the exciton and photon modes of the cavity was $\delta = -2$ meV. The sample was placed into the optical cryostat at the temperature 7 K.

The pump beam has excited the sample resonantly at the angle 14° relative to the cavity normal (that corresponds to the in-plane wave-vector $k = 1.96 \times 10^4$ cm^{-1}). The duration of the pump pulse is ∼1 ns, its halfwidth is ∼1 meV, and the repetition rate is 5 kHz. The pump beam focused onto the spot with diameter of ∼100 μm. The signal from the microcavity was detected in the direction normal to the MC plane by the streak camera with spectral resolution 0.28 meV and time resolution ∼100 ps.

2. Experimental results

Fig. 1 shows time dependences of the pump pulse transmission and the luminescence at $\mathbf{k} = 0$ for the excitation density of $P = 9.2$ kW/cm^2, pump is polarized circularly (σ^+), and the signal is detected at σ^+ polarization, for both luminescence and transmission.

The system dynamics reveals two remarkable transitions, namely, first an unusual growth of the laser transmission and then its sharp decrease (c.f. Fig. 1(a)) that occur at $t = 0.27-0.57$ ns and $t = 0.57-0.97$ ns, correspondingly.

During the first time region (from 0.27 ns to 0.57 ns) the pump transmission is increasing sharply. At the same time both transmission (Fig. 1c) and luminescence (Fig. 1d) energies shift upward. As the transmission shows a magnitude of electric field on the quantum well, $T \propto |\mathcal{E}_\mathrm{QW}(\mathbf{k}_\mathrm{p})|^2$, its increase corresponds to growth of intra-cavity field. It is essential that

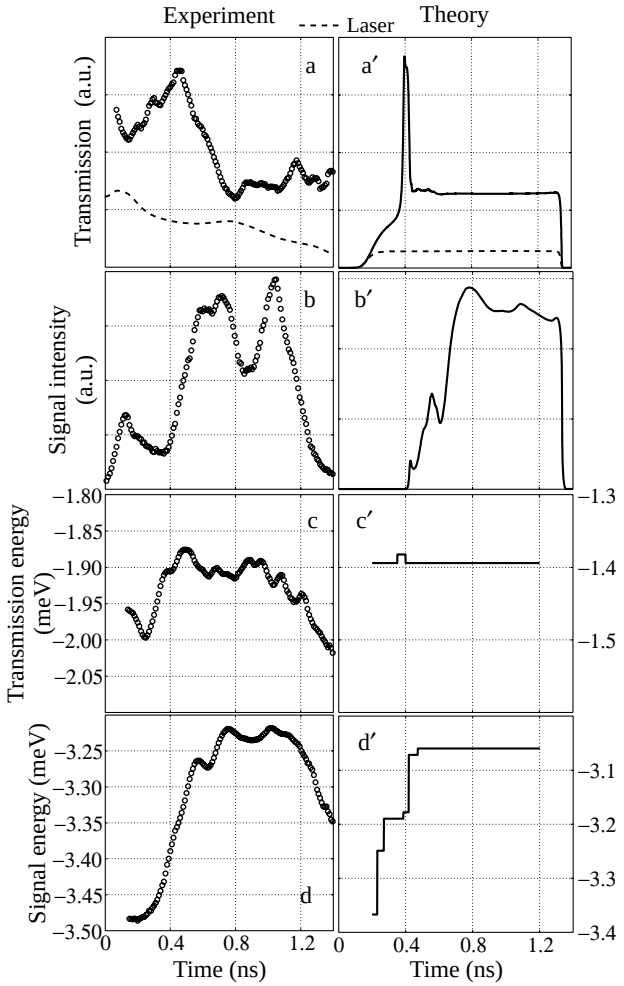

Fig. 1. Time dependences of pump transmission (a,a′), luminescence signal in the direction normal to the cavity (b,b′), frequencies of the transmitted pump (c,c′) and the signal (d,d′). The energies are counted off from the free exciton level. Experimental data were obtained for the case of circular pumping slightly above the threshold (*left* panel). *Right* panel shows the results of numerical modelling.

the laser intensity (i.e. an *external* field) is smoothly decreasing during this time. Such a behavior of an intra-cavity field can be connected with reaching the point of a bistable transition. The energy shift of both luminescence and transmission lines comes from the renormalization of polariton spectrum (the so-called "blue shift" [1–5]).

During the second time region (from 0.57 ns to 0.92 ns), the transmission through the MC falls down, which indicates the decrease of the *pumped* harmonic of intra-cavity field ($\mathbf{k} = \mathbf{k}_\mathrm{p}$). At the same time the signal of luminescence at $\mathbf{k} = 0$ increases strongly. Obviously, this behavior is connected with a redistribution of excitation inside the cavity, which comes from the break-up of excited mode onto 'signal' and 'idler'.

3. Discussion

The above experiments reveal a quite complicated kinetics of MC exciton-polariton system. Namely, the signal of parametric scattering (the sharp peak at $\mathbf{k} = 0$) is lagged as regard to reaching the threshold value of pump intensity. The delay time $t_\mathrm{d} \gtrsim 10^2$ ps exceeds significantly the lifetime of MC polaritons ($\tau \approx 3$ ps), which indicates the presence of essentially collective effects in the system. To realize it, we try an analogy with a system simulated numerically for the case of purely harmonic (single-mode) pumping slightly above the resonance. The latter system exhibits a bistable response to excitation that makes a drastic impact on scenario of parametric scattering. As was shown in [5], the bistability can cause fast population of numerous polariton modes (in a wide k-space area). Consequently, the scattering becomes quite stochastic with time, so the system evolves in presence of a strong noise. Its evolution takes a shape of a self-organization, and results eventually in macrooccupation of the ground mode ($\mathbf{k} \approx 0$), regardless of the pump frequency and wave vector. Typically, the time of passing to quasi-stationary regime may reach $t_\mathrm{d} \gtrsim 10^2$ ps, which corresponds roughly to the delay observed in considered experiment.

To summarize, we note the main features of the discussed system.

1. The sharp increase of the internal field is observed in region of a smooth change of external (laser) intensity. Such a behavior is typical for a system with a bistable response to excitation (compare Fig. 1(a) and (a′)).

2. The signal of parametric scattering at $\mathbf{k} = 0$ appears with a significant delay as compared with the excited mode (compare Figs. 1(a) and 1(b)). This behavior is similar to that modelled numerically for the system under a coherent single-mode excitation (Figs. 1(a′) and (b′)). The delay covers a lot of polariton lifetimes that allows one to suppose the presence of essentially collective phenomena acting on evolution of the polariton system.

Acknowledgements

The authors thank M. S. Skolnick for the samples, S. G. Tikhodeev, D. N. Krizhanovskii, and M. N. Makhonin for fruitful discussions.

References

[1] P. G. Savvidis *et al*, *Phys. Rev. Lett.* **84**, 1547 (2000).
[2] C. Ciuti *et al*, *Phys. Rev. B* **62**, R4825 (2000).
[3] V. D. Kulakovskii *et al*, *Nanotechnology* **12**, 475 (2001).
[4] N. A. Gippius *et al*, *Europhys Lett* **67**, 997 (2004).
[5] S. S. Gavrilov *et al*, to be published in *JETP* (2007).

15th Int. Symp. "Nanostructures: Physics and Technology"
Novosibirsk, Russia, June 25–29, 2007

Analytical theory of density of states in disordered one-dimensional photonic crystals

A. A. Greshnov[1], M. A. Kaliteevski[1,2], R. A. Abram[2], S. Brand[2] and G. G. Zegrya[1]

[1] Ioffe Physico-Technical Institute, St Petersburg, Russia
[2] Department of Physics, Durham University, Durham, DH1 3LE, UK

Abstract. Analytical theory of density of states (DOS) in disordered 1d photonic crystals has been developed using so-called phase formalism. It is shown that the problem of DOS calculation reduces to solution of Fokker–Planck equation under the assumption of small dielectric contrast. Exact analytical expression for DOS and its asymptotic forms in the depth of band gap and allowed bands are obtained. Our results agree with semi-empirical formula obtained previously from numerical studies [1] and disorder-free case.

1. Introduction

Photonic crystals being periodic structures with modulated refractive index are very perspective for numerous optical applications due to their band gaps — the ranges of frequencies with exponentially decreasing transmission. The structure of real photonic crystals is often far from periodic due to fluctuations of refractive index, dimensions of structural elements (layers, cylinders or spheres), their forms and distances between them. All these factors lead to absence of strict ordering and existence of optical eigenmodes within the band gaps. This implies narrowing of the band gaps and can adversely affect operation of devices. In present work we have calculated DOS in 1d disordered photonic crystals as analytically solvable and applicable (VCSELs) case.

2. The model and phase formalism

For the sake of simplicity we consider normal propagation (in fact standing wave) of linearly polarized light $\mathbf{E}(\mathbf{r},t) = E(z)\cos(\omega t+\varphi_0)\mathbf{e}_x$ in 1d photonic crystal with $D/2$ layers, where D is a period of the crystal (Fig. 1). Also we consider the following model of disorder:

$$n_{\mathrm{A,B}}(s) = n_0(1\pm\eta)\,(1+\delta_n P(s))\,, \tag{1}$$

where $n_{\mathrm{A,B}}(s)$ are refractive indices of "A" and "B" layers of $D/2$ width, formative the structure, n_0 is mean refractive index, s is layer number, $\eta = (n_\mathrm{A}-n_\mathrm{B})/(n_\mathrm{A}+n_\mathrm{B})$ is layer number independent quantity which we call dielectric contrast, δ_n is disorder parameter, $P(s)$ is distribution of disorder. We assume uncorrelated distribution $P(s)$ to have zero mean value $\langle P(s)\rangle = 0$ and unit dispersion $\langle P(s)P(s')\rangle = \delta_{ss'}$. The fluctuations of layer widths could be considered in the same way. Propagation of electromagnetic wave of frequency ω along the axis of structure (z) is described by wave equation

$$\frac{d^2E}{dz^2} = -\frac{n^2\omega^2}{c^2}E, \tag{2}$$

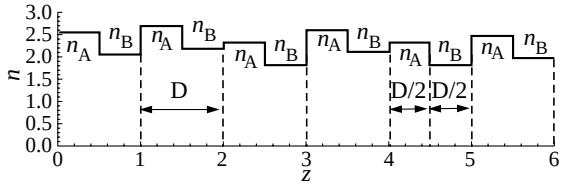

Fig. 1. The model of 1d disordered photonic crystal.

which can be solved through the structure using transfer matrix method. Hereafter we use so-called phase formalism adopting "electronic" theory of Ref. [2]. The quantity which is essential for DOS calculation is a logarithmic derivative of electric field $L(z)$ (or phase $\tilde\Psi(z)$),

$$L(z) = \frac{D}{\pi}\frac{dE/dz}{E} = \cot\left(\frac{\tilde\Psi(z)}{2}\right). \tag{3}$$

The equation for $L(z)$ transforms to

$$\frac{dL}{dz} = -L^2 - \frac{n^2\omega^2}{c^2}. \tag{4}$$

By analogy with transfer-matrix method we can derive discrete version of Eq. (4):

$$L(z_{s+1}) = \frac{A_1L(z_s)+A_2}{A_3L(z_s)+A_4}, \quad z_s = Ds, \tag{5}$$

where $A_{1..4}$ are some cumbersome coefficients. Eq. (5) is not very convenient due to its discreteness, but fortunately it can be reduced to differential equation in the case of small dielectric contrast $\eta \ll 1$ and disorder $\delta_n = K\eta \ll 1$, $K\sim 1$, and also frequencies not too far away from center of the first band gap $\omega_0 = \pi c/(n_0 D)$, so as

$$\omega = \omega_0\left(1+\frac{2G}{\pi}\eta\right), \quad G \lesssim 1. \tag{6}$$

The values of $G<1$ correspond to the band gap while $G>1$ correspond to the allowed bands. Under all the above mentioned assumptions the following differential equation

$$\frac{d\Psi}{ds} = 2\pi\frac{\omega-\omega_0}{\omega_0} + 4\frac{n_\mathrm{A}-n_\mathrm{B}}{n_\mathrm{A}+n_\mathrm{B}}\sin\Psi + 2\pi\delta_n P(s). \tag{7}$$

together with $L(z_s) = \cot(\Psi(s)/2)$ gives the solution of equation Eq. (5) with $O(\eta^2)$ accuracy. Being slow function of s, $\Psi(s)$, which we call *modified phase*, differs from the phase $\tilde\Psi(z)$, given by Eqs. (3,4), so as

$$\tilde\Psi(z_s) = \Psi(s) + 2\pi s \quad (s \text{ is integer}). \tag{8}$$

As we shall see below, this difference is irrelevant for DOS calculation.

Earlier non-linear equations with "random force" similar to Eq. (7) were derived in the area of Josephson contacts to describe thermal noise [3]. Below we proceed to statistical (Fokker–Planck) description of *modified phase* variation and calculation of DOS.

3. Fokker–Planck equation and oscillation theorem

In order to derive Fokker–Planck equation for distribution function of *modified phase* $F(\Psi)$ we use standard approach by analogy with the problem of brownian motion in viscous liquid [4]. First we write the solution of Eq. (7) in the implicit form

$$\Psi(s) = \Phi(\Psi(s+1), P(s)), \tag{9}$$

reflecting that $P(s)$ is constant on the intervals between two adjacent integers. Using Eq. (9) we can calculate increment of distribution function $F(\Psi, s)$:

$$F(\Psi, s+1) = \int F(\Phi(\Psi, P), s) \frac{\partial \Phi}{\partial \Psi} f(P) dP, \tag{10}$$

where $f(P)$ is a distribution function of random quantity $P(s)$, describing the fluctuations of refractive index (remember that $P(s)$ is uncorrelated $\langle P(s)P(s')\rangle = \delta_{ss'}$). Making Taylor expansion in the l.h.s. and r.h.s. of Eq. (10) up to the first and second orders respectively, we come to Fokker–Planck equation [4]:

$$\frac{\partial F}{\partial s} = 2\pi^2 \delta_n^2 \frac{\partial^2 F}{\partial \Psi^2} - 4\eta \frac{\partial}{\partial \Psi} \left[(G + \sin \Psi) F \right]. \tag{11}$$

In fact we shall use conjugated Fokker–Planck equation

$$2\pi^2 \delta^2 \frac{d^2 M}{d\Psi^2} + 4\eta (G + \sin \Psi) \frac{dM}{d\Psi} = -1,$$
$$M(\Psi_L = -\infty) = M(\Psi_R = 2\pi) = 0. \tag{12}$$

which gives an average number of periods $M_0 = M(0)$ needed for modified phase Ψ to get 2π shift [4]. Eq. (12) has the following solution:

$$M_0 = \frac{1}{2\pi^2 \delta_n^2} \int_{-\infty}^{0} dx \exp\left(-\frac{2\eta (Gx - \cos x)}{\pi^2 \delta_n^2} \right) \times \left[C - \int_{-\infty}^{x} dx' \exp\left(\frac{2\eta (Gx' - \cos x')}{\pi^2 \delta_n^2} \right) \right],$$
$$C = \left[\int_{-\infty}^{2\pi} dx \exp\left(-\frac{2\eta (Gx - \cos x)}{\pi^2 \delta_n^2} \right) \right]^{-1} \times \int_{-\infty}^{2\pi} dx \exp\left(-\frac{2\eta (Gx - \cos x)}{\pi^2 \delta_n^2} \right) \times \int_{-\infty}^{x} dx' \exp\left(\frac{2\eta (Gx' - \cos x')}{\pi^2 \delta_n^2} \right). \tag{13}$$

Fortunately these cumbersome integrals can be evaluated in the depth of band gap $|G| < 1$, which gives

$$M_0 = \frac{\pi \exp\left(\frac{4\eta}{\pi^2 \delta_n^2} \left[\sqrt{1-G^2} + |G| \arcsin |G| - \frac{\pi}{2} |G| \right] \right)}{2\eta \sqrt{1-G^2} \left(1 + \exp\left(-\frac{4\eta |G|}{\pi \delta_n^2} \right) \right)}, \tag{14}$$

where $G = \dfrac{\omega - \omega_0}{\Delta\omega/2}$, $\Delta\omega = \dfrac{4\eta}{\pi}\omega_0 = \dfrac{4(n_A - n_B)c}{n_0(n_A + n_B)D}$

is a width of the first band-gap.

The next step in our calculations is the relation between phase variation and DOS given by oscillation theorem holding in photonics as well as in electronic case [2]. According to this theorem, the number of a solution $E(z)$ of 1d wave equation Eq. (2) is given by the number of zeros of this solution on a fixed interval $(0, l)$. Zero values of E mean $L(z) = \infty$, i.e. $\tilde{\Psi}(z) = 2\pi n$, n is integer. These arguments lead to the following expression for DOS:

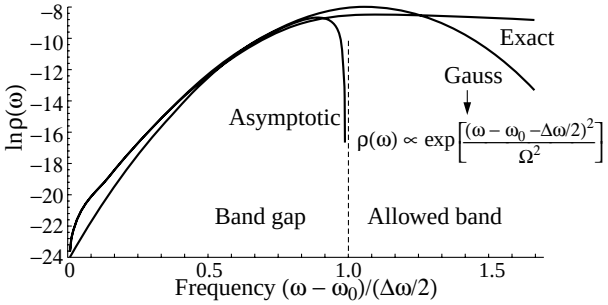

Fig. 2. Density of states in 1d disordered photonic crystal calculated for $\eta = \delta_n = 0.025$.

$$\rho(\omega) = \frac{1}{l} \frac{d(\langle N \rangle - N_0)}{d\omega} = \frac{1}{D} \frac{d}{d\omega} \frac{1}{M_0} = \frac{\pi}{2D\omega_0 \eta} \frac{d}{dG} \frac{1}{M_0}, \tag{15}$$

where $\langle N \rangle$ is an average number of zeros on $(0, l)$ interval, $N_0 = l/D$ is a constant due to the difference between $\tilde{\Psi}(z)$ and $\Psi(s)$ (cf. Eq. (8)), M_0 is given by Eqs. (13,14). Eq. (15) generalizes well-known disorder-free formula $\rho(\omega) \propto dk/d\omega$.

Finally we would like to compare analytical expressions with gaussian formula of Ref. [1], obtained from numerical calculations. For this purpose we estimate DOS in the center of the first bang gap (with exponential accuracy) using Eqs. (14,15):

$$\frac{\rho(\omega_0)}{\rho(\omega_0 + \Delta\omega/2)} \sim \frac{M_0(G=1)}{M_0(G=0)} \sim \exp\left(-\frac{4\eta}{\pi^2 \delta_n^2} \right). \tag{16}$$

This gives us estimation for tail width $\Omega = \delta_n \sqrt{\eta} \omega_0$, which is in very good agreement with Ref. [1]. Furthermore we can compare gaussian approximation with exact solution given by Eq. (13) and approximate solution of Eq. (14) (Fig. 2). We see that Eq. (14) works excellent everywhere within the band gap except narrow region close to the edge, while gaussian formula is a fairly good approximation but following neither of two asymptotics. Also note that exact solution given by Eq. (13) works not only inside the band gap but also in the allowed bands $|\omega - \omega_0| > \Delta\omega/2$. This can be verified explicitly expanding Eq. (13) at $G > 1$ and then comparing it with disorder-free formula for DOS. Proper (decreasing) behavior of DOS given by Eq. (13) at $|\omega - \omega_0| > \Delta\omega/2$ is also seen from Fig. 2.

Acknowledgements

This work has been supported by RFBR (05-02-16679), Federal Programme on Support of Leading Scientific Schools and Grant of Royal Society. One of the authors (A. A. Greshnov) appreciates the support of Dynasty Foundation and Russian Science Support Foundation.

References

[1] M. A. Kaliteevski *et al*, *Phys. Rev. E* **73**, 056616 (2006).
[2] I. M. Lifshits, S. A. Gredeskul, L. A. Pastur, *Introduction to the theory of disordered systems (Vvedenie v teoriu neuporyadochennyh system)*, §6. Moscow: Nauka, 1982.
[3] U. M. Ivanchenko, L. A. Zilberman, *Jetp. Lett.* **8**, 113 (1968); A. C. Biswas, S. S. Jha, *Phys. Rev. B* **2**, 2543 (1970).
[4] M. A. Leontovich, *Introduction to thermodynamics. Statistical Physics. (Vvedenie v termodinamiku. Statisticheskaya fizika.)*, chapter 6. Moscow: Nauka, 1983.

15th Int. Symp. "Nanostructures: Physics and Technology"
Novosibirsk, Russia, June 25–29, 2007

Fractal photonic quasi-crystals and their optical properties

A. A. Grunin[1], A. G. Zhdanov[1] and A. A. Fedyanin[3]

[1] Dept. of Physics, M. V. Lomonosov Moscow State University, Moscow 119992, Russia

Abstract. One-dimensional photonic microstructures with optical thicknesses, chosen according to the fractal sequence of the Cantor's ladder are considered. Experimental samples made by electrochemical etching of porous silicon are studied. Both numerical calculations and experimental results demonstrate self-similarity in optical response, caused by self-similarity in morphology.

Introduction

Quasi-periodic structures are attracting much attention in modern optics [1,2]. It is caused by the fact that such structures represent intermediate situation between periodic ones (photonic crystals) and totally disordered (inhomogeneous) structures. These structures exhibit interesting effects in optical response which can not be observed in photonic crystals or in disordered structures [2]. In the present work one-dimensional optical quasi-crystals with optical thicknesses of layers chosen according to the fractal sequence made from porous silicon are studied. They are called below as "photonic quasi-crystals".

1. Results and discussion

Studied photonic quasi-crystals with self-similarity in morphology are constructed according to the Cantor's ladder as shown in Fig. 1. In this case self-similarity is expected.

Numerical calculations of reflectance spectrum are carried out utilizing transfer matrix technique [3]. Refractive indices of layers forming the stacks are supposed to be $n_1 = 1.75$ and $n_2 = 2.1$, those are close to experimental values for porous silicon layers. An example of calculated reflection spectrum for the 15-layered sample corresponding to the third order of Cantor's ladder is shown in Fig. 2.

Reflectance spectrum (solid line) exhibits self-similarity properties. After scaling it turns out to be an envelope curve for the system of 3 peaks (dashed-dot line), by-turn the resulted peak can be scaled for the whole photonic band gap (dashed line). Such system exhibits self-similarity of the second order. Generally, the order of the self-similarity is equal to $n - 1$, where n is the order of the structure. Numerical results are experimentally proved on several samples fabricated from porous silicon by electrochemical etching. Refractive indices of the layers were controlled by the etching current density and the thicknesses of the layers were defined by the etching duration. The process of self-similarity destruction was observed by varying the thicknesses of the layers of the structure both numerically and experimentally. The calculations of time-and-space optical field distribution in photonic fractals are also performed. Both space distribution and time-resolved response demonstrate self-similarity caused by self-similarity in morphology. This can be experimentally observed utilizing femtosecond lasers and near-field microscopy.

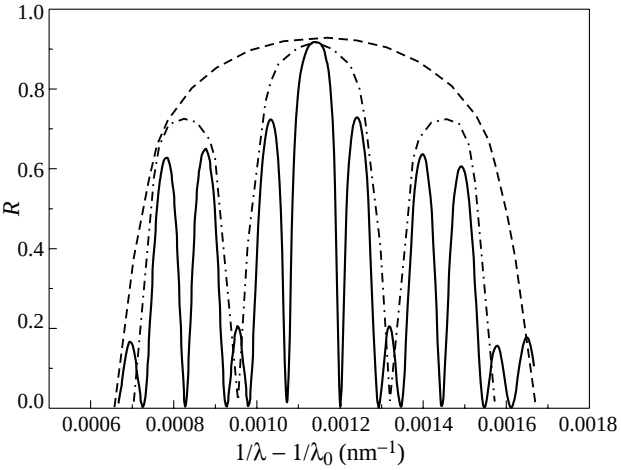

Fig. 2. Calculated reflection spectrum for the 15-layered sample corresponding to the third order of Cantor's ladder.

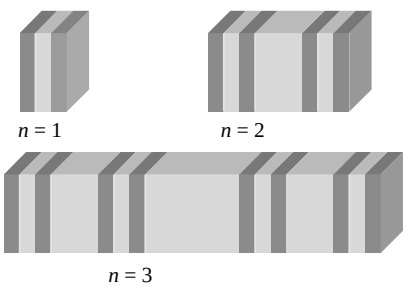

Fig. 1. Sketch of stacks of layers formed according to the Cantor's ladder of order of $n = 1$, $n = 2$, $n = 3$.

References

[1] Luca Dal Negro, Claudio J. Oton, Zeno Gaburro, Lorenzo Pavesi, Patrick Johnson, Ad Lagendijk, Roberto Righini, Marcello Colocci, and Diederik S. Wiersma, *Phys. Rev. Lett.* **90**, 055501-1 (2003).

[2] W. Gellermann, M. Kohomoto, B. Suthrland, *Phys. Rev. Lett.* **72**, 633 (1994).

[3] D. S. Bethune, *J. Opt. Soc. Am.* **6**, 910 (1989).

15th Int. Symp. "Nanostructures: Physics and Technology"
Novosibirsk, Russia, June 25–29, 2007

Enhanced emission from a planar microresonator induced by pumping via a cavity eigenmode

A. V. Medvedev[1], A. A. Dukin[1], N. A. Feoktistov[1], S. A. Grudinkin[1], A. B. Pevtsov[1], C. Sibilia[2] and V. G. Golubev[1]

[1] Ioffe Physico-Technical Institute, St Petersburg, Russia
[2] INFM at Dipartimento di Energetica, Università di Roma 'La Sapienza', Via Scarpa 16 00161 Roma, Italy

Abstract. Strong enhancement of 1.54 μm-emission in a resonant mode of a planar a-Si:H/a-SiO_x microcavity with an Er-doped active layer is induced by optical pumping via a cavity eigenmode. The theoretical analysis shows that the enhancement is due to large value of the overlap integral between electric fields of the pump radiation and erbium emission in the active layer of the microcavity designed.

Introduction

An increase of quantum efficiency of compact light sources remains one of the important goals of optoelectronics. There are two basic approaches to achieve this goal. The first one uses microcavities (MCs) to concentrate emitted light into a MC eigenmode and enlarge intensity of luminescence due to Purcell effect [1]. The second approach uses an enhancement of absorption of phosphor when pump radiation traverses through a MC eigenmode [2].

In the present work we combined both approaches that allowed us to increase the photoluminescence (PL) intensity of a phosphor placed into the MC active layer more than two orders of magnitude. Our idea is based on using of the cavity eigenmodes both for input of optical excitation and for output of phosphor emission. a-Si:H/a-SiO_x microcavities with an erbium-doped a-SiO_x:Er active layer were chosen as a model object [3,4]. The cavity eigenmode wavelengths were tuned to the 1540 nm emission line of Er^{3+} ions and the 980 nm absorption band of a-SiO_x:Er at normal and oblique incidence angles of light, respectively.

1. Experimental

The a-Si:H/a-SiO_x microcavities were grown by plasma-enhanced chemical vapor deposition technique and composed of two quarter-wave distributed Bragg reflectors (DBRs) of 2 periods each and an a-SiO_x:Er half-wave active layer in between [3,4]. The wavelength of the MC eigenmode under normal light incidence was in resonance with 1540 nm emission of 4f electronic transition of Er^{3+} ions in a-SiO_x. It provided an efficient output of Er^{3+} ions PL from the active layer along normal direction to the plane of the MC layers.

Reflection and PL spectra were measured at room temperature using a computer-controlled optical grating spectrometer equipped with a Hamamatsu InGaAs photodiode and lock-in amplifier. The PL of erbium ions was excited by a TE-polarized 980 nm semiconductor laser. The choice of TE-polarization is caused by stronger concentration of TE-polarized eigenmode field in the active layer as compared with TM-mode. The angle φ between the excitation beam and the cavity axis (Z) could be varied from 20 to 60°, as indicated in Fig. 1(a). To tune the excitation wavelength to the TE eigenmode at the incidence angle accessible in experiment, the structure was immersed in CCl_4 (dielectric constant $\varepsilon_{CCl_4} = 2.01$). The liquid is transparent in near IR and has sufficiently large refractive index to provide

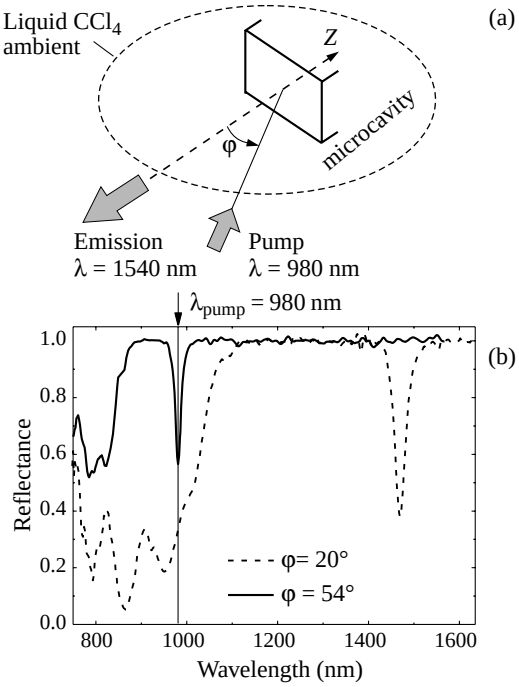

Fig. 1. (a) Experimental configuration of an Er-doped a-Si:H/a-SiO_x microcavity optically pumped by a 980 nm semiconductor laser. The microcavity is immersed in CCl_4. φ is the angle of incidence of light in the liquid CCl_4 ambient. (b) The microcavity reflectance spectra in TE-polarization. Incidence angles of light from the CCl_4 ambient are 20° (dashed line), 54° (solid line). The arrow marks the excitation wavelength.

the desirable wavelength matching [5] at $\varphi \approx 54°$ (Fig. 1(b)). The PL of erbium ions from the MC at 1540 nm was directed along the optical axis Z of the MC.

2. Results and discussion

The reflectance spectra of the fabricated MCs are shown in Fig. 1(b). The DBRs produce almost a total reflection band — a stop-band in the near IR spectral range. The reflectance in the stop-band region is close to unity. In addition, the reflectivity exhibits a sharp dip resulted from the fundamental resonance mode of the cavity (Fig. 1(b)). The eigenmode wavelength shifts uniformly to shorter wavelength as the incidence angle increases (inset in Fig. 2) [6]. The shift is due to confinement of light wavevector along the Z axis of the MC. Under the

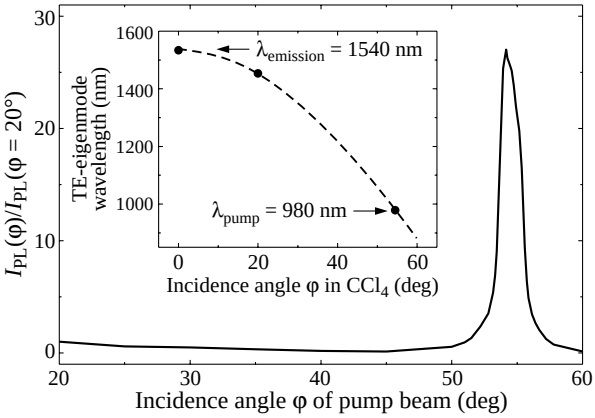

Fig. 2. The ratio $I_{PL}(\varphi)/I_{PL}(\varphi = 20^\circ)$ vs the incidence angle φ of TE-polarized pump beam ($\lambda = 980$ nm) in the CCl_4 ambient. $I_{PL}(\varphi)$ is PL intensity ($\lambda = 1540$ nm) from the Er-doped a-Si:H/a-SiO_x microcavity at an incidence angle φ of pump beam. Inset: angular dependence of the TE-polarized microcavity eigenmode wavelength in the CCl_4 ambient (dots). Dashed line is an approximation of the experimental data by the expression: $\lambda(\varphi) = \lambda(\varphi = 0)\sqrt{1 - \varepsilon_{CCl_4}(\sin\varphi/n_{eff})^2}$, where $n_{eff} = 1.5$ is an effective refractive index [7].

incidence angle $\varphi \leq 20^\circ$ the excitation wavelength (980 nm) is outside the TE-stop-band (Fig. 1(b), dashed line). When $\varphi = 54^\circ$ the TE-eigenmode wavelength coincides with the pumping wavelength (Fig. 1(b), solid line).

Figure 2 shows the erbium PL intensity depending on the incidence angle of the excitation beam. The Er emission line at 1540 nm has maximum intensity at the excitation angle $\varphi = 54^\circ$, when the 980 nm laser beam transverses through the MC eigenmode. In this case the pump electric field concentrates in the active layer. Figure 3 shows that the erbium PL intensity excited through the MC eigenmode exceeds by 25 times the PL intensity excited outside the stop band ($\varphi = 20^\circ$).

Combination of two factors (Purcell effect and "eigenmode excitation technique") has allowed us to increase the Er^{3+} ions emission intensity from the MC by 500 times as compared with a single a-SiO_x:Er film which thickness is equal to that of the MC active layer (Fig. 3).

The theoretical analysis of the observed PL enhancement

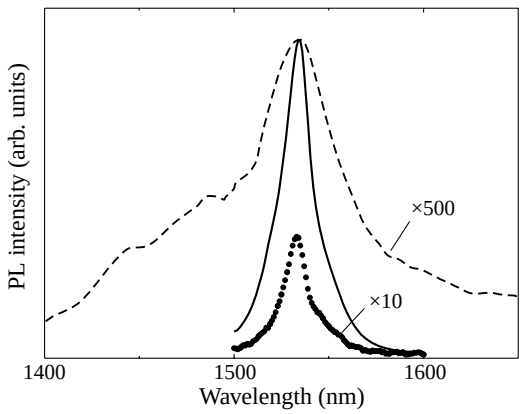

Fig. 3. Photoluminescence spectra from the Er-doped a-Si:H/a-SiO_x microcavity at different incidence angles of pump beam in the CCl_4 ambient: 20° — dotted line, 54° — solid line. Dashed line shows the Er PL spectrum from a single a-SiO_x:Er film which thickness is equal to that of the microcavity active layer.

was performed. The spatial distribution of electromagnetic field inside the MC structure was calculated by the transfer matrix method. It is established that the PL intensity of emitting centers placed into the active layer of MC is proportional to the overlap integral between pump and emission fields inside the active layer. The large value of the overlap integral originates from strong concentration of the eigenmode fields within the MC active layer.

In conclusion, we have offered and experimentally realized a novel way of increasing photoluminescence intensity of phosphors introduced into active layer of a planar microcavity. The method combines an optical excitation via a cavity mode with emission output through an another resonant mode of the same cavity. As a result, an enhancement of the Er^{3+} ions emission intensity from the Er-doped a-Si:H/a-SiO_x microcavity by two orders of magnitude as compared with a single a-SiO_x:Er film is observed. The enhancement can be quantitatively described by consideration of spatial distribution of the microcavity eigenmode fields.

Acknowledgements

The work was supported by the Russian Foundation for Basic Research (Grant # 05-02-17803) and the EC-funded project PHOREMOST (FP6/2003/IST-2-511616).

References

[1] K. J. Vahala, *Nature* **424**, 839 (2003).
[2] E. F. Schubert, N. E. Hunt, A. M. Vredenberg, T. D. Harris, J. M. Poate, D. C. Jacobson, Y. H. Wong, G. J. Zydzik, *Appl. Phys. Lett.* **63**, 2603 (1993).
[3] A. A. Dukin, N. A. Feoktistov, V. G. Golubev, A. V. Medvedev, A. B. Pevtsov, A. V. Sel'kin, *Appl. Phys. Lett.* **77**, 3009 (2000).
[4] V. G. Golubev, A. A. Dukin, A. V. Medvedev, A. B. Pevtsov, A. V. Sel'kin, N. A. Feoktistov, *Semiconductors* **35**, 1213 (2001).
[5] A. A. Dukin, N. A. Feoktistov, A. V. Medvedev, A. B. Pevtsov, V. G. Golubev, A. V. Sel'kin, *J. Opt. A: Pure Appl. Opt.* **8**, 625 (2006).
[6] A. A. Dukin, N. A. Feoktistov, V. G. Golubev, A. V. Medvedev, A. B. Pevtsov, A. V. Sel'kin, *Phys. Rev. E* **67**, 046602 (2003).
[7] G. Panzarini, L. C. Andreani, A. Armitage, D. Baxter, M. S. Skolnick, V. N. Astratov, J. S. Roberts, A. V. Kavokin, M. R. Vladimirova, M. A. Kaliteevski, *Phys. Rev. B* **59**, 5082 (1999).

15th Int. Symp. "Nanostructures: Physics and Technology"
Novosibirsk, Russia, June 25–29, 2007

Computer simulation of inorganic photoresist based on chalcogenide glass As_2S_3 development

D. V. Myagkov, M. O. Nestoklon and E. L. Portnoi
Ioffe Physico-Technical Institute, St Petersburg, Russia

Abstract. Development of the photoresist exposed by interference picture of coherent light is simulated and revealed good agreement with experement. The influence of exposure dose and development parameters on photoresist profile are analyzed. The possibility of decreasing the effect of standing light wave by means of additional homogeneous light irradiation is demonstrated.

High spatial frequency two-dimensional periodical structures, also known as crossed gratings, are celebrated for their ability to reduce light reflection and to increase light extraction [1, 2]. However, the advantages are useless for optoelectronics unless there is no cost-effective technology for large-scale production of high spatial frequency two-dimensional periodical structures. Interference photolitography using phase mask for exposition [2] and nanoimprinting [3] are the possible solutions of the problem. Both of the technologies can be easily built in photolithographic process of optoelectronic devices manufacturing. The technologies are based on the reproduction of the master grating by imprinting or photolithography. Interference photolithography with phase mask requires a structures periodical only in one dimension to produce both conventional and crossed gratings in contrast to the nanoimprinting technology.

The high spatial frequency master gratings periodical in one dimension can be fabricated by interference photolithography as the ability of interference photolithography to produce periodical structures with period of 250 nm and stripe width of 80 nm was demonstrated [4]. The key point that allowed to produce the grating with such a small features and sharp fringes was negative inorganic photoresist — chalcogenide glass As_2S_3. The photoresist was chosen, since it has high resolution, developing contrast and threshold of photoresist sensitivity. In order to produce the grating with nanoscale features the dependence of groove profile on exposure parameters: wavelength, incidence angle, thickness of the photoresist, contrast ratio; and photoresist parameters: dependence of photoresist dissolution velocity on exposure, optical absorption and refractive index should be thoroughly investigated. Thus, the computer simulation of photoresist development is required.

The dependence of developing rate of inorganic photoresist based on chalcogenide glass As_2S_3 on exposure was found experimentally like the other parameters of the photoresist — thickness of the photoresist, refraction index, absorption index.

Since the interference picture of two coherent light beams creates exposure dose distribution in the photoresist that is invariant along one of the axis, only a cross section of the photoresist should be simulated. The cross-section of developing photoresist is divided into small squares that are treated as elementary units (Fig. 1) whose exposition dose is calculated from their coordinates [5]. Size of units ($H = 1.5$ nm) is chosen, because such discretization provides adequate accuracy of simulation at an optimal simulating time. For every unit the development time is evaluated on the basis of the dependence of development rate on exposition dose of the unit [5],

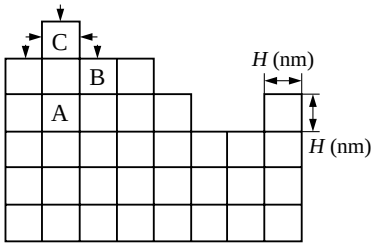

Fig. 1. Fragment of photoresist in contact with the developer. A — Elementary unit within photoresist. B — Elementary unit contacts with developer by only one side. C — Elementary unit contacts with developer by two opposite sides, this kind of units dissolves two times faster.

which is calculated according to coordinates of the point in the center of the unit. Unit development time also depends on its position relative to the interface between the photoresist and a developer.

Therefore, there are three kinds of units (Fig. 1). A — units within photoresist, which means they are not in contact with the developer and they are not dissolving, B — units at an interface between the photoresist and the developer, which means they are dissolving and their dissolution time depends on their thickness and development rate, and C — units with two opposite interfaces in contact with developer. Such a unit dissolves two times faster than B. A crucial event during the photoresist development is the complete dissolution of any unit. To simulate the photoresist development, an array of dissolving units is used. Every point that is in contact with the developer is imported into the array. Beginning with the moment of a contact of the developer with the photoresist, the program sorts the array out according to dissolution time of every unit in the array. The minimal dissolution time is assumed as a time for the next iteration. Neighbors of the dissolved units are put into the array, and the dissolved ones are deleted from the array. The sequence of these iterations repeats until the current computer dissolution time achieves the time defined by the user. The result of the computer simulation is a photoresist profile for any defined time. Dynamics of the development can be seen from a sequential set of photoresist profiles calculated for different times with equal intervals (Fig. 2). It helps to determine some crucial events: substrate opening, destruction of the mask by damaging the stripe at the substrate, reaching the desired mask dimensions.

The simulation can help to produce a phase mask for photolithography, but for nanoimprinting technology the master grating should be a crossed grating. Thus a computer simula-

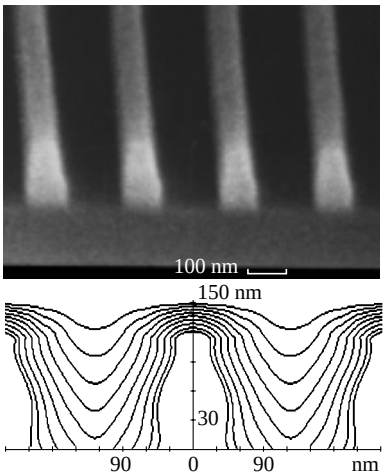

Fig. 2. (a) Periodical grating with 80 mn wide line. (b) Developing photoresist profiles, calculated with equal time intervals.

tion of crossed grating developing is required. We are about to develop such a program which is also based on experimental data of the photoresist properties determination. However, we can not afford to simulate a whole piece of the photoresist in the above described way due to the lack of the memory of usual PC and insufficient time of the simulating. Instead of discretisation of whole photoresist we have triangulated the surface of the resist that is in contact with the developer and then tracing the nodes of the mesh in course of development adding or deleting the triangles according to curvature of an area where it is located.

We have developed simple but effective way of inorganic photoresist — chalcogenide glass As_2S_3, developing simulation that enabled us to produce gratings that can be used as a phase mask for large-scale fabrication of high spatial frequency two-dimensional periodical structures on LED surface. By further developing of the described simulation approach we intend to investigate mask formation during the developing of crossed grating and thus produce a master grating for nanoimprinting technology.

References

[1] C. G. Bernhard, 1967 Structural and functional adaptation in a visual system Endeavor, v. 26, pp. 79–84.
[2] M. Ishimori, Y. Kanamori, M. Sasaki and K. Hane, *Jpn. J. Appl. Phys.* **41**, 4346–4349 (2002); Part 1, No. 6B (2002).
[3] R. Hershey, Compound Semiconductor.net October 2006.
[4] S. I. Nesterov, D. V. Myagkov and E. L. Portnoi, *Int. J. of Nanoscience* **3**, N. 1 & 2 (2004).
[5] L. F. Johnson, G. W. Kammlot, and K. A. Ingersoll, *Appl. Optics.* **17**, No. 8, 1165 (1978).

15th Int. Symp. "Nanostructures: Physics and Technology"
Novosibirsk, Russia, June 25–29, 2007

Exciton-polaritonic propagation and absorption in periodic and disordered multiple-quantum-well structures

V. A. Kosobukin and *A. N. Poddubny*
Ioffe Physico-Technical Institute, St Petersburg, Russia

Abstract. Exciton-polaritonic transfer and absorption are theoretically studied in short-period, Bragg-type and disordered multiple-quantum-well (MQW) structures. In all cases, the integral absorptivity is shown to increase monotonously with the nonradiative decay rate of quasi-2D excitons and the number of QWs. The scale and growth rate of integral absorptivity depend essentially on the type of MQW structure under consideration.

Introduction

Theoretically, the integral over the exciton absorption line is independent of the inverse exciton lifetime (temperature) in media with infinite translational mass of excitons and in nanostructures with infinite number of QWs. Experimentally, the integrated absorptivity is known to depend on temperature in bulk semiconductor crystals [1], solid solutions [2] and in structures with a finite number of QWs [3]. The presence of temperature-dependent integral absorptivity can be considered as an indication of electromagnetic (exciton-polaritonic) mechanisms of energy transfer. For short-period MQW structures, exciton-polaritonic effects in absorption were theoretically studied [4]. In this work, preliminary results of the theory [5] are reported concerning exciton-polaritonic transfer and integral absorptivity in the regular and disordered Bragg structures (one-dimensional resonant photonic crystals).

1. General relations

Consider an array of N QWs with the middle planes $z = z_n$ $(1 \le n \le N)$. A monochromatic wave

$$\mathbf{E}\,(\mathbf{r}, t) = \hat{\mathbf{y}}\; E\,(z; \omega)\; \exp\,(-i\omega t) \qquad (1)$$

with the frequency ω is assumed to propagate along the normal $\hat{\mathbf{z}}$ to the QWs in the background dielectric medium whose permittivity is ε_b. The excitonic polarization is of the form (1) with

$$P\,(z, \omega) = \frac{\sqrt{\varepsilon_\mathrm{b}}}{2\pi k_0} \sum_n \delta\,(z - z_n)\; \chi_n^{(0)}(\omega) E(z_n, \omega), \qquad (2)$$

$k_0 = \omega/c$. The susceptibility of the n-th QW

$$\chi_n^{(0)}(\omega) = \frac{\Gamma_n}{\omega_n - \omega - i\gamma} \qquad (3)$$

includes the frequency ω_n of quasi-2D exciton, as well as its radiative Γ_n and nonradiative γ decay rates. Within this basic model, the transfer matrix technique [4,5] is applied to calculate the spectra of reflection $R_\mathrm{N}(\omega)$, transmission $T_\mathrm{N}(\omega)$ and absorption

$$A_\mathrm{N}\,(\omega) = 1 - R_\mathrm{N}\,(\omega) - T_\mathrm{N}\,(\omega)\;. \qquad (4)$$

Given the exciton resonance frequency $\omega_0 \approx \omega_n$ and the related wavelength of light $\lambda = 2\pi c/\left(\sqrt{\varepsilon_\mathrm{b}}\omega_0\right)$, the optical problem is discussed for the quasi-Bragg ($d \propto \lambda$) MQW structures in comparison with short-period ($d \ll \lambda$) ones, where d is a characteristic inter-well distance.

Using Eq. (4), the dimensionless integral absorptivity is defined for a MQW structure as follows

$$I_\mathrm{N}\,(\gamma) = \int \frac{d\omega}{2\pi\Gamma_0} A_\mathrm{N}\,(\omega, \gamma)\;. \qquad (5)$$

It is a function of the nonradiative decay rate γ taken the same for all QWs, the energy being scaled by a typical radiative decay rate Γ_0. The integral absorptivity as a function of temperature should look like the function (5) of γ. It is because γ associated with exciton-phonon interaction grows monotonously with temperature, and so does the total decay rate $\gamma + \Gamma_0$ of exciton.

2. Absorption in resonant Bragg structures

Next, treated are regular MQW structures, in which cases $\omega_n = \omega_0$ and $\Gamma_n = \Gamma_0$ in Eq. (3) and $z_n = nd$ in Eq. (2). Under these conditions, the exciton-polaritonic absorption is studied for the resonant Bragg structures ($d = \lambda/2$) versus short-period ones ($d \ll \lambda/2$). In the former case, integration (5) over the absorption line

$$A_\mathrm{N}\,(\omega, \gamma) = \frac{2\gamma N\Gamma_0}{(\omega_0 - \omega)^2 + (\gamma + N\Gamma_0)^2} \qquad (6)$$

gives

$$I_\mathrm{N}\,(\gamma) = \frac{\gamma N}{\gamma + N\Gamma_0}\,. \qquad (7)$$

Figure 1 demonstrates the minima of integral absorptivity I_N at the periods $d = m\lambda/2$ satisfying the condition of m-th order Bragg diffraction in the spectral range of exciton resonance. The larger is N, the relatively deeper and narrower are the minima of I_N at the integers of $2d/\lambda$. The features of I_N occur because absorption is caused by different polaritonic modes in the resonant Bragg and short-period MQW structures. In the Bragg structures with finite numbers N, the integral absorptivity (7) is due to the only normal mode allowed for exciting by light with absorption spectrum (6) having the width $\gamma + N\Gamma_0$. This mode called super-radiant is a result of constructive interference of waves reradiated by QW excitons.

Dependences of the integral absorptivity on γ/Γ_0 and N are shown in Figs. 2(a),(b) by curves 1 and 2 for short-period and the resonant Bragg MQW structures, respectively. Given N, the integral absorptivity (7) of the Bragg structures grows monotonously with γ/Γ_0 up to $I_\mathrm{N} \to N$ at $\gamma/N\Gamma_0 \gg 1$. As

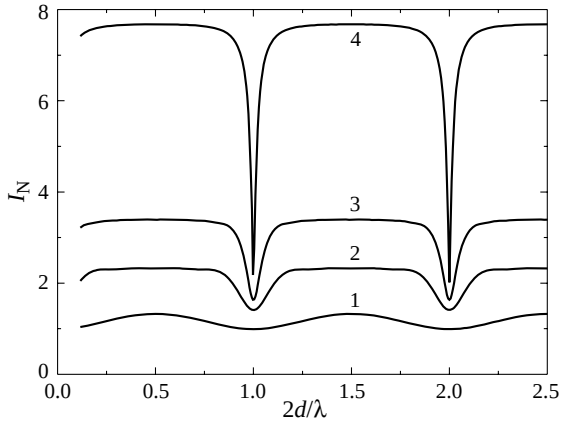

Fig. 1. Integral absorptivity I_N depending on the dimensionless period $2d/\lambda$ of MQW structures with the following N: 2 (1), 5 (2), 10 (3) and 50 (4). Calculated at normal light incidence with the parameters $\hbar\omega_0 = 1.51$ eV, $\hbar\Gamma_0 = 0.05$ meV, $\hbar\gamma = 0.1$ meV, $\varepsilon_b = 12$, typical of excitons in AlGaAs/GaAs QWs.

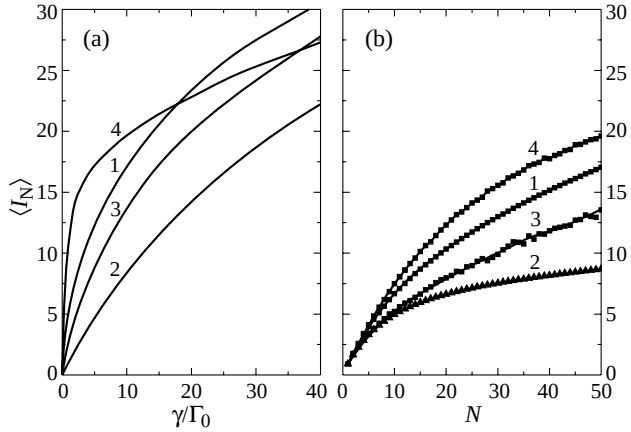

Fig. 2. Averaged integral absorptivity $\langle I_N \rangle$ depending on γ/Γ_0 at $N = 50$ (a) and on N at $\gamma/\Gamma_0 = 10$ (b). Curves correspond to the following MQW structures: short-period with $d = 0.1\lambda$ (1), Bragg-type with $d = \lambda/2$ (2), quasi-Bragg with inter-well disorder, $\delta_d/d = 0.06$ (3) and quasi-Bragg with intra-well disorder, $\delta_\omega/\Gamma_0 = 60$ (4). The exciton parameters are the same as in Fig. 1.

well, the integral absorptivity grows monotonously with N up to γ/Γ_0 at $N\Gamma_0/\gamma \gg 1$. The dependences of I_N on γ/Γ_0 and N can be treated as a radiative (polaritonic) effect until the MQW structure under study stays open to radiate. The dependences I_N saturate, when the radiation becomes inefficient, i.e. at very large γ/Γ_0 and N. The analytical forms of (5) are rather different for short-period and the resonant Bragg MQW structures: at $\gamma/N\Gamma_0 \ll 1$ these are estimated as $I_N \propto \sqrt{\gamma N/\Gamma_0}$ and $I_N \propto \gamma/\Gamma_0$, respectively.

3. Influence of disorder

In real MQW structures, optical spectra and the integral absorptivity (5) can be influenced by two kinds of disorder. *Inter-well* disorder implies the identical resonant QWs to be randomly spaced with the mean period d and the r.m.s. fluctuation δ_d of spacings. On the contrary, *intra-well* disorder means the QWs to form a lattice with a period d, while the exciton frequency ω_n entering Eq. (3) is a random variable in the n-th QW with the mean value ω_0 and r.m.s. fluctuation δ_ω. When neglecting any disorder, we deal with a regular "reference" MQW structure.

With the Bragg MQW structure ($d = \lambda/2$) as a "reference", we discuss how the averaged integral absorption varies in disordering from curves 2 in Fig. 2. Inter-well disorder ($\delta_d \neq 0$) makes the averaged absorption spectra $\langle A_N \rangle$ near $\omega = \omega_0$ larger in value and structured. It is because extra normal modes other than the super-radiant one become active in absorption owing to disorder. As a consequence, if δ_d increases, the averaged integral absorptivity $\langle I_N \rangle$ in Figs. 2(a),(b) varies from curves 2 to curves 3, with the latter tending further to curves 1 due to multi-mode absorption.

In turn, intra-well disorder leads to inhomogeneous broadening of absorption spectrum consisting of multiple maxima belonging to localized excitons. For intra-well disorder, the averaged integral absoprtivity $\langle I_N \rangle$ is shown by curves 4 in Fig. 2. If the disorder is strong ($\delta_\omega \gg N\Gamma_0$), $\langle I_N \rangle$ tends to $I_N = \gamma N/(\gamma + \Gamma_0)$ that is much larger than (7). The increase of integral absorptivity is also explained as a transition to multi-mode absorption regime in suppressing the resonant interactions between excitons.

In conclusion, a theory was developed for the resonant energy transfer and absorption in structures with finite numbers of QWs. It was established that the dependences of integral absorptivity on the nonradiative decay rate of quasi-2D excitons are qualitatively similar for short-period and Bragg-type MQW structures, both periodic and influenced by either inter-well or intra-well disorder. Also, significant differences in the integral absorptivity behavior were found due to different regimes of resonant reradiation of excitons in the above MQW structures.

Acknowledgements

This work was supported by the Russian Foundation for Basic Research, grant No. 07-02-00053, and the Dynasty Foundation-ICFPM.

References

[1] A. S. Davydov, *Theory of Solid State*, M. (1976).
[2] R. P. Seisyan, V. A. Kosobukin, S. A. Vaganov, M. S. Markosov, T. S. Shamirzaev, K. S. Zhuravlev, A. E. Bakarov, A. I. Toropov, *Phys. Stat. Sol. (c)* **2**, 900 (2005).
[3] V. A. Kosobukin, R. P. Seisyan, S. A. Vaganov, *Semicond. Sci. Technol.* **8**, 1235 (1993).
[4] V. A. Kosobukin, *Phys. Stat. Sol. (b)* **108**, 271 (1998).
[5] V. A. Kosobukin, A. N. Poddubny, *Phys. Solid State* **49** (2007), to appear.

15th Int. Symp. "Nanostructures: Physics and Technology"
Novosibirsk, Russia, June 25–29, 2007

Refocusing of a qubit system coupled to an oscillator

L. P. Pryadko and G. Quiroz
Department of Physics & Astronomy, University of California, Riverside, California, 92521, USA

Abstract. Refocusing, or dynamical decoupling, is a coherent control technique where the internal dynamics of a quantum system is effectively averaged out by an application of specially designed driving fields. The method has originated in nuclear magnetic resonance, but it was independently discovered in atomic physics as a "coherent destruction of tunneling". Present work deals with the analysis of the performance of "soft" refocusing pulses and pulse sequences in protecting the coherence of a qubit system coupled to a quantum oscillator.

Introduction and background

Quantum coherent control has found way into many applications, including nuclear magnetic resonance (NMR), quantum information processing (QIP), spintronics, atomic physics, etc. The simplest control technique is dynamical decoupling (DD), also known as refocusing, or coherent destruction of tunneling. The goal here is to preserve coherence by averaging out the unwanted couplings. This is achieved most readily by running precisely designed sequences of specially designed pulses [1].

In a closed system this can be analyzed in terms of the average Hamiltonian theory in the "rotating frame" defined by the controlling fields [2]. To leading order, the net evolution over the refocusing period is indeed described by the Hamiltonian of the system averaged over the controlled dynamics. For an open system, the dynamics associated with the bath degrees of freedom can be also averaged out, as long as they are sufficiently slow. This can be understood by noticing that the driven evolution with period $\tau = 2\pi/\Omega$ shifts some of the system's spectral weight by the Floquet harmonics, $\omega \to \omega + n\Omega$. With the average Hamiltonian for the closed system vanishing, the original spectral weight at $n = 0$ disappears altogether, and the direct transitions with the bath degrees of freedom are also suppressed as long as Ω exceeds the bath cut-off frequency, $\Omega \gtrsim \omega_c$ [3].

For a *closed* system, the refocusing can be made more accurate by designing higher-order sequences, where not only the average Hamiltonian ($k = 1$), but all the terms of order $k \le K$ in the Magnus (cumulant) expansion of the evolution operator over the period τ are suppressed. The corresponding simulation can be done efficiently by constructing time-dependent perturbation theory on small clusters [4]. The quantum kinetics of the corresponding *open* system with order-K DD, $K \le 2$, was analyzed by one of the authors using the non-Markovian master equation in the rotating frame defined by the refocusing fields [5]. This involved a resummation of the series for the Laplace-transformed resolvent of the master equation near each Floquet harmonic, with subsequent summation of all harmonics.

The results of Ref. [5] can be summarized as follows. With $K \ge 1$ refocusing, there are no direct transitions, which allows an additional expansion in powers of the small adiabaticity parameter, ω_c/Ω. In this situation the decoherence is dominated by reactive processes (dephasing, or phase diffusion). With $K = 1$, the bath correlators are modulated at frequency Ω. This reduces the effective bath correlation time, and the phase diffusion rate is suppressed by a factor $\propto \omega_c/\Omega$. With $K = 2$ refocusing, all 2nd-order terms involving instantaneous correlators of the bath coupling are cancelled. Generically, this leads to a suppression of the dephasing rate by an additional factor $\propto (\omega_c/\Omega)^2$, while in some cases (including single-qubit refocusing) all terms of the expansion in powers of the small adiabaticity parameter (ω_c/Ω) disappear. This causes an *exponential* suppression of the dephasing rate, so that an excellent refocusing accuracy can be achieved with relatively slow refocusing, $\Omega \gtrsim \omega_c$.

The conclusions in Ref. [5] were based on the analysis of the oscillator bath with a featureless spectral function, with the cut-off frequency ω_c serving as the only scale describing the bath correlations. They do not apply in the presence of sharp spectral features which appear if the controlled system is coupled to a local high-Q oscillator. On the other hand, the situation where the controlled system is coupled to a local oscillator mode is quite common. This situation is realized in atomic physics, where the oscillator in question is the cavity mode, while the continuous-wave (CW) excitation is used to suppress the coupling. In several quantum computer designs, nearly-linear oscillator modes are inherently present (e.g., mutual displacement in ion traps, or QCs based on electrons on helium). Finally, there are suggestions to include local high-Q oscillators in the QC designs to serve as "quantum memory" or "quantum information bath" [6].

In this work we consider refocusing of a qubit system where the spectral function of the oscillator bath has a sharp resonance. More specifically, we include the resonant mode in the system Hamiltonian, and consider the quantum kinetics of the resulting system in the presence of a featureless low-frequency oscillator bath driven by the refocusing pulses applied to the qubits only. Such a system can be analyzed with the help of the general results [5], as long as one is able to construct a $K = 1$ or $K = 2$ refocusing sequence to decouple the oscillator and other degrees of freedom. To this end, and having in mind sequences of soft pulses, we consider the analytical structure of the evolution operator for a closed system of arbitrary complexity, where one of the qubits is driven by a single one-dimensional π-pulse. An analysis of any refocusing sequence is then reduced to computing an ordered product of evolution operators for individual pulses. We illustrate the technique by analyzing the controlled dynamics of a qubit coupled to an oscillator. One of the constructed sequences provide order $K = 2$ qubit refocusing for any form of qubit-oscillator coupling, and was also shown to provide an excellent decoupling in the presence of a thermal bath.

Single π-pulse

Consider a qubit with generic couplings,

$$H_S = \sigma_x A_x + \sigma_y A_y + \sigma_z A_z + A_0, \tag{1}$$

where σ_μ are the qubit Pauli matrices and A_ν, $\nu = 0, x, y, z$ are the operators describing the degrees of freedom of the rest of the system which commute with σ_μ, $[\sigma_\mu, A_\nu] = 0$. The qubit evolution is driven by a one-dimensional pulse,

$$H_C = \tfrac{1}{2}\sigma_x V_x(t), \quad 0<t<\tau_p, \tag{2}$$

where the field $V_x(t)$ defines the pulse shape. The evolution due to the pulse is dominant; the unitary evolution operator to zeroth order in H_S is simply

$$U_0(t) = e^{-i\sigma_x\phi(t)/2}, \quad \phi(t) \equiv \int_0^t dt'\, V_x(t'). \tag{3}$$

When acting on the spin operators, this is just a rotation, e.g., $U_0(t)\sigma_y U_0^\dagger(t) = \sigma_y \cos\phi(t) + \sigma_z \sin\phi(t)$. Suppose $V_x(t)$ be symmetric, $V_x(\tau_p - t) = V_x(t)$, π-pulse, $\phi(\tau_p) = \pi$, and it additionally satisfies the first-order self-refocusing condition $s \equiv \langle \sin\phi(t)\rangle_p = 0$, where $\langle f(t)\rangle_p$ denotes the time-average over pulse duration. Then, the evolution operator $X \equiv U_0(\tau_p)$ expanded to second order in $\tau_p H_S$ reads

$$\begin{aligned} X^{(2)} = & -i\sigma_x - \tau_p(A_x + \sigma_x A_0) + \frac{i}{2}\tau_p^2\{A_0, A_x\} \\ & + \frac{i}{2}\tau_p^2\sigma_x(A_0^2 + A_x^2) + \tau_p^2\alpha\Big(A_y^2 + A_z^2 + i\sigma_x\,[A_y, A_z]\Big) \\ & + \tau_p^2\zeta\Big(\,[A_0, \sigma_y A_z - \sigma_z A_y] + i\{A_x, \sigma_y A_y + \sigma_z A_z\}\Big). \quad (4) \end{aligned}$$

Here $\alpha \equiv \langle\theta(t-t')\sin[\phi(t)-\phi(t')]\rangle_p$, $\zeta \equiv \langle\theta(t-t')\cos\phi(t')\rangle_p$ parametrize the evolution properties of the pulse at second order. The values of the parameters computed for some pulse shapes are listed in Tab. 1.

Common pulse sequences

Transforming Eq. (4) appropriately, we can now easily compute the result of application of any pulse sequence. In particular, the π-pulse $\overline{X}$ applied along the $-x$ direction can be obtained from $(-X)$ with a substitution $\alpha \to -\alpha$. As a result, e.g., the expansion of the evolution opeator for the one-dimensional sequence $\overline{X}X$ can be written as

$$\overline{X}X = 1 - 2i\tau_p(A_0 + \sigma_x A_x) - 2\tau_p^2(A_0 + \sigma_x A_x)^2 + \mathcal{O}(\tau_p^3),$$

or it can be re-exponentiated as evolution with the effective Hamiltonian

$$H_{\overline{X}X} = A_0 + \sigma_x A_x + \mathcal{O}(\tau_p^2). \quad (5)$$

The corresponding calculation with the usual finite-width pulses (e.g., Gaussian) where $s \neq 0$ produces a correction to the effective Hamiltonian already in the leading order,

$$\delta H_{\overline{X}X} = s(\sigma_z A_y - \sigma_y A_z) + \mathcal{O}(s^2\tau_p).$$

This can be corrected by constructing a longer sequence, e.g., $\overline{X}X\overline{X}\overline{X}$. Returning to pulses with $s = 0$, we list the expansions computed for several two-dimensional sequences:

$$\begin{aligned} H_{X\overline{Y}XY} = & A_0 + \tau_p\Big(\frac{i\alpha}{2}[A_z, A_y] - \frac{i}{2}\,[A_0, \sigma_x A_x - \sigma_y A_y] \\ & - \frac{\alpha}{2}\sigma_y(A_x^2 + A_y^2) + \frac{1+4\zeta}{4}\sigma_z\{A_x, A_y\}\Big) + \mathcal{O}(\tau_p^2), \quad (6) \end{aligned}$$

$$H_{YX\overline{Y}X\overline{X}\overline{Y}XY} = A_0 - \frac{\alpha\tau_p}{2}\Big(\sigma_y(A_x^2 + A_z^2) + i[A_y, A_z]\Big), \quad (7)$$

$$H_{\overline{Y}\overline{X}Y\overline{X}X\overline{Y}XY} = A_0 + \mathcal{O}(\tau_p^2). \quad (8)$$

Table 1. Parameters of several common pulse shapes. The first line represents the "hard" δ-function pulse, G_{001} denotes the Gaussian pulse with the width $0.01\tau_p$, while S_n and Q_n denote the 1st and 2nd-order self-refocusing pulses from Ref. [4].

pulse	$s \equiv \langle\sin\phi(t)\rangle_p$	$\alpha/2$	ζ
$\pi\delta(t-\tau_p/2)$	0	0	0.25
G_{001}	0.0148978	0.00735798	0.249979
G_{010}	0.148979	0.0653938	0.247905
S_1 [4]	0	0.0332661	0.238227
S_2 [4]	0	0.0250328	0.241377
Q_1 [4]	0	0	0.239889
Q_2 [4]	0	0	0.242205

Atom in a cavity example

Consider an atom placed in a lossless cavity with a single resonant mode. The resonance part of the Hamiltonian can be written in the form (1), where $A_x = g(b + b^\dagger)$, $A_y = ig(b - b^\dagger)$, $A_z = 0$, $A_0 = \Delta\, b^\dagger b$, g is a coupling constant, and Δ is the cavity frequency bias. Contrary to the conclusions of Ref. [7], such a coupling cannot be suppressed with any one-dimensional pulse sequence.

On the other hand, the two-dimensional four-pulse sequence (6) provides a leading-order refocusing of the coupling. The subleading-order correction is present (the order of the sequence is $K = 1$), and it is not particularly small even for 2nd-order self-refocusing pulses with $s = \alpha = 0$. The eight-pulse sequences (7) and (8) have equal accuracy with 2nd-order pulses but the 2nd-order accuracy of the latter sequence is also retained with 1st-order pulses.

After tracing out the oscillator degrees of freedom, we can apply the results of Ref. [5] and expect the two 2nd-order sequences to provide an excellent refocusing accuracy even in an open system, as long as the refocusing rate is sufficiently high. We confirmed this expectation by a numerical simulation, where the bath was modeled as a classical correlated random field.

Conclusions

The main result of this work is the expansion (4) and the classification of the corresponding parameters in Tab. 1. This allows an explicit computation of the error operators associated with refocusing in systems of arbitrary complexity. We illustrated the approach for several sequences applied to a qubit coupled to an oscillator. The 8-pulse sequence (8) provides 2nd-order refocusing for any form of the coupling between the qubit and the oscillator.

Acknowledgements

This research was supported in part by the NSF grant 0622242 (LP) and the Dean's Undergraduate Research fellowship (GQ).

References

[1] C. P. Slichter, *Principles of Magnetic Resonance* (Springer-Verlag, Berlin, 1992), 3rd ed.; L. M. K. Vandersypen and I. L. Chuang, *Rev. Mod. Phys.* **76**, 1037 (2005).

[2] J. S. Waugh, L. M. Huber, and U. Haeberlen, *Phys. Rev. Lett.* **20**, 180 (1968); J. S. Waugh, C. H. Wang, L. M. Huber, and R. L. Vold, *J. Chem. Phys.* **48**, 662 (1968).

[3] A. G. Kofman and G. Kurizki, *Phys. Rev. Lett.* **87**, 270405 (2001); **93**, 130406 (2004).

[4] P. Sengupta and L. P. Pryadko, *Phys. Rev. Lett.* **95**, 037202 (2005).

[5] L. P. Pryadko and P. Sengupta, *Phys. Rev. B* **73**, 085321 (2006).

[6] See, e.g., A. T. Sornborger, A. N. Cleland, and M. R. Geller, *Phys. Rev. A* **70**, 052315 (2004) and references therein.

[7] M. Thorwart, L. Hartmann, I. Goychuk, P. Hänggi, *J. Mod. Opt.* **47**, 2905 (2000).

15th Int. Symp. "Nanostructures: Physics and Technology"
Novosibirsk, Russia, June 25–29, 2007

Effective ε and μ from the general scattering matrix of a metamaterial slab

S. G. Tikhodeev[1] and N. A. Gippius[1,2]

[1] A. M. Prokhorov General Physics Institute RAS, Vavilova 38, 119991 Moscow, Russia
[2] LASMEA, UMR 6602 CNRS, Université Blaise Pascal, 24 av. des Landais, 63177 Aubière, France

Abstract. Retrieval of effective electric permittivity ε and magnetic permeability μ of metamaterials is discussed basing on general scattering matrix of a photonic crystal slab in long wavelength (zero diffraction) case. It is shown that a possibility to describe the electromagnetic response of metamaterial slabs in near-infrared and optical ranges by local ε and μ is very limited, and more general nonlocal description is needed.

Recently, a lot of interest is attracted to the electromagnetic response of short period metallic-dielectric photonic crystals — metamaterials. For example, they can demonstrate so called left-handed or negative index behaviour [1]: the refractive index may become negative, and unusual lensing (Veselago lens) becomes possible. Another interesting possibility is cloaking of objects from the electromagnetic fields [2].

However, the problem of effective medium description of metamaterials is very nontrivial [3]. On the one hand, it is known that the wavelength of light has to exceed significantly the period of such structures, in order that a description within spatially local ε and μ becomes valid, see, e.g., a recent analysis in [4, 5, 6]. On the other hand, any photonic crystal slab in zero diffraction limit behaves like a homogeneous slab, in a sense that the incoming light is only refracted and transmitted, and it is very tempting to retrieve effective ε and μ from the corresponding optical coefficients [7]. Do then such retrieved ε and μ have any physical sense, and is it possible to use them to engineer something like a Pendry's cloak, or at least to distinguish a modulated slab from a homogenous one, are important questions.

In this paper, we analyse the effective electromagnetic response of the metamaterials basing on the scattering matrix theory [8, 9, 10, 11] and using the retrieval idea of [7, 12]. The results will be illustrated on examples of several metamaterial metal-dielectric structures, for which the effective negative refractive behaviour has been established in recent works, e.g. [13, 14]. We show that, in agreement with analysis in [3], the electromagnetic response of metamaterials near the magnetic resonances is actually significantly nonlocal and lossy. As a result, e.g., it appears to be hardly possible to use such metamaterials for light cloaking.

Acknowledgements

This work was supported by the Russian Foundation for Basic Research (Grant No. 06-02-17211) and by the Presidium of Russian Academy of Sciences (Program "Quantum Nanostructures").

References

[1] V. G. Veselago, *Sov. Phys.–Uspekhi* **10**, 509 (1968).
[2] J. B. Pendry, D. Schurig, and D. R. Smith, *Science* **312**, 1780 (2006).
[3] V. M. Agranovich, Y. N. Gartstein, *Phys.–Uspekhi* **49**, 1029 (2006).
[4] D. Felbacq and G. Bouchitte, *Phys. Rev. Lett.* **94**, 183902 (2005).
[5] A. I. Căbuz, D. Felbacq, and D. Cassagne, *Phys. Rev. Lett.* **98**, 037403 (2007).
[6] X. Hu, C. T. Chan, J. Zi, M. Li, and K.-M. Ho, *Phys. Rev. Lett.* **96**, 223901 (2006).
[7] D. R. Smith, S. Schultz, P. Markoš and C. M. Soukoulis, *Phys. Rev. B* **65**, 195104 (2002).
[8] S. G. Tikhodeev, A. L. Yablonskii, E. A. Muljarov, N. A. Gippius, and T.Ishihara, *Phys. Rev. B* **66**, 045102 (2002).
[9] A. Christ, S. G. Tikhodeev, N. A. Gippius, J. Kuhl, and H. Giessen, *Phys. Rev. Lett.* **91**, 183901 (2003).
[10] N. A. Gippius, S. G. Tikhodeev, and T. Ishihara, *Phys. Rev. B* **72**, 045138 (2005).
[11] S. G. Tikhodeev and N. A. Gippius, to be published.
[12] D. R. Smith, D. Schurig, and J. J. Mock, *Phys. Rev. E* **74**, 036604 (2006).
[13] S. Zhang, W. Fan, N. C. Panoiu, K. J. Malloy, R. M. Osgood, and S. R. J. Brueck, *Phys. Rev. Lett.* **95**, 137404 (2005).
[14] U. K. Chettiar, A. V. Kildishev, T. A. Klar, and V. M. Shalaev, *Optics Express* **14**, 7872 (2006).

15th Int. Symp. "Nanostructures: Physics and Technology"
Novosibirsk, Russia, June 25–29, 2007

Photoluminescence of one-dimensional photonic crystals doped with resonance centres

M. M. Voronov
Ioffe Physico-Technical Institute, St Petersburg, Russia

Abstract. A general method of photoluminescence (PL) spectra calculation of one-dimensional (1D) photonic crystals has been developed. This approach is based on application of thermal radiation Kirchhoff's law to 1D systems and appears to be suitable for practical analysis. The analytical expression for PL spectral function and its decomposition nearby the real parts of eigenfrequencies have been obtained. The origin of frequency shifts between PL and transmission spectral peaks has been discussed.

Introduction

In most papers on PL of photonic crystals the calculations of spontaneous emission have been done by using the concept of electromagnetic density of states (DOS) [1–3]. However, its physical meaning and criterion for validity are not always clear, because the typical definition of DOS relates to Bloch states in an infinite crystal [1]. The problem of theoretical calculation of DOS in partly disordered 1D periodic structures, let alone 3D-structures, apparently looks rather complicated. The approach developed in the present paper is based on using Kirchhoff's law for thermal radiation to PL calculations of 1D-structures. It appears to be very convenient for a large class of systems, in particular, for MQW structures [4], planar microcavities and may also be generalized on 2D and 3D photonic crystals.

In this work numerical calculations are performed for the distributed Bragg reflector (DBR) which as well known works as dielectric mirror and thereby strongly modifies electromagnetic-radiation. This structure consists of alternating quarter-wavelength layers A and B with refractive indices n_a, n_b of the compositional materials and thicknesses $a = \bar{\lambda}/4n_a$, $b = \bar{\lambda}/4n_b$, respectively. The wavelength $\bar{\lambda}$ is a parameter which governs the photonic band and spontaneous emission. In more detail such a system and some experiments on its spontaneous emission are described in [5]. Let us consider layers A as active ones, since they contain some resonant emitting centres, which may be atoms in a dielectric or excitons in a semiconductor. We note that in our theory the specific nature of resonance centres (RCs) is of no importance and can always be taken into account.

1. General theory of PL spectra of 1D photonic crystals

The PL intensity $I(\omega)$ is conveniently presented as a sum of partial contributions $I_n(\omega)$ from the n-th active layer,

$$I_N(\omega) = \sum_{n=1}^{N} I_n(\omega)\,, \tag{1}$$

where N is the number of layers A in the structure. The partial intensity I_n is further written as

$$I_n(\omega) \propto \omega A'_n(\omega)\, f(\omega) F_n(\omega_0)\,, \tag{2}$$

Let us explain the meaning of each of these functions. Here $F_n(\omega_0)$ defines excitation intensity of RCs at frequency ω_0 in n-th layer and, in particular, can have the form $\exp(-\alpha n)$, where α is the Buger law attenuation coefficient. An expression for $F_n(\omega_0)$ will be given below. Another function $f(\omega)$ is the occupation of the excited RC states emitting at the frequency ω. Note that in equilibrium $f(\omega)$ should be replaced by the Bose–Einstein distribution function $[\exp(\hbar\omega/k_{\mathrm{B}}T) - 1]^{-1} \approx \exp(-\hbar\omega/k_{\mathrm{B}}T)$. Finally, $A'_n(\omega)$ is the contribution to the absorbance in the n-th layer from RCs. If the RCs concentration in layers is not great, as well as value of the excitation intensity, the imaginary part of the refractive index $n_a(\omega)$ in the active layers is a sum $n''_m(\omega) + n''_{\mathrm{RC}}(\omega)$, where $n''_m(\omega)$ is independent of and $n''_{\mathrm{RC}}(\omega)$ is proportional to the concentration of RCs. Since $n''_{\mathrm{RC}}(\omega)$ is small one can keep in $A'_n(\omega)$ only the first order in $n''_{\mathrm{RC}}(\omega)$. It follows then that $A'_n(\omega)$ in (2) and the total absorbance $A_n(\omega)$ due to the n-th layer are related by

$$A'_n(\omega) = \Phi_n(\omega)\, n''_{\mathrm{RC}}(\omega)\,, \quad \Phi_n(\omega) = \frac{dA_n(\omega)}{dn''_a(\omega)}\,, \tag{3}$$

It is obvious that $\Phi_N(\omega) = \sum_n \Phi_n(\omega)$. In case of small n''_m one can consider $\Phi_N(\omega)$ is independent of n''_m and without taking into account emission line form of the single RC is proportional to $A_N(\omega) = \sum_n A_n(\omega)$. For practical calculations $f(\omega)$ can be approximated by a function of the Gaussian form $\exp[-\beta(\omega - \omega_{\mathrm{RC}})^2]$, where β is a fitting constant and ω_{RC} is the emission frequency of a single RC.

Now we describe the calculation procedure of the spontaneous emission from the finite periodic structure in detail. For simplicity we will study a normal incidence of light from semi-infinite medium B on the structure.

It is advisable to present the expression for

$$A_N(\omega) = \sum_n A_n(\omega) = 1 - |r_N(\omega)|^2 - |t_N(\omega)|^2,$$

where r_N and t_N are reflection and transmission coefficients for the structure with N active layers. It may be useful to give here their expressions for arbitrary number, m, of layers A $r_m = r_1 \sin mQd/Z_m$, $t_m = t_1 \sin Qd/Z_m$,

$$Z_m(\omega) = \sin mQd - t_1 \sin(m-1)Qd\,,$$

where Q is the polaritonic wave vector in an infinite structure The reflection and transmission coefficients for a single A-layer are

$$r_1 = 2\mathrm{i}\mathrm{e}^{\mathrm{i}(\phi_a+\phi_b)} r \sin\phi_a/\xi\,,\ t_1 = \mathrm{e}^{\mathrm{i}(\phi_a+\phi_b)}(1-r^2)/\xi\,.$$

The other notations are as follows: $\phi_a = \omega n_a a/c$, $\phi_b = \omega n_b b/c$, $r = (n_a - n_b)/(n_a + n_b)$, $t = 2n_b/(n_a + n_b)$,

$\xi = 1 - r^2 e^{2i\phi_a}$, $|\xi|^2 = 1 - 2r^2\cos 2\phi_a + r^4$. Let us introduce an auxiliary function $\eta_n = t_n/(1 - r_n r_{N-n})$ with the help of which one can get the following expressions: $F_n(\omega_0) = |\eta_{n-1}|^2(1 - |r_{N-n+1}|^2) - |\eta_n|^2(1 - |r_{N-n}|^2)$ and partial PL intensity $I_n(\omega) \propto \omega^2|te^{i\phi_a/2}/\xi|^2(n_a/n_b)^2[g_1(|\eta_{n-1}|^2 + |\eta_n r_{N-n}|^2) + 2g_2\mathrm{Re}(\eta_n\eta^*_{n-1}r_{N-n})]n''_{RC}(\omega)$, where $g_1 = 1+r^2+r\sin 2\phi_a/\phi_a$ and $g_2 = (1+r^2)\sin\phi_a/\phi_a + 2r\cos\phi_a$ (when $F_n = \mathrm{const}$ and $f = \mathrm{const}$). This method is equivalent to direct calculation of the function Φ_N.

In a situation when light falls on the structure from vacuum so that the distance between vacuum and outermost interface of the first A-layer is equal to b' the expression (1) for PL intensity should be multiplied by the factor $|\tau/(1 - \varrho r_N e^{i\phi})|^2$, where $\varrho = (n_b - 1)/(n_b + 1)$, $\tau = 2n_b/(n_b + 1)$ and $\phi = (2b' - b)\omega n_b/c$.

2. PL spectral function in photonic band

The calculation of the derivative (3) gives the following expression for the PL spectral function in photonic band

$$\Phi_N(\omega) = \frac{C_1 N + C_2 \sin NQd}{|\xi|^2|Z_N|^2}\,. \qquad (4)$$

Below we write the expressions for functions C_1 and C_2:

$$\begin{aligned}
C_1 &= [(1/n_b - n_b/n_a^2)\sin\phi_a\sin\phi_b \\
&\quad +(2\sin\phi_a\cos\phi_b + (n_a/n_b + n_b/n_a)\sin\phi_b\cos\phi_a)\omega a/c] \\
&\quad \times(1 - r^2)[r^2\sin(\phi_b - \phi_a) - \sin(\phi_a + \phi_b)]\,, \\
C_2 &= B_0\sin NQd + B_1\sin(N-1)Qd \\
&\quad + B_2\sin(N-2)Qd - C_1(\sin NQd + \cos NQd\cot Qd), \\
B_0 &= 4[rt\sin 2\phi_a/(n_a + n_b) + r^2(1 - r^2)(\omega a/c)]\,, \\
B_1 &= -2(1-r^2)[3r^2\cos(\phi_b - \phi_a) - \cos(\phi_a + \phi_b)](\omega a/c) \\
&\quad -8rt\sin\phi_a\cos\phi_b/(n_a + n_b)\,, \\
B_2 &= -2(1 - r^2)^2(\omega a/c)\,.
\end{aligned}$$

The general expression for $\Phi_N(\omega)$ allowing for both the allowed and forbidden photonic band is too cumbersome to show it here.

As is seen in Eq. (4), the denominator of $\Phi_N(\omega)$ has some function $|Z_N|^2$. It is known that the equation $Z_N(\omega) = 0$ define all complex eigenfrequencies $\omega_j = \omega'_j + \mathrm{i}\omega''_j$ of this system. Therefore there is another way to present PL spectral function, namely, by decomposition nearby the real values ω'_j of the eigenfrequencies ω_j. One can show that

$$\Phi_N(\omega) = \sum_j \frac{a_j + b_j(\omega - \omega'_j)}{|\omega - \omega_j|^2}\,,$$

where coefficients a_j and b_j can be found from the real and imaginary parts of the following expression

$$a_j + \mathrm{i}b_j\omega''_j = \lim_{\omega\to\omega_j}\frac{[(\omega - \omega'_j)^2 + \omega''^2_j]P(\omega)}{Z(\omega)Z(-\omega)}\,,$$

where $P(\omega) = (C_1 N + C_2\sin NQd)/|\xi|^2$. The analysis shows that frequencies at which the function $|Z(\omega)|^2$ is minimal are very close to ω'_j, and the shift between $\omega_{PL,j}$, corresponding to a maximum of $\Phi_N(\omega)$, and ω'_j arises due to a smooth frequency dependence of the function $P(\omega)$. We also note that a similar explanation is valid for a frequency shift between a maximum in the transmission $T_N = |t_N|^2$ and ω'_j. In the latter case, instead of $P(\omega)$, the function $|t_1|^2\sin^2 Qd$ is responsible for the shift, owing to the dependence $Q(\omega)$. This is why the frequency at which $T_N \approx 1$ (if the absorption is small) is clearly distinguished from ω_{PL}, see inset and caption in Fig. 1. The mentioned shift between transmission and PL peaks have been observed experimentally in [5]. At the same time such a shift in the maxima positions for structure with micro-resonator is absent, as it indeed occured in experiment in [6].

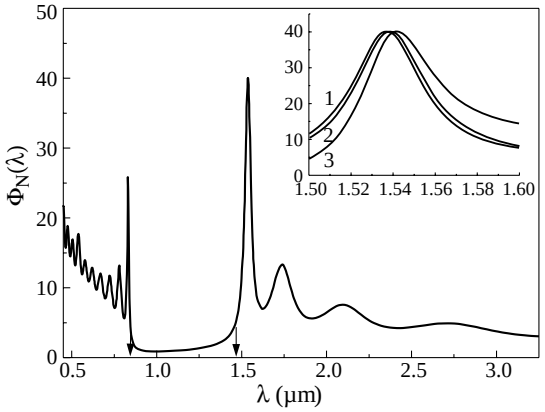

Fig. 1. The dependence of PL spectral function on wavelength (in vacuum) for DBR-structure with $N = 7$ A-layers. The refractive indices of materials A and B are $n_a = 3.46$ and $n_b = 1.46$ and the wavelength $\bar{\lambda} \approx 1078.5$ nm. The forbidden photonic band is indicated by two vertical arrows. Inset shows three different spectra reduced to the same maximum value, namely: $I_N \propto \Phi_N$ (curve 1), $|Z_N|^{-2}$ (curve 2) and T_N (curve 3).

In conclusion, we have developed a theory which can explain the spontaneous emission behaviour in dependence on the frequency of light emitted by doped resonance centers and the geometry of a $1D$ photonic crystal, in particular, a DBR-structure. In this paper the theory has been illustrated for conditions close to the experiment [5] and a good qualitative agreement has been achieved. The results on quantitative comparison between the theory and experiment, including a fitting procedure to find the optimal set of parameters, will be published elsewhere.

Acknowledgements

The author is grateful to E. L. Ivchenko and A. B. Pevtsov for helpful discussions. This work is supported by RFFI 05-02-17803 and program of RAS.

References

[1] C. H. Raymond *et al*, *Phys. Rev. E* **62**, 7405 (2000).
[2] J. M. Bendickson *et al*, *Phys. Rev. E* **53**, 4107 (1996).
[3] A. Settimi *et al*, *Phys. Rev. E* **68**, 26614 (2003).
[4] M. M. Voronov *et al*, *J. Lumin.* **125**, 112 (2007).
[5] A. B. Pevtsov *et al*, *Proc. 13th Int. Symp. "Nanostructures: Physics and Technology"*, Ioffe Institute, St Petersburg, Russia, p. 137, 2005.
[6] A. A. Dukin *et al*, *Appl. Phys. Lett.* **77**, 3009 (2000).

15th Int. Symp. "Nanostructures: Physics and Technology"
Novosibirsk, Russia, June 25–29, 2007

XAFS spectroscopy for study quantum dots microstructure and energy spectrum peculiarities

S. B. Erenburg[1], N. V. Bausk[1], A. I. Nikiforov[2], A. V. Dvurechenskii[2], V. G. Mansurov[2], K. S. Zhuravlev[2] and S. Nikitenko[3]

[1] Nikolaev Institute of Inorganic Chemistry SB RAS, Lavrentiev Ave. 3, Novosibirsk 630090, Russia
[2] Institute of Semiconductors Physics SB RAS, Lavrentiev Ave. 13, Novosibirsk 630090, Russia
[3] KU Leuven, DUBBLE-CRG & ESRF, BP 220, F38143, Grenoble, France

Abstract. Parameters of quantum dots (QDs) and heterostructures appeared during their formation by molecular beam epitaxy (MBE) depend on substrate pretreatment, temperature conditions and composition variations have been determined using EXAFS and XANES spectroscopy method. Lowering of the Si spacer deposition temperature from 500 to 300 °C leads to a substantial decrease of the diffusion between the phases Ge/Si and the formation of sharp phase boundaries. It was established that microstructure parameters of heterosystems containing three-dimensional islands and (or) two-dimensional thin films depend on AlN-substrate temperature and peculiarities of GaN-deposition process.

Introduction

Developments of techniques allowing the determination of spatial and electronic structural parameters on the surface or interfaces of materials will provide tools to control and check the fabrication of structures containing nanoclusters with discrete electronic spectra. The fabrication of such systems can be an important step in the pathway towards miniaturization and engineering for quantum computer systems.

The goal of this research is to determine parameters of quantum dots (QD) and heterostructures appeared during their formation by molecular beam epitaxy (MBE) depend on substrate pretreatment, temperature conditions and composition variations. In present work Ge/Si-, GaN/AlN- and InAs/AlAs-sandwich heterostructures formed from components with the lattice constant mismatch have been studied. EXAFS and XANES spectra at the GeK, GaK and InK edges have been measured using surface sensitive fluorescent yield detection mode [1,2].

Local structural changes in thin layers and nanoclusters are not detectable by traditional X-ray structural analysis or electron diffraction, due to the absence of long-range ordering. EXAFS spectroscopy provides a unique possibility for solving such problems [1,2]. This experimental technique allows determination of parameters regarding the local environment of atoms and electronic parameters of nanoclusters. In particular, our previous experiments using GeK XAFS showed that Ge QDs are characterized by interatomic Ge-Ge distances of 2.41 Å which is 0.04 Å less than in bulk Ge [1].

1. Experimental

EXAFS spectra of the GeK-, GaK-, InK-edges were measured at the VEPP-3 storage ring of the Budker Institute of Nuclear Physics (Novosibirsk, Russia) and at the DUBBLE beamline of the European Synchrotron Radiation Facility (Grenoble, France). Both beamlines are equipped with a Si(111) double-crystal monochromator. In all experiments the samples were placed under an angle of 3 degrees relative to the incoming X-ray beam and the detector was mounted in horizontal plane in such a way to achieve the best signal to noise ratio. Atoms local arrangement in these systems have been determined using the fitting procedure in the EXCURV program of Fourier filtered experimental data.

2. Results and discussion

Microstructure of Ge/Si sandwich geterostructures has been studied depend on effective thickness of Ge thin films deposited on Si(001) and Si(111) at 300 °C. This films are separated and protected by Si spacer layers. It has been detected a monotonic growth of the of Ge-Ge effective coordination number in parallel with the effective thickness of the germanium film increase from 4 to 10 monolayers which indicates monotonic size evolution of germanium nanoclusters. Lowering of the Si spacer deposition temperature from 500 to 300 °C leads to a substantial decrease of the diffusion between the phases Ge/Si and the formation of sharp phase boundaries between Si and Ge.

The spectra have been measured on GaN/AlN heterosystems which contain GaN two-dimensional layers or nanoclusters on AlN substrates. These samples have been produced using molecular beam epitaxy (MBE) on (0001) sapphire substrate. The samples consist of a few layers (from 1 to 20) with each an effective thickness from 2 to 5 GaN monolayers. These layers are separated and protected by AlN layers with a thickness of about 100 Å.

It has been found that the first shell RGa-N interatomic distance in heterostructure GaN/AlN is equal to $\sim$ 1.93 Å, which is 0.02 Å smaller compared to crystalline GaN. For the second Ga-Ga shell an interatomic distance $R_{\mathrm{Ga-Ga}} \sim 3.14$ Å was found, which is 0.04 Å smaller than in crystalline GaN. The coordination number $N_{\mathrm{Ga-Ga}}$ was found to be from 5.9 to 10.7. It was established that heterostructure contains three-dimensional islands or two-dimensional thin films depending of temperature of AlN-substrate during GaN-deposition. Our results suggest that average size of GaN clusters and elastic strains and deformations depend of preparation conditions, such as temperature of AlN-substrate and time of deposition, or effective thickness of GaN film.

The Ge/Si and GaN/AlN quantum dots vertical (in the growth direction) and lateral alignment have been recently demonstrated. The coupled dots are formed by depositing a single layer of dots followed directly by a small amount of barrier

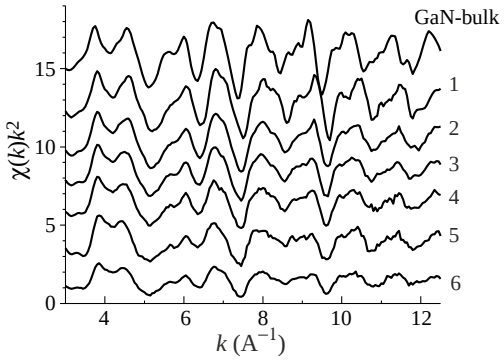

Fig. 1. Experimental k^2-weighted GaK EXAFS spectrum ($\chi(k)k^2$ for bulk crystalline GaN and for GaN/AlN heterostructures.

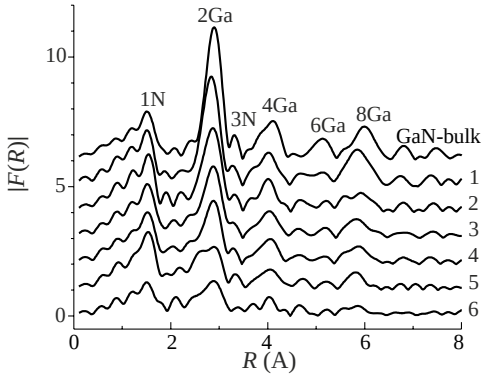

Fig. 2. Fourier transform modules of $\chi(k)k^2$ GaK EXAFS without phase shift: for bulk crystalline GaN and for GaN/AlN heterostructures. The respective peaks are marked by the shell numbers and types of surrounding atoms.

material (Si or AlN) then immediately another layer of dots. Due to the strain field of the first dot, the new dots form directly over the first dots. For two layers of closely coupled dots separated by a thin ($\sim$ 30 Å) Si or AlN barrier the electron wave function become highly delocalized along the z direction so that each coupled dot pair is very similar to a single quantum dot with the larger aspect ratio. Such coupled, tripled and so on nanostructures are also known as "artificial" or "macro" molecules.

Therefore, interpretation of peculiarities of QDs experimental energy spectra must take into account the variation in local structure of "macromolecule" with vertically adjoint aligned QDs in comparison with the ordinary QDs heterostructure.

Semiconductors sandwich heterostructures (from 1 up to 20 monolayers) were prepared by the growing procedure with follow-up deposition of blocking Si, AlN layers (from 30 up to 500 Å).

Microstructure of Ge/Si and GaN/AlN sandwich geterostructures contains vertically aligned QDs has been studied depend on number of Ge or GaN layers in sandwich and effective thickness of Si or AlN barrier material. It was established an influence of blocking layers (Si, AlN) thickness and number of QDs layers (Ge, NaN) in geterostructure on the microstructure characteristics of quantum dots. The coordination number NGe-Ge was found to be $\sim$ 2 for samples with thin barrier Si films (30–50 Å) in contrast with samples with thick Si films (500 Å), which have smaller NGe-Ge coordination number. This result is in accordance with electron spectroscopy and electron diffraction results. It has been found the same, but more feebly marked results, for GaN/AlN heterostructure. This result suggests increasing of average GaN clusters size for structures with thin AlN films ($\sim$ 30 Å).

An information concerning quantum dots free states energy structure was obtained by XANES data analysis of the samples doped with boron. It was supposed that the GeK XANES preedge maximum is appeared due to free levels formation at the top of the bulk Ge valence band and at a depth of 0.2–0.4 eV from the top of the valence band for the samples with quantum dots. The microstructure parameters and the energy spectrum peculiarities of heterosystems with discrete electronic spectra largely influenced by the elastic deformation at the boundaries of the nanoclusters and substrate was detected by the direct method showing that EXAFS spectroscopy is very perspective tool to study materials containing nanostructures.

Acknowledgements

Financial support from the Siberian Branch of Russian Academy of Sciences Program "Integration" No. 101 and from the Russian Foundation of Basic Research (grant 06-03-32793) is greatly appreciated.

References

[1] S. Erenburg, N. Bausk, L. Mazalov, A. Nikiforov and A. Yakimov, *J. Synchrotron Rad.* **10**, 380 (2003).

[2] S. B. Erenburg, N. V. Bausk, L. N. Mazalov, A. I. Toropov, K. S. Zhuravlev, V. G. Mansurov, T. S. Shamirsaev, W. Bras, S. Nikitenko, *Nucl. Instr. & Meth. Phys. Res.* **A 543**, 188 (2005).

15th Int. Symp. "Nanostructures: Physics and Technology"
Novosibirsk, Russia, June 25–29, 2007

Ge islands on Si(001): stability, evolution, elastic relaxation, and dislocation injection

F. Montalenti[1], S. Cereda[1], R. Gatti[1], A. Marzegalli[1], G. Vastola[1], V. A. Zinovyev[1,2] and Leo Miglio[1]

[1] L-NESS and Dipartimento di Scienza dei Materiali, Università di Milano-Bicocca,
Via Cozzi 53, 20125 Milano, Italy
[2] Institute of Semiconductor Physics, Novosibirsk, 630090 Russia

Abstract. Ge islands evolution on Si(001) is investigated by a synergic use of different theoretical approaches, followed by a direct comparison with experimental data. Based on ab initio calculations, we suggest an atomic-scale path explaining why Ge (105) pyramids are observed to grow from top to base, and how a fast step-flow mechanism allows for facets completion. Then, we consider the evolution of larger-volume islands. Exploiting three-dimensional elastic-theory calculations, we discuss why on a pit pre-patterned Si(001) substrate it is possible to delay misfit-dislocation insertion, allowing coherent high aspect-ratio islands to be formed, as observed in intriguing recent experiments.

Introduction

Deposition of Ge on Si(001) induces the formation of three-dimensional (3D) coherent islands. After the formation of a thin wetting layer (WL), indeed, a simple tetragonal relaxation is not sufficient to relax the elastic energy induced by the lattice-parameter mismatch [1]. In general, low height-to-base aspect-ratio islands are favored at small volumes. A moderate facet inclination, indeed, limits the excess in exposed surface with respect to the WL. Shallow islands with low surface-energy facets, are thus expected to show up right after the completion of the WL. Islands of larger dimensions, on the other hand, tend to increase in steepness since the higher volumetric strain relaxation dominates the overall energy balance [2]. This simple picture is confirmed by the observation of small Ge islands being characterized by {105} facets, forming an angle of only $\sim 11^\circ$ with the substrate [3]. In a joint theoretical and experimental work [4], it was shown that {105} facets are characterized by a complex rebonded-step (RS) reconstruction, which helps in decreasing the surface energy and in stabilizing the whole Ge islands [5] until its volume reaches a critical value. At this point, flat {105} pyramids smoothly transform into a different shape. Material is first observed to accumulate towards the top of pyramid [6], creating an upper region separated from the rest of the island by several steps bunched together. This step bunching induces the formation of steeper facets, which ultimately evolve into the multifaceted dome shape, characterized by ~ 0.2 aspect ratio. Such experimental observations were nicely explained [6] by a local-thermodynamic model which quantitatively considered the base-to-top lattice relaxation and the step formation energy. In Section 1 we shall go beyond this model, providing ab-initio based calculations suggesting a possible atomic-scale path leading to preferential nucleation at the top of the islands, without destroying the RS reconstruction [7].

Once the pyramid-to-dome transition takes place, the above discussed energy balance between volumetric relaxation and surface-energy cost would suggest a further morphological evolution from domes to higher aspect-ratio islands. At the large volumes needed to observe such transition, however, another channel for strain relaxation becomes competitive: the system can lower the elastic energy load by introducing misfit dislocations into the islands, and interrupting its evolution towards formation of very steep facets. This issue is tackled in Section 2 where we shall discuss a model for island stability based on elasticity theory (solved by Finite Element Methods), and on ab-initio estimates of surface energies. By considering both a flat and a pit-patterned Si(001) substrate, our results show that the presence of a non-flat substrate can delay misfit-dislocation injection into high aspect-ratio islands. These results allow for a direct interpretation of a very recent experimental evidence concerning the crucial dependence of the evolution of dome islands on the substrate. Our colleagues Zhong, Schwinger, Schäffler, and Bauer of the Johannes Kepler University (Linz, Austria), indeed, have observed that on a suitably pit-patterned substrate, domes evolve into exceptionally high aspect-ratio (~ 0.37) coherent (111) truncated pyramids while, on the flat substrate, misfit dislocations are shown to stop the evolution towards high steepness [8].

1. Working at the atomic scale: nucleation of a new layer and step flow at the Ge(105)RS surface

As recalled in the Introduction, the Ge(105) surface at pyramids facets displays the so-called RS reconstruction which is characterized, as shown in Fig. 1a, by the formation of U-shaped structures (U_{ss}). In order to look for possible stable nuclei, able to trigger growth of a new layer on such surface, we have investigated, by ab initio calculations using the Local Density Approximation (LDA), possible adsorption sites for adatoms [9], ad-dimers, ad-trimers and larger two-dimensional structures [7]. We found the ad-trimer configuration displayed in Fig. 1b to be of particular interest since it provides a binding energy per adatom lower than any of the sampled one- or two-adatom configuations. Besides, it is easy to recognize that the ad-trimer already contains the footprints of a new Uss, thus being a promising seed for nucleation of an entire new layer. Due to lateral elastic interactions, ad-trimers tend to align along the [010] direction, as illustrated in Fig. 1c, and demonstrated in [7]. At this stage our calculations, based on the use of the Nudged Elastic Band Method [10], show that the arrival of a further adatom is able to trigger a low-barrier (~ 0.5 eV, lower than the isolated-adatom one [9]) kinetic process leading to the configuration pictured in Fig. 1d, where two one-layer higher Uss are formed. If one of such mechanisms takes place for each ad-trimer, the configuration of panel e) is

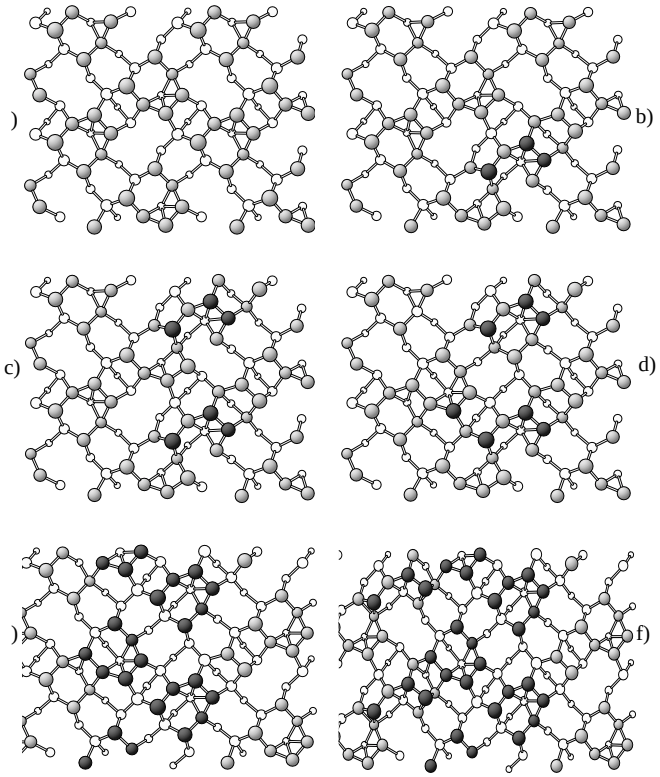

Fig. 1. a) Clean (105)RS surface. b) Ad-trimer minimum-energy configuration c) Adjacent ad-trimers configuration. d) Evolution of configuration c) After the arrival of a further adatom. e) One-layer higher stripe bounded by two steps. f) Step-flow produced by nucleation of trimers at the left step edge of configuration e). In all of the panels, the vertical direction is [010], the direction exiting from the paper is [105], while the horizontal one is [-501].

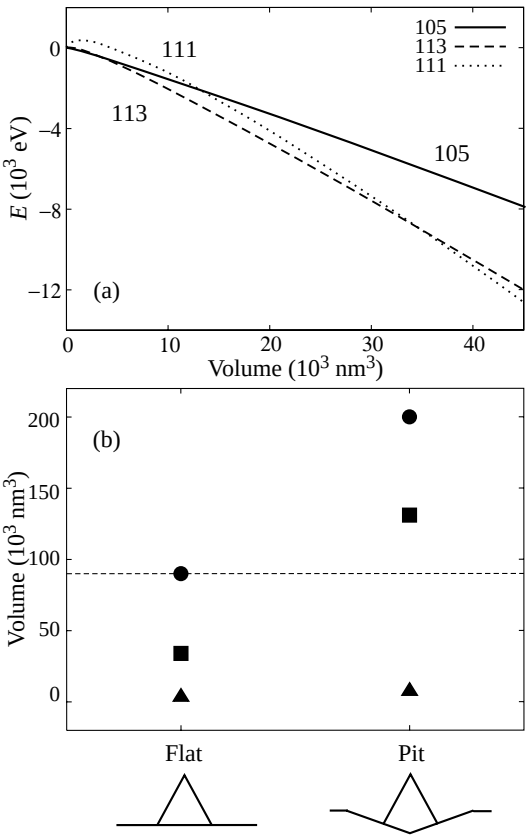

Fig. 2. a) Energy vs volume curve for three differently shaped 65% Ge-islands on Si(001). b) Critical volumes for the (105)–(113) (triangles), and for the (113)–(111) (squares) shape transformation for both flat and (1,1,10) pit-patterned substrates. Full circles indicate volumes of experimental islands taken from Ref. [8]: on the flat substrate such islands are dislocated, while on the pit they are coherent (111) pyramids. The dashed line evidently indicates an experimentally-derived upper bound for the critical volume for dislocation injection on the flat substrate. If the same critical volume would apply also to the pit substrate, coherent islands should not be observed: the pit induces a delay in dislocation formation.

reached. In such panel, we have painted atoms of the same (105) layer using identical grey darkness, in order to emphasize that a terrace bounded by steps on the left and on the right side is obtained. The step on the left side is of particular interest since it corresponds to the typical monoatomic (105) step which is predicted to play a key role at pyramids facets [11]. Notice that if a new set of trimers, positioned and oriented as our minimum-energy configuration of Fig. 1b, is formed at the step edge, this causes the step propagation along the [501] direction, i.e. in the top-to-bottom direction in a typical Ge pyramid. While the above mentioned calculations were first performed on a (105) slab at the Ge lattice parameter, i.e. at the situation encountered at the relaxed top of a Ge pyramid, in order to understand where nucleation preferentially takes place at a pyramid facet, we have re-computed the energy of our *magic* unit, the ad-trimer, also considering a $\sim$ 4% compression, representative of the strained bottom of the island. The energy gain per adatom turned out to be $\sim$ 0.15 eV/adatom higher in the presence of strain. We have therefore demonstrated that atoms climbing along the facets of a Ge(105) pyramids are more likely to nucleate in ad-trimers towards the top of the islands. Further evolution involves alignement of ad-trimers to form steps, and a fast step-flow process completing the facet from top to bottom, while keeping the perfect RS reconstruction. Our results are in very nice agreement with the reported experimental evidence for nucleation at the top of Ge islands, and for a fast step-flow process allowing for facets completion without altering the reconstruction [4,6].

2. Working at the islands full scale: pit-induced dislocation delay in Ge/Si(001)

While in the previous Section we have investigated nucleation at low aspect-ratio Ge (105) pyramids, here we shall focus our attention on larger-volume islands, with the aim of investigating the relative stability of different morphologies on both a flat and a pit-pre-patterned Si(001) substrate. Our work was inspired by recent experiments [8], showing that when islands are grown on (1,1,10) pits created by etching followed by further deposition, the sequence (105) pyramids (aspect ratio: 0.1) — (113) domes (aspect ratio: $\sim$ 0.2) — (111) truncated pyramids (aspect ratio: 0.37) is observed, while on the flat substrate islands larger than domes are typically dislocated, forming the so-called superdomes (very recently a new *barn* shape was also reported [12] for coherent islands). Following, e.g. Ref. [2], we can evaluate the difference in energy between an island of volume V and the equivalent volume of a flat WL as

$$E = (E_S \times S) + (E_V \times V)\,, \qquad (1)$$

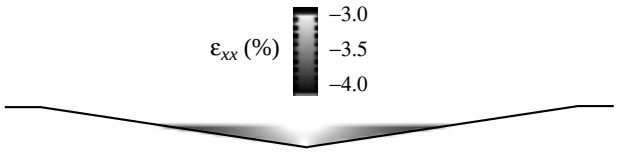

Fig. 3. Grey-scale map of the ϵ_{xx} component of the strain tensor for a (1,1,10) pit carved in Si(001) and half-filled with Ge. Dark regions correspond to as compression close to the misfit strain between Ge and Si (4%), while light gray and white regions are less compressed. Only the strain values within the filled pit are shown.

where $E_S \times S$ is the exposed-facet dependent energy associated with creation of an extra surface S, and E_V is the volumetric density of relaxation energy (given by the difference between the energy density of the elastically relaxed island and the WL). Ab initio calculations have shown that several reconstructed surfaces typically appearing in islands, such as (001), (111), (113) [13], and (105) [5] are roughly characterized by the same surface energy (~ 62.5 meV/Å^2). Therefore, we have used this common value in our calculations for all the involved exposed facets. Instead, we have evaluated E_V by elasticity theory, using the Comsol Multiphysics Finite Element Method code. We considered the three kinds of coherent islands observed in the experiments on both the flat substrate and on the pit-patterned substrate. Following the experiments, we tuned the elastic paramaters in order to take into account that the real islands were estimated to be 65% rich in Ge, due to intermixing with Si. The results of such calculations in terms of $E = E(V)$ are displayed in Fig. 2a for the flat substrate case. As it is evident from the curves, the well known transformation from pyramid to dome is predicted to take place around $V \sim 3.2 \times 10^3$ nm^3, while the (111) islands should appear around $V \sim 3.4 \times 10^4$ nm^3. However, this last transformation was not observed. As emphasized by the full circle in Fig. 2b, indeed, dislocated islands were observed within the range of domes stability. After repeating the same calculations on the pit, we found that (111) coherent islands are predicted to be stable in a range which nicely includes the experimental volume of a real (111) pyramid. From Fig. 2b, it is quite evident that a delay in dislocation injection has occurred in the pit-grown islands, allowing for the observation of a very high aspect ratio for a coherent island. While we are presently working on a quantitative modeling of dislocation injection in islands, and preliminary results confirm the above considerations, here we shall at least offer a qualitative justification for the dislocation delay. It is well known that the energy gain obtained by introducing a dislocation in an island is proportional to the square of the misfit strain generated by the difference in lattice parameter between the island and the substrate [14]. The corresponding energy cost, on the other hand, can be considered as strain-independent (at least as a first approximation). A lowering of the effective misfit strain, therefore, would produce larger critical volumes for dislocation injection. This is exactly the effect produced by the pit, as demonstrated in Fig. 3, where the ϵ_{xx} component of the strain tensor (x being the [110] direction) is reported for a half-filled (1,1,10) pit. At the pit surface, the strain is indeed lower than the one of the flat WL ($\sim 4\%$), the pit showing a relaxation process inverse with respect to a typical upward island. Islands forming on pit, therefore, find a less compressed substrate lowering its elastic load. These results demonstrate the possibility of extending the volumetric and aspect-ratio range for coherent islands grown on Si(001) by a suitable control of the pit-patterned substrate, an issue of particular importance for the development of future nano-devices.

Acknowledgements

The work has been supported by the d-DotFet European STREP project and by the Cariplo Foundation.

References

[1] V. A. Shchukin, N. N. Ledenstov, and D. Bimberg, *Epitaxy of Nanostructures*, (Berlin: Springer), 2003.
[2] J. Stangl, V. Holy, and G. Bauer, *Rev. Mod. Phys.* **76**, 725 (2004).
[3] Y. W. Mo, D. E. Savage, B. S. Swartzentruber, and M. G. Lagally, *Phys. Rev. Lett.* **65**, 1020 (1990).
[4] P. Raiteri, D. B. Migas, L. Miglio, and H. von Känel, *Phys. Rev. Lett.* **88**, 256103 (2002).
[5] D. B. Migas, S. Cereda, F. Montalenti, and L. Miglio, *Surf. Sci.* **556**, 121 (2004).
[6] F. Montalenti, P. Raiteri, D. B. Migas, H. von Känel, A. Rastelli, C. Manzano, G. Costantini, U. Denker, O. G. Schmidt, K. Kern, and L. Miglio, *Phys. Rev. Lett.* **93**, 216102 (2004); 245313 (2004).
[7] S. Cereda and F. Montalenti, *Phys. Rev. B*, in press.
[8] Z. Zhong, W. Schwinger, F. Schäffler, G. Bauer, G. Vastola, F. Montalenti, and L. Miglio, *Phys. Rev. Lett.*, in press.
[9] F. Montalenti, D. B. Migas, F. Gamba, and L. Miglio, *Phys. Rev. B* **70**, 245315 (2004).
[10] G. Henkelman, B. P. Uberuaga, and H. Jònsson, *J. Chem. Phys.* **113**, 9901 (2000).
[11] S. Cereda, F. Montalenti, and L. Miglio, *Surf. Sci.* **591**, 23 (2005).
[12] M. Stoffel, A. Rastelli, J. Tersoff, T. Merdzhanova, and O. G. Schmidt, *Phys. Rev. B* **74**, 155326 (2006).
[13] A. A. Stekolnikov and F. Bechstedt, *Phys. Rev. B* **72**, 125326 (2005).
[14] K. Tillmann and A. Föster, *Thin Solid Films* **368**, 93 (2000).

15th Int. Symp. “Nanostructures: Physics and Technology”
Novosibirsk, Russia, June 25–29, 2007

Electron- and near edge x-ray adsorption fine structure spectroscopy of InN- near surface layers

V. M. Mikoushkin[1], V. V. Bryzgalov[1], Yu. S. Gordeev[1], V. V. Shnitov[1], V. Yu. Davydov[1], C.-L. Wu[2], C.-H. Shen[2] and S. Gwo[2]

[1] Ioffe Physico-Technical Institute, St Petersburg, Russia
[2] Department of Physics, National Tsing-Hua University, Hsinchu 300, Taiwan, Republic of China

Abstract. A set of InN films was studied by Auge-, photoelectron- and near edge x-ray adsorption fine structure spectroscopy with using synchrotron radiation. Effects of oxidation and degradation of near surface layers with formation of InNO alloy, In metallic clusters and molecular N_2 bubbles were revealed. It has been shown that degradation rate is less in monocrystalline InN films with low carrier densities. Fine structure and corresponding density of unoccupied states on InN were obtained. Auger- and photoelectron spectra of pure InN-bulk were measured and core-level binding energies were found.

Introduction

Recent revision of InN band gap has turned high activity in researching this material [1]. However, nano-applications of InN are restrained by the problem of fabrication of InN films of sufficient quality. The evident progress in technology of InN fabrication has been achieved recently on the basis of comprehensive research of the material by a wide range of analytic instruments. Unfortunately surface sensitive methods of electron spectroscopy providing information about electronic structure proved to be aside the activity till recently because of problems in preparation the surface. Progress in InN surface preparation was achieved by atomic hydrogen cleaning (AHC) [2]. The electronic structure of clean InN surface has been investigated by x-ray photoelectron spectroscopy [3] and high-resolution electron-energy-loss spectroscopy [4]. As a result, some of core-level binding energies, density of states and an intrinsic surface electron accumulation layer were found. Unfortunately surface element composition depends on the parameters of AHC technology, and AHC technique can’t move away In extra- stochiometric atoms. In addition, degradation of InN surface with segregation of In atoms was found to be efficiently occur [5]. We present here another approach of study of InN electronic structure, which is based on combination of electron spectroscopy without surface preparation and near edge x-ray adsorption fine structure(NEXAFS) spectroscopy. The first one characterizes near surface layer and the second one describes mainly the bulk. As one of the main results, diminishing degradation of near-surface layer was found for rather perfect InN monocrystalls characterized by low carrier concentrations, and information about InN bulk was obtained by surface sensitive electron spectroscopy.

Experimental details and samples under study

Study of InN films by Auger electron spectroscopy (AES) was performed using electron spectrometer LHS-11. Ion beam sputtering allowed measuring depth concentration profiles of samples. X-ray photoelectron spectra (XPS) of InN films were measured in parallel with NEXAFS spectra using synchrotron radiation (SR) at BESSY-II (Berlin). All of the measurements were made at high-vacuum conditions ($P \sim 10^{-10}$ Torr). Hexagonal InN epilayers grown by different techniques on different substrates have been analyzed in this study. The main parameters of the sample are collected in Tab. 1. The other details can be found in Refs. [6,7,8]. X-ray and Raman scattering were used to characterize the crystal structure of InN layers.

Table 1. Sample characteristics (type of substrate, InN thickness (h), carrier concentration (n), and FWHM of (00.2) x-ray rocking curve).

	Samples	Substr.	h (μm)	n (cm^{-3})	FWHM of ω (arcmin)
1	CUI570	Al_2O_3	1.7	1.5×10^{19}	34
2	040406	Si(111)	0.34	5.8×10^{18}	20
3	Gs2060	Al_2O_3	12	3.6×10^{17}	8
4	050118	Si(111)	0.65	3.8×10^{18}	17

Degradation of InN near surface layer

Degradation of InN near surface layer of the sample 1 with relatively high carrier density was studied by AES. Intensities and shapes of Auger lines give information about element and chemical compositions of material. Figure 1 illustrates decomposition of nitrogen NKVV line into contributions of nitrogen to InN and to molecular N_2 — bubbles. Auger energy of nitrogen in N_2 — bubbles was taken from the research of nitrogen implantation into GaAs [9]. One can see that thin initial near

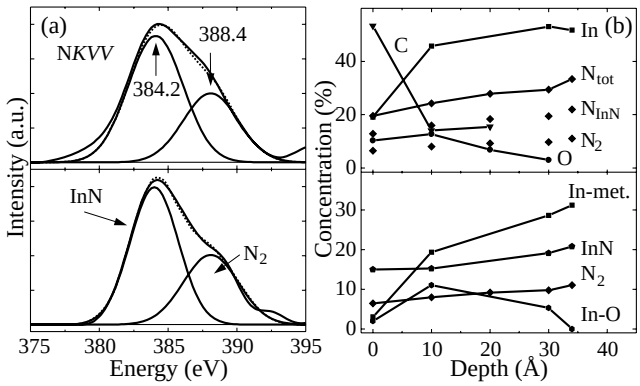

Fig. 1. (a) NKVV Auger spectra of the sample 1 before (top panel) and after (bottom panel) ion sputtering of 1nm thickness surface layer. The spectrum is decomposed into the spectra of InN and molecular nitrogen. (b) Element concentration (top panel) and chemical composition (bottom panel) depth profiles of the sample 1.

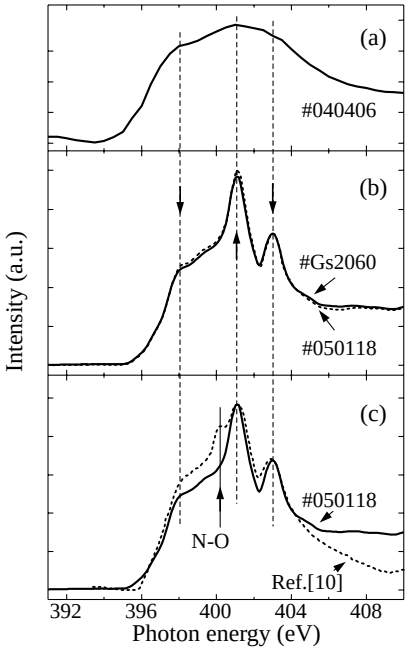

Fig. 2. NEXAFS spectra of samples 2, 3, 4 and that from [10].

surface layer ($\sim$1.5 nm) of the sample contains N_2 — bubbles even before the ion bombardment. Some amount of In atoms in metallic and oxidized states are seen in this layer being covered by the 1–2 monolayer of carbon containing molecules. Besides the composition of initial near-surface area, the depth profiles of element concentration and chemical composition were measured up to several nanometers by ion etching the sample (Fig. 2). Figure 2 shows the effect of ion- induced creation of the In-metallic phase manifesting itself in drastic increase of the concentration of metallic In atoms just after the first ion bombardment [8]. Indium metallic clusters are formed due to destruction of In–N bonds followed by segregation. Nitrogen atoms form N_2 — nano-bubbles or leave the sample. Despite this effect, the concentration and composition profiles give information about degradation of InN near surface layer due to oxidation. Oxygen replaces nitrogen spreading through defects and inter-grain boundaries. As a result $InN_{1-x}O_x$ alloy and N_2 — bubbles are created. The comparable concentrations of these two phases confirm this conclusion. The assumption was made that the degradation rate must be lower in more perfect monocrystalline InN films.

Relationship between surface and bulk properties

Samples 2, 3, and 4 of InN monocrystalline films with intermediate and low carrier concentrations were studied by combination of NEXAFS and XPS (Figs. 2 and 3). NEXAFS spectra characterize density of unoccupied states in thick bulk layer and XPS spectra give information about chemical states in thin near surface layer. One can see that, contrary to the spectrum 2, NEXAFS spectra 3 and 4 show sharp structure and practically coincide with each other and with the spectrum published in Ref. [10]. Excellent reproducibility of NEXAFS spectrum for samples fabricated by different techniques at different laboratories evidences obtaining a reference NEXAFS spectrum of pure InN. Though the spectrum published in Ref. [10] shows a bit larger oxygen concentration.

Contrary to the sample 1, samples 2, 3 and 4 don't contain

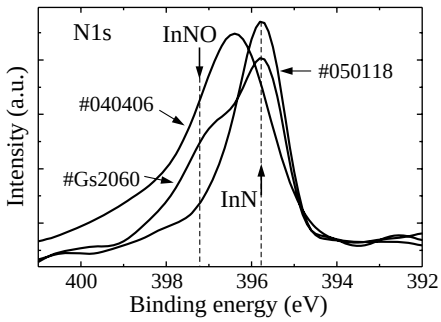

Fig. 3. N1s XPS spectra of samples 2, 3, 4 measured at the photon energy $h\nu = 600$ eV.

essential amount of molecular nitrogen: N_2 line wasn't found in XPS spectra (Fig. 3). Nevertheless, XPS spectra of samples 2 and 3 include contribution of $InN_{1-x}O_x$ alloy besides InN. This indicates some oxidation of the sample 2 and minor oxidation of the sample 3 in $\sim$1$-$2 nm surface layer. The surprising fact is that the near surface spectrum of the sample 4 proved to be practically consisting of the single InN phase. Low oxidation rate seems to be a result of high crystallinity of material, low defect concentration and low density of crystallite boundaries, through which oxygen can effectively diffuse into the bulk. In the first approximation, these defects correlate with carrier concentration. Therefore the sample 1 characterized by relatively high carrier concentration (Tab. 1) shows high degradation rate. But for for more accurate characterization of the material quality, one needs additional parameters. One of them might be XPS spectra of near surface layer.

Conclusions

Effects of degradation of near surface layers with formation of InNO alloy, In metallic clusters and molecular N_2 bubbles were revealed. It has been shown that degradation effects are suppressed in InN films with low carrier concentrations. Fine structure and corresponding density of unoccupied states on InN were obtained. Auger- and photoelectron spectra of pure InN-bulk were measured and core-level binding energies and chemical shifts were found.

Acknowledgements

The authors express gratitude to Bill Schaff, Cornell University, and Jochan Aderhold, Hannover University, for supplying the InN samples for the research. This work was supported by BESSY-II, RFBR (project 05-08-65522-a) and NSC-RFBR (Joint Research Project 94WFA0400128).

References

[1] Abstracts of The 6th International Conference on Nitride Semiconductors, August 28–September 2, 2005, Bremen, Germany.
[2] L. F. J. Piper *et al*, *J. Vac. Sci. Technol. A* **23**, 617 (2005).
[3] L. F. J. Piper *et al*, *Phys. Rev. B* **72**, 245319 (2005).
[4] I. Mahboob *et al*, *Phys. Rev. Lett.* **92**, 036804 (2004).
[5] V. M. Mikoushkin, V. V. Bryzgalov *et al*, *Nanostructures*, 2005, Proceedings, p. 274.
[6] J. Aderhold *et al*, *J. Cryst. Growth* **222**, 701 (2001).
[7] Hai Lu *et al*, *Appl. Phys. Lett.* **82**, 1736 (2003).
[8] S. Gwo *et al*, *Appl. Phys. Lett.* **84**, 3765 (2004).
[9] Yu. S. Gordeev, V. V. Bryzgalov *et al*, *Nanostructures*, 2003, Proceedings, p. 289.
[10] I. J. Lee *et al*, *J. Appl. Phys. Lett.* **82**, 2981 (2003).

15th Int. Symp. "Nanostructures: Physics and Technology"
Novosibirsk, Russia, June 25–29, 2007

STM studies of interaction of Ge with surface Si(7 7 10), containing ordered triple steps

S. A. Teys, K. N. Romanuk and B. Z. Olshanetsky
Rzhanov Institute of Semiconductor Physics, Novosibirsk, 630090, Russia

Abstract. The initial stages of growth of Ge on Si(7 7 10) was investigated by scanning tunnelling microscopy in the range of temperatures from room to 600 °C. The elongated islands of Ge were formed along triple steps before formation of a wetting layer. The effect of decomposition of the triple steps of Si into two alternating steps of height in 1 and 2 belayers (BL) was observed after adsorption about 0.3 BL of Ge.

Introduction

The application of substrates with the well-defined relief of a surface can increase uniformity of nanoobjects during the self-organized growth mode. One of interesting surfaces is the surface Si(7 7 10), with ordered steps with the height of three interplanar distances (triple steps) [1]. Earlier was considered, that such surface has orientation Si(557) [2]. The surface Si(7 7 10) is vicinal a facet of Si(111) and inclined at 10° relative to the (111) towards the [11-2] direction. A system of monolayer steps is transformed in the system ordered of triple steps during cooling the surface Si(7 7 10) below temperature 870 °C. The triple steps are spaced of the (111) terraces with a width equal to that of a unit cell of the Si(111)-7 × 7 surface structure (Fig. 1).

The formation of Ag nanoislands of various form on the surface Si(7 7 10) was shown in Ref. [3]. The control of growth conditions has allowed produce of the Ag islands of identical width and elongated along the triple steps. The purpose of this work is formation of nanoislands (nanowires) of Ge, lengthened along ⟨110⟩ directions on the surface Si(7 7 10).

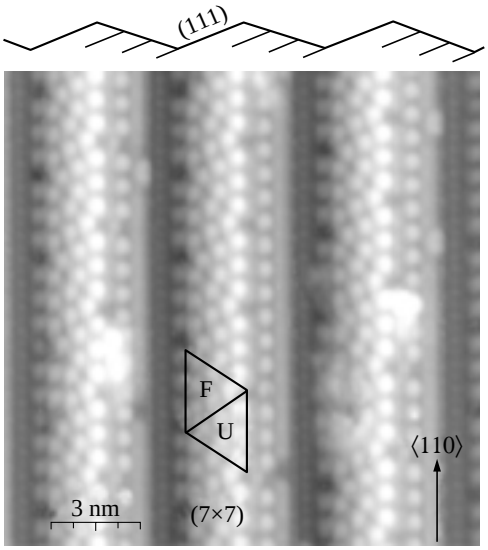

Fig. 1. STM image of the Si(7 7 10) surface consisting of triple-layer-height steps are separated by (111) terraces with a width of that of the Si(111)-7 × 7 unit cell. Sample bias $U = +2.0$ V (unoccupite surface states). *F* — faulted half of unit cell, *U* — unfaulted half of unit cell.

1. Experimental

The experiments were performed in ultra high vacuum systems equipped with an scanning tunnelling microscope (STM) (OMICRON). The pressure of the residual atmosphere in the STM chamber was 9×10^{-11} Torr. Silicon samples, inclined relative to the (111) plane towards the [11-2] direction at 10° with an accuracy of ±0.5°, were used. Samples were resistively heated by a direct current. The temperature of a sample was monitored by an optical-disappearing filament pyrometer. Clean surfaces were prepared by carefully degassing a sample at 600 °C followed by a short flash to 1250 °C to desorb the native oxide. Si(7 7 10) surface were prepared following the procedure described in Ref. [2]. Ge was deposited in the range of temperatures from room to 600 °C within a deposition rate range 10^{-2}–10^{-3} BL/min. STM images were fixed at room temperature. All STM images were recorded in the constant-current mode using an electrochemically etched tungsten tip.

2. Results

The formation of Ge nanoislands was shown on a surface Si(111) in the solid phase epitaxy mode. The nanoislands of Ge with size 5–20 nm and height 1 BL was organized after annealing of amorphous layer of Ge. It was expected, that the similar growth mode and presence of the relief of surface will result in formation of elongated nanoislands of Ge along steps on the Si(7 7 10) surface. However, initial relief of the surface was disorder after annealing, because the atoms of Ge were chaotic incorporated into edges of steps. The disorder growth of Ge was observed in a molecular-beam epitaxy growth mode up to temperatures 350 °C, because surface diffusion of Ge was weak. The atoms of Ge were incorporated mainly into edges of the triple steps. The width of terraces (111) decreased non-uniformly and the lines of step edges obtained corrugated shape. The tendency to ordering and elongation of Ge nanoislands up to 100 nm along steps was observed after adsorbed of Ge in temperatures range 350–500 °C (Fig. 2) before formation of a wetting layer.

We observed formation of two kinds of elongated Ge islands with cross sizes 5 and 10 nm and length up to 100 nm along steps at coverings less 1.3 BL. Two kinds of islands differed by a means of location of Ge between terrace of (111) and edge of the triple steps. The formation of large triangular pyramids of Ge with size 100 nm and height 20 nm was observed at coverings of Ge more 1.5 BL. The beginning growth of pyramids of Ge was observed at smaller thickness of a wetting layer in comparison with a smooth Si(111) surface. The effect of

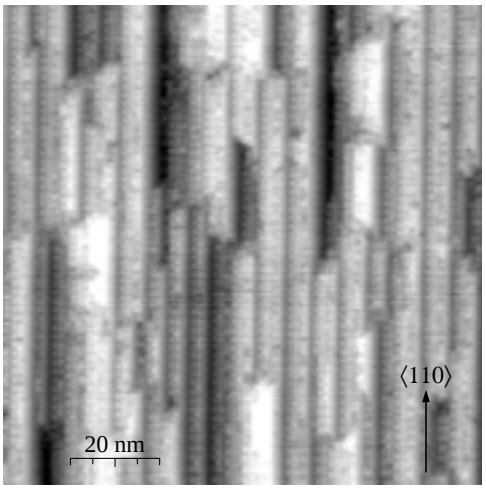

Fig. 2. STM image of the Si(7 7 10) surface after adsorption of 1.3 BL of Ge at 450 °C; $U = +1.1$ V, $I = 0.025$ nA.

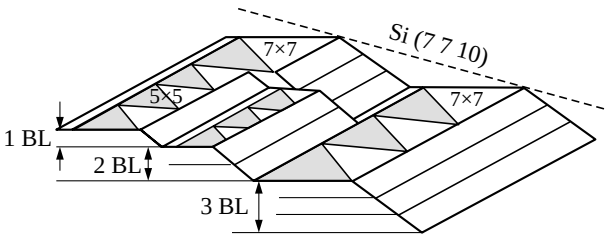

Fig. 3. Scheme of transformation of the triple step into two alternating steps of height in 1 and 2 BL on Si(7 7 10) after adsorption of Ge.

decomposition of the triple steps was observed at change of surface structure of the (111) terraces. The each triple step was transformed into two alternating steps of height in 1 and 2 BL (Fig. 3). Surface structure of terraces (111) on the new steps was transformed from structure (7×7) to (5×5). Complete transformation of the surface structure on the Si(7 7 10) surface occurred at temperature 600 °C and covering 0.3 BL of Ge.

Acknowledgements

This work has been supported by the Russian Foundation for Basic Research (05-08-502278, 07-02-00274) and by the Ministry of Education and Science of Russia (Russian Federal Program).

References

[1] S. A. Teys *et al*, *Surf. Sci.* **600**, 4878 (2006).
[2] A. Kirakosian *et al*, *Appl. Phys. Lett.* **79**, 1608 (2001).
[3] R. A. Zhachuk *et al*, *Surf. Sci.* **565**, 37 (2004).

15th Int. Symp. "Nanostructures: Physics and Technology"
Novosibirsk, Russia, June 25–29, 2007

Controllable growth of C_{60} thin films on Bi(001)/Si(111) surface

R. Z. Bakhtizin[1], A. I. Oreshkin[2], J. T. Sadowski[3] and T. Sakurai[3]

[1] Department of Physical Electronics, Bashkir State University, 450074 Ufa, Russia
[2] Moscow State University, Department of Physics, Moscow, 119992 , Russia
[3] Institute for Materials Research, Tohoku University, Sendai, 980-8577, Japan

Abstract. Surface morphology and controllable growth of C_{60} thin films on Bi(001)/Si(111)–7×7 template have been studied under ultra high vacuum (UHV) conditions using scanning tunneling microscopy (STM) and a low-energy electron microscopy (LEEM). Submonolayer, monolayer and thick layer coverages of C_{60} were imaged in this study with atomic resolution. It has been shown that the most favorable sites for C_{60} nucleation are the twin domain boundaries of Bi and the double steps. These results may be the basis for further developing of fullerene-based thin-film transistors.

Introduction

An understanding of the growth of organic thin films and organic nano-scale structures on Si surface is important for potential applications in micro- and opto-electronic devices using the flexibility of molecular structures and their properties. Among others, thin films of fullerenes are very promising in fabrication of electro-active elements in solar cells and active layers in organic thin-film transistors. In addition, C_{60} fullerene molecules with their closed-cage geometry and uniform size can be considered as probable candidates for use as building blocks in nano-science applications. The most significant problem in C_{60} field effect carrier injection technique is how to form a good interface between substrate and solid C_{60}, so one particularly essential issue is the initial stage of formation of thin films. That is why some level of morphological control is desired for the growth optimization and improvement of organic devices. However controllable fabrication of highly ordered homogeneous nanostructures on surfaces still remains a difficult challenge. Usually, the interaction between a semiconductor surface and an adsorbed fullerene molecule is rather strong due to high concentration of dangling bonds at the surface, and may have a strong influence on the morphology of thin solid films of weak van der Waals-bonded C_{60}. To reduce such an interaction and allow a growth of film in a bulk-like phase we used a semi-metallic Bi(001)/Si(111) template as a substrate for the deposition of C_{60} and preparation of C_{60} nanostructures with long-range order and uniform size. Starting point for this study is a weak interaction between Bi and organic molecules (e.g., pentacene [1]). Here we present the results of our UHV LEEM/STM investigations of the initial stages of nucleation, formation and growth of C_{60} films.

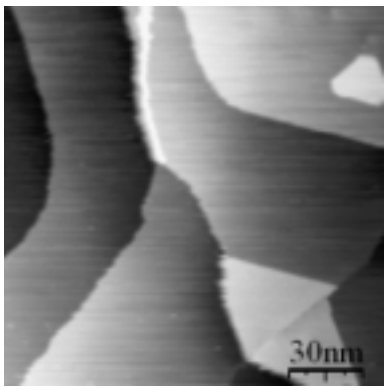

Fig. 1. C_{60} islands on the Bi(001)/Si(111) surface (V_S = 1.5 V). Heights of islands correspond to Bi steps.

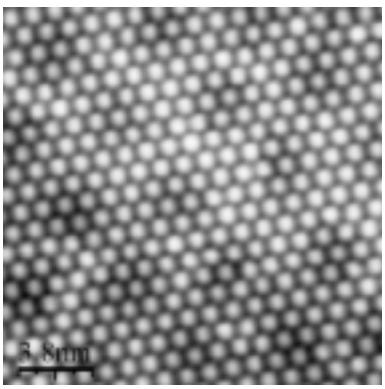

Fig. 2. STM image of a surface with one monolayer of C_{60} (V_S = 2.6 V).

1. Experimental

All the experiments have been carried out at room temperature in two ultra high vacuum systems, using a home-built field ion-scanning tunneling microscope (base pressure 2×10^{-11} Torr) and low-energy electron microscope (base pressure 2×10^{-10} Torr) equipped with standard surface preparation facilities. A clean Si(111)–7×7 surface was obtained by fashing the sample at 1200 °C several times, followed by slow cooling in both systems. Bi was deposited from an alumina-coated tungsten basket on a clean Si(111)–7×7 surface (P-doped n-type 1.6 Ω cm wafer) kept at room temperature. The morphology of the resulting well-ordered Bi(001) film was finally improved by moderate annealing at 120 °C. The self-epitaxial nucleation and growth of C_{60} films have been performed at substrate temperature of 120 °C. Fullerene molecules deposited on well-ordered Bi films interact only weakly with the substrate through van der Waals forces. C_{60} molecule is free to diffuse on this surface and forms highly ordered islands even at less than one monolayer(ML) coverage but the initial nucleation of deposited molecules occurs preferentially in some regions, and these special sites can be viewed as "anchor sites". Therefore, to find the most favorable sites for C_{60} nucleation the LEEM investigation has been performed first.

The corresponding data showed that C_{60} nucleation occurs on the Bi twin domain boundaries mainly. To verify this observation on an atomic scale we used scanning tunneling microscopy. Fig. 1 (taken after deposition of 0.12 monolayer of

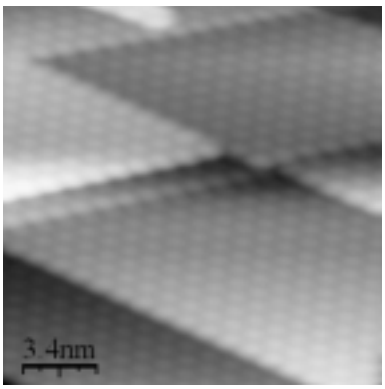

Fig. 3. STM image ($V_S = 2.3$ V; $I_t = 20$ pA) of C_{60} thick film (5 ML) on the Bi/Si(111)–7×7 substrate.

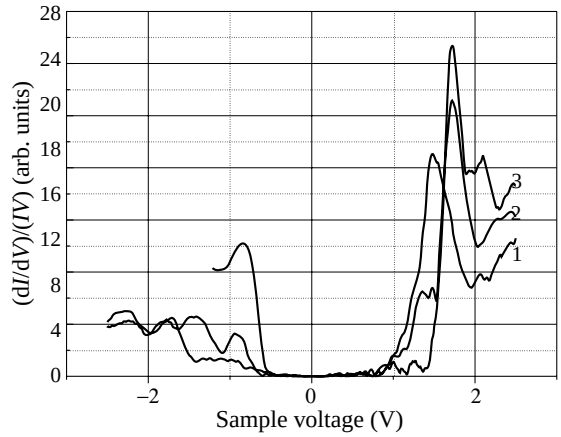

Fig. 4. Normalized conductivity tunneling spectra measured above Bi bilayer (1), C_{60} sub-monolayer coverage (2) and C_{60} thick layer coverage (3).

C_{60}) shows clearly that most favorable sites for C_{60} nucleation are indeed double steps and Bi domain boundaries while a Bi template is clearly seen. One of the islands demonstrates a specific defect (screw dislocation). These observations agree well with our LEEM data. A careful analysis of that and similar images enabled us to single out the six directions of C_{60} domains on the Bi(001)/Si(111)–7×7 surface with hexagonally close-packed structures. To further investigate the growth mode, we carried out a series of experiments with C_{60} coverages ranging from 0.1 ML to above full monolayer coverage and more. Fig. 2 shows a typical STM image of the surface with one monolayer coverage of C_{60} on the Bi/Si(111)–7×7 surface with a characteristic modulation pattern coming from the epitaxial relation between C_{60} and Bi unit cells (5:11), while step heights correspond to Bi steps. Besides, the formation of the second layer of C_{60} could start directly above the C_{60} chains located along the steps filling the intermediate sites between two neighbor molecules. After that the C_{60} growth above smooth terraces became possible. In contrary to that the STM images of thick layers of C_{60} (45 monolayers) did not exhibit any manifestation of modulation. The corresponding STM image showed that C_60 molecules completely cover Bi template forming a good quality film. The step height in this case was the same as for the Bi layer (0.39 nm) which indicates directly that the interaction between C_{60} film and the substrate is not so strong. To estimate the possible charge transfer between fullerenes in molecular layers and the substrate we carried out the scanning tunneling spectroscopy measurements above Bi bilayer, thin C_{60} film (with coverage of 1 ML or less) and thick C_{60} layer (coverage about 5 ML). If charge transfer takes place, the position of peaks at LUMO states should be different for various C_{60} coverages due to the interaction of the first layer with the substrate [2]. But the interaction between first layer and subsequent layers are mainly van der Waals, since the first layer is not modified greatly by substrate bonding. The spectra taken from these layers did not show any shift which confirms evidently the miserable charge transfer filling up the LUMO states. In summary, we have successfully prepared C_{60} epitaxial thin films with long-range order on a semi-metallic Bi(001)/Si(111) template surface. It has been proved that most favorable sites for C_{60} nucleation are double steps and Bi twin domain boundaries. All the observations constitute a concept of site-selective molecular anchoring and provide the perspective of fabricating molecular nanostructures being of technological relevance by site-selective anchoring and self-assembly methods.

Acknowledgement

This work has been supported in part by the Russian Fond for Basic Research.

References

[1] J. T. Sadowski *et al*, *Appl. Phys. Lett.* **86**, 073109 (2005).
[2] T. R. Ohno *et al*, *Phys. Rev. B* **44**, 13747 (1991).

15th Int. Symp. "Nanostructures: Physics and Technology"
Novosibirsk, Russia, June 25–29, 2007

High-density, uniform InSb quantum dots in GaSb emitting in the midinfrared regiont

M. S. Dunaevskii[1], V. Tasco[2], N. Deguffroy[2], A. N. Baranov[2], E. Tournie[2], B. Satpati[3], A. Trampert[3] and A. N. Titkov[1]

[1] Ioffe Physico-Technical Institute, St Petersburg, Russia
[2] Intistut d'Electronique du Sud, Université Montpellier 2-CNRS, UMR 5214, Place Eugene Bataillon, F-34095 Montpellier cedex 5, France
[3] Paul-Drude-Institut für Festkörperelektronik, Hausvogteiplatz 5-7, D-10117 Berlin, Germany

Abstract. There have been developed a multistep MBE growth procedure for InSb QD formation in GaSb. This technique consists in the deposition of InSb at very low temperature followed by an annealing step. We have obtained the highest density ever achieved ($> 7\times10^{10}$ cm^2) of small, fully strained InSb QDs with narrow monomodal size distribution. The QD structures demonstrated PL emission near 3.5 μm up to room temperature.

InSb small band gap makes it attractive as active medium for light emitting diodes and lasers operating in the midinfrared region, in particular, in the 3–5 μm band-II region where several technological applications (such as gas analysis, free space communication, laser assisted surgery, or imaging) find room. InSb/AlInSb quantum well light emitting diodes have recently shown efficient emission in this region at low temperature [1], but the Auger effect strongly affects such kind of devices, limiting their performances at high temperature. Another appealing approach is the use of InSb quantum dots (QDs) as active medium for light emitting devices. One then expects both an emission in the 3–5 μm region and the improvement of device performances, due to low dimensional properties of semiconductor QDs [2].

However, despite the potential advantages of InSb QD material system, only few reports are available in the literature, in marked contrast to the InAs/GaAs case-study materials. The growth of InSb QDs has been investigated, both by molecular beam epitaxy (MBE) and metal organic vapor phase epitaxy, on different substrates: GaAs [3], GaSb [4,5], InP [6], and InAs [3,7]. In the work [7] it has been obtained InSb submonolayer insertions by shortly exposing the InAs growth surface to an Sb_4 flux. They report a density of 10^{12} cm^2 of extremely small insertions and observed PL between 3 and 4 μm up to room temperature [8].

If InSb QDs in GaSb are considered [4,5], all groups working in the field have obtained QD densities in the 10^9 dot/cm^2 range with typically large dot lateral size (50–100 nm). These nanostructures exhibit photoluminescence (PL) emission only at low temperature and around 0.75 eV. To summarize the published data, the growth of high quality InSb QDs, especially on GaSb, has proven impossible up to now whatever the epitaxial technique. This arises from the comparatively weak In–Sb binding energy which, in turn, results in a long migration length of In adatoms on an Sb-terminated surface [3,9]. This is confirmed by the fact that some improvement may be obtained when nucleating InSb QDs on an As-terminated surface [7,10]. In this work, we show that high density, uniform, fully strained, InSb/GaSb QDs can be grown by means of a particular MBE technique, consisting of a deposition at an extremely low temperature followed by a properly designed annealing step.

The samples have been grown on GaSb(100) substrates by solid source MBE. Each sample contains either one plan of uncapped InSb QDs or one plan of InSb QDs inserted in the center of a GaSb barrier layer, itself confined on both sides by 100 nm thick AlGa(As)Sb lattice-matched claddings. In situ reflection high-energy electron diffraction (RHEED) has been used for monitoring the sample surface evolution. The surface morphology and structural properties of the as-grown samples have been investigated by atomic force microscopy (AFM) and transmission electron microscopy (TEM).

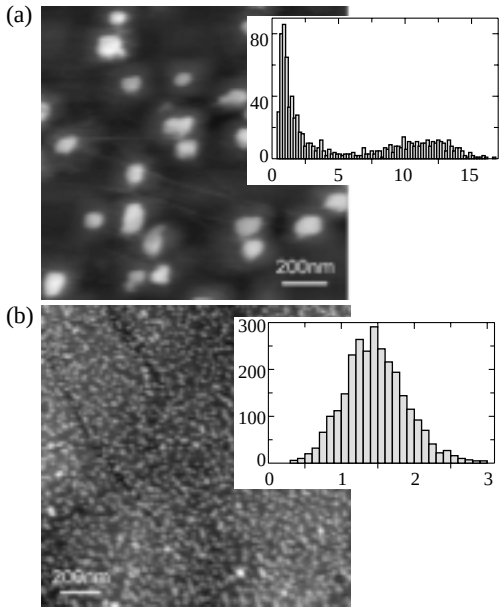

Fig. 1. AFM scan on 2.6 ML of InSb deposited by the usual growth at 450 °C (a) and deposited following the two step procedure (b). The insets are the related histograms for the height expressed in nm.

During the MBE growth of InSb QDs on GaSb at a substrate temperature around 450 °C we observe a Stranski–Krastanow growth mode with a two dimensional to three dimensional transition occurring after about 1.7 ML of InSb coverage. We show in Fig. 1(a) an AFM scan taken from 2.6 ML of InSb deposited at 450 °C with a growth rate of 0.33 ML/s. The QD density is 4×10^9 dot/cm^2 with typical diameters of about 40–80 nm and heights of about 10–15 nm. Further, the InSb QDs exhibit a bimodal distribution, as shown by the size histogram in the inset of Fig. 1(a). Finally, plan-view as well as cross-section TEM reveal that all QDs are plastically relaxed. Such results

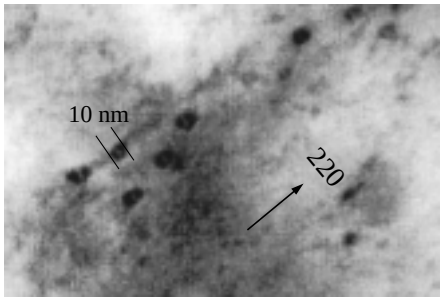

Fig. 2. TEM cross-sectional images of 3 ML InSb QDs grown with the two step technique. Cross-sectional projectional view of tilted QDs layer ($g = 220$) in bright-field mode to visualize the isolated QDs.

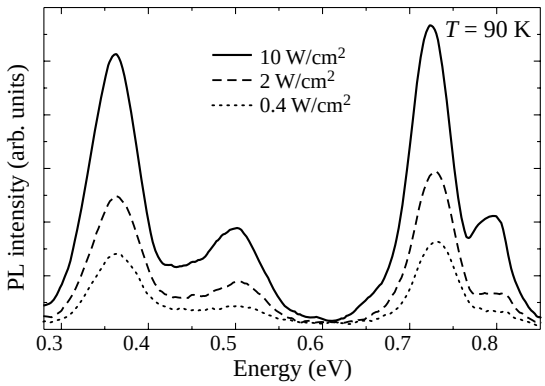

Fig. 3. PL spectra taken from the high density InSb/GaSb QD sample at 90 K under different excitation intensities.

are in perfect agreement with previously published data [4,5].

In order to increase the density of nucleation centers, and thus the QD density, the In-adatom migration length should be reduced. Typical MBE growth parameters which can affect the kinetics of the system are the growth temperature, the growth rate, and the amount of deposited InSb. We have varied these parameters from 365 to 450 °C, from 0.3 to 1.2 ML/s, and from 1.8 to 2.6 MLs, respectively. Nevertheless, the InSb QD morphological properties are independent of such variations of the growth conditions, even if very wide. This behavior is in marked contrast to the well known InAs/GaAs system which has, however, a comparable lattice mismatch (6.3% for InSb/GaSb versus 7.1% for InAs/GaAs). This confirms the very long diffusion length of In adatoms on an Sb-terminated surface and shows that no significant improvement in the InSb QDs population can be achieved under usual MBE growth conditions.

To overcome this limitation we have developed an innovative growth procedure with parameters far away from usual MBE conditions. The main key of this technique is the deposition of InSb below the Sb-condensation temperature followed by an annealing step. After the completion of the GaSb buffer layer we reduce the substrate temperature down to 300 °C. A few monolayers of InSb are then deposited. The RHEED pattern then becomes very faint. Indeed, at this temperature an amorphous or polycrystalline InSb film is expected. AFM (not shown here) reveals a uniform surface with a root mean square roughness of about 1 ML. Immediately after InSb deposition, the substrate temperature is increased up to the Sb-desorption value (390 °C) where an annealing is performed during 20–50 s. The RHEED pattern evolves toward a spottylike pattern indicating the formation of well developed QDs. Figure 1(b) shows the AFM image (scan size of 1×1 μm^2) taken from 2.5 ML of InSb deposited according to this procedure. The uniform surface observed after the InSb deposition at low temperature has been replaced by well defined nanostructures after the annealing step. A dot density of 7.4×10^{10} cm^{-2}, i.e., one order of magnitude higher than that ever reported, and a narrow monomodal distribution [inset of Fig. 1(b)] are obtained. Their average sizes are strongly reduced down to 13 ± 3 nm for the radius and 1–3 nm for the height. Therefore, this two step growth technique enables a noticeable improvement of the dot distribution, with respect to any other reported conditions. At a temperature as low as 300 °C, not only the In-migration length is naturally reduced but also Sb-solid clusters are formed which further suppress In migration. The annealing step allows the evaporation of the excess Sb. The InSb film crystallizes and evolves toward its lowest energy state, i.e., formation of well developed QDs.

Plan-view and cross-section TEM analyses have also been performed on such QDs buried within GaSb layers. By tilting the sample to get the QDs layer inclined to the electron beam and to adjust $g = 220$ diffraction conditions, as shown in Fig. 2, the InSb QDs are clearly detected due to the effect of the strain field on diffracted intensity. The InSb QDs appear to be very uniform, with an average diameter of about 10 nm. No threading dislocations are observed in contrast to the previous results for usual MBE growth conditions. The lattice strain field around the InSb QDs appears as lobes of dark contrast with lines of no contrast perpendicular to g. This particular strain effect corresponds to fully strained InSb QDs with an ovoid or almost spherical shape.

Finally, Fig. 3 shows PL spectra taken under different excitation intensities at 90 K from this high density InSb QD sample. Even under low optical excitation intensity (4×10^{-1} W/cm^2), the sample exhibits PL emission peaked at 360 meV with a full width at half maximum of 47 meV which we attribute to transitions involving the QD ground state (GS). A second peak is also evident at higher energy (500 meV) and its band filling dynamics at different excitation intensities suggests that it is likely due to the first excited state transition in the QDs. The other peaks in the 0.7–0.8 eV region are related to GaSb and its native defects. The QD emission can be detected up to room temperature. The QD GS integrated intensity only decreases by a factor of 4 when the temperature increases from 90 to 300 K, suggesting a good thermal stability.

Acknowledgement

Part of this work is supported by the European Commission (Project No. FP6-017383, DOMINO).

References

[1] S. J. Smith *et al*, *Appl. Phys. Lett.* **88**, 081909 (2006).
[2] Y. Arakawa *et al*, *Appl. Phys. Lett.* **40**, 939 (1982).
[3] F. Hatami *et al*, *Appl. Phys. Lett.* **89**, 133115 (2006).
[4] N. Bertru *et al*, *Appl. Phys. Lett.* **68**, 31 (1996).
[5] E. Alphandery *et al*, *Appl. Phys. Lett.* **74**, 2041 (1999).
[6] Y. Qiu *et al*, *Appl. Phys. Lett.* **84**, 1510 (2004).
[7] S. V. Ivanov *et al*, *J.Cryst.Growth* **278**, 72 (2005).
[8] V. A. Solov'ev *et al*, *Appl. Phys. Lett.* **86**, 011109 (2005).
[9] N. Deguffroy *et al*, *Inst. Phys. Conf. Ser.* **187**, 93 (2006).
[10] V. Tasco *et al*, *Phys. Status Solidi B* **243**, 3959 (2006).

15th Int. Symp. "Nanostructures: Physics and Technology"
Novosibirsk, Russia, June 25–29, 2007

AFM investigation of micro- and nanoparticle formation on silicon surface under femtosecond laser pulses action

A. A. Ezhov, L. A. Golovan, P. K. Kashkarov, P. K. Kolmychek, V. I. Panov, V. Yu. Timoshenko and S. V. Zabotnov

Physics Department, M. V. Lomonosov Moscow State University, 119992 Moscow, Russia

Abstract. The structures formed by femtosecond laser pulses irradiation of the monocrystalline silicon surface were studied by atomic force microscopy. It was demonstrated that the nanoparticles were formed in addition to the microstructures. The height of the nanoparticle is 2–30 nm and the lateral size is 70–200 nm. These values agree qualitatively with the estimation based on the previously obtained optical data.

Introduction

The high-intensity femtosecond laser radiation is an effective tool to treat solid state surfaces with micron and submicron accuracy [1,2]. Radiation absorption and thermal diffusion in the matter are time-separated under femtosecond laser pulse processing, that is a very important feature of femtosecond irradiation. As a result, femtosecond treatment gives the best quality of the formed microstructures [3].

Nanostructure formation caused by the high-intensity femtosecond treatment of the surface is another subject of interest especially in the case of the silicon surface. The electronic and optical properties of the silicon nanoparticles are greatly different from the bulk silicon. These properties are investigated intensively at present.

The detailed investigation of the structures formed on the femtosecond laser modified silicon surface by means of atomic force microscopy (AFM) was the main of the presented work.

1. Experimental

In our work we study the silicon wafers irradiated by the femtosecond laser pulses. The Cr4+:forsterite laser with wavelength 1250 nm, pulse duration 80 fs and tunable pulse energy up to 0.250 mJ was employed as a femtosecond pulse source [4]. The pulse frequency was 10 Hz. Laser light was linearly polarized. Slightly focused laser beam was incident normal to the silicon surface. Femtosecond modification was produced at ambient conditions in air. From 1 to 100 femtosecond laser shoots were used for the modification.

Scanning probe microscope Solver PRO which operated in AFM mode was used for the modified surface investigation. Semicontact mode was chosen for scanning to decrease the interaction between the probe and the sample surface.

2. Results

Three types of the low-dimensional structures are presented on the irradiated silicon surface (Fig. 1): disordered objects with the lateral size about micron, ripples with a period about laser wavelength (Fig. 1) and nanoparticles covered surface. The ripple formation is a well-known phenomenon caused by the interference between the incident and scattered surface electromagnetic waves [5]. The period of the ripples measured by AFM increases when the number of shoots are increased. This fact may be explained in the terms of the change of the efficient optical properties of the surface after the previous shoots.

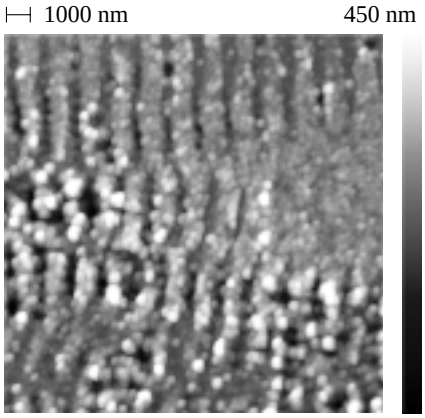

Fig. 1. AFM image of the silicon surface after 10 femtosecond shoots. Both ripples and nanoparticles are clearly resolved.

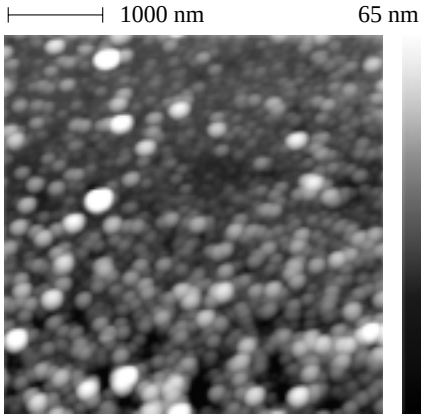

Fig. 2. AFM image of the silicon surface after 10 femtosecond shoots. Area situated outside of stripes region is shown.

Nanoparticles have a lateral size 70–200 nm and height 2–30 nm. They cover all microstructures by persistent layer which extends out of the irradiated area. Recent Raman scattering and photoluminescence data [6] allow to estimate the size of the silicon nanoparticles formed by the same femtosecond modification. This estimation give the value in order to few nanometers which agrees with the height of the nanoparticles.

Nanoparticle formation and their direct observation have been achieved in our work for the first time.

3. Conclusion

Thus, it has been demonstrated by means of AFM that 1250 nm wavelength femtosecond irradiation of silicon surface at ambient conditions in air leads to the formation of both ordered and disordered microstructures and nanoparticles. The sizes of the nanoparticles are qualitatively agree with the estimation produced from alternative techniques data.

Acknowledgements

The authors give gratitude to M. A. Lastovkina for her contribution to the measurements.

This work has been supported in part by the RFBR grants 05-02-17035-a, 06-02-16960-a, 06-02-17179-a, 06-02-08306-obr and 06-02-39022-NNSF-a.

References

[1] P. P. Pronko *et al*, *Optics Communications* **114**, 106 (1995).
[2] F. Korte *et al*, *Applied Physics A* **77**, 229 (2003).
[3] C. Momma *et al*, *Optics Communications* **129**, 134 (1996).
[4] S. V. Zabotnov *et al*, *Quantovaya Electronica* **35**, 943 (2005) *in Russian*.
[5] J. Bonse *et al*, *Appl. Phys. A* **74**, 19 (2002).
[6] S. V. Zabotnov *et al*, *Pis"ma v ZhETP* **83**, 76 (2006) *in Russian*.

15th Int. Symp. "Nanostructures: Physics and Technology"
Novosibirsk, Russia, June 25–29, 2007

Formation of the current image in combined STM/AFM of the metal nanoclusters in dielectric films

M. A. Lapshina, *D. O. Filatov* and D. A. Antonov

Research and Educational Center for Physics of the Solid State Nanostructures, University of Nizhniy Novgorod, Nizhniy Novgorod, Russia

Abstract. The current image formation in Combined Scanning Tunnelling Atomic Force Microscopy (STM/AFM) of the metal nanoclusters in a thin dielectric film was studied theoretically in the quasi classic approximation. It was shown that the size of the spots in the current image related to the electron tunnelling through the nanoclusters are determined primarily by the probe size and by the position of the nanoclusters relative to the film surface rather than the cluster size. The results of modelling were compared to the experimental data on STM/AFM investigations of the Au nanoclusters in SiO_2 films on the n^+-Si substrates.

Introduction

The metal nanoclusters in the dielectric films are interesting because of a number of fundamental effects peculiar to the nanoscale systems such as Coulomb blockade, resonant tunneling, etc. [1] From the viewpoint of possible applications they are promising for the single electronic devices, data storage, non linear optics, etc. Characterization of the clusters' morphology (i.e. their shape. sizes, and concentration) is an essential component of their investigation. In this purpose, Transmission Electronic Microscopy (TEM) is applied usually [2]. In Ref. [3] Scanning Capacitance Microscopy (SCM) was applied to visualize the Sn nanoclusters in SiO_2 formed by ion implantation.

In Ref. [4] Combined Scanning Tunnelling/Atomic Force Microscopy (STM/AFM) was applied to visualize the Au nanoclusters in a tunnel transparent SiO_2 films on the n^+-Si substrates formed by Pulsed Laser Deposition (PLD). The film surface was scanned by a conductive Pt coated AFM probe in the contact mode. Simultaneously, the tunnel current between the probe and the substrate was measured. The spots of increased conductivity (or the current channels, Fig. 1) related to the electron tunnelling from the probe to the substrate through the Au nanoclusters (Fig. 2) have been observed in the current images. However, the mechanism of the current image formation, in particular, the relation of the current channels' sizes to the nanoclusters' sizes, to the probe to cluster separation, etc. has been still unclear until recently.

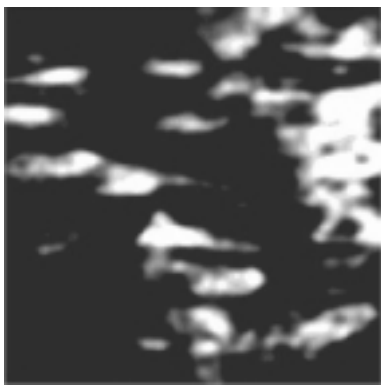

Fig. 1. A current image of a n^+-Si/SiO_2/Au nanoclusters/SiO_2 obtained by Combined STM/AFM [4]. $U_g = 2$ V. Frame size 100×100 nm^2.

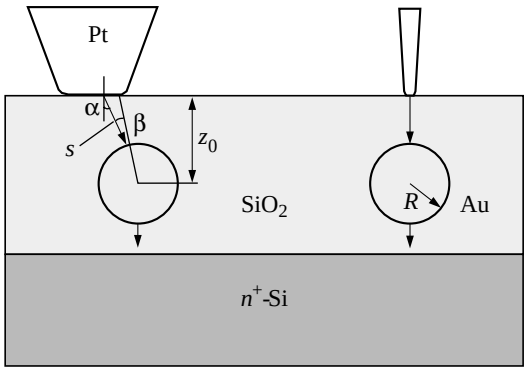

Fig. 2. Schematic of electron tunnelling through the Au nanoclusters in SiO_2 film.

In the present work we have modelled the tunnelling of the electrons between the AFM probe and the substrate through the metal nanoclusters in the dielectric film taking into account the actual shape of the contact of the AFM probe to the dielectric film, the clusters' sizes, and the position of the clusters relative to the film surface.

1. Modelling

The contact area between the probe and the dielectric film was assumed to be a circle. Its diameter D was calculated within the framework of Hertz' problem [5]. For the loading force $F \approx 2$ nN used in the experiment [4] $D \approx 10$ nm.

The Coulomb blockade effect observed in the investigated samples [4] was neglected in the present work and was analyzed in Ref. [4]. The size quantization was neglected as well so the clusters were treated to be the bulk metal spheres with the radius $R \sim 1$ nm. TEM investigations of the structures formed in similar conditions revealed $R \approx 1.1$ nm [4]. The estimate of R from the Coulomb staircase period gave a close value [4].

An element of tunnel current between an element of the probe surface $rdrd\varphi$ and an element of the cluster surface $\sin\Theta d\Theta d\phi$ [6]

$$dI = C \int_{E_F}^{E_F+eV} \rho_p(E+eV)\rho_c(E)T(E,eV) \times \cos\alpha \cos\beta dE rdrd\varphi \sin\Theta d\Theta d\phi\,, \qquad (1)$$

where C is a constant, e is the elementary charge, E_F is the Fermi level in the probe material, ρ_p and ρ_c are the densities

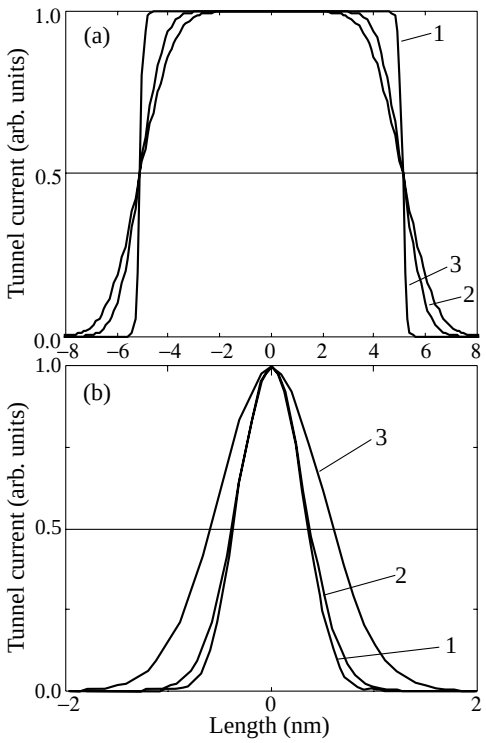

Fig. 3. The calculated normalized profiles of the tunnel current along the diameter of a spherical Au nanoclusters in SiO_2 film: (a) in the flat probe limit ($D \gg R$); (b) in the point probe one ($D \ll R$). The cluster radius $R = 1$ nm. The probe size D, nm: (a) 10; (b) 0.1. z_0, nm: 1 — 0.1, 2 — 2, 3 — 5. $V = 2$ V.

of states in the probe and in the cluster, respectively, T is the tunnelling probability, and V is the voltage between the probe and the cluster. Neglecting the Coulomb blockade, $V \approx U_g$ where U_g is the gap voltage. When $eV < A_{Au}, A_{Pt}$ where A_{Au} and A_{Pt} are the work functions in the cluster and in the probe materials, respectively, $T \cong \exp(-ks)$, where $k = 2\sqrt{2m\overline{X}}/\hbar$, $\overline{X} = (A_{Au} + A_{Pt} - eV)/2 - X_{SiO_2}$, s is the tunnelling path, m and X_{SiO_2} are the electron effective mass and the electron affinity in SiO_2, respectively. In the quasi classic limit α and β take the meaning of the incident angles of the electrons onto the probe and cluster surfaces, respectively (see Fig. 2).

The total current between the probe and the cluster is given by summation of dIs over the whole probe area and over the side of the cluster exposed to the probe:

$$I = C \int_0^{D/2} \int_0^{2\pi} \int_0^{\pi/2} \int_0^{2\pi} \int_{E_F}^{E_F+eV} \rho_p(E+eV)\rho_c(E) \times \exp(-ks) r \cos\alpha \cos\beta \sin\Theta dE d\phi d\Theta d\varphi dr \,. \quad (2)$$

2. Results and discussion

It was found that the size of the current channels is determined primarily by the size of the contact between the probe and the sample D. This effect is a manifestation of a more general convolution effect [7]. When $D \gg R$ (that takes place in the STM/AFM experiments reported in Ref. [4]), the observable size of the current channels can exceed the cluster size essentially (Fig. 3a). In addition, the current channel size depends on the position of the cluster under the film surface z_0: the less z_0, the wider range of the probe positions $(x.y)$ which electron tunnelling is possible in (Fig. 2, left). On the contrary, when $D \ll R$ (a point probe limit, which takes place, in particular, in STM investigations of the metal nanoclusters dispersed in the dielectric films with percolation conductivity [8,9]) the current channel size can be less than the actual cluster size that can be understood easily taking into account that because of small $k \sim 0.1$ nm only the elements of the cluster surface closest to the probe contribute into the total tunnelling current essentially (Fig. 2, right). Again, the observable current channel size depends on z_0: the less z_0, the sharper the current image (Fig. 3b).

Acknowledgement

The work was supported by Russian Agency of Education (RNP2.1.1.6055).

References

[1] B. Prevel *et al*, *Scripta Materialia* **44**, 1235 (2001).
[2] J. C. H. Spencer *Mat. Sci. Eng. R* **26**, 1 (1999).
[3] G. Tallarida *et al*, *MRS Proc.* **738**, G5.1.1 (2003).
[4] D. A. Antonov *et al*, *Bull. RAS: Phys.* **71**, 61 (2007).
[5] L. D. Landau and E. M. Lifshitz, *Course of Theoretical Physics* v. 7. *Theory of Elastisity 3rd Edition*, (Oxford: Butterworth-Heinemann) 54, 1986.
[6] J. A. Kubby and J. J. Boland, *Surf. Sci. Reports* **26**, 61 (1996).
[7] P. Markievicz *et al*, *Probe Microscopy* **1**, 355 (1999).
[8] E. Bar-Sadeh *et al*, *Phys. Rev. B* **50**, 8961 (1994).
[9] H. Imamura *et al*, *Phys. Rev. B* **61**, 46 (2000).

15th Int. Symp. "Nanostructures: Physics and Technology"
Novosibirsk, Russia, June 25–29, 2007

Anomalous calorimetric properties of one-dimension molecular nanochains at low temperatures

I. E. Paukov, Yu. A. Kovalevskaya and *S. P. Gabuda*
A. V. Nikolaev Institute of Inorganic Chemistry, SB RAS, 630090 Novosibirsk, Russia

Abstract. The data of precision low-temperature calorimetric study of series of nanoporous materials are presented. Abnormal behavior of specific heat at lowest temperatures was found for the case, when nanocapillaries in the studied systems are filled by molecular subsystem represented by 1D Ice. It is shown that in this case the heat capacity is proportional to the absolute temperature, but not to the cube of temperature, as it is predicted by P. Debye law. The anomaly disappears if molecular subsystem is removed.

Introduction

Heat capacity of 3D systems at lowest temperatures is proportional to T^3, but in 2D systems (like graphene) is proportional to T^2, and in one-dimension ones is linearly dependent of absolute temperature (Tarasov law). It may be expected, that molecular substances in the ultrathin capillaries in nanotubes also can display the linear dependence $C_p(T)$. In this report we confirm such expectations.

Experimental

Series of natural nanoporous tuff minerals of zeolite family, and some other non-framework porous crystal were studied by adiabatic low-temperature calorimetric method [1]. Typical crystal structure of nanoporous crystal is shown in Fig. 1.

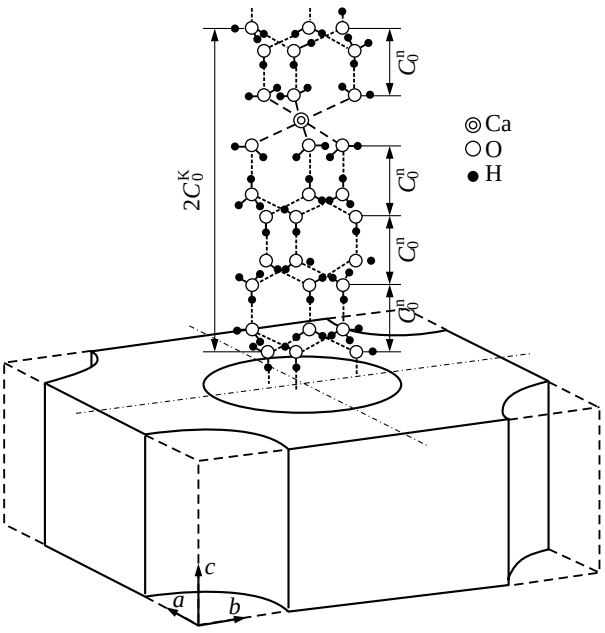

Fig. 1. Nanotubes in crystal structure of mordenite. The lower part of figure show the unit cell, the circle indicate the section of nanochannel. The upper part of figure show the 1D Ice needle built of chains of water molecules that probably forms a part of ice-similar structure in the zeolite channels [1].

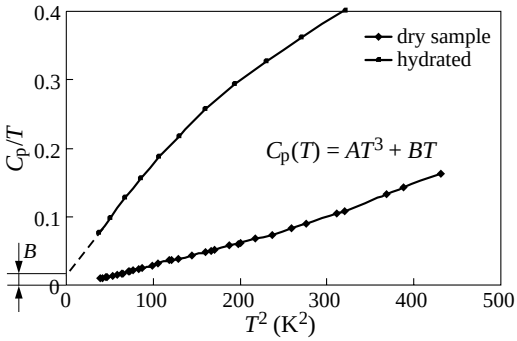

Fig. 2. Experimental temperature dependences of the specific heat of hydrated cordierite (upper line) and of dry cordierite (down line) at low temperatures [2].

Results

Typical experimental data of $C_p(T)$ are shown in Fig. 2 representing the heat capacity of synthetic gem crystal of hydrated cordierite, $Mg_2Al_3[AlSi_5O_{18}]\cdot H_2O$, containing a chains of water molecules, and of other synthetic gem crystal cordierite $Mg_2Al_3\,[AlSi_5O_{18}]\cdot[*]$ of the same structure, but water-free (asterisk indicates the water holes). One can see, that heat capacity of dry sample at 10 K is nearly an order lower of the hydrated form, and the difference must be related to the presence of one-dimensional subsystem of water molecules in the nanopores.

In discussed nanocomposite system the temperature dependence of specific heat may be represented by combination of two contributions: of Debye part, AT^3, related to presence of the host lattice, and of Tarasov part, or BT, related to presence of perfect one-dimensional subsystem:

$$C_p(T) = AT^3 + BT, \qquad (1)$$

or $C_p(T)/T = AT^2 + B$.

The simplest way to visualize the one-dimensional subsystem is to represent the data in coordinates $C_p(T)/T$ plotted as the function of T^2. In such a case the temperature dependence of heat capacity of perfect nanocomposite systems will be represented by straight lines intersecting the ordinate axis at positive value which is equal to constant B. The B constant is characterizing the basic interaction in the 1D-chain.

Other studied systems are structurally similar narrow-pored zeolites edingtonite, $[BaAl_2Si_3O_{10}]\cdot 4H_2O$, and of tetranatrolite, $Na_2[Al_2Si_3O_{10}]\cdot 2H_2O$ (Figure 2).

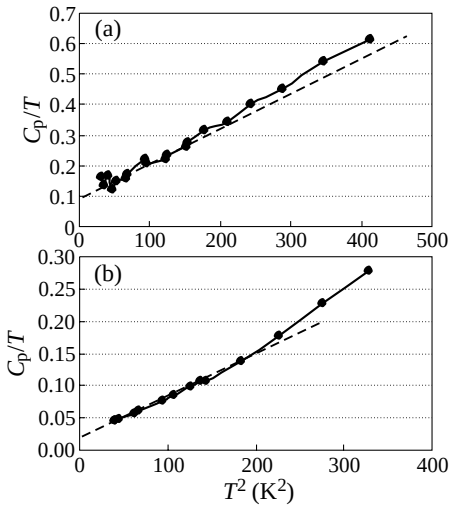

Fig. 3. Experimental temperature dependences of the specific heat of nanoporous minerals edingtonite and tetranatrolite (points). Dotted lines represents their linear approximations according to Tarasov law (1).

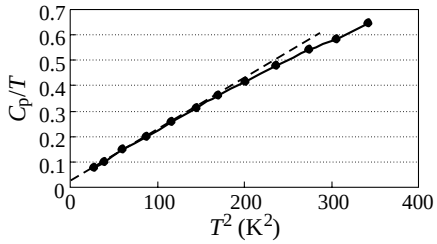

Fig. 4. Experimental temperature dependence of the specific heat of hydrated mordenite.

From comparison of the data of Figs. 2 and 3 one can conclude that the observed values of experimental parameter B in cordierite, tetranatrolite and edingtonite are roughly proportional to the number n of H_2O molecules falling on the one formula unit in studied samples:

$$B \sim nkE_0, \tag{2}$$

where k is some constant, and E_0 may be related to the pair intermolecular interaction of H_2O in nano chains.

To check the empirical finding (2), we have studied series of wide-pored zeolites mordenite, $Ca[AlSi_5O_{12}]\cdot 7H_2O$ [1] (structure is shown in Fig. 1), stellerite $Sr[Al_2Si_7O_{18}]\cdot 7H_2O$, epistilbite $Ca[Al_2Si_6O_{16}]\cdot 5H_2O$, and erionite $NaCa\,[Al_3Si_9O_{24}]\cdot 9H_2O$ [3]. In every case it was found the linear dependence of $C_p(T)/T$ versus T^2 (Fig. 4), and each time the linear contribution to C_p disappears if the water is removed even partially. However, the parameters B in studied wide-porous systems are practically independent of n and all have the order of ~ 0.02 J/mole·K^2.

Acknowledgements

The work was supported by financial support from Russian Fund for Basic Researches (grant No. 05-03-32263) and Interdisciplinary integration project No. 81 of SB RAS.

References

[1] I. A. Belitsky, S. P. Gabuda *et al*, *Proceedings of the Institute of Geology ad Geophysics of SB RAS* **487**, 167 (1981).

[2] I. E. Paukov, Yu. A. Kovalevskaya, N. S. Rahmoun, C. A. Gaiger, *American Mineralogist* **91** N 1, 35 (2006).

[3] I. E. Paukov *et al*, *Phys. Chem. Minerals* **29** N 4, 300 (2002).

15th Int. Symp. "Nanostructures: Physics and Technology"
Novosibirsk, Russia, June 25–29, 2007

Structure and optical properties of $CrSi_2$ nanocrystallites in silicon matrix and point defects generated by the growth

N. G. Galkin[1], L. Dozsa[2], T. V. Turchin[1], D. L. Goroshko[1], B. Pecz[2], L. Toth[2], L. Dobos[2] and N. Q. Khanh[2]

[1] Institute for Automation and Control Processes of FEB RAS, Vladivostok, Russia
[2] Research Institute for Technical Physics and Materials Science, Budapest, Hungary

Abstract. Semiconducting $CrSi_2$ nanocrystallites were grown by reactive deposition epitaxy in silicon. The structure, morphology and optical properties of grown structures were investigated by TEM, AFM and optical reflectance spectroscopy. The point defects were investigated by deep level spectroscopy and by RBS. The $CrSi_2$ crystalline structure is identified by high resolution TEM as hexagonal fitted to the silicon lattice. Energy filtered TEM shows that most of the Cr is localized in the nanocrystals. RBS and DLTS measure significant concentration of Cr point defects in the covering epitaxial silicon layer. Lower silicon cap layer growth temperature may reduce the Cr content in the top epitaxial silicon layer.

Introduction

Chromium disilicide ($CrSi_2$) is a narrow band semiconductor ($E_g = 0.35$ eV [1]), which was epitaxially grown on Si(111) [2]. The strong increase of hole mobility and decrease of hole concentration have been observed in $CrSi_2$ epitaxial films on Si(111) [3], that corresponds to considerable alterations in their band structure. In a previous study of 0.06–0.12 nm Cr deposition on Si(111) surface the formation of self-organization of semiconductor $CrSi_2$ islands has been observed by differential optical spectroscopy (DOS) and the threshold for 3D nanosize island formation has been determined [4]. The preservation of $CrSi_2$ phase in silicon matrix after the growth of cap silicon layer has been observed by UPS data [4] after ion etching the cap layer. Quantum size $CrSi_2$ crystallites with high density ($10^{10}-10^{11}$ cm^{-2}) in the silicon crystalline lattice is expected to change the optical, electrical, photoelectrical and thermoelectrical properties of such a material.

In this work $CrSi_2$ nanosize islands were grown by reactive deposition epitaxy (RDE) on Si(111) surface and covered with 100 nm epitaxial silicon. The structures with buried $CrSi_2$ nanocrystallites (NC's) are investigated by atomic force microscopy (AFM), TEM, by optical reflectance spectroscopy to determine the structure and by RBS and DLTS to identify the point defects.

1. Experimental

The growth of structures was carried out in ultra high vacuum (UHV) chamber. Optical properties of samples were studied in UHV chamber VARIAN with base pressure of 2×10^{-10} Torr equipped with AES and DOS [5] facilities.

Samples were cut from Si(111) substrates of n-type conductivity and 7.5 Ω cm resistivity. The silicon cleaning procedure was as follows: annealing at 700 °C during 4–5 hours, cooling during 12 hours, flashes at 1250 °C (5 times). Surface purity was controlled by AES method. Chromium was deposited on hot (500 °C) silicon substrate from Ta tube in the thickness range of 0.1–1.5 nm at rate about 0.04 nm/min in all experiments controlled by quartz sensor.

Silicon film growth was performed by MBE method at temperature 750 °C. Silicon deposition rate was 3–4 nm/min. Silicon film thickness was 100 nm. Influence of Cr thickness (0.1–1.5 nm) on the growth and properties of Si(111)/$CrSi_2$–NC's/Si structures was studied. Morphology of uncovered and silicon covered samples was studied by AFM (Solver P47), by planar and cross sectional transmission electron microscopy (TEM) (Philips CM 20) at 200 keV energy, and at 300 keV energy in a JEOL 3010 high resolution transmission electron microscope (HRTEM) equipped with energy filtering facility (EFTEM).

The point defects were studied by deep level transient spectroscopy (DLTS) in Schottky junctions prepared by evaporation of 0.4×0.4 mm gold dots onto the top silicon layer. Rutherford backscattering (RBS) was measured using 1.5 MeV $^4He^+$ analyzing ion beam with spot size of 0.5×0.5 mm^2. Backscattered He^+ ions were detected at scattering angles $\Theta = 165^\circ$ and $\Theta = 97^\circ$.

2. Results and discussion

For a study of surface morphology after 3D $CrSi_2$ island formation samples with 0.1–0.6 nm Cr thicknesses were grown. Square form $CrSi_2$ nanoislands with density $(4-9) \times 10^9$ cm^{-2}, height of 2.0–6.0 nm and lateral sizes of 20–60 nm were measured by AFM before growing the top silicon layer.

LEED pattern Si(111)1×1 for 0.02–0.2 nm Cr thickness samples with increased background corresponds to the partial disordering of silicon surface between $CrSi_2$ islands due to surface diffusion of silicon atoms into the reaction zone. Since the maximal intensity LEED pattern and minimal background was observed at 750 °C [4], the silicon over the $CrSi_2$ NC's was grown at this temperature. For all samples LEED Si(111)7×7 pattern was preserved after the growth of silicon overlayer that corresponds to a monolithic Si(111)/ $CrSi_2$–NC's/Si(111) structure. The AFM study of Si covered $CrSi_2$–NC's has shown a few uncovered NC's on the surface. They usually had hexagonal form and partially buried in silicon.

Comparison of the reflectance spectra of grown layers with the spectra of $CrSi_2$ epitaxial film has shown a new peak at 1.8 eV that corresponds to the $CrSi_2$ segregation near the silicon surface. Intensity of this peak has a maximum at 0.6 nm Cr thickness. For Cr thicknesses 0.1–0.6 nm displacement of $CrSi_2$ NC's towards silicon surface was proved, since the maximal density of NC's was observed by AFM also at 0.6 nm. At higher Cr thicknesses (1–1.5 nm) a coalescence of $CrSi_2$ NC's was observed and decrease of density of uncovered $CrSi_2$ NC's. Therefore different depth distributions of $CrSi_2$ NC's were found in the grown structures.

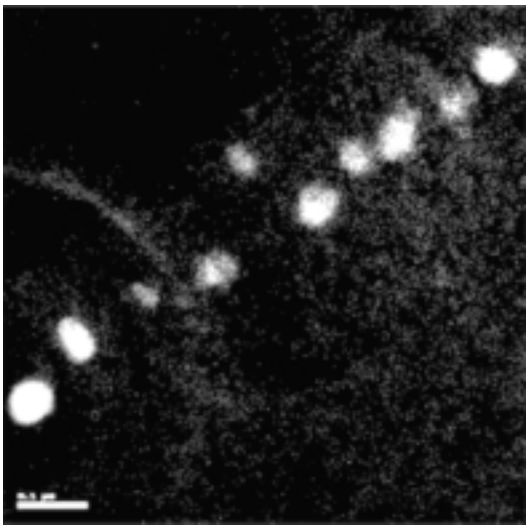

Fig. 1. Cross sectional EFTEM image (Cr map) showing the distribution of buried $CrSi_2$ nanocrystals.

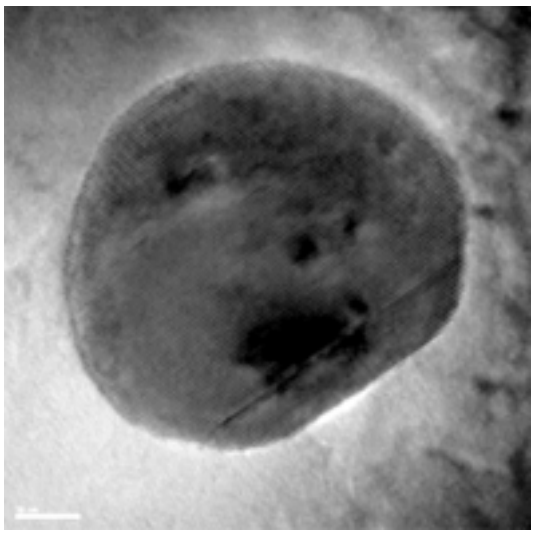

Fig. 2. HRTEM image of a $CrSi_2$ NC fitted into the Si lattice.

This interpretation has been confirmed by the cross sectional TEM images. It was shown that NC's are frustum of a sphere and their sizes increases with the Cr thickness. Most of NC's are lying about 100 nm below the surface as expected but some of them are definitely shifted toward the surface. The Cr map shown in Fig. 1 proves that majority of the Cr is localized in the NC's.

The HRTEM image (Fig. 2) of a NC grown from 1.5 nm Cr shows the $CrSi_2$ hexagonal phase ($a = 0.4428$ nm, $c = 0.6369$ nm) epitaxially fitted to the Si(111) spacing ($d = 0.3135$ nm). The lattice constant in the c direction is with good approximation double of the Si lattice. By DLTS point defects are detected at about 0.25 eV above the valence band, which is attributed to Cr related defects. The defect concentration is so large in the epitaxial silicon layer that the layer is resistive manifested as a double peak in the DLTS spectra due to slow relaxation DLTS excitation pulses. By RBS large concentration (10^{19}/cm^3 range) of Cr was measured in the top 100 nm silicon.

The growth at 750 °C was optimized by the LEED pattern of the grown silicon. The observed large concentration of Cr in the epitaxial silicon shows that for improving the quality of the top silicon the growth temperature has to be reduced and/or some annealing process has to be applied to improve the crystal quality before the growth of the top silicon layer.

3. Conclusions

Monolithic Si(111)/NC's $CrSi_2$/Si(111) structures with buried $CrSi_2$ NC's were grown and optically investigated after $CrSi_2$ island formation and after silicon overgrowth. It was shown that semiconductor properties of $CrSi_2$ NC's preserves inside silicon matrix independently of deposited Cr thickness (0.1–1.5 nm). The silicide NC's have been measured to be hexagonal phase $CrSi_2$ fitted to the silicon. By DLTS and RBS large concentration of Cr was measured in the top silicon layer. The growth temperature and the Si thickness (100 nm) optimized earlier by the LEED pattern have to be refined to reduce the Cr concentration in the epitaxial silicon layer.

Acknowledgements

The work was performed with financial support from FEB RAS grants No. 06-02-P1-001 and Program between the Russian Academy of Sciences and the Hungarian Academy of Sciences (2005–2007, project No. 22) and L. Dobos for OTKA grant No. 67827.

References

[1] *Semiconducting Silicides*, ed. by V. E. Borisenko, (Berlin, Springer-Verlag), 2000.
[2] P. Wetzel, C. Pirri, J. C. Peruchetti, D. Bolmont, and G. Gewinner, *Sol. State Commun.* **65**, 1217 (1988).
[3] N. G. Galkin *et al*, *Thin Solid Films* **280**, 211 (1996).
[4] N. G. Galkin, K. N. Galkin, A. M. Maslov, A. I. Cherednichenko, and V. A. Davydov, *Asia-Pacific Conference on Semiconductor, Extended abstracts, July 29–31, 2006, Kyoto, Japan*, Kyoto University, 105–106 (2006).
[5] S. A. Dotsenko, N. G. Galkin, A. S. Gouralnik, and L. V. Koval, *e-J. Surface Science and Nanotechnology* **3**, 113 (2005).

15th Int. Symp. "Nanostructures: Physics and Technology"
Novosibirsk, Russia, June 25–29, 2007

Fano resonance study in impurity photocurrent spectra of InGaAsP/GaAs heterostructures doped with shallow donors

V. Ya. Aleshkin, A. V. Antonov, *L. V. Gavrilenko* and V. I. Gavrilenko

Institute for Physics of Microstructures Russian Academy of Sciences, Nizhny Novgorod, GSP-105, 603950, Russia

Abstract. The results of experimental and theoretical study of the impurity photocurrent peaks in the spectral region corresponding to the longitudinal optical phonon energy in InGaAsP/GaAs quantum wells doped with silicon are presented. We demonstrate that Fano peak in photocurrent spectra in a quantum well structure is wider than that in a bulk semiconductor. Impurity location dispersion weakly influence on the peak shape.

Introduction

In the impurity photocurrent spectra of n-GaAs and n-InP doped with the shallow donors were observed asymmetric peaks in the spectrum range where the photon energy is close to the longitudinal optical (LO) phonon one [1]. It should be noted that analogous features in the photoexcitation spectra of acceptors in silicon were reported in 1958 [2]. In contrast to n-GaAs in p-Si these features appear as minimums in the photocurrent and absorption spectra [3–5]. Similar features were observed in the absorption and photocurrent spectra in n-Si, doped with deep donors [6]. The authors of Refs. [3–5] explained the appearance of the above spectral features by the interaction of carriers with optical phonons. They suggested using the term "Fano resonances" to denote these features. However, any suitable theory for a quantitative description of the observed Fano resonances in p-Si is not yet created. The famous expression from Fano's work [7], where the configuration interaction between a resonant level and a continuum was considered, is often used to qualitatively describe these spectral features.

In this paper the investigations of Fano resonances in photocurrent spectra of InGaAsP/GaAs quantum well heterostructures doped with shallow donors are presented. We discovered that narrowing of quantum well (QW) leads to the resonance peak broadening that is due to the growth of the probability of electron-phonon scattering. It is also shown that impurity location dispersion weakly influence on Fano peak position and shape.

1. Experiment

The photocurrent spectra were measured on a bulk n-GaAs sample and InGaAsP/GaAs heterostructures. Bulk n-GaAs layer was grown by the liquid phase epitaxy on a semi-insulating GaAs substrate. The epilayer was doped with silicon at a concentration of 8.3×10^{14} cm^{-3} and had a thickness of 70 μm. The electron mobility was 5.9×10^4 cm^2/V s at 77 K. The heterostructures under investigation were grown on semi-insulating GaAs substrate and consisted of 30 GaAs quantum wells and separated by the lattice matched 400 Å $In_{0.1}Ga_{0.9}As_{0.8}P_{0.2}$ barriers. Structure 1 contains 200 Å wide QWs, while structure 2 contains 90 Å wide QWs. The central parts of quantum wells were delta-doped with silicon. The sheet donor concentration measured by Hall effect was 3.3×10^{10} cm^{-2} per quantum well. The photocurrent spectra were measured by using the BOMEM DA3.36 Fourier-transform spectrometer at 4.2 K.

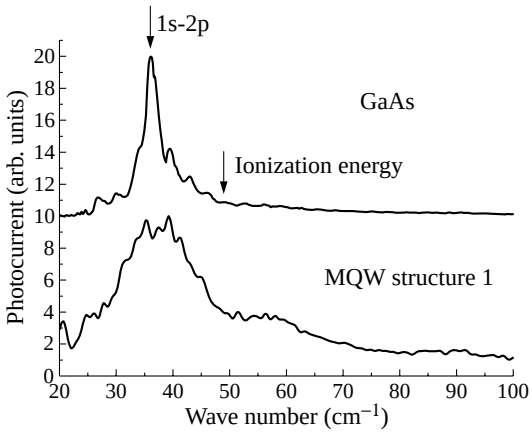

Fig. 1. The measured (long-wave) photocurrent spectra in the epitaxial GaAs (top curve) and in structure 1 (bottom curve).

Impurity photocurrent spectra contain two bands: long-wave band corresponds to transitions from ground donor state to excited states up to continuum while short-wave band is situated close to LO phonon energy and corresponds to Fano resonance.

The measured photocurrent spectra in the area of long-wave band for structure 1 and epitaxial GaAs layer are presented in Fig. 1. The arrows point 1s-2p donor transition in GaAs (36 cm^{-1}) and donor ionization energy (48 cm^{-1}). It is seen from the figure that photocurrent band in quantum well structure is much wider than that in bulk GaAs. The reason for it is the real dispersion of donor location which leads to different binding energies for donor in the center of QW and on heterointerface.

The photocurrent spectra around the LO photon energy in quantum well heterostructures and in the epitaxial GaAs are shown in Fig. 2. Whereas long-wave photocurrent band in QW is more than two times wider than bulk photocurrent band (see Fig. 1), Fano peak width is 2 cm^{-1} in the epitaxial GaAs and 2.5 cm^{-1} in the structure 1. It shows that Fano resonance shape weakly depends on donor location and binding energy.

2. Theoretical investigations

Further narrowing of QW leads to Fano peak width increasing (in structure 2 full width is about 5 cm^{-1}). For explaining this fact we considered simple model which allows to derive analytical expressions for Fano peak in photocurrent spectrum. We assumed, that the wave function of a donor states in the

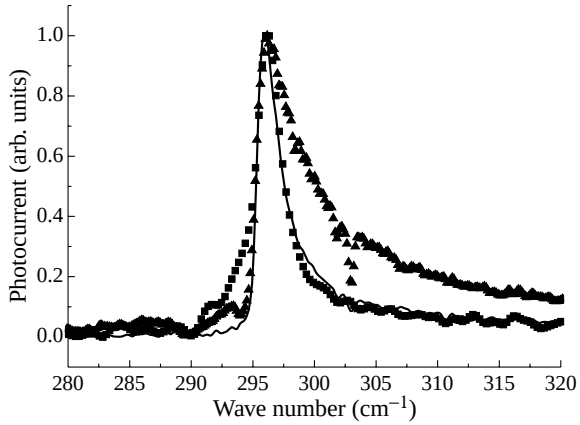

Fig. 2. The measured photocurrent spectra in quantum well heterostructures (structure 1 — squares, structure 2 — triangles) and in the epitaxial GaAs (solid line).

quantum well $-d/2 < z < d/2$ may be presented in the form

$$\Psi(\boldsymbol{\rho}, z) = f(\boldsymbol{\rho})F(z), \tag{1}$$

where $\boldsymbol{\rho}$ is the radius vector in the quantum well plane. Approximation (1) is valid in the case when the quantum well width is much smaller than Bohr radius and the quantum well is deep enough; so the wave function is localized inside QW.

Taking into account reflection in the vicinity of Fano resonance the photocurrent can be expressed as

$$J(\omega) = BI(\omega)\frac{W(\omega)}{|\mathcal{E}|^2}\left[1 - R(\omega)\right], \tag{2}$$

where B is a frequency-independent constant, $I(\omega)$ is the incident light intensity, $R(\omega)$ is reflection coefficient, $\mathcal{E}$ is electric field amplitude, and $I(\omega)$ is a phonon absorption probability which can be expressed in the form

$$W(\omega) \approx \frac{2\pi}{\overline{h}}\frac{|\langle\psi_{1,1}(\overline{h}\omega + E_i)|V_{\rm ph}|i\rangle|^2}{1+x^2}|\alpha + i + x|^2, \tag{3}$$

where $x = 2(\overline{h}\omega - \overline{h}\omega_0)/\Gamma$ is the dimensionless energy. Here constant α is

$$\alpha = \sum_{q,f}\frac{\langle\psi(E_\phi)|V_{\rm LO}^+|\phi_q\rangle}{\Gamma/2\langle\psi(E_\phi)|V_{\rm ph}|i\rangle} \times 2\left(P\int_{E_i}^{\infty} dE'\frac{\langle\phi_q|V_{\rm LO}^+|\psi(E')\rangle\langle\psi(E')|V_{\rm ph}|i\rangle}{E_\phi - E'} + \int_{E_i}^{\infty} dE'\frac{\langle\phi_q|V_{\rm ph}|\psi(E')\rangle\langle\psi(E')|V_{\rm LO}^+|i\rangle}{-\overline{h}\omega_0 + E_i - E'}\right)$$

symbol P denotes the principal value of an integral, E_i, E_ϕ are the energies of donor ground state and resonant state respectively, $\Gamma/\overline{h}$ is the frequency of electron transition between the state in continuum $|\psi(E_\phi)\rangle$ and the resonant state $|\phi_q\rangle$ due to the spontaneous LO-phonon emission,
$\Gamma = 2\pi\sum_q |\langle\phi_q|V_{\rm LO}^+|\psi(E_\phi)\rangle|^2$, $V_{\rm ph}$, $V_{\rm LO}^+$ are the light absorption and LO-phonon emission operators, respectively (for details see [8]).

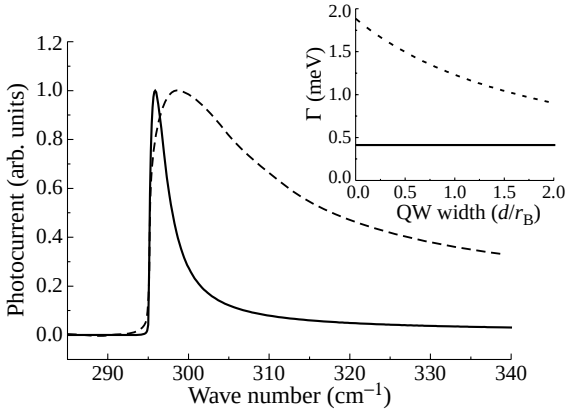

Fig. 3. The photocurrent spectra calculated for the bulk n-GaAs (solid curve) and for narrow QW (dashed curve). The insert shows dependence of Γ on the QW thickness (dashed line). The straight line stands for Γ in bulk n-GaAs.

The 2D hydrogen atom wave functions were used to calculate the absorption spectrum [9]. In Figure 3 calculated photocurrent spectra for bulk GaAs and narrow QW are shown. The peak width is determined by value of Γ, i.e. by electron-phonon scattering frequency. In a narrow QW Γ is approximately four times larger than in bulk n-GaAs. The calculated dependence of $\Gamma(E_\phi)$ on d for GaAs quantum well are shown in the insert of Fig. 3.

The observed Fano resonance in the photocurrent spectra of the quantum well heterostructures demonstrats a double peak width comparing with that for a bulk semiconductor which qualitatively agrees with the theory prediction.

Acknowledgements

This work has been supported by RFBR (07-02-00549, 05-02-17341), the Dynasty foundation (grant for L. V. Gavrilenko).

References

[1] K. Jin, J. Zhang, Z. Chen *et al*, *Phys. Rev. B* **64**, 205203 (2001).
[2] H. J. Hrostowski, R. H. Kaiser, *J. Phys. Chem. Solids* **4**, 148 (1958).
[3] A. Onton, P. Fisher, A. K. Ramdas, *Phys. Rev.* **163**, 686 (1967).
[4] H. R. Chandrasekhar, A. K. Ramdas, S. Rodriguez, *Phys. Rev. B***14**, 2417 (1976).
[5] G. D. Watkins, W. B. Fowler, *Phys. Rev. B* **16**, 4524 (1977).
[6] E. Janzen, G. Grossmann, R. Stedman, H. G. Grimmeiss, *Phys. Rev. B* **31**, 8000 (1985).
[7] U. Fano, *Phys. Rev.* **124**, 1866 (1961).
[8] V. Ya. Aleshkin, A. V. Antonov, L. V. Gavrilenko and V. I. Gavrilenko, *Phys. Rev. B*, accepted (2007).
[9] X. L. Yang, S. H. Guo and F. T. Chan, K. W. Wong, W. Y. Ching, *Phys. Rev. A* **43**, 1186 (1991).

15th Int. Symp. "Nanostructures: Physics and Technology"
Novosibirsk, Russia, June 25–29, 2007

Determination of the structural properties of multiple quantum dot ensembles based on a rigorous X-ray specular and diffuse scattering analysis and comparison with measurements

L. I. Goray[1,2], G. E. Cirlin[1,3], E. Alves[4], Yu. B. Samsonenko[1,3], A. A. Tonkikh[3], N. K. Polyakov[1,3] and V. A. Egorov[3]

[1] Institute for Analytical Instrumentation, St Petersburg 190103, Russia
[2] International Intellectual Group, Inc., Penfield, New York 14526, USA
[3] St Petersburg Physics and Technology Center for Research and Education of RAS, Khlopina 8/3, 194021, St Petersburg, Russia
[4] Instituto Tecnológico e Nuclear, Sacavém 2686-953, Portugal

Abstract. Multiple and multi-wave diffraction, absorption, and resonances influence significantly X-ray scattering from multiple quantum dots (QDs), and these effects are taken into account by known theories only approximately. The present report dwells on application of a rigorous theoretical analyses of X-ray reflection from In(Ga)As/GaAs QD ensembles to the investigation of their structural properties. The angle dependences of diffuse scattering exhibit very strong peaks near the angles corresponding to specular reflection from the QD facets (the so-called blaze condition for gratings). These peaks exist at nearly the same diffraction angles for QDs with the equal slope angle; their intensities, however, may differ by a few times for vertically correlated and non-correlated QDs.

Introduction

Further progress in investigation of self-assembled quantum dots (QDs) and of other low-dimension structures with typical sizes of the order of 10-nm and having unique optoelectronic properties requires development of methods that would provide more accurate characterization of structural details. Non-destructive X-ray diffraction generally has the potential to measure the chemical composition and strain field distributions. In many cases, however, the complete intensity distribution has to be calculated using a structural model with a large number of free fitting parameters [1], and it falls short from predicting absolute values exactly. For example, the widely used Takagi–Taupin formalism [2], which was developed for the analysis of strained crystals, is not capable of predicting directly the influence of the height h and width L of QDs, as well as their vertical correlation rate. Multiple and multi-wave diffraction, absorption, and resonances influence significantly X-ray scattering from multiple QDs, and these effects are taken into account by known theories only approximately. The present report dwells on application of comprehensive theoretical and experimental analysis of X-ray scattering from QD ensembles to the investigation of growth processes of QDs in In(Ga)As/GaAs systems and of their structural properties.

1. Theory

Rigorous computation of the field scattered by X-rays from rough surfaces is a problem of daunting complexity in the area of electromagnetism and optics even for modern computers because of the small wavelength-to-period λ/d and wavelength-to-height λ/h ratios on the one hand [3] and large number of accountable asperities, especially at grazing incidence, on the other [4]. The rigorous integral equation method employed in the analysis of diffraction grating efficiency [5] is extended here to the case of quasi-periodical and non-periodical structures of any kind [6]. The software developed allows one to operate with exact models (viz based on Maxwell's equations, exact boundary conditions, and radiation conditions) to study X-ray scattering from multilayer structures in real space [7], in particular ensembles of QDs having different shapes, lateral and vertical correlation lengths, surface densities, and fractal dimensions, with the use of a low- or mid-end workstation in a reasonable computation time.

It was shown that in perfect crystalline structures with vertically correlated QD ensembles there is an additional long-range QD ordering in lateral planes which gives rise to corrugation of crystalline planes and results in a quasi-periodical distribution of the elastic deformation and QDs [8]. To rigorously include the quasi-periodicity of QD ensembles, we used the model in which the rough surface is represented by a grating, the large period of which contains a few or a large number of irregularities [4]. Thus, the program deals with a structure which, while being a grating from a mathematical point of view, can model a rough surface provided d becomes large compared with the lateral correlation length (width) L of the asperities. Moreover, if L is about or greater than λ, the number of diffraction orders is large, and the continuous speckle of the rough surface is simulated by the discrete speckle of the grating. Border profiles with QDs have both a periodic and a random component, and random samples have to be averaged to obtain the exact scattered field. The model assumed permits also to use corrugated interfaces having QDs as irregularities.

The time required to calculate one reflectance for all scattering angles for a 20-border QD structure (with the energy balance error of $\sim 1.e-5$) was about 3.5 hours when using a workstation with two Intel(R) Pentium(R) 2 GHz processors, 2 Mbyte cache, 400 MHz bus clock, 2 Gbyte RAM and controlled by OS Windows(R) XP Pro.

2. Experimental

Two samples were grown by molecular beam epitaxy. Both of them consisted of 10 InAs QD sheets (two mono layers of InAs were deposited for each QD layer) separated with 10 nm (sample F667) and 40 nm (sample F668) of GaAs allowing

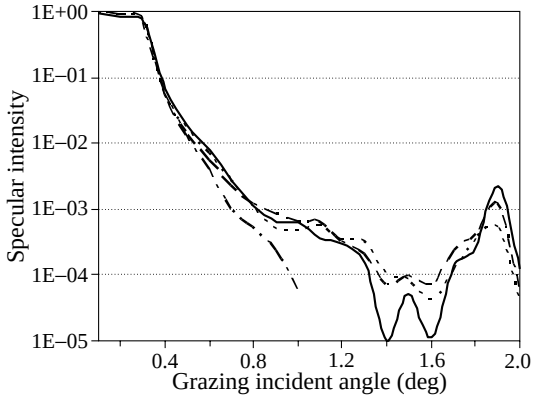

Fig. 1. Absolute specular reflectivity for sample F668 with vertically non-correlated GDs at a 0.154-nm wavelength vs grazing angle of incidence: perfect plane structure model (short-dashed line); Névot–Croce approximation with rms roughness of 1.45 nm for triangles (long-dashed line); rigorous calculation with QD height $h = 5$ nm and width $L = 16.7$ nm (full line); measurement (long-short-dashed line).

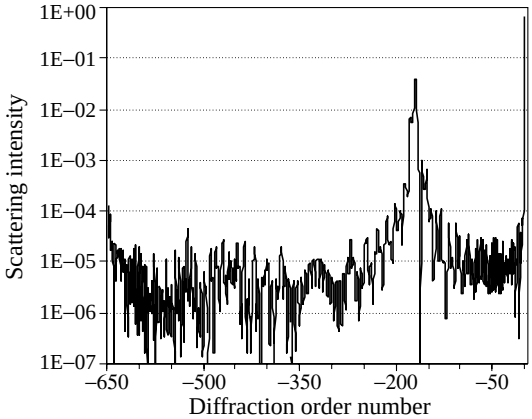

Fig. 2. Absolute specular and non-specular reflectivity calculated for sample F667 with vertically correlated GDs at a 0.154-nm wavelength and a 0.5° grazing incidence vs diffraction angle in the range from −85.7° to +89.7°. The strong peak exists near a scattering angle of 28.5° that corresponds to specular reflection from QD facets.

to get correlated and non-correlated QD arrays. In the first case (10 nm), the dots are perfectly aligned vertically (which is confirmed by transmission electron microscopy), in the second case they are arranged more or less randomly.

Measurements of both specular and diffuse X-ray intensities in different geometries and spaces were performed on chosen samples using the grazing incidence X-ray diffraction techniques at a wavelength of Cu $K\alpha_1$ ($\lambda = 0.1541$ nm) by the Hotbird diffractometer and position sensitive detector [9]. The beam's divergence is 0.01° and the angular resolution of 0.005° or 0.001° has been chosen for different experiments.

3. Results and discussions

By comparing the theoretical with experimental X-ray reflectances (Fig. 1), the average values of $h = 5.0$ nm and $L = 16.7$ nm determined in the Stranski–Krastanow growth model [10], as well as the superlattice parameters were borne out and refined by the fitting procedure for two different samples. Calculations have revealed a weaker dependence of specular scattered intensities on L and a stronger one on h, a feature that is especially noticeable at high grazing angles. Also, noticeable differences appearing at these angles between both approximate (Névot–Croce model) and rigorous calculation methods, on the one hand, and the theory and experiment, on the other, find adequate explanation.

The angle dependences of diffuse scattering exhibit very strong peaks near the angles θ_{diff} corresponding to specular reflection from the QD facets (Fig. 2), the so-called blaze condition for gratings:

$$2\alpha = \theta_{\text{inc}} - \theta_{\text{diff}} ,$$

where α is the facet angle of QDs ($\tan\alpha = 2h/L$), θ_{inc} is the incident angle and θ_{diff} is the diffraction (scattering) angle corresponding to a strong intensity peak. The good coincidence for the results obtained from the blaze equation with those obtained numerically indicates the validity of computations and possibility to extract QD slope angles from measurements of X-ray diffuse scattering.

These peaks exist at nearly the same diffraction angles for QDs with the equal slope angle; their intensities, however, may differ by a few times for correlated and non-correlated QD structures. This determination of the QD slope angle and vertical correlation rate, as well as of other structural parameters, can be performed with a high accuracy, provided the data sample to be averaged is statistically large enough. So the proposed approach appears promising.

Acknowledgements

Partial support of the Russian Foundation for Basic Research and Quantum Nanostructures Scientific Program of the Russian Academy of Sciences is gratefully acknowledged.

References

[1] I. Kegel, T. H. Metzger, A. Lorke *et al*, *Phys. Rev. Lett.* **85**, 1694 (2000).
[2] Z. Xu, D. Birkedal, J. M. Hvam *et al*, *App. Phys. Lett.* **82**, 3859 (2003).
[3] A. Rathsfeld, G. Schmidt and B. H. Kleemann *et al*, *Commun. Comput. Phys.* **1**, 984 (2006).
[4] M. Saillard and A. Sentenac, *Waves Random Media* **11**, R103 (2001).
[5] L. I. Goray, J. F. Seely and S. Yu. Sadov, *J. Appl. Phys.* **100**, 094901 (2006).
[6] L. I. Goray, *Optical Metrology (Germany, Munih, 18–21 June, 2007)*, SPIE Proc. **6617** (2007).
[7] L. I. Goray, *Nuclear Instrum. Methods Phys. Research A* **536**, 211 (2005).
[8] N. N. Faleev, K. M. Pavlov, V. I. Punegov *et al*, *Semiconductors* **33**, 1229 (1999).
[9] A. D. Sequeira and N. Franco, *Mat. Sci. Forum* **206**, 378 (2001).
[10] V. G. Dubrovski, G. E. Cirlin, Yu. G. Musikhin *et al*, *J. Crystal Growth* **267**, 47 (2004).

15th Int. Symp. "Nanostructures: Physics and Technology"
Novosibirsk, Russia, June 25–29, 2007

Optical manifestation of quasi-2d accumulation layers of n-InN

A. A. Klochikhin[1,2], V. Yu. Davydov[1], A. V. Sakharov[1], A. N. Smirnov[1], C.-H. Shen[3], H.-Y. Chen[3] and S. Gwo[3]

[1] Ioffe Physico-Technical Institute, St Petersburg, Russia
[2] Nuclear Physics Institute, 188350, St Petersburg, Russia
[3] Department of Physics, National Tsing-Hua University, Hsinchu 300, Taiwan, ROC

Abstract. It is shown that quasi-2D surface accumulation layers strongly affect optical characteristics of thin epilayers of n-InN. We present model calculations and experimental data demonstrating that the PL band shapes are sensitive to the presence of accumulation layers.

InN, in contrast to GaN and AlN, has been the least studied of the group III-nitrides. It has been recently established that the characteristic features of InN are nano-size thick surface accumulation layers for the undoped n-type InN or n-type surface inversion layers for the p-type Mg-doped InN. We present the first evidences of the optical observation of electron accumulation layers in n-InN.

Electron accumulation in n-InN has been detected by different experimental techniques [1,2,3,4,5,6,7]. It can be supposed that surface and, probably, interface accumulation layers account for a considerable discrepancy between the conduction electron density in InN thin film derived from Hall measurements and the density obtained from optical methods reported in Refs. [8,9].

Data on the carrier concentration for three InN samples estimated from Hall measurements and from analysis of PL band shapes [9] are presented in Table 1. Assuming that Hall measurements give the concentration $n_{\rm H}$ averaged over the sample thickness L, whereas the PL band shape depends on the free carrier concentration $n_{\rm PL}$ within the bulk part of the sample, we can ascribe the difference $\Delta n = (n_{\rm H} - n_{\rm PL})L$ to the surface or interface (or both) accumulation layers. As shown in Table 1, the difference Δn between the estimates from Hall and PL measurements can be as high as $\sim 10^{14}$–10^{15} cm^{-2}. If the accumulation (or inversion) layer thickness is of the order of a few nanometers, the 3D concentration within the accumulation layer can be of the order of 10^{20}–10^{21} cm^{-3}. In fact, the values of such an order of magnitude were reported in Refs. [1,2,3,4,5,6,7].

Accumulation layers are formed due to an electrostatic potential well near a sample surface (and interface). The attractive potential near the surface of a degenerate semiconductor was studied by a number of authors [10,11,12]. However, the attractive potential origin is still understood incompletely. We assume that ionized donors and free electrons create the potential due to the Coulomb interaction. Then, following [13], we can write

$$\begin{aligned} \Phi(\mathbf{r}) &= -\int d^3r' \left[N^{\rm D}(\mathbf{r}') - n(\mathbf{r}')\right] e/\varepsilon_0 |\mathbf{r}-\mathbf{r}'|, \\ \Delta\Phi(\mathbf{r}) &= -4\pi/\varepsilon_0 \left[-N^{\rm D}(\mathbf{r}) + n(\mathbf{r})\right], \end{aligned} \qquad (1)$$

where $N^{\rm D}(\mathbf{r})$ and $n(\mathbf{r}')$ are the ionized donor and free electron densities, respectively, ε_0 is the lattice dielectric constant, and $\int d^3r[-N^{\rm D}(\mathbf{r}) + n(\mathbf{r})] = 0$ is the electro-neutrality condition. The spatial distribution of the electrons $n(E,\mathbf{r})$ with kinetic energy E is now

$$n(E,\mathbf{r}) = 1/\left(\exp\left\{[E - e\Phi(\mathbf{r}) - \mu]/kT\right\} + 1\right)^{-1},$$

where μ is the chemical potential and k is the Boltzmann constant.

Of particular interest is the inhomogeneity of the charge distribution in the growth direction. We regard an epilayer of thickness L as a box filled by a free electron liquid and restricted by infinite walls. The model potential inside the box $\Phi(z)$ is presented using the Morse potential in the form symmetrical with respect to the sample surface and interface

$$\begin{aligned} \Phi(z) &= [\phi(\lambda z) + \phi(\lambda|z-L|) - 2\phi(\lambda L/2)], \\ \phi(\lambda z) &= 2V_0\{\exp(-\lambda z) - 1/2\,\exp(-2\lambda z)\}, \end{aligned} \qquad (2)$$

where $V_0 = \Phi(z=0)$. Parameter λ allows one to vary the accumulation layer thickness. The choice of the potential in the form of Eq. (2) means that $\Phi(L/2) = 0$ and derivatives $\frac{\partial\Phi(z)}{\partial z} = 0$ at $z = 0$, $z = L/2$, and at $z = L$.

Table 1. Parameters of samples used in experiment.

Sample	$n_{\rm H}$ (cm^{-3})	$n_{\rm PL}$ (cm^{-3})	t (nm)	Δn (cm^{-2})
050110	1.0×10^{19}	1.0×10^{18}	220	$2.\times10^{14}$
050118	4.2×10^{18}	1×10^{18}	650	$2.\times10^{14}$
UCI-507	3×10^{19}	$9.\times10^{18}$	600	1.3×10^{15}

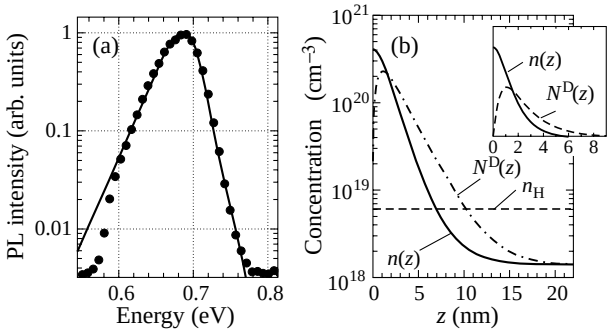

Fig. 1. (a) PL band shape for sample 050110. Symbols present experimental data, the solid lines are the calculated shape. (b) Semi-logarithmic plots of inhomogeneous distributions of electrons $n_{\rm e}(z)$ and ionized donors $N^{\rm D}(z)$ near the surface of sample 050110, the dashed line $n_{\rm H}$ gives the Hall concentration. The inset presents the linear plots of the concentration data.

The values of $n_{\rm H}$, $n_{\rm PL}$, and difference $\Delta n = (n_{\rm H} - n_{\rm PL})L$ appreciably restrict the potential parameters in Eq. (2). Electroneutrality gives an additional connection between the electron density $n(z) = \int \rho(E) n(E, z) dE$ and donor density $N^{\rm D}(z) = n(z) + (\epsilon_0/4\pi)\, \partial^2 \Phi(z)/\partial z^2$ which has to be positively defined. Data on the accumulation layer width or on the potential well depth V_0, or on the maximum electron concentration allow one to establish the shape of the accumulation layer unambiguously.

The calculation procedure is as follows. The PL band shape of a sample is fitted using the approach described in [9]. The non-parabolic conduction band is assumed to have the effective mass at the $\Gamma-$point equal to 0.07 of the free electron mass. For the sample with a given Hall concentration we vary the potential amplitude V_0 at fixed λ and calculate the PL band shape for the bulk region of the sample. Simultaneously the sum of the charge densities is found from the Poisson equation. Variation of λ starting from $\lambda = 2.25$ nm^{-1} is used to obtain the non-negative values of $N^{\rm D}(z)$ at arbitrary z.
The shape of the PL band for the "bulk" region ($10 < z < 210$ nm) for the 220-nm thick sample is shown in Fig. 1(a). The Hall concentration is seen to be higher than $n_{\rm PL}$ by an order of magnitude. Potential parameter λ was chosen so that the electron distribution given in Fig. 1(b) was similar to that given in Ref. [7]. The condition $N^{\rm D}(z) \geq 0$ restricts the maximum electron density in the accumulation layer from above and the potential well width from below.

The photoluminescence formed partially in the accumulation layer can be observed for some samples. This can be explained by the fact that the electric field of the accumulation layer is not able to move photo-holes toward the center of the film because of their localization on deep traps. Figure 2 demonstrates results of such observations together with calculated curves. The fact that the surface layer contains the greatest part of electrons makes the luminescence observable even from a small region of the accumulation layer. Figure 3 demonstrates the experimental and calculated PL bands of the non-intentionally doped sample with a high electron concentration. The calculated PL band is obtained under the assumption that emission begins at $z > 6$ nm, and the luminescence from the bulk region of the sample is essentially suppressed. Comparison of Fig. 1(b) and Fig. 3(b) shows that the difference between electron and donor distributions decreases for the sample with a high electron concentration.

To summarize, the PL spectra of InN epilayers together with Hall data allow one to establish the free carrier content in the accumulation layer. The model calculations based on the parameterized potential well give quantitative information about such interconnected characteristics of the accumulation layer as its width and maximum electron concentration, as well as the band bending.

Acknowledgements

This work was supported by NSC-RFBR Project 94WFA0400 128 and the Programs of RAS "Quantum nanostructures" and "New materials and structures".

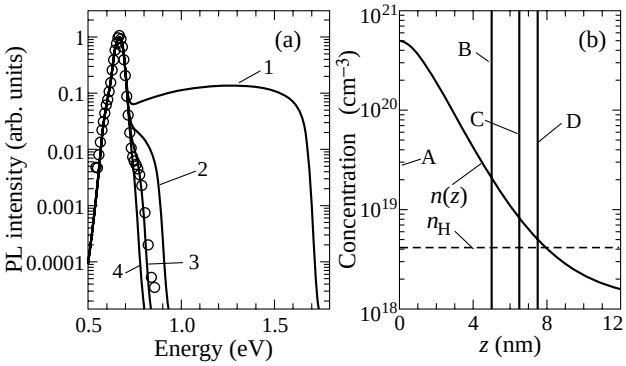

Fig. 2. (a) PL band shape for sample 050118. Symbols present experimental data, solid lines are the calculated shapes. (b) Inhomogeneous distribution of electron density near the surface (solid line). Vertical lines A, B, C, and D correspond to the boundaries of the regions taken into account in calculations of the PL shapes given in Fig. 2(a) by curves 1, 2, 3, and 4, respectively.

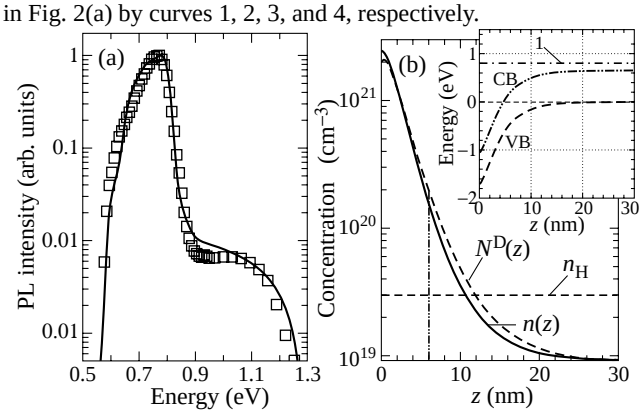

Fig. 3. (a) PL band shape for sample UCI-507. Symbols present experimental data, the solid line is the calculated shape. (b) inhomogeneous distributions of electron (solid line) and ion (dashed line) densities near the surface. The inset shows the band bending effect, curve 1 is the chemical potential level for the conduction band.

References

[1] Hai Lu, W. J. Schaff, L. F. Eastman, and C. E. Stutz, *Appl. Phys. Lett.* **82**, 1736 (2003).
[2] I. Mahboob, T. D. Veal, C. F. McConville, H. Lu, and W. J. Schaff, *Phys. Rev. Lett.* **92**, 036804 (2004).
[3] L. F. J. Piper, T. D. Veal, I. Mahboob, C. F. McConville, H. Lu, and W. J. Schaff, *Phys. Rev. B* **70**, 115333 (2004).
[4] C. H. Swartz, R. P. Tompkins, N. C. Gilesa, T. H. Myersa, Hai Lu, W. J. Schaff, L. F. Eastman, *J. Cryst. Growth* **269**, 29 (2004).
[5] I. Mahboob, T. D. Veal, L. F. J. Piper, C. F. McConville, Hai Lu, W. J. Schaff, J. Furthmüller and F. Bechstedt, *Phys. Rev. B* **69**, 201307(R) (2004).
[6] S. X. Li, K. M. Yu, J. Wu, R. E. Jones, W. Walukiewicz, J. W. Ager III, W. Shan, E. E. Haller, H. Lu, and W. J. Schaff, *Phys. Rev. B* **71**, 161201 (2005).
[7] W. Walukiewicz, J. W. Ager III, K. M. Yu, Z. Liliental-Weber, J. Wu, S. X. Li, R. E. Jones, and J. D. Denlinger, *J. Phys. D: Appl. Phys.* **39**, R83 (2006).
[8] B. Arnaudov, T. Paskova, P. P. Paskov, B. Magnusson, E. Valcheva, B. Monemar, H. Lu, W. J. Schaff, H. Amano, and I. Akasaki, *Phys. Rev. B* **69**, 115216 (2004).
[9] A. A. Klochikhin, V. Yu. Davydov, V. V. Emtsev *et al*, *Phys. Rev. B* **71**, 195207 (2005).
[10] J. A. Appelbaum and G. A. Baraff, *Phys. Rev. B* **4**, 1235 (1971).
[11] G. A. Baraff and J. A. Appelbaum, *Phys. Rev. B* **5**, 475 (1972).
[12] H. Übensee, G. Paasch, J.-P. Zöllner, and S. Handschack, *Phys. Rev. B* **39**, 1955 (1989).
[13] P. Hohenberg and W. Kohn, *Phys. Rev. B* **136**, B864 (1964).

15th Int. Symp. “Nanostructures: Physics and Technology”
Novosibirsk, Russia, June 25–29, 2007

MOVPE growth and characterization of ZnCdS/ZnSSe QW structures

V. I. Kozlovsky, V. I. Kuntsevich, V. P. Martovitsky, D. A. Sannikov and D. E. Sviridov
P. N. Lebedev Physical Institute, Leninsky pr. 53, 119991 Moscow, Russia

Abstract. ZnCdS/ZnSSe heterostructures, ZnCdS/ZnSSe SQW and MQW structures were grown by metal-organic vapour-phase epitaxy (MOVPE) on GaAs substrates at 400–425 °C. Strong short-wavelength shift of the interface emission line (up to 200 meV) with increasing electron beam current density and QW thickness was observed in low-temperature cathodoluminescence (CL) spectra. By CL method and X-ray diffraction analysis it has been found that $Zn_xCd_{1-x}S$ composition of the epilayers or the QW layers changes with distance from the ZnCdS/ZnSSe interface, x being about 0.4 near the interface with weak dependence on Zn/Cd relation in gas phase.

Introduction

CdS/ZnSe II-type heterostructures are of interest last time because of their rather high conduction band offset with about 0.8 eV [1]. Such a heterostructure shows remarkable luminescence properties depending on interface design. A possibility of two-dimensional electron gas formation may be a basis of using such heterostructures in high electron mobility transistors [2]. Intersubband transitions in the (CdS/ZnSe)BeSe system have attracted much attention due to their potential for applications to ultrafast photonics devices [3]. Starting from the CdS/ZnSe system, here we concentrated on MOVPE growth of ZnCdS/ZnSSe heterostructures and study their luminescence properties.

These heterostructures may be used as active layers of electron beam pumped lasers. Such lasers are promising as monochromatic light sources for display applications. All layers of the ZnCdS/ZnSSe MQW structure may be matched to GaAs substrate. Such a structure is potentially unstrained. The internal stress as one of driving forces of degradation processes in ZnCdSe/ZnSe lasers will be absent in the ZnCdS/ZnSSe structures. However the II-type of band alignment in this structure may be a problem to achieve high optical gain.

1. Experimental

Single and multi quantum well heterostructures were grown by MOVPE on the GaAs substrates misoriented by 10° from (001) to $(111)_A$ plane. The ZnSSe buffer, barrier and cap layers were practically matched to GaAs. Their thickness was 100–200 nm. The QW thickness varied from 3 to 15 nm. The Zn content in QWs was up to 50%. The ZnCdS/ZnSSe heterostructure without any cap layer and periodic 47 ZnCdS/ZnSSe QW structure with total thickness of 5 μm was grown also. The growth runs were carried out at hydrogen atmospheric pressure in a custom built horizontal quartz reactor with optical window for *in situ* reflectometry control of the layer thickness and roughness. $ZnEt_2$, $CdMe_2$, Et_2S and Me_2Se were used as precursors. The growth temperature was 400–425 °C. As-grown structures were studied by cathodoluminescence (CL), X-ray diffraction and atom force microscopy (AFM) techniques.

2. Results and discussion

The dependence of the average lateral force signal on structure depth was presented in Fig. 1. It is the result of AFM image processing. The 0.7×0.7 μm scan of the cleaved surface of the 47 ZnCdS/ZnSSe QW structure was made in the lateral force (LF) mode. The LF signal was averaged along the QW direction. The QWs are displayed as sharp peaks in Fig. 1. The ZnCdS QW thickness was about 5 nm while the ZnSSe barrier thickness was about 100 nm.

The low-temperature CL spectra of the two different heterostructure containing the bulk (40 nm) ZnCdS layer on the ZnSSe buffer are presented in Fig. 2 at different electron beam current densities from 10^{-6} to 10^{-1} A/cm^2. The spectra consist of the line near 440 nm due to the ZnSSe layer emission, the line ($\lambda_{max} \approx 455$ and 475 nm for different structures) due to the bulk ZnCdS layer and the line which maximum shifts to short-wavelength side with increasing the current density. We interpret this last line as ZnCdS/ZnSSe interface emission. Intensity of this emission increases strongly with increasing excitation level in some samples. Note that the spectral range of the interface emission is practically the same for two samples with ZnCdS composition being different far from the interface. The X-ray analysis of the MQW structures displays that the Zn content in the $Zn_xCd_{1-x}S$ QWs is close to $x = 0.4$. This composition is matched to GaAs. It means that the ZnCdS composition near the interface changes weak with changing Zn/Cd relation in gas phase but is determined by the crystal lattice of the ZnSSe (GaAs) layer.

In Fig. 3 the CL spectra of different SQW structures were presented at two different current densities. We intend to grow pure CdS QW layers in these structures. However the X-ray analysis and CL measurements found that these layers really

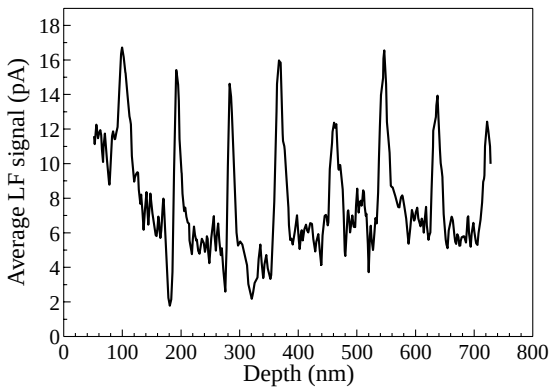

Fig. 1. Average lateral force (LF) signal depending on MQW structure depth. The LF scan was made from a cleaved surface by AFM. Averaging was fulfilled along the QW direction.

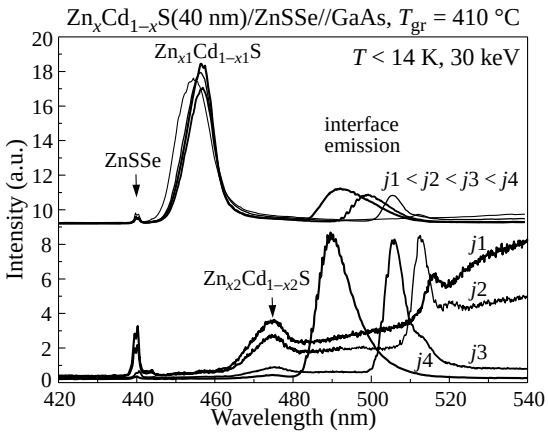

Fig. 2. CL spectra of two different ZnCdS(40 nm)/ZnSSe heterostructures at $T \approx 14$ K, $E_e = 30$ keV and different current densities from 10^{-6} ($j1$) to 10^{-1} A/cm^2 ($j4$).

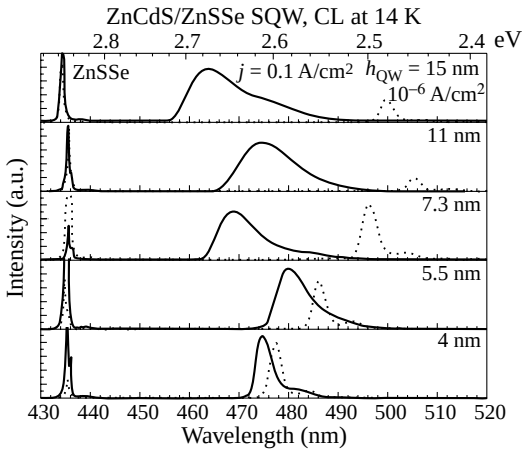

Fig. 3. CL spectra of ZnCdS/ZnSSe SQW structures with different QW thickness at $T \approx 14$ K, $E_e = 10$ keV and two current densities 10^{-6} and 10^{-1} A/cm^2.

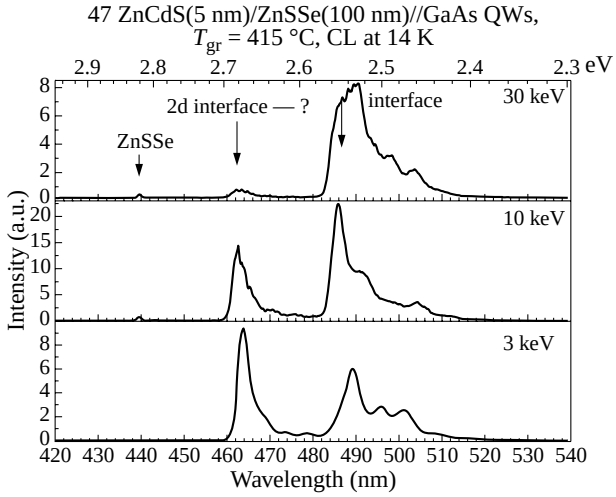

Fig. 4. CL spectra of the 47 ZnCdS(5 nm)/ZnSSe(100 nm) QW structure at $T \approx 14$ K, $j = 10^{-6}$ A/cm^2 and $E_e = 3, 10, 30$ keV.

contain Zn of some concentration. As seen from Fig. 3 the short wavelength shift of interface emission line depends strongly on the QW thickness h_{QW}. The maximum shift was as high as 200 meV for $h_{QW} = 15$ nm while the shift is only 13 meV at 4 nm. The shift is determined by a formation of internal electric field by a space separation of nonequilibrium electrons and holes due to the II-type band offset. The 28 meV shift was observed at $h_{QW} = 4.5$ nm and optical excitation of practically the same excitation levels [1]. This value is close to those we observe at $h_{QW} = 4$ and 5.5 nm. However, the emission line maximum of our structures at low excitation level is 2.55–2.6 eV that is different from 2.06 eV in [1]. This is additional argument of high Zn content attendance in thin QWs. Then long wavelength shift of the emission line at low excitation level with increasing h_{QW} may be ascribed to a decrease of Zn entering in QW layer during the growth. If it is true then the triangular shape QW is formed and electrons recombine with holes at the second interface preferably. At higher excitation levels the QW is filled by electrons, average electron density displaces to the first interface, overlapping of electron and hole wave functions decreases and recombination time becomes higher. As a result, higher electron concentration is achieved in thicker QWs at the same excitation level.

Fig. 4 shows the CL spectra of the 47 ZnCdS/ZnSSe QW structure at different electron energies E_e. The spectra consist of weak emission line due to the ZnSSe barrier layers and two structured lines with maxima at 462–464 nm and 486–490 nm. The relative intensity of the short wavelength line decreases with increasing E_e from 3 to 30 keV. At that the electron penetration depth increases from about 0.03 to 2.3 μm. We relate this intensity decrease to high absorption of the structure in 460–485 nm range. The observed structure of these lines is due to the interference of the light rays reflected from the structure surface and the GaAs-ZnSSe interface. Besides the lines have LO-phonon replicas seen in Fig. 3 at low-level excitation. We relate both lines to emission due to ZnCdS/ZnSSe interfaces, one to the first interface and other to the second interface. If the ZnCdS composition changes in the QW weakly, electrons recombine with holes on both interfaces.

Acknowledgements

We thank P. I. Kuznetsov for useful consultation on MOVPE. The work was supported by RFBR (grants 05-02-16390, 07-02-01139), the program "Scientific Schools of Russia" (grant 6055.2006.02), the programs of basic research of RAS and Educational Scientific Facility of P. N. Lebedev Physical Institute.

References

[1] H. Priller *et al*, *phys. stat. sol.* (c) **1**, 747 (2004).
[2] M. Dremel *et al*, *Appl. Phys.* **93**, 6142 (2003).
[3] R. Akimoto *et al*, *Appl. Phys. Lett.* **81**, 2998 (2002).

15th Int. Symp. "Nanostructures: Physics and Technology"
Novosibirsk, Russia, June 25–29, 2007

Swift heavy ion track-based nanostructures in SiO_2/Si system for spintronic applications

V. V. Malyutina-Bronskaya[1], J. A. Ivanova[2], D. K. Ivanou[2], E. A. Streltsov[2], A. K. Fedotov[2], A. V. Petrov[3], S. E. Demyanov[3] E. Yu. Kaniukov[3] and D. Fink[4]

[1] Institute of Electronics, NAS Belarus, Minsk, Belarus
[2] Belarusian State University, Minsk, Belarus
[3] Joint Institute of Solid State and Semiconductor Physics, NAS Belarus, Minsk, Belarus
[4] Hahn-Meitner-Institute, Berlin, Germany

Abstract. The swift heavy ion track technology is used for creation of new types of magnetic-field-sensitive spintronic structures on the base of SiO_2/Si system. A "TEMPOS" ("Tunable Electronic Material with Pores in Oxide of Semiconductors") concept is used for the preparation of these structures. First samples of the structures with ion tracks (pores) in the SiO_2 layers, filled with metallic nanoparticles were created and their investigations have been started.

Introduction

At present an intensive search for the new technologies, which makes it possible to lower the dimensions of electronic devices down to the nanometric size range, takes place worldwide. On this concern, an interest to the development of non-traditional technologies of formation of nanomaterials, nanostructures and their arrays, increases. In this way, here is used the so called swift heavy ion track technology which is connected with formation of narrow trails of radiation damage ("latent ion tracks") as a result of the high-energy ions impact. Further, by means of the chemical etching of latent tracks, pores of various forms and dimensions (typically 10 to 1000 nm), depending on irradiation parameters, etching conditions and substrate type, are formed. Later on, functional elements for nanoelectronics can be created on the base of these structures [1].

1. Expected properties and preparation of the SiO_2/Si-based nanostructures

New types of spintronic materials and structures, which can be used in magnetoresistive sensors, motion detectors, memory devices, etc., are of a special interest for industry at present. For the creation of such devices, one need to use the structures containing magnetic nanoparticles and their alternating layers, having giant magnetoresistance or tunnel magnetoresistance, and being able to function at high frequencies. The elaboration of the swift heavy ion tracks technology should be quite prospective for this sake. Therefore, goal of the present research is to develop and create the new types of magnetic-field-sensitive spintronic structures on the base of the etched ion tracks in silicon oxide, inside of which homogeneous nanocompositions or multilayered structures with alternating layers of ferromagnetic (Ni, Co, Fe) and non-magnetic (Cu, Ag, Se, $A_{II}B_{VI}$ and $A_{IV}B_{VI}$) nanoparticles. For the creation of these structures, it is planned to use the "TEMPOS" ("Tunable Electronic Material with Pores in Oxide of Semiconductors") concept, which has been developed earlier at the Hahn-Meitner-Institute (Berlin, Germany) and the University of Hagen (Germany). According to this concept [1–3], the structure used in our research consists of the following components: (1) a n- or p-doped silicon wafer, (2) a SiO_2 layer on top of the silicon wafer, (3) very narrow conducting connections traversing the whole dielectric layer, thus connecting top and bottom (etched ion tracks, filled with metallic nanoparticles), and (5) three electrical contacts, two of them being on the top of the sample and one of them being on its back side (Fig. 1). The "TEMPOS"-concept is used for the creation of MOS-type structures, having non-linear I/V characteristics, and in this number, with negative differential resistance, which is important for the present research.

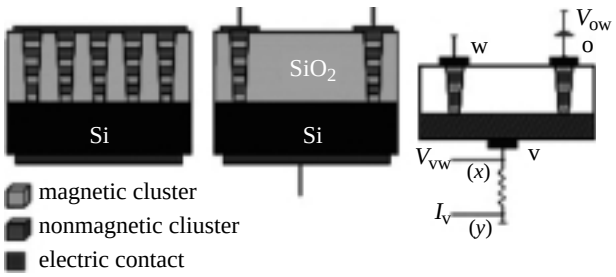

Fig. 1. A sketch of the preparation and measurement of "TEMPOS"-type structures on the base of SiO_2/Si system with etched swift heavy ion tracks.

Following steps in realization of the described above research concept have been already taken by us. First, the samples of SiO_2/n-Si and SiO_2/p-Si have been prepared by a standard technology of Si thermal oxidation at 1100 °C during 10 hours, and SiO_2 layer thickness was 0.7 μm. Then, the obtained samples were irradiated with $^{197}Au^{26+}$ having energy 350 MeV and fluence 5×10^8 cm^{-2} at the "Ion Beam Laboratory" Center of the Hahn-Meitner-Institute. During the next stage of the research realization, the latent ion tracks, formed in the SiO_2 layer after irradiation, have been etched with fluoric acid (HF) with concentrations 1.35 wt.% 2.7 wt.% during 40 min. and 20 min. correspondingly. As a result, stochastically placed conical pores, reaching the Si layer, having diameters 250 nm and height 200 nm, have been formed. Further on, the method of underpotential electrochemical deposition, developed at the Chemistry Department of the Belarusian State University, is used for the deposition of metallic nanoparticles [4]. Due to precise measurements of current flowing in an electrochemical cell, this method provides a highly effective control of thickness, stoichiometric composition and grain dimensions of deposited substances, and can also provide a high purity of deposited metals and semiconductors. The electrochemical deposition of metals and semiconductors to form a

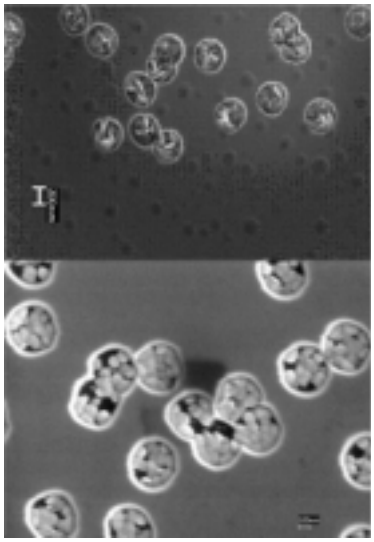

Fig. 2. SiO_2/Si structures with Cu (upper part of the figure) and Ni (lower part of the figure) nanoparticles in the etched swift heavy ion tracks in SiO_2 layer.

multicluster/multilayered structure is conducted at relatively low temperatures, which diminishes a possibility of interdiffusion of different components in heterostructures. In this way, the first samples with Cu and Ni nanoparticles deposited in the pores in SiO_2 were prepared (Fig. 2), and their microscopic and electrical-physical investigations have been started by our group.

References

[1] D. Fink, A. Petrov *et al*, *Nucl. Instr. Meth.* **218**, 355 (2004).
[2] A. V. Petrov, D. Fink *et al*, *Proc."Nanostructures: Phys. Technol."*, St Petersburg, Russia, 318 (2004).
[3] D. Fink, D. Sinha *et al*, *Proc."Nanomeeting"*, Minsk, Belarus, 474 (2005).
[4] D. K. Ivanou, E. A. Streltsov *et al*, *Thin Solid Films* **490**, 154 (2005).

15th Int. Symp. "Nanostructures: Physics and Technology"
Novosibirsk, Russia, June 25–29, 2007

Influence of quantum size effects on complex dielectric susceptibility function of GeO_2 films with Ge nanoclusters: spectral ellipsometry studies

D. V. Marin, E. B. Gorokhov, A. G. Cherkov, A. G. Borisov and V. A. Volodin
Institute of Semiconductor Physics of SB RAS, pr. ak. Lavrentjeva 13, Novosibirsk 630090, Russia

Abstract. The developed more accurate many-angle and many-thickness approaches for scanning and spectral ellipsometry were used to measure refraction and absorption coefficients of GeO_2 films with Ge nanoclusters. The applied technology of deposition of the films from oversaturated GeO vapor with decomposition of germanium monoxide allow to know exactly molar ratio Ge to GeO_2 in the films as 1 to 1. It allows us to calculate complex dielectric susceptibility, and, consequently, refraction and absorption coefficients of the films using Bruggeman model. One can affirm, that, the observed significant difference between the measured and the calculated data is caused by influence of quantum size effects.

Despite of great efforts in study of Si quantum dots (QDs) in SiO_2 to find very promising applications in optoelectronic and nano-scaled memory devices, the very-matched Ge QDs in GeO_2 heterosystem is poorly known. But some properties of last system allow considering it as perspective for the applications. For studying of quantum-size effects for semiconductor QDs in dielectric matrix one need precise, not destructive and express methods. This work is an attempt to develop such method, mainly based on ellipsometry and, for control using Raman scattering spectroscopy and high resolution transmission electron microscopy (HRTEM).

The original technology of deposition of Ge:GeO_2 films from GeO supersaturated gas flow was developed. The technology has some advantages for band gap engineering approach. Usually, there is a problem to define volume ratio between QDs and matrix in heterostructures. Our heterostructure have remarkable property — due to (2GeO(solid) $\rightarrow$ Ge+GeO_2) growth procedure it has molar ratio between Ge and GeO_2 as 1:1, independently on growth condition [1]. So, the volume part of c-Ge or a-Ge clusters is $\sim 30,7\%$. So, the average distance between QDs is about $\sim 1/2$ of QD diameter. Thermal budget of deposition is relatively low ($T < 600\,^{\circ}$C). Homogeneity of films is very high; films with thickness from several nm up to micron can be deposited. Varying the gas flow and substrate temperature one can controllable change the average size and phase composition of Ge clusters. Using proposed ex-situ treatments one can change not only the QDs, but also the matrix structural parameters (like barriers width and height).

Raman spectra were taken at room temperature using double spectrometer DFS-52 equipped with cooled photo electron amplifier with pulse counting electronics and Ar laser as a pump (wavelength is equal to 514.5 nm). Quasi-backscattering geometry was used with angle of light falling equal to Brewster angle. The incident light was linearly polarised, polarization of scattered light was not analysed. The study of structure of the films was carried out using high-resolution electron microscope JEOL-4000EX. The using voltage was equal to 250 keV, the spatial resolution was equal to 0.19 nm.

The Ge nanoparticle phase composition and sizes Ge nanocrystals were estimated from Raman spectra. The ratio c-Ge/a-Ge ($\mathbf{f}_{a-Ge}/\mathbf{f}_{c-Ge} = \gamma(l)$) can be measured from Raman spectra from ratio of integral intensity of amorphous peak (275–280 cm^{-1}) and nanocrystal-peak (300 cm^{-1}). The Raman spectra were registered from different part of the Ge:GeO_2 film grown in condition of temperature and GeO concentration gradient (Fig. 2). The difference in phase composition and thickness is caused by temperature gradient and difference in GeO pressure along the flow. To estimate the sizes of Ge nanoclusters, we use the model of efficient density of folded vibration states in nanocrystals of spherical shapes. The nanocrystalline peak is narrow and its position depends on nanocrystal size (Fig. 3).

The HREM data confirm the Raman data that for used growth condition the GeO_2 films contain Ge nanocrystals with sizes from 8–9 to 5–6 nm.

The optical constant of the films were studied using scanning ellipsometry with step $\delta l = 0.5$ mm, He-Ne laser (633 nm) and the results were interpreted using described method and specially developed algorithm [2]. We can find on the films the area with almost constant thickness and optical constant for wavelength 633 nm. These areas were used for studies by spectral ellipsometry.

Spectral dependence of refraction and absorption coefficients from diameter of Ge nanoclusters $n(D)$ and $k(D)$ can give useful information about the quantum size effect influence. But usually, the accuracy of measurement of n and k is not enough to reveal this influence for all spectral diapasons.

Original special approach for many-angle, many-thickness

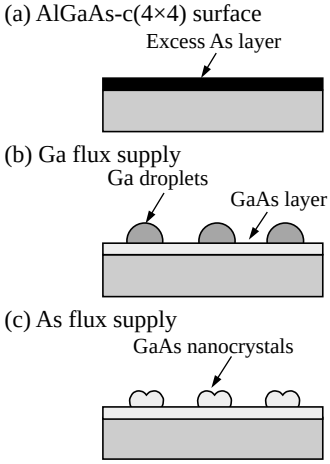

Fig. 1. Scheme of growth reactor.

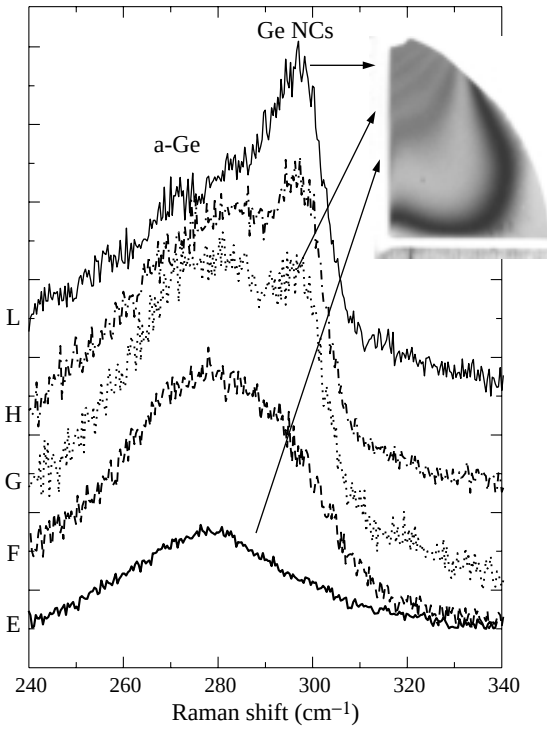

Fig. 2. Raman spectra from different parts of a Ge:GeO_2 film.

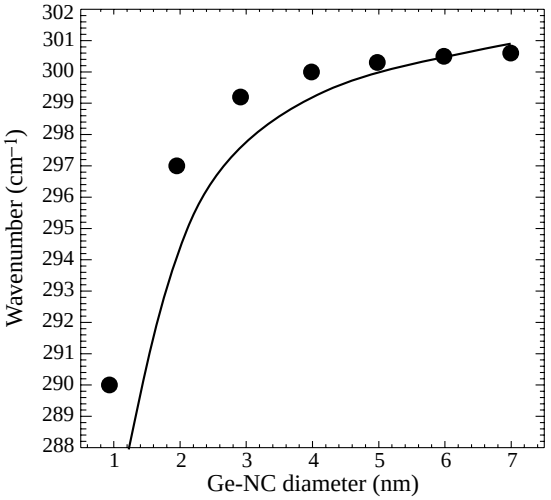

Fig. 3. Dependence of Raman scattering peak for opticl phonons localized in Ge nanocrystals versus its diameter.

spectral (250–800 nm) scanning ellipsometry was developed. The developed mathematical approach allows measuring the ellipsometry data with an order of magnitude better accuracy, comparing in the case of measuring in one point (not scanned by wedge). The accuracy worsens if the ellipsometryy nomogramms pass close to each other. But changing the wavelength one can shift in the area of good accuracy. On the film with different thickness $h(l)$ but almost identical $n(l)$ and $k(l)$ one can chose the area of good accuracy for spectral measurements for any given spectral region. In this area the spectral ellipsometry angles $\Psi(h)$ and $\Delta(h)$ can be measured with high accuracy, and, consequently, one can get n and k with high accuracy for all spectral diapasons.

Knowing spectral dependencies of $n(l)$ and $k(l)$ for pure

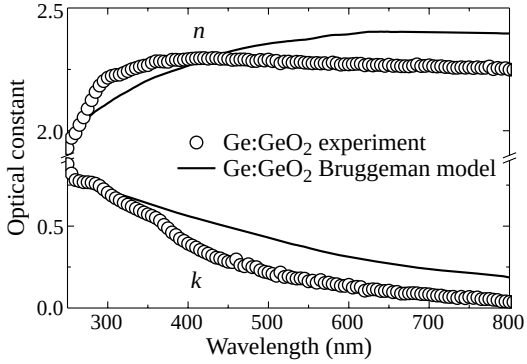

Fig. 4. Calculated from for Bruggeman model (without taking into account quantum size effect) and experimental data for n — upper curves and k — bellow curves.

GeO_2 (media a) and for crystal Ge (c-Ge) and amorphous Ge (a-Ge) (media b) and also volume ratio of Ge (f_b Ge$\sim 30,7\%$), one can calculate from Bruggeman model $n(l)$ and $k(l)$ for Ge:GeO_2 hetero-films:

$$0 = f_a \frac{\varepsilon_a - \varepsilon}{\varepsilon_a + 2\varepsilon} + f_b \frac{\varepsilon_b - \varepsilon}{\varepsilon_b + 2\varepsilon}.$$

In our case $f_a = \text{const} = 0.693$, $f_b = \text{const} = 0.307$. One can calculate real and imaginary parts of dielectric permittivity ε from n and k. The difference in calculated (for a-Ge) and experimentally measured data is easily seen (Fig. 4) and is supposed to be due to quantum size effect, because in Bruggeman model this effect is not taken into account. Due to enhanced accuracy it was possible to find the influence of quantum size effects in Ge QDs on optical properties of hetero-films.

The difference is qualitative clear, the experimental absorption in long-wave region is lower than the calculated absorption. Even for amorphous Ge nanoclusters, the quantum size effects lead to broadening of optical gap in absorbance. For quantitative analysis the well known theoretical models (for example Penn model) are planned to use in future. It should be noted, that early influence of quantum size effect on photoluminescence properties of the GeO_2 films with Ge nanoclusters was observed [1].

So, the use of scanning ellipsometry methods (with analytical interpretation and calculations based on Bruggeman model) consequently with using of HREM and Raman data allows us to obtain experimental evidence of the quantum-size effect on optical properties of heterostructure Ge:GeO_2. Broadly speaking, the developed methods can be applied for study of others heterostructures like semiconductor QDs in dielectric matrix.

References

[1] E. B. Gorokhov *et al*, *12th International Symposium "Nanostructures: Physics and Technology"*, St Petersburg, Russia, 310–311 (2004).

[2] E. B. Gorokhov *et al*, *14th International Symposium "Nanostructures: Physics and Technology"*, St Petersburg, Russia, 170–171 (2006).

15th Int. Symp. "Nanostructures: Physics and Technology"
Novosibirsk, Russia, June 25–29, 2007

Intervalley deformation potentials in $(AlAs)_n(GaAs)_m(001)$ superlattices

S. N. Grinyaev, *L. N. Nikitina* and V. G. Tyuterev
Tomsk Polytechnical University, Tomsk State University, Tomsk, Russia

Abstract. Intervalley electron scattering by phonons in $(AlAs)_n(GaAs)_m(001)$ superlattices is studied using the pseudopotential method and a phenomenological model of the bonding forces. The deformation potentials between the conduction band extrema of superlattices involving short and long-wavelength phonons are calculated. Is shown that due to quantum size effects the mixing of states from the zinc-blende L of valleys plays a greater role in intervalley scattering in superlattices than $\Gamma - X$ mixing. Thereof the superlattice transitions $\Gamma_1 - X_1$, $\Gamma_1 - X_3$ with participation of a symmetric state in a quantum L-well being analogs zinc-blende states $\underline{\Gamma} - \underline{L}$ of transitions, have major intensity, than analogs $\underline{\Gamma} - \underline{X}$ of transitions ($\Gamma_1 - M_5$, $\Gamma_1 - \Gamma_3$). United on phonons and averaged on related valleys the deformation potentials in superlattices are compounded with the relevant potentials in solid solutions, but for the lower states all transitions in superlattices are more intensive because of localization of wave functions in quantum wells.

Intervalley scattering of electrons on phonons plays the important role at tunneling electrons in multilayer structures, relaxation of photoexcited carriers, resonant Raman scattering, hot electron photoluminescence etc. [1,2]. In superlattices due to quantum-confinement effects are accompanied by the essential reconstruction of electronic and phonon spectrums, there appear new type of interface states and addition scattering channels. As a result electron-phonon interaction in superlattices has composite character with specific features caused by mixing of zinc blende states.

To date, scattering of electrons on phonons in superlattices has been investigated theoretically mainly for a case of long-wavelength polar optical vibrations; the scattering by short-range deformation potential has been studied only by the wave-function envelope method [2] for superlattices GaAs/AlAs (001) with rather thick layers (>5 nm). The study of similar scattering in the thinlayer's superlattices and establishment of dependences of the parameters an electron-phonon interaction from their composition and thickness of layers represents considerable interest. For this purpose it is more preferably to use the microscopic description of crystalline potential and vibration of atoms.

In this paper, the study of the features of a electronic-phonon scattering in the ultrathin superlattices $(AlAs)_n(GaAs)_m$ ($n + m = 4$) and relevant composition alloys is presented.

Intensity of intervalley scattering of electrons from an initial state $|\mu k\rangle$ (μ — is the band number, k — is the wave vector) to the final state $|\mu' k'\rangle$ is determined by deformation potentials as:

$$\left|D^s_{\mu k,\mu' k'}\right|^2 = \left|\sum_{i,\alpha}\left(\frac{M}{m_\alpha}\right)^{1/2}\left(e^\alpha_i(s,k-k')\cdot d^\alpha_i(\mu k,\mu' k')\right)\right|^2,$$

where m_α and M — mass of α-th ion and unit cell, $e^\alpha_i(s,k)$ — a vector of polarization (s — number of a phonon branch, $i = x, y, z$), d^α_i — matrix element of gradient of atom potential in functions of initial and finale states.

The calculation of deformation potentials was carried out such as [3]. The quantum size effects lead to composite multivalley character of a conduction band and 4 multiple number of phonon branches in superlattices in comparison with binary compounds.

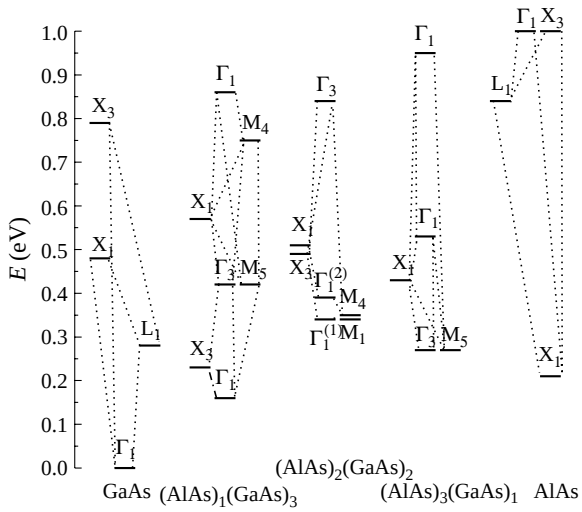

Fig. 1. The scheme of levels in the conduction bands GaAs, AlAs and superlattices.

The electronic states of superlattices are originated from hybridization of virtual crystal states of the relevant alloy compositions. The especially appreciable changes arise in states that undergo large offsets at the heterointerfaces. It happens for the states related to the $\underline{\Gamma}_1$ and $\underline{L}_1$ zinc blende valleys (here and in what follows, zinc blende states are underlined), since a GaAs layer is a rather deep quantum well for the $\underline{\Gamma}_1$ states ($\sim$ 1 eV deep) and $\underline{L}_1$ states (0.56 eV deep).

In a conduction band of superlattices arise the competing valleys (Γ_1, Γ_3, M_5, X_3, X_1) with close energies. The bottom of conduction band in a superlattice $(AlAs)_1(GaAs)_3$ is corresponding to state originated from Γ_1 virtual crystal state $Al_{0.25}Ga_{0.75}As$. In superlattices $(AlAs)_2(GaAs)_2$ and $(AlAs)_3(GaAs)_1$ central (Γ_1) and lateral (M_5) of a valley the close energies have and occur from Γ zinc blende states $Al_{0.5}Ga_{0.5}As$ and $Al_{0.75}Ga_{0.25}As$ accordingly.

The scheme of levels in the conduction bands GaAs, AlAs and superlattices relative to bottom of conduction band GaAs ($\underline{\Gamma}^c_1$) is shown in Fig. 1. By dashed lines are designated possible intervalley transitions relevant $\underline{\Gamma} - \underline{X}$, $\underline{\Gamma} - \underline{L}$, $\underline{X} - \underline{X}$, $\underline{L} - \underline{L}$, $\underline{X} - \underline{L}$ to transitions in binary crystals The most intensive scattering between these valleys occurs with a participation of phonons of

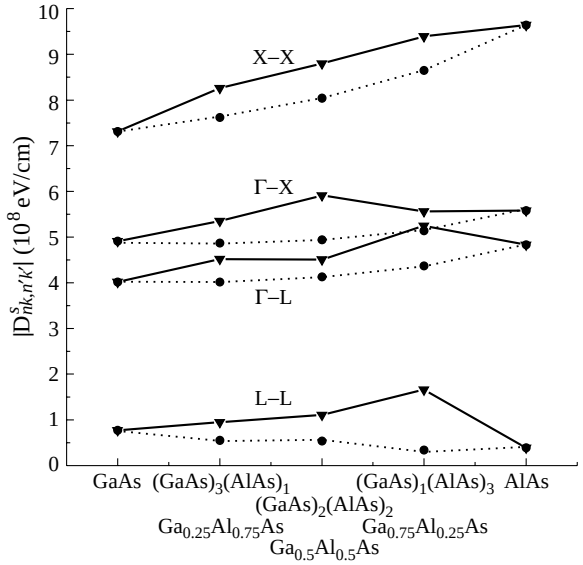

Fig. 2. The averaged intervalley deformastion potentials in superlattices and corresponding potentials alloys.

symmetry M_5, X_1, X_3. Channels of scattering $\Gamma_1 - M_5$, $\Gamma_1 - X_1, \Gamma_1 - X_3, X_1 - X_1, X_1 - X_3, \Gamma_3 - M_5$ basically are connected with oscillations of cations, and channels of scattering $X_1 - M_5$, $X_3 - M_5$, $\Gamma_3 - X_1$, $\Gamma_3 - X_3$ are connected with oscillations of As.

The potentials for transition involving various phonons are given in the Table 1. The intervalley scattering of electrons in a numbers of alloys (dashed lines) and relevant by them average on related electronic transitions in superlattices (continuous lines) is shown in Fig. 2.

As follows from the received results, in intervalley scattering of superlattices the mixing L zinc blende states by potential tetragonal compound plays in more essential role, than mixing Γ and X states. Therefore superlattice transitions $\Gamma_1 - X_1$ and $\Gamma_1 - X_3$ which related to zinc blende $\underline{\Gamma} - \underline{L}$ transition would have most intensity than analogs $\underline{\Gamma} - \underline{X}$ transition ($\Gamma_1 - M_5$, $\Gamma_1 - \Gamma_3$). The greatest intervalley scattering constants in superlattices answer transitions $\Gamma_3 - M_5$, $M_5 - M_5$ and are related to $\underline{X} - \underline{X}$ deformation potentials. The long-wave optical vibrations with symmetry Γ_1 participate in direct transitions $\Gamma_1^{(1)} - \Gamma_1^{(2)}$ and $\Gamma_1 - \Gamma_3$ which corresponding with short-wave zinc blende $\underline{X}-$phonon.

Fig. 2 shows that the intervalley scattering in superlattices are more intensively of scattering in the respective alloys. Analogs of the $\underline{\Gamma} - \underline{L}$, $\underline{\Gamma} - \underline{X}$ and $\underline{L} - \underline{L}$ transitions depend on composition not monotonously as result of the localization of wave functions in enough deep $\underline{\Gamma}$ and $\underline{L}$ quantum wells.

In conclusion, due to close arrangement of competing valleys and increased values of intervalley deformation potentials a superlattice $(AlAs)_1(GaAs)_3$ is of interest as material for development Gunn's generator. In pseudodirect superlattices $(AlAs)_2(GaAs)_2$ and $(AlAs)_3(GaAs)_1$ intensive intervalley transitions $\Gamma_1 - M_1$, $\Gamma_1 - M_4$, $\Gamma_3 - M_5$ should give in amplification of optical absorption. The deformation potentials obtained can be used to simulate the transport and optical properties of heterostructures and superlattices GaAs/AlAs (001) with the account of two basic mechanisms of a scattering of electrons on interfaces and phonons.

Table 1. Intervalley deformstion potentials in superlattices $(AlAs)_n(GaAs)_m$, (10^8 eV/cm).

Transition	$n = 1, m = 3$	$n = 2, m = 2$	$n = 3, m = 1$
$\Gamma_1 - M_5$	5.35	5.91	5.56
$\Gamma_1 - \Gamma_3$	5.12	5.15	3.49
$\Gamma_3 - M_5$	8.26	8.80	9.39
$M_5 - M_5$	8.30	4.06	9.23
$\Gamma_1 - X_3$	5.56	4.75	5.28
$\Gamma_1 - X_1$	3.15	3.71	5.21
$X_3 - X_3$	0.73	0.92	2.38
$X_1 - X_1$	1.21	1.08	1.77
$X_1 - X_3$	0.90	1.21	1.07
$X_3 - X_1$	0.90	1.21	1.07
$X_1 - M_5$	3.85	4.17	4.16
$X_3 - M_5$	4.33	3.96	3.93
$\Gamma_3 - X_1$	3.82	4.44	4.55
$\Gamma_3 - X_3$	4.53	3.95	3.84

Acknowledgement

The work was supported by grant of RFBR No. 06-02-16627.

References

[1] Z. S. Gribnikov, O. E. Raichev, *Fiz. Tekh. Poluprovodn.* **23**, 2171 (1989); O. E. Raichev, *Fiz. Tekh. Poluprovodn.* **25**, 1228 (1991); I. A. Akimov, V. F. Sapega, D. N. Mirlin, V. M. Ustinov, *Physica E* **10**, 505 (2001).

[2] O. E. Raichev, *Phys. Rev. B* **49**, 5448 (1994).

[3] L. N. Nikitina, S. N. Grinyaev, V. G. Tyuterev, *Phys. Solid State* **48**, 129 (2006).

15th Int. Symp. "Nanostructures: Physics and Technology"
Novosibirsk, Russia, June 25–29, 2007

Meniscus in AFM based nanolithography

E. A. Sergeeva[1], D. V. Sheglov[2] and A. V. Latyshev[2]

[1] Novosibirsk State University, 630090 Novosibirsk, Russia
[2] Institute of Semiconductor Physics, SB RAS, 630090 Novosibirsk, Russia

Abstract. Atomic force microscope has been applied to investigate the role of water meniscus on AFM tip-induced local anodic oxidation at ambient condition. The number of parameters such as applied voltage, relative humidity, tip-surface press force was under consideration. The peculiarities of meniscus formation were investigated in frame of optimizing of AFM tip-induced local anodic oxidation. Some examples of nanostructures fabrication are demonstrated.

Introduction

There are various approaches of SPM probe for nano-scaled modifications of semiconductor and metal surfaces, for example, anodic selective oxidation [1–6]. The potential possibilities of AFM for lithography and fabrication of low-dimensional structures for nanoelectronics and nanomechanics are not realized completely in spite of large number of publications in that field.

This work demonstrates some results about optimizing of tip-induced local anodic oxidation of the semiconductor and metal films at the atmospheric condition via determination of the water meniscus role in this process.

1. Experimental

The AFM experiments are carried out with a Solver P-47H and P-47 PRO (NT-MDT) microscopes with lithography software. The both contact and semi-contact modes were realised at ambient conditions. Standard silicon cantilevers ($\nu = 150-450$ kHz) and ones with conductive covering were used for imaging and lithography by AFM. An applying electric potential (± 10 V) on conductive AFM-tip with variation of potential pulse from 10 to 1000 ms was used for local anodic oxidation. The sample holder has a contact pad to connect the sample to electric wires of the microscope. Only standard cleaning treatments to the sample were used. Wet-chemical etching procedure did not apply to the sample because it can effect on tip-sample interaction. All experiments were carried out at the room temperatures.

The sample, a plate $0.3\times1\times8$ mm^3 in size, was cut from a silicon wafer with a misorientation angle of less than 1° from a (111) plane. The sample has been cleaning at temperature 1200 °C in UHV chamber and after cleaning procedure the silicon surface contains system of equidistantly distributed monatomic steps 0.31 nm in height. Sample was evacuated from ultrahigh vacuum chamber and was investigated by AFM technique at atmospheric conditions. To minimize noise contribution of external electromagnetic fields on the image formation during scanning, the AFM apparatus used for these studies has been placed in side of a metal box having good electric connection to the ground. For the humidity control this chamber was completed by humidity sensor and humidifier.

2. Results and discussion

The meniscus formation is one of the factors that affect the current passing through the tip-sample junction during local anodic oxidation. The high density of current requires a careful design of the experiments, especially control of meniscus geometry. It is known fact, that AFM tip-induced oxidation is characterized by the extra growth of the oxide at initial point of oxidation. This is speaking that it is the one of main factors of oxidation process optimizing consists of the initial meniscus form control. In the following, we describe an experimental procedure to measure meniscus geometry with and without any electrical potential and field during contact forming. Measurements are performed by acquiring simultaneously measurements of the cantilever deflection and the applied to it potential (i.e. the simultaneous acquisition of a force-versus-distance curve and a determination of the applied potential). Figure 1 illustrates the cantilever impact height via relative humidity for approach and remove. The AFM tip first approaches and then retracts from the substrate.The Figure 1 shows the cantilever curve or force dependence via relative humidity as for mutual approaching as for their recession. Simple calculation shows the abnormal high meniscus force at the retracting process. We speculate that this fact is founded on spontaneous extra damping of large area of cantilever and initiating of process spontaneous capillarity diffusion for water.

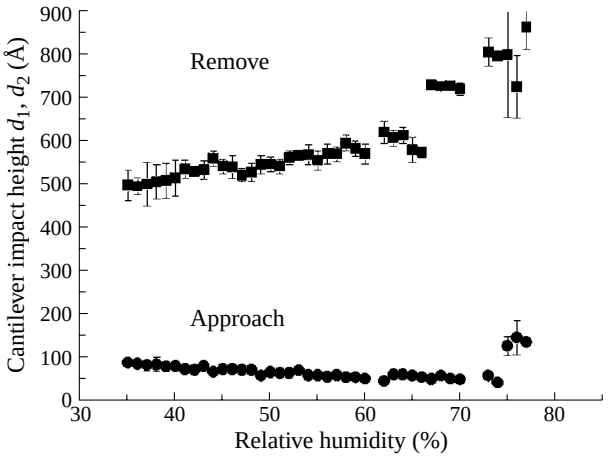

Fig. 1. The cantilever impact height via relative humidity for approach and remove.

We investigate the force curve dependence on electrical potential too. Figure 2 shows the cantilever impact to the surface height via relative humidity for approach under different applied potential. The applied potential increases the tip-sample impact distance and this fact agreements our speculation about spontaneous capillarity diffusion as one of the critical mechanisms for meniscus formation. It was founded that Coulombian field perfectly determines low of tip-sample force curve and critically impact on the meniscus formation too. If we

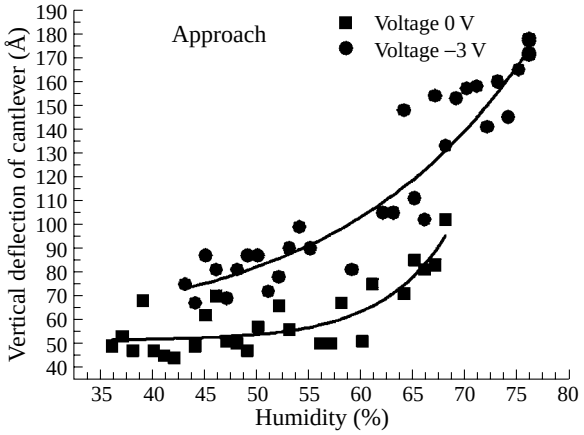

Fig. 2. The cantilever impact height via relative humidity for approach under different applied potential.

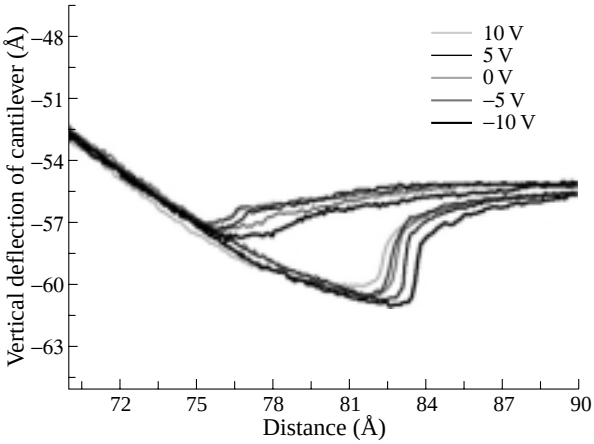

Fig. 3. The vertical deflection of the cantilever via cantilever-surface distance for different applied voltage.

firstly measure and build the cantilever vertical deflection via cantilever-surface distance for different applied voltage (Fig. 3) and then deduct from these all curves those which is obtained under zero potential, we find the effective Coulombian force which acts on the cantilever during approach and remove processes. Figure 4 shows the comparison of that effective force with model Coulomb order curve (dots). It is clear that the increasing of applied potential brings to increasing of tip-sample interaction longitude.

3. Conclusion

We have shown that the meniscus geometry can be analyzed by the simultaneous acquisition of cantilever deflection and electrical potential under condition of various humidity, when approaching and retracting the tip from the surface under the application of a constant voltage.

It has been shown that, the meniscus force is abnormal high at the retracting process that may speak about spontaneous extra damping of large area of cantilever.

We find the effective Coulombian force which acts on the cantilever during approach and remove processes.

This information can be used to study and to optimize AFM related experiments, in special AFM based nanopatterning (like AFM induced oxidation or dip pen nanolithography).

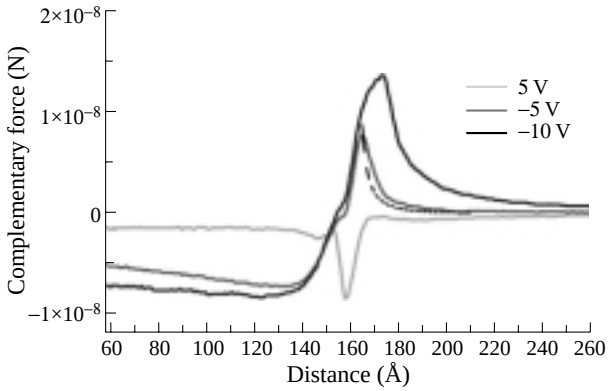

Fig. 4. The effective Coulomb force dependence on the cantilever height due to surface.

Acknowledgements

We would like to acknowledge the valuable assistance in sample preparation of Mr. Kosolobov S. S. This work was partly supported by Russian Found of Basic Researches and by the programs of “Physics of Solid Nanostructures” and “Surface Atom Structures”.

References

[1] J.-I. Shirakashi, K. Matsumoto, M. Konagai, *Appl. Phys. A* **66**, 1083 (1998).
[2] D. Sarid, in: *Scanning Force Microscopy*, Oxford series in optical and imaging sciences, Oxford University Press, Oxford (1994).
[3] R. Wiesendanger, *Appl. Surf. Sci.*, **54** 271 (1992).
[4] G. Abadal, F. Peres-Murano, N. Barniol, X. Aymerich, *Appl. Phys. A*, **66** 792 (1998).
[5] W. Y. Yu *et al*, *Phys. Rev. B* **51**, 9722 (1995).
[6] C. F. Quate, *Surf. Sci.* **386**, 259 (1997).
[7] A. P. Volodin, *Instrum. Exp. Tech.* **41**, 745 (1998).

15th Int. Symp. "Nanostructures: Physics and Technology"
Novosibirsk, Russia, June 25–29, 2007

Nanostructures characterization by phase contrast of atomic force microscopy

D. V. Sheglov and A. V. Latyshev
Institute of Semiconductor Physics, SB RAS, 630090 Novosibirsk, Russia

Abstract. The phase shift of the resonant atomic force microscope (AFM) tip is studied as a velocity function during lateral moving on the surface. Lateral mechanism of phase shift forming is presented. It was found that the lateral phase shift is initiated by friction increasing during increasing of AFM tip moving velocity on the surface. The AFM lateral phase contrast imaging allows to obtain the Cu-dopant distribution on the silicon (111) surface under atmospheric condition.

Introduction

The semi-contact atomic force microscopy (AFM) mode of surface scanning allows obtaining notable progress in the surface morphology diagnostic [1]. This method is founded on the AFM tip amplitude and phase registration during it vibration on eigenfrequency and interaction with investigated surface [2]. The registration of phase shift for the vibrated tip under condition of interaction with surface was named as the phase contrast mode of AFM. Tip vibration phase shift at interaction with surface is depended on many parameters: chemical compound, hardness, absorption layer and other [3,4] and discussed in frame of the model, which assumes the main role for dissipative factor influence [5,6]. But at the present the physical orders of such phase shift is not enough clear. It makes hard the correct interpretation of achieved information about the surface [7,8]. This work is directed on AFM tip phase shift mechanism study during it interaction with surface.

1. Experimental

The AFM experiments are carried out with a Solver P-47H (NT-MDT) microscope which was completed with electromagnetic and vibro-acoustic noises reduction chamber with humidity control system. The semi-contact mode was realized at ambient conditions. Standard silicon cantilevers (150 $\pm$ 450 kHz) was used for AFM-imaging. All experiments were carried out at the room temperatures. The silicon was chosen as a model material for investigations with well-studied surface structure and morphology. The sample was cut from a silicon wafer with a misorientation angle of less than 10 from a (111) plane. Contamination free silicon surface with a system of monatomic steps was achieved by thermal annealing in home-built ultra high vacuum (UHV) chamber at high temperature. The copper were evaporated on the silicon surface from the well outgased evaporators in the UHV chamber. Sample was evacuated from ultrahigh vacuum chamber and was investigated by AFM technique at atmospheric conditions.

Particularly, the average roughness of the silicon surface with natural oxide measured by AFM was less than 0.06 nm at the area between monatomic steps. That is less than the interlayer distance for the silicon (111) plane equaled to 0.31 nm. Thereby, we can speculate that the natural oxide uniformly replicates the initial stepped surface [9].

2. Results and discussion

Remarkable that the phase contrast of AFM-image of the same area on the stepped silicon (111) surface indicates position of monatomic steps too (Fig. 1(a)). The steps are look to be smooth in AFM topography whereas steps clearly show wavelength in the phase image [10]. The both topographic and phase AFM-images don't show any other contrast on the terrace of the real surface. Direct measuring of phase shift in the points without any moving along the surface doesn't show any difference between various points of this surface area, — all measurements were equivalent (Fig. 1(b)). We speculate that only moving of AFM tip in lateral direction on the surface during its interaction can produce such type of phase shift — lateral phase shift. For inspection this hypothesis the silicon (111) surface with submonolayer copper covering was chosen as the investigated surface.

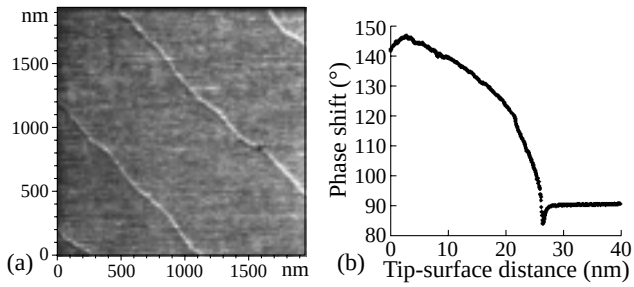

Fig. 1. Phase contrast AFM-image of the silicon (111) surface. Bright lines are monoatomic steps (a). Typical phase shift of vibrate AFM-tip at such surface in any point (b).

Early it was shown that such type of surface demonstrates good AFM phase shift variance between copper covered areas and clean ones when it was investigated by this method [11]. But measuring of phase shift on this surface at the point (without moving) doesn't show any phase shift difference between various types of surface too. Arising and increasing of AFM tip moving velocity along the surface during its interaction pro-

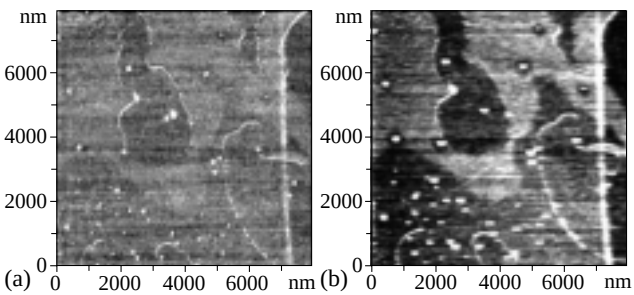

Fig. 2. Phase contrast AFM-images of the silicon(111) surface covered by submonolayer quantity of copper: (a) AFM-tip lateral moving velocity 0.3 μm/s, (b) 10 μm/s.

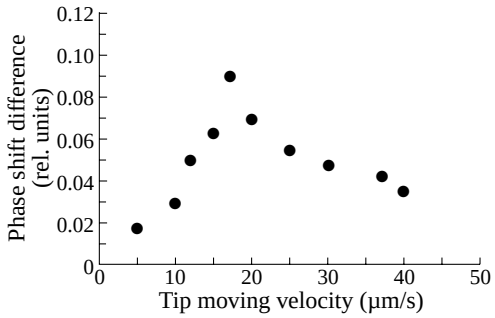

Fig. 3. Phase shift difference via AFM-tip lateral moving velocity.

duces the arising and increasing of phase shift difference between various type of surface covering (Fig. 2(a), (b)). Fig. 3 demonstrates the phase shift difference dependence on the tip moving velocity on the surface in lateral direction. The growth of the lateral phase shift with increasing of velocity comports with Bhushan–Tambe model [12], which determines this kind of interaction as friction based on "aspheric" inelastic deformation.

3. Conclusion

The phase shift of the resonant atomic force microscope (AFM) tip is studied as a velocity function during lateral moving on the surface. Lateral mechanism of phase shift forming is presented. It was found that the lateral phase shift is initiated by friction increasing during increasing of AFM tip moving velocity on the surface. The AFM lateral phase contrast imaging allows obtaining the Cu-dopant distribution on the silicon (111) surface under atmospheric condition.

Acknowledgements

We would like to acknowledge the valuable assistance of Mr. S. S. Kosolobov and Dr. V. Popkov. This work was partly supported by Russian Found of Basic Researches and by the programs of "Physics of Solid Nanostructures" and "Surface Atom Structures".

References

[1] Q. Zhong, D. Iniss and V. B. Elings, *Surf. Sci.* **290**, L688 (1993).
[2] J. Tamayo, R. Garcia, *Appl. Phys. Lett.* **71**, 2374 (1997).
[3] F. Dubourg, J. P. Aime, S. Marsaudon, R. Boisgard, P. Leclere, *Eur. Phys. J.* **E 6**, 49 (2001).
[4] J. Tamayo, R. Garcia, *Appl. Phys. Lett.* **73**, 2926 (1998).
[5] J. Tamayo, R. Garcia, *Langmuir* **12**, 4430 (1996).
[6] N. W. Nelson, P. G. Schroeder, R. Shalf, B. A. Parkinson, C. W. Almgren, A. N. Erickson,*Appl. Phys. Lett.* **74**, 1421 (1999).
[7] J. P. Cleveland, B. Anczykowski, E. Schmid, V. Elings, *Appl. Phys. Lett.* **73**, 2926 (1998).
[8] B. Anczykowski, B. Gotsmann, H. Fuchs, J. P. Cleveland, V. Elings, *Appl. Surf. Sci.* **140**, 376 (1999).
[9] D. V. Sheglov *et al*, *Phys. Low-Dim. Str.* **5/6**, 239–247, (2002).
[10] D. Sarid *et al*, *J. Vac. Sci. Technol. B* **14**, 864–867, (1996).
[11] D. V. Sheglov, S. S. Kosolobov, E. E. Rodyakina, A. V. Latyshev, *Microscopy and analysis*, **9**, 9 (2005).
[12] N. S. Tambe, B. Bhushan, *Nanotechnology* **16** , 2309 (2005).

15th Int. Symp. "Nanostructures: Physics and Technology"
Novosibirsk, Russia, June 25–29, 2007

Recent developments in III–V MOSFET technology

R. J. W. Hill, M. Holland, X. Li, D. McIntyre, D. A. J. Moran, C. R. Stanley, S. Thoms, H. Zhou and I. G. Thayne

Nanoelectronics Research Centre, University of Glasgow,
Rankine Building, Oakfield Avenue, G12 8LT, Glasgow, UK

Abstract. We report data from 1μm gate length enhancement mode III–V MOSFETs. The devices utilise a Pt metal gate, a 5 nm GaGdO high-κ dielectric ($\kappa = 20$), and an implant free δ-doped, AlGaAs/InGaAs/AlGaAs/GaAs heterostructure. Typical device figures of merit are; saturation drive current, $I_{\mathrm{d,sat}} = 325$ μA/μm, threshold voltage, $V_t = +0.1$ V, extrinsic transconductance, $g_m = 315$ μS/μm, gate leakage current, $J_{\mathrm{g}} = 2.2 \times 10^{-5}$ A/cm^2, sub-threshold slope of 158 mV/V and $I_{\mathrm{on}}/I_{\mathrm{off}}$ ratio of 1000. Electron mobility in excess of 1200 cm^2/V s over the full gate bias operating range with a peak value of 2145 cm^2/Vs was extracted from low drain bias measurements on 20 μm long channel devices. These transport and device data are highly encouraging for future high performance n-channel CMOS solutions based on III–V MOSFETs.

Introduction

No viable solution has yet been proposed for the manufacture of devices with performance meeting the targets at and beyond the 32 nm technology generation of the ITRS. Recent research into Ge-channel devices has yielded promising improvements in pMOS performance [1], but has failed to deliver similar results in the n-channel case. This is due largely to inefficient doping and low mobility resulting from the poor quality of the high-κ dielectric-semiconductor interface and a corresponding increase in the interface state density in the upper half of the Ge bandgap. The development of III–V compatible high-κ dielectric stacks with an unpinned interface and low leakage has drawn attention to high mobility III–V materials for the n-channel CMOS solution [2]. This has prompted the formation of several powerful consortia to investigate III–V devices for digital applications, including the Non-Classical CMOS Research Center led by the University of California at Santa Barbara [3], and the Materials, Structures and Devices Marco Research Center at MIT [4]. Various alliances have also been forged, including one between IMEC and Riber to examine III–V and Ge-based technologies for beyond silicon CMOS [5], and Intel and QinetiQ focussing on InSb-based HEMTs for logic applications [6]. Simultaneously, the need for equivalent oxide thicknesses of <1 nm forces the introduction of high-κ dielectrics and metal gates.

Monte Carlo simulation of implant free III–V MOSFETs have revealed the scalability of this architecture to sub-20 nm, physical gate lengths exploiting the benefits of the high mobility channel [7,8].

1. Experimental

Material growth was carried out by MBE on a 4" semi-insulating GaAs substrate, using a dual chamber system, by the method detailed in [2]. The III–V heterostructure was grown in one chamber before transfer under ultra-high vacuum conditions to a second chamber, where oxide deposition took place. The Ga_2O_3/GaGdO (GGO) gate stack consists of three layers; a crystalline Ga_2O template layer, which unpins the GaAs surface [9], an amorphous Ga_2O_3 layer, which protects the interface from Gd migration, and an amorphous GaGdO layer, which controls leakage current [10].

Figure 1 gives the layer structure of the epitaxial material, which confines a 2 dimensional electron gas in the low band-gap $In_{0.3}Ga_{0.7}As$ channel, spatially separating the electrons from the δ-doping planes by the use of large band-gap $Al_{0.45}Ga_{0.55}As/Al_{0.2}Ga_{0.8}As$ barrier/buffer layers.

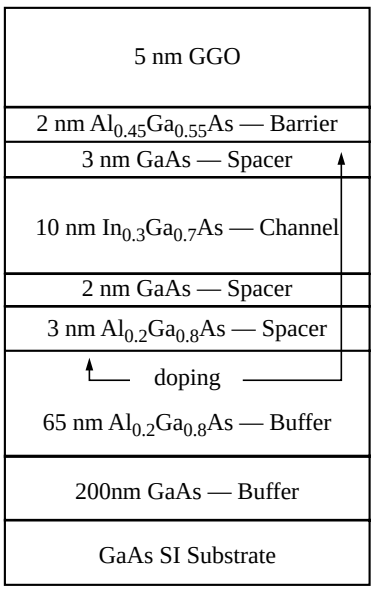

Fig. 1. MOSFET epitaxial layer structure.

A two-level wrap-around gate design (where the gate encircles the drain) was used to simplify the device process flow, removing the need for isolation. Firstly, the Pt/Au gate level was patterned by direct-write electron beam lithography and lift-off. Subsequently, the ohmic contact layer, with a source drain separation of 2.7 μm, was defined by a similar process. The GGO dielectric was removed by wet etching prior to deposition of Ni/Ge/Au ohmic contacts, which underwent rapid thermal annealing at 430 °C for 60 s. Optical and SEM micrographs of a completed device are given in Fig. 2.

2. Results

Transmission line measurements (TLM) yielded a contact resistance (R_{c}) of 366 Ω-μm, and a sheet resistance for the access regions (R_{sh}) (identified in Fig. 2) of 513 Ω/sq. Using these figures and the device geometry, the parasitic access resistance (R_{sd}) was calculated to be 1600 Ω-μm.

Fig. 3 shows the $I_{\mathrm{ds}}(V_{\mathrm{ds}}, V_{\mathrm{gs}})$ and Fig. 4 shows the $I_{\mathrm{ds}}(V_{gs})$, and $g_m(V_{\mathrm{gs}})$ characteristics of a 1 μm gate length III–V MOS-

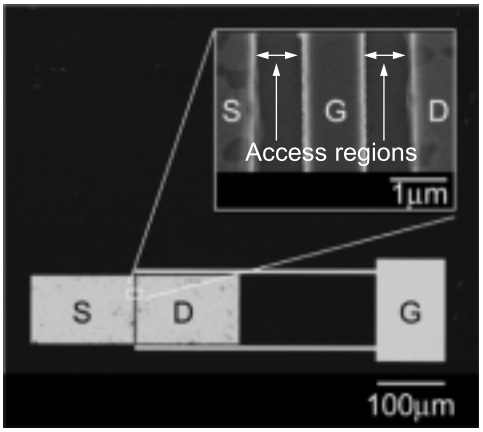

Fig. 2. Optical and SEM micrographs of a 1 μm gate length III–V MOSFET.

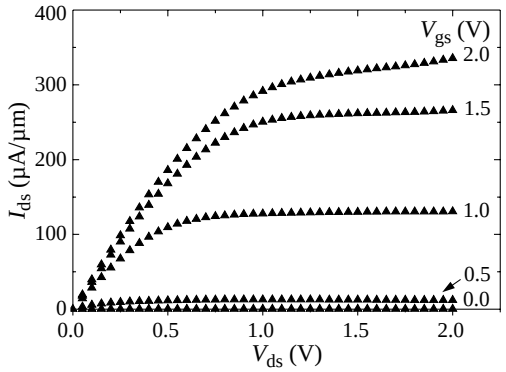

Fig. 3. $I_{ds}(V_{ds}, V_{gs})$ characteristic of a 1 μm III–V MOSFET.

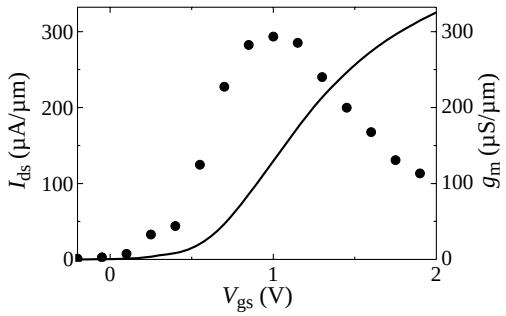

Fig. 4. $I_{ds}(V_{gs})$ and $g_m(V_{gs})$ ($V_{ds} = 2$ V) characteristics of a 1 μm III–V MOSFET.

FET. The $I_{ds}(V_{ds}, V_{gs})$ characteristics are well behaved, and give an $I_{ds,sat}$ of 325 μA/μm.

The $I_{ds}(V_{gs})$ characteristics show a threshold voltage, V_t (defined at 1 μA/μm drain current), of +0.1 V and a peak transconductance g_m of 315 μS/μm.

Fig. 5 shows a log $I_{ds}(V_{gs})$ plot for a 1 μm III–V MOSFET, from which a sub-threshold slope of 158 mV/V is extracted, along with an I_{on}/I_{off} ratio of 1000. At $V_{gs} = 2$ V, $V_{ds} = 2$ V, the gate leakage current, J_g is 2.2×10^{-5} A/cm^2.

Low drain bias (0.1 V) $I_{ds}(V_{gs})$ measurements of 20 μm gate length devices were used to extract gated mobility data. The wrap around gate design precludes the use of the standard split-CV method of mobility extraction, as the entire gate pad is on active material. A simplified method, based on the long channel MOSFET equation, given in Eq. (1) was used to extract

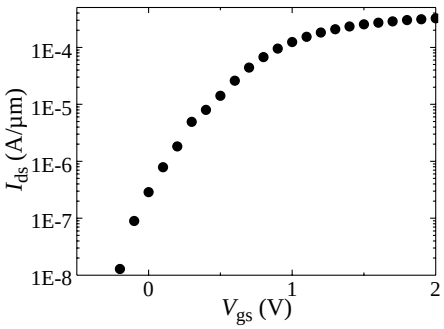

Fig. 5. Log scale $I_{ds}(V_{gs})$ characteristics ($V_{ds} = 2V$) of a 1 μm III–V MOSFET.

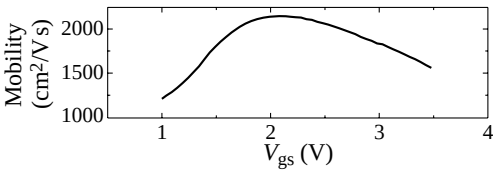

Fig. 6. Gate voltage dependent mobility extracted from 20 μm III–V MOSFET.

the effective mobility, μ:

$$I_{ds} = \frac{W}{L}\mu C_{ox}\left(V_{gs} - V_t\right)V_{ds}, \qquad (1)$$

where W is the device width, L the gate length, and C_{ox} the gate-to-channel capacitance (calculated from the permittivity and thicknesses of the gate dielectric and semiconductor layers separating the gate from the channel). This method does not include the effect of any residual interface or bulk oxide traps, so predicts an artificially high carrier concentration and hence low mobility. Nevertheless, good agreement is found between the V_{gs}/carrier concentration relationship calculated using Eq. 1, and self-consistent Poisson–Schrödinger simulations of the complete layer structure.

Using this method, the gate bias dependent mobility was extracted (Fig. 6). To our knowledge, this is the highest extracted mobility from enhancement mode III–V MOSFETs reported to date. For the full operating gate voltage range of the device, mobility values in excess of 1200 cm^2/Vs, with a peak of 2145 cm^2/Vs are observed, significantly higher than those obtained from contemporary silicon/high-κ solutions.

3. Conclusion

Well behaved, 1 μm gate length enhancement mode III–V MOSFETs were demonstrated with V_t of +0.1, $I_{ds,sat}$ of 325 μA/μm, g_m of 315 μS/μm and sub-threshold slope of 158 mV/dec. Peak effective electron mobilitiy of 2145 cm^2/Vs was extracted from long channel devices. The latter is the highest mobility data reported for n-channel III–V MOSFETs, and significantly outperform contemporary Si/high-κ n-channel solutions. These transport and device data are highly encouraging for future, high mobility n-channel solutions based on III–V MOSFETs.

Acknowledgements

We are grateful to Matthias Passlack, Ravi Droopad, Mel Miller and Karl Johnson of Freescale Semiconductor, Wireless Systems and Packaging Laboratory, Tempe, Arizona for stimulating discussions and to the UK Engineering and Physi-

cal Sciences Research Council, Scottish Funding Council and Freescale Semiconductor who have funded this work.

References

[1] P. Zimmerman, High performance Ge pMOS devices using a Si-compatible process flow, in *IEDM Tech. Dig.* 2006.

[2] M. Passlack *et al*, Development methodology for high-k gate dielectrics on III–V semiconductors: $Gd_xGa_{0.4-x}O_{0.6}/Ga_2O_3$ dielectric stacks on GaAs, *Journal of Vacuum Science and Technology B: Microelectronics and Nanometer Structures* **23** 1773–1781 (2005).

[3] www.src.org/member/news/center_cmos06.asp

[4] https://www-mtl.mit.edu/MSD/

[5] www.imec.be/wwwinter/mediacenter/en/riber2006.shtml

[6] S. Datta *et al*, 85 nm gate length enhancement and depletion mode InSb quantum well transistors for ultra high speed and very low power digital logic applications, in *IEDM Tech. Dig.* (2005).

[7] K. Kalna, *Nanotechnol.* **7** (2007).

[8] M. Passlack *et al*, Implant-free high-mobility flatband MOSFET: principles of operation. *Electron Devices, IEEE Transactions on* **53** (10) 2452 (2006).

[9] M. J. Hale *et al*, Scanning tunneling microscopy and spectroscopy of gallium oxide deposition and oxidation on GaAs(001)-c(2×8)/(2×4). *The Journal of Chemical Physics*, **119** (13) 6719–6728 (2003).

[10] M. Passlack *et al*, Role of Ga_2O_3 template thickness and gadolinium mole fraction in $Gd_xGa_{0.4-x}O_{0.6}/Ga_2O_3$ gate dielectric stacks on GaAs. *Applied Physics Letters*, **83** (25) 5262–5264 (2003).

15th Int. Symp. "Nanostructures: Physics and Technology"
Novosibirsk, Russia, June 25–29, 2007

Nano local stable high density charge storage in a two-dimensional Si and Ge nanocrystal networks in thin SiO_2 layers performed by electrostatic force microscopy in vacuum

A. N. Titkov[1], M. S. Dunaevskii[1], A. Claverie[2], C. Bonafos[2], S. E. Alexandrov[3], A. N. Speshilova[3], M. Ramonda[4] and P. Girard[4]

[1] Ioffe Physico-Technical Institute, St Petersburg, Russia
[2] CEMES/CNRS, Toulouse, France
[3] St Petersburg State Technical University, St Petersburg, Russia
[4] LAIN, University of Montpellier II, 34095 Montpellier, France

In recent decade the electrostatic force microscopy (EFM) method [1,2] have been applied to perform many studies on local charging of thin oxide layers beneath the EFM probe The main interest to these studies arises in the connection with intention to create electrical memory systems of super high density and develop materials suitable for electrostatically directed local assembly of nanostructures. The main system studied up to now is nano thin SiO_2 oxide layers with embedded Si nanocrystals [3–5]. There was achieved locality of charging on the level of 100 nm with charge retention time of 1 hour on dry oxide surfaces in vacuum conditions. In our work we show that the both charging locality and retention time in that system can be considerably improved if certain modifications in sample preparation and measurement procedure will be undertaken.

Nano local stable high density charge storage has been realized in thin SiO_2 oxide layers with embedded Si or Ge nanocrystals fabricated by low energy ions implantation (1–5 keV) and subsequent annealing in N_2 gas containing few percents of oxygen. The mentioned modifications of traditional technology of nanocrystals fabrication in oxide matrix have improved the integrity of the oxides, made narrow the size distribution of the nanocrystals, produced them well laterally separated.

For the such prepared oxide layers with embedded Si or Ge nanocrystal networks it was found that local charging in vacuum in the contact with an EFM probe creates in oxide layer nano local charged areas which do not show any lateral spreading in time. The charged areas with the diameter as small as 35 nm and charge retention time over 10 hours have been registered in electrostatic force gradient mode at the tip-surface distance of 15 nm. It should be mentioned that due to a long-range nature of the electrostatic interactions and certain volume of the EFM probe the experimental conditions strongly influence the detected size of charged area. The detected values are increasing with increasing the probe-surface distance, for example, in our case from 35 nm to 80 nm with probe lifting over surface from 15 nm up to 70 nm. As well, measurements in a simple electrostatic force non-gradient mode also cause broadening of detected charged areas by 2–3 times at the same probe-surface distances. Measurments in vacuum are essentials to realize the smallest probe-surface distances.

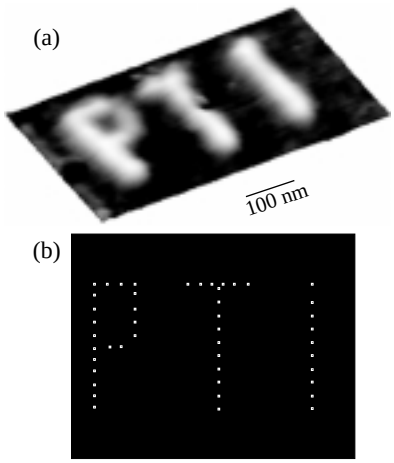

Fig. 1. Charge patterning on the surface of $Si0_2$ film with embedded Si nanocrystals: (a) detected EFM image, (b) point map of charging with application of 4 V on probe during 100 msec at each point.

Furthermore, we have experimental evidences that an actual charged area is still smaller then the detected one. The detected by us charged areas demonstrate an internal structure which varies with probe transformation during measurements or probe change by the new one. It means that the actual charged area is smaller then the probe ending and detected charged area images, in the reality, reflect the shape of probe ending. From the known value of probe ending radius of 10 nm nearly the same estimation comes for actual charged area size. Quantitative estimation of the electrostatic interaction between probe and charged area brings estimation of the number of charges in that area on the level of several tens. The number of nanocrystals in the charged area is of the same range and it is possible to propose that most of nanocrystals are charged. That expectation correlates with the experimentally found saturation of local surface charging with a raise of voltage or time of charging.

The effect of nano local charging beneath the EFM probe opens a new promising possibility for characterization of nano thin and laterally small oxide layers. Indeed, oxide layer local charging with subsequent time control of charged area lateral spreading and reduction of total injected charge permit to characterize the charges diffusion and transport in the plain of oxide layer and their escape into the Si substrate. As an example of

application, the local analysis of gate oxide in nanotransistors can be mentioned.

Presented results demonstrate also a great potential of the studied system as a stable tunable electrets suitable for nanoscale charge patterning and electrostatically directed assembly of complex nanostructures. Charge retention time of 10 hours is quite sufficient to perform many technological processes. In Fig. 1 we present the EFM image of charge patterning on the surface of $Si0_2$ film with embedded Si nanocrystals. Charge patterning image in Fig. 1(a) presents the abbreviation of Ioffe Physico-Technical Institute. The lateral resolution is better then 50 nm. Charging was performed via point map, shown in Fig. 1(b).

References

[1] Y. Martin, D. W. Abraham, H. K. Wickramasinghe, *Appl. Phys. Lett.* **52**, 1103 (1988).
[2] P. Girard, A. N. Titkov, *Applied Scanning Probe Methods II*, Eds. Bh. Bhushan and H. Fuchs, Springer-Verlag, Berlin Ch. 9, 282–320 (2006).
[3] E. Boer *et al*, *Appl. Phys. Lett.* **79**, 791 (2001).
[4] C.Ng *et al*, *Appl. Phys. Lett.* **85**, 2941 (2004).
[5] R. Dianoux *et al*, *Phys. Rev. B.* **71**, 125303 (2005).

15th Int. Symp. "Nanostructures: Physics and Technology"
Novosibirsk, Russia, June 25–29, 2007

Quantum detector of noise based on a system of asymmetric Al superconducting rings

V. L. Gurtovoi, S. V. Dubonos, A. V. Nikulov and V. A. Tulin
Institute of Microelectronics Technology and High Purity Materials, Russian Academy of Sciences,
142432 Chernogolovka, Moscow District, Russia

Abstract. Multiple asymmetric superconducting ring structures are proposed as quantum detectors of noise (QDN). Calibration of QDN has been done for different bias current and temperature. The maximum rectification efficiency of QDN is 0.25 and diminishes as temperature approaches T_c.

The future realization of quantum computers is closely connected with solid-state quantum bit (qubit) and coupled qubit fabrication and investigation of their functionality. The most promising candidates for solid-state qubits are two-level superconducting structures which act like artificial atoms with quantized energy levels [1,2]. To carry out quantum computations, decoherence time for superposition of macroscopic quantum states in superconducting structures should be longer than computation time. Decoherence is determined by the equilibrium and nonequilibrium noise environment, which have to be investigated and strictly controlled. Although, the intensity of equilibrium thermal fluctuations vanishes linearly with temperature, nevertheless, there are quantum fluctuations due to zero-point motion even at zero temperature. To detect nonequilibrium and vanishing with temperature equilibrium thermal fluctuations and separate them from quantum fluctuations, one should use a quantum system, i.e. a quantum detector of noise (QDN).

As a basic element of the QDN, we propose to use an asymmetric superconducting ring (ASR) with or without Josephson junctions. Analogous to SQUID structures in magnetic field [3], ASR structures are able to rectify applied ac current or both external and internal noise without bias current when narrow part of the ASR is in the resistive state induced by the magnetic flux quantization persistent current. In this work, we have investigated magnetic field, temperature, and ac bias current dependence of the sensitivity for the ASR structures as QDsN. Calibration of the noise detector and optimization of the sensitivity has been carried out. Connected in series 18 ASRs have been investigated for the sensitivity improvement.

Investigated test structures (without Josephson junctions) consisted of asymmetric aluminum rings (45–50 nm thick, thermally evaporated on oxidized Si substrates) with semi-ring width of 200 and 400 nm for narrow and wide parts, respectively. 4 μm diameter single ASR and 20 ASR structures were fabricated by e-beam lithography and lift-off process. Fig. 1 shows an SEM image of the 20 ring structure.

Measurements were carried out by applying 5 or 40 kHz sinusoidal bias current to current leads, whereas, rectified dc signal was measured in a frequency band from 0 to 30 Hz by home made preamplifier (followed by low-noise preamplifier SR560) at potential leads. Noise level of the amplification system was 20 nVpp for $f_b = 0$ to 1 Hz. It should be noted that rectification effects do not depend on frequency of the bias current at least up to 1 MHz [4]. Magnetic field direction was perpendicular to the ring's plane.

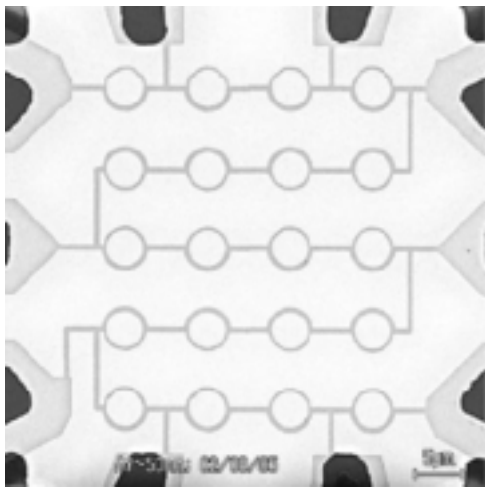

Fig. 1. An SEM image of a superconducting structure with 20 asymmetric aluminium rings.

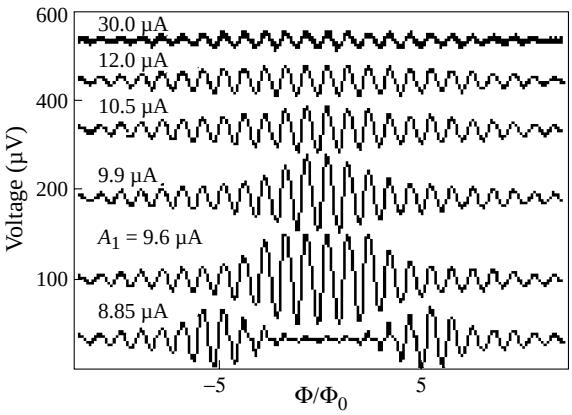

Fig. 2. The rectified voltage for 18 ASRs in magnetic field (f = 5 kHz and amplitudes I_0 = 8.85; 9.6; 9.9; 10.5; 12; 30 μA) at T = 1.244 K = 0.98T_c. Except for I_0 = 9.6 μA, all curves are vertically shifted.

To make calibration of the QDN, ac bias current with different amplitude was applied to substitute noise with different amplitude level. Fig. 2 shows typical oscillations of the rectified voltage as a function of magnetic field at different ac bias currents for the 18 ASRs in series (T = 1.244 K = 0.98T_c). The oscillations are periodic with period equals to the superconducting flux quantum $\Phi_0 = h/2e$, the positive and negative maxima being observed at $\Phi \approx (n \pm 1/4)\Phi_0$, ($n = 0, \pm 1$), showing points of magnetic field with maximum rectification

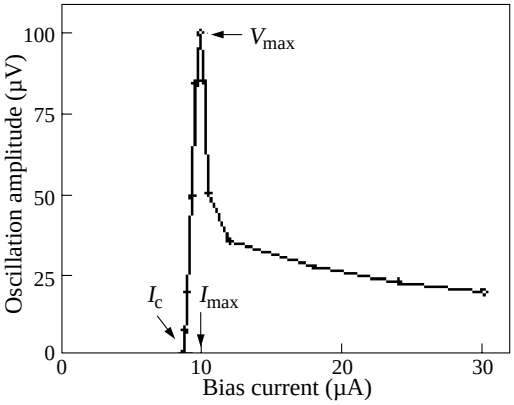

Fig. 3. AC bias current dependence of the oscillation amplitude ($\Phi \approx \Phi_0/4$) for the single ARS at $T = 1.214$ K $\approx 0.98T_c$.

efficiency. The rectified voltage crosses zero at $\Phi = n\Phi_0$ and $\Phi = (n + 1/2)\Phi_0$. Our experiments have shown that the rectified voltage for N ASRs is approximately N times higher compared to that for a single ASR fabricated in the same technological process. Therefore, in Fig. 3 we present the amplitude of the rectified voltage oscillations at $\Phi \approx \Phi_0/4$ as a function of the bias current amplitude for a single ARS. This dependence is nonmonotonous with sharp peak at near the critical current value. At low bias currents, the rectified voltage is zero since the ASR is in superconducting state.

To determine the exact position of the maximum in Fig. 3 with respect to the critical current value, in Fig. 4 we present temperature dependence of both the critical current of the single ASR obtained from current-voltage characteristics and the amplitude of the bias current I_{max} at which the maximum of the rectified oscillations is observed. As clearly seen from Fig. 4, the maximum of the oscillations is achieved when the bias current amplitude is slightly higher than the critical current of the ASR, having practically the same temperature dependence. Temperature dependence of the maximum rectified voltage V_{max} is also shown in Fig. 4. The maximum voltage increases with temperature decrease in a way similar to the bias current I_{max}, having linear dependence on the bias current (not shown hear). To the accuracy of measurement errors, the ratio $V_{max}/I_{max} \approx 1.45$ Ohm is independent of temperature for $T < 0.98T_c$. When the amplitude of the bias current I_0 is equal to I_{max}, this ratio determines the maximum rectification efficiency, which is equal to $V_{max}/I_0R_n = V_{max}/I_{max}R_n \approx 0.25$, where $R_n = 5.5$ Ohm is the resistance of the ASR in the normal state. It has been shown that rectified voltage is proportional to persistent current in the ring [5]. Since $I_{max} \approx I_c$, the maximum rectification efficiency could be increased using ARS with smaller radius where persistent current is higher and could be close to I_c.

By fitting the critical current temperature dependence in Fig. 4, one can get that $I_{max} \approx I_c = 4.4$ mA $\times (1-T/T_c)^{3/2}$. Since the bias current or noise only shift the QDN total current to near critical value I_{max} where it has the maximum rectification efficiency, measurements of noise at different temperatures near T_c allows amplitude profiling of the noise pulses in accordance with I_c temperature dependence. Thus, the noise with the lower level will be detected by the QDN without biasing at lower temperature. In case of high level of intrinsic noise in the amplification system, the QDN with N ASRs could

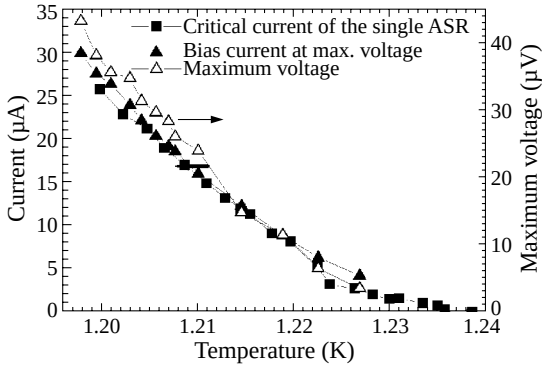

Fig. 4. Temperature dependence of the I_c, I_{max}, V_{max} for the single ASR (explanation of I_c, I_{max}, and V_{max}, see at Fig. 3).

overcome this lack of the amplifier sensitivity. Finally, let us estimate the level of the equilibrium noise. The square root mean value of the equilibrium Nyquwist noise can be determined from $R\langle I^2_{Ny}\rangle = k_BT\Delta\omega$ for the frequency range from 0 to the quantum limit $k_BT/\hbar$, i.e. $\langle I^2_{Ny}\rangle^{1/2} = k_BT/(\hbar R)^{1/2}$ which is equal to ~ 0.4 μA at $T \approx 1$ K and $R \approx 10$ Ohm. Our preamplifier noise level allows reliable measurement of 30 nV voltage signal. Therefore at the point of the maximum rectification efficiency (~ 0.25) and $V_{max} \approx 30$ nV, one could measure the current noise $I_{max} = V_{max}/(0.25R_n) \approx 20$ nA at different temperatures T/T_c. As a result, even a QDN based on a single ASR is able to detect temperature dependent equilibrium thermal fluctuations and separate them from temperature independent quantum fluctuations.

Acknowledgements

This work has been supported by a grant of the Program "Quantum Nanostructures" of the Presidium of RAS, grant "Quantum bit on base of micro- and nano-structures with metal conductivity" of the Program "Technology Basis of New Computing Methods" of ITCS department of RAS and a grant 04-02-17068 of the Russian Foundation of Basic Research.

References

[1] Y. Makhlin, G. Schoen, and A. Shnirman *Rev. Mod. Phys.* **73**, 357 (2001).
[2] D. V. Averin, *J. Low Temp. Phys.* **118**, 781 (2000).
[3] A. Th. A. M. de Waele *et al*, *Physica* **37**, 114 (1967).
[4] S. V .Dubonos *et al*, *Pisma Zh. Eksp. Teor. Fiz.* **77**, 439 (2003) (*JETP Lett.* **77**, 371 (2003)).
[5] V. L. Gurtovoi *et al*, *Izvestiya RAN, Ser. Physicheskaya* **71**, 21 (2007).

15th Int. Symp. "Nanostructures: Physics and Technology"
Novosibirsk, Russia, June 25–29, 2007

Nanometer-sized Hall probe with a high spatial field resolution

V. N. Matveev, V. I. Levashov, O. V. Kononenko, *V. T. Volkov*, S. V. Dubonos, A. V. Chernykh, G. M. Michailov, M. A. Knjazev and S. V. Pjatkin

Institute of Microelectronics Technology and High Purity Materials, Russian Academy of Sciences, 142432 Chernogolovka, Moscow District, Russia

Abstract. Nano-sized Hall probe was prepared from ultra thin FePt film. The magnetic field sensitivity of the probe was 150 Ω/T. Induction of magnetic field around the cantilever tip with deposited SmCo film was measured with aid of this Hall probe. The spatial field resolution of the probe was better then 100 nm.

Introduction

Mesoscopic Hall probe have proved themselves as a valuable experimental tool for studies flux distribution in macroscopic and submicron superconductors and for studies of the magnetic properties of individual nanometer-sized magnets and their arrays [1]. At room temperature a noteworthily alternative to Hall probe made from Au films was found Hall probes from ferromagnetic films. We believe that at present no other micromagnetization measurement technique can provide highest field resolution. This paper presents an experimental study of magnetic field around the tip of cantilever by Hall probe made from Fe–Pt ultra thin films.

1. Experiment

Ultra thin Fe–Pt films (∼2 nm) were grown at 0.04 nm/s on SiO_2 substrates of by laser ablation of a rotary iron target (diameter 40 mm) with Pt segment on top, the target — substrate separation being 90 mm. The process employed a 1.06 μm laser delivering 10 ns pulse with a repetition rate of 15 Hz. A long-focus lens placed in front of the vacuum deposition chamber was used to provide a radial-flux density of 10^9 W/cm^2 on the target. The base pressure was 10^{-5} bar. Hall probes 60 × 60 nm in size made from ultra thin film (∼20 nm thickness) using electron beam lithography procedure and method of contamination. When Hall probe patterned into nanometer scale the magnetic properties are the same as in millimeter scale.

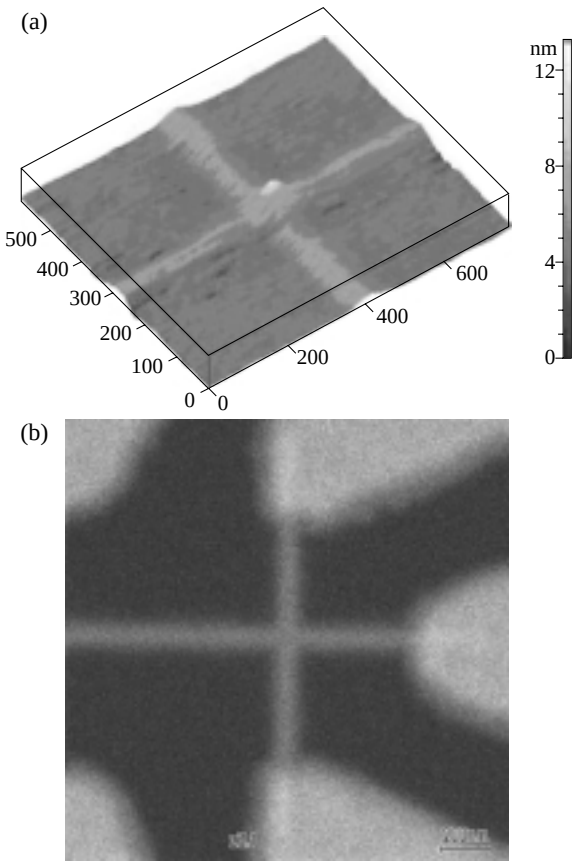

Fig. 1. AFM (a) and SEM (b) images of the Hall probe.

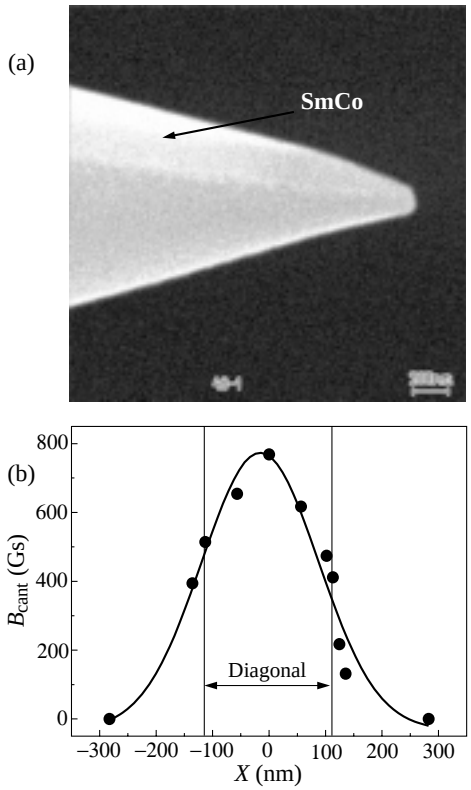

Fig. 2. Cantilever tip with deposited SmCo film (a). Induction of magnetic field around cantilever along diagonal of the Hall probe (b).

2. Results and discussion

AFM and SEM images of work region of Hall probe are shown in Fig. 1. The size of the probe is 60 × 60 nm. The maximum sensitivity to magnetic field of such probe was $S = 150$ Ω/T.

For characterization of the magnetic induction space resolution of the nano-sized Hall probe improved atomic-force microscope P4-NTMDT with capability of electrical measurements of nanostructures was applied. For local measurements of mag-

netic induction at first sensitivity of nanoprobe in uniform magnetic field from the calibrated Sm–Co magnet was defined. Then specially made magnet cantilever with Sm–Co coating was approached to surface of microchip with nanoprobe in contact mode. The nanoprobe atomic-force image was obtained and magnet cantilever was placed in adjusted in plane and on height points over nanostructure. Measured in these positions Hall signals allowed to build the space picture of the magnet cantilever field with resolution of order of 10 nm.

References

[1] K. S. Novoselov *et al*, *Nanoscience* **3**, 123 (2004).

15th Int. Symp. "Nanostructures: Physics and Technology"
Novosibirsk, Russia, June 25–29, 2007

Generation of THz radiation in submicron HEMTs with two-dimensional electron gas

M. L. Orlov[1], K. V. Maremyanin[1], *S. V. Morozov*[1], V. I. Gavrilenko[1], N. Dyakonova[2], W. Knap[2], A. Shepetov[3], Y. Roelens[3] and S. Bollaert[3]

[1] Institute for Physics of Microstructures RAS, 603950 Nizhniy Novgorod, Russia
[2] GES-UMR, CNRS — Université Montpellier 2, Place E. Bataillon 34950 Montpellier, France
[3] Institut d'Electronique, de Microelectronique et de Nanotechnologie, 59652 Villeneuve d'Ascq, France

Abstract. Current-voltage characteristics and THz emission of submicron InGaAs/AlGaAs and GaAs/AlGaAs HEMTs with two-dimensional electron gas were studied at $T = 4.2$ K. Spectral studies were carried out with n-GaAs cyclotron resonance rejection filter tuned by the magnetic field. The emission was found to arise abruptly at the saturation part of the source-to-drain current-voltage characteristic after current drop that is ascribed to the development of Gunn instability. In addition to a broadband emission of radiation by hot carriers relatively narrow THz emission bands were discovered in the spectra that is attributed to Gunn current oscillations in the transistor channel due to the high electric field domain traveling the short interspace between gate and drain.

Introduction

The cut-off frequency in the usual mode of operation of a High Electron Mobility Transistor (HEMT) is governed by the inverse transit time. Dyakonov and Shur suggested to use plasma effects to increase the operation frequency of submicron HEMTs [1,2] since the plasma wave velocity could be of 10^8 cm/s that is much more than a typical electron drift velocity in a HEMT channel. Resonant detection of THz radiation by plasma waves was already demonstrated in submicron HEMTs [3,4] and in a field effect transistor with a grating gate [5]. A significant increase of HEMT response to THz radiation was observed in commercial GaAs/AlGaAs HEMTs and in InGaAs/InAlAs HEMTs with nanoscales gate when the source-to-drain voltage fell into the saturation range of the current-voltage characteristic [6,7], the response being resonant even at room temperature. This effect was explained in terms of decreasing the effective scattering rate due to plasma wave amplification. Under similar conditions, again at the current saturation, an intensive THz radiation was discovered [8]. The spectral studies in InGaAs/AlGaAs HEMTs with a tunable by the magnetic field cyclotron resonance n-InSb detector have revealed that the emission spectrum is rather broad with two spectral features nearby 1 and 6 THz, the lower frequency peak being attributed again to the Dyakonov–Shur plasma wave instability. The present paper is devoted to the emission spectral studies with better resolution provided by a narrow band n-GaAs rejection filter.

1. Experimental

The transistors under investigations were $In_{0.5}Ga_{0.5}As/In_{0.5}Al_{0.5}As$ [9] and GaAs/AlGaAs (Fujitsu FHX06X) devices with two-dimensional electron gas with gate length 60 nm and 250 nm respectively. Current-voltage I–V characteristics and THz emission were measured at $T = 4.2$ K. The emission was detected by a broad-band Si bolometer. The spectral measurements were carried out with n-GaAs cyclotron resonance rejection filter tunable by the magnetic field (up to 10 T) with a resolution of 2 to 3 cm^{-1} that is one order of magnitude better than of previously used n-InSb detector [8].

2. Results and discussion

Typical I–V characteristics of InGaAs/AlGaAs HEMT at different gate voltages are given in Fig. 1. In contrast to [8,10] we observed the negative differential conductivity (NDC) at the positive gate voltage only. The THz emission signal at Si bolometer was shown to arise at the applied source-to-drain voltages corresponding to NDC part of I–V curve (cf. [8]). The results of spectral measurements with n-GaAs rejection filter are plotted in Fig. 2 for the gate voltage $U_G = 0.05$ V. One can see two minima (corresponding to maximums in the emission spectrum) at 0.87 and 1.36 THz. It is worth mentioned that these spectral features were observed at high enough source-to drain voltages $U_D > 0.5$ V only, their amplitude being increased with U_D as one can see in Fig. 2.

In Figure 3 I–V characteristics of GaAs/AlGaAs Fujitsu HEMT measured at different gate voltages are presented together with source-to-drain voltage dependencies of the of the emission intensity (measured at the zero magnetic field at the filter). Again one can see a prominent current saturation followed by an abrupt current drop (kink). Similar current kinks have been observed in InGaAs/AlGaAs HEMT with a long (3 mm) channel and attributed to the origin of the Gunn instabilities [11]. In Fig. 3 one can see that the overall emission

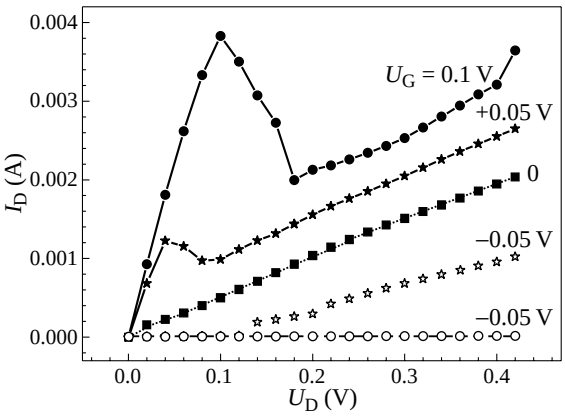

Fig. 1. I–V characteristics of InGaAs/AlGaAs HEMT at different gate voltages (U_G) at 4.2 K.

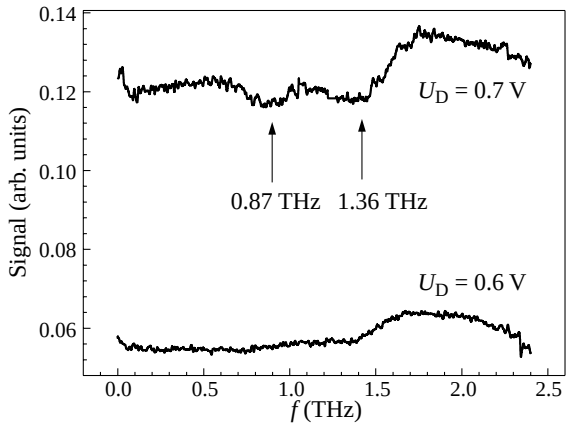

Fig. 2. The THz emission signal of InGaAs/AlGaAs HEMT at dependences n-GaAs rejection filter at the applied source-to-drain voltages $U_D = 0.6$ V (curve 1) and 0.7 V (curve 2) for the gate voltage $U_G = 0.05$ V at 4.2 K.

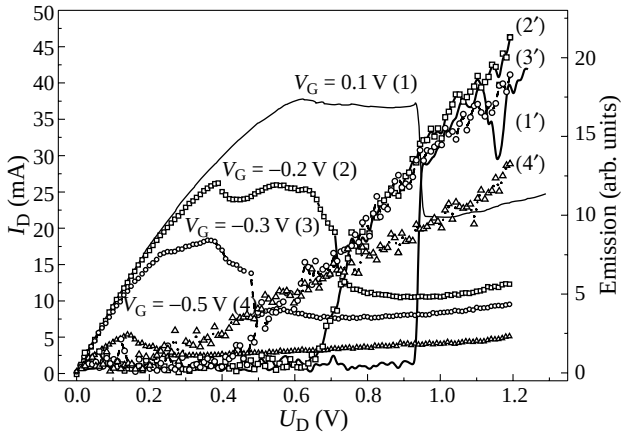

Fig. 3. I–V characteristics of GaAs/AlGaAs Fujitsu HEMT measured at different gate voltages (curves 1–4) and dependences of the emission intensity (curves $1'-4'$, correspondently) versus source-to-drain voltage at 4.2 K.

arises steeply at the source-to-drain voltage corresponding to the kinks. Spectral studies showed that the emission intensity dependencies on the rejection filter frequency are in general rather flat (Fig. 4) that corresponds to the broad emission spectrum (hot carrier emission, the electric field in the channel being of the order of 10^4 V/cm).

However at some applied gate and source-to-drain volt-ages we have observed narrow dips corresponding to narrowband emission at about 1.25 THz (Fig. 4). Since it is unlikely that such narrowband emission (Figs. 2, 4) could be explained by a plasma instability we proposed a hypothesis that it results from Gunn oscillations. To the present Gunn oscillations have never been observed at such high frequencies.

However the results of recent Monte Carlo simulations of the drain current noise showed that in submicron HEMTS at drain-to-source voltages exceeding some threshold value Gunn oscillations takes place [12,13] owing to the high electric field domain traveling in the gap between gate and drain. The high frequency of the Gunn oscillations results from the quasiballistic motion of G-electrons in the transistor channel with an average velocity about 10^8 cm/s.

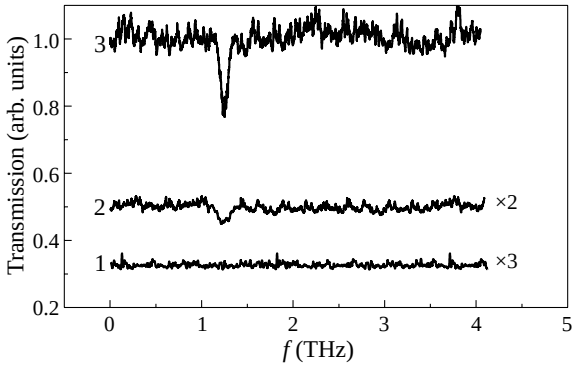

Fig. 4. The transmission spectra of emission of GaAs/AlGaAs Fujitsu HEMT dependences on the rejection filter frequency at difference source-to-drain voltages $U_D = -0.1$ V (curve 1), $U_D = 1$ V (curve 2), $U_D = 1.15$ V (curve 3) at 4.2 K.

Acknowledgements

The work has been financially supported by RFBR (#05-02-17374) and RFBR-CNRS (#05-02-22001) projects and by Russian Academy of Sciences.

References

[1] M. Dyakonov *et al*, *Phys. Rev. Lett.* **71**, 2465 (1993).
[2] M. Dyakonov *et al*, *IEEE Trans. on Electr. Dev.*, **43**, 380 (1996).
[3] W. Knap *et al*, *Appl. Phys. Lett.* **30**, 3433 (2002).
[4] A. El Fatimy *et al*, *Appl. Phys. Lett.* **89**, 131926 (2006).
[5] X.G.Peralta *et al*, *Appl. Phys. Lett.* **81**, 1627 (2002).
[6] F. Teppe *et al*, *Appl. Phys. Lett.* **87**, 052107 (2005).
[7] F. Teppe *et al*, *Appl. Phys. Lett.* **89**, 222109 (2006).
[8] W. Knap *et al*, *Appl. Phys. Lett.* **84**, 2331 (2004).
[9] N. Dyakonova *et al*, *Appl. Phys. Lett.* **88**, 141906 (2006).
[10] J. Lusakowski *et al*, *J. App. Phys.* **97**, 064307 (2005).
[11] G. M. Dunn *et al*, *Semicond. Sci. Technol.* **16**, 562 (2001).
[12] J. Mateos *et al*, *SAIP Conf. Proc.* **800**, 423 (2005).
[13] http://www.iemn.univ-lille1.fr/workshop/exposes/knap.ppt.

15th Int. Symp. "Nanostructures: Physics and Technology"
Novosibirsk, Russia, June 25–29, 2007

Antireflective gratings with diffraction orders in transmitted light for optoelectronic applications

D. V. Myagkov[1], V. E. Grikurov[2], S. I. Nesterov[1] and E. L. Portnoi[1]

[1] Ioffe Physico-Technical Institute, St Petersburg, Russia
[2] Institute on Physics, St Petersburg University, 1 Uljanovskaia Ave. St Petersburg-Petrodvoretz, 198504 Russia

Abstract. The idea of an antireflective grating transmitting a greatest part of incident light into diffracted orders is presented. Possible design of such a grating for devices operating at 1.06 μm was developed using effective medium theory (EMT). The diffraction efficiency was rigorously calculated and compared with EMT predictions. Application of such a grating as a phase mask for interference photolithography was considered. The grating revealed high contrast between diffracted and zero order in transmitted light.

High spatial frequency two-dimensional periodical structures, also known as crossed gratings or photonic crystals, are appreciated for their ability to reduce light from the optical surface on which they are formed. This is so called moth-eye effect, which has been first reported on by biologists [1]. The periodical structures can be etched into device material that gives them the advantage of thermal stability. Antireflection properties of crossed gratings have been intensively studied, due to their polarization independence [2]. However, conventional gratings with high spatial frequency also exhibit antireflection properties [3]. The defining property of the high spatial frequency grating is that its wavelength to period ratio is large enough so that all non-zero diffracted orders are cut off. Thus, the grating can be treated as an antireflection layer with equivalent refractive index, which can be calculated applying effective medium theory (EMT) [4]. The equivalent refractive index can be controlled by choosing of the groove width.

Using the generalized grating equation and keeping in mind light wavelength shortening in a medium with higher refraction index a grating period can be found, so that the grating gives only reflected orders in the incoming medium and diffracted orders in the material [5] (Fig. 1). The grating can be also made antireflective, that is achieved by choosing filling factor and grating groove height according to EMT. So, the grating has diffracted orders in the material and transmits greatest part of incoming light into the grating material. Thus, if the most part of transmitted light is directed into the diffraction order the effectiveness of photoconversion in photoactive region of optoelectronic device could be increased due to the increasing of the absorption path. Once the operating wavelength for the optoelectronic device is defined, the other parameters are fixed by above mentioned conditions and diffraction efficiency can be calculated by solving the Helmholz equation in closed

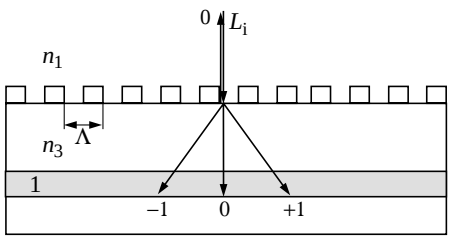

Fig. 1. Cross-section of optoelectronic device with diffraction grating formed on the surface. L_i — incident light, Λ — period of the grating, 1 — photoactive layer.

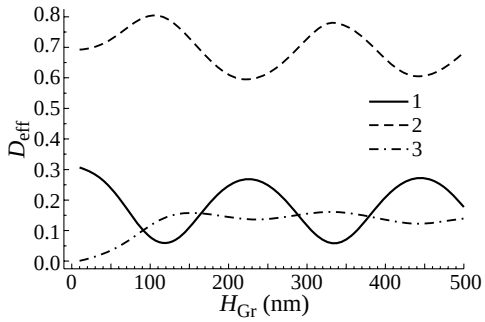

Fig. 2. Dependence of the diffraction efficiency D_{eff}, of different diffraction orders on the grating height H_{Gr} (wavelength — 1.06 μm, refraction index — 2.5, period — 700 nm, normal incidence, TE polarization, rectangle profile shape, groove width — 75 nm), 1 — reflected light, 2 — the zero order of tramsmitted light, 3 — the first diffracted order of transmitted light.

region with artificial boundary conditions [6, 7]. The calculated dependence of the diffraction efficiency on the grating height is shown in Fig. 2. The dependence is periodical and its peaks positions are in satisfactory agreement with the EMT predictions. Thus, the EMT is applicable as a simplest model for understanding reflection reduction from the gratings with high spatial frequency in case of diffraction order's presence in the grating's material. The grating reduces reflection from the semiconductor material, but the main part of transmitted light is directed in the zero order [5]. Possibly, the better results can be obtained by optimization of groove shape. Moreover, the further improvement of the gratings combining the antireflection and diffraction properties requires a more complex analytical model for diffraction efficiency calculations than EMT.

The same approach could be used to create a grating that could be used as a phase mask and can be easily built in photolithographical process of optoelectronic devices manufacturing (Fig. 3). Such grating was designed and revealed that the intensity of the zero order is 20 times lower than the intensity of the first order (Fig. 4). Implementation of such gratings allows increasing the intensity of exposing light by lowering of the losses on the zero order which is usually damped by nontransparent screen (Fig. 3).

Usually, a diffraction grating formed on the input window of optoelectronic devices has two different purposes: to reduce the reflection from the surface and to increase the photoconversion by increasing of the absorption path in the photoactive

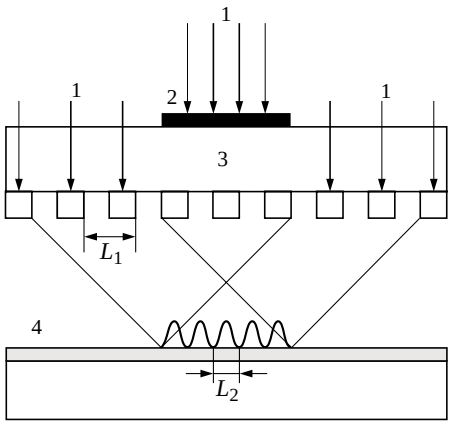

Fig. 3. Scheme of interference photolithography using phase mask with nontransparent screen for exposition. 1 — Exposing Light, 2 — Nontransparent screen, 3 — Phase Mask, 4 — Photoresist, L_1 — phase mask period, $L_2 = L_1/2$ — period of exposing interference picture.

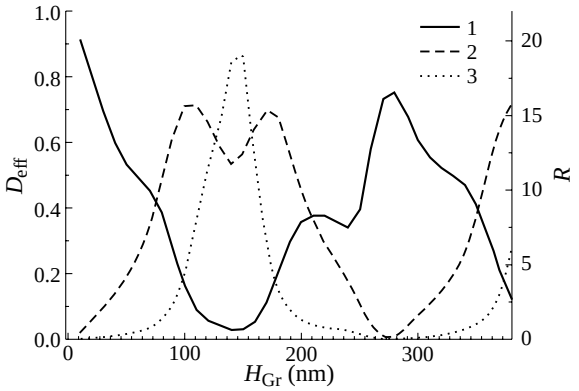

Fig. 4. Dependence of the diffraction efficiency D_{eff}, of light transmitted into the material, on the grating height H_{Gr} of diffraction grating made from chalcogenide glass on the quartz glass substrate (period — 700 nm, filling factor — 0.5, refraction index — 2.5, normal incidence, TE polarization, rectangle profile shape). 1 — the zero order, 2 — the second order, 3 — intensity ratio between the first and the zero order (R).

layer due to directing of the light in diffracted order propagating angular to the semiconductor surface. A grating that is suited for both of the purposes is proposed and investigated by numerical calculations of diffraction efficiency.

References

[1] C. G. Bernhard, 1967 Structural and functional adaptation in a visual system Endeavor, v. 26, pp. 79–84.
[2] S. J. Wilson and M. C. Hutley, *Optica Acta* **29**, 993–1009 (1982).
[3] R. C. Enger and K. Case, *Appl. Opt.* **22**, No. 20, 3220–3228 (1983).
[4] D. L. Brundet, E. N. Glystys and T. K. Gaylord, *Appl. Opt.* **33**, No. 13, 2695–2706 (1994).
[5] D. V. Myagkov, V. E. Grikurov, S. I. Nesterov, E. L. Portnoi, *Technical Physics Letters*, **32**, No. 24, pp. 62–67.
[6] V. E. Grikurov, E. Heikkola, P. Neittaanmaki, B. A. Plamenevskii, *Numerische Mathematik*, **94**, 269–288 (2003).
[7] V. E. Grikurov, *Scattering trapped modes and guided waves in waveguides and diffraction gratings*, Proceedings of the First East-West Workshop on Advanced Techniques in Electromagnetics, 2004, Warsaw, May 20–21. [quant-ph/0406019].

15th Int. Symp. "Nanostructures: Physics and Technology"
Novosibirsk, Russia, June 25–29, 2007

High performance polarized electrons photocathode

D. A. Vasiliev[1], Yu. P. Yashin[1], Yu. A. Mamaev[1], L. G. Gerchikov[1], V. V. Kuzmichev[1], V. M. Ustinov[2], A. E. Zhukov[2] and V. S. Mikhrin[3]

[1] State Polytechnic University, 195251, St Petersburg, Russia
[2] St Petersburg Physics and Technology Center for Research and Education of RAS, Khlopina 8/3, 194021, St Petersburg, Russia
[3] Ioffe Physico-Technical Institute, St Petersburg, Russia

Abstract. New photocathode for highly polarized electron emission has been developed, fabricated and studied. Polarized electron source is based on short-period strained AlInGaAs/AlGaAs superlattice grown by MBE method. Deformation of AlInGaAs quantum well results in 60 meV energy splitting between heavy hole and light hole minibands. Electron emission from the developed photocathode demonstrates maximal polarization of 92% with quantum efficiency of 0.85%.

Introduction

Polarized electrons have been extensively used in the last thirty years to investigate the spin-dependent structure of the nucleons, to probe the electro-weak interaction, to study the surface and thin-film magnetism, the electronic structure of metal and semiconductor surfaces and films [1]. There is no question but that having the highest possible value of polarization will have an enormous impact on the physics capabilities of a future International linear Collider (ILC) [2]. At collision energies of about 500 GeV in the center of mass, the cross sections for many processes depend on polarization. Within supersymmetry (SUSY), the production of right-handed sleptons and neutralinos dominates for a right-handed beam, whereas left-handed sleptons and charginos dominate for left-handed. Thus polarization will be very useful for sorting out SUSY signals. Moreover, polarized beams enhance the luminosity of a collider. The principal reason for the effectiveness of polarized electrons for energies $> M_Z$ is that right-handed electrons have no weak interaction whereas left-handed electrons do. Consequently, above the Z_0 mass, right-handed and left-handed electrons behave as distinctly different particles. Wherever cross sections have a strong dependence on polarization, about half the particles in an unpolarized beam are useless. By choosing only the desired particles for an interaction, the luminosity for a given beam intensity is effectively increased.

Strained GaAs-based superlattices (SL) are known to be most effective as photoemitters of spin-polarized electron beams [1]. Spin orientation of photoelectrons generated in the SL conduction band by circularly polarized light arises due to the splitting of the SL valence band. Though the theoretically predicted initial electronic polarization in the conduction band the near the absorption edge is expected to be close to $P = 100\%$, the experimentally observed values of the emitted electron polarization are typically in the interval from 80 to 86%. The main effect responsible for the substantial decrease of the initial electron polarization is the smearing of the interband absorption, which is mainly due to the fluctuations of SL layers compositions and to the valence band tails [3]. Polarization losses during electron extraction to the surface layer and emission into vacuum amount in the best photocathodes to an additional 6% [3,4|. These mechanisms set a sizeable limitation for the maximum polarization of emitted electrons.The initial polarization can be increased by choosing strongly strained structures with a higher valence band splitting. However the deformation of SL layers is limited by some critical value, deformation beyond this level result in structural defects, smaller residual strain and lower polarization.

The energy splitting between heavy hole (hh) and light hole (lh) minibands is provided both by the effects of strain and quantum confinement. The contributions of these effects do not combine additively and the resulting energy splitting is a complicated function of SL composition and layer thickness. The choice of the optimal SL structure assuring good transport properties and sufficient valence band splitting without strain relaxation is based on the reliable calculations of SL energy spectrum [5]. To combine the effects of strain and quantum confinement several types of SLs have been proposed: the SLs with strained quantum wells [1], strained barriers [3] and so-called strain-compensated SLs with opposite sign of deformation in quantum well and barrier [4]. Together with polarization of electron emission the quantum efficiency (QE) of the photocathode is the main parameter of polarized electron source. It is determined by the processes of electron extraction to the surface band bending region (BBR) and emission into the vacuum. Besides the transport properties of SL the crucial importance for these processes has the configuration of BBR and activation of the photocathode surface. Activation of the GaAs surface produces the negative electron affinity (NEA) and, hence, determines the band bending value and transparency of photocathode surface for the emitted electrons

In the present work we developed the optimized photocathode structure with working layer based on the AlInGaAs/AlGaAs SL with strained quantum wells. We report the highest level of polarization of the photoelectrons $P = 92\%$ in combination with the largest quantum efficiency at polarization maximum QE $= 0.85\%$. The obtained results are the best up to date achieved parameters of the polarized electron sources.

1. Design and fabrication

The photocathode structures were grown on a p-type (100) GaAs substrate by Molecular Beam Epitaxy (MBE) at RIBER 32P. The photocathode design is shown in Fig. 1. It consists of a 500 nm thick $Al_{0.35}Ga_{0.65}As$ buffer layer, AlInGaAs/AlGaAs SL working layer and surface GaAs layer for BBR. The superlattice contains 12 pairs of strained $Al_{0.19}In_{0.2}Ga_{0.61}As$ quantum well layers and unstrained $Al_{0.4}Ga_{0.6}As$ barrier layers. The layer compositions and thickness were optimized to achieve the

As cap		
GaAs	BBR	6 nm
$Al_{0.19}In_{20}Ga_{0.61}As$	SL 12X	5.4 nm
$Al_{0.4}Ga_{0.6}As$		2.1 nm
$Al_{0.35}Ga_{0.65}As$	Buffer	500 nm
GaAs substrate		

Fig. 1. Composition of the photocathode.

maximal valence band spitting with minimal risk of stain relaxation and structural defects and sufficient electron mobility along the SL axes. The Sl's energy spectrum has been calculated using the multiband Kane model, including the conduction band Γ_6, the states of light and heavy holes of the valence band Γ_8 and also the states of the spin-orbit splitted Γ_7 band [5]. According to these calculations the energy splitting between hh1 and lh1 minibands in the present structure is equal to 75 meV.

The photocathode structure was Zn-doped with heterogeneous doping profile. The highest doping level 7×10^{18} cm^{-3} was used in 6-nm thick GaAs to produce thin BBR. The lowest Zn concentration 3×10^{17} cm^{-3} was deposited in working layer to minimize the smearing of the absorption band edge. The fabricated structure was characterized by photoluminescence measurements. We control the actual SL parameters by comparison of the position of photoluminescence peak with the results of band energy calculations. The photoluminescence line width was used to control the structure quality. Finally the GaAs surface was activated by repeating deposition of cesium and oxygen to achieve the NEA.

2. Results and discussion

The polarization and quantum efficiency spectra as a function of the photon energy are shown in Fig. 2. The spectra show all the typical features of SL emission including high-polarization peak at the band edge absorption and a second peak at higher energies with a well-pronounced dip between them. The main polarization maximum originates from the optical transition from the first heavy-hole miniband hh1 to the first electron miniband e1, while the second maximum is connected with hh2–e2 optical transitions. The polarization decrease in between is connected with the optical transitions from light-hole miniband lh1 to electronic states of e1 miniband with opposite spin orientation. The spectrum of quantum efficiency exhibits a typical smooth behavior above the absorption edge with a sharp cutoff below which indicates a high structure quality of the fabricated photocathode. The cutoff of the QE corresponds to the photoabsorption edge and its position correlates with the position of the main polarization maximum. The absolute value of the QE at the polarization maximum is about 1%, which is best result reported for the polarized electron sources. The maximal electron polarization $P = 92\%$ demonstrated by the developed photocathode is also not exceeded by any other polarized electron sources. We did analyze the origin of the observed 8% polarization losses. Polarization losses during the electron transport to the BBR are less than 1%. Typical polarization losses in the BBR region of photocathodes with similar surface layer are about 5–6%. Thus the polarization

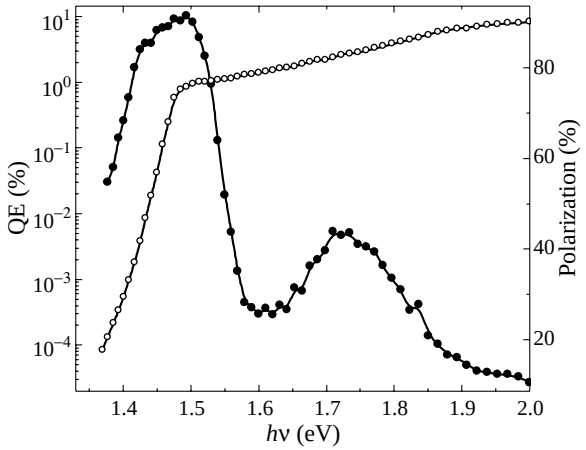

Fig. 2. Polarization (solid circles) and quantum efficiency (open circles) spectra of the emitted photoelectrons at room temperature.

losses on the photoabsorption stage amounts 2%. This fact indicates the optimized design and high quality of the developed working layer.

3. Conclusions

We have developed an optimized photocathode based on InAlGaAs/AlGaAs SL with strained quntum wells. The maximal polarization of the electron emission together with high value of quantum efficiency is the best combination of parameters demonstrated up to date by polarized electron sources. The obtained results show the advantages of the developed photocathode as a perspective candidate for practical spin polarized electron sources.

Acknowledgements

This work was supported by Russian Ministry of Education and Science under grant N.P. 2.1.1.2215 and by Swiss National Science Foundation under grant SNSF IB7420-111116.

References

[1] A. V. Subashiev *et al*, *Low-Dimentional Structures* **1/2**, 1 (1999).
[2] G. Moortgat-Pick *et al*, *SLAC-PUB-11087* (2005).
[3] L. G. Gerchikov *et al*, *Semiconductors* **40** 11, 1326 (2006).
[4] A. V. Subashiev *et al*, *Appl. Phys. Lett.* **86**, 171911 (2005).
[5] A. V. Subashiev *et al*, *J. Appl. Phys.* **96**, 1511 (2004).

15th Int. Symp. "Nanostructures: Physics and Technology"
Novosibirsk, Russia, June 25–29, 2007

Noise characteristics of a single-electron transistor based on highly doped silicon-on-insulator

V. A. Krupenin[1], D. E. Presnov[2], *V. S. Vlasenko*[1], N. N. Afanasiev[1] and D. N. Erkhov[1]

[1] Laboratory of Cryoelectronics, Moscow State University, 119899 Moscow, Russia
[2] Nuclear Physics Institute, Moscow State University, 119899 Moscow, Russia

Abstract. This work introduces fabrication and investigation of a single-electron transistor based on highly doped silicon on insulator material (SOI). The comparison of noise and electrical characteristics of SOI based SET transistors with the traditional SET transistors with $Al/AlO_x/Al$ junctions were carried out.

Introduction

Single-electron transistors have been demonstrated in numerous experiments using a wide variety of device geometries, materials, and techniques. We have developed and studied SOI based SET transistor structures that demonstrate classical behavior: changes between Coulomb blockade and fully conductive states and periodical modulation of transport current controlled by the gate electrode voltage. This type of SET transistor can be used as ultra-sensitive electrometer. Advantages of the chosen fabrication method compared with other types of SET devices [1–2]: simpler fabrication technology, mechanical solidity, higher stability to overvoltage, higher operating temperatures at the same sizes of structure elements, the opportunity to manufacture suspended devices.

1. Samples fabrication

The experimental structures were fabricated from highly doped (10^{20} cm^{-3}) silicon-on insulator film. We used SOI material with 55 nm thick silicon layer and 150 nm insulating SiO_2 layer placed on a silicon substrate. The fabrication method for the SET structures includes the following stages:

— ion implantation of SOI film with Ph^+ ions;
— e-beam lithography for the structure patterning;
— forming a metal mask by the deposition of Al thin film through the suspended 2-layers resist mask prepared with an electron- and photolithography;
— forming nanostructures by the reactive-ion etching of SOI film through the formed metal mask;
— reactive-ion etching process of Si for further downsizing of the fabricated structure and final adjustment of the transistor parameters.

2. Results and discussion

For the effective comparison several SOI based SET transistors were fabricated with a characteristics extremely close to those of the $Al/AlO_x/Al$ based transistors, e.g. without further downsizing of the structures. Size of the central island was about 100 nm.

IV-curves of the investigated samples were measured with different gate voltages applied and in the wide temperature range: from 30 mK to 1 K. The offset voltage of the Coulomb blockade was about 1 mV. The charge energy estimated from the offset voltage were 10 K. This means that such SET transistor shows the single-electron effects, observable on the temperature fluctuation environment, at temperatures of 1 K and lower.

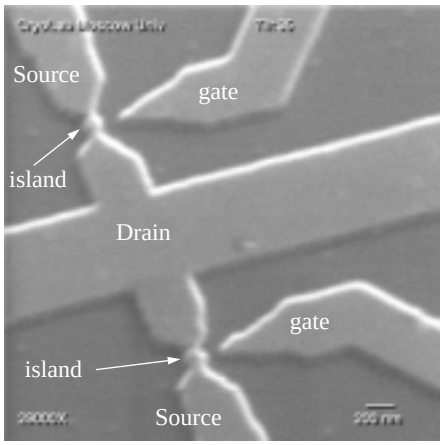

Fig. 1. Layout of fabricated SET transistor structures (SEM image).

The IV-curves shape and their behavior versus gate voltage were close to those of traditional $Al/AlO_x/Al$ SET transistors. SOI based SET transistor demonstrated blockade and completely conductive states at $V < V_{\text{off}}$ depending on the applied gate voltage. Such behavior shows that fabricated structures had geometry close to the geometry of a traditional $Al/AlO_x/Al$ SET transistors: one island and two tunnel junctions.

The modulation curves of the transistor demonstrate current oscillations depending on the bias voltage. The modulation amplitude increases with the increasing of the bias voltage. Its maximum corresponds to the bias voltage very close to the offset. This behavior correlates well with the behavior of the traditional SET transistor modulation curve. Maximum amplitude of the modulation curve was about 4.5 nA with a bias voltage 1 mV. Its period was about 400 mV. The maximum charge sensitivity SET transistor demonstrates with a bias voltage of 1 mV in the highest slope point of the modulation curve. This value was estimated to be 15 nA/e, which is 5–6 times greater than typical charge sensitivity of traditional SET transistors.

The charge noise of the highly doped SOI based SET transistor at 10 Hz was measured as 2.7×10^{-4} e/$\sqrt{\text{Hz}}$ at bias voltage of 1 mV and 2.3×10^{-4} e/$\sqrt{\text{Hz}}$ at 0.15 mV and temperature 30 mK (Figs. 2,3). The increasing of the current through SOI SET transistor causes the increasing of its charge noise exactly as in the traditional SET transistor case. The spectrum of this noise was close to the $1/f$ function in the voltage range from 0.1 Hz to 100 Hz. This is a common behavior for the traditional $Al/AlO_x/Al$ SET transistors where the sources of such charge noise are located in the dielectric substrate. Probably the suspended structures could solve the problem of excess charge

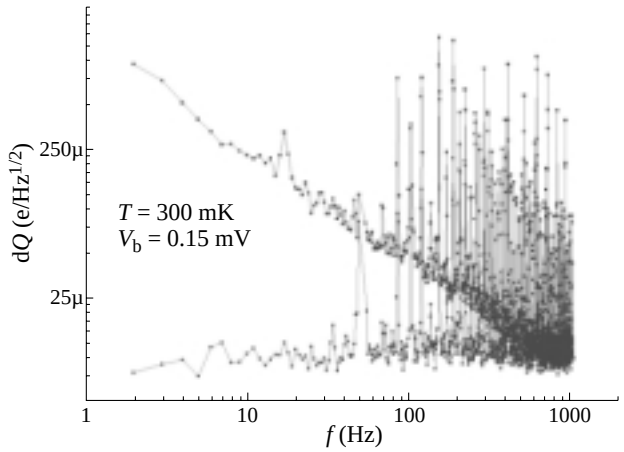

Fig. 2. Charge noise characteristic of a typical SET transistor based on SOI at bias voltage 0.15 mV and different gate voltages (maximum and minimum sensitivity of transistor).

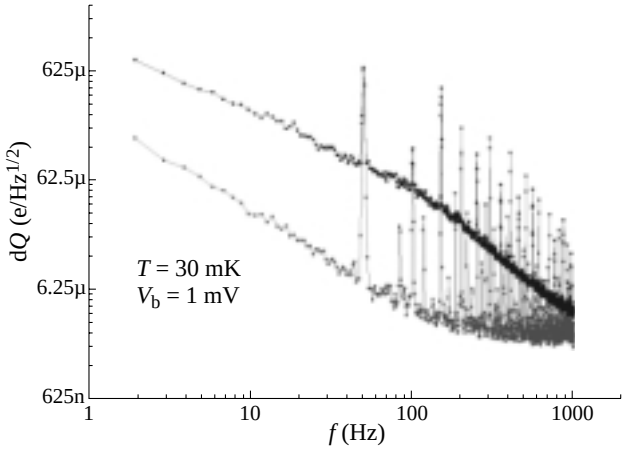

Fig. 3. Charge noise characteristic of a typical SET transistor based on SOI at bias voltage 1 mV and different gate voltages (maximum and minimum sensitivity of transistor).

noise for SOI based SET devices [1].

3. Conclusions

We fabricate and characterize SET transistor based on highly doped silicon on insulator, which has electric and noise characteristics very close to traditional SET transistors characteristics and sometimes even better than those. This fact with the mentioned above advantages of the introduced technology allows us to consider this device very promising in the future micro and nanoelectronics investigations and applications.

Acknowledgement

Authors wish to express their gratitude to professor M. Yu. Kupriyanov for useful discussions.

References

[1] V. A. Krupenin, D. E. Presnov, M. V. Savvateev, H. Scherer, A. B. Zorin, J. Niemeyer, "Noise in Al single-electron transistor of stacked design", *J. Appl. Phys.* **84**, 3212–3215 (1998).

[2] Yukinori Ono, Kenji Yamakazi, Masao Nagase, Seiji Horiguchi, Kenji Shiraishi, Yasuo Takahashi, "Single-electron and quantum SOI devices", *MEE* **59**, 435–442 (2001).

15th Int. Symp. "Nanostructures: Physics and Technology"
Novosibirsk, Russia, June 25–29, 2007

Silicon microchannel array for optical DNA-sensors

N. V. Vandysheva[1], S. I. Romanov[1], A. V. Bublikov[1], A. A. Lomzov[2] and D. V. Pyshnyi[2]

[1] Institute of Semiconductor Physics, Siberian Branch of Russian Academy of Sciences, Novosibirsk, Russia
[2] Institute of Chemical Biology and Fundamental Medicine, Siberian Branch of Russian Academy of Sciences, Novosibirsk, Russia

Abstract. The assumption that a silicon microchannel array (Si-MCA) offers the greatest promise for developing the methods of DNA hybridization analysis has been substantiated. A cell with Si-MCA for FTIR spectra measurements was made. FTIR absorption spectra of Si-MCA with amino-containing silane and immobilized DNA had been obtained.

Introduction

Up-to-date diagnostics of different diseases is based on DNA analysis using a method of molecular hybridization [1]. The method involves detection of complementary complexes formed by the oligonucleotide probes and DNA targets in a highly parallel fashion. More recently, to enhance the hybridization reactions as well as to provide increased sensitivity and dynamical range, higher throughput and shorter assay times, three-dimensional microchannel arrays were developed [2–6]. So far, microchannel glass substrates [2–4] and anodic porous alumina membranes [5,6] were used for multiplexed nucleic acid fluorescence hybridization assays. When compared to glass or porous alumina arrays, the Si-MCA provides a much wider choice of its structural parameters, functional materials and can be easily integrated with different nano- and microelectromechanical systems. Previously, it was shown that immobilization capacity of 160 μm-thick Si-MCA was 40 times higher then the capacity of glass slides [7].

In this report, we demonstrate analytical power of a newly emerged Si-MCA for DNA analysis using FTIR spectrometry. An experimental simulation of DNA hybridization (functionalization of 3D-substrate and an occurrence of DNA therein) was carried out.

1. Experimental

The 250 μm-thick MCA was made of (100) Si wafer through special techniques and had a highly ordered structure of square cross-section microchannels 7×7 μm^2 with $\{011\}$ fac-es and $\langle 100 \rangle$ axis, Fig. 1.

The surface of Si-MCA was modified with 3-aminopro-pyltrimethoxysilane (amino-containing silane). Then FTIR spectra of Si-MCA were recorded in the region of 1800–800 cm^{-1} using an Infralum FT-801 Fourier-spectrometer equip-ped with an infrared microscope. A DNA isolated from calf thymus was immobilized on this functionalized sudstrate due to electrostatic interaction with positively charged surface of Si-MCA. FTIR spectra of Si-MCA were recorded repeatedly. For reference, a planar unpenetrable substrate was processed in the same manner. IR-cell with the Si-MCA and the measuring system are shown in Fig. 1.

2. Results and discussion

IR spectra of the functional amino-containing silane appear in Fig. 2. The two reference and one "microchannel" curves are demonstrated. The reference spectrum 2 was obtained after three cycles of "deposition/drying" whereas the "microchan-

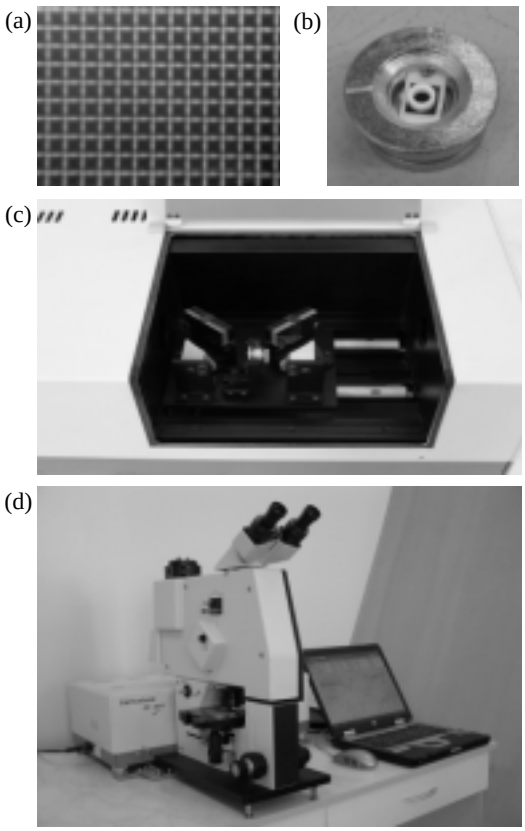

Fig. 1. Plane view of the Si-MCA (a), IR-cell with Si-MCA (b) and the measuring system (c,d).

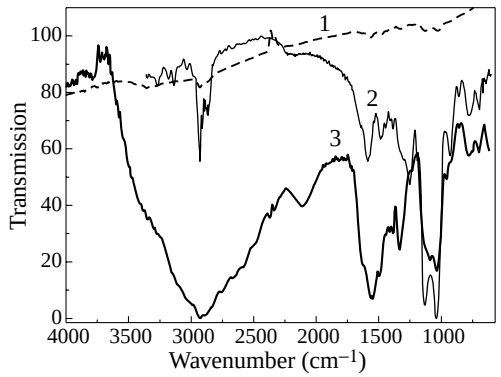

Fig. 2. FTIR spectra in the region of 1800–800 cm^{-1} for amino-containing silane chemisorbed on a planar substrate after one (1), three (2) cycles of "deposition/drying" and in the Si-MCA after one cycle (3).

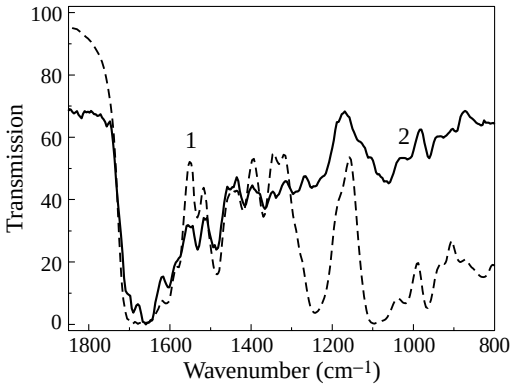

Fig. 3. FTIR spectra in the region of 1800–800 cm^{-1} for reference DNA (1) and the Si-MCA with DNA and amino-containing silane (2).

nel" spectrum 3 was at once recorded after one cycle. It is obvious that these spectra are identical. However, optical absorption in the Si-MCA "microchannel" curve is more pronounced.

FTIR spectra of reference DNA and the Si-MCA with DNA and amino-containing silane are shown in Fig. 3. There are the absorption band and lines at 11705–1636 and 1531, 1485, 1415, 1369 cm^{-1} in the spectra of reference DNA. These features are assigned to vibrations of the nucleic bas-es. The identical band and lines can be seen to be present in the spectrum of the Si-MCA, but its signal modulation is lesser. The presence of identical absorption band and lines proves the occurrence of DNA in our 3-D substrates.

3. Conclusion

We have shown that Si-MCA can be successfully employed as optical sensor for direct detection of DNA and functional groups with reasonably high sensitivity.

Acknowledgements

This work was supported by a grant of the MCB Program of RAS, the integration grants of SB RAS No. 55 and No. 73.

References

[1] M. J. Heller, *Annu. Rev. Biomed. Eng.* **4**, 129 (2002).
[2] V. Benoit V *et al*, *Analytical Chemistry* **73**, 2412 (2001).
[3] H. L. Fredrickson *et al*, *The Science of the Total Environment* **274**, 137 (2001).
[4] B. J. Cheek *et al*, *Analytical Chemistry* **73**, 5777 (2001).
[5] F. Matsumoto *et al*, *205th Meeting*, Abs. **745**, The Electrochemical Society, Inc., (2004).
[6] I. Vlassiouk *et al*, *Langmuir* **20**, 9913 (2004).
[7] A. Lomzov *et al*, *Mater. Res. Soc. Symp. Proc.* **915**, 0915-R03-06 (2006).

15th Int. Symp. "Nanostructures: Physics and Technology"
Novosibirsk, Russia, June 25–29, 2007

DNA as a building block for single molecule electronics; From transistor effect to a single molecule Esaki diode

Andrey V. Malyshev

GISC, Departamento de Física de Materiales, Universidad Complutense, Madrid, Spain
(on leave from Ioffe Institute, St Petersburg, Russia)

Abstract. The combination of electronic and self-assembly properties as well as its true nanoscale dimensions makes the DNA a promising candidate for the building block of single molecule electronics. We argue that the intrinsic double helix conformation of the DNA strands makes it possible to drive the electric current through the DNA by the perpendicular electric (gating) field, suggesting such applications as the field-effect transistor. The transistor effect is demonstrated for the gated poly(G)-poly(C) synthetic DNA within a simple model approach. We put forward experimental set-ups to observe the predicted effect and discuss possible device applications of the DNA. In particular, we propose a design of the single molecule analog of the Esaki diode.

Introduction

Charge transport through DNA molecules has extensively been studied lately (see Refs. [1–3] for an overview). Recent advances in experimental techniques allowed measurements on a single DNA molecule [4,5] and consolidated the expectation that DNA double helices can be particularly useful for single molecule electronics [3,6–8]. Many effects useful for molecular device applications have been predicted and demonstrated: rectification, the Kondo effect, the Coulomb blockade, etc. (see Ref. [8] for a recent overview).

In this contribution, it is demonstrated that the intrinsic helix conformation of the DNA strands determines transport properties of gated DNA molecules (subjected to an electric field perpendicular to the molecule axis). In particular, we show that the electric current through the double-helix DNA (in the base stacking direction) can be driven by the perpendicular gating field. We put forward new experimental set-ups to reveal the predicted effect and discuss possible applications of the DNA for molecular devices. In particular, we propose a design of the single DNA molecule analog of the Esaki diode.

The model

Here we address electronic properties of periodic poly(G)-poly(C) artificially created [9] DNA molecules which reveal wide-band-gap semiconductor behavior [4,5] and are probably one of the best candidates for novel single molecule device applications. We use the *minimum* tight-binding ladder model [10–12] that accounts for the double-stranded structure of the DNA. The tight-binding Hamiltonian of the N-base-pair DNA reads:

$$\sum_{s,n} \left(\varepsilon_{sn}|sn\rangle\langle sn| - t|sn+1\rangle\langle sn| + \text{h.c.} - \tau|-sn\rangle\langle sn|\right),$$

where ε_{sn} are on-site energies of the base molecules with index $n \in [1, N]$ labeling a pair and index $s = \pm 1$ labeling a strand, t and τ are inter-base hoppings parallel and perpendicular to the base stacking direction, respectively, while $\langle sn|$ and $|sn\rangle$ are bra and ket vectors of an electron at site n of the strand s.

The traditional ladder model neglects the helix geometry of the strands. In the case when the molecule is subjected to the perpendicular electric field the helix conformation becomes determinant and should be accounted for. Here we consider the B form of the DNA with the 10-base-pairs full-twist period. Neglecting the difference between major and minor grooves we set the on-site energies ε_{sn} as follows:

$$\varepsilon_{sn} = \varepsilon_{sn}^{(0)} + eE_n sr\cos\left(\frac{2\pi n}{10} + \varphi_0\right), \qquad (1)$$

where $\varepsilon_{sn}^{(0)}$ is site energy of the sn-th base molecule at zero field, E_n is the perpendicular gating field (for simplicity, let it be homogeneous: $E_n = E_0$), and $r \sim 1$ nm is the strand radius. Hereafter, we use the notation $V_g = 2E_0 r$ for the *gate* voltage drop across the double helix. The phase φ_0 that determines the orientation of the molecule with respect to the field is set to 0 from now on. Thus, the gated DNA is described by the Harper-type Hamiltonian with commensurate harmonic modulation of the on-site potential.

The DNA was supposed to be sandwiched between two metallic contacts and the field-dependent transmission coefficient of the system, $T(V_g, E)$, was calculated using the transmitting quantum boundary method . The transmission coefficient was then used to calculate the current-voltage characteristics of the device in the framework of the scattering formalism (see Ref. [13] for details):

$$I\left(V_g, V_{sd}\right) = \frac{2e}{h}\int T(V_g, E)\left[f_s(E, V_{sd}) - f_d(E, V_{sd})\right]dE,$$

where $f_{s,d}(E, V_{sd}) = (1+\exp(E_F \pm eV_{sd}/2 - E)/kT)^{-1}$ are Fermi functions of source and drain contacts, V_{sd} is the *source-drain* voltage drop, and E_F is the Fermi energy at equilibrium taken to be in the middle of the band gap, as for Au contacts [14]. The temperature T was set to 4 K.

Throughout the paper, the electron transport through a 31-base-pairs poly(G)-poly(C) DNA molecule is addressed with the following LUMO state on-site energies which are used as a starting point: $\varepsilon_{-1n}^{(0)} = \varepsilon_g = 1.14$ eV, $\varepsilon_{+1n}^{(0)} = \varepsilon_C = -1.06$ eV [15]. Hopping integrals t and τ are not considered as bare tight-binding parameters, rather as effective ones [12] and are adjusted to reproduce the voltage gap of about 2 V which was observed in experiments on the dry poly(G)-poly(C) DNA [4,5]: $t = 0.27$ eV, $\tau = 0.25$ eV. These values are within reasonable parameter intervals [16].

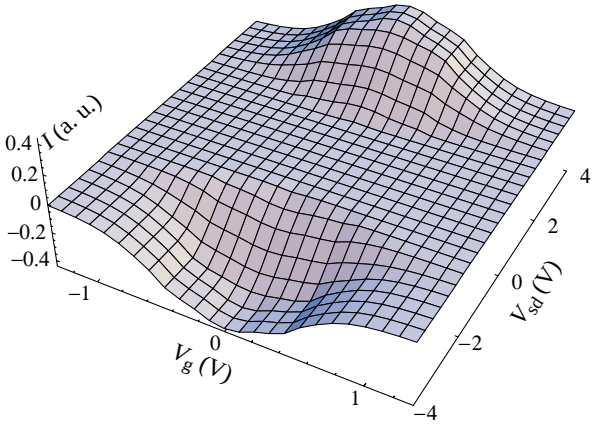

Fig. 1. Current-voltage characteristics of the 31-base-pairs poly(G)-poly(C) DNA molecule within a wide range of source-drain (V_{sd}) and gate (V_g) voltages.

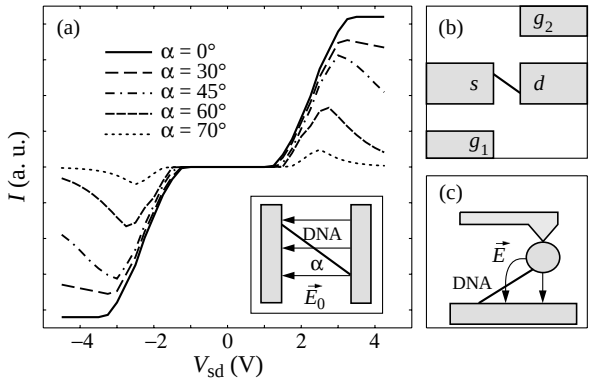

Fig. 2. (a) Non-monotonous current-voltage characteristics of the tilted DNA for different angles α between the molecule and the inter-contact electric field (see the text and the inset of the panel (a) where a single molecule analog of the Esaki diode is shown schematically). (b),(c) Proposed experimental configurations to observe the predicted non-monotonous $I-V$ curves: (b) a DNA molecule trapped between two contacts by asymmetric electrostatic trapping method [13], and (c) a DNA molecule trapped between a substrate and a golden nano-particle suspended from the metal coated AFM tip [5].

Results and discussion

Figure 1 demonstrates $I-V$ characteristics within a wide range of source-drain and gate voltages. Semiconducting behavior can be observed for $|V_g| \leq 0.7$ V as well as strong gating effect for $|V_{sd}| \geq 1.2$ V: for all such values of V_{sd} a typical hat-like $I-V_g$ characteristic is observed (consider cross-sections of the surface parallel to the V_g axis). Strong dependence of the source-drain current on the gate voltage suggests the usage of the gated double helix DNA as a field-effect transistor.

Current-voltage characteristics of the tilted DNA for different angles α between the molecule and the homogeneous inter-contact field are presented in Fig. 2(a). The inset of Fig. 2(a) shows the sketch of the device design. The $I-V$ curves of the device are non-monotonous and have a region with the negative differential resistance, similar to those of the tunneling diode, which suggests that the proposed device is a single molecule analog of the Esaki diode.

Panels (b) and (c) of Fig. 2 show experimental set-ups which we put forward to observe the non-monotonous $I-V$ characteristics. In particular, panel (b) illustrates the four contact configuration that is proposed for *asymmetric* electrostatic trapping of a DNA molecule: applying appropriate biases to all four contacts a tilted electrostatic trapping field can be induced between the electrodes "s" and "d". Then, the polarized molecule aligns with the field and gets trapped between contacts "s" and "d" being tilted with respect to them. Electrodes "s" and "d" can then be used for measurements, resulting in the experimental configuration presented in the inset of panel (a).

Conclusions

In summary, the predicted gating effect opens a possibility to use the DNA for various novel single molecule devices such as the field effect transistor, the Esaki-type diode, etc. The same argumentation and conclusions may also apply to G4-DNA and proteins, many of which have the α-helix conformation [17].

Acknowledgements

The author is grateful to F. Domínguez-Adame, E. Maciá, R. Gutierrez, and V. Malyshev for fruitful discussions, VM's constant encouragement throughout the study is greatly appreciated. The study was supported by the MEC under projects Ramón y Cajal and MOSAICO.

References

[1] M. A. Ratner, *Nature* **397**, 480 (1999).
[2] D. Porath *et al*, *Top. Curr. Chem.* **237**, 183 (2004).
[3] R. G. Enders *et al*, *Rev. Mod. Phys.* **76**, 195 (2004).
[4] D. Porath *et al*, *Nature* **403**, 635 (2000).
[5] H. Cohen *et al*, *Proc. Natl. Acad. Sci.* **102**, 11589 (2005).
[6] M. Mertig *et al*, *Eur. Phys. J. D* **9**, 45 (1999).
[7] K. Keren *et al*, *Science* **302**, 1380 (2003).
[8] G. Cuniberti, G. Fagas, and K. Richter (Eds.), *Introducing Molecular Electronics* (Berlin: Springer) 2005.
[9] D. B. Tippin *et al*, *J. Mol. Biol.* **270**, 247 (1997).
[10] K. Iguchi, *Int. J. Mod. Phys. B* **11**, 2405 (1997); *ibid* **17**, 2565 (2003); *ibid* **18**, 1845 (2004).
[11] H. Yamada, *Int. J. Mod. Phys. B* **18**, 1697 (2004); *Phys. Lett. A* **332**, 65 (2004).
[12] R. Gutiérrez *et al*, *Phys. Rev. B* **74**, 235105 (2006).
[13] A. V. Malyshev, *Phys. Rev. Lett.* 98, 096801 (2007).
[14] M. S. Xu *et al*, *Appl. Phys. Lett.* **87**, 083902 (2005).
[15] H. Mehrez and M. P. Anantram, *Phys. Rev. B* **71**, 115405 (2005).
[16] E. Maciá and S. Roche, *Nanotech.* **17**, 3002 (2006).
[17] C. Branden and J. Tooze, *Introduction to Protein Structure* (New York: Garland Publishing), ed. 2, 1999.

15th Int. Symp. "Nanostructures: Physics and Technology"
Novosibirsk, Russia, June 25–29, 2007

Nano-tubes for nanomechanics

M. Willander[1,2], O. Nur[1], Y. E. Lozovik[3], A. M. Popov[3] and M. Riaz[1]

[1] Department of Science and Technology (ITN), Campus Norrköping, Linköping University, SE-601 74 Norrköping, Sweden
[2] Department of Physics, Gothenburg University, SE-412 96 Gothenburg, Sweden
[3] Institute of Spectroscopy, Russian Academy of Science, 142190, Troitsk, Moscow, Russia

Abstract. We will discuss the possible applications of multi wall carbon nano-tubes (MWCNs) and ZnO nanorods for future nano-mechanical and nano-electro-mechanical systems (NEMS). The basic special mechanical properties of these two nano-materials will be briefly presented. Some theories of interest to NEMS are to be highlighted. Examples of some NEMS based on these two nano-materials will be presented.

Introduction

Carbon nano-tubes (CNs) have both unique electronic and mechanical properties, which makes them suitable for many applications in nano-electro-mechanics i.e. for NEMS [1]. For example, the value of both the Young modulus and the bending elastic modulus of CNs are of the order of about 1 TPa. In addition, the walls of CNs can be metallic or semiconducting, depending on the category of the CNs and the wall structure. The employment of CNs as elements for electronic applications, such as, nano-diodes, nano-transistor, and nano-logic gates, has been discussed for some time. In addition, the use of CNs for NEMS systems utilizing both the electronic as well as the mechanical properties likes electrical nano-switches; nano-tweezers and a variety of field emission devices have also been proposed and analyzed [2]. In this talk we will present and analyze NEMS based on the weak van de Waals interaction between different walls of multi-wall carbon nanotubes (MWCNs) [2,3]. Such property allows CNs to easily slide and/or rotate with respect to each other. This property allows a new family of possible NEMS, to mention few, nano-bearings, nano-gears, constant force nano-springs, nano-motors etc. [5]. Due to the fact that walls of CNs are atomically precise; the life time of this new family is not limited by the wear of the surfaces.

On the other hand, ZnO nano-rods with a variety of unique properties, is of interest particularly the piezoelectric property. In addition, ZnO with its hexagonal structure possesses one of the most ideal packing factors. This makes ZnO to have stable mechanical properties. ZnO nano-structures can be synthesized by different methods [6,7]. Among the ZnO nanostructures of interest for NEMS are nano-propellers, nano-rings, nano-combs etc... These different ZnO nano-structures can be grown with polar and non-polar surfaces. Different aspects of ZnO nano-structures of interest for NEMs are to be presented and discussed.

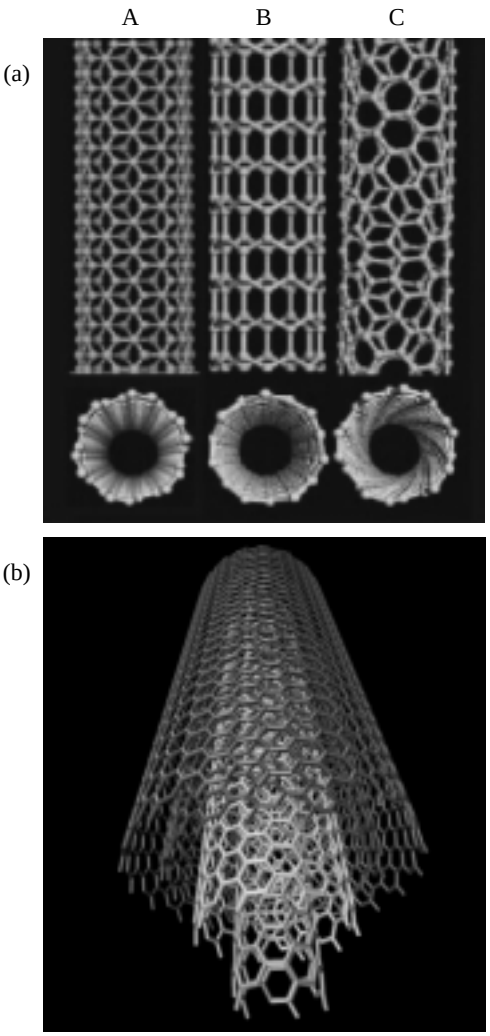

Fig. 1. (a) Three different types of CNs, A is armchair (n, n), B is zigzag $(n, 0)$ and C is chiral (n, m). (b) Shows a typical multi-wall CN.

Carbon nanotubes structures, properties, interwall interactions, and some future nano-devices

The structure of CN walls is determined by a pair of integers (n, m) corresponding to a lattice vector $\mathbf{c} = n\mathbf{a}_1 + m\mathbf{a}_2$ on the graphene plane used to perform conformal mapping, where $\mathbf{a}_1$ and $\mathbf{a}_2$ are the unit vector of the graphene sheet (see Fig. 1). The corresponding wall radius of the CN is determined from the length of the graphite lattice vector together with the integers n and m. Since the CN wall is a one dimensional crystal the neighboring walls can be commensurate or non-commensurate. The commensurability is in fact an essential property that determines the relative motion of walls. The role of this property in the relative motion between walls in double wall CNs is to be highlighted.

The excellent elastic properties of different types of CNs are to be discussed. The dependence of the elastic properties on the geometrical dimensions of CNs will be presented. The published theories concerning interwall interaction between two

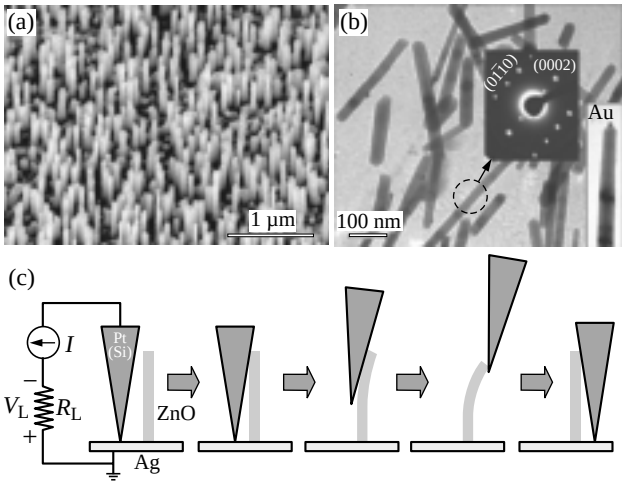

Fig. 2. Experimental design for converting nanoscale mechanical energy into electrical energy by a vertical piezoelectric (PZ) ZnO NW. (a) Scanning electron microscopy images of aligned ZnO NWs grown on a-Al_2O_3 substrate. (b) Transmission electron microscopy images of ZnO NWs, showing the typical structure of the NW without an Au particle or with a small Au particle at the top. Each NW is a single crystal and has uniform shape. Inset at center: an electron diffraction pattern from a NW. Most of the NWs had no Au particle at the top. Inset at right: image of a NW with an Au particle. (c) Experimental setup and procedures for generating electricity by deforming a PZ NW with a conductive AFM tip. The base of the NW is grounded and an external load of RL is applied, which is much larger than the resistance RI of the NW. The AFM scans across the NW arrays in contact mode [6].

walls in CNs by potential relief are to be reviewed. The influence on the barriers to the relative motion between two walls in CNs in relation to the symmetry of the interwall interaction energy through potential relief will be considered. In addition, other related important issues concerning the dynamics of the relative motion are also to be mentioned. The available experimental results on the relative motion are to be presented. Finally the theories of mechanical nano-device operation will be discussed, with review of some examples of these NEMS based on CNs.

ZnO nano-structures for NEMS applications

As mentioned above, ZnO having a hexagonal crystal structure is possessing excellent mechanical properties. Among the many interesting mechanical properties of ZnO, the piezoelectricity is of importance to this presentation. As ZnO nanostructures are of recent interest compared to CNs, we will review the few examples of ZnO based NEMS published in the literature and highlight the potential for future applications as a NEMS element. The most recent example of nano-generator will be discussed in details (see Fig. 2).

References

[1] W. E. Wong, P. E. Sheehan, C. M. Lieber, *Science* **277**, 1971 (1997).
[2] J. Koohsorkhi, H. Hoseinzadegan, S. Mohajerzadeh, E. Asl Soleimani, E. Arzi, *Fullerenes, Nanotubes, and Carbon Nanostructures*, **13**, suppl. 1, 355 (2005).
[3] Y. E. Lozovik, A. V. Mingon, A. M. Popov, *Phys. Lett. A*, in press (2007).
[4] A. V. Belikov, A. G. Nikolaev, Y. E. Lozovik, and A. M. Popov, *Chem. Phys. Lett.* **385**, 72 (2004).
[5] T. D. Yuzvinsky , A. M. Fennimore, A. Zettl, *AIP Conference Proceedings* **723**, 512 (2004); Y. E. Lozovik, A. M. Popov, M. Willander, to be publish.
[6] W. L. Hughes, and Z. L. Wang, *Applied Physics Letters*, **86** (4), 43106 (2005).
[7] Q. X. Zhao, P. Klason, and M. Willander, *Applied Physics A: Materials Science & Processing*, in press (2007).

15th Int. Symp. "Nanostructures: Physics and Technology"
Novosibirsk, Russia, June 25–29, 2007

Room-temperature ferromagnetism in InMnAs layers

O. V. Vikhrova[1], Yu. A. Danilov[1,2], *A. V. Kudrin*[1], B. N. Zvonkov[1], V. V. Podolskii[1], Yu. N. Drozdov[2] and M. V. Sapozhnikov[2]

[1] Physico-Technical Research Institute, University of Nizhny Novgorod, 603950, Nizhny Novgorod, Russia
[2] Institute for Physics of Microstructures, RAS, 603950, Nizhny Novgorod, Russia

Abstract. The InMnAs layers have been fabricated by laser deposition. X-ray diffraction measurements shows reasonably high crystal quality of these layers on GaAs(100) substrates. Room-temperature ferromagnetism was observed with magneto-optical Kerr effect and anomalous Hall effect measurements. The mesa structures with p-InMnAs layer fabricated by deposition on n-type InAs substrate show positive magnetoresistance up to 90% at 77 K and 70% at 300 K.

Introduction

Previously the formation of ferromagnetic InMnAs layers by MOVPE at growth temperatures of 475 °C was reported [1]. In this paper, we report about the possibility of formation of room-temperature ferromagnetic InMnAs layers by laser deposition.

1. Samples and experimental

InMnAs layers were grown by pulse Q-switched YAG:Nd laser ($\lambda = 1.06\ \mu$m) sputtering of Zn-doped InAs ($p \sim 10^{17}$ cm^{-3}) and metal Mn targets, placed in the quartz reactor with the flow of hydrogen and arsine. Semi-insulating GaAs (100) was used as substrate. The substrate temperature (T_g) was varied from 200 to 500 °C. A content of Mn depended on relation of the times for periodical sputtering of Mn and InAs ($X_{\mathrm{Mn}} = t_{\mathrm{Mn}}/t_{\mathrm{InAs}}$). The InMnAs layers thickness ranged from 50 to 400 nm. Electrical properties of the layers were studied by Hall effect measurements at room temperature (RT) and 77 K and sheet resistance measurements at temperature range of 77–370 K. Magneto-optical properties were investigated by longitudinal magneto-optical Kerr effect (MOKE) at RT.

2. Results and discussion

Sheet resistance (R_{S}) of InMnAs films as a function of deposition temperature (T_g) is shown in Fig. 1. As can be seen from this figure, the R_{S} value is minimum (10^4 Ohm/sq at $X_{\mathrm{Mn}} = 0.5$) in rather narrow deposition temperature range of 280–330 °C. Decreasing the growth temperature to 200 °C or increasing to 500 °C gives high-resistance InMnAs layers. Similar behavior of electrical properties of samples, in our opinion, can be associated with strong temperature influence on manganese incorporation in the InAs matrix. Apparently, temperature range 280–330 °C is optimal for InAs doping of

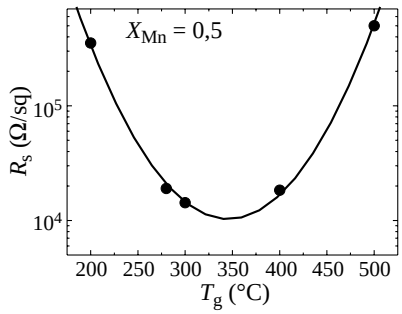

Fig. 1. The sheet resistance of InMnAs films grown at different deposition temperatures. $X_{\mathrm{Mn}} = 0.5$.

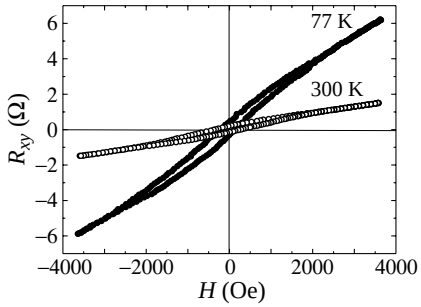

Fig. 2. Hall resistance dependence on magnetic field for InMnAs sample at 77 and 300 K. The thickness of InMnAs layer is 460 nm, $T_g = 320$ °C, $X_{\mathrm{Mn}} = 0.33$.

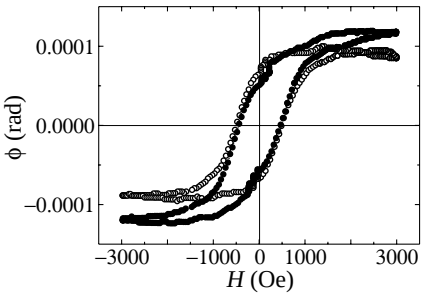

Fig. 3. Kerr angle versus external magnetic field for two perpendicular directions of field in sample plane ($T_g = 320$ °C, $X_{\mathrm{Mn}} = 0.33$).

Mn, and at these temperatures occurs effective substitution of In by Mn atoms. Samples InMnAs, grown in this temperature range, exhibited p-type semiconducting behavior with carrier concentrations as high as $\sim 5 \times 10^{18}$ cm^{-3}.

The structures grown at $X_{\mathrm{Mn}} = 0.3-0.5$ and $T_g = 280-330$ °C exhibit ferromagnetism at 300 K and 77 K. This is evident from nonlinear Hall resistance dependence on magnetic field with hysteresis loop (Fig. 2).

The magnitude of coercive field is equal to ≈ 330 Oe. The MOKE measurements showed that there is a hysteresis loop in the dependence of Kerr angle on the value of external magnetic field. Fig. 3 shows the dependence of Kerr angle for two perpendicular directions of field in sample plane. From Fig. 3 it can be conclude what there is no strong anisotropy of hysteresis curves in sample plane when magnetic field direction changes from axis $\langle 1\bar{1}0\rangle$ to $\langle 110\rangle$.

Crystal structure of InMnAs films was analyzed by X-ray diffraction. Fig. 4 shows $\Theta/2\Theta$ scans for InMnAs and InAs films for comparison. Both spectra contain GaAs(002) substrate and InAs(002) epitaxial layer peaks near 2Θ val-

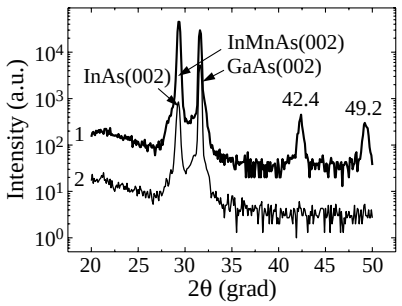

Fig. 4. X-ray diffraction spectra for InMnAs (1) and InAs (2) layers grown by laser deposition ($T_g = 320$ °C).

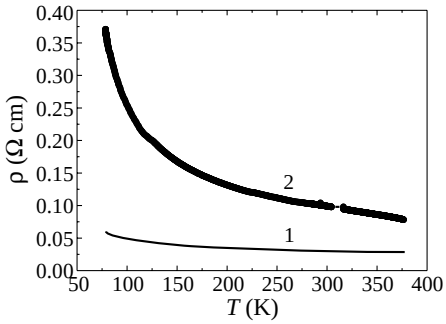

Fig. 5. Resistivity of InMnAs samples ($X_{\mathrm{Mn}} = 0.5$) with thickness of 50 nm as a function of measurement temperature. T_g (°C): 1 — 300, 2 — 280.

ues of 31.6 and 29.5, respectively. Furthermore, two additional peaks that locate near the values of 42.3 and 48.9 were recorded. Most probable identification of these peaks is associated with presence of hexagonal MnAs phase reflexes of $(10\bar{1}2)$ and $(11\bar{2}0)$, respectively. Thus X-ray diffraction shows that InMnAs films grown at $T_g = 280{-}330$ °C and $X_{\mathrm{Mn}} = 0.3{-}0.5$ has rather high crystal quality; but they are not single-phase.

The resistivity measurements InMnAs layers ($X_{\mathrm{Mn}} = 0.5$; $T_g = 300$ °C or 280 °C) as a function of temperature show semiconductor type behavior (Fig. 5). The resistivity decreases by one order of magnitude with increasing of the growth temperature of 20 °C. From the resistivity vs. temperature dependences the activation energy of conduction was estimated at 6 and 12 meV for samples with $T_g = 300$ °C and 280 °C, respectively. Measured activation energy is smaller what 23 meV energy of acceptor Mn level energy in InAs [2]. It can be attributed to the formation of an impurity band above the valence band. Further, it should be noted that InMnAs samples heating up to 370 K did not reveal any local resistance maximum in the Curie temperature range (318 K) for MnAs hexagonal phase [3]. This fact suggests that room-temperature ferromagnetism in InMnAs layers, which causes the anomalous Hall effect, is not associated with MnAs cluster presence.

One the possible way of practical application obtained InMnAs layers is fabrication of magnetic field sensors [4]. We formed the structure with resistance dependence on magnetic field. For this structure, a 400 nm thick p-InMnAs layer was deposited on a n-InAs substrate. The p-InMnAs was patterned into $\sim$ 300 μm diameter mesa. A big positive magnetoresistance about $\sim$ 90% at 77 K and 70% at 300 K was observed in magnetic field of 1 T, applied perpendicularly to structure surface (Fig. 6). Similar magnetoresistance was attributed by authors [4] with carrier scattering arising from compositional

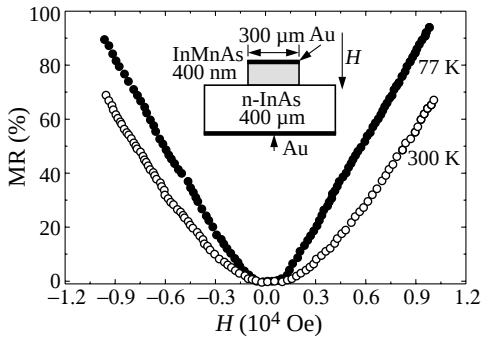

Fig. 6. Magnetoresistance of p-InMnAs/n-InAs structure vs. magnetic field at 77 K and 300 K. The inset shows the schematic illustration of the p-InMnAs /n-InAs structure.

inhomogeneities at the InMnAs/InAs interface.

Acknowledgements

The work was supported by the Russian foundation for basic research (Grants Nos. 05-02-16624, 03-02-16777) and by CRDF-RUX0-001-NN-06/BP1M01.

References

[1] A. J. Blattner, B. W. Wessels, *Appl. Surf. Science* **221**, 155 (2004).

[2] S. J. May, A. J. Blattner, B. W. Wessels, *Physica B* **340–342**, 870 (2003).

[3] F. Iikawa, P. V. Santos, M. Kastner, F. Schippan, L. Daweritz, *Phys. Rev. B* **65**, 205328 (2002).

[4] S. J. May, B. W. Wessels, *Appl. Phys. Lett.* **88**, 072105 (2006).

15th Int. Symp. "Nanostructures: Physics and Technology"
Novosibirsk, Russia, June 25–29, 2007

Quantum ring complexes grown by droplet epitaxy

T. Mano[1], T. Kuroda[1,2], T. Ochiai[1], K. Sakoda[1,3] and N. Koguchi[1]

[1] Quantum Dot Research Center, National Institute for Materials Science, 1-2-1 Sengen, Tsukuba, Ibaraki, Japan
[2] PRESTO, Japan Science and Technology Agency, 4-1-8 Honcho Kawaguchi, Saitama, Japan
[3] Graduate School of Pure and Applied Science, University of Tsukuba,
1-1-1 Tennodai, Tsukuba 305-8577, Japan

Abstract. We demonstrate self-assembly of quantum ring (QR) complexes in a lattice-matched GaAs/AlGaAs system by droplet epitaxy. Focusing on the crystallization mechanisms of the droplets, we have successfully created single QRs and concentric quantum double rings by simply supplying As_4 flux to the hemispherical Ga droplets. We have also found that the size of these rings can be tuned independently. These unstrained quantum ring complexes are ideal for the further understandings of quantum interference phenomena specifically found in the semiconductor QR systems.

Introduction

The use of self-assemblies during the crystal growth allows us to create high quality quantum nanostructures without lithographical techniques. Therefore, self-assembling technologies have been intensively studied for the basic physics and practical device applications. The physical properties of the quantum nanostructures strongly depend on their size and shapes [1]. By combining various crystal growth technologies, a variety of nanostructures have been successfully created and their characteristic properties have been demonstrated. Among them, quantum ring (QR) systems have recently attracted a great deal of attention because fascinating properties have been predicted and demonstrated [2,3]. In lattice-mismatched systems, self-assembled single ring structures have been realized by using modified Stranski–Krastanow (S–K) growth mode [4–6]. In these systems, however, the real ring structures are complex due to the heavy intermixing of the materials [4]. Also it has been predicted that the electrons and/or the holes might localize in particular in-plane directions in these strained systems [7]. These will make it difficult to analyze the properties of the QR systems. From these viewpoints, strain-free self-assembled QRs are also desired for the studies of basic physics of the semiconductor QR systems. In contrast to the S–K growth mode, we have proposed and developed another self-assembled growth techniques, termed *droplet epitaxy*, for the formation of high quality self-assembled nanostructures [8,9]. Since the mechanism of dropet epitaxy is based on the formation of liquid metal particles (droplets) and their crystallization, this method has been widely applied to various compound semiconductor systems both in the lattice-matched and mismatched systems [8–14]. While we had mainly focused on the formation of simple dot-shaped quantum nanostructures (quantum dots (QDs)), the droplet epitaxy technique has a potential for the growth of more complex nanostructures [15], when we take note a characteristic properties of the crystallization processes. In this reports, we will show our recent achievements on the self-assembly of GaAs QR complexes in a lattice-matched system.

1. Experimental

The samples were grown by conventional solid-source molecular beam epitaxy on GaAs (100) substrates. For the precise control of As_4 flux intensity, a valved-cell was used for the As source. After the growth of a 100 nm thick $Al_{0.3}Ga_{0.7}As$ buffer layer at 580 °C, As-stabilized $c(4\times4)$ surface was formed by reducing the substrate temperature (Fig. 1(a)). For the Ga droplet formation, nominally 3.75 ML (0.5 ML/s) Ga was supplied to the $c(4\times4)$ surface at 200 or 350 °C without As_4 flux (Fig. 2(b)). The background pressure was kept below 1×10^{-8} torr. The droplets are, then, crystallized into GaAs by supply of As_4 flux with various intensities at 200 °C (Fig. 1(c)). To improve the crystalline qualities, the samples were annealed at 350 °C for 10 min under As_4 flux, where the surface nanostructures almost keep their shapes. For the structural characterization, the surface morphologies of the samples after the annealing process were observed by non-contact mode atomic force microscope (AFM) in air.

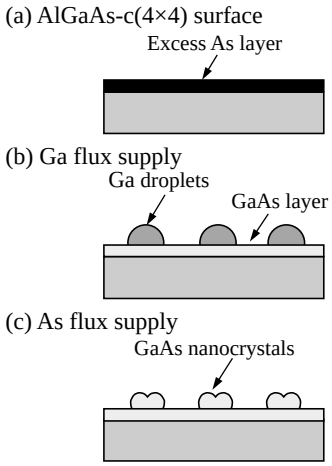

Fig. 1. Schematic illustration of the droplet epitaxy technique to form GaAs nanostructures on AlGaAs surface.

2. Results and discussion

Figure 2(a) shows the AFM image of the surface after the supply of 3.75 ML Ga on the $c(4\times4)$ surface at 200 °C. Many hemispherical shaped Ga droplets are formed on the surface with the density of $\sim1\times10^{10}$ /cm^2. The average base size and height are 20 and 7 nm, respectively. The size distribution of the droplets is ∼20%. On the $c(4\times4)$ surface, there is 1 ∼ 2 ML of excess As layer [16]. The first supplied 1 ∼ 2 ML Ga changes into two-dimensional GaAs layer and the rest of Ga form droplets [9]. After the supply of As_4 flux to the droplets with different intensities at 200 °C, these Ga droplets change into GaAs nanostructures with various shapes (Figs. 2(b)–(e)) [15,17,18]. Since the densities of the droplets

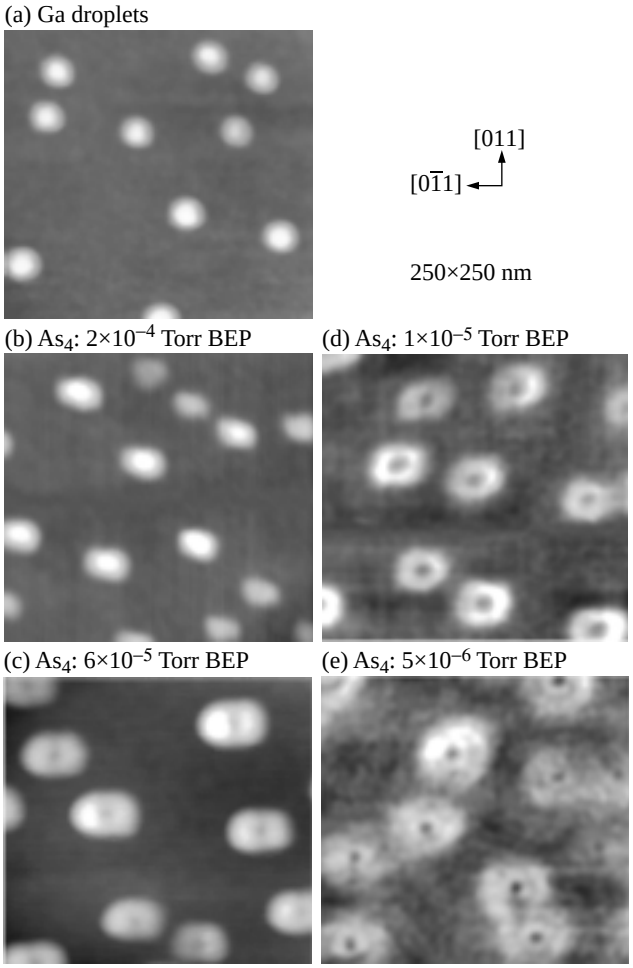

Fig. 2. 250×250 nm AFM images of the surfaces. (a) Ga droplets, (b) GaAs QDs, (c) GaAs DQDs, (d) GaAs single QRs, and (e) GaAs CQDRs. The black-to-white height contrast is (a) 16.0 nm, (b) 10.0 nm, (c) 10.0 nm, (d) 4.0 nm, and (e) 2.5 nm.

and GaAs nanostructures are almost identical, we believe that a droplet is crystallized into each GaAs nanostructure.

When we supply intense As_4 flux (2×10^{-4} torr beam equivalent pressure (BEP)), cone-shaped GaAs nanostructures (standard QDs) are formed (Fig. 2(b)) [15]. In contrast, by reducing the As_4 flux intensities for crystallization, central holes become visible. When we crystallize the droplets with the intensity of 1×10^{-5} torr BEP, the central holes become very clear and well-defined single QRs are formed (Figs. 2(d) and 3) [15,17]. The single QRs exhibit excellent rotational symmetry. The average peak size and height of the single QRs is ∼22 and ∼2 nm, respectively. The size of the single QRs is almost the same as base size of the original Ga droplet and changes with the droplet size [17,18]. These suggest that the effective crystallization occurs at the edges of the droplets [19].

Here, we would like to additionally point out the formation of double QDs (DQDs). When we crystallized the droplets with As_4 flux of 6×10^{-5} torr BEP, the shape of the nanostructures become highly anisotropic, as seen in Fig. 2(c). They are not a ring but laterally coupled two QDs [20,21]. We believe that these DQDs are the good candidate for the formation of artificial molecules.

When we use further reduced intensity of 5×10^{-6} torr BEP for the crystallization of the droplets, the mean height of nanostructures decreases (Fig. 2(e)). Although the nanostructures are not so well-defined due to the extremely low-height, it is visible that other rings appear outside of the initial rings, forming concentric quantum double rings (CQDRs) with a well-defined central holes [15,18]. The respective diameters of the inner and outer rings are ∼20 and ∼50 nm.

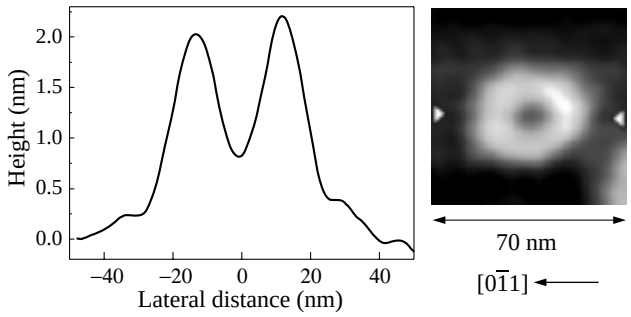

Fig. 3. Cross-section profiles along the [0$\bar{1}$1] direction of a single QR (indicated by white arrowheads in the right-hand side of magnified AFM image).

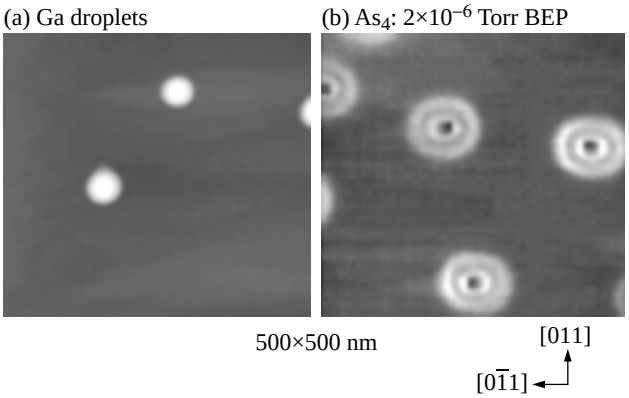

Fig. 4. 500×500 nm AFM images of the surfaces. (a) Ga droplets and (b) GaAs CQDRs. The black-to-white height contrast is (a) 25.0 nm and (b) 8.5 nm.

When larger Ga droplets are prepared as an initial structure, more well-defined CQDRs are formed [18]. Figure 3 shows AFM images of the (a) Ga droplets formed by supply of 3.75 ML Ga on the $c(4\times4)$ surface at 350 °C and (b) GaAs nanostructures formed using As_4 flux (2×10^{-6} torr BEP) supply to the droplets at 200 °C. After crystallization of the Ga droplets (density: $\sim1\times10^9$ /cm^2, base size: ∼50 nm, height: ∼17 nm), well-defined CQDRs are formed (Figs. 4(b) and 5). The respective diameters of the inner and outer rings are ∼45 and ∼100 nm; both rings are ∼5 nm high. The rings also show a good circular symmetry. In the CDQRs, the size of the inner rings is also almost the same as the base size of the initial droplets, which may be caused by the effective crystallization at the edges of the droplets. However, we should note that the diameter of the outer ring exceeds the diameter of the original Ga droplet. This indicates the migration of Ga atoms away from the droplet. In the crystallization stage, Ga atoms are mainly in the droplets, and As atoms are densely dispersed on the surface far from the droplet. This concentration gradient might cause the migration of Ga atoms away from the droplet, and that of the As atoms, toward the droplet. Efficient counter flows of Ga and As atoms results in the crystallization of GaAs outside the original droplet, i.e., formation of the outer rings. This inter-

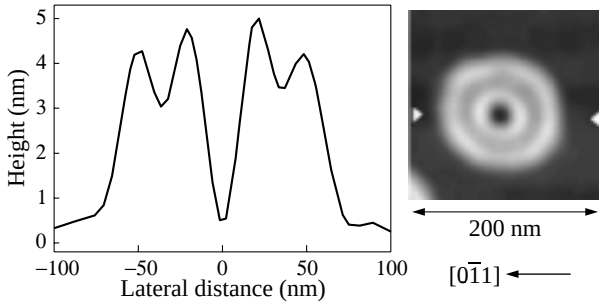

Fig. 5. Cross-section profiles along the [0$\bar{1}$1] direction of a CQDR(indicated by white arrowheads in the right-hand side of magnified AFM image.

pretation is supported by the fact that diameter of the outer ring is found to increase with decreasing As_4 flux intensity, while that of the inner ring is almost unchanged [18]. These findings suggest that the diameters of both inner and outer rings can be independently controlled by tuning the initial droplet sizes and As_4 flux intensities, respectively.

3. Summary

Well-defined GaAs quantum ring (QR) complexes are created by droplet epitaxy in a lattice-matched system. By adjusting the As_4 flux intensity, the crystallization was enhanced at the edge and/or outside of the droplets, resulting in the formation of single QRs or concentric quantum double rings (CQDRs). We also found that the size of the rings can be independently controlled. From the capped QR complexes, we have observed efficient photoluminescence (PL) emission, which indicates the high quality. From the high quality QRs, recently, we have demonstrated photo-pumped lasing at room temperature [22]. We have also performed micro-PL measurements on single CQDR and successfully observed distinct PL emission from inner and outer rings [18,23].

Although further studies of crystallization processes are necessary, droplet epitaxy is a highly promising method for the QR complexes in lattice-matched systems, which are ideal for the studies of physics of semiconductor QRs.

Acknowledgements

The authors wish to acknowledge T. Noda, K. Mitsuishi, M. Kawabe, M. Yamagiwa, T. Tateno, J. Kim, A. Ohtake, M. Gurioli, and S. Sanguinetti. The works was partly supported by a Grant-in-Aid from the Ministry of Education, Culture, Sports, Science and Technology of Japan.

References

[1] D. Bimberg *et al*, *Quantum Dot Heterostructures* (John Wiley & Sons Ltd. Chichester), (1999).
[2] M. Bayer *et al*, *Phys Rev. Lett.* **90**, 186801 (2003).
[3] E. Ribeiro *et al*, *Phys Rev. Lett.* **92**, 126402 (2004).
[4] J. M. García *et al*, *Appl. Phys. Lett.* **71**, 2014 (1997).
[5] A. Lorke *et al*, *Jpn. J. Appl. Phys.* **40**, 1857 (2001).
[6] S. Kobayashi *et al*, *Jpn. J. Appl. Phys.* **43**, L662 (2004).
[7] J. A. Barker *et al*, *Phys. Rev. B* **69**, 035327 (2004).
[8] N. Koguchi *et al*, *J. Crystal Growth* **111**, 688 (1991).
[9] N. Koguchi and K. Ishige, *Jpn. J. Appl. Phys.* **32**, 2052 (1993).
[10] T. Mano *et al*, *Appl. Phys. Lett.* **76**, 3543 (2000).
[11] Y. Nonogaki *et al*, *Appl. Surf. Sci* **117**, 665 (1997).
[12] I. Pietzonka *et al*, *Jpn. J. Appl. Phys.* **40**, 6531 (2001).
[13] K. Ueno *et al*, *Jpn. J. Appl. Phys.* **40**, 1888 (2001).
[14] K. Kawasaki *et al*, *Appl. Phys. Lett.* **79**, 2243 (2001).
[15] K. Watanabe *et al*, *Jpn. J. Appl. Phys.* **39**, L79 (2000).
[16] A. Ohtake *et al*, *Phys Rev. Lett.* **92**, 236105 (2004).
[17] T. Mano and N. Koguchi, *J. Crystal Growth* **278**, 108 (2005).
[18] T. Mano *et al*, *Nano Letters* **5**, 425 (2005).
[19] T. Mano *et al*, *J. Crystal Growth* **209**, 504 (2000).
[20] T. Mano *et al*, *Thin Solid Films* **515**, 531 (2006).
[21] M. Yamagiwa *et al*, *Appl. Phys. Lett.* **89**, 113115 (2006).
[22] T. Mano *et al*, *Appl. Phys. Lett.* **89**, 183102 (2006).
[23] T. Kuroda *et al*, *Phys. Rev. B* **72**, 205301 (2005).

15th Int. Symp. "Nanostructures: Physics and Technology"
Novosibirsk, Russia, June 25–29, 2007

MBE growth and properties of InP/InAsP/InP nanowire heterostructures

G. E. Cirlin[1,2], M. Tchernycheva[2], G. Patriarche[2], L. Travers[2], V. Zwiller[3], U. Perinetti[3] and J.-C. Harmand[2]

[1] St Petersburg Physics and Technology Center for Research and Education of RAS, St Petersburg, Russia
[2] CNRS-LPN, Route de Nozay, 91460 Marcoussis, France
[3] Kavli Institute of Nanoscience, Delft University of Technology, P.O. Box 5046, 2600 GA Delft, The Netherlands

Abstract. The fabrication technology of InP nanowires, including embedded InAsP nanoinsertions by Au-assisted molecular beam epitaxy is presented. The growth temperature affects the nucleation on the nanowire facets allowing to change the wire shape from pencil-like (at 390 °C) to cylindrical (at 420 °C) and to control the InAsP insertion geometry and composition. The InAsP alloy composition was varied between $InAs_{0.35}P_{0.65}$ and $InAs_{0.5}P_{0.5}$ by changing the As/P flux ratio and substrate temperature. The InAsP segments show strong room-temperature photoluminescence with a peak wavelength tunable from 1.2 to 1.6 μm. Low-temperature micro-photoluminescence performed on isolated single wires shows narrow peaks with a linewidth as low as 120 μeV.

Introduction

Semiconductor nanowires (NWs) are attracting an increasing attention due to their emerging applications to nano-scale devices. A technique for NW fabrication relies on the catalytic mechanism usually referred to as vapor-liquid-solid (VLS) growth, whereby liquid particles are formed by alloying of the catalyst with the semiconductor constituents. The one dimensional growth is driven by the fast local precipitation of adsorbed species at the liquid-semiconductor interface under the droplets. Moreover, VLS technique provides the possibility to fabricate heterostructures in both NW axial and radial directions. As concern to InAsP, its band gap can be tailored from 3.5 to 0.92 μm by adjusting the alloy composition and, in particular, can cover the 1.3–1.55 μm wavelength range of technological importance for optical telecommunications.

In this paper we report on the synthesis of InP/InAsP/InP heterostructures in InP nanowires by Au-assisted molecular beam epitaxy. The InP/InAsP/InP heterostructures demonstrate strong room-temperature photoluminescence with the peak wavelength tunable from 1.2 to 1.6 μm by adjusting the As content. The micro-photoluminescence performed at 4 K on isolated single wires show narrow peaks with a linewidth as low as 120 μeV.

1. Experimental procedure

NWs were grown on InP (111)B substrates in an MBE system equipped with solid sources supplying In atoms, and cracker As and P sources to produce dimers. The substrate surface was first deoxidized at 530 °C, then a 100 nm thick InP buffer layer was grown to achieve atomically flat surface. A total amount of Au equivalent to 1 nm layer was deposited under phosphorus flux at 420 °C using an Au effusion cell installed directly into the growth chamber. The substrate temperature was then set to the desired value for the growth. This procedure results in the formation of droplets containing Au alloyed with the substrate constituents. The typical distribution of droplet sizes ranges between 30 and 40 nm. The NW growth was initiated by opening simultaneously the In and P sources. For all samples the nominal growth rate, i.e. the growth rate on a clean and Au-free InP surface, was fixed at 0.2 nm/s.

For InP/InAsP/InP heterostructure formation, the growth started with 20 min of InP, then the As source was opened for desired time in order to form an InAsP segment. The As to P flux ratio was varied from sample to sample to investigate different alloy compositions. The growth was completed with 5 min deposition of InP.

The resulting morphology of NW ensembles was investigated by scanning electron microscopy (SEM). The crystallographic structure was analyzed by transmission electron microscopy (TEM) equipped with an energy dispersive X-ray (EDX) spectrometer for composition measurements. The photoluminescence (PL) of NW ensemble was investigated using the following setup. The sample was excited at normal incidence with 532 nm line of frequency doubled NdYag laser at low excitation density ($\sim$ 0.1 W cm^{-2}). The luminescence signal was dispersed with Jobin Yvon spectrometer and detected with nitrogen cooled Ge photodetector. For micro-PL measurements, NWs were removed from their substrate, dispersed on a Si-oxide/Si substrate with the average density of $\sim$ 0.1 NW per μm^2 and placed in a continuous LHe flow cryostat The signal was collected with the same objective, dispersed with a 0.75 m spectrometer and detected with an InGaAs detector.

2. Influence of temperature on the nanowire morphology

First the temperature domain where binary InP NWs can be formed was investigated. A set of 7 samples was grown at temperatures ranging from 330 to 440 °C with a constant growth time equal to 20 min. The NW formation was observed only in a relatively narrow temperature window, between 350 and 420 °C. The growth at 330 °C produced only a rough two-dimensional layer that covered the deposited Au catalyst. At 440 °C the catalyst droplets were found segregating on the growing surface without giving rise to NW formation. In the intermediate range of temperature, NW growth is induced by diffusion of adatoms from the surface to the catalyst droplets and by their subsequent precipitation at the catalyst-semiconductor interface.

For temperatures below 410 °C, NWs develop a pencil-like shape. The diameter in the lower part of the wire is two-three times larger than that of the catalyst particle and the NW end is tapered. This morphology indicates that at low temperatures, concomitantly with the vertical growth governed by the catalyst, the nucleation on the lateral facets also takes place. This phenomenon occurs when the mean diffusion length of species on the lateral NW facets becomes shorter than the NW height. In this case, most of In adatoms cannot reach the catalyst droplets. Instead, the species can nucleate on the NW sidewalls giving rise to a significant lateral growth. To reduce this lateral growth, temperature must be raised to increase the adatom diffusion length. At temperatures higher than 410 °C InP NWs present cylindrical shape with the diameter equal to that of the catalyst. This means that by raising the substrate temperature it is possible to switch from the mixed axial/lateral growth to almost pure axial growth.

For heterostructure formation, two temperatures corresponding to the two morphologies of InP NWs discussed above were chosen: 390 and 420 °C. Fig. 1(a) shows the SEM cross-sectional image of typical InP/InAsP/InP NWs grown at 390 °C. The resulting NW

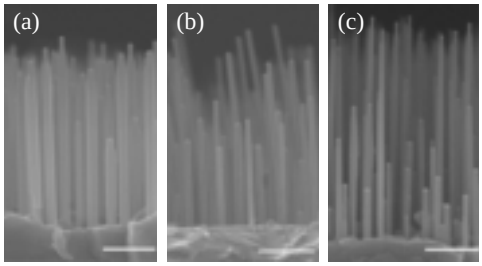

Fig. 1. Cross-sectional SEM images of InP/InAsP/InP nanowires grown (a) at 390 °C, (b) at 420 °C and (c) at 420 °C overgrown with InP at 390 °C. Scale bar corresponds to 0.4 μm.

height is about 1 μm, the diameter varies from 50 to 80 nm. The InAsP insertion has little influence on the NW morphology, the NWs present the typical pencil-like shape observed in binary InP NWs grown at this temperature. When the growth proceeds at 420 °C (Fig. 1(b)), the NWs keep a cylindrical shape with 30–40 nm diameter equal to that of the catalyst droplets, a sign that lateral growth is inhibited.

In a third sample, we have intentionally promoted the lateral growth by decreasing the temperature after the InAsP insertion. Fig. 1(c) presents a SEM image of these InP/InAsP/InP NWs that were grown at 420 °C until the formation of InAsP segments was completed. The last 5 min of InP growth were performed at 390 °C. The resulting NW diameter (40–55 nm) is larger than that of the catalyst especially for long wires, confirming that lateral growth took place.

3. Photoluminescence of nanowires

The macro-PL measurements were performed on the NW ensembles grown at different temperatures. For samples grown at 390 °C and thus having an InP shell around the InAsP insertions, the luminescence spectra show two peaks (Fig. 2). The high energy peak, situated around 1.35 eV at 300 K, has the same position in all the samples. The linewidth is about 150 meV. This peak is also present in the PL spectrum of a reference sample containing binary InP NWs. The peak energy corresponds to the bulk InP band gap. It should mainly originate from the two dimensional InP buffer layer. One cannot also exclude a luminescence signal coming from InP NWs. Because of their wurtzite structure, their PL contribution is expected at a slightly different energy than that of cubic InP. This may contribute to the large peak broadening of the 1.35 eV peak. However, a residual concentration of As in InP may also explain the PL broadening. The low energy peak is ascribed to the luminescence of the embedded InAsP segments. To ascertain that this peak does not originate from the emission of the two-dimensional layer, which can still grow between the NWs, we have removed all the NWs from the surface using an ultrasonic bath. After this treatment, the PL spectrum showed only the short wavelength peak; this excludes the possibility of the emission of two-dimensional InAsP layer.

The PL spectra for NW heterostructures grown at 420 °C and overgrown with InP at 390 °C look similar as in case of growth a 390 °C. However, for samples grown entirely at 420 °C only the high energy peak at 1.35 eV is present, no emission from the InAsP insertions is observed. This should be related to the suppression of the lateral growth at high temperature. The InP shell acts as an energy barrier that confines the carriers in the InAsP insertion and prevents their diffusion to the NW surfaces. When the InP shell is suppressed, the fast recombination of photogenerated carriers via surface states might hinder the PL emission from InAsP insertions. In addition, the oscillator strength of the exciton is much lower in a shell-free structure because the strain inhomogeneities tend to separate the electron from the hole. The InP shell limits the strain relaxation of InAsP insertions, resulting in a better overlap of carrier wave

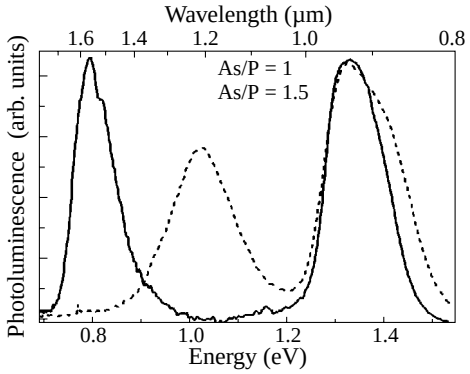

Fig. 2. Room temperature luminescence of InP/InAsP/InP NWs grown at 390 °C with As to P flux ratio equal to 1 (dashed line) and to 1.5 (full line).

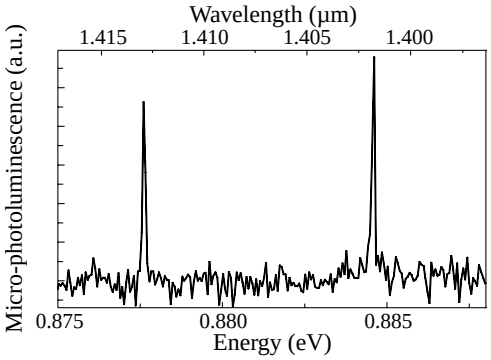

Fig. 3. Micro-photoluminescence at 4 K of an individual NW containing 2 InAsP insertions of a different length.

functions.

Fig. 2 shows the room-temperature PL spectra of two samples grown at 390 °C with InAsP insertions synthesized at different As to P flux ratio. By changing the As to P flux ratio from 1 to 1.5, the peak emission energy was tuned from 1.025 eV (1.2 μm) to 0.8 eV (1.55 μm). This demonstrates the potential of the InP/InAsP/InP heterostructures for fabrication of emitters in the telecommunication wavelength range 1.3–1.55 μm. The InAsP peak has an inhomogeneous broadening of 100–150 meV, which should be related to the wire-to-wire composition fluctuations of the InAsP alloy.

Finally, we have performed micro-PL measurements on NWs grown at 390 °C and containing two InAsP insertions of different lengths (growth time of 30 and 45 s). Fig. 3 presents the emission spectrum taken at 4 K with 3.6 μW excitation on an individual NW. Two sharp lines attributed to the emission of the InAsP insertions are observed at 1.401 and 1.412 μm with the full width at half maximum as small as 0.19 nm.

In conclusion, we fabricated 25–30 nm high InAsP insertions in InP nanowires by Au-assisted MBE. The wire shape was shown to change from pencil-like for 390 °C growth to cylindrical for 420 °C growth. The alloy composition was adjusted between $InAs_{0.35}P_{0.65}$ and $InAs_{0.5}P_{0.5}$ by changing the As to P flux ratio. The presence of InP shells around the InAsP insertions is essential to observe efficient PL emission. In that case, the InAsP insertions show room temperature photoluminescence peaked in the 1.2–1.55 μm domain. The micro-photoluminescence from isolated nanowires shows narrow lines with full width at half maximum as small as 0.19 nm.

Acknowledgements
The financial support of PNANO Filemon35 project, SANDiE European project, RAS scientific programs (“Quantum macrophysics” and “Quantum nanostructures”) and that of RFBR grants is acknowledged and State Contract No. 02.513.11.3042.

15th Int. Symp. "Nanostructures: Physics and Technology"
Novosibirsk, Russia, June 25–29, 2007

Polarization transformation by arrays on the basis of precise metal-semiconductor microhelices

E. V. Naumova[1], V. Ya. Prinz[1], V. A. Seleznev[1], S. V. Golod[1], A. F. Buldygin[1], R. A. Soots[1], V. V. Kubarev[2], B. A. Knyazev[2], G. N. Kulipanov[2], S. A. Kuznetsov[2] and N. A. Vinokurov[2]

[1] Institute of Semiconductor Physics, SB RAS, Lavrent'eva, 13, 630090 Novosibirsk, Russia
[2] G. I. Budker Institute of Nuclear Physics, SB RAS, Lavrent'eva, 11, 630090 Novosibirsk, Russia

Abstract. Arrays on the basis of precise thin-film metal-semiconductor microhelices were fabricated by recently developed method of 3D nanostructuring from strained bifilms. Rotation of polarization plane of radiation by arrays of helices in microwave and THz ranges was studied. Prospects of application of demonstrated effect are discussed.

Introduction

Development of micro- and nanostructuring brought into life novel artificial electromagnetic media — materials with negative refractive index, high-frequency magnetics, chiral materials, nonreflective materials, non-reciprocating artificial media etc [1,2]. They are often called metamaterials so as to emphasize that their properties are gained not from atomic or molecular level structure, but from the artificial structure of larger scale, that is still not large in comparison with the wavelength of radiation and allows describing it's electromagnetic properties with some integral characteristics used for common materials, such as absorption coefficient or dielectric permittivity. Metamaterials are expected to find applications in telecommunication, information storage and processing, lithography, microscopy, biomedicine and other areas.

Chiral asymmetry (impossibility to superimpose object with its mirror reflection) of material microstructure leads to rotation of polarization plane of electromagnetic wave. That effect was firstly observed in natural optically active substances. Now it is widely used in liquid crystal devices, however, technical difficulties in liquid-crystal phase handling and operation encourage to seek for their solid-state analogues.

Artificial chiral media constructed by Lindman was one of the first metamaterials [3]. That composite of metal helical inclusions in dielectric matrix was intended to model natural optical activity: helical molecules were mimicked by metal wire helices, while visible light wave was scaled up to the radio range ($\lambda = 30$ cm). This structure rotated polarization plane of transmitted radiation. Later, there were some more experiments on artificial chirality demonstrated by arrays of metal wire helices in radio and microwave ranges (Tinoco [4], Lagarkov [5] and others).

Due to chiral asymmetry a secondary wave reradiated by helix has polarization different from polarization of primary incident wave. Near the half-wave resonance (i.e. when the length of unwound metal helix is equal to the half of the wavelength in host dielectric media) the amplitude of currents in helix and corresponding intensity of secondary radiation is maximal. At resonance the phase shift between charge oscillations in helix and electric field of primary wave (as driving force of charge oscillations in helix) changes its sign and phase of secondary wave as well as direction of polarization plane rotation change correspondingly. Resonant frequency spread unavoidable for any real array leads to dramatic damping of half-wave resonance. As far as the rotation angle function is sign-changing and steep, helices have to be finely tuned to the same resonant frequency.

Interest to artificial chiral structures was intensified by demonstration of significant advantages of chiral structures as elements of negative refractive index metamaterials [6]. Artificial chiral structures can not compete with traditional aids for polarization control in radiorange, while for THz and higher frequencies they are very promising as solid-state analogues of liquid crystals. Device base for THz optics is still not well developed — it is so called "THz gap". Efficient control over polarization could broaden possibilities of traditional applications of THz radiation such as imaging (to reveal anisotropic structure and improve contrast), spectroscopy (to use vibrational circular dichroism techniques), telecommunications (to add one more degree of freedom in coding) and bring up novel ones such as high-capacity information processing and sensing. Proceeding from radio and microwaves to THz and higher frequency ranges requires miniaturization, high Q-factor and precise tuning of all chiral elements of the structure.

1. Experimental

Fabrication of uniform arrays of metal-semiconductor helices was based on the recently developed method of fabrication of precise three-dimensional micro- and nanoshells [7]. Helices were rolled from plane stripes of metal-semiconductor films formed on the substrate by subsequent molecular-beam epitaxial growth of pseudomorphous semiconductor layers (sacrificial layer and two layers with certain lattice mismatch), vacuum deposition of metal layers, and lithographic patterning of strips. Driving force of rolling was relaxation of internal strains in semiconductor bilayer that took place when strips were detached from the substrate by etching of sacrificial layer. Metal layers were intended for strong interaction of helices with radiation, while semiconductor bilayer served as carcass of helix. For strained monocrystal semiconductor bilayer (100) with zinc blend structure the anizotropy of Young modulus makes rolling in direction with minimal Young modulus (direction $\langle 010 \rangle$) energy-optimal. Being detached from the substrate the strips of bifilm inclined to this direction roll as helices with pitches strictly determined by inclination angle and with diameters set by internal strains, Young modulus and thicknesses of layers.

Two-dimensional array of helices fabricated from metal-semiconductor film $In_{0.2}Ga_{0.8}As/GaAs/Ti/Au$ (8/45/3/50 nm) for experiments in THz range had the following parameters:

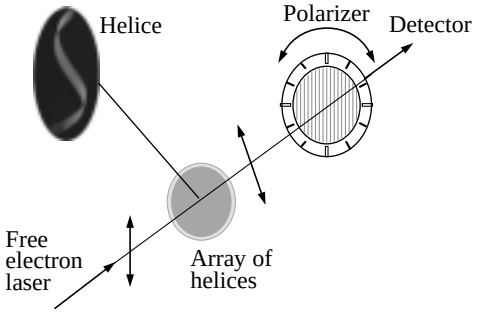

Fig. 1. Scheme of experiment in THz range.

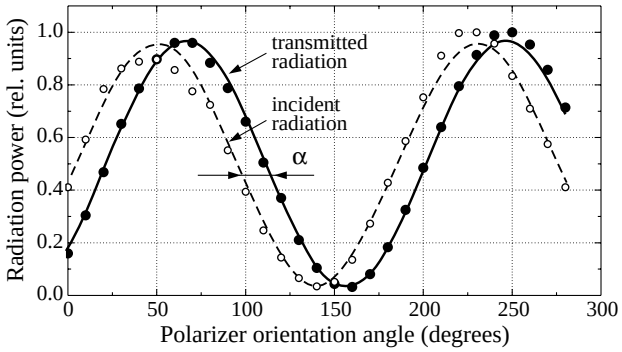

Fig. 2. Radiation power as a function of polarizer orientation angle ($\lambda = 142$ μm, $\alpha = 17^\circ$).

unwound helix's length: 75 μm; width: 3 μm; diameter: 10 μm; pitch: 40 μm; density of array: 500 helices/mm^2; distribution of helices over substrate was two-dimensional, uniform, and chaotic with axes of helices parallel to the substrate. Experiments were carried out on the Novosibirsk free electron laser (1.6–2.3 THz). Polarization plane orientation was measured with rotating polarizer and detector (Fig. 1). Dependence of rotation angle on the wavelength had strong resonant character. Maximal rotation of 17° was observed at $\lambda = 142$ μm (see Fig. 2), while at the $\lambda = 139$ μm the rotation angle fell to 3°.

Experiments in microwave range (135–145 GHz) were aimed at modeling of interaction of radiation with helices of significantly longer length than wavelength. Different orientations of metal wire helices relative to propagation direction and polarization plane of radiation were studied. Principle of polarization measurements was the same, but free-space scheme was changed with quasioptical microwave line. Maximal angle of polarization plane rotation in microwave range achieved 90° for array of parallel helices with pitch close to the wavelength oriented parallel to the wave line. For monolayer of helices perpendicular to the wave line the maximal rotation of 34° was obtained for helices with helix angle $\psi = 40^\circ$ and diameter $d = 480$ μm at wavelength $\lambda = 2.1$ mm, that is in well agreement with resonance condition for cylinders with helical conductivity $\psi = \pi\lambda/d$ [8]. Direction of rotation for arrays of left-handed helices and right-handed helices were opposite, array with racemic mixture of left and right-handed helices showed no significant rotation.

2. Discussion

Sharpness of polarization rotation angle resonance in THz range was due to the high Q-factor of helices and precise tuning of all helices in array to the same resonant frequency. Polarization rotation angle demonstrated by monolayer of helices with thickness just 1/10 of wavelength was by factor of some tens more than rotation angle for the best liquid crystals of comparable thickness (in wavelengths). The significant rotation angle and sharp resonance make observed effect promising for different THz applications and open up new possibilities in communication, biomedicine, chemistry, security, imaging and spectroscopy. Full compatibility of used method with IC technology facilitates high-speed dynamic control over polarization. Rotation of polarization plane of microwave radiation has no such practical value as artificial chirality effect demonstrated in THz range, however, these experiments are useful for modeling of interaction of helices with radiation.

Scalability of the effect and used nanostructuring technique allows fabrication of such "solid-state liquid crystals" for different spectral ranges — from microwave to optical one.

Acknowledgement

This work has been supported by RFBR.

References

[1] V. G. Veselago, *Sov. Phys. Usp.* **10**, 509–514 (1968).
[2] D. R. Smith *et al*, *Science* **305**, 788 (2004).
[3] K. F. Lindman, *Annalen der Physik* **63**, 621 (1920).
[4] I. Tinoco *et al*, *J. Phys. Chem.* **61**, 1196 (1957).
[5] A. N. Lagarkov *et al*, *Dokl. Phys.* **46**, 163 (2001).
[6] J. B. Pendry, *Science* **306**, 1353 (2004).
[7] V. Ya. Prinz *et al*, *Physica E* **6**, No. 1–4, 828 (2000).
[8] A. N. Sivov *et al*, *Radiotechnika i electronika* **39**, No. 10, 1534 (1994).

15th Int. Symp. "Nanostructures: Physics and Technology"
Novosibirsk, Russia, June 25–29, 2007

Electronic states induced by cesium on atomically rough and flat GaAs(001) surface

V. L. Alperovich[1,2], A. G. Zhuravlev[1,2], I. O. Akhundov[2], N. S. Rudaya[1], D. V. Sheglov[1,2], A. V. Latyshev[1,2] and A. S. Terekhov[1,2]

[1] Institute of Semiconductor Physics, 630090 Novosibirsk, Russia
[2] Novosibirsk State University, 630090 Novosibirsk, Russia

Abstract. Atomic flattening of semiconductors at equilibrium conditions was applied to obtain GaAs(001) surfaces with ordered arrays of atomically flat terraces separated by steps of monatomic height. The electronic states on atomically rough and flat As-rich and Ga-rich GaAs(001) surfaces with adsorbed cesium are studied by measuring the evolution of band bending under Cs deposition. The non-monotonic variations of band bending caused by adatom-induced surface states are observed on the flat surface, whereas on the rough surface the amplitude of these variations is substantially reduced by the defect-induced electronic surface states.

Introduction

Atomically clean and flat semiconductor surfaces with given atomic superstructures are needed for nanotechnologies and are the basis for studying fundamental electronic properties of the surfaces. An ideally smooth semiconductor surface consists of a regular set of atomically flat terraces separated by straight steps of monatomic height. The terrace width is determined by the miscut of the crystal surface from the singular face. Atomically flat silicon surfaces very close to the ideal can be obtained by thermal smoothing in vacuum [1]. The preparation of atomically flat surfaces of III–V semiconductors is still a problem, because annealing in vacuum often leads to roughening rather than smoothing due to different evaporation rates of the III and V components. Up to now the preparation of such surfaces was performed by using MOCVD [2] and MBE [3] growth techniques. However, for many purposes an atomically clean, flat and ordered semiconductor surface should be prepared without epitaxial technologies, starting from a surface oxidized in air. A useful technique for preparation of atomically clean GaAs surfaces with various superstructures consists in removal of oxides in HCl-isopropanol (HCl-iPA) solution in nitrogen atmosphere, transfer to the UHV setup without exposure to air and subsequent annealing in vacuum [4, 5]. This technique is efficient for the technology of GaAs(Cs,O) photocathodes with negative electron affinity. On the GaAs(001) surfaces prepared by the HCl-iPA technique the evolution of the surface band bending φ_S under deposition of cesium was studied by photoreflectance (PR) spectroscopy [6]. This study revealed qualitative differences in the electronic surface states induced by cesium on the As-rich and Ga-rich surface reconstructions, and an unusual non-monotonic behavior ("fine structure") in the evolution of φ_S with the increase of Cs coverage θ [6, 7]. To clarify the origin of these phenomena and their relation to the morphology of the GaAs(001) surface, in the present work we studied the evolution of the band bending under Cs deposition on the atomically rough and flat GaAs(001) surfaces with various reconstructions.

1. Experimental

The experiments were performed on GaAs(001) epi-ready substrates and epitaxial layers. The morphology of the surfaces was studied *ex-situ* by the atomic force microscopy (AFM), using the scanning probe microscope Solver-P47H. The thermal smoothing of GaAs(001) was done in a quartz reactor under the flow of hydrogen. To prevent surface roughening because of different evaporation rates of the III and V components, the conditions close to equilibrium were provided by two methods. In the first method the GaAs surface was covered with another GaAs sample. Thus, within the narrow slit ("capillary") between the two samples quasi-equilibrium between the solid and vapor phases was realized during annealing. The main problem of smoothing in a capillary is gradual depletion of the near-surface region with arsenic due to incongruent evaporation of GaAs and restricted diffusion flow of As from the GaAs bulk to the surface. To overcome this problem, in the second method the equilibrium pressures of arsenic and gallium vapors during the thermal smoothing were provided by a saturated Ga-GaAs melt placed in a graphite cassette.

The evolution of the band bending was measured by means of PR spectroscopy, using the Fourier transform of Franz–Keldysh oscillations. To provide uniform electric field near the surface, epitaxial UP^+ structures with thin ($\sim$ 100 nm) undoped surface layers were used [6]. A modification of the PR spectroscopy technique to a "real-time" version allowed us to measure the band bending evolution during the process of Cs deposition with a high precision.

2. Results and discussion

We proved experimentally that both methods of thermal smoothing of GaAs surfaces (in a capillary and in the presence of Ga-GaAs melt) led to the morphology with atomically flat terraces separated by monatomic steps. Fig. 1 shows the AFM images measured on the "as is" epi-ready GaAs substrate (a) and after annealing in the capillary for two hours at $T = 575\ ^\circ$C (b) and 650 $^\circ$C (c). Although the root mean square roughness of the substrate before and after annealing remained almost the same $R_q \approx 0.12 \pm 0.02$ nm, the morphology of the surface changed substantially. Distinct "islands" and "lakes" bounded by steps of monatomic height ($\sim$ 0.3 nm) are formed at $T \geq 500\ ^\circ$C (Fig. 1b). Further increase of the annealing temperature led to the decrease of the concentration of islands and lakes and to the formation of atomically flat terraces. Consequently, the surface morphology approached the "ideal" one with flat terraces of $\sim 1\ \mu$m width separated by approximately equidistant and relatively straight monatomic steps (Fig. 1c). Annealing

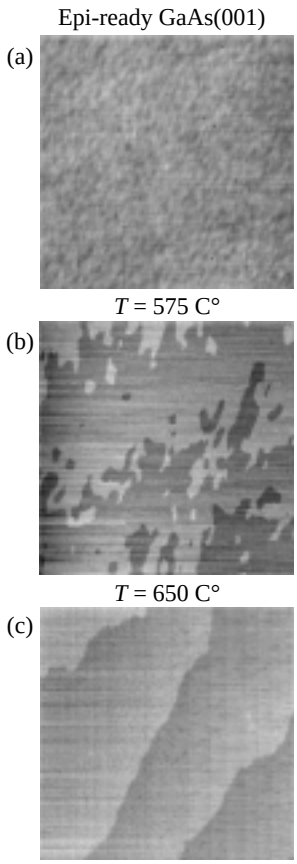

Fig. 1. 3×3 μm^2 AFM images of the epi-ready GaAs(001) surface before (a) and after thermal smoothing in quasi-equilibrium conditions at $T = 575$ °C (b) and $T = 650$ °C (c).

in the capillary at $T > 650$ °C led to surface roughening, probably due to strong deviation from the equilibrium between the crystal and the gas phase because of the depletion of the near-surface region with arsenic. Annealing in the presence of the Ga-GaAs melt yielded more reproducible flattening up to higher temperatures $T \sim 750$ °C.

To study the relation between the morphology and electronic states of the Cs/GaAs(100) surface, we measured the evolution of the band bending under Cs deposition on the atomically flat (as-grown and annealed in equilibrium conditions) UP$^+$ structures with $R_q \sim 0.2$ nm, and on the rough UP$^+$ structures ($R_q \sim 1$ nm) annealed in non-equilibrium conditions. The results are shown in Fig. 2 for Cs deposition on As-rich (a) and Ga-rich (b) surfaces. It is seen that the shape of $\varphi_S(\theta)$ is different for the As-rich and Ga-rich surfaces [6, 7]. On the flat As-rich surfaces φ_S increased steeply at small $\theta < 0.1$ ML and went through a maximum at larger coverages, while on the flat Ga-rich surfaces several distinct maxima and minima ("fine structure") were reproducibly observed. The shape of $\varphi_S(\theta)$ was similar for the as-grown sample and for the sample annealed in equilibrium, as expected, because both were atomically flat, though they had different sizes and shapes of monatomic islands and steps. On the rough surface the shape of $\varphi_S(\theta)$ was distinctly different, with a substantially higher initial value of φ_S on the clean surface, reduced amplitude of φ_S variations with Cs coverage, and less pronounced "fine structure". A possible reason for the distinction is much higher density of the defect-induced surface states in the middle of the band gap on the rough surface. These states cause the initial band

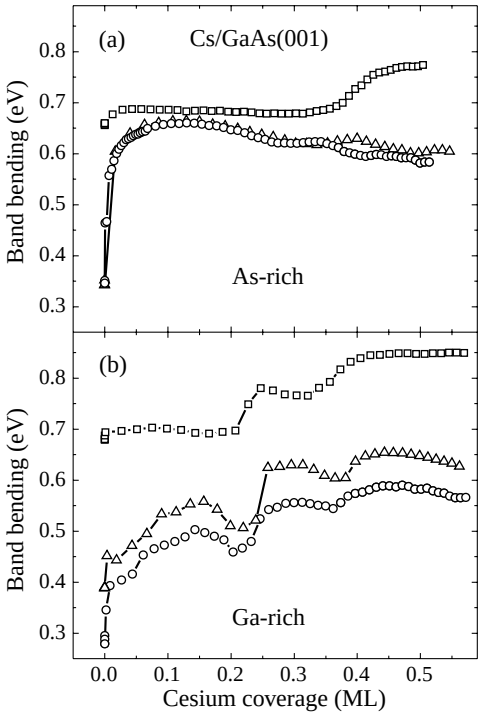

Fig. 2. Evolution of the band bending φ_S under Cs deposition on the as-grown GaAs(001) UP$^+$ structures (circles), on the structures annealed in equilibrium conditions (triangles), and on the rough UP$^+$ structures (squares) with As-rich (a) and Ga-rich (b) reconstructions.

bending and restrict its variations under Cs deposition.

In conclusion, the technique for preparation of atomically flat GaAs(001) surfaces by annealing in equilibrium conditions was developed. The comparison of the band bending behavior under Cs deposition on the atomically flat and rough surfaces proved that surface roughness produced defect-induced surface states which restricted the adatom-induced variations of φ_S.

Acknowledgement

This work was partly supported by the Russian Foundation for Basic Research (grant No. 05-02-17265).

References

[1] A. V. Latyshev, A. L. Aseev, A. B. Krasilnikov and S. I. Stenin, *Surf. Sci.* **213**, 157 (1989).
[2] J. E. Epler, T. A. Jung and H. P. Schweizer. *Appl. Phys. Lett.* **62**, 143 (1993).
[3] Z. Ding *et al*, *Phys. Rev. Lett.* **90** 216109 (2002).
[4] O. E. Tereshchenko, S. I. Chikichev and A. S. Terekhov, *J. Vac. Sci. Technol. A* **17**, 2655 (1999).
[5] V. L. Alperovich, O. E. Tereshchenko, N. S. Rudaya, D. V. Sheglov, A. V. Latyshev and A. S. Terekhov, *Appl. Surf. Sci.* **235**, 249 (2004).
[6] O. E. Tereshchenko, V. L. Alperovich, A. G. Zhuravlev, A. S. Terekhov and D. Paget *Phys. Rev. B* **71**, 155315(7) (2005).
[7] V. L. Alperovich, A. G. Zhuravlev, O. E. Tereshchenko, H. E. Scheibler and A. S. Terekhov, *Proc. 28th Int. Conf. Phys. Semicond.*, Vienna, Austria, July 24–28 (2006).

15th Int. Symp. "Nanostructures: Physics and Technology"
Novosibirsk, Russia, June 25–29, 2007

A promising SOI technology for producing nanostructures

M. N. Cheyukov, S. I. Romanov, V. V. Kirienko and A. K. Gutakovskii
Institute of Semiconductor Physics, SB RAS, Novosibirsk, Russia

Abstract. We present a new silicon-on-insulator (SOI) technology which can be promising for producing nanostructures. Conceptually the technology is different from the well-known methods. The key principle of our technology is to use high temperature annealing for sintering porous layers of silicon and silicon dioxide. Structural and electrical properties of SOI wafers have been analyzed. The results show high quality of received SOI nanostructures.

Introduction

SOI technologies offer the greatest promise for producing a wide variety of nanostructures. SOI wafers with ultrathin Si and SiO_2 layers have many advantages over bulk Si substrates for isolation, process simplicity, for short channel device performance, and for applications involving low power, high speed, high temperature and radiation hardness. There are several competitive technologies for SOI wafer fabrication where SIMOX and Wafer Bonding are currently the front running techniques.

We have been developing SOI technology referred to as SIPOL-technology (SIntering of POrous Layers) conceptually different from the above. We have no need of implantation, epitaxy, bonding and splitting. The principle of the method is to form SOI structure by means of high temperature sintering (densification) of porous layers of silicon and silicon dioxide. In this work, we describe the SOI material technology which is believed to can be quite competitive with other present-day technologies for the commercial production of nanodevice grade substrates.

1. Process flow

The process flow is very simple and includes only four basic steps. It is shown schematically in Fig. 1. Anodic etching of p^+-type Si (100) wafer is used to form a porous silicon layer (PSL) with different porosity in depth. PSL consists of top and bottom layers. The porosity (void fraction) of the top-PSL is lower than that of the bottom-PSL. As a result of anodic oxidation of PSL the continuous porous layer of silicon dioxide is formed at an interface of the bottom-PSL with bulk silicon. The capping is necessary to an avoidance of environment-borne contaminants. After capping, the wafer is annealed at 1300–1370 °C to fabricate SOI structure. This process occurs due to the fundamental feature of porous materials on heating, namely: a sintering of porous mass into solid body. In our case the formation of continuous separate layers of monocrystalline silicon and silicon dioxide is taking place at high temperature annealing.

2. Results and conclusion

Most of the available diagnostic techniques including electron microscopy (TEM, SEM), current-voltage and capacity voltage measurements, EDX method and specific plasma etching have been applied to characterize the received SOI structures.

The TEM study of SIPOL wafers has shown reasonable quality single crystalline top Si layer and the continuous buried oxide. There were no extended defects, such as dislocations, stacking faults and discrete oxide precipitates, in the Si matrix. The buried oxide layer was always free of silicon islands.

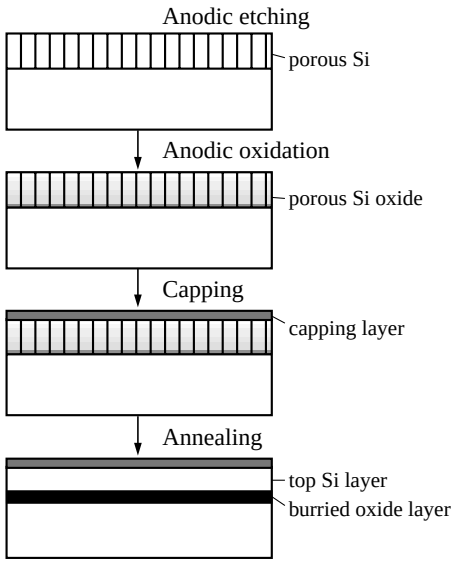

Fig. 1. Schematic process route for SIPOL-technology.

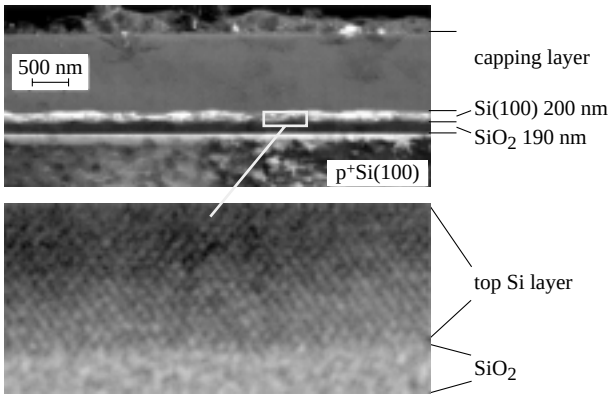

Fig. 2. Typical cross-sectional (a) and high-resolution (b) TEM images of SIPOL sample.

A typical cross-sectional TEM micrograph of the SOI sample is shown in Fig. 2. It should be pointed out that both the layers are about 200 nm thick and may be substantially reduced, which are sufficient for producing nanodevices.

The roughness of interface between the top Si layer and the buried oxide was estimated at less ±20 nm using specific plasma etching. This feature may be significantly improved when elaborating the SIPOL-technology.

Current-voltage measurements were made across the SOI structure to determine leakage currents and breakdown voltage. The results recorded from a typical SIPOL wafer are shown in

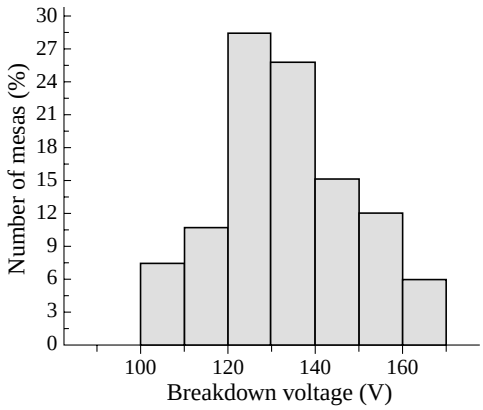

Fig. 3. Histogram of breakdown voltage for 300 × 300 μm^2 mesa.

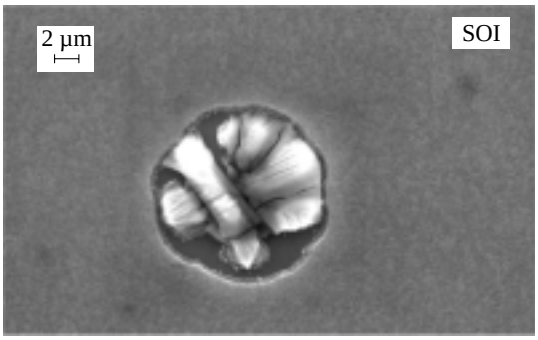

Fig. 4. SEM image of SIPOL structure with micro-defect.

Fig. 3. Some of the characteristics of current SIPOL material are the following:

thickness of top Si layer $\sim$150$-$200 nm,
thickness of buried oxide $\sim$200 nm,
average breakdown voltage $\sim$130 V,
breakdown electrical field strength $\sim 6.4\times10^6$ V/cm,
roughness of interfaces $< \pm$20 nm.

As for now, one macro-defect is typical of SIPOL structures. It can be seen in Fig. 4 and measures $\sim$16 μm. Their density is about 10^3 cm^{-2}. As was apparent after SEM and EDX studies, these macro-defects were due to the presence of crystalline SiO_2, which destroys SOI structure. This crystalline phase of silicon dioxide appears to form as a result of impurity contaminations of initially amorphous buried oxide during high temperature annealing. The design of high-temperature furnaces used to anneal the SIPOL material has been optimized in order to minimize the diffusion of metallic contaminants from the heating elements into the furnace tubes.

In summary, SIPOL-technology is described which incorporates the techniques of porous silicon and porous silicon oxide. This simple technology is substantiated with experimental results. We believe that SIPOL-technology will be available for producing nanostructures.

Acknowledgements

We thank T. Gavrilova for technical assistance with SEM and EDX analysis, and F. Dultsev for study of SOI structures with specific plasma etching.

15th Int. Symp. "Nanostructures: Physics and Technology"
Novosibirsk, Russia, June 25–29, 2007

Non-standard scaling of the 2D Si island density on Si(111)-7×7

S. N. Filimonov[1], V. Cherepanov[2], Yu. Yu. Hervieu[1] and B. Voigtländer[2]

[1] Department of Physics, Tomsk State University, 634050 Tomsk, Russia
[2] Institute of Bio- and Nanosystems (IBN 3), and Center of Nanoelectronic Systems for Information Technology, Research Centre Jülich, 52425 Jülich, Germany

Abstract. Submonolayer density of 2D islands in Si/Si(111)-7×7 molecular beam epitaxy is measured using scanning tunneling microscopy. At a relatively low deposition temperature of 673 K the density of 2D islands is a power function of the deposition flux $N_{2D} \propto F^{\chi}$ with the exponent $\chi = 0.24$ being smaller than that predicted by the standard nucleation theory. The nonstandard scaling of the 2D island density is explained by the multistage character of the nucleation process on the Si(111)-7×7 surface.

Introduction

Nucleation of 2D islands in epitaxial growth is a process that may be utilized for creation of various nanostructures [1]. To achieve a better control over the properties of 2D islands, i.e. their size and number density, it is important to understand how the nucleation develops on the atomic level. The problem here is that on real surfaces the nucleation pathways may be different from those commonly considered by the nucleation theories. An interesting example is the nucleation of Si islands on the (7×7) reconstructed Si(111) surface. At typical growth temperatures (600–900 K) submonolayer deposition of silicon on Si(111)-7×7 results in formation of a high density of small clusters occupying the half unit cells (HUC) of the surface reconstruction which coexist with the "normal" 2D islands that extend over plural HUCs [2]. Markedly, the clusters show no epitaxial arrangement of the constituting atoms and occur to be relatively stable both against decomposition and against further growth. Small clusters play an important role in the nucleation process serving as precursors for 2D islands [3], so that the 2D Si nucleation on Si(111)-7×7 occurs to be a multistage process. In the present work we specify the details of this multistage nucleation mechanism with the help of scanning tunneling microscopy and a theoretical rate equation analysis.

1. Nucleation mechanism

Small Si clusters and 2D Si islands were created on Si(111)-7×7 by deposition of 0.2 BL Si at $T = 673$ K and deposition rates ranging from 0.2 to 4.35 BL/min. In accordance with our earlier observations [4] three types of objects were identified on the surface (Fig. 1(a)): the epitaxial 2D islands, alone standing small clusters (single clusters), and pairs of clusters occupying neighboring half unit cells. The densities of those objects at different deposition rates are shown in Fig. 1(b). One can see that the density of 2D islands N_{2D} obeys a power-law dependence on the deposition flux F: $N_{2D} \sim F^{\chi}$. Interestingly, the measured scaling exponent $\chi = 0.24 \pm 0.03$ is smaller than the smallest value of 1/3 predicted by the standard nucleation theory [5]. This nonstandard scaling results from the multistage character of the nucleation process as will be shown below.

A detailed analysis of the cluster population shows that the pairs of clusters are present on the surface at a density larger than one would expect if they were created by a random allocation of single clusters. Thus, there is a preference in the filling of a half unit cell nearby the HUC already occupied by a cluster. This preferable formation of cluster pairs together with the fact that the smallest 2D island observed by STM has a size of two HUCs [4] suggests that the nucleation of a 2D Si island on Si(111)-7×7 is a multistage process that includes (1) formation of a stable cluster in an unoccupied HUC, (2) formation of the second stable cluster in a neighboring HUC, (3) formation of the critical nucleus consisting of the cluster pair and some number of atoms loosely bonded to the clusters, and, finally, (4) local reconstruction removal in the HUC occupied by the critical nucleus (Fig. 1(a)).

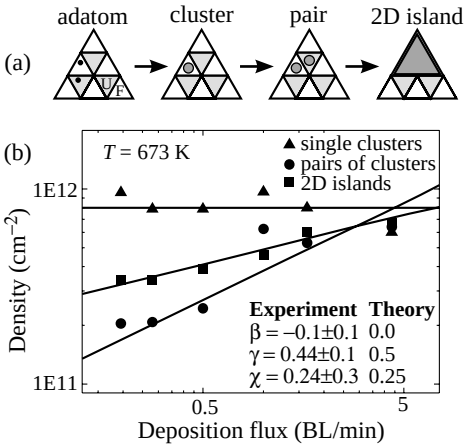

Fig. 1. (a) Multistage nucleation pathway on Si(111)-7×7. (b) Densities of single clusters, cluster pairs and 2D islands vs. the deposition flux. Symbols — experiment, lines — theory.

2. Rate equations

To describe the proposed multistage nucleation mechanism quantitatively we construct the set of rate equations for the densities of adatoms n_1, single clusters n_s, cluster pairs n_p and 2D islands N_{2D}

$$\frac{dn_1}{dt} = F - G^* - G, \quad (1)$$

$$\frac{dn_s}{dt} = J_s - J_p, \quad (2)$$

$$\frac{dn_p}{dt} = J_p - J_{2D}, \quad (3)$$

$$\frac{dN_{2D}}{dt} = J_{2D}. \quad (4)$$

Here G is the flux of adatoms incorporating into the 2D islands: $G = \sigma_{av} D n_1 N_{2D}$, where σ_{av} is the average capture number of

2D islands and $D = \nu \exp(-E_d/k_B T)$ is the surface diffusion coefficient [5]. The flux G^* describes accumulation of adatoms in single clusters and cluster pairs together with the consumption of adatoms in course of the transformation of cluster pairs into 2D islands. J_s, J_p and J_{2D} are the rates of formation of single clusters, cluster pairs and 2D islands, respectively. This set of equations extends the rate equations used in the standard nucleation models by including Eqs. (2) and (3) which describe birth and death of stable single clusters and cluster pairs.

The cluster formation rate J_s is calculated in the standard way using the critical nucleus approximation. If i is the size of the critical nucleus to form a stable cluster, then

$$J_s = \sigma_i D e^{E_i/k_B T} n_1^{i+1}, \tag{5}$$

where E_i is the energy to dissociate the nucleus into single adatoms and σ_i is the capture number. The formation of cluster pairs represents a heterogenous process where single clusters serve as the nucleation centers for the pairs. Therefore, the rate of pair formation must be proportional to the density of single clusters n_s. Assuming that the formation of the stable cluster nearby an already occupied HUC proceeds through the formation of the critical nucleus of size j one writes

$$J_p = \sigma_j D e^{E_j/k_B T} n_1^{j+1} n_s. \tag{6}$$

It should be noted that the critical sizes i and j, as well as the dissociation energies E_i and E_j may be different. Moreover, even when $i = j$ the dissociation energies are not necessary equal, because the presence of a cluster in a HUC may modify the bonding configuration in the neighboring HUCs.

While single clusters serve as precursors for cluster pairs, the pairs itself are precursors for 2D islands. However, the fact that we observed cluster pairs at temperatures so high as 780 K, suggests that the pair by itself cannot launch the cluster-to-2D island transformation. Instead, somewhat bigger associate — the pair plus some number of adatoms weakly bonded to it — has to be formed.

One may consider two limiting cases. First, the associates are unstable up to the characteristic size — pair plus m atoms — which should be achieved to start the local removal of the reconstruction. Second, a critical associate consisting of the pair plus l ($l < m$) atoms is formed so that bigger associates rather participate in the transformation than dissolve. In both cases the rate of formation of 2D islands is given by

$$J_{2D} = \sigma_k D e^{E_k/k_B T} n_1^{k+1} n_p \tag{7}$$

with $k + 1 = m$ (unstable associates) and $k = l$ (the critical associate of size l).

3. Results and discussion

We are searching for the solutions of rate equations (1)–(4) which allow power-law dependencies of the densities of single clusters, pairs and 2D islands on the deposition flux: $n_s \sim F^\beta$, $n_p \sim F^\gamma$ and $N_{2D} \sim F^\chi$. Let us note that except for the very beginning of growth the atoms entering the surface from the molecular beam incorporate, for the most part, into the edges of 2D islands [5]. In this case

$$\frac{dn_1}{dt} \approx F - \sigma_{av} D n_1 N_{2D} \approx 0. \tag{8}$$

Table 1. Scaling exponents.

	β	γ	χ
Regime I	$2\frac{i-j}{i+2}$	$2\frac{i-k}{i+2}$	$\frac{i}{i+2}$
Regime II	$3\frac{i-j}{i+k+3}$	$\frac{2i-k}{i+k+3}$	$\frac{i+k}{i+k+3}$
Regime III	$\frac{2i-j}{i+j+3}$	$\frac{2i+2j-3k}{i+j+3}$	$\frac{i+j}{i+j+3}$
Regime IV	$\frac{3i-j-k}{i+j+k+4}$	$2\frac{i+j-k}{i+j+k+4}$	$\frac{i+j+k}{i+j+k+4}$

Then the power-law dependencies take place in the following four regimes of nucleation:

I. $J_s \approx J_p$ ($dn_s/dt \approx 0$) and $J_p \approx J_{2D}$ ($dn_p/dt \approx 0$).
II. $J_s \approx J_p$ ($dn_s/dt \approx 0$) and $J_p \gg J_{2D}$.
III. $J_s \gg J_p$ and $J_p \approx J_{2D}$ ($dn_p/dt \approx 0$).
IV. $J_s \gg J_p$ and $J_p \gg J_{2D}$.

The power-law exponents corresponding to these four regimes are given in the Table 1.

As can be seen from the Table 1 the best fit to the experimental dependencies in Fig. 1(b) is achieved in the Regime II with $i = j = 1$ and $k = 0$. In this regime the formation of single clusters is balanced by their transformation to cluster pairs. On the contrary, the accumulation of pairs still takes place, only a minor part of them transforms in the 2D islands. As $i = j = 1$, the Si dimer represents the stable nucleus both for formation of a single stable cluster and the second stable cluster in a neighboring HUC. The zero value of k indicates that only one additional atom is required to trigger the reconstruction removal beneath the cluster pair. This atom either is a part of an unstable associate waiting for the overcoming the activation barrier for reconstruction removal, or its attachment to the pair (presumably with an increased activation barrier) results in appearance of the stable associate which grows rapidly up to the characteristic size m when, finally, the reconstruction is removed.

Acknowledgements

This work was partially supported by INTAS under grant No. 03-51-5015 (S.F. and Yu.H.), by the Russian Federal Agency for Science and Innovations under grant No. MK-6647.2006.2 (S.F.), and by the Alexander von Humboldt Stiftung (S.F.).

References

[1] V. A. Shchukin, N. N. Ledentsov and D. Bimberg, *Epitaxy of nanostructures*, (Berlin: Springer) 2003.
[2] U. Köhler, J. E. Demuth and R. J. Hamers, *J. Vac. Sci. Technol. A* **7**, 2860 (1989).
[3] H. Tochihara and W. Shimada, *Surf. Sci.* **296**, 186 (1993).
[4] S. N. Filimonov, V. Cherepanov, Yu. Yu. Hervieu, and B. Voigtländer, *Surf. Sci.* to be published.
[5] J. A. Venables, G. D. T. Spiller, M. Hanbücken, *Rep. Prog. Phys.* **47**, 399 (1984).

15th Int. Symp. "Nanostructures: Physics and Technology"
Novosibirsk, Russia, June 25–29, 2007

Nanostructures and quantum dots based on $A^{II}B^{VI}$ and $A^{III}B^{VI}$ semiconductors for nanoelectronics

G. V. Lashkarev
Institute for Problems of Material Science, Kiev, Ukraine

Zinc oxide is a prominent wide gap direct band semiconductor for UV and blue lasers, light-emitting diodes, UV detectors, solar cells, electron field emitters and transparent thin film transistors. ZnO nanostructured films were deposited by PEMOCVD, magnetron sputtering (MS) and reactive thermal evaporation on sapphire (0001) and SiN_x/Si. ZnO nanostructures were grown on Si substrates out of gas phase. The photoluminescence (PL) of ZnO films deposited by PEMOCVD and MS were studied. Optical excitation was carried out by femptosecond laser Al_2O_3:Ti.

Influence of film texture on PL spectra of ZnO film deposited on sapphire substrate was revealed. For ZnO (110) film, grown on the c-plane Al_2O_3 (0001), the misfit between identity periods of a film and a substrate is small (0.08%) what leads to good interface and crystal quality of ZnO film in this case and thus to strong UV PL. In opposite case for ZnO (002) film grown on the same c-plane of Al_2O_3 (0001) the large misfit (18%) deteriorate crystal quality leading to low UV PL. The film ZnO/SiN_x/Si, revealed the most intensive near band emission (symmetric peak at 3.27 eV) due to the recombination of free excitons without any PL related to defects (DLE). It proves the high crystal quality of ZnO films. However, ZnO on Si (100), Si (111), grown within the same experimental conditions display weak UV PL and intense broad DLE. In most cases annealing leads to improvement of UV PL, but in our case it degrade the UV PL and leads to DLE. This can be explained by diffusion mechanism which eventually impair stoichiometrical composition of films. As-grown ZnO films deposited by reactive thermal evaporation and from the gas phase by carbothermal reduction process demonstrate DLE due to interstitial zinc and oxygen ions. Post-growth annealing of this films improves UV PL but do not suppress DLE. Thus high quality films for optoelectronic applications can be deposited on sapphire and SiN_x/Si substrate at certain conditions.

Volt-Ampere characteristics of cold electron emission current undergo to Fauler–Nordgeim law. Two parts of curve with different slopes are observed for nanostructures grown from gas phase. Repetition of measurements led to lowering of threshold emitter electrical field E_{th} from 9.3×10^5 V/cm to 6×10^4 V/cm. It testifies to additional forming of nanoemitters during their study. E_{th} is close to ones of diamond and diamond-like films. Improvement of electron emission from Si tips covered by ZnO films was discovered and is due to lowering of work function (from 4.15 eV for Si tips to 2.9 for ZnO coated Si tips). The improving of the emission current stability for the Si structures after ZnO coating is also observed. Density of emission current from ZnO nanostructures achieves 0.6 mA/cm^2 at electric field $E = 2.1\times10^5$ V/cm testifying the ability of ZnO to be used in panel displays as effective cold cathodes.

Magnetic structure of sophisticated InSe⟨Mn⟩ 2D-dimensional ferromagnetics consisted of ferromagnetic nanoclusters for spintronics was studied by SQUID magnetrometry, ESR and neutron diffraction. Curie temperature exceeding 350 K was achieved. The appearance of weak ferromagnetism of α-MnSe nanoclusters at $T < 70$ K obliged to lowering of magnetic lattice parameter was established by neutron dsifractometry.

The use of Hot Wall Epitaxy technology for $A^{IV}B^{VI}$ QDs growth was proposed by us for the first time in 2003 (G. Lashkarev *et al* Proc. of the E-MRS Spring Meeting, Strasbourg, 2003). This method allows to grow semiconductor layers in the conditions close to thermodynamic equilibrium at low supersaturation of vapor phase and to realize the independent control of growth temperature and supersaturation at the condensation area. The analysis of mass transfer processes has shown that QDs growth occurs by Volmer–Weber mechanism without formation of wetting layer. The growth rate out of the molecular flow is (0.01–0.1) ML/s what is comparable with parameters of MBE growth (0.05–0.15) ML/s. The effect of substrate deformation on parameters of PbTe/BaF_2 QDs ensemble was studied. It was supposed that dislocations appear on BaF_2 side opposite to the loaded side. Single atom steps ($\sim$ several Å) are created in the places of intersection of sliding planes (100) with the surface of BaF_2 (111). The volume of PbTe QDs deposited on the nondeformed substrate exceeds ~ 5 times the volume of PbTe, deposited in the case of deformation. The latter increases the barrier for surface diffusion. In the conditions of low vapor supersaturation in the area of condensation and under plastic deformation of substrate the dense (~ 1011 cm^{-2}) uniform QDs population was formed. It relates to a creation of sliding steps and to an effect of deformation on kinetic processes on substrate's surface.

At the study of single crystal surface of InSe by AFM contact mode in an air the formation of a new phase was observed in the form of hillocks. The repetition of scanning by the probe has resulted in an appearance of new structures. Then the scanning field, which includes the previous one, was increased. The earlier scanning field has considerably more large density of new phase. An altitude of hillocks achieved 0.7 nm. The further scanning increases density of hillocks, without increase of their altitude. The similar phenomena were observed on GaSe samples. The differences consist only in the more sharp form of hillocks, instead of smoothed form for InSe. The hillocks altitude achieve a size of 1.4 nm. The results can be connected with layer lattice structure of InSe and GaSe. A surface atomic layer in both materials is selenium one. It is possible to assume, that the selenium vacancies, formed owing to disturbance of a surface layer by the probe, are nucleus of formation for oxygen complexes. The principal possibility of quantum structure growth by the help of Atomic Force Microscope is shown.

The use of CdS Quantum Dots (QD) in optoelectronics and laser technics is related to the manifestation of their unique op-

tical properties caused by exciton confinement. CdS nanocrystals were grown by dissolving of polyethylene in hydrocarbon oil (in inert gas medium). After that the precursor solution containing Cd and S ions was introduced. Composites with CdS nanocrystals having diameters $d = 4.0$ nm; 5.0 nm; 6.2 nm were studied. XRD researches demonstrated high structure perfectness of CdS nanocrystals. MS and ESR investigations testify to the absence of paramagnetic impurities.

In Raman scattering spectra of CdS QDs incorporated in polyethylene, the band is observed which has a frequency 301 cm^{-1} for $d = 6.2$ nm and 299 cm^{-1} for $d = 4.0$ nm. For CdS single crystal the corresponding band, due to light scattering on LO phonons, is situated at 305 cm^{-1}. The softening of LO phonon mode is clearly seen. It is related to the effect of confinement on phonon spectrum as well as blue shift of of near band photoluminescecence. The assymmetry and spectral position of RS band are tuned also by surface phonons light scattering and nanocrystals distribution by dimensions.

15th Int. Symp. "Nanostructures: Physics and Technology"
Novosibirsk, Russia, June 25–29, 2007

Plasma-assisted molecular beam epitaxy of AlGaN layers and quantum well heterostructures for ultraviolet spectral range

A. M. Mizerov, V. N. Jmerik, A. N. Semenov, T. V. Shubina, S. B. Listoshin, A. V. Sakharov, M. V. Zamoryanskaya, A. A. Sitnikova, P. S. Kop'ev and S. V. Ivanov
Ioffe Physico-Technical Institute, St Petersburg, Russia

Abstract. The plasma-assisted molecular beam epitaxy (PA MBE) growth of AlGaN layers and quantum well (QW) heterostructures with relatively high Al-content (up to $x = 0.7$) is reported. The growth conditions, which allow obtaining the atomically smooth surface and continuous sharp interfaces, are determined. The intense room-temperature photoluminescence from AlGaN layers and QW structures with the peak wavelength within ultraviolet (UV) range (280–340 nm) was observed. UV light emitting diode prototype has been fabricated and demonstrated room temperature electroluminescence at 320 nm.

Introduction

High-efficiency AlGaN-based light-emitting devices (LED) for the deep UV wavelength range (210–360 nm) still remains an actual problem despite the significant progress in III-nitrides technology [1–3]. In comparison with commercial blue-violet InGaN-based LEDs, the UV ones demonstrate the much worse quantum efficiency that is explained by lowering the structural quality of $Al_xGa_{1-x}N$ at high Al-content ($x > 0.2$) and, until recently, the absence of carrier localization effects [4, 5].

This paper is devoted to plasma-assisted MBE (PA MBE) growth of AlGaN layers and QW heterostructures with relatively high Al-content (up to $x = 0.7$), which demonstrate photo-, cathodo- and electro-luminescence in the 280–340 nm range.

Experiment

$Al_xGa_{1-x}N$ ($x \leq 0.7$) epitaxial layers with typical thickness of $\sim$1 μm and QW heterostructures were grown directly on annealed nitridiated c-sapphire by PA MBE growth technique using Compact 21 T (Riber) setup. In some experiments, 3-μm-thick GaN-layers grown by MOCVD on c-sapphire were used as buffers. The different substrate temperatures ($T_s = 650-740\,^\circ$C), growth rates (0.3–0.4μm/h, group III flux to activated nitrogen (III/N) as well as Al/Ga flux ratios were employed. QW structures had 1–1.6 μm-thick n-type AlGaN:Si buffers ($n_e \sim 10^{18}$ cm^{-3}). For p-type doping, the standard Mg-doping using the solid-state cell and $T_s = 650\,^\circ$C was employed. *In-situ* monitoring of the growth rate and surface morphology was performed using laser reflectometry system and reflection high energy electron diffraction (RHEED), respectively, that gives the convinient way to control Al-content in the layers and QWs with rather high accuracy [6]. The structural and optical properties of the structures were analyzed using scanning electron microscopy (SEM), transmission electron microscopy (TEM), X-ray diffraction (XRD), photo-, cathodo- and electroluminescence spectroscopy (PL, CL and EL respectively).

Results and discussion

We have found that PA MBE of AlGaN epilayers allows one to achieve the Al-content up to 0.7 at growth rate of 0.4 μm/h. Comparative study of the growth kinetics during PA MBE of AlGaN and binary alloys (GaN and AlN) has revealed the strong difference in the epitaxy conditions for two-dimensional growth of epilayers. Whereas for the 2D growth of binary alloys at $T_s = 700\,^\circ$C the III/N value should be maintained at 1.1 and this value is limited by the occurrence of the metallic microdroplet formation (Ga or Al respectively), for the growth of the $Al_xGa_{1-x}N$ the much higher III/N values (at least 1.5) are necessary to provide the 2D growth conditions (without micro-droplet phase formation till III/N of 1.7) at the same T_s. Also, it has been found the complete Al incorporation in AlGaN layer at the used T_s (less 740 $^\circ$C). These data indicate the strong difference between Ga desorption from the surface of the binary and ternary alloys.

Study of the structural properties of the $Al_xGa_{1-x}N$ layers revealed that the samples grown using MOCVD-templates possesed much narrower XRD peaks in comparison with ones grown atop of c-sapphire. In the case of layers with $x = 0.42$ the FWHM of symmetric reflex (0002) measured in θ-scanning mode was of 248$''$ for AlGaN/GaN-template whereas the the layers grown on c-sapphire demonstrated analogous value of 1750$''\theta$ only. However, the former demonstrated micro-cracking and PA MBE buffers were mainly used.

It has been found that the flatness of the $Al_xGa_{1-x}N$ layers could be improved by the insertion of the several 2-ML-thick AlN layers or 30$\times$$Al_xGa_{1-x}N$(6 nm)/AlN(2 nm) super lattices (SL). In addition, TEM data demonstrate that the introduction of such SL results in the one order lowering the density of the threading dislocations atop SL down to 2.5×10^9 cm^{-2}.

QW structures consist of 3 $Al_xGa_{1-x}N$ wells (nominally 3-nm-thick) and $Al_yGa_{1-y}N$ barriers (nominally 8-nm-thick), with the maximum values of x and y being of 0.45 and 0.55, respectively. No variation of Al flux was used, and the QW structures were grown using a sub-monolayer digital alloying technique with Al and Ga cell temperature kept constant, with the average composition being defined by an employed AlGaN/GaN sub-monolayer SL. The typical (y-x) difference was kept constant at 0.15. The QW structures were capped by either a 50-nm-thick $Al_yGa_{1-y}N$ layer for PL and CL studies or a 20-nm-thick electron blocking layer followed by a 200-nm-thick p-GaN:Mg layer with hole concentration of $\sim10^{18}$ cm^{-3} for EL measurements.

PL spectra of AlGaN QWs have a complicated shape with two separated bands and a tail extending deep inside the optical gap (Fig. 1). PL temperature dependence has demonstrated that the higher-energy band is related to the near-band-edge

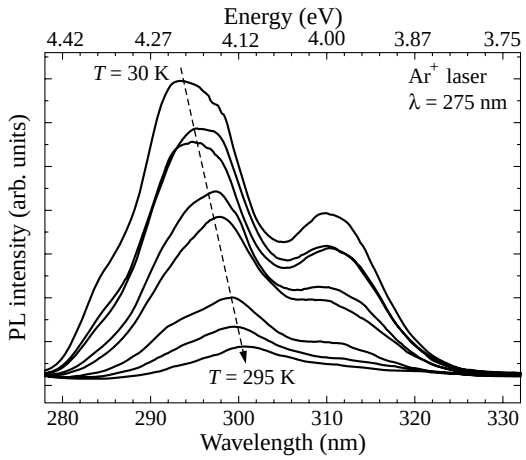

Fig. 1. Temperature dependence of PL spectra for $3\times Al_{0.42}Ga_{0.58}N/Al_{0.56}Ga_{0.44}N$ QW structure.

transitions, as its position shifts to the red by ∼0.1 eV with temperature variation from 15 to 300 K. The lower-energy band position varies slightly with temperature that permits us to ascribe it to the transitions involving deep localization centers.

The wafer-test of the EL ability has been performed using QW structures grown by PA MBE directly on sapphire (for TEM cross-view see Fig. 2).

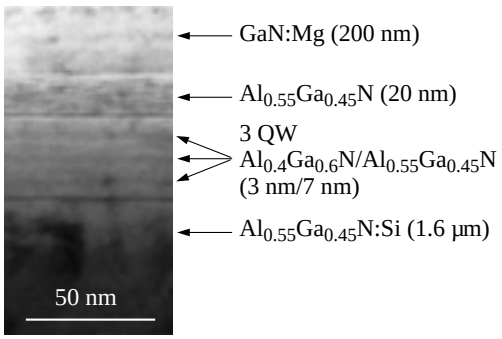

Fig. 2. TEM cross-view image of prototype LED structure with $3\times Al_{0.4}Ga_{0.6}N/Al_{0.55}Ga_{0.45}N$ QWs.

The EL spectrum, shown in Fig. 3, has been registered at 1.5 mA *cw* electrical pumping. It is dominated by a peak at 320 nm with a 25 nm line width, presumably related to the AlGaN QWs.

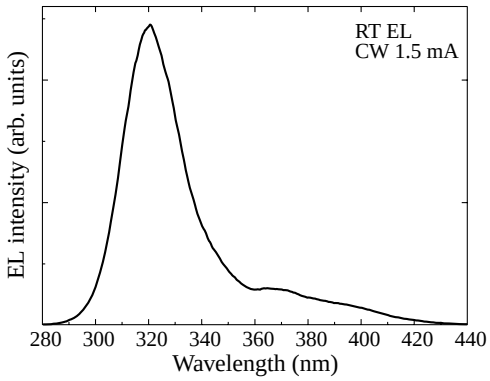

Fig. 3. Electroluminescence spectrum of prototype LED structure with $3\times Al_{0.4}Ga_{0.6}N/Al_{0.55}Ga_{0.45}N$ QWs.

Conclusion

These results illustrate perspectives of the PA MBE growth technique for AlGaN-based UV LEDs.

Acknowledgements

The work was supported partly by RFBR, Program of PSD of RAS, FASI and the Foundation for Assistance to Small Innovative Enterprises (FASIE).

References

[1] Y. Taniyasu, M. Kasu, T. Makimoto, *Nature* **441**, 325 (2006).
[2] S. Nikishin, M. Holtz, H. Temkin, *Jpn. J. Appl. Phys.*, Part 1 **44**, 7221 (2005).
[3] W. H. Sun, V. Adivarahan, M. Shatalov *et al*. *Jpn. J. Appl. Phys.*, Part 2 **43**, L1419 (2004).
[4] A. V. Sampath, G. A. Garrett, C. J. Collins *et al*. *J. Electron. Material.* **35**, 641 (2005).
[5] B. Borisov, S. Nikishin, V. Kuryatkov, H. Temkin *Appl. Phys. Lett.* **87**, 191902 (2005).
[6] S. V. Ivanov, V. N. Jmerik, A. M. Mizerov *et al*., *Abstr. ISGN-I* Linkopping, WeP-26, 2006.

15th Int. Symp. "Nanostructures: Physics and Technology"
Novosibirsk, Russia, June 25–29, 2007

Photoluminescence from MBE-grown HgCdTe films in the short infrared range

V. I. Ivanov-Omskii[1], *K. D. Mynbaev*[1], N. L. Bazhenov[1], V. A. Smirnov[1], V. S. Varavin[2], A. A. Babenko[2], D. G. Ikusov[2] and G. Yu. Sidorov[2]

[1] Ioffe Physico-Technical Institute, St Petersburg, Russia
[2] Institute of Semiconductor Physics SB RAS, 630090, Novosibirsk, Russia

Abstract. Infrared (1.5–1.8 μm wavelength) photoluminescence (PL) of HgCdTe films grown by molecular beam epitaxy is studied. It is shown that annealing of the as-grown films at 270 °C for 20 hours leads to considerable changes both in the structure of the PL spectra and in the PL intensity. The former effect can be explained by smoothing of non-uniformity of chemical composition along the thickness the films, while the latter results from the improvement in their structure.

Introduction

HgCdTe alloys still hold their position as one of the basic materials for infrared photodetectors [1]. Furthermore, recently, there has been much interest in these alloys as promising materials for fabricating light emitters, mostly for 1.5–1.8 μm wavelength, which are of much importance for environment control [2–5]. Mainly, this trend was stimulated by substantial improvements in HgCdTe technology and, first of all, by the progress of molecular beams epitaxy (MBE). Also, it was shown [6], that the radiation quantum efficiency in $Hg_{1-x}Cd_xTe$ with $0.4 < x < 0.74$ has a maximum at $\lambda \simeq 1.5$ μm at $T \simeq 300$ K. This maximum is caused by the suppression of the Auger-recombination mechanisms due to a specific relation between the bandgap and spin-orbit splitting in the material. It should be noted that this spectral range is of current importance for fiber-optics communications.

It is known that fabrication of HgCdTe-based devices requires solving problems related to the post-growth annealing. This necessity is caused by the dependence of the concentration of intrinsic defects in HgCdTe on external conditions, which is typical for $A^{II}B^{VI}$ compounds. Deviations from stoichiometry, which appear during the growth, need compensating by post-growth annealing. In this paper, we studied photoluminescence (PL) of MBE-grown HgCdTe in order to assess the prospects of light emitters based on this material. We considered the effect of the post-growth annealing on the PL of HgCdTe in the 1.5–1.8 μm wavelength range.

1. Experiment

The experimental samples were grown with the technology described in [8], and represented multi-layer structures grown on GaAs and Si substrates (50 mm in diameter) with ZnTe and CdTe buffer layers. A typical composition profile as measured during the growth using an automatic ellipsometer is presented in Fig. 1. At the left part of the image one can see a vary-gap layer, corresponding to the transition between the CdTe buffer layer and the HgCdTe layer with homogeneous composition. The latter demonstrates composition fluctuations of about 2% from the mean x value. In the samples studied, HgCdTe films had an average x value of 0.58 to 0.64 and after the growth demonstrated n-type conductivity with the electron concentration $\sim 10^{14}$ cm^{-3}.

After the growth, samples for optical measurements with the area of $\sim$ 1 cm^2 were cut from the wafers, and a part

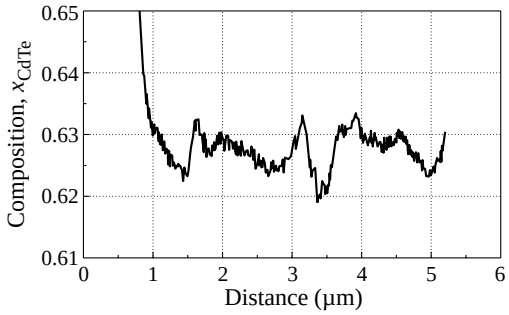

Fig. 1. HgCdTe composition along the thickness of the sample; the distance is measured from the CdTe buffer layer.

of the samples was annealed for 20 h at 270 °C in the helium atmosphere. Such annealing is normally used to convert MBE-grown $Hg_{1-x}Cd_xTe$ with $x < 0.4$ into p–type conductivity [9].

PL was studied in the 4.2 to 300 K temperature range under pulse excitation with InGaAs/GaAs semiconductor laser emitting at 1.03 μm. The spectra were recorded with an optical installation based on MDR-23 monochromator. PL signal was measured with Ge photodiode.

2. Results and discussion

It was found that the annealing had a double effect on the PL spectra. Firstly, it caused evolution in the spectrum structure, which was especially clearly seen at temperatures under 100 K. Secondly, the PL intensity of the samples subjected to the annealing was strongly changed, and at the room temperature the PL intensity of the annealed samples increased greatly.

The first effect is illustrated in Fig. 2, which shows PL spectra of a HgCdTe sample before and after the annealing, as recorded at 93 K. For clearness, the spectra were normalized before plotting. As is seen, the PL band after the annealing was narrowed and blue-shifted (see curves 1 and 3). This can be explained by levelling of the composition along the thickness of the film, caused by Cd and Hg diffusion in the layer adjacent to the substrate and by out-diffusion of Hg. As to composition fluctuations, in the as-grown samples they should be accompanied by the fluctuations of energy bands. The laser radiation is absorbed at a distance of about 1 μm from the surface, and generated carriers diffuse into the bulk of the specimen. However, the energy barriers hinder the diffusion. As the barrier height may be as high as 30 meV (Fig. 1), at low temperatures they prevent the diffusion of photogenerated carriers; so

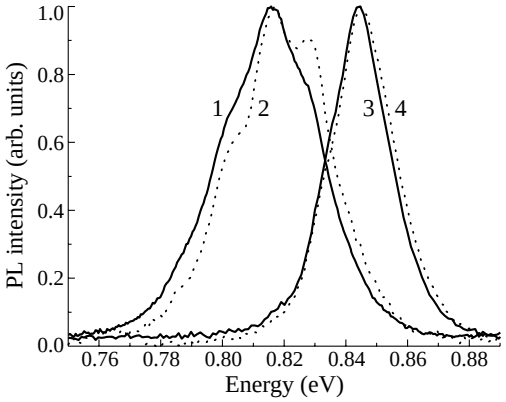

Fig. 2. PL spectra at 93 K: 1, 2 — before annealing; 3, 4 — after annealing. Spectra 1 and 3 were measured under excitation and with recording PL signals from the epitaxial layer; 2 and 4, from the substrate.

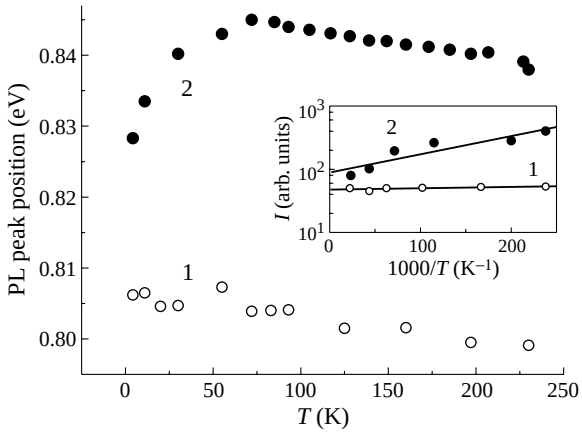

Fig. 3. Dependence of the position of dominant PL peaks on temperature. 1 — before annealing, 2 — after annealing. Temperature dependences of the amplitudes of the corresponding peaks were shown in the insert.

the concentration of the latter is much more at the side under radiation. Also, the carriers accumulate in local potential wells and recombine from there, giving luminescence peaks at the wavelengths, which correspond to the areas with minimum composition. As a result, at $T = 4.2$ K for the as-grown sample we observed PL band with FWHM of 25 meV. With increasing the temperature, when the thermal energy of the carriers reaches the value big enough to overcome the barriers, the spectrum broadens, yet its shape is still depending on the side, from which the sample is irradiated. This can be seen in Fig. 2, curves 1 and 2. It is seen that the spectra comprise similar bands but their relative intensity changes, depending on irradiated side, which is obviously caused by different filling of potential wells. As the temperature increases further, the thermal energy of the carriers becomes high enough to overcome most of the barriers, and the PL band broadens even more.

After the annealing, the potential relief smoothes down; the diffusion of the carriers takes place more "easily", and now, the shape of the spectrum does not depend on the excitation side. This is clearly seen in Fig. 2, curves 3 and 4.

The second effect, i.e. the change in the PL intensity after the annealing, is probably related to the improvement in the material structure and reduction of the intrinsic defect concentration. In Fig. 3, examples of the temperature dependence of the position of major PL band in as-grown and annealed samples are shown. It is seen that the dependence before and after the annealing is different. In the as-grown sample, it is monotonous with the slope close to that of $E_g(T)$. After the annealing, the peak of the PL band under consideration experiences a blue shift in the 4.2–70 K temperature range, but at higher temperatures becomes red-shifted with the slope similar to that of the as-grown sample. Also, the integral intensity of the two peaks depends on the temperature T differently; such dependence is presented in the inset in Fig. 3. It is seen there, that in the as-grown sample the peak intensity in the 4.2–20 K temperature range does not depend on T, while in the annealed sample it is thermally activated with 1.6 meV activation energy. The results presented allow us to suggest that after the annealing the defect structure of the sample improves so greatly, that at low temperatures formation of excitons becomes possible. Excitons were observed in structurally perfect HgCdTe samples with similar composition previously [10,11]. Most probably, it is the drastic improvement of structural properties of the layers and reduction of the density of non-radiation recombination centers that is responsible for the increase in PL intensity of the annealed samples at the room temperature.

3. Conclusion

Thus, low-temperature annealing strongly affects the photoluminescence of MBE-grown HgCdTe films by improving the structure of the films and reducing the density of non-radiation recombination centers.

Acknowledgements

This work was supported by RFBR grant 07-02-00400-a.

References

[1] A. Rogalski, *Rep. Progr. Phys.* **68**, 2267 (2005).
[2] Yu. N. Nozdrin, A. V. Okomel'kov, A. P. Kotkov *et al*, *Semiconductors*, **38**, 1374 (2004).
[3] A. A. Andronov, Yu. N. Nozdrinov, A. V. Okomel'kov *et al*, *Semiconductors* **40**, 1266 (2006).
[4] J. P. Zanatta, F. Noel, P. Ballet *et al*, *J. Electron. Mater.* **32**, 602 (2003).
[5] J. Bleuse, J. Bonnet-Gamard, G. Mula *et al*, *J. Cryst. Growth.* **197**, 529 (1999).
[6] N. L. Bazhenov, V. I. Ivanov-Omskii, A. I. Izhnin *et al*, *Sov. Phys. Semicond.* **25**, 667 (1991).
[7] K. D. Mynbaev, V. I. Ivanov-Omskii, *Semiconductors* **40**, 1 (2006).
[8] Yu. G. Sidorov, V. S. Varavin, S. A. Dvoretskii *et al*, *Semiconductors* **35**, 1045 (2001).
[9] P. A. Bakhtin, S. A. Dvoretskii, V. S. Varavin *et al*, *Semiconductors* **38**, 1168 (2004).
[10] V. I. Ivanov-Omskii, I. A. Petroff, V. M. Pogorletskii *et al*, *Sol. Stat. Comm.* **76**, 1159 (1990).
[11] A. Lusson, F. Fuchs, J. Mairfang, *J. Cryst. Growth.* **101**, 673 (1990).

15th Int. Symp. "Nanostructures: Physics and Technology"
Novosibirsk, Russia, June 25–29, 2007

The heteroepitaxial growth of silicon carbide nanocrystals of fixed sizes on the porous silicon

Yu. S. Nagornov, B. M. Kostishko and E. S. Pchelinscheva
Ulyanovsk State University, Ulyanovsk, 432000, Russia

It is well known that the melting temperature of nanocrystallites decreases with their size. It's experimental established that T_m decreases to 900 °C for the silicon nanocrystals with 5 nm diameter [1]. The melting point decreasing effect was observed for porous silicon (por-Si), which keeps the crystals with a diameter in range of 1–1000 nm. Authors of work [2] discovered that silicon particles melt under 800 °C for por-Si with 50% porosity. Thus we can suppose that nanocrystallites, which are smaller than critical diameter, melt under the high temperature epitaxy on the porous silicon. It is obvious that the critical diameter is defined by equality of the ambience temperature and his melting point. Evidently the speed of the diffusion in the crystal volume and the coalescence in the liquid nanocrystals are much more than in the solid crystals. Therefore the formation of new substance phase will happen with participation of nonacrystallites in the first place. In this work we discuss the formation of cubic silicon carbide (3C-SiC) nanocrystals of fixed sizes under high temperature carbonization of porous silicon.

The samples, formed on the basis of n-type Si wafers with the 4.5 T cm resistivity, (100) oriented, were used in the experiments. Porous silicon was prepared by the electrochemical anodization in the electrolyte containing HF and C_2H_5OH in volumetric relation 1:1 under the 20 mA/cm^2 electric current density for 30 minutes. After the formation of the porous layer, the samples were placed in the chamber with CCl_4 gas atmosphere and carrying agent (hydrogen) for carbonization at temperatures in the range from 800 to 1350 °C, for 2 to 60 minutes. In the process, the samples were doped by the atoms of Ga, P and B up to 10^{18} cm^{-3} concentrations.

The formation of the cubic silicon carbide crystallites with 5–7 nm size during carbonization of porous silicon under 1200–1300 °C is investigated by X-ray diffraction, Auger spectroscopy, Raman scattering and scanning tunneling microscopy. Single particles with sizes of 20–110 nm and quantum wires consisting of particles with sizes of 20–50 nm are presented on the porous silicon. The specific feature of carbonized por-Si is the appearance of SiC nanoparticles with sizes of 70–110 nm which have grain form. After the scan magnification we saw that all SiC particles consist of the fragments with sizes of 20–40 nm. The distribution of SiC particles has Gauss form and it is in the range of 10–100 nm contrary to Si particles distribution. The average size of SiC quantum dots was calculated from Raman scattering spectra by numerical simulation of the peak form. It is interesting that the peak of SiC is greatly changed contrary to silicon peak during the Raman spectra measurement. At first, the maximum of SiC peak shifts from 960 to 967 cm^{-1}, the second, the peak linewidth decreases from 51 to 26 cm^{-1}, and the third, the peak intensity grows greatly. All the modifications occur during 2–3 hours and then they don't change for a long time. The numerical simulation coincides with experimental data, thus the average size of SiC nanocrystallites decreases from 5.2 to 7.3 nm under laser light with power of 1–5 W/cm^2.

Proposed model of the crystallites formation includes the following stages. The first one is the melting of the silicon crystallites with 3–7 nm diameters due to the size effect of the melting temperature decreasing. The second is the participation of the liquid crystallites in fast growth of silicon carbide particles. And the third stage includes the growth stop when the SiC crystallites reach critical diameter depending on the carbonization temperature.

References

[1] C. C. Yang, G. Li, Q. Jiang, *J. of Physics: Condensed Matter* **15** (29), 4961 (2003).
[2] V. Yu. Timoshenko, Th. Dittrich *et al*, *Phys. status sol. (a)* **182**, 325 (2000).

15th Int. Symp. "Nanostructures: Physics and Technology"
Novosibirsk, Russia, June 25–29, 2007

Monte Carlo simulation of silicon nanowhiskers growth

A. G. Nastovjak[1,2], I. G. Neizvestny[1], N. L. Shwartz[1], Z. Sh. Yanovitskaya[1] and A. V. Zverev[1]

[1] Institute of Semiconductor Physics RAS SB, Novosibirsk, 630090, Russia
[2] Novosibirsk State Technical University, Novosibirsk, Russia

Abstract. Examination of silicon nanowhiskers growth on Si(111) surface activated by gold was carried out using Monte Carlo simulation. Dependences of nanowhisker length on gold drop size and deposition conditions were obtained. It was shown that for given temperature and deposition rate there is optimal drop size corresponding to maximal whisker growth rate. Existence of optimal deposition conditions providing maximal growth rate of nanowhiskers was demonstrated.

Introduction

Much attention has been given for understanding mechanisms of silicon nanowhiskers (NWs) growth due to their promising applications: in sensors and microelectronicmechanical systems, as effective emitters for vacuum electronic devises and flat displays, etc. Semiconductor NWs are generally grown by chemical vapor deposition (CVD) or molecular beam epitaxy (MBE) with predeposited Au drops [1–4]. Gold is used as catalyst, growth rate under catalyst-drop is higher than on the free substrate. This results in the formation of semiconductor columns with Au drops on the top. According to vapor-liquid-solid (VLS) mechanism [1] metal catalyst must become supersaturated with semiconductor material. Excess material then precipitates at the liquid-solid interface. Semiconductor atoms may get into the drop both directly from the vapor phase and due to diffusion from the substrate along the sides of NWs [1,3,4]. Different aspects of NWs growth were investigated theoretically: analytic kinetic models of CVD and MBE growth of NWs were suggested [1,5], thermodynamic size limit of NWs was estimated [6], ab-initio calculations of their electronic and structural properties were fulfilled [7] and energy favorable shape of whiskers with small diameter was found [8]. However for controlled technology of NWs growth atomic scale consideration of the process is desirable. In this work atomic-scale investigation of nanowhiskers growth was fulfilled using Monte Carlo simulation.

1. Monte Carlo model

Simulations were carried out using program package SilSim 3D-7comp, developed for atomic processes modeling during growth and annealing on the surface of multicomponent crystal substrates. Molecules containing silicon atoms (precursors P) were deposited by CVD on Au activated Si(111) substrate with diamond-like crystal lattice and with sizes up to 100×100 atomic sites (a.s.). Under the surface layer there was perfect Si semi-infinite crystal in Z direction that was not changed during simulation. Cyclic boundary conditions were applied in lateral $X-Y$ direction. The main atomic events considered in the model are adsorption, diffusion and chemical reactions. To realize growth of vertical Si crystals following aspects were considered: golden drop poorly wets Si surface; crystal silicon was not dissolved in the drop, diffusion coefficient of adsorbed molecules through the substrate was higher than along drop surface.

Two growth mechanisms differently considering the role of gold were studied. For both mechanisms after decomposition at the surface of precursor molecules P intermediate matter M containing silicon was created and volatile by-products were removed from the model system. Diffusion of M particles through gold drop was realized due to exchange diffusion with activation energy 0.8 eV and Si precipitation at the interface Au/Si was realized using chemical reaction: $M + \mathrm{Si} \rightarrow \mathrm{Si} + \mathrm{Si}$ ($E_\mathrm{r} = 1.2$ eV). This reaction was possible at any atomic site containing silicon atom. In the first mechanism 3 component system was considered: 1 — Si, 2 — Au, 3 — intermediate matter (M). Decomposition of gas transport molecules with M particles formation was possible at any atomic site. The gold particle only provides energy favorable place for silicon atoms embedding. In the second mechanism model system was 4 compound system: 1 — Si, 2 — Au, 3 — Precursor (P), 4 — intermediate matter (M). Decomposition of P particles takes place only on the drop in the presence of gold: $P + \mathrm{Au} \rightarrow M + \mathrm{Au}$ ($E_\mathrm{r} = 0.8$ eV). The chemical nature of P and M particles is not discussed in this work.

Diffusivity is determined by interaction energies E_{ij} between different sorts of atoms. The simulations were carried out for following energy values: $E_{\mathrm{SiSi}} = 0.6$ eV; $E_{\mathrm{SiAu}} = 0.4$ eV (1 mechanism), $E_{\mathrm{SiSi}} = E_{\mathrm{SiAu}} = 0.6$ eV (2 mechanism); $E_{P\mathrm{Si}} = E_{M\mathrm{Si}} = 0.6$ eV, $E_{M\mathrm{Au}} = E_{P\mathrm{Au}} = 1$ eV. Lower interaction energies of Au atom with other sorts of atoms than between atoms of gold provide poor gold wettability and guarantee formation of constriction around the Au/Si interface and sites for silicon embedding under the drop. Temperature and precursor deposition rates were varied in the ranges: $650\ \mathrm{K} < T < 925\ \mathrm{K}$, $5 \times 10^{-3}\ \mathrm{ML/s} \leq V \leq 5 \times 10^{-1}\ \mathrm{ML/s}$, according to experimental works [2,3].

2. Results and discussion

Fig. 1(a) illustrates NWs morphology for two sizes of gold drop, and Fig. 1(b) demonstrates NW length dependence on initial drop diameter d_0 for two growth mechanisms. There is minimal diameter lower which no whiskers can be grown. Existence of minimal drop diameter in the model system is due to high mobility of small drop. Small gold drop permanently migrates through the surface without crystal growth activation at some definite surface place. With the increase of drop diameter whiskers length increases and when diameter achieves some definite value (in our case approximately equal 3 nm) whisker length is maximal. At larger diameters $L(d_0)$ is decreasing function as in [3–5]. Descending $L(d_0)$ dependence is due to diffusion induced nature of growth. The character of $L(d_0)$ dependence is similar for both mechanisms of growth.

Fig. 2 demonstrates dependences of NWs lenght on deposition rate for two growth mechanisms. This dependence is

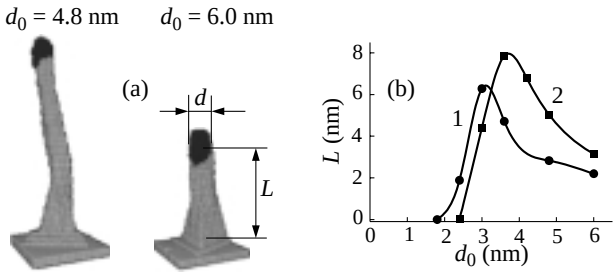

Fig. 1. (a) Morphology of nanowhisker grown according mechanism 1 at $T = 800$ K, $V = 0.05$ ML/s after 155 s deposition for two initial diameters of gold drop d_0; (b) nanowhisker length L versus initial drop diameter d_0: 1, 2 — growth mechanism number, $T = 800$ K, $V = 0.05$ ML/s, $t = 23$ s.

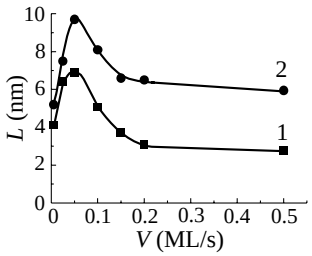

Fig. 2. Nanowhisker length L versus deposition rate V at $T = 800$ K: 1, 2 — growth mechanism number ($d_0 = 3.6$ nm, deposited dose $\Theta = 1.5$ ML).

determined by relation between deposition rate, drop mobility and silicon rate precipitation at interface Au/Si. The main contribution to whiskers length growth give silicon atoms embedded in the constriction around the Au/Si interface. Such constriction was observed in experimental works [4]. At optimal deposition rate all silicon atoms deposited on the surface are embedded at the gold-silicon interface. For lower flux concentration of silicon atoms in the region of constriction around the Au/Si interface is not enough for silicon nucleus formation at the interface, so portion of silicon atoms diffuses along side walls of whisker and embeds into silicon kinks far off the drop. For high flux of precursors only part of silicon can be embedded under the drop, since precursor atoms occupy all accessible atomic sites at constriction area around the Au/Si interface. And portion of Si atoms are embedded at whisker side walls or at the substrate and make no contribution in whisker length growth. It should be noted that NW length L is the distance between Au/Si interface and flat silicon surface, corresponding to silicon layer grown between Au drops. Second growth mechanism gives longer whiskers than the first one since in first mechanism part of silicon atoms can be embedded in the kinks of whisker column or at the substrate before they reach Au/Si interface.

With temperature elevation growth rate raises due to the increase of silicon segregation rate from transport molecules and diffusion coefficient. However with rising temperature mobility of gold drops increases and whisker growth is not observed at temperatures higher than some definite temperature. So there are optimal deposition conditions providing maximal growth rate.

In the model system a number of effects defining by mobile gold drop behavior were observed: branching of growing crystal, diffusion overflow of small drops into large ones, capture of gold atoms by growing silicon NW. The lower is growth temperature the more gold portion stays inside the model whisker. Example of growing crystal branching is shown in Fig. 3. Faceting of whiskers column is clearly seen in this figure. Gold drop can slip down from the flat facet formed on the top of the whisker, accumulate on the sidewall of whisker and initiate branch growth. In [2] sizes of experimental NWs were comparable with our model consideration and NWs branching was observed, in [3] one can see faceting of whiskers column.

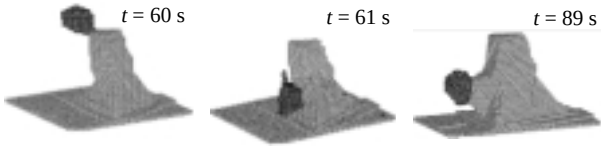

Fig. 3. Initial stages of nanowhisker branching ($T = 800$ K, $V = 0.05$ ML/s, $d_0 = 3.6$ nm).

3. Summary

Kinetic Monte Carlo model of CVD growth of silicon nanowhiskers, on the assumption of high surface diffusion on Si(111) surface activated by Au, was realized. The model takes into account that diffusion coefficient of adsorbed molecules through the substrate is higher than along drop surface and that golden drop poorly wets silicon surface. Effects observed in experiments were found in the model system, like faceting of whiskers side walls, drop migration from the top to the sides of whisker, NW branching, diffusion overflow of small gold drops into large ones and entrapping of gold atoms inside growing crystal. Existence of minimal size of Au drop lower which NWs don't grow can be explained by high mobility of small gold drop along silicon surface. Sliding of gold drop from the top of the whiskers with following branch growth may be result of flat facet formation on the top of NW.

Acknowledgement

This work was supported by the RFBR (05-02-16455).

References

[1] E. I. Givargizov, *J. Crystal Growth* **31**, 20 (1975).
[2] J. Kikkawa, Y. Ohno, S. Takeda, *Appl. Phys. Lett.* **86**, 123109 (2005).
[3] N. D. Zakharov, P. Werner, L. Sokolov, U. Gosele, *Physica E* (2006), doi:10.1016/j.physe.2006.07.018.
[4] L. Schubert, P. Werner, N. D. Zakharov, G. Gerth, F. M. Kolb, L. Long, U. Gosele, T. Y. Tan, *Appl. Phys. Lett.* **84**, 4968 (2004).
[5] V. G. Dubrovskii, N. V. Sibirev, G. E. Cirlin, J. C. Harmand, V. M. Ustinov, *Phys. Rev. E* **73**, 021603 (2006).
[6] T. Y. Tan, N. Li, U. Gosele, *Appl. Phys. Lett.* **83**, 1199 (2003).
[7] T. Vo, A. J. Williamson, G. Galli, *Phys. Rev. B* **74**, 045116 (2006).
[8] J. X. Cao, X. G. Gong, J. X. Zhong, R. Q. Wu, *Phys. Rev. Lett.* **97**, 136105 (2006).

15th Int. Symp. "Nanostructures: Physics and Technology"
Novosibirsk, Russia, June 25–29, 2007

Array properties of the vertical ordering of Ge nanoclusters on Si(100) surface

A. I. Nikiforov, V. V. Ulyanov, S. A. Teys, A. K. Gutakovsky and O. P. Pchelyakov
Rzhanov Institute of Semiconductor Physics, SB RAS, Lavrentjeva 13, 630090 Novosibirsk, Russia

Abstract. Variations of in plane lattice constants in the course of the growth of the Si/Ge/Si heterosystem were studied. The thickness of the silicon film where elastic strains are relaxed is determined as dependent on the germanium layer thickness. HRTEM studies indicate the vertical ordering of the germanium island layers when the thickness of the Si layer in between Ge layers is not sufficient to provide the full strain relaxation. The vertical ordering of Ge islands in the multilayer structure results in a decrease in the island density at reduced of their size.

1. Introduction

The silicon structures with germanium quantum dots is of interest to practical optoelectronic applications due to their potential covering the regions from IR [1] through the wavelengths used in fiber-optic communications [2]. The vertical ordering of quantum-sized objects gives rise to changing the band diagram as compared to that of single and disordered nano objects. As a result, optical properties of these heterostructures change considerably, for example, the photoluminescence intensity increases remarkably [3]. Thus, new potentialities arise in the areas of band engineering and development of new principles for creation of up-to-date devices.

The traditionally used technique in MBE is reflection high-energy electron diffraction (RHEED). The unique features of the RHEED technique enabled oscillations of the in-plane lattice constant to be detected for the Ge film growing according to the 2D mechanism on the silicon surface [4]. The strains can be estimated from variations of in plane lattice constant in the growing Ge film. While silicon grows over the germanium layer, the irregular strain distribution on its surface above the nanoclusters produces nanocluster nucleation sites in the next growing germanium layer. This phenomenon is of particular importance for synthesis of multilayer heterosystems with alternating vertically ordered germanium nanocluster layers. AFM and TEM were used earlier to study the dependence of the preferable arrangement of germanium islands on the thickness of the silicon layer grown above the preceding island layer [5–7]. The strained state of the overgrown silicon layer causes not only the vertical ordering but also a change in the thickness of the wetting germanium layer. This effect was discussed in detail with "dome"-clusters as an example [8]. The aim of the present work is to study the influence of the vertical ordering of "hut"-clusters on their properties.

2. Results and discussion

A MBE installation Katun-C equipped with two electron beam evaporators for Si and Ge was used for synthesis. Analytical equipment of the chamber included a quadrupole mass spectrometer, a quartz thickness monitor and a high energy electron (20 kV) diffractometer. Diffraction patterns were monitored during the growth using a CCD camera on line with a PC. RHEED technique allows the deformation to be *in situ* registered as a variation in the size of the in-plane lattice constant ($\boldsymbol{a}_{||}$). To do that, variations in the intensity of the diffraction pattern was recorded along the line going across the streaks and bulk spots. A variation of in plane constant lattice $\boldsymbol{a}_{||}$ of Ge film relative to the Si lattices as a function of effective thickness of the growing layer was shown earlier [9]. Relaxation of elastic strains in the silicon film grown over the germanium layer was identified similar way.

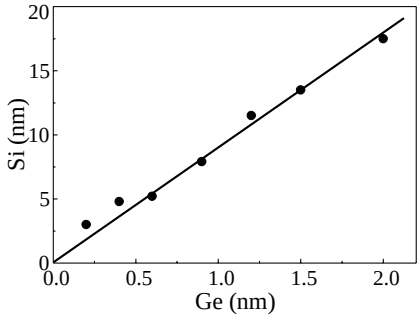

Fig. 1. Dependence of the thickness of the silicon epitaxial layer necessary for full relaxation of elastic strains in the system as a function of the thickness of underlying germanium layer.

Variations in the in plane lattice constant were determined from the RHEED pattern during the formation of both the germanium layer and of the following silicon layer. During the measurements, the Si(100) substrate was at the temperature of 500 °C. The Ge thickness was 5 monolayers in the multilayer structures. As the silicon layer grows over the germanium layer, parameter $\boldsymbol{a}_{||}$, which tends progressively to the value characteristic of the bulky material, illustrates the process of elastic strains relaxation. The full relaxation of strains in the silicon film, which are caused by the presence of germanium, depends on the thickness of the underlying germanium layer. The thickness of the silicon epitaxial layer necessary for full relaxation of elastic strains in the system is shown in Fig. 1 as a function of the thickness of underlying germanium layer. Relevant experimental data (points in Fig. 1) are described well enough by a linear dependence (a straight line in Fig. 1) going through zero point. Thicker germanium films are of no interest because of potential appearance of misfit dislocations. TEM studies indicate the vertical ordering of the germanium island layers when the thickness of the Si layer in between Ge layers is not sufficient to provide the full strain relaxation. Therefore, the elastic strains, which are distributed in irregular manner through the growing Si film surface due to the presence of Ge islands, propagate deeper than the silicon layer thickness that makes the quantum dots growing one above another.

The presence of the "hut"-type islands on the surface only is

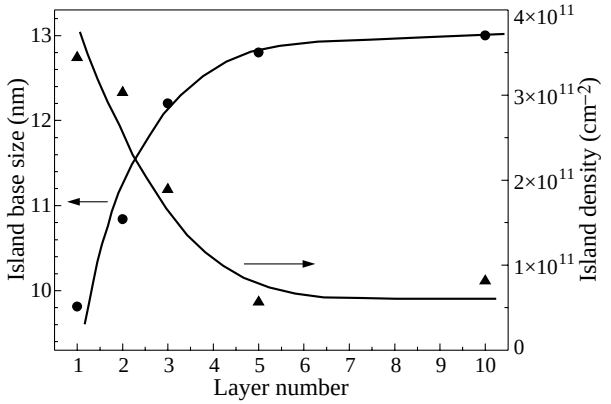

Fig. 2. Density and size of "hut"-clusters versus the number of replications in the multilayer structure with the silicon interlayer thickness of 3 nm.

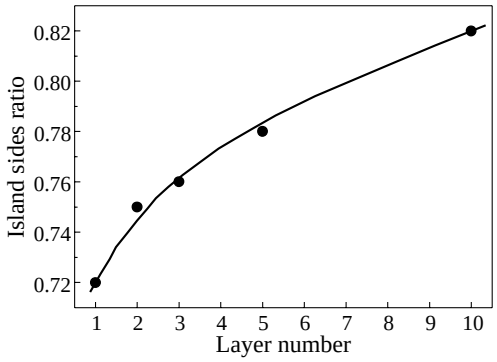

Fig. 3. Changes in the side ratio of "hut"-clusters depending on the number of replications in the multilayer structure with the silicon interlayer thickness of 3 nm.

established by ex situ STM studies of the fist and the following germanium layers. Figure 2 illustrates variations in the density and size of "hut"-clusters depending on the number of replications in the multilayer structure with the silicon interlayer of 3 nm in thickness. A considerable decrease in the nanocluster density is accounted for by the site competition for preferable island nucleation in the regions with different strain gradient on the silicon surface, the gradient being higher above larger islands arranged in the underlying germanium layer. As the number of layers increases, the side ratio of the "hut"-clusters bases also increases (Fig. 3) along with changes in the density and size. As the number of germanium layers increases, the base shape of most islands comes close to square. It looks like irregular elastic strains on the silicon surface suppress the anisotropy of germanium diffusion through the Si(100) surface.

Acknowledgements

The work is supported by the Russian Foundation for Basic Research (Grants 06-02-17412 and 06-02-17275), INTAS (Grant 03-51-5051), and State Contract No. 02.513.11.3156.

References

[1] A. I. Yakimov *et al*, *J. Appl. Phys.* **89**, 5676 (2001).
[2] A. I. Yakimov *et al*, *Semiconductors* **37**, 1345 (2003).
[3] K. Eberl *et al*, *Thin Solid Films* **373**, 164 (2000).
[4] A. I. Nikiforov *et al*, *Mat. Sci. Engineering B* **89**, 180 (2002).
[5] F. Liu *et al*, *Surf. Sci.* **386**, 169 (1997).
[6] M. Miura *et al*, *Thin Solid Films* **369**, 104 (2000).
[7] O. G. Schmidt *et al*, *Phys. Rev. B* **61**, 13721 (2000).
[8] V. Le Thanh *et al*, *Physica E* **23**, 401 (2004).
[9] A. I. Nikiforov *et al*, *Thin Solid Films* **380**, 158 (2000).

15th Int. Symp. "Nanostructures: Physics and Technology"
Novosibirsk, Russia, June 25–29, 2007

Instabilities of stepped silicon surface under sublimation, growth and equilibrium

E. E. Rodyakina[1], S. S. Kosolobov [1] and A. V. Latyshev[1,2]

[1] Institute of Semiconductor Physics, SB RAS, 630090 Novosibirsk, Russia
[2] Novosibirsk State University, 630090, Novosibirsk, Russia

Abstract. Analysis of the structural elementary (atomic) processes on silicon surface during homoepitaxial growth, sublimation, and annealing at thermodynamic equilibrium conditions at high temperatures has been done. The experiments have been carried out by means of *in situ* ultrahigh vacuum reflection electron microscopy and *ex situ* atomic force microscopy at ambient condition. The structural transformations of silicon surface under conditions in flat capillary, consisting two close situated silicon wafers independently heated by electric current, has been analysed. Formation of anti-bunches, containing steps of the opposite sign in comparison with ones in bunches, has been found under homoepitaxial growth and quasi-equilibrium on silicon (111) surface. Anomalous large distance (more then 95 μm) between steps have been registered.

Introduction

One of the problems of nanoparticles formation technology is spontaneous roughening of substrate surface morphology under thermal annealing, homo- and heteroepitaxial growth and other treatments. Understanding of atomic processes been responsible for roughening initial clean silicon surface consist of regularly distributed atomic steps could help us to govern the surface morphology. Insight the processes governing the motion of vicinal surface steps has been a long standing problem of fundamental interest in surface science. For semiconductors, understanding the behavior of the steps is technologically critical for the growth of epitaxial overlayers and for devices processing.

It has been well known about redistribution of atomic steps (step bunching) on Si(111) surface under heating by passing direct electric current (DC) [1]. Still controversial is the physical origin of temperature and current direction dependences of the phenomena. Especially there have been a lot of discrepancies about impact of outer silicon atoms flux on surface morphology transformation [2]. Long-time heating stepped silicon surface by DC leads to forming bunches of the steps of opposite sing (anti-bunches) relative to original step direction [3], but the phenomena is still not understood. Influence of silicon deposition on such surface structure could help us to understand elementary processes governing steps redistribution, but it is not investigated early. This work presents the investigation of step behavior on silicon(111) surface consisting step bunches and anti-bunches under sublimation, homoepitaxial growth and quasi-equilibrium.

1. Experimental

Near-equilibrium and growth conditions at high temperatures (up to 1350 °C) were realized by using system of flat capillary consisting two silicon substrates placed parallel on small distance (about 100 μm). The substrates were separated on the edges by a dielectric material and heated independently by passing electric current. Near-equilibrium conditions were achieved on a sample surface when sublimation atom flux off investigated sample is compensated by atom flux from neighbor substrate, so net flux is equal by zero. As a result it was observed by *in situ* reflection electron microscope (REM), that regularly distributed steps didn't move and only fluctuated thermal near its mean position under near-equilibrium conditions.

The samples, $10 \times 1.2 \times 0.3$ mm^3 in sizes, were cut from Si(111) wafer (miscuts angle less then 0.5°) with the long edge near perpendicular to atomic steps line. After standard chemical treatment samples were fixed in home-made flat capillary holder and placed into an ultrahigh vacuum chamber of REM (with base pressure less then 10^{-9} Torr) [4]. Its were annealed at different temperatures and current directions and morphology transformations were *in situ* investigated by REM. Then samples were quenched to room temperature, evacuated to atmosphere conditions and investigated *ex situ* at ambient condition by atomic force microscope (AFM, Solver P-47H) with using semicontact and phase contrast regimes. Thin silicon dioxide covered silicon surface uniformly and didn't influence on AFM resolution [5].

2. Results and discussion

AFM-images (phase contrast) of stepped silicon surface after annealing under sublimation (a), growth (b) and near-equilibrium (c) conditions are presented in Fig. 1. The annealing temperature was about 1270 °C. Wide white regions on the image represent step bunches, black regions, parallel to white ones, — step anti-bunches. Thin grey lines are atomic steps. The schematic profiles of topography along slash lines, perpendicular to step bunch, are presented near each of AFM-image. The step anti-bunches are formed in parallel with bunches from the upper side of bunches under sublimation (Fig. 1(a)). For the first time, the step anti-bunches have been observed to form from the lower side of bunches under growth and near the centre between two neighbors bunches under quasi-equilibrium on the surface (see Fig. 1(b), (c)). It have been observed that under changing the conditions on the surface from sublimation to growth at constant temperature, anti-bunch moved to upper bunch and stopped on some distance from it. If condition were changed to near-equilibrium the step anti-bunch were stopping near the center between bunches and its width were increasing. So we can control the anti-bunch position by changing supersaturation on the surface.

It is also seen on Fig. 1(c) that width of anti-bunch forming at equilibrium is much more then it into anti-bunch form-

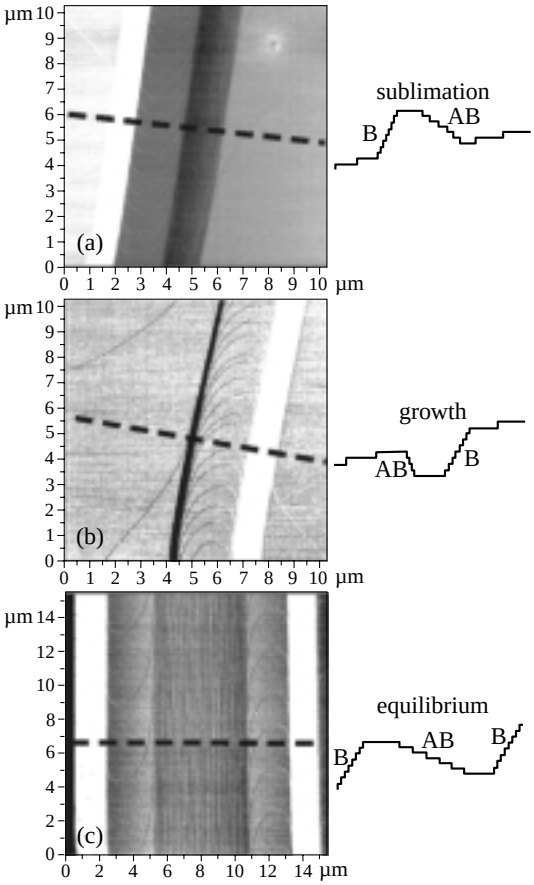

Fig. 1. AFM-images (phase contrast) Si(111) surface with step bunches and anti-bunches and schematic profiles of topography along slash lines. On profiles denoted: B — steps bunch, AB — steps anti-bunches.

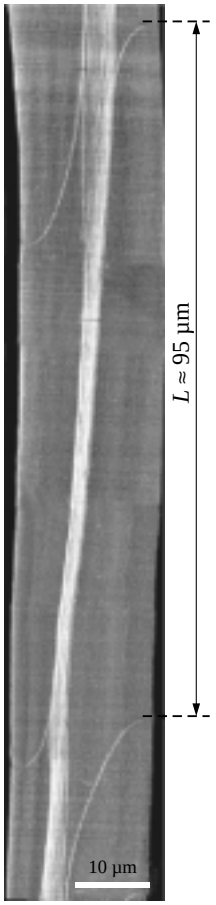

Fig. 2. AFM-image (phase contrast) Si(111) surface with step anti-bunch (light horizontal zone), formed at near-equilibrium condition, and crossing steps (light thin lines).

ing at growth because of number of steps is about equal in Fig. 1(b) and (c), the average distance between steps into the anti-bunches is much greater at equilibrium. We believe that such differences of interstep distances are due to moving steps at growth while under equilibrium steps almost stand at the place. Monoatomic steps between bunches are called crossing steps. Maximum distance between crossing steps are defined by a diffusion length of adatoms on silicon surface. At sublimation that distance have been experimentally observed less then 30 μm at temperatures above 1250 °C [6]. Anomalous large distance (more then 95 μm) between crossing steps at the area between bunch and anti-bunch at equilibrium conditions have been observed (see Fig. 2). The diffusion length of adatom is proportional to lifetime of adatom before desorption from surface or incorporating it into step edge. We believe that under equilibrium the adatom lifetime are effectively increased thus adatom diffusion length and distance between steps are also increased. So we can create large step free area on Si(111) surface by controlling supersaturation on the surface.

3. Summary

The phenomenon of step anti-bunching have been investigated under sublimation, homoepitaxial growth and quasi-equilibrium on stepped Si(111) surface by means of both *in situ* ultrahighvacuum REM and *ex situ* AFM. It has been found that anti-bunch position between bunches depended from supersaturation on the surface. Anomalous large distance between crossing steps between bunch and anti-bunch have been observed under near-equilibrium conditions. Formed large step free areas can be used not only for fundamental research, but for technical application for nanostructure formation on ideal silicon substrate.

References

[1] See for review A. V. Latyshev *et al*, *Surf. Sci.* **213**, 157 (1989), Y. Homma, *Phys. Rev. B* **62**, 8323 (2000).
[2] See for example S. Stoyanov *et al*, *Surf. Sci.* **440**, 200 (1999) and B. J. Gibbons *et al*, *Surf. Sci.* **575**, L51 (2004).
[3] A. V. Latyshev *et al*, *Surf. Sci.* **311**, 395 (1994).
[4] A. V. Latyshev *et al*, *Microsc. Res. Technique* **20**, 341 (1992).
[5] D. Sheglov *et al*, *Microscopy and Analysis* **19/5**, 9 (2005).
[6] Y. Homma *et al*, *Phys. Rev. B* **55**, 10237 (1997).

15th Int. Symp. "Nanostructures: Physics and Technology"
Novosibirsk, Russia, June 25–29, 2007

Analysis of growth conditions influence on the nanowhiskers morphology

N. V. Sibirev[1,2], V. G. Dubrovskii[2,3], G. E. Cirlin[1,2,3] and I. P. Soshnikov[2,3]

[1]Institute for Analytical Instrumentation RAS, Rizhsky 26, 190103, St Petersburg, Russia
[2] St Petersburg Physics and Technology Center for Research and Education of RAS, Khlopina 8/3, 194021, St Petersburg, Russia
[3] Ioffe Physico-Technical Institute, St Petersburg, Russia

Abstract. The results of theoretical study of the growth conditions influence on the structural properties of GaAs nanowires in different growth technologies are presented.

Semiconductor nanowhiskers, or vertical nanowires (NWs) are a new attractive object in modern nanotechnology due to their potential applications in microelectronics and optoelectronics.

Investigation of the NW growth mechanism is very significant problem [3,4,6] and up to this day it is not completely solved. In different growth conditions NW obtain different shapes prism(see Fig. 1), "pencil-like"(see Fig. 2), cone (see Fig. 3) [5,7,4].

In papers [4,6] is described a model, which explains the growth of "pencil-like" nanowires. The model unifies the conventional adsorption-induced model, the diffusion-induced model and the model of nucleation-mediated growth on the liquid-solid interface. The concentration of deposit atoms in the liquid alloy, the nanowire diameter and all other characteristics of the growth process are treated dynamically as functions of the growth time. It is shown that the nanowires taper [6] when their length becomes comparable with the adatom diffusion length on the sidewalls.

In paper [7] we described the model, which explains the growth of conical nanowires. This theoretical model, which describes the growth of conical nanowires, also takes into account nucleation on the nanowires sidewalls [7]. A model solution for the NW geometrical shape enables to describe the dependence of process on the value of adatom diffusion flux from the substrate surface to the NW base. The substrate temperature dependence of the effect is studied theoretically. It is demonstrated that nucleation becomes pronounced at lower temperatures and changes the shape of growing wires to conical, while the overall length of the wire decreases. Obtained theoretical results are qualitatively compared to the available experimental data on the GaAs nanowires, grown by molecular beam epitaxy on the GaAs(111)B surface and activated by Au seed drops within the temperature range from 400 to 600 °C.

In the paper is shown the existence of the growth condition under which periodical oscillation of the NW diameter can be observed.

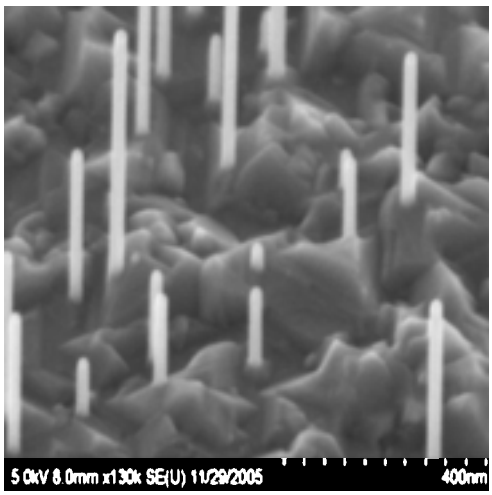

Fig. 1. Prismatic nanowire (InAs, $T = 350$ °C).

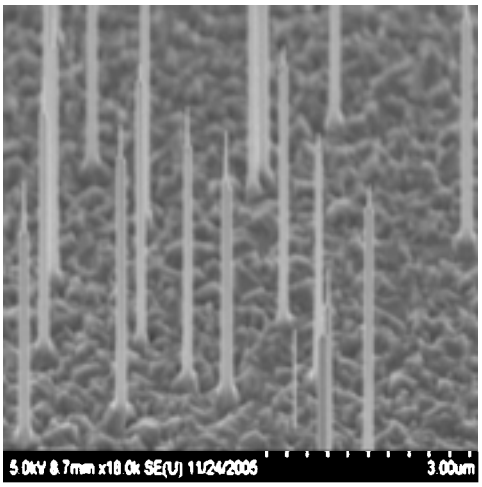

Fig. 2. "Pencil-like" nanowire (InAs, $T = 355$ °C).

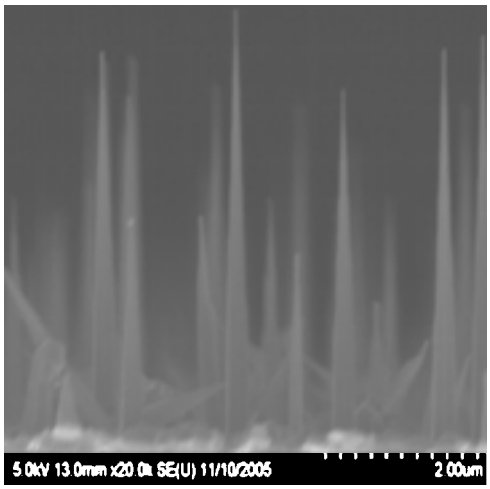

Fig. 3. Conical nanowire (InAs, $T = 300$ °C).

Acknowledgements

The authors are grateful to the financial support received from RFBR grants Nos. 05-02-16495-a, 06-08-01198-a and 05-02-08090-OFI, and Russian Federal Agency for Science and Innovations within the frame of Contracts Nos. 02.442.11.7428 and 02.442.11.7399 and low dimension quantum-size program supported by RAS different scientific programs of RAS. N.V.S acknowledges the support of the Dynasty Foundation.

References

[1] A. B. Greytak, L. J. Lauhon, M. S. Gudiksen and C. M. Lieber, *Appl. Phys. Lett.* **84**, 4176 (2004).
[2] M. T. Bjork, B. J. Ohlsson, T. Sass, A. I. Persson, C. Thelander, M. H. Magnusson, K. Deppert, L. R. Wallenberg and L. Samuelson, *Appl. Phys. Lett.* **80**, 1058 (2002).
[3] J. Johansson, B. A. Wacaser, K. A. Dick and W. Seifert, *Nanotechnology 17*, S355 (2006).
[4] J. C. Harmand, G. Patriarche, N. Péré-Laperne, M. -N. Mérat-Combes, L. Travers and F. Glas, *Appl. Phys. Lett.* **87**, 203101 (2005).
[5] I. P. Soshnikov, G. E. Cirlin, V. G. Dubrovskii, A. V. Veretekha, A. G. Gladyshev, V. M. Ustinov, *Physics of the Solid State* **48** (4), 737 (2006).
[6] V. G. Dubrovskii, N. V. Sibirev, G. E. Cirlin, J. C. Harmand, and V. M. Ustinov, *Phys. Rev. E* **73**, 021603 (2006).
[7] V. G. Dubrovskii, I. P. Soshnikov, N. V. Sibirev, G. E. Cirlin, V. M. Ustinov, M. Tchernycheva, J. C. Harmand *Semiconductors* **41** (7), 888 (2007).

15th Int. Symp. "Nanostructures: Physics and Technology"
Novosibirsk, Russia, June 25–29, 2007

Growth of GaAs nanowhiskers on GaAs and Si substrate by magnetron pre-sputtering deposition

I. P. Soshnikov[1,2], G. E. Cirlin[1,2,3], V. G. Dubrovskii[1,2], A. V. Veretekha[4], V. T. Barchenko[4], A. Galisultanov[5] and V. M. Ustinov[1,2]

[1] St Petersburg Physics and Technology Center for Research and Education of RAS, Khlopina 8/3, 194021, St Petersburg, Russia
[2] Ioffe Physico-Technical Institute, St Petersburg, Russia
[3] Institute for Analytical Instruments of RAS, Russia
[4] St Petersburg State Electrotechnical University (LETI), Russia
[5] St Petersburg State Politechnical University, Russia

Nanowhisker arrays are interested for different applications, for example as field emitters, chemical and biological sensors, opto- and microelectronics, nanomechanical systems [1–4]. Typical methods of semiconductor nanowhiskers growth are molecular beam epitaxy (MBE) [5,6] and chemical vapor deposition [2,4,7–9] while they are expensive and ecology problematic. This work is devoted to the investigation of GaAs nanowhiskers growth on GaAs and Si substrates by magnetron sputtering deposition (MSD).

The growth process of GaAs is realized in three stages: preparations of substrate surface, formation of disperse array nanoclusters by deposition of ultrathin Au film ($\sim$ 1 nm) following by the growth of GaAs nanowhiskers by magnetron sputter deposition. Argon is used as working gas in DC magnetron.

Morphology of nanowhiskers is studied using scanning electron microscope Camscan Series 4-90FE. The structure of nanowhiskers is examined by electron diffraction.

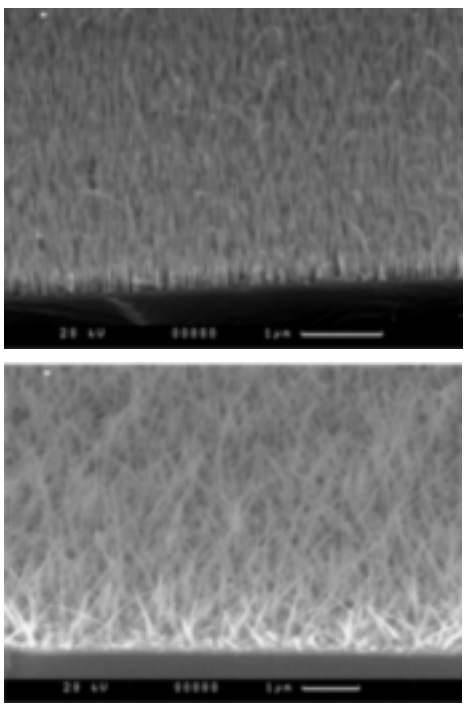

Fig. 1. Nanowhisker morphology grown by magnetron sputtering deposition of 100 nm GaAs on GaAs(111)B and Si(111) substrates.

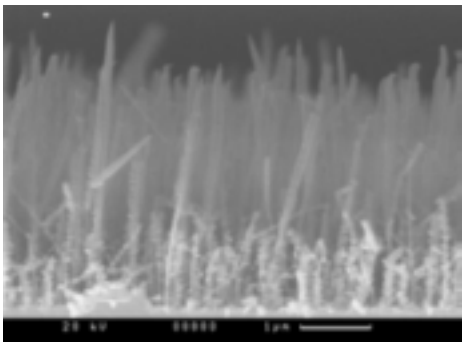

Fig. 2. Nanowhiskers with block crystaline grown by magnetron sputtering deposition of 270 nm GaAs on GaAs(111) substrate.

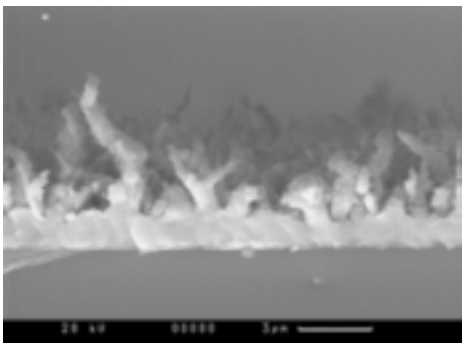

Fig. 3. Dendrite and blister whisker morphology grown by magnetron sputtering deposition about 1000 nm GaAs on Si(111) substrate.

Series of the samples on GaAs (111)B, (100) and Si (111), (100) substrate with variation of GaAs deposited layer thicknesses and substrate temperature were grown. Fig. 1 demonstrates an example of the surface morphology with nanowhiskers array grown on GaAs (111)B and Si (111). The preferred orientation for the substrates is vertical (normal), along $\langle 111 \rangle$ axis. Additionally, we have found other oriented nanowhiskers on Si substrates: along $\langle 211 \rangle$, $\langle 311 \rangle$ and $\langle 511 \rangle$ axes. A habitus of the nanowhiskers is defined hexahedral prism with (110) facet having an AuGa nanodroplet on the top. Sometimes, nanowhiskers exhibit different blocks (Fig. 2). At relatively high argon pressure ($p \sim 10^{-1}$ Torr) the structure of whiskers can be dendrite and/or blister (Fig. 3). The growth on GaAs (100) substrates results to formation of two groups of nanowhiskers oriented along $\langle 111 \rangle$B axes. In contrast, the growth on Si (100) gives four groups of the nanowhiskers oriented along four $\langle 111 \rangle$

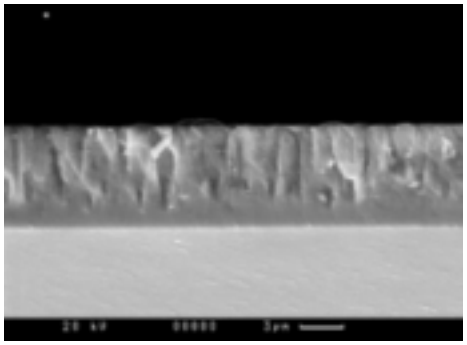

Fig. 4. Texture layer morphology grown by magnetron sputtering deposition about 2000 nm GaAs on Si(111) substrate.

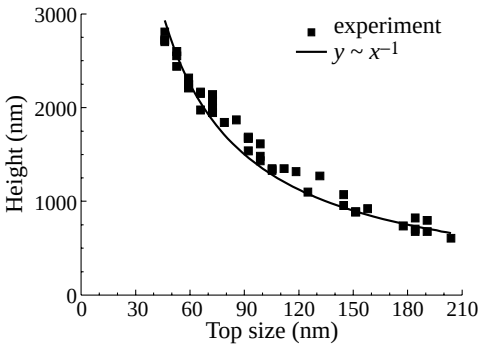

Fig. 5. Size relation for nanowhisker by magnetron sputtering deposition about 200 nm GaAs on Si(111) substrate.

axes and additional close to ⟨211⟩, ⟨311⟩ and ⟨511⟩ axes. We note that habitus of nanowhiskers oriented along ⟨211⟩, ⟨311⟩ axes has a step facet form.

The growth at higher deposition rate (4 ML/s) demonstrates a formation of the texture layer with thickness similar to the effective thickness of the deposited layer (Fig. 3). The morphology transformation from nanowhiskers array to texture layer on Si substrates occurs at higher deposition rate in comparison to the growth on GaAs substrates. The formation of texture layer morphology is likely to be explained by the relatively low ratio of the surface diffusion to the deposition rate.

Characteristic size of NW depends on the growth conditions and can attain from 10 to 500 nm across and as high as 15000 nm in length. The characteristic length of nanowhisker depends on the effective thickness of deposited layer and can be about 10 times larger. The analysis of NW size (Fig. 5) demonstrates following dependence of the length of NW (L) on their diameter (D):

$$L \cong A + \frac{B}{D}, \tag{1}$$

where A and B are parameters. The dependence cannot be explained by classic vapor-liquid-solid theory [9]. However, the experimental curves can be explained whitin the Dubrovskii's–Sibirev's diffusion model [5,6]. The observed effect is even more pronounced when Si substrate is used. This result can be explained by the additional stress introduced by a lattice mismatch between nanowhisker (GaAs) and substrate (Si) materials.

Acknowledgements

The work is supported by Russian Foundation for Basic Research and different RAS scientific programs ("Quantum macrophysics" and "Quantum nanostructures").

Authors are acknowledgment V. Busov and S. Troshkov for SEM investigations.

References

[1] Y. Cui and C. M. Lieber, *Science* **291**, 851 (2000).
[2] T. Bryllert, L.-E. Wernersson, L. E. Froberg and L. Samuelson, *IEEE letters* **27**, 323 (2006).
[3] Q. Wan *et al*, *Appl. Phys. Lett*, **84**, 3654 (2004).
[4] C. M. Lieber, *Nature* **414**, 142 (2001).
[5] V. G. Dubrovskii, G. E. Cirlin, I. P. Soshnikov, N. V. Sibirev, A. A. Tonkikh, Yu. B. Samsonenko, and V. M. Ustinov, *Phys. Rev. B* (2005).
[6] V. G. Dubrovskii, N. V. Sibirev, G. E. Cirlin, J. C. Harmand, V. M. Ustinov, *Phys. Rev. E* **73**, 021603 (2006).
[7] K. Hiruma, M. Yazawa, K. Haraguchi, K. Ogawa, T. Katsuyama, M. Koguchi, and H. Kakibayashi, *J. Appl. Phys.* **74**, No. 5, 3162–71 (1993).
[8] B. J. Ohlsson, M. T. Bjork, M. H. Magnusson, K. Deppert, L. Samuelson L. R. Wallenberg, *Appl. Phys. Lett.* **79** 20, 3335–37 (2001).
[9] E. I. Givargizov, *J. Cryst. Growth* **31** 20, (1975).

15th Int. Symp. "Nanostructures: Physics and Technology"
Novosibirsk, Russia, June 25–29, 2007

Size control of Ge nanocrystals formed on SiO_2 during pulse ion-beam assisted deposition for non-volatile memory

N. P. Stepina, A. V. Dvurechenskii, V. A. Armbrister, V. V. Kirienko, P. L. Novikov, Z. V. Smagina, V. G. Kesler and A. K. Gutakovskii

Institute of Semiconductor Physics, Novosibirsk, Russia

Abstract. Using pulsed low-energy (100–200 eV) ion-beam-induced nucleation, Ge nanocrystals (NCs) homogeneous arrays were grown on thin SiO_2 films during deposition in UHV chamber. Analysis of growth parameters allowed to control the nanocrystal size and NCs array density required for non-volatile memory device. The tuning of the Ge nanocrystal size is demonstrated by transmission electron microscopy as well as by Electron Spectroscopy for Chemical Analysis (ESCA). The memory effect of a metal-oxide-semiconductor (MOS) structure containing Ge NCs was investigated via capacitance-voltage measurements after oxidation of $Si/SiO_2/Ge(NCs)/a\text{-}Si$ structure. Voltage flat-band shift of 2.8 V was founded.

Introduction

Layered arranged Si or Ge nanocrystals in a dielectric matrix are discussed as one of the candidates to replace conventional flash memories. Ge-based single-electron memory device (SEMD) has the superior properties over Si-based SEMD in terms of the writing/erasing time and the operating voltage [1]. When using NCs for charge storage devices, the general requirements that can be placed upon the control are the size of NCs and theirs density as well as the homogeneity in growth plane. In our previous works [2] we offered a method of formation of the Ge nanoclusters homogenous array on SiO_2 using pulsed low energy ion-beam induced molecular-beam deposition (MBD) in ultra-high vacuum (UHV). It was shown [3] that variation of temperature and Ge flux change only the NCs array density keeping NCs size practically invariable. In this work, in order to control the island size and optimize the structural parameters of NCs for memory device, we analyzed the process of NCs nucleation and their following overgrowth. MOS structure containing Ge NCs of 5–6 nm diameter and 1.5×10^{12} cm^{-2} density formed after oxidation $Si/SiO_2/Ge(NCs)/a\text{-}Si$ structure exhibits capacitance-voltage hysteresis of 2.8 V.

1. Experimental setup

A 4.5 nm thick SiO_2 film was grown by thermal oxidation on (111) p-type silicon substrates at 850 °C (tunnel insulator). After dioxide formation the wafers were washed, dried-up and inserted into the UHV chamber. A $\sim$ 1 nm-thick SiO_2 layer was removed from the top surface in situ using a Si flux of $\sim$ 0.04 ML/s at 820 °C before Ge deposition. Molecular beam deposition (MBD) was carried out in an ultra-high vacuum chamber of molecular beam epitaxy setup equipped with effusion cell (boron nitride crucible) for Ge. A pulse accelerating voltage supply unit generated ion-current pulses with duration of 0.5–1 s and ion energy of 200 eV. Pulsed ion-beam actions were applied in series at the effective Ge layer thickness of 3 ML, 4 ML and 5 ML. Details of deposition were described in [3]. The substrate temperature of Ge deposition was varied from 200 to 400 °C. Effective Ge layer thicknesses $\sim 3-20$ ML were intended for deposition. To form the memory device, $Si(100)/SiO_2(3.5\text{ nm})/Ge(NCs)/a\text{-}Si(10\text{ nm})$ structure was oxidized in dry oxygen at 850–950 °C. Oxidation time was found in the way allowing to oxidize a-Si layer and not disturb Ge NCs.

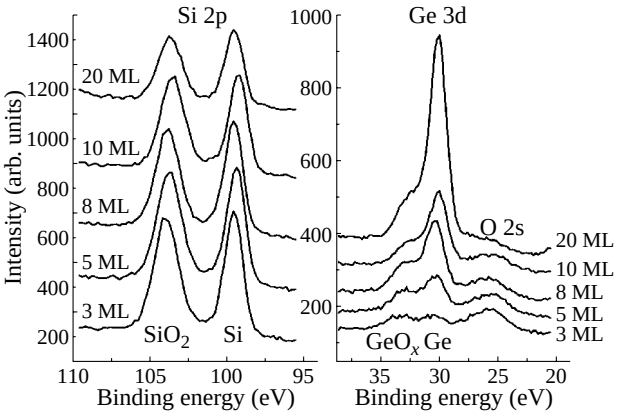

Fig. 1. ESCA spectra for Ge deposition on SiO2 at 200 °C. Left — peak of 2p Si, right — peak of 3d Ge.

2. Experimental results and discussion

Fig. 1 shows the detailed ESCA spectra of Ge 3d dou-blet for samples grown with ion-beam assisted MBD at $T = 200$ °C and different amount of deposited Ge. Effective Ge thicknesses determined from the spectra in accordance to

$$d_{\mathrm{Ge}} = 2.7 \ln\left(1 + 1.52 \frac{I_{\mathrm{Ge}}}{I_{\mathrm{Si}}}\right) [\mathrm{nm}]$$

indicate on the absence of Ge adsorption at this temperature.

To control NCs size 5 samples with 3, 5, 8, 10 and 20 ML of Ge were grown at 200 °C. Fig. 2 shows plan-view HREM images of samples after deposition of 5, 8 and 20 Ge ML. The density of NCs array estimated from HREM images for all samples gives practically the same value $\sim 1.5 \times 10^{12}$ cm^{-2} and addition of Ge from 3 to 20 ML leads only to overgrowth of nuclei from 3 to 5.5 nm. To clarify the mechanism of Ge NCs formation, we have carried out the kinetic Monte Carlo (MC) simulation. "Lattice gas" model [4] was used, including Ge atoms deposition on SiO_2 surface, their surface diffusion, desorption, precipitation, and ion-beam action. Ge atoms and SiO2 cells were restricted to faced-centered cubic (FCC) lattice, which is well suited to describe precipitation in isotropic

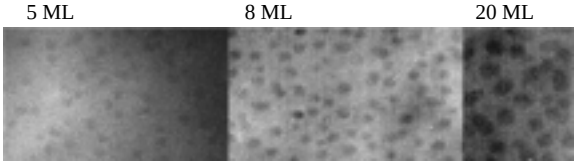

Fig. 2. Plan-view HREM images of samples with 5, 8, and 20 ML of deposited Ge on SiO_2.

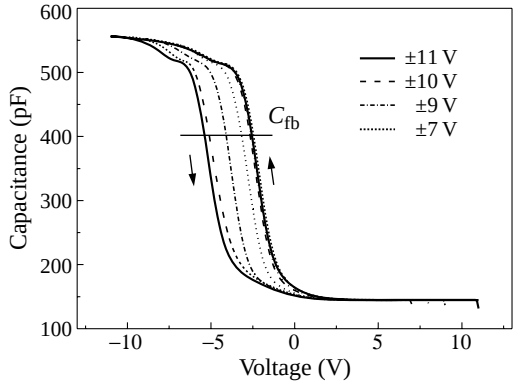

Fig. 3. CV characteristics of MOS sample formed by dry oxidation of $Si/SiO_2/Ge(NCs)/a\text{-}Si$ structure.

amorphous matrices (e.g. SiO_2). An irradiation effect was included in terms of the concept of collisional mixing (CM), i.e. the displacements of atoms. In the simulation, an ion-beam action results in the smaller NCs size and the higher NCs density due to precipitation and nucleation of new NCs by atoms knocked out from initial NCs to the SiO_2 surface. At the low temperature (200 °C) the desorption is sup-pressed and Ge atoms attached to an island become immobile. Therefore the dominating kinetic processes are surface diffusion and growth of Ge islands. Thus, the effect of NCs size increase upon the amount of Ge deposited, which was reproduced in simulation, looks quite expectable.

To form the MOS structure containing Ge NCs, 10 nm a-Si layer were grown on a top of germanium. Oxidation procedure was carried out keeping in mind that Si is known to have a stronger thermodynamic tendency to be oxidized in comparison to Ge. HREM results show that Ge nanocrystals are buried in silicon dioxide after oxidation at 950 °C. Fig. 3 shows CV characteristics of such structure after oxidation at 950 °C during 20 minutes. The CV counterclockwise hysteresis is caused by the trapping, storing and detrapping of carriers to and from the germanium nanocrystals. One can see that hysteresis appeared after applying a bias higher than 6 V and continue to increase with increase a bias volt-age up to 11 V. Maximum of flat band shift corresponds to 2.8 V. Total trapping charge estimated from measured voltage shift and total oxide capacitance is $\sim 1 \times 10^{-9}$ C that corresponds to single charges captured by 1.3×10^{12} cm^{-2} NCs. Last value is very close to that determined from HREM data.

In conclusion we have shown the formation of dense homogeneous size-controlled Ge NCs arrays on thin SiO_2 films by low-temperature pulsed ion-beam-assisted deposition. Due to negligible Ge desorption, size of NCs is easily controlled by the amount of Ge deposited. CV characteristics of MOS structure with embedded Ge NCs exhibit memory effect.

Acknowledgement

The work was supported by RFBR (Project 06-02-08077).

References

[1] Y. C. King *et al*, *IEEE Trans. Electron Devices.* **48**, 696 (2001).
[2] A. V. Dvurechenskii *et al*, *Proc. SPIE* **6260**, 626006–626006A–8 (2006).
[3] A. V. Dvurechenskii *et al*, *Proc. 14th Int. Symp. "Nanostructures: Physics and Technology" St Petersburg, Russia, June 26–30*, 101–102 (2006).
[4] P. Novikov *et al*, *Nucl. Instrum. Methods Phys. Res. B* **191**, 462 (2002).

15th Int. Symp. "Nanostructures: Physics and Technology"
Novosibirsk, Russia, June 25–29, 2007

Digital etching of GaAs(001) with a monolayer precision facilitated by selective interaction of iodine and cesium with Ga-rich and As-rich surface reconstructions

O. E. Tereshchenko[1,2], N. N. Velker[2], K. V. Toropetsky[2], V. L. Alperovich[1,2] and D. Paget[3]

[1] Institute of Semiconductor Physics, 630090 Novosibirsk, Russia
[2] Novosibirsk State University, 630090 Novosibirsk, Russia
[3] Laboratoire de Physique de la Matière Condensée, Ecole Polytechnique, 91128 Palaiseau, France

Abstract. Reversible transitions between Ga-rich and As-rich GaAs(001) surface reconstructions facilitated by alternate deposition of cesium and iodine followed by annealing at moderated temperatures $T \leq 470$ °C are studied experimentally by low-energy electron diffraction and x-ray photoelectron spectroscopy. The observed phenomenon stems from the selective interaction of halogen and alkali metal adsorbates with group III and group V elements of compound III–V semiconductors, respectively. Each transition leads to the removal of a monolayer of surface atoms. Thus, this procedure may be considered as digital etching of GaAs(001) with a monolayer precision.

Introduction

The fabrication of nanostructures is essentially based on the developments of semiconductor epitaxial techniques. The advanced modifications of these techniques allow one to grow semiconductor structures in which the interface smoothness and the thickness of layers are controlled with the ultimate precision of one monolayer [1,2]. Along with the atomic-layer growth, for modern nanotechnology it is important to develop techniques of a layer-by-layer removal of a semiconductor with monolayer resolution, keeping atomically smooth surface morphology. These techniques are also referred to as atomic-layer or "digital" etching. Atomic layer etching with monolayer resolution can be realized, in principle, on the polar faces of III–V semiconductors by using adsorbates which selectively react with the elements of III and V groups and, thus, allow selective removal of surface cations and anions. It was shown in Ref. [3] that iodine adsorbed on the Ga-rich GaAs(001) surface was bonded predominantly with gallium atoms. Low-temperature annealing of the iodine-covered surface led to the desorption of gallium iodides GaI_x and conversion to the As-rich surface with a (2×4)/c(2×8) reconstruction. Similar results were obtained for iodine adsorption on various III–V semiconductors [3, 4]. On the other hand, electropositive alkali metal adatoms may react selectively with group V atoms, weaken their bonds with the substrate and, thus, facilitate a reverse conversion from the anion-rich to cation-rich surface by the removal of a monolayer of group V atoms at reduced annealing temperatures. This reverse transition was observed on the Cs/GaAs(001) surface [5,6]. The goal of the present paper is to show that it is possible to combine these two opportunities in one experiment in order to realize atomic layer etching of GaAs(001) by alternate adsorption and desorption of cesium and iodine.

1. Experimental

The experiments were performed on epitaxial p-GaAs(001) layers. The preparation of the clean surface included the removal of oxides by a solution of HCl in isopropyl alcohol (HCl-iPA) under dry nitrogen atmosphere, transfer to the ultra-high vacuum (UHV) without air contact and subsequent annealing in vacuum [7]. Cesium deposition was performed using dispensers thoroughly outgassed in a vacuum not exceeding 10^{-10} mbar. Iodine was generated from a UHV compatible solid-state electrochemical cell with a silver iodide crystal [3,4]. The surface composition and atomic structure were determined in the electron spectrometer ADES-500 by x-ray photoelectron spectroscopy (XPS) and by low-energy electron diffraction (LEED), respectively.

2. Results and discussion

To realize reversible transitions between anion- and cation-stabilized surface reconstructions, we performed Cs and I_2 depositions on the As-rich and Ga-rich GaAs(001) surfaces, respectively. Each deposition was followed by annealing in UHV. The evolution of LEED patterns measured under this procedure is shown in Fig. 1. Fig. 1(a) shows the initial As-stabilized GaAs(100)-(2×4)/c(2×8) reconstruction, which was obtained by removal of oxides in HCl-iPA and subsequent annealing at $T = 440$ °C. The deposition of Cs on this surface led to its fast disordering, which revealed itself in the degradation of the diffraction pattern (Fig. 1(b)). Specifically, at small Cs coverage $\theta_{Cs} \sim 0.1$ ML the diffuse background increased by a factor of ~ 3 with respect to the diffraction spot intensities, and at $\theta_{Cs} \sim 0.5$ ML the fractional spots disappeared. Subsequent annealing of the cesiated surface at $T = 450-470$ °C yielded a clear (4×2)/c(8×2) reconstruction characteristic of the Ga-rich surface (Fig. 1(c)). It should be noted that this annealing temperature is by 100 °C lower than that required to obtain the same reconstruction by heating without preliminary Cs deposition [7,6].

The adsorption of about 1 ML of iodine on the Ga-rich surface led to a sharp (1×1) structure with weak $2\times$ fractional spots (Fig. 1(d)). Heating the sample at $T = 440$ °C removed the adsorbed iodine and converted the surface structure back to the initial (2×4)/c(2×8) reconstruction, which is characteristic of the As-rich surface (Fig. 1(e)). XPS measurements proved that after deposition of Cs and heating at $T \sim 450-470$ °C about ~ 0.1 ML of Cs was left on the surface, while subsequent adsorption of iodine and heating at 440 °C yielded a clean surface with no traces of cesium or iodine within the accuracy of XPS (≤ 0.01 ML).

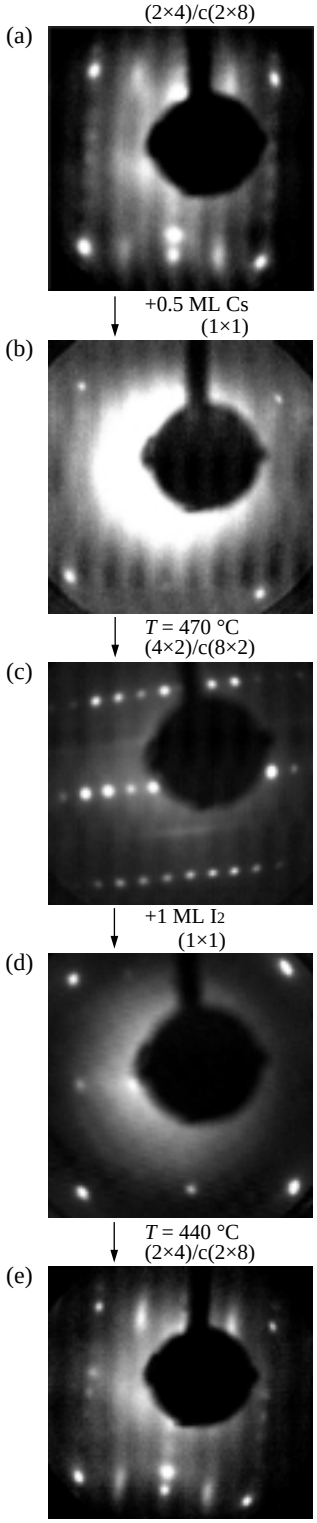

Fig. 1. Transitions between the As-rich and Ga-rich reconstructions of the GaAs(001) surface facilitated by alternate depositions of cesium and iodine followed by annealing. (a) initial surface with (2×4)/c(2×8) reconstruction; (b) disordered (1×1) reconstruction after deposition of 0.5 ML of Cs; (c) (4×2)/c(8×2) reconstruction after heating at 470 °C; (d) (1×1) reconstruction after adsorption of 1 ML of iodine; (e) (2×4)/c(2×8) reconstruction after heating the iodated surface at 440 °C.

The observed cesium and iodine-induced transitions between the As-rich and Ga-rich GaAs(001) surface reconstructions can be explained in a general way, by adatom-induced weakening of the bonds between the uppermost layer of surface atoms and the substrate [5,6]. According to this explanation, deposition of cesium leads to the decrease of the binding energy of arsenic atoms with the substrate and, thus, facilitates the conversion to the Ga-rich surface at reduced temperature. On the contrary, on the Ga-rich surface iodine adatoms bind preferably with Ga atoms and weaken their bonds with the substrate. This leads to the removal of uppermost Ga atoms and reverse conversion to the As-rich surface.

Thus, depositions of cesium and iodine followed by annealing at moderate temperatures constitute a closed cycle of conversions from the As-rich to Ga-rich and back to As-rich GaAs(001) surface. At each half of the cycle one monolayer of atoms is removed from the crystal surface, so this procedure represent a method of digital etching of GaAs(001). By successive deposition of cesium and iodine and subsequent annealing we performed several cycles of layer-by-layer GaAs etching without deterioration of the quality of LEED images.

3. Conclusions

Reversible transition between the As-rich and Ga-rich reconstructions are experimentally observed under adsorption of cesium and iodine on the GaAs(001) surface followed by heating in vacuum at moderate temperatures $T = 440-470$ °C. These transitions are explained by the element-specific selectivity in the interaction of iodine and cesium with group III and group V elements of GaAs(001). This effect opens up opportunities for the atomic layer etching of polar faces of III–V compounds.

Acknowledgements

This work was partly supported by the Russian Foundation for Basic Research (grant No. 06-02-16093) and by the Russian Science Support Foundation.

References

[1] J. R. Arthur, *Surf. Sci.* **500**, 189 (2002).
[2] M. Ritala and M. Leskelä, *Nanotechnology* **10**, 19 (1999).
[3] P. R. Varekamp, M. C. Håkansson, J. Kanski, D. K. Shuh, M. Björkqvist, M. Gothelid, W. C. Simpson, U. O. Karlsson, and J. A. Yarmoff, *Phys. Rev. B* **54**, 2101 (1996).
[4] W. K. Wang, W. C. Simpson, and J. A. Yarmoff, *Phys. Rev. Lett.* **81**, 1465 (1998); *Phys. Rev. B* **61**, 2164 (2000).
[5] O. E. Tereshchenko, V. L. Alperovich, and A. S. Terekhov, *JETP Lett.* **79**, 131 (2004).
[6] O. E. Tereshchenko, V. L. Alperovich, A. G. Zhuravlev, A. S. Terekhov and D. Paget, *Phys. Rev. B* **71**, 155315 (7) (2005).
[7] O. E. Tereshchenko, S. I. Chikichev, and A. S. Terekhov, *J. Vac. Sci. Technol. A* **17**, 2655 (1999).

15th Int. Symp. "Nanostructures: Physics and Technology"
Novosibirsk, Russia, June 25–29, 2007

The synthesis, micromorphology and structure of hexagonal molybdenum (VI) oxide nanorods

V. V. Atuchin[1], *I. B. Troitskaia*[1], L. D. Pokrovsky[1], T. A. Gavrilova[1] and V. G. Kostrovsky[2]

[1] Institute of Semiconductors Physics SB RAS, Novosibirsk, Russia
[2] Institute of Solid State Chemistry and Mechanochemistry SB RAS, Novosibirsk, Russia

Abstract. h-MoO_3 nanorods with good crystallinity have been obtained by precipitation from water solution of ammonium paramolybdate with and without ultrasonics agitation. Final product was characterized by X-ray diffraction (XRD), scanning electron microscopy (SEM), transmission electron microscopy (TEM), IR- and Raman spectroscopy.

Introdution

Generation of nanocrystals on a basis of transition metals oxides gives a way to futher diminishing of electronic devices, an increase of catalysis efficiency and production of sophisticated nanocompositions which will possess new functional properties. The nanostructures based on the molybdenum oxides are among most interesting objects for this purpose [1,2]. This oxide possesses pronounced electrochromic and photochromic abilities, can be used in gas sensor devices and catalysis.

There are several polymorphous modifications of molybdenum oxide, α-phase stable under ordinary condition, metastable β-phase, and hexagonal modification, h-MoO_3, with practically unknown physical and chemical characteristics. Most published ways for synthesis of nanocrystals MoO_3 yield α-phase [3], β-phase [4], or their mixture [5,6]. Only under autoclave conditions during a several hours with subsequent heating in the vacuum up to 350 °C well crystallized hexahedral shaped rods of h-MoO_3 were prepared [8,9]. In this work the low-temperature way ($T = 105$ °C) is suggested for preparation of hexagonal modification h-MoO_3 and structural and morphologic characterization of the crystals has been produced.

1. Experimental

Examples of h-MoO_3 nanocrystalls were obtained by precipitation of molybdenum oxide from ammonium paramolybdate water solution by nitric acid. A deposit was washed by distilled water to $pH = 6$ of wash water and dried in air under room temperature. As a result, white crystals having a shape of straight hexahedral rods 10 μm in lenght and 500 nm in diameter were fabricated (see Fig. 1). An agglomeration into sea nanourchin structures is evident.

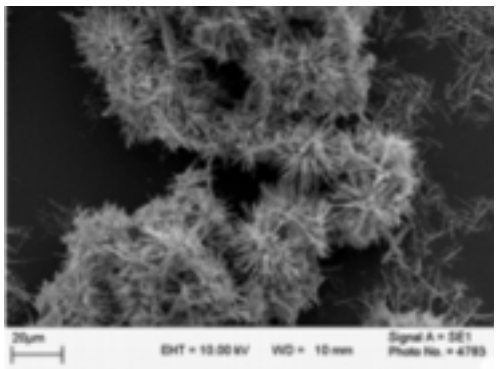

Fig. 1. SEM images of as-prepared h-MoO_3 deposit.

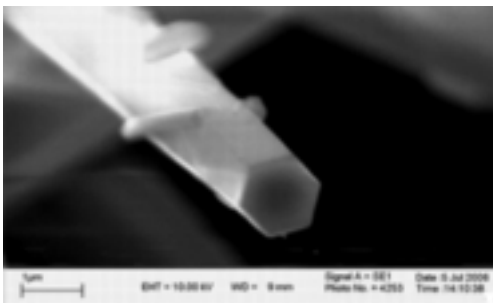

Fig. 2. SEM images of nanorod cross section of as-prepared h-MoO_3.

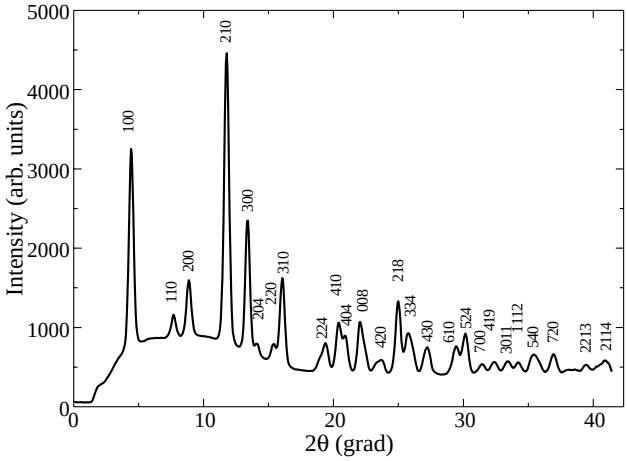

Fig. 3. XRD pattern of as-prepared h-MoO_3.

It is especially ought to note about the flat fasets of h-MoO_3 nanocrystals. An example is shown in Fig. 2. It is probable that under the crystallization conditions the formation of equilibrium rod shape of h-MoO_3 nanocrystals is achieved in the mother liquor used for synthesis. The formation of pure h-MoO_3 has been confirmed by XRD analysis. In Fig. 3 the X-ray diffraction pattern recorded for molybdenum oxide deposit is shown. All diffraction peaks were successfully indexed in hexagonal system with d-spacings of hexagonal modification of MoO_3 [9]. Typical transmission electron diffraction pattern is shown in Fig. 4. The results of TEM analysis confirm the presence of only h-MoO_3phase.

An attempt to diminish nanorod size by the compulsory stopping of deposition process was unsuccessful. In this case the nanoparticles lose a regular shape without significant rod size decreasing.

Ultrasonic agitation at 20 kHz during 30 minutes starting

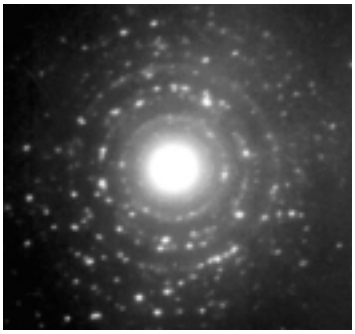

Fig. 4. TEM image for as-prepared h-MoO_3.

from the moment of crystal seeds formation in mother liquor induces a decrease of nanorod diameter up to 300 nm. Thus the low-temperature way of precipitation of hexagonal modification h-MoO_3 is suggested and a totality of factors defining the morphology of nanorods is established. It is found that ultrasonic treatment results in essential decreasing of nanocrystal sizes supposedly owing to the crushing of forming crystal seeds which are distributed in the mother liquor.

References

[1] A. M. Taurino, A. Forleo, L. Francioso, P. Siciliano, M. Stalder, R. Nesper, *Appl. Phys. Lett.* **88**, 152111 (2006).
[2] W. Dong, W. Dong, Z. Shi, J. Ma, Ch. Hou, Q. Wan, Sh. Feng, A. Cogbill, Z. R. Tian, *J. Phys. Chem.* **B 110**, 5845 (2006).
[3] L. Kihlborg, *Ark. Kemi* **21**, (34) 357 (1963).
[4] J. B. Parise, E. M. McCarron III, R. Von Dreele, J. A. Goldstone, *J. Solid State Chem* **93** 193 (1991).
[5] Q. P. Ding, H. B. Huang, J. H. Duan, J. F. Gong, S. G. Yang, X. N. Zhao, Y. W. Du, *J. Cryst. Growth* **294** 304 (2006).
[6] H. A. Therese, N. Zink, U. Kolb, W. Tremel, *Solid State Sci* **8**, 1133 (2006).
[7] J. Song, X. Wang, X. Ni, H. Zheng, Z. Zhang, M. Ji, T. Shen, X. Wang, *Mater. Res. Bull* **40**, 1751 (2005).
[8] J. Song, X. Ni, D. Zhang, H. Zheng, *Solid State Sci* **8**, 1164 (2006).
[9] X. W. Lou, H. C. Zeng, *J. Am. Chem. Soc.* **125**, 2697 (2003).

15th Int. Symp. "Nanostructures: Physics and Technology"
Novosibirsk, Russia, June 25–29, 2007

AFM tip-induced surface nanostructuring initiated by ethyl alcohol oxyanions

A. S. Vasilyev[1], D. V. Sheglov[2] and A. V. Latyshev[2]

[1] Novosibirsk State University, 630090 Novosibirsk, Russia
[2] Institute of Semiconductor Physics, SB RAS, 630090 Novosibirsk, Russia

Abstract. Atomic force microscope has been applied to investigate the possibilities of AFM tip-induced local anodic oxidation of semiconductor surfaces at ethyl alcohol atmosphere. The number of parameters such as applied voltage, applied voltage time in each point, tip-surface press force was under consideration. The peculiarities of ethyl alcohol using for nanostructuring were investigated in frame of optimizing of AFM tip-induced local anodic oxidation. Some examples of nanostructures fabrication are demonstrated.

Introduction

There are various approaches of SPM probe for nano-scaled modifications of dielectric, semiconductor and metal surfaces: extraction, deposition, and displacement of atoms by SPM [1], anodic selective oxidation [2–7], local recharging [8], mechanical scraping [9] so on. The most promised technique for a lithography application in nanometer range is atomic force microscopy method that does not demand conductivity of the sample as scanning tunneling microscopy.

The potential possibilities of AFM for lithography and fabrication of low-dimensional structures for nanoelectronics and nanomechanics are not realized completely in spite of large number of publications in that field. This method of surface nanosrucTurization is developed in frame of depth and resolution increasing for nanoobjects creation on the surface. For example, the work [10] shows the extra increasing of AFM tipinduced nanooxidation depth by using of extra pressforce during of applying the anodic potential. Other work [11] shows the giant growth rate of such nanooxidation process by using of ethyl alcohol atmosphere. This paper is dedicated to study of peculiarities of silicon films tip-induced local anodic oxidation by using of ethyl alcohol vapour as source of anions.

1. Experimental

The AFM experiments are carried out with a Solver P-47H (NT-MDT) microscopes with lithography software. The both contact and semicontact modes were realised at ambient conditions. Standard silicon cantilevers ($\nu = 150 \pm 450$ kHz) and ones with conductive covering were used for imaging and lithography by AFM. An applying electric potential (± 40 V) on conductive AFM-tip with variation of potential pulse from 0,1 to 1000 ms was used for local anodic oxidation. The sample holder has a contact pad to connect the sample to electric wires of the microscope.

Only standard cleaning treatments to the sample were used. Wet-chemical etching procedure did not applied to the sample because it can effect on tip-sample interaction. All experiments were carried out at the room temperatures. The sample, a plate $0.3 \times 1 \times 8$ mm^3 in size, was cut from a silicon wafer with a misorientation angle of less than 1° from a (111) plane, and was cleaned by heating in UHV chamber. After cleaning procedure the silicon surface contains system of equidistantly distributed monatomic steps 0,31 nm in height. Sample was evacuated from ultrahigh vacuum chamber and was investigated by AFM technique at atmospheric conditions. For producing the ethyl alcohol atmosphere at the tip-sample contact area the microscope was situated in hermetic chamber connected with ethyl alcohol vapour source and liquid nitrogen balloon. For drying the chamber space from the water vapour the dry nitrogen gas was flowed from the balloon and replaced the ambient atmosphere in chamber to dry nitrogen. This process didn't change the temperature in the chamber drastically. After the drying second source of ethyl alcohol (98%) was opened and alcohol vapour was leaked through the chamber (Fig. 1).

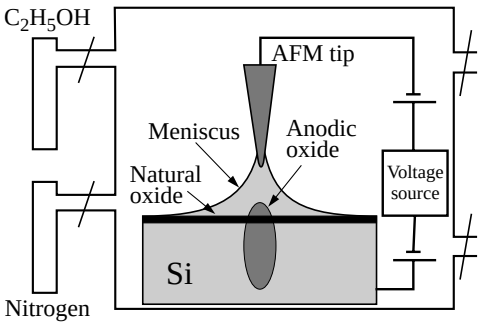

Fig. 1. The scheme of AFM tip-induced nanooxidation in alcohol atmosphere.

2. Results and discussion

The presence of the oxyanions source is the critical factors that affect the oxide growth and current passing through the tip-sample junction during local anodic oxidation. The alcohol (for example, ethyl) dissociation energy and oxyanions formation energy is lower than in the water and high density of oxyanions allows hoping for high oxidegrowth rate during this process. Other important factor of oxidation rate and resolution increasing based on the tip-sample liquid meniscus form control.

The water and alcohol difference in surfacetension parameters, possibilities for surface moistening and capillarity condensation conditions makes important for experimental procedure of measuring the meniscus formation with and without any electrical potential and field during contact forming. Investigations were carried out on the clean silicon (111) surface. The permanent tip-induced anodic oxidation of the silicon (111) surface with natural oxide coating was observed in wide range of applied tip-sample voltage and oxidation time. The height of the obtained oxide patterns was studied as a function of the

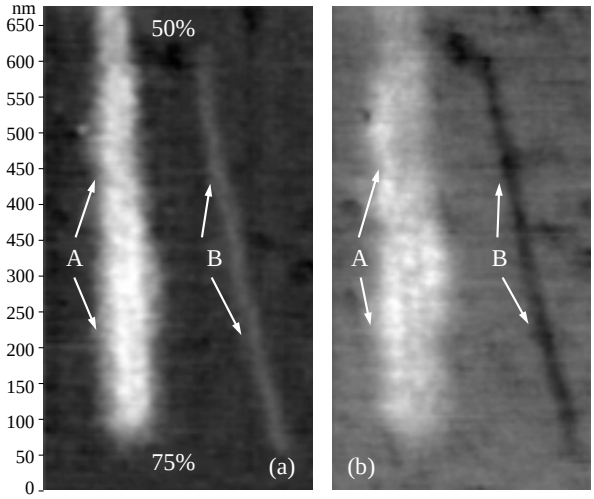

Fig. 2. AFM topography (a) and phase (b) images of silicon(111) surface with anodic oxide lines: A — obtained in ethanol atmosphere, B — at ambient condition. The ethanol partial pressure was changed from 50% to the 75% from top to the bottom of A-line.

applied voltage and the velocity of the tip movement. Especial attention was directed to the oxidation differences between water and alcohol based processes. Figure 2 shows the AFM topography (a) and phase (b) images of silicon(111) surface with anodic oxide lines: A — obtained in ethanol atmosphere, B — at ambient condition. The ethanol partial pressure was changed from 50% to the 75% from top to the bottom of A-line. We found that the oxidation process based on alcohol is in 3 times more intensive than on water atmosphere. This result agreements with known work [11].

The difference in AFM phase contrast images for A-line and B-line (Fig. 2) speaks about some structural differences between ethanol-induced and water-induced oxide lines. We speculate that not only ethanol oxyanions migrate to the surface in oxidation process but unstable $C_2H_5^+$ cations is destroyed on more simple parts and some derivative carbon substance is drifting to the surface too. From analysis of the oxide line height dependences on oxidation time and applied voltage magnitude, parameters for the anodic oxidation nanolithography were optimised. We investigate the force curve dependence for AFM tip at the alcohol atmosphere.

3. Conclusion

Tip-induced local anodic oxidation of silicon films surfaces in conditions of ethyl alcohol presence is studied. It was found that the presence of oxyanions source in tip-surface contact area is the critical parameter for anodic nanometre scale oxidation process. Oxide patterns on silicon were obtained. The ability of using tip-induced oxidation method for fabrication nanoscale structure is demonstrated in alcohol atmosphere. The height of the oxide patterns is studied as a function of the applied tip-sample voltage and the velocity of the tip movement. The force curve dependence for AFM tip at the alcohol atmosphere is obtained and analyzed.

Acknowledgements

We would like to acknowledge the valuable assistance in sample preparation of Mr. Kosolobov S. S. This work was partly supported by Russian Found of Basic Researches and by the programs of “Physics of Solid Nanostructures” and “Surface Atom Structures”.

References

[1] M. Aono, D. Huang, T. Nakayama, *Microelectronic Eng.* **32**, 1–4 00191 (1996).
[2] J.-I. Shirakashi, K. Matsumoto, M. Konagai, *Appl. Phys. A* **66**, 1083 (1998).
[3] D. Sarid, *in: Scanning Force Microscopy, Oxford series in optical and imaging sciences, Oxford University Press*, Oxford (1994).
[4] R. Wiesendanger, *Appl. Surf. Sci.* **54**, 271 (1992).
[5] G. Abadal, F. Peres-Murano, N. Barniol, X. Aymerich, *Appl. Phys. A* **66**, 792 (1998).
[6] C. F. Quate, *Surf. Sci.* **386**, 259 (1997).
[7] A. P. Volodin, *Instrum. Exp. Tech.* **41**, 745 (1998).
[8] H. J. Wintle, *Measurement Science and Technology* **8** 5, 508 (1997).
[9] A. Notargiacomo *et al*, *Nanotechnology* **10**, 458 (1999).
[10] D. V. Sheglov, A. V. Latyshev and A. L. Aseev, *Appl. Surf. Sci.* **243**, 1–4 138 (2005).
[11] M. Tello, R. Garcia, *Appl. Phys. Lett.* **83**, 12 2339 (2003).

15th Int. Symp. "Nanostructures: Physics and Technology"
Novosibirsk, Russia, June 25–29, 2007

Analysis of current progress and trends in development of atomic layer depoisition equipment and technology for microelectronic applications

V. Yu. Vasilyev[1,2], S. H. Chung[1] and Y. W. Song [1]

[1] Korea Polytechnic University, 2121, Jeongwang-Dong, Shiheung-City, Kyungki-Do, 429-793, Korea
[2] Novosibirsk State Technical University, Novosibirsk, 630092, Russia

Abstract. A review of current progress and trends in development of the atomic layer deposition technique.

Introduction

This review is focused on microelectronic applications of Atomic Layer Deposition (ALD) technique. Advances in microelectronics have been a locomotive of equipment development. All the successful tools and technology become essential in the other modern technology fields, such as MEMS, nanotechnology, etc. Thus, taking progression in microelectronics technology as an instrument for analysis, the main directions, basic issues and their solutions in ALD development for any applications can be recognized.

1. Forecasts of the International Technology Roadmap for Semiconductors

Chemical Vapor Deposition (CVD) technique is the major technique for thin film deposition in modern Integrated Circuits (IC) technology. Small gaps between device elements with a spacing below 0.1 micron and aspect ratio (AR) higher than 5 have already become typical features of IC. Limitations of thin film CVD techniques with respect to very tight gaps in IC have already been analyzed [1]. It was shown that conformal thin film growth in deep trenches with extremely high AR is not feasible by the traditional CVD technology. Non-conformal film deposition causes voiding in the gaps. ALD technique has recently become very popular for semiconductor applications [2]. The core of ALD is the fact that at certain conditions chemisorption-based surface limiting reactions are strongly dominant. Hence, ALD processes should not depend on mass-transport phenomena and they should provide an inherent monolayer deposition, i.e. 100% conformal thin film step coverage in high AR gaps. In this respect, ALD technique is considered to be the most competitive alternative for future IC thin film technology applications. However, taking into account severe strengthening of technological requirements forecasts of the International Technology Roadmap for Semiconductors (ITRS) [3] (see examples in Fig. 1), it looks reasonable to perform a careful tracing of ALD issues in parallel with successes in ALD tool and technology development.

2. Limitations of the traditional CVD techniques

Systematic studies on thin film conformality and gap-fill capability [1] covered the most implemented CVD methods such as TEOS-based and silane-based atmospheric pressure (APCVD), sub-atmospheric pressure (SACVD), low pressure (LPCVD), plasma enhanced (PECVD), and High-Density Plasma (HDP-CVD), as well as thin films of silicon dioxide and glasses, polysilicon, silicon nitride, etc. Based on the results of the

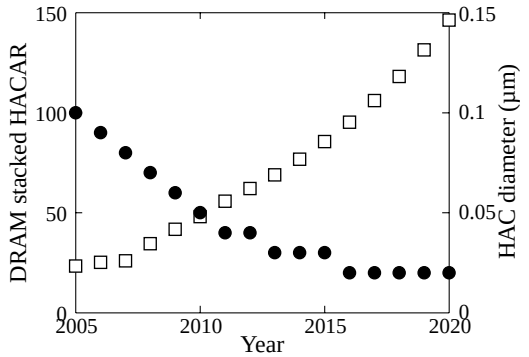

Fig. 1. ITRS forecast for the most critical DRAM IC element (HAC — High Aspect Contact).

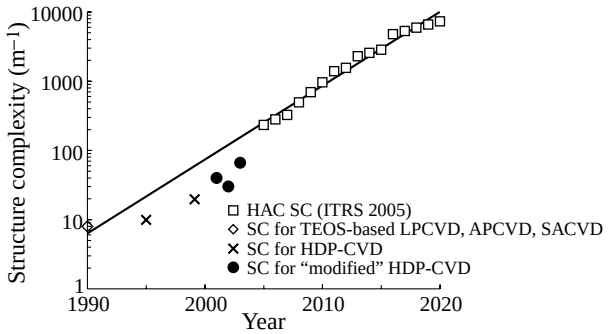

Fig. 2. SC values for ITRS example in Fig. 1 and for some CVD processes, revealing best gap-fill features.

analysis, a simple common parameter for IC gaps quantification and void-free gap-fill characterization was proposed. It was defined for the gaps with vertical shape as the ratio of AR to the gap size and named a Structure Complexity, SC. These SC values for some CVD processes are placed on the graph in Fig. 2 at approximate time when these processes were implemented in IC technology for the first time. The same SC parameter allows us to interpret the data from ITRS. In Fig. 2, opened squares represent the SC values of proposed future DRAM IC elements, calculated from the data presented in Fig. 1. It is clear that taking into account the decrease of gap size along with the increase of AR, the changes of SC look much stronger, being about 2 orders of magnitude higher compared to just 6 times increase forecast for AR. Moreover, data in Fig. 1 and Fig. 2 present just starting values of AR and SC, which will be drastically increase along with shortening of the gap size during thin film deposition on the gap side walls.

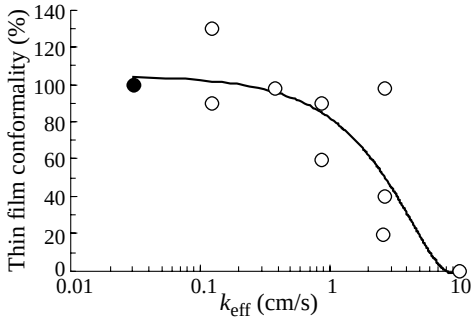

Fig. 3. Positioning of ALD technique (dark circular dot on the left) among other numerically characterized CVD techniques using conformality vs. k_{eff} data.

3. Evaluation of ALD technique

There are not too many differences between CVD and ALD in apparatus, precursors, general deposition methodology. The main differences between them are: a) an ALD process is intentionally performed by consecutive short pulsing mode precursor injection into reaction chamber, and b) a substrate is heated to less temperature than in traditional CVD processes. Considering ALD technique to be just a case of more common CVD technique, we can outline its position among the other known CVD methods using previously introduced parameter k_{eff} (an effective constant of the deposition rate) [1,4]. Experimentally obtained k_{eff} values for some CVD methods were found to correlate with thin film conformality values, as shown in Fig. 3. Undoubtedly, k_{eff} can be applied for ALD technique characterization as well as for the other types of thin films. Based on general ALD process conditions, our evaluation gives us an ALD k_{eff} range of about 0.01–0.05 cm per second. This is much lower values compared to the values obtained for the studied CVD processes. Using this k_{eff} range and commonly adopted for ALD technique 100% film conformality, one can see that ALD position in graph in Fig. 3 falls into a logical sequence with previously studied CVD processes. Being generally the slow chemical process, an ALD process can be characterized to have the following main features: very low efficiency of precursor usage; sensitivity to the surface status; excellent thickness uniformity; no gas-phase particle issues; intensive film growth on the wafer backside; excellent step coverage; good gap-fill. ALD technique position among other CVD techniques and its features is believed a core of some engineering issues and trends in ALD development.

4. Review on ALD engineering trends

Basic trends in ALD tool development seems to be caused by very low deposition rate. For instance, vacuum pump issues [4] are the consequence of very low k_{eff} that corresponds to very low reaction efficiency and wasting a lot of precursors. In fact, in most of cases the real ALD technique deposition rate is much lower compare to a monolayer forecast for 1 deposition cycle. For very thin films, single-wafer chamber design is preferable as long as it allows to integrate an ALD unit with a few other films deposition or film treatment units (for instance, Rapid Thermal Anneal) in the same cluster tools. However, for relatively thick films single-wafer chamber approach looks like rather disadvantage because of low tool productivity. From this point of view, the interest to multi-batch hot-wall reactors is quite reasonable. In fact, their design is close enough to well-known and routinely used tubular LPCVD reactors, which are relatively simple, reliable, and highly productive.

5. Likely future trends and topics in ALD development

It is believed that the most complicated issues of ALD developments in a future will be linked to the thin film conformality, quality and characterization of material properties in deep trenches (gaps) of ICs. It is expected that more efforts will be focused on the searching of a balance between the ALD tool productivity and thin film quality.

References

[1] V. Y. Vassiliev, J. L. Sudijono, and A. Cuthbertson, *Solid State Technol.* **44**, 129 (2001).
[2] D. Volger , P. Doe, *Solid State Technol.* **46**, 35 (2003).
[3] ITRS 2005, http://www.itrs.net.
[4] V. Y. Vasilev, S. M. Repinsky, *Uspekhi Khimii (Russian Chemical Reviews)* **74(5)**, 413 (2005).
[5] C. Bailey, K. Hutchison, and M. Wilders, *Solid State Technol.* **49**, 30 (2006).

15th Int. Symp. "Nanostructures: Physics and Technology"
Novosibirsk, Russia, June 25–29, 2007

SiGe/Si undoped and modulation-doped micrometer and submicrometer tubes and spirals

Yu. S. Yukecheva[1], A. B. Vorob'ev[1], V. Ya. Prinz[1], G. Mussler[2], V. Shushunova[2], A. Weber[2], E. Deckardt[2] and D. Grützmacher[2]

[1] Institute of Semiconductor Physics, 630090 Novosibirsk, Russia
[2] Paul-Sherrer Institute, 5232 Villigen, Switzerland

Abstract. The SiGe/Si undoped and modulation-doped tubes and spirals of micro-and submicron diameters were fabricated using the method of stress-driven rolling. Methods, allowing preparation of such structures electrically isolated from the substrate, and local well-controlled variation of curvature radii, are developed. The presented structures might be useful for magnetotransport investigations of holes on cylindrical surface and applications in novel types of sensors.

Introduction

Modulation-doped tubes and spirals of submicron and nanometer curvature radius are new physical objects that are of interest both for practical applications and for the study of electron transport in a non-uniform magnetic field [1]. The system Si/SiGe is attractive for the solution of these problems since the present-day IC technology and microelectromechanical systems are based on this semiconductor. In the system SiGe/Si, both electron and hole 2D gases of high mobility ($>10^5$ cm^2/V s for electrons [2] and $>10^4$ cm^2/V s for holes [3]) can be obtained. This work is aimed at the development of a technology for fabricating SiGe/Si-based modulation-doped tubes and spirals of submicron radius with 2D hole gas.

1. Experimental results and discussion

The submicron tubes and spirals in the present study were fabricated using the method proposed in [4]. For such structures to be formed, a sacrificial layer is necessary that can be removed with high selectivity ($>10^3$) with respect to the active part of the heterostructure. To satisfy this condition, two types of the structures were chosen: with Ge-rich, and with Si dioxide sacrificial layers.

It is well-known that Ge forms soluble oxide, and thus, it is very favorable as a sacrificial layer for Si/SiGe systems. Yet, because of the considerable mismatch in the lattice constant with Si it is hardly possible, if at all, to grow a sufficiently thick structure on a Si substrate in pseudomorphic regime. To solve the posed problem, "virtual substrates" prepared as metamorphic $Si_{0.2}Ge_{0.8}$ layers were chosen. The heterostructure, consists of additional Ge strain-compensating layer, strained $Si_{0.5}Ge_{0.5}$ and modulation-doped or undoped Si layers. The growth was performed by MBE at $T = 300$ °C. The subsequent evaporation of Ti, SiO_2, or Si_3N_4 was performed on some samples in order to raise the mechanical strength of the tubes and helixes. These additional layers could be selectively removed from the already rolled-up structure.

Using the expressions given in [5], the band offset values for strained $Si_{0.5}Ge_{0.5}$/Si grown on $Si_{0.2}Ge_{0.8}$ substrates, were evaluated to be 100 meV for valence band and about 400 meV for the conductance band. After the detachment, i.e. in the rolled structures, the strain redistribution leads to the considerable change in the band diagram: valence band offset increases up to 240 meV, and conductance band offset decreases down to 270 meV. These estimations show that in p-doped structures after the film detachment holes should be still localized in $Si_{0.5}Ge_{0.5}$ quantum well. The same material system, but n-doped, could be used to get two-dimensional electron gas, what is attractive because of mobility enhancement in stretched Si.

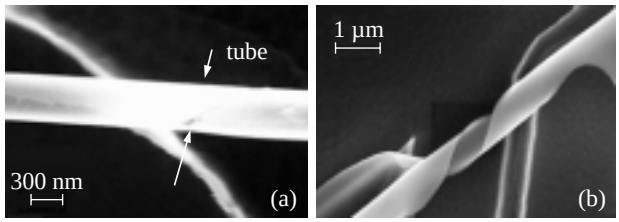

Fig. 1. a) Si/SiGe/Ti tube, $R = 225$ nm; b) SiGe/Si/SiO_2 spiral, $R = 280$ nm.

Tube and helix, fabricated by anisotropic etching [6], are shown on Fig. 1. To make magnetotransport measurements on such structures possible, contacts and electrical isolation from the substrate are implicitly needed. To fabricate structures with contacts, we used directional rolling procedure to wrap tubes and helices onto metallic contact pads. To exclude the substrate conductance, we have developed an original technology the key point of which was withdrawal of the contact pads from the heterostructure onto additionally evaporated thick oxide layer. Such structures make it possible to examine the conductance of the fabricated tubes and helices in a broad temperature range. Apart from improved mechanical strength, the top SiO_2 provides an additional advantage: during the exposure of $Si_{0.5}Ge_{0.5}$/Si/SiO_2 cylindrical sector to the electron beam, SiO_2 contracts, and thus the diameter of the whole structure decreases. Exposing only small tube areas, the cylindrical sector diameter was locally varied (Fig. 2), and since the beam placement and its intensity in scanning electron microscope is very well controlled, the method is promising for the fabrication of complex shape structures.

Another way toward the fabrication of micrometer and submicrometer Si/SiGe tubes electrically insulated from substrate is using advanced silicon-on-insulator (SOI) substrates for heterofilm growth [7]. Here, the SiO_2 layer is used the sacrificial layer. The initial Si layer (70 nm) was given a thermal oxidation treatment so that to decrease its thickness to 30 nm and, after the removal of the oxide, a heterofilm was grown comprising p-doped Si layers, Si spacers, and a Si_xGe_{1-x} with $x = 0.4...0.5$ quantum well. The structure was accomplished with additional Si layer of 60–70 nm thickness which was is necessary for the films to be rolled "upward", i.e., in the di-

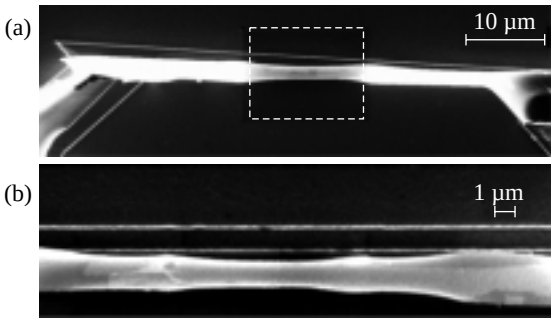

Fig. 2. Electron-beam assisted local modification of the stress in a SiGe/Si/SiO_2 tube: a) single exposure, the corresponding area is marked with a white frame; b) several exposures, the cylindrical sector diameter diminishes by a factor of two.

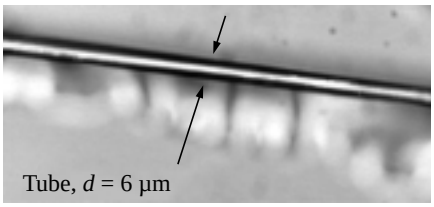

Fig. 3. Si/SiGe/Si p-type modulation-doped tube on SOI.

rection from the substrate. By etching SiO_2, the so thick film was rolled in scrolls with diameters >100 μm. Then Si was etched from both sides, the scroll diameters decreased down to several micrometers (Fig. 3).

The modulation-doped tubes and spirals of submicrometer and nanometer curvature radius fabricated by the method of strain-driven film rolling may prove useful in device applications as accelerometer components, components of magnetic field and magnetic-field gradient sensors, and building blocks for various MEMS. Undoped structures may be used for the investigations of passivation influence on the Fermi level pinning and electron distribution in the free-standing thin films.

Acknowledgements

This work was supported by SCOPES and Russian Foundation for Basic Research (Grant No. 06-02-16005).

References

[1] M. L. Leadbeater, C. L. Foden, J. H. Burroughes, M. Pepper, T. M. Burke, L. L. Wang, M. P. Grimshaw, and D. A. Ritchie, *Phys. Rev. B* **52**, R8629 (1995).

[2] F. Schaffler, *Semicond. Sci. Technol.* **12**, 1515 (1997), and references therein.

[3] W. C. Tsai, C. Y. Chang, G. W. Huang, F. F. Fang, Y. H. Chang, C. F. Huang, *Jpn. J. Appl. Phys.* **36**, L323 (1997).

[4] V. Ya. Prinz, V. A. Seleznev, A. K. Gutakovsky, A. V. Chehovskiy, V. V. Preobrazhenskii, M. A. Putyato, T. A. Gavrilova, *Physica E* **6**, 828 (2000).

[5] V. L. Yang, J. R. Watling, R. C. W. Wilkins *et al*, *Semicond. Sci. Tech.* **19**, 1174 (2004).

[6] S. V. Golod, V. Ya. Prinz, V. I. Mashanov, *Semicond. Sci. Tech.* **19**, 1174 (2004).

[7] A. Vorob'ev, P. O. Vaccaro, K. Kubota, T. Aida, T. Tokuda, T. Hayashi, Y. Sakano, J. Ohta, and M. Nunoshita, *J. Phys. D* **36**, L67 (2003).

15th Int. Symp. "Nanostructures: Physics and Technology"
Novosibirsk, Russia, June 25–29, 2007

Electronic Raman scattering by InAs/AlAs quantum dots

A. G. Milekhin[1], A. I. Toropov[1], A. K. Bakarov[1], N. V. Surovtsev[2], M. Lentze[3], J. Geurts[3] and D. R. T. Zahn[4]

[1] Institute of Semiconductor Physics, 630090 Novosibirsk, Russia
[2] Institute of Automation and Electrometry, 630090 Novosibirsk, Russia
[3] Physikalisches Institut, Universität Würzburg, 97074 Würzburg, Germany
[4] Institut für Physik, Technische Universität Chemnitz, 09126 Chemnitz, Germany

Abstract. Resonant Raman scattering by intersubband electronic excitations in InAs/AlAs quantum dots is observed in the acoustic spectral region. With increasing temperature (from 1.7 to 90 K) the energy position of the intersubband electronic excitations is blue shifted manifesting size selective resonant electronic Raman scattering.

Introduction

Structures with quantum dots (QDs) attract much attention due to their unique physical properties [1] and potential application in opto- and microelecronic devices such as lasers [2], infrared photodetectors [3], memory elements [4] *etc*. The study of the QD phonon spectrum has become a subject of special interest because it determines the processes of carrier relaxation. Raman spectroscopy is traditionally considered as the most informative tool for the investigation of the vibrational spectrum of semiconductors.

In InGaAs/AlGaAs QDs first-order Raman scattering by optical [5,6,7], interface [8,9] and acoustic [10] phonons and multiple-phonon Raman scattering [11] were investigated. Electronic Raman scattering was first observed and investigated for GaAs/AlGaAs QDs fabricated by etching of GaAs/AlGaAs structures with a two-dimensional electron gas [12,13]. Recently [14,15], the results of a study of electronic Raman scattering by self-assembled InGaAs/GaAs QDs was reported.

The InAs/AlAs combination is an ideal system for studying electronic excitations in InAs QDs. First, InAs/AlAs QDs fabricated at growth temperatures of 400–520 °C have a small size for which the quantization effect of the electronic spectrum is significant. Second, a deep quantum well for electrons (about 1 eV) allows the electronic transitions between quantized levels in the conduction band in a wide energy region to be studied. Third, a low atomic intermixing in the InAs/AlAs heterosystem in comparison with InAs/GaAs system simplifies the interpretation of the results. Finally, the interband transition energy E_0 in InAs/AlAs QDs lies in the visible (red) spectral region allowing the resonant Raman scattering to be studied. The latter argument has a principal importance because electronic Raman scattering is observed only under resonant conditions.

In this paper, we present the results of investigation of electronic intersubband excitations in InAs/AlAs QDs.

1. Experimental

The nanostructures studied were grown by molecular beam epitaxy (MBE) on (001)-oriented GaAs substrates using a Riber 32P system. Samples consisting of 10 periods of InAs QDs embedded in AlAs were grown at a substrate temperature of 510 °C. Each period contains an InAs QD layer (nominal thickness 2.25 monolayers) and a 30 nm thick AlAs layer. Each AlAs layer was delta-doped with Si atoms at a distance of 2 nm below the QD layer. The whole structure was capped by 15 nm of GaAs.

The Raman spectra were recorded at $T = 1.7-150$ K using a Dilor XY800 triple spectrometer. Several lines of Ar^+ and Kr^+ lasers in the spectral range of 476.2–752.5 nm (1.65–2.6 eV) were used for excitation. A dye (DCM) laser was used for excitation in the vicinity of the E_0 transitions in the energy range of 1.83–1.95 eV. Raman spectra were measured in backscattering using polarized $(z(xx)\bar{z})$ or depolarized $(z(yx)\bar{z})$ configurations where x, y, z are parallel to the [100], [010], [001] directions, respectively. Nonzero in-plane vector transfer $q = 4\pi \sin\alpha/\lambda$ was achieved by tilting the sample by an angle α with respect to the linearly polarized incident laser beam of wavelength λ. The spectral resolution was 2 cm^{-1} over the entire spectral range.

2. Results and discussion

Fig. 1 shows Raman spectra of the InAs/AlAs QDs measured in the $z(x, x)\bar{z}$ and $z(y, x)\bar{z}$ scattering geometries. Beside the features near 250, 296, 407 and 390 cm^{-1} corresponding to LO phonons in InAs, GaAs and AlAs and interface phonons in AlAs, respectively, discussed in [2, 6, 8] in detail, intensive peaks are observed at 175 cm^{-1} (in polarized) and 157, 196 cm^{-1} (in depolarized geometry).

As it was shown earlier [12], single particle, charge- and spin-density electronic excitations (SPEs, CDEs, SDEs, respectively) in nanostructures can be identified by their Raman selection rules. The SPEs are observed in both polarized and depolarized geometries. Their energies correspond to the energy difference between two confined electronic states. CDEs are active in the polarized geometry. Their energies are

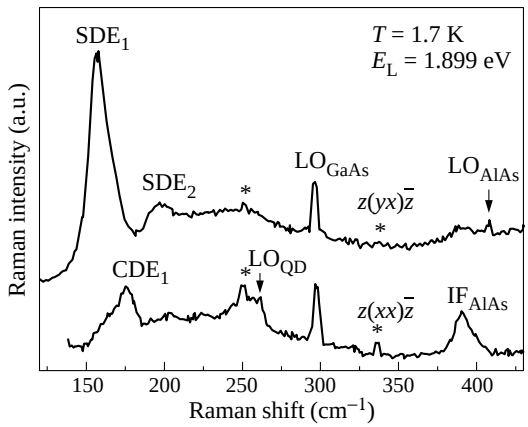

Fig. 1. Raman spectra of InAs/AlAs QDs measured in the $z(xx)\bar{z}$ and $z(yx)\bar{z}$ scattering geometries at an excitation energy of 1.889 eV and a temperature of 1.7 K. The stars show laser plasma lines.

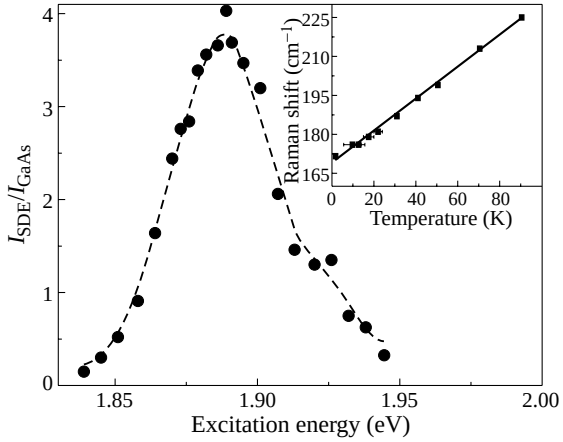

Fig. 2. Dependence of the SDE_1 peak intensity on the laser excitation energy. The inset to the figure shows the temperature dependence of SDE_1 peak energy.

determined by the Coulomb interaction and, therefore, blue shifted with respect to the SPEs energies. The energies of SDEs observed in the depolarized geometry are also renormalized with respect to SPEs but reveal an opposite (red) shift due to the exchange interaction. Using the selection rules considered above, the peaks observed in Fig. 1 can be interpreted in terms of Raman scattering by intersubband CDEs and SDEs (depicted in Fig. 1 as CDE_1 and SDE_1, SDE_2). In order to confirm the zero-dimensional character of the electronic excitations angle-dependent measurements were performed. The incidence angle of the laser beam was varied in the range of $\alpha = 28^\circ - 80^\circ$ which corresponds to an in-plane vector transfer $q = (0.91 - 1.92) \times 10^5$ cm^{-1}. However, no energy change of electronic excitation peaks was observed thus confirming the zero-dimensional character of the electronic excitations.

The SDE and CDE peaks are observed in Raman spectra measured in both Stokes and anti-Stokes regions allowing the Raman signal to separate from the features related with the photoluminescence.

Electronic Raman scattering has a resonant behavior and occurs in a narrow region of excitation energies. Fig. 2 shows the dependence of the SDE_1 peak intensity as a function of the laser excitation energy. It is worth mentioning that the SDE_1 peak intensity is normalized to the peak of LO phonon from GaAs substrate recorded with the same excitation energy. As one can see from Fig. 2, the intensity maximum is observed at 1.88 eV. At this value the incident photon energy approaches the first excited electron-hole transitions in the QDs. The shoulder at about 1.92 eV can be due to a contribution in the Raman scattering by a resonance with higher-lying interband transitions.

With increasing temperature a blue shift of the electronic excitation energies is observed. As one can see from the inset in Fig. 2, this shift is linear for SDE_1 in a wide range of temperatures (1.7–90 K). Such behavior can not be explained by an increasing number of thermalized electrons in the conduction band because this causes an opposite shift of the electronic excitations energies [14]. Moreover, the energy of the intersubband transitions obtained from IR absorption experiments [16] decreases also with temperature. However, this bevavior becomes obvious if one takes into account the resonant character of Raman scattering by an array of QDs inhomogeneous in size. Indeed, with increasing temperature the band gap of InAs as well as the interband transition energy in QDs decreases. As a result, the QDs having a smaller size and thus larger interband and intersubband transition energies get into a resonance with the excitation energy. Consequently the increase of the intersubband electronic excitations via temperature is observed in the Raman spectra (Fig. 2). Contrary to Raman measurements IR spectroscopy probes nonresonantly the intersubband transition energies in the QDs having the dominant size in the array. Therefore, the intersubband transition energies derived from the IR experiments decrease with temperature in accordance with decreasing interband transition energies of QDs.

In conclusion, resonant Raman scattering by intersubband CDEs and SDEs in self-assembled InAs/AlAs QDs was observed. The energy positions of the Raman peaks attributed to these excitations are shifted towards higher energy with increasing temperature due to size-selective Raman scattering.

Acknowledgements

This work has been supported in part by the Russian Foundation for Basic Research (grant 06-02-90870 Mol a), SFB-410 and Deutscher Akademischer Austauschdienst (DAAD).

References

[1] D. Bimberg, M. Grundmann, and N. N. Ledentsov, *Quantum Dot Heterostructures*, Wiley, New York (1999).
[2] N. N. Ledentsov *et al*, *Semiconductors* **32**, 343 (1998).
[3] E. Finkman *et al*, *Phys. Rev. B* **63**, 045323 (2001).
[4] G. Yusa *et al*, *Appl. Phys. Lett.* **70**, 345 (1997).
[5] D. A. Tenne *et al*, *Phys. Rev. B* **61**, 13785 (2000).
[6] A. Milekhin, D. Tenne, D. R. T. Zahn, in *Quantum Dots and Nanowires*, American Scientific Publishers, 375 (2003).
[7] J. Ibanez *et al*, *Phys. Rev. B* **83**, 3069 (2003).
[8] M. Yu. Ladanov *et al*, *JETP* **101**, 554 (2005).
[9] A. G. Milekhin *et al*, *Phys. Rev. B* **70**, 085314 (2004).
[10] A. Milekhin *et al*, *Proceedings of 12th Int. Conference on Narrow Gap Semiconductors*, 3–7 July, 2005, Toulouse, France, IOP Conference Series, New York, **187**, 99 (2006).
[11] A. Milekhin *et al*, *JETPL* **83**, 505 (2006).
[12] C. Schueller *et al*, *Phys. Rev. Lett.* **80**, 2673 (1998).
[13] D. J. Lockwood *et al*, *Phys. Rev. Lett.* **77**, 354 (1996).
[14] T. Brocke *et al*, *Phys. Rev. Lett.* **91**, 257401 (2003).
[15] L. Chu *et al*, *Appl. Rev. Lett.* **77**, 3944 (2000).
[16] F. Bras *et al*, *Appl. Rev. Lett.* **80**, 4620 (2002).

15th Int. Symp. "Nanostructures: Physics and Technology"
Novosibirsk, Russia, June 25–29, 2007

High-density InSb/InAs quantum dots grown by liquid-phase epitaxy for the mid-ir spectral range 3–4 μm

K. D. Moiseev, Ya. A. Parkhomenko, M. P. Mikhailova, A. V. Ankudinov, S. S. Kizhaev, E. V. Gushchina, A. S. Vlasov, E. V. Ivanov, D. A. Razumovsky, N. A. Bert, A. N. Titkov and Yu. P. Yakovlev
Ioffe Physico-Technical Institute, St Petersburg, Russia

Abstract. We report first results on structural and optical properties of the InSb quantum dots (QDs) grown on InAs(100) substrate by liquid-phase epitaxy. Characterization of InSb/InAs QDs was performed using atomic force microscopy (AFM) and transmission electron microscopy (TEM) methods. Two types of self-assembled, small and large, QDs were observed. The uniform small QDs with high density ($0.7-1.9 \times 10^{10}$ cm^{-2}) with dimensions of 3–5 nm in height and 11–13 nm in diameter were obtained in the temperature range $T = 420-445$ °C. The large QDs with dimensions of 12–14 nm in height and 25–30 nm in diameter appear to be at a much lower density (5×10^{8} cm^{-2}). The density, the form and the size of the strain-induced QDs were found to change with growth temperature, supercooling value and cooling rate. Capsulation of self-assembled InSb QDs by InAs(Sb,P) capping layer was obtained using metal-organic vapour phase epitaxy. The results of AFM study are well agreed with TEM images. Photoluminescence and electroluminescence from capsulated InSb QDs in InAs based matrix were observed in the spectral range 3–4 μm at $T = 77$ K.

Introduction

Self-assembled quantum dots (QD) have attended a great interest for both fundamental sciences and potentional applications due to their unique properties as 0-dimensional nanoobjects in the 3D-matrix [1]. Most of investigations was focused on structural and optical study of InAs/GaAs, InGaAs/GaAs, InP/GaAs, InAs/InP and InSb/GaSb quantum dots grown mainly by molecular beam epitaxy (MBE) or metal-organic vapour phase epitaxy (MOVPE) [2–5]. The main goal of these studies was to create QD lasers [1] and photodetectors [6] for the telecommunication in the spectral range $1.1-1.3$ μm. QD lasers exhibited lower threshold current, operation wavelength tuning, low-energy consumption and high temperature stability. Last years a great attention of researchers was paid to use quantum dots in biology and medicine [7].

To penetrate in the longwavelength region ($\lambda > 2$ μm) it needs to produce quantum dots based on the narrow-gap semiconductors such as InSb and InAsSb that are promising for the fabrication of emitters and detectors for mid-infrared spectral range $3-4$ μm. However, up to now there are a few works devoted to the study of such quantum dots grown by MBE and MOVPE [8–11]. The density of InSb/GaSb, InSb/InP and InSb/InAs quantum dots did not exceeded 10^{9} cm^{-2} [11–13]. The liquid phase epitaxy (LPE) method was used for the growing of InAsSb/InAs and InAs/GaAs quantum dots [14,15]. The main difficult is to obtain the capsulated InSb QDs using LPE method. Here we report on the high-density uniform InSb/InAs QDs grown by the combine technology using LPE and MOVPE methods to get the structures emitting in the spectral range 3–4 μm.

Experimental results and discussion

To obtain InSb QDs our experiments were carried out in a horizontal LPE system equipped with a standard slider graphite boat under H_2 flow atmosphere. The growing was made from indium-enriched melt. Epitaxial growth runs were performed in the wide temperature range $T = 420-450$ °C [16]. Self-assembled InSb QDs were grown on InAs (100) substrates according with Stranski–Krastanov's growth model due to the lattice mismatch between InSb and InAs as large as 7.2%.

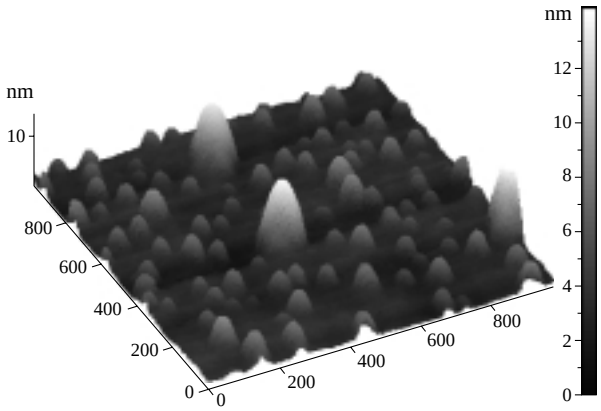

Fig. 1. Topography of the surface for MP-3/1 sample with square 1×1 μm^2 obtained by contactless AFM method.

Structural characterization of uncapped InSb/InAs QDs was made using scanning probe microscopy (SPM) and atomic-force microscopy (AFM) methods reported elsewhere [17]. The distribution of the QDs samples on the size and the density was evaluated by AFM method and analyzed by the special program SPM — Image Magic.

As one can see from Figure 1 there is enough uniform distribution of nanoobjects on sizes. Small and large QDs are observed, the resulting structures being generally similar to those produced by MBE and MOVPE techniques. Small uniform InSb QDs are characterized by average height $H = 3.4 \pm 1.2$ nm and average diameter $R = 13.2 \pm 3.5$ nm, number of objects in the field of view was $N = 102$ which corresponds to average density $n = 10^{10}$ cm^{-2}. The large QDs with dimensions of 12–14 nm in height and 25–30 nm in diameter appear to be at a much lower density ($\sim 5\times10^{8}$ cm^{-2}). The density of the small QDs were found to increase from 0.7×10^{10} to 1.9×10^{10} cm^{-2} with growth temperature decreasing from 445 down 420 °C. High-density small dots should be self-assembled and dislocation-free, whereas the larger dots may contain defects that help to consume the residual strain. Therefore LPE method allows to get more density of QDs in

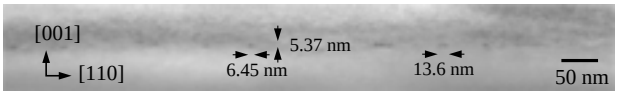

Fig. 2. Dark-field electron micrograph of cross-section sample performed in ⟨220⟩ direction. Substrate-layer interface can be ascribed to the fine dark line. Dark contrast spots at the interface represent InSb QDs.

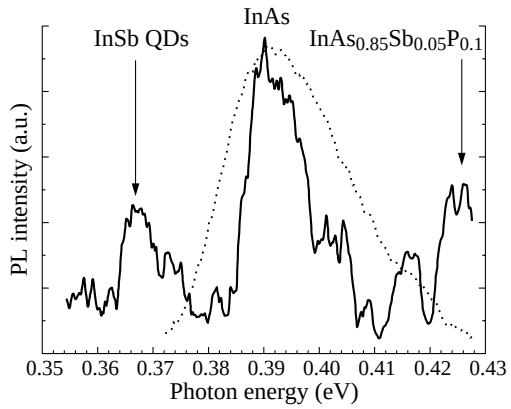

Fig. 3. PL spectra from the capsulated InSb QDs (solid line) and InAs substrate (dot line) measured at $T = 77$ K.

comparison with MBE and MOVPE [9,12]. From these results we can conclude that we have successfully grown InSb QDs on the InAs substrate by LPE method.

Capping of the InSb QDs by $InAs_{0.85}Sb_{0.05}P_{0.1}$ epilayer lattice-matched with InAs substrate was performed using MOVPE method. The cap layer with thickness of about 0.5 μm was grown at $T = 500\,^{\circ}$C. Trimethylindium (TMIn), maintained at $10\,^{\circ}$C, phosphine (PH_3) and arsine (AsH_3) were used as sources of indium, phosphorus and arsenic, respectively. Growth was performed at V/III ratio of 120.

Cross-section transmission electron microscopy (TEM) was used to identify capsulated InSb QDs after capping by InAsSbP layer. TEM study was carried out in JEM 2100 instrument at accelerating voltage 200 kV using both diffraction and high-resolution modes. Cross-sectional TEM (XTEM) samples were prepared in conventional manner by preliminary mechanical grinding-polishing followed by 4 keV Ar^+ ion milling.

XTEM observations demonstrated small (nanometer-sized) inclusions situated at InAs/InAsSbP substrate-layer interface (Fig. 2). Two types of inclusions can be seen in the image: (i) globular-like ones with a characteristic size of around 6–7 nm; (ii) larger inclusions with a height of about 6 nm and lateral size 10–15 nm. It is important to notice that in addition to pyramidal shape QDs lens-like shaped ones were also observed. High-resolution image of such a large inclusion provides some evidence of dome-like shape of large inclusions. Sizes for small InSb QDs were evaluated as 5.37 nm and their length as 6.45 nm. These data are in good agreement with AFM results. Although some dislocations and stacking faults were observed in the epitaxial layer no extended defects associated with inclusions were found.

Photoluminescence from capsulated InSb QDs was measured at $T = 77$ K. Nd:YAG laser operating on second order harmonic ($\lambda = 535$ nm) with output power 200–240 mW was used for pumping. Incident light was focused in the spot with lateral sizes 100×200 ^{2}. PL spectra were recorded by 1/4 m monochromator using a PbSe detector and Lock-in amplifier. PL spectrum of the capsulated InSb/InAs QDs exhibited three pronounced emission bands in the mid-infrared spectral range (Fig. 3). Maximum of the emission band at $h\nu = 390$ meV (FWHM = 12 meV) for the QDs sample and substrate relates to radiation transitions in the bulk InAs. We suppose that the longwavelength band at $h\nu = 366$ meV (FWHM = 19 meV) can be ascribed to the InSb quantum dots, whereas the short-wavelength one at $h\nu = 427$ meV is from InAsSbP capping layer. This result agrees with our electroluminescence data where intensive emission was observed at $T = 77$ K in the spectral range 3–4 μm.

Conclusions

In conclusion we would like to notice that we obtained high-density ($\sim 10^{10}$ cm^{-2}) InSb/InAs uniform QDs with parameters better than it was obtained by MBE and MOVPE methods. The advantage of the proposed LPE technology method is simplicity and low cost of technological processes as well as low defects concentration in contrary to other growth methods. It is important for mass production of mid-ir semiconductor optoelectronic devices on the base of quantum dot nanostructures.

References

[1] N. N. Ledentsov *et al*, *Semiconductors* **32**, 385 (1998).
[2] J. M. Moison *et al*, *Appl. Phys. Lett.***64**, 196 (1994).
[3] F. Hatami *et al*, *Appl. Phys. Lett.* **67**, 656 (1995).
[4] G. Saint-Giroris *et al*, *Appl. Phys. Lett.* **89**, 03192379 (2006).
[5] D. E. Eaglesham *et al*, *Phys. Rev. Lett.* **65**, 1020 (1995).
[6] P. Bhattacharya *et al*, in book *Mid-infrared optoelectronics*, Springer Series in Optical Sciences. Ed. A. Krier, 487–513 (2006).
[7] G. G. Zegrya , *Tech. Phys. Lett.* **32**, 75 (2006).
[8] V. Tasco *et al*, *Appl. Phys. Lett.* **90**, 021658 (2007).
[9] F. Hatami *et al*, *Appl. Phys. Lett.* **89**, 133115 (2006).
[10] S. V. Ivanov *et al*, *Proc. IOP Conf. ser.* **187**, 89 (2005).
[11] E. Alphandery *et al*, *Appl. Phys. Lett.* **74**, 2041 (1999).
[12] C. W. Warren *et al*, *Science* **281**, 2016 (1998).
[13] T. Ultzunger *et al*, *Appl. Phys. Lett.* **69**, 2674 (1996).
[14] A. Krier *et al*, *Appl. Phys. Lett.* **77**, 3791 (2000).
[15] I. E. Maronchuk *et al*, *Surface. Roentgen synchrotron and neutron study* **12**, 97 (2005).
[16] K. D. Moiseev *et al*, *Tech. Phys. Lett.* **33**, 295 (2007).
[17] A. Ankudinov *et al*, *Phys. Low-Dim. Struct.* **3/4**, 9 (2001).

15th Int. Symp. "Nanostructures: Physics and Technology"
Novosibirsk, Russia, June 25–29, 2007

Finger-print of the Auger recombination process in semiconductor InAs/GaAs quantum dots

A. S. Shkolnik[1], K. A. Kupriyanov[1], L. Ya. Karachinsky[1], S. Pellegrini[2], G. S. Buller[2], N. Yu. Gordeev[1], G. G. Zegrya[1] and V. P. Evtikhiev[1]

[1] Ioffe Physico-Technical Institute, St Petersburg, Russia
[1] School of Engineering and Physical Sciences, Heriot-Watt University, Riccarton, Edinburgh EH14 4AS, United Kingdom

Abstract. We present the results of the detailed investigations of the directly estimated Auger recombination time dependence on the size of semiconductor quantum dots. The internal quantum efficiency and the lifetime of nonequilibrium charge carriers in semiconductor InAs/GaAs quantum dots at different levels of excitation have been investigated experimentally and theoretically. It is shown, that depending on excitation level non-radiative Auger recombination can play a significant role in recombination processes in quantum dots.

Introduction

By virtue of strong carrier localization in quantum dots (QDs), arrays of QDs represent an ideal system for the Auger processes (AP) realization. Theoretical investigations of AP in QD heterostructures have been provided earlier [1,2]. Recently also in experimental papers devoted to the QD's laser diodes investigations appears calculations denotes on necessity of the Auger recombination being taken into account [3,4]. For the detailed investigation of AP influence on QD's luminescence characteristics we have performed the measurements of carriers lifetime in QDs and photoluminescence quantum efficiency at different level of excitation in wide temperature range.

1. Experimental

InAs QD single layer arrays were grown simultaneously in the same process using the Stransky–Krastanow method using molecular beam epitaxy (MBE) on an exactly oriented GaAs (001) substrate (sample A) and on substrates intentionally misoriented by 2, 4 and 6 degrees to the [010] direction (samples B, C and D, respectively). The average thickness of the InAs layer was 2.9 monolayer (ML). The InAs QD growth temperature was 470 °C and the III/V element flux ratio was 2. The InAs QD array was confined by GaAs barriers (20 nm) surrounded by 250 nm thick AlAs/GaAs graded band-gap superlattices and by $Al_{0.7}Ga_{0.3}As$ cladding layers (200 nm). The structure was completed by GaAs cap layer (5 nm). Application of the misoriented substrates allows us to grow in the same epitaxy process a set of the samples with different average size of quantum dots. The size of the QDs was calculated from atomic force microscopy (AFM)images and was found in range of 15–30 nm in lateral size and 1.4–3 nm in height.

Steady state photoluminescent (PL) measurements were performed with an Ar^+ ion laser ($\lambda = 514.5$ nm) in wide excitation energy range. Detailed description of the time-resolved photoluminescence (TRPL) measurements is presented in [5,6]. TRPL measurements of the ground state (GS) QD emission were performed in wide incident energy range (0.7–47 000 pJ cm^{-2}). Narrow band pass filters (few nanometres width) were used to spectrally discriminate the luminescence signal. Measurements were performed at the maximum of the PL spectra, which corresponds to the carrier recombination via the ground state.

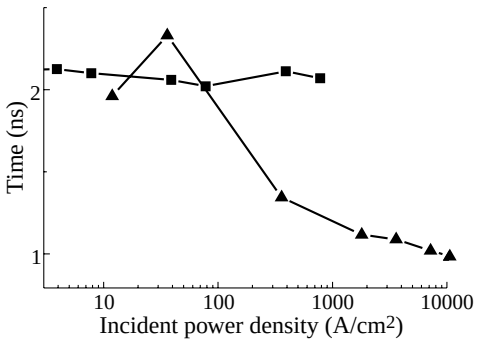

Fig. 1. Carriers life-time dependence of the incident power density. Triangles $T = 77$ K, squares $T = 5$ K.

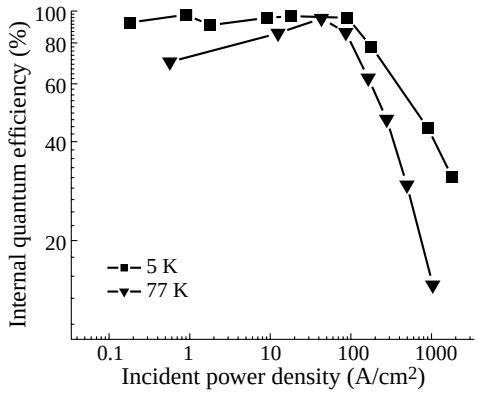

Fig. 2. Internal quantum efficiency dependence on the incident power density. Triangles $T = 77$K, squares $T = 5$ K.

2. Results and discussion

Dependences of the lifetime of the non-equilibrium carriers and internal quantum efficiency on the incident power density for the sample C at the temperatures 5 and 77 K are shown in Fig. 1 and Fig. 2, respectively.

The dependence of the internal quantum efficiency on the incident power density at the $T = 77$ K turned out to be qualitatively close to the same dependence measured at the $T = 5$ K. At the small concentrations of injected carriers (in contrast to the $T = 5$ K, where the value of the internal quantum efficiency is practically equal to 100% and the decreasing is due the band filling effect [7]) internal quantum efficiency increases with

the incident power density increasing. At the injected carriers concentrations closed to the filling of the ground state the internal quantum efficiency achieves the value of 100% whereupon it starts to decrease. This decreasing is more abrupt than at $T = 5$ K and cannot be explained only by ground state filling effect [7]. At the same time there is a great difference in carrier life-time versus incident power density dependences measured at $T = 5$ K and $T = 77$ K.

The value of the charge carriers life-time τ and the internal quantum efficiency η are bounded with radiative/non-radiative charge carriers life-times by the following equations:

$$\tau^{-1} = \tau_{\mathrm{RR}}^{-1} + \tau_{\mathrm{NR}}^{-1}, \quad \eta = \frac{\tau_{\mathrm{RR}}^{-1}}{\tau_{\mathrm{RR}}^{-1} + \tau_{\mathrm{NR}}^{-1}}, \tag{1}$$

where τ_{RR} — radiative charge carriers life-time and τ_{NR} — non-radiative charge carriers life-time. Using experimental internal quantum efficiency and life-time dependencies on the injected carriers concentration ($\eta(n)$ and $\tau(n)$) we can obtain the dependencies of the radiative/non-radiative life-times on the incident power density $\tau_{\mathrm{RR}}(n)$ and $\tau_{\mathrm{NR}}(n)$, correspondingly. Those dependencies are presented in the Fig. 3. As it can be seen in the Fig. 3 the radiative life-time stays practically constant while non-radiative lifetime one has pronounced maximum near the ground state filling of the quantum dots. The first part of the dependence — increasing of the non-radiative life-time is due to the saturation of the Shokley–Reed non-radiative recombination channel and the following decreasing is the evidence of the new non-radiative channel turning on. It is necessary to point out the fact that those experiments allow us to measure the time of the non-radiative recombination process. As it can be seen the turning on of the new non-radiative channel occurs while temperature changes from 5 up to 77 K. Additionally performed experiments (for example, constancy of the internal quantum efficiency and FWHM of the PL spectra from the ground state up to 100 K and so on) allow us to exclude the influence of the thermal escape of the charge carriers from the ground state. We supposed that predicted earlier Auger non-radiative recombination [1, 2] is the reason of the internal quantum efficiency decreasing at the ground state filling. Measurements of the samples with different average size of quantum dots allowed us to find out the experimental dependence of the time of this new non-radiative process on the average size of quantum dots. This dependence is shown in the Fig. 4. Theoretically calculated dependence of Auger recombination time on the size of quantum dot is also presented in the Fig. 4. As it can be seen those dependencies have qualitative similarity and it is necessary to mention that in QD's only Auger recombination process has such dependence on quantum dot size. In our previous theoretical work it has been shown that such character of the behavior of the recombination rate on the quantum dot size dependence explained by the increasing of the electron-hole overlap integral on the first part and by decreasing of the electron localization in QD on the second part. This is the reason why we can declare that decreasing of the internal quantum efficiency at the filling of the ground state in quantum dots is caused by Auger recombination. It is necessary to point out the high efficiency of this non-radiative channel — the time of the non radiative Auger recombination process is in the range of nanoseconds (2–6 ns) and is comparable with time of radiative recombination.

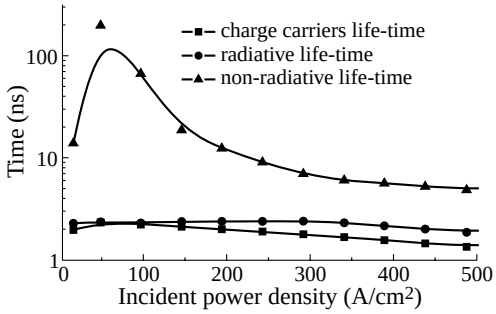

Fig. 3. Radiative (squares) and non-radiative (triangles) life-times dependencies of the incident power density.

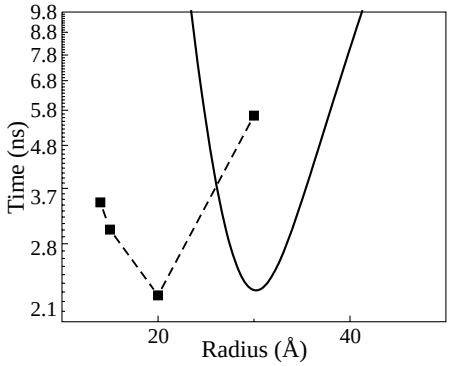

Fig. 4. Experimental (squares) and theoretical (line) Auger time dependencies on the quantum dot size.

3. Conclusions

Internal quantum efficiency and the carriers life-time in the ground state of InAs/GaAs quantum dots arrays with different average size in the wide excitation range have been investigated. It was shown that at the high excitation levels Auger process has a significant influence on the charge carriers life-time. For the quantum dots with the average height of about 20–30 A the time of Auger recombination in quantum dots is comparable with the time of radiative recombination.

Acknowledgements

This work was supported in different parts by Grant from St Petersburg Scientific Center RAS and The Russian Foundation for Basic Research. L.Ya.K. acknowledges financial support from the Grant of the President of the Russian Federation for the support of young scientists (MK-4232.2007.2).

References

[1] A. S. Shkolnik, V. P. Evtikhiev G. G. Zegrya, *Technical Physics Letters* **32**, 51, (2006).
[2] D. I. Chepic, *et al*, *J. Luminescence* **47**, 113 (1990).
[3] I. I. Novikov, *et al*, *Semiconductors* **39**, 507 (2005).
[4] I. P. Marko, *et al*, *IEEE J. Select. Topics Quant. Electron.* **9**, 1300 (2003).
[5] L. Ya. Karachinsky, *et al*, *Appl. Phys. Lett.* bf 84, 7 (2004).
[6] A. S. Shkolnik, *et al*, *Appl. Phys. Lett.* **86**, 211112 (2005).
[7] A. S. Shkol'nik, *et al*, *Nanotechnology* **12**, 512–514 (2001).

15th Int. Symp. "Nanostructures: Physics and Technology"
Novosibirsk, Russia, June 25–29, 2007

Fine structure of exciton in doubly charged CdSe/ZnSe/ZnMnSe quantum dots

E. A. Chekhovich, A. S. Brichkin, A. V. Chernenko and V. D. Kulakovskii
Solid State Physics Institute, RAS, Chernogolovka, 142432, Russia

Abstract. Photoluminescence of single doubly charged CdSe/ZnSe/ZnMnSe quantum dots (QDs) with various magnitude of sp-d exchange interaction of QD carriers and Mn ions has been investigated in magnetic fields up to 6 T. The fine energy structure of doubly charged exciton in the QD has been determined and the effect of interaction with Mn ions on Zeeman splitting and spin relaxation has been investigated in detail.

Introduction

Semiconductor quantum dots (QD) are artificial atoms whose properties are determined by their solid-state environment [1]. To manipulate the charge and spin of an exciton confined to a QD, it is necessary to clarify the effect of the Coulomb interactions between electrons and holes. In particular, the exchange interaction between electrons (e) and holes (h) determines the polarization and entanglement of the emitted photons [2]. In the case of exciton in a neutral QD, the e-h exchange interaction splits the exciton state into states with total spin $J = 1$ and 2. Only the states with $J = 1$ can emit a photon as a consequence of the selection rules. The e-h exchange interaction of a QD exciton has typically been measured by breaking the symmetry, either with a strong magnetic field or with a highly anisotropic strain field, mixing the bright and dark states. In the case of a doubly charged exciton, the e-h exchange interaction also splits the exciton into a few states, but unlike the case of a neutral exciton, all states are now bright. That helps one to extract the parameters of the exchange interactions between the hole in the ground shell and the electron in the second shell from the photoluminescence (PL) spectra. An addition of Mn ions into the barrier layer close to the QD allows one to control the spin relaxation in the exciton complex and determine the fine structure of the doubly charged QD exciton. On the other hand, the strong sp-d exchange interaction of QD carriers with Mn ion spins can result in a qualitative change of the exciton level structure. To keep the sp-d exchange interaction weak, an intermediate nonmagnetic ZnSe barrier has been placed between the nonmagnetic CdSe QD and diluted magnetic semiconductor (DMS) barrier ZnMnSe.

1. Experiment and results

A sample with CdSe QDs in $Zn_{0.89}Mn_{0.11}Se$ barriers was grown by molecular beam epitaxy. Additional non-magnetic 1.75 nm thick ZnSe layers were placed on both sides of the QD. Chemical etching was used to achieve spatial resolution sufficient to study single QDs.

Experiments were carried out in superfluid liquid helium at $T = 1.8$ K. PL was excited by UV emission of a HeCd laser with intensity $J \approx 35$ W/cm^2 and collected in the direction normal to the sample surface. The spectra were analyzed using 0.6 m single monochromator with a CCD camera. Magnetic field up to 6 T was applied either perpendicular (Faraday geometry) or parallel (Voigt geometry) to the sample surface.

PL spectra from one of the single QDs are shown in Fig. 1. Without external magnetic field, the spectrum consists of two

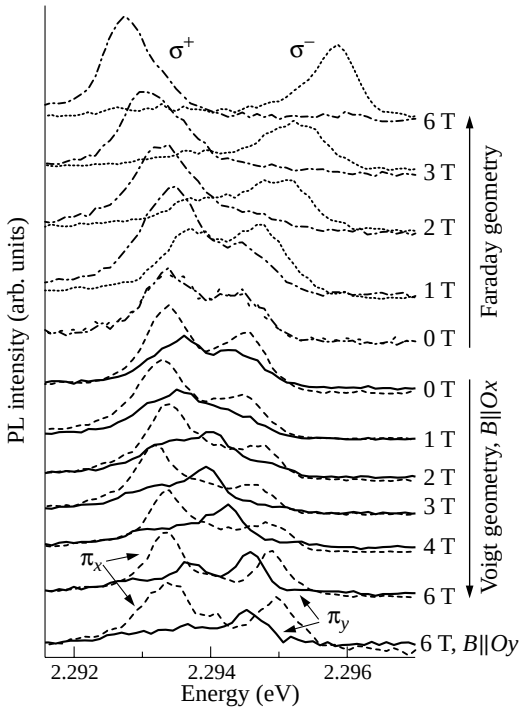

Fig. 1. Magneto-PL spectra of a doubly-charged QD. The spectra are recorded in two circular polarizations σ^+, σ^- in Faraday geometry and in two linear polarizations π_x, π_y in Voigt geometry ($Ox \parallel [110]$, $Oy \parallel [1\bar{1}0]$). Magnetic field is directed along Ox axis in range 0–6 T, additional spectra for $B = 6$ T along Oy are shown.

lines with splitting $\delta_0 = 1.1$ meV and spectral widths ~ 0.7 meV. Measurements performed in linear polarization showed however, that δ_0 varies slightly with an analyzer angle. Amplitude of this variation was found to be $\delta_1 \approx 150$ μeV, with extremal directions corresponding to [110] and [1$\bar{1}$0] crystallographic axes. This fact suggests that both lines have a doublet structure with splitting $\leq \delta_1$. For different investigated QDs δ_0 and δ_1 are in range 0.2−1.7 meV and 60−180 μeV, respectively. A relative intensity of a high-energy doublet increases with temperature, which indicates its origination from an excited state.

Magnetic field in Faraday geometry increases the splitting of both doublets. Fig. 1 shows that the intensity of two inner components rapidly decreases until they totally vanish at $B \approx 3$ T. Behavior of spectra in a Voigt geometry is more complicated. Fine structure of PL lines can't be resolved due to large spectral widths of components caused by fluctuation of Mn magnetization. In the highest magnetic fields only four

linearly polarized components are observed.

2. Discussion

Fine structure of PL from QDs presented above is inconsistent with that of neutral and single-charged QDs [2]. To explain it we assume that emission comes from QDs with two excess electrons X^{2-}. They are permanently trapped in the QD due to background n-type doping of the sample and form a singlet state. When e-h pair is localized in the doubly charged QD the third electron occupies an excited (second) shell due to Pauli principle. E-h exchange interaction appears only between the hole and electron with unpaired spins in the second shell. Thus the initial state of X^{2-} should resemble that of neutral exciton with a main e-h exchange splitting between the states with $J = 1$ and 2. When the hole recombines with one of electrons in the first shell two electrons remain in excited state that is split by an e-e exchange interaction into a singlet ($S = 0$) and triplet ($S = 1$) ones. It was shown [3] that the singlet state is well above the triplet one and has a short lifetime resulting in its strong broadening. Hence, we can attribute two observed lines with a relatively small splitting δ_0 to transitions from doubly charged exciton states with $J = 1$ and 2 into the triplet state of two electrons. Its energy subsequence will be determined below from magnetic field measurements.

Magnetic field normal to the QD plane splits both initial and final states of the transition. When Zeeman splitting exceeds the e-h exchange one, momentum projections become good quantum numbers and the transitions obey the spin selection rules. Energy level scheme and allowed optical transitions are shown in Fig. 2. Zeeman transition energies can be written as:

$$E_{J=1} = -\frac{\delta_0}{2} \pm \frac{1}{2}\sqrt{\delta_1^2 + (\mu\,(g_\mathrm{h} - g_\mathrm{e})\,B)^2}\,,$$
$$E_{J=2} = \frac{\delta_0}{2} \pm \frac{1}{2}\sqrt{\delta_2^2 + \left(\mu\left(g_\mathrm{h} - g'_\mathrm{e}\right)B\right)^2}\,,$$

where g_h, g_e, g'_e are effective g-factors accounting for the contribution from sp-d exchange interaction of QD carriers with Mn ion spins, respectively. It follows from the sequence of σ^+ and σ^- that $g_\mathrm{e} > 0$, $g'_\mathrm{e} > 0$ whereas $g_\mathrm{h} < 0$ and $|g_\mathrm{h}| > g_\mathrm{e}$. An opposite sign of g_h compared to that in nonmagnetic CdSe/ZnSe QDs is due to the effect of the p-d exchange interaction of a QD hole with neighboring Mn^{2+} ions that gives a large negative contribution to the hole g-factor [4]. Fitting gives: $|g_\mathrm{h}| + g_\mathrm{e} = 6.9$, $|g_\mathrm{h}| + g'_\mathrm{e} = 8.8$, so that $g'_\mathrm{e} - g_\mathrm{e} \approx 1.9$. We attribute this difference in g-factors to larger contribution of s-d exchange interaction for excited state, originating from larger penetration of the electron wave function into semimagnetic barriers.

As can be seen in Fig. 2, inner spectral components correspond to transitions from X^{2-} with excited electron spin (dashed lines), while outer ones (solid lines) correspond to those with the electron in the ground spin state. The vanishing of inner components in a magnetic field suggests that the electron spin relaxation time $\tau_{s,e2}$ is much smaller than exciton emission time τ_l. (Time resolved studies at zero magnetic field give $\tau_l \approx 300$ ps.) In contrast, similar intensities of outer Zeeman components in the whole range of magnetic fields indicate that the hole spin relaxation rate remains very weak even in the high magnetic fields.

Analysis of magnetic field dependencies of Zeeman polarized components' energies using scheme in Fig. 2 shows that

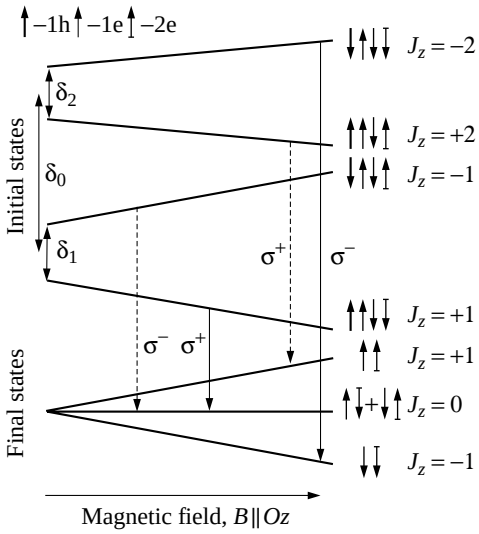

Fig. 2. Zeeman splitting of energy levels in Faraday geometry. Spin states are shown for hole (1h) $j_\mathrm{h} = \pm 3/2$, electron in first (1e) and second (2e) shells $s_\mathrm{e} = \pm 1/2$. Optically allowed transitions and their polarizations are represented by arrows. Dashed arrows correspond to transitions from the states with an electron in the excited spin state ($s_\mathrm{e} = +1/2$).

the lowest X^{2-} state has $J = 1$. That is opposite to the case of excitons in neutral QDs where the lowest state has $J = 2$. The reason for the opposite sign of δ_0 is not clear.

Figure 1 shows that the spectra in a Voigt geometry are more complicated as momentum projections on the growth axis are no longer good quantum numbers and all transitions are allowed. In high magnetic fields there remain only four strong components. These correspond to transitions from two states of doubly charged QD exciton with an electron in the lowest spin state and for each of them the hole can recombine with each of two electrons in the first shell.

3. Conclusions

The fine energy structure of doubly charged exciton in the QD and the effect of interaction with Mn ions on Zeeman splitting and spin relaxation have been determined basing on magneto PL measurements.

Acknowledgements

We thank S. V. Ivanov and A. A. Toropov for the QD samples, and A. Koudinov, K. Kavokin, and E. Ivchenko for helpful discussions.

References

[1] L. Jacak, P. Hawrylak, and A. Wojs, *Quantum Dots* (Springer-Verlag, Berlin, 1998).
[2] M. Bayer *et al*, *Phys. Rev. B* **65**, 195315 (2002).
[3] R. J. Warburton *et al*, *Nature* **405**, 926 (2000).
[4] J. K. Furdyna, *J. Appl. Phys.* **64**, R29 (1988).

15th Int. Symp. "Nanostructures: Physics and Technology"
Novosibirsk, Russia, June 25–29, 2007

Power dependence of photoluminescence from single hexagonal GaN quantum dots formed in an AlN matrix

K. S. Zhuravlev[1], V. G. Mansurov[1], A. Yu. Nikitin[1], M. Larsson[2] and P. O. Holtz[2]

[1] Institute of Semiconductor Physics, 13, Lavrentiev Avenue, 630090 Novosibirsk, Russia
[2] Linköping University, S-581 83 Linköping, Sweden

Abstract. In the present work we have studied the optical properties of single GaN/AlN quantum dots (QDs) grown by a particular MBE mode. Sharp emission lines have been found on the low energy side of a broad photoluminescence (PL) band originating from the QDs. Most of the PL lines do not shift with the excitation power while a peculiar PL line is considerably blue-shifted with increasing excitation power. The blue shift is interpreted as being due to local electric fields induced by charged defects placed in the vicinity of the QD.

Introduction

GaN-based quantum dots (QDs) are promising for applications in optoelectronic devices such as visible and ultraviolet (UV) light emitters, and infrared intersubband detectors. Localization of carriers into the QDs leads to a reduced internal quantum yield degradation of the light emitters due to a decreasing nonradiative recombination probability and to a reduced dark noise of detectors due to a decreasing probability of thermal ionization of confined charge carriers from the QDs.

Hexagonal GaN QDs are peculiar because of a giant internal electric field with a strength of several MV/cm, which is caused by the difference of both the spontaneous and piezoelectric polarizations between the barrier and the dot materials. This internal electric field strongly influences the properties of nitride based QDs, e.g. causing red-shifts of the transition energy, increasing the recombination carrier time. However, this field is partly screened by spatially separated excited carriers. It has been proposed that the screening of the internal electric field by non-equilibrium carriers causes a giant red-shift (at about 1 eV) of the photoluminescence (PL) spectrum from QDs formed in an AlN matrix at varying carrier densities in QDs [1]. To the best of our knowledge, this energy shift is the largest known for semiconductors structures. On the other hand, such a shift may be caused by other reasons, for example, a carrier lifetime dependent on the QDs size or by states filling. The uncertainty in the value of internal polarization field, its inhomogeneity, and nonuniformity of QDs make experimental investigations of screening effects in QDs difficult. Microphotoluminescence (μ-PL) spectroscopy is accordingly an important tool to reduce the number of QDs involved during an experiment and hence the effect of the size distribution.

1. Experimental

In the present work, we have studied the optical properties of GaN/AlN QDs grown by a particular MBE mode. Recently, we reported that self-organized GaN/AlN QDs could form without wetting layer at relatively low growth temperatures [2]. We have grown samples on sapphire (0001) substrates with a single layer of GaN QDs to decrease the volume probed in μ-PL experiments. The typical dot density measured by high resolution transmission electron microscopy is a few 10^{11} cm^{-2}. The mean height of the QDs is 1.3–0.2 nm and the mean aspect ratio (height/diameter) is about 1/3. The excitation of the μ-PL was carried out using a Nd:YAG laser with a wavelength of 266 nm (4.66 eV), i.e. a photon energy between the GaN (3.5 eV) and AlN (6.2 eV) band gaps. The laser spot was about 1.5 mm in diameter. The excitation power and sample temperature were varied. The μ-PL signal was detected by a liquid-nitrogen cooled UV-enhanced CCD camera.

2. Experimental results and discussion

PL spectra of our QDs samples contain a bright UV band, which position varies in the range of 3.3–4.0 eV with variation of the QDs size. A typical value of full width at half maximum (FWHM) of this PL band was about 400 meV. On the low energy side of this PL band, sharp emission lines have been observed. FWHM of these PL lines is less than 10 meV. With increasing temperatures, the narrow PL lines quench faster than the main PL band. We suppose that the narrow PL lines can originate from single QDs with larger sizes, or some strong localization centers, which have been observed earlier in InGaN/GaN QWs and QDs [3]. From the number of single emission lines which are detected in the illuminated area of the sample corresponding to the laser spot size the density of QDs/centers can be deduced to 10^9 cm^{-2}. Figure 1 shows μ-PL spectra taken at a temperature of $T = 4.5$ K for different excitation powers. It is seen from the figure that most of the PL lines do not shift with a varying excitation power (up to four orders of magnitude), while one PL line blue-shifts with increasing excitation power and vanishes under a neighbor PL line.

Nevertheless, one particular PL line is blue-shifted by about

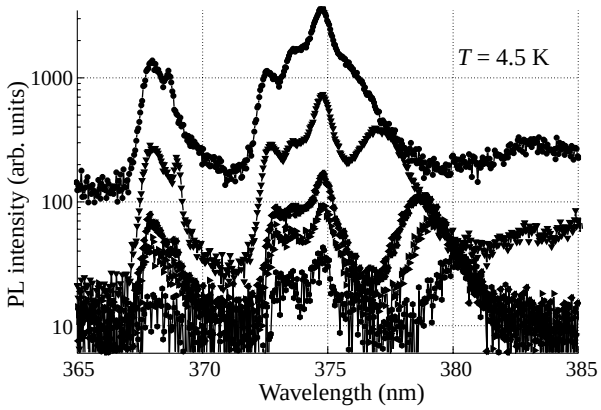

Fig. 1. PL spectra of GaN QDs for different excitation powers (with background subtracted), mW (bottom-up): 1.5, 2.6, 3.4, 24, 215.

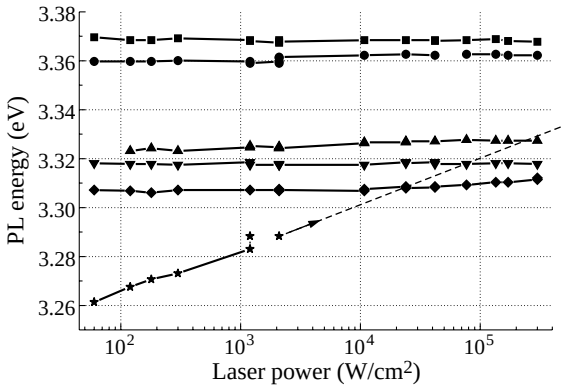

Fig. 2. Dependencies of PL line's energy position of the excitation power measured at $T = 5$ K.

25 meV with increasing excitation power (from 6×10^2 up to 6×10^2 W/cm^{-2}. It is seen from the Figure 2 that the power dependence for this PL line is not linear. The blue shift can be caused by local electric fields due to trapping of charge carrier at neutral defects at a distance of a few nm from the QD/center responsible for this line. Referring to recent works [5,6], we estimate that an electric field of strength of 200 kV/cm applied along the growth axis against the built-in field is needed to shift the excitonic transition by 25 meV. Such a field can be induced in the dot by a point charge placed at approximately 2.5 nm from the QD. A continuous nonlinear power dependence is consistent with the presence of a few defects located at different distances from the QD/center.

Acknowledgement

This work is supported by the RFBR (grant No. 05-02-16901).

References

[1] S. Kalliakos *et al*, *Appl. Phys. Lett.* **96**, 180 (2004).
[2] V. G. Mansurov *et al*, *Phys. Status Solidi C* **3**, 1548 (2006).
[3] K. Sebald *et al*, *Mater. Res. Soc. Symp. Proc.* **892**, 0892-FF25-02.1 (2006).
[4] J. Simon *et al*, *Phys. Rev. B* **68**, 035312 (2003).
[5] T. Nakaoka *et al*, *Phys. Rev. B* **73**, 121305R (2006).
[6] T. Nakaoka *et al*, *Physica E* **32**, 148 (2006).

15th Int. Symp. "Nanostructures: Physics and Technology"
Novosibirsk, Russia, June 25–29, 2007

Potential of nano structured composites for room temperature applications

E. Baskin, V. Garber, A. Fayer and N. Shuall
Sirica Corporation, 2 Hatamar St., Yoqneam 20692, Israel

The paper presents theoretical and experimental evidence of using nanostructures for nanoelectronics applications at room temperature (RT). These evidence are based on harnessing *stationary non-equilibrium* state of free carriers within nano inclusions embedded in host material. The concept is based on three typical time scales for such carriers: (a) energy relaxation time τ_ε; (b) the time of free carriers transition between neighboring inclusions $\tau_{\rm tr}$; and (c) the lifetime of non-equilibrium carriers inside the inclusions τ. The relations between these three time scales are governed by the size of the inclusions and the state of their surface.

If $\tau_{\rm tr} < \tau$, these inclusions can form percolation clusters although there is no real geometrical percolation in the system. For example, this effect may increase the efficiency of solar cells based on amorphous hydrogenated silicon (a-Si:H) with nano-scale inclusions of crystalline silicon (c-Si) [1].

If the lifetime of free carriers continuously pumped with external energy, is shorter than their energy relaxation time $\tau \ll \tau_\varepsilon$ ($\tau < \min(\tau_{\rm tr}, \tau_\varepsilon)$) they can recombine before thermalizing. This would result in a "nose-like" steady state energy distribution of non-equilibrium carriers. The maximum of this distribution is defined by the pumping energy $\hbar\omega_{\rm pm}$ and by the physical properties of the inclusions (i.e. bandgap energy $E_{\rm G}^{\rm in}$, free carriers effective mass m^*). The high-energy tail of this distribution has typical scale $T_{\rm eff}$ which is lower than the lattice temperature $T_{\rm L}$. This type of distribution can be used for detecting infra-red radiation at RT [2].

References

[1] E. Baskin, *J. Non-Cryst. Solids* **352**, 1117 (2006).
[2] Patent No. US 6,995,371 B2, dated Feb. 7 (2006).

15th Int. Symp. "Nanostructures: Physics and Technology"
Novosibirsk, Russia, June 25–29, 2007

The exiton potoluminescence spectrum of multilayer planarly ordered quantum dot InAs/GaAs at the hydrostatic pressure

V. A. Gaisin[1], V. G. Talalaev[1,2,3], B. V. Novikov[1], V. A. Shugunov[1], N. D. Zakharov[3], G. E. Cirlin[1,4,5], Yu. B. Samsonenko[4,5], G. G. Zegrya[4], R. M. Peleschak[4], O .O. Dankiv[4], A. A. Tonkikh[1,4,5], V. A. Egorov[4,5], N. K. Polyakov[4,5] and V. M. Ustinov[4]

[1] Institute of Physics State University St Petersburg, Russia
[2] Max Born Institut für Nichtlineare Optik und Kurzzeitspektroskopie, 12489 Berlin, Germany
[3] Max Planck Institut für Mikrostrukturphysik, 06120 Halle (Saale), Germany
[4] Ioffe Physico-Technical Institute, St Petersburg, Russia
[5] Institute for Analytical Instrumentation, Russian Academy of Science, St Petersburg Russia

Abstract. Photoluminescence spectra of InAs/GaAs quantum dot at $T = 77-300$ K were studied in the hydrostatic pressure range 0–20 kbar. The samples under study were grown by the molecular beam epitaxy method and were formed by 10 layers of InAs quantum dots separated by 7.5 nm GaAs spacer layers. The baric coefficients were found.

Introduction

Systems of self-assembled InAs quantum dots (QD's) have been intensively studied in recent years. Of special interest are the heterostructures involving the massive of planar and vertical bounded QDs. Planar and vertical bounded QDs structures are new quantum mechanical objects, that have considerable pramice for optoelectronics. Planar and vertical bounded QDs contains of 2 types species: i) the columns of QDs in contact with wetting layer (CQD), whose sizes increase monotonously in direction of growth axis with layer number and ii) QDs of large sizes, which are not closed by spacer layer and envelop next layers-associated (AQD). In [1,2] the dependence of baric coefficient (BC) on energy for two-dimensional massive of QDs was found out. The analogous anomalies of BC were found out in photoluminescence (PL) spectra of multiplayer structures with different distances between layers and in the transitions to ground states of quantum molecules [3].

In present papers the results of investigation of planar and vertical bounded QDs structures with maximum size for used method of synthesis and respectively with minimum energies of transitions to ground states are gives.

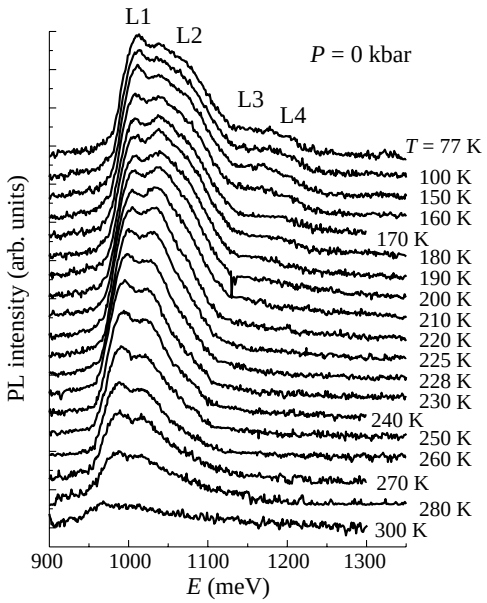

Fig. 1. The temperature dependences of PL spectra at $P = 0$ kbar at 77–300 K.

1. Experimental

The samples ware grown by MBE method and contained 10 layers of InAs QDs separated by 7.5 nm thin GaAs spaces layers [4]. Measurement ware performed at $T = 77$ K in the energy range 1.0–1.4 eV and hydrostatic pressure (P) was applied up to 16 kbar. The PL spectrum at $P = 0$ consists of wide slightly structured band (90–1300 meV) with maximum 1009 meV. As P increases the short-waved shift of the band is observed and its structure changes. Temperature increase gives rises to the band displacement of PL band to low-energy side. At $T > 200$ K the emission of short waved wing disappears completely. In Figs. 1 and 2, two series of PL spectra at $P = 0$ and 15.5 kbar at 77–300 K are given.

On the basic of analysis of PL spectra at different temperatures the separation of spectra into components (L1, L2, L3, L4 lines) has been performed and dependences of spectral position of their maximum on applied hydrostatic pressure have been constructed. Their baric coefficients (BC), BC(L1) = 5.24 meV/kbar, BC(L2) = 5.38 meV/kbar, BC(L3) = 4.68 meV/kbar, BC(L4) = 6.1 meV/kbar, have been defined. A correlation has been obtained between the results and date measured previously (Fig. 3). BC of L1 and L2 lines are well within the linear dependency BC(E); BC of L3 and L4 lines depart very appreciably from this dependence. It was supposed formerly that BC anomalies are due to internal strain in QD and barrier, resulting in an additional contribution to the transition energy. The value of this contribution is proportional to total energy in the range of wave function localization. The external hydrostatic pressure decreases the range of localization owing to lattice constants decrease and as a result decreases the additional contribution to the energy in strained QD and consequently values of the transition energy and BC. Evidently the value of the additional has to be more and the value of BC is less for the QD of lager size. The calculations carried out by G. G. Zegrya, R. M. Peleschak and O. O. Dankiv with regard to deformation effects the model of InAs QD confirmed into InAs/GaAs heterostructures was constructed in framework of with the dependence of BC on sizes R0 was calculated.

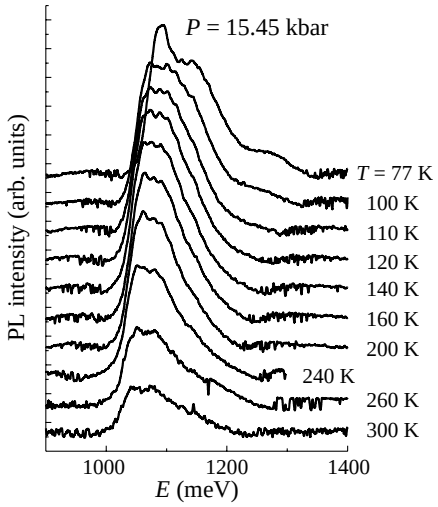

Fig. 2. The temperature dependences of PL spectra at $P = 15.5$ kbar at 77–300 K.

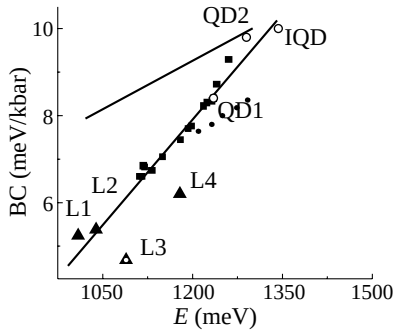

Fig. 3. Dependence of BC on the energy of transition to ground state for QDs on vicinal QD1, QD2 and IQD [1], singular [2] surfaces and planar and vertical bounded QDs L1,L2,L3,L4. The upper line is the numerous calculations carried out for QD with energy transition to ground state 1.2–1.3 eV.

The numerous calculations carried out for QD with energy transition to ground state 1.2–1.3 eV were found to be in good agreement with character of dependence of BC on sizes, the experimental and calculated corves have similar slopes. The same unusual energy dependence of BC on energy in multilayer (2 and 10 layers) allow to suppose that the BC(E) is connected with the distribution of tensions in plane layers on which two-dimensional massives of QD are formed. Such supposition explains the lack of deviation from dependences BC(E) obtained previously for 2 layer massive, for the planar ordering of QDs proposes the change of character of distribution of internal tensions in direction of growth axis compared to that in isolated QDs. The good agreement between experimental and calculated values of BC of L2 allows to interpret this eviation of BK value in L4 from the BK(E) dependence is due to the difference of QD form from the typical for isolated QDs form — proper pyramid in which a height is equal to half a base side. The increase of geometric sizes of QD both in plane of layer and in the direction perpendicular to it as a number of layers increases is typical for manylayer structures. This results in the relative decrease of pyramid height in comparison with its base side. At same value of BK the energy of transition to ground state increases.

2. Conclusions

The investigation of temperature and baric dependences of PL spectra allowed to divide the complex band into components — L1–L4 lines and to measure their BC. The following conclusions was drawn: baric coefficient in QD do not coincide with those in bulk InAs (11.6 meV/kbar) and in bulk GaAs (10.4 meV/kbar) — their values are found to be approximately half as much as those expectancy (5.23 meV/kbar, 5.28 meV/kbar, 4.68 meV/kbar and 6.1 meV/kbar for lines L1, L2, L3 and L4. These results confirmed the anomalous dependence of one of fundamental characteristics of matter on the wavelength of observation.

Acknowledgement

This work was supported by the Russian Foundation for Basic Research (grant No. 05-02-17780).

References

[1] V. A. Gaisin *et al*, *Vest. St Petersburg Univer. ser. 4. Fyzika, himiya. vip. 4* **25**, 65 (2000).
[2] V. A. Gaisin *et al*, *Vest. St Petersburg Univer. ser. 4. Fyzika, himiya. vip. 2* **12**, 115 (2001).
[3] V A. Gaisin *et al*, *Proc. 13th Int. Symp. "Nanostructures: Physics and techology"* **175/176**, 352 (2005).
[4] V. G. Talalaev *et al*, *Appl. Phys. Lett.* **85**, 284 (2004).

15th Int. Symp. "Nanostructures: Physics and Technology"
Novosibirsk, Russia, June 25–29, 2007

Cyclotron resonance in InAs/AlSb QW heterostructures in high magnetic fields

M. L. Orlov[1,4], *A. V. Ikonnikov*[1], Yu. B. Vasilyev[2], S. S. Krishtopenko[1], V. Ya. Aleshkin[1], Yu. G. Sadofyev[1], V. I. Gavrilenko[1], M. L. Sadowski[3] and W. Knap[4]

[1] Institute for Physics of Microstructures of Russian Academy of Sciences, 603950 N. Novgorod, Russia
[2] Ioffe Physico-Technical Institute, St Petersburg, Russia
[3] Grenoble High Magnetic Field Laboratory, CNRS, Grenoble, France
[4] GES, University of Montpellier 2 & CNRS, Place Eugene Bataillon, 21, F34095, Montpellier, France

Abstract. Cyclotron resonance in InAs/AlSb quantum well heterostructures in quantizing magnetic fields up to 13 T under visible light illumination was studied for the first time. In the sample grown on GaSb buffer the transition energies between the lowest Landau levels are shown to depend on electron concentration. Additional cyclotron resonance line splitting resulted from the polaron effect was found.

Introduction

InAs/AlSb quantum well (QW) heterostructures exhibit a number of remarkable properties such as high electron mobility (up to 9×10^5 cm^2/V s at $T = 4.2$ K [1]), low electron effective mass ($0.03m_0$) and large electron effective g^*-factor [2] that makes them promising for various electronic, optoelectronic and spintronic devices. Cyclotron resonance (CR) is an effective tool for studying both the conduction band nonparabolicity and the spin-related phenomena [3–7]. In this paper we present results of CR measurements in InAs/AlSb QWs in magnetic fields up to 13 T, the illumination with visible light being used to change the electron concentration in QW due to the negative persistent photoconductivity (NPPC) effect [8].

1. Experimental

InAs/AlSb heterostructures under study were grown by MBE technique on semi-insulating GaAs(100) substrates on thick metamorphic AlSb (or GaSb in the case of B824 sample) layer followed by a ten-period smoothing GaSb/AlSb super-lattice [2]. The active part of the structure consists of a lower AlSb barrier 12 nm wide, an InAs QW with a nominal thick-ness of 15 nm, an upper AlSb barrier 30 to 40 nm wide and a GaSb cap layer 6 nm wide. CR spectra were measured with Bruker 113V FT spectrometer. We used square samples with an area 5.5 mm^2 with two strip ohmic contacts for magnetoresistance measurements. The samples were mounted in the light-pipe insert in the liquid helium cryostat in the center of superconducting solenoid, the sample can be illuminated either by blue LED or by green light via optical fiber. In our setup we have to illuminate the sample with visible light permanently to decrease the electron concentration due to NPPC effect probably because of parasitic IR background. All measurements were carried out at $T = 2$ K. The radiation transmitted through the structure was detected with a Si composite bolometer. Transmission signals measured in magnetic fields were normalized to that measured in the absence of the magnetic field. The two-terminal magnetoresistance of the samples was recorded to determine the two-dimensional (2D) electron concentration before and after illumination.

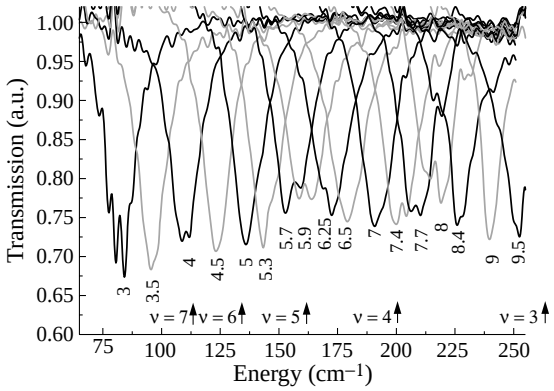

Fig. 1. CR spectra in the sample A692 ($n_s = 7.1 \times 10^{11}$ cm^{-2}) measured at different magnetic fields (the field values in Tesla are given below the curves). Arrows indicate integer values of the LL filling factor ν.

2. Theory

To calculate Landau levels (LLs) in rectangular InAs/AlSb QW we used 8-band Kane model [9] accounting the deformation terms and electron magnetic moment interaction with the magnetic field [10]. The calculations were performed using the transfer matrix technique neglecting in the Hamiltonian the terms proportional to the square of the hole wavevector. The InAs lattice constant in the plane of the structure was assumed to be equal to that of AlSb or GaSb. Also we calculated LLs for the self-consistent QW profile (cf. [11]). We found that the band bending as well as deformation term practically does not affect LLs spectra in the 1st subband, but significantly changes the intersubband spacing that is to be taken into account for doped samples (cf. [7]).

3. Results and discussion

The measured CR spectra in the sample A692 are given in Fig. 1. It is clearly seen that a marked CR line splitting is observed at the integer values of LL filling factor $\nu = 4, 5, 7$ that is a typical Δm^* and Δg^* CR line splitting in quantizing magnetic fields at odd and even ν respectively (cf. [3–5]). The measured CR line energies as well as calculated transition energies between the lowest LLs versus the magnetic field are presented in Fig. 2. It's clearly seen that in magnetic fields

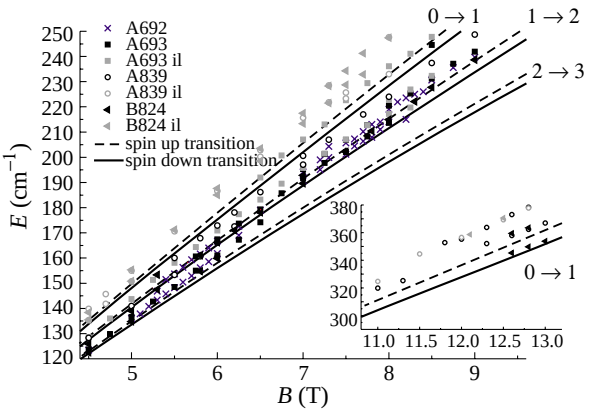

Fig. 2. Spectral positions of the observed CR lines in different InAs/AlSb samples with the dark electron concentration about 7.1×10^{11} cm^{-2} (symbols) versus the magnetic field ("il" means measurements under illumination with visible light). Lines correspond to calculated CR transitions between the lowest LLs pairs.

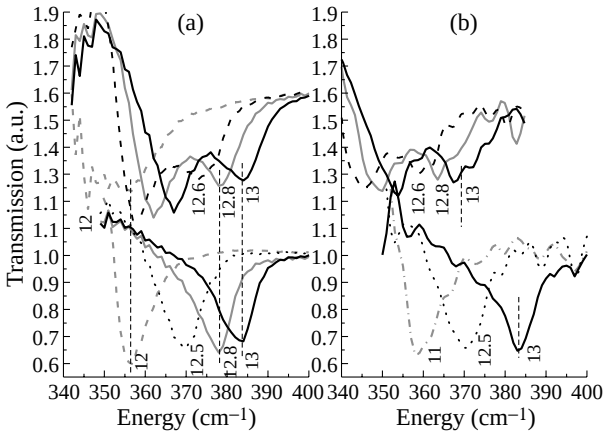

Fig. 3. CR spectra in the samples A839 (a) and B824 (b) before (upper curves) and under (lower curves) illumination by blue LED (magnetic field values in Tesla are given below the curves).

up to 9 T the experimental data (before the illumination with visible light) are in a good agreement with calculations results for most of the samples. In the magnetic fields up to 6 T the CR absorption results from $2 \rightarrow 3$ transitions, at higher fields up to 9 T $1 \rightarrow 2$ ones dominate and over 11 T we observe the $0 \rightarrow 1$ transitions from two lowest spin-split LLs. Some systematic discrepancies between measured and calculated line positions could result from a deviations of the actual InAs QW width form its nominal value of 15 nm.

Fig. 3 illustrates the effect of illumination by blue LED on CR spectra in the samples A839 & B824 in ultra quantum limit ($0 \rightarrow 1$ transitions). In the dark 2D electron concentrations in these samples were 7.0×10^{11} cm^{-2} and 6.8×10^{11} cm^{-2} respectively. Under the illumination it was 3.5×10^{11} cm^{-2} in both samples. Before the illumination in the magnetic fields of Fig. 3 12 to 13 T the LL filling factor ν is a little bit over 2 and two CR lines corresponding $0 \rightarrow 1$ transitions from two lowest spin-split LLs are observed (see insert in Fig. 2, cf. [5]). Under the illumination the concentration decreases 2 times ($\nu \sim 1$) and the upper (spin down) 0^{th} LL is practically depopulated. So only spin-up $0 \rightarrow 1$ transition is observed. In the sample A839 its spectral position is just the same as in the dark. However in the sample B824 it shifts by 15 cm^{-1} to the higher energy (and

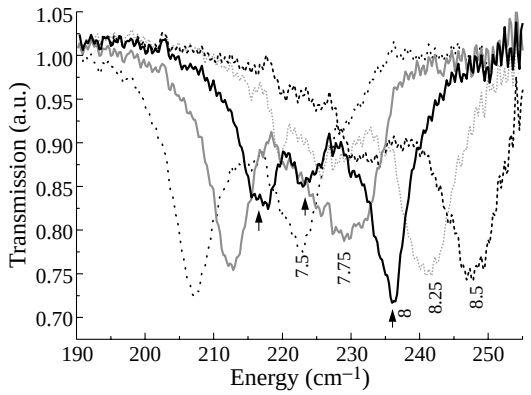

Fig. 4. CR spectra in the sample A693 under permanent illumination by green light ($n_s = 5.6 \times 10^{11}$ cm^{-2}; magnetic field values in Tesla are given below the curves). It's clearly seen that 3 absorption lines present in the 8 T spectrum.

its position now coinsides with that in the sample A839). The only apparent reason of such a varied behavior is the different buffer layers: AlSb in the sample A839 and GaSb B824 one. Evidently, this problem requires further studies.

In the sample A693 under green light illumination in magnetic fields in between 7.5 and 8.5 T ($\nu \sim 3$) we observed an additional splitting of the CR line — Fig. 4 (cf. [12]). In other samples in this spectral range we observed a marked CR line broadening. The initial CR line splitting (e.g. at 7.5 and 8.5 T in Fig. 4) into two lines at $\nu \sim 3$ (Δm^* splitting) results from the difference in the energies of $0 \rightarrow 1$ and $1 \rightarrow 2$ transitions due to the conduction band nonparabolicity. The additional splitting seems to result from the polaron effect (electron-LO phonon interaction) that is observed near the photon energy 227 cm^{-1}. This value is less than LO-phonon energy in InAs 243 cm^{-1} and is close to the TO-phonon energy 217 cm^{-1} that is attributed to the strong screening effects of 2D electron gas (cf. [4]).

Acknowledgements

This work was financially support by RFBR(grants 05-02-17531, 07-02-01382), INTAS (YS Fellowship 04-83-3169) and by Russian Academy of Sciences. The measurements at GHMFL are supported by EC from the 6^{th} framework program "Transnational Access Specific Support Action", contract No. RITA-CT-2003-505474 (ref SE3806).

References

[1] C. Nguyen *et al*, *J. Electron. Mater.* **22**, 255 (1993).
[2] Yu. G. Sadofyev *et al*, *Appl. Phys. Lett.* **81**, 1833 (2002).
[3] J. Scriba *et al*, *Semicond. Sci. Technol.* **8**, S133 (1993).
[4] M. J. Yang *et al*, *Phys. Rev. B* **47**, 1681 (1993).
[5] M. J. Yang *et al*, *Phys. Rev. B* **47**, 6807 (1993).
[6] Y. B. Vasilyev *et al*, *JETP Lett.* **79**, 674 (2004).
[7] V. Ya. Aleshkin *et al*, *Semiconductors* **39**, 71 (2005).
[8] V. Ya. Aleshkin *et al*, *Semiconductors* **39**, 30 (2005).
[9] E. O. Kane, *J. Phys. Chem. Solids* **1**, 249 (1957).
[10] H.-R. Trebin *et al*, *Phys. Rev.* **20**, 2 (1979).
[11] R. Winkler, *Surf. Sci.* **361/362**, 411 (1996).
[12] C.-M. Hu *et al*, *Phys. Rev. B* **67**, 201302 (2003).

15th Int. Symp. "Nanostructures: Physics and Technology"
Novosibirsk, Russia, June 25–29, 2007

Photoelectric properties of heterostructures with multylayer self-assembled InAs/AlAs QDs

S. V. Karpov[2], V. A. Gaisin[2], T. S. Shamirzaev[1], K. S. Zhuravlev[1], B. S. Kulinkin[2], B. V. Novikov[2], S. V. Mikushev[2], A. S. Batyrev[2], E. V. Ubyivovk[2] and V. M. Alzheev[2]

[1] Institute of Semiconductor Physics, pr. Lavrentieva 13, 630090 Novosibirsk, Russia
[2] Fock Institute of Physics, St Petersburg State University, 198904 St Petersburg, Russia

Abstract. Effect of an electric field applied along the growth direction of the structure on photoluminescence (PL) and photoconductivity (PC) of multiplayer structure with InAs/AlAs QDs was studied. Bands relating to transitions at QDs, spacer layers of AlAs and buffer layer of GaAs was observed in PC spectra at spectral region of 500–800 nm. An oscillation of PL intensity along the spectrum connected with Franz–Keldysh effect in cap GaAs layer was observed under electric field of 30 kV/cm.

Introduction

Systems of self-assembled InAs quantum dots (QD's) have been intensively studied in recent years due to its importance for fabrication micro- and optoelectronic devices [1]. The most investigated system with such QD's is system of InAs QD's embedded in GaAs matrix. The system of InAs QD's embedded in AlAs matrix is very close to the system of InAs/GaAs QD's from point of view of the Stranski–Krastanov growth mode, since AlAs has practically the same lattice constant as GaAs. However the system of InAs/AlAs QD's demonstrates millisecond recombination dynamics and strong no-monotonic shift of photoluminescence (PL) band with change in excitation power density the quite different from that of the InAs/GaAs QD's system. Recently we explain these differences by feature of energy levels structure in heterostructure with InAs/AlAs QDs [2]. In present work, in order to obtain additional information about structure of energy levels in heterostructure with InAs/AlAs QD's we study photoluminescence and photoconductivity (PC) of this structure under electric field (E) applied along growth direction.

1. Experimental

Structure with self-assembled InAs/AlAs QDs was grown by the molecular beam epitaxy on semi-insulating (001)-oriented GaAs substrates using a Riber-32P system. The structure consists of five layers of InAs QDs separated by 8 nm thick AlAs spacer layers. The QD layers were deposited with a nominal amount of InAs of 2.5 monolayers (ML). A 20 nm GaAs cap layer was grown on top of the structure in order to prevent oxidation of AlAs. In order to apply electric field (0–30 kV/cm) the samples are pressed to quartz plate covered with translucent contact of SnO_2. Backside of the sample was covered by silver past to form the opposite contact. The radiation of a He-Cd laser (441.6 nm) was used to excite PL.

2. Results and discussions

PC spectra of the structure with QDs measured at temperatures of 77 K and 300 K and different strength of E are shown in Fig. 1. The PC spectra contain several broad bands related to transitions in: (i) spacer layers of AlAs (in spectral region $>$2.2 eV), (ii) wetting layer ($h\nu = 2.1$ eV); and (iii) QDs (in spectral region of 1.4–2 eV).

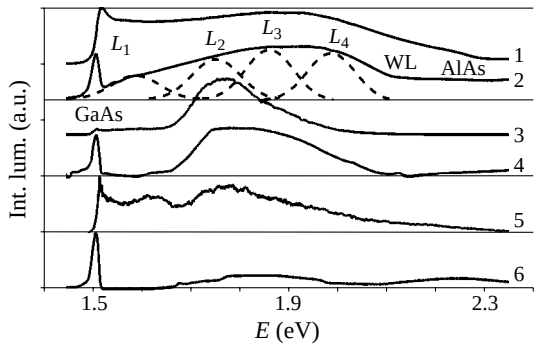

Fig. 1. PC spectra of the structure measured at different T and E: 1 — 300 K E — 3 kV/cm; 2 — 300 K, E — 5 kV/cm; 3 — 77 K, E — 6 kV/cm; 4 — 77 K E — 4 kV/cm; 5 — 77 K, E — 2 kV/cm; 6 — 77 K, E — 0.5 kV/cm.

Two bands L_1 ($h\nu = 1.628$ eV) and L_2 ($h\nu = 1.764$ eV) in PC spectra have, while the other two L_3 ($h\nu = 1.884$ eV) and L_4 ($h\nu$=1.991 eV) have not the counterparts in the PL spectra. Relative intensity of the bands L_3 and L_4 increase with increasing in temperature or with increasing in apply electric field above 3 kV/cm. Clearly registered signal of PC evidences that QDs and WLs belonged to different layers are vertically coupled and form superlattice with mini-bands produced by states of electrons and holes in QDs. The relatively large intensity of the L_1 and L_2 bands at low temperature or relatively small electric field demonstrates that mini-bands formed by the ground states of electrons and holes in QDs provide larger conductivity of the carriers than that of excited states. We suppose that this difference in conductivity is a result of change in QDs size form layer to layer that takes place in multiplayer structures [3]. The difference in QDs size results in energy difference of electronic layers for QDs in different layers. This energy difference increases for excited levels that hamper to move the carriers across layers via states of the excited levels. We suppose that the signal related to light absorption in excited levels of QDs arises due to relaxation of the carries from excited to ground states of QDs with next transport across layers via these ground states. The rate of the relaxation increase with increase in temperature or electric field strength that results in increase relative intensity bands L_3 and L_4 connected with excited states of QDs. Formation of coupled states across layers of QDs means that shift of the PL line with changing in excitation density observe in Ref. 2 can be explain by redistribution

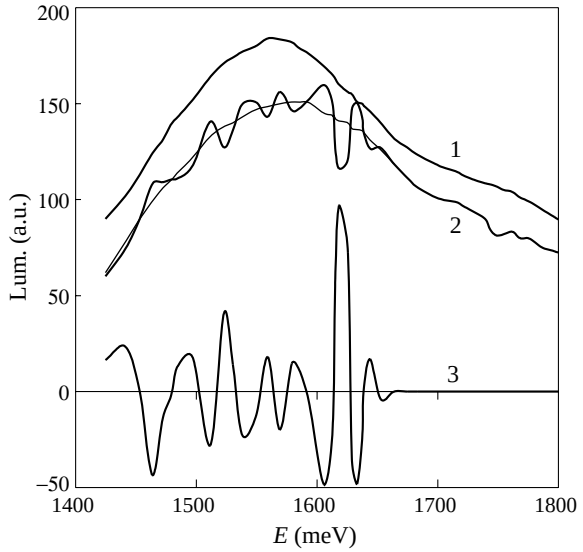

Fig. 2. PL spectra of InAs/AlAs QD's measured at 77 K at E kV/cm: 1 — 0, 2 — 30, 3 — an additional absorption causes by FK effect.

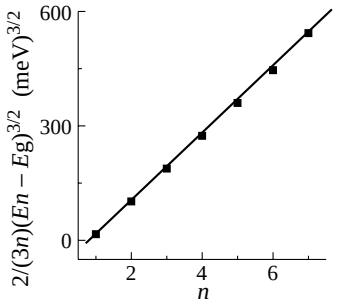

Fig. 3. Energy positions of FK oscillation extremums (E_n) for E with strength of 30 kV/cm. The points are experimental data, and the slope of the solid line corresponds to $E = 30.2$ kV/cm in accordance with calculation with using a theory from Ref. 4.

of carriers between adjacent QDs not only in plane of the QDs growth but also between layers.

Fig. 2 shows PL spectra of InAs/AlAs QD's measured at 77 K with (curve 2) and without (curve 1) applying of E with strength of 30 kV/cm. We subtract curve 1 form curve 2 and built differented spectrum depicted in Fig. 2 as curve 3. One can see that electric field results in decrease of the PL intensity. Besides, application of the electric field leads to appearance of an oscillation of PL intensity along the spectrum. We suppose that the oscillation is a result of spectral modulation of light absorption in cap GaAs layer due to Franz–Keldysh (FK) effect [4]. In order to test this supposition we calculate absorption causes by FK effect in layer of GaAs with thickness 20 nm equals to thickness of cap layer of our structure. Calculated energy positions of FK oscillation extremums $E_n - E_g$, where E_g is a bang gap of the layer and n is number of extremum, for E with strength of 30 kV/cm are demonstrated Fig. 3. The slope of the line fitted via experimental data corresponds to electric field with strength of 30.2 kV/cm in accordance with calculation with using a theory from Ref. 4. One can see that the calculated value of E is in good agreement with experimental data.

3. Conclusions

Photoluminescence and photoconductivity at the temperature of 77 K and 300 K heterostructures with five layers of InAs/AlAs QDs have been studied. The PC bands related to transitions in spacer layer of AlAs, wetting layer and QDs have been observed. We showed that the QDs belonged to different layers are vertically coupled and that PC bands connected with QDs results from light absorption at ground and excited levels of QDs. The oscillation of intensity arises along PL spectra at application of the electric field explain by modulation of light absorption in cap GaAs layer due to Franz–Keldysh effect.

Acknowledgements

This work has been supported in part by the Deutsche Forschungsgemeinschaft and RFBR grant No. 07-02-00134 and No. 07-02-00564.

References

[1] D. Bimberg, M. Grundmann, and N. N. Ledentsov, *Quantum Dot Heterostructures* (Wiley, New York, 1999).
[2] T. S. Shamirzaev, A. M. Gilinsky, A. I. Toropov, A. K. Bakarov, D. A. Tenne, K. S. Zhuravlev, C. von Borczyskowski, and D. R. T. Zahn, *JETP Lett.* **77**, 389 (2003).
[3] N. N. Ledentsov, V. M. Ustinov, V. A. Shchukin, P. S. Kop'ev, Zh. I. Alferov and D. Bimberg, *Semiconductors* **32**, 343 (1998).
[4] J. Hader, N. Linder, G. H. Döhler, *Phys. Rev. B* **55**, 6960 (1997).

15th Int. Symp. "Nanostructures: Physics and Technology"
Novosibirsk, Russia, June 25–29, 2007

Ferromagnetism and anomalous magnetotransport in GaAs structures with InAs quantum dots or GaAs/$In_xGa_{1-x}As$/GaAs quantum well delta-doped with Mn and C

V. A. Kulbachinskii[1], P. S. Gurin[1], R. A. Lunin[1], I. S. Vasil'evskii[1], O. V. Vikhrova[2], Yu. A. Danilov[2], B. N. Zvonkov[2], Y. Horikoshi[3] and K. Onomitsu[3]

[1] M. V. Lomonosov Moscow State University, Low Temperature Physics Department, 119992, GSP-2, Moscow, Russia
[2] Physico-Technical Research Institute, University of Nizhny Novgorod, 603950, Nizhny Novgorod, Russia
[3] School of science and engineering, Waseda university, 3-4-1, Okubo, Tokyo 169-8555, Japan

Abstract. We report on the transport, magnetotransport and magnetic properties of two type structures: i) with a layer of InAs quantum dots (QD) embedded in GaAs matrix and ii) with $In_{0.17}Ga_{0.83}As$ quantum well (QW) in GaAs. Both types of structures were δ-doped by Mn and carbon to provide magnetic properties and enhanced p-type conductivity. The ferromagnetic phase up to 400 K was detected by SQUID magnetometer. Anomalous Hall-effect and negative magnetoresistance was observed at low temperatures.

Introduction

Mn-doped GaAs is an attractive diluted magnetic semiconductor (DMS) for a new spin-based electronics. It has been shown that the Curie temperature (T_c) in $Ga_{1-x}Mn_xAs$ can be raised by increasing the hole concentration as well as Mn concentration [1]. Although Mn acts as an acceptor in GaAs, the hole activation ratio is much less than unity and the hole concentration tends to saturate due to the compensation of Mn acceptors by the defects [2]. Therefore, some additional doping of acceptor impurity is needed to achieve a high hole concentration. One of the method is the molecular beam epitaxy growth of the GaAs based heterostructures. Such procedure leads to the value of $T_c = 250$ K [3].

In the present study we investigated the influence of Mn delta-doping on magnetic and galvanomagnetic properties of GaAs structures with InAs quantum dot layer or GaAs/$In_xGa_{1-x}As$/GaAs quantum well.

1. Samples and experimental

All samples were prepared with the combined method of MOC-hydride epitaxy and laser deposition. This method of fabrication of structures has been published previously [4]. Samples were grown on GaAs (100) substrate and contain InAs quantum dot layer, carbon δ-layer (to provide enhanced p-type conductivity in the quantum dot layer) and laser-deposited Mn layer separated by GaAs spacers with width d=10 nm. A schematic diagram of the structure is given in Fig. 1. In $In_xGa_{1-x}As$ quantum well ($x \approx 0.17$) with width 10 nm, laser-deposited Mn layer was separated by $d = 3$ nm GaAs spacer. The Mn concentration controlled by duration time of Mn laser-deposition. Thus Mn concentration was different in the samples. Temperature dependence of resistance was measured in the temperature interval of 4.2–300 K, magnetoresistance and Hall effect for $4.2 \le T \le 77$ K in magnetic fields up to 6 T. Some parameters of the samples with quantum dot layer are listed in Table 1 and with quantum well in Table 2. For measurements of the magnetization in the temperature interval 4.2–400 K in magnetic fields up to 7 T, a SQUID magnetometer was used. The measurements were performed by applying the magnetic field parallel to the surface of samples. Temperature dependences of resistance have been measured in the temperature range $4.2 \le T \le 300$ K. Magnetoresistance and Hall effect have been measured by a conventional four probe technique in the temperature range $4.2 \le T \le 300$ K in magnetic field B up to 6 T applied perpendicular to the sample surface.

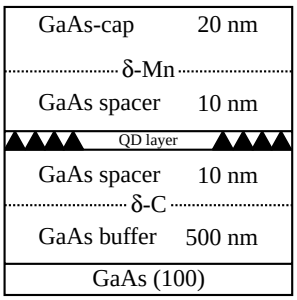

Fig. 1. Schematic diagram of GaAs structure with InAs quantum dot layer.

2. Results and discussion

All samples had p-type conductivity. When temperature decreased sheet resistivity R_S samples increased (Fig. 2). In the temperature range between 50 and 110 K a kink is visible in $R_S(T)$, which is a characteristic of the ferromagnetic transition [5]. At $T < T_c$ the spin flip scattering disappears [6], mobility increases and resistance decreases. This effect results in a kink for an activation type of the experimental dependence of $R_S(T)$ as we have observed.

All samples showed ferromagnetism, as indicated by hys-

Table 1. Duration of Mn deposition t_{Mn}, Hall density p, Hall mobility μ at $T = 300$ K and 4.2 K for QD structures.

No	t_{Mn} (s)	p (300 K), (10^{12} cm^{-2})	μ (300 K) (cm^2/V s)	p (4.2 K) (10^{12} cm^{-2})	μ (4.2 K) (cm^2/V s)
612	0	0.3	200	—	—
615	0.5	1.7	450	1.8	2580
616	1	3.7	285	1.5	3270
617	2	4.0	330	1.6	490

Table 2. Duration of Mn deposition t_{Mn}, Hall density p, Hall mobility μ at different temperatures for QW structures.

No	t_{Mn} (s)	p (300 K) (10^{12} cm^{-2})	μ (300 K) (cm^2/V s)	μ (cm^2/V s)	p (10^{12} cm^{-2})
415	0	1.8	300	—	—
419	2	3.4	450	4670 (4.2 K)	0.35 (4.2 K)
420	4	5.7	190	1930 (77 K)	1.2 (77 K)
417	6	6.8	160	1920 (77 K)	1.4 (77 K)
421	8	7.9	150	95 (16 K)	0.58 (16 K)

teresis loop in the magnetization (all samples studied showed qualitatively similar magnetic behavior). The hysteresis loops show clear temperature dependence over the entire range of temperatures studied for QW samples, as can be seen in Fig. 3 for sample 419. In insert to Fig. 3 we plot magnetization of saturation on temperature. There are different magnetic phases in the samples, one with T_c about 70 K, others with T_c above room temperature. The first value of T_c is very typical for hole mediated ferromagnetism in $Ga_{1-x}Mn_xAs$ solid solutions. Next phase is due to formation of MnAs clusters. The Curie temperature for bulk MnAs is about 315 K. Above this temperature ferromagnetism survived die to $Ga_{1-x}Mn_x$ clusters. T_c for such clusters depends on Mn content and may be as high as 600 K for $x = 0.6$ [7].

One of the manifestation of the existence of the spin-polarized carriers is the anomalous Hall effect [8]. In investigated structures anomalous Hall effect appears at the temperature interval 25–80 K. Above 80 K we observed in structures only ordinary Hall effect in spite of the ferromagnetism in clusters of MnAs and $Ga_{1-x}Mn_x$. Hole mobility in QD samples less as compared with QW samples due to additional disorder introduced by QD in the conducting layer. But anomalous Hall effect was observed in the same temperature range, magnetic properties, $R_S(T)$ dependences and magnetoresistance are very similar.

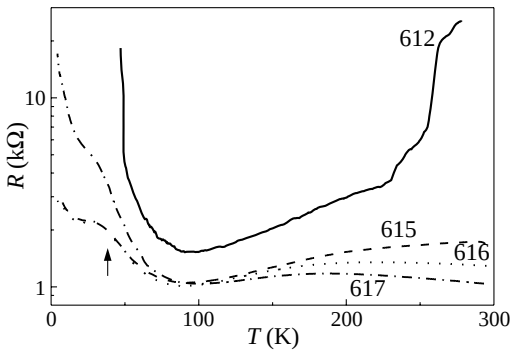

Fig. 2. Temperature dependence of sheet resistivity R_S for QD samples (arrow marks a kink, see text).

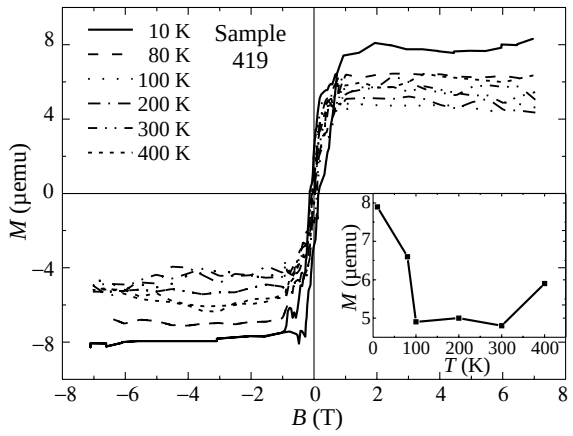

Fig. 3. Magnetization loops at different temperatures for sample 419 (diamagnetic background was subtracted). Insert shows the magnetization of saturation as a function of temperature.

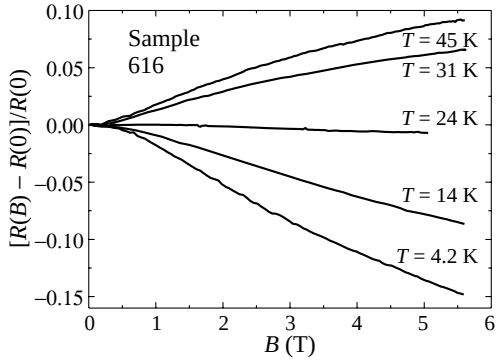

Fig. 4. Magnetoresistance of sample 616 at different temperatures.

Magnetoresistance in all samples changes a sign from negative to positive when temperature increases. In the temperature interval 4.2–30 negative magnetoresistance is observed, transferring to the positive magnetoresistance. At temperatures above 30 K it is observed positive magnetoresistance. As an example in Fig. 4 we plot magnetoresistance of sample 616 at different temperatures. Complicated dependence of resistance on magnetic field may be explained by the contribution to magnetoresistance spin-dependent scattering of carriers for two phase sample [9]. In our opinion, the observable experimental facts testify that the presence of the fluctuation potential in the 2D channel of the structures, formed by QD layer or quantum well, *caused by non- uniform distribution of Mn ions* plays a significant role in the magnetotransport phenomena.

Acknowledgements

The work was supported by RFBR, grants 04-02-19964a, and 05-02-17021a.

References

[1] T. Jungwirth, Jairo Sinova, J. Mašek, J. Kučera, and A. H. MacDonald, *Rev. Mod. Phys* **78**, 809 (2006).
[2] H. Shimizu, T. Hayashi, T. Nishinaga, and M. Tanaka, em Appl. Phys. Lett. **74**, 398 (1999).
[3] A. M. Nazmul, T. Amemiya, Y. Shuto, S. Sugahara, and M. Tanaka, *Phys. Rev. Lett.* **95**, 017201 (2005).
[4] Yu. V. Vasilieva, Yu. N. Danilov, Ant. A. Ershov *et al*, *FTP* **39**, 87 (2005).
[5] F. Matsukura, H. Ohno, A. Shen, and Y. Sugawara, *Phys. Rev. B* **57**, R2037 (1998).
[6] M. N. Baibich, J. M. Broto, A. Fert *et al*, *Phys. Rev. Lett.* **61**, 2472 (1988).
[7] M. Tanaka, J. P. Harbison, J. De Boeck *et al*, *Appl. Phys. Lett.* **62**, 1565 (1993).
[8] B. A. Aronzon, V. A. Kulbachinskii, P. V. Gurin *et al*, *Pisma v ZETF* **85**, 32 (2007).
[9] A. O. Sboichakov, A. L. Raikhmanov, K. I. Kugel *et al*, *JETP* **95**, 753 (2002).

15th Int. Symp. “Nanostructures: Physics and Technology”
Novosibirsk, Russia, June 25–29, 2007

Anomalous absorption in CdSe/ZnS quantum dots: the effect of intensity dependent exciton lifetime

V. S. Dneprovskii, *D. A. Kabanin*, V. L. Lyskovskii, T. Wumaier and E. A. Zhukov
Physics Faculty, Moscow State University, Moscow, Russia

Abstract. We have explained the peculiarities of the observed dependence of colloidal CdSe/ZnS quantum dots' (QDs') absorbtion upon the intensity of input laser pulses in the case *of one-photon resonant excitation* of $1S_{3/2}(\mathrm{h}) \rightarrow 1S(\mathrm{e})$ exciton optical transition — the linear absorbtion at low intensity is replaced by nonlinear decreasing and then *increasing of absorbtion (!)* — by *saturation effect (state filling)* of two-level system *with variable lifetime of the excited state (variable saturation intensity).* The saturation intensity is inverse proportional to the lifetime of the excited state. The lifetime decreases at high excitation due to Auger nonradiative recombination.

Introduction

Nonlinear effects in quantum dots (QDs) are of great interest both from their fundamental properties and from their important possible applications (optical switches, optical limiters, saturable absorbers for Q-switched and mode-locked lasers etc.).

Nonlinear decreasing of absorption in the case of one-photon resonant excitation of ground exciton transition has been observed and explained [1] by saturation effect (state filling) of two-level system with invariable lifetime of the excited state (invariable saturation intensity). Saturation intensity is inverse proportional to the lifetime of the excited state [2]. However, the lifetime of the excited state in semiconductor QDs depends (!) on the excitation intencity and decreases at high excitation [3]. Auge nonradiative recombination dominates. The goal of the work is the investigation of the peculiarities of nonlinear absorption in colloidal CdSe/ZnS QDs in the case of resonant excitation of excitons by powerful ultra-short laser pulses.

Experimental setup

A method of QDs' nonlinear transmission measurement using the train of variable intensity picoseconds pulses of mode-locked Nd^{3+}:YAG-laser has been utilized. QDs were synthesized by organometallic method. The spectra of transmission and excitation of luminescence (PLE) of CdSe/ZnS QDs colloidal solution are presented in Fig. 1. The considerable width of these spectra is determined by inhomogeneous broadening as a result of QDs' size dispersion. The radius of QDs

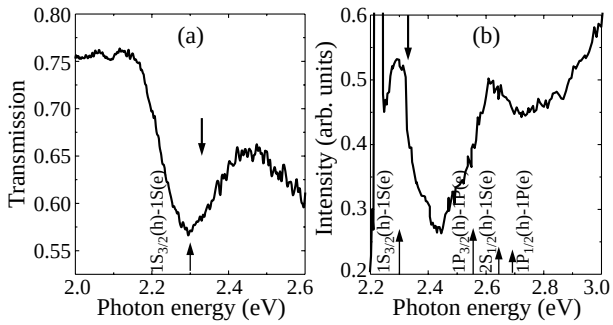

Fig. 1. The transmission (a) and photoluminescence excitation (b) spectra of CdSe/ZnS QDs' colloidal solution. The energy of the second harmonic of Nd^{3+}:YAG-laser photon is pointed by bold arrow.

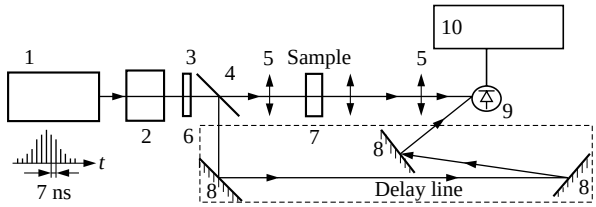

Fig. 2. Experimental setup: 1 — mode-locked Nd^{3+}:YAG-laser; 2 — KDP-crystal; 3 — colour filter; 4 — beam splitter; 5 — lens; 6 — optical delay line; 7 — the cell with CdSe/ZnS QDs colloidal solution; 8 — mirror; 9 — avalanche photodiode; 10 — high speed oscillograph.

$(2.6 \pm 0.4$ nm) was determined using theoretical results [4]. The density of QDs in colloidal solution was about 10^{15} cm^{-3}. The experimental setup is shown in Fig. 2. The second harmonic of mode-locked Nd^{3+}:YAG-laser ($\hbar\omega = 2.33$ eV) was used for resonant excitation of $1S_{3/2}(\mathrm{h}) \rightarrow 1S_{1/2}(\mathrm{e})$ exciton transition of CdSe/ZnS QDs. The measured pulse duration of single pulses (30 ps) didn't vary at least for the first half of the train. The axial period of pulses in the train was 7 ns. The energies of transmitted through the sell with colloidal solution of CdSe/ZnS QDs in toluene pulses and the energies of corresponding exciting pulses were measured simultaneously using optical delay line (3 ns) and photodiode operated in the linear regime. The delay time is longer than the measured lifetime of excited excitons. Photodiode was coupled with fast-acting oscillograph. The time-resolution of the system was about 1 ns. Oscillogram of the trains of transmitted and the part of the delayed input pulses is shown in Fig. 3.

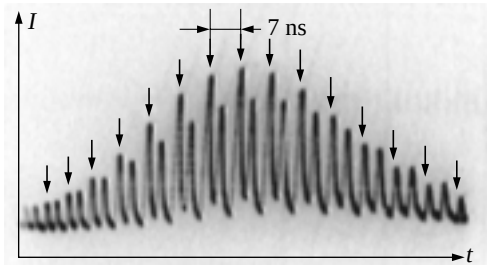

Fig. 3. Oscillogram of the trains of transmitted (pointed by arrows) and the part of the delayed of input pulses.

Results

The dependence of CdSe/ZnS QDs' colloidal solution transmission $T \equiv I_T/I_0$ upon the intensity of exciting pulses I_0 (Fig. 4) is characterized by the replacing of its increasing by decreasing followed by a new increasing (parts I, II and III in Fig. 4). The data (parts I and II) were fit to the simple saturable absorption (state filling) model [1] with a saturable α and non-saturable background α_0 absorption. But we have taken into account the dependence of saturation parameter on the changing relaxation time of the excited state τ. The saturation parameter $I_s \sim 1/\tau$ and at high excitation $\tau \sim N^{-2} \sim I^{-2}$ (N is the number of electron-hole pairs excited in QD) due to Auger-recombination [3]. Thus

$$\frac{dI}{dz} = -\alpha_0 I - \frac{\alpha I}{1 + \frac{I}{I_s + \gamma I^2}}. \qquad (1)$$

After integration of (1) one can receive the final equation for numerical solution:

$$\alpha d + \frac{\alpha}{\alpha_0 + \alpha} \ln\left(\frac{I_T}{I_0}\right) + \frac{\alpha^2}{\gamma(\alpha_0+\alpha)^2} \cdot \frac{1}{\sqrt{\Theta(\gamma)}} \times \left[\operatorname{arctg}\left(\frac{I_T + \frac{\alpha_0}{2\gamma(\alpha_0+\alpha)}}{\sqrt{\Theta(\gamma)}}\right) - \operatorname{arctg}\left(\frac{I_0 + \frac{\alpha_0}{2\gamma(\alpha_0+\alpha)}}{\sqrt{\Theta(\gamma)}}\right)\right] = 0, \qquad (2)$$

where $\Theta(\gamma) = \frac{I_s}{\gamma} - \frac{\alpha_0^2}{4\gamma^2(\alpha_0+\alpha)^2}$.

Using (2) we have calculated the dependence of CdSe/ZnS QDs' colloidal solution transmission $T \equiv I_T/I_0$ upon the intensity of exciting pulses I_0 and got agreement between the theory and experimental data, that show the transition from increasing to decreasing of transmission. The arising increasing of $T(I_0)$ in part III may be attributed to the Stark shift of the exciton absorption band in the charged QDs [5]. In this case the red shift of the spectra in Fig. 1 leads to the increasing of transmission.

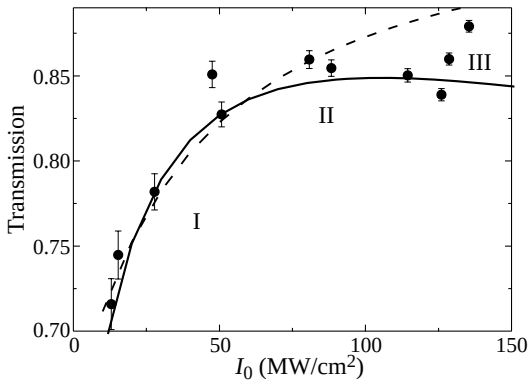

Fig. 4. The measured and calculated (using Eq. (2)) dependence of CdSe/ZnS QDs' transmission vs the intensity of exciting laser pulses: $\gamma = 0$ (dashed line) and $\gamma = 16 \times 10^{-4}$ cm^2/MW (solid line); $I_s = 15$ MW/cm^2.

Acknowledgement

This work was supported by Russian Foundation for Basic Research (grants 02-05-17604 and 02-06-90869).

References

[1] N. Peyhambarian, S. W. Koch "Semiconductor Nonlinear Materials" in "Nonlinear photonics" H. M. Gibbs, G. Khitrova, N. Peyhambarian ed. (Springer-Verlag, Berlin Heidelberg, 1990).

[2] D. N. Klysko, "The physical foundation of quantum electronics", russian edition, "Nauka" (1986).

[3] V. S. Dneprovskii, Al. L. Efros, A. I. Ekimov, V. I. Klimov, I. A. Kudriavtsev and M. G. Novikov, *Solid State Commun.*, **74**, 555-557, (1990).

[4] A. I. Ekimov, F. Hache, M. C. Schanne-Klein, D. Ricard, C. Flytzanis, I. A. Kudryavtsev, T. V. Yazeva, A. V. Rodina, and Al. L. Efros, *J. Opt. Soc. Am.* **B 10**, 100 (1993).

[5] D. J. Norris, A. Sacra, C. B. Murray, and M. G. Bawendi, *Phys. Rev. Lett.*, **72**, 2612–2615, (1994).

15th Int. Symp. "Nanostructures: Physics and Technology"
Novosibirsk, Russia, June 25–29, 2007

Effect of composition fluctuations on emission properties of GaAs(In,Sb)N QWs

A. Mintairov[1,2], K. Sun[1], J. Merz[1], G. Peak[2], H. Yuen[2], S Bank[3], M. Wistey[3], J. Harrisa[3], A. Egorov[4] and V. Ustinov[4]

[1] Department of Electrical Engineering, University of Notre Dame, IN 46556, USA
[2] Sandia National Laboratories, Albuquerue, NM 87185, USA
[3] Stanford University, Stanford, CA 94305, USA
[4] Ioffe Physico-Technical Institute, St Petersburg, Russia

Abstract. Using high spatial resolution and temperature-dependent photoluminescence spectroscopy we studied carrier localization in GaAs(In,Sb)N quantum wells (QWs) having different structural uniformity (phase separation). We reveal important role of quantum-dot like composition fluctuation in suppressing of the lateral carrier transport to non-radiative recombination centers and achieving high emission intensity at room temperature in these QWs.

Introduction

Heterostructures based on GaAs(In,Sb)N alloys having nitrogen composition of a few percent are very attractive for long wavelength emitters. It has been shown using high spatial resolution near-field photoluminescence that in these dilute nitride materials strongly localized quantum-dot-like composition fluctuations can exist, arising from nitrogen clustering [1]. In GaAsN and GaInAsN epi-layers with In composition up to 10%, which have emission energies 1–1.2 μm, such composition fluctuations have size $\sim$ 15 nm, activation energy $\sim$ 30 meV and density $\sim 100\,\mu\text{m}^{-3}$, which implies their spontaneouse formation (phase separation) [2]– [4]. For achieving longer emission wavelengths $\sim$ 6 nm thick quantum wells (QWs) with In composition up to 40%, and incorporation of the antimony, are used. In such QWs a phase separation can be controlled and very uniform material can be obtained [5].

In the present paper we used high spatial resolution and temperature dependent photoluminescence (PL) spectroscopy to study compositional fluctuations and their effect on emission properties in GaAs(In,Sb)N quantum wells emitting at 1.2–1.3 nm.

Samples and experimental details

We studied here three GaAs(In,Sb)N QW samples (thickness $d \sim 6$ nm) having nitrogen composition $\sim$ 1.5% and different combinations of In ($\sim$ 30−40%) and Sb (2 and 50%). The emission wavelengths of these QWs at 300 K ($\lambda_{300\text{ K}}$) are $\sim 1.2-1.3\,\mu$m. We also used GaAsN (N $\sim$ 1.5%) QW ($d = 10$ nm) and "bulk" layer ($d = 100$ nm) having $\lambda_{300\text{ K}} \sim 1.0\,\mu$m. The InAs quantum dots (QDs) structure ($\lambda_{300\text{ K}} \sim 1.2\,\mu$m) having density 5×10^{10} cm^{-2} was also used. The

Table 1. GaAs(In,Sb)N samples (N $\sim$ 1.5%).

Samples	In(Sb) %	d, nm	γ^*_{PLLT}, meV
GaAsN (MBE)	0(0)	10	16
GaInAsN (MBE)	40(0)	6	25(15)*
GaAsSbN (MOCVD)	0(50)	6	21**
GaInAsSbN (MBE)	40(2)	7	6
GaAsN (MBE)	0(0)	100	15**

* before (after) annealing;

** for high enegry component.

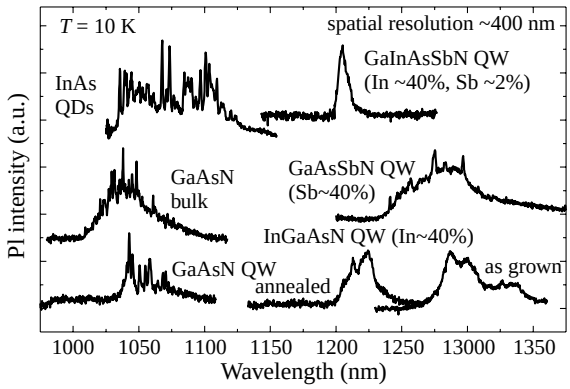

Fig. 1. Low temperature, high spatial resolution ($\sim$ 400 nm) spectra of GaAs(In,Sb)N QW and reference GaAsN and InAs QD samples.

GaAsSbN sample was grown by MOCVD, while the rest of the samples were grown by MBE. The GaInAsN sample was annealed and measured before (as grown) and after annealing. The In and Sb compositions, the thickness (d) and a reduced half-width of photoluminescence (PL) peak at 10 K ($\gamma^*_{\text{PLLT}} = \gamma_{\text{PLLT}}/\sqrt{2}$) are presented in Table 1. The transmission microscopy measurements reveal very high structural uniformity of GaInAsSbN QW.

High spatial resolution (HSR) spectra were taken using NSOM photoluminescence (PL) technique [1] or μ-PL through metallic apertures having diameters 200–700 nm deposited directly on the samples using e-beam lithography.

High spatial resolution PL spectra

The HSR PL spectra of all samples including GaInAsN sample before and after annealing are shown in Fig. 1. Single QD sharp lines, similar to those observed in reference InAs QD sample, are clearly seen in bulk and QW GaAsN. Much weaker QD lines are also observed in GaAsSbN QW. These lines are related to QDs formed by nitrogen clustering [2–4]. The density of such QDs in estimated from the number of sharp lines ($\sim 10^{10}$ cm^{-2}) is comparable to the dot density in InAs QD sample. These sharp lines are strongly suppressed in In containing GaInAsN and GaInAsSbN QWs. Instead in these samples a series of wider (15–25 meV) peaks separated by $\sim$ 20 and $\sim$ 40 meV are observed. Only single peak observed in GaInAsSbN QW, which characterizes its high structurally

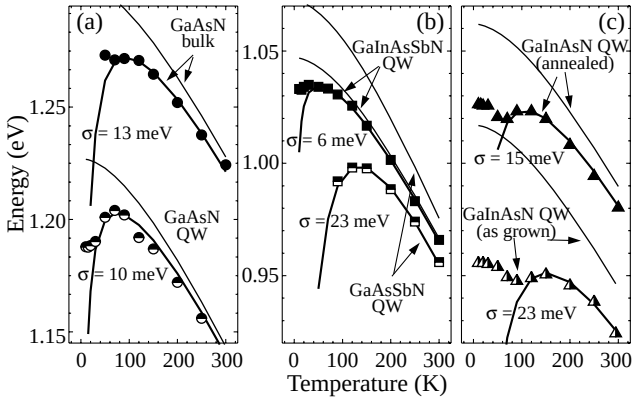

Fig. 2. Temperature dependence of PL peak position (circles, squares and triangles), band-tail model [7] (thick curves) and band gap (thin curves) for GaAsN structures (a) and GaAs(In,Sb)N QWs (b and c). For bulk GaAsN and GaAsSbN QW the data for higher energy peak are presented.

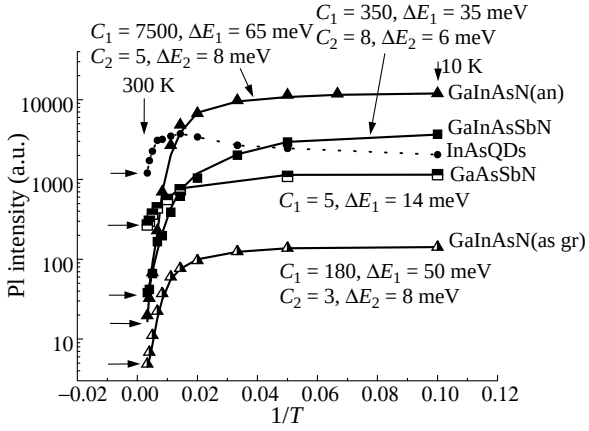

Fig. 3. Measured intensity of PL peak position versus temperature (triangles and squares) and Arrhenius plot fitting (curves) for GaInAsN, GaAsSbN and GaInAsSbN QWs. Circles experimental data for reference InAs QD (circles).

uniformity. In GaInAsN QWs the multiple peaks separated by $\sim$ 20 meV can be related to the fluctuations of the well thickness. The 40 meV peak separation can be assigned to different nearest-neighbor In and Ga atoms arrangements [6]. Reducing the number of peaks indicates higher structural uniformity of annealed GaInAsN QW.

Carrier localization in temperature dependent PL spectra

Using measurements of PL peak position versus temperature, presented in Fig. 2 we study effects of QD formation on carrier localization. For all of the samples so-called S-behavior was observed. It represents a red temperature shift near some "critical" temperature T_0, ranging from 20 K (for GaInAsSbN) to 120 K (for GaAsSbN and as grown GaInAsN). The red shift corresponds to a thermal population of the composition fluctuations forming a band tail. For a Gaussian distribution of a band tail with dispersion σ^2, the shift of PL peak can be described by the expression $E_{\rm PL} = E(T) - \sigma^2/kT$, where $E(T)$ is a regular temperature dependence of the band gap (Varshni model) and σ^2/kT is a Stokes shift [7]. This expression is valid for nongenerate carrier occupation, which is not fulfilled at low temperatures. In the case of multiple PL peak (bulk GaAsN and GaAsSbN QW, see Table 1) the using of the Gaussian distribution is not straightforward. The fitting of this expression to experiment (see Fig. 2) in the valid temperature range ($T > T_0$) allows determine energy dispersion of composition fluctuations and their Stokes shift ΔE. As expected we obtained small values (6 and 15 meV) of σ and $\Delta E_{\rm S}$ for structurally uniform GaInAsSbN layer and large values (23 and 60 meV) for highly non-uniform GaAsSbN and as grown GaInAsN QWs. The values presented in Fig. 2 agree well with related quantity $\gamma^*_{\rm PLLT}$ (see Table 1). For GaInAsSbN and GaInAsN QW the values of and $\gamma^*_{\rm PLLT}$ coincide, which to our opinion confirm the absence of QD formation in these samples.

Non-radiative recombination in temperature dependent PL intensity

Figure 3 shows a dependence of the PL peak intensity for GaInAsN (as grown and annealed), GaAsSbN and GaInAsSbN QWs and InAs QDs in logarithmic scale versus reciprocal temperature (Ahhrenius scale). The results of the thermal activation model fitting [8] and fitting parameters En and Cn (activation energies and relative scattering rate for n-th non-radiative recombination channel) are also shown. At room temperature the strongest intensity have InAs QDs and GaAsSbN QW, having nitrogen related QDs. At 10 K the strongest emission have GaInAsSbN and annealed GaInAsN QWs, which are structurally uniform. These two samples show very strong temperature dependence of the emission intensity, which corresponds to high density of non-radiative recombination centers of MBE grown material. More efficient room temperature emission of samples with QDs indicates the effect of suppressing of the lateral carrier transport to non-radiative recombination centers due to strong carrier localization. The efficient low temperature emission of GaInAsSbN and annealed GaInAsN QWs corresponds to freezing of non-radiative centers, when most of the material becomes emissive.

Conclusions

Using high spatial resolution photoluminescence (PL) spectroscopy and temperature-dependent PL we studied effects of carrier localization in GaAs(In,Sb)N quantum wells (QWs) having different structural uniformity (phase separation). We reveal important role of quantum-dot like composition fluctuation in suppressing of the lateral carrier transport to non-radiative recombination centers and achieving high emission intensity at room temperature in these QWs.

Acknowledgement

This work has been partially supported by a Subaward under NSF/DMR06-06406.

References

[1] A. M. Mintairov *et al*, *Phys. Rev. Lett.* **87** 277401 (2001).
[2] A. M. Mintairov *et al*, *Physica E* **21**, 385 (2004).
[3] J. Merz *et al*, *IEE Proc. Optoelectronics* **151**, 346 (2004).
[4] A. Mintairov *et al*, *Mater. Res. Soc. Symp. Proc.* **838E**, Warrendale, PA, O3.1 (2005).
[5] X. Yang *et al*, *Appl. Phys. Lett.* **78**, 4068 (2001).
[6] P. J. Klar *et al*, *Phys. Rev. B* **64**, 121203 (2001).
[7] P. G. Eliseev, *J. Appl. Phys.* **93**, 5404 (2003).
[8] G. Bacher *et al*, *Phys. Rev. B* **43**, 9312 (1991).

15th Int. Symp. "Nanostructures: Physics and Technology"
Novosibirsk, Russia, June 25–29, 2007

Exciton states in CdTe/ZnTe quantum wells with self-assembled quantum dots

A. Reznitsky[1], A. Klochikhin[1,2], S. Permogorov[1], L. Tenishev[1], *K. Mironenko*[1], W. Loeffler[3], H. Kalt[3] and C. Klingshirn[3]

[1] Ioffe Physico-Technical Institute, St Petersburg, Russia
[2] Nuclear Physics Institute, 188350, St Petersburg, Russia
[3] Institut für Angewandte Physik, Universität Karlsruhe (TH), 76128 Karlsruhe, Germany

Abstract. We have studied the ensemble averaged and spatially resolved photoluminescence (PL) and PL-excitation (PLE) spectra of narrow CdTe/ZnTe quantum wells (QW's). We have shown that the obtained results can be used for characterization of exciton states and character of energy relaxation in the system. Micro-PL spectra indicate the presence of Cd-rich dot-like islands. The analysis of the PL and PLE spectra allow us to restore the profiles of CdTe content in the lateral and growth directions and CdTe concentration within- and between the islands.

We have studied the PL and PLE spectra of MBE-grown CdTe/ZnTe structure containing seven QW's (from A to G) with progressively increasing CdTe content w_{CdTe} (from 1.8 to 12 monolayers (ML)), separated by thick (60 nm) ZnTe barriers. Transmission electron microscopy has shown that only three narrowest QW's (A, B, and C) with w_{CdTe} equal to 1.8, 2.5, and 4.3 ML were coherently strained [1].

In Fig. 1(a) the PL spectrum of the sample is shown in logarithmic scale. Besides the emission from QW's A, B, and C, one can see another two PL bands resulting from the recombination in QW's D and E. These PL bands are weaker than the preceding ones by the factor of ~ 50, and no photoluminescence are registered from the more thicker QW's F and G. This had been attributed to the increase of non-radiative recombination due to the defect formation in the process of the structural relaxation of these QWs [1].

The micro-PL spectra were registered for QW's A, B, and C. These spectra shown in Fig. 1(b) give the evidence of highly inhomogeneous distribution of CdTe over the QW plane resulting in the quantum dot formation. Sharp, resolution limited (< 0.2 meV) lines in recombination spectra of the QW's indicate the existence of excitons localized in individual quantum dots.

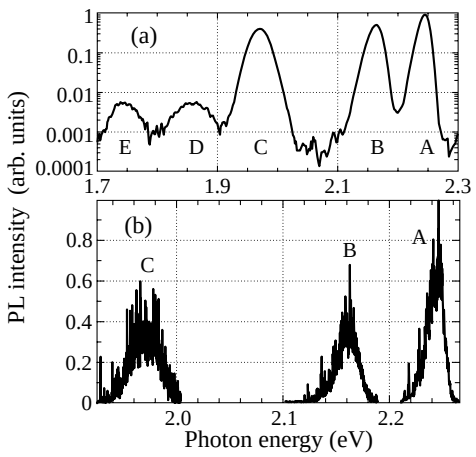

Fig. 1. (a) Semi-logarithmic plot of emission spectra of QW's from A to E at $T = 2$ K and at above ZnTe-barrier excitation. (b) Micro-PL spectra of QW's A, B, and C from the 0.5-μ-diameter spot at $T = 7$ K and at excitation above ZnTe-barrier.

In order to characterize the averaged parameters of the ensemble of the islands in CdTe QW's we have studied its PLE spectra.The PLE spectra of QW's A, B, and C for different detector positions within corresponding PL bands are demonstrated in Fig. 2 (a–c). The PLE spectra for each of QW's are normalized so that to obtain the equal intensity at the excitation energy which is slightly below the exciton transition in the ZnTe barrier. After such normalization the different PLE spectra for each QW coincide at excitation energies above some energy E_{ME} and show a strong divergence at $E < E_{\mathrm{ME}}$. As it was discussed in Ref. [2, 3, 4], the point of divergence of PLE spectra E_{ME} can be identified with the exciton mobility edge, which separates the extended exciton states in the "wetting" layer from the states localized within quantum dots.

The PLE spectra of states forming the low energy part of the PL band do not depend on the detector position. This result shows that the energy dependence of these PLE spectra can be attributed only to the variation in the absorption of the QW. Therefore, these PLE spectra can be regarded as the absorption spectrum of the ensemble of island states.

In Table 1 the main characteristics of optical spectra of the QW's under the study are presented.

We have assumed that the distribution of CdTe content along the growth direction can be described by the function $c(z) \sim 4/\cosh^2(2z/L)$ like in the CdSe/ZnSe system. This leads to the potential distribution $V(z) = -\Delta E_{\mathrm{G}} c(z)$, where ΔE_{G} is the band gap offset. With this potential we have calculated the dependence of the confinement energy of the heavy

Table 1. Characteristics of quantum wells discussed in the paper: E_{PL} and E_{abs} are the maximum positions of PL and absorption spectra, E_{ME} is position of the mobility edge, c_{QD} and c_{WL} are the estimated CdTe concentration within- and between dots (see text).

QW	w_{CdTe} (ML)	E_{PL} (eV)	E_{abs} (eV)	E_{ME} (eV)	c_{QD}	c_{WL}
A	1.8	2.250	2.262	2.310	0.23	0.15
B	2.5	2.165	2.188	2.310	0.34	0.15
C	4.3	1.973	2.006	2.152	0.62	0.40
D	6.5	1.864	1.905 (estim.)	—	0.76	—
E	8.6	1.749	1.793 (estim.)	—	0.88	—

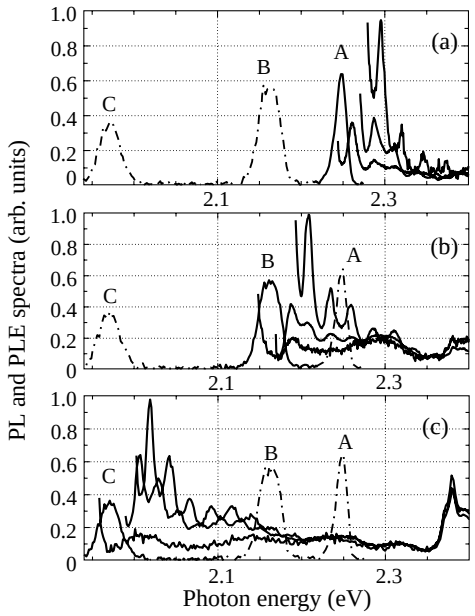

Fig. 2. PL spectra of QW's A, B, and C. The PLE spectra of these QW's are presented in panels *a*, *b*, and *c*, respectively. PLE spectra of each QW are given for three different detector positions (at maximum and the points below and above the maximum where the intensity is 0.5 of that at maximum).

hole exciton on the CdTe concentration in CdTe/ZnTe QWs at $\Delta E_G = 0.78$ eV for different values of L.

In Fig. 3(a) the observed energies of the absorption peak E_{abs} in the PLE spectra in various QW's are plotted as functions of the amount of deposited CdTe w_{CdTe}. These values are compared with the theoretical curve giving the energy position of the ground state of the heavy-hole exciton in a single QW. The latter was calculated at the assumtion that the well width L do not depend on the amount of CdTe deposited. This assumption is based on the results obtained by high resolution transmission electron microscopy of narrow CdSe/ZnSe QW's [5]. The experimental results for three narrow QW's are in good agreement with calculation. However, for $w_{CdTe} > 5$ ML systematic deviations of experimental positions to higher energies with respect to the calculated exciton energies is seen. These deviations can be attributed to the onset of the structural relaxation of QW's resulting in the increase of the island height in the growth direction with the increase of w_{CdTe}.

In Fin. 3b the calculated concentration dependence of the heavy-hole exciton energy is shown by the inclined solid line. We have assumed that the QW width do not depend on CdTe content for QW's with $w_{CdTe} < 5$ ML and linearly increases for QW's with $w_{CdTe} > 5$ ML. In the same figure the energies of E_{abs} and E_{ME} for QW's A, B and C and estimated positions of E_{abs} for QW's D and E are shown by horizontal lines. The intersections of these lines with calculated heavy-hole exciton energy dependence give the estimate for the CdTe concentrations within islands c_{QD}. Similarly, intersections of dashed horizontal lines E_{ME} with this curve estimate concentration between islands c_{WL}. The obtained concentrations are listed in Table 1.

In conclusion, we have shown that the optical study of narrow CdTe/ZnTe quantum wells can be used for characterization of exciton states in these systems. The study of PLE spectra for different emission energies within PL band allows to determine

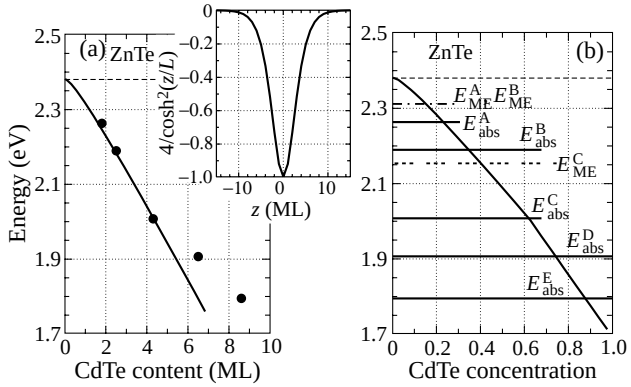

Fig. 3. (a) PL peak positions in QW's from A to E versus w_{CdTe} (closed circles). Solid line presents the exciton confinement energy. Inset: the normalized shape of the QW potential in the growth direction used in calculations. (b) The inclined solid line is the composition dependence of the h-h exciton transition energies for potential well profile shown in inset of Fig. 3(a). Parameters of potential wells are: $L = 7$ ML for QW's A, B, and C and $L = 8.5$ ML and 9.3 ML for QW's D and E, respectively. Horizontal solid lines give positions of E_{abs} and horizontal dashed lines give positions of E_{ME}. Estimated concentrations of CdTe within- and between the islands for different QW's are presented in Table 1 (see text).

the energy position of the exciton mobility edge for lateral motion separating the mobile and localized exciton states. Using the model for exciton states in QW's we have estimated the mean concentrations of CdTe within and between the quantum dots forming in the QW's.

References

[1] J. Cibert, Y. Gobil, Le Si Dang *et al*, *Appl. Phys. Lett.* **56**, 292 (1990).

[2] A. Reznitsky, A. Klochikhin, S. Permogorov, L. Tenishev *et al*, *phys. stat. sol. (b)* **229**, 509 (2002).

[3] A. Klochikhin, A. Reznitsky, B. Dal Don, H. Priller *et al*, *Phys. Rev. B* **69**, 085308 (2004).

[4] A. Reznitsky, S. Permogorov, A. Klochikhin, H. Kalt *et al*, to be published in *Intern. J. of Nanoscience* (2007).

[5] N. Peranio, A. Rosenauer, D. Gerthsen, S. V. Sorokin *et al*, *Phys. Rev. B* **61**, 16015 (2000).

[6] L. Marsal, L. Besombes, F. Tinjod, K. Kheng *et al*, *J. Appl. Phys.* **91**, 4936 (2002).

15th Int. Symp. "Nanostructures: Physics and Technology"
Novosibirsk, Russia, June 25–29, 2007

Strain distribution in quantum dot of arbitrary shape: analytical solution

A. V. Nenashev and A. V. Dvurechenskii
Institute of Semiconductor Physics, Novosibirsk State University, Novosibirsk, Russia

Abstract. An analytical expression of the strain distribution due to lattice mismatch is obtained in infinite isotropic elastic medium (matrix) with a three-dimensional polyhedron-shaped inclusion (a quantum dot) for the first time. This expression was obtained utilizing the analogy between electrostatic and elastic theory problems. The main idea is based on similarity between the electric field of a point charge and the strain field induced by a point inclusion in the matrix. It opens a way to simplify the structure of the expression for strain tensor. In the solution the strain distribution consists of contributions related to faces and edges of the inclusion. A contribution of each face is proportional to the solid angle at which the face is seen from the point where the strain is calculated. A contribution of an edge is proportional to the electrostatic potential which would be induced by this edge if it was charged with a constant linear charge density. The solution is valid for the case of inclusion having the same elastic constants as the matrix. Three particular cases of the general solution are considered — for inclusions of pyramidal, truncated pyramidal, and "hut-cluster" shapes. For a pyramid and a truncated pyramid considerable simplification was achieved in comparison with previously published solutions. The solution for a hut-cluster-shaped inclusion is obtained here for the first time.

Introduction

From a point of view of elasticity theory self-assembled quantum dots are three-dimensional lattice-mismatched inclusions of one material in other one (matrix). The lattice mismatch is an origin of a built-in strain field. Knowledge of the strain distribution is of crucial importance for analysis of electronic structure of quantum dots (especially of type-II dots).

There are a lot of theoretical works considering the strain distribution in quantum dot structures (see review [1,2]). But an analytical closed form solutions were found so far only in few instances of inclusion shapes: an ellipsoid, a cuboid, a pyramid, a truncated pyramid, and a variety of quantum-wire-like structures. Moreover, the known solutions for pyramidal inclusions are extremely complicated.

The aim of our paper is to develop a novel approach to constructing the solutions, to obtain a solution for the general case of polyhedral inclusion, and to propose a new insight into the structure of a solution.

The problem considered in our paper is the following. There is an infinite elastically isotropic medium (a matrix) with a finite polyhedron-shaped inclusion. The crystal lattice of the inclusion matches the lattice of the matrix without any defects. Elastic moduli of the inclusion are assumed to be equal to that of the matrix, but the inclusion has a different lattice constant. This produces an elastic strain in both the inclusion and the matrix, and the task is to determine the strain tensor as a function of coordinates, $\varepsilon_{\alpha\beta}(\mathbf{r})$.

1. The method

The starting point of our investigation is a well-known analogy between the elastic inclusion problem and the electrostatic problem (Poisson equation). Namely, the *displacement vector* $\mathbf{u}(\mathbf{r})$ induced by the inclusion is proportional to the *electric field* $\mathbf{F}(\mathbf{r})$ induced by charge uniformly distributed over the volume of the inclusion:

$$\mathbf{u}(\mathbf{r}) = \frac{\varepsilon_0(1+\nu)}{4\pi(1-\nu)}\mathbf{F}(\mathbf{r}) \equiv \frac{\varepsilon_0(1+\nu)}{4\pi(1-\nu)}\int\limits_V \frac{\mathbf{r}-\mathbf{r}'}{|\mathbf{r}-\mathbf{r}'|^3}\,d\mathbf{r}',$$

where ε_0 is the lattice mismatch, ν is the Poisson ratio, V denotes volume of the inclusion. Then, we introduce an auxiliary "electrostatic potential"

$$\varphi(\mathbf{r}) = \int\limits_{\mathbf{V}} \frac{\mathbf{dr}'}{|\mathbf{r}-\mathbf{r}'|} \equiv \int \frac{\mathbf{dr}'}{|\mathbf{r}-\mathbf{r}'|}\,\chi(\mathbf{r}),$$

where $\chi(\mathbf{r})$ is equal to 1 inside the inclusion and to 0 outside it. The displacement vector $\mathbf{u}(\mathbf{r})$ is proportional to gradient of φ, therefore the strain tensor $\varepsilon_{\alpha\beta}(\mathbf{r})$ is expressed via second derivatives of φ:

$$\varepsilon_{\alpha\beta}(\mathbf{r}) = -\Lambda\partial^2\varphi(\mathbf{r})/\partial\mathbf{x}_\alpha\partial\mathbf{x}_\beta - \varepsilon_0\delta_{\alpha\beta}\chi(\mathbf{r}), \qquad (1)$$

where $\Lambda = \varepsilon_0(1+\nu)/4\pi(1-\nu)$. Second derivatives of φ can be regarded as integrals

$$\frac{\partial^2\varphi(\mathbf{r})}{\partial x_\alpha\,\partial x_\beta} = \int \frac{\partial^2\chi(\mathbf{r}')}{\partial x'_\alpha\,\partial x'_\beta}\,\frac{d\mathbf{r}'}{|\mathbf{r}-\mathbf{r}'|}. \qquad (2)$$

Second derivatives of $\chi(\mathbf{r})$ vanish inside and outside the inclusion and tend to infinity on the inclusion surface. So, the integration in (2) is actually an integration over the surface.

Then, the integral (2) breaks down into separate integrals over all faces and edges of the inclusion surface. Therefore the strain field can be presented as a sum of contributions of the faces and edges. This is the main point of our method; it gives a possibility to construct expressions for strain distributions in inclusions of complicated shapes.

The detailed consideration of the face and edge contributions is beyond the present paper, here we present the results only. The contribution of a face can be considered as a potential of dipolar layer spread uniformly over the face. It is known that the electrostatic potential induced by such a dipole layer at point $\mathbf{r}$ is equal to $d\,\Omega(\mathbf{r})$, where d is a dipole moment per unit area of the face, and $\Omega(\mathbf{r})$ is a solid angle at which the face is seen from the point $\mathbf{r}$. We imply that $\Omega(\mathbf{r})$ is positive if the outer side of the face is seen from the point $\mathbf{r}$, and negative otherwise. In an analogous way, the contribution of an edge is equal to a potential induced by the edge as if it was uniformly charged.

2. General solution

By evaluating the integration in Eq. (2), as described in the previous Section, and substituting the results into Eq. (1), we obtain the following expression for the strain tensor $\varepsilon_{\alpha\beta}$:

$$\varepsilon_{\alpha\beta}(\mathbf{r}) = -\Lambda \sum_i n^i_\alpha n^i_\beta \Omega_i - \Lambda \sum_k \gamma^k_{\alpha\beta} \Phi_k - \varepsilon_0 \delta_{\alpha\beta} \chi(\mathbf{r}), \quad (3)$$

where i runs over faces of the inclusion surface, and k runs over its edges; $\Omega_i(\mathbf{r})$ is a solid angle subtended by the i-th face from the point $\mathbf{r}$ (positive if the outer side of the face is seen from the point $\mathbf{r}$, and negative otherwise);

$$\Phi_k(\mathbf{r}) = \log \frac{r_{k1} + r_{k2} + L_k}{r_{k1} + r_{k2} - L_k}$$

is the electrostatic potential of uniformly charged edge k (with unit linear charge density) at the point $\mathbf{r}$; r_{k1} and r_{k2} are distances from the point $\mathbf{r}$ to the end points of the k-th edge; L_k is a length of the k-th edge; $\mathbf{n}^i$ is a normal unit vector to the i-th face directed outside the inclusion; $\gamma^k_{\alpha\beta} = n^{k1}_\alpha b^{k1}_\beta + n^{k2}_\alpha b^{k2}_\beta$; $\mathbf{n}^{k1}$ and $\mathbf{n}^{k2}$ are normal unit vectors (directed outside the inclusion) to the two faces intersecting at the k-th edge; $\mathbf{b}^{k1}$ is a unit vector perpendicular to the k-th edge and to $\mathbf{n}^{k1}$ directed out of the $k1$-th face; analogously, $\mathbf{b}^{k2}$ is a unit vector perpendicular to the k-th edge and to $\mathbf{n}^{k2}$ directed out of the $k2$-th face:

$$\mathbf{b}^{k1} = \frac{\mathbf{n}^{k2} - \mathbf{n}^{k1}(\mathbf{n}^{k1}\mathbf{n}^{k2})}{|\mathbf{n}^{k2} - \mathbf{n}^{k1}(\mathbf{n}^{k1}\mathbf{n}^{k2})|}, \quad \mathbf{b}^{k2} = \frac{\mathbf{n}^{k1} - \mathbf{n}^{k2}(\mathbf{n}^{k2}\mathbf{n}^{k1})}{|\mathbf{n}^{k1} - \mathbf{n}^{k2}(\mathbf{n}^{k2}\mathbf{n}^{k1})|},$$

$\Lambda = \varepsilon_0(1+\nu)/4\pi(1-\nu)$; ν is the Poisson ratio; ε_0 is the lattice mismatch between inclusion and matrix; $\delta_{\alpha\beta}$ is the Kroneker delta; $\chi(\mathbf{r})$ is equal to 1 inside the inclusion and to 0 outside it.

Equation (3) is the main result of the present paper. It gives a closed-form analytical expression for strain distribution inside and around a polyhedral inclusion in infinite isotropic elastic medium.

3. Application to pyramidal and hut-cluster inclusions

Among all the polyhedrons the three ones most often are used as geometrical models of quantum dots: square-based pyramid (Fig. 1a), truncated square-based pyramid (Fig. 1b), and so-called "hut-cluster" (Fig. 1c).

First, let us consider a pyramidal inclusion. The tensors $n^i_\alpha n^i_\beta$ and $\gamma^k_{\alpha\beta}$ are easily expressed via the dihedral angle θ between the pyramid base and any of its side faces (Fig. 1a). Introducing abbreviations $s = \sin\theta$ and $c = \cos\theta$, we get the following expressions for the strain distribution inside the pyramidal inclusion and its surrounding:

$$\begin{aligned}
\varepsilon_{xx} &= -s^2\Lambda(\Omega_1+\Omega_3) - sc\Lambda(\Phi_1+\Phi_3) + \tfrac{sc^2\Lambda}{\sqrt{1+c^2}}\Phi_{5-8} - \varepsilon_0\chi, \\
\varepsilon_{yy} &= -s^2\Lambda(\Omega_2+\Omega_4) - sc\Lambda(\Phi_2+\Phi_4) + \tfrac{sc^2\Lambda}{\sqrt{1+c^2}}\Phi_{5-8} - \varepsilon_0\chi, \\
\varepsilon_{zz} &= -\Lambda\Omega_0 - c^2\Lambda\Omega_{1-4} + sc\Lambda\Phi_{1-4} - \tfrac{2sc^2\Lambda}{\sqrt{1+c^2}}\Phi_{5-8} - \varepsilon_0\chi, \\
\varepsilon_{xy} &= -\tfrac{s\Lambda}{\sqrt{1+c^2}}(\Phi_5 - \Phi_6 + \Phi_7 - \Phi_8), \qquad (4) \\
\varepsilon_{xz} &= sc\Lambda(\Omega_1-\Omega_3) + s^2\Lambda(\Phi_1-\Phi_3) - \tfrac{s^2c\Lambda}{\sqrt{1+c^2}}(\Phi_5-\Phi_6-\Phi_7+\Phi_8), \\
\varepsilon_{yz} &= sc\Lambda(\Omega_2-\Omega_4) + s^2\Lambda(\Phi_2-\Phi_4) - \tfrac{s^2c\Lambda}{\sqrt{1+c^2}}(\Phi_5+\Phi_6-\Phi_7-\Phi_8).
\end{aligned}$$

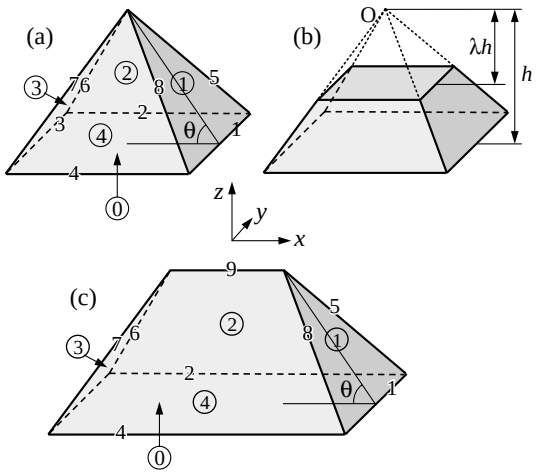

Fig. 1. Inclusions of most common shapes: (a) a pyramid with square base; (b) a truncated pyramid with square base; (c) a "hut-cluster". Numbers in circles refer to faces (with number 0 corresponding to the base), italic numbers refer to edges.

Here we use a shorthand notation: $\Omega_{1-4} = \Omega_1+\Omega_2+\Omega_3+\Omega_4$, and so on. To get the solution for the *truncated* pyramid, $\varepsilon^{(\mathrm{trunc})}_{\alpha\beta}$, the easiest way is to start from the solution for a pyramid, $\varepsilon^{(\mathrm{pyr})}_{\alpha\beta}$, and apply the superposition principle. Let the point of origin be the point O in Fig 1b. Then

$$\varepsilon^{(\mathrm{trunc})}_{\alpha\beta}(\mathbf{r}) = \varepsilon^{(\mathrm{pyr})}_{\alpha\beta}(\mathbf{r}) - \varepsilon^{(\mathrm{pyr})}_{\alpha\beta}(\mathbf{r}/\lambda),$$

where the truncation parameter λ is explained in Fig 1b.

Finally, we consider the hut-cluster. The hut-cluster is a figure that consists of the base (a parallelogram) and four side faces. Slope angles of all the side faces are the same. Therefore orientations of faces and edges of the hut-cluster are the same as of pyramid except the top (9th) edge. So, the solution for a hut-cluster is very similar to the one for a pyramid. The only difference is the addition of the contribution of 9th edge. Namely, to get the solution for the hut-cluster from Eq. (4), it is sufficient to add the term $2sc\Lambda\Phi_9$ to ε_{yy}, and to add the term $-2sc\Lambda\Phi_9$ to ε_{zz}. It demonstrates the flexibility of the general solution (3). This is a property that does not inherent in previous particular solutions [3]. In the present paper the solution for a hut-cluster was obtained for the first time.

4. Summary

We propose a new, more general, simple, and flexible expression for strain field inside and around an inclusion in an infinite isotropic medium.

Acknowledgements

This work was supported by RFBR (grant 06-02-16988), the Dynasty foundation, and the President's program for young scientists (grant MK-4655.2006.2).

References

[1] J. Stangl, V. Holý, and G. Bauer, *Rev. Mod. Phys.* **76**, 725 (2004).
[2] R. Maranganti and P. Sharma, *Handbook of Theoretical and Computational Nanotechnology*, Chapter 118 (2006).
[3] G. S. Pearson and D. A. Faux, *J. Appl. Phys.* **88**, 730 (2000).

15th Int. Symp. "Nanostructures: Physics and Technology"
Novosibirsk, Russia, June 25–29, 2007

Light scattering and resonant absorption by quantum dots

S. T. Pavlov[1,2], I. G. Lang[3] and L. I. Korovin[3]

[1] P. N. Lebedev Physical Institute, Russian Academy of Sciences, 119991 Moscow, Russia
[2] Facultad de Fisica de la UAZ, Apartado Postal C-580, 98060 Zacatecas, Zac., Mexico
[3] Ioffe Physico-Technical Institute, St Petersburg, Russia

Abstract. The cross section of light absorption by semiconductor quantum dots is calculated in the resonance with $\Gamma_6 \times \Gamma_7$ excitons in cubic crystals T_d. The interference of stimulating and induced electric and magnetic fields is taken into account. The cross section is proportional to the exciton nonradiative damping γ.

Introduction

At light irradiation of size-quantized low-dimensional semiconductor objects (quantum wells, quantum wires, quantum dots), elastic light scattering and absorption amplify resonantly if the light frequency ω_l equals to the exciton frequency ω_0. The resonant peak width is determined by the exciton damping Γ, which consists of nonradiative and radiative broadenings, i.e., $\Gamma = \gamma + \gamma_\mathrm{r}$. An important role of the radiative damping γ_r was proved for the first time in [1,2]. Light reflection by some structures, consisting of quantum wells, quantum wires, quantum dots, was considered in [3]. In [4], theoretically the elastic light scattering by quantum dots of any forms and sizes is investigated in a resonance with excitons with the help of the quantum perturbation theory. However, the quantum method does not allow to leave the limits of the lowest approximation on the light electron interaction, which is admissible only under condition $\gamma_\mathrm{r} \ll \gamma$.

The semiclassical method allows to calculate the classic electric and magnetic fields, while the description of the electron system is quantum one. It allows also to introduce the nonradiative damping γ into the theory and to calculate the light absorption. The version of the semiclassical method (the method of retarded potentials) is used, which allows to avoid the problem of boundary conditions.

1. The method of retarded potentials

We calculate the current $\mathbf{j}(\mathbf{r},t)$ and charge $\rho(\mathbf{r},t)$ densities induced by the electric field inside of a semiconductor object and averaged on the ground state of a crystal [5,6]. If in expressions for these densities to substitute the stimulating electric field $\mathbf{E}_0(\mathbf{r},t)$, we shall be limited by the lowest order on light-electron interaction. We obtain exact results , having substituted in these expressions true fields $\mathbf{E}(\mathbf{r},t) = \mathbf{E}_0(\mathbf{r},t) + \Delta\mathbf{E}(\mathbf{r},t)$ inside objects. We write down the induced electric and magnetic fields through the vector $\mathbf{A}(\mathbf{r},t)$ and scalar $\varphi(\mathbf{r},t)$ potentials and use the standard formulas for retarded potentials with the light refraction, which is identical inside and outside of a quantum dot.

The resonance situation is considered, when the light frequency ω_l is close to the exciton frequency ω_0. We obtain the integral equation for the electric field $\Delta\mathbf{E}(\mathbf{r},t)$ inside of the quantum dot. Having calculated the field inside of the quantum dot, we determine electric and magnetic fields on large distances from the quantum dot.

2. Electric and magnetic fields for excitons $\Gamma_6 \times \Gamma_7$ in cubic crystals of $\mathbf{T_d}$ class

Let us consider excitons, formed by electrons from the twice degenerated conductivity band Γ_6 and holes from the twice degenerated valence band Γ_7, chipped off by the spin-orbital interaction. The exciton $\Gamma_6 \times \Gamma_7$, described in [4], is the most simple object in its structure: All the measurable values do not depend on a direction of crystallographic axes, i.e., the crystal plays a role of the isotropic medium.

For the sake of simplicity, we use one more restriction. In the theory the values $P(\mathbf{k}) = \int d^3 r e^{-i\mathbf{kr}} F(\mathbf{r})$, are essential, where $F(\mathbf{r})$ is the real exciton wave function $\mathbf{r}_\mathrm{e} = \mathbf{r}_\mathrm{h} = \mathbf{r}$, $\mathbf{r}_\mathrm{e}(\mathbf{r}_\mathrm{h})$ is the electron (hole) radius vector. So named "envelope" wave function $F(\mathbf{r})$ is calculated in the effective mass approximation. Let us assume that $P(\mathbf{k})$ depends only on k, i.e., $P(\mathbf{k}) = P(k)$.

This condition is carried out, if the function $F(\mathbf{r})$ is spherically symmetric or if the quantum dot sizes are much less than the stimulating light wave length, and $P(\mathbf{k}) \simeq P(0)$. For the monochromatic irradiation we obtain

$$\Delta\mathbf{E}_{r\to\infty}(\mathbf{r},t) = -\frac{3}{4}E_0\frac{\gamma_\mathrm{r}}{k_\mathrm{l} r}\left[(\mathbf{e}_\mathrm{l}\mathbf{e}_s^-)\mathbf{e}_s^+ + (\mathbf{e}_\mathrm{l}\mathbf{e}_s^+)\mathbf{e}_s^-)\right] \times \frac{e^{i(\mathbf{k}_\mathrm{l}\mathbf{r}-\omega_\mathrm{l}t)}}{\omega_\mathrm{l} - \tilde{\omega}_0 + i\Gamma/2} + c.c., \quad (1)$$

$$\Delta\mathbf{H}_{r\to\infty}(\mathbf{r},t) = \frac{3iv}{4}E_0\frac{\gamma_\mathrm{r}}{k_\mathrm{l} r}\left[(\mathbf{e}_\mathrm{l}\mathbf{e}_s^-)\mathbf{e}_s^+ - (\mathbf{e}_\mathrm{l}\mathbf{e}_s^+)\mathbf{e}_s^-)\right] \times \frac{e^{i(\mathbf{k}_\mathrm{l}\mathbf{r}-\omega_\mathrm{l}t)}}{\omega_\mathrm{l} - \tilde{\omega}_0 + i\Gamma/2} + c.c., \quad (2)$$

where E_0 is the amplitude of stimulating light, $k_\mathrm{l} = \omega_\mathrm{l} v/c$, $\mathbf{e}_\mathrm{l}(\mathbf{e}_s)$ is the vector of circular polarization of stimulating light, $\tilde{\omega}_0$ is the exciton frequency, renormalized by the light-electron interactions, $\Gamma = \gamma + \gamma_\mathrm{r}$,

$$\gamma_\mathrm{r} = \frac{8v}{9}\frac{e^2}{\hbar c}\left(\frac{p_{cv}}{m_0 c}\right)^2 \frac{\omega_\mathrm{l}^2}{\omega_\mathrm{g}}|P(k_\mathrm{l})|^2, \quad (3)$$

$p_{cv} = i\langle S|\hat{p}_z|X\rangle$ is the interband matrix element of the quasimomentum operator in designations of [7, page 73], $\hbar\omega_\mathrm{g}$ is the energy gap.

3. The Pointing vector and the light scattering section

On the large distances from a quantum dot, the Pointing vector equals $\mathbf{S}_{r\to\infty} = \mathbf{S}_0 + \mathbf{S}_\mathrm{interf} + \mathbf{S}_\mathrm{scat}$, where

$$\mathbf{S}_0 = \frac{c}{4\pi}[\mathbf{E}_0 \times \mathbf{H}_0] = \frac{cv}{2\pi}E_0^2\mathbf{e}_z,\ \mathbf{S}_\mathrm{scat} = \frac{c}{4\pi}[\Delta\mathbf{E} \times \Delta\mathbf{H}], \quad (4)$$

$$\mathbf{S}_{\rm interf} = \frac{c}{4\pi}(\mathbf{E}_0 \times \Delta\mathbf{H} + \Delta\mathbf{E} \times \mathbf{H}_0), \quad (5)$$

With the help (4) and (5) we obtain

$$\mathbf{S}_{\rm scat} = \frac{9\pi}{4} S_0 \frac{\gamma_{\rm r}^2}{(k_{\rm l} r)^2} \frac{\mathbf{r}}{r} \frac{|\mathbf{e}_{\rm l}\mathbf{e}_s^-|^2 + |\mathbf{e}_{\rm l}\mathbf{e}_s^+|^2}{(\omega_{\rm l} - \tilde{\omega}_0)^2 + \Gamma^2/4}. \quad (6)$$

The magnitude of the total flux of scattered light in time unit is

$$\Pi_{\rm scat} = \frac{3\pi}{2} S_0 \frac{\gamma_{\rm r}^2}{k_{\rm l}^2} \frac{1}{(\omega_{\rm l} - \tilde{\omega}_0)^2 + \Gamma^2/4}\,. \quad (7)$$

Having divided $\Pi_{\rm scat}$ on S_0 and using the ratio $k_{\rm l} = 2\pi/\lambda_{\rm l}$, we obtain the total scattering section

$$\sigma_{\rm scat} = \frac{3}{2\pi}\lambda_{\rm l}^2 \frac{\gamma_{\rm r}^2/4}{(\omega_{\rm l} - \tilde{\omega}_0)^2 + \Gamma^2/4}\,. \quad (8)$$

The differential sections of light scattering are determined in [4].

4. The interference contribution into the Pointing vector

The semiclassical approach allows to determine the light absorption section by quantum dots. At monochromatic irradiation, the absorption equals 0 at $\gamma = 0$. The same result is true for a quantum well [2]. The reason is that the energy dissipation spent by light on the exciton creation is absent at $\gamma = 0$, and the energy comes back at the exciton annihilation. The process of reabsorption and reradiation proceeds infinitely. In the case of the pulse irradiation at $\gamma = 0$, the integrated absorption is equal 0 [8].

At calculation of the light absorption coefficient of a quantum well, it was found out that it is necessary to take into account the interference of stimulating and induced electromagnetic fields. Let us show that the last statement is true for the quantum dot also. Using (1) and (2), we have

$$\mathbf{S}_{\rm interf} = \mathbf{S}_z + \mathbf{S}_\perp, \quad \mathbf{S}_z = -\frac{3}{4}\frac{\gamma_{\rm r}}{k_{\rm l} r} S_0 \mathbf{e}_z |\mathbf{e}_{\rm l}^+ \mathbf{e}_s^-|^2 \times \left(\frac{e^{i(\mathbf{k}_{\rm l}\mathbf{r} - k_{\rm l} r)}}{\omega_{\rm l} - \tilde{\omega}_0 - i\Gamma/2} + c.c. \right), \quad (9)$$

$$\mathbf{S}_\perp^\pm = -\frac{3}{4}\frac{\gamma_{\rm r}}{k_{\rm l} r} S_0 \times \left(\mathbf{e}_{\rm l}^\pm (\mathbf{e}_{\rm l}^\mp \mathbf{e}_s^\pm)(\mathbf{e}_s^\mp \mathbf{e}_z) \frac{e^{i(\mathbf{k}_{\rm l}\mathbf{r} - k_{\rm l} r)}}{\omega_{\rm l} - \tilde{\omega}_0 - i\Gamma/2} + c.c. \right), \quad (10)$$

where the indexes $+(-)$ correspond to the right (left) circular polarization Stimulating light. Since the formulas (9) and (10) correspond to the case $r \to \infty$, it is obvious that only the angles $\Theta \to 0$ can contribute into the constant energy flux because of the factor $e^{i(\mathbf{k}_{\rm l}\mathbf{r} - k_{\rm l} r)}$. However, in the RHS of (10) there is the factor $\mathbf{e}_{\rm l}^\mp \mathbf{e}_z$, which equals 0 at $\Theta = 0$. Therefore, the constant energy flux on large distances from a quantum dot corresponds only to the vector $\mathbf{S}_z$, which direction is opposite to direction of an axis z, conterminous with $\mathbf{k}_{\rm l}$. It proves to be true by direct calculation.

Let us calculate the energy flux $\Pi_z = \int ds \mathbf{S}_z$, passing through a surface, perpendicular to the direction z of stimulating light in time unit on a very large distance z behind the quantum dot. The surface element is equal $ds = \rho d\rho d\varphi$, and $\rho = z\tan\Theta$, $r = z/\cos\Theta$, where Θ is the angle between $\mathbf{k}_{\rm l}$ and $\mathbf{r}$. Having executed integration on the angle φ, which gives a factor 2π, using (20) and passing from the variable ρ to the variable Θ, we obtain

$$\Pi_z = -\frac{3\pi}{8}\frac{\gamma_{\rm r} z}{k_{\rm l}} \mathbf{e}_z \frac{S_0}{\omega_{\rm l} - \tilde{\omega}_0 - i\Gamma/2} \int_0^{\pi/2} d\Theta \times \frac{\sin\Theta(1+\cos\Theta)^2}{\cos^2\Theta} e^{ik_{\rm l} z[1-(1/\cos\Theta)]} + c.c. \quad (11)$$

Further, let us pass to the variable $t = \cos^{-1}\Theta - 1$ from the variable Θ. At $z \to \infty$, having executed integration on t, we obtain

$$\Pi_z = -\frac{3\pi}{2}\frac{1}{k_{\rm l}^2} S_0 \mathbf{e}_z \frac{\gamma_{\rm r}\Gamma}{(\omega_{\rm l} - \tilde{\omega}_0)^2 + (\Gamma/2)^2}, \quad (12)$$

independent on z. In (12), the contributions approaching to 0 at $z \to \infty$ are omitted, as well as the contributions oscillating very rapidly on z.

Thus, we obtain that the interference contribution to the Pointing vector at $z \to \infty$ results into the constant energy flux directed oppositely to the axis z. It means that the energy flux of stimulating light decreases on the value Π_z. From the formulas (11), it is obvious that at $z \to \infty$ the basic contribution into the integral on Θ is brought in by the very small angles, when $e^{i(\mathbf{k}_{\rm l}\mathbf{r} - k_{\rm l} r)}$ approaches to the unit.

5. The light absorption cross section

Since $\Gamma = \gamma_{\rm r} + \gamma$, the energy flux consists of two parts: $\Pi_z = -\mathbf{e}_z \Pi_{\rm scat} - \mathbf{e}_z \Pi_{\rm abs}$, where $\Pi_{\rm abs}$ is defined in (7).

It is obvious that the energy flux $-\mathbf{e}_z \Pi_{\rm scat}$ compensates the total flux of the scattered energy, and $-\mathbf{e}_z \Pi_{\rm abs}$ is the energy flux absorbed by a quantum dot during the time unit. Having divided $\Pi_{\rm abs}$ on the density S_0 of the stimulating energy flux, we obtain that the total light absorption cross section results in

$$\sigma_{\rm abs} = \frac{3}{2\pi}\lambda_{\rm l}^2 \frac{\gamma_{\rm r}\gamma/4}{(\omega_{\rm l} - \tilde{\omega}_0)^2 + (\Gamma/2)^2}. \quad (13)$$

At $\gamma = \gamma_{\rm r}$ in the resonance, $\sigma_{\rm scat}^{\rm res} = \sigma_{\rm abs}^{\rm res} = \frac{3}{8\pi}\lambda_{\rm l}^2$.

6. Conclusion

The cross sections of light scattering and absorption by quantum dots are obtained. The results are applicable for spherically symmetric envelope exciton wave functions and for quantum dots of any sizes, if the light wave length exceeds these sizes.

References

[1] L. C. Andreani *et al*, *Solid State Commun.* **77**, 641 (1991).
[2] L. C. Andreani *et al*, *Phys. Rev. B* **57**, 4670 (1998).
[3] E. L. Ivchenko *et al*, *Soviet Physics Solid State* **34**, 968 (1992).
[4] S. T. Pavlov *et al*, *Proc. 14th Int. Simposium "Nanostructures: Physics and Technology"*, St Petersburg, 144 (2006); cond-mat/0605650.
[5] I. G. Lang *et al*, *JETP* **96**, 268 (2003).
[6] I. G. Lang *et al*, *Physics of the Solid State* (St Petersburg) **46**, 1761 (2004).
[7] I. M. Tsidilkovsky, *The band structure of semiconductors* Nauka, Moscow (1978).
[8] D. A. Contreras-Solorio *et al*, *Phys. Rev. B.* **62**, 16815 (2000).

15th Int. Symp. "Nanostructures: Physics and Technology"
Novosibirsk, Russia, June 25–29, 2007

Effect of the homogeneous broadening of localized electron states on the spin relaxation processes of excitons in CdSe/ZnSe quantum dots

A. Klochikhin[1,2], A. Reznitsky[1], *S. Permogorov*[1], K. Mironenko[1], E. Tsitsishvili[3], R. v. Baltz[3], H. Kalt[3] and C. Klingshirn[3]

[1] Ioffe Physico-Technical Institute, St Petersburg, Russia
[2] Nuclear Physics Institute, 188350, St Petersburg, Russia
[3] Institut für Angewandte Physik, Universität Karlsruhe (TH), 76128 Karlsruhe, Germany

Abstract. Spin relaxation of excitons and/or trions in semiconductor CdSe/ZnSe quantum dots has been studied both theoretically and experimentally. We have demonstrated that the spin relaxation processes are strongly influenced by the homogeneous broadening of localized electronic levels caused by the multi-phonon processes. Such broadening relaxes the limitations on the energy of phonons participating in one-phonon transitions between the spin sublevels. With the account for the multi-phonon broadening of spin sublevels we were able to give a model description of the temperature dependence of polarization degree in the PL spectra of CdSe/ZnSe quantum dots and to restore from experimental data the characteristic function describing the interaction of localized electronic states with phonons.

Presently the study of spin relaxation of localized carriers in quantum dots attracts a considerable interest due to the perspectives of development of spin-memory devices. In present work we have studied, both experimentally and theoretically, the processes of spin relaxation of excitons and trions confined in the self-organized CdSe/ZnSe quantum dots (QD's). The spin relaxation rates, as well as its temperature dependence were monitored through the study of the degree of linear or circular polarization (PD) of the photoluminescence (PL) appearing at resonant excitation of the samples by linearly or circularly polarized laser light in resonance with the main PL band. The inhomogeneously broadened PL band arises due to the radiative recombination of carriers localized in quantum dots, formed by ZnCdSe solution. The distribution of QD's on sizes and composition essentially depends on the technology of the dot growth. The high-energy part of the PL band is formed by the emission of neutral excitations (excitons) whereas the low-energy tail of the band corresponds mostly to the emission of charged excitations (trions) [1]. The linear polarization of PL arises due to the optical alignment (OA) of exciton states. The contribution of excitons to the circular polarization is usually rather small due to the anisotropy of localizing potential leading to the splitting of $m = \pm 1$ spin sublevels. So, the circular polarization is mainly due to the optical orientation (OO) of trion states for which the OA is not possible due to the odd number of spins. Due to the inhomogeneous nature of the PL band the observed value of polarization degree (PD), as well as the relative value of linear and circular polarization strongly depend on the position of exciting laser line within the PL band. The spectrum of PL and the spectral distribution of PD are shown in Fig. 1 for resonant excitation around the maximum of the PL band when both linear and circular PD of emission are observable.

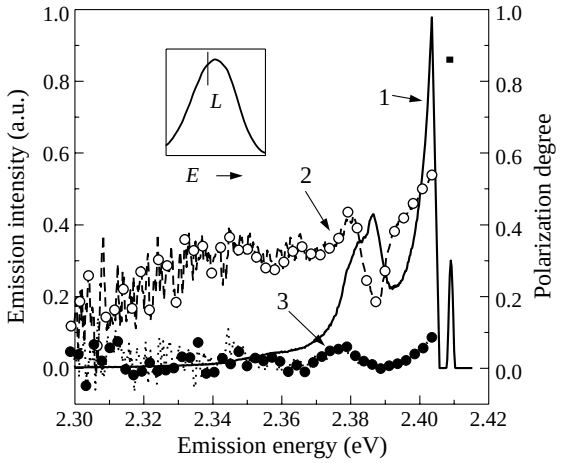

Fig. 1. Emission spectrum of CdSe/ZnSE QD's at resonant excitation (1) and spectral distribution of circular (2) and linear (3) PD. Insert shows the position of exciting line in the PL spectrum. $T = 7$ K.

At the increase of temperature the decrease of both linear and circular PD is observed indicating the increase of the spin relaxation rate $w_{1,2}$ between the spin sublevels of the localized states. The spin relaxation rate $w_{1,2}$ is strictly related to the observable value of PD $\rho(T)$ as:

$$\rho(T) = \frac{\rho_0 + \tau\,[w_{21}(T) - w_{12}(T)]}{1 + \tau\,[w_{12}(T) + w_{21}(T)]}, \qquad (1)$$

where τ is the total life-time of excitations and the values $w_{1,2}$ and $w_{2,1}$ are transition rates between the sublevels 1 and 2 and $w_{2,1} = w_{1,2}\exp(-E_{1,2}/kT)$.

Fig. 2 shows the temperature dependence of linear and circular PD along with the temperature dependence of parameter $(\tau w_{1,2})$, which characterizes the rate of spin relaxation. The spin sublevels responsible for the optical transitions with opposite polarization sense are either degenerate or have the splitting much less than 1 meV. The energy conservation law imposes severe restrictions on the energy of phonons which can participate in one-phonon spin-flip transitions limiting it by the level splitting. For such phonons a linear dependence of the relaxation rate on the temperature is expected.

However, as it can be seen from the Fig. 2, the spin relaxation rate demonstrates a strongly nonlinear increase with

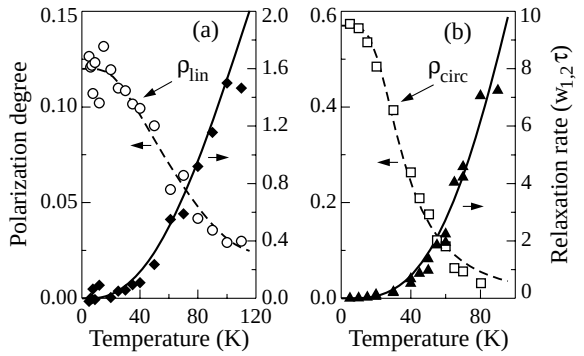

Fig. 2. Temperature dependence of linear (a) and circular (b) PD (open symbols) measured at resonant excitation at energy 2 meV below the excitation line. Dotted lines show the results of model fit. Temperature dependence of relaxation parameter $\tau w_{1,2}$ is shown by filled symbols.

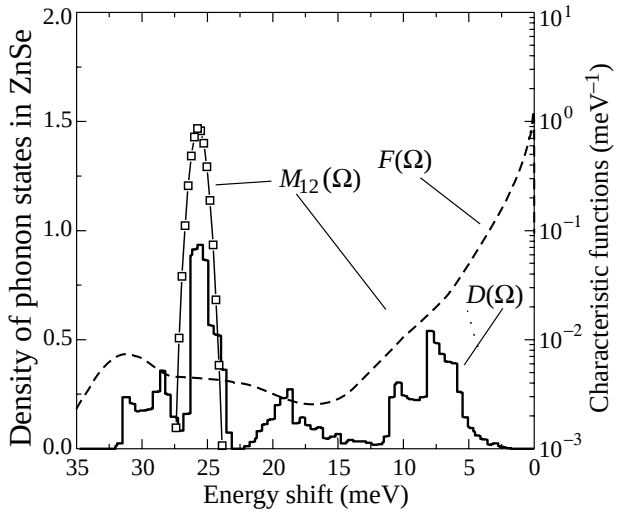

Fig. 3. Phonon density of states in ZnSe crystals (histogram $D(\Omega)$) and the characteristic functions $F(\Omega)$ and $M_{1,2}(\Omega)$.

temperature (nearly as T^3) and the observable PD persists up to the temperatures of about 100 K. These experimental results indicate that the phonons with the energies of at least several meV take part in the spin-flip transitions between the spin sublevels of the localized states.

To explain our experimental results we have developed a new approach, which explicitly takes into account the homogeneous broadening of spin sublevels due to the multiphonon exciton-phonon interaction. The account for the level broadening essentially widens the set of phonon states which can participate in spin-flip transitions. The probability of one-phonon spin-flip transitions between sublevels 1 and 2 can be written as:

$$w_{12}(T) = \int_0^\infty \Omega^2 d\Omega \mathcal{M}_{12}(\Omega)\Delta(\Omega - E_{12}/\hbar)[N(\Omega)+1]. \quad (2)$$

Here Ω is the phonon frequency, $N(\Omega)$ is the Bose factor, $\mathcal{M}_{12}(\Omega)$ is the function giving the probability of spin-flip transitions between sublevels 1 and 2 with the emission or absorption of one phonon with the energy $\hbar\Omega$. The factor $\Delta(\Omega - E_{12}/\hbar)$ under the integral replaces the δ-function and represents the continuous density of spin-flip transitions between the sublevels 1 and 2.

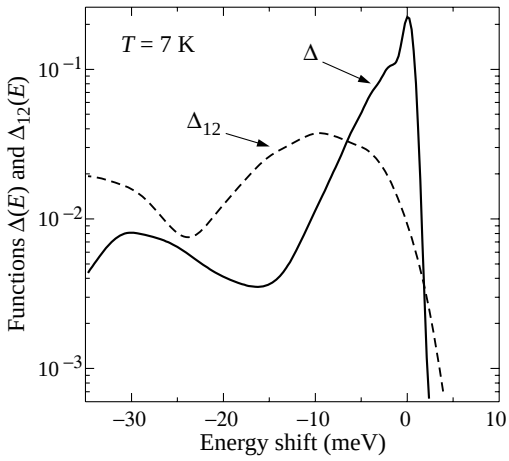

Fig. 4. Semi-logarithmic plot of the line-shape of the spin sublevel calculated with the help of the function $F(\Omega)$ and the spectral density of one-phonon transitions between the levels 1 and 2 ($\Delta_{1,2}$).

The homogeneous broadening of spin sublevels by multiphonon processes can be calculated with the help of the function $F(\Omega)$ describing the probability of interaction of localized states with phonons of the energy $\hbar\Omega$. This function allows to describe the effect of the multiphonon processes on the homogeneous broadening of the localized states.

The calculation of the functions $F(\Omega)$ and $\mathcal{M}_{12}(\Omega)$ from the first principles is very difficult. To find these functions we have used a numerical trial procedure based on the available experimental data. The function $F(\Omega)$ has been chosen in the form providing the best description of the temperature dependence of the line-shapes of narrow lines in μ-PL spectra and the phonon wings in PL spectra at resonant excitation. The trial function $\mathcal{M}_{12}(\Omega)$ has been reconstructed using the information on the energy distribution of the density of phonon states $D(\Omega)$ in ZnSe matrix. The characteristic functions $F(\Omega)$ and $\mathcal{M}_{12}(\Omega)$ providing the best description of the experimental results on the temperature dependence of the line-shapes are shown in Fig. 3. Using these function we were also able to perform a model description of our experimental data on the temperature dependence of PD (dashed curves on the Fig. 2).

The main conclusion of our work is that the account for the homogeneous broadening of the spin sublevels due to the multiphonon processes gives the possibility to describe the nonlinear temperature dependence of the spin-relaxation rates and the persistence of the observable polarization of PL in CdSe/ZnSe quantum dots up to relatively high temperatures.

References

[1] A. Reznitsky, A. Klochikhin, S. Permogorov *et al*, Proc. of the 27-th Int. Conf. on the Phys. of Semicond., pt. B, 935–936 (2005).

15th Int. Symp. "Nanostructures: Physics and Technology"
Novosibirsk, Russia, June 25–29, 2007

Effect of annealing on the localization volume of electrons in InAs/GaAs quantum dots

M. Yu. Petrov and I. V. Ignatiev
Institute of Physics, St Petersburg State University, 198504 St Petersburg, Russia

Abstract. Inter-diffusion of In and Ga atoms due to annealing of self-assembled quantum dots (QDs) InAs/GaAs is modeled by the numerical solution of a diffusion equation. Electron and hole wave functions and the energy of optical transition are calculated by the numerical solution of a Schrödinger equation. The QD shape and size as well as the diffusion parameters are determined by comparison of the numerical results with the available experimental data about the optical transition energies. The localization volume of electron in the annealed QDs is calculated and the modification of the hyperfine interaction of the electron and nuclear spins due to the annealing is analyzed.

Introduction

Annealing of nanostructures with InAs/GaAs quantum dots (QDs) at the temperatures above $\sim 800\,^{\circ}$C is observed to cause the blue shift of optical transitions in the QDs [1]. This effect is related to the efficient inter-diffusion of In and Ga atoms due to which the potential wells for electrons and holes become more shallow. Simultaneously the localization volume for electrons should be changed in the annealed QDs which may result in modification of various properties of the QDs. We discuss here only effect of the annealing on the hyperfine interaction of the electrons and nuclei in the QDs.

The hyperfine interaction is proposed to be the most important physical reason of the efficient spin relaxation of electrons localized in QDs [2]. Because of limited number of the nuclear spins in QDs, random orientation of the nuclear spins creates small nuclear polarization fluctuating from dot to dot. Electron spin precession in the effective field, B_f, of the fluctuations results in the fast dephasing of the electron spins in ensemble of QDs [3].

In this paper, we report on the numerical modeling of the annealing process and on the calculations of the electron and hole wave functions in QDs. We modeled the InAs/GaAs self-assembled QDs by appropriate choice of the QD shape and size. The calculations allowed us to obtain the annealing temperature dependence of the optical transition energies and of the localization volume for electrons in the QDs.

1. Modeling the QD annealing

The first step of our calculation as the appropriate choice of the QD shape and size. We considered the bell-like QD with cylinder symmetry. The QD is arranged on the one-monolayer wetting layer (see Fig. 1). The height, $h_{\mathrm{QD}} = 4.5$ nm, and base diameter (at $0.1h_{\mathrm{QD}}$), $d_{\mathrm{QD}} = 10.5$ nm, of the QD are optimized to obtain the best correspondence between the calculated and measured energies of the two lowest optical transitions for the unannealed QDs.

The second step is modeling the Ga-In inter-diffusion due to annealing. We describe the diffusion by the time-dependent equation:

$$\frac{\partial x(\mathbf{r},t)}{\partial t} - \nabla D(\mathbf{r}) \nabla x(\mathbf{r},t) = 0, \qquad (1)$$

where $x(\mathbf{r},t)$ is the fraction of In in the $\mathrm{In}_x\mathrm{Ga}_{1-x}\mathrm{As}$ solid solution obtained after annealing during the time t in the point $\mathbf{r}$.

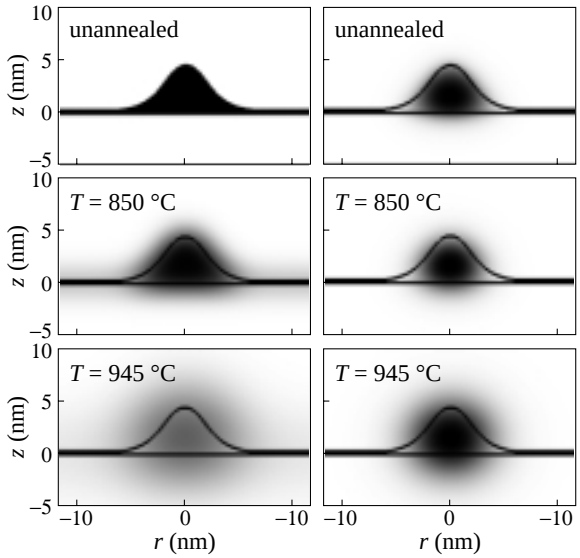

Fig. 1. Left column: calculated distribution of the In content x over the heterostructure an different annealing temperatures given at each panel. The unannealed case corresponds to the growth temperature $T = 500\,^{\circ}$C. Right column: calculated distribution of electron density for the QDs annealed at different temperatures. As seen the distribution acquires the spherical-like shape.

It is assumed that $x = 1$ inside the QD and $x = 0$ outside before annealing ($t = 0$).

The annealing is performed at different temperatures, T, and the fixed annealing time interval, $t_0 = 30$ s [1]. To connect our calculation procedure to the annealing one, we introduced an effective annealing time, $\tau = Dt_0$. We assume that the diffusion coefficient D does not depend on $\mathbf{r}$ and depends on temperature by usual law: $D = D_0 \exp(-\Delta E/kT)$ where ΔE is the activation energy of the inter-diffusion process. The numerical solution of Eq. (1) is performed using the finite element approximation for different effective annealing time τ. We used ΔE and prefactor D_0 as the fitting parameters. Left column in Fig. 1 shows examples of the In distribution over the heterostructure calculated for the unannealed QD (upper panel) and for the QDs annealed at different temperatures.

The third step of the calculations is the modeling of potential profiles for carriers. Using the results of calculations of the In content distribution $[x(\mathbf{r})]$ for the annealed QDs, we modeled the three-dimensional potential profile for the conduction and valence bands. For this purpose, we used a linear

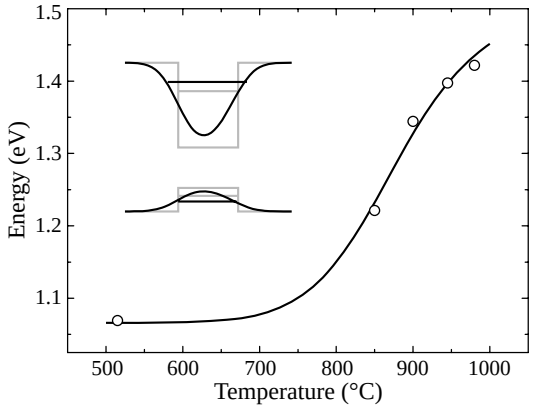

Fig. 2. Calculated temperature dependence of the energy of the lowest optical transition (solid line). Fitting parameters are: $D_0 = 2.7 \times 10^{-10}$ cm^2/s, $\Delta E = 1.7$ eV. Circles are the experimental data obtained from the photoluminescence spectra of the annealed samples. Inset shows the potential profile cross-sections at $r = 0$ (see Fig. 1) and the energy levels for unannealed QD (gray lines) and for the QD annealed at $T = 850$ °C (black lines).

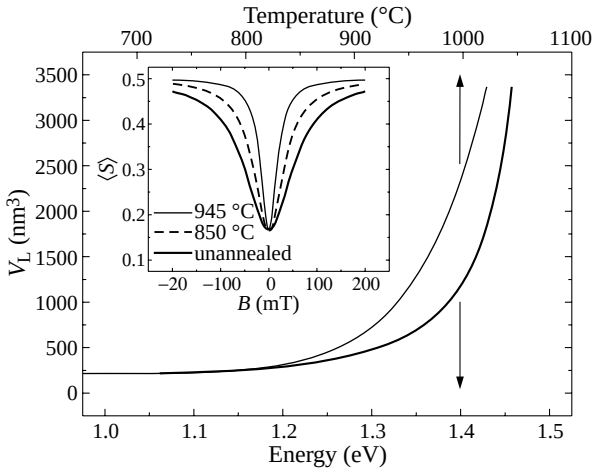

Fig. 3. Calculated electron localization volume as a function of the optical transition energy (black curve) and as a function of the annealing temperature (gray curve). Inset shows the magnetic field dependence of the electron spin polarization for the QDs annealed at different temperatures.

approximation for bandgap of $In_xGa_{1-x}As$ and for effective masses of carriers in the conduction and valence bands with the use of know values for InAs and GaAs crystals. Ratio of the band offsets for conduction and valence bands was set 3.5:1 in accordance to Ref. [5]. No strain effects was considered for simplicity though they cause considerable modification of energy structure of unannealed QDs [5]. First, this allowed us to simplify the calculations and to minimize the number of fitting parameters. Second, we assume that the annealing strongly reduces the strain in the QD structures.

2. Electron localization volume

We calculated the electron and hole wave functions for the lowest energy states in the annealed QDs by solving the Schrödinger equation with the three-dimensional potential calculated as described above. The right column in Fig. 1 shows the electron density distributions for the QDs annealed at different temperatures. The dependence of the optical transition energies on the annealing temperature is shown in Fig. 2. As seen the calculations well reproduce the dependence obtained experimentally.

The hyperfine interaction of electron in a QD is determined the electron localization volume defined as [3]:

$$V_L = \left(\int |\psi(\mathbf{r})|^4 \, dV \right)^{-1}, \qquad (2)$$

where $\psi(\mathbf{r})$ is the electron wave function. We calculated V_L as a function of the annealing temperature (Fig. 3). As seen, this volume rapidly increases with at annealing. Correspondingly, the effect of the nuclear spins on the electron spin is rapidly decreases. To illustrate this effect more quantitatively, we calculated the effective magnetic field of the nuclear spin fluctuations, $B_f = B_N/\sqrt{N_L}$ where B_N is the effective magnetic field of the totally polarized nuclear spins and $N_L = V_L/v_0$; v_0 is the unit cell volume. The effective field B_f gives rise to the three-fold decrease of the electron spin orientation in the QD ensemble. The external field, B, directed along the initial electron spin orientation suppresses the effect of nuclear spins and restores the electron spin orientation. This effect is really observed for InGaAs QDs [7]. The field dependence of the spin orientation can be approximated by a phenomenological function: $\langle S \rangle = S_0 \left(1 - 0.67/[1 + (B/B_f)^2]\right)$ where S_0 is the initial value of the electron spin. We modeled this dependence for QDs annealed at different temperatures (see inset in Fig. 3). For this purpose we calculated B_N taking into account the partial contributions of different nuclei, $B_N = x\, b_N^{\mathrm{In}} + (1-x)\, b_N^{\mathrm{Ga}} + b_N^{\mathrm{As}}$, where x is the average fraction of the In content in the annealed QDs and b_N for In, Ga, and As nuclei are taken from Ref. [6]. The calculated dependences show dips around zero magnetic field with full width at half maximum of the order of several tens of mT, in good correspondence with experimental observations [7]. The dip becomes more narrow with increasing temperature of the annealing.

Acknowledgements

This work has been supported in part by RFBR and ISTC (grant No. 2679).

References

[1] W. Langbein *et al*, *Phys. Rev. B* **69**, 161301(R) (2004).
[2] D. Gammon *et al*, *Phys. Rev. Lett.* **86**, 5176 (2001).
[3] I. A. Merkulov, Al. L. Efros, and M. Rosen, *Phys. Rev. B* **65**, 205309 (2002).
[4] B. Pal *et al*, *J. Phys. Soc. Jpn.* **75**, 054702 (2006).
[5] O. L. Lazarenkova *et al*, *Appl. Phys. Lett.* **85**, 4193 (2004).
[6] R. Oulton *et al*, *Phys. Rev. Lett.* **98**, 107401 (2007).
[7] R. Oulton, R. V. Cherbunin, A. Greilich *et al*, *Proceedings of the 14th Int. Symp. "Nanostructures: Physics and Technology"*, Ioffe Inst., St Petersburg, p. 129 (2006).

15th Int. Symp. "Nanostructures: Physics and Technology"
Novosibirsk, Russia, June 25–29, 2007

Theory of spin interaction in coupled quantum dots

I. V. Ponomarev[1], M. Scheibner[1], M. F. Doty[1], A. Bracker[1], D. Gammon[1], V. L. Korenev[2] and T. L. Reinecke[1]

[1] Naval Research Laboratory, Washington DC, 20375, USA
[2] Ioffe Physico-Technical Institute, St Petersburg, Russia

Abstract. We discuss the interaction between electron and hole spins in a vertically coupled InAs/GaAs asymmetric quantum dots. This interaction manifests itself in distinctive fine structure patterns in photoluminescence spectra. We construct effective Hamiltonians in terms of a minimal number of physical parameters that provide the basis for a description of the energies and intensities of the observed optical transitions in charged excitons.

Introduction

A confined electron spin in a quantum dot (QD) is one of the leading candidates for the realization of a quantum bit (qubit). Spin, unlike charge, interacts weakly with its environment and better maintains quantum coherence. When more than one particle is present in a system, a purely quantum-mechanical interaction, called exchange interaction, becomes important. It entangles different spins and manifests itself in spectroscopic fine structure [1].

While much of the progress to date toward the realization of quantum gates has been made in electrostatically gated quantum dots through transport measurements and fast electrical switching [2], the use of optical techniques in self-assembled QDs has several advantages. The most important of them are speed, coherent control, and possibility to transmit quantum information through free space or optical fibers. On the other hand, optical excitation implies that two different kinds of particles are involved (electrons and holes). Therefore, the number of physically important parameters becomes larger compared to transport experiments in electrostatically defined QDs. The physical picture becomes even more intricate in coupled quantum dots (CQDs) where tunneling and inter-dot Coulomb interactions result in the formation of molecular quantum dot states. In this paper we derive an effective Hamiltonian that describes the low energy excitations of this system in terms of a small number of physical parameters.

The model

In optically addressed CQDs tuned by applied electric field, an electron-hole (e–h) pair is created in the presence of the previously existing spins. Due to variations in growth conditions the sizes and the shapes of QDs vary from dot to dot. This inherent asymmetry in CQD system causes electron and hole resonances to occur at different fields. When the electric field brings the bottom (B) and the top (T) hole levels into resonance, the electron level of the top dot is shifted to much higher energies relative to that of the bottom dot, and the electron remains localized in one dot. This results in additional large single-particle electron and hole detuning parameters, which were not considered in previous theoretical models for identical QDs [3, 4].

In the envelope-function approximation we choose a truncated single-particle basis consisting of only the 'atomic' s-shell orthonormalized orbitals for the electron localized primarily in the bottom dot, $\varphi^{\rm e}_{\rm B}(\mathbf{r}_{\rm e})$, and for the holes in both dots: $\varphi^{\rm h}_{\rm B}(\mathbf{r}_{\rm h})$, $\varphi^{\rm h}_{\rm T}(\mathbf{r}_{\rm h})$. Bra-ket notations for these single-particle states are $|B^{\rm e}\rangle$, $|B^{\rm h}\rangle$, $|T^{\rm h}\rangle$. For the electron spin functions we use the following notations: $|\alpha^{\rm e}\rangle \equiv |S^{\rm e}_z = -1/2\rangle$, $|\beta^{\rm e}\rangle \equiv |1/2\rangle$. The heavy hole spin function ($J = 3/2$, $J_z = \pm 3/2$) is treated as a fermion with pseudo-spin 1/2. To avoid phase multipliers in the pseudospin representation the correspondence of the projections are: $|\alpha^{\rm h}\rangle \equiv |-1/2\rangle = |J^{\rm h}_z = +3/2\rangle$, $|\beta^{\rm h}\rangle \equiv |1/2\rangle = |J^{\rm h}_z = -3/2\rangle$. For two-particle spin states we will use an orthogonal set of singlet and triplet spin wave functions

$$\begin{aligned}
\left|s_{ij}\right\rangle &= 2^{-1/2}\left(|\beta_i\rangle|\alpha_j\rangle - |\alpha_i\rangle|\beta_j\rangle\right),\\
\left|\tau^{(0)}_{ij}\right\rangle &= 2^{-1/2}\left(|\beta_i\rangle|\alpha_j\rangle + |\alpha_i\rangle|\beta_j\rangle\right),\\
\left|\tau^{(+1)}_{ij}\right\rangle &= |\beta_i\rangle|\beta_j\rangle,\ \left|\tau^{(-1)}_{ij}\right\rangle = |\alpha_i\rangle|\alpha_j\rangle.
\end{aligned}$$

We take the applied electric field, F, to change only the difference between two hole energies by $f = |e|F\tilde{d}$ (e is the charge of the electron, $\tilde{d} = d + (h_{\rm B} + h_{\rm T})/2$ is the distance between the centers of the two dots). The zero of electric field occurs when the two hole energies would cross in the absence of coupling between the dots.

The many-body basis configurations for each molecule are constructed from antisymmetrized products of single-particle states. To describe these many-body basis state in CQDs we use the following nomenclature. ${}^{(n_1,n_2)}_{(m_1,m_2)}X^q$ denotes the CQD system with $n_1(m_1)$ electrons (holes) in the bottom QD and $n_2(m_2)$ electrons (holes) in the top QD with total charge $q = (m_1 + m_2) - (n_1 + n_2)$. In order to label excitonic transitions between charge states and to indicate which charges are involved, the corresponding electron(hole) index is underlined. For example, the abbreviation ${}^{(1,0)}_{(2,\underline{1})}X^{2+}$ means e-h recombination ${}^{(1,0)}_{(2,1)}X^{2+} \rightarrow {}^{(0,0)}_{(2,0)}X^{2+}$ in doubly positively charged exciton.

Because we consider the electrons to be distinguishable from the holes we add the electron-hole exchange interaction in the form of the short-range effective Hamiltonian:

$$\hat{H}^{\rm eh}_{\rm exch} = A\sum_{i,j}\delta(\mathbf{r}_{{\rm e}i} - \mathbf{r}_{{\rm h}j})\hat{\sigma}^{(i)}_{{\rm e}z}\hat{\sigma}^{(j)}_{{\rm h}z}, \qquad (1)$$

where A is a coupling constant, $\hat{\sigma}_{{\rm e(h)}z}$ are Pauli matrices, and z is the growth direction, the strongest confinement direction for electrons and holes. In the envelope wave function approximation and in effective atomic units, the many-particle Hamiltonian of the CQD system consists of three parts:

$$\hat{H} = \sum_{\alpha,l}\mathbf{h}^{\alpha}_{l} + \sum_{\alpha,\beta,l,m}\frac{e_\alpha e_\beta}{|\mathbf{r}_{\alpha l} - \mathbf{r}_{\beta m}|} + \hat{H}^{\rm eh}_{\rm exch}, \qquad (2)$$

where $\alpha, \beta = e$ or h; $l, m = 1, 2\ldots$ The first sum represents single-particle Hamiltonians for the electrons and holes, the second part gives the Coulomb interactions between particles ($e_{\alpha,\beta}$ are electron or hole charges), and the third part is electron-hole exchange Hamiltonian, Eq. (1). The single-particle Hamiltonians have the following matrix elements: $\langle B^\alpha|\mathbf{h}^\alpha|B^\alpha\rangle=\varepsilon_\alpha$, $\langle T^{\rm h}|\mathbf{h}^{\rm h}|T^{\rm h}\rangle=\varepsilon_{\rm h}-f$, $\langle B^{\rm h}|\mathbf{h}^{\rm h}|T^{\rm h}\rangle=t_{\rm h}$, where ε_α are the electron or hole confinement energies in the bottom QD, and $t_{\rm h}$ is the hole tunneling rate. The Coulomb part of the many-particle Hamiltonian generates Coulomb integrals: $V_{ijkl}^{\alpha,\beta} = \pm\int d\mathbf{r}d\mathbf{r}'|\mathbf{r}-\mathbf{r}'|^{-1}\varphi_i^{\alpha*}(\mathbf{r})\varphi_k^{\beta*}(\mathbf{r}')\varphi_j^{\alpha}(\mathbf{r})\varphi_l^{\beta}(\mathbf{r}')$. The electron-hole exchange interaction is given by $J_{ij}^{\rm eh} = A\int d\mathbf{r}|\varphi_{\rm B}^{\rm e}|^2\varphi_i^{\rm h*}\varphi_j^{\rm h}$

We find from model calculations that there is a hierarchy in the magnitudes of the parameters $t_{\rm h}$, $V_{ijkl}^{\alpha,\beta}$, $J_{ij}^{\rm eh}$, which is determined by their different dependences on distance between QDs. When the distance between QDs is 6 nm the smallest ($\sim 1\,\mu$eV) matrix elements are $J_{TT}^{\rm eh}$ and $V_{\rm BTBT}^{\rm hh} \equiv J^{\rm hh}$, which are responsible for exchange between particles in the two different QDs. The off-diagonal Coulomb matrix elements $V_{\rm BBBT}^{\alpha\beta}$, $J_{\rm BT}^{\rm eh}$ are larger ($\sim 10\ \mu$eV). They are responsible for small Coulomb corrections to tunneling. The intra dot electron-hole exchange constant $J_{\rm BB}^{\rm eh}$ and the hole tunneling rate are about ~ 0.4 meV. The absolute values of the diagonal Coulomb integrals $V_{\rm BBBB}^{\alpha,\beta}$, $V_{\rm BBTT}^{\alpha,\beta} \sim 10{-}20$ meV are comparable with single-particle energy splitting and are almost independent of inter dot distances. However, these integrals always appear in the diagonal matrix elements of the many-particle Hamiltonian as combinations of differences (see next Section). Thus, the magnitudes of the physical parameters, which come from the diagonal Coulomb integrals, are effectively smaller ($\sim 1{-}5$ meV).

Doubly positively charged exciton $\mathbf{X^{2+}}$

As an illustration here we consider the case of a doubly positively charged exciton X^{2+} in CQDs [5]. In order to obtain PL energy transitions we calculate the initial states (with 3 holes + 1 electron) and the final states (with 2 holes). The basis many-particle states of the initial Hamiltonian are

$$|1\rangle = \frac{|B^{\rm e},\beta^{\rm e}\rangle}{\sqrt{3}}\left[|B_1B_2T_3s_{12}\beta_3\rangle + |B_1T_2B_3s_{31}\beta_2\rangle + |T_1B_2B_3s_{23}\beta_1\rangle\right],$$
$$|2\rangle = \frac{|B^{\rm e},\beta^{\rm e}\rangle}{\sqrt{3}}\left[|T_1T_2B_3s_{12}\beta_3\rangle + |T_1B_2T_3s_{31}\beta_2\rangle + |B_1T_2T_3s_{23}\beta_1\rangle\right],$$
$$|3\rangle = \frac{|B^{\rm e},\beta^{\rm e}\rangle}{\sqrt{3}}\left[|B_1B_2T_3s_{12}\alpha_3\rangle + |B_1T_2B_3s_{31}\alpha_2\rangle + |T_1B_2B_3s_{23}\alpha_1\rangle\right],$$
$$|4\rangle = \frac{|B^{\rm e},\beta^{\rm e}\rangle}{\sqrt{3}}\left[|T_1T_2B_3s_{12}\alpha_3\rangle + |T_1B_2T_3s_{31}\alpha_2\rangle + |B_1T_2T_3s_{23}\alpha_1\rangle\right].$$

Here we omitted the superscript "h" from hole wave functions. We count energies from the absolute value of the first basis state (without the small $e{-}h$ inter-dot exchange): $H_{11} = 3\varepsilon_{\rm h}+\varepsilon_{\rm e}-f+V_{\rm BBBB}^{\rm hh}+2V_{\rm BBTT}^{\rm hh}-2V_{\rm BBBB}^{\rm eh}-V_{\rm BBTT}^{\rm eh}-J^{\rm hh}$. Then, the Hamiltonian has a block-diagonal form with

$$\hat{H}^{\pm} = \begin{pmatrix} \pm J_{\rm TT}^{\rm eh} & \tilde{t}^{\pm} \\ \tilde{t}^{\pm} & E_{\rm BTT} \pm J_{\rm BB}^{\rm eh} \end{pmatrix}, \qquad (3)$$

where $E_{\rm BTT} = -f + V_{\rm BBBB}^{\rm eh} - V_{\rm BBTT}^{\rm eh} + \Omega^{\rm hh}$, $\tilde{t}^{\pm} = -t_{\rm h} + V_{\rm BBBT}^{\rm eh} - V_{\rm BBBT}^{\rm hh} - V_{\rm TTBT}^{\rm hh} \pm J_{\rm BT}^{\rm eh}$, and we have introduced a parameter $\Omega^{\rm hh} = V_{\rm BBBB}^{\rm hh} - V_{\rm TTTT}^{\rm hh}$ that is responsible for the asymmetry induced difference of hole-hole Coulomb interaction ($\Omega^{\rm hh} = 0$ for identical QDs).

The basis of the final states for the two holes consists of three singlet and three triplet states:

$$|1\rangle = |T_1T_2, s_{12}\rangle, \quad |2\rangle = |B_1B_2, s_{12}\rangle,$$
$$|3\rangle = |2^{-1/2}(B_1T_2 + T_1B_2), s_{12}\rangle,$$
$$|4\rangle = |2^{-1/2}(B_1T_2 - T_1B_2), \tau_{12}^{(0)}\rangle,$$
$$|5\rangle = |2^{-1/2}(B_1T_2 - T_1B_2), \tau_{12}^{(+1)}\rangle,$$
$$|6\rangle = |2^{-1/2}(B_1T_2 - T_1B_2), \tau_{12}^{(-1)}\rangle.$$

In this basis the triplet states are eigenstates of the Hamiltonian $\hat{H} = \mathbf{h}_1^{\rm h} + \mathbf{h}_1^{\rm h} + |\mathbf{r}_1 - \mathbf{r}_2|^{-1}$. They are degenerate and are decoupled from singlets:

$$E_{4,5,6} = 2\varepsilon_{\rm h} - f + V_{\rm BBTT}^{\rm hh} - J^{\rm hh}. \qquad (4)$$

The matrix for singlets is

$$\begin{pmatrix} \Omega^{\rm hh} - 2f & J^{\rm hh} & t_{2\rm h}^{\rm T} \\ J^{\rm hh} & 0 & t_{2\rm h}^{\rm B} \\ t_{2\rm h}^{\rm T} & t_{2\rm h}^{\rm B} & -\delta_{\rm hh} - f + J^{\rm hh} \end{pmatrix}, \qquad (5)$$

where energies are counted from

$$H_{22} = 2\varepsilon_{\rm h} + V_{\rm BBBB}^{\rm hh}, \quad \delta_{\rm hh} = V_{\rm BBBB}^{\rm hh} - V_{\rm BBTT}^{\rm hh},$$
$$t_{2\rm h}^{\rm T} = \sqrt{2}\left(t_{\rm h} + V_{\rm TTBT}^{\rm hh}\right), \quad t_{2\rm h}^{\rm B} = \sqrt{2}\left(t_{\rm h} + V_{\rm BBBT}^{\rm hh}\right).$$

The energy differences between initial and final states determine the energy positions of PL spectrum. These transitions reveal the characteristic "X" pattern observed in the experiment [5]. The PL intensities are calculated using the Fermi Golden rule:

$$\sum_{\rm in,fin}\left|\langle\psi_{\rm fin}|M_{\rm BB}\hat{\mathbf{c}}_{\rm B\uparrow}^{\rm e}\hat{\mathbf{c}}_{\rm B\uparrow}^{\rm h} + M_{\rm BT}\hat{\mathbf{c}}_{\rm B\uparrow}^{\rm e}\hat{\mathbf{c}}_{\rm T\uparrow}^{\rm h}|\Psi_{\rm in}\rangle\right|^2$$
$$\times N_{\rm in}\delta(E_{\rm in} - E_{\rm fin} - E),$$

where $\hat{\mathbf{c}}_{\rm B(T)\uparrow}^{\rm e(h)}$ are the electron (hole) annihilation operators in the bottom (top) QD, and $M_{\rm BB(T)} = \int d\mathbf{r}\varphi_{\rm B}^{\rm e}\varphi_{\rm B(T)}^{\rm h*}$ are e–h overlap integrals. We use a Boltzmann thermalization $N_{\rm in}(T)$ for the initial states and the same Lorentzian broadening for all energies with average experimental linewidth $\Gamma = 50\ \mu$eV. We have found that the PL intensities are in a good agreement with experimental data.

Acknowledgements

We acknowledge the financial support by NSA/ARO, ONR, and NRC.

References

[1] E. A. Stinaff *et al*, *Science* **311**, 636 (2006).
[2] R. Hanson *et al*, cond-mat/0610433 (2006).
[3] Y. B. Lyanda-Geller, T. L. Reinecke, and M. Bayer, *Phys. Rev. B* **69**, 161308(R) (2004).
[4] B. Szafran *et al*, *Phys. Rev. B* **71**, 205316 (2005).
[5] M. Scheibner *et al*, cond-mat/0607241 (2006).

15th Int. Symp. "Nanostructures: Physics and Technology"
Novosibirsk, Russia, June 25–29, 2007

Nanohelices and Aharonov–Bohm quantum rings in a transverse electric field

V. L. Campo Jr[1], M. Rosenau da Costa[1], O. V. Kibis[2], S. V. Malevannyy[2], L. Huggett[3] and *M. E. Portnoi*[3]

[1] International Center for Condensed Matter Physics, University of Brasilia, 70904-970 Brasilia DF, Brazil
[2] Department of Applied and Theoretical Physics, Novosibirsk State Technical University, Novosibirsk 630092, Russia
[3] School of Physics, University of Exeter, Exeter EX4 4QL, United Kingdom

Abstract. We find a striking similarity between the electronic energy spectrum of a helical nanostructure in a transverse electric field and the spectrum of a quantum ring pierced by a magnetic flux in the presence of an in-plane electric field. Optimal parameters of a quantum ring are found, so that a weak in-plane electric field can be used for observation of the pronounced Aharonov–Bohm oscillations of electric dipole moment in the ring.

The widespread fascination with helical nanostructures probably stems from the miracle of the DNA, the majestic double-helix underlying the life on Earth. It has recently become possible to fabricate artificial nanohelices in different material systems, including InGaAs/GaAs [1], Si/SiGe [2], ZnO [3] and pure carbon [4]. Soon after the discovery of carbon nanotubes (CNTs), it was realized that a chiral CNT can be viewed as a helical motif [5], which becomes a single helix containing all elementary cells of the rolled graphene sheet in a special case of a $(n, 1)$ CNT [6].

We show that a quasi-one-dimensional helical nanostructure in the presence of an electric field normal to the helix axis behaves as a superlattice with parameters controlled by the applied field. This behavior includes Bragg scattering of electrons on a periodic potential created in a helix by the field, which results in the energy gap opening at the edge of the superlattice Brillouin zone. The gap is proportional to the helix radius and the strength of the applied electric field, $\Delta\varepsilon = eER$. In Fig. 1, the three lowest energy subbands for an electron confined to an ideal helix of radius R and pitch d in a transverse electric field E are plotted as a function of dimensionless parameter k/g, where k is the electron wave number along the helical line, $g = 2\pi/l_0$ and $l_0 = \sqrt{4\pi^2R^2 + d^2}$ is the length of one coil of the helix. Only the first Brillouin zone of the superlattice is shown.

The energy spectrum of an electron, which is confined in an infinitely-narrow ring pierced by a magnetic field flux (Aharonov–Bohm quantum ring) and subjected to an in-plane electric field, is exactly the same as the energy spectrum of an electron in a helix in a transverse electric field. Here the magnetic flux $\Phi = \pi R^2 B$ through the ring of radius R plays the same role as the electron momentum along the helical line. The spectrum shown in Fig. 1 is applicable to the ring if the dimensionless parameter $f = \Phi/\Phi_0$, where $\Phi_0 = h/e$, is used instead of k/g. The spectrum is periodic in f and only one period is shown in the figure. The linear in electric field splitting in the energy spectrum of the ring occurs when Φ is equal to an odd number of $\Phi_0/2$. This splitting takes place when the electric field mixes two states with the values of the angular momentum m differing by one, which are degenerate when $f = (2m+1)/2$ in the absence of electric field. The two resulting states, which are separated by the gap $\Delta\varepsilon = eER$, have the same absolute value but the opposite sign of the electric dipole moment. At zero temperature, the discussed effect

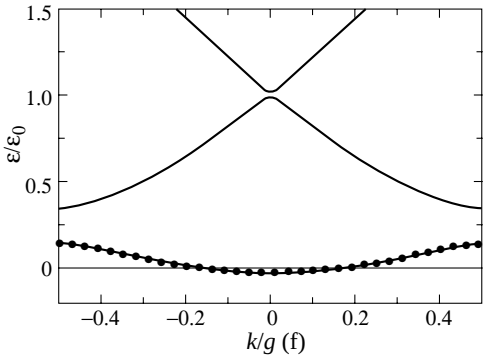

Fig. 1. The energy spectrum of an electron confined to an ideal helix in a transverse electric field and the spectrum of an electron in the infinitely narrow Aharonov–Bohm ring in an electric in the plane of the ring. For the helix $\varepsilon_0 = \hbar^2 g^2/2M$ and for the ring $\varepsilon_0 = \hbar^2/2MR^2$, where M is the electron effective mass. In both cases $eER = 0.2\varepsilon_0$. Red dots show the results obtained from a simple analytic formula.

results in the periodic in magnetic flux increase of the dipole moment P up to its maximum value of eR in the arbitrary weak electric field. With increasing temperature these oscillations become suppressed, since the population of the two states with opposite dipole moments becomes effectively the same, unless $eER > k_B T$. However, to observe pronounced oscillations the field should not be too large, so that it does not mix the states with different angular momenta for $\Phi = 0$, which requires $eER \ll \hbar^2/2MR^2$. At higher electric fields all traces of the Aharonov–Bohm effect are completely eliminated from the ground state spectrum [7]. The latter condition shows that the effect of magnetic flux oscillations of the dipole moment becomes stronger with decreasing the ring radius R. The smallest nanoring radius achievable by existing growth techniques [8,9] is about 10 nm. In fact, the further reduction of the ring size will make it difficult to achieve a flux through the ring of the order of the flux quantum at experimentally attainable magnetic fields of several Tesla. Our analysis shows that pronounced oscillations of the dipole moment can be observed in the nanorings with radius between 10 and 20 nm in relatively weak electric fields in the range of 100–200 V/cm and temperatures below 4 K. Figure 2 shows the magnetic flux dependence of the dipole moment of the 20 nm ring for two values of the in-plane field E and several temperatures. As discussed above

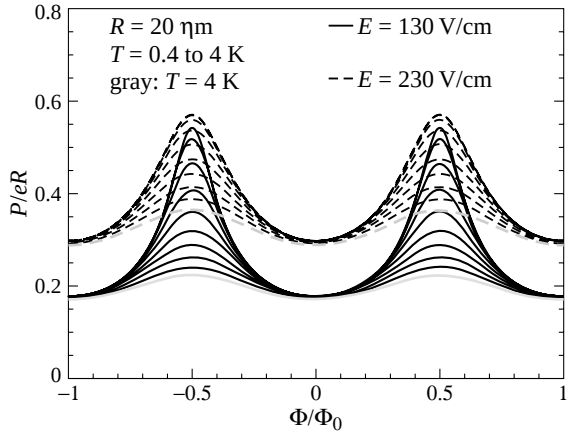

Fig. 2. Magnetic flux oscillations of the electric dipole moment P of a quantum ring of radius $R = 20$ nm, pierced by a magnetic flux Φ and subjected to an in-plane electric field $E = 130$ V/cm or $E = 230$ V/cm at T from 0.4 to 4 K.

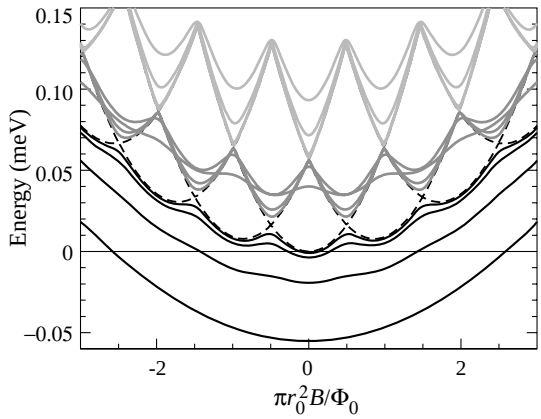

Fig. 3. A finite-width ring in a magnetic field for different values of in-plane electric field strength: $E = 1$, 2, 5 and 10 V/cm. The ring radius is $r_0 = 100$ nm and its width is 20 nm.

the oscillations are more pronounced in weaker electric fields and their amplitude is strongly temperature-dependent.

It is important to emphasize that the discussed effect is not an attribute of the infinitely-narrow ring model, but it persists in finite-width rings in a uniform magnetic field. Indeed, the essential feature required for this effect is the degeneracy of the states with the angular momenta differing by one at certain magnetic field values. This degeneracy is well-known to take place for finite-width rings. In Fig. 3 we show the energy spectrum of a finite-width ring in a uniform magnetic field normal to the plane of the ring for several values of in-plane electric fields. In our calculations we adopted the 'soft-edge' ring model of Ref. [10], which allows for analytical solutions in the absence of electric field. Not-too-large electric fields open the gaps linear in field, whereas large fields destroy the oscillations completely.

The discussed mixing of two states, which are degenerate in the absence of electric field, is completely controlled by the direction of the in-plane field with respect to a fixed axis. This brings the potential possibility for creating nanoring-based qubits, which do not require weak spin-orbit coupling between the electric field and electron spin. Arrays of the Aharonov–Bohm rings can also be used for polarization sensitive single-photon detection.

Acknowledgements

This work is supported by the INTAS Foundation (Grants 03-50-4409 and 05-1000008-7801), the Royal Society (UK), the Russian Foundation for Basic Research (Grants 06-02-16005 and 06-02-81012), the Russian Ministry for Education and Science (Grant RNP.2.1.1.1604), and MCT and FINEP (Brazil).

References

[1] V. Ya. Prinz *et al*, *Physica E* **6**, 828 (2000).
[2] V. Ya. Prinz *et al*, *Nanotechnology* **12**, 399 (2001).
[3] P. X. Gao *et al*, *Science* **309**, 1700 (2005).
[4] G. Zhang, X. Jiang, and E. Wang, *Appl. Phys. Lett.* **84**, 2646 (2004).
[5] C. T. White, D. H. Robertson, and J. W. Mintmire, *Phys. Rev. B* **47**, 5485 (1993).
[6] O. V. Kibis, D. G. W. Parfitt, and M. E. Portnoi, *Phys. Rev. B* **71**, 035411 (2005).
[7] Z. Barticevic, G. Fuster, and M. Pacheco, *Phys. Rev. B* **65**, 193307 (2002).
[8] A. Lorke *et al*, *Phys. Rev. Lett.* **84**, 2223 (2000).
[9] T. Mano *et al*, *Nano Lett.* **5**, 425 (2005).
[10] W.-C. Tan and J. C. Inkson, *Phys. Rev. B* **60**, 5626 (1999).

15th Int. Symp. "Nanostructures: Physics and Technology"
Novosibirsk, Russia, June 25–29, 2007

IR reflection spectra of multilayered epitaxial heterostructures with quantum dots InAs and GaAs and internal stress crystalline lattice calculation

P. V. Seredin[1], E. P. Domashevskaya[1], A. N. Lukin[1], I. N. Arsentyev[2], D. A. Vinokurov[2] and I. S. Tarasov[2]

[1] Voronezh State University, Universitetskaya pl., 1 394006, Voronezh, Russia
[2] Ioffe Physico-Technical Institute, St Petersburg, Russia

Abstract. IR reflection spectra of lattice vibrations were investigated in multilayered epitaxial heterostructures obtained by MOVPE epitaxy.

Introduction

The self-organized fabrication of the low dimensional semiconductor structures with nanoscale islands has been a subject of intensive investigations during the last years. These structures have a unique electrophysical and optical properties because of low dimensional confinement of carriers in the island volume. The most extensively studied heterostructures with nanoscale islands (NI's) are (Ga)InAs/GaAs [1], (Ga,In,Al)Sb/GaAs [2], InP/GaInP [3]. One of the widely applied methods for the study of the fine lattice properties and estimation of structural quality of epitaxial films is infrared optical vibration spectroscopy allowing to consider not only molecular composition of a substance but also internal stresses in its lattice since this method is very sensitive to them. Due to a high penetration ability of IR-radiation IR-reflection spectra of lattice vibrations allow to obtain information on the real state of the crystal microstructure at the appreciable depth. The aim of our work was the study of the influence of InAs and GaAs nanolayers on IR-lattice reflection spectra in multi-layer heterostructures.

1. Objects and methods of investigations

Investigated heterostructures were grown at Ioffe Institute. Epitaxial single-crystalline films of AlInAs/InAs/AlInAs InGaAs/GaAs/InGaAs and AlInAs/InGaAs/GaAs/InGaAs/AlInAs with InAs and GaAs nanolayers were grown by MOVPE on InP (100) substrates doped with sulphur providing concentration about 5×10^{17} cm^{-3}. Growth rate was of about 2.5 mcm/sec, the ratio of V/III was 50, while for growing of the "dots" the rate of growth was 2.5 Å/min and the ratio of V/III was of 200. The temperature of growth was the same of about 725 °C. Atomic composition of epitaxial films was determined by X-ray microanalysis. IR reflection vibration lattice spectra of the investigated epitaxial heterostructures were obtained at FIR-spectrometer Vertex 70 (Bruker) at room temperature in the range of 200 to 600 cm^{-1} with a resolution of 1 cm^{-1}.

2. IR-reflection spectra of the multi-layer epitaxial structures

Analysis of the obtained data, results of dispersion analysis IR-spectra in the model of "a semi-infinite substrate with the permittivity function s, and a surface thin film with the thickness d and the permittivity function f" and results of internal stress crystalline lattice calculation allows to make a next conclusions. IR reflection spectra of lattice vibrations from the multi-layer epitaxial structures of AlInAs/InAs/AlInAs/InP (100) with InAs quantum dots are presented in Fig. 1(a). As it is seen from the Fig. 1(a), three different basic modes of vibrations can be observed in the spectra: In-As, Al-As and In–P. Dispersion analysis demonstrated that with an increase of the number of InAs monolayers (from 6 to 8) LO-mode of Al-As vibrations considerably changes its position (from 397 to 416 cm^{-1}) (Table 1). All other LO and TO modes of the main vibrations change quite insignificantly.

Table 1. Composition and thickness of the layers in multi-layer heterostructures.

Composition and thickness of heterostructure layers	TO/LO vibration modes (cm^{-1})			
	In-As	Ga-As	In-P	Al-As
AlInAs/InAs/AlInAs 0.2 μ/6 ML/0.4 μ	228/ 251		307/ 325	360/ 397
AlInAs/InAs/AlInAs 0.2 μ/8 ML/0.4 μ	229/ 253		308/ 329	359/ 416
InGaAs/GaAs/InGaAs 0.2 μ/8 ML/0.6 μ	225/ —	253/ 267	311/ 369	
InGaAs/GaAs/InGaAs 0.2 μ/12 ML/0.6 μ	226/ —	253/ 266	312/ 373	
AlInAs/InGaAs/GaAs/ InGaAs/AlInAs 0.2 μ/300 Å/8 ML/300 Å/0.4 μ	227/ 256	– / –	308/ 329	358/ 399
AlInAs/InGaAs/GaAs/ InGaAs/AlInAs 0.2 μ/100 Å/8 ML/100 Å/0.4 μ	226/ 246	– / –	308/ 327	356/ 387

Fig. 1(b) represents IR reflection spectra for heterostructures of InGaAs/GaAs/InGaAs/InP (100) with GaAs quantum dots. These spectra also include three basic vibration modes: In-As, Ga-As and In–P. Analysis of the spectra demonstrated insignificant changes for TO and LO vibration modes. However, one should note that the mode of vibrations for InAs is splitted and there appears a fine structure for this mode.

IR reflection spectra of multi-layer heterostructures of AlInAs/InGaAs/GaAs/InGaAs/AlInAs/InP (100) with w-grooves are represented in Figure 1c. Analysis of the spectra demonstrated that they include three basic modes of vibrations: In-As, Al-As and In–P. Fourth Ga-As mode of vibrations is not practically observed and it is active only in the spectrum with less thickness of adjacent InGaAs layers (100 Å).

As for the frequencies of TO and LO the basic modes for all of vibrations they do not practically change except for the frequency of Al-As LO mode which considerably changes its

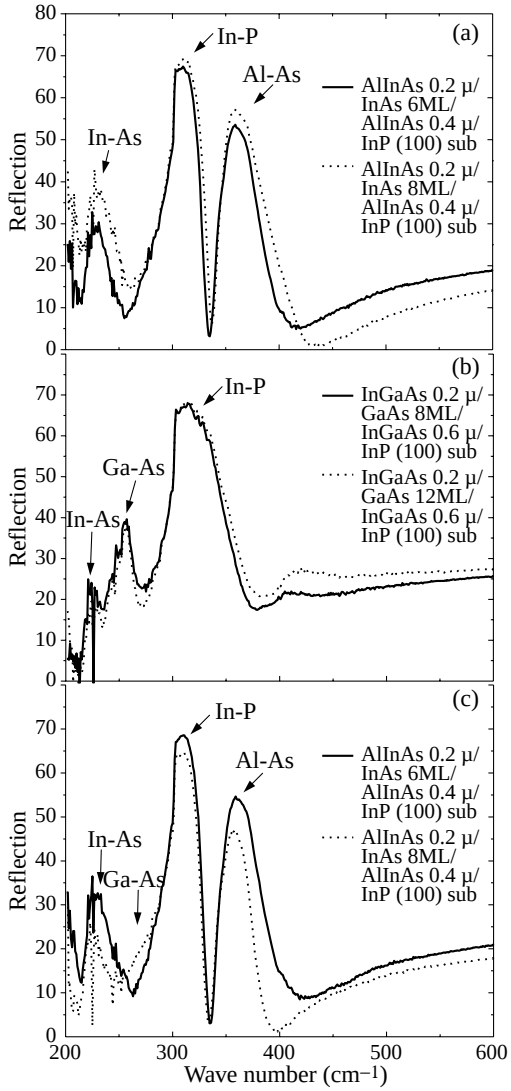

Fig. 1. IR reflection spectra of multilayered epitaxial heterostructures with embedded nanolayers InAs and GaAs.

position with a decrease of the thickness of InGaAs layer (from 399 to 387 cm^{-1}) (Table 1). Moreover, the splitting of In-As mode takes place just as in the spectra of heterostructures with GaAs layers. Analysis of the obtained data allows to make a conclusion the change (increase) of LO modes of Al-As vibrations in heterostructures AlInAs/InGaAs/GaAs/InGaAs/AlInAs/InP (100) with an increase of the number of embedded InAs layers the stresses in the adjacent layers of InGaAs è AlInAs also increase due to the difference in lattice parameters ($a_{\mathrm{AlInAs}} < a_{\mathrm{InAs}}$). Decrease of LO modes of Al-As vibrations in the spectra of the structures with embedded GaAs layers is due to the fact that at the decrease of thickness of InGaAs layer and, hence, mismatch of lattice parameters in the layers ($a_{\mathrm{AlInAs}} < a_{\mathrm{InGaAs}} < a_{\mathrm{GaAs}}$) AlInAs layer is subjected to rather high compression tensions. Appearance of the fine structure for In-As mode in the structures with GaAs embedded layers occurs since GaAs monolayers result in stretching tensions in the layers of InGaAs thus leading to separation of AlGaAs alloys and localizing of the optic phonons in these alloys as it takes place in the case of superlattices [4]. A dispersion analysis of all samples has allowed to determine frequencies of plasma oscillations and the characteristic lifetimes of plasmons

Table 2. Result of internal stress crystalline lattice calculation.

Composition and thickness of heterostructure layers	Internal stress crystalline lattice for atomic bond		
	In-As	Ga-As	Al-As
AlInAs/InAs/AlInAs 0.2 μ/6 ML/0.4 μ AlInAs/InAs/AlInAs 0.2 μ/8 ML/0.4 μ	0.053		0.035
InGaAs/GaAs/InGaAs 0.2 μ/8 ML/0.6 μ InGaAs/GaAs/InGaAs 0.2 μ/12 ML/0.6 μ	−0.028	0.021	
AlInAs/InGaAs/GaAs/InGaAs/AlInAs 0.2 μ/300 Å/8 ML/300 Å/0.4 μ AlInAs/InGaAs/GaAs/InGaAs/AlInAs 0.2 μ/100 Å/8 ML/100 Å/0.4 μ			−0.041

arising in monocrystalline InP (100) substrates. A result of internal stress crystalline lattice calculation is given in Table 2.

Acknowledgement

This work has been supported in part by RFFI grant 06-02-96313-r_center_a.

References

[1] A. Madhukar *et al*, *Appl. Phys. Lett.* **64**, 2727 (1994).
[2] F. Hatami *et al*, *Appl. Phys. Lett.* **67**, 656 (1995).
[3] D. A. Vinokurov *et al*, *Semiconductors* **35**, 235 (2001).
[4] U. Pusep *et al*, *Pisma v JETF* **52**, 9 (1991).

15th Int. Symp. "Nanostructures: Physics and Technology"
Novosibirsk, Russia, June 25–29, 2007

Photoluminescence of single InAs quantum dot in an AlAs matrix

K. S. Zhuravlev[1], *T. S. Shamirzaev*[1], M. Larsson[2] and P. O. Holtz[2]

[1] Institute of Semiconductor Physics, pr. Lavrentieva 13, 630090 Novosibirsk, Russia
[2] Department of Physics and Measurement Technology, Linkoping University, Sweden

Abstract. Micro-photoluminescence (μ-PL) of a simple InAs/AlAs quantum dot (QD) has been studied. It has been found that the μ-PL emission related to the recombination in a single QD is strongly broadened due to spectral diffusion. Emissions related to the recombination of biexcitons and excitons occupying excited levels of the QD are observed in μ-PL spectra at high excitation power densities. A red shift of the μ-PL emissions related to recombination of excitons in the ground and excited levels of the QD with increasing excitation power gives clear evidence for type I alignment of the InAs/AlAs QD.

Introduction

The system of InAs quantum dots (QD's) embedded in an AlAs matrix is very close to the system of InAs/GaAs QD's what concerns the Stranski–Krastanov growth mode, since AlAs has practically the same lattice constant as GaAs. Nevertheless, the increase in the QD barrier height leads to a stronger electronic confinement in the InAs/AlAs dots, and to significant changes in their electronic and optical properties as compared with the InAs/GaAs QD system [1–3]. Recently microsecond [2] and even millisecond-scale [3] non-exponential photoluminescence (PL) decays have been observed in InAs/AlAs QD's at low temperatures. To explain the long nonexponential PL decays in InAs/AlAs QD's three models have been proposed in the literature [2–4]. Dawson *et al* [2] attributed the long decay times to the recombination involving electrons and holes localized in spatially separated QD's. Later, the long QD PL decay was explained in terms of type II indirect transitions of electrons localized in the AlAs matrix with holes in the QD's [4]. A third explanation is based on the exchange splitting of excitonic levels in a QD, as proposed in our previous study [3]. In the latter case a long PL decay results from a long lifetime of an exciton in the optically inactive state in a QD. Since QD structures with type II alignment exhibit an energy blue-shift with filling QD by non-equilibrium carriers, which should be proportional to the cube root of the excitation power density (P) [5], one can test the type of alignment for InAs/AlAs QD's. However, due to significant dispersion of the QD's sizes, the PL emission of the InAs/AlAs QD's array demonstrates a considerable width ($>$ 200 meV) that hampered the observation of a relatively small energy shift of the emission with increasing excitation power. In this work, the type of alignment of InAs/AlAs QD's is studied by means of μ-PL of the QD's as a function of excitation power density.

1. Experimental

A sample with self-assembled InAs QD's in AlAs matrix was grown by molecular beam epitaxy on semi-insulating (001)-oriented GaAs substrates using a Riber-32P system. The sample consisted of one layer of InAs QD's sandwiched between two 25 nm thick layers of AlAs grown on top of a 200 nm buffer layer of GaAs. The first AlAs layer in all the samples was grown at $T_S = 600$ °C. The QD's were formed at $T_S = 530$ °C. To prevent InAs evaporation, the growth temperature was not increased during the deposition of a few initial monolayers of the second AlAs layer covering the QD's. The rest of the cover layer was grown at $T_S = 600$ °C. A 20 nm GaAs cap layer was grown on top of the sandwich in order to prevent oxidation of AlAs. The average QD density of about 10^8 cm^{-2} was found from transmission electron microscopy (TEM) plane view image demonstrated in Fig. 1.

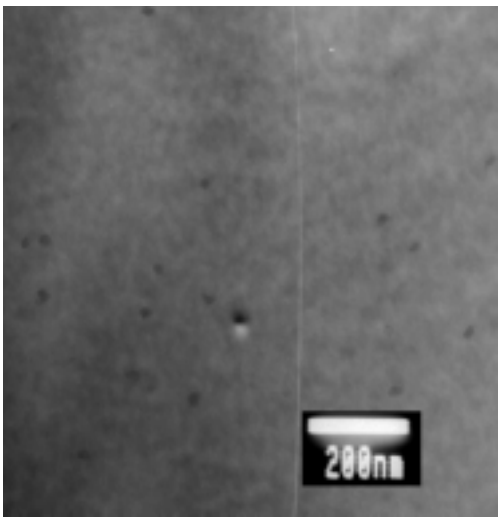

Fig. 1. TEM plan view image of the structure with InAs/AlAs QD's.

The excitation of μ-PL was carried out by a Verdi/MBD laser system with wavelength of 266 nm ($h\nu = 4.66$ eV). The laser spot was about 1.5 mm in diameter that will illuminate one or two QD's. The excitation power was varied from 5×10^{-4} to 6 mW. The emission was collected by a microscope, dispersed by monochromator and detected by a CCD. A temperature of 60 K was established using a closed-cycle helium cryostat.

2. Results

μ-PL spectra of a single InAs/AlAs QD as a function of excitation power density are depicted in Fig. 2. A single PL band (labeled as QD_0) related to the recombination of electrons and holes occupying the ground levels of QD is observed in the μ-PL spectrum at $P = 1$ kW/cm^{-2}. The line width (15 meV) exceeds resolution of our monocromator as a result of spectral diffusion [6]. An increase of P results in the appearance of additional lines in the μ-PL spectra (labeled as WL, QD_1, QD_2 and XX in Fig. 2). The intensities of these lines increase with increasing P stronger than the intensity of the QD_0 line. The XX line becomes dominating in the PL spectra

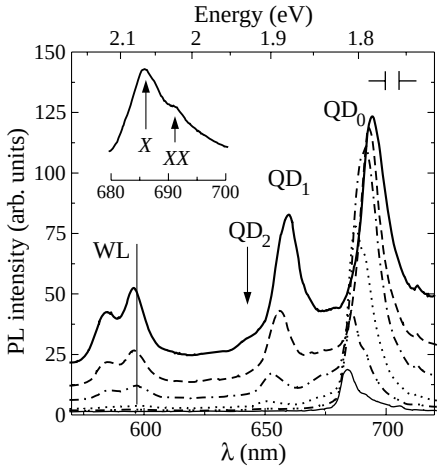

Fig. 2. μ-PL spectra of InAs/AlAs QD's as a function of excitation power P, top-down kW/cm^{-2}: 300, 170, 80, 19, 9, 1. Inset demonstrates QD0 and XX lines at $P = 9$ kW/cm^{-2}.

at $P > 40$ kW/cm^{-2}. The energy position of the WL line and the shift of the XX line with respect to the QD_0 line evidence that these lines are due to the recombinations of charge carriers in the wetting layer and of biexcitons [7], respectively. The QD_1 and QD_2 lines were identified as the recombination of carriers originating from the excited levels of QD. With increasing P, the WL line demonstrates a small blue shift due to filling of the wetting layer bands by non-equilibrium carriers [8]. On the other hand, the QD (XX, QD_0 and QD_1) bands demonstrate a significant red shift and broadening with filling of the QD by charge carriers. The observation of the excited levels of the QD and the emission red shift give unambiguously evidence for type I alignment of the structure.

Acknowledgement

This work is supported by the RFBR (grant No. 07-02-00134).

References

[1] P. Ballet *et al*, *J. Appl. Phys.* **90**, 481 (2001).
[2] P. Dawson *et al*, *Appl. Phys. Lett.* **82**, 2349 (2002).
[3] T. S. Shamirzaev *et al*, *Physica E* **20**, 282 (2004).
[4] P. Dawson *et al*, *J. Appl. Phys.* **98**, 013541 (2005).
[5] N. N. Ledentsov *et al*, *Phys. Rev. B* **52**, 14058 (1995).
[6] P. G. Blome *et al*, *Phys. Rev. B* **61**, 8382 (2000).
[7] D. Sarkar *et al*, *J. Appl. Phys.* **100**, 023109 (2006).
[8] S. K. Brieley, *J. Appl. Phys.* **74**, 2760 (1993).

15th Int. Symp. "Nanostructures: Physics and Technology"
Novosibirsk, Russia, June 25–29, 2007

Raman study of strain relaxation in Ge quantum dot array

A. B. Talochkin, V. A. Markov, A. G. Cherkov and V. I. Mashanov
Institute of Semiconductor Physics, pr. Lavrentieva 13, 630090 Novosibirsk, Russia

Abstract. We have studied Raman spectra of Si/Ge/Si structures with Ge quantum dots (QDs) obtained using a molecular beam epitaxy. In the spectra of structures grown at different growth conditions, features related to an inelastic strain relaxation in a QD array were observed. Two mechanisms of this relaxation were distinguished. It was shown that the strain relaxation is strongly non-uniform and results in a broad residual strain distribution in a QD array. As a result, an overall spectrum of electron states of a QD array differs considerably from the discrete levels of a separate QD.

Introduction

For device application of Ge quantum dot (QD) array being synthesized by the self-ordering growth in a molecular beam epitaxy (MBE) process, it is necessary to ensure uniformity of QD sizes and other parameters [1,2]. The mechanical strain of Ge QDs is a key parameter determining not only the QDs self-ordering mechanism but also an electronic state energy spectrum of individual QD. Thus, the valence band offset between pseudomorphic Ge and Si is $E = 0.75$ eV, and it is reduced by 0.2 eV for the case of full relaxation of the Ge strain [2]. A strain value is usually measured from the optical phonon line position observed in Raman spectrum. Raman spectra of Ge QDs obtained at sufficiently high growth temperatures (400–600 °C) have been studied in numerous experiments [1]. For this temperature range, interdiffusion of the components and also Ge-Si intermixing are appreciable. As a result, a solid solution Ge:Si, whose broad phonon lines complicate observation of strain relaxation in Ge QD array, is formed.

1. Experimental

In this work, we have studied Raman spectra of Si/Ge/Si structures with Ge QDs obtained by using MBE. The Ge QD arrays were grown at sufficiently low temperature of a substrate ($T_s = 300-250$ °C) at a deposition rate of 5 Å/min. An effective thickness of Ge layer was varied in the range of 4–15 ml. The grown QDs array was covered with Si layer 20 Å thick at the same temperature. A protective Si layer 200 Å thick was deposited last at $T_s = 450$ °C. Variation of the mentioned growth parameters (T_s, d) allows us to obtain the pseudomorphic Ge QD array with perfectly abrupt Ge/Si interfaces, and also to observe strain relaxation, which turns out to be strongly nonuniform and causes residual strain distribution in QD array.

2. Results

Fig. 1 shows the Raman spectra of the Si/Ge/Si structures obtained at different growth conditions. For the sample (a), $T_s = 250$ °C and $d = 8$ ml, for the sample (b), $T_s = 250$ °C and $d = 12$ ml, and for the sample (c), $T_s = 300$ °C and $d = 8$ ml. The optical phonon lines of Ge (304–318 cm^{-1}), the phonon lines of Ge/Si interface vibrations (a) (420 cm^{-1}), the Ge–Si mode of Ge:Si solid solution (c) (420 cm^{-1}), and the phonon line of Si substrate (525 cm^{-1}) are observed. The frequency shift of the Ge phonon line (Fig. 1(a)) from the bulk position indicated in Fig. 1 by the vertical arrow is 16 cm^{-1}. This shift corresponds to the value of biaxial deformation of

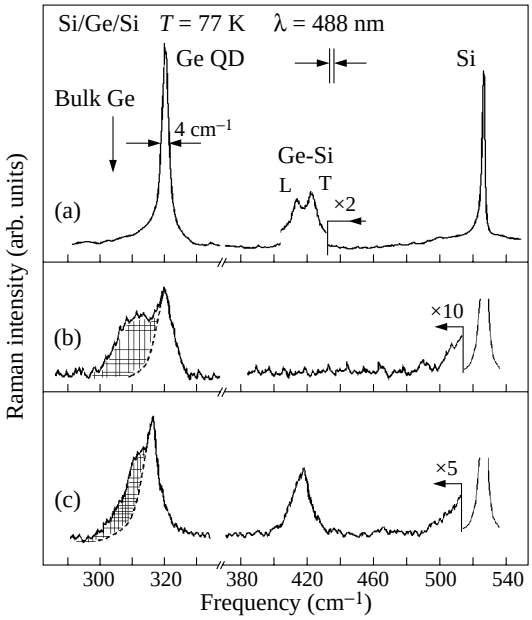

Fig. 1. Raman spectra of the Si/Ge/Si structures with Ge quantum dots obtained at different growth conditions.

Ge in the (100) plane equals 0.04, which is defined by pseudomorphic state of Ge islands. Besides, the doublet structure of the Ge-Si mode observed in the first sample (Fig. 1(a)) indicates that the Ge-Si interfaces are ideally-abrupt, as it has been shown by theoretical calculations [3]. The observed intensity of the Ge phonon line is anomalous high, being by five times grater than the bulk intensity measured with the same excitation wavelength. The half-width of this phonon line is 4 cm^{-1}, whereas that of the bulk phonon line is somewhat smaller (1.5 cm^{-1}). This broadening is probably uniform and determined by phonon life-time reducing appeared due to phonon interaction with interfaces and crystal imperfections. Thus, the QDs of the sample (a) have the identical stain state (pseudomorphic) with ideally-abrupt interfaces, and all the QDs give the nearly equal contribution to the observed phonon line.

Fig. 1(b),(c) shows the Raman spectra of the Si/Ge/Si structures with strain relaxation. In the first case (b, $d = 12$ ml), strain is relaxed by misfit dislocation formation at interfaces as a result of exceeding of the Ge effective thickness above the critical value (10 ml). The Ge phonon line intensity is reduced by factor of 20 with changing of line shape. The observed contour may be decomposed into two regions. The first one shown in Fig. 1(b) by the dashed line is attributed to Ge islands remaining in the pseudomorphic state. The second part (the

shaded area) results from partially relaxed Ge islands. As it is seen, the phonon frequency is varied from the bulk (304 cm^{-1}) position up to the nearly maximal value (320 cm^{-1}) for this part of QD array. The observed frequency shift is defined by residual strain value of Ge island. It is clear that, the residual strain distribution has an essentially nonuniform character in the relaxed part of QD array. The strain relaxation exhibits itself by a similar way with growth temperature increasing (Fig. 1(c)). In this case, QD strain is relaxed due to interdiffusion of Ge and Si, which results in formation of Ge:Si solid solution at interfaces. The discrete energy levels of individual QD should be dispersed over the range of 0.2 eV for relaxed part of QD array. This results in unfitness of such QD array for device application.

The observed non-uniformity may be explained taking into account the statistical nature of the relaxation process. The dislocation formation and interface intermixing of the components occur due to local temperature fluctuations, which fill an energy deficiency for overcoming of some energetic threshold. The occasional nature of this fluctuations may produce a considerable deviation of different parameters of a system from theirs average values. For example, for the full strain relaxation of a small size (200 Å) Ge island, it is required that $N = 4$ dislocations are formed at the interface. Supposing that the fluctuations of the value N is described by a regular distribution (Poisson's distribution), we can find that its deviation from the average value is $N^{0.5}$. This magnitude is comparable with the average one. This indicates that the residual strain distribution is broad, i.e. the strain relaxation is strongly non-uniform. For the case of diffusion intermixing, the fluctuating parameter is average composition of Ge:Si solid solution formed at the interface of a Ge island.

Acknowledgement

This work was supported by Russian Foundation for Basic Research (Grant No. 07-02-00299).

References

[1] J-M. Baribeau *et al*, *J. Phys.: Cond. Matt.* **18**, R139 (2006).
[2] K. Brunner, *Rep. Prog. Phys.* **65**, 27 (2002).
[3] S. de Gironcoli, *Phys. Rev. B* **48**, 8959 (1993).

15th Int. Symp. "Nanostructures: Physics and Technology"
Novosibirsk, Russia, June 25–29, 2007

Effect of bulk inversion asymmetry on infrared optical transitions in InAs/GaSb quantum wells

I. Semenikhin[1], *A. Zakharova*[1], K. Nilsson[2] and K. A. Chao[2]

[1] Institute of Physics and Technology of the Russian Academy of Sciences,
Nakhimovskii Avenue 34, Moscow 117218, Russia
[2] Department of Physics, Lund University, Sölvegatan 14A, S-223 62 Lund, Sweden

Abstract. We investigate the influence of bulk inversion asymmetry terms in the eight-band $\mathbf{k}\cdot\mathbf{p}$ Hamiltonian on subband dispersions and optical matrix elements for the infrared transitions in semiconductor quantum well structures, using InAs/GaSb quantum wells sandwiched by AlSb barriers as an example. We have found a considerable contribution from spin-flip processes to the probability of intersubband transitions caused by linearly polarized light with the electric field amplitude along the growth direction. In addition we found an essential anisotropy of the subband dispersions and optical matrix elements with respect to different directions of the in-plane wave vector of 2D hybridized electron-hole states.

Introduction

In the past there have been many studies on InAs/GaSb quantum wells sandwiched between two AlSb barriers. The strongly hybridized electron-hole levels in these structures are due to the overlap between the InAs conduction band and the GaSb valence band. The conduction and valence band edges of the InAs/GaSb quantum well under flatband conditions is shown in Fig. 1. If at zero in-plane wave vector $\mathbf{k}_\parallel$ the lowest electron level in InAs is below the highest hole level in GaSb, the electron-like and hole-like levels anticross at some finite $k_\parallel$. This creates hybridization gaps in the in-plane dispersion. The strong hybridization around these gaps significantly influences the intersubband optical transitions [1].

The bulk inversion asymmetry produces additional spin splits in the energy levels and mingles of states with different spin orientations. Also, the difference between the second and the third Luttinger parameters causes warping terms in the Hamiltonian. These factors modify the optical matrix elements for the intersubband transitions in InAs/GaSb quantum wells, but were not considered in previous calculations with radiation polarized along the growth direction. These effects will be included in the present work.

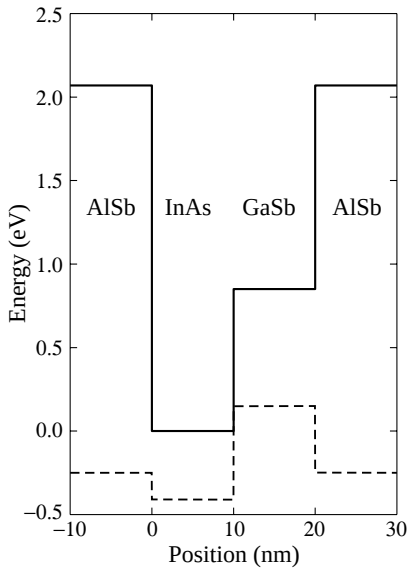

Fig. 1. The conduction and valence band edges of a InAs/GaSb quantum well with a 10 nm InAs layer and a 10 nm GaSb layer.

1. Model Hamiltonian and subband dispersions

We use the eight-band $\mathbf{k}\cdot\mathbf{p}$ model and Burt–Foreman envelope function theory, taking into account the strain induced by lattice-mismatch, to calculate subband dispersions and optical matrix elements. All electron states, light-hole states, heavy-hole states and split-off states are included in our model. We add to the Hamiltonian in Ref. [2] the bulk inversion asymmetry terms which are proportional to Kane's B-parameter, and the terms of the form $k_i\epsilon_{lj}$, where k_i is the wave vector component and ϵ_{lj} is the strain tensor component. The small linear-in-k_i terms in the valence band Hamiltonian, which do not depend on strain, are neglected. For a quantum well grown on InAs along the [001] direction, with a 10 nm InAs layer and a 10 nm GaSb layer, the calculated self-consistently subband dispersions for the in-plane wave vector along the [10] direction and the [11] direction are shown in Fig. 2.

According to the wave function properties at $\mathbf{k}_\parallel$=0, the six subbands in Fig. 2 are labeled as 1e and 2e for the electron states, 1hh, 2hh, and 3hh for the heavy-hole states, and 1lh for the light-hole states. Since at $\mathbf{k}_\parallel$=0 the 1e level is lower than the 1hh level, anticrossings of subbands occur at finite $\mathbf{k}_\parallel$, resulting in hybridization gaps between the 1hh subband and the 1e-like subband. Around these gaps the electron-like and the heavy-hole-like states are strongly hybridized. The hybridized wave functions have large amplitudes in both the InAs layer and the GaSb layer. After the anticrossing, the states of the 1hh subband become the 1e-like. The hybridization significantly affects the optical transitions between the 1hh subband and the 2e subband, generated by linearly polarized light.

We see in Fig. 2 a large spin-split of the levels for finite $\mathbf{k}_\parallel$. This split is due to the spin-orbit interaction, structural asymmetry and bulk inversion asymmetry. We also found an essential anisotropy in the 2e subband dispersion. This type of anisotropy in the dispersion curves also appears in other subbands in the region of large $\mathbf{k}_\parallel$, and is produced by the bulk inversion asymmetry terms in the Hamiltonian and the difference between the second and the third Luttinger parameters in bulk InAs, GaSb, and AlSb.

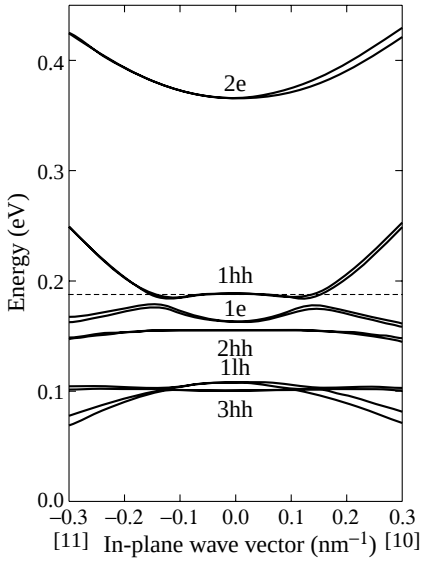

Fig. 2. Subband dispersions in the InAs/GaSb quantum well grown on InAs obtained self-consistently at temperature $T = 4.2$ K. Fermi level is shown as the dashed line.

2. Optical matrix elements for the infrared transitions

We have investigated the optical matrix elements, using the transitions between the $1hh$ subband and the $2e$ subband as an example. For small values of $k_\parallel$ the $2e$ subband is the second electron-like subband and the $1hh$ subband is the first heavy-hole-like subband. As shown in Fig. 2, after anticrossing around $k_\parallel \simeq 0.15$ nm^{-1}, the $1hh$ subband becomes the first electron-like subband. We choose the polarization of light along the growth direction. The $1hh \rightarrow 2e$ optical transition is forbidden at $k_\parallel = 0$. With increasing $k_\parallel$ the transition probability is enhanced because of the increasing hybridization between the $1hh$ subband and the $1e$ subband. The absolute value of the optical matrix element reaches its maximum when the $1hh$ subband states turn into $1e$-like. Then it decreases with further increase of $k_\parallel$ because of the strong nonparabolicity of bulk dispersions in the narrow-gap InAs layer. Such results were obtained in Ref. [1].

When the bulk inversion asymmetry and the difference between the second and the third Luttinger parameters are taken into account, in contrary to Ref. [1] we obtained a significant probability of spin-flip optical transitions, induced by the linearly polarized light, from all states except those with $\mathbf{k}_\parallel$ along the [11] direction. If the bulk inversion asymmetry terms in the Hamiltonian are neglected, the spin-flip optical transitions from the states with $\mathbf{k}_\parallel$ parallel to the [10] direction are also forbidden. However, for any other direction of $\mathbf{k}_\parallel$ the spin-flip transition probability is still finite. This phenomenon is connected to the important contribution of the warping terms in the Hamiltonian to the optical matrix elements. Since the second and third Luttinger parameters are not equal in each of the bulk materials InAs, GaSb, and AlSb, the Hamiltonian can be block diagonalized only if $\mathbf{k}_\parallel$ is along the [10] or the [11] direction. Under this situation the spin-up states and the spin-down states are coupled to yield a finite spin-flip optical transition probability, which can be comparable to the spin-conserved optical transition probability.

The spin-flip optical transition, produced by the bulk inversion asymmetry terms in the Hamiltonian, can be equally large if $\mathbf{k}_\parallel$ is along the [10] direction. The reason is the mixing of states with different spin orientations as well as the influence of bulk inversion asymmetry on the group velocity operator. This spin-flip optical transition probability is again comparable to the spin-conserved transition probability. Both terms proportional to the Kane's B-parameters, and the strain-dependent bulk inversion asymmetry terms give a large contribution to the spin-flip optical transitions. The maximum value of the matrix elements for the spin-flip transition from an initial states in the $1hh$ subband are achieved when these states are near the hybridization gap. Note that the effects of the low C_{2v} symmetry of interfaces [3] can produce only some quantitative change of results for the $1hh$–$2e$ optical matrix elements with the light polarization along the growth direction.

Acknowledgement

This work was financially supported by the RFBR.

References

[1] E. Halvorsen, Y. Galperin, and K. A. Chao, *Phys. Rev. B* **61**, 16743 (2000).
[2] A. Zakharova, S. T. Yen, and K. A. Chao, *Phys. Rev. B* **66**, 85312 (2002).
[3] E. L. Ivchenko and M. O. Nestoklon, *Phys. Rev. B* **70**, 235332 (2004).

15th Int. Symp. "Nanostructures: Physics and Technology"
Novosibirsk, Russia, June 25–29, 2007

SiGe nanostructures for optoelectronic applications

Detlev Grützmacher[1], Gregor Mussler[1], Hans Sigg[2], Soichiro Tsujino[2], Maxi Scheinert[2], Christian Dais[2], Elisabeth Müller[2], Harun Solak[2], Thomas Fromherz[3], Julian Stangl[2] and Günter Bauer[3]

[1] Institute for Bio- and Nanosystems, Forschungszentrum Jülich, 52425 Jülich, Germany
[2] Laboratory for Micro- and Nanostructures, Paul Scherrer Institute, 5232 Villigen, Switzerland
[3] Institute for Semiconductor Physics, Johannes Kepler University Linz, A-4040 Linz, Austria

Abstract. The integration of SiGe nanostructures with a high Ge content into Si offers new paths for optoelectronic devices based on Si. Here, strain compensated Si/SiGe quantum well structures and their potential for optical components such as modulators and quantum cascade lasers are discussed. The ordering of Ge quantum dots on pre-patterned substrates allows the fabrication of 3-dimensional quantum dot crystals. Patterns with periodicities down to 25 nm have been fabricated using EUV-interference lithography. Dense arrays of ordered Ge quantum dots might be applicable for sensitive photodetectors as well as for THz emitters. All these structures require high Ge concentration, thus build up large strain throughout the structure, which makes them challenging for epitaxial growth. New developments may arise from the availability of bulk SiGe substrates.

1. Introduction

Si based optical components attracted strong interest lately triggered by the findings of an all Si based Raman laser [1], the observation of a strong quantum confined Stark effect [2], the option to construct a quantum cascade laser [3] and the description of a possible generic optical logic gate [4]. These efforts indicate that the incorporation of optical devices in mature Si electronics might be feasible in the near future. Here we discuss the options and challenges using Si/SiGe nanostructures for the construction of optical devices. Ge has a 4% lattice mismatch towards Si which puts constrains to the design of Si/SiGe structures with high Ge content. The latter is typically needed in order to achieve large bandoffsets, a prerequisite for the observation of the desired quantum effects. Moreover, in pure Ge the direct band gap is energetically close to the fundamental indirect gap and absorption via the direct bandgap of Ge has been observed in Ge/SiGe quantum well structures [2,5], opening a new path to overcome the indirect nature of the fundamental bandgap in Si.

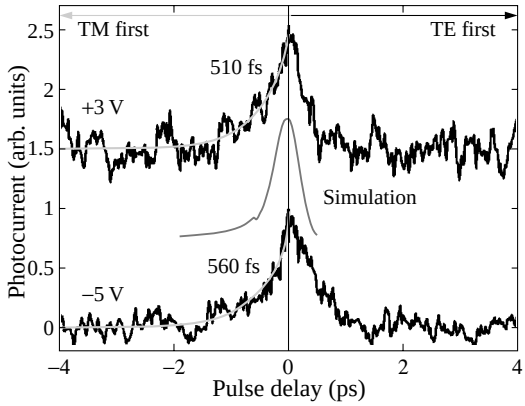

Fig. 1. Plot of the photocurrent of a quantum cascade structure as a function of the delay between the TM and TE pump pulses for different bias voltages.

2. Results and discussion

2.1. Si/SiGe/Ge *quantum well structures*

Three types of Si/SiGe/Ge quantum well structures were investigated, namely for quantum cascade structures, quantum fountain structures for optically pumping and Ge/SiGe quantum wells for modulators. Whereas the first two explore intersubband transitions, the later is used to study the direct band gap of pure Ge wells. Quantum cascade (QC) structures for electrical carrier injection typically contain 28 layers per cascade and 15 cascades. Here intersubband transition of holes were employed, since the effective tunnel mass of electrons in these structures was considered to be too high for efficient carrier injection. The growth of such a structure with several hundred layers is already challenging, however, the required design freedom at appropriate wavelength in the MIR to FIR regime require large band offsets which are only achievable if Ge concentrations above 70% are used, which leads to strain accumulation in the QC structure. To avoid relaxation in the thick QC structure it has to be deposited strain symmetrised on a relaxed $Si_{0.5}Ge_{0.5}$ buffer layer (pseudosubstrate) [6]. The growth conditions are rather critical and low temperature growth is required to avoid buckling and island formation with the films of high Ge concentration. Careful analysis of the structural properties using x-ray diffractometry and transmission electron microscopy have been performed. Despite excellent structural properties only electroluminescence was observed from these structures but no lasing. This is mainly attributed to the carrier relaxation via heavy hole (HH) to light hole (LH) transitions, instead of the required HH to HH transition, leading to a strongly reduced lifetime of holes in the upper HH state. To confirm this assumption the lifetime has been directly measured using a 2 photon absorption experiment at FELIX. In this experiment a TM polarized light pulse is used to excite carriers from the HH ground state to the first excited HH state. The second TE polarized pulse is used to excite the carriers from the excited state into the continuum, note that the TE pulse will not excite carriers from the HH ground state to the HH excited state. By shifting the time delay between these pulses and measuring the photocurrent of the sample the lifetime of holes in the excited state can be probed. In our experiments a lifetime of 510–560 fs has been established as shown in Fig. 1. To overcome this problem, either designs have to be chosen with a minimum of LH states spread between the active HH states, or intersubband transitions other than HH-HH transi-

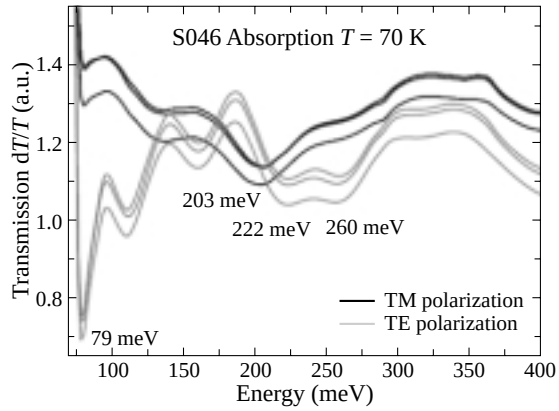

Fig. 2. Differential absorption spectra for TM and TE polarized light of a Si/SiGe/Ge quantum fountain structure embedded in a waveguide.

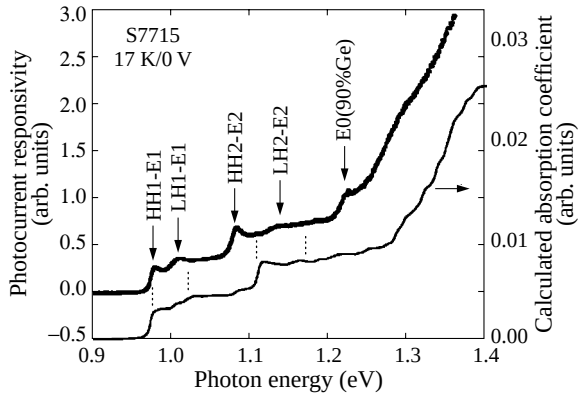

Fig. 3. Photocurrent spectroscopy of a SiGe/Ge modulator structure.

tion have to be employed. To study the latter, quantum well structures for LH-HH hole transitions have been designed. The structure contains an asymmetric quantum well with a section of pure Ge and a section of a SiGe alloy. They were subject to absorption and optically pumped emission experiments. Fig. 2 shows the differential absorption spectra using a waveguide structure fabricated by etching a mesa into the 60 period multiple quantum well structure. Clear absorption peaks for the HH_0 ground state to excited HH_1 and LH_1 states are visible. Only little absorption is found in the energy range of the HH_1 to LH_1 transitions where the emission should occur.

Next to laser structures also structures for optical modulators based on SiGe/Ge quantum well structures were investigated. Thick relaxed SiGe buffer layers were deposited by CVD. These pseudosubstrates were mounted into a MBE system and the Ge/SiGe quantum well structure was deposited. The well width of Ge QW was varied and the direct transition energy of the direct-gap interband transitions between the Γ_{8v}^{+} edge and the Γ_{7c}^{-} edge in SiGe heterostructures was monitored by photocurrent and absorption spectroscopy using Fourier transform infrared spectroscopy. Fig. 3 shows the photocurrent spectrum of a sample measured at 17 K when the bias voltage is equal to 0 V. A series of steps is observed above 0.97 eV, which is ~ 0.2 eV above the indirect fundamental band gap of Ge. In addition, the onset of steps is decorated by a peak structure indicating an excitonic effect. For comparison also a calculated spectrum (lower curve) is shown in Fig. 3. The good overall agreement between theory and experiment confirms the

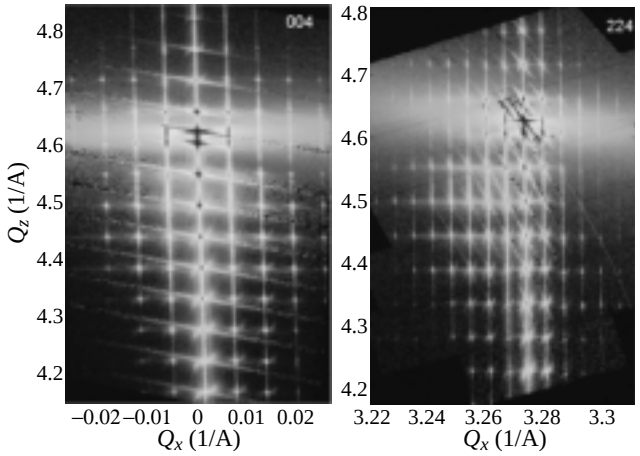

Fig. 4. Reciprocal space maps around the symmetric (004) and asymmetric (224) reflex of a 3-dimensional Ge quantum dot crystal.

peak assignment for photon energies below ~ 1.2 eV. Further improvements of this kind of structures may arise from the development of bulk SiGe crystals. First experiments growing resonant tunnelling diodes (RTD) on $Si_{0.15}Ge_{0.85}$ bulk wafers reveal excellent electronic properties showing negative differential resistance up to room temperature.

2.2. Ge *quantum dot structures*

The bandstructure of an artificial quantum dot crystals containing densely packed dots may open another path for the realisation of optical devices based on Si. Substrates have been patterned using EUV-IL and reactive ion etching with regular shallow patterns. Using this technique patterns with a pitch of 25 nm have been fabricated. Growth was performed on patterned Si wafers and regular 3-dimensional arrangements of Ge dots are observed by AFM and TEM analysis. Fig. 4 shows reciprocal space maps (RSM) obtained from grazing incidence diffractometry along the (004) and the (224) direction. Both RSM show diffraction peaks and Pendellösungen up to high orders, indicating the excellent periodicity within the 3-d quantum dot crystals. The valence and conduction band edges of stacked Ge islands were calculated by the nextnano 3 simulation package. A Ge concentration of 50% is assumed in the dots and the dots were modelled as a pyramid with the dimensions corresponding to the dot dimensions observed by cross sectional TEM. Due to the narrow (10 nm) Si spacer layer between the dots the local Δ_z^1 and Δ_z^2 minima for the electron overlap and the increased strain accumulation between the dots shifts the state to slightly lower energies compared to single dots. Also the Δ_{xy} valleys of the electrons overlap in stacked dots, forming extended states in 3-d dot arrangements. The energy values will depend on the Ge concentration in the buried SiGe islands. For the assumed 50% of Ge in the dots a transition energy of 823 meV is computed, which is higher than the observed 746 meV obtained from the PL measurements, indicating that the Ge concentration in reality is higher than 50%.

Acknowledgements

The financial support of this work by the Swiss National Science Foundation and the European Community (Shine project) is highly acknowledged.

References

[1] O. Boyraz, B. Jalali, *Optics Express* **12**, 5269 (2004).
[2] Y. H. Kuo, Y. K. Lee, Y. S. Ge *et al*, *Nature* **437** 1334 (2005).
[3] G. Dehlinger, L. Diehl, U. Gennser *et al*, *Science* **290**, 2277 (2000).
[4] H. J. Caulfield, R. A. Soref, C. S. Vikram, *Phot. and Nanostr. — Fund. and App.* **5**, 14 (2007).
[5] S. Tsujino, H. Sigg, and G. Mussler, *Appl. Phys. Lett* **89**, 262119 (2006).
[6] H. von Känel, C. Rosenblad, M. Kummer *et al*, *Jap. J. of Appl. Phys.* **39**, 2050 (2000).

15th Int. Symp. "Nanostructures: Physics and Technology"
Novosibirsk, Russia, June 25–29, 2007

Self-assembly of adsorbate atoms into ordered nanostructures on semiconductor surfaces

A. A. Saranin and A. V. Zotov
Institute of Automation and Control Processes, Vladivostok, Russia

Abstract. Self-organization of atoms adsorbed on atomically-clean semiconductor surfaces in ultra-high vacuum has been used to fabricate the main principal nanostructures, including nanofilms, nanowires and nanodots. The most principal results obtained with this technique and prospects of its development are discussed in detail.

Introduction

Recent progress, achieved in the ordered nanostructure formation using self-organization of atoms adsorbed on semiconductor surfaces in ultra-high vacuum (UHV), allows to consider this technique as a prototype technology for fabrication of nanoelectronic devices. Combination of the extra-clean UHV conditions and surface monitoring with scanning tunneling microscopy (STM) ensures controlling the growth processes on atomic scale. In the present report, we review the recent results obtained in this field in the Department of Surface Science in the Institute of Automation and Control Processes. We consider how using self-assembly of adsorbate atoms on semiconductor surfaces one can fabricate the main principal nanostructures, including nanofilms, nanowires and nanodots.

1. Nanofilms

Nanofilms having thickness on atomic scale are represented by a wide set of surface phases (reconstructions) formed in monolayer and submonolayer adsorbate/silicon and adsorbate/germanium systems. Surface phases have been an object of extensive researches for more than 40 years. As a result, a considerable body of manifold information has been accumulated by scientific community: for many systems the phase diagrams have been constructed; for the phases of the greatest interest the phase composition, atomic structure and electronic properties have been elucidated [1]. Current researches are directed towards reaching the greater structural perfection of the surface phases, as well as controlling their properties. As an example, we can refer to the results of our recent work on Au/Si(111) system, which demonstrate that adding the second adsorbate (In) alters the domain wall structure, which in turn affects electronic properties of the surface phase [2] (see Fig. 1).

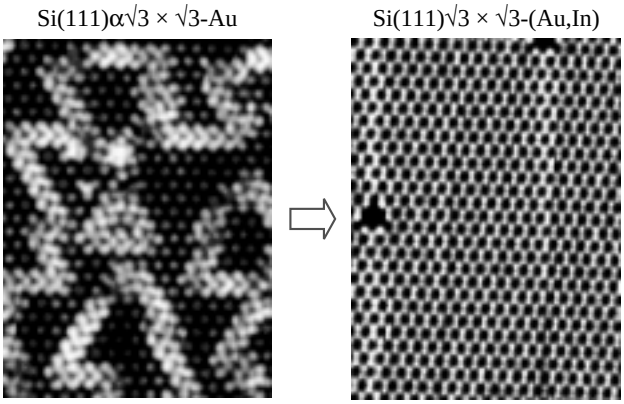

Fig. 1. Structural transformations in the Si(111) $\alpha\sqrt{3} \times \sqrt{3}$-Au surface phase induced by adsorption of 0.15 ML of In at 600 °C.

2. Nanowires

For self-assembly formation of the nanowires, one can use highly anisotropic growth, say, as in the case of growing nanowires made of silicides of metals (e.g., Er, Dy, Sm) on Si(100) surface. To reach the same goal, we have used alternative approach, namely preferential metal island nucleation at the atomic steps, which takes place, for example, in the Cu/Si(111) system.

3. Nanodots

Nanodots, which are represented by various nanocluster arrays, attract currently a great interest and a number of the vivid results have been obtained in this field. In particular, highly-ordered arrays of the identical-size nanoclusters (i.e., magic-cluster 2D crystals) have been successfully fabricated with Group-III adsorbates on Si surfaces. Modification of the magic-cluster composition leading to the changeover of its electronic properties (i.e., cluster doping) has been demonstrated [3]. It has been found that dynamic behavior of the doped cluster in In/Si(100) system (see Fig. 2) opens a prospect for using the cluster as an atomic-scale memory cell [4]. Nanocluster growth on the various modified Si surfaces has also been studied.

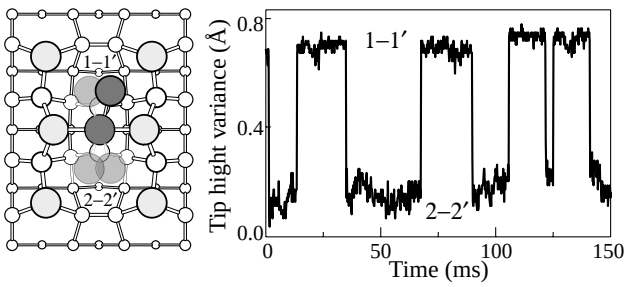

Fig. 2. Modified (doped) In/Si(100) nanocluster has an asymmetric configuration, in which one In atom (shown by dark gray circle) is relatively mobile and hope between four equivalent sites (labeled 1, 1′, 2 and 2′). Other In atoms are shown by light gray circles, Si atoms are shown by white circles. According to the calculations, energy barrier between 1-1′ and 2-2′ sites is about 0.7 eV, that allows at room temperature direct monitoring In-atom hopping between these sites by STM.

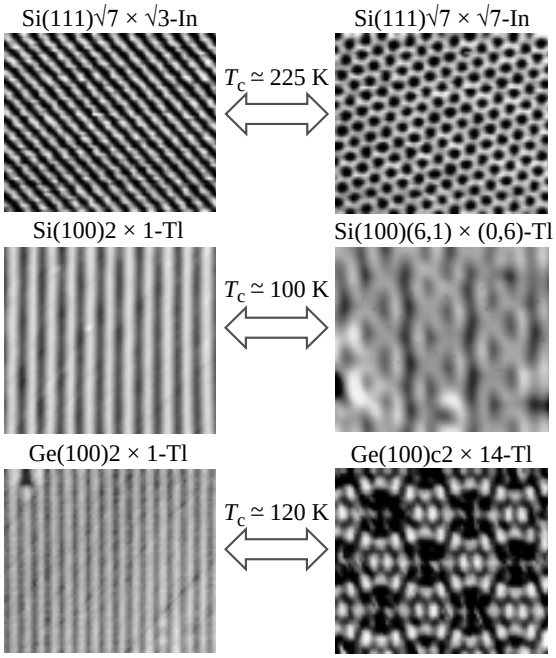

Fig. 3. Low-temperature reversible phase transitions in the metal (In, Tl) monolayers on Si(111), Si(100) and Ge(100) surfaces.

4. Structural phase transitions

Besides the application tasks, self-assembly of adsorbates can be used in the fundamental studies of the critical phenomena in the low-dimensional systems. For example, Fig. 3 shows STM images of the unusual reversible phase transitions that have recently been found in the surface phases developed in the Tl/Si(100) [5], Tl/Ge(100) [6] and In/Si(111) [7] systems.

5. Perspectives

Further development of the above directions are believed to be associated with expansion of the adsorbate types, with various modifications of the substrate surfaces, as well as with developing of the STM technique, say, with using STM tips made of carbon nanotubes covered by thin layers of the functional (e.g., metallic, magnetic or superconducting) materials.

References

[1] V. G. Lifshits, A. A. Saranin, and A. V. Zotov, *Surface Phases on Silicon*, John Wiley & Sons, Chichester, 450 (1994).
[2] D. V. Gruznev, I. N. Filippov, D. A. Olyanich, D. N. Chubenko, I. A. Kuyanov, A. A. Saranin, A. V. Zotov, and V. G. Lifshits, *Phys. Rev. B* **73**, 115335 (2006).
[3] V. G. Kotlyar, A. V. Zotov, A. A. Saranin, T. V. Kasyanova, E. N. Chukurov, I. V. Pisarenko, and V. G. Lifshits, *Phys. Rev. Lett.* **91**, 026104 (2003).
[4] A. A. Saranin, A. V. Zotov, I. A. Kuyanov, M. Kishida, Y. Murata, S. Honda, M. Katayama, K. Oura, C. M. Wei, and Y. L. Wang, *Phys. Rev. B* **74**, 125304 (2006).
[5] A. A. Saranin, A. V. Zotov, I. A. Kuyanov, V. G. Kotlyar, M. Kishida, Y. Murata, H. Okado, I. Matsuda, H. Morikawa, N. Miyata, S. Hasegawa, M. Katayama, and K. Oura, *Phys. Rev. B* **71**, 165307 (2005).
[6] A. A. Saranin, A. V. Zotov, M. Kishida, Y. Murata, S. Honda, M. Katayama, and K. Oura, *Surf. Sci.* **601**, 595 (2007).
[7] A. A. Saranin, A. V. Zotov, M. Kishida, Y. Murata, S. Honda, M. Katayama, K. Oura, D. V. Gruznev, A. Visikovsiy, and H. Tochihara, *Phys. Rev. B* **74**, 035436 (2006).

15th Int. Symp. "Nanostructures: Physics and Technology"
Novosibirsk, Russia, June 25–29, 2007

Localization of electrons in type-II Ge/Si quantum dots stacked in a multilayer structure

A. I. Yakimov, A. V. Dvurechenskii, A. I. Nikiforov and *A. A. Bloshkin*
Institute of Semiconductor Physics, 630090 Novosibirsk, Russia

Abstract. Space-charge spectroscopy was employed to study the electronic structure of single and multiple layers of Ge/Si quantum dots embedded in a n-type Si(001) matrix. For a multilayer sample, the evidence for an electron localization in strained Si in the vicinity of Ge dots was found. From the temperature- and frequency-dependent measurements the electron binding energy was determined to be 40–70 meV for different quantum states. The electron accumulation was not observed in a sample with a single layer of Ge dots. Existence of localized electronic states is explained by a modification of the conduction band alignment induced by inhomogeneous tensile strain in Si around the buried Ge dots.

There are two main types of band-edge alignment, in heterostructures with semiconductor quantum dots (QDs). In type-I QDs, the band gap of the narrow-gap material lies entirely within the gap of the wide-gap semiconductor, and both electron and hole are confined inside the same region. A typical example of type-I band-edge line-up is the InAs QDs in GaAs matrix. For type-II QDs, the localization inside the dot occurs only for one of the charge carriers, whereas the dot forms a potential barrier for the other particle. A system like this is that of Ge/Si(001) dots formed by strain epitaxy, in which the holes are strongly confined in the Ge region, and the electrons are free in the Si conduction band. The above consideration disregards possible modification of the band structure due to inhomogeneous strain in the dots and the surrounding matrix. Tensile strain in the nearby Si causes splitting of the sixfold-degenerate Δ-valleys ($\Delta 6$) into the fourfold-degenerate in-plane $\Delta 4$-valleys and the twofold-degenerate $\Delta 2$-valleys along the [001] growth direction. The lowest conduction band edge just above and below the Ge island is formed by the $\Delta 2$-valleys yielding the triangle potential well for electrons in Si near the Si/Ge boundary. Thus one can expect three-dimensional localization of electrons in the strained Si near the Ge dots. The electron binding energy in a strain-induced potential well in a single Ge/Si QD was predicted to be very small ($<$10 meV) [1]. This value is expected to enlarge vastly in multilayer Ge/Si structures with vertical stacking of Ge islands due to accumulation of strain energy from different dot layers in a stack and increase of the potential well depth. In this work we employ space-charge spectroscopy to study electronic states in samples with different number of Ge dot layers embedded in a n-type Si(001) matrix.

Ge/Si heterostructures with self-assembled Ge QDs were fabricated by molecular-beam epitaxy on a n^+-Si(001) substrate with a resistivity of 0.01 Ω cm doped with antimony up to a concentration of $\sim 10^{19}$ cm^{-3}. A fourfold stack of Ge islands was inserted into the 0.8-μm epitaxial n-Si layer at a distance of 0.5 μm from the substrate. The amount of deposited Ge was gradually reduced from 6 ML (1 ML=1.41 Å) in the first layer to about 4 ML in the fourth layer to ensure Ge islands with equal islands sized and densities in all layers. The Ge growth rate was chosen to be as large as 2 ML/s to provide the high Ge content in the islands and hence the larger strain. The n-type remote doping was achieved by insertion of a Sb δ-doping Si layer of 0.2 μm below the Ge QD layer. The first and second Ge layers in the stack as well as the third and fourth Ge layers are separated by 3 nm Si spacers, while the distance between the second and third Ge layers is 5 nm. Ge nanoclusters fabricated by such a way demonstrate good vertical correlation and have almost equal size. From cross-sectional transmission electron micrographs, we observe the Ge dots to be approximately 20 nm in lateral size and about 2 nm in height. The scanning tunneling microscopy of a sample without the Si cap layer showed that the Ge islands have the shape of hut-clusters. The density of the dots is about 10^{11} cm^{-2}. The average Ge content of 80% in the islands was determined from Raman measurements. To separate response from the stacked Ge/Si islands, the reference sample was fabricated under conditions similar to the multilayer sample, except that only a single layer of Ge QDs was grown. For the admittance measurements, Pd Schottky gates with the area of 7.5×10^{-3} cm^2 were deposited on top of the samples through a shadow mask.

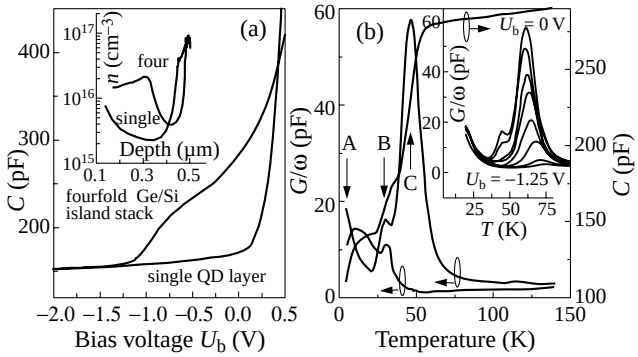

Fig. 1. (a) Capacitance-voltage characterisctics measured at modulation frequency of 10 kHz and at $T = 77$ K for the single-layer and multilayer samples. The inset displays the apparent electron distribution derived from the measured C–V curves using the full depletion approximation. (b) Temperature dependence of conductance (G) and capacitance (C) measured at bias voltage $U_b = 0$ V and modulation frequency of 1 MHz for the single-layer sample (broken line, only conductance) and fourfold Ge/Si island stack (solid lines). Inset: Conductance spectra of the multilayer sample at the frequency of 1 MHz under different bias voltages. The voltages are 0, −0.2, −0.5, −0.7, −0.9, −1.0, −1.2, and −1.25 V from top to bottom.

Figure 1(a) shows experimental capacitance-voltage (C–V) characteristics for the reference and the multilayer samples. The dependence of the capacitance on voltage for the single-layer sample shows no specific features and has the form of the

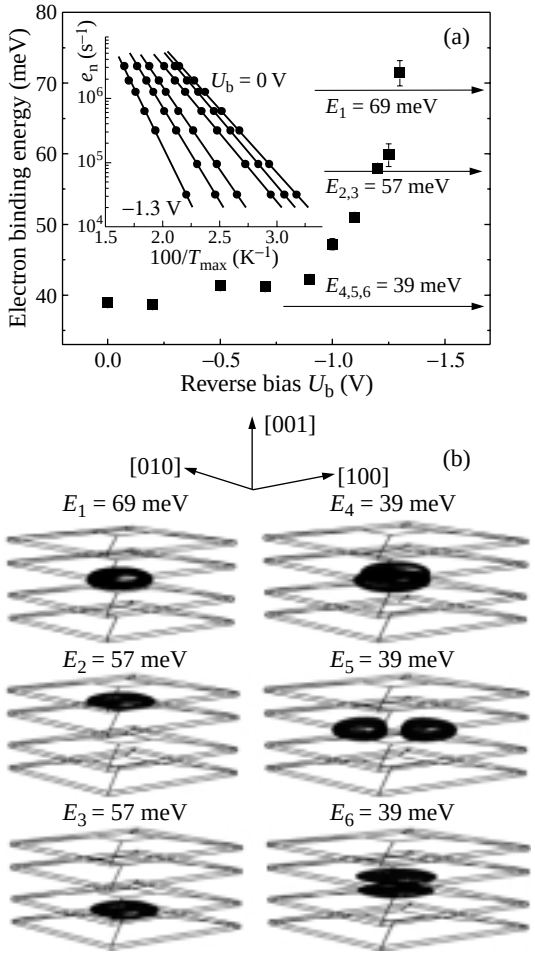

Fig. 2. (a) Bias dependent activation energies of electron emission rate. Inset displays the Arrhenius plots of the electron emission rate e_n obtained from $G-T$ spectra with different bias voltages. The voltages are 0, −0.5, −0.9, −1.1, −1.2, and −1.3 V. (b) Three-dimensional view of the isosurface of the electron charge density for the six lowest conduction states. The isosurface level is selected as $1/e$ ($e = 2,71828\ldots$) of the maximum wave-function amplitude $|\psi_{max}(\mathbf{r})|$. The probability of finding the electron inside is 70–77% dependent on the state. E_i is the single-electron binding energy of the i-th state, determined with the error of ±1 meV.

conventional C–V characteristic of a n-type Schottky diode. For the multilayer sample, we observe a steplike structure caused by an additional capacitance, which we associate with the negative charge accumulation in the Si layers between the stacked Ge islands [see, inset of Fig. 1(a)]. Due to the n-type doping in the Si matrix, the stacks of Ge QDs will be charged by electrons at a zero bias. When a reverse bias is applied to the diode, the electrons are gradually swept out. At $U_b > 1$ V electrons escape from the stack of Ge/Si dots and the latter become neutral. The QD contribution to the capacitance disappears at temperatures below $\sim$ 50 K [Fig. 1(b)] due to "freezing" the electrons in the $\Delta 2$ bound states in the strained Si. The corresponding step on the temperature dependence of capacitance is accompanied by the conductance maximum [peak C in Fig. 1(b)] which is not seen for the reference sample. Thus we may attribute the conductance peak C to the ac response of electrons confined in Ge/Si QDs stacked in a multilayer structure. With increasing reverse bias, the position of peak C shifts towards higher temperatures, its amplitude gradually decreases and the peak disappears at voltages $|U_b| > 1$ V just after the ending of the QD-related capacitance plateau in C–V characteristic. Peaks A and B are observed in both samples. They are assigned to a dopant-related admittance signal associated with the carrier freeze-out effect in the highly doped δ-doping Si layer (peak A) and in Si layers with a lower doping Sb concentration (peak B) [2]. Admittance signal originated from electron traps can be used to extract the trap energy level. For a given measurement frequency $\omega = 2\pi f$, the conductance reaches a maximum at a temperature T_{max} which corresponds to the condition $e_n(T_{max}) \approx \omega/2$, where $e_n = e_0 \exp(-E_a/kT)$ is the emission rate of electrons from the bound to extended states which depends on the electron binding energy E_a. Thus, by measuring $G(T)$ dependencies at various ω, the activation energies of the electron emission rate can be deduced from the Arrhenius plots of $e_n(T_{max})$ vs $1/T_{max}$. Arrhenius plots necessary for deriving the activation energy are depicted in inset of Fig. 2(a). The activation energies of the electron emission rate were found from the slope of the approximating straight lines. The resulting values of E_a are shown in Fig. 2(a) as a function of reverse bias voltage.

To support experimental results we performed numerical analysis of three-dimensional strain distribution and electronic structure of the samples under investigation. The strain distribution was found in terms of atomic positions using valence-force-field model with a Keating interatomic potential. The electronic energy levels were calculated by solving three-dimensional effective-mass Schrödinger equation. The carrier confinement potential in this equation is modified by the strain distribution. Details of theoretical consideration can be found elsewhere [3]. In Fig. 2(b) we show the isosurface plots of the charge density for the first 6 electronic states with the respective electron binding energies E_i. The same energies are shown in Fig. 2(a) by arrows. Obviously, the calculated values of E_i agree well with the experimental data providing the evidence for the electron confinement in Ge/Si QDs stacked in a multilayer structure.

Acknowledgement

The authors are much obliged to V. A. Volodin for Raman measurements and A. V. Nenashev for assistance in development of a simulation procedure. This work was supported by the Russian Foundation for Basic Research (Grant No. 06-02-16143) and State Contract No. 02.513.11.3156. A.I.Y. acknowledges financial support from Russian Science Support Foundation.

References

[1] A. I. Yakimov *et al*, *Semicond. Sci. Technol.* **15**, 1125 (2000).
[2] D. V. Singh *et al*, *J. Appl. Phys.* **85**, 985 (1999).
[3] A. I. Yakimov *et al*, *Phys. Rev. B* **73**, 115333 (2006).

15th Int. Symp. "Nanostructures: Physics and Technology"
Novosibirsk, Russia, June 25–29, 2007

Interband photoconductivity of Ge/Si structures with self-organized quantum rings

O. A. Shegai[1], V. I. Mashanov[1], H. -H. Cheng[2] and O. P. Pchelyakov[1]

[1] Institute of Semiconductor Physics, 630090 Novosibirsk, Russia
[2] Center for Condensed Matter Sciences and Graduate Institute of Electronic Engineering, National Taiwan University, Taipei, 106, Taiwan, Republic of China

Abstract. At low temperatures a lateral photoconductivity (PC) of Ge/Si (100) self-organized quantum ring (QRs) structures as a function of interband light intensity have been investigated for the different values of lateral voltage U, and temperature T. In contrast to self-organized Ge/Si quantum dots (QDs) structures where the stepped PC is registered for the QRs structures essential smoothing of steps were observed. In addition, a resonance PC of QRs structure has been observed at $U = 90$ V for T in the interval about 5.5−12.5 K.

Semiconductor structures based on self-organization of Si/Ge hetero-junction known as quantum dots (QDs) or islands are perspective low dimensional structures for investigation and future applications [1]. A further developing of the self-organization conception is a recent growth of Ge/Si (100) structures with the quantum rings (QRs) [2–4]. In this report an influence of the intensity of interband light illumination on low temperature photoconductivity (PC) of QDs and QRs of Ge/Si (100) was investigated.

The growth of structures with the QDs and QRs were performed in molecular beam epitaxy (MBE) system (Riber SIVA 32) with two electron beam evaporators for Ge and Si. For all the samples, thin Si buffer layer of 30 nm is deposited at 700 °C. Low growth flux is employed for the structure with a rate of 0.01 and 0.06 nm/s for Ge and Si, respectively. The structure consists of (a) a layer of 0.7 nm Ge, (b) a thin layer of 0.05 nm of Ge, and (c) a Si cap layer of 2.5 nm. Between the layer (a) and (b), both Si and Ge shutter is closed for 5 min to ensure the uniformity of the Ge layer. Four samples are grown at various temperatures of 640, 660, 680 and 700 °C [4]. We note that for the PC measurements the QDs and QRs structures with the thick Si capped layers (20 nm, 400 °C) were used.

A red LED was mounted near the studied structure and was used for measurements of stationary photoconductivity (PC). The power of illumination was varied by the current through the LED and its density on the surface of the structures not exceeds the magnitude of 3 mW/cm^2. In addition an illuminated area is about 2×2 mm^2 and the distance between the two linear contacts is about 2 mm. Ohmic contacts were made by evaporating of Al and followed annealing in H_2 atmosphere. More details of measurements were described in [5].

In Fig. 1 (3×3 μm^2) AFM image of QRs structure grown at $T_s = 680$ °C is shown. Estimates show that an outside diameter of QRs is about 300 nm, a height 2−4 nm, a surface density is $\approx 2 \times 10^8$ cm^{-2}. It is seen that not all QDs were transformed to QRs and the both types of low dimension object are observed at the surface of structure. Figure 2 shows the typical dependence of PC on light intensity of sample #46 grown at $T_s = 640$ °C and contained only QDs at $T = 5$ K for the $U = 66-100$ V. It is seen that as for early measurements of QDs structures [5,6] a PC curve has a stepped dependences. For the explanation of the stepped PC in QDs structures we used percolation approach [7]. The most of photoexcited holes fill the QDs localized states, whereas electrons localized in the

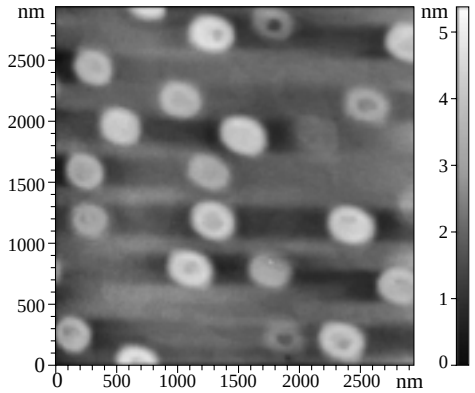

Fig. 1. AFM scan of surface structure with the quantum rings ($T_s = 680$ °C).

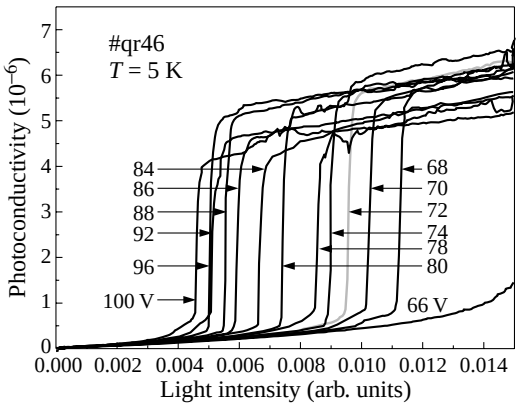

Fig. 2. Dependence of photoconductivity of the structure with the quantum dots on interband light intensity; $U = 66-100$ V, $T = 5$ K.

2D states near the wetting layer. Due to spatial strain relaxation around QDs the energetic relief in these structures so that the potential minima appeared between the neighboring QDs. The stepped increase of PC is explained by filling of the electrons confined states up to percolation level. Increase of U lead to shift PC step to lower light intensity. Early [6], like stepped PC was observed for others Si/Ge structures with QDs. However for the QRs structure (#45) grown at the same condition as the QDs structure (#46) a smooth stepped PC is observed as shown in Fig. 3 for the same experimental conditions. For this structure in contrast to QDs structure (#46) the increase of

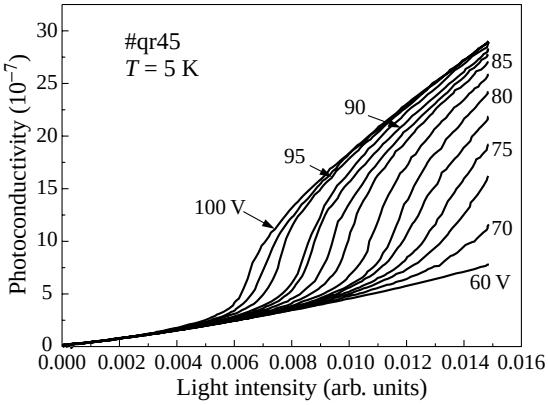

Fig. 3. Dependence of photoconductivity of the structure with the quantum rings on interband light intensity; $U = 60-100$ V, $T = 5$ K.

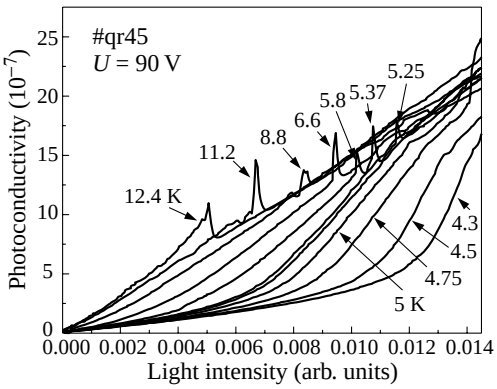

Fig. 4. Dependence of photoconductivity of the structure with the quantum rings on interband light intensity; $T = 4.3-12.4$ K, $U = 90$ V.

the temperature up to ≈ 10 K the stepped PC disappeared entirely and only monotonous growth of PC was registered with intensity of illumination. The QDs transform to QRs due to escaping a large numbers of Ge atoms of the QDs center. It leads to decreasing of strain around the QRs in Si matrix.

A resonant PC for QRs structures (#45) at large voltage ($U = 90$ V) and different temperatures in the interval of $5.3-12.4$ K is appeared as shown in Fig. 4. Increasing of the temperature lead to shift of the resonance to the lower light intensity. We note that such resonance was not observed for the QDs structures (#46). Zone diagram of the QRs for the electrons in contrast to holes (for which it indeed ring-like) can be considered as QDs, when the confined states are appeared due to Ge/Si hetero-interface in lateral direction and Coulomb potential of the holes localized in QRs states in vertical direction. Resonant PC of the QRs structure we explain by electron tunneling from these states into the percolation level. Shift of PC resonance to the lower light intensity with the growth of T can be explained by the growth of electron thermal energy of localized in QRs states and lower level of light intensity need to fill up the level from which tunneling is effective occurred.

Acknowledgement

This work was supported by RFBR (#07-02-01106).

References

[1] O. P. Pchelyakov, Yu. B. Bolkhovityanov *et al*, *Semiconductors* **34**, 1229 (2000).
[2] J. Cui, Q. He, X. M. Jiang *et al*, *Appl. Phys. Lett.* **83**, 2907 (2003).
[3] S. W. Lee, L. J. Chen *et al*, *Appl. Phys. Lett.* **83**, 5283 (2003).
[4] V. I. Mashanov, H. -H. Cheng *et al*, *Physica E* **28**, 531 (2005).
[5] O. A. Shegai, V. A. Markov *et al*, *Phys. Low Dim. Struct.* **1–2**, 261 (2002).
[6] O. A. Shegai, V. A. Markov *et al*, *Phys. Sol. St.* **46**, 74 (2004).
[7] B. I. Shklovskii and A. L. Efros, *Electronic Properties of Doped Semiconductors.*, (Berlin: Springer), 1984.

15th Int. Symp. "Nanostructures: Physics and Technology"
Novosibirsk, Russia, June 25–29, 2007

Growth and photoluminescence of the SiGe/Si self-assembled nanoclusters grown by sublimation molecular beam epitaxy in GeH_4 ambient

M. V. Kruglova[1], D. O. Filatov[1], S. V. Siprova[1], M. A. Isakov[1], M. O. Marychev[1], V. G. Shengurov[2], V. Yu. Chalkov[2] and S. A. Denisov[2]

[1] Research and Educational Center for Physics of the Solid State Nanostructures, University of Nizhniy Novgorod, Nizhniy Novgorod, Russia
[2] Physics Technical Research Institute, University of Nizhniy Novgorod, Nizhniy Novgorod, Russia

Abstract. The dependence of morphology and photoluminescence (PL) of the SiGe/Si(001) heterostructures with self-assembled nanoclusters grown by Sublimation Molecular Beam Epitaxy in GeH_4 ambient on the growth conditions has been investigated. The growth conditions providing uniform nanocluster arrays have been determined. The dependence of PL spectra on the amount of deposited Ge in the range of transition from 2D growth to islanding and on the measurement temperature within the range of 9–300 K has been studied. The PL signal from SiGe nanoclusters at 0.8–0.9 eV has been observed in all the range of the temperatures up to 300 K.

The self-assembled SiGe/Si nanoclusters are considered now to be one of the promising approaches in Si-based optronics [1]. Due to quantum size effect, a significant increase in the efficiency of the radiative recombination is expected in these structures.

Usually, the SiGe/Si nanoclusters are grown by Molecular Beam Epitaxy (MBE) [2]. In this work, the dependence of morphology and photoluminescence (PL) spectra of the SiGe/Si(001) heterostructures grown by Sublimation MBE (SMBE) in GeH_4 ambient [3] on the growth conditions has been studied. The Si layers were deposited from the sublimation source, for deposition of Ge, GeH_4 was introduced into the growth chamber. Recently this method was demonstrated to be promising for growing the structures for Si optronics (in particular, p-i-n diodes [4]). However, while a lot of work has been devoted to investigation of the SiGe/Si nanoclusters grown by MBE [1], the growth mechanisms of the SiGe/Si nanoclusters by SMBE in GeH_4 ambient have not been studied so thoroughly to date.

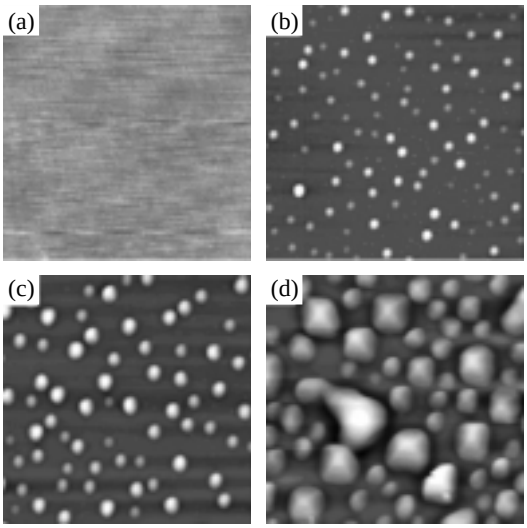

Fig. 1. AFM images of the SiGe/Si heterostructures with surface nanoclusters. $T_g = 700$ °C, $p_g = 9 \times 10^{-4}$ Torr. d_{Ge}, ML: (a) 4,0; (b) 4,8; (c) 10,3; (d) 77. Frame size 5×5 μm^2.

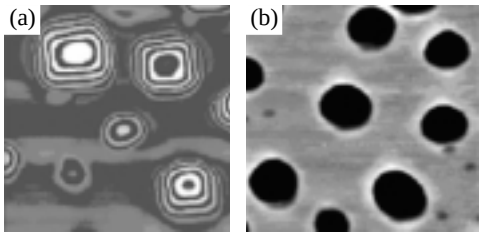

Fig. 2. AFM images of the SiGe/Si surface nanoclusters. $T_g = 700$ °C, $p_g = 9 \times 10^{-4}$ Torr. d_{Ge}, ML: (a) 27; (b) 10.3. Frame size 1.5×1.5 μm^2.

To investigate the dependence of the morphological parameters of the clusters (the cluster height h, the base diameter D, and their surface density N_S) and of their PL spectra on the growth conditions (the partial pressure of GeH_4 inside the growth chamber p_g, the time of Ge deposition t_g, and the substrate temperature T_g), the two sets of samples were grown. One set with the surface clusters was destined for Atomic Force Microscopy (AFM) investigations. Another one was grown in the same conditions on the low conductive substrates for PL measurements. The clusters in these samples were overgrown by Si cladding layer 40 nm thick. The Si buffer layers were 400 nm thick with the hole concentration of $(1-3) \times 10^{15}$ cm^{-3}. The Ge nominal thickness d_{Ge} was determinate by Rutherford Backscattering (RBS). The AFM investigation were carried out using NT-MDT Solver Pro^{TM} ambient air AFM. For PL spectroscopy Acton SP-558 grating monochromator with Janis CCS-150 closed cycle cryostat was employed. PL was excited by 1.4 W Ar^+ CW laser (514 nm).

Fig. 1 presents the AFM images of the structures with the surface Ge layer of different nominal thickness. At $d_{Ge} = 4,0$ monolayers (ML) a two-dimensional Ge/Si layer was formed (Fig. 1(a)). The clusters began nucleating on the Ge wetting layer (WL) at $d_{Ge} = 4,8$ ML (Fig. 1(b)). The critical nominal thickness of Ge layer when transition from layer-by-layer growth mode to islanding takes place in MBE process is accepted commonly to be ≈ 5 ML [2].

As a rule, the SiGe nanoclusters were featured by a bi-modal size distribution (Figs.1b,c), which is typical for the clusters

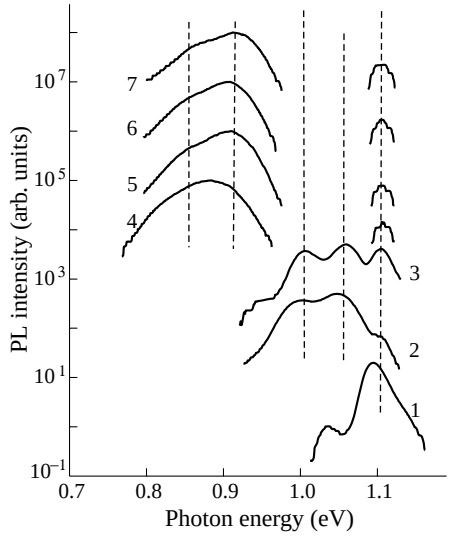

Fig. 3. PL spectra (77 K) of the SiGe/Si heterostructures with different amount of deposited Ge. d_{Ge}, ML: 1 — 0; 2 — 4.0; 3 — 4.8; 4 — 10.3; 5 — 27; 6 — 60; 7 — 77.

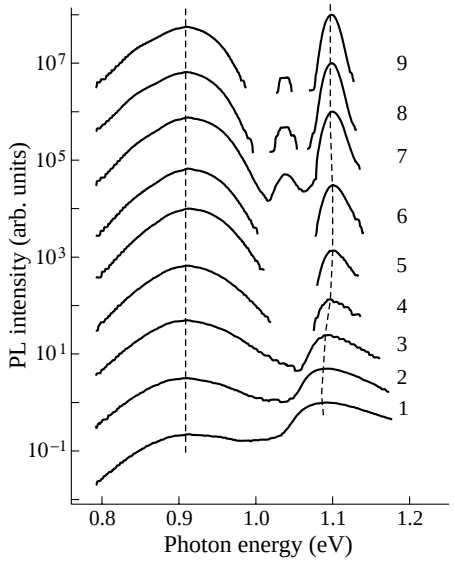

Fig. 4. Temperature dependence of the PL spectra of a SiGe/Si structure. $T_{\mathrm{g}} = 700\ ^{\circ}\mathrm{C}$, $d_{\mathrm{Ge}} = 10.3$ ML, T K: 1 — 295; 2 — 250; 3 — 200; 4 — 150; 5 — 100; 6 — 77; 7 — 40; 8 — 15; 9 — 9.

grown by MBE as well [2]. In the latter case it is related to existence of two types of the clusters: the "pyramid" clusters and "dome" ones. In our case the smaller clusters were similar in shape to the "dome" clusters grown by MBE. As well as the latter ones they were well uniform. The scatter in size was 7–10%, that was close to the lowest values reported for the MBE grown structures [5]. The larger clusters had a pyramid shape with the facets defined by {101} planes (Fig. 2(a)). With further increasing d_{Ge}, the size of the large clusters increased and their coalescence began (Fig. 1(d)).

The AFM measurements revealed that the dome-shaped clusters sd well as the pyramidal ones were surrounded by the trenches $\approx 5{-}10$ nm deep (Fig. 2(b)). Similar trenches were also reported for the clusters grown by MBE [6]. Formation of these trenches promotes the relief of the elastic strain in the clusters and the substrate.

In the PL spectrum of the sample with $d_{\mathrm{Ge}} = 4.0$ ML (Fig. 3, curve 2) the PL lines related to phonon assisted transitions and to zero phonon ones from the conduction band in Si to the quantum confined hole levels in the two-dimensional Ge layer were observed. The identification of the PL lines was based on calculations of the energy spectrum of $\mathrm{Ge}_x\mathrm{Si}_{1-x}$ layer in Si(001) taking into account the size quantization and the elastic strain [6]. At $d_{\mathrm{Ge}} = 4.8$ ML the PL line at ≈ 0.93 eV related to the transitions to the quantum confined hole states in the Ge clusters appears in the PL spectrum (Fig. 3, curve 3). At $d_{\mathrm{Ge}} = 10.3$ ML (Fig. 3, curve 4) the PL from the wetting layer disappeared and the PL from the SiGe clusters (at ≈ 0.87 eV) dominated in the PL spectrum. With further increasing d_{Ge} the PL spectra didn't change essentially (Fig. 3, curves 5 to 7).

In Fig. 4 the temperature dependence of PL in the sample with $d_{\mathrm{Ge}} = 10.3$ ML is presumed. Besides the phonon assisted edge PL in Si, the PL peak from the SiGe nanoclusters have been observed even at room temperature. Its intensity increased with decreasing T and exceeds the Si edge PL at $T = 200$ K.

Acknowledgements

The work was supported by CRDF (BRHE RUX-0-001-NN-06/BP1MO1 and RESC RUR1-1038-NN-03) and by Federal Agency of Education RF (RNP.2.1.1.4737). Authors are grateful to Paul Tchernykh (Research Institute for Nuclear Physics, Moscow State University) for RBS measurements.

References

[1] Y. Shiraki and A. Sakai, *Surf. Sci. R* **59**, 153 (2005).
[2] O. P. Pchelyakov *et al*, *Semicond.* **34**, 1229 (2000).
[3] S. P. Svetlov *et al*, *Bull. RAS: Phys.* **65**, 204 (2001).
[4] G. A. Maksimov *et al*, *Phys. Sol. St.* **47**, 22 (2005).
[5] N. V. Vostokov *et al*, *J. Cryst. Growth* **209**, 32 (2000).
[6] S. A. Chaparro *et al*, *Appl. Phys. Lett.* **76**, 3534 (2000).
[7] V. Ya. Aleshkin and N. A. Bekin, *Semicond.* **31**, 132 (1997).

15th Int. Symp. "Nanostructures: Physics and Technology"
Novosibirsk, Russia, June 25–29, 2007

Molecular state of a hole in vertically coupled Ge/Si quantum dots produced by strain-driven self-assembly

A. I. Yakimov, *G. Yu. Mikhalyov*, A. V. Dvurechenskii, A. V. Nenashev and A. I. Nikiforov
Institute of Semiconductor Physics, Siberian Branch of the Russian Academy of Science,
630090 Novosibirsk, Russia

Abstract. We investigated both theoretically and experimentally the ground state of a hole in vertically self-aligned double Ge quantum dots separated by a Si barrier of thickness t_{Si}. For a dot layer separation above 2 nm, we observed reduction of the hole binding energy below the value of the single dot. It was demonstrated that formation of single-particle hole states in self-organized molecules is governed by the interplay among two effects. The first is the quantum mechanical coupling between the individual states of two dots constituting the molecule. The second one originates from asymmetry of the strain field distribution within the top and bottom dots due to the lack of inversion symmetry with respect to the medium plane between the dots. We found that the molecularlike hole state delocalized over the two dots is formed only at $t_{Si} < 3$ nm and at $t_{Si} > 3.5$ nm. For the intermediate distances ($3 < t_{Si} < 3.5$ nm), the molecular bond becomes disrupted, and the hole turns out to be confined entirely inside the bottom most strained Ge dot.

1. Introduction

Coherent two-level systems and the quantum logic gates are suggested to serve as the building blocks of a quantum information processing. Two vertically or laterally coupled quantum dots (QDs) confined electrons, holes, or excitons have been proposed as a basis for entangled quantum bit operations. The electronic coupling between QDs brought closely together arises from the process of quantum-mechanical tunneling and appears as a formation of bonding and antibonding molecular-type orbitals from the single-dot states by an analogy with the covalent bonds in natural molecules. The bonding molecular state has a larger binding energy than the energies of the original states of the individual dots, thus creating the binding force between the two dots.

The phenomenon of strain-induced self-assembly of semiconductor nanostructures provides a method that allowed for the fabrication of high-quality vertically aligned QDs whose size is extremely small ($\sim$ 10 nm) and the electronic state resembles certainly those of an atom even at room temperature. During heteroepitaxial growth of lattice mismatched materials strain field of a dot in a first layer penetrates into the barrier material and makes it favorable for the dot on the upper layer to form above the buried QD, thus forming a vertical QD molecule. Inhomogeneous spatial strain distribution is a characteristic feature of self-assembled molecules that distinguish them from electrostatically confined nanostructures. Since the strain modifies the confinement potential and the carrier effective masses it may cause considerable deviations from the simplified molecular behavior which implies a coupling of identical QDs.

In this paper we analyzed both theoretically and experimentally the hole ground state of double Ge/Si quantum dots. We observed that the ground-state configuration undergoes nontrivial transformations as a function of the interdot distance due to the competition of the tunneling and deformation effects.

2. Sample preparation

Samples were grown by molecular-beam epitaxy on a p^+-Si(001) substrate with a resistivity of 0.005 Ωcm doped with boron up to a concentration of $\sim 10^{19}$ cm^{-3}. The active region consists of two nominally pure Ge layers separated by Si spacer layer of thickness t_{Si}. To separate response from coupled dots, the reference sample was grown under conditions similar to the double-dot samples, except that only a single Ge layer was deposited. The scanning tunneling microscopy (STM) of samples without the Si cap layer was employed to assess the morphology of Ge layers. Figures 1(a) and 1(b) shows the STM images of the topmost Ge layer for single and double-layer samples, and the lateral size histogram derived derived for each image. The dots have a typical base length $\langle l \rangle \simeq 10-11$ nm and an areal density $n_{QD} \approx 1.5 \times 10^{11}$ cm^{-2}. The non-uniformity of island size is estimated to be about 16–18%. The average Ge content of 90% in the nanoclusters was determined from Raman measurements. Figure 1(e) shows a representative cross-sectional transmission electron micrograph (TEM) of a double-layer sample with $t_{Si} = 4$ nm. The image clearly demonstrates the formation of double-dot molecules with a high vertical correlation between "hut"-shaped Ge islands. For the capacitance and conductance measurements, Al contacts were deposited on top of the samples through a shadow mask to form a Schottky diode, while the Ohmic back contact was fabricated by alloying indium to the p^+-type Si substrate.

3. Results and discussion

To determine the hole binding energy we studied the hole thermal emission rates using the admittance spectroscopy. In these experiments, the ac conductance of a Schottky diode with the hole states of interest is measured as a function of temperature, gate voltage, and test frequency [1]. The average number of extra holes per each molecule (the filling factor ν) was found from analysis of the capacitance-voltage characteristics in low- and high-frequency limits.

Dispersion of the QD size is a dominating force for inhomogeneous broadening of the density of states (DOS) in ensembles of QDs produced by strain-driven self-assembly. For the ground-state energy levels, DOS has a maximum at energies which correspond to the typical dot size. On the other hand, in arrays of quantum dots, DOS oscillates as a function of filling factor and is peaked at half integer ν [2]. Therefore, to analyze the ground state of a molecule occupied with only one hole, we

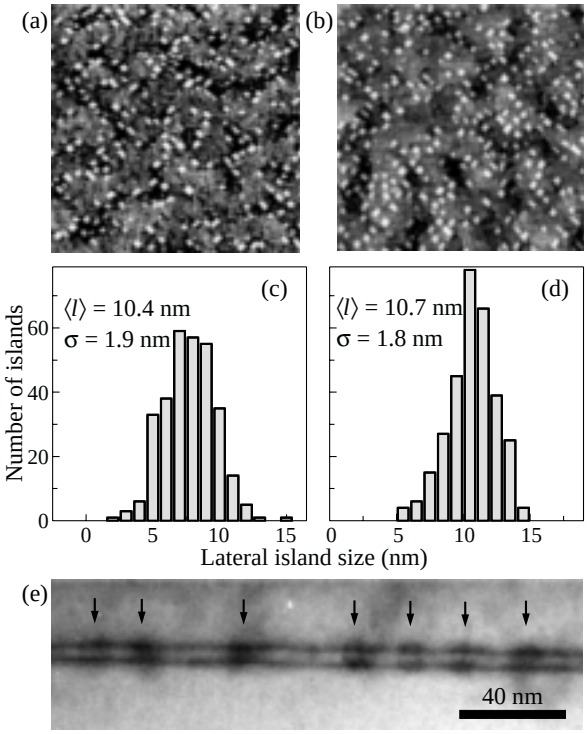

Fig. 1. 400 × 400 nm^2 STM images (a,b) and size distribution histograms (c,d) from topmost uncapped Ge layer of single (a,c) and double (b,d) island layers deposited at a substrate temperature of 500 °C with the rate of $R = 1$ ML/s. For the two-fold stack in panels (b) and (d), the separation between Ge layers is 3.5 nm. (e) Cross-section TEM image in (001) direction of coupled Ge QDs separated by a Si barrier with 3.5-nm thickness. Arrows indicate vertically coupled double quantum dots.

considered the data taken at $\nu = 0.5$. Increasing of the ground state hole energy due to formation of a bonding molecular orbital was found to be as large as $\sim$ 50 meV at $t_{\rm Si} = 1.5$ nm (Fig. 2). For a dot layer separation exceeding 2.5 nm the hole binding energy of the double-dot molecules becomes smaller than the ionization energy of the single Ge dot, contrasting with a simplified quantum-mechanical molecular model.

The interpretation of experimental results is based on the application of sp^3 tight-binding approach in combination with the valence-force-field model (Fig. 2). We considered two *identical* vertically aligned pyramidal GeSi islands with four {105}-oriented facets and a (001) base embedded into the Si matrix. Each pyramid lies on a 4 ML GeSi wetting layer and contains 10% Si atoms randomly distributed within QD. The islands are separated by a Si barrier of thickness $t_{\rm Si}$ measured from wetting layer to wetting layer. Theoretical analysis showed that (i) biaxial strain inside QDs is reduced when the two dots are brought closely together, leading to hole levels with smaller localization energies in the double-dot system; (ii) the strain field is different on both geometrically identical dots due to the lack of inversion symmetry with respect to the medium plane between the dots. Thus, the observed anomalous decreasing of the hole binding energy below the value of the single dot with increasing interdot separation is caused by the partial strain relaxation upon dot stacking accompanied by the strain-induced reduction of the hole confinement potential.

There are two effects which influence the formation of a molecular-type orbital in opposite way. The first one, characterized by the overlap integral Q, is the quantum mechanical coupling between the individual states of two dots constituting the molecule. The second is the difference of the original hole energy levels of the dots, ΔE, originated from asymmetry of the strain field distribution within the top and bottom dots. Both Q and ΔE vanish with increasing the interdot separation $t_{\rm Si}$. Our modeling revealed that, at $t_{\rm Si} < 3$ nm and at $t_{\rm Si} > 3.5$ nm, the overlap integral is larger than the individual energy difference, resulting in formation of the molecular-type hole state delocalized fairly over the two dots. For the intermediate distances ($3 < t_{\rm Si} < 3.5$ nm), the strain anisotropy shifts the ground states of the dots far from resonance with one another, and the hole state becomes confined entirely inside the bottom, most strained Ge dot. The overall agreement between theory and experiment turns out to be quite good, indicating the crucial role played by strain fields in electronic coupling of self-assembled quantum dot molecules.

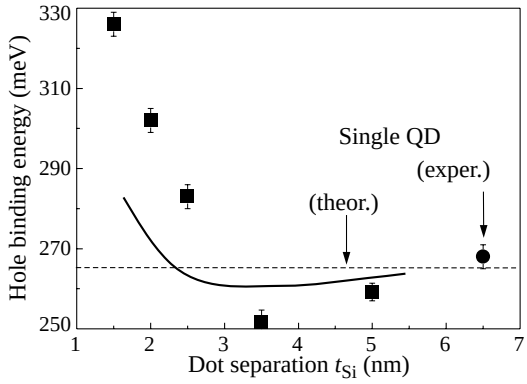

Fig. 2. Evolution of the hole binding energy for $\nu = 0.5$ as a function of the distance between QD layers. As reference, also the energy of single dot is shown. Circle and squares denote experimental data. The solid line is the result of theoretical modeling of double-dot molecules. The dashed line corresponds to the single dot.

Acknowledgements

We thank A. K. Gutakovskii for TEM measurements, S. A. Teys for STM experiments, V. A. Volodin for providing us with the data obtained using Raman spectroscopy, and A. F. Zinovieva for helpful discussion of simulation procedure. This work was supported by RFBR (Grant No. 06-02-16143) and State Contract No. 02.513.11.3156. A.I.Y. acknowledges support from Russian Science Support Foundation.

References

[1] A. I. Yakimov *et al*, *Phys. Rev. B* **72**, 115318 (2005).
[2] J. Zhang and B. I. Shklovskii, *Phys. Rev. B* **70**, 115317 (2004).

15th Int. Symp. "Nanostructures: Physics and Technology"
Novosibirsk, Russia, June 25–29, 2007

Optimized Ge nanowire arrays on Si by modified surfactant mediated epitaxy

K. Romanyuk[1], J. Mysliveček[1], V. Cherepanov[1], B. Voigtländer[1], T. Sekiguchi[2], S. Yoshida[2] and K. M. Itoh[2]

[1] Institute of Bio- and Nanosystems (IBN 3), and CNI — Center of Nanoelectronic Systems for Information Technology, Research Centre Jülich, 52425 Jülich, Germany
[2] Department of Applied Physics and Physico-Informatics, 3-14-1, Hiyoshi, Kohoku-ku, Yokohama, 223-8522, Japan

Abstract. We demonstrate the formation of Ge nanowire arrays on highly ordered kink-free Si stepped surfaces. The nanowires are grown using Bi-surfactant mediated epitaxy. The nanowires are single-crystalline and feature minimal kink densities allowing them to span lengths larger than 1 μm at a width of $\sim$ 4 nm. To achieve desired growth conditions for the formation of such nanowire arrays, we introduce a novel concept in surfactant mediated epitaxy: controlling the surfactant coverage in the surface and/or at step edges to modify growth properties of surface steps.

Introduction

In order to fabricate ever-smaller nanoscale device structures, there is an enormous interest in finding ways to build devices from the bottom up rather than fabricate from the top down. One of the concepts followed in the bottom-up formation of nanowire arrays is to create a highly ordered atomic-step template on a vicinal single crystal surface and to form the wires along the step edges decorating the step edges by a selected material [1,2,3]. A suitable template is the vicinal surface of a Si(111) single crystal, since the structure of the step train on this surface can be controlled to a a large extent [4,5,6]. In this work, we show how it is possible to create a highly ordered array of Ge nanowires on the Bi-covered Si(111) surface. In standard epitaxy of Ge on Si(111) the step structure of the initial well ordered stepped surface is not maintained during growth. We developed a new growth method which prevents this normally occurring loss of the control over step directions. The important point is to conserve the long-range order of the initial Si template. Using surfactant mediated epitaxy an additional parameter becomes available to control the growth — the amount of surfactant at the surface. Changing the amount of the surfactant during growth enables to modify the growth process in the desired direction. The surfactant termination has also two other advantageous properties: it prevents the mutual Ge-Si intermixing and mediates a chemical contrast between Si and Ge allowing to observe the lateral Ge-Si nanostructures in the scanning tunneling microscope (STM). We show that it is possible to grow Ge nanowires on a highly ordered kink-free stepped Si template that follow the ideal geometry of the template. Such Ge nanowires are largely equidistant, have a width of 4 nm and length in micrometer range.

We can divide the procedure of preparation of the Ge nanowire array to three stages: *i*) preparation of the highly-ordered Si(111) template, *ii*) termination of the template by 1 ML Bi, *iii*) growth of Ge nanowires on the Bi-terminated template.

Preparation of the highly-ordered Si(111) template and termination of the template by 1 ML Bi

(i) The highly ordered Si(111)-7 $\times$ 7 template was prepared as in [6]. We polished a Si(111) wafer to 1° miscut (θ_m) toward a [$\bar{1}\bar{1}2$] direction with an intentional azimuthal misorientation ($\phi_m = 4°$) to orient all kinks at the surface steps in the same direction. The samples were cleaned in vacuum with flash heating to 1300 °C and rapidly quenched. Afterwards, the samples were annealed at 800–830 °C for about 10 h with dc current flowing parallel to the steps in the "kink-up" direction [6] to extend atomically straight step edges by surface electromigration of Si. The resulting surface step structure is shown on the Fig. 1(a). The "kink-up" direction was used for dc sample heating in all subsequent preparation steps.

(ii) The standard Bi-surfactant mediated epitaxy [3,7,8] on the Si(111)-7 $\times$ 7 surface starts by terminating the surface with 1 ML of Bi that forms a $\sqrt{3} \times \sqrt{3}$ surface structure [9,10,11]. This is associated with a significant surface mass transport of Si, because 0.24 ML of Si atoms are released as a result of the lifting of the 7 $\times$ 7 surface reconstruction [12]. The steps become wavy on a short length scale and the initial step ordering is completely lost. This shows that the standard Bi termination is not useful to retain the straight step structure of the Si template. We solve the above problem by a careful control of the Bi coverage at the terraces during Bi termination. We make use of the fact that Bi readily desorbs from the Si(111) surface at elevated temperatures. Thus, for a constant Bi flux we can control the Bi coverage in a steady state regime adjusting the Bi desorption rate by choosing the appropriate substrate temperature. In the optimized Bi termination procedure we heat the substrate to $T_s = 700$ °C and start to deposit Bi at $F_{Bi} = 3$ ML/min. At this high temperature the Bi coverage is virtually zero. Afterwards, we slowly reduce T_s to 650 °C over 10 min. This leads to a slow increase of the Bi coverage allowing a gradual Si mass transport during the lifting if the Si(111)-7 $\times$ 7 reconstruction and the conversion to the 1 $\times$ 1 structure below the Bi layer. The surface steps remained straight indicating that during the slow increase of the Bi coverage the released Si atoms had enough time to evenly distribute along the step edges.

Growth of Ge nanowires on the Bi-terminated template

(iii) In the last preparation step we grow the Ge nanowires along the step edges of the 1 ML Bi terminated template using surfactant mediated epitaxy. In standard surfactant mediated epitaxy, materials are deposited under a constant supply of the surfactant to maintain the (saturated) 1 ML surfactant coverage

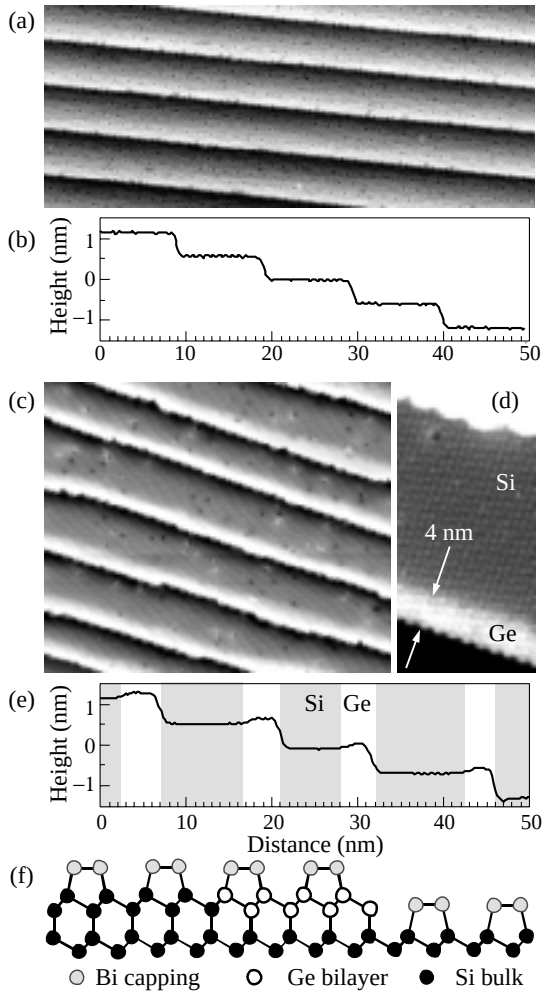

Fig. 1. (a) Si(111)-7 × 7 template with highly ordered step structure. (b) Corresponding height profile. (c), (d) Ge nanowires (light colored stripes at the step edges) grown on this template by modified surfactant mediated epitaxy. The long range order of the starting template remains conserved. The Bi surfactant changes the surface reconstruction to $\sqrt{3} \times \sqrt{3}$ (d). (e) Apparent height difference measured by STM between Si and Ge areas. The Ge nanowires are a Ge bilayer attached to the step edges of the template under the Bi capping (f). They measure $\sim$ 4 nm ($\sim$ 20 atoms) in width, and 0.3 nm in height. The width of the STM topographs is 100 nm, 75 nm, and 15 nm in (a), (c), (d), respectively.

during growth [7,8,11]. However, performing the Ge deposition in the standard way at $F_{\mathrm{Ge}} = 0.08$ ML/min, $T_{\mathrm{s}} = 450\,^{\circ}$C, and the Bi flux $F_{\mathrm{Bi}} = 3$ ML/min does not yield the straight Ge nanowires of homogenous width. In Fig. 2(a) we can observe, that Ge nanowires grown by standard surfactant mediated epitaxy develop step edges in $\langle 1\bar{1}0 \rangle$ directions which are 30° off the step direction of the template. This leads to undesired variations of the Ge nanowire width. To obtain the desired regular growth of Ge nanowire arrays we consider reducing the Bi surfactant coverage. We switch off the Bi flux during Ge evaporation and deposit Ge at $T_{\mathrm{s}} = 400\,^{\circ}$C, $F_{\mathrm{Ge}} = 0.02$ ML/min for 10 min. Afterwards, we cool the sample rapidly to room temperature. We show the result of this preparation step in Figs. 2(b), and 1(c),(d). We obtain the optimized growth of Ge at the template step edges resulting in single-crystalline, high aspect-ratio, low kink-density Ge nanowires with width of about 4 nm.

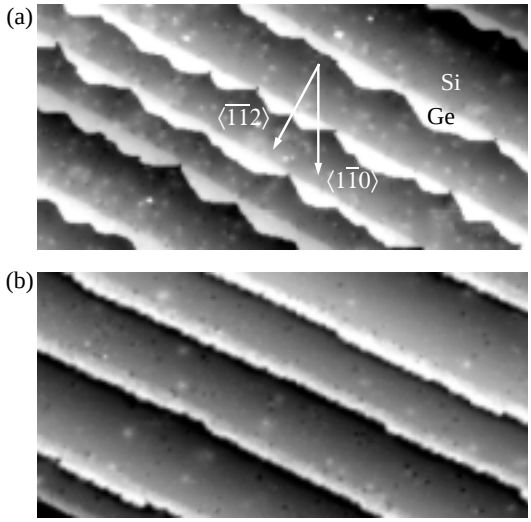

Fig. 2. Deposition of Ge on the ordered Bi-terminated surface. (a) Standard surfactant mediated epitaxy. Ge and Bi are deposited simultaneously. The light areas at the step edges are Ge decoration. The Ge step edges develop facets in $\langle 1\bar{1}0 \rangle$ directions that are 30 ° off the original $\langle \bar{1}12 \rangle$ step direction. (b) Modified surfactant mediated epitaxy. Ge is deposited without Bi flux. The light uniform stripes at step edges correspond to the Ge stripes. The Ge step edges retain the original $\langle \bar{1}12 \rangle$ step direction. The width of the STM topographs is 200 nm in (a), and 100 nm in (b).

The success of the last preparation step shows that switching off the Bi flux at $T_{\mathrm{s}} = 400\,^{\circ}$C is sufficient to change the Ge growth scenario. We cannot observe any significant reduction of Bi concentration on the terraces after this growth step. The $\sqrt{3} \times \sqrt{3}$ surface structure is homogeneous, indicating the saturation 1 ML Bi coverage [10] [Fig. 1(d)]. Therefore, we attribute the change of growth scenario to a reduction of Bi coverage at step edges.

References

[1] T. Jung, R. Schlittler, J. K. Gimzewski, F. J. Himpsel, *Appl. Phys. A.* **61**, 467–474 (1995).
[2] F. J. Himpsel, T. Jung, J. E. Ortega, *Surface Review and Letters* **4** (2), 371–380 (1997).
[3] M. Kawamura, N. Paul, V. Cherepanov, B. Voigtländer, *Phys. Rev. Lett.* **91** (9), 096102-1-096102-4 (2003).
[4] J.-L. Lin, D. Y. Petrovykh, J. Viernow, F. K. Men, D. J. Seo, F. J. Himpsel, *J. Appl. Phys.* **84** (1), 255–260 (1998).
[5] H. Omi, T. Ogino, *J. Vac. Sci. Technol. A* **17** (4), 1610–1614 (1999).
[6] S. Yoshida, T. Sekiguchi, K. M. Itoh, *Appl. Phys. Lett.* **87** (3), 031903-1-031903-3 (2005).
[7] N. Paul, H. Asaoka, J. Mysliveček, and B. Voigtländer, *Phys. Rev. B* **69** (19), 193402-1-193402-4 (2004).
[8] N. Paul, H. Asaoka, and B. Voigtländer, *Surface Science* **564** (1–3), 187–200 (2004).
[9] K. J. Wan, T. Guo, W. K. Ford, J. C. Hermanson, *Phys. Rev. B* **44** (7), 3471–3474 (1991).
[10] R. Z. Bakhtizin, Ch. Park, T. Hashizume, T. Sakurai, *J. Vac. Sci. Technol. B* **12** (3), L290–L293 (1994).
[11] T. Schmidt, J. Falta, G. Materlik, *Appl. Phys. Lett.* **74** (10), 1391–1393 (1999).
[12] S. Hasegawa, R. G. Ryland, E. D. Williams, *Appl. Phys. Lett.* **65** (20), 2609–2611 (1994).

15th Int. Symp. "Nanostructures: Physics and Technology"
Novosibirsk, Russia, June 25–29, 2007

Room temperature photo- and electroluminescence of Ge(Si)/Si(001) self-assembled islands

A. N. Yablonskiy, D. N. Lobanov, A. V. Novikov, K. E. Kudryavtsev, M. V. Shaleev, V. B. Shmagin, D. V. Shengurov, Yu. N. Drozdov and Z. F. Krasilnik

Institute for Physics of Microstructures, Nizhny Novgorod, Russia

Abstract. In this work we present the results of the comparative investigations of photo- (PL) and electroluminescence (EL) of multilayer Ge(Si)/Si(001) structures with self-assembled Ge(Si) islands. Multilayer diode structures with 20 layers of Ge(Si) islands separated by 25 nm thick silicon spacers have been grown by MBE at 600 °C. The effect of additional annealing of the structures on the intensity, spectral characteristic and temperature dependence of the PL and EL signal has been studied.

The intensive PL and EL signal originated from the radiative recombination in Ge(Si) islands was observed in the spectral range 1.3–2 μm up to room temperature (Fig. 1). It has been shown that the position of the PL and EL peak from the islands strongly depends on the pumping power. The maximum of the PL and EL signals shifts to higher energies upon an increase of the pumping power (the power of the pumping laser radiation in case of PL and the current density for EL). This shift is typical for semiconductors heterostructures with type II band alignment [1] and can be explained by an increase of the number of photo-generated carriers and, as a result, populating of the higher excited energy states in the islands and additional bending of the conduction and valence bands in the vicinity of the islands. The maximum of the EL signal from the islands is shifted to higher energies in comparison with the PL signal, which can be explained by more effective injection of carriers into the islands by electrical current then by laser radiation with wavelength of 532 nm. In case of electrical pumping the carriers are injected from the contact layers directly to the undoped region with Ge(Si) islands.

It has been found that in the samples subjected to annealing during 1 minute at the temperatures 650 °C and 700 °C the maximum of the PL and EL signal from Ge(Si) islands shifts to higher energies and the shift is more pronounced for higher annealing temperature (700 °C) (Fig. 2). This shift can be explained by additional diffusion of silicon to the islands during the annealing, which results in decrease of the band offset on the interface between Ge(Si) islands and Si layers and leads to an increase in the energy of the optical transitions in the islands [2].

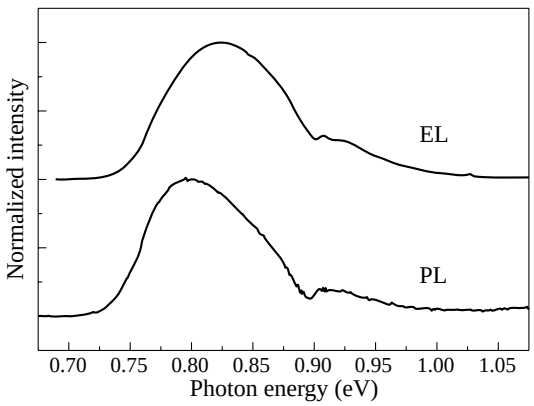

Fig. 1. Room temperature PL and EL spectra of the "as grown" structure with Ge(Si) islands. The spectra were measured using Ge detector.

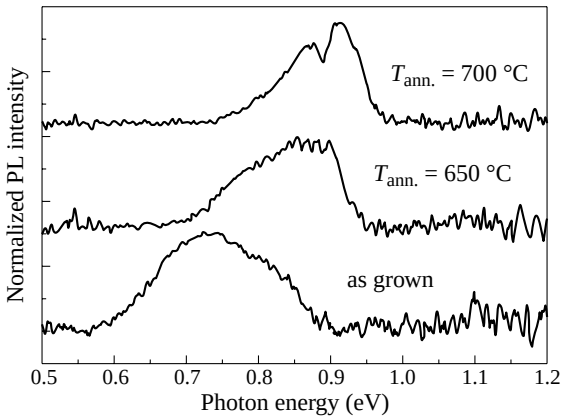

Fig. 2. PL spectra of the multilayer structure with Ge(Si) islands before annealing and after annealing at 650 °C and 700 °C. The spectra were measured using InSb detector at 77 K.

It has been demonstrated that intensive PL and EL signal from the Ge(Si) islands can be observed up to room temperature (Fig. 1). The studies of the temperature dependences of the integral PL and EL intensity have shown that the "as grown" structure is characterized by low temperature quenching of the PL signal (Fig. 3) and demonstrated almost independent on temperature EL signal (Fig. 4). For the structures annealed at 650 °C and 700 °C the temperature quenching of the PL signal was found to be much stronger (Fig. 3). The analysis of the temperature curves has shown that the activation energy of the PL temperature quenching decreases from 192 meV for the "as grown" structure down to 141 meV and 113 meV for the islands annealed at 650 °C and 700 °C, respectively. It has been shown that the activation energies of the PL temperature quenching well coincides with the difference between the energy levels for holes in the islands and in the wetting layers, which has been obtained from energy band calculations and the PL studies of the structures with wetting layers. This result evidences that the temperature quenching of the PL signal from the islands is caused by thermal release of the photo-generated holes from the islands to the wetting layers. The lower activation energies of the PL quenching in the annealed structures can be explained by decrease of the Ge content in the islands after annealing and, as a result, decrease of the well depth for holes in the islands. This suggestion is supported by the fact that the activation energy of

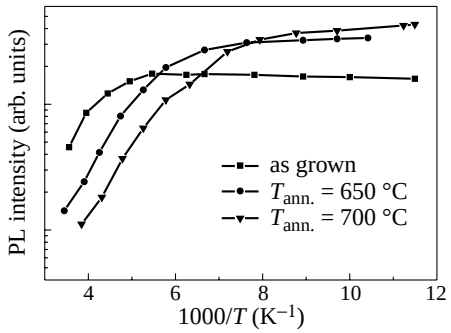

Fig. 3. Temperature dependences of the integrated PL intensity from the "as grown" and annealed structures with Ge(Si) self-assembled islands.

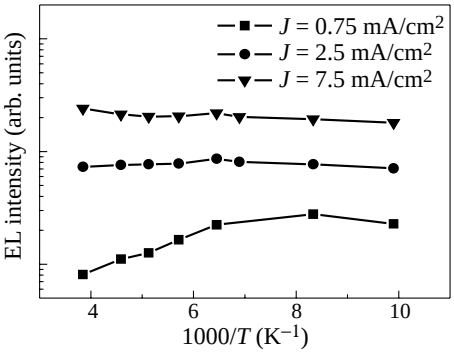

Fig. 4. Temperature dependences of the integrated EL intensity from the "as grown" structure with Ge(Si) islands at different current densities.

the PL quenching decreases also with an increase of the growth temperature and, consequently, with decrease of the Ge content in the islands. As an example for the structure grown at 650 °C the activation energy of the PL quenching amounts to 120 meV.

It has been shown that the temperature quenching of the integral EL signal from Ge(Si) islands decreases with an increase of the current density and for the value ~ 2.5 A/cm^2 the EL signal becomes almost independent on temperature (Fig. 4). Such behavior is concerned with saturation of the non-radiative recombination channels at high current densities. The slight increase of the EL intensity with temperature observed at high current densities (>2.5 A/cm^2) can be explained as in [3] by an increase in the lifetime of the injected carriers due to their thermal release from the deep non-radiative recombination centers.

The external quantum efficiency of the room temperature EL for the "as grown" structure was found to be 1.2×10^{-5} at the current density of 7.5 A/cm^2.

It should be noted also that considerable photoconductivity signal in the spectral range 1.3–1.55 μm has been observed at room temperature in the "as grown" structure with Ge(Si) self-assembled islands.

Acknowledgements

This work has been financially supported by RFBR (grant 05-02-17336-a) and by Russian Academy of Sciencies.

References

[1] C.-K. Sun *et al*, *Appl. Phys. Lett.* **68**, 1543 (1996).
[2] P. Boucaud *et al*, *Phys. Rev. B* **64**, 1555310 (2001).
[3] M. C. Bresler *et al*, *Phys. of the Solid State* **46/1**, 10 (2004).

15th Int. Symp. "Nanostructures: Physics and Technology"
Novosibirsk, Russia, June 25–29, 2007

Excited excitonic states in Mn-doped quantum dots

M. M. Glazov[1], E. L. Ivchenko[1], L. Besombes[2], Y. Léger[2], L. Maingault[2] and H. Mariette[2]

[1] Ioffe Physico-Technical Institute, St Petersburg, Russia
[2] CEA-CNRS group "Nanophysique et Semiconducteurs", Laboratoire de spectrométrie physique, CNRS and Université Joseph Fourier-Grenoble 1, BP 87, F-38402 St Martin d'Hères, France

Abstract. The fine structure of excited excitonic states in a quantum dot containing a Mn ion is studied theoretically and experimentally. The developed theory takes into account the direct Coulomb and exchange interaction in the zero-dimensional exciton, and the exchange interaction of the electron and the hole with the d-electrons of the Mn ion inserted into the dot. The experimental results and theoretical predictions show good quantitative agreement.

Introduction

Semiconductor quantum dots (QDs) with embedded magnetic ions attract a special interest owing to the possibility of the single spin manipulation by optical means [1]. The fine structure of the exciton ground state has been studied in detail both experimentally and theoretically [1, 2]. The aim of the the present joint theoretical-experimental investigation is to analyze the energy energy levels and photoluminescence excitation spectra of the excited excitonic states in the Mn-doped quantum dots.

1. Model

We consider heavy-hole exciton states in a single quantum-well quantum dot. The carriers are confined by the *coaxial parabolic* potentials with z as the principal axis. In what follows we concentrate on QDs of sizes small enough to have the in-plane localization lengths for electrons (a_e) or holes (a_h) smaller than the two-dimensional (2D) exciton Bohr radius a_B.

The exciton state can be described as a product of the orbital envelope determined by the confinement potential of the QD and a Bloch function which is conveniently denoted by the spin of electron, s, and hole angular momentum, j. We are interested in the fine structure of the ground, ss-shell, state and of the excited, pp-shell, states, the latter formed by the electron and hole occupying the p-orbitals in the QD. We focus on the case of slightly anisotropic quantum dot where pp-orbital states are split due to the difference of the localization lengths $a_{\mathrm{e},i}$, $a_{\mathrm{h},i}$ ($i = x, y$) in the x and y directions. The anisotropy is characterized by the ratios $\beta_\mathrm{e} = (a_{\mathrm{e},y} - a_{\mathrm{e},x})/2a_\mathrm{e}$, $\beta_\mathrm{h} = (a_{\mathrm{h},y} - a_{\mathrm{h},x})/2a_\mathrm{h}$, where $a_\mathrm{e} = (a_{\mathrm{e},y} + a_{\mathrm{e},x})/2$, $a_\mathrm{h} = (a_{\mathrm{h},y} + a_{\mathrm{h},x})/2$. For simplicity we assume $\beta_\mathrm{e} = \beta_\mathrm{h} \equiv \beta$ and $\beta \ll 1$. The splitting between two bright states $D_{xx}(\boldsymbol{\rho}_\mathrm{e}, \boldsymbol{\rho}_\mathrm{h})$ and $D_{yy}(\boldsymbol{\rho}_\mathrm{e}, \boldsymbol{\rho}_\mathrm{h})$ (formed of the P_x electron and P_x hole, and P_y electron and P_y hole, respectively) is given to the lowest order in β by

$$E_a = E_{xx} - E_{yy} = \left(1 + \frac{\sigma}{\zeta^2}\right) \frac{4\hbar^2\beta}{m_\mathrm{e} a_\mathrm{e}^2}\,, \qquad (1)$$

where $\sigma = m_\mathrm{e}/m_\mathrm{h}$ and $\zeta = a_\mathrm{h}/a_\mathrm{e}$.

2. Exciton fine structure

Let us introduce the characteristic value of the long-range exchange for pp-shell states

$$\mathcal{E} = \left(\frac{e\hbar|p_0|}{m_0 E_\mathrm{g}}\right)^2 \frac{\sqrt{\pi}}{16\kappa_\infty a_\mathrm{e}^3 \zeta\sqrt{1+\zeta^2}}\,, \qquad (2)$$

where e is an elementary charge, p_0 is an interband momentum matrix element, m_0 is a free electron mass, E_g is a band gap, κ_∞ is the high-frequency dielectric constant.

If the QD possesses an anisotropy in the axes x, y the radiative doublet of the ground state is split into a pair of linearly polarized sublevels with the microscopic oscillating dipole momentum parallel to x and y as [3]

$$\delta E_s = 24\beta\mathcal{E}\,, \qquad (3)$$

and is proportional to the anisotropy degree β. Each optically active pp-shell (D_{xx} and D_{yy}) is split into radiative sublevels $|D_{xx}, x\rangle$, $|D_{xx}, y\rangle$ or $|D_{yy}, x\rangle$, $|D_{yy}, y\rangle$ according to

$$\delta E_d = E_{|D_{xx},x\rangle} - E_{|D_{xx},y\rangle} = E_{|D_{yy},y\rangle} - E_{|D_{yy},x\rangle} = 3\mathcal{E}\,. \qquad (4)$$

Comparing Eqs. (3) and (4) we conclude that splittings of the ss- and pp-shells differ by 8β.

In a QD with an embedded Mn ion, fine structure of the excitonic states is determined by the interplay between the QD anisotropy and the exchange coupling with the Mn ion. From now on we consider the case where the ground state anisotropic splitting (3) is negligible as compared with the coupling with a magnetic ion. The exciton-Mn interaction splits this state into 12 doubly-degenerate sublevels half of which, namely, those with the exciton angular-momentum component $m \equiv s + j = \pm 1$, are optically active (or bright). Their energies are given by

$$E^{(S)}_{m,M} = E^{(S)}_0 + \delta_s m M\,,\ \delta_s = (3I^{(s)}_\mathrm{h} - I^{(s)}_\mathrm{e})/2\,, \qquad (5)$$

where $E^{(S)}_0$ is the ss-shell exciton energy, $I^{(s)}_\mathrm{e}$ and $I^{(s)}_\mathrm{h}$ are the interaction constants which depend on the position, $\mathbf{r}_0 = (x_0, y_0, z_0)$, of the Mn ion in the quantum dot.

The fine structure of the pp-shell exciton excited states is determined by a combined effect of the exciton-Mn and the electron-hole (long-range) exchange interactions. In the general case an overlap between exciton and Mn ion is different for these two orbitals and one needs to introduce two coupling constants for each type of the carriers, as e.g., $I^{(xx)}_\mathrm{e} = (x_0/a_\mathrm{e})^2 I^{(s)}_\mathrm{e}$, $I^{(xx)}_\mathrm{h} = (x_0/a_\mathrm{h})^2 I^{(s)}_\mathrm{h}$. The eigen energies are determined by the interplay of the exciton-Mn interaction described by the parameter

$$\delta_{ii} = 3I^{(ii)}_\mathrm{h} - I^{(ii)}_\mathrm{e}, \quad (i = x, y), \qquad (6)$$

and the long-range exchange splitting (4). For a fixed orbital D_{ii} one should observe six doubly-degenerated non-equidistant lines.

3. Experimental results and discussion

We use micro-spectroscopy to analyze the optical properties of individual Mn-doped self-assembled CdTe/ZnTe QDs. Single Mn atoms are introduced in CdTe/ZnTe QDs [1] by adjusting, during the growth process, the density of Mn atoms to be roughly equal to the density of QDs. The PL of individual QDs is excited with a tunable dye laser and collected through aluminium shadow masks with 0.2. . .1.0 μm apertures. The PL is then dispersed by a 2-m additive double monochromator and detected by a nitrogen cooled Si charge-coupled device (CCD).

The experimental findings for a particular Mn-doped QD which shows clear linearly polarized excited states can be summarized as follows. The ground state PL demonstrates 6 equidistant lines positioned at $\sim$ 2086 meV. These lines correspond to different projections of Mn spin, see Eq. (5). Their approximately equal intensities and regular energy spacing evidence the negligible anisotropic splitting of the ground state. The splitting between these lines suggests the value $\delta_s \approx 0.2$ meV being in a good agreement with previous studies [1].

Now we proceed with the discussion of the excited-states fine structure. Two excited states with energies $\approx$ 2118 meV and 2120 meV are observed in photoluminescence excitation (PLE) experiments. We relate them with the D_{yy}- and D_{xx}-orbital states. From their energy spacing we evaluate the quantum dot anisotropy degree β to be ≈ 0.02 which supports the assumption that the anisotropic splitting of ss-shell state is not observed. Figure 1 clearly demonstrates the splitting of D_{yy} state into a pair of lines. The splitting of D_{xx} state is not observed.

The comparison between the experimental data (Fig. 1) and theoretical predictions (Fig. 2) shows that the best possible agreement of the data is obtained for anisotropic splitting $\delta E_{\rm d} = 0.05$ meV and $\delta_{yy} = 0.04$ meV. Other parameters are shown in the caption to Fig. 2. The order of magnitude of $\delta E_{\rm d}$ is consistent with the quantum dot size $a_{\rm e} = 45$ Å and $a_{\rm h} = 90$ Å (i.e. $\zeta = 2$). The experimentally observed PLE intensity distribution for the higher energy state D_{xx} is almost

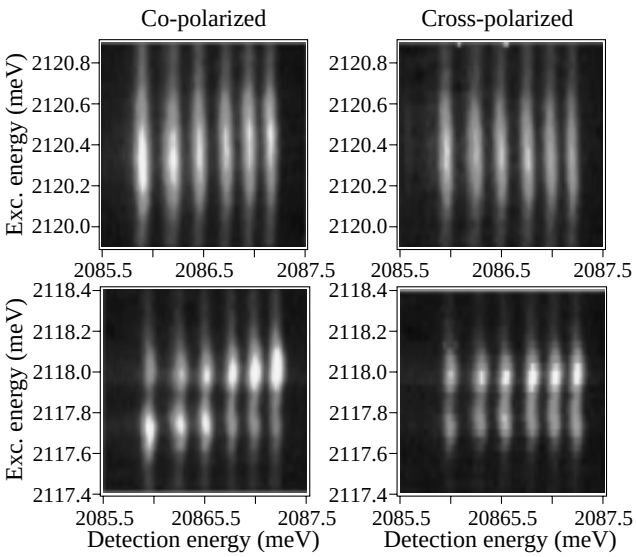

Fig. 1. PLE contour plots for excited states D_{xx} (upper panel) and D_{yy} (lower panels) obtained for co-polarized (left panels) and cross-polarized (right panels) circular excitation.

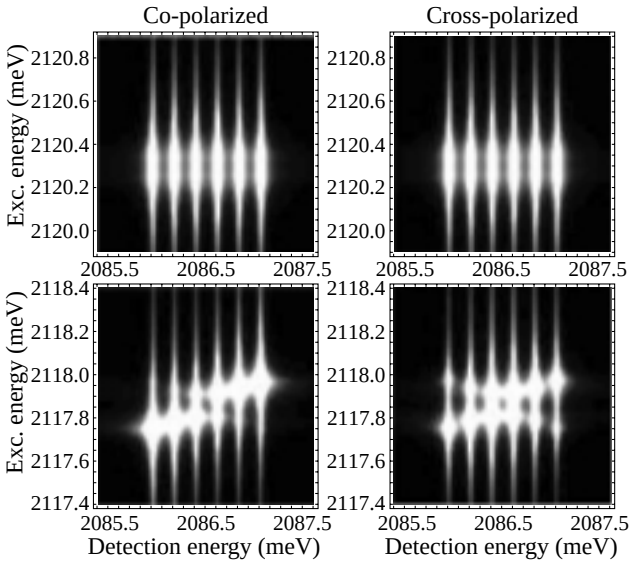

Fig. 2. Calculated PLE spectra in co-polarized (left) and cross-polarized (right) configuration. The parameters used are as follows: $E_{yy} = 2117.86$ meV, $E_{xx} = 2120.30$ meV, $\delta E_{\rm d} = 0.05$ meV, $\delta_{xx} = 0.01$ meV, $\delta_{yy} = 0.04$ meV, $\delta_s = 0.2$ meV and $E_0^{(S)} = 2086.5$ meV. The lines are Lorentzian-broadened with the widths $\Gamma_s = 0.03$ meV and $\Gamma_{xx} = 0.06$ meV, $\Gamma_{yy} = 0.03$ meV.

uniform, therefore we conclude that the exciton-Mn ion coupling is negligible for this state. Taking into account the fitted value $\delta_{yy} = 0.04$ meV we deduce that the Mn-ion is positioned at $y_0 \approx 0.3a_{\rm h}$, $x_0 \ll y_0$.

In conclusion, we have performed a combined experimental and theoretical study of the fine structure of exciton excited states in the QDs containing a single magnetic ion. Theoretical predictions and experimental findings are in the quantitative agreement with each other.

Acknowledgements

The work was partially supported by RFBR, "Dynasty" foundation — ICFPM and French ANR contract MOMES.

References

[1] L. Besombes, Y. Léger, L. Maingault, D. Ferrand, H. Mariette and J. Cibert, *Phys. Rev. Lett.* **93**, 207403 (2004). L. Besombes , Y. Léger, L. Maingault, D. Ferrand, H. Mariette and J. Cibert, *Phys. Rev. B* **71**, 161307(R) (2005). Y. Léger, L. Besombes, L. Maingault, D. Ferrand and H. Mariette, *Phys. Rev. Lett.* **95**, 047403 (2005). Y. Léger, L. Besombes, L. Maingault, D. Ferrand and H. Mariette, *Phys. Rev. B* **72**, 241309(R) (2005). Y. Léger, L. Besombes, J. Fernández-Rossier, L. Maingault and H. Mariette, *Phys. Rev. Lett.* **97**, 107401 (2006).

[2] A. O. Govorov, *Phys. Rev. B* **70**, 035321 (2004). J. Fernández-Rossier, *Phys. Rev. B* **73**, 045301 (2006).

[3] M. M. Glazov, E. L. Ivchenko, R. v. Baltz, and E. G. Tsitsishvili, *Int. J. Nanosci.* (2007) cond-mat/0501635.

15th Int. Symp. "Nanostructures: Physics and Technology"
Novosibirsk, Russia, June 25–29, 2007

ODMR investigation of tunneling recombination processes in ZnO nanocrystals

P. G. Baranov[1], *D. O. Tolmachev*[1], N. G. Romanov[1], C. de Mello Donegá[2], A. Meijerink[2], S. B. Orlinskii[3] and J. Schmidt[3]

[1] Ioffe Physico-Technical Institute, St Petersburg, Russia
[2] Debye Institute, Utrecht University, Utrecht, The Netherland
[3] Huygens Laboratory, Department of Physics, Leiden University, Leiden, The Netherlands

Abstract. Optically detected magnetic resonance was applied to study radiative recombination in ZnO nanocrystals (quantum dots) obtained by colloid chemistry technique. Long-lasting spin-dependent recombination afterglow has been found in light-excited ZnO nanocrystals. A giant increase in the intensity of afterglow upon a change in the spin orientation of electron and hole centers has been observed under electron paramagnetic resonance conditions, which allowed these centers to be identified.

Introduction

In this work, long tunneling afterglow (TA) in ZnO quantum dots (nanocrystals) exposed to short-term irradiation with ultraviolet (UV) light with a quantum energy in the interband absorption region was detected and studied. Previously, long TA was observed only in bulk crystals after x-ray irradiation, and it was induced by tunneling recombination between electron and hole centers generated by x-ray irradiation [1]. The long duration (many hours) of TA in these systems was due to the long distance between recombining partners. It was shown that TA is a spin-dependent process; therefore, the magnetic quenching of afterglow is observed in strong magnetic fields at low temperatures due to the spin polarization of electron and hole centers in according to the Boltzmann distribution. Thus it became possible to detect optically the electron paramagnetic resonance (EPR) of the recombining partners and, thus, to identify these defects (optically detected magnetic resonance, ODMR) [2].

Electron paramagnetic resonance (EPR) of electron and hole centers (donors and acceptors) in ZnO nanocrystals have recently been studied by the high-frequency electron spin echo (ESE) technique [3–5].

1. Results and discussion

As in [3–5], we studied dry powders of free-standing $Zn(OH)_2$-capped ZnO nanocrystals obtained by colloid chemistry technique (the sample preparation procedure was described in [3–5]). ZnO nanocrystals were 3.5 nm in size, and the scatter in their sizes was no more than 10%. Fig.1 (a) presents a TEM micrograph of these nanocrystals dispersed in ethanol.
The photoluminescence (PL) excited with UV light ($\sim$ 300 nm) and afterglow spectra recorded at a temperature of 5 K for 3.5 nm ZnO nanocrystals are shown in Fig. 1(b). The TA intensity drops by more than three orders of magnitude in the first seconds after the termination of excitation and then slowly decreases for a long time (for several hours). The shape of the spectrum and its intensity remained virtually unchanged in the temperature range 1.5–5 K.

Magnetic quenching of the afterglow has been found in strong magnetic fields at low temperatures, which implies that recombination is a spin-dependent process. The magnetic field dependence of the afterglow at a temperature of 2 K is presented

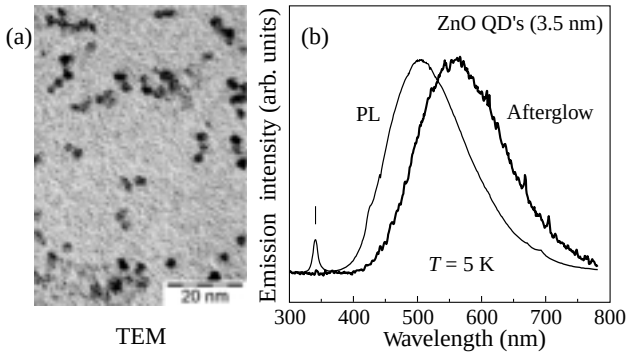

Fig. 1. a) TEM image of 3.5 nm ZnO nanocrystals dispersed in ethanol. b) photoluminescence (PL) and tunneling afterglow of 3.5 nm ZnO nanocrystals.

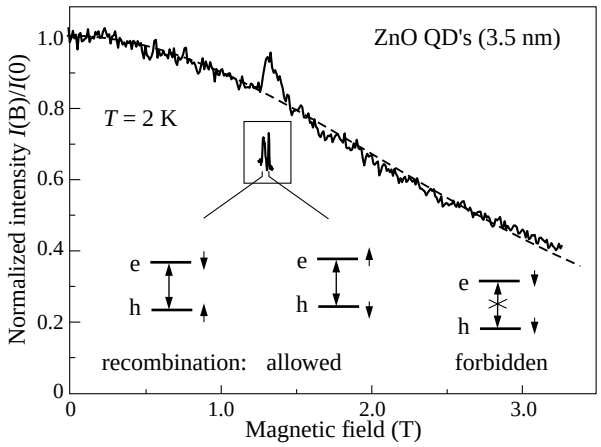

Fig. 2. Magnetic field dependence of tunneling afterglow of 3.5 nm ZnO nanocrystals in presence of 35.2 GHz microwaves at 2 K. Inset shows ODMR signal recorded at low sweep rate.

in Fig. 2. It is corrected with regard to the slight decrease in the TA intensity with time during the magnetic field sweep. The the field dependence can be described with the expression $I = I_0(1 - P_e P_h)$, where I_0 is the TA intensity in a zero magnetic field and P_e and P_h are the spin polarizations of electron and hole centers in the magnetic field. The calculated dependence for the recombination of two centers with spins $S_e = S_h = 1/2$ and g factors $g_e = 1.965$ and $g_h = 2.003$ is shown in Fig. 2 by dashed line.

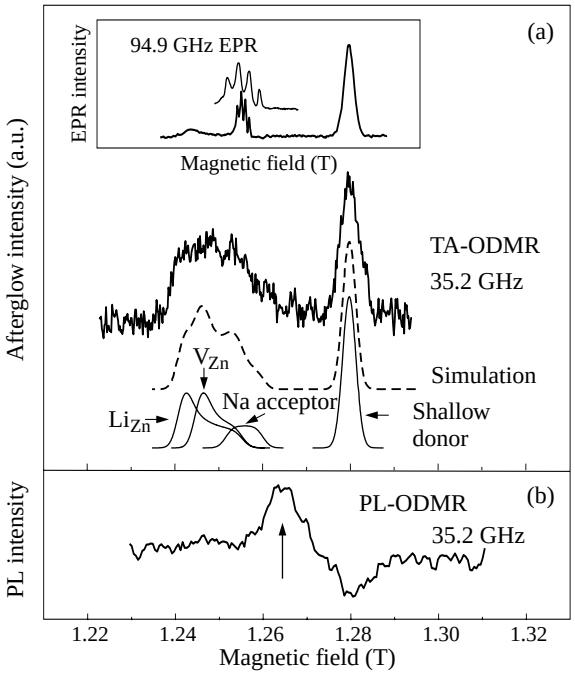

Fig. 3. a) 35.2 GHz ODMR spectrum recorded by monitoring total afterglow and simulated ODMR signals (below) for shallow donors and different types of acceptors. Inset shows the 95 GHz EPR spectrum recorded by ESE technique for the same nanocrystals. b) ODMR of 3.5 nm ZnO nanocrystals recorded by monitoring total photo-luminescence. The arrow marks ODMR of exchange-coupled DA pairs. $T = 2$ K.

In strong magnetic fields the spins of the most of the electron and hole centers are parallel due to thermalization and the recombination is forbidden. The application of microwaves leads to an increase in the TA intensity in magnetic fields corresponding to EPR transitions for electron (e) and hole (h) centers due to the reorientation of their spins, which increase an amount of pairs with antiparallel spins. In the region of magnetic fields of 1.2–1.3 T, a strong increase in the TA intensity (up to 10%) is observed in the presence of a microwave field with a frequency of 35.2 GHz. Insert shows a part of the dependence recorded at a slower sweep rate.

The ODMR spectrum recorded by the overall TA spectrum two hours after the UV excitation is presented in Fig. 3. The inset presents the EPR spectrum at 2 K recorded by the electron spin echo (ESE) technique at a frequency of 94.9 GHz for the same ZnO nanocrystals after short-term UV irradiation. The scale of magnetic fields is decreased according to the ratio of the microwave frequencies 94.9/35.2. Since the hyperfine splitting does not depend on frequency, the real 35.2 GHz EPR for surface acceptors associated with sodium is also shown (above).

Shallow donors with a g-factor of 1.965 coinciding with the g factor obtained by high-frequency EPR are detected in the ODMR spectra. The g-factor shift relative to the bulk ZnO is due to confinement effects. Shown below are simulated ODMR spectra of shallow donors and three types of deep acceptors that were previously discussed in [5]: centers associated with Na atoms localized near the interface (Na acceptors), zinc vacancies V_{Zn}, and lithium atoms at zinc positions Li_{Zn}. The overall simulated spectrum is shown with a dashed line. A correlation between the two methods can be seen from the figure; however, the ratios of intensities for various acceptor signals differ significantly. ODMR is directly linked to the recombination efficiency for defects of a certain type at the instant of detection, while in conventional EPR all defects remaining in the sample at the instant of detection are observed.

Fig. 3b shows a weak ODMR signal (the change in the PL intensity at resonance $\sim 10^{-2}$% observed by monitoring the PL intensity. Exchange-coupled electron-hole pairs composed of a shallow donor and an acceptor of the Li_{Zn} or V_{Zn} type, that is, pairs that were not observed in high-frequency EPR experiments, is detected in the ODMR spectrum.

The probability of tunneling recombination of electron-hole pairs and, hence, the intensity of tunneling recombination afterglow I are rapidly decreasing functions of the distance between recombining partners. The dependence $I(t) \sim C/t$ is fulfilled in bulk materials for large time intervals passed after the termination of (x-ray) excitation [1]. In subsequent studies, it will be of interest to consider specific features of the time dependence of the TA intensity $I(t)$ in quantum dots, that is, under conditions when the distances between recombining partners are spatially confined.

Thus, long spin-dependent tunneling recombination afterglow is found in ZnO nanocrystals excited by short-term UV irradiation. Because of the giant increase in the intensity of tunneling afterglow upon the spin flip in electron and hole centers participating in recombination, these centers were identified by their ODMR spectra. It was shown that recombination involves shallow donors and deep acceptors of two types: (i) deep acceptors conventional for bulk ZnO crystals, namely, lithium atoms substituted for zinc atoms Li_{Zn} and zinc vacancies V_{Zn}, and (ii) deep acceptors associated with sodium located near the interface.

Acknowledgements

This work was supported by the Russian Foundation for Basic Research (project 05-02-17817) and by the Russian Academy of Sciences (programs “Spin-Dependent Effects in Solids and Spintronics” and P-03 “Quantum Macrophysics”).

References

[1] C. J. Delbecq, Y. Toyozawa, and P. H. Yuster, *Phys. Rev. B* **9**, 4497 (1974).
[2] P. G. Baranov, Yu. P. Veshchunov, and N. G. Romanov, *Sov. Phys. Solid State* **22**, 2186 (1980).
[3] S. B. Orlinskii, J. Schmidt, P. G. Baranov *et al*, *Phys. Rev. Lett.* **92**, 047603 (2004).
[4] S. B. Orlinskii, J. Schmidt, E. J. J. Groenen *et al*, *Phys. Rev. Lett.* **94**, 097602 (2005).
[5] S. B. Orlinskii, H. Blok, J. Schmidt *et al*, *Phys. Rev. B* **74**, 045204 (2006).
[6] O. F. Schirmer and D. Zwingel, *Solid State Commun.* **8**, 1559 (1970).
[7] L. Taylor, G. Filipovich, and G. K. Lindeberg, *Solid State Commun.* **8**, 1359 (1970).
[8] N. G. Romanov, V. A. Vetrov, and P. G. Baranov, *JETP Lett.* **37**, 386 (1983).

15th Int. Symp. "Nanostructures: Physics and Technology"
Novosibirsk, Russia, June 25–29, 2007

Influence of Mn ions on lifetime and spin relaxation of exciton-hole complexes in semimagnetic quantum dots

A. V. Chernenko[1], A. S. Brichkin[1], E. A. Chekhovich[1], P. S. Dorozhkin[1], V. D. Kulakovskii[1], S. V. Ivanov[2] and A. A. Toropov[2]

[1] Institute of Solid State Physics, RAS, 142432, Chernogolovka, Russia
[2] Ioffe Physico-Technical Institute, St Petersburg, Russia

Abstract. Photoluminescence measurements on individual CdSe/ZnSe/ZnMnSe quantum dots in a magnetic field up to 11 T both parallel and perpendicular to the sample growth plane at 1.6 K reveal a qualitative difference between samples with different strength of the *sp-d* exchange interaction controlled by means of varying the thickness of the nonmagnetic ZnSe layer. The observed difference is explained by taking into account the dependence of the non-radiative Auger recombination and spin relaxation rate on magnetic field and the strength of the exchange interaction.

Introduction

Studies of quantum dots(QDs) are attractive because of possibility to utilize carriers spin states in a QD in various fields of spintronics [1]. Incorporation of Mn ions into CdSe QDs allows one to strongly increase the Zeeman splitting and obtain spin-polarized states in relatively weak magnetic fields.

However, in addition to the increase of Zeeman splitting the exchange interaction accelerates the electron and hole spin relaxation. Furthermore, the presence of Mn ions leads to the substantial reduction of photoluminescence (PL) intensity since the energy of optical transition in the Cd(Mn)Se/Zn(Mn)Se QDs usually exceeds the energy of the internal Mn transition ~ 2.15 eV. It is found that this mechanism is spin-dependent and can be controlled by magnetic field. These additional factors depend on probability to find the carriers inside the ZnMnSe barrier $\eta_{\mathrm{e,h}}$ and obviously affect the spin polarization of the carriers and its dependence on the magnetic field B. Hence, one can expect to observe substantially different PL spectra for the samples with various $\eta_{\mathrm{e,h}}$.

1. Experimental

The CdSe/ZnSe/ZnMnSe samples are grown by MBE pseudomorphically on a GaAs(001) substrate. A nominal thickness of the CdMnSe QD layer is 2 monolayers. The Mn content was $x = 0.07$. The thickness of ZnSe buffer layer is $\sim$ 1.6 nm. The sample is immersed in superfluid He in a cryostat with superconducting magnet. PL is excited with ultraviolet lines of Ar^+-ion laser The PL signal is dispersed by a monochromator with a 2400 gr/mm grating and detected by a nitrogen cooled CCD camera.

Three types of lines are identified in PL spectra of individual QDs in the samples under study: two of them are doublets (X) and (XX) with the opposite order of linearly polarized lines. The lines of the first type (X) are most common in PL spectra. They are associated with exciton recombination whereas lines of the second type (XX) are related with the biexciton luminescence. Lines of this type are located 22–25 meV down on the energy scale from the exciton lines and demonstrate superlinear dependence of the intensity on the excitation power [2].

The third type of lines corresponds to the recombination of negatively charged excitons X^-. The initially single trion line splits apart into two σ^+ and σ^- polarized lines in the magnetic field parallel to the sample growth direction $B \parallel Oz$ (Faraday geometry). Experimental results indicate that evolution of the exciton and trion lines in a magnetic field depends on $\eta_{\mathrm{e,h}}$.

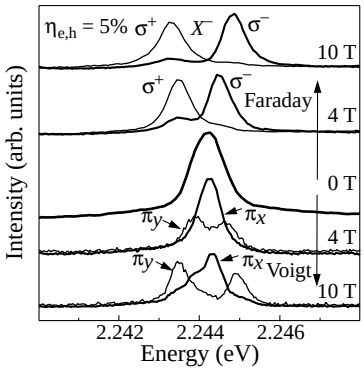

Fig. 1. PL spectra of X^- trion in the sample with $\eta_{\mathrm{e,h}} \sim 5\%$ recorded with the magnetic field applied both in the Faraday and Voigt geometries.

Indeed, the spectra presented in Fig. 1 and Fig. 2 show trion lines in the samples with $\eta_{\mathrm{eh}} \simeq 5\%$ and 12%, respectively. The value of $\eta_{\mathrm{e,h}}$ was estimated from the comparison of the Zeeman splitting in the QDs under study and CdSe/ZnMnSe QDs with known $\eta_{\mathrm{e,h}}$ [2]. The numerical model gives us $\eta_{\mathrm{e}} \simeq \eta_{\mathrm{h}}$.

Similar to X and XX lines the trion lines in PL spectra of the samples with different $\eta_{\mathrm{e,h}}$ presented in Fig. 1 and Fig. 2 split into two circularly polarized lines in the magnetic field $B \parallel Oz$.

The PL spectra of the sample with $\eta_{\mathrm{e,h}} \simeq 5\%$ in the Voigt geometry $B \perp Oz$ shown in Fig. 1 differ from those of the sample with $\eta_{\mathrm{e,h}} \simeq 12\%$ in two kinds: intensities of both lines in the Faraday geometry in Fig. 1 are equal whereas intensities of the higher energy line is larger than that of the low energy line for the sample $\eta_{\mathrm{e,h}} \simeq 12\%$ (Fig. 2). Besides this the quartet of lines is observed in the spectra of the sample with $\eta_{\mathrm{e,h}} \simeq 5\%$, whereas only two lines is visible in the spectra of the another sample. Exciton spectra for these two samples are also different. Thus, the spectra of exciton lines in the sample with $\eta_{\mathrm{e,h}} \simeq 5\%$ demonstrate two equally intensive lines, while the high energy line is almost invisible in the spectra of the sample with $\eta_{\mathrm{e,h}} \simeq 12\%$ presented in Fig. 3.

2. Auger recombination and spin relaxation

The observed peculiarities can be understood on the basis of Mn mediated spin-relaxation and non-radiative recombination

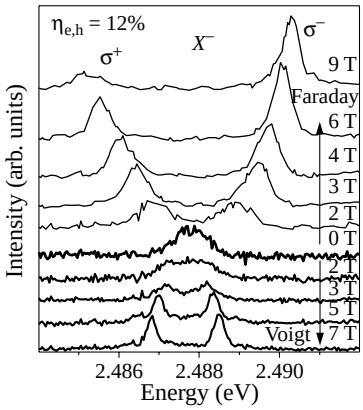

Fig. 2. Magneto-PL spectra of a X^- in the sample with $\eta_{eh} \sim 12\%$ recorded in Voigt and Faraday geometries.

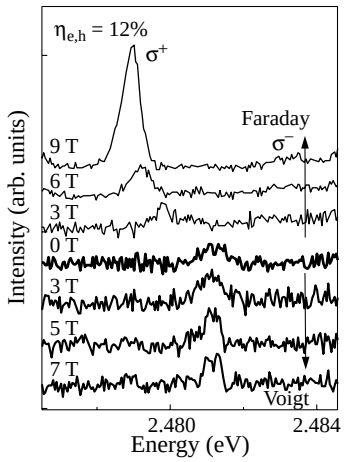

Fig. 3. PL spectra of neutral exciton in the CdSe/ZnSe/ZnMnSe sample with $\eta_{e,h} \sim 12\%$ recorded with magnetic field applied in both Faraday and Voigt geometries.

of $e-h$ pairs. Particularly, the surprising behavior of the trion excited spin state shown in Fig. 1 is related with different non-radiative Auger-recombination probabilities of $j_z = 3/2$ and $j_z = -3/2$ trion states. Indeed, selection rules of the Auger-recombination at $B \parallel Oz$ with the excitation of Mn ion from the ground ${}^6A_1(-5/2)$ to the excited ${}^4T_1(-3/2)$ state predict that transitions involving electron-heavy-hole pairs are allowed if the total spin projection of the system conserves [3,2]. The Auger-recombination originates from the mixing of Mn $3d$-orbitals with valence band p-like states. In the magnetic field which is enough to split Mn ions spin states ($g_{\rm Mn}\mu_{\rm B}B > kT$) the recombination of the trion $j_z = 3/2$ state is allowed whereas it is forbidden for the $j_z = -3/2$ trion. Here $g_{\rm Mn} \simeq 2$ is g-factor of d-electrons.

Indeed, in the initial trion state $j_z = 3/2$ the spin projection $s_z = 1/2$, the Mn spin projection $S_{{\rm Mn}z} = -5/2$, thus $S_z = S_{z{\rm Mn}} + s_z = -2$, whereas for the excited trion state $j_z = -3/2$, $s_z = -1/2$ and $S_z = -3$. The final state has the total spin $S_z \geq -2$. Hence, the Auger transition is allowed for the $j_z = 3/2$ trion and forbidden for the $j_z = -3/2$ state.

The intensity of trion line depends on the radiative time $\tau_{\rm r}$, the time of Auger-recombination $\tau_{\rm Auger}$ and the spin-relaxation time $\tau_{\rm s}$. For instance, a relative increase of the population of the trion excited state occurs when $\tau_{\rm Auger} < \tau_{\rm s}/2$. Experimental results indicate that Mn localized inside the ZnMnSe barrier modifies the Auger recombination rate stronger than the $e-h$ spin-relaxation does.

The hole spin relaxation rate in nonmagnetic QDs is relatively low because of requirement for the hole moment projection to be changed on $\Delta j_z = 3$. The addition of Mn does not substantially increase it. The magnetic field $B \perp Oz$ mixes trion $j_z = \pm 3/2$ states, which leads to a faster spin relaxation, whereas Auger-recombination remains allowed from both trion levels splitted by magnetic field. As the result, only two lines associated with transitions from the ground trion state are visible in the Voigt geometry.

The Mn mediated recombination and relaxation also mo difies exciton PL spectra. The strong magnetic field $B \parallel Oz$ splits the exciton line from PL spectrum of the sample $\eta_{\rm e,h} \sim 5\%$ into σ^+ and σ^- polarized lines at $B \parallel Oz$. Both of them remains well visible in the spectra up to $B = 10$ T. However, the spectra of the sample with $\eta_{\rm e,h} \sim 12\%$ presented in Fig. 3. contain only one low energy line which intensity increases with $B \parallel Oz$. The observed increase of the intensity of the σ^+ line is caused by suppression of the Auger recombination in a magnetic field. Indeed, the Auger recombination is forbidden for excitons in the Faraday geometry since the initial spin projection is $S_z = -5/2$ whereas final $S_z \geq -3/2$. The absence of the line corresponding to the excited state is related with the increased spin relaxation in the sample with higher $\eta_{\rm e,h}$.

In summary, incorporation of Mn ions into QDs structures modifies not only g-factors of electrons and holes but also spin-relaxation and recombination rates of $e-h$ complexes. PL spectra from samples with various $\eta_{\rm e,h}$ can be qualitatively different since both these mechanisms depend on $\eta_{\rm e,h}$.

Acknowledgement

This work has been supported by RFBR grants.

References

[1] D. D. Awschalom, D. Loss, N. Samarth, *Semiconductor Spintronics and Quantum Computations*, Springer-Verlag, Berlin (2002).
[2] A. S. Brichkin *et al*, to be published in *JETP*, **131** (2007).
[3] A. V. Chernenko *et al*, *Phys. Rev. B* **72**, 045302 (2005).

15th Int. Symp. "Nanostructures: Physics and Technology"
Novosibirsk, Russia, June 25–29, 2007

Tilted magnetic field quantum magnetotransport in a double quantum well with the sizable bulk *g*-factor: $In_xGa_{1-x}As/GaAs$

M. V. Yakunin[1,2], G. Galistu[2] and A. de Visser[2]

[1] Institute of Metal Physics, RAS, Ural branch, 620041 Ekaterinburg, Russia
[2] Van der Waals–Zeeman Institute, University of Amsterdam, 1018 XE Amsterdam, The Netherlands

Abstract. Rich patterns of transformations in the structure of quantum Hall effect and magnetoresistivity under tilted magnetic fields were obtained in the $In_xGa_{1-x}As/GaAs$ double quantum well at mK temperatures. Local transformations correspond to the calculated intersections of Landau levels from different subbands and are due to the sharp motion of their (anti-)crossing points with parallel field component. Also some additional features of different nature were revealed and analyzed.

Introduction

The double quantum well (DQW) is a unique object to study inter-particle interactions (since interlayer correlations may be regulated here), magnetotransport for the occupied upper subband (since the antisymmetric subband can be made arbitrarily close to the symmetric one) and, in general, to study effects of additional degree of freedom on the quantum magnetotransport [1]. Interest to a DQW made in the $In_xGa_{1-x}As/GaAs$ heterosystem is due to the $In_xGa_{1-x}As$ bulk g-factor, which is considerably larger than that of GaAs while almost all the researches in DQW physics have been performed on the GaAs/AlGaAs heterosystem so far. The spin effects observed in the latter DQW [2] are due to the spin splitting that could be more than an order of magnitude enhanced at local magnetic fields because of correlation effects. The initially greater g-factor value (i.e. the bulk value) for $In_xGa_{1-x}As$ leads to a more stable behavior of quantum magnetotransport and sheds a new light on the spin-splittings in the (quasi)-2D electron gas.

1. Experimental

We consider the influence of the magnetic field component $B_{||}$ parallel to the layers as an effective tool to investigate specific features of a quasi-2D object and of the spin splittings since there should be no effects at all for the ideal 2D spinless system. Especially informative such experiments should be when, additionally to $B_{||}$, there is a perpendicular component B quantizing the energy spectrum. Intricate transformations in the $In_xGa_{1-x}As/GaAs$ DQW magnetoresistivity ρ_{xx} as a function of two variables ($B_\perp$, $B_{||}$) have been revealed from thorough scans of the ($B_\perp$, $B_{||}$)-plane at 1.8 K [3], and a strong interference with the magnetic breakdown effect was found. To increase resolution, we extended measurements of the quantum Hall effect (QHE) in DQW under tilted magnetic fields down to 50 mK in fields up to 16 T, with the results presented here as functions of the total field under its different fixed orientations φ relative to the sample normal. The sample is the same as in [3]: $In_{0.2}Ga_{0.8}As/GaAs$ DQW with 5 nm wide quantum wells and 10 nm barrier, symmetrically doped in both GaAs surroundings with 19 nm spacers. The electron density n_S in the sample could be increased more than twice by infra-red illumination at low temperatures, and the sample quality improved drastically. The data presented here are for the longest illumination that corresponds to $n_S \approx 5.1 \times 10^{15}$ m^{-2}.

2. Effects of tilted magnetic field

The most pronounced manifestations of addition the parallel field component are local transformations in the structure of magnetoresistance peaks within restricted ranges of $B_\perp$ and $B_{||}$ (or $B_\perp$ and φ) — see Fig. 1 with angle values indicated as they were obtained from the Hall effect in its classical linear part. To analyze these data, we calculated magnetic level patterns for the DQW energy dispersions at fixed $B_{||} = B_x$ values [4]:

$$E_M = \frac{\hbar^2(k_x^2+k_y^2)}{2m} + \frac{E_S+E_A}{2} \pm \frac{1}{2}\sqrt{\Delta_{SAS}^2 + \left(2\hbar\frac{eB_{||}d}{m}k_y\right)^2}$$

with $M = S, A$ denoting the symmetric and antisymmetric subbands with edges E_S, E_a and the tunneling gap Δ_{SAS} between them; k_x, k_y — the wave vector projections onto the DQW planes; $m = 0.058m_0$ — the effective mass; d — an effective interlayer distance.

First, for a given $B_{||}$ value, the Landau levels formed in each of the subbands were calculated quasi-classically from the following condition for the number of states $N_M(E)$ in the area within the E_M projection onto the (k_x, k_y)-plane:

$$N_M(E) = \oint k_x(E_M)dk_y/4\pi^2 = \frac{eB_\perp}{h}(N+1/2),\ N = 0, 1, \ldots$$

Second, the spin splitting $\pm 1/2 g^* \mu_B B$, with B — the total

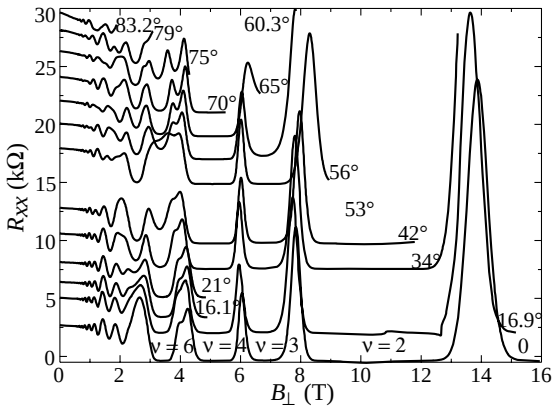

Fig. 1. Longitudinal magnetoresistance vs. perpendicular magnetic field component for different angles of the field relative to the sample normal (indicated). The curves are vertically shifted. Note (i) sharp local transformations of the peaks with $B_{||}$ and (ii) damping of the $\nu = 3$ minimum at the highest $B_{||}$ available.

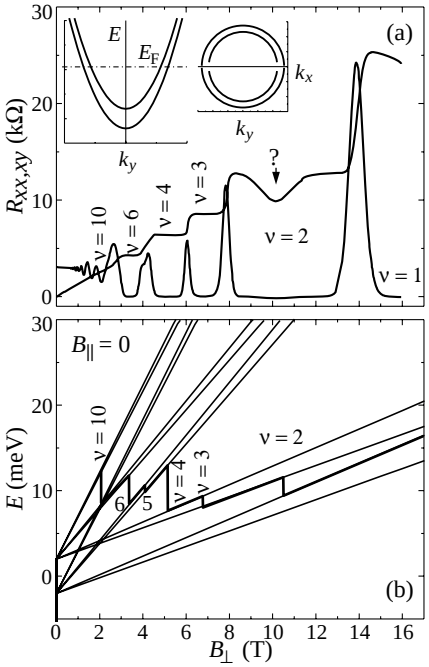

Fig. 2. (a) Quantum Hall effect under pure perpendicular field. The values of filling factor ν indicated. The inserts: energy dispersion and its Fermi energy cross-section. (b) The calculated magnetic level pattern with the Fermi level (bold) moving through it.

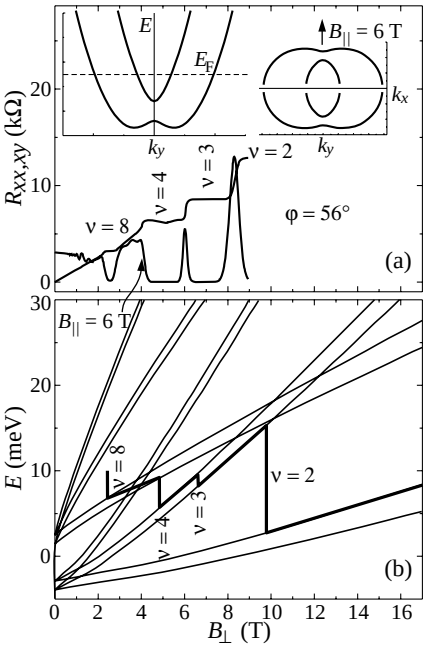

Fig. 3. (a) The same as Fig. 2, but for the field tilted 56° from the sample normal. (b) Calculated magnetic level pattern for the constant component $B_{||} = 6$ T with the curved arrow indicating the $B_\perp$ position corresponding to this $(B_{||}, \varphi)$ combination. Inserts in (a) are for $B_{||} = 6$ T. Note the correspondence between the intricate shaped peak around 4 T and the transition of Fermi level through the magnetic level crossings.

field, was added to each of the $E^{\pm}_{\mathrm{M,N}}(B_\perp)$ Landau level. We used a tentative value $g^* = 3$, as it was obtained in [3]. The results of calculations are presented in Figures 2–4 together with calculated energy dispersions and their cross-sections at the Fermi energy E_F. Intricate-shaped peaks coincide in their position in $B_\perp$ with the calculated intersections between mag-

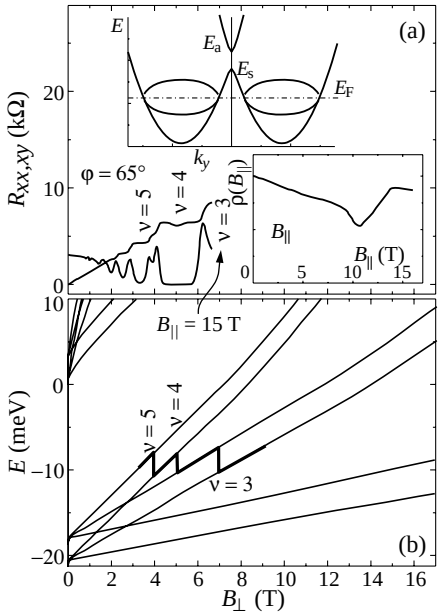

Fig. 4. The same as Fig. 3, but for $\varphi = 65^\circ$. Calculations and upper insert in (a) are for $B_{||} = 15$ T. Note that there are no crossings of different subband magnetic levels around $\nu = 3$, so the damping of the $\nu = 3$ minimum is not due to this. Lower insert in (a): magnetoresistivity for the pure parallel field.

netic levels of *S*- and *A*-subbands (Fig. 3), indicating that just this is the cause for the sharp transformations. Contrary, there are no intersections for the $\nu = 3$ minimum at the highest $B_{||}$ available (Fig. 4) where its damping is observed. The resonant structures observed in $\rho_{xx}(B_{||})$ under pure parallel field (Fig. 4) correlate with our analysis. Thus, the damping of $\nu = 3$ minimum should be due to some different reason. Notably, this minimum starts damping when $B_{||}$ exceeds the value for E_F going below the tunneling gap when the Fermi cross-sections of *shape two* paraboloids part (Fig. 4, upper insert). Separation of the electron gas into two independent sheets should lead to a disappearance of the odd-numbered QH states. Although concomitant retaining of the $\nu = 5$ minimum indicates that the physics is more complicated here, probably due to a competition between intra- and interlayer interactions [2]. Some unusual minima are observed at QH plateaus (Figs. 2–4): they exist only at even numbered plateaus and only in the DQW, contrary to the single QWs in the same heterostructure. Now we are analyzing them as being due to the reentrant QHE (see, e.g., [5]).

Acknowledgements

The samples were grown by B. N. Zvonkov at NIFTI, Nizhnii Novgorod State University. The work is supported by RFBR, project 05-02-16206; M.V.Y. also acknowledges support by the Dutch NWO foundation.

References

[1] S. Girvin and A. H. MacDonald, in *Perspectives in Quantum Hall Effect*, Ed. S. Das Sarma and A. Pinczuk (N. Y.: Wiley), 161–224, 1997.
[2] G. S. Boebinger *et al*, *Phys. Rev. Lett.* **64**, 1793 (1990).
[3] M. V. Yakunin *et al*, *Proc. 14-th Int. Symp. "Nanostructures: Physics and Technology" (St Petersburg, 2006)*, Ioffe Institute, 77, 2006.
[4] G. S. Boebinger *et al*, *Phys. Rev. B* **43**, 12673 (1991).
[5] G. A. Csathy *et al*, *Phys. Rev. Lett.* **94**, 146801 (2005).

15th Int. Symp. "Nanostructures: Physics and Technology"
Novosibirsk, Russia, June 25–29, 2007

Lifetime of electron spins in quantum dots in small magnetic field

R. V. Cherbunin[1,2], I. V. Ignatiev[1,2], D. R. Yakovlev[1,3] and M. Bayer[1]

[1] Fachbereich Physik, Universität Dortmund, 44221 Dortmund, Germany
[2] Institute of Physics, St Petersburg State University, 198504 St Petersburg, Russia
[3] Ioffe Physico-Technical Institute, St Petersburg, Russia

Abstract. Longitudinal spin lifetime of the resident electrons in InGaAs quantum dots are experimentally studied in conditions when the nuclear spin effect on the electron spin dynamics is considerably suppressed. The spin lifetime of about 100 μs is observed at magnetic field of 30 mT.

Introduction

Electron spins localized in quantum dots (QDs) are proposed to be useful for storage of information [1]. Several reports are published, in which the long-lived electron spin memory is observed [2,3,4]. At the same time, physical origin of high stability of electron spins in QDs is still under discussion. Problem is that the strong localization of electrons considerably enhances the effects of hyperfine interaction of the electron and nuclear spins [5]. The nuclear spins may be considerably polarized under the repeated polarization of the electron spin. The dynamically polarized nuclear spin system may give feedback to the electron spin thus stabilizing the electron spin orientation. The nuclear spin systems is highly decoupled to phonon reservoir and can retain its polarization for extremely long time (minutes and hours [6]). Correspondingly, the electron spin orientation might be saved by the hyperfine interaction in the same time scale. Recording and readout of information are very slow processes in this case because of slow polarization/depolarization of the nuclear spin system. This circumstance makes the electrons coupled with the polarized nuclear spin system not attractive for the information storage. The suppress this effect, the nuclear spin can by intentionally depolarized by the optical excitation with alternatively modulated (from σ^+ to σ^-) polarization. Frequency of the modulation may be relatively low (units or tens of Hz [5]).

The non-polarized nuclei still can efficiently affect the electron spin polarization due to effective magnetic field of the nuclear spin fluctuations [7]. Random orientation of the nuclear spins may create a small nuclear polarization fluctuating from dot to dot. Electron spin precession in the effective field, B_f, of the fluctuations results in the fast dephasing (units of nanoseconds [7,8] of the electron spins in ensemble of QDs. The effect of these fluctuations can be suppressed by an external magnetic field, B applied along the optically oriented electron spins if the field $B \gg B_f$ [7,8]. So, both the effects of the dynamic nuclear polarization and of the nuclear spin fluctuations can be considerably suppressed by a proper choice of experimental conditions. We shall call the electron spin lifetime observable in this as the *intrinsic* lifetime. In the high quality nanostructures with QDs, the intrinsic spin lifetime is determined solely by the electron-phonon interaction. We should note here that the electron-phonon interaction strength increases with increasing magnetic field [2,9]. Therefore the intrinsic lifetime is determined by competition of the relaxation processes due to interaction with phonons and with fluctuating nuclear field.

In this paper we report on the *direct* measurements of the spin lifetime of electrons localized in the (In,Ga)As QDs in the experimental conditions when there is no dynamic nuclear polarization and the effect of the nuclear spin fluctuations is considerably suppressed. We found that this time exceeds 100 μs in the longitudinal magnetic field of 30 mT.

1. Experimental

A heterostructure with 20 layers of self-assembled (In,Ga)As QDs containing one resident electron per dot on the average has been studied. The photoluminescence (PL) of these QDs reveal the strong negative polarization [see Fig. 1(a,b)] under the optical excitation into the low-energy wing of the wetting layer absorption band. The PL polarization is calculated by a standard manner: $\rho_c = (I^{++} - I^{+-})/(I^{++} + I^{+-})$ where I^{++} (I^{+-}) is the PL intensity in the co- (cross-) polarization. Analysis shows [3] that the negative circular polarization (NCP) of the PL is observed due to the optical orientation of the resident electron spin. The amplitude of the NCP, $A_{\rm NCP}$ [see Fig. 1(b)], may be used as a measure of spin polarization of the resident electrons.

For study of the electron spin relaxation in the microsecond timescale, we used a modified version of the PL pump-probe method described in Ref. [3]. A long circularly polarized pulse (pump) creates an optical orientation of electrons and a short co- or cross-polarized pulse (probe) delayed relative to the pump is used to detect it. The PL circular polarization excited by the probe pulses is measured to obtain information about the electron spin polarization. To achieve the total suppression of the nuclear spin polarization, the pump and probe pulses were repeated with opposite (cross) polarization as it is shown in Fig. 1(c). The pump (probe) pulse duration is 20 μs (1 μs). The leading and falling edges of the pulses did not exceed 0.2 μs. The relatively low pump-power density of about 0.3 W/cm^2 has been used in these experiments. Though the probe beam power density corresponded to several absorbed photons per QD per pulse, the probe pulses were able to partially destroy the spin orientation created by the pump pulses. Therefore we studied the PL polarization under excitation of the co- and cross-polarized pump and probe pulses and used the difference of the PL polarization, $\Delta A_{\rm NCP} = A_{\rm NCP}({\rm co}) - A_{\rm NCP}({\rm cross})$ as a measure of the electron spin orientation. In this case, the orientation created by the probe pulses is subtracted and the difference $\Delta A_{\rm NCP}$ reflects the orientation created by the pump

pulses only.

The external magnetic field was applied to the sample along the growth axis (Faraday geometry). The field dependences of the PL polarization [the examples are shown in Fig. 1(d)] demonstrate a dip related to the effect of the nuclear spin fluctuations mentioned above. The effect is seen to be considerably suppressed by the external magnetic field of about 30 mT for the QDs under study. At this field, the difference $\Delta A_{\rm NCP}$ between the PL polarizations measured at co- and cross-polarized excitations is clearly observable. It is related to the electron spin orientation created by the pump pulses. We studied the lifetime of the orientation measuring the delay dependence of $\Delta A_{\rm NCP}$.

2. Intrinsic lifetime

The dependence of $\Delta A_{\rm NCP}(t_{\rm d})$ is present in Fig. 2. It is clearly seen that $\Delta A_{\rm NCP}(t_{\rm d})$ has non-zero value and, correspondingly, the spin orientation is observed with good signal-to-noise ratio even at delay $t_{\rm d} \sim 100$ μs. The accuracy of the measurements can be estimated from inset in Fig. 2. This result means that the lifetime of the electron spin in the (In,Ga)As QDs is really large and lies in the hundred-microsecond time scale at low temperature and at the relatively small magnetic field. The obtained dependence cannot be approximated by the single-exponential curve which is probably due to the inhomogeneous spread of the QD parameters in ensemble. Some contribution of about 0.01 to the long-lasting signal in Fig. 2 can be related to the electron spin thermalization between Zeeman levels in the external magnetic field.

In conclusion, we performed the direct measurement of the electron spin lifetime in the InGaAs QDs in absence of the nuclear spin polarization and considerable suppression of the nuclear spin fluctuations effect by an external magnetic field. The lifetime is found to exceed 100 μs at field $B = 30$ mT.

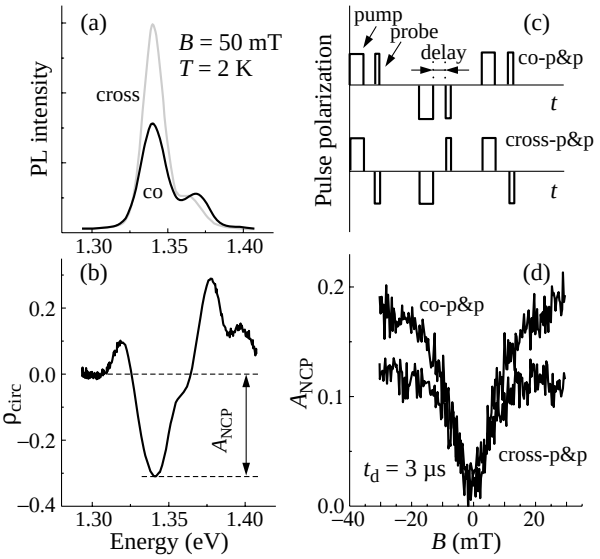

Fig. 1. (a) PL spectra measured in the co and cross circular polarizations to that of excitation. (b) Degree of circular polarization. (c) Time diagram of the pump and probe pulses used in the experiment. The pulses with the opposite circular polarization are shown from different sides of the time axis. (d) Magnetic field dependence of the PL polarization amplitude for the co- and cross-polarized excitation.

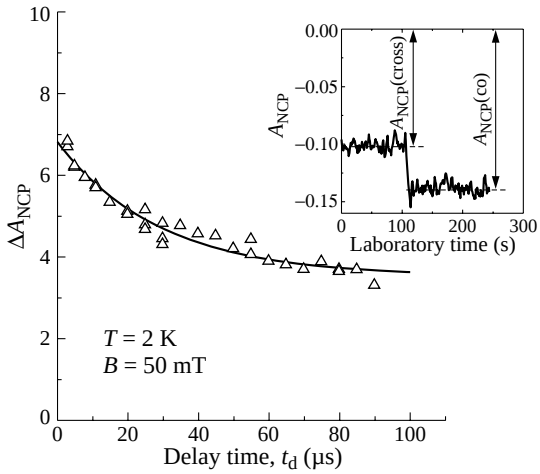

Fig. 2. Measured time dependence of spin polarization $S \propto \Delta A_{\rm NCP}$ (symbols). Solid line is guide to the eye. Inset shows the NCP amplitude for co- and cross-pump probe for time delay $t_{\rm d} = 85$ μs. At time $t \sim 100$ s, polarization of the probe pulses are switched to opposite helicity. Dashed lines are guides to the eye.

Acknowledgements

This work has been supported by the BMBF "nanoquit" program, by the Deutsche Forschungsgemeinschaft (grant 436 RUS 17/144/05), by Russian Ministry of Sci. & Edu., grant RNP.2.1.1.362, and by RFBR, grant 06-02-17137-a.

References

[1] *Semiconductor Spintronics and Quantum Computation.* Edited by D. D. Awschalom, D. Loss, and N. Samarth (Berlin: Springer, 2002).

[2] M. Kroutvar, Y. Ducommun, D. Heiss, M. Bichler, D. Schuh, G. Abstreiter, and J. J. Finley, *Nature* (London) 432, 81 (2004).

[3] M. Ikezawa, B. Pal, Y. Masumoto, I. V. Ignatiev, S. Yu. Verbin, I. Ya. Gerlovin, *Phys. Rev. B* **72**, 153302 (2005).

[4] R. Oulton, A. Greilich, S. Yu. Verbin, R. V. Cherbunin, T. Auer, D. R. Yakovlev, M. Bayer, V. Stavarache, D. Reuter, and A. Wieck, *Phys. Rev. Lett.* **98**, 107401 (2007).

[5] D. Gammon, Al. L. Efros, T. A. Kennedy, M. Rosen, D. S. Katzer, D. Park, S. W. Brown, V. L. Korenev, and I. A. Merkulov, *Phys. Rev. Lett.* **86**, 5176 (2001).

[6] *Optical Orientation.* Edited by F. Meier and B. P. Zakharchenya (Amsterdam: North Holland, 1984).

[7] I. A. Merkulov, Al. L. Efros, and M. Rosen, *Phys. Rev. B* **65**, 205309 (2002).

[8] P.-F. Braun, X. Marie, L. Lombez, B. Urbaszek, T. Amand, P. Renucci, V. K. Kalevich, K. V. Kavokin, O. Krebs, P. Voisin, and Y. Masumoto, *Phys. Rev. Lett.* **94**, 116601 (2005).

[9] B. Pal, M. Ikezawa, Y. Masumoto, and I. V. Ignatiev, *J. Phys. Soc. Jpn.* **75**, 054702 (2006).

15th Int. Symp. "Nanostructures: Physics and Technology"
Novosibirsk, Russia, June 25–29, 2007

Electron spin manipulation in GaAs/AlGaAs coupled quantum wells with bias

A. V. Larionov[1,2], V. E. Bisti[1], M. Bayer[2], J. Hvam[3] and K. Soerensen[3]

[1] Institute of Solid State Physics RAS, 142432 Chernogolovka, Russia
[2] Experimentelle Physik II, Dortmund University, D-44221, Germany
[3] Microelectronic Centre, DK 2800 Lyngby, Denmark

Abstract. The electron spin relaxation process has been investigated in GaAs/AlGaAs coupled quantum wells. The electron spin relaxation rate as function of electrical bias at different temperatures has been measured by means of the spin-beats spectroscopy based on a time-resolved Kerr rotation technique. It was found that spin dephasing time strongly depends on electron localisation. Spin relaxation mechanism is defined by the bulk inversion asymmetry and structure inversion asymmetry which are controlled by means of electric field.

Introduction

Topic point of spintronics investigations from fundamental point of view is a control of electron spin relaxation rate by means of electric and magnetic fields, temperature and structural features of semiconductor heterostructures. It takes as well to know spin relaxation mechanism and as far as possible to affect upon it.

Among the quasi-two-dimensional objects based on semiconductor heterostructures, coupled quantum wells (CQWs) with bias are of special interest because they provide spatial separation of photoexcited electrons and holes in neighboring quantum wells (CQWs). GaAs/AlGaAs CQWs with bias allow to tune the electron-hole overlap integral through the tunneling barrier height and in a such way to control the electrons escape from quantum well due to radiative annihilation with holes. Additionally in such structures there is a possibility to have an influence on structure inversion asymmetry, that is useful for spin relaxation mechanism control.

In the present work we demonstrate some particularities of electron spin dynamics that are controlled by means of electric fields and temperature and a consequence of structure inversion asymmetry.

1. Experimental

The CQWs system studied here consists of two GaAs quantum wells (width ≈120 Å) separated by a narrow (4 monolayers) AlAs barrier. The QWs were separated from the Si-doped (10^{18}cm^{-3}) GaAs layers by 0.15 μ thick AlGaAs ($x = 0.33$) barriers. The upper part of the structure was covered with a 100 Å GaAs layer. Mesa structures were fabricated on the as-grown structure by a lithographic technique. Metal contacts of Au + Ge + Pt alloy were deposited as a frame on the upper part of the mesa and also the doped buffer layer.

The electron spin relaxation rate has been measured by means of a time-resolved Kerr rotation technique. This setup consists of a high precision mechanical delay line (OWIS, LIMES 170), an elasto-optical modulator (PEM, I/FS50). The detection of the nonlinear signal is provided by a Si p-i-n photodiodes balanced detector (Nirvana-2007) with a lock-in detector. As source of pulsed photoexcitation we have used a pulsed Ti-Sapphire laser (Mira-900) with pulse duration of about 1 ps.

Set of time-resolved spin beats in CQWs detected in a magnetic field of 1T (Voigt configuration) is given in Fig. 1 for three different bias. The energy of pump and probe picosecond laser beams was the same and has been scanned along the photoluminescence line contour corresponding to radiative an-

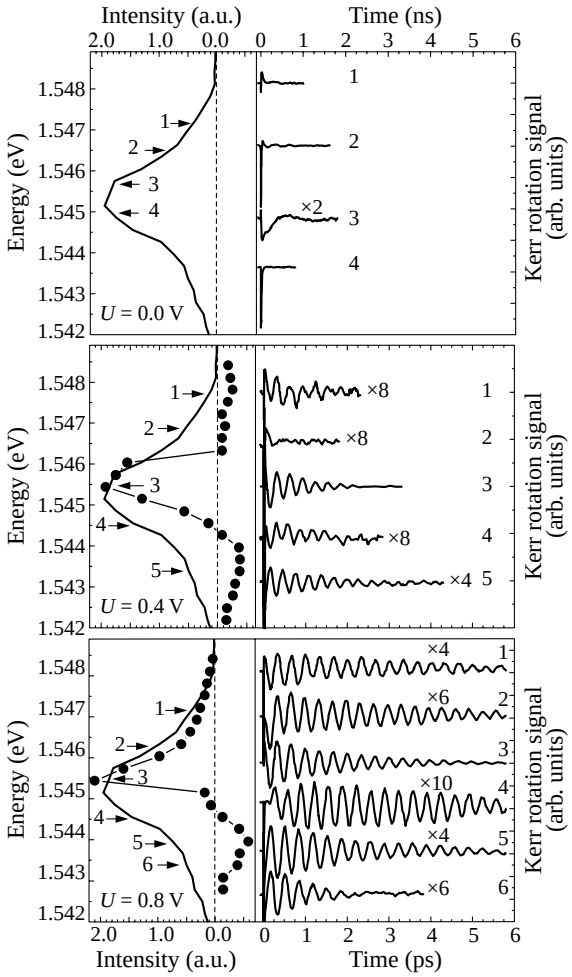

Fig. 1. Kerr rotation signal for 3 sets applied bias. Solid lines on the left plots part correspond to PL line, circular points correspond to Kerr rotation signal amplitude after 160 psec laser pulse coming detected along PL line contour (arrows with numbers). Oscillation curves on the right plots part are Kerr rotation signal for 3 applied bias detected at different points of PL line contour. Experimental curves have been recorded at $T = 1.8$ K and photoexcitation power density $P \approx 2 \times 10^3$ W/cm^2.

nihilation of the 1sHH exciton (left Fig. 1 part, arrows with numbers). The periodic oscillations (right Fig. 1 part) are due to the precession of coherently excited electron spins around the external magnetic field. The period of the oscillations is proportional to the electron spin splitting ΔE in the conduction band. This experimental technique is not sensitive to the sign of the g-factor, but allows to measure the g-factor value in the quantum well plane (g_e^{xy}) with high precision, as the precession frequency ω ($\omega = 2\pi/T$ with the oscillation period T is given by: $\hbar\omega = \Delta E = \mu_B g_e^{xy} B$.

The set of experimental data can be fitted by an exponentially damped oscillation containing the beat frequency ω and a single decay time:

$$I = I_0 \exp(-t/\tau) \times \cos(\omega t). \quad (1)$$

As we have been mentioned early Kerr rotation signal at smaller bias (<0.27 V) has exciton spin-flip oscillations type while at bigger bias (>0.27 V) takes place spin oscillations according to the electronic g-factor value $g_e^{xy} \approx 0.2$. One can see than electron spin relaxation time is rather complicate along PL line contour and has features at every fixed bias. Summarizing the whole data set we can conclude that with increasing applied voltage spin relaxation time on high energy PL line edge becomes shorter whereas spin relaxation time on low energy PL line edge aspires to bigger value.

We believe that it might be connected with electron localisation effect originated from small- and large-scale random potential fluctuations. This assumption is confirmed in Fig. 2, which presents temperature dependence of spin relaxation time at fixed bias. As temperature increases spin relaxation time decreases. In the temperature range from 10 to 15 K spin relaxation time drops more than 2 times and at 15 K almost the same along PL line contour.

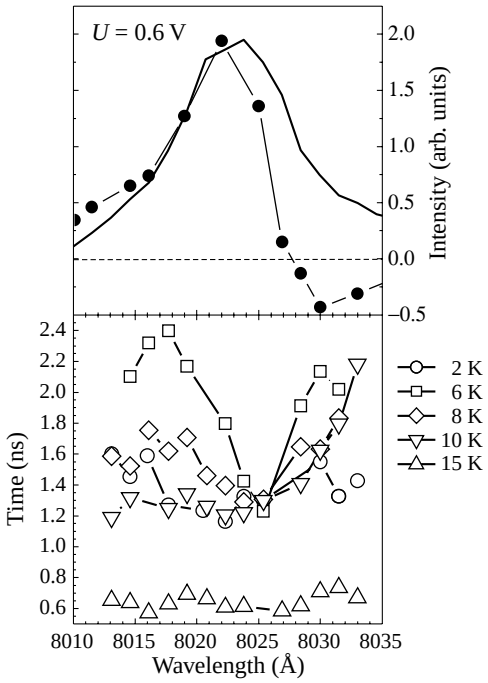

Fig. 2. Temperature dependence of electron spin-flip time (down figure part) along PL line contour at applied bias $U = 0.6$ V and $P \approx 2 \times 10^3$ W/cm^2. Solid line on the upper figure part corresponds to PL line, circular points correspond to Kerr rotation signal amplitude after 160 psec laser pulse coming detected in different points of PL line contour.

So, we would like to emphasize that in CQWs with bias the interconnection of external electric field and disorder are main factor determinated electron spin dynamics.

2. Discussion and summary

Observed electron spin-flip time dependence for the selected field direction along the (110) axis (for an ordinary (001) quantum well) has been reported in [1] as consequence of an interference of two types of spin-orbit interaction (bulk inversion asymmetry, independent on electric field, and structure inversion asymmetry, strongly dependent on applied electric field). This mechanism can be efficient in our case, too. In work [1] authors have been shown that for in-plane relaxation, if the electron gas is degenerate, there is electron spin-flip time asymmetry:

$$\frac{1}{\tau_\pm} = \frac{2\tau_{tr}}{\hbar^2}\left(\gamma\left\langle k_z^2\right\rangle \pm \alpha_0 eF\right)^2 k_F^2,$$

here $\tau_{tr} = 100$ ns — transport relaxation time, and $N_s = 10^{10}$ cm^{-2}.

For used GaAs-AlGaAs structures (two quantum wells 120 Å with barrier 12 Å) the bulk inversion asymmetry (BIA) term ($\gamma = 27$ eV A^3); the structure inversion asymmetry (SIA) term ($\alpha_0 = 5.33$ A^2).

For model of triangle well dependence $\langle k_z^2\rangle$ on electric field F is

$$\left\langle k_z^2\right\rangle = \left(\frac{meF}{\hbar^2}\right)^{2/3}$$

and H_{BIA} is dominant.

In conclusion, a strong dependence of spin dephasing time on electron localisation in quantum well plane versus applied bias has been observed.

Acknowledgements

This research was supported by RFBR, the Russian Science Support Foundation and by Russian President grant for young scientists.

References

[1] N. S. Averkiev, L. E. Golub and M. Willander, *Journ. of physics: condensed matter* **14**, R271–283 (2002).

15th Int. Symp. "Nanostructures: Physics and Technology"
Novosibirsk, Russia, June 25–29, 2007

Electric field effect on valley-orbit and spin splittings in SiGe quantum wells

M. M. Nestoklon[1], E. L. Ivchenko[1], J.-M. Jancu[2] and P. Voisin[2]

[1] Ioffe Physico-Technical Institute, St Petersburg, Russia
[2] Laboratoire de Nanophotonique et Nanostructures, 91460 Marcoussis, France

Abstract. Effect of electric field on spin splitting in SiGe quantum wells (QWs) is analyzed. Microscopical calculations of valley-orbit and spin splittings were performed in the efficient $sp^3d^5s^*$ tight-binding model. The splittings oscillate as a function of the QW width due to inter-valley reflection of the electron off the interfaces. In accordance with symmetry considerations additional electric-field-induced terms appear in the electron spin-dependent Hamiltonian. The splitting oscillations are suppressed in rather low electric field. The tight-binding calculations are analyzed by using the envelope function approach extended to asymmetrical QWs.

Introduction

Recently it has been demonstrated [1] that ideal symmetric QWs grown from Si (with an odd number of atomic planes) allow spin-dependent linear-in-**k** terms in the electron effective Hamiltonian due to interface effects. Microscopical analysis in the simple sp^3s^* tight-binding model has showed [2] that the splitting oscillates with the QW width and its behavior is strongly affected by valley-orbit splitting of the electron subbands. However, experimental studies of such systems are performed for asymmetric QWs [3] where an additional spin-dependent contribution appears which is called the Rashba term.

In the virtual-crystal approximation for the SiGe alloy, an ideal (001)-grown SiGe/Si/SiGe QW structure with an odd number N of Si atomic planes is characterized by the D_{2d} symmetry which allows spin-dependent term $\alpha(\sigma_x k_x - \sigma_y k_y)$ in the electron effective Hamiltonian, where σ_x, σ_y are the spin Pauli matrices, **k** is the two-dimensional wave vector with the in-plane components k_x, k_y, and $x \parallel [100]$, $y \parallel [010]$. The QW structures with even N have the D_{2h} point symmetry containing the space-inversion center and the constant α is zero. Under electric field applied along z, the symmetry of structures with both odd and even number of Si monoatomic layers reduce to the C_{2v}-point group and the spin-dependent linear-**k** Hamiltonian becomes

$$\mathcal{H}_s(\mathbf{k}) = \alpha(\sigma_x k_x - \sigma_y k_y) + \beta(\sigma_x k_y - \sigma_y k_x)\,. \qquad (1)$$

For odd N the coefficient α is an even function of the electric field F_z whereas α for odd N and β for arbitrary N are odd functions of F_z. The aim of this work is to calculate and analyze the electric field dependencies of α and β. For this purpose we use the precise nearest-neighbor $sp^3d^5s^*$ tight-binding model [4] and calculate valley-orbit and spin splittings in symmetrical QWs in the absence and presence of an external electric field.

1. Microscopical calculation

In the tight-binding method the electron Hamiltonian is presented by a set of matrix elements taken between the atomic orbitals. For diamond crystals the basis functions are constructed of functions centered on each atom in the crystal. It is assumed that the only nonzero Hamiltonian matrix elements are those between orbitals on the same or neighboring atoms. Then the electron Hamiltonian in a heterostructure grown along [001] direction for a given lateral wave vector **k** can be written as a matrix. Its eigenvalues give the electron energy dispersion. The constants α and β can be found from

$$\alpha = \frac{\Delta_{so}(\mathbf{k} \parallel [110]) + \Delta_{so}(\mathbf{k} \parallel [1\bar{1}0])}{4|\mathbf{k}|}\,,$$
$$\beta = \frac{\Delta_{so}(\mathbf{k} \parallel [110]) - \Delta_{so}(\mathbf{k} \parallel [1\bar{1}0])}{4|\mathbf{k}|}\,, \qquad (2)$$

where $\Delta_{so}(\mathbf{k})$ is the splitting between the spin-up and spin-down states which may be of arbitrary sign depending on the relative energy position of these states.

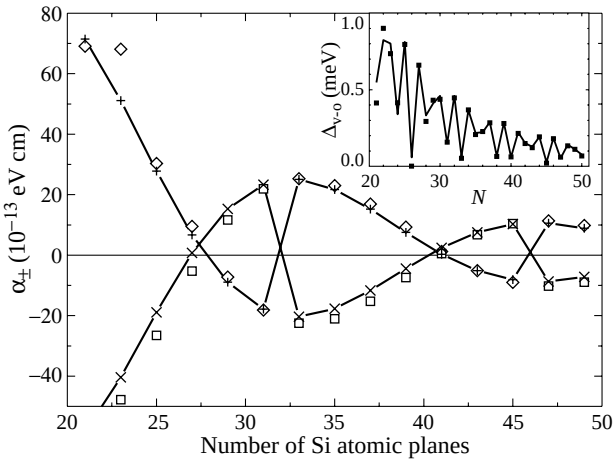

Fig. 1. Spin-splitting constants $\alpha_\pm$ versus the number N of Si monoatomic layers in a $Si_{1-x}Ge_x$/Si/$Si_{1-x}Ge_x$ ($x = 0.25$) QW structure in the absence of an electric field (odd N are taken in account only). The spin splitting is shown by diamonds ($sp^3d^5s^*$ tight-binding calculation) and conventional crosses (envelope function approximation) for the lower valley-orbit split $e1$ subband, and by squares and x-shaped crosses for the higher subband. Inset illustrates valley-orbit splitting Δ_{v-o} as a function of N in the same system (for both even and odd N). Black squares and vortices of the broken line represent results of calculations using the tight-binding method and envelope function approximation, respectively.

Figure 1 shows the zero-field results of calculation of the valley-orbit splitting Δ_{v-o} and the constants $\alpha_\pm$ for the valley-orbit split $e1$ subbands in symmetrical structure containing a single QW with N Si atomic planes sandwiched between the

thick $Si_{0.75}Ge_{0.25}$ barriers. The splittings as a function of N exhibits oscillations, in agreement with Refs. [2,5]. Crosses in Fig. 1 and vortices of the broken line in the inset represent the calculation in the envelope-function approximation, see below.

Fig. 2 demonstrates the effect of an electric field on the spin splitting for the lower valley-orbit split $e1$ subband. In order to determine the coefficients α and β in accordance with Eqs. (2) we performed the tight-binding calculations of the spin splittings for the electron wave vectors $\mathbf{k} \parallel [110]$ and $\mathbf{k} \parallel [1\bar{1}0]$. At zero electric field, the coefficient β_- vanishes for arbitrary value of N, similarly $\alpha = 0$ for even N. In this case the spin splitting $\Delta_{so}(\mathbf{k})$ is independent of the azimuthal angle of the vector $\mathbf{k}$. Note that, for $N = 31$ and $N = 33$ the zero-field values of α have opposite signs. However, with increasing the field the scatter in values of α and β for QWs with $N = 31$, 32, 33, 34 remarkably decreases.

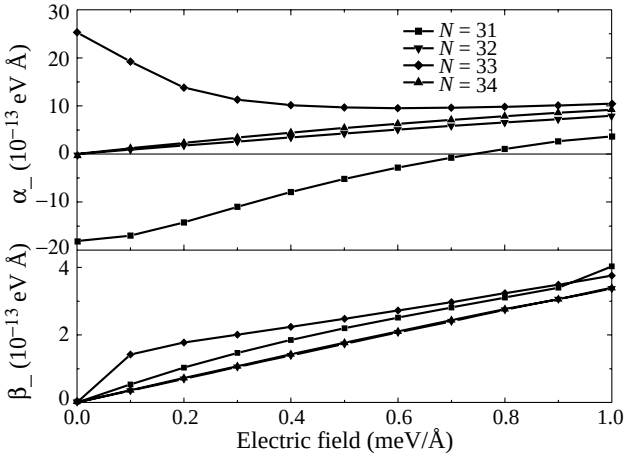

Fig. 2. Spin-splitting constants α_- and β_- for the lowest conduction subband versus the electric field F_z calculated for the four QWs with 31, 32, 33 and 34 Si monoatomic planes.

2. Discussion

We have extended the envelope function method [2] to include effects of the electric field and present here the final equations. By using the notations of Refs. [2] the valley-orbit splitting can be written as

$$\Delta_{v-o} = 2|\lambda|\sqrt{\chi_L^4 + \chi_R^4 + 2\chi_L^2\chi_R^2 \cos[2(k_0 L - \phi_\lambda)]} \quad (3)$$

and, for the coefficients $\alpha_\pm$, $\beta_\pm$ in the Hamiltonian (1) describing the spin splitting of the valley-orbit split subbands, we obtain

$$\alpha_\pm = (\chi_R^2 - (-1)^N \chi_R^2) S \pm |p| F_\alpha(\phi_p)\,, \quad (4)$$

$$\beta_\pm = (\chi_R^2 - \chi_L^2) S' \mp |p'| F_\beta(\phi_{p'})\,,$$

where χ_L, χ_R are the values of the electron zero-order envelope function $\chi(z)$ (i.e., neglecting the splittings) at the left- and right-hand side interfaces,

$$F_\alpha(\phi) = \chi_R^2 \cos(k_0 L - \phi + \Phi) - (-1)^N \chi_L^2 \cos(k_0 L - \phi - \Phi),$$

$$F_\beta(\phi) = \chi_R^2 \cos(k_0 L - \phi + \Phi) - \chi_L^2 \cos(k_0 L - \phi - \Phi)\,,$$

$$\Phi = \arg\left(\chi_L^2 e^{i(k_0 L - \phi_\lambda)} + \chi_R^2 e^{-i(k_0 L - \phi_\lambda)}\right)\,,$$

N is the number of monoatomic layers in the QW, k_0 is the extremum point on the line Δ in the Brillouin zone, L is the QW thickness, the parameters S, S' describe the intra-valley contributions to the interface-induced electron spin mixing and the parameters $\lambda = |\lambda| e^{\phi_\lambda}$, $p = |p| e^{\phi_p}$, $p' = |p'| e^{\phi_{p'}}$ describe the inter-valley spin-independent and spin-dependent mixing. Oscillatory dependence of the valley-orbit and spin splittings on the QW thickness L is caused by interference of electron waves arising from inter-valley reflection off the left- and right-hand side interfaces.

In the absence of the electric field, one has $\chi_L^2 = \chi_R^2$, $\Phi = 0$ for positive and $\Phi = \pi$ for negative $\cos(k_0 L - \phi_\lambda)$, and Eqs. (3), (4) reduce to, see [2],

$$\Delta_{v-o} = 4\chi_L^2 |\lambda \cos(k_0 L - \phi_\lambda)|\,,$$

$\alpha_\pm = \beta_\pm = 0$ for even N, and

$$\alpha_\pm = 2\chi_L^2 [S \pm \eta |p| \cos(k_0 L - \phi_p)]\,, \quad \beta_\pm = 0\,,$$

for odd N, where $\eta = \mathrm{sign}\{\cos(k_0 L - \phi_\lambda)\}$. The curves in Fig. 1 are calculated by using the following best-fit set of parameters: $|\lambda| = 37$ meV Å, $\phi_\lambda = 0.576\,\pi$, $|p| = 40$ meV Å^2, $\phi_p = -1.05\,\pi$, $S = 4$ meV Å^2.

In the high-field limit $\chi_L \chi_R / (\chi_L^2 + \chi_R^2) \to 0$ so that either $\chi_L^2 \ll \chi_R^2$ or $\chi_L^2 \gg \chi_R^2$, Eqs. (3), (4) transfer to

$$\Delta_{v-o} = 2|\lambda| \max\{\chi_L^2, \chi_R^2\}\,,$$

$$\alpha_\pm = 2\mathrm{sign}\{F_z^{N+1}\} [S \pm |p| \cos(\phi_p - \phi_\lambda)] \max\{\chi_L^2, \chi_R^2\}\,,$$

$$beta_\pm = 2\mathrm{sign}\{F_z\} [-S' \mp |p'| \cos(\phi_{p'} - \phi_\lambda)] \max\{\chi_L^2, \chi_R^2\}\,.$$

Since one of the interfaces becomes inaccessible to the electron the oscillatory behavior vanishes in strong fields which explains the suppression of oscillatory behavior with the increasing field seen in Fig. 2.

It should be stressed that the parity of the coefficients $\alpha_\pm$ and $\beta_\pm$ following from the above equations completely agrees with the general symmetry considerations. We also note that a monoatomic shift as a whole of the QW position in the structure results in the change of sign of $\alpha_\pm$ while the values of $\beta_\pm$ remain unchanged.

Acknowledgements

This work has been supported in part by the RFBR/CRNS project, "Dynasty" Foundation — ICFPM and programmes of RAS.

References

[1] L. E. Golub and E. L. Ivchenko, *Phys. Rev. B* **69**, 115333 (2004).
[2] M. O. Nestoklon *et al*, *Proc. 14th Int. Symp. "Nanostructures: Physics and Technology"*, St Petersburg, Russia, 2006, p. 63.; *Phys. Rev. B* **73**, 235334 (2006).
[3] Z. Wilamowski *et al*, *Phys. Rev. B* **66**, 195315 (2002).
[4] J.-M. Jancu *et al*, *Phys. Rev. B* **57**, 6493 (1998).
[5] T. B. Boykin *et al*, *Appl. Phys. Lett.* **84**, 115 (2004); *J. Appl. Phys.* **97**, 113702 (2005).

15th Int. Symp. "Nanostructures: Physics and Technology"
Novosibirsk, Russia, June 25–29, 2007

Effect of interplay between spin-orbit and Zeeman interactions on the magnetotransport in two-dimensional electron gas

S. G. Novokshonov[1] and A. G. Groshev[2]

[1] Institute of Metal Physics, Ural Division of RAS, Ekaterinburg, Russia
[2] Physical-Technical Institute, Ural Division of RAS, Izhevsk, Russia

Abstract. An analytical approach to calculation of the conductivity tensor, σ, of a two dimensional electron gas with Rashba spin–orbit interaction (SOI) in an orthogonal magnetic field is proposed. The electron momentum relaxation is assumed to be due to electron scattering by a random field of short-range impurities The analytical expressions for the density of states (DOS) in the self-consistent Born approximation (SCBA) and σ in the ladder approximation are obtained. This expressions hold true in a wide range of magnetic fields, from the weak up to the quantizing ones. In the ladder approximation, the Rashba SOI has no effect on the conductivity magnitude in the whole range of classical (non quantizing) magnetic fields. The Shubnikov–de Haas (SdH) oscillation period is shown to be related to the total charge carrier concentration by the conventional formula, irrespective of the SOI magnitude. A simple equation defining the location of the SdH oscillation beating nodes is obtained. The results are in good agreement with the experimental and recent numerical investigations.

Introduction

The spin-orbit interaction (SOI) is responsible for many interesting effects in the transport and spin-related phenomena and, particularly, for beatings in the SdH oscillations of kinetic coefficients [1]. This feature of SdH oscillations in two-dimensional (2D) electron systems carries more information about spin-orbit and Zeeman couplings. But up to now, there has been no satisfactory analytical description of the kinetic phenomena in 2D electron systems with SOI in strong and especially in quantizing magnetic fields. The direct employment of the eigenstates basis [1] for calculation of kinetic properties of the 2D Rashba system in a strong magnetic field leads to very complicated expressions. It is forced almost from the first steps either to turn to numerical calculations [2,3], or to make approximations like the momentum-independent spin-splitting energy [4,5]. This makes more difficult the interpretation of the results obtained in such a way, as well as the understanding of the whole physical picture.

In the present work, we obtain the analytical expressions for the conductivity tensor of a 2D Rashba system in the ladder approximation. The spin-orbit as well as the Zeeman splitting of the electron energy are properly allowed for in our calculations. On the basis of these results, we perform the analysis of the beatings of the SdH oscillations of the kinetic coefficients, as well as of their behavior in the classical magnetic fields region. The results are in good agreement with the experimental data [7,8], and with the results of a recent numerical investigation [3].

1. Model

We consider an 2D electron gas in the presence of the Rashba SOI. The electrons move in an external orthogonal magnetic field $\mathbf{B} = \nabla \times \mathbf{A}$ and in a random field $U(\mathbf{r})$ due to pointlike impurities. The one-particle Hamiltonian of the considered system has the form

$$\mathcal{H} + U = \frac{\boldsymbol{\pi}^2}{2m} + \alpha(\boldsymbol{\sigma} \times \boldsymbol{\pi}) \cdot \mathbf{n} + \frac{1}{4} g \omega_c \sigma_z + U(\mathbf{r}) . \quad (1)$$

Here $\boldsymbol{\pi} = \mathbf{p} - e\mathbf{A}/c$ is the operator of the kinematic electron momentum; $\boldsymbol{\sigma}$ is the vector formed by the Pauli matrices; α and g are the Rashba spin-orbit and Zeeman couplings, respectively; $\omega_c = |e|B/mc$ is the cyclotron frequency; $\mathbf{n}$ is the unit normal vector to the considered 2D system.

The eigenspinors and energy levels of the Hamiltonian $\mathcal{H}$ (1) of a free ($U(\mathbf{r}) = 0$) Rashba electron in a magnetic field are well known [1]. But they are very inconvenient to use for analytical calculations. However, $\mathcal{H}$ commutes with Hamiltonian of the "ideal" electron in a magnetic field

$$\mathcal{H}_0 = \frac{\boldsymbol{\pi}^2}{2m} + \frac{1}{2}\omega_c \sigma_z , \quad g_0 = 2 . \quad (2)$$

It allows us to perform the all calculations in the more convenient Landau basis. Indeed, it is easy to check that resolvent of Hamiltonian $\mathcal{H}$ can be expressed in the following form

$$\hat{G}(E) = \frac{E - \mathcal{H}_0 + \left[\alpha(\boldsymbol{\pi} \times \mathbf{n}) + \omega_c \delta \mathbf{n}\right] \cdot \boldsymbol{\sigma}}{(E + m\alpha^2 - \mathcal{H}_0)^2 - \Omega_B^2/4} , \quad (3)$$

where $\delta = (g-2)/4$ is the relative deviation of the effective Zeeman coupling from its ideal value $g_0 = 2$;

$$\Omega_B = 2\sqrt{2m\alpha^2 E + m^2\alpha^4 + \omega_c^2\delta^2} = \sqrt{\Omega^2 + 4\omega_c^2\delta^2} . \quad (4)$$

is the magnetic field-dependent frequency of the spin precession of the electron with energy E; Ω is the same frequency in the absence of a magnetic field. Expanding the right hand side of (3) into the partial fractions, one can express it through resolvent of the "ideal" electron Hamiltonian (2). The same representation can be obtained for the averaged resolvent of the Rashba system in the SCBA [6]. It opens up the way for analytical calculations of the kinetic properties of 2D Rashba system in a strong magnetic field.

2. Results and discussion

Using this observation, we have obtained the analytical expression for the oscillating part of the DOS of an 2D Rashba electron in a magnetic field. In the case of large filling numbers ($E \gg \omega_c$), it has the following form

$$\Delta n(E_F) = \frac{2m}{\pi} \exp\left(-\frac{\pi}{\omega_c \tau}\right) \cos 2\pi \frac{E_0}{\omega_c} \cos \pi \frac{\Omega_B}{\omega_c} . \quad (5)$$

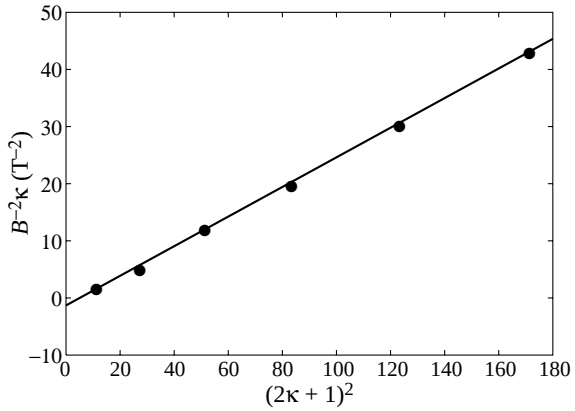

Fig. 1. Measured locations, B_k, of the SdH oscillation beating nodes as compared to the behavior predicted by Eq. (6). The points correspond to the values $B_1 = 0.873$ T, $B_2 = 0.460$ T, $B_3 = 0.291$ T, $B_4 = 0.227$ T, $B_5 = 0.183$ T, $B_6 = 0.153$ T, measured for the $In_{0.65}Ga_{0.35}As/In_{0.52}Al_{0.48}As$-heterostructure [7]. The straight line is the result of least-squares fitting of Eq. (6).

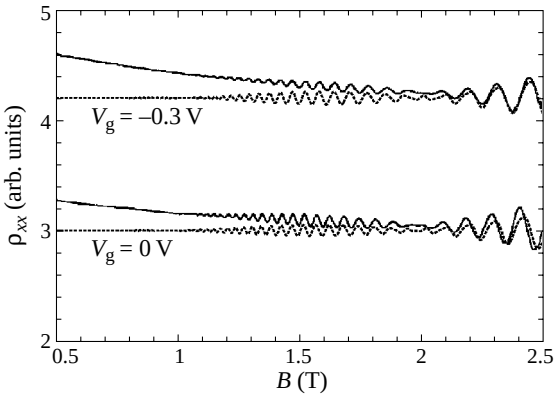

Fig. 2. The theoretical curves of the ρ magnetooscillation as compared with the measured [8] results for the InGaAs/InAlAs-heterostructure at gate voltages $V_g = 0$ V and $V_g = -0.3$ V. The experimental data are denoted by the solid lines and the theoretical ones by dashed lines.

It follows from (5) that the main period of the SdH oscillations is determined by the total electron concentration $n = m(E_F + m\alpha^2)/\pi = mE_0/\pi$, regardless of the spin-orbit interaction magnitude. On the other hand, the period of the SdH oscillation beatings (5) is determined by the spin precession frequency (4) which depends on the magnetic field even in the absence of Zeeman splitting. The location of the k-th node of beatings is determined by the condition

$$B_k = \frac{2mc}{|e|}\frac{\Omega}{\sqrt{(2k+1)^2-(g-2)^2}}\,. \qquad (6)$$

We have calculated the conductivity tensor σ in the ladder approximation. The obtained expression for σ looks as if the current were generated by charge carriers of one type with total concentration n and mobility $\mu = |e|\tau/m$, where τ is the lifetime of the one-electron states. In the classical magnetic fields region ($\omega_c\tau \ll 1$), it takes the usual Drude–Boltzmann form. Therefore, the Rashba SOI has no effect on the conductivity magnitude (in the ladder approximation) everywhere over this region of magnetic fields.

Let us proceed now to the discussion of the magnetotransport in the 2D Rashba system in the quantizing magnetic fields region. In the large filling factors ($E \gg \omega_c$) region, we extract in the linear approximation the oscillating part of the longitudinal resistance that is expressed through oscillating part of DOS (5)

$$\frac{\Delta\rho(B)}{\rho_0} = \frac{\Delta n(E_F)}{n_F^{(0)}}\,. \qquad (7)$$

Here, ρ_0 and n_F^0 are the resistance and DOS in zero magnetic field, respectively.

Let compare our results with experimental data obtained in [7, 8]. The equation (6) allows the couplings α and g to be found from the measured beating nodes location B_k. This is illustrated Fig. 1 which presents the results of least-squares fitting of (6) in variables B^{-2}, $(2k+1)^2$ to the measured [7] locations of the SdH oscillation beating nodes of the longitudinal resistance of a InGaAs/InAlAs-type heterostructure. The slope of the fitted straight line and the point of its intersection with the ordinate axis yield the values $\Omega = 2.47$ meV and $g = 4.25$ for the spin precession frequency in the absence of magnetic field and the g-factor, respectively. This values are in good agreement with the results $\Omega = 2.46$ meV and $g = 4.4 \pm 0.2$ obtained in [7].

We have performed numeric analysis of the SdH oscillations of the longitudinal resistance ρ (Fig. 2) for parameters ($g = 4$, $E_0 = 108.93$ meV, $\Omega = 5.13$ meV, and $g = 3.8$, $E_0 = 98.85$ meV, $\Omega = 5.59$ meV) corresponding to the gate voltages $V_g = 0$ V and $V_g = -0.3$ V for the InGaAs/InAlAs-heterostructure investigated in [8]. The parameters g and Ω were calculated from the positions of two successive nodes B_1, and B_2, using (6), while E_0 was adjusted to the SdH oscillation period. At $V_g = 0$ V, the calculated value $\Omega = 5.13$ meV is close to the result $\Omega = 5.4$ meV of [8], whereas at $V_g = -0.3$ V, the calculated value $\Omega = 5.59$ meV is in excellent agreement with the value $\Omega = 5.6$ meV obtaned in [8]. The results of ρ calculation are compared in Fig. 2 to the experimental curves from [8]. It can be seen that the theoretical results reproduce well the period and beating nodes location of the measured magnetoresistance oscillations. Some difference in oscillation amplitude is due to the fact that the temperature smearing of the Fermi level was not taking into account in our analysis for simplicity. The negative magnetoresistance observed in [8] lies outside the ladder approximation.

Acknowledgement

This work was supported by the RFBR, grant 06–02–16292.

References

[1] E. I. Rashba, *Fiz. Twerd. Tela* **2**, 1224 (1960).
[2] X. F. Wang *et al*, *Phys. Rev. B* **67**, 085313 (2003).
[3] W. Yang *et al*, *Phys. Rev. B* **73**, 045303 (2006).
[4] S. A. Tarasenko *et al*, *Pis'ma ZhETF* **75**, 669 (2002).
[5] M. Langenbuch *et al*, *Phys. Rev. B* **69**, 125303 (2004).
[6] S. G. Novokshonov *et al*, *Phys. Rev. B* **74**, 245333 (2006).
[7] B. Das *et al*, *Phys. Rev. B* **41**, 8278 (1990).
[8] J. Nitta *et al*, *Phys. Rev. Lett.* **78**, 1335 (1997).

15th Int. Symp. “Nanostructures: Physics and Technology”
Novosibirsk, Russia, June 25–29, 2007

Manifestation of spin-orbit interaction in tunneling between 2D electron layers

I. V. Rozhansky and N. S. Averkiev
Ioffe Physico-Technical Institute, St Petersburg, Russia

Abstract. An influence of spin-orbit interaction on the tunneling between two 2D electron layers is considered. Particular attention is payed to the relation between the contribution of Rashba (γ_R) and Dresselhaus (γ_D) terms in spin-orbit Hamiltonian. It is shown that without scattering of the electrons, the tunnel conductivity can either exhibit resonances at certain voltages or be totally suppressed over the whole voltage range, depending on the relations between γ_R and γ_D. The elastic scattering broadens the resonances in the first case and restores the conductivity to a finite magnitude in the latter one. It is demonstrated that these effects open possibility to determine the parameters of spin-orbit interaction and electron quantum lifetime in experiments on tunneling between low-dimensional electron layers without external magnetic field.

Introduction

Spin-orbit interaction (SOI) plays an important role in the widely studied spin-related effects and spintronic devices. In the latter it can be either directly utilized to create spatial separation of the spin-polarized carries or indirectly influence the device performance through spin-decoherence time. In 2D structures two kinds of SOI are known to be of the most importantce, namely Rashba and Dresselhaus mechanisms. The first one characterized by parameter γ_R is due to the structure design asymmetry while the second one characterized by γ_D is due to the bulk crystallographic asymmetry. The energy spectra splitting due to SOI can be obtained in rather well-developed experiments as that based on Shubnikov–de Haas effect. However, these experiments can hardly tell about the partial contribution of the two mechanisms. Determination of γ_R and γ_D separately is a more challenging task. Still, in some important cases spin relaxation time τ_s and spin polarization depend on the relation between γ_R and γ_D. In this paper we put our attention on the tunneling between 2D electron layers, which turns out to be sensitive to γ_R and γ_D. The feature of the system considered is that the energy and in-plane momentum conservation put tight restrictions on the tunneling. Without SOI the conductivity exhibits delta-function-like maximum at zero bias broadened by elastic scattering in the layers [1]. Different situation is realized when there is SOI of Rashba type with γ_R having the opposite signs for the two layers [2]. In this case the peak of the conductivity occur at voltage corresponding to the energy of SOI. In this work we consider arbitrary Rashba and Dresselhaus contributions and show how qualitatively different situations can be realized. In some cases the structure of the electrons eigenstates supresses the tunneling at ever voltage. At that the scattering is important as it restores the features of conductivity containing information about SOI parameters. Finally the parameters γ_R and γ_D can be obtained in the tunneling experiment which unlike other spin-related experiments requires neither magnetic field nor polarized light.

Calculation

We consider the system of 2D electron layers separated by a wide enough barrier at zero temperature (Fig. 1). Its quantum state can be described by the Hamiltonian [1]:

$$H = H_0^l + H_0^r + H_T, \tag{1}$$

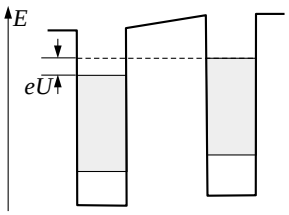

Fig. 1. Energy diagram of two 2D electron layers at $T = 0$.

where H is the total Hamiltonian of the system, H_0 is exact Hamiltonian for the layer, H_T is the tunnel coupling term. Indices r, l stay for the right and left layer respectively. In representation of secondary quantization (1) can be expanded with account for the elastic scattering and SOI (we omit expressions for H_0^l, they are similar to H_0^r):

$$\begin{aligned} H_0^r &= \sum_{k,\alpha} \varepsilon_k^r c_{k\alpha}^{r+} c_{k\alpha}^r + \sum_{k,k',\alpha} V_{kk'}^r c_{k\alpha}^{r+} c_{k'\alpha}^r + H_{SO}^r\,, \\ H_T &= \sum_{k,\alpha} t \left(c_{k\alpha}^{r+} c_{k\alpha}^l + c_{k\alpha}^{l+} c_{k\alpha}^r \right), \end{aligned} \tag{2}$$

where k is the wavevector, α is spin variable, t is transparency of the barrier and V is the scattering potential. The term H_{SO}^r describes the spin-orbit part of the Hamiltonian:

$$\hat{H}_{SO}^r = \gamma_R^r \left(\sigma \times k\right)_z + \gamma_D^r \left(\sigma_x k_x - \sigma_y k_y\right), \tag{3}$$

where σ_i are the Pauli matrices. The operator of the tunnel current can be expressed as [1]:

$$I = \frac{ie}{\hbar} t \sum_{k,\alpha} c_{k,\alpha}^{r+} c_{k,\alpha}^l - c_{k,\alpha}^{l+} c_{k,\alpha}^r\,. \tag{4}$$

In order to calculate the current we solve the equations which describe the time evolution of the creation and annihilation operators averaged over ensemble of impurities with uncorrelated arrangement.

Results

We have performed the calculation of tunnel current for arbitrary relation between Rashba and Dresselhaus contributions in the layers. The results show that qualitatively different situations are possible depending on the relations between γ_R and γ_D in the layers. In the absence of SOI ($\gamma_R^r = \gamma_R^l = 0$,

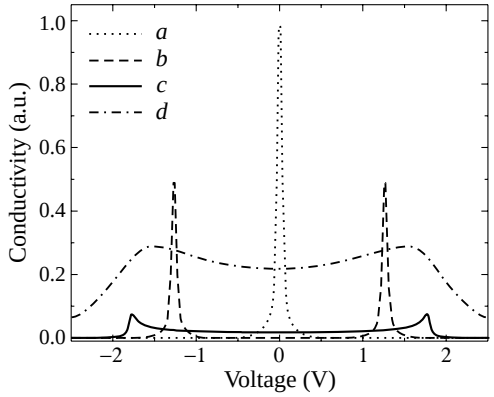

Fig. 2. Tunnel conductivity, a: $E_F = 10$ meV, $\gamma_R = \gamma_D = 0$, $\tau = 2 \times 10^{-11}$ s; b: same as a, but $\gamma_R k_F = 0.6$ meV; c: same as b, but $\gamma_D = \gamma_R$; d: same as c, but $\tau = 2 \times 10^{-12}$ s.

$\gamma_D^r = \gamma_D^l = 0$) and without scattering the energy spectrum for each of the layers forms a paraboloid:

$$E(k_\parallel) = E_0 + \frac{\hbar^2 k_\parallel^2}{2m} \pm eU, \qquad (5)$$

where $k_\parallel$ is in-plane wavevector, E_0 is the size quantization level, m is the electron's effective mass and U is the external voltage. Energy and momentum conservation requires $E^r = E^l$, $k_\parallel^r = k_\parallel^l$. It is satisfied at $U = 0$ only so that a nonzero external voltage does not produce any current despite it produces empty states in one layers aligned to the filled states in the other layer (Fig. 1). The differential conductivity dI/dU would have a resonance at $U = 0$ as shown in Fig. 2(a). This figure except for the curve d shows the results of the calculation for very small scattering yet not strictly equal to zero for the reasonances to be of a visible width. The corresponding quantum lifetime of the electrons τ is taken $\tau \approx 10^{-11}$ s. SOI complicates this picture as it splits the spectra into two subbands. If there is no Dresselhaus contribution and the Rashba terms in the layers are of the opposite sign, i.e. $\gamma_D^r = \gamma_D^l = 0$, $\gamma_R^r = -\gamma_R^l$ the spectra consist of two paraboloid-like subbands "inserted" into each other. Fig. 3 shows their cross-sections for both layers. The right layer is shifted higher on the energy scale by external voltage so that the cross-section of the "outer" subband of the right layer coincides with that of the "inner" subband of the left layer (solid curves). At that the conditions $E^r = E^l$, $k_\parallel^r = k_\parallel^l$ are satisfied. Moreover the orientation of the spins in these states (shown by the arrows in Fig. 3) is the same also. This situation, pointed out in [2], reveals itself in sharp maximum of the conductivity at $eU = \pm 2\gamma_R k_F$, $k_F = \sqrt{2mE_F}/\hbar$, E_F being the Fermi energy (Fig. 2(b)). From this dependence γ_R can be immediately obtained by the position of the peak.

Another special case occurs if additionally Dresselhaus term of the same magnitude exist in the layers so that $\gamma_R^l = -\gamma_R^r$, $\gamma_D^l = \gamma_D^r = \gamma_R^r$. The corresponding energy spectra and spin orientations are shown in Fig. 4. In this case the tunneling is allowed only at few points of intersection between spectra shown in Fig. 4(a) and (b) and the conductivity remains negligibly small over the whole voltage range (Fig. 2(c)). The elastic scattering on impurities plays a significant role in the tunneling phenomena under study as it partly removes the restrictions of momentum conservation. For the first two of the cases discussed above this results in broadening of the

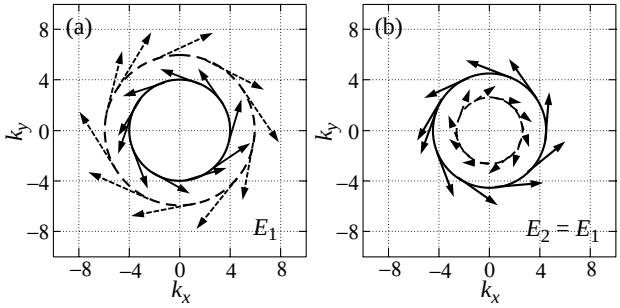

Fig. 3. Cross-section of electron energy spectra in the left (a) and right (b) layer for the case $\gamma_R^l = -\gamma_R^r$, $\gamma_D^l = \gamma_D^r = 0$.

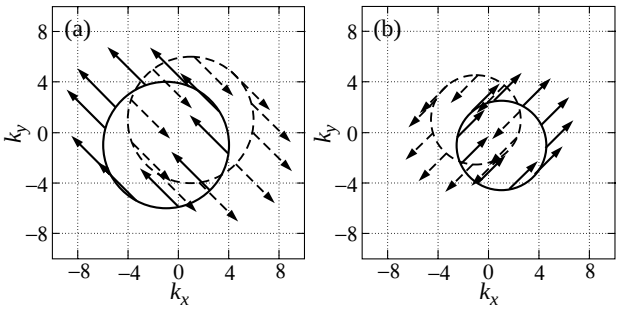

Fig. 4. Cross-section of electron energy spectra in the left (a) and right (b) layer for the case $\gamma_R^l = -\gamma_R^r$, $\gamma_D^l = \gamma_D^r = \gamma_R^r$.

peaks into Lorentz shaped curves with the characteristic width $\delta = \hbar/(e\tau)$. For the third case the weakening of momentum conservation restores the manifestation of SOI in the dependence of conductivity on voltage, the maximum appears at the splitting energy as shown in Fig. 2(d). As the calculations show, for arbitrary γ_R and γ_D the dependence has a complicated form with a number of maxima, being very sensitive to both contributions individually. The origin of such sensitivity is the interference of spin angular dependencies in the electron's eigenstates in the layers.

Conclusions

It has been demonstrated that in the system of two 2D electron layers separated by a potential barrier SOI in the layers can reveal itself in the tunneling current. The difference in spin structure of eigenstates in the layers results in a kind of interference in the tunnel conductivity being sensitive to the parameters of SOI. In some cases an elastic scattering can play a positive role as it brings up the traces of SO interaction otherwise not seen due to destructive interference.

Acknowledgements

This work has been supported in part by INTAS, RFBR, President of RF support (grant MK-8224.2006.2) and Scientific Programs of RAS.

References

[1] L. Zheng, A. H. MacDonald, *Phys. Rev. B* **47**, 10619 (1993).
[2] V. A. Zyuzin, E. G. Mishchenko, M. E. Raikh, *Phys. Rev. B* **74**, 205322 (2006).

15th Int. Symp. "Nanostructures: Physics and Technology"
Novosibirsk, Russia, June 25–29, 2007

Evanescent states and spin-dependent tunnelling in 2D electron systems with spin-orbit coupling

V. A. Sablikov and Yu. Ya. Tkach

Kotel'nilov Institute of Radio Engineering and Electronics, Russian Academy of Sciences,
Fryazino, 141190 Russia

Abstract. We show that total spectrum of electron states in 2D system with spin-orbit coupling contains two branches of evanescent states in addition to propagating states. One branch is described by imaginary while the wave vector of the other branch is complex, i.e. these states do not only decay with distance but also oscillate. The evanescent states manifest themselves in the tunneling through a barrier giving rise to such features as an oscillatory dependence of the transmission probability on the barrier width, spin polarization of tunnel current.

Introduction

Generation of spin-polarized currents in nonmagnetic nanostructures attracts presently considerable interest. Several ways are used to solve this problem such as spin injection from ferromagnet or semi-magnetic semiconductors, optical excitation by polarized light, but of most interest is the idea to use spin-orbit coupling for this purpose. In this direction, much attention is paid to the structures, in which the strength of spin-orbit coupling is spatially non-uniform. In the simplest case, this is a 3D layered structure or a strip structure in 2D systems. Perel' *et al* [1] have shown that an electron beam is polarized as it tunnels through a barrier layer with Dresselhaus spin-orbit coupling. However, the total electron flow turns out to be unpolarized if the distribution function of incident electrons is symmetric with respect to the momentum parallel to the barrier, i.e. if the current is normal to the layer. The spin polarization of electrons passing trough a 2D strip with Rashba spin-orbit coupling has been considered by Khodas *et al* [2] for over-barrier transport. An initially unpolarized beam splits into two polarized beams as it passes through the strip, so that the spin polarization of high degree can be obtained for some directions of the transmitted beam.

In the present paper, we show that high spin polarization can be obtained in 2D system if electrons tunnel through a strip barrier with Rashba spin-orbit coupling, even if the momentum distribution function is symmetric in the transverse direction. This result follows from the analysis of the total spectrum of electron states in a 2D system with spin-orbit coupling, including evanescent states. They exist in the forbidden energy band and are important for bounded systems and tunnelling processes. We find two branches of the evanescent states, one of which decays monotonously with distance and the other oscillates decaying. These states result in unusual features of the tunnelling, such as an oscillatory dependence of the transmission probability on the barrier width and the generation of spin flow.

1. Complex band structure

Consider a 2D electron gas with Rashba spin-orbit coupling caused by an electric field perpendicular to its plane. Electron states are defined by the Hamiltonian:

$$H = \frac{\hbar^2(p_x^2 + p_y^2)}{2m} + \frac{\alpha}{\hbar}(p_y\hat{\sigma_x} - p_x\hat{\sigma_y})\,.$$

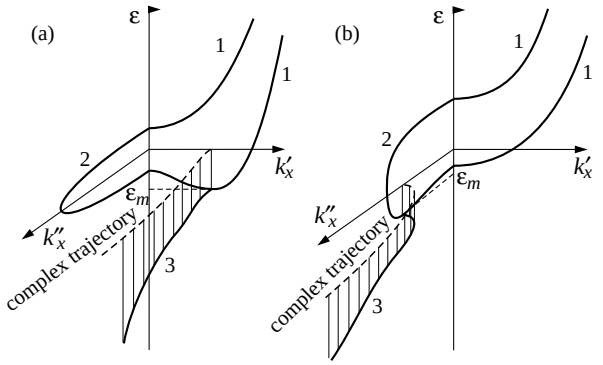

Fig. 1. A schematic view of complex band structure of 2D electron gas with spin-orbit interaction. Energy is shown as a function of k'_x and k''_x for: (a) $k_y<a$ and (b) $k_y>a$. Branch 3 is presented by a line along the real energy trajectory on complex plane (k'_x, k''_x).

The energy depends on wave vector $k = (k_x, k_y)$ and spin variable s: $\varepsilon(k_x, k_y, s)$. It is important that k can be complex, since a bounded system is considered. For simplicity, suppose that the system is infinite in y-direction and bonded in x direction, hence only x-component can be complex, $k_x = k'_x + ik''_x$. The energy spectrum contains three branches shown in Fig. 1:

1. Propagating states defined at $k''_x = 0$. This branch is splitted by spin. The energy gap at $k'_x = 0$ depends on k_y.

2. Decaying states defined at $k'_x = 0$. This branch connects the branches of extended states along the imaginary axis. Branch 2 is also splitted by spin. The minimal energy for first and second branches is $\varepsilon_{\min} = -m\alpha^2/2\hbar^2$.

3. Decaying and oscillating states, which exist at certain trajectories in the complex plane (k'_x, k_x) for the energy below the minimal value $\varepsilon_{\min}$. These trajectories are real energy lines, which are defined by the following equation:

$$(a^2 - {k'_x}^2)(a^2 + {k''_x}^2) = a^2k_y^2\,,$$

where a is a characteristic wave vector of spin-orbit splitting, $a = m\alpha/\hbar^2$. There are four pairs of values (k'_x, k''_x), which correspond to one value of energy. They differ by signs of k'_x and k''_x, For a given value of k'_x or k_x, the states of branch 3 are doubly degenerate by spin. The spin functions are as follows:

$$|s\rangle = \begin{pmatrix}\chi\\ 1\end{pmatrix}, \quad \text{where} \quad \chi = -a\frac{k_y - k''_x + ik'_x}{a^2 + ik'_xk''_x}\,.$$

Though the wave number $|k'_x|$ describing the oscillations and

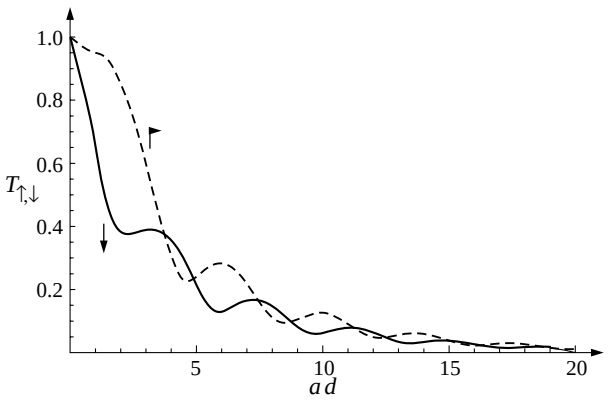

Fig. 2. The transmission coefficients for up and down polarized electrons as a function of the barrier width (the barrier height is $2.25\,\varepsilon_{\min}$, the electron energy is $1.21\,\varepsilon_{\min}$ and $k_y = 0.55a$).

the spatial decrement $|k_x''|$ are connected, their ratio is not restricted and changes strongly along the trajectories. In particular, close to the top of branch 3, $|k_x'| > |k_x''|$ if $k_y < a$, i.e. the wave functions oscillate and slowly decrease with distance. It worth noting that the particle current is absent for each state of branch 3.

2. Tunnel currents

The oscillations of the wave functions in the forbidden energy band give rise to nontrivial features of the tunnelling through a barrier with spin-orbit coupling. Consider two half-planes of 2D electron gas without spin-orbit coupling separated by a barrier strip with spin-orbit coupling and the barrier higher that the Fermi energy. An electron incident from the left is described by the wave function $|k_x, k_y, s\rangle$. The wave function of a reflected electron is a superposition of states with opposite spins, $|\psi_{r,s}\rangle = \sum_{s'} r_{s,s'}|{-k_x}, k_y, s'\rangle$. Similarly, the wave function of transmitted electrons has the form $|\psi_{t,s}\rangle = \sum_{s'} t_{s,s'}|k_x, k_y, s'\rangle$. The wave function in the barrier region is a superposition of four states corresponding to branch 3 of the spectrum with complex wave vectors. Boundary conditions for wave functions give an equation set for the matrices of reflection coefficients $r_{ss'}$ and transmission coefficients $t_{s,s'}$. Finally, the particle and spin currents through the barrier are obtained.

The below-barrier oscillations of the wave functions give rise to unusual feature of the transmission coefficients of electrons with a wave vector k_x, k_y and spin directed up and down, $T_\uparrow = (|t_{\uparrow,\uparrow}|^2 + |t_{\uparrow,\downarrow}|^2)^{1/2}$ and $T_\downarrow = (|t_{\downarrow,\downarrow}|^2 + |t_{\downarrow,\uparrow}|^2)^{1/2}$. Owing to the four-wave interference, the transmission coefficients oscillate with increasing the barrier width d, as Fig. 2 shows. These oscillations may be observed if the electron beam is incident on the barrier at some angle. If the incident electron beam is unpolarized, the transmitting beam acquires a polarization, which depends on the incident angle and the barrier width.

Of more interest is other case when the electron flow is directed normally to the barrier. Consider the particle and spin flows produced by a voltage V applied to left a right electron 2D reservoirs. The electric current J is determined by the partial currents of states $|k_x, k_y, s\rangle$ averaged over the electron distribution function in the energy layer eV and over spin states. This current decreases monotonously with the width d. The oscillations of the partial currents disappear in the total current because of the averaging. However the spin current through

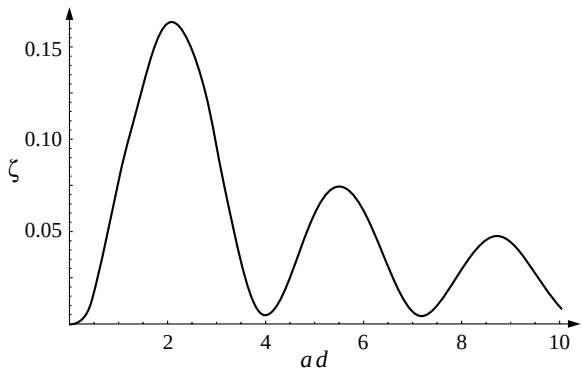

Fig. 3. The polarization efficiency ζ as a function of the barrier width for the barrier height $9\,\varepsilon_{\min}$ and electron energy $6.25\,\varepsilon_{\min}$.

the barrier is not trivial. First, it is nonzero even if the distribution function is symmetric with respect to k_y and 2D electron gases are unpolarized. Second, its spin polarization unusually depends on the barrier width and Fermi energy. As soon as we consider the spin averaged over quantum states and distribution function, the spin current is a tensor. In the experiment under discussion, the spin current is directed along x-axis. The x-component of the spin current is a vector $\langle \vec{J}_S \rangle$, which has all three components defined. The partial spin currents polarized in x and z directions are odd functions of the transverse momentum k_y. For this reason, the components $\langle J_{S,x} \rangle$ and $\langle J_{S,z} \rangle$ turn to zero if the electron distribution function is symmetric about k_y momentum. The partial spin current with y-polarization is an even function of k_y and therefore the y-polarized component of the spin current $\langle J_{S,y} \rangle$ is not zero. Thus the spin flow is polarized in y-direction. The polarization efficiency, defined as

$$\zeta = \frac{\langle J_S \rangle}{J},$$

oscillates with the barrier width d, as it is shown in Fig. 3. The oscillations of ζ are caused by the interference of the evanescent states. The amplitude of polarization efficiency increases with the Fermi energy, until ε_F is far below the bottom of the third branch $\varepsilon_{\min}$. But in the vicinity of $\varepsilon_{\min}$, the polarization efficiency oscillates with ε_F.

Acknowledgements

This work was supported by the Russian Foundation for Basic Research, Russian Academy of Sciences (programs "Quantum nanostructures", "Strongly correlated electrons in semiconductors, metals, superconductors, and magnetic materials"), and RF Ministry of Education and Science.

References

[1] V. I. Perel, S. A. Tarasenko, I. N. Yassievich *et al*, *Phys. Rev. B* **67**, 201304 (2003).

[2] M. Khodas, A. Shekter, and A. M. Finkel'stein, *Phys. Rev. Lett.* **92**, 086602 (2004).

15th Int. Symp. "Nanostructures: Physics and Technology"
Novosibirsk, Russia, June 25–29, 2007

Spin injection and depolarization mechanisms in ferromagnetic Schottky diodes

S. V. Zaitsev[1], M. V. Dorokhin[2], V. D. Kulakovskii[1], P. B. Demina[2], N. V. Baidus[2], E. A. Uskova[2] and B. N. Zvonkov[2]

[1] Institute of Solid State Physics, Russian Academy of Sciences, 142432 Chernogolovka, Russia
[2] Physical-Technical Research Institute, N. I. Lobachevskii University, 603950 Nizhny Novgorod, Russia

Abstract. Detailed investigations of electroluminescence (EL) in composite ferromagnetic (Au/Co/Au)/GaAs Schottky contacts with near-surface n-doped InGaAs/GaAs quantum wells, located at depth $d_C = 20-100$ nm, have been performed in magnetic fields B up to 10 T and low temperature $T = 1.5$ K. The EL band, corresponding to recombination of 2DEG with injected holes, at $B > 2$ T shows circular polarized Landau levels (LLs) with polarization degree P_C significantly larger than that in the nonmagnetic Au/GaAs contact, thus evidencing about efficient spin injection. The dependencies of $P_C(B)$ systematically decrease with increasing d_C and show non-monotonic character at high B correlated with filling of the LLs, reaching maximum values of P_C at $B = 7-8$ T ($\approx 40\%$ for $d_C = 20$ nm).

Introduction

Circular-polarized semiconductor light sources are of a great importance for spintronics [1]. They use the carrier spin degree of freedom, possibility to control of which promises fast and low power elements for future opto-electronics. Many interesting device schemes had been proposed during last years [2]. To realize such devices an efficient spin injection into the active area is required. Many problems have to be solved, in first order the problem of the conductivity mismatch at a metal-semiconductor interface [3]. One of the promising ways to solve the problem of electrical spin injection is to use a Schottky diode (SD) with the contact made of a ferromagnetic metal (FM) having sufficiently high Curie temperature [4, 5, 6]. It was established also that a thin oxide tunnel layer between the FM contact and semiconductor can help to overcome the conductivity mismatch problem [7]. The first observation of the spin injection in a forward biased diode was reported in Ref. [5] These studies emphasized the problem related to a low quality of the FM-semiconductor interface and resulting low quantum efficiency of the FM SD.

In this contribution we present results of investigations of spin injection in the composite FM (Au/Co/Au)/GaAs Schottky contacts with near-surface GaAs/InGaAs/GaAs quantum well (QW) active region, located at different depth $d_C = 20-100$ nm from the contact. Previously we have shown that introducing of the intermediate Au layer between the FM and semiconductor results in a significant increase of the interface quality and higher EL quantum efficiency in the FM SDs [8]. We have found that the values of P_C of the circular polarized EL significantly exceed ones in the nonmagnetic Au/GaAs SD, thus evidencing about efficient spin injection.

1. Experimental

Nominally undoped $In_xGa_{1-x}As$/GaAs QWs with thickness of 7 nm and indium content $x = 0.16-0.2$ were grown on the n-type doped (Si: 3×10^{17} cm^{-3}) buffer GaAs layer by a metal-organic vapor phase epitaxy at atmospheric pressure [9]. The n-doped capping GaAs layer with thicknesses $d_c = 20$, 30 and 100 nm for different samples has smaller donor (Si) concentration of 8×10^{16} cm^{-3}. In this work, SDs with FM Au/Co/Au sandwich structure and reference sample with non-magnetic Au contact were studied. Total metal sandwich thickness did not exceed 120 nm. Before metal deposition the heterostructures were exposed to air to form a natural GaAs surface oxide layer of ≈ 2 nm in thickness [9]. The ohmic contacts to the n-doped GaAs substrates were formed by alloying of tin pads.

EL in a Faraday geometry (perpendicularly to the sample surface and the easy magnetization axis of the FM film) was measured in a magnetic cryostat, in superfluid He (temperature $T \simeq 1.5$ K) with magnetic fields up to $B = 10$ T. EL emission was measured from the substrate side. The degree of circular polarization $P_C(B)$ was defined as $P_C(B) = (I^+ - I^-)/(I^+ + I^-)$, where I^+ and I^- — are the intensities of the right- and left-hand polarized interband emission spectrum.

2. Electroluminescence in a magnetic field

Independently on type of the contact metal, DSs begin to emit at a threshold forward bias of ≈ 1.3 V [8]. We suggest that this occurs when the Fermi level in the FM is aligned with the valence band of the semiconductor as shown in the band diagram in Fig. 1(a). The injected holes transport and relax to the InGaAs/GaAs QW where they recombine with a 2DEG, present in the QW due to doped barriers. At low B the EL band is wide and structureless while at $B > 2$ T it splits into several lines (0-0, 1-1, ...), corresponding to transitions between different LLs of electrons and holes. The total EL intensity increases with B. Also, P_C decreases for higher LLs. This fact points that the recombination is not connected with the acceptor-bound hole for which P_C is the same for different LLs [10]. Contrary, the decrease of P_C for higher LLs evidences about partial spin relaxation of holes, injected and relaxed in the QW: higher LLs correspond to higher values of k-vector with more effective spin relaxation due to hh-lh mixing [12].

Several distinct features of the EL band has to be emphasized. First, the EL is circular polarized (Fig. 1(b)) with a polarization degree $P_C(B)$ in the FM SDs significantly larger than that in the reference Au/GaAs Schottky contact for all values of d_C (Fig. 2). While in the nonmagnetic DS P_C is related to the Zeeman splitting of the hole QW levels, much higher value of P_C in the FM DSs unambiguously evidences about efficient injection of spin-polarized carriers, obtained in the studied FM DSs. Similar behavior of $P_C(B)$ in SDs with

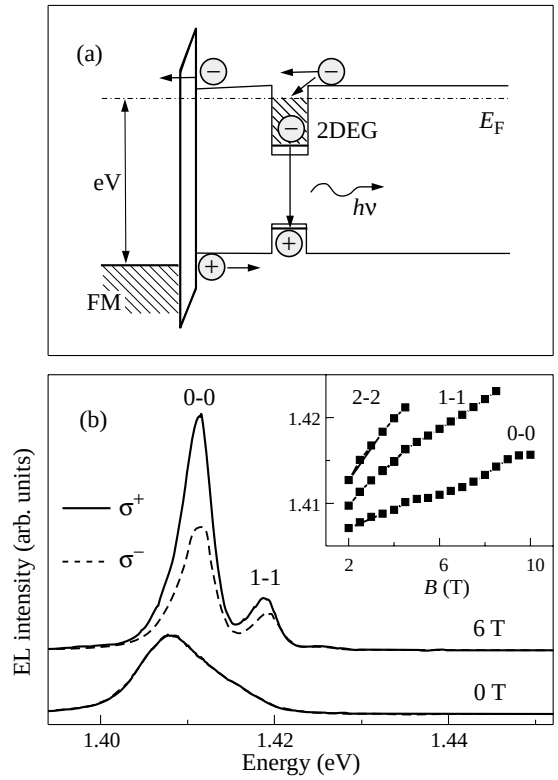

Fig. 1. (a) Schematic band alignment in forward biased DS. Arrows show injection of holes from the FM and their recombination with electrons in the QW. (b) EL spectra at $B = 0$ and 6 T of the DS with $d_C = 30$ nm $T = 1.5$ K. The inset shows B-dependence of the LLs transitions.

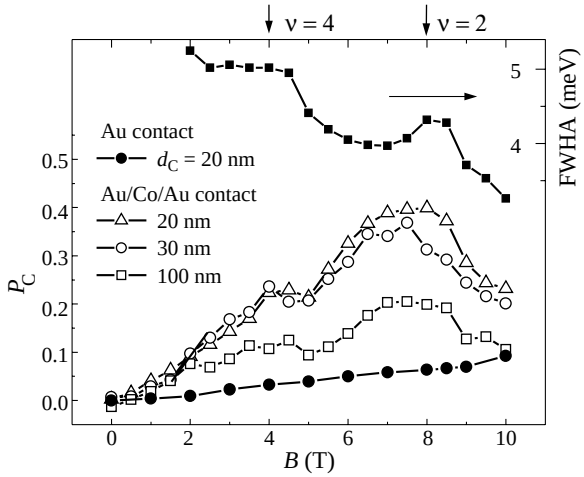

Fig. 2. Left scale — polarization degree $P_C(B)$ dependencies for the first LL in different Schottky contacts (marked in figure). Injection current is 10 mA. On the right scale — the linewidth FWHA for the 1st LL in the Au/Co/Au contact with $d_c = 30$ nm.

different d_C, which systematically decreases with increasing of the d_C, points to the fact that the spin relaxation during transport of injected holes can be accounted for by some depolarization factor, approximately constant at $B > 2$ T. Absence of saturation in $P_C(B)$, as usually observed at $B = 2{-}4$ T [13], when the FM film is fully magnetized, evidences about the main role of the spin relaxation processes during transport of the injected spin-polarized holes and their relaxation into QW's states before recombination.

It is seen that $P_C(B)$ shows non-monotonic behaviour with smooth maxima at $B \approx 4$ T and 7–8 T (Fig. 2). An analysis of the EL spectra shows that the following minima of $P_C(B)$ correlate with a disappearance of the 3rd and 2nd LLs in the spectra, at filling factors $\nu = 4$ and 2, correspondingly. From the observed ν one can estimate 2DEG density $n_{2D} = \nu eB/h \approx 4 \times 10^{11}$ cm^{-2} for all DSs. The peculiarities of $P_C(B)$ correlate also with the divergence of the LLs energies from the linear dependencies, expected for the single-particle electron states (inset, Fig. 1(b)). The observed non-linearities at even ν-s were explained by a many-body effects [11]. Simultaneously with emptying of the LLs a significant increase of the LL linewidth occurs (Fig. 2, right scale). This is attributed to the absence of free carriers (electrons) in the 2DEG system which screen the long-range coulomb potential fluctuations at these particular conditions, when the electron Fermi-level E_F passes in between the LLs (at even ν values) [14]. Correlation of the P_C peculiarities and screening effect points to a significant contribution of the spin scattering on the coulomb centers (donors) in spin relaxation of the injected holes. On the other hand, a gradual decrease of $P_C(B)$ takes place at high $B > 8$ T, when the linewidth continues to drop due to effective screening by 2DEG at $\nu < 2$. It is related to the spin polarization of electrons in a partially filled 1st and 2nd LLs, which leads to relative reducing of the I^+ as compare to the I^-.

Thus, efficient spin injection have been demonstrated in the heterostructures with a forward biased composite Au/Co/Au FM Schottky contact. For small distances (20–30 nm) from the contact to the active QW layer the polarization degree of the electroluminescence can be as high as 40% at high B and low temperature. Major influence of transport and intra-QW processes on spin relaxation of injected carriers is found and discussed.

References

[1] I. Žutić *et al*, *Rev. Mod. Phys.* **76**, 323 (2004).
[2] D. D. Awschalom *et al*, *Semiconductor spintronics and quantum computation*, (Springer-Verlag, series: NanoScience and Technology (2002).
[3] E. I. Rashba, *Phys. Rev. B* **62**, R16267 (2000).
[4] A. T. Hanbicki *et al*, *Appl. Phys. Lett.* **80**, 1240 (2002).
[5] V. F. Motsnyi *et al*, *Appl. Phys. Lett.* **81**, 265 (2002).
[6] C. H. Li *et al*, *Appl. Phys. Lett.* **86**, 132503 (2005).
[7] V. F. Motsnyi *et al*, *Phys. Rev. B* **68**, 245319 (2003).
[8] N. V. Baidus *et al*, *Appl. Phys. Lett.* **89**, 181118 (2006).
[9] I. A. Karpovich *et al*, in *Trends in Nanotechnology Research*, (Nove Science, Hauppauge, NY), Chap. 8 (2004).
[10] I. V. Kukushkin *et al*, *Phys. Rev. B* **40**, 7788 (1989).
[11] T. Uenoyama and L. J. Sham, *Phys. Rev. B* **39**, 8418 (1989).
[12] R. Ferreira and G. Bastard, *Phys. Rev. B* **43**, 9687 (1991).
[13] A. T. Hanbicki *et al*, *Appl. Phys. Lett.* **82**, 4092 (2003).
[14] I. V. Kukushkin and V. B. Timofeev, *Adv. Phys.* **45**, 147 (1996).

15th Int. Symp. "Nanostructures: Physics and Technology"
Novosibirsk, Russia, June 25–29, 2007

Inverse population of the spin subbands in magnetic junctions with spin injection

E. M. Epshtein, Yu. V. Gulyaev, A. I. Krikunov, A. I. Panas and *P. E. Zilberman*
Institute of Radio Engineering and Electronics of the Russian Academy of Sciences,
Fryazino, Moscow District, 141190, Russia

Abstract. Conditions are found which provide inverse population of the spin subbands in spin-valve type magnetic junctions at experimentally attainable current densities $\sim 10^7-10^8$ A/cm^2. The conditions correspond to effective spin injection at the input boundary of the collector ferromagnetic layer and suppressed injection at its another boundary. The proper matching conditions between the ferromagnetic layers under their antiparallel orientation assure stability of the magnetic fluctuations at any currents.

Introduction

Spin injection in magnetic junctions breaks spin equilibrium in the ferromagnetic layers and can lead to inverted spin population of the spin subbands and lasing effect. Such a possibility was discussed in [1], where rates were calculated of the radiative transitions between spin subbands, and small optical interaction length ($\sim 10^{-7}$ cm) was found. However, a problem remains of finding the conditions which provide high enough spin injection level without instability of the magnetic fluctuations in ferromagnetic layer. We show that some specific choice of the layer materials is needed that assures required boundary conditions at the layer interfaces.

1. Spin injection

We consider a spin-valve type magnetic junction, containing a ferromagnetic layer **1** with pinned lattice magnetization, free ferromagnetic layer **2** and nonmagnetic contact layer **3**. The semi-infinite layer **1** placed in $-\infty < x < 0$ range contacts with the finite thickness layer **2** in $0 < x < L$ range, that, in its turn, contacts with the layer **3** in $L < x < \infty$ range. A very thin spacer is placed between layers **1** and **2** to prevent direct exchange interaction between the layers. The current flows along positive direction of the x axis (**1** $\rightarrow$ **2**) perpendicular to the layers (CPP mode).

The nonequilibrium part of the electron spin polarization $\Delta P(x)$ in the layers satisfies spin diffusion equation [2]

$$\frac{d^2\Delta P_i}{dx^2} - \frac{\Delta P_i}{l_i^2} = 0 \quad (i = 1,\ 2,\ 3), \tag{1}$$

where l_i are longitudinal spin diffusion lengths.

The boundary conditions at the interface between layers **1** and **2** under current flowing in **1** $\rightarrow$ **2** direction take the following form [3]:

$$J_1 \cos\chi = J_2, \tag{2}$$

$$N_1 \Delta P_1 = N_2 \Delta P_2 \cos\chi, \tag{3}$$

where

$$J_i(x) = \frac{\hbar}{2e}\left\{Q_i\, j - e n_i D_i \frac{d\Delta P_i(x)}{dx}\right\} \tag{4}$$

are spin current densities, $N_i = (n_i/2)\left(g_{i+}^{-1} + g_{i-}^{-1}\right)$, $g_{i\pm}$ are partial density of states at the Fermi level for spin up (+) and spin down (−) subbands, χ is the angle between the magnetization vectors of the contacting layers, Q_i are conductivity polarizations, n_i are electron densities, D_i are spin diffusion constants. The $\cos\chi$ factor in (2), (3) is due to change in quantization axis under electron passing from one layer to another. At the interface between layers **2** and **3** such a change is absent, so $\cos\chi = 1$ should be put there. Under the opposite current direction (**2** $\rightarrow$ **1**), $\cos\chi \rightarrow (\cos\chi)^{-1}$ substitution in Eqs. (2), (3) should be made.

We confine ourselves to the case of thin layer **2**, $\lambda \equiv L/l_2 \ll 1$. The solution of Eq. (1) with boundary conditions (2) and (3) for the layer **2** takes the form

$$\Delta P_2(x) = \frac{j}{j_{D2}} \frac{Q_1 \nu_{12} \cos\chi}{\nu_{12}\nu_{23} + \cos^2\chi}, \tag{5}$$

where $j_{D2} = e n_2 D_2/l_2$. The $\nu_{12} = (j_{D2}/j_{D1})(N_1/N_2)$ and $\nu_{23} = (j_{D3}/j_{D2})(N_2/N_3)$ parameters describe spin current matching at the interfaces. They can be taken in the form of a spin resistance ratio [3]:

$$\nu_{ik} = \frac{Z_i}{Z_k}, \qquad Z_i = \frac{\rho_i l_i}{1 - Q_i^2}, \tag{6}$$

where ρ_i are resistivities.

At $Z_1 \gg Z_2$ the layer **1** works as an ideal injector, in which the spin polarization is equilibrium ($\Delta P_1 = 0$), while the spin equilibrium breakdown occurs in the layer **2**. In the opposite case, $Z_1 \ll Z_2$, an ideal collector regime takes place, when the spin equilibrium is disturbed in layer **1** and remains unchanged in layer **2**.

Earlier (see, e.g., [4]), the injection from ferromagnetic metal to semiconductor was considered, when $Z_1 \ll Z_2$, as well injection from a ferromagnetic metal to the same metal with antiparallel orientation of the magnetic moment ($Z_1 = Z_2$, $\chi = 180^\circ$). In those cases, as can be seen from Eq. (5), $\Delta P_2 \leq j/j_{D2} \ll 1$ estimate is valid, so that the injection efficiency is rather low.

2. Inversion of the spin subband population

Under inverted population conditions, the magnetic junction emits, rather than absorbs, electromagnetic radiation on an average. For simplicity, we consider an isotropic energy dependence on the crystal momentum $\varepsilon_\pm(\mathbf{p})$. Then the net emission condition can be write down in the following form:

$$|\mathbf{p}_{F-}| > |\mathbf{p}_{F+}|, \tag{7}$$

where $\mathbf{p}_{F\pm}$ are the Fermi momenta for the spin subbands of the layer **2**. This condition can be represented as

$$\Delta P_2 < -\bar{P}_2 < 0, \tag{8}$$

where $\bar{P}_2$ is equilibrium spin polarization in layer **2**.

The diffusion equation (1) refers to the case $|\Delta P| \ll 1$. To satisfy that condition and (8), we should have negative ΔP_2 and $|\bar{P}_2| \ll 1$. Under forward current (in the **1** $\rightarrow$ **2** direction), $\chi = 180^\circ$, i.e. antiparallel magnetization orientation is needed.

As it was noted, j/j_{D2} ratio is small. However, the second multiplier in the right-hand side of Eq. (5) can take large value at $\nu_{12} \gg 1$, $\nu_{12}\nu_{23} \ll 1$ (or $Z_2 \ll Z_1 \ll Z_3$). Therefore, despite the smallness of the j/j_{D2} ratio, the $|\Delta P|$ quantity may be larger significantly than that small ratio. Such an effect allows a simple physical interpretation. Under fulfillment of the conditions indicated, effective injection from layer **1** to layer **2** takes place, while the injection from layer **2** to layer **3** is suppressed.

To realize the conditions $Z_2 \ll Z_1 \ll Z_3$ corresponding to high spin injection efficiency, a half-metal [5] may be chosen for the layer **1** (the Heusler alloys or chromium dioxide are possible candidates), in that case spin resistance Z_1 is high because the conduction spin polarization Q_1 is close to 1 (see Eq. (6)). Semiconductor such as silicon with large Z_3 value may be taken for the nonmagnetic layer **3**. Large Z_3 value can be achieved in the case due to high resistivity and larger spin diffusion length. The layer **2** in which nonequilibrium spin polarization appears may be a ferromagnet such as gadolinium with $\bar{P} \approx 0.14$ [6]. Thus, the current induced spin injection level can be enhanced significantly by proper choice of the layer material and parameters.

The current density j_{inv}, which is necessary to reach spin inversion, may be estimated from (5) as $j_{inv} \approx j_{D2}\bar{P}/Q_1\nu_{12}$. At $\bar{P} = 0.14{-}0.35$, $j_{D2} \approx 10^{10}$ A/cm^2, $Q_1 \approx 1$ and $\nu_{12} \approx 100$, that corresponds to nearly complete spin polarization of the layer **1**, we obtain $j_{inv} \sim (1.4{-}3.5) \times 10^7$ A/cm^2.

Rough estimates made in free electron approximation give the following frequencies for resonant transitions between spin subbands: 120 THz, 80 THz and 46 THz in Co, Ni and Gd, respectively.

3. Stability of magnetic fluctuations

To realize inverted population and laser effect, the magnetic junction is to be stable against fluctuations. In accordance with Refs. [7,8], two factors affect the fluctuation stability, namely: i) spin torque due to current driven transverse spins [9,10], and ii) effective exchange field due to injected longitudinal spins. As estimates show, under required matching conditions $Z_2 \ll Z_1 \ll Z_3$ the role of the first mechanism is small, so that we may take only the effective exchange field into account.

In such a case, the stability against magnetic fluctuations corresponds to minimum of the magnetic energy [11]. The energy U per unit area of the layer is

$$\frac{U}{4\pi M^2 L} = -h\cos\chi - \frac{h_a}{2}\cos^2\chi - \left(\frac{j}{j_0}\right)\frac{\nu_{12}\cos\chi}{\nu_{12}\nu_{23} + \cos^2\chi}, \tag{9}$$

where $h = H/4\pi M$, $h_a = H_a/4\pi M$, H and H_a are the external magnetic field and anisotropy field, respectively, M is the saturation magnetization in layer **2**,

$$j_0 = \frac{4\pi M j_{D2}}{\mu_B \alpha_2 n_2 Q_1} \sim 6 \times 10^7 \text{ A/cm}^2, \tag{10}$$

α_2 is *sd* exchange constant, μ_B is Bohr magneton. The energy as a function of the χ angle with different current densities and $\nu_{12} \gg 1$, $\nu_{12}\nu_{23} \ll 1$ is shown in Fig. 1. At zero current, there are two minima at $\chi = 0$ and $\chi = 180^\circ$. The minimum at $\chi = 0$ disappears with the current rising, so that the only minimum at $\chi = 180^\circ$ remains, which corresponds to antiparallel orientation of the magnetic layers. Under these conditions, both inverted spin population and stability are assured.

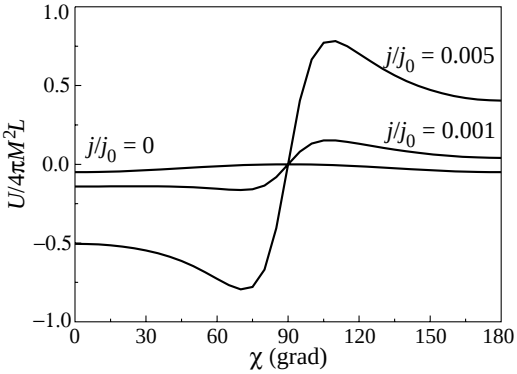

Fig. 1. The junction magnetic energy as a function of the magnetic layer relative orientation ($h = 0$, $h_a = 0.1$, $\nu_{12} = 100$, $\nu_{23} = 0.001$).

Acknowledgements

The authors are grateful to Yu. G. Kusraev and V. A. Sablikov for interesting discussions.

The work was supported by RFBR (Grant No. 06-02-16197).

References

[1] A. K. Kadigrobov, Z. Ivanov, T. Claeson *et al*, *Europhys. Lett.* **67**, 948 (2004).
[2] Yu. V. Gulyaev, P. E. Zilberman, E. M. Epshtein and R. J. Elliott, *JETP Lett.* **76**, 155 (2002).
[3] Yu. V. Gulyaev, P. E. Zilberman and E. M. Epshtein, *Doklady — Physics* **51**, 496 (2006).
[4] G. Schmidt, D. Ferrand, L. W. Molenkamp *et al*, *Phys. Rev. B* **62**, R4790 (2000).
[5] A. M. Haghiri-Gosnet, T. Arnal, R. Soulimane *et al*, *Phys. stat. sol. (a)* **201**, 1392 (2004).
[6] R. Meservey and P. M. Tedrow, *Phys. Reports* **238**, 174 (1994).
[7] Yu. V. Gulyaev, P. E. Zilberman, E. M. Epshtein and R. J. Elliott, *JETP* **100**, 1005 (2005).
[8] E. M. Epshtein, Yu. V. Gulyaev and P. E. Zilberman, cond-mat/0606102.
[9] J. C. Slonczewski, *J. Magn. Magn. Mater.* **159**, L1 (1996).
[10] L. Berger, *Phys. Rev. B* **54**, 9353 (1996).
[11] R. J. Elliott, E. M. Epshtein, Yu. V. Gulyaev and P. E. Zilberman, *J. Magn. Magn. Mater.* **271**, 88 (2004).

15th Int. Symp. "Nanostructures: Physics and Technology"
Novosibirsk, Russia, June 25–29, 2007

ESR of electrons localized on Ge/Si quantum dots

A. F. Zinovieva[1], A. V. Dvurechenskii[1], N. P. Stepina[1], A. S. Deryabin[1], A. I. Nikiforov[1], R. Rubinger[2,3], N. A. Sobolev[2], J. P. Leitão[2] and M. C. Carmo[2]

[1] Institute of Semiconductor Physics, 630090 Novosibirsk, Russia
[2] Departamento de Fisica e I3N, Universidade de Aveiro, Aveiro, Portugal
[3] 3DFQ UNIFEI, 37500-000 Itajuba, Brazil

Abstract. The electron spin resonance (ESR) of electron states in the Ge/Si system with Ge quantum dots (QD's) has been investigated. To localize electrons in potential well at the Si/Ge interface near Ge QD, two types of QD samples were grown: 1) a four-layer stacked QD's structure; 2) a SiGe/Si/SiGe quantum well structure with QD's embedded in the middle of the strained Si channel. Both structures show similar ESR signals, which we attribute to electrons localized in the Si quantum well the at Ge/Si interface. The linewidth ΔH is about 0.6 G that gives the lower limit of transverse spin relaxation time of $\sim 10^{-7}$ s. This type of signal was not observed in the reference structures without QD's. The g-tensor is axially symmetric with the principal values $g_{zz} = 1.9995$ and $g_{xx} = g_{yy} = 1.9984$, where $Z \parallel [100]$ is the growth direction of structure.

Introduction

Strong confinement in low-dimensional structures such as quantum wells (QW's) and quantum dots (QD's) leads to a significant increase of spin lifetimes [1]. Extremely long spin lifetime is expected in Ge/Si QD's system due to weak spin-orbit (SO) coupling in Si. Ge/Si QD's are formed by strain epitaxy and exhibit a type II band lineup, where localization inside the dot occurs only for holes. Electrons can localized in nearby Si due to strains around QD's. Tensile strain in Si around Ge QD's causes splitting of the sixfold-degenerate Δ-valley and separation two lower Δ-valleys along the [001] growth direction and four upper in-plane Δ-valleys. The conduction band edge in Si just above and below the Ge QD is formed by two lower Δ-valleys yielding the triangle potential well for electrons near the Si/Ge boundary. The spin of electron strongly confined in all three dimensions in Si is excellent candidate for solid state spintronics and future quantum computation applications. However, the binding energy of electrons in this potential well is very small (<10 meV) [2]. One way to enlarge of electron binding energy is growth of vertical stack of Ge QD's. An accumulation of strains from different QD's layers in a stack leads to increase of the potential well depth. Second way to confine electron is embedding of Ge QD's layer in the middle of strained Si channel in the SiGe/Si/SiGe QW structure.

For successive spin manipulation in QD it is necessary to know such fundamental spin properties as effective g-factor, which defines the duration of a π pulse, and spin relaxation time. These values usually are obtained from ESR-measurements. Commonly used opinion is that the size dispersion of self-assembled QD's leads to broadening of ESR-line and makes impossible its observation. Here we show that this factor has no significance for electrons in Si/Ge system with QD's in contrast to other semiconductor systems, where SO interaction have more higher value. We performed direct ESR-measurements on both types of structures with electrons localized at the Ge/Si interface nearby Ge QD's. We demonstrate that the strains in the structure have a crucible effect on the g-factor value of electron on Ge/Si QD's. Contrary, a binding energy of electron plays negligible role.

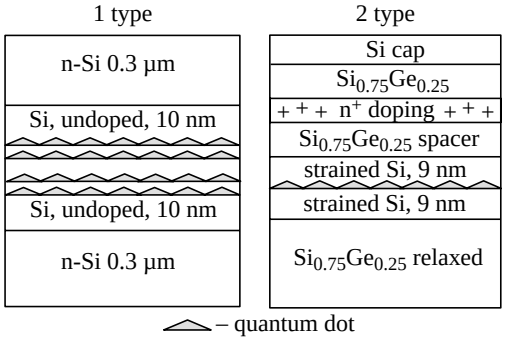

Fig. 1. Samples structure.

1. Samples and experiment

Two types of structures with self-assembled Ge/Si QD array were prepared for ESR measurements: 1) four-layer stacked QD's structure, 2) SiGe/Si/SiGe QW structure with QD's.

Samples were grown by molecular-beam epitaxy on n-Si(001) substrate with a resistivity of 1000 Ω cm. The density of QD's is $\sim 10^{11}$ cm^{-2} in both structures. The STM shows that the average QD lateral size is $l = 20$ nm and height is $h = 1.5$ nm. The details of growth is described in papers [2,3] and samples structure is shown in Fig. 1.

According to calculations using effective-mass approximation [2] the localization of electron in 1 type structure occurs between second and third layer of QD's at the top of Ge QD's. The binding energy of electron in this structure is ≈ 60 meV. In the second structure the binding energy for electrons is ≈ 100 meV. We investigate ESR with a standard Bruker X-band spectrometer operating at frequency close to 9.38 GHz at sample temperatures 3.9–20 K.

2. Results and discussion

Both structures with QD's show similar ESR signals, which we attribute to electrons localized in the Si potential well at Ge/Si interface near the top of Ge dot (Fig. 2). The observed ESR line has inhomogeneous broadening. The width of ESR line ΔH is about 0.6 G for magnetic field $\mathbf{H} \parallel Z$, where Z is the growth direction [001] of structure. For in-plane magnetic field $\mathbf{H} \perp Z$ ESR lines become broader and weaker. The linewidth ΔH for $\mathbf{H} \perp Z$ is approximately two times larger, than ΔH for $\mathbf{H} \parallel Z$. The g-tensor is axially symmetric with the

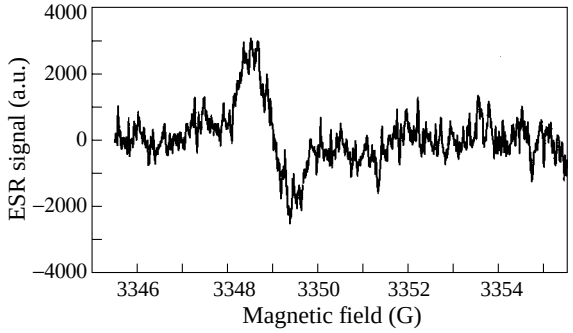

Fig. 2. ESR signal from electrons localized on Ge/Si QD's in four-fold stack structure.

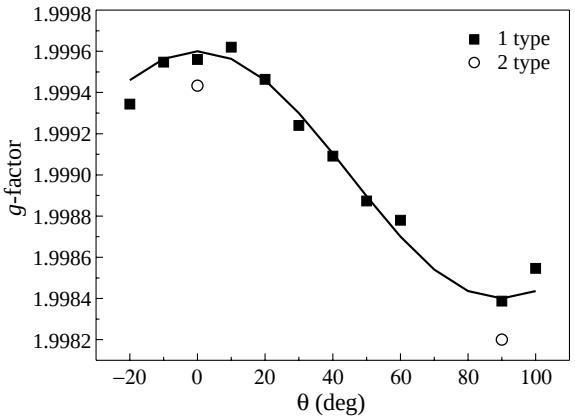

Fig. 3. Angular dependence of electron g-factor.

principal values $g_{zz} = 1.9995$ and $g_{xx} = g_{yy} = 1.9984$. The difference between g-factors in 1 and 2 structures is about $\approx 10^{-4}$. The angular dependence of g-factor is described by: $g = (g_{zz}^2 \cos^2(\Theta) + g_{xx}^2 \sin^2(\Theta))^{\frac{1}{2}}$, where Θ is the angle between magnetic field and axis Z (Fig. 3). This type of signal was not observed in the reference structures without QD's.

The obtained value of g_{zz} is exactly coincided with parallel component of g-factor in Si $g_{\parallel} = 1.9995$. This is explained by coincidence of growth direction of structure Z with axis of electron's ellipsoid. A value of $g_{xx} = g_{yy}$ is coincided with $g_{\perp} = 1.9984$. So the symmetry of g-tensor is the same as symmetry of isoenergetic surface. Electron g-factor in the bulk Si is 1.9987 and its value is determined from ESR experiments, which are generally carried out on donors. The donor state is built from wave functions of six Δ-valleys and its g-factor is a consequence of mixing ellipsoids: $\frac{1}{3}g_{\parallel} + \frac{2}{3}g_{\perp} = 1.9987$. In our case the strains in Si due to buried Ge QD's lead to separation of two lower Δ-valleys along [001]-direction and four in-plane Δ-valleys. Thus no mixing of ellipsoids is occurred, and we observed pure $g_{\parallel}$, when **H** is parallel to ellipsoid's axis, and $g_{\perp}$, when **H** is perpendicular to this axis.

So, the strains in Si around a Ge QD strongly affect the magnitude of the g-factor. The splitting between Δ-valleys depends on the value of biaxial strain $(\varepsilon_{zz} - \varepsilon_{xx})$ [4]. A decrease of biaxial strain can caused a narrowing energy gap between Δ-valleys and increasing contribution of upper Δ-valleys to the electron g-factor. This can lead to a change of electron g-factor. The value of biaxial strain is practically the same for all QD's in the array, because it is determined by the aspect ratio h/l. Namely this fact gives a chance to observe the ESR signal of electrons localized on Ge QD's.

The change of electron binding energy has negligible effect on the value of g-factor. A shift of electron energy due to difference of potential wells in two types of investigated structures is ~ 50 meV. One can estimate the g-factor value from following equation: $\delta g \approx \frac{\lambda}{\Delta E}$, where λ is the constant of SO interaction, and ΔE is the energy gap between electron level and nearest band. In Si $\lambda \approx 44$ meV and $\Delta E \approx 4$ eV. The change ΔE on ≈ 50 meV has not a noticeable effect on g-factor. That is why the difference in binding energy of electrons in our samples does not lead to difference of g-factor values.

The second important parameter for value of g-factor is a Ge content in the localization area of electron. In Ge the SO interaction is an order larger than in Si, and small amount of Ge can lead to a significant change of electron g-factor. According to our theoretical calculations g-factor in Δ-valley in Ge is determined as $g_{\parallel}^{Ge_{\Delta}} = 2.04$. The tails of electron wave function penetrate barrier of potential well. Then g-factor is determined by: $g_{el} = \alpha \times g_{\mathrm{Si}} + \beta \times g_{\mathrm{SiGe}}$, where α is the part of wave function inside Si potential well, β is the part penetrating a SiGe barrier, $\alpha + \beta = 1$. In our experiments the growth temperature of Ge QD's in 1 and 2 structures differs: four-fold stack QD's structure has the higher growth temperature 500 °C and QW structure — 300 °C. The higher temperature leads to mixing of Ge and Si inside QD's. Analysis of Raman measurements shows that a Ge content in high temperature QD's is ~ 0.7. Then the wave function penetration is higher. A calculation give $\beta = 0.0025$ in this case. Finally the change of g-factor due to this effect is $\approx 10^{-4}$, that is observed in experiments.

The time $\sim 10^{-7}$ s, calculated from width $\Delta H = 0.6$ G, is the lower limit of the transverse spin relaxation time T_2. The observed linewidth is determined by disorder in QD's array. Based on the above discussion we conclude that the strain fluctuations in array of QD's and deviation of Ge content in QD's can result in inhomogeneous broadening of ESR line.

Well pronounced anisotropy of ESR linewidth $\Delta H(\mathbf{H} \perp Z)/\Delta H(\mathbf{H} \parallel Z) \approx 2$ is explained by anisotropy of spin relaxation processes, arising from a special form of SO interaction, similar to Rashba interaction for electrons in asymmetric QW's. This signifies that the spin relaxation is controlled by fluctuating effective in-plane magnetic field, related to asymmetry of QD's. Decoherence in QD's can be caused by perturbation of ground state by time-varying fields and mixing in exited states with higher angular momentum due to SO interaction.

Acknowledgements

This work was supported by INTAS (Project No. 03-51-5015), RFBR (Grants Nos. 05-02-16285, 06-02-16988, 05-02-39006-GFEN), FCT (Projecto POCI/FIS/58524/2004) and SANDiE Network of Excellence.

References

[1] M. Kroutvar *et al*, *Nature* **432**, 81 (2004).
[2] A. I. Yakimov *et al*, *Phys. Rev. B* **73**, 115333 (2006).
[3] Z. Wilamowski *et al*, *Phys. Rev. B* **66**, 195315 (2002).
[4] C. G. Van de Walle and R. M. Martin, *Phys. Rev. B* **34**, 5621 (1986).

15th Int. Symp. "Nanostructures: Physics and Technology"
Novosibirsk, Russia, June 25–29, 2007

Spectroscopic evidence of extended states in the quantized Hall phase of the weakly-coupled GaAs/AlGaAs multilayers

Y. A. Pusep, F. E. G. Guimarães, H. Arakaki and C. A. de Souza
Instituto de Fisica de Sao Carlos, Universidade de Sao Paulo, 13560-970 Sao Carlos, SP, Brazil

Abstract. The influence of the inter-layer coupling on formation of the quantized Hall conductor phase at the filling factor $\nu = 2$ was studied in the multilayer GaAs/AlGaAs heterostructures. The disorder broaden Gaussian photoluminescence line due to the localized electrons was observed in the quantized Hall phase of the isolated multi-quantum well structure. On the other hand, the quantized Hall phase of the weakly-coupled multilayers emitted the unexpected asymmetrical line similar to that one exhibited by the metallic electron systems. We demonstrated that the observed asymmetry is caused by a partial population of the extended electron states formed in the quantized Hall conductor phase due to the inter-layer percolation. A sharp decrease of the single-particle scattering time associated with these extended states was observed at the filling factor $\nu = 2$.

Introduction

The integer quantum Hall effect is observed in layered structures consisting of weakly-coupled two-dimensional electron layers when the magnetic field induced gaps ($\hbar\omega_c$, with ω_c being the cyclotron frequency) are larger than the inter-layer tunneling bandwidth (t) [1]. The phase diagram determining the behavior of the weakly-coupled layered systems in a high magnetic field was put forward in Ref. [2] where two principal phases corresponding to a miniband metal state and an isolating quantized Hall state were distinguished. As compared to the 2DEG, the electronic phases of the layered systems reveal several novel properties. Contrary to the 2DEG, where the metallic phase exists at a single energy, the phase diagram of the layered system exhibits the metallic phase for a finite range of energies and magnetic fields. Furthermore, in the layered system the disorder influences the electron tunneling between different layers resulting in a third phase, which separates the metallic and quantized Hall phases and in which the electrons are localized quantum mechanically, but their classical trajectories are extended [3]. While the modification of the metallic quantum Hall phase predicted in the layered three-dimensional electron system were confirmed experimentally [4], no influence of the inter-layer electron correlations on the insulating quantized Hall phase was reported to date.

1. Experimental

The aim of this work is to investigate experimentally the density of states (DOS) and the nature of the electron states in the quantized Hall phase of the layered quantum Hall systems and to verify theoretical predictions cited above. We studied GaAs/AlGaAs semiconductor superlattices (SL) where the inter-layer tunneling can be easily tailored by variations of the barrier widths and heights. The magneto-PL and the magneto-resistance were measured in the structures with t varying from 0 [isolated multi-quantum wells (MQW)] to 55 meV (strongly-coupled SL). Moreover, the effect of the inter-layer coherence on the formation of the quantized Hall phase was studied in the weakly-coupled multilayer structures where the inter-layer coherence was controlled by as grown random variations of the barrier thicknesses.

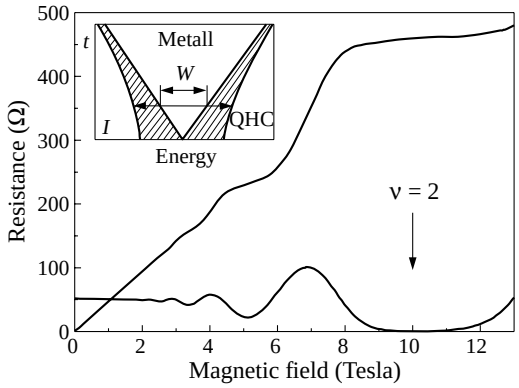

Fig. 1. Transversal and Hall resistances measured in the weakly-coupled $(GaAs)_{65}(Al_{0.18}Ga_{0.82}As)_{15}$ SL at $T = 0.3$ K. Inset schematically demonstrates the phase diagram of the quantum Hall layered system presented in Ref. [3]. The shaded areas are the regions of the quantized Hall conductor where the extended states were predicted. The intervals shown by solid and dash arrow lines indicate the regions of the extended states with and without the disorder driven inter-layer tunneling.

2. Results and discussion

The magneto-resistance data obtained in one of the weakly-coupled SLs ($t = 1$ meV) are shown in Fig. 1. At the magnetic field 10 T the transverse and Hall resistivities develop a clear zero-resistance state and a plateau respectively, corresponding to the filling factor $\nu = 2$. In the MQW the analogous plateau was found at 8 T. In quantizing magnetic field the electron system of the weakly-coupled SL transforms to the electrons localized in isolated quantum wells; their two-dimensionality was proved by PL measured with the magnetic field inclined by the angle $\alpha = 45^\circ$. Therefore, in the regime of the quantum Hall effect the optical response of the weakly-coupled SL is expected similar to that one of the MQW structure.

The PL spectra obtained in some of the heterostructures studied here are shown in Fig. 2. The broad PL lines due to the recombination of the electron-hole pairs in the respective minibands were detected in the strongly-coupled SL. No important influence of the magnetic field was found in this SL. The observed asymmetry of the PL line is caused by a partial occupation of the electron miniband and indicates the metallic character of the electron system. At this, the high-energy side

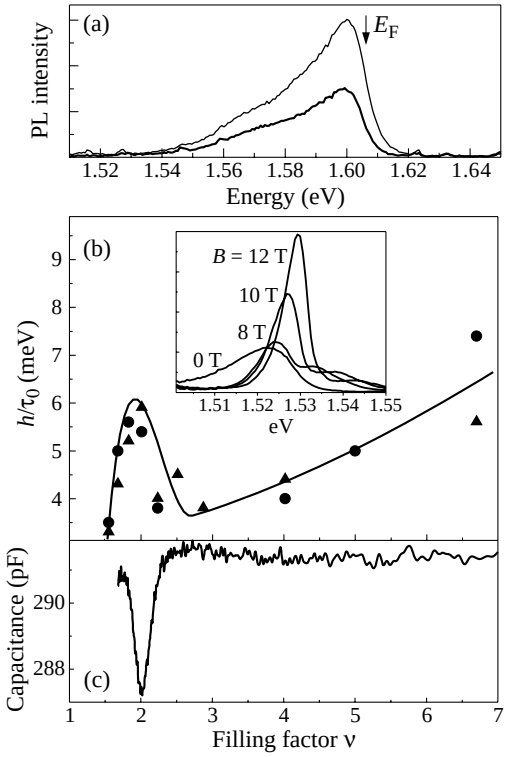

Fig. 2. PL spectra measured at $T = 1.6$ K: (a) in the strongly-coupled SL at $B = 0$ T (thick line) and $B = 10$ T (thin line); (b) characteristic broadenings of the Fermi edge $\hbar/\tau_o$ measured in the weakly-coupled $(GaAs)_{65}(Al_{0.18}Ga_{0.82}As)_{15}$ SL at $T = 1.6$ K, corresponding PL spectra are shown in inset; (c) magneto-capacitance measured in the same weakly-coupled SL.

of the PL line is determined by the broadenings of both the electron states on the Fermi surface and the holes recombining with the electrons. In such case the intensity of the PL line can be calculated according to Ref. [5]:

$$I(\omega) = I_0 \left[1/2 - 1/\pi \operatorname{arctg}(2\tau_o \delta\Omega)\right], \qquad (1)$$

where I_0 is the PL intensity of the completely occupied miniband, $\delta\Omega = \hbar\omega - 2E_F$, where E_F is the Fermi energy and τ_o is the characteristic relaxation time which determines the Fermi edge broadening. This relaxation time is defined by the formula:

$$\hbar/\tau_o = \left[(\hbar/\tau_e)^{0.5} - (\hbar/\tau_h)^{0.5}\right]^2, \qquad (2)$$

where $\tau_{e(h)}$ is the electron (hole) single-particle scattering time. Thus, the asymmetry of the PL lines caused by the broadening of the Fermi edge provides a spectroscopic evidence of the metallic phase and consequently, of the extended electron states at the Fermi energy.

As expected, the zero-field PL measured in the MQW structure and in the weakly-coupled SL revealed the same kind asymmetry indicating the Fermi edge as in the strongly coupled SL.

In the regime of quantum Hall effect the metallic phase of the 2DEG shrinks to a single energy state. In such case a partial occupation of the metallic phase is impossible to observe and therefore, a symmetric Gaussian (due to the unavoidable random character of the MQW) PL line is anticipated. Indeed, the PL observed in the MQW structure in quantizing magnetic fields revealed the Gaussian line associated with the disorder broadened lowest Landau level. On the contrary, the quantized Hall phase created in the weakly-coupled multilayers emitted an unexpected PL line with asymmetry increasing with the increasing magnetic field [shown in inset to Fig. 2(b)]. Comparison of the PL measured in the quantized Hall phase with the zero-field PL demonstrated that the observed asymmetry is caused by a partial population of the extended electron states formed in the insulating quantized Hall phase of the weakly-coupled multilayer system. In such case, according to Eq. (1) the shape of the high-energy side of the asymmetrical PL line is determined by the broadenings of the electron states on the Fermi surface. The fit of the PL performed by Eq. (1) resulted in determination of the characteristic relaxation time τ_o associated with the single-particle scattering time of the electrons at the Fermi energy. A sharp increase of the characteristic broadening $\hbar/\tau_o$ and consequently, decrease of the single-particle scattering time was observed at the filling factor $\nu = 2$. This is caused by the corresponding decrease of the screening efficiency in the quantized Hall phase. No variation of the single-particle scattering time was found in the strongly-coupled structure where the quantum Hall effect was not observed. The magneto-PL data were completely consistent with the sharp minimum of the magneto-capacitance observed at the filling factor $\nu = 2$ [shown in Fig. 2(c)], which is also associated with the decrease of the screening efficiency in the quantized Hall phase. Both the tunneling strength and the inter-layer coherence were shown to significantly influence formation of the observed extended states.

3. Conclusion

We demonstrated a remarkable modification of the spectral shape of the PL lines in the quantizing magnetic fields, which is associated with the formation of the extended states at the Fermi surface of the quantized Hall phase of the weakly-coupled SLs. These extended states may be caused by the disorder driven inter-layer tunneling predicted in [3]. Our data demonstrate that the extended states expand over a large energy range of the quantized Hall phase.

Acknowledgement

This work has been supported by the Brazilian agencies FAP ESP and CNPq.

References

[1] H. L. Stormer, J. P. Eisenstein, A. C. Gossard, W. Wiegman, and K. Baldwin, *Phys. Rev. Lett.* **56**, 1870 (2001).
[2] J. T. Chalker and A. Dohmen, *Phys. Rev. Lett.* **75**, 4496 (1995).
[3] Y. Meir, *Phys. Rev. B* **58**, R1762 (1998).
[4] D. P. Druist, P. J. Turley, K. D. Maranowski, E. G. Gwinn, and A. C. Gossard, *Phys. Rev. Lett* **80**, 365 (1998).
[5] Y. A. Pusep, F. E. G. Guimaraes, M. B. Ribeiro, H. Arakaki, C. A. de Souza, S. Malzer, and G. H. Dohler, *Phys. Rev. B* **70**, 092301 (2004).

15th Int. Symp. "Nanostructures: Physics and Technology"
Novosibirsk, Russia, June 25–29, 2007

Anomalous magnetoconductance beyond the diffusion regime in 2D systems with spin-orbit coupling

A. V. Germanenko[1], G. M. Minkov[2], O. E. Rut[1] and A. A. Sherstobitov[2]

[1] Institute of Physics and Applied Mathematics, Ural State University, Ekaterinburg 620083, Russia
[2] Institute of Metal Physics RAS, Ekaterinburg 620219, Russia

Abstract. The interference quantum correction to the conductivity and its temperature and magnetic-field dependence with taking into account the spin relaxation processes is investigated. The results of numerical and real physical experiments are reported. We show that the shape of the magnetoresistance is nonuniversal beyond the diffusion regime, when the close trajectories with small number of collisions are of importance. It is sensitive to anisotropy of scattering and correlation of impurity distribution.

Interference quantum correction to the conductivity arises from interference of electron waves scattered along closed trajectories in opposite directions. An external magnetic field applied perpendicular to the two-dimensional (2D) layer destroys the interference and, thus, influences the quantum correction. In systems of spin-less particles this results in anomalous negative magnetoresistance. In the systems, in which the spin-orbit coupling is relatively strong and the spin relaxation processes cannot be neglected, the magnetoconductivity is nonmonotonic. Its shape is determined by the relationship between the phase and spin relaxation times, τ_ϕ and τ_s, respectively.

Theoretically, this problem was studied only for the case of random distribution of scattering centers and isotropic scattering. As a rule, these conditions are not fulfilled in real semiconductor structures. The scattering by ionized impurities dominates often in semiconductors at low temperatures. This scattering is strongly anisotropic in high-mobility heterostructures with remote doping layers. Besides, the impurity distribution is correlated to some extend due to the Coulomb repulsion of the impurity ions at the temperatures of crystal growth.

In this paper we investigate the interference quantum correction to the conductivity beyond the diffusion regime with taking into account the spin relaxation processes. The results of numerical and real physical experiments are reported.

The weak-localization phenomenon is described in the framework of quasiclassical approximation which is justified under the condition $k_F l \gg 1$, where k_F is the Fermi wave vector, l is the transport mean-free path. In this case the conductivity correction is expressed through the classical *quasi*probability density W for an electron to return to the area of the order $\lambda_F l$ around the start point [1,2,3]

$$\delta\sigma = -\sigma_0 \frac{\lambda_F l}{\pi} W = -2\pi l^2 G_0 W, \qquad (1)$$

where $G_0 = e^2/(2\pi^2\hbar)$, $\lambda_F = 2\pi/k_F$, and $\sigma_0 = \pi G_0 k_F l$ is the Drude conductivity. Prefix *quasi-* means that W takes into account the dephasing of interfering waves caused by external magnetic field and inelastic processes. To find W and l, we simulate the motion of a particle over the 2D plane with scattering centers in it. This technique was described in details in [4]. Here is outline only. The plane is represented as a lattice. The scatterers with a given cross-section are placed in a part of lattice sites with the use of a random number generator. A particle is launched from some random point, then it moves with a constant velocity along straight lines, which happen to be terminated by collisions with the scatterers. After collision it changes the motion direction. If the particle passes near the starting point at the distance less than $d/2$ (where d is a prescribed value, which is small enough), the path is perceived as being closed. Its length, l_i, and enclosed algebraic area, S_i, are calculated and kept in memory. The particle walks over the plane until it escapes the lattice. As this happens one believes that the particle has left to infinity and will not return. A new start point is chosen and all is repeated.

This approach was used to study the weak localization for the spin-less particle in [4]. It has been shown that obtaining from the simulation procedure the parameters of closed paths, one can calculate the interference quantum correction to the conductivity and its magnetic field dependence (see Eq. (20) in [4]). Taking into account the spin relaxation processes leads to the following expression for the correction:

$$\delta\sigma(b) = -\frac{2\pi l G_0}{d\,N} \sum_i \cos(bS_i) \left[\exp(-l_i\gamma_s) + \frac{1}{2}\exp(-2l_i\gamma_s) - \frac{1}{2} \right] \exp\left(-l_i\gamma_\phi\right). \qquad (2)$$

Here, the summation runs over all closed paths, N is the total number of paths, γ_ϕ and γ_s are the phenomenological parameters describing the phase and spin relaxation and corresponding in real systems to the ratios τ/τ_ϕ and τ/τ_s, respectively, where τ is the transport relaxation time. The lengths and areas in Eq. (2) are measured in units of l and l^2, respectively, the magnetic field b is measured in units of transport magnetic fields, $B_{tr} = \hbar/(2el^2)$.

The simulation has been carried out for three systems. In system A the scatterers are distributed randomly, the scattering is isotropic that physically corresponds to a short-range scattering potential. In the system B the scatterers are distributed randomly and scattering is anisotropic. The angle dependence of scattering probability for this case corresponds to that for the heterostructure with δ doped barrier in which impurities are spaced from the 2D gas of density of about 10^{12} cm^{-2} by a distance of 7 nm. The ratio between the transport and quantum relaxation time for this anisotropy is equal to two. Finally, the system C is characterized by isotropic scattering, but the distribution of scatterers is quite correlated.

Figure 1 shows the magnetoconductivity $\Delta\sigma(b) = \delta\sigma(b) - \delta\sigma(0)$ calculated from Eq. (2) for system A with $\gamma_s = 1/3$

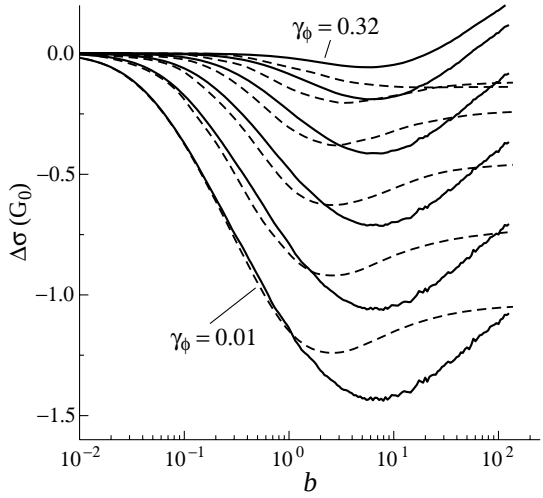

Fig. 1. The $\Delta\sigma$-vs-b dependence for $\gamma_s = 1/3$ and different values of γ_ϕ: 0.01, 0.02, 0.04, 0.08, 0.16, and 0.32. The solid lines are the simulation results for the system A. The dashed lines are calculated according to [5].

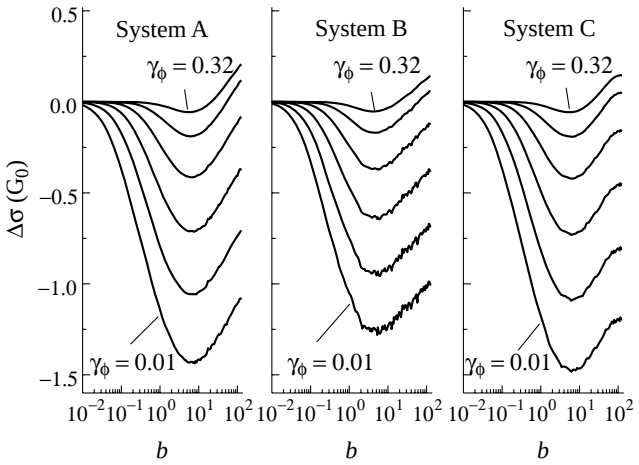

Fig. 2. The dependences $\Delta\sigma(b)$ for systems A, B, and C calculated from Eq. (2) with $\gamma_s = 1/3$ and different values of γ_ϕ: 0.01, 0.02, 0.04, 0.08, 0.16, and 0.32.

and different τ_ϕ/τ values (that is equivalent to the different temperatures). In the same figure the curves calculated within framework of the diffusion approximation [5] are presented. It is clearly seen that the diffusion theory is failed. The higher the temperature is, the stronger the discrepancy is evident. In the high magnetic field, $b \gg 1$, the results differ qualitatively. This is because that the one or several conditions of the diffusion regime ($\gamma_\phi \ll 1$, $\gamma_s \ll 1$, and $b \ll 1$) are not fulfilled in the numerical experiment. Thus, the expression from [5] being applied by experimentalist beyond the diffusion regime can give inadequate information about the spin and phase relaxation times.

Let us compare the magnetoconductivity obtained for systems A, B, and C (see Fig. 2). As one would expected the behavior of $\delta\sigma(b)$ beyond the diffusion regime, when the magnetoconductivity is determined by the closed paths with small number of collisions, depends on scattering details. So the depth of the antilocalization minimum is less in the system B with anisotropic scattering. The magnetoconductivity for the system C demonstrates the saturation of $\Delta\sigma$ at $b > 40-50$. Analysis of the statistics of closed paths shows that such peculiarities directly follow from the difference in the area distribution functions at $S < l^2$. There is a appreciable deficit of the paths with small area enclosed in systems B and C as compared with system A.

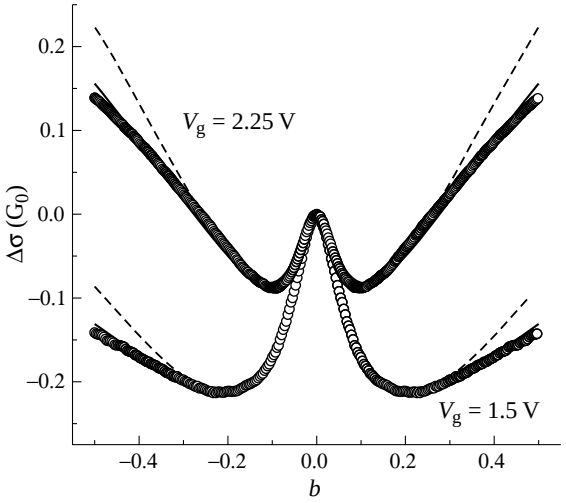

Fig. 3. The magnetoconductivity as a function of normalized magnetic field measured at $T = 0.44$ K for the two values of hole density $p = 8 \times 10^{11}$ cm^{-2} and 5.8×10^{11} cm^{-2} (symbols). Dashed lines are the best fit by the expression from [5] with $\gamma_s = 0.051$ and $\gamma_\phi = 0.016$. Solid lines are the results of the simulation procedure with $\gamma_s = 0.040$ and $\gamma_\phi = 0.014$.

The real experiment has been performed on gated heterostructure GaAs/$In_xGa_{1-x}As$/GaAs of p-type. The heterostructure consists of a 250 nm-thick undoped GaAs buffer layer, carbon δ-layer, a 7 nm spacer of undoped GaAs, a 8 nm $In_{0.2}Ga_{0.8}As$ well, a 7 nm spacer of undoped GaAs, a carbon δ-layer and 200 nm cap layer of undoped GaAs. In order to treat the experimental results (see Fig. 3), we have used the parameters of closed paths l_i and S_i obtained during the simulation for the model system B. Then, the experimental $\Delta\sigma$-vs-b plots have been fitted by Eq. (2) with γ_ϕ and γ_s as the fitting parameters. The results of the best fit are shown in Fig. 3 by the solid lines. It is seen that the simulation procedure describes the data more adequately as compared with the standard diffusion theory [5] (shown by the dashed lines).

In summary, the study of interference quantum correction to the conductivity beyond the diffusion regime shows that the shape of the magnetoresistance curves in systems with the fast spin relaxation is nonuniversal and sensitive to the scattering details.

We are grateful to I. V. Gornyi for very useful discussions. This work was supported in part by the RFBR (Grant Nos. 07-02-00528, 05-02-16413, and 06-02-16292).

References

[1] L. P. Gorkov, A. I. Larkin, and D. E. Khmelnitskii, *Pis'ma Zh. Eksp. Teor. Fiz.* **30**, 248 (1979).
[2] M. I. Dyakonov, *Solid State Commun.* **92**, 711 (1994).
[3] A. P. Dmitriev, V. Yu. Kachorovskii, and I. V. Gornyi, *Phys. Rev. B* **56**, 9910 (1997).
[4] G. M. Minkov, A. V. Germanenko, V. A. Larionova, S. A. Negashev, and I. V. Gornyi, *Phys. Rev. B* **61**, 13164 (2000).
[5] S. Hikami, A. I. Larkin, and Y. Nagaoka, *Prog. Theor. Phys.* **63**, 707 (1980).

15th Int. Symp. "Nanostructures: Physics and Technology"
Novosibirsk, Russia, June 25–29, 2007

Non-Markovian corrections to the Hall coefficient

A. P. Dmitriev and *V. Yu. Kachorovskii*
Ioffe Physico-Technical Institute, St Petersburg, Russia

Abstract. We show that non-Markovian effects lead to dependence of the Hall coefficient R on the magnetic field B. Two types of the non-Markovian effects, specific, respectively, for diffusive and ballistic processes, are discussed. Both types of the effects can be interpreted in terms of small change of the effective scattering cross-section $\sigma_{\rm eff}(\theta)$. In the presence of the magnetic field this cross-section becomes asymmetric: $\sigma_{\rm eff}(\theta) \neq \sigma_{\rm eff}(-\theta)$, which leads to the correction to the Hall coefficient δR. We show that the diffusive processes lead to a small correction $\delta R^{\rm diff}/R \sim C_1 + C_2(\omega_c\tau)^2$ (here $C_1 \ll 1$, $C_2 \ll 1$ are numerical coefficients which depend on the type of disorder, ω_c is the cyclotron frequency, and τ is the transport scattering time). This correction depends parabolically on B and exists in all range of classically weak magnetic fields. At the same time ballistic returns lead to a sharp dependence $\delta R^{\rm ball}$ on B, concentrated in the region of very weak B where $\omega_c\tau \leq \beta_0$ (here $\beta_0 = a/l \ll 1$ is the gas parameter, a is the characteristic size of the scattering centers, and l is the mean free path). This dependence does not have parametrical smallness in β_0: $\delta R^{\rm ball}/R \sim 1$ for $\omega_c\tau \leq \beta_0$.

Introduction

The magnetotransport properties of the 2D semiconductor systems has been intensively discussed in literature during the past three decades. Most of the publications were devoted to the case of the degenerate 2D electron gas where the electrons move in the plane perpendicular to the magnetic field and scatter on a random impurity potential. In this situation only the electrons with energy close to the Fermi energy participate in conductance. The simplest theoretical approach to the problem is based on the Boltzmann equation which yields the following expressions for the components of the conductivity tensor: $\sigma_{xx} = \sigma_0/(1+\omega_c^2\tau^2)$, $\sigma_{xy} = \sigma_0\,(\omega_c\tau)/(1+\omega_c^2\tau^2)$. Here $\sigma_0 = e^2 n\tau/m$ is the Drude conductivity at $B = 0$ and n is the electron concentration. The resistivity tensor, which can be obtained by inverting the conductivity tensor, has even simpler form:

$$\rho_{xx} = \frac{m}{e^2 n\tau}, \quad \rho_{xy} = \frac{m\omega_c}{e^2 n} = RB, \tag{1}$$

where $R = 1/enc$ is the Hall coefficient. Hence, in the frame of Boltzmann equation ρ_{xx} and R do not depend on magnetic field. Measurements of ρ_{xx} and R in experiment are widely used to find n and τ.

It is known, however, that ρ_{xx} and R might become field-dependent due to several reasons of both classical and quantum nature. The most beautiful quantum phenomenon leading to sharp dependencies of R and ρ_{xx} on B is the Quantum Hall Effect, which is observed in strong magnetic fields. Another quantum effect — weak localization, leads to negative magnetoresistance (MR): the decrease of ρ_{xx} with B, concentrated in the region of weak magnetic fields [1]. At the same time, weak localization does not lead to dependence of R on B [2]. The dependencies of both ρ_{xx} and R on B might be also caused by the quantum effects related to electron-electron interaction [3].

Besides quantum effects, there exist some purely classical phenomena, leading to violation of Eqs. (1). In particular, these formulae do not work in systems with several types of charge carriers and in systems with macroscopic inhomogeneity. Another type of classical phenomena, which can be obtained in homogeneous system with one type of charge carriers, are non-Markovian phenomena (so called "memory effects"). Though such phenomena have classical nature, they are not accounted for by the Boltzmann equation. Corrections to the kinetic coefficients arising due to the memory effects are usually proportional to the gas parameter $\beta_0 = a/l$ (where a is the size of the scattering potential and l is the mean free path) which is typically small: $\beta_0 \ll 1$. Nevertheless, the non-Markovian effects are known to lead to a number of non-trivial magnetotransport phenomena in 2D disordered systems such as magnetic-field-induced classical localization [4, 5], high-field negative [4, 5, 6, 7, 8] and positive [9] MR, low-field anomalous MR [10, 11, 12, 13, 14], and non-Lorentzian shape of cyclotron resonance [15].

The MR, caused by non-Markovian effects, arises due to repeated returns to the impurity which was already visited by the diffusing electron. It was studied both in classically strong ($\omega_c\tau \gg 1$) [4, 5, 6, 7, 8, 9, 15] and classically weak ($\omega_c\tau \ll 1$) [10, 11, 12, 13, 14] magnetic fields. Diffusive returns, involving closed paths with a large number of scatterings, usually lead to smooth MR, while the ballistic returns might lead to a sharp MR, concentrated in region of the small magnetic fields [10, 11, 12, 13, 14]. In particular, for the case when electrons scatter on hard disks of radius a, the ballistic MR can be expressed in terms of a dimensionless function $f(z)$ (the analytical expression for this function was given in Ref. [11]) via $\delta\rho_{xx}/\rho = -\beta_0 f\,(\omega_c\tau/\beta_0)$. This MR is caused by memory effects specific for ballsitic returns after one scattering act (see Fig. 1(c), (c′)) [10]. It is concentrated in the region of low fields, where $\omega_c\tau \sim \beta_0 \ll 1$. In spite of large number of works, devoted to the study of the role of the non-Markovian effects in the MR, the dependence of R on B, induced by non-Markovian effect, was studied (to the best of our knowledge) only in the case $\omega_c\tau \gg 1$ [4].

1. Theoretical results

In this paper we present a theoretically calculated dependence of R on B, caused by non-Markovian effects, for the case of weak fields ($\omega_c\tau \ll 1$). Two types of the non-Markovian effects, specific, respectively, for diffusive and ballistic returns, are discussed. Both types of the effects can be interpreted in terms of small change of the effective scattering cross-section $\sigma_{\rm eff}(\theta)$ as illustrated in Fig. 1. In the frame of the usual Boltzmann equation, the scattering on one disk is described by differential scattering cross-section $\sigma_0(\theta)$, (see Fig. 1(a)), the scattering acts on different impurities being independent. The important property of the single scattering act is the symmetry

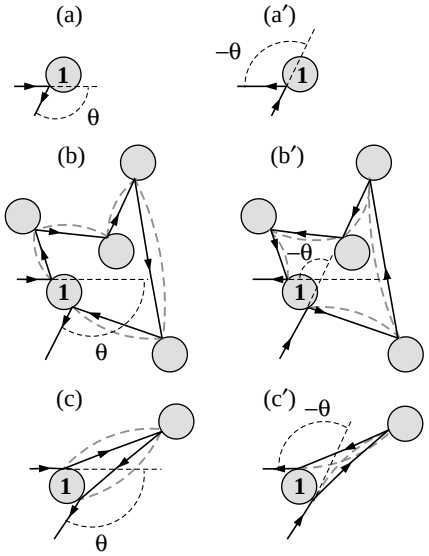

Fig. 1. Processes of single scattering on impurity 1 and processes of diffusive (b), (b′) and ballistic (c,) (c′) scattering on a complex of impurities including double scattering on impurity 1. Single scattering cross-section is symmetric $\sigma_0(\theta) = \sigma_0(-\theta)$ both for the case $B = 0$ and for the case $B \neq 0$. Multi-scattering processes can be accounted for in terms of effective cross-section which remains symmetric in the absence of field: $\sigma_{\rm eff}(\theta) = \sigma_{\rm eff}(-\theta)$ for $B = 0$. Magnetic field curves trajectories as shown in (b), (b′), (c), (c′) by dashed lines. As a result, the symmetry with respect to inversion of θ fails: $\sigma_{\rm eff}(\theta) \neq \sigma_{\rm eff}(-\theta)$ for $B \neq 0$.

with respect to replacement of θ by $-\theta$ (reciprocity theorem): $\sigma_0(\theta) = \sigma_0(-\theta)$ Indeed, the inversion in time of the process shown in Fig. 1(a) leads to a process shown in Fig. 1(b), corresponding to the scattering on the angle $-\theta$,. This is the property which provides that R does not depend on B.

The Drude–Boltzmann approach does not take into account processes of double scattering on a certain impurity after diffusive (Fig. 1(b), (b′)) or ballistic (Fig. 1(c), (c′)) return to it. These are typical non-Markovian processes, since an electron, propagating along closed loop (ballistic or diffusive) "keeps memory" about position of the impurity which it already visited before (impurity 1 on Fig. 1(b), (b′), (c), (c′)). Such processes are not accounted for by usual Boltzmann equation. However, they can be included in the frame of the Drude–Boltzmann approach by introducing of the effective scattering cross-section $\sigma_{\rm eff}(\theta)$ on the impurity where double scattering takes place (impurity 1 in Fig. 1(b), (b′), (c), (c′) [11,16]. For $B = 0$, the effective cross-section remains symmetric for the processes shown in Fig. 1(b), (b′), (c), (c′): $\sigma_{\rm eff}(\theta) = \sigma_{\rm eff}(-\theta)$. However, in the presence of the field this cross-section becomes asymmetric: $\sigma_{\rm eff}(\theta) \neq \sigma_{\rm eff}(-\theta)$ (for $B \neq 0$). The point is that the influence of the magnetic field is different for the processes where closed return path is passed clockwise (see Fig. 1(b), (c)) and counterclockwise (see Fig. 1(b′), (c′). As a result, there appear a correction to R.

The calculation of the field-dependent effective cross-section can be done with the use of the methods developed in Refs. [11,17]. As a result, one can find that diffusive (Fig. 1(b), (b′)) and ballistic (Fig. 1(c), (c′)) processes lead to the correction $\delta R = \delta R_{\rm diff} + \delta R_{\rm ball}$, where

$$\frac{\delta R_{\rm diff}}{R} = C_1 + C_2(\omega_{\rm c}\tau)^2, \quad \frac{\delta R_{\rm ball}}{R} = g\,(\omega_{\rm c}\tau/\beta_0)\,. \qquad (2)$$

Here C_1 and C_2 are dimensionless coefficients which depend on the type of the disorder (in particular, for isotropic scattering $C_1 = \beta_0/2\pi$, $C_2 = 0$) and $g(z)$ is the monotonous dimensionless function such that $g(0) \sim 1$ (this implies that ballistic correction does not have parametric smallness in β_0) and $g(z) \sim 1/z^{3/2}$ for $z \to \infty$. We have found analytical expression for $g(z)$ in the case of scattering on hard disks.

2. Conclusions

We show that the diffusive processes lead to small correction $\delta R_{\rm diff}$ which depends parabolically on B and exists in the range of classically weak magnetic fields ($\omega_{\rm c}\tau \ll 1$). At the same time, ballistic returns lead to very sharp dependence $\delta R_{\rm ball}$ on magnetic field, concentrated in the region of very small magnetic fields, where $\omega_{\rm c}\tau \leq \beta_0$. This dependence does not have parametrical smallness in the β_0: $\delta R_{\rm ball}/R \sim 1$ for $\omega_{\rm c}\tau \leq \beta_0$.

Acknowledgements

The work was partially supported by RFBR, by grant of Russian Scientific School, and by programmes of the RAS.

References

[1] B. L. Altshuler, D. Khmelnitskii, A. I. Larkin, and P. A. Lee, *Phys. Rev. B* **22**, 5142 (1980).
[2] H. Fukuyama, *J. Phys. Soc. Jap.* **49**, 644 (1980).
[3] B. L. Altshuler and A. G. Aronov, in *Electron-Electron Interactions in Disordered Systems*, eds. A. L. Efros and M. Pollak, North-Holland, Amsterdam (1985).
[4] E. M. Baskin, L. N. Magarill, and M. V. Entin, *Sov. Phys. JETP* **48**, 365 (1978); E. M. Baskin and M. V. Entin, *Physica B* **249**, 805 (1998).
[5] M. M. Fogler *et al*, Phys. Rev. B **56**, 6823 (1997).
[6] A. V. Bobylev *et al*, *Phys. Rev. Lett.* **75**, 197 (1995); *J. Stat. Phys.* **87**, 1205 (1997); A. Kuzmany and H. Spohn, *Phys. Rev. E* **57**, 5544 (1998).
[7] A. D. Mirlin *et al*, *Phys. Rev. Lett.* **87**, 126805 (2001); D. G. Polyakov *et al*, *Phys. Rev. B* **64**, 205306 (2001).
[8] A. Dmitriev, M. Dyakonov, R. Jullien, *Phys. Rev. B* **64**, 233321 (2001).
[9] A. D. Mirlin, J. Wilke, F. Evers, D. G. Polyakov, and P. Wolfle, *Phys. Rev. Lett.* **83**, 2801 (1999).
[10] A. Dmitriev, M. Dyakonov, R. Jullien, *Phys. Rev. Lett.* **89**, 266804 (2002).
[11] V. V. Cheianov, A. P. Dmitriev, V. Yu. Kachorovskii, *Phys. Rev. B* **68**, 201304(R) (2003); *Phys. Rev. B* **70**, 245307 (2004).
[12] G. Gusev *et al*, *Surface Science* **305**, 443 (1994).
[13] N. M. Sotomayor *et al*, *Phys. Rev. B* **70**, 235326 (2004).
[14] H. Cho *et al*, *Phys. Rev. B* **71**, 245323 (2005).
[15] D. G. Polyakov, F. Evers and I.V. Gornyi, *Phys. Rev. B* **65**, 125326 (2002).
[16] I. S. Lyubinskiy and V. Yu. Kachorovskii, *Phys. Rev. B* **73**, 041301(2006).
[17] A. P. Dmitriev, M. Dyakonov, and R. Jullien, *Phys. Rev. B* **71**, 155333 (2005).

15th Int. Symp. "Nanostructures: Physics and Technology"
Novosibirsk, Russia, June 25–29, 2007

Nonlinear current-voltage characteristics and current instabilities in the side-gated quantum wire

V. I. Borisov[1], A. I. Chmil'[1], V. A. Martyakhin[1] and A. I. Toropov[2]

[1] Institute of Radioengineering and Electronics Russian Academy of Science,
Vvedenskii sq. 1, Fryazino, Moscow region, 141190, Russia
[2] Institute of Semiconductor Physics Siberian Branch of Russian Academy of Science,
Novosibirsk, 630090, Russia

Abstract. We study the current-voltage characteristics ($I(V)$) of a quasi-one-dimensional channel in a transistor structure with in-plane side gates (IPGT), created on the bases of AlGaAs/GaAs heterostructures with a two-dimensional electron gas (2DEG), in nonlinear conditions. We have found an asymmetric $I(V)$ and negative differential conductivity (NDC), which can be explained by the asymmetry of the potential of the gates with respect to the source and drain, and by the heating of the electrons in the percolation net in the δ-doped layer in AlGaAs, which brings about the transfer of electrons into the pits of the fluctuating potential and, as a result, the accumulation of charge.

Introduction

Studies into the nonlinear conductivity of quantum conductors and quantum contacts are currently being paid special attention, because this nonlinearity is thought to be connected to the processes of electron-electron interaction in one-dimensional systems. Measurements of the conductance characteristics ($G(U_G)$, U_G — the gate voltage) are conducted under small (as compared to the intersubband and Fermi energies) voltage of the source and drain (U_{SD}), which are applied along the quantum conductor. There have also been many studies which propose to use a quantum channel for injecting hot electrons into a 2D- system or into a quantum dot. In these applications, the voltage U_{SD} may be significantly higher. Theory predicts that for $U_{SD} > E_F$ (where E_F is the Fermi energy of electrons in the source reservoir) it may be possible to observe the appearance of a section on the $I(V)$ with negative differential conductance, both when the current flows in one one-dimensional subband [1], and when it flows along several subbands [2].

1. Experimental

In this work we study the transport of electrons in a quasi-one-dimensional channel of a transistor with side gates, created on the basis of a heterostructure GaAs/AlGaAs with a 2DEG. In the initial structures with 200 Å AlGaAs spacer layer and two delta layers doped with Si the concentration of the two-dimensional electron gas and the mobility of electrons at temperature 10 K were: $n \sim 1.4 \times 10^{11}$ cm^{-2} and $\mu \sim 3 \times 10^5$ cm^2/V s. In this work, the transistors were made in two stages. First mesa-structures of size 100×100 μm were formed by using optical lithography and conventional AuGeNi Ohmic contacts to the source, drain and gates regions were added. Afterwards, insulating grooves dividing channel and gates were formed by using the methods of electron-beam lithography and ion etching by a low energy Ar^+-ion beam. An image of the resulting structure, obtained by using a scanning probe microscope (SPM), is shown in Fig. 1. The length of the channel (0.7 μm) is several times less than the length of the free-path of the electrons, which is estimated to be 2 μm. The geometric width of the channel that resulted after etching was about 0.3 μm. The measurements were conducted by attaching

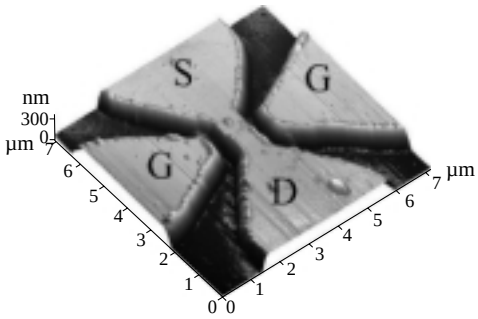

Fig. 1. SPM image of the IPGT.

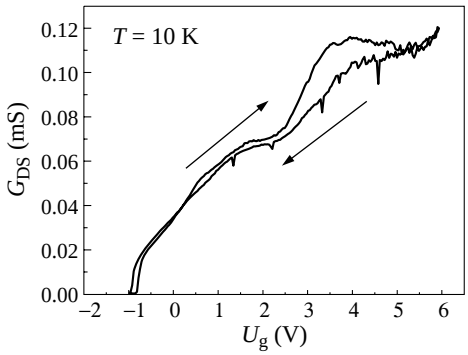

Fig. 2. Variation of conductance $G_{SD}(U_G)$ of the IPGT, obtained while sweeping U_G in different directions.

electrodes in the following way. The source (S) was grounded, and potentials with respect to S were applied to the gates (G) and the drain (D), so that the sum of the constant and alternating ($f = 130$ Hz) voltages, $U_{SD} = V_= + V_\sim$, was applied to the drain in order to measure the differential conductivity. In addition, the structure was illuminated by an infrared LED of output $P < 100$ μW during the measurements, if not indicated otherwise.

The dependence of the channel conductivity $G_{SD}(U_G) = dI_{SD}/dU_{SD}$ on the gate voltage U_G for alternating voltage amplitude of $V_\sim = 100$ μV and $V_= = 0$ V is shown in Fig. 2. It can be seen that this dependence has two clearly defined plateaus for gate voltages $U_G \approx 1.5{-}2$ V and $U_G \approx 3.5{-}5$ V. We also note that the conductivity corresponding to the first plateau is very close to the value $G_0 = 2e^2/h \approx 0.077$ mS

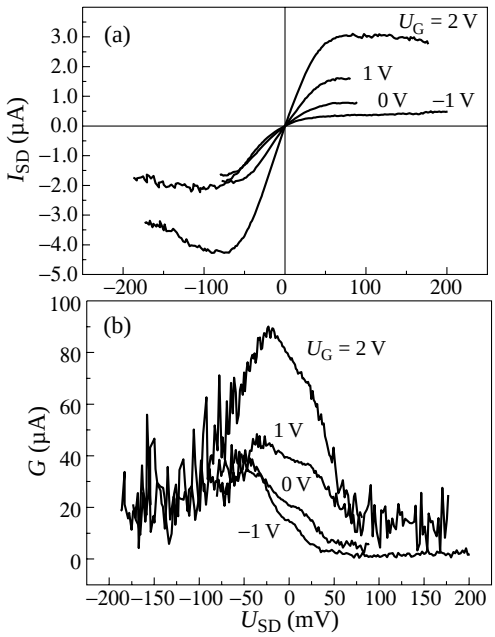

Fig. 3. Current-voltage (a) and differential conductivity (b) dependencies on drain voltage obtained for different constant gate voltages.

(e is the charge of an electron, h is Plank's constant), which corresponds to the conductivity of the quantum point contact (wire) for the first subband.

Measurements of $I(V)$ (the dependence on the voltage U_{SD} of the constant current component of the drain I_{SD}) and of the differential conductivity of the structure $G(U_{SD})$ were conducted for fixed gate voltages $U_G = 2$ V, and thus we would expect that only one subband would influence the conductivity of the channel, and the maximum current should not exceed $I_{max} = G_0 E_F$. For our samples this is about $I_{0max} \sim 0.3{-}0.4$ μA. However, as can be seen from the measurement results shown in Fig. 3a, the current at the peak of the characteristic is significantly higher than I_{0max}. This leads us to suppose that with increase in the voltage U_{SD} subbands other than the first also begin to transfer electrons, and the inclusion of each successive subband does not bring about the appearance of peculiarities on the $I(V)$. These peculiarities with a period of about 0.2 μA appear on the $I(V)$ shown in Fig. 4, which were obtained for our same sample but without illumination.

Another interesting feature of the $I(V)$ shown in Fig. 3a is the significant asymmetry with respect to the polarity of the voltage U_{SD}. In addition, for the $I(V)$ obtained at gate voltage $U_G = +2$ V, there are regions with a negative slope for both polarities of the U_{SD} voltage and for all other $I(V)$ s with a negative bias voltage. $I(V)$ measurements are carried out for constant (average) current through the structure; however, the presence of NDC and the current instabilities that it gives rise to are confirmed by the dependencies of differential conductivity of the channel on the U_{SD} shown in Fig. 3b.

2. Discussion

Asymmetry in the $I(V)$ of quantum channels has been observed earlier [2,3]. It was explained by the fact that the gate voltage is fixed with respect to the source, while the drain voltage with respect to the source may change during the measurements. The instability of the current through the channel had been observed by Kelly *et al* [3] and was explained by the presence of NDC that had to do with the decrease in the transparency of the potential barrier with an increase in U_{SD}. We note, however, that the $I(V)$ shown in Fig. 4 and obtained without illumination is different in that it displays significant hysteresis; this indicates that the redistribution of the charge in the structure and its localization changed during the measurements(about 20 min). It may be shown that the reason for the redistribution of charges in the structure for such low U_{SD} cannot be the transport of electrons in real space from the 2DEG layer to the AlGaAs layer but it could be the accumulation and redistribution of charges in the fluctuation potential in the AlGaAs layer which was δ-doped with silicon. A similar situation was considered in [4] when analyzing the instability of currents observed in structures with 2DEG.

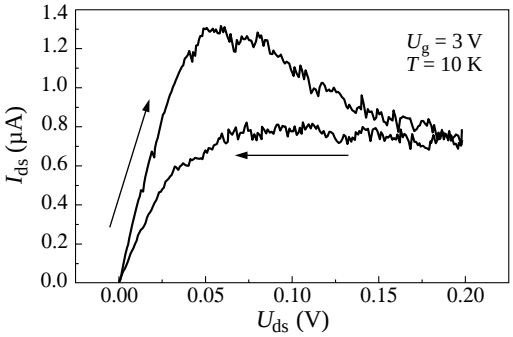

Fig. 4. $I(V)$ characteristic of the structure obtained while sweeping U_G in different directions in darkness.

Analysis shows that the charge density and the width of the stripe of the layer with positively charged Si^+ donors close to the conducting quasi-one-dimensional channel determines the shape and width of the potential profile of the channel, and also, as a result, the intersubband energies. The positive charge distributed in the layer is compensated by the charge in the DX-centers and by the free electrons which are in the percolational net of channels and "lakes" formed by the fluctuation potential. A change in the drain voltage brings about not only a change in the potential of the drain, but also a change in the density of charge in the doped layer.

Acknowledgements

This work was supported by the Russian Foundation for Basic Research and Russian Academy of Sciences (programs "Quantum Nanostructures" and "Strongly Correlated Electrons in Semiconductors, Metals, Superconductors, and Magnetic Materials"). We thank Prof. V. A. Sablikov for valuable dicscussions.

References

[1] R. J. Brown *et al*, *J. Phys.: Condens. Matter* **1**, 6285 (1989).
[2] T. Heinzel *et al*, *Semicond. Sci.Technol.* **9**, 1220 (1994).
[3] M. J. Kelly *J. Phys.: Condens. Matter* **1**, 7643 (1989).
[4] V. I. Borisov *et al*, *Physica E* **8**, 376 (2000).

15th Int. Symp. "Nanostructures: Physics and Technology"
Novosibirsk, Russia, June 25–29, 2007

Scanning Gate microscopy/spectroscopy of quantum channel with constriction: steering of electron wave controlled by the tip voltage

O. A. Tkachenko[1,2,3], V. A. Tkachenko[1], V. T. Renard[3], J.-C. Portal[3,4] and A. L. Aseev[1]

[1] Institute of Semiconductor Physics, 630090 Novosibirsk, Russia
[2] Université Joseph Fourier - BP 53 - 38041 Grenoble Cedex 9, France
[3] GHMFL, CNRS, BP 166, F-38042, Grenoble Cedex 9, France
[4] INSA, 135 Avenue de Rangueil, F-31077, Toulouse Cedex 4, Institut Universitaire de France, France

Abstract. We present the results of numerical modelling for scanning gate microscopy/spectroscopy (SGM/SGS) of quantum channel with constriction. Calculations show that a small quantum dot with three outlets can be formed when the tip of SGM is approached to quantum point contact (QPC). The steering of electron wave is found in this system with increasing voltage on the tip or the Fermi energy.

Introduction

Scanning Gate microscopy (SGM) uses the conducting tip of an Atomic Force Microscope as a moveable local gate that scatters electron waves in nanostructures based on two-dimensional electron gas (2DEG) [1]. We report on computer simulation of the SGM tip effect on a quasi-one-dimensional channel with constriction in SGM/SGS techniques. We have recently demonstrated electron wave steering in small three-terminal quantum dots formed at a Y-junction [2]. Here we suggest a similar device in which the three-terminal system can be controlled by the SGM tip. Both the tip position and more importantly the amplitude of the potential perturbation induced by the tip can be used to intentionally send electrons to one of the outlets.

Results

We modelled a GaAs/AlGaAs structure in which 2DEG is located in 8 nm GaAs quantum well, 35 nm beneath the surface. We supposed that the QPC and quantum channel were created by local anodic oxidation. A cone-shaped tip was scanned above the oxide layer with a negative voltage applied with respect to the 2DEG. The oxide thickness was 11 nm. A 300 nm thick vacuum layer was taken into account in the model. The distance between the tip and the 2DEG was about 52 nm.

Our 3D electrostatic modelling shows that the tip perturbation (both shape and height) strongly depends on the position of the tip; especially close to depletion regions. In addition, contrary to previous calculations [3] we obtain that the

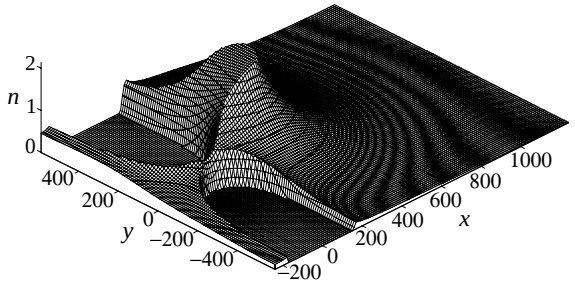

Fig. 1. Perturbation of electron density in QPC [10^{11} cm^{-2}] induced by SGM tip. Correction to electron density is nonzero near depletion regions forming constriction. Distance is plotted in nm.

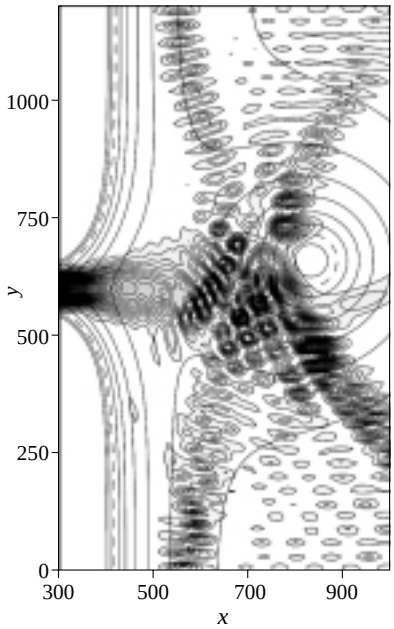

Fig. 2. Probability density and effective potential in the plane of 2DEG for the tip position $x_t = 830$ nm, $y_t = 660$ nm. Conductance is $G = 1.94e^2/h$.

half width of the tip perturbation in the 2DEG plane occurs at a radial distance 2 times larger than the 2DEG depth (half width a is 115 nm). This means that in small nanostructures (narrow quantum channels, dots or ring interferometers) the perturbation from the tip is no longer localized and has an influence on symmetry of the whole electron system. It is can not be considered as a small additional spot of confining potential (Fig. 1). Also, in a homogeneous 2DEG an expression $U_t = V_0/(1+(r/a)^{1.75})$ approximates the tip perturbation better than a Lorentzian [3]. Here r is radial distance from the tip, V_0 is height of the induced potential perturbation determined by the voltage on the tip. The conductance is calculated by recursive Green's function method [4] for 2D effective potential, obtained for fixed position of the SGM tip from 3D electrostatics modelling. The conductance response $\delta G(x, y)$ as a function of the tip position is computed for a QPC situated in a 1200 nm wide channel with rigid walls. A strong modulation of the conductance is obtained when the tip is scanned in the

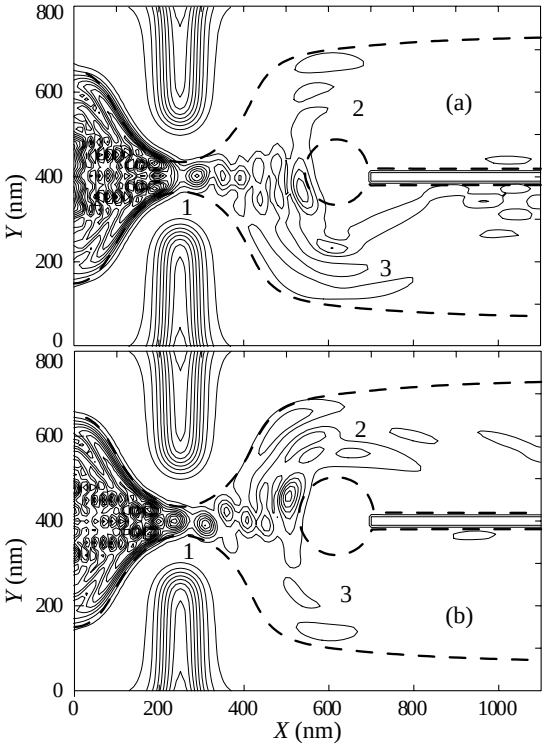

Fig. 3. Distribution of probabilty density and effective potential in the plane of 2DEG. Dashed line shows the Fermi level (E_F = 11 meV in 2DEG). The tip position is $x_t = 625$ nm, $y_t = 410$ nm. Magnetic field is $B = 0.03$ T. a) Height of the tip bump is $V_0 = 12.5$ meV, $G_{12} = 0.6e^2/h$, $G_{13} = 1.3e^2/h$. b) $V_0 = 13.8$ meV, $G_{12} = 1.2e^2/h$, $G_{13} = 0.54e^2/h$.

region close to a QPC. It originates from the complex interference pattern generated by multiple reflections between the tip potential and the boundaries (both the walls of the channel and the QPC). Figure 2 shows that the tip bump can split electron wave into several narrow directed beams: an open quantum billiard is formed.

An interesting situation is arisen when the tip and the QPC define a small quantum dot with three terminals. The parameters of the dot (size and coupling to the reservoirs) are easily tuned by the tip position and voltage. The obtained dot has two peculiarities: first, its conductance can be much smaller than $2e^2/h$ even if both inlet and outlet (or even two outlets) are open. Secondly, the ballistic transport of electrons is extremely sensitive to small displacement of the tip away from the symmetry axis. Also, the electron flow changes outlet if the voltage on the tip or magnetic field is changed. It is worthy of note that electrons can move to narrower constriction and against Larmor gyration.

This effect can be monitored in the resistance of the device if one performs a three-terminal measurement. For this purpose the 2DEG should be cut a bit farther from potential of the tip (Fig. 3). As shown in Fig. 4 and 5 the transmission coefficients through outlets 2 and 3 change in antiphase and the difference $G_{12}-G_{13}$ oscillates around zero when the voltage on the tip is varied. This effect becomes stronger in a weak magnetic field even if magnetic field doesn't change total conductance $G_{12} + G_{13}$ significantly.

In summary, we have performed numerical modelling of the influence of SGM tip on electrostatics and conductance of

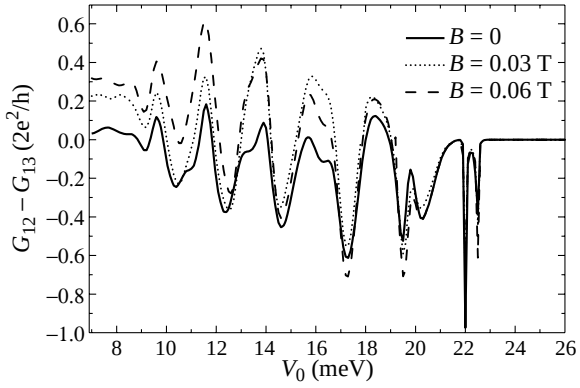

Fig. 4. Conductance difference $G_{12}-G_{13}$ as a function of the height of the tip bump V_0. The tip position is $x_t = 625$ nm, $y_t = 410$ nm. The effect becomes more pronounced in a weak magnetic field.

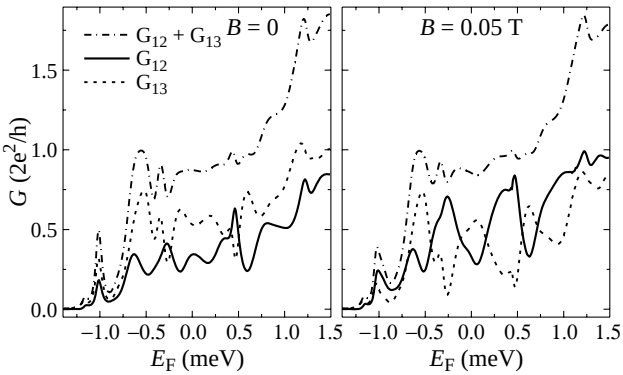

Fig. 5. Conductance G_{12}, G_{13}, $G_{12} + G_{13}$ as a function of the Fermi energy at zero and weak magnetic field. The tip position is $x_t = 650$ nm, $y_t = 410$ nm, $V_0 = 15$ meV.

quantum channel with constriction. The microscopic behavior of electron flow in a small quantum dot formed between SGM tip and QPC was considered. We suggested an experiment that allows to observe switching of the electron current between the output ports of three-terminal quantum dot with increasing the voltage on the SGM tip.

Acknowledgements

We are very grateful to D. G. Baksheev and Yu. Krupko for help and discussions. O.A.T. acknowledges Supercomputing Siberian Centre, Novosibirsk, Russia and IDRIS Supercomputing Center, Orsay, France (project 61778) for the possibility of performing the calculations. This work at Novosibirsk was supported by programs "Quantum nanostructures" of RAS, and "Russian Scientific School" Grant No. 8401.2006.8. The work at Grenoble was funded partially by CNRS.

References

[1] M. A. Topinka, B. J. Le Roy *et al*, *Science* **289**, 2323 (2000); *Nature* **410**, 183 (2001); R. Crook, C. G. Smith *et al*, *Phys. Rev. Lett.* **91**, 246803 (2003).

[2] O. A. Tkachenko, Z. D. Kvon *et al*, 13th Int. Symp. Nanostructures: Physics and Technology, St Petersburg, 8–10 (2005).

[3] M. A. Eriksson, R. G. Beck, M. Topinka *et al*, *Appl. Phys. Lett.* **69**, 671 (1996).

[4] T. Usuki, M. Saito, M. Takatsu *et al*, *Phys. Rev. B* **52**, 8244 (1995).

15th Int. Symp. "Nanostructures: Physics and Technology"
Novosibirsk, Russia, June 25–29, 2007

I–V characteristics and current instabilities of semiconductor superlattices with narrow minigaps

A. A. Andronov[1], *E. P. Dodin*[1], D. I. Zinchenko[1] and Yu. N. Nozdrin[1]

[1] Institute for Physics of Microstructures, Russian Academy of Sciences,
Nizhny Novgorod GSP 105 603600, Russia

Abstract. Vertical electron transport under the condition of strong Zener tunneling in constant electric field has been studied experimentally. Some effects typical for weakly coupled superlattices (SLs) have been found. Transport properties are analyzed based on models of charged walls and electric field domains dynamics.

Introduction

One of the main obstacles for creating THz Bloch generator on the basis of semiconductor superlattices (SLs) [1] is the low frequency current instability due to negative differential conductivity (NDC) of the structure. The current instability results in inhomogenity in the field distribution up to domain formation and, consequently, leads to spontaneous appearance of parasitic low frequency current oscillations. Traditional studies of active properties of Bloch oscillator in constant electric field E are mainly focused on finding the generation on the frequencies lower than the Bloch frequency, $\omega < \omega_B = eEd/\hbar$, where the SL differential conductivity is negative [2]. Attempts of suppression of low-frequency instability by using different ways and regimes of pumping by electric field haven't lead to desired results yet [3].

In [4] it has been shown that in the SL with narrow minigap and substantial interminiband tunneling it's possible to realize *dynamic* NDC that is positive on low $\omega < \omega_B$ frequencies and negative on the frequencies higher than Bloch $\omega > \omega_B$. Corresponding energy spectrum can be achieved by using SL on the base of GaAs/Al_xGa_{1-x}As with wide quantum wells and narrow barriers with Al concentration $\sim 10-15\%$. The spectrum of such SLs contains minigaps $\sim 10-20$ meV wide and first and second minibands ~ 10 and ~ 40 meV wide consequently. Here it has to be noted that studied structures cannot be unambiguously considered as strongly or weakly coupled SLs (see def. in [5]). In spite of relatively strong coupling between neighboring wells (narrow, $< 20A$, and low, < 100 meV, potential barriers), even in relatively weak electric field interminiband Zener tunneling becomes important enough that some effects typical for weakly coupled SLs are observed in studied structures. In particular, such effects include sawtooth-like plateaus on I–V characteristic, hysteresis, multistability and spontaneous generation of low-frequency current oscillations with wide (and even stochastic) spectrum.

In the report some properties of the electron transport in weakly doped SLs with narrow minigaps under constant and pulsed voltages are identified and analyzed based on models of space-time dynamics of charged layers and domains of electric field.

1. Experimental

1.1. Structures

Transport properties of weakly doped GaAs/Al_xGa_{1-x}As SL samples with different number of periods N, well width w and barrier width b (Table 1) have been studied. The structures were grown by MOCVD on the n^+-GaAs (100) substrate with concentration $N_i = (1.0-3.5) \times 10^{18}$ cm^{-3} (Si). On both sides the SL is adjoined with n^+-GaAs layers $N_i = (1.5-4) \times 10^{18}$ cm^{-3} (Si). Carrier concentration in the SL region is about 1.0×10^{15} cm^{-3}.

Table 1. Sample parameters.

Sample	426	502	698	816
E_0 (meV)	3.2	3.7	6.5	6.2
ΔE_1 (meV)	11.2	14.8	11.8	10.7
E_1 (meV)	14.4	18.5	18.3	16.9
E_{gap} (meV)	7.1	7.9	18.0	13.9
E_2 (meV)	21.3	26.4	31.6	30.8
ΔE_2 (meV)	34.9	45.0	38.4	34.9
$d = w + b$, A	185+10	163+10	155+20	161+20
N	100	150	500	1000

Here E_0, E_1 — energies of the bottom and the top of first miniband, E_2 is the energy of the second miniband bottom, $\Delta E_{1,2}$ is the width of the first (second) miniband, E_{gap} is the width of the minigap. The energy spectra were calculated using the transfer matrix method.

1.2. Results

In the report the I–V characteristics of SLs measured under 4 and 77 K are presented.

The sawtooth dependence of average current on applied voltage is established (Fig. 1): first, NDC regions alternate

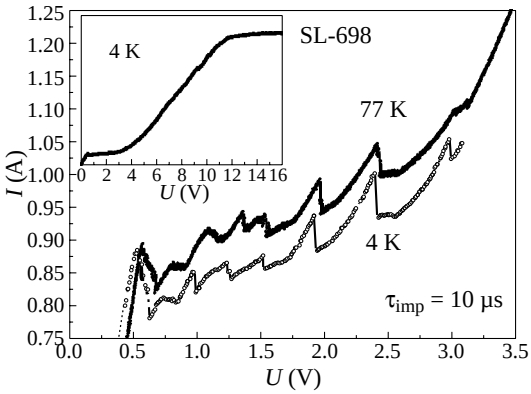

Fig. 1. Low-field time-averaged I–V curves for sample 698 at 4 and 77 K. *Inset*: Full I–V curve for 698 structure.

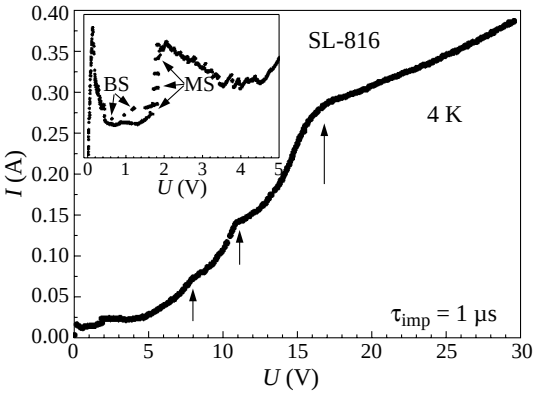

Fig. 2. Full time-averaged I–V curves for sample 816 at 4 K. *Inset:* Low-field part of I–V curve for 816 structure. BS, MS- bi- and multistability. Arrows point to the regions of resonant tunneling discussed in [6].

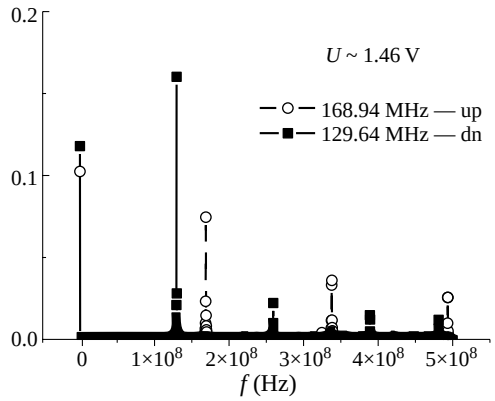

Fig. 3. Current oscillations spectrum for sample 816 at 4 K under up (principal frequency 169 MHz) and down (−130 MHz) voltage sweeps at 1.46 V.

with positive DC regions and then with the increase of applied voltage the jumps of average current are observed. These jumps are caused by size increase of monopole — charge accumulation layer that divides the SL into high and low electric field domains. The monopole size depends on the doping level and can amount to tens of superlattice periods. The observations of current response under constant and pulse voltage allowed to establish the existence of both static and dynamic modes of strong and weak electric field domains. In some SL samples hysteresis of I–V, effects of bi- and multistability (BS and MS) (Fig. 2, inset) that directly define the sawtooth plateau shape have been observed.

Outside of sawtooth region of I–V regular peculiarities were found for voltages $U \sim N\times(35\,\mathrm{meV})/en$, here $n = 4,\ 3,\ 2$, e — electron charge (Fig. 2). These peculiarities are manifestation of resonant tunneling effect of electrons between minibands levels $1 \to 2$, $1 \to 3$, $2 \to 3$ of quantum wells located n SL periods apart [6].

In NDC regions the spontaneous current oscillations are observed; their principal frequency has non-monotonous dependence on the applied voltage, and the full frequency spectrum can contain several tens of harmonics. Here as an example the frequency spectra for some of the observed current oscillations waveforms are presented: from discrete for quasiharmonic oscillations (Fig. 3) to almost continuous — for chaotic (Fig. 4). In narrow voltage regions bifurcational multiplication of current oscillations frequency has been observed, and with the additional applied AC field halving of the frequency has been observed also.

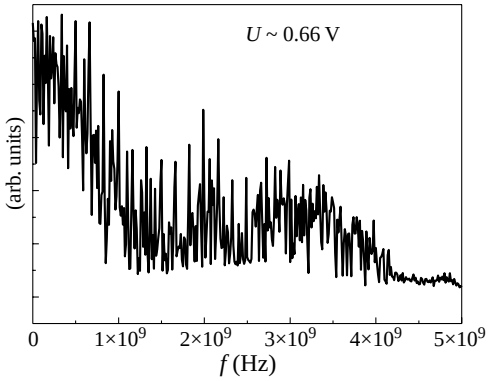

Fig. 4. Example of stochastic spectrum for 816 sample at 77 K at 0.66 V.

The peculiarities of sawtooth region of I–V characteristic caused by complex space-time dynamics of charged layers (dipoles, monopoles, tripoles) are discussed based on numerical simulation of drift-diffusion transport in $n^+ - n - n^+$ structures. Possible reasons for appearance of periodic structures on I–V characteristic for electron transport in SL with narrow minigaps are analyzed on the models of resonant emission of polar optical phonons with transverse (relative to the electric field) heating and interminiband resonant tunneling.

Acknowledgements

This work is supported by RFBR grant 05-02-16468 and by RAS Program "Low dimensional structures". The authors are grateful to A. A. Marmalyuk and A. A. Padalitsa for growing of the samples, Yu. N. Drozdov for X-Ray characterization of the samples and to I. Yu. Shuleshova, V. V. Rogov and A. Yu. Klimov for processing the samples.

References

[1] L. Esaki and R. Tsu *IBM J. Res. Develop.* **14**, 61 (1970).
[2] S. A. Ktitorov *et al*, *Sov. Phys. Solid State* **13**, 1872–1874 (1971).
[3] H. Kroemer, *cond-mat/0009311* 2000; *cond-mat/0007482* (2000).
[4] A. Andronov, I. Nefedov and A. Sosnin, *Semiconductors* **37**, 378–384 (2003).
[5] L. L. Bonilla, H. T. Grahn, *Rep. Prog. Phys.* **68**, 577–683 (2005).
[6] A. A. Andronov *et al*, these Proceedings.

15th Int. Symp. "Nanostructures: Physics and Technology"
Novosibirsk, Russia, June 25–29, 2007

Electrons in vibrating quantum wells: absolute reflectivity, true local quasienergy states, and related physical effects in passive and active electron transport

L. S. Braginsky, *M. V. Entin* and M. M. Mahmoodian
Institute of Semiconductor Physics, Siberian Division of Russian Academy of Sciences,
Novosibirsk, 630090, Russia

Abstract. We have found positive answers to the following questions: 1. Can vibrating finite quantum well keep electrons in a local state? 2. Can be the absolute reflectivity for electrons with positive energy, colliding with a potential which has zero asymptotics on infinity?
The consequence of these statements are: 1. The vibrating potential well can be treated in the same way as a well with constant potential, in particular for 2D, 1D or 0D confinement. 2. This well can serve as controlling ideal mirror for Fabri–Perro electron interferometer. 3. The conductivity through this well is positive and vanishes for some values of the Fermi level. 4. In asymmetric double-well structure the reflectivities from left and right vanishes for different electron energies. 5. The active transport (photogalvanic effect) has at the same points zero derivative with respect to the Fermi level.

We study one-dimensional systems with vibrating potentials:

$$U(x) = (u + v\sin(\omega t))\delta(x), \tag{1}$$
$$U(x) = (u_1 + v_1(t))\delta(x+d) + (u_2 + v_2(t))\delta(x-d). \tag{2}$$

Here $v_1(t) = v_1\sin(\omega t)$, $v_2(t) = v_2\sin(\omega t + \varphi)$, t is time, $\hbar = m = 1$. The model (1) is used for the problem about conductance of the structure, the model (2), besides that, for the problem of quantum pump.

The vibrating potential barriers were under study in connection with quantum pumps of photon- and phonon-assisted tunnelling, quantum pumps [1]– [7], and resonant reflection [8]. The present study is concentrated on the properties of such systems determined by the absolute reflection of particles (high-frequency blockade).

In the problem of scattering the wave function on the left and on the right of the well reads

$$\Psi = \sum_n e^{-i(E+n\omega)t} \times \begin{cases} \delta_{n,0}e^{ip_n x} + r_n e^{-ip_n x} & \text{left,} \\ t_n e^{ip_n x} & \text{right.} \end{cases} \tag{3}$$

Here $p_n = \sqrt{p^2 + 2n\omega}$, $p = \sqrt{2E}$. In general, the scattering is multichannel; each channel corresponds to emission or absorption of some oscillating field quanta ω. The multichannel transmission amplitudes in the problem (1) obeys equations

$$t_n(p_n + iu) + \frac{v}{2}(t_{n+1} - t_{n-1}) = p_n\delta_{n,0}. \tag{4}$$

Similar equations for the problem (2) were found in [5].

At low temperature the conductance G and the derivative of the stationary photogalvanic current J_0 with respect to the Fermi level E_F are

$$G = \frac{G_0}{2}(\mathcal{T}^{\rightarrow} + \mathcal{T}^{\leftarrow})|_{E=E_F}, \tag{5}$$
$$e\frac{\partial}{\partial E_F}J_0 \equiv \mathcal{G} = G_0(\mathcal{T}^{\rightarrow} - \mathcal{T}^{\leftarrow})|_{E=E_F}. \tag{6}$$

Here $\mathcal{T} = \sum_n |t_n|^2$, G_0 is a conductance quantum. The right and the left arrows denote the direction of propagation of an electron.

Unexpected feature of the considered systems is presence of states with absolute ideal reflection. They can be searched in the form (3) with all $t_n = 0$ for $n \geq 0$, $r_0 = -1$ and $r_n = 0$ for $n > 0$:

$$e^{-iEt}\theta(-x)\sin px + \sum_{n<0} t_n e^{-|p_n||x| - i(E+n\omega)t}, \tag{7}$$

where

$$t_n(p_n + iu) + \frac{v}{2}(t_{n+1} - t_{n-1}) = 0 \tag{8}$$

for $n < 0$. The Eqs. (8) have normable solutions exponentially decaying with n for $n \to -\infty$. These solutions correspond to

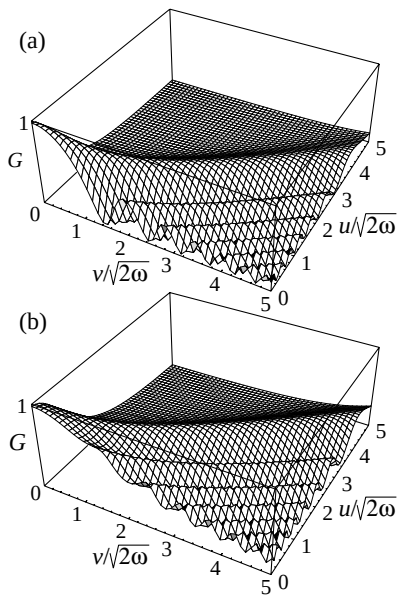

Fig. 1. Conductance of vibrating delta-well in units G_0 *vs* parameters of the potential u and v. The Fermi energy has values 0.5ω (a), 1.5ω (b). The minima of G achieve zero at $E_F = 0.5\omega$, but not at $E_F = 1.5\omega$.

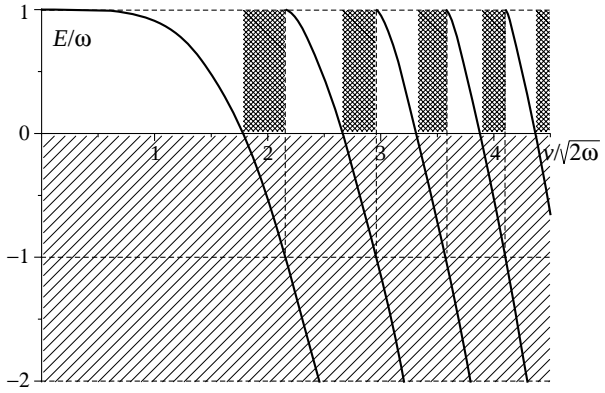

Fig. 2. Quasienergies of blockade states versus amplitude of alternating signal v. For convenience the expanded-bands scheme is depicted. Vertical dashed lines mark the values v, when the local states appear. Transmission coefficients are defined in the domain of positive energies (white). Non-physical domain of negative energies is single-dashed. Cross-dashing marks forbidden values of v (forbidden band), where conductance does not vanish for any E_F.

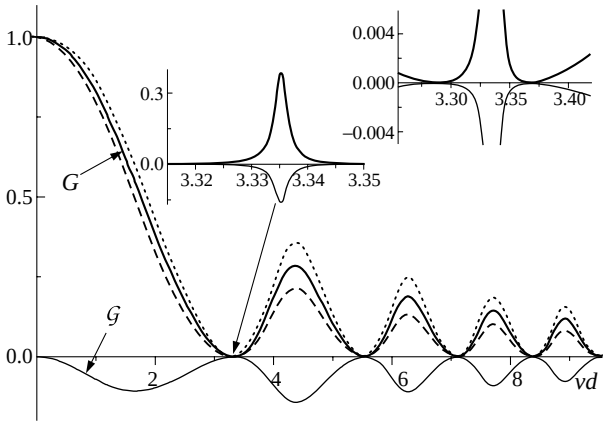

Fig. 3. The conductance (bold) and the derivative of photogalvanic current on chemical potential (thin) in units of G_0 as a function of amplitude in the double-well structure. Dashed and dotted lines show the transmission coefficients from left and right $\mathcal{T}^{\rightarrow}$ and $\mathcal{T}^{\leftarrow}$. The inserts show the neighborhood of conductance zeroes with different magnification. The parameters of the graph are: $\omega = 5$, $p_F = \pi/2d$, $\varphi = \pi/2$, $u_1 = u_2 = 0$, $v = v_1 = v_2$.

absolute reflection with conservation of electron energy. The demand of absolute reflection determines isolated eigenvalues of incident particle energy. This blockade is explained by interference of different channels of reflection.

The Fig. 1 shows the conductance for different energies. In the first quasienergy band $0 < E < \omega$ the conductance vanishes on the curves in (u, v) plane. These zeroes correspond to the eigenvalues for the Eq. (8), see the Fig. 2.

The double-well structure was subject of study as a simplest example of quantum pumps [5, 6]. Here we consider the case of strong alternating signal. The figure 3 shows the conductance G and the derivative of photocurrent with respect to the Fermi level $\mathcal{G}$ as functions of $v = v_1 = v_2$ at $u = 0$. The resonant case is chosen when just half of Fermi wavelength is equal to the distance between the wells and the electrons can be confined there.

In rough approximation the dependence of G is similar to the case of single well (Fig. 1). The situation changes in the

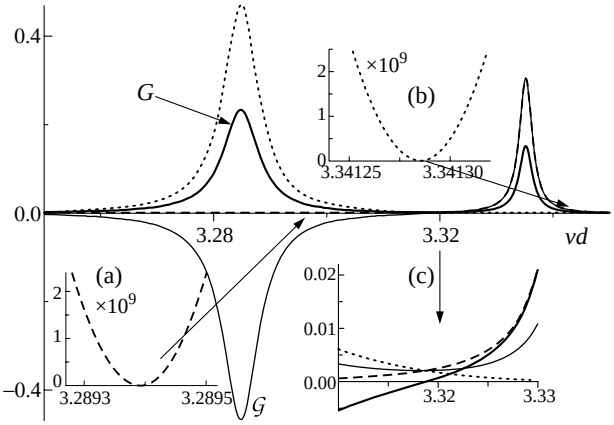

Fig. 4. The same domain as in the Fig. 3 for weak asymmetry of the potentials: $v = v_1 = v_2 - 0.1/d$, the other parameters correspond to Fig. 3. For these values the main picture does not change, while the neighborhood of conductance zeroes undergoes strong changes: $\mathcal{T}^{\rightarrow}$ has only right peak, while $\mathcal{T}^{\leftarrow}$ has left peak. Zeroes of $\mathcal{T}^{\rightarrow}$ and $\mathcal{T}^{\leftarrow}$ (inserts a) and b)) become separated (insert c)).

vicinity of zeroes (inserts to 3). In a symmetric case the zero is replaced by very narrow peak, surrounded by two zeroes of G and $\mathcal{G}$. This structure is explained by the splitting of single-well local states due to overlapping of their wave functions. That results in typical behavior of the stationary current: it vanishes near the local level of a single well which is double-splitted. The resonances are exclusively narrow.

The Fig. 4 shows the influence of weak asymmetry: $v_1 = v = v_2 - 0.1/d$. The rough picture does not change, while the fine structure change essentially: the transparency of the well from the left $\mathcal{T}^{\rightarrow}$ and from the right $\mathcal{T}^{\leftarrow}$ vanish but for different values of amplitude. Hence the asymmetric system plays role of "single-sided ideal mirror". The quantity $\mathcal{G}$ vanishes in the point where $t^{\rightarrow} = t^{\leftarrow}$.

Thus, we have demonstrated that the vibrating potential well (wells) can in resonant conditions produce full blockade of transport through the structure. The absolute reflectivity can be utilized for controlled confinement in low-dimensional structures of electrons with positive energies.

Acknowledgements

The work was supported by the Program for support of scientific schools of the Russian Federation grant No. 4500.2006.2, by the Russian Foundation for Basic Research grant No. 04-02-16398, by the President of the Russian Federation grant No. MK-8112.2006.2 and the Dynasty Foundation.

References

[1] D. J. Thouless, *Phys. Rev. B* **27**, 6083 (1983).
[2] P. W. Brouwer, *Phys. Rev. B* **58**, R10135 (1998).
[3] M. Moskalets and M. Büttiker, *Phys. Rev. B* **66**, 205320 (2002).
[4] S. W. Kim, *Int. J. Mod. Phys. B* **18**, 3071 (2004).
[5] L. S. Braginsky, M. M. Mahmoodian, M. V. Entin, *JETP* **100**, 920 (2005).
[6] M. M. Mahmoodian, L. S. Braginsky, M. V. Entin, *Phys. Rev. B* **74**, 125317 (2006).
[7] M. M. Mahmoodian, M. V. Entin, *Europhys. Lett.* **77**, 67002 (2007); cond-mat/0610832.
[8] O. A. Tkachenko, V. A. Tkachenko, and D. G. Baksheev, *Phys. Rev. B*, **54**, 13452 (1995).

15th Int. Symp. "Nanostructures: Physics and Technology"
Novosibirsk, Russia, June 25–29, 2007

Ponon dispersion in graphene

L. A. Falkovsky

L. D. Landau Institute for Theoretical Physics, Moscow 117334, Russia
Max-Planck-Institut für Physik Komplexer Systeme, Dresden, Germany

Abstract. Taking into account constraints imposed by the lattice symmetry, the phonon dispersion is calculated for graphene with interactions between first and second nearest neighbors. We show that only five force constants give a very good fitting to elastic constants and Raman frequencies observed in graphite.

Introduction

Since the discovery of graphene — a single atomic layer of graphene, main attention has been devoted to its electronic properties. More recently, Raman spectroscopy extends to investigations of graphene. For interpretations of the Raman scattering as well as of the transport phenomena, the detailed knowledge of the lattice dynamics and the electron-phonon interactions is needed.

The first-principles calculations of dynamical properties for graphite and graphene (and also for diamond) show that distinctions between the phonon frequencies in graphene and relating ones in graphite are negligible in comparison with the experimental errors for that frequencies in graphite. This could be intuitively expected for the highest frequencies because interactions between the layers in graphite are weak.

Our aim here is to find an analytical description of the phonon dispersion in graphene. This can be done within the framework of the Born–von-Karman model for the honeycomb graphene lattice with interactions only between first and second nearest neighbors, but the constraints imposed by the lattice symmetry should be taken into account.

1. Symmetry constraints on the dynamical matrix

Graphene consists of two atoms in the unit cell and correspondingly two sublattices. Each atom, for instance, $\mathbf{A}_0$ has three first neighbors in the other sublattice, i.e., B and six second neighbors in the same sublattice A. For the nearest neighbors (in the B sublattice), the Fourier transform of the dynamical matrix has the form

$$\phi_{ij}^{\mathrm{AB}}(\mathbf{q}) = \sum_{\kappa=1}^{3} \Phi_{ij}^{\mathrm{AB}}(\mathbf{B}_\kappa) \exp(i\mathbf{q}\mathbf{B}_\kappa), \tag{1}$$

and similar form for the next neighbors (in the A sublattice).

Symmetry group C_{6v} of the honeycomb lattice places constraints on the dynamical matrix. To obtain them, we introduce variables $\xi, \eta = x \pm iy$ transforming under the rotation $\mathbf{C}_3$ around the z-axis (taken at the $\mathbf{A}_0$ atom in the A sublattice) as follows $(\xi, \eta) \to (\xi, \eta)\exp(\pm 2\pi i/3)$. In the rotation, the atoms change their positions $\mathbf{B}_1 \to \mathbf{B}_2 \to \mathbf{B}_3$, $\mathbf{A}_1 \to \mathbf{A}_3 \to \mathbf{A}_5$, and $\mathbf{A}_2 \to \mathbf{A}_4 \to \mathbf{A}_6$. Therefore, all the force constants $\Phi_{\xi\eta}^{\mathrm{AB}}(\mathbf{B}_\kappa)$ with the different κ (as well as $\Phi_{zz}^{\mathrm{AB}}(\mathbf{B}_\kappa)$) are equal to one another, but the force constants with the coincident subscripts ξ or η transform as covariant variables. For instance,

$$\begin{aligned} \Phi_{\xi\xi}^{\mathrm{AB}}(\mathbf{B}_1) &= \Phi_{\xi\xi}^{\mathrm{AB}}(\mathbf{B}_2)\exp(2\pi i/3) \\ &= \Phi_{\xi\xi}^{\mathrm{AB}}(\mathbf{B}_3)\exp(-2\pi i/3). \end{aligned} \tag{2}$$

The relation between $\Phi_{\xi\xi}^{\mathrm{AA}}(\mathbf{A}_\kappa)$ with $\kappa = 1, 3, 5$ (and also for $\kappa = 2, 4, 6$) has the same form. The constants $\alpha_z = \Phi_{zz}^{\mathrm{AB}}(\mathbf{B}_1)$, $\gamma_z = \Phi_{zz}^{\mathrm{AA}}(\mathbf{A}_1)$, $\alpha = \Phi_{\xi\eta}^{\mathrm{AB}}(\mathbf{B}_1)$, and $\gamma = \Phi_{\xi\eta}^{\mathrm{AA}}(\mathbf{A}_1)$ are evidently real. The constant $\beta = \Phi_{\xi\xi}^{\mathrm{AB}}(\mathbf{B}_1)$ is real because the reflection $(x, y) \to (x, -y)$ with $\mathbf{B}_1 \to \mathbf{B}_1$ belongs to the symmetry group. Besides, for the first and second neighbors, we have one complex force constant $\delta = \Phi_{\xi\xi}^{\mathrm{AA}}(\mathbf{A}_1)$.

Two force constants $\Phi_{zz}^{\mathrm{AA}}(\mathbf{A}_0)$ and $\Phi_{\xi\eta}^{\mathrm{AA}}(\mathbf{A}_0)$ for the atom $\mathbf{A}_0$ can be excluded with the help of conditions imposed by invariance with respect to the translations of the layer as a whole in the x/z directions. Using the equations of motion and Eqs. (1),(2), we find this stability condition

$$\Phi_{\xi\eta}^{\mathrm{AA}}(\mathbf{A}_0) + 6\Phi_{\xi\eta}^{\mathrm{AA}}(\mathbf{A}_1) + 3\Phi_{\xi\eta}^{\mathrm{AB}}(\mathbf{B}_1) = 0 \tag{3}$$

and the similar form for the zz components.

The force constants $\alpha, \beta, \gamma, \delta$ obey another condition

$$\alpha - \beta + 6[\gamma - \mathrm{Re}\,\delta] = 0\,. \tag{4}$$

resulting from invariance with respect to the rotation of the layer around the z axis

2. Dispersion of the bending out-plane modes

In the first and second neighbor approximation, the out-plane vibrations u_z^{A}, u_z^{B} in the z direction are not coupled with the in-plane modes. The corresponding dynamical matrix for the out-plane modes has the form

$$\begin{pmatrix} \phi_{zz}^{\mathrm{AA}}(\mathbf{q}) & \phi_{zz}^{\mathrm{AB}}(\mathbf{q}) \\ \phi_{zz}^{\mathrm{AB}}(\mathbf{q})^* & \phi_{zz}^{\mathrm{AA}}(\mathbf{q}) \end{pmatrix}, \tag{5}$$

where

$$\begin{aligned} &\phi_{zz}^{\mathrm{AA}}(\mathbf{q}) \\ &= 2\gamma_z[\cos(\sqrt{3}q_y) + 2\cos(3q_x/2)\cos(\sqrt{3}q_y/2) - 3] - 3\alpha_z, \\ &\phi_{zz}^{\mathrm{AB}}(\mathbf{q}) \\ &= \alpha_z[\exp(iq_x) + 2\exp(-iq_x/2)\cos(\sqrt{3}q_y/2)]. \end{aligned} \tag{6}$$

The phonon dispersion for the out-plane modes is found

$$\omega_{\mathrm{ZO,ZA}}(\mathbf{q}) = \sqrt{\phi_{zz}^{\mathrm{AA}}(\mathbf{q}) \pm |\phi_{zz}^{\mathrm{AB}}(\mathbf{q})|}. \tag{7}$$

Expanding Eq. (7) in powers of the wave vector $\mathbf{q}$, we find the velocity of the acoustic out-plane mode propagating in the layer

$$s_z = a\left[-.75\alpha_z - 4.5\gamma_z\right]^{1/2} = \sqrt{C_{44}/\rho}, \tag{8}$$

where we use the well-known formula for the velocity of the acoustic z-mode propagating in the x-direction in terms of the elastic constant C_{44} and dencity ρ of a hexagonal crystal. Because the interaction between the layers in graphite is weak, we can correspond the values of C_{44} and ρ to graphite.

3. Dispersion of the in-plane modes

The dynamical matrix for the in-plane vibrations has the form similar to that for the in-plane mode (5), but instead of the functions $\phi_{zz}^{\rm AA}(\mathbf{q})$ and $\phi_{zz}^{\rm AB}(\mathbf{q})$ we have to substitute respectively the 2×2 matrices

$$\phi^{\rm AA}(\mathbf{q}) = \begin{pmatrix} \phi_{\xi\eta}^{\rm AA}(\mathbf{q}) & \phi_{\xi\xi}^{\rm AA}(\mathbf{q}) \\ \phi_{\xi\xi}^{\rm AA}(\mathbf{q})^* & \phi_{\xi\eta}^{\rm AA}(\mathbf{q}) \end{pmatrix}, \tag{9}$$

$$\phi^{\rm AB}(\mathbf{q}) = \begin{pmatrix} \phi_{\xi\eta}^{\rm AB}(\mathbf{q}) & \phi_{\xi\xi}^{\rm AB}(\mathbf{q}) \\ \phi_{\eta\eta}^{\rm AB}(\mathbf{q}) & \phi_{\xi\eta}^{\rm AB}(\mathbf{q}) \end{pmatrix}. \tag{10}$$

The matrix elements $\phi_{\xi\eta}^{\rm AA}(\mathbf{q})$ and $\phi_{\xi\eta}^{\rm AB}(\mathbf{q})$ are obtained from $\phi_{zz}^{\rm AA}(\mathbf{q})$ and $\phi_{zz}^{\rm AB}(\mathbf{q})$, Eqs. (6), respectively, with substitutions γ and α instead of γ_z and α_z. The off-diagonal elements are given by

$$\begin{aligned} &\phi_{\xi\xi}^{\rm AA}(\mathbf{q}) \\ &= \delta\left[\exp(i\sqrt{3}q_y)+2\cos(3q_x/2+2\pi/3)\exp(-i\sqrt{3}q_y/2)\right] \\ &+\delta^*\left[\exp(-i\sqrt{3}q_y)+2\cos(3q_x/2-2\pi/3)\exp(i\sqrt{3}q_y/2)\right], \\ &\phi_{\xi\xi}^{\rm AB}(\mathbf{q}) \\ &= \beta\left[\exp(iq_x)+2\exp(-iq_x/2)\cos(\sqrt{3}q_y/2-2\pi/3)\right]. \end{aligned} \tag{11}$$

The matrix elements for the B sublattice can be obtained from that ones for the A sublattice by C_2 rotation $(x, y)\to -(x, y)$ from the graphene symmetry group.

The optical phonon frequencies for the in-plane branches at Γ and K are found

$$\begin{aligned} \omega_{1,2}^{\rm in-pl}(\Gamma) &= \sqrt{-6\alpha}, \quad \text{doublet}, \\ \omega_{1,2}^{in-pl}(K) &= \sqrt{-3\alpha-9\gamma}, \quad \text{doublet}, \\ \omega_{3,4}^{in-pl}(K) &= \sqrt{-3\alpha-9\gamma\pm 3\beta}. \end{aligned} \tag{12}$$

Using Eqs. (9)–(11), we find in the explicit form the in-plane mode dispersion for the $G-K$ direction and an algebraic equation of the forth order have to be solved for the M point as well as for points of the general position.

The in-plane vibrations make a contribution into the elastic constants C_{11} and C_{12}. The corresponding relation between the dynamical matrix elements and the elastic constants can be deduced taking the long-wavelength limit ($\mathbf{q}\to 0$) in the matrices (9) and (10). We write the squared velocities of the LA and TA in-plane modes in the form

$$\begin{aligned} C_{11}/\rho &= a^2(s_1+|s_2|),\ (C_{11}-C_{12})/2\rho = a^2(s_1-|s_2|), \\ s_1 &= -4.5\gamma-.75(\alpha-|\beta|^2/\alpha),\ s_2 = 2.25\mathrm{Re}\,\delta-.375\beta, \end{aligned}$$

corresponding them to elastic constants and density of graphite.

The calculated phonon dispersion is shown in Fig. 1. Notice, first, that the sound velocities (for the long waves, $q\to\Gamma$) are isotropic in the $x-y$ plane as it should be appropriate for the C_6 symmetry of graphene. Second, the in-plane LO/TO modes at Γ, the in-plane LO/LA modes at K, and the out-plane ZA/ZO modes at K are doubly degenerate, because graphene is the non-polar crystal and the C_{3v} symmetry of these points in the Brillouin zone admits the two-fold representation (observation of splitting of that modes in graphene would display the symmetry braking of the crystal).

For lack of information about graphene, we compare the present theory with experiments on graphite. We prefer to obtain more accurate fitting for the higher frequencies because the absence of the neighboring layers in graphene affects more intensively the low frequencies. Moreover, the low frequencies in graphene for the out-plane branches have to be less than their values in graphite,

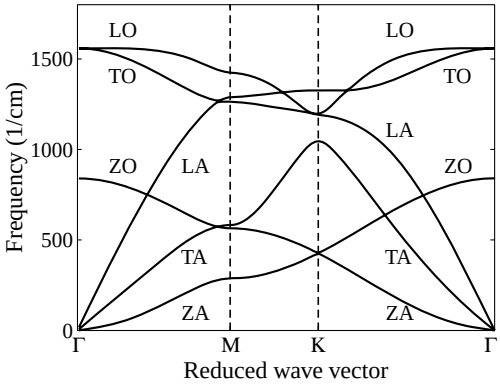

Fig. 1. Calculated phonon dispersion for graphene.

since the atoms are more free to move in the z direction in graphene comparatively with graphite.

Thus, we have only two force constants α_z and γ_z to fit four Raman frequencies of the out-plane modes and one elastic constant C_{44}. The constant α_z is determined by the Raman frequency $\omega_{\rm ZO}$, Eq. (7). The sound velocity s_z, Eq. (8), is very sensitive to the small variation of γ_z and becomes complex for $\gamma_z > 0.2\times 10^5$ cm^{-2}, that is only 10% greater than the value used for Fig. 1. This indicates that graphene is nearly unstable with respect to transformation into a phase of the lower symmetry group at Γ. From the results of fitting, one can see also that the phonon frequencies for the z modes turn out less than their values in graphite.

Fitting of the in-plane branches is unsensitive to the imaginary part of the constant δ. Therefore, it is taken as a real parameter. Thus, for the in-plane mode, we have to fit eight Raman frequencies and two elastic constants using three force constants. Results of fitting are presented in Fig. 1. Notice, that the extent of agreement of the present theory with the data obtained for graphite corresponds to the comparison level between the first-principal calculations for graphite and their experimental data. We see only qualitative discrepancy in the subsequence of the levels at M: in Fig. 1 the highest level is the LO mode, whereas the crossover of the TO and LO modes is found in the first-principl calculations on the Γ-M line (similar to Γ-K line), yielding the TO mode higher at M. We examined versions with the crossover. The agreement with experiments is not so good in these cases as for one that shown in Fig. 1, but the discrepancies of the order of 50 cm^{-1} between the different experiments as well as the distinctions between graphene and graphite do not allow us to choose the version conclusively. The experiment on graphene would clarify this point.

15th Int. Symp. "Nanostructures: Physics and Technology"
Novosibirsk, Russia, June 25–29, 2007

Quantum Hall plateau-plateau transition in p-Ge/$Ge_{1-x}Si_x$ and n-$In_xGa_{1-x}As$/GaAs heterostructures

Yu. G. Arapov, G. I. Harus, *I. V. Karskanov*, V. N. Neverov, N. G. Shelushinina and M. V. Yakunin
Institute of Metal Physics RAS, Ekaterinburg, GSP-170, 620219, Russia

Introduction

The quantum Hall effect (QHE) regime may be regarded as a sequence of quantum phase insulator-metal-insulator transitions when the density of states of 2D system in quantizing magnetic fields is scanned by the Fermi energy. In terms of this conception the transition regions between adjacent QHE plateaux, as well as the width of appropriate $\rho_{xx}(B)$ peaks, should get more and more narrow as the temperature approaches zero. In the theoretical framework of scaling [1] the width of the transition regions goes to zero as

$$\delta B_{i\to(i+1)} \sim T^{\kappa}, \tag{1}$$

where $\kappa = 1/zn$, $n = 7/3$ is the critical index of localization length and $z = 1$ is the dynamical critical index.

The pioneer experimental study of Wei *et al* [2] on low mobility InGaAs/InP heterostructures has strongly supported the power law behavior of Eq. (1). The evolution of the width of the ρ_{xx} peaks and of the inverse maximal slope of the ρ_{xy} steps, $(d\rho_{xy}/dB)^{-1}_{\max}$, as a function of temperature corresponds to (1) with nearly universal value of exponent $\kappa = 0.42 \pm 0.05$ for several Landau levels. The scaling behavior with $\kappa = (0.42-0.46)$ has been reported later for QHE plateau-to-plateau transition in GaAs/AlGaAs heterostructures and in p-SiGe quantum wells, but in series of experimental works the universality of exponent κ was questioned (see references in review article [1]).

In a work of Shahar *et al* [3] a transport regime distinct from the critical scaling behavior was reported to exist asymptotically close to the transition at very low temperatures. Studying the QHE-to-insulator transition in a variety of GaAs/AlGaAs and InGaAs/InP samples at temperatures down to 70 mK, they found an exponential dependence of ρ_{xx} on filling factor (FF) on the both sides of the critical FF value ν_c ($\Delta\nu = |\nu - \nu_c|$):

$$\rho_{xx} = \exp(-\Delta\nu/\nu_0(T)) \tag{2}$$

and emphasized that the effective transition width $\nu_0(T)$ appears to vary as $\alpha T + \beta$ rather than to exhibit T^{κ} scaling behavior. It means that even at $T = 0$ the transition is of a finite width.

Experimental results and discussion

To estimate the width of a band of delocalized states in our n-InGaAs/GaAs and p-Ge/$Ge_{1-x}Si_x$ samples we have analyzed magnetoresistance data in transition region between the first and second ($1 \to 2$) QHE plateaux. We used the description of $\sigma_{xy}(B)$ dependences in terms of so-called scattering parameter

$$s = \exp(-\Delta\nu/\nu_0(T)). \tag{3}$$

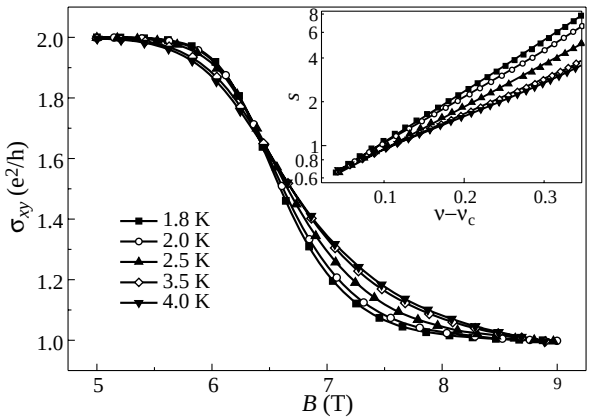

Fig. 1. Hall conductivity plotted as a function of magnetic field for InGaAs/GaAs sample at different temperatures. The inset shows a scattering parameter s, derived from σ_{xy} according to (4), as a function of filling factor ν ($\nu_c = 1.5$).

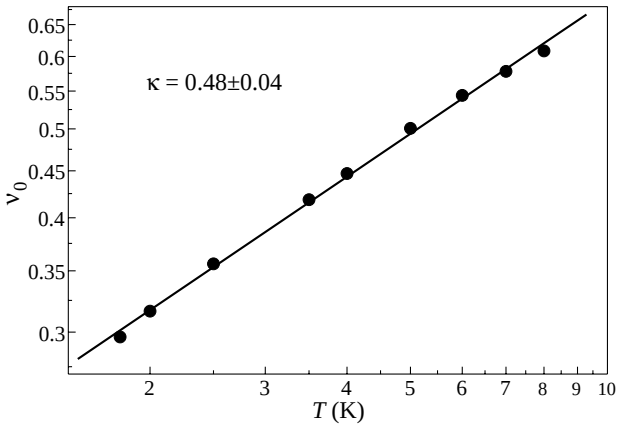

Fig. 2. Temperature dependence of $\nu_0(T)$ plotted in a log-log scale for InGaAs/GaAs sample.

For $1 \to 2$ plateau-to-plateau transition the scattering parameter can be extracted according to

$$\sigma_{xy} = 2 - s^2/\left(1 + s^2\right). \tag{4}$$

On Fig. 1 the Hall conductivity in transition $1 \to 2$ plateau-plateau region as a function of magnetic field at different temperatures for n-InGaAs/GaAs heterostructure with electron density $n_s = 2.3\times10^{11}$ cm^{-2} and mobility $\mu = 1\times10^4$ cm^{2}V/s is presented. The dominant contribution to disorder for investigated InGaAs/GaAs samples is of short-range character (a scattering on interface roughness [4]).

Fig. 2 shows $\nu_0(T)$ dependence extracted according to Eq. (3) for the same sample as in Fig. 1. We see a rather good power-law scaling in the temperature range from 1.8 K to 8 K with a

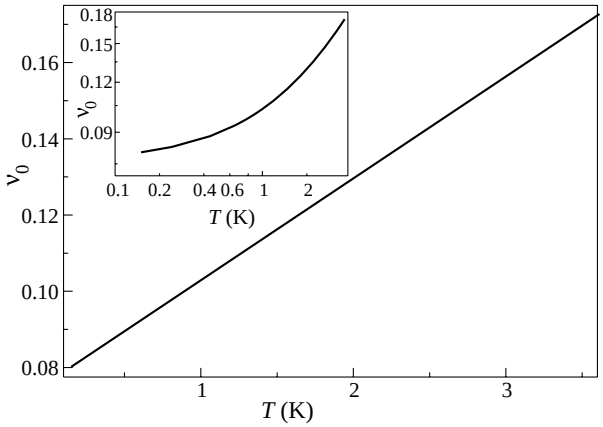

Fig. 3. A linear graph of $\nu_0(T)$ plotted against T for Ge/GeSi sample. Solid line is the best fit. Inset: dependence of $\nu_0(T)$ plotted in a log-log scale.

critical exponent $\kappa = 0.48 \pm 0.04$.

Fig. 3 depicts $\nu_0(T)$ dependences presented on a log-log graph (see inset) and in a linear scale for p-Ge/$Ge_{1-x}Si_x$ heterostructures with hole density $p_s = 2.4 \times 10^{11}$ cm^{-2} and mobility $\mu_p = 1.1 \times 10^4$ cm^{2}V/s and predominantly long-range impurity potential (a scattering on remote impurities [5]). It is seen that the data cannot be satisfactorily described by a power law $\nu_0(T) \sim T^\kappa$ (it is not a straight line on a log-log plot). On the other hand the data are much more compatible with a linear dependence

$$\nu_0(T) = \alpha T + \beta \qquad (5)$$

with $\alpha = 0.027$, $\beta = 0.076$.

In the theoretical work of Pruisken *et al* [6] and in recent works [7–9] it is emphasized an essential importance of *short-range* random potential scattering for experimental probing of scaling phenomena as the long-range potential fluctuations dramatically complicate the observability of the quantum critical phenomenon. The art experiments of W. Li *et al* [9] on $Al_xGa_{1-x}As/Al_{0.33}Ga_{0.67}As$ quantum wells with controlled short-ranged alloy potential fluctuations confirmed universal scaling with $\kappa = 0.42 \pm 0.01$ for plateau-plateau transitions in the range $0.0065 < x < 0.016$. For larger values of x an exponent κ increases to ~ 0.58 due to clustering of Al atoms which introduces correlation in the sample that may change the nature of disorder destroying therefore the universal scaling.

On the other hand, in opinion of Pruisken *et al* [6] the linear in T behavior of $\nu_0(T)$ is semiclassical in nature and should be observed in samples with predominantly slowly varying potential fluctuations. The most simple and natural reason of the linear $\nu_0(T)$ dependence, namely, the thermal broadening of a quantum critical phase transition, is suggested and confirmed by calculation in the work of Coleridge and Zawadzki [10].

The answer on the main question about the finite $T \to 0$ width of QHE transitions, we think, may be found in the works treating the influence of Coulomb interactions on the screening of smooth disorder potential [11]. The theory includes screening within Thomas–Fermi approximation appropriate for a smooth disorder.

The effect of electron-electron interaction manifests in that the regions of the third kind occur in the sample in addition to the local areas of full and empty Landau levels presented in the noninteracting system. The new "metallic" regions are ones in which the local electron density is between zero and that of the full Landau level. Then the percolation description must be revised as the metallic region percolates through the sample over a finite range of magnetic field near the critical value. One therefore expects transition between QHE plateaux to have a finite width in filling factors even in the low temperature limit.

Conclusions

In summary, qualitatively different temperature dependences of QHE plateau-to-plateau transition width $\nu_0(T)$ are observed for investigated n-InGaAs/GaAs heterostructures with predominantly short-range scattering potential and for p-Ge/GeSi heterostructures with predominantly smooth character of disorder. As the real scaling behavior, $\nu_0(T) \sim T^\kappa$, with exponent $\kappa = 0.48 \pm 0.04$, close to the theoretical value, has been observed for InGaAs/GaAs, the semiclassical in nature linear temperature dependence of $\nu_0(T)$ takes place for Ge/GeSi samples. Thus, our results are in accordance with conclusions of Refs. [6–9] that the dominant scattering mechanism of electrons should be of a short-range character in order to experimentally observe the true low-temperature asymptotics of the quantum phase transition — the scaling behavior of $\nu_0(T)$.

Acknowledgements

The work was supported by: Russian Foundation for Basic Research RFBR, grant No. 05-02-16206; program of Russian Academy of Sciences "Low-dimensional quantum heterostructures".

References

[1] B. Huckestein, *Rev. Mod. Phys.* **67**, 357 (1995).
[2] H. P. Wei, *et al*, *Phys. Rev. Lett.* **61**, 1294 (1988).
[3] D. Shahar, *et al*, *Sol. St. Commun.* **107**, 19 (1998).
[4] G. M. Minkov, *et al*, *Phys. Rev. B* **70**, 035304 (2004).
[5] Yu. G. Arapov, *et al*, *Nanotechnology* **13**, 86 (2002).
[6] A. M. M. Pruisken, B. Ŝcoriĉ, M. A. Baranov, *Phys. Rev. B* **60**, 16838 (1999).
[7] A. M. M. Pruisken, *et al*, *Sol. St. Commun.* **137**, 540 (2006).
[8] A. de Visser, *et al*, *cond-mat*/0608482.
[9] Wanli Li, G. A. Csáthy, *et al*, *Phys. Rev. Lett.* **94**, 206807 (2005).
[10] P. T. Coleridge and P. Zawadzki, *cond-mat*/9903246.
[11] N. R. Cooper and J. T. Chalker, *Phys. Rev. B* **48**, 4530 (1993).

15th Int. Symp. “Nanostructures: Physics and Technology”
Novosibirsk, Russia, June 25–29, 2007

Photogalvanic effect in 2D lattice of artificial scatterers: theory and numerical simulations

A. D. Chepelianskii[1], M. V. Entin[2], *L. I. Magarill*[2,3] and D. L. Shepelyansky[4]

[1] Ecole Normale Supérieure, 45, rue d'Ulm, 75231 Paris Cedex 05, France
[2] Institute of Semiconductor Physics, Siberian Division of Russian Academy of Sciences, Novosibirsk, 630090, Russia
[3] Novosibirsk State University, Novosibirsk, 630090, Russia
[4] Laboratoire de Physique Théorique, UMR 5152 du CNRS, Univ. P. Sabatier, 31062 Toulouse Cedex 4, France

Abstract. The stationary photocurrent is studied both analytically and by computer simulations in 2D regular and random system of asymmetric antidots: oriented semidisks and cuts with different reflectivity of sides.

The problem of stationary flow created by monochromatic fields in the systems with no inversion symmetry has a long history [1]– [4], but recently the interest to it has been renewed in connection to quantum pumps [5]– [8] and artificial 2D antidot lattices [9]– [12].

In the present report we study a 2D system of artificial scatterers in a monochromatic electric field. Namely, such scatterers are considered as oriented semidisks or cuts with one specular and another diffusive sides like those depicted in Fig. 1. The case of rare scatterers is studied analytically in the framework of kinetic equation approximation. The comparison of results for cuts and semidisks exhibits different polarization dependence. In particular, the linear polarization in x and y directions results in opposite values of electric current for the case of semidisks and different values for the model of cuts.

The stationary current is described by expression $j_i = \alpha_{ijk} E_j E_k^* + c.c.$ At $T = 0$ (a degenerate Fermi gas) the expressions for components of photogalvanic tensor α_{ijk} read

$$\alpha_{xxx} = -A\Big[(2-2s) + C\Big]a_{xxx} \qquad (1)$$

$$\alpha_{xyy} = A\Big[(2-2s)a_{xxx} - Ca_{xyy}\Big] \qquad (2)$$

$$\mathrm{Re}(\alpha_{yxy}) = -A\Big[(2-2s)a_{xyy} + \frac{C}{2}(a_{xyy} - a_{xxx})\Big]. \qquad (3)$$

Here, $A = e^3 V_F \tau^3/(\pi\tau_c(1+\omega^2\tau^2))$, $C = s(1-\omega^2\tau^2)/(1+\omega^2\tau^2)$, $\tau_c = 1/n_c v$ (cuts) or $\tau_c = \sqrt{3}R^2/(8r_d v)$ (semidisks) is the characteristic scattering time on asymmetric scatterers (n_c is the concentration of cuts, D is the cut length, R is the distance between semidisks, r_d is the radius of semidisk, $v = \sqrt{2\varepsilon/m}$ is the electron velocity), $\tau = \tau_i\tau_c/(\tau_i + \tau_c)$, where τ_i is the relaxation time of scattering on impurities; τ and τ_c are taken at $\varepsilon = \varepsilon_F$. We assume the power dependence of τ_i on electron energy, $\tau_i \propto \varepsilon^s$. The quantities a_{ijk} depend on the model of asymmetric scatterers. For the cuts model these quantities are equal to: $a_{xxx} = 1/48$, $a_{xyy} = -1/16$. For semidisks $a_{xxx} = -a_{xyy} = 1/12$. The formulas (1–3) with $s = -1/2$ follow also from the exact solution of the problem for cuts obtained in [12].

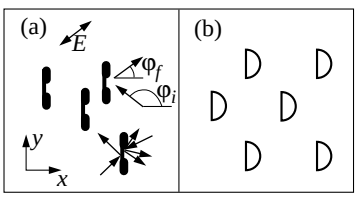

Fig. 1. Considered models of oriented scatterers. Left panel: model of vertical cuts with specular left side and diffusive right side. Right panel: model of triangular lattice of oriented semidisks. The electric field $\mathbf{E}\cos(\omega t)$ is linear-polarized under angle θ to $x-$axis.

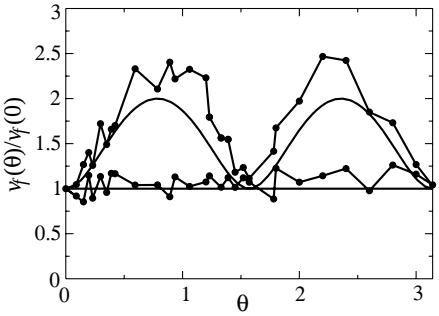

Fig. 2. Dependence of the rescaled absolute value of ratchet velocity $v_f(\theta)/v_f(\theta = 0)$ on the polarization angle θ for the cuts (top points at $\theta = 0.7$) and semidisks (bottom points at $\theta = 0.7$) models; corresponding theory is shown by smooth curves.

We performed numerical simulations of the cuts and semidisks models. The regular triangular lattice of semidisks is studied by computer simulations. This study was concentrated mostly on the case of moderately dense system. Nevertheless, the intersection of the applicability domains of analytical theory and simulations were also examined.

The Newton equations were solved numerically between collisions. The Maxwell (or Fermi–Dirac) equilibrium at temperature T is generated with the help of the Metropolis thermalization algorithm as it is described in [11]. The computation time along one trajectory is about few hundred thousands of microwave periods. Some results are shown in Figs. 2 and 3. They are in a very good agreement with the obtained theoretical expressions both for the cuts and semidisks models.

We also studied the effect of external magnetic field on electron dynamics in considered systems in presence of alternating electric field. The dense system exhibits many features of dynamic chaos. In particular, strong geometric resonances are observed in magnetic field caused by commensurability of the cyclotron radius and the lattice period.

For experiments on photogalvanic current in asymmetric nanostructures it is important to know what are the effects of

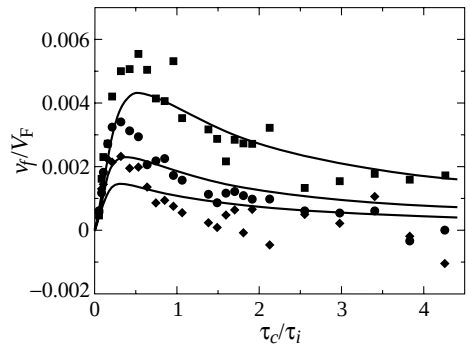

Fig. 3. Dependence of the rescaled velocity of ratchet v_f/V_F on the rescaled collision time τ_c/τ_i obtained by numerical simulations of the cuts mode (symbols) for $\omega\tau_i = 4.7; 7.05; 9.4$ (from top to bottom respectively at $\tau_c/\tau_i = 1$). The full curves show the theoretical dependence for corresponding $\omega\tau_i$ multiplied by a numerical factor $Q = 0.54$. Here, the equilibrium Fermi–Dirac distribution has the temperature $T/E_F = 0.1$ and $eE\tau_i V_F/E_F = 4.2$; the polarization angle $\theta = 0$.

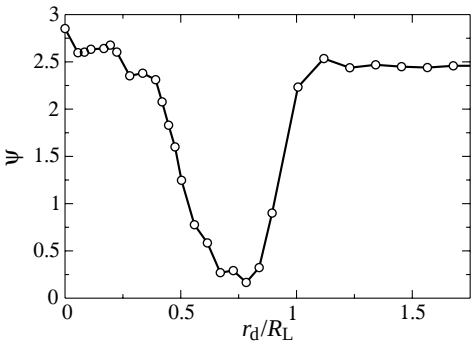

Fig. 4. Dependence of ratchet current angle ψ on a rescaled magnetic field $r_d/R_L \propto B$ at $\theta = 0$; curve with circles shows numerical data for the semidisks model with $R/r_d = 2.5$.

a magnetic field **B** perpendicular to the 2DES plane on the strength of current and its directionality. An analytic solution of the kinetic equation becomes much more complicated compared to the cases considered above. This is especially the case when the Larmour radius R_L of electron motion becomes comparable with the size of asymmetric antidots. Therefore, the numerical simulations in this case become especially important. For the semidisks Galton board the effects of magnetic field have been studied in [11]. They clearly show that the ratchet current becomes quite weak when the Larmor radius R_L becomes smaller then the semidisk radius r_d. This follows from so called "memory effects", the suppression of transport in conservative 2D system due to multiple returning of electron in strong magnetic field to the starting point.

However, in the regime with $r_d/R_L \sim 1$ a relatively weak magnetic field can significantly affect the directionality of photogalvanic current. This is illustrated in Fig. 4, where a moderate magnetic field changes the direction of current almost on 180 degrees. We attribute the origin of this strong angular dependence to a significant change of scattering process in the regime when $r_d/R_L \sim 1$ related to multiple collisions of electron with a semidisk.

For a structure of width 100 μm a microwave field of strength $eE = 1$ V/cm generates a current of about 20 nA at $R \sim 1$ μm and electron density $n_e = 2.5 \times 10^{11}$ cm^{-2}. At $R \sim 100$ nm the mean free path at room temperature becomes larger than the size of semidisks. Thus, the photogalvanic effect can be used for creation of room temperature detectors of radiation in teraherz range.

This work was supported in part by the ANR PNANO project MICONANO and (for MVE and LIM) by the grant of RFBR No. 04-02-16398, Program for support of scientific schools of the Russian Federation No. 4500.2006 and INTAS No. 03-51-6453.

References

[1] A. M. Glass, D. Linde and T. J. Negran, *Appl. Phys. Lett.* **25**, 233 (1974).
[2] V. I. Belinicher, V. K. Malinovskii and B. I. Sturman, *Sov. Phys. — JETP* **46**, 362 (1977); V. I. Belinicher and B. I. Sturman, *Sov. Phys. — Usp. Fiz. Nauk* **23**, 199 (1980).
[3] E. M. Baskin, M. D. Blokh, M. V. Entin, and L. I. Magarill, *Phys. Stat. Sol. (b)* **83**, K97 (1977).
[4] E. L. Ivchenko, G. E. Pikus, in Semiconductor Physics, V. M. Tushkevich and V. Ya. Frenkel, Eds., Cons. Bureau, p. 427, New York (1986).
[5] D. J. Thouless, *Phys. Rev. B* **27**, 6083 (1983).
[6] P. W. Brouwer, *Phys. Rev. B* **58**, R10135 (1998).
[7] M. Moskalets and M. Büttiker, *Phys. Rev. B* **66**, 205320 (2002).
[8] L. S. Braginskii, M. M. Makhmudian and M. V. Entin, *JETP* **100**, 920 (2005); M. M. Mahmoodian, L. S. Braginsky and M. V. Entin, *Phys. Rev. B* **74**, 125317 (2006).
[9] A. D. Chepelianskii and D. L. Shepelyansky, *Phys. Rev. B* **71**, 052508 (2005).
[10] G. Cristadoro and D. L. Shepelyansky, *Phys. Rev. E* **71**, 036111 (2005).
[11] A. D. Chepelianskii, *Eur. Phys. J. B* **52**, 389 (2006).
[12] M. V. Entin and L. I. Magarill, *Phys. Rev. B* **72**, 205206 (2006).

15th Int. Symp. "Nanostructures: Physics and Technology"
Novosibirsk, Russia, June 25–29, 2007

Acoustoelectric current through anisotropic quantum wire: effect of impurities

V. A. Margulis and I. A. Kokurin
Mordovian State University, 430000 Saransk, Russia

Abstract. The acoustoelectric (AE) current through an anisotropic parabolic quantum wire contained a system of ionized impurities is investigated. Using the kinetic approach the formula for impurity-assisted component of AE current is obtained. It was shown that presence of impurities leads to appearance of new oscillation peaks on the dependence of AE current on the chemical potential (which is controlled by the gate voltage) due to the fact that transitions between any dimensional sub-bands are allowed. The effect of temperature on the impurity-assisted current is studied.

Introduction

The interaction of surface acoustic waves (SAW) with electrons in mesoscopic systems has been attracting growing attention. In particular, the acoustoelectric (AE) effect (dc current induced by the SAW) was investigated experimentally in quantum channels defined in GaAs-Al$_x$Ga$_{1-x}$As heterostructures [1,2]. It was shown the AE current undergoes giant quantum oscillations as a function of the applied gate voltage [1], having maxima between the plateaux of the quantized conductance. The experimental study [2] presents step-like behavior of the AE current through a channel.

This problem has been considered theoretically in several papers [1,3–9]. The most of authors [6–9] used kinetic approach to describe the electron-SAW interaction, and the SAW was represented as a flux of monochromatic ultrasonic phonons with frequency $\omega_{\mathbf{q}} = sq$, where s is the sound velocity, $\mathbf{q}$ is the phonon wave vector. We will keep to above approach too.

Taking into account the potential possibility of the creation of various nanodevices based on AE effect it is necessary to investigate the effects of various defects of the structure on AE current. We know only one paper [8] where effect of impurities on AE current through low-dimensional system was investigated. Furthermore, very sophistical mathematical technique (non-equilibrium Green's function method) has been used to take into account effect of impurities on AE current. Here we offer a simple approach that does not pretend to the presentation of the exact solution, but it will facilitate (as we assume) the qualitative interpretation of the problem.

1. Statement of the problem

The aim of the present work is to study the behavior of the AE current through an anisotropic parabolic quantum wire in the presence of the ionized impurities inside the wire. We consider a system that consists of two bulk electronic reservoirs connected by a quantum wire. We assume that the reservoirs temperatures are equal, the same is true for electrochemical potentials. Thereby we exclude from consideration all transport effects except the acoustoelectric one. To model the quantum wire we use anisotropic parabolic confining potential, $V(x, y) = (m^*/2)(\omega_x^2 x^2 + \omega_y^2 y^2)$, where m^* is the effective mass of the electron; ω_x, ω_y are the characteristic frequencies of the parabolic potential.

We consider wire that contains N_i impurities modelled by the potential $V(\mathbf{r}) = \sum_{j=1}^{N_i} U(\mathbf{r} - \mathbf{R}_j)$, where $U(\mathbf{r} - \mathbf{R}_j)$ is the potential of a single impurity located at point $\mathbf{R}_j$. In our case $U(\mathbf{r})$ is screened Coulomb potential

$$U(r) = \frac{ze^2}{\epsilon r} \exp(-r/r_0), \tag{1}$$

where ze is the impurity charge, ϵ is the dielectric constant and r_0 is the screening radius that in our case is of the order of Thomas–Fermi screening length.

It is convenient to use the Fourier transformation for the impurity potential

$$U(r) = \sum_{\mathbf{q}} C_{\mathbf{q}} e^{i\mathbf{qr}}, \qquad C_{\mathbf{q}} = \frac{4\pi z e^2}{V_0 \epsilon} \frac{1}{q^2 + r_0^{-2}}. \tag{2}$$

Here V_0 is the normalization volume.

Eigenfunctions of the one-particle spinless Hamiltonian in a quantum wire are given by

$$|mnk\rangle = \Phi_m(x)\Phi_n(y)\frac{1}{\sqrt{L}} e^{ikz}, \tag{3}$$

where L is the wire's length, and $\Phi_n(x)$ are the eigenfunctions of harmonic oscillator, k is the electron wave vector along the wire. The spectrum corresponding to wave functions (3) has the form

$$E_{mnk} = \hbar\omega_x(m + 1/2) + \hbar\omega_y(n + 1/2) + \hbar^2 k^2/2m^*, \tag{4}$$

where $m, n = 0, 1, 2, \ldots$

2. Calculation of AE current

To calculate AE current through the quantum wire we use kinetic approach [6,7]

$$J = 2e \sum_{mn} \int_{-\infty}^{\infty} \frac{dk}{2\pi} v \Delta f_{mnk}(z). \tag{5}$$

Here Δf is the non-equilibrium component of electron distribution function that is the solution of the kinetic equation $v\partial\Delta f/\partial z = I[f]$ [6], with the boundary condition $\Delta f = 0$ for $z = \mp L/2$ [at $k > 0 (k < 0)$], $v = \partial E_{mnk}/\partial(\hbar k)$ is the electron velocity, $I[f]$ is the collision integral. Phonons obey the distribution $N_{\mathbf{q}} = N_0 \delta_{\mathbf{q},\mathbf{q_0}}$ [8] with $N_0 = SV_0/\hbar s^2 q_0$, S is the sound intensity. We assume the phonon beam propagates along a wire, $\mathbf{q_0} = (0, 0, q_0)$.

To calculate transition probability that determines the collision integral we use the second order of perturbation theory. The matrix element of such transition is given by

$$W^{\pm}_{\alpha\alpha'} = \sum_{\alpha''} \frac{\langle\alpha'|H^{\mathrm{e-i}}|\alpha''\rangle\langle\alpha''|H^{\mathrm{e-ph}}|\alpha\rangle}{E_{\alpha''} - E_{\alpha} \mp \hbar\omega_{\mathbf{q}}} + \sum_{\alpha''} \frac{\langle\alpha'|H^{\mathrm{e-ph}}|\alpha''\rangle\langle\alpha''|H^{\mathrm{e-i}}|\alpha\rangle}{E_{\alpha''} - E_{\alpha'} \pm \hbar\omega_{\mathbf{q}}}, \quad (6)$$

where $H^{\mathrm{e-ph}}$ and $H^{\mathrm{e-i}}$ are electron-phonon and electron-impurity coupling operator, respectively, and $|\alpha\rangle = |mnk\rangle$. The first term in Eq. (6) describes transitions where at first the electron absorbs (emits) phonon and then interacts with impurity, and the second term describes processes occurred in reverse sequence.

We have for the collision integral $I[f] = I^{+}[f] + I^{-}[f]$, where the sign $+(-)$ corresponds to processes of phonon absorption (emission)

$$I^{\pm}[f] = \frac{2\pi}{\hbar} \sum_{\alpha'} \left|W^{\pm}_{\alpha\alpha'}\right|^2 \Big[f^{\mathrm{F}}(E') - f^{\mathrm{F}}(E) \Big] \delta\left(E' - E \mp \hbar\omega_{\mathbf{q}}\right), \quad (7)$$

where $f^{\mathrm{F}}(\varepsilon) = [e^{(\varepsilon-\mu)/T} + 1]^{-1}$ is the Fermi distribution function, μ is the chemical potential, T is the temperature.

In the case of electron-phonon interaction we have for the matrix element

$$M^{\pm q}_{\alpha,\alpha'} = D_{\mathbf{q}}(N_{\mathbf{q}} + 1/2 \mp 1/2)^{1/2} \delta_{k',k\pm q_0} \delta_{m'm} \delta_{n'n}, \quad (8)$$

where $D_{\mathbf{q}}$ is the electron-phonon coupling constant that for the case of piezoelectric (PE) interaction and for the deformation potential (DP) is given by

$$D^{\mathrm{PE}}_{\mathbf{q}} = M_{\lambda}(\mathbf{e}_q)(\hbar/2\rho_0 V_0 \omega_{\mathbf{q}})^{1/2},$$
$$D^{\mathrm{DP}}_{\mathbf{q}} = D(\hbar q^2/2\rho_0 V_0 \omega_{\mathbf{q}})^{1/2},$$

where ρ_0 is the mass density, $M_{\lambda}(\mathbf{e}_q)$ is the PE coupling tensor (in our case it is the constant $M_{\lambda}(\mathbf{e}_q) \to M$), D is the DP constant. Note that for relatively small frequencies (1–3 GHz, as in the experiments in Refs. [1,2]), the PE interaction dominates.

For the electron-impurity interaction, we have

$$\langle\alpha'|V(r)|\alpha\rangle = \sum_{j=1}^{N_i} \sum_{\mathbf{q}} C_{\mathbf{q}} e^{-i\mathbf{q}\mathbf{R}_j} \langle\alpha'|e^{i\mathbf{q}\mathbf{r}}|\alpha\rangle. \quad (9)$$

These matrix elements were calculated exactly, but we do not write them because of the cumbersome form.

Combining Eqs. (5)–(9) we obtain the expression for the impurity-assisted component of the AE current. This expression is very cumbersome and we do not write it here. Some analysis of this expression is presented in the next section.

3. Discussion

The analysis of the expression for the impurity-assisted current shows that its dependence on the chemical potential is oscillatory one in the general case. The presence of the impurities leads to appearance of new oscillation peaks because transitions between any dimensional sub-bands are allowed.

Note that the use of kinetic approach gives the following fact: AE current through the perfect channel decays at sound frequencies ω_q less than threshold value $\omega_{\mathrm{th}} = 2m^* s^2/\hbar$ [6]. It is well-known that this restriction can be broken if the current will be calculated with regard to impurity scattering [8], or scattering in the region of conducting-channel contact with electronic reservoirs [7]. Our consideration leads to breakdown of the above restriction too, namely, we have non-zero current for the case of any sound frequency.

Let us note that it is not enough to sum only impurity-assisted current and AE current under ballistic regime [9]. To find the correct total current it is necessary to take into account that presence of the impurities does not change the total number of electron transitions, but they are redistributed among different scattering mechanisms. It is clear that the probability of the second-order processes is much smaller than the first-order one. Thus, our consideration represents the small correction to the current due to impurity scattering.

The analysis shows that decreasing of the lateral size of the system leads to increasing of the impurity-assisted current that can be associated with growing role of the impurity scattering in thin wires. The amplitudes of the oscillation peaks strongly correlate with location of each scattering center.

Note that our consideration does not pretend to the presentation of the exact solution. Using this approach we want to display the qualitative features in behavior of the impurity-assisted AE current. The main complexity of our model is the difficulty in application of the first Born approximation in Eq. (9). However we hope that our consideration represents qualitatively correct results.

Acknowledgement

This work has been supported by the Russian Foundation for Basic Research.

References

[1] J. M. Shilton, D. R. Mace, V. I. Talyanskii *et al*, *J. Phys.: Condens. Matter* **8**, L337 (1996).
[2] V. I. Talyanskii, J. M. Shilton, M. Pepper *et al*, *Phys. Rev. B* **56**, 15180 (1997).
[3] F. A. Maaø, and Yu. M. Galperin, *Phys. Rev. B* **56**, 4028 (1997).
[4] O. Entin-Wohlman, Y. Levinson, P. Wölfle, *Phys. Rev. Lett.* **85**, 634 (2000).
[5] O. Entin-Wohlman, Y. Levinson, P. Wölfle, *Phys. Rev. B* **64**, 195308 (2001).
[6] V. L. Gurevich, V. B. Pevzner, and G. J. Iafrate, *Phys. Rev. Lett.* **77**, 3881 (1996).
[7] V. L. Gurevich, V. I. Kozub, and V. B. Pevzner, *Phys. Rev. B* **58**, 13088 (1998).
[8] Ø. L. Bø, H. Totland and Yu. Galperin, *J. Phys.: Condens. Matter* **9**, 8381 (1997).
[9] V. A. Margulis, M. P. Trushin, and A. V. Shorokhov, *JETP* **94**, 1160 (2002).

15th Int. Symp. "Nanostructures: Physics and Technology"
Novosibirsk, Russia, June 25–29, 2007

Electron transport in crossed nanocylinders with point contact

V. A. Margulis and M. A. Pyataev
Mordovian State University, 430000 Saransk, Russia

Abstract. Electron transport in a four-terminal nanodevice consisting of two crossed conductive nanocylinders is considered. The evident formula for the ballistic conductance of the device is found from the first principles. Sharp conductance dips stipulated by resonance scattering on the contact are shown to appear in the conductance of the first cylinder. The conductance between the cylinders has resonant behavior. The form and the positions of resonant peaks are studied. We have shown that the maximal value of the conductance between the cylinders does not exceed a unit of conductance quantum due to the limited transparency of the point contact.

Introduction

The theoretical interest to the electron in transport crossed nanocylinders is stipulated by recent experimental studies of crossed carbon nanotubes [1–2]. A number of interesting theoretical models based on tight-binding approximation has been suggested to study physical properties of the contacts between nanotubes [3–6]. However the most of theoretical investigations are focused on the electron transport in nanotubes of sufficiently small diameter. At the same time, the diameter of tubes used in some experiments [1] were in the range of 25–30 nm. The application of the tight-binding approach to this systems is somewhat difficult because it requires considerable amount of computer time. Furthermore physical meaning of the phenomenon is sometimes smeared in sufficiently accurate but very complicated models. Thus it should be useful to study the electron transport through the contact between two nanotubes using a simple model which allows an exact analytical solution. The purpose of the present paper is the theoretical investigation of the electron transport in a four-terminal nanodevice consisting of two crossed nanotubes with a point contact between them. Each tube is modelled by a conductive cylindrical surface of radius r_j $(j = 1, 2)$.

1. Hamiltonian and conductance

If we ignore the contact between cylinders then electronic states are described by the unperturbed Hamiltonian $H_0 = H_1 \oplus H_2$ where H_1 and H_2 are electron Hamiltonians in the first and the second cylinder respectively. The electron wave function in this case consists of two independent parts ψ_1 and ψ_2. The Hamiltonian H of contacted nanocylinders is a point perturbation of the operator H_0. To define this perturbation we use linear boundary conditions at the point of contact.

We introduce two independent cylindrical coordinate systems and denote the point on the cylinder by $\mathbf{q} = (z, \varphi)$. Then the Hamiltonian H_j has the form

$$H_j = \frac{p_z^2}{2m^*} + \frac{L_z^2}{2m^* r_j^2}, \tag{1}$$

where m^* is the electron effective mass, p_z and L_z are the projections of the momentum and the angular momentum onto the axis of the cylinder.

The spectrum of the Hamiltonian H_j is given by the sum of the continuous part $p_z^2/(2m^*)$ and the discrete part $E_m^{(j)} = \varepsilon_j m^2$ where $\varepsilon_j = \hbar^2/(2m^* r_j^2)$ and m is the magnetic quantum number.

The boundary values for the wave function ψ_j of the electron in j-th cylinder are determined with the help of the zero-range potential theory [7–9]. The theory shows that the electron wave function $\psi_j(\mathbf{q})$ has the logarithmic singularity in a vicinity of the contact point $\mathbf{q}_0$

$$\psi_j(\mathbf{q}) = -u_j \ln \rho(\mathbf{q}, \mathbf{q}_0) + v_j + R(\mathbf{q}), \tag{2}$$

where $\rho(\mathbf{q}, \mathbf{q}_0)$ is geodesic distance between the points $\mathbf{q}$ and $\mathbf{q}_0$, u_j and v_j are complex coefficients, and $R(\mathbf{q}) \to 0$ with $\mathbf{q} \to \mathbf{q}_0$.

It is clear that the boundary conditions at the point of contact are some linear relations between u_1, v_1, u_2, and v_2. In the paper, we use the following form for the boundary conditions

$$\begin{cases} v_1 - b_1 u_1 = a u_2, \\ v_2 - b_2 u_2 = a^* u_1. \end{cases} \tag{3}$$

Here the coefficients b_1 and b_2 determine the strength of the zero-range potential at the point of contact and a is a dimensionless parameter responsible for the coupling of the wave functions in different cylinders. According to the zero-range potential theory [7] the parameters b_j can be represented in terms of the scattering lengths λ_j by the relation $b_j = 2 \ln \lambda_j$. It should be noted that the zero-range potential is attractive and the strength of the potential decreases with increasing of λ_j. The limit $\lambda_j \to \infty$ corresponds to the absence of the point perturbation.

In the paper, we investigate the conductance G_{11} of the first cylinder and the conductance G_{21} from the first cylinder to the second one. According to the Landauer–Büttiker formula the zero-temperature conductance G_{ji} can be expressed in terms of transmission coefficients $T_{m'm}^{ji}$ from the state with magnetic quantum number m in i-th cylinder to the state with m' in j-th cylinder. Solving the Schrödinger equation for the Hamiltonian H with the boundary conditions (3), we obtain transmission coefficients of the system. Using Landauer's formula we get the following equation for the conductance $G_{11}(\mu)$

$$\frac{G_{11}(\mu)}{G_0} = N(\mu) - \frac{(\operatorname{Im} Q_1)^2 |Q_2|^2}{|Q_1 Q_2 - |a|^2|^2} - 2\frac{|a|^2 \operatorname{Im} Q_1 \operatorname{Im} Q_2}{|Q_1 Q_2 - |a|^2|^2}. \tag{4}$$

Here $N(\mu)$ is the number of states with energy less than μ and $Q_j(E)$ is the Krein's Q-function that is the renormalized Green function of the Hamiltonian H_j. The explicit form for $Q_j(E)$ may be found in Ref. [9]

$$Q_j(E) = \frac{i}{r_j k_0^{(j)}} + 2\sum_{m=1}^{\infty} \left(\frac{i}{r_j k_m^{(j)}} - \frac{1}{m} \right) + 2 \ln \frac{r_j}{\lambda_j}, \tag{5}$$

where $\hbar k_m^{(j)} = \sqrt{2m^*(E - E_m^{(j)})}$, $\mathrm{Re}\, k_m \geq 0$ and $\mathrm{Im}\, k_m \geq 0$.

2. Results and discussion

Conductance G_{11} as a function of the Fermi energy μ is represented in Fig. 1. If the contact between the cylinders is absent ($a = 0$) then equation (4) contains only the first term and the dependence $G_{11}(\mu)$ is step-like (dotted line in Fig. 1). The second term in equation (4) is responsible for the back-scattering on the contact point and the last term is stipulated by the transmission of electrons from the first cylinder to the second one.

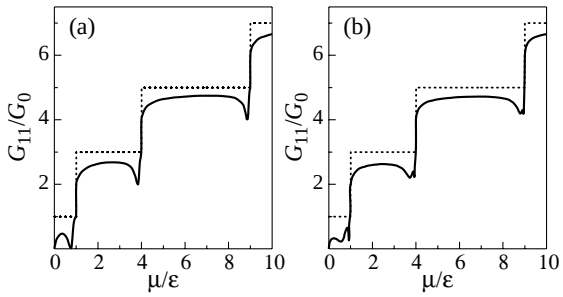

Fig. 1. Conductance G_{11} as a function of the chemical potential μ: (a) $r_1 = r_2$, $\lambda_1 = \lambda_2 = 3r_1$, $a = 0.1$; (b) $r_1 = r_2$, $\lambda_1 = \lambda_2 = 5r_1$, $a = 5$. Dotted line represents the conductance of the unperturbed cylinder.

The presence of the zero-range perturbation at the point of contact leads to appearance of virtual levels $\tilde{E} = E_\mathrm{R} - i\Gamma$ in the spectrum of the Hamiltonian H. Positions of the virtual levels are defined by equation

$$Q_1(\tilde{E})Q_2(\tilde{E}) - |a|^2 = 0. \tag{6}$$

The scattering on the virtual levels lead to a number of dips on the dependence $G_{11}(\mu)$. If the coupling between the wave functions on different cylinders is weak ($|a| \ll 1$) then the virtual level $\tilde{E}$ is situated in the vicinity of the root $\tilde{E}_1$ of the equation $Q_1(\tilde{E}_1) = 0$. The conductance has only one dip on each plateau in this case (Fig. 1(a)). The dip is situated near the point $\mathrm{Re}\, Q_1(E_1) = 0$. The maximal depth of the dip equals G_0. If $\lambda_1 \gg r_1$ then the dip is situated near the right edge of the conductance plateau. With decreasing λ_1, the dip shifts to the lower energies and disappears reaching the left edge of plateau.

An additional conductance minima appears on the graph $G_{11}(\mu)$ if the coupling between the wave functions on different cylinders is sufficiently strong $|a| \geq 1$ (Fig. 1(b)). These minima are stipulated by splitting of the virtual levels due to the interaction between electron states on the different cylinders. In the case of strong point perturbation ($\lambda_j \ll r_j$) and weak interaction between the wave functions ($a \ll 1$) the dips of the conductance are absent.

Let us consider now the conductance G_{21} which corresponds to the transmission of electrons from the first cylinder to the second one. Using the asymptotics of the wave function in the second cylinder and Landauer's formula, we obtain the following equation

$$G_{21}(\mu) = 4G_0 \frac{|a|^2\, \mathrm{Im}\, Q_1\, \mathrm{Im}\, Q_2}{|Q_1 Q_2 - |a|^2|^2}. \tag{7}$$

The conductance $G_{21}(\mu)$ vanishes when the Fermi energy μ coincides with $E_m^{(2)}$. The asymmetric resonance peak appears

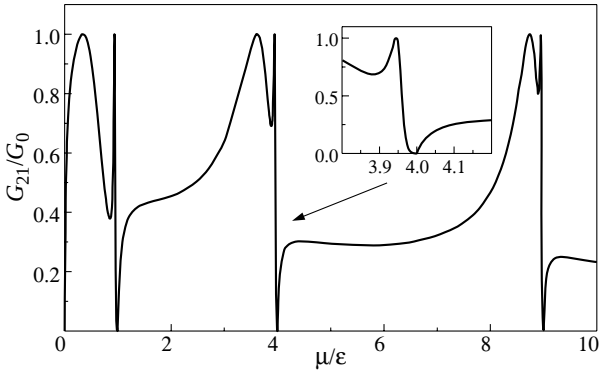

Fig. 2. The dependence $G_{21}(\mu)$. All parameters of the system are the same as in Fig. 1(a). The inset shows a fragment of the same curve in a vicinity of $\mu = 4\varepsilon$.

in a vicinity of the zero $\mu = E_m^{(2)}$ (Fig. 2). The form of the peak is similar to the Fano resonance line shape, however the dependence $G_{21}(\mu)$ at $T = 0$ is not smooth in contrast to the Fano curve.

Our analysis shows that the maximal value of the conductance $G_{21}(\mu)$ never exceed G_0. We relate this fact to limited transparency of the point contact. Similar results have been obtained in Ref. [6] for several crossed junctions of small nanotubes. It should be noted, that the resistance of the value 16.8 kΩ $\approx G_0^{-1}$ has been observed experimentally in crossed carbon nanotubes at $T = 4.2$ K [1].

Acknowledgement

The work is supported by the Russian Foundation for Basic Research (grant No. 05-02-16145).

References

[1] J. Kim *et al*, *Phys. Rev. Lett.* **90**, 166403 (2003).
[2] B. Gao *et al*, *Phys. Rev. Lett.* **92**, 216804 (2004).
[3] F. Y. Meng *et al*, *Phys. Rev. B* **70**, 125418 (2004).
[4] G. Kim *et al*, *Phys. Rev. B* **71**, 205415 (2005).
[5] H. T. Yang *et al*, *Phys. Rev. B* **71**, 073401 (2005).
[6] S. Dag *et al*, *Phys. Rev. B* **70**, 205407 (2004).
[7] Y. N. Demkov and V. N. Ostrovsky, *Zero-Range Potentials and Their Applications in Atomic Physics* (Plenum, New York, 1988).
[8] V. A. Geyler, V. A. Margulis, and M. A. Pyataev, *JETP* **97**, 763 (2003).
[9] V. A. Margulis and M. A. Pyataev, *Phys. Rev. B* **72**, 075312 (2005).

15th Int. Symp. "Nanostructures: Physics and Technology"
Novosibirsk, Russia, June 25–29, 2007

Hole-hole interaction at decreasing Drude conductivity

G. M. Minkov[1], A. A. Sherstobitov[2], A. V. Germanenko[2], O. E. Rut[2] and B. N. Zvonkov[3]

[1] Institute of Metal Physics RAS, 620219 Ekaterinburg, Russia
[2] Ural State University, 620083 Ekaterinburg, Russia
[3] Physical-Technical Research Institute, University of Nizhni Novgorod, 603600 Nizhni Novgorod, Russia

Abstract. The diffusion contribution of the hole-hole (h-h) interaction to conductivity is analyzed in gated GaAs/InGaAs/GaAs heterostructures. We show that the decrease of the interaction correction to the conductivity with the lowering Drude conductivity results from both the compensation of the singlet and triplet channels and from the arising of the prefactor $\alpha_i < 1$ in the conventional expression for the interaction correction.

The new interest in the electron-electron (e-e) and hole-hole (h-h) interaction is associated with discussion of the nature of metal-like temperature dependence of the conductivity observed at low temperature in some 2D systems, e.g., in n-Si MOSFET and in dilute 2D hole gas in AlGaAs/GaAs and GeSi/Ge structures (see [1] and references therein). One of the reason for such behavior of $\sigma(T)$ can be the renormalization of the interaction correction at lowering of the temperature and/or changing of the conductivity. Such renormalization was theoretically studied in framework of the theory of the renormalization group (RG) in [2, 3]. Two terms coming from the singlet and triplet channels and having different sign in favor of the localization and antilocalization, respectively, determine the value and sign of the correction. In conventional conductors at high value of the Drude conductivity $\sigma_0 = \pi k_F l G_0 \gg G_0$ (where k_F and l are the Fermi quasimomentum and the mean free path, respectively, and $G_0 = e^2/(2\pi^2\hbar)$) the initial value of the amplitude γ_2, which controls the triplet channel, is small, and the net effect is in favor of localization. At $\sigma_0 \lesssim (10-15)G_0$ or in dilute systems this amplitude may be enlarged due to e-e correlations and may lead to metallic sign of $d\sigma/dT$ [3].

The role of the interaction correction in disordered 2D systems when $k_F l$ tends to 1, i.e., at crossover from weak to strong localization was studied significantly less. Experimentally it was studied in the simplest single-valley electron 2D system GaAs/InGaAs/GaAs with small g-factor [4]. It was shown that at $\sigma_0 \lesssim (12-15)G_0$ [$k_F l \lesssim (4-5)$] the net value of the interaction correction decreases rapidly with decreasing σ_0. Such behavior can result from the compensation of the contributions from the singlet and triplet channels or from suppression of the both contribution with decreasing σ_0. It is impossible to separate these effects in the systems with small g-factor. The situation changes drastically for the case of large enough g-factor because the contribution from triplet channel can be strongly reduced in available magnetic field while the contribution from singlet channel is not changed. The hole 2D gas in strained GaAs/InGaAs/GaAs structures meets this requirement.

In this paper, we present the results of experimental study of the h-h contribution to the conductivity in the heterostructures GaAs/InGaAs/GaAs which were grown by metal-organic vapor phase epitaxy on semi-insulator GaAs substrate. Two field-effect transistors in the form of the Hall bar with aluminium gate electrode prepared from each of the waffles 3856, 3857 with close parameters were investigated.

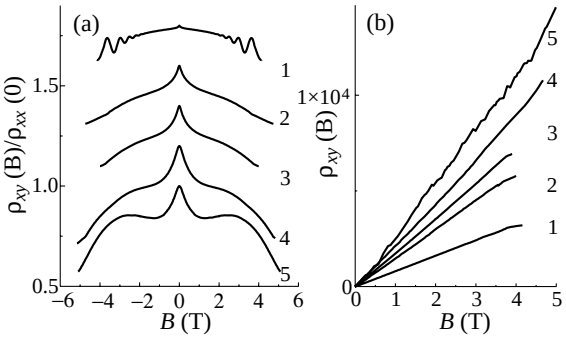

Fig. 1. The B-dependences of ρ_{xx} (a) and ρ_{xy} (b) measured at $T = 1.4$ K for different hole density controlled by the gate voltages. The parameters for different curves are $p = 8 \times 10^{11}$ cm^{-2}, $\sigma_0 = 59.6G_0$, $\sigma(T = 1.4\text{ K}) = 56.9G_0$ (curves 1); 4.5×10^{11}, $9.9G_0$, $6.8G_0$ (curves 2); 3.9×10^{11}, $8.1G_0$, $4.37G_0$ (curves 3); 3×10^{11}, $3.9G_0$, $0.36G_0$ (curves 4); 2.6×10^{11}, $3.2G_0$, $0.027G_0$ (curves 5).

The magnetic field dependences of ρ_{xx} and ρ_{xy} at $T = 1.4$ K for different gate voltages for one of the samples investigated are presented in Fig. 1. It is clearly seen that despite the very large difference in the conductivity values at $B = 0$, the magnetoresistance (MR) curves are very similar: the sharp negative MR at low magnetic field, which results from suppression of the interference contribution to the conductivity, is followed by the parabolic-like MR which results from interaction correction.

The unique property of this correction is that it contributes to σ_{xx} but not to σ_{xy}. This fact opens a straightforward way to extract interaction correction reliably even when the correction value is small. One has to find such contribution to σ_{xx} which is absent in σ_{xy}. The weak localization (WL) correction and ballistic part of the interaction corrections are reduced to renormalization of the transport relaxation time and can be accounted through the temperature and magnetic field dependence of the mobility for. Thus σ_{xx} and σ_{xy} can be written as

$$\sigma_{xx}(B,T) = \frac{ep\mu(B,T)}{1+\mu^2(B,T)B^2} + \delta\sigma_{xx}^{\rm hh}(B,T), \quad (1)$$

$$\sigma_{xy}(B,T) = \frac{ep\mu^2(B,T)B}{1+\mu^2(B,T)B^2}. \quad (2)$$

The value of the interaction correction $\delta\sigma_{xx}^{\rm hh}(B,T)$ depends on the Fermi-liquid parameter F_0^σ and on the magnetic field through the Zeeman splitting

$$\frac{\delta\sigma_{xx}^{\rm ee}}{G_0} = \alpha_i F(F_0^\sigma, B)\ln T\tau, \quad (3)$$

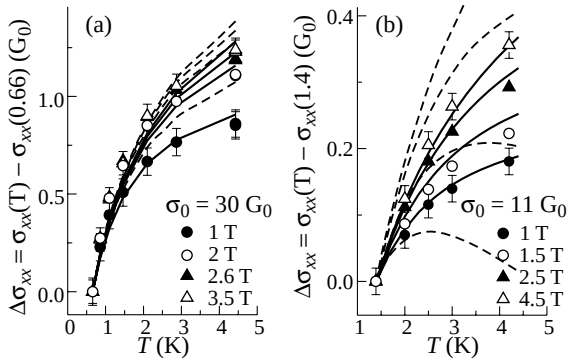

Fig. 2. The T-dependences of $\Delta\sigma_{xx}$ at different magnetic fields for two σ_0 values. The symbols are the experiment; the curves are calculated dependences with: (a) $\alpha_i = 1$, $F_0^\sigma = -0.4$ (solid curves); $F_0^\sigma = -0.35$ (dotted curves); (b) $\alpha_i = 1$, $F_0^\sigma = -0.4$ (dotted curves); $\alpha_i = 0.5$, $F_0^\sigma = -0.43$ (solid curves).

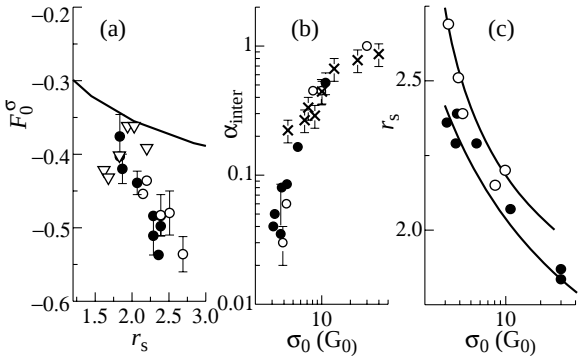

Fig. 3. (a) The r_s dependences of the F_0^σ. Symbols are the experimental data; the curve is theoretical dependence. (b) The prefactor α_i as a function of the Drude conductivity for the structures investigated (circles) and for 2D electron structure from [4]. (c) The Drude conductivity dependence of r_s.

where $\alpha_i = 1$ for $\sigma_0 \gg G_0$, and $F(F_0^\sigma, B)$ is obtained in [5].

Thus, knowing the hole density p we can find $\mu(B, T)$ from experimental σ_{xy}-vs-B dependences using Eq. (2) and calculate the first term in Eq. (1). The difference between experimental value of σ_{xx} and this term should give the h-h correction to the conductivity. The change in $\delta\sigma_{xx}$ with temperature

$$\Delta\sigma_{xx}(T, B) = \delta\sigma_{xx}(T, B) - \delta\sigma_{xx}(T_0, B)$$

(where T_0 is lowest temperature) at different magnetic fields are presented in Fig. 2(a) for large enough σ_0 value, $\sigma_0 \simeq 30G_0$. Comparison with the theory (solid curves) shows that the data are well described with $\alpha_i = 1$ and $F_0^\sigma = -0.4$.

Analogous data treatment was carried out for lower conductivity. As Fig. 2(b) shows one cannot obtain reasonable agreement with prefactor $\alpha_i = 1$ for any F_0^σ-values. It is not surprising because theory predicts $\alpha_i = 1$ only for large σ_0. However, one can fit the data perfectly with $\alpha_i = 0.5$ and $F_0^\sigma = -0.43$ [shown by solid curves in Fig. 2(b)].

To assure that the found change of F_0^σ and α_i has not occasional character we carried out systematical studies at successive decrease of hole density and σ_0. There was recognized that Eq. (3) with two fitting parameters, α_i and F_0^σ, well describes the experimental data down to $\sigma_0 \approx 3.5 \pm 0.3$. All results for α_i and F_0^σ are summarized in Fig. 3.

Firstly, let us discuss the behavior of F_0^σ. It is seen that F_0^σ decreases with decreasing hole density, i.e., with increasing r_s. The sign of the interaction correction in Eq. (3) changes at $F_0^\sigma = -0.454$ [5]. For structures investigated it occurs at $r_s \approx 2$. Positive sign of $\delta\sigma_{xx}^{\rm hh}$ at $r_s > 2$ should lead to the fact that the positive low-magnetic-field MR should transform to the negative MR in higher magnetic field because of suppression of the triplet channel. This fact graphically manifests itself in behavior of $\rho_{xx}(B)$ as local maximum evident for $\sigma_0 \simeq 3.5G_0$ at $B \simeq 2.8$ T [Fig. 1(a)]. However, experimentally such MR is observed at noticeably larger r_s-value, $r_s \approx 2.5$. This occurs due to the suppression of the interference quantum correction that results in strong negative MR. That is why the change of the MR sign happens when the curvature of the positive MR due to interaction becomes larger than that of the interference induced negative MR.

Fig. 3(a) shows that the experimental dependence of F_0^σ strongly deviates down from theoretical curve with increasing r_s. The possible reason of the deviation is the renormalization of the Fermi liquid constant F_0^σ with decreasing Drude conductivity which strongly changes with r_s [see Fig. 3(c)]. This effect was studied in the framework of RG theory [2,3] and our experimental data are in qualitative agreement with this theory.

Let us now call attention to the behavior of the prefactor in Eq. (3). Fig. 3(b) shows that α_i decreases sharply when σ_0 lowers. The interaction correction with decreasing σ_0 was studied experimentally in the n-type 2D structures [4]. The recalculated data of this paper presented in Fig. 3(b) demonstrate analogous decreasing also. The possible reason of the α_i-versus-σ_0 dependence is the interplay of the interference and the interaction which is not taken into account in the RG theory [2, 3]. As shown in [6, 7], the prefactor in WL magnetoresistance appears just due to this interplay. For the best of our knowledge the role of the interplay of the interaction and the interference in the interaction correction to the conductivity was not studied yet.

Thus, the decrease of interaction contribution to the conductivity with decreasing σ_0 results from both renormalization of interaction constant F_0^σ and decrease of the prefactor in Eq. (3), therewith the last effect is more pronounced.

Acknowledgements

We thank Igor Gornyi for useful discussion. This work was supported in part by the RFBR (Grant 06-02-16292) and the CRDF (Grants EK-005-X1 and Y1-P-05-11).

References

[1] V. M. Pudalov *et al*, Chapter 19 (pp. 309–327) in: Fundamental Problems of Mesoscopic Physics. Interaction and Decoherence, Nato sci. series, Kluwer (2004).
[2] A. M. Finkelstein, *Zh. Eksp. Teor. Fiz.* **84**, 168 (1983); *Z. Phys. B* **56**, 189 (1984).
[3] A. Punnoose, A. M. Finkel'stein, *Science* **310**, 289 (2005).
[4] G. M. Minkov *et al*, *Phys. Rev. B* **63**, 205306 (2003).
[5] C. Castellani *et al*, *Phys. Rev. B* **57**, R9381 (1998).
[6] I. L. Aleiner, B. L. Altshuler, and M. E. Gershenzon, *Waves in Random Media* **9**, 201 (1999).
[7] G. M. Minkov, A. V. Germanenko and I. V. Gornyi, *Phys. Rev. B* **70**, 245423 (2004).

15th Int. Symp. "Nanostructures: Physics and Technology"
Novosibirsk, Russia, June 25–29, 2007

Localization of the single-particle and collective electron excitations

Y. A. Pusep[1] and A. R. Gonzalez[2]

[1] Instituto de Fisica de Sao Carlos, Universidade de Sao Paulo, 13560-970 Sao Carlos, SP, Brazil
[2] Dpto. de Fisica Fundamental, Universidad de Salamanca, 37008 Salamanca, Spain

Abstract. The localization properties of the single-particle and collective excitations were investigated in the AlGaAs alloys and in the intentionally disordered GaAs/AlGaAs superlattices by magnetoresistance and Raman scattering. It was shown that the Landau damping determines the localization length of the collective plasmon-like excitations in bulk AlGaAs alloy. Meanwhile, the localization lengths of both, the single-particle and collective excitations are limited by disorder in the intentionally disordered superlattices. In this case the localization length of the individual electron was found to be considerably larger than the localization length of their collective excitations. This suggests that the disorder has weaker effect on the electrons than on their collective motion and that the interaction which gives rise to the collective effects increases localization.

Introduction

One of the long staying problems of solid state physics is the simultaneous influence of electronic interactions and disorder on transport properties. It is well known that each of them acting separately produces localization of carriers decreasing the conductivity. Whereas, when both of them act simultaneously, their effect depends on a particular arrangement of a disordered electron system. In this work we present the experimental evidence that in the presence of the disorder the interaction between electrons increases their localization. We compared the localization properties of the low-lying excited states of the Fermi system, such as the single-particle with those of the collective electron excitations. In the fermion system the interaction does not considerably influence the transport properties of a single electron, while it is fundamental for the formation of the collective excitations (plasmons). Therefore, the comparison between the localization properties of the electrons and the plasmons subject to the same random potential reveals how the interaction influences localization.

1. Experimental

We measured the localization lengths of the electrons and their collective excitations in a variety of samples in different disordered electron systems such as AlGaAs alloys and GaAs/AlGaAs intentionally disordered SLs. In the alloys the disorder was provided by the alloy potential fluctuations, while in the superlattices the vertical (along the growth direction) disorder was produced by a random variation of the well thicknesses. Differently doped 0.5 μm thick $Al_{0.11}Ga_{0.89}As$ films were grown by molecular beam epitaxy on semi-insulating (001) GaAs substrates. The intentionally disordered $(GaAs)_m(Al_{0.3}Ga_{0.7}As)_6$ SLs (where the thicknesses of the layers are expressed in monolayers, ML) with various strengths of the disorder were grown on semi-isolating and doped (001) GaAs substrates used to measure Raman scattering of the plasmon-like modes and the magnetoresistance respectively. In this case the disorder was produced by a random variation of the well thicknesses (m) around the nominal value 17 ML according to a probability distribution. Such a disorder let us to control the spatial extent of the wave functions of the elementary excitations propagating normal to the layers. The disorder strength was characterized by the disorder parameter $\delta_{SL} = \Delta/W$, where Δ is the full width at half maximum of a Gaussian distribution of the electron energy calculated in the isolated quantum wells and W is the miniband width of the nominal SL in the absence of disorder. In order to form the degenerate electron system the samples were homogeneously doped with Si.

2. Results and discussion

In a three-dimensional metallic system the electron phase-breaking length coincides with the localization length. Therefore, the electron phase-breaking lengths determined by the weak-field magnetoresistance were used to acquire the localization lengths of the single-particle electron excitations. While, the localization lengths of the collective electron excitations were obtained by Raman scattering [1]. It was shown that in most of the bulk AlGaAs alloys the Landau damping determines the localization lengths of the collective plasmon-like excitations, while the electron localization was found due to the random alloy potential. Because of the different nature of the localization of the electrons and the plasmons, the direct comparison between them was not possible. At the same time, in certain conditions (when the plasmon energy is placed in the range of the minigap of the single-particle spectrum) the Landau damping is absent in the SLs. In such case the superlattice disorder determines the localization of the plasmons and the electrons. When the disorder limits the localization properties of both the elementary excitations their localization lengths may be compared.

The localization length of the single-particle and collective electron excitations obtained in the intentionally disordered SLs are shown in Fig. 1. The phase-breaking lengths of the electrons propagated perpendicular to the surface of the disordered SLs associated with the corresponding electron localization lengths are depicted in Fig. 1(a) as function of the disorder strength. These data exhibit remarkable decrease of the phase-breaking length with the increasing disorder. The electron localization lengths were calculated in the SLs with different disorder strengths basing on the transmission matrix technique. The transmission matrix has been used to obtain the energy of the electron in the isolated well, the miniband width of the periodic SL and the transmission probability of the structure as a function of the energy $T(E)$. From this quantity the

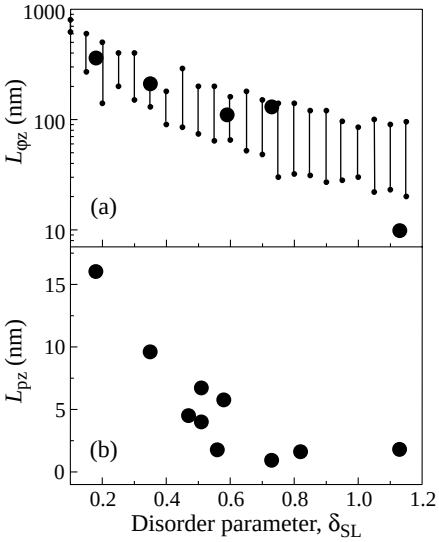

Fig. 1. Localization lengths of the single electrons (a) and their collective excitations (b) measured in the $(GaAs)_m(Al_{0.3}Ga_{0.6}As)_6$ superlattices with different disorder strengths and the fixed electron densities $n = 5.0\times10^{17}$ cm^{-3} and $n = 1.7\times10^{18}$ cm^{-3} respectively. The bars show the calculated localization lengths of the electrons.

electronic localization can be characterized by the Lyapunov exponent defined as:

$$\lambda(E) = -\frac{1}{2L}\ln T(E)\,, \qquad (1)$$

where L is the length of the system. For a given energy the electron localization length was determined as $L_z(E) = 1/\lambda(E)$. The electron localization lengths calculated by this way and averaged over all the occupied electron states below the Fermi energy are depicted in Fig. 1(a). The bars indicate the fluctuations of the localization length obtained with different disorder realizations. A good agreement between the calculated and experimental data was obtained without use of any fitting parameter.

The localization lengths of the plasmons coupled to the AlAs LO phonons (which reveal mostly the plasmon character) were obtained in the SLs with different disorder strengths by the fits of the Raman scattering intensities as in Ref. [1]. They are shown in Fig. 1(b). These data also reveal significant decrease of the localization length of the collective plasmon-like excitations with the increasing disorder.

Moreover, in the whole range of the disorder variation we found the localization lengths of the collective excitations much smaller than those of the single-particle ones. The difference between the single-particle and collective excitations is due to the electron polarization which basically determines the properties of the collective excitations. This suggests that the interaction which gives rise to the collective effects increases localization.

3. Conclusion

We demonstrated that the localization lengths of the collective electron excitations measured in the metallic AlGaAs alloys is limited by the Landau damping. In such case the calculated wave number cutoff of the collective excitations was found in good agreement with that one determined by their localization length obtained by the Raman scattering experiments. This proves the ability of the Raman scattering to determine the localization length of corresponding collective excitations. The localization lengths of the single-particle and collective electron excitations were properly compared in the intentionally disordered superlattices where, due to the absence of the Landau damping, both of them were limited by the disorder. In this case we found the electron localization length significantly larger than that of the collective plasmon-like excitations. Our data show that the disorder influences the collective excitations in a stronger way than that of the individual electron and consequently, the interaction increases the localization. The electron localization lengths calculated in the disordered SLs were found in good agreement with the experimental data.

Acknowledgement

This work has been supported by the Brazilian agencies FAP ESP and CNPq.

References

[1] Y. A. Pusep, M. Ribeiro, V. Carrasco, G. Zanelatto, and J. C. Galzerani, *Phys. Rev. Lett.* **94**, 136407 (2005).

15th Int. Symp. "Nanostructures: Physics and Technology"
Novosibirsk, Russia, June 25–29, 2007

Electron-electron interaction in multi-mode quantum point contacts

O. A. Tkachenko[1,2,3], V. T. Renard[3,4], K. S. Pyshkin*, I. V. Gornyi[5,6], A. P. Dmitriev[6], V. A. Tkachenko[1] and J.-C. Portal[3,7]

[1] Institute of Semiconductor Physics, 630090 Novosibirsk, Russia
[2] Université Joseph Fourier - BP 53 - 38041 Grenoble Cedex 9, France
[3] GHMFL, CNRS, BP 166, F-38042, Grenoble Cedex 9, France
[4] NTT Basic Research Laboratories, NTT corporation 3-1 Morinosato Wakamiya, Atsugi 243-0198, Japan
[5] Institut für Nanotechnologie, Forschungszentrum Karlsruhe, 76021 Karlsruhe, Germany
[6] Ioffe Physico-Technical Institute, St Petersburg, Russia
[7] INSA, Institut Universitaire de France, F-31077, Toulouse Cedex 4, France
* Formerly at Cavendish Laboratory, United Kingdom

Abstract. The strong temperature dependence of the conductance observed in multi-mode QPCs is explained by electron-electron interaction — coherent scattering on the Friedel oscillations originating from the boundaries of the QPC. Results of numerical modelling are reported.

Introduction

It is generally recognized that the conductance of quantum point contacts (QPC) or quasi-one-dimensional constrictions in two-dimensional electron gases (2DEG) is well described by one-particle quantum physics. An exception to this rule is the "0.7 feature" below the first conductance step. Starting from Ref. [1], "0.7 anomaly" has been the subject of numerous experimental and theoretical papers, while the high conductance steps were neglected. However some measurements indicate that even the high conductance regime [2,3] does not always agree with single-electron picture. The measurements in QPCs at low electron density ($n = 10^{11}$ cm^{-2}) in high mobility 2DEG ($\mu > 10^6$ cm^2/Vs) show that starting from the second quantization step the average slope of the conductance versus gate voltage is increased with increasing temperature (Fig. 1). This temperature increase of the conductance can not be explained by simple thermal averaging. Besides a non-monotonic temperature dependent magneto-resistance was surprisingly observed at very low magnetic fields [3]. This anomalous temperature and magnetic field behavior requires taking into account electron-electron interactions.

Results

It is known that, in the case of strong scattering, interaction effects in open low-dimensional systems share a common origin: coherent scattering on Friedel oscillations [5,6]. Solving this problem analytically in nano-constrictions is very difficult because the potential is strongly position dependant. We report on a fully numerical approach to take into account Friedel oscillations in multi-mode QPC. Friedel oscillations originating from the boundaries of the QPC are considered and those coming from impurities are neglected.

A self-consistent calculation of 3D electrostatics and transport in nanostructures in presence of e-e interaction is very complicated. The wave functions were therefore calculated for some smooth potential of QPC $U_0(x, y)$ in a one-particle approach. Electron densities $n(x, y)$ were then computed at different values of Fermi energy E_F and temperature T (Fig. 2). The interaction correction to 2D potential was determined by

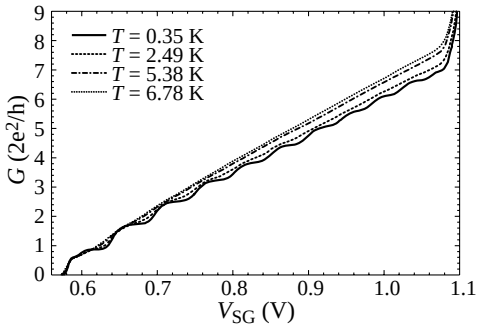

Fig. 1. Experimental $G(V_{SG})$ for different temperatures T, series resistance is not subtracted (data taken from Ref. [2] with permission). Lithography size of split-gate window is 0.4×0.4 μm^2. This nanostructure was modelled in [4].

simple a formula:

$$\delta U(x, y) = \alpha \Delta / D,$$

where $\Delta = n(x, y, E_F, T) - n(x, y, E_F, T^*)$ (Fig. 3), T^* is a high temperature, $D = em/(2\pi h^2)$ is 2D density of states, $\alpha = 1/2(1 + 3F_0^\sigma/(1 + F_0^\sigma))$ is electron-electron interaction factor, F_0^σ is the interaction constant in the triplet channel which depends on the interaction strength. Finally, the conductance was computed solving the one-particle scattering problem with the new potential $U(x, y) = U_0(x, y) + \delta U(x, y, E_F, T, T^*)$ which takes into account interactions. Influence of weak magnetic field was also studied.

The computation requires large computing resources. For example, determining Friedel oscillations requires solving several thousands of 2D scattering problems and integrating on energy the local density of states. We therefore modeled e-e-interaction in constrictions smaller than those studied experimentally. The calculation region was 3 microns long and 0.7 microns wide. Size of mesh was chosen 5 nm. Two-dimensional reservoirs were modeled by 500 nm clean channels (Figs. 2,3). Disorder was neglected.

To control the accuracy of computation we compared one-dimensional electron densities n_{1D} calculated in channel far from QPC at different temperatures. At $k_B T < 0.5$ meV $n_{1D}(E_F)$ almost doesn't depend on temperature (Fig. 2(b)).

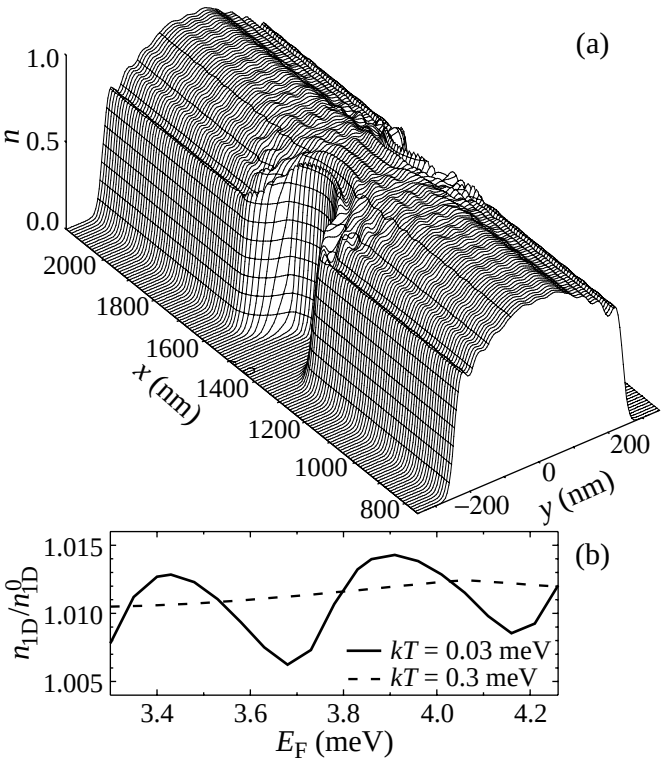

Fig. 2. (a) Calculated electron density $n(x, y, E_F, T)$ [10^{11} cm^{-2}] in clean channel with multi-mode QPC: $E_F = 3.3$ meV, $k_BT = 0.03$ meV (0.35 K). (b) 1D electron density ratio in the channel vs E_F, n_{1D} is calculated by averaging of $n(x, y)$ far from constriction, n^0_{1D} is quasiclassical density at $T = 0$.

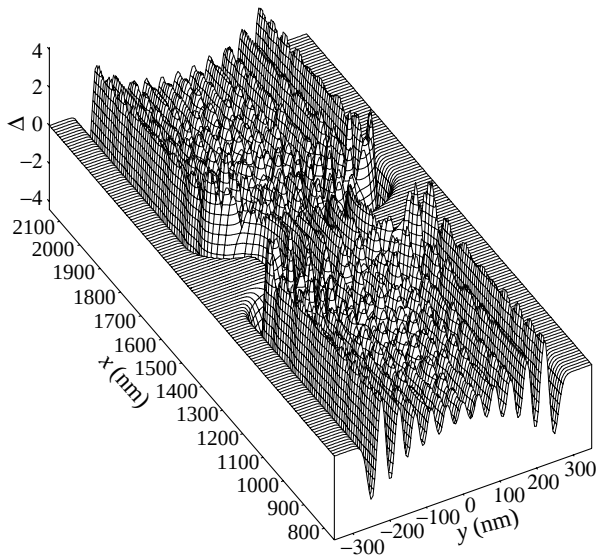

Fig. 3. Electron density difference $\Delta = n(E_F,T) - n(E_F,T^*)$ [10^9 cm^{-2}] in channel with QPC: $E_F = 3.3$ meV, $k_BT = 0.03$ meV, $k_BT^* = 0.4$ meV.

The deviation from some average line is within 0.5%.

Numerical modelling reproduces qualitatively the experimental temperature dependence of the conductance [2,3]. Not only the conductance curves are smoothed by increasing temperature but they are also offset with respect to the centers of quantization steps (Fig. 4a). The temperature-dependent part of the correction to the conductance, associated with interactions, is negative (insulating) and grows with decreasing

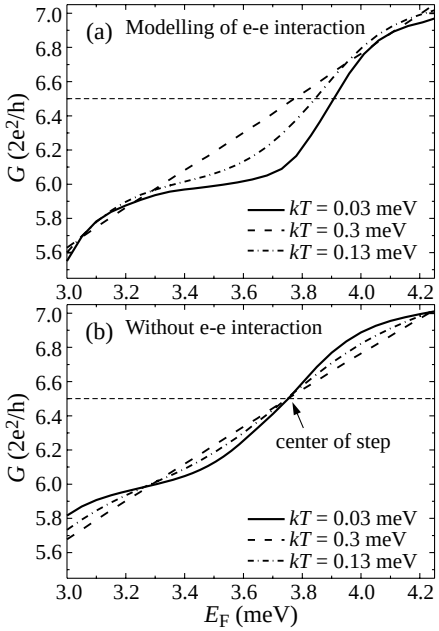

Fig. 4. Calculated conductance of clean channel with QPC as a function of E_F at different T: (a) for $U = U_0(x, y) + \alpha\Delta(T, T^*)/D$, $k_BT^* = 0.4$ meV, $\alpha = -6$ ($F_0^\sigma = -0.8$, i.e. the spin-exchange interaction is strong enough); (b) for $U = U_0(x, y)$.

temperature.

When e-e interactions are absent ($\delta U(x, y) = 0$) the smoothing of the conductance steps is only observed with increasing temperature (Fig. 4b). It is interesting that presence of e-e interaction makes conductance steps steeper. Thus we conclude that scattering on Friedel oscillations formed around clean QPC contribute substantially to the observed temperature effects.

Acknowledgement

We are very grateful to D. G. Baksheev and A. L. Aseev for help and discussions. O.A.T. acknowledges Supercomputing Siberian Centre, Novosibirsk, Russia and IDRIS Supercomputing Center, Orsay, France (project 61778) for the possibility of performing the calculations. This work at Novosibirsk was supported by programs "Quantum nanostructures" of RAS, and "Russian Scientific School" Grant No. 8401.2006.8.

References

[1] K. J. Thomas *et al*, *Phys. Rev. Lett* **77**, 135 (1996).
[2] K. S. Pyshkin, Induced Quantum Wires, PhD thesis, University of Cambridge (2000).
[3] V. T. Renard, T. Ota, N. Kumada, and Y. Hirayama, International Workshop Tera- and Nano-Devices: Physics and Modeling, October 16–19, 2006, University of Aizu, Aizu-Wakamatsu, Japan (unpublished).
[4] O. A. Tkachenko *et al*, *J. Appl. Phys.* **89**, 4993 (2001).
[5] B. L. Altshuler and A. G. Aronov, Electron-electron interaction in disordered systems (A. L. Efros, M. Pollak, Amsterdam, 1985); G. Zala, B. N. Narozhny, and I. L. Aleiner, *Phys. Rev. B* **64**, 214204 (2001); I. V. Gornyi and A. D. Mirlin, *Phys. Rev. Lett.* **90**, 076801 (2003); *Phys. Rev. B* **69**, 045313 (2004).
[6] Dongxiao Yue, L. I. Glazman, K. A. Matveev, *Phys. Rev. B* **49**, 1966 (1994); Anton Yu. Alekseev and Vadim V. Cheianov, *Phys. Rev. B* **57**, R6834 (1998); I. L. Aleiner and L. I. Glazman, *Phys. Rev. B* **57**, 9608 (1998); V. A. Sablikov, *JETP Letters* **84**, 404 (2006).

15th Int. Symp. "Nanostructures: Physics and Technology"
Novosibirsk, Russia, June 25–29, 2007

Study of electrical conductivity of surface phases on silicon in situ

D. A. Tsukanov, M. V. Ryzhkova and S. V. Ryzhkov
Institute for Automation and Control Processes FEB RAS, 690041, Vladivostok, Russia

Abstract. In present paper the dependence of electric conductivity of the Si(100)c(4 × 12)-Al surface phase on the surface morphology has been studied using LEED and four-point probe conductivity measurement techniques after the deposition of Al on this surface. The growth of adsorbate islands acting as additional centers of charge carrier scattering leads to a decrease in the conductivity. The conductivity of surface phases Si(111)$\sqrt{3} \times \sqrt{3}$-In and Si(111)4 × 1-In was investigated by LEED and four-point probe method in situ in accordance with crystallographic directions of silicon (111) surface. It was pointed out that directions in which conductivity has maximum magnitude for Si(111)$\sqrt{3} \times \sqrt{3}$-In surface phase are coincident with one for the maximum In atomic density, where as for Si(111)4 × 1-In surface phase the directions of maximum conductivity are coincident with directions of one-dimensional chaines of In atoms.

Introduction

The investigation of electric conductivity of surface superstructures (surface phases) on silicon is of the great interest from the fundamental as well as technological viewpoint. It is connected with the active development of silicon semiconductor devices' technology and construction the new elements for microelectronics as two-dimensional diode, two-dimensional transistor etc. The surface phases on silicon are very perspective due to its unique properties such as ultra small thickness (order of atomic dimension), well-ordered structure, its own electronic structure and so on [1]. The study of the electrical properties for such materials begins in last time, see for example [2–5]. The fundamental problem is a clarification the mechanisms of electrical conductivity. As basic the four-point probe method for measurements of resistivity *in situ* is used with ultrahigh vacuum technologies. It was shown [5] that surface phases of adsorbates on silicon (for example, surface phases Si(100)2 × 1 and Si(100)-Au) are additional conducting channels on the silicon substrate. Also it was shown that the physical processes on the surface (adsorption, formation of ordered structures, diffusion etc.) have strong influence on the conductance for such structures.

In this paper the correlated changes in the conductivity and morphology of Si(100)c(4 × 12)-Al surface phase and anisotropy of surface conductivity for In/Si(111) submonolayer system was studied by low energy electron diffraction (LEED) and four-point probe method in ultrahigh vacuum (UHV).

1. Experimental

The experiments were carried out in UHV chamber with base pressure 5×10^{-10} Torr equipped by (LEED) and four-point probe system. As substrates the Si(100) ($15 \times 5 \times 0.5\,\mathrm{mm}^3$) wafers n-type (P-doped) with resistivity 20 Ohm cm and Si(111) ($15 \times 5 \times 0.5$ mm^3) wafers n-type (P-doped) with resistivity 45 Ohm cm. Prior to introduction into the UHV chamber, the substrates were cleaned in organic solvents. The final cleaning was effected in UHV by flash heating at 1550 K. The thus pretreated samples exhibited a clear 2 × 1 and 7 × 7 LEED patterns characteristic of the atomically clean Si(100) and Si(111) crystal surface, respectively. The electrical conductivity of samples was measured *in situ* using the four-point probe technique at 150 K by passing a direct current in the range from 10 to 150 A. The distance between the tungsten probes situated in square cones was about 1 mm. The surface phase Si(100)c(4 × 12)-Al was formed by depositing aluminum to an 0.5 ML coverage onto the Si(100)2 × 1 substrate surface. The surface phases Si(111)$\sqrt{3} \times \sqrt{3}$-In and Si(111)4 × 1-In were formed by deposition of 1/3 ML and 1 ML In atoms, respectively, onto the Si(111)7 × 7 surface at room temperature (RT) and subsequent annealing of the substrate at 750 K. The Al and In coverage was determined in accordance with phase diagrams for submonolayer Al/Si(100) and In/Si(111) system [1].

2. Influence of indium islands on surface conductivity of Si(100)c(4×12)-Al surface phase

Fig. 1 shows plots of the change of the conductivity of the Si(100)c(4 × 12)-Al surface phase versus coverage of In deposited at RT. As can be seen, the conductivity exhibits a sharp drop in the very early stage of In deposition, reaching a level ($\Delta\sigma = 0$) characteristic of the initial clean Si(100)2 × 1 surface. However, the decrease in the conductivity was much less pronounced if the deposition of In was followed by vacuum annealing of the sample at 700 K. The STM investigations [6] of the In/Si(100)c(4 × 12)-Al surface showed that at RT deposition of In led to the appearance of a high concentration (about 5×10^{11} cm^{-2}) of three-dimensional (3D) In islands on the surface. Upon subsequent annealing at 400 K and lower, the number of islands decreased to about 1×10^{11} cm^{-2} and the remaining islands were arranged predominantly at the steps. The variation of conductivity was analyzed using a model system comprising a Si(100) substrate with a c(4 × 12)-Al surface phase and the 3D adsorbate islands that played the role of additional centers of charge carrier scattering. It was assumed that only the change in the scattering from islands contributes to the conductivity variations.

The total conductivity of a sample was defined as $\sigma = \sigma_1 + \sigma_2$, where σ_1 is the conductivity of a bulk substrate and σ_2 is a contribution due to the surface phase. As is well known, the n-type conductivity can be expressed as $\sigma = en\mu$, where e, n, and μ are the electron charge, density, and mobility, respectively [7]. In the case of scattering on neutral centers, the electron mobility can be determined using the formula $\mu = T^k m e^3 / 20\epsilon\hbar^3 N_0$ [8], where T is the temperature, k is a constant, m is electron mass, ϵ is the permittivity, $\hbar$ is the Planck constant, and N_0 is the concentration of neutral scat-

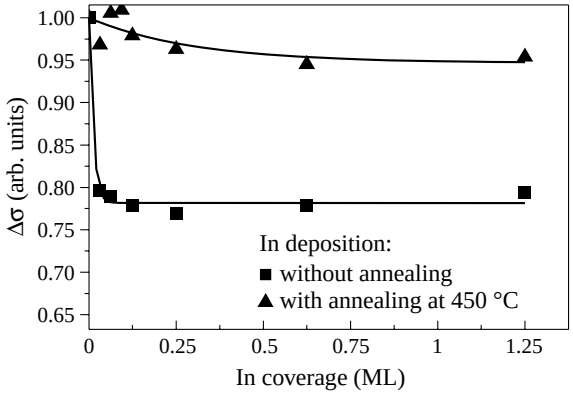

Fig. 1. Plots of the conductivity changes $\Delta\sigma$ of the Si(100)c(4×12)-Al surface phase versus coverage of In deposited without annealing and with annealing at 450 °C.

tering centers. According to this formula, the experimentally measured conductivity is inversely proportional to the concentration of scattering centers.

3. Study of anisotropy of In/Si(111) surface phases conductivity

The surface phase Si(111)$\sqrt{3}\times\sqrt{3}$-In has interest for the study of conductivity anisotropy due to its "quasy" one-dimensional structure. So it was proposed that for this system the anisotropy in surface conductivity can be observed as well as for single-domain surface phases [9]. It is known that In atoms in this surface phase take places in T_4 sites on unreconstructed Si surface, and In coverage is 1/3 ML [10].

In Fig. 2 the changes in surface conductivity vs. an angle of direction of probes for Si(111)$\sqrt{3}\times\sqrt{3}$-In surface phase are shown. In this case the maxima of conductivity are observed in directions closed to $[1\bar{2}1]$ and $[2\bar{1}\bar{1}]$. In the direction closed to $[10\bar{1}]$ and $[1\bar{1}0]$ the minimum of conductivity magnitude were observed. It is seen that maximums and minimums of conductivity repeat through 60°. If we compare this data with model of this surface phase it is seen that crystallographic directions in which the conductivity has maximum coincidences with directions in which the distance between adsorbate atoms is minimal ($[1\bar{2}1]$ and $[2\bar{1}\bar{1}]$).

It is known that free path for charge carriers is reversely proportional to the distance between atoms in the cell [8,11]. It is seen from the experimental data: the directions where maximum density of atoms coincidence with directions with higher conductivity (Fig. 2).

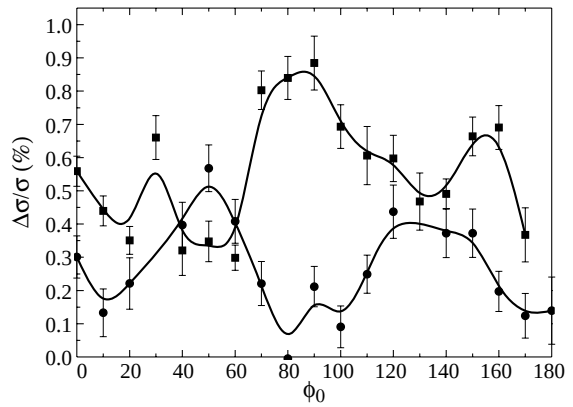

Fig. 2. Dependences of the changes in conductivity of surface phases Si(111)4 × 1-In (■) and Si(111)$\sqrt{3}\times\sqrt{3}$-In (•) versus the angle of the rotation of four-point probe head in relation to crystallographic orientation on the sample surface.

The anisotropy of conductivity of Si(111)4 × 1-In surface phase also was studied. This phase is formed at 1 ML of In and consists from one-dimensional chains of In atoms separated by Si rods [12]. As was shown in [9], the current along direction ⟨110⟩ flow through the In chains, and along direction ⟨211⟩ flow through the subsurface region. In such manner the conductance along In chains has to more higher than that in previous case. It is also seen in our work. The conductivity maximums observed in directions $[10\bar{1}]$, $[1\bar{1}0]$, $[0\bar{1}1]$ (Fig. 2). Because the Si(111)4 × 1-In surface phase in our experiment has the three-domain structure, the conductance peaks repeated with period 60°. In that time if we consider atomic structure of surface phases, the peaks in conductivity for the Si(111)$\sqrt{3}\times\sqrt{3}$-In and Si(111)4 × 1-In surface phases must have a difference in 30°, as we can see on Fig. 2.

Acknowledgements

The work was done at financial support from Russian Foundation for Basic Research (No. 05-02-17823), grants NSh-4755.2006.2, MK-4743.2006.2.

References

[1] V. G. Lifshits *et al*, *Surface Phases on Silicon*, (Chichester: Wiley) 450 (1994).
[2] S. Hasegawa *et al*, *Progr. Surf. Sci.* **60**, 89 (1999).
[3] S. V. Ryzhkov *et al*, *Phys. Low-Dim. Struct.* **7/8**, 109 (1998).
[4] S. Hasegawa *et al*, *Surf. Sci.* **500**, 84 (2002).
[5] D. A. Tsoukanov *et al*, *Appl. Surf. Sci.* **162–163**, 168 (2000).
[6] M. V. Lavrinaitis *et al*, *Tech. Phys. Lett.* **31**, 1068 (2005).
[7] C. Kittel, *Introduction to Solid State Physics* (New York: Wiley) (1978).
[8] V. L. Bonch-Bruevich, S. G. Kalashnikov, *Semiconductor physics* (Moscow: Nauka) (1990).
[9] T. Kanagawa *et al*, *Phys. Rev. Lett.* **91**, 3 (2003).
[10] M. S. Finney *et al*, *Surf. Sci.* **291**, 99 (1993).
[11] K. V. Shalimova, *Semiconductor physics* (Moscow: Energoatomizdat) (1985).
[12] O. Bunk *et al*, *Phys. Rev. B* **59**, 12228 (1999).

15th Int. Symp. "Nanostructures: Physics and Technology"
Novosibirsk, Russia, June 25–29, 2007

Influence of thin heterolayer insertion on the electron transport properties of GaAs/InGaAs/GaAs shallow quantum wells

I. S. Vasil'evskii[1], G. B. Galiev [1], V. G. Mokerov[1], V. A. Kulbachinskii [2], R. A. Lunin [2], G. Galistu [3] and A. de Visser[3]

[1] Institute of UHF Semiconductor Electronics, 117105, Moscow, Russia
[2] Low Temperature Physics Department, Moscow State University, 119992, GSP-2, Moscow, Russia
[3] Van der Waals-Zeeman Institute, University of Amsterdam, 1018 XE Amsterdam, The Netherlands

Abstract. Electron transport properties of shallow pseudomorphic double-side delta-doped GaAs/$In_{0.12}Ga_{0.88}As$/GaAs quantum wells (QWs) with thin heterolayers in the QW center are studied. The influence of a 3 AlAs monolayers barrier or 3 $In_{0.7}Ga_{0.3}As$ monolayers deep well in the QW center on the transport properties is investigated. Such insertions are shown to change the subband structure, notably the envelope wave functions. This leads to the change in the dominant scattering process and drastically affects the mobility.

Introduction

Quantum wells with complex potential profiles have attracted substantial interest. Thin barriers or "deep" layers grown inside the QW, thereby forming coupled or stepped QWs, may tune the subband structure and give rise to desirable optical properties [1,2]. Other studies intended to employ thin barriers as phonon walls in order to suppress electron-optical phonon coupling and scattering [3,4]. Only few experimental studies are devoted to the influence of the barriers on the transport properties, but the conclusions are contradictory [5,6].

In this work the temperature dependence of the resistance and the magnetoresistance at low and quantizing magnetic fields B has been investigated for shallow pseudomorphic quantum wells. The AlAs barrier or InGaAs deep well insertion in the QW center are found to change the subband structure and electron mobility.

1. Samples

The structures investigated here are based on GaAs/$In_{0.12}$ $Ga_{0.88}As$/GaAs pseudomorphic QWs grown by molecular-beam epitaxy on semi-insulating (100) GaAs substrates. First a GaAs buffer layer of 0.6 μm was grown. An $In_{0.12}Ga_{0.88}As$ QW was grown with different well width L_{QW}(11 or 16 nm) and was symmetrically delta-doped by Si through 8.5 nm thick GaAs spacer layers. The Si doping sheet concentration was 1×10^{12} cm^{-2}. The capping layers are 75 nm thick i-GaAs and 8 nm thick Si-doped GaAs. The substrate temperature was 510 °C for the pseudomorphic QW and 590 °C for the other layers. Samples with (#4, #6) and without AlAs barrier (#3, #5) were prepared for each well width. The barrier consists of $b = 3$ monolayers (ML) of AlAs grown in the center of the QW. Sample #9 was grown with 3 ML of $In_{0.7}Ga_{0.3}As$ deep well in the center of QW. Its thickness is below the critical one for this composition, thus no quantum dot appears. Some structural and transport parameters (at $T = 4.2$ K) of the samples are reported in Table 1.

Table 1. Structural and transport parameters of the samples.

#	3	4	5	6	9
L_{QW} (nm)	16	16	11	11	11
b (ML)	0	3, AlAs	0	3, AlAs	3, $In_{0.7}Ga_{0.3}As$
ρ_0 (Ω/sq)	1586	5140	1338	8770	55800
n_H (10^{12} cm^{-2})	0.52	0.57	0.59	0.73	0.62
μ_H (m^2/Vs)	1.0	0.21	0.8	0.15	0.018

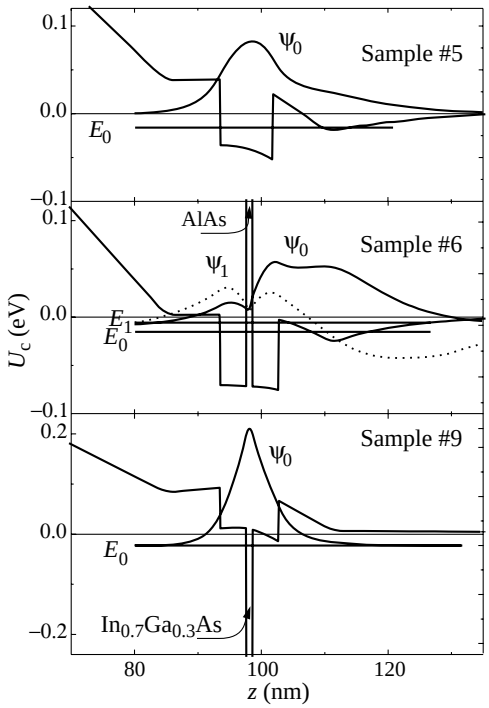

Fig. 1. Subband structure of samples #5, #6 and #9.

Here n_H and μ_H are the Hall concentration and mobility, respectively. Self-consistent calculations were performed to determine the subband structure and envelope wavefunctions (WF) for all samples. The conduction band profiles and the WFs for samples #5, #6 and #9 are shown in Fig. 1.

2. Electronic transport

The temperature dependence of the resistance was measured for all samples in the range 0.25–300 K. The samples with a single QW (SQW) #3 and #5 show metallic behavior, i.e. the resistance decreases (approximately linearly) with decreasing T. The resistance of the corresponding samples with central AlAs barrier (#4 and #6) increases with decreasing T by a factor

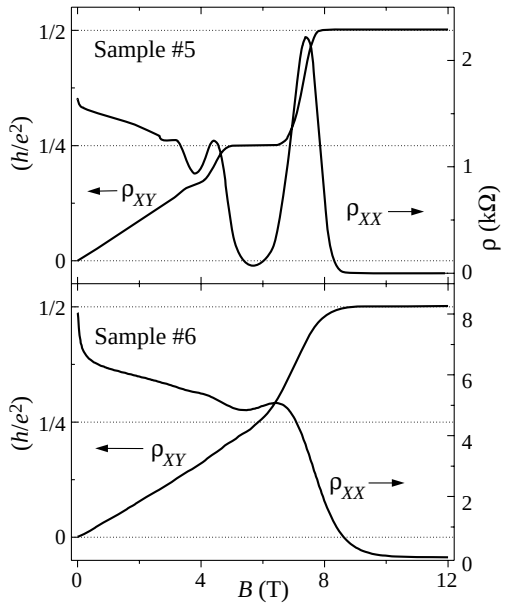

Fig. 2. Magnetoresistivity ρ_{xx} and Hall resistivity ρ_{xy} for samples #5 and #6 at temperature $T = 0.25$ K.

$\sim 3-7$ at the lowest temperatures. The sample #9 shows the most pronounced increase of the resistance by a factor ~ 19. Instead of the value of conductivity, the temperature variation of the conductivity below $T \sim 10$ K follows logarithmical law which corresponds to manifestation of quantum corrections for the two-dimensional systems.

The magnetoresistance and Hall effect were measured in the T interval 0.25–4.2 K. From these data, for all structures, the 2D Hall electron concentration $n_{\rm H}$ and mobility $\mu_{\rm H}$ were determined. The subband concentration $n_{\rm SdH}$ was determined from the Fourier spectra of the SdH oscillations for the subband with the highest mobility. It was found that in all samples thin barrier or deep well insertions do not affect the subband concentration. As an example, in Fig. 2, the magnetoresistivity and Hall resistivity for samples #5 and #6 are shown. Subband concentration is close to measured Hall concentration and agrees with the calculated values.

In low applied B fields a large negative magnetoresistance (NMR) is observed in all samples. Sharp component of NMR is more pronounced in the samples with low conductivity and has the order of magnitude $\sim e^2/h$. The experimental dependence $\Delta\sigma(B)$ is in a good agreement with the calculated according to weak localization theory curves with appropriate dephasind parameter τ_ϕ. For samples #3–#6 the resistance decreases about linearly in moderate field, before SdH oscillations appear in the signal. At higher B fields quantum Hall plateaus appear with integer factors $i = 4$ and $i = 2$.

In samples #3, #5 and #9 only one QW subband is filled at low temperatures. As shown in Fig. 1, the central AlAs barrier leads to a strong reconstruction of the wavefunction with hybrid states formation, when the WF magnitudes become equal in the QW and in the delta-doped V-shape well (WF ψ_0 and ψ_1). This changes the dominant scattering mechanism from phonon scattering (which is inherent in single QW) to ionized impurity scattering on Si dopant in the δ-layer. Calculations of electron mobility due to ionized impurity scattering show strong enhancement of the scattering for the hybrid states. This effect weakens in the sample with a larger QW due to better confinement of the electrons because the subband level has lower energy. Thus, hybrid state is originated from the shallowness of the QW.

In sample #9 the introduction of the 3 ML of $In_{0.7}Ga_{0.3}As$ results in the strong mobility reduction (see Table 1) by a factor $\sim$40 compared with the SQW sample #5. Calculation shows that in this case the wavefunction increases strongly in the area of the deep well (see Fig. 1). It is the layer with small additional well thickness, so the well width and depth fluctuations are significant. So, interface roughness scattering and potential fluctuations contribute into mobility decrease and lead to the change of temperature dependence of the resistance. Note that Hall concentration holds when deep layer is introduced, thus, no carrier capture occurs.

In summary, the influence of a thin barrier or thin deep well layer in the QW center on the electron transport and subband structure is studied for shallow QWs with different widths. AlAs thin barrier effectively displaces WF maximum, while $In_{0.7}Ga_{0.3}As$ deep well concentrates WF at the insertion. The strong reconstruction of the wave function spatial profiles and insertion of the novel heterointerfaces give a pronounced change of dominant scattering mechanism and involve impurity or interface roughness scattering.

Acknowledgements

This work was supported by Russian Foundation for Basic Research, grant 05-02-17029-a and by Program of RAS "Quantum Nanostructures".

References

[1] A. Patanè, D. Sherwood, L. Eaves, T. M. Fromhold, M. Henini, P. C. Main *et al*, *Appl. Phys. Lett.* **81**, 661 (2002).
[2] Q. X. Zhao, S. Wongmanerod, M. Willander, P. O. Holtz, E. Selvig *et al*, *Phys. Rev. B* **62**, 10984 (2000).
[3] J. Požela, A. Namajunas, K. Požela *et al*, *J. Appl. Phys.* **81** 1775 (1997).
[4] J. Požela, V. Juciene, A. Namajunas *et al*, *Fiz. Tekhn. Poluprovodnikov* **31** 85 (1997).
[5] X. T. Zhu, H. Goronkin, G. N. Maracas, R. Droopad *et al*, *Appl. Phys. Lett.* **60** 2141 (1992).
[6] T. Noda, M. Tanaka *et al*, *J. of Cryst. Growth* **95** 60 (1989).

15th Int. Symp. "Nanostructures: Physics and Technology"
Novosibirsk, Russia, June 25–29, 2007

Direct observation of the transition from the diffusive to the ballistic regime in a p-Ge/$Ge_{1-x}Si_x$ and n-$In_{1-x}Ga_xAs$/GaAs quantum wells

Yu. G. Arapov, G. I. Harus, I. V. Karskanov, V. N. Neverov, N. G. Shelushinina, M. V. Yakunin and S. M. Podgornyh

Institute of Metal Physics RAS, Ekaterinburg, GSP-170, 620041, Russia

Abstract. For the dilute 2D-hole gas in a GeSi/p-Ge/GeSi multi-quantum-well, a low-temperature transition from a metallic ($d\rho/dT > 0$) to an insulator ($d\rho/dT < 0$) behavior of resistivity $\rho(T)$ was observed at $T^* = 1.5$ K. Contrary, a 2D-elecron gas within a n-InGaAs/GaAs double-quantum-well exhibits a monotonous "insulator-like" dependence of mobility $\mu(T)$ ($d\rho/dT < 0$) at $T = 1.8-70$ K in zero field. Temperature dependence of the Hall constant $R_{H0}(T)$ has a non-monotonous character. These temperature intervals for our samples correspond to the transition from the diffusive regime ($2\pi k_B T\tau/h \ll 1$) to the ballistic one ($2\pi k_B T\tau/h > 0.1$). The value of temperature (T^*) that corresponds to maximum $\rho(T)$, a change in $\delta\sigma_{ee}(T)$ and $\mu(T)$ slopes, and the temperature dependence of $B_{CR}(T)$, defined as $\rho_{xx}(B_{CR}, T) = \rho_{xy}(B_{CR}, T)$, are used for estimation the parameter $k_B T^*\tau/\hbar$ at the transition between the two regimes.

Introduction

In contrast to the extensively studied two-dimensional n-, p-GaAs/AlGaAs heterostructures (HS), the transport and magnetotransport properties of n-InGaAs/GaAs and p-Ge/GeSi HS remain much less understood. So far the electron-electron interaction (eei) that gives a quantum corrections to the Drude conductivity has been investigated, both theoretically and experimentally, only within the diffusive regime, which is applicable to the low mobility (μ) (small τ — transport relaxation time) 2DE(H)G and low temperatures [1]. More recently, a systematic theory for the eei in the ballistic and intermediate regimes has been developed [2–4]. Largely motivated by these theories the experimental activity splash is observed [5–7 and Refs. within]. However, we know only one experimental work [6], where two regimes transition have been clearly observed and the parameter $2\pi k_B T\tau/\hbar$ value have been estimated. It is more difficult to extract experimentally the parameter value because the theories do not divide the interaction corrections into the diffusion and ballistic parts and do not predict any specific features of these corrections. In accordance the theories [3,4] crossover between the two regimes is expected to occur at $k_B T\tau/\hbar \ll 1/2\pi \ll 0.1$. For strong interaction $(F_\sigma^0)^2/(1+F_\sigma^0) \gg 1$ (in particular, in the vicinity of "metal-insulator" transition (2D MIT $B = 0$) a condition of the crossover between two regimes is modified $k_B T\tau/\hbar \ll (1+F_\sigma^0)1/2\pi$ [3,4].

Some questions are rises. What experiments present an evidence of the apparent transition between two regimes and that it allow to estimate the critical value of $k_B T\tau/\hbar$? Is this critical value universal for various 2D systems? How one is agreement with the experimental data?

First of all, the outstanding and recent experiments on the study of the dephasing rate $\tau_\varphi - 1(T)$ temperature dependence. According to the Fermi-liquid theory the $\tau_\varphi^{-1}(T)$ due to e-e scattering is dominated either by a linear or quadratic term, depending on regime: diffusive or ballistic, hence the $k_B T\tau/\hbar$ value you have. In the experiment [5] for the GaAs/AlGaAs HS with the low density 2DHG the parameter $k_B T\tau/\hbar$ varies with temperature from 0.06 to 0.8 for the lowest density and from 0.1 to 0.9 for the highest density and the τ_φ, extracted from the magnetoresistance, is dominated by the T^2 term due to p-p scattering in the ballistic regime Thus, the highest limit of parameter $k_B T\tau/\hbar$ value is 0.06–0.1 ($k_B T\tau/\hbar < 0.06-0.1$).

Further, Renard *et al* [6] has reported an experimental study of quantum conductivity corrections in a low mobility, high density 2DEG in a GaAs/AlGaAs QW in a wide T range (1.5 K–110 K). These temperatures cover both diffusive and ballistic interaction regimes for their samples. It has been therefore possible to study the crossover between these regimes for both the longitudinal conductivity (σ_{xx}) and the Hall effect. They perform a parameter free comparison of experimental data for σ_{xx} at zero magnetic field, the Hall coefficient and the magnetoresistivity with the recent theories of interaction-induced corrections to the transport coefficients. This change of behavior is observed at $T = 20$ K. This is in a qualitative agreement with the theory [3,4], predicting the crossover to occur at $k_B T\tau/\hbar = 0.1$ which corresponds to $T = 30$ K.

Experimental results and discussion

We performed the experiments on two 2D systems: multi-quantum-well (MQW) p-Ge/GeSi and double-quantum-well (DQW) n-InGaAs/GaAs.

1. Experimental data are presented for two samples p-Ge/GeSi with $p_s = 1.1(1.4)10^{11}$ cm^{-2}, $\mu_p = 4.0(3.1)10^3$ cm^2/Vs, zero field resistivity $\rho_0 = 15(16)$ k$\Omega/\square$ (per layer) and low field Hall $\rho_{xy}(T)$. The longitudinal and Hall resistivities have been investigated in magnetic fields $B_\perp \le 5.0$ T at temperatures $T = (0.2-4.2)$ K. A non-monotonous temperature behavior resistivity is revealed (Fig. 1). The "metallic" behavior ($\delta\rho/\delta T > 0$) takes place from 0.2 to 1.5K and changes to the "insulating" behavior ($\delta\rho/\delta T < 0$) at higher temperatures.

We believe that in our experiment the crossover between diffusive and ballistic regimes with an assumption of smooth character of random impurity potential may be responsible for the non-monotonous $\rho(T)$ dependence. Critical value of $k_B T\tau/\hbar = 0.04$.

2. We study n-InGaAs/GaAs DQW samples with $n_s = 2.3\times10^{11}$ cm^{-2} and $\mu = 1.2\times10^4$ cm^2/Vs. The measure-

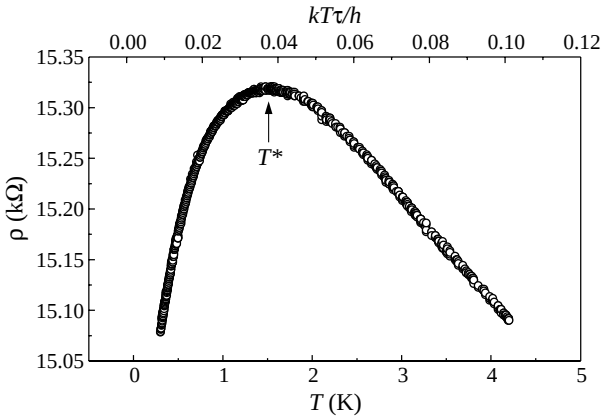

Fig. 1. Temperature dependence of zero-field resistivity.

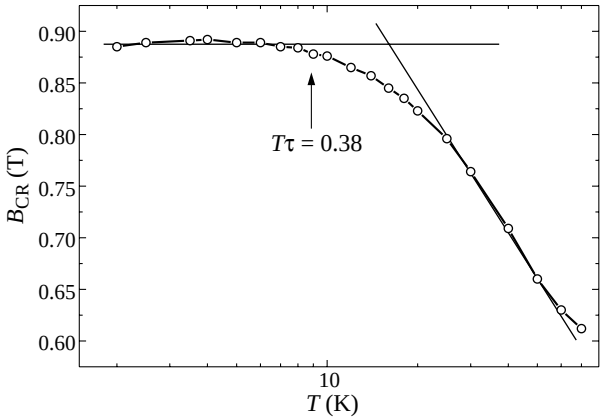

Fig. 2. Experimental temperature dependence of the critical magnetic field, for which $\rho_{xx}(B,T) = \rho_{xy}(B,T)$.

ment of $\rho_{xx}(B,T)$, $\rho_{xy}(B,T)$ and calculation of $\sigma_{xx}(B,T)$, $\sigma_{xy}(B,T)$ were carried out in a wide T-interval (1.8–70) K. In a low $B_\perp$. the negative magnetoresistance (NMR) on a $\rho_{xx}(B,T)$ was observed. The so-called T-independent point ($T_{\rm ind}$) is seen at some $B_{\rm CR}$. At this value of magnetic field we have also $\rho_{xx}(B,T) = \rho_{xy}(B,T)$, i.e. $\omega_c\tau = 1$. With temperature increasing above 9 K $B_{\rm CR}$ moves to low magnetic fields (see Fig. 2). We think that $B_{\rm CR}(T)$ is connected with the beginning of the $\tau(T)$ dependence that, i.e. with the beginning of the transition from diffusive to ballistic regime.

3. Extrapolation of the B^2 dependences of the high-field NMR ($B \gg B_{\rm tr}$) to zero field is used to separate the weak localization and eei parts of the total quantum correction to the conductivity as in the diffusive and ballistic regimes [8]. In Fig. 3. we plot the experimental temperature dependence of eei quantum correction to conductivity. As can be seen, the logarithmic diffusive part vanishes at $T > 9.0$ K when the ballistic part starts to vary linearly with temperature (see the inset of Fig. 3). Therefore we believe that Fig. 3 establishes a crossover from the diffusive to the ballistic limit in the behavior of the interaction-induced correction to the zero-B conductivity. This change of behavior is observed at $T = 10$ K ($k_{\rm B}T\tau/\hbar = 0.36$).

Conclusions

The critical parameters $k_{\rm B}T\tau/\hbar$ for the p-Ge/GeSi MQW and n-InGaAs/GaAs DQW differ an order of magnitude. It is doubtful that critical value is universal for various 2D systems.

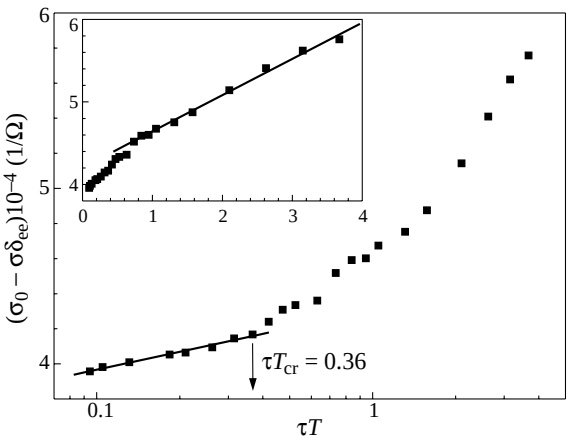

Fig. 3. Experimental temperature dependence of eei quantum correction to conductivity (black dots) in a logarithmic scale. The same data are plotted in a linear scale at the inset. The lines corresponds to the $\ln(T\tau)$ law at $T\tau < 0.38$ and linear law at $T\tau > 0.38$.

Acknowledgement

The work was supported in part by: RFBR No. 05-02-16206; program of RAS “Low-dimensional quantum heterostructures”.

References

[1] B. L. Altshuler and A. G. Aronov, *Electron-Electron Interaction in Disordered Systems*, edited by A. L. Efros and M. Pollak (North-Holland, Amsterdam, 1985).
[2] A. Gold *et al*, *Phys. Rev. B* **33**, 1076 (1986).
[3] G. Zala *et al*, Phys. Rev. B **64**, 214204 (2001); *Phys. Rev. B* **64**, 201201 (2001); *Phys. Rev. B* **65**, 020201 (2002).
[4] I. V. Gornyi *et al*, *Phys. Rev. Lett.* **90**,076801 (2003); *Phys. Rev. B* **69**, 045313 (2004), *ibid. B* **64**, 214204 (2001).
[5] Y. Y. Proskuryakov *et al*, *Phys. Rev. Lett.* **89**, 076406 (2002).
[6] V. Renard *et al*, *Phys. Rev. B* **72**, 075313 (2005).
[7] G. M. Minkov *et al*, *Phys. Rev. B* **74**, 045314 (2006).
[8] Yu. G. Arapov *et al*, *Semiconductors* **33**, 978 (1999), *Low Temperature Physics* **33**(2/3), (2007).

15th Int. Symp. "Nanostructures: Physics and Technology"
Novosibirsk, Russia, June 25–29, 2007

Numerical simulation of electron transport in disordered Cr granular films

V. A. Krupenin[1], *V. O. Zalunin*[1,4], S. A. Vasenko[1] and A. B. Zorin[2,3]

[1] Laboratory of Cryoelectronics, Moscow State University, 119899 Moscow, Russia
[2] Physikalisch-Technische Bundesanstalt, 38116 Braunschweig, Germany
[3] Nuclear Physics Institute, Moscow State University, 119899 Moscow, Russia
[4] Mirantis Inc, 107023, Moscow, Russia

Abstract. In this paper we report the results of numerical simulation of electron transport in a two dimensional Cr granular films. Theoretical model based on two-dimensional array of Coulomb-blockade islands was developed. Potential and $I-V$ curves were numerically calculated and matched with experimental results. Transition from quasi-one-dimensional to two-dimensional transport regime was observed and discussed.

Introduction

Granular films are promising candidates to replace lithographically defined islands and tunnel barriers in various single-electron devices. Typical size of grains in such structures is in the range of 2–20 nm, enabling operation of these devices at temperatures higher than 4.2 K. The properties of granular single-electron devices strongly depend on its parameters, i.e. self capacitance of islands (grains), mutual capacitance and resistance between grains, operation temperature, etc. For example, granular structures with relatively low intergrain resistance and high mutual capacitance were used as resistive elements instead of traditional tunnel junctions in original SET transistor (see Ref. [1]), more resistive structures were proposed to build memory cell (see, for example [2]). In this paper we present the results of numerical simulation of Cr two-dimensional structures which were earlier studied experimentally [3].

1. Experimental results overview

Our Cr films had the sizes of 1000 × 100, 500 × 100 and 200 × 100 nm^2, while their thickness was 7–8 nm. The average grain size according to TEM image (Fig. 1a) was found to be in the range of 10–15 nm. One can find detailed description of the sample preparation technique in [3]. $I-V$ curves of the samples measured at low temperature ($T_{\text{bath}} = 25$ mK) demonstrated Coulomb blockade phenomena. The Coulomb blockade threshold was measured to be 3–6 mV. Samples demonstrated abrupt current switching from the blockade to the conductive state. The typical amplitude of these current jumps varied from 200 pA to 900 pA. Hysteretic behavior was also observed: switching from the conducting to the blockade state occurred at lower voltages than switching from the blockade to conducting state. This behavior was reported for the first time in Ref. [3].

2. Theoretical model and simulation results

We suppose that the observed peculiarities of single-electron transport are related to the influence of the local charge traps formed in the film. Fabrication technique allows "large" grain formation, i.e., fusion of two or more grains together (Fig. 1a). In our study we will follow the approach developed in [4] and approximate our chromium granular film by a two-dimensional array of conducting islands separated by tunnel junctions. "Large" grain in contrast to other grains will be connected with more than 4 neighbors depending on it's geometry. Such a configuration is shown in Fig. 1b.

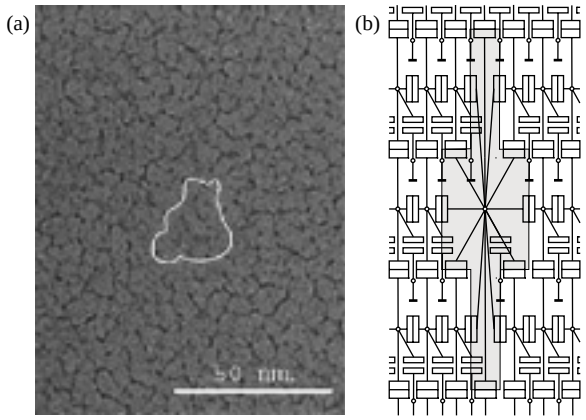

Fig. 1. a) TEM image of the studied chromium film. One of the "large" grains is bounded by the white line. b) Equivalent scheme of "large" grain.

The crossection of potential barrier formed by an array of islands with "large" grain, i.e. the energy of the electron consecutively placed in every island of the array are represented in Fig. 2. Without a loss of generality we placed "large" grain symmetrically between the side boundaries of the array. One can see a well pronounced minimum of potential, forming a potential well. The depth of this potential well is about 0.5 meV. With increasing the bias voltage (when it becomes equal to the height of the potential barrier) the first electron passes a part of the array and getting trapped in the potential well .

The potential curve of the array with one electron, trapped in the potential well, is shown in the Fig. 2. It should be noted that the height of the potential barrier near the "large" grain increases by approximately 1 meV. Every excess electron on the island of the array has a finite screening length ($\Lambda = 5-6$ elementary cells for our structures) and acts as a soliton repulsing from other soliton. So, the excess electron, trapped in the "large" grain, will block the electrical transport through the array. When this electron leaves the trap, the blockade is taken down sharply and current starts to flow. Let us note that the actual situation depends on temperature and position of other electrons. For example, second electron can be trapped in the "large" grain (one can see a small minimum shown by grey curve in Fig. 2).

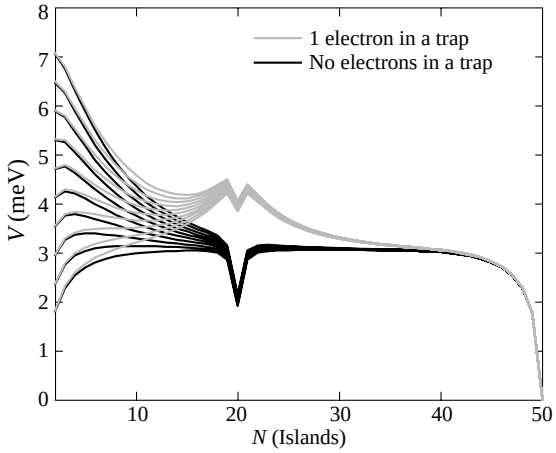

Fig. 2. Crossection of the potential profile of the array with a "large" grain for various bias voltages V_b.

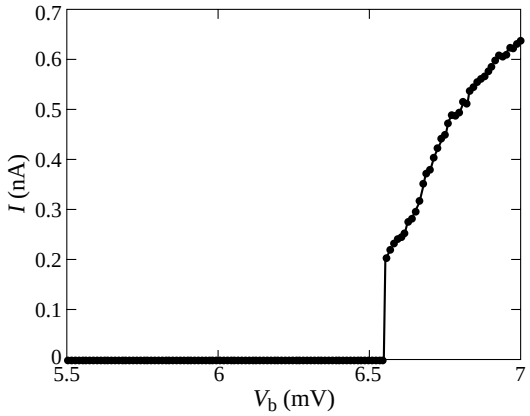

Fig. 3. $I-V$ curve of the array calculated using Monte-Carlo technique. Experimentally observed current jump is reproduced.

To reproduce the dynamic behavior of the system we have used Monte-Carlo technique. Typical $I-V$ curve is presented in Fig. 3. The abrupt switching between the blockade and conductive states is clearly visible. In our simulation model we were unable to take into account all factors affecting actual experimental result, for example, background charge fluctuations. Moreover, in real experiments these factors are smoothly changing in time, so two subsequent measured $I-V$ curves can be slightly different [3]. So, we compare only typical switching parameters. One can see that the typical switching voltage of 5–6 mV and current jump amplitude of $200-300$pA agree quite well with our experiment. To move towards more realistic situation one has to take into account the existence of multiple "large" grains of arbitrary form located in an different points of the array. It should be noted that, again in spite of a big parameters number ("large" grains number, its form and position), $I-V$ curves look similarly . All "large" grains increased the total potential barrier height, switching voltage and the amplitude of current jump. The calculated charge distributions over the array are represented in Fig. 4. Discrete charges in the blockade state (upper panel) are placed at the points where the self-consistent potential is minimal. Slightly above the blockade threshold one can see the excess charges distributed along two pathways (bottom panel). They are repulsed from the side boundaries of the array and the trapped electron. Therefore, current flows through very narrow pathways and the system

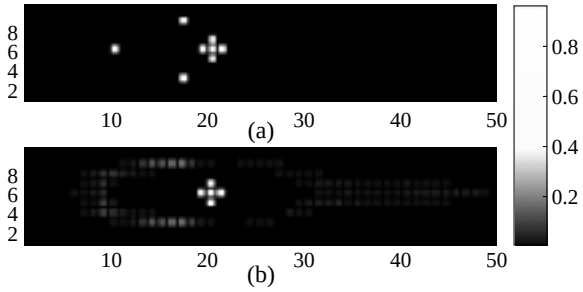

Fig. 4. Average charge of the array islands in elementary charge units. Bias voltage V_b slightly below blockade threshold (upper panel) and above the blockade threshold (bottom panel). One can see quasi-one-dimensional behavior.

can be considered as quasi one dimensional. With further increasing of the bias voltage other tunnel junctions are becoming unblocked and current starts to flow through the entire array. As a result, system switches from quasi one dimensional state to pure two dimensional state.

3. Conclusion

In this paper we have developed the numerical model describing the sharp current jumps from the blockade to the conducting state in non-regular two-dimensional tunnel junctions array. Applying "large" grain model we have calculated potential distribution and $I-V$ curves of our structures. Typical parameters including the blockade threshold and current jump amplitude agree well with the experimental results. Quasi-one-dimensional and two-dimensional transport regimes were observed and discussed.

References

[1] V. A. Krupenin, A. B. Zorin, M. N. Savvateev, D. E. Presnov and J. Niemeyer, *Journal of Applied Physics* **90(5)**, 2411 (2001).

[2] V. A. Krupenin, V. O. Zalunin, V. S. Vlasenko, D. E. Presnov, A. B. Zorin, *Proc. of 13th Int. Symposium "Nanostructures: Physics and Technology"*, Ioffe Institute (2005).

[3] V. A. Krupenin , V. O. Zalunin and A. B. Zorin, *Microelectronic Engineering* **81**, 218 (2005).

[4] N. S. Bakhvalov, G. S. Kazacha, K. K. Likharev, S. I. Serdyukova, *Sov. Phys. JETP*, **68** 581 (1989).

15th Int. Symp. "Nanostructures: Physics and Technology"
Novosibirsk, Russia, June 25–29, 2007

Integer quantum Hall effect with correlated disorder

A. A. Greshnov and *G. G. Zegrya*
Ioffe Physico-Technical Institute, St Petersburg, Russia

Abstract. The influence of disorder shape upon longitudinal σ_{xx} and Hall σ_{xy} conductivities has been studied theoretically in the regime of integer quantum Hall effect (IQHE). It is shown that widths of IQHE plateaus as well as peak values of longitudinal conductivity strongly depend on the ratio of disorder correlation length λ to magnetic length $a_{\rm H}$. In the case of short-wavelength disorder, $\lambda \ll a_{\rm H}$, peak values of $\sigma_{xx}^{(N)}$ are proportional to Landau level (LL) number $N \geqslant 1$, $\sigma_{xx} = 0.5Ne^2/h$. In the case of long-wavelength disorder, $\lambda \gg a_{\rm H}$, $\sigma_{xx}^{(N)}$ are LL number independent with values considerably less than $0.5e^2/h$. Our results are in good agreement with available experimental data.

1. Introduction

Despite the considerable progress in IQHE, there is no comprehensive theory of this intriguing phenomena up to date. An essential component of understanding of IQHE is localization of carriers by disorder potential of impurities [1]. In the regime of IQH localization length $\xi_N(E) \propto (E - E_N)^{-\nu}$, where $N \geqslant 1$ is LL number, $\nu \approx 2.3$ is universal exponent [2,3]. Due to this power law it becomes possible to distinguish between bands of localized and extended states only considering samples of finite dimensions $L_x \times L_y$ or (more naturally) non-zero temperature $T \neq 0$. As a result of localization the regions of zero diagonal conductivity $\sigma_{xx} = 0$ and constant Hall conductivity σ_{xy} ("plateaus") as well as the regions of $\sigma_{xx} \neq 0$ and varying σ_{xy} ("P-P transitions") can be observed.

In this paper we present numerical study of the problem of plateau widths and peak values of longitudinal conductivity supporting it by essential theoretical arguments. This problem is of great interest [2] because plateau widths and peak values of σ_{xx} reflect peculiarities of localization in magnetic field. It was argued for the first time in the works of Khmelnitskii and Pruisken *et al* [4] that peak values of longitudinal conductivity are universal, i.e. independent of details of disorder and LL number $N \geqslant 1$, $\sigma_{xx}^{(N)} = 0.5e^2/h$. Eight years later this relationship was confirmed by numerical study of Huo *et al* [5] for $N = 1$ in the case of short-range disorder. However, experimental situation is not so clear. Peak values considerably less than $0.5e^2/h$ were found in Refs. [6,7,3] and explained [7] by long-range nature of disorder in the studied samples. At the same time IQH plateaus corresponding to $N \geqslant 2$ are usually absent in the samples showing strict fulfillment of "0.5 law" for the lowest LL $N = 1$ [8], which impedes the verification for arbitrary N. Below we provide consecutive theoretical study of the mentioned problem.

2. Model

Let us consider two-dimensional electron gas of finite dimensions $L_x \times L_y$ at zero temperature $T = 0$ taking into account only elastic impurity scattering of electrons, described by two-dimensional disorder potential $V(\mathbf{r})$. In fact this model allows one to describe not only the effect of finite dimensions [9] at $T = 0$, but also the effect of finite-temperature assuming $L_x = L_y = L_\phi$, $L_\phi \propto T^{-p/2}$ being so-called phase-breaking length [2]. Below we consider gaussian model of disorder, modelling $V(\mathbf{r})$ as

$$V(\mathbf{r}) = V_0 \sum_{\mathbf{k}} F(|\mathbf{k}|) \exp(i\varphi_{\mathbf{k}}) \exp(i\mathbf{kr}), \qquad (1)$$

with $F(k) = \exp(-(k/k_0)^2)$ and uniformly distributed random phases $\varphi_{\mathbf{k}} = -\varphi_{-\mathbf{k}}$, which gives zero mean value $\langle V(\mathbf{r})\rangle = 0$ and gaussian form of correlators $\langle V(\mathbf{r})V(\mathbf{r}+\mathbf{l})\rangle/\langle V^2(\mathbf{r})\rangle = \exp(-l^2/2\lambda^2)$, $\lambda = \sqrt{2}/k_0$ being a correlation length of disorder. The restriction applied to the shape of disorder potential allows to describe it using two parameters, *viz.* the amplitude $\overline{V} = \sqrt{\langle V^2(\mathbf{r})\rangle}$ and correlation length λ.

Absolute value of λ depends on type and degree of disorder in a particular sample. In strong magnetic fields of several Tesla typical value of magnetic length is $a_{\rm H} = \sqrt{\hbar c/eB} \sim 100$ Å. This means both cases of short-wavelength disorder, $\lambda \ll a_{\rm H}$, and long-wavelength disorder, $\lambda \gg a_{\rm H}$, can be realized in the heterostructures. The case of short-wavelength disorder realizes in $In_xGa_{1-x}As$ samples where it is due to randomness in In and Ga positions, so $\lambda \sim 20$ Å. Long-wavelength disorder typically realizes in modulation-doped GaAs quantum wells, where we can estimate $\lambda \sim 500$ Å.

The hamiltonian of noninteracting electrons in magnetic field $\mathbf{B}$ and disorder potential $V(\mathbf{r})$ is

$$\hat{H} = \frac{(\hat{\mathbf{p}} - e/c\mathbf{A})^2}{2m^*} + V(\mathbf{r}), \quad \mathrm{rot}\mathbf{A} = \mathbf{H} = \mathbf{B}. \qquad (2)$$

Applying appropriate gauge and (quasi)periodic boundary conditions we obtain eigenenergies and eigenfunctions of hamiltonian Eq. (2) by direct numerical diagonalization. The diagonal and Hall conductivities are given at $T = 0$ by the following linear-response formulas [10,11]:

$$\sigma_{xx}(\omega) = \frac{\pi e^2}{S\omega} \sum_{i<F,f>F} |(v_x)_{if}|^2 \delta(\hbar\omega + E_i - E_f), \qquad (3)$$

$$\sigma_{xy} = \frac{e^2\hbar}{S} \sum_{i<F,f>F} \frac{2Im\{(v_x)_{if}(v_y)_{fi}\}}{(E_i - E_f)^2}. \qquad (4)$$

Here indices i and f refer to the (microscopic) electronic states, F is Fermi level, $S = L_xL_y$ is area of a sample. Since direct evaluation of static conductivity using Eq. (3) gives senseless (zero or infinite) answer in the case of finite system we redefine static longitudinal conductivity as $\sigma_{xx} = \lim_{\Omega\to 0}\int_0^\Omega \sigma_{xx}(\omega)d\omega/\Omega$, keeping in mind $\hbar\Omega \gg \delta E$, where $\hbar\Omega$ plays the role of Fermi surface width, δE is mean distance between (microscopic) energy levels. Using this definition we can write σ_{xx} in terms of velocity matrix element squared and averaged over Fermi surface $\langle|v_x|^2\rangle$ and density of states (DOS) $D(E)$ [10,14]:

$$\sigma_{xx} = \pi e^2\hbar S D^2(E_{\rm F})\langle|v_x|^2\rangle. \qquad (5)$$

3. Results and discussion

As follows from Eq. (5), diagonal conductivity σ_{xx} can be expressed as a product of DOS and typical value of velocity matrix element $\overline{v} = \sqrt{\langle |v_x|^2 \rangle}$. The first factor, $D(E)$, reflects broadening of LLs due to the presence of disorder. Calculated DOS is shown in Fig. 1 for the cases of (a,b) long-wavelength and (c,d) short-wavelength disorder. Our numerical results are in qualitative agreement with analytical formulas of Ref. [12] and Ref. [13] in the long-wavelength and short-wavelength cases respectively. In the first case cyclotron motion of electrons can be described semiclassically and $D(E)$ is given by LL number independent formula [12]

$$D_n(E) \propto \mathrm{Prob}\{V(\mathbf{r}) = E - \overline{\hbar}\omega_c(n+1/2)\}, \quad n \geqslant 0. \quad (6)$$

In the opposite case of short-wavelength disorder semi-elliptical shape of DOS was obtained in Ref. [13]:

$$D_n(E) \propto \sqrt{\Gamma_n^2 - (E - \overline{\hbar}\omega_c(n+1/2))^2}, \quad n \geqslant 0. \quad (7)$$

Components of conductivity tensor calculated for (a) long-wavelength and (b) short-wavelength disorder are presented in Fig. 2. The calculation was conducted for $L_x = L_y = 50a_H \sim 10^{-4}$ cm and quite small amplitude $\overline{V} = 0.1\overline{\hbar}\omega_c$ taking into account 6 LLs. Results were averaged over 400 realizations and it was checked that variations of sample length and disorder amplitude (up to $\overline{V} \sim \overline{\hbar}\omega_c$) affect weakly.

In the case of long-wavelength disorder all the five shown plateaus on σ_{xy} plot are highly pronounced. The peak values of diagonal conductivity $\sigma_{xx}^{(N)}$ are independent of LL number N, being approximately $0.35e^2/h$ for $\lambda = 4a_H$ and decreasing with the growth of λ. Such a behavior of both diagonal and Hall conductivities is entirely consistent with the experiments on high-mobility samples [6,3].

In the opposite case of short-wavelength disorder only one developed plateau is seen on the calculated σ_{xy} plot. Peak values of diagonal conductivity $\sigma_{xx}^{(N)}$ grow linearly with N. The first peak value is approximately $0.5e^2/h$, the second e^2/h *etc*. These results are consistent principally with experiment since only one or two IQH plateaus corresponding to $N = 1$ are seen usually in the experiments on samples with short-wavelength disorder and the value of $0.5e^2/h$ is believed to be exact for the first peak of σ_{xx} [8].

To conclude, we would like to present an explanation of obtained dependencies [15]. First, as it is seen from Fig. 1 peak values of DOS weakly depend on LL number, therefore we can hold $\sigma_{xx}^{(N)} \propto \langle |v_x^{(N)}|^2 \rangle$. Second, the structure of different LLs

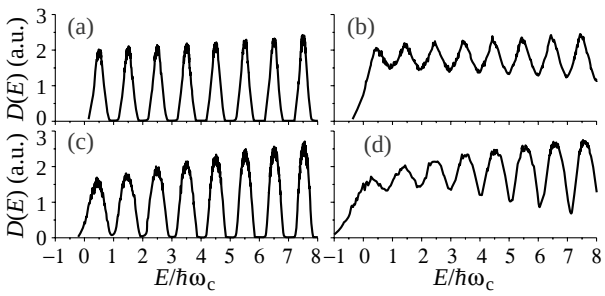

Fig. 1. Calculated density of states (a) $\lambda \gg a_H$, $V \ll \overline{\hbar}\omega_c$; (b) $\lambda \gg a_H$, $V \gtrsim \overline{\hbar}\omega_c$; (c) $\lambda \ll a_H$, $V \ll \overline{\hbar}\omega_c$; (d) $\lambda \ll a_H$, $V \gtrsim \overline{\hbar}\omega_c$.

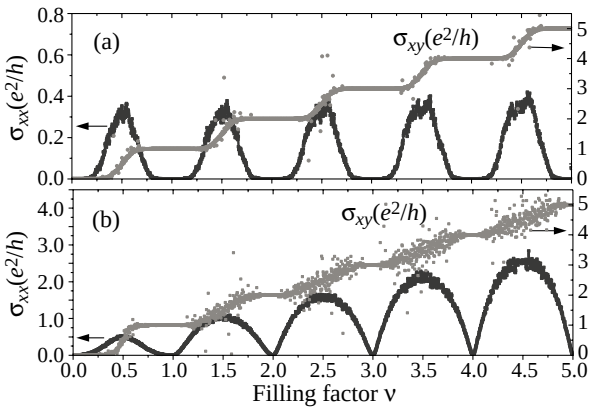

Fig. 2. Calculated longitudinal and Hall conductivities for (a) long-wavelength disorder, $\lambda = 4a_H$, and (b) short-wavelength disorder, $\lambda = 0.25a_H$.

(set of allowed trajectories) is identical in the long-wavelength case [12], so $\langle |v_x^{(N)}|^2 \rangle$ is LL number independent in this case. Moreover, $\langle |v_x^{(N)}|^2 \rangle$ depends considerably on λ due to its nature, reflecting mixing of adjacent LLs. In the limit of large correlation length this mixing (but not broadening) becomes negligible, so $\lim_{\lambda\to\infty} \sigma_{xx}^{(N)} = 0$. Third, correlation length of the wave functions cannot be less than magnetic length a_H therefore we can use statistical approach and treat microscopic wave functions belonging to different LLs as random superpositions of basis functions of harmonic oscillator [15]. As a result $\sigma_{xx}^{(N)} \propto \langle |v_x^{(N)}|^2 \rangle \propto N$ by direct analogy with the matrix elements of harmonic oscillator.

Acknowledgements

This work has been supported by RFBR (05-02-16679) and Federal Programme on Support of Leading Scientific Schools. A. A. Greshnov appreciates the support of Dynasty Foundation and Russian Science Support Foundation.

References

[1] R. E. Prange and S. M. Girvin Ed., *The Quantum Hall Effect, 2nd Ed.*, New York: Springer-Verlag, 1990.
[2] B. Huckestein, *Rev. Mod. Phys.* **67**, 357 (1995).
[3] S. Koch *et al*, *Phys. Rev. Lett.* **67**, 883 (1991).
[4] D. E. Khmelnitskii, *JETP. Lett.*, **38**, 552 (1983); chapter 5 of Ref. [1] and references therein.
[5] Y. Huo *et al*, *Phys. Rev. Lett.* **70**, 481 (1993).
[6] L. P. Rokhinson *et al*, *Solid State Comm.* **96**, 309 (1995); P. T. Coleridge, *Phys. Rev. B* **60**, 4493 (1999); F. Hols *et al*, *Physica B* **298**, 88 (2001).
[7] H. P. Wei *et al*, *Phys. Rev. B* **45**, 3926 (1992).
[8] D. Shahar *et al*, *Phys. Rev. Lett.* **74**, 4511 (1995); R. B. Dunford *et al*, *Physica E* **6**, 297 (2000); E. Peled *et al*, *Phys. Rev. Lett.* **90**, 246802 (2003); S. S. Murzin *et al*, *Phys. Rev. B* **66**, 233314 (2002).
[9] A. A. Greshnov *et al*, *Semiconductors* **40**, 89 (2006).
[10] Y. Imry, *Introduction to Mesoscopic Physics*, Oxford University Press, 2002.
[11] Q. Niu *et al*, *Phys. Rev. B* **31**, 3372 (1985).
[12] M. Tsukada, *J. Phys. Soc. Jpn.* **41**, 1466 (1976).
[13] T. Ando, Y. Uemura, *J. Phys. Soc. Jpn.* **36**, 959 (1974) and consecutive papers.
[14] S. R. E. Yang *et al*, *Phys. Rev. Lett.* **74**, 3229 (1995).
[15] A. A. Greshnov and G. G. Zegrya, submitted to *JETP. Lett.*

15th Int. Symp. "Nanostructures: Physics and Technology"
Novosibirsk, Russia, June 25–29, 2007

Effects of Wannier–Stark localization and resonant interminiband tunneling in transport properties of GaAs/AlGaAs superlattices with weak barriers

A. A. Andronov, *D. I. Zinchenko*, E. P. Dodin and Yu. N. Nozdrin
Institute for Physics of Microstructures, Russian Academy of Sciences,
Nizhny Novgorod GSP-105 603600, Russia

Abstract. The electron transport in GaAs/$Al_xGa_{1-x}As$ superlattices with weak barriers was studied at 4K. It is shown that resonant interminiband tunneling plays an important role in the shape of I–V curves for such structures. The correspondence between positions of current peaks and calculated anticrossings of Wannier–Stark levels is established.

Introduction

Study of vertical transport in semiconductor superlattices (SL) with narrow minibands and narrow minigaps is of great interest as a way of realization of dynamic negative differential conductivity (NDC) caused by Bloch oscillations of electrons at Terahertz frequency and construction of Terahertz oscillator on this basis [1]. Quasiclassical Monte-Carlo numerical simulation [1] shows the possibility of dynamic NDC at the Bloch frequency together with positive static differential conductivity in SL with the optical phonon energy lying below the bottom of the second miniband and under strong interminiband Zener tunneling. On the other hand, this simulation takes into account only non-resonant interminiband Zener tunneling. In this work we studied the effects of resonant Zener tunneling between localised Wannier–Stark states of different minibands on the transport properties of such SLs.

1. Experimental

We've studied GaAs/$Al_{0.1}Ga_{0.9}As$ superlattices with the parameters shown in Table 1 (we used transfer matrix method to calculate dispersion relation). Here E_0 is the bottom of the first miniband, E_1 is the top of the first miniband, E_2 is the second miniband bottom, ΔE_1 is the first miniband width, ΔE_2 is the second miniband width, E_{gap} is the minigap between first two bands, d is the superlattice period, w and b are well and barrier widths respectively, N is the number of periods.

The GaAs/$Al_{0.1}Ga_{0.9}As$ superlattices consisting of 100 and 1000 periods were mounted in n^+-n-n^+ structures. The superlattice itself was undoped with background concentration $n \approx 1 \times 10^{15}$ cm^{-3} and the n^+ contact regions were doped with $n = 3 \times 10^{18}$ cm^{-3}. Studied samples are processed into mesas 500 and less micrometers in diameter. The ohmic contacts are provided by standard Au-Ni-Si deposition and thermal treatment.

Table 1. Sample parameters.

Sample	426	816
E_0 (meV)	3.2	6.2
ΔE_1 (meV)	11.2	10.7
E_1 (meV)	14.4	16.9
E_{gap} (meV)	7.1	13.9
E_2 (meV)	21.3	30.8
ΔE_2 (meV)	34.9	34.9
$d = w + b$ (Å)	185+10	161+20
N	100	1000

2. Transport properties

In this work we studied the I–V curves of different superlattice samples in the region of strong interminiband tunneling. Some similar studies were reviewed in the work [2]. However most of the works on this subject are dedicated to the weakly coupled superlattices where quantum wells are separated by strong barriers and usually only transitions between neighboring wells are significant for the electron transport. Also such superlattices are usually divided into high and low electric field regions (domains). In our work we used SL with weak barriers (and narrow minigaps) which allowed us to observe rich structures on the I–V caused by resonant tunneling between Wannier–Stark levels of different minibands located several SL periods apart of each other.

The I–V curves for 2 samples 426 and 816 are shown in Fig. 1. We can divide these curves into 3 main regions: 1) low

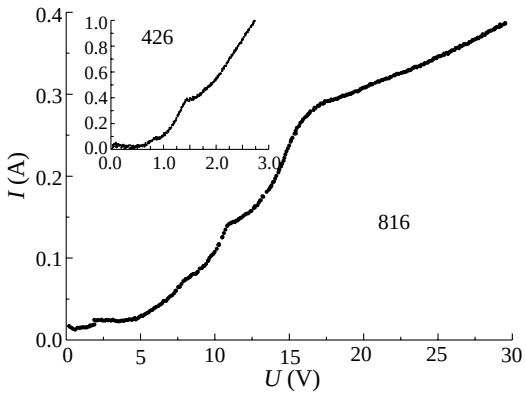

Fig. 1. I–V curve for sample 816 at 4 K. *Inset:* I–V curve for sample 426 at 4 K.

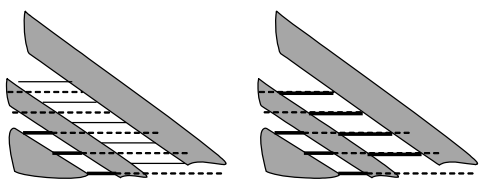

Fig. 2. Non-resonant and resonant alignment of Wannier–Stark levels in different minibands.

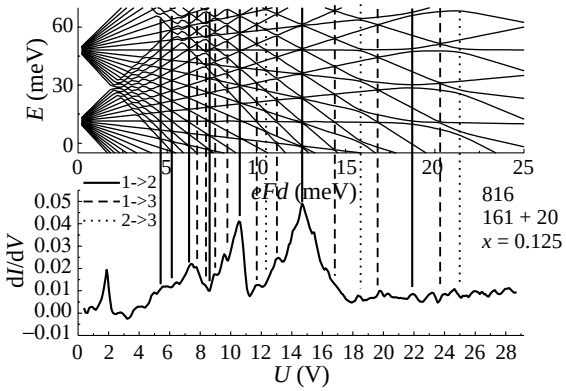

Fig. 3. *Upper part:* calculated "fan chart" of energy levels of first 3 minibands in SL 816. *Lower part:* numerical derivative of experimental I–V curve for SL 816. Lines show anticrossing positions of WS levels.

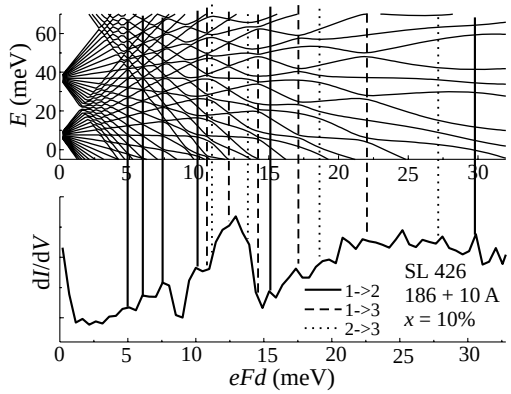

Fig. 4. *Upper part:* calculated "fan chart" of energy levels of first 3 minibands in SL 426. *Lower part:* numerical derivative of experimental I–V curve for SL 426. Lines show anticrossing positions of WS levels.

field region with miniband transport; 2) rising intermediate region where interminiband tunneling takes place and 3) high field region that shows some sort of saturation behavior. In this report we will discuss the form of the I–V in the second region (in intermediate fields).

It is well known [3] that when we apply electric field together with periodic potential of the superlattice, the minibands split into the series of so-called Wannier–Stark levels (or Wannier–Stark resonances). Each band gives rise to the equidistant series of levels, their number equals to the number of sites in the lattice. When we change the electric field strength the levels of different minibands shift against each other, and for some values of the electric field the resonances between levels of different minibands can occur (Fig. 2). It happens approximately when the condition $E_i - E_j = n\,eFd$ is fulfilled. Here E_i and E_j are the energies of i's and j's levels in the quantum well (more precisely it's the "center-of-mass" energy of the corresponding miniband), e is the electron charge, F is the field strength and d is the period of superlattice.

To find the resonance positions more precisely, the numerical algorithm was developed to calculate the positions of energy levels in superlattice with applied field. First we calculated the Bloch functions of field-free SL with the transfer matrix method, next we used them to calculate Wannier functions for several lowest minibands, and finally we diagonalised the Hamiltonian with the field in the basis of these Wannier functions. Similar process was used in [4].

The result of calculations is shown in the upper parts of Figs. 3 and 4. Here we can see the dependence of levels position on the applied field (so-called "fan chart" of Wannier–Stark levels). When the levels of different minibands get close, anticrossing of energy levels occurs. Set of anticrossings at fixed field F accounts for resonant interaction of levels of corresponding minibands in quantum wells located n periods apart. The distance n equals to the number of anticrossings between levels E_i and E_j of corresponding minibands (shown by dotted lines in Fig. 3). In these calculations we used levels of first 3 minibands as a basis, so the resonances of levels of first 3 minibands have been identified ($1 \to 2$, $1 \to 3$, $2 \to 3$). In the lower part of these figures the derivative of experimental I–V curve shown in Fig. 1 is plotted. Most of the I–V peaks correspond to the positions of anticrossings of the upper part. Also there is a correlation between peak size on dI/dV and distance between levels at anticrossing because both of them are proportional to the wavefunction overlap at the resonance.

3. Conclusions

It has been shown in this report that both resonant and nonresonant parts of Zener tunneling play important role in the electron transport in superlattices with weak barriers.

A numerical algorithm that allows to establish resonance positions with high precision was developed. The traces from transitions between WS levels located up to 5 SL periods apart of each other and transitions to different higher minibands were identified in the experimental I–V curves.

Acknowledgements

This work is supported by RFBR grant 05-02-16468 and by RAS Program "Low dimensional structures". The authors are grateful to A. A. Marmalyuk and A. A. Padalitsa for growing of the samples, Yu. N. Drozdov for X-Ray characterization of the samples and to I. Yu. Shuleshova, V. V. Rogov and A. Yu. Klimov for processing the samples.

References

[1] A. A. Andronov, I. M. Nefedov, A. V. Sosnin *Semiconductors* **37**, 378 (2003).
[2] A. Sibille, C. Minot, F. Laruelle, *Int. J. of Mod. Phys.* **14**, 909–942 (2000).
[3] G. Wannier, *Rev. Mod. Phys.* **34**, 645 (1962).
[4] K. Hino, N. Toshima, *Phys. Rev. B.* **71**, 205326 (2005).

15th Int. Symp. "Nanostructures: Physics and Technology"
Novosibirsk, Russia, June 25–29, 2007

Probing the electron eigenstates and the chemical potential in GaMnAs/GaAs heterostructures by magnetotunneling and photocurrent spectroscopy

O. Makarovsky
School of Physics and Astronomy, University of Nottingham, NG7 2RD, UK

Abstract. We use a combination of optical, electrical and magneto-tunnelling measurements on p-i-n resonant-tunelling diodes (RTD) incorporating a $Ga_{1-x}Mn_xAs$ p-layer with $x = 3\%$, to study the effect of substitutional and interstitial Mn ions on the electronic properties of GaMnAs heterostructures. The high density of substitutional Mn acceptors affects significantly the electrostatic potential profile of the heterostructure and inhibits hole tunneling from GaMnAs into the quantum well of the RTD. We use photoconductivity to probe this potential and to precisely measure the hole chemical potential in GaMnAs relative to the band edges of the adjacent undoped GaAs layers. We also investigate a new type of quantum dot formed by a nanocluster of interstitial Mn ions which we diffuse into the active region of the diode. We measure the energy levels and image the wavefunctions of the electrons confined in the electrostatic potential of this quantum dot.

Introduction: ferromagnetic GaMnAs

The emerging field of spintronics utilises the quantised spin and associated magnetic dipole moment of an electron. The successful manipulation of spin offers the prospect of a new class of magnetic semiconductor devices, e.g. ultra-fast non-volatile magnetic memory devices and quantum information devices. Particularly interesting spintronic effects have been achieved using semiconducting ferromagnetic GaMnAs [1–4]. In the GaAs lattice, Mn can be incorporated substitutionally on the Ga site or form an interstitial defect [2,3]. Substitutional Mn in GaAs, Mn_{Ga} is an acceptor impurity with a hole binding energy of 110 meV [5]. At high Mn_{Ga} concentrations, the acceptor impurity band tends to merge with the valence band. Hence the holes become mobile, even at low temperatures, and act as itinerant carriers of the ferromagnetic interaction between the Mn^{2+}_{Ga} ions [2,3]. At present there is no firm consensus concerning the dependence on Mn content of the energy gap of $Ga_{1-x}Mn_xAs$ and the location of the chemical potential (μ_p) relative to the conduction and valence band edges. Optical spectroscopy measurements [6] indicate that μ_p is within the Mn-impurity band for high x ($x = 5\%-7\%$). Room temperature scanning tunneling microscopy has measured a band gap of 1.23 ± 0.05 eV for $x = 3\%$ [7].

The key parameter for ferromagnetic semiconductors is the Curie transition temperature, T_c. In $Ga_{1-x}Mn_xAs$, T_c is determined by the concentration of holes, p, and roughly proportional to $p^{1/3}$ [2]. GaMnAs is grown by low temperature ($\sim 250\,^\circ$C) molecular beam epitaxy (MBE) in order to achieve above equilibrium concentrations of Mn. This lead to a high concentration of interstitial Mn defects (Mn_i) [8,9]. These are double donors, which inhibit ferromagnetism by compensating the holes provided by Mn_{Ga} [2,8,9]. Mn_i is a rather mobile defect and can diffuse through the lattice at relatively low temperatures ($T < 200\,^\circ$C) [8]. A Curie temperature of up to 173 K has recently been achieved for GaMnAs with $x = 9\%$ annealed at $T = 190\,^\circ$C for about 50 hours [2].

In this work we investigate the electronic and optical properties of a p-i-n double barrier resonant tunneling diode (RTD) incorporating an AlAs/GaAs/AlAs quantum well, QW, and a p-doped $Ga_{1-x}Mn_xAs$ layer with $x = 3\%$. The high density of Mn acceptors in the p-type layer affects significantly the electrostatic potential profile of the diode and inhibits the injection of holes from $Ga_{1-x}Mn_xAs$. Photoconductivity (PC) measurements allow us to probe the potential profile and to locate precisely the position of the chemical potential in $Ga_{1-x}Mn_xAs$ with respect to the band edges in the adjacent GaAs layers [4]. This information is particularly useful as it determines the bias required for hole injection into the QW subbands, and is an important material parameter for the design, modeling, and operation of $Ga_{1-x}Mn_xAs$ heterostructure devices.

Our experiments have also revealed some novel quantum phenomena in $Ga_{1-x}Mn_xAs$ p-i-n RTDs: by careful annealing, we are able to create a new type of quantum dot formed by a nanocluster of interstitial Mn ions which we diffuse into the active region of the diode. Using magnetotunneling spectroscopy we measure the energy levels and image the wavefunctions of the electrons confined in the electrostatic potential of this quantum dot.

Layer structure of our devices and thermal annealing conditions

The sequence of layers, grown by MBE on (100) semi-insulating GaAs substrates, is as follows (see inset of Fig. 1): a 300 nm Si-doped GaAs layer $n = 2 \times 10^{18}$ cm^{-3}; 100 nm of Si-doped GaAs $n = 2 \times 10^{17}$ cm^{-3}; an undoped intrinsic i region consisting of a 20 nm GaAs spacer layer, a 6 nm GaAs QW formed between two 5 nm AlAs barriers, and a 10 nm GaAs spacer layer; the top 50 nm $Ga_{1-x}Mn_xAs$ layer with $x = 3\%$ was grown at 250 °C. We have also studied a control sample of similar design, except that the $Ga_{1-x}Mn_xAs$ layer was replaced by a 1 μm layer of carbon-doped GaAs $p = 2 \times 10^{18}$ cm^{-3}. We have studied both annealed and unannealed devices. Annealing has been shown to significantly reduce compensation in $Ga_{1-x}Mn_xAs$ through Mn_i out-diffusion [2,8] and can lead to hole densities close to the Mn concentration of $\sim 6 \times 10^{20}$ cm^{-3} for $x = 3\%$ [9]. In this work, we only consider samples that were unannealed or else annealed only for a short time, $\sim$ 3 hours, at relatively low temperatures $T = 140\,^\circ$C–$180\,^\circ$C. Under these annealing conditions, only a small amount Mn interstitials diffuse out of the $Ga_{1-x}Mn_xAs$ layer; therefore it can be considered as a source with constant

concentration of Mn_i.

Experimental results and discussion

Figure 1 compares the low-temperature ($T = 4.2$ K) current-voltage, ($I(V)$) curve of an unannealed p-i-n diode containing the p-$Ga_{1-x}Mn_xAs$ layer with that of the control sample in which the p-layer is doped with shallow carbon acceptors. For the control sample, the strongest peak in $I(V)$ corresponds to electron tunneling into the lowest conduction subband E1; the three weaker peaks, HH1, LH1, and HH2, arise from resonant hole tunneling [10] where LHn and HHn refer to QW subbands with light (L) or heavy (H) hole character at wave vector $k = 0$ and $n = 1, 2$ is the subband quantum number, see Figure 2a. In contrast, the diode incorporating the $Ga_{1-x}Mn_xAs$ layer reveals only a single resonance in $I(V)$ due to electron tunneling into E1. To understand this unusual behavior we consider the effect of the high density of Mn_{Ga} acceptors on the electrostatic potential profile of the diode.

Figure 2 shows a schematic diagram of the band edges of the heterostructure at a voltage V_{FB} corresponding to the flat-band condition at which the electric field in the intrinsic region is zero. In this diagram, we assume that the band gap of $Ga_{1-x}Mn_xAs$ is smaller than that of GaAs, as indicated by recent experiments [7]. The potential step at the interface between $Ga_{1-x}Mn_xAs$ and the GaAs spacer layer is made up of two contributions: the band-edge discontinuity due to the smaller band gap of $Ga_{1-x}Mn_xAs$, and the dipolar charge at the edge of the $Ga_{1-x}Mn_xAs$ layer created by negatively ionized Mn_{Ga} acceptors and holes which diffuse into GaAs. Since the chemical potential on the n-type side of the barriers is very close (within a few meV) to the energy E_c of the GaAs conduction band edge, at $V = V_{FB}$ the hole chemical potential in

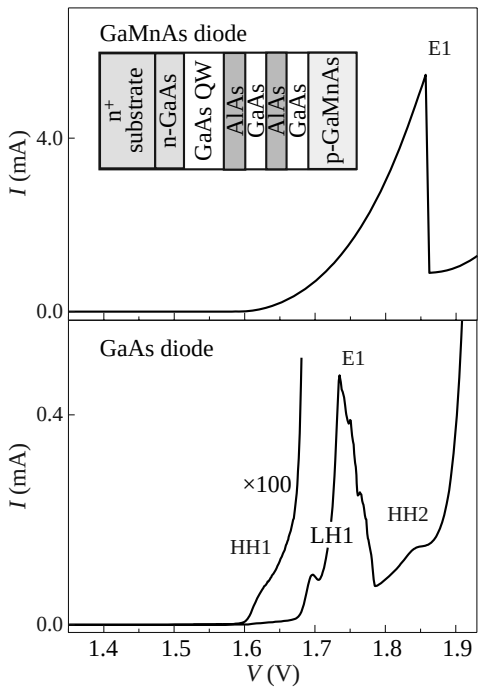

Fig. 1. Low-temperature ($T = 4.2$ K) $I(V)$ curve of the p-i-n diode containing the $Ga_{1-x}Mn_xAs$ layer (upper curve) and of the control sample in which the p-layer is doped with shallow carbon acceptors (bottom curve). The inset is a sketch of the layer composition of the p-i-n diode containing the p-$Ga_{1-x}Mn_xAs$ layer.

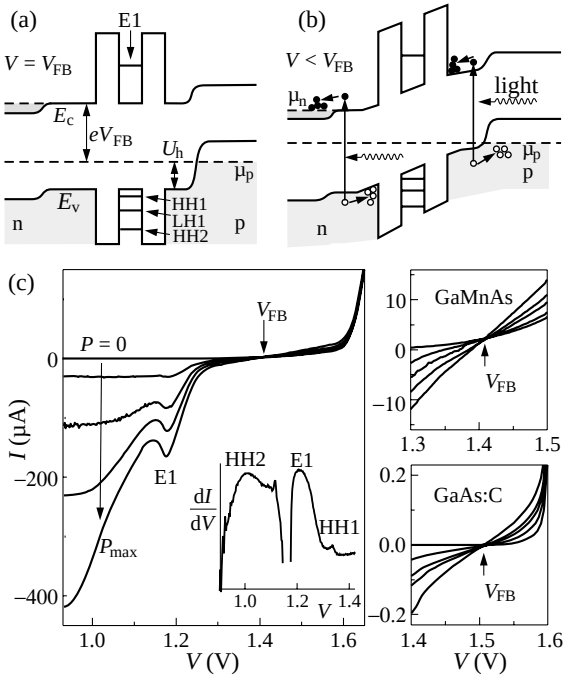

Fig. 2. (a) Schematic diagram of the conduction and valence band edges of our p-i-n diode containing the p-$Ga_{1-x}Mn_xAs$ layer biased at $V = V_{FB}$, for which the electric field in the intrinsic region of the device is zero. (b) Schematic of the dynamics of photoexcited electrons and holes when the diode is biased at $V < V_{FB}$. (c) Low-temperature ($T = 4.2$ K) $I(V)$ characteristics for different intensities of laser excitation $P = 0$, 4, 11, 18, and 35 W/cm^2. The inset shows the hole and electron resonances in the differential conductance, dI/dV, plot for $P_{max} = 35$ W/cm^2. The right insets show the intersection point, V_{FB}, in photocurrent for our p-i-n diode containing the p-$Ga_{1-x}Mn_xAs$ layer (top inset) and for our control sample in which the p-type GaAs layer is doped with shallow carbon acceptors (bottom inset).

$Ga_{1-x}Mn_xAs$ lies at a well-defined energy $\mu_p = eV_{FB}$ below E_c in the adjacent GaAs layers (see Fig. 3a). For $V > V_{FB}$, hole injection from $Ga_{1-x}Mn_xAs$ into the QW is inhibited by the potential step at the $Ga_{1-x}Mn_xAs$-spacer layer interface. Hence the current is dominated by resonant transmission of electrons through E1, as is evident from Fig. 1. These electrons recombine with holes in the $Ga_{1-x}Mn_xAs$ and GaAs layers on the p side of the diode, thus reducing further the density of holes near the barrier that are available for tunneling into the QW.

The hole chemical potential energy μ_p, is a key parameter of our $Ga_{1-x}Mn_xAs$ heterostructure, which we derive from the bias dependence of the PC response at $T = 4.2$ K. For $V < V_{FB}$, the photocreated electrons and holes are swept by the electric field in opposite directions and form accumulation layers adjacent to the tunnel barriers, see Fig. 2b. Since the dark current is negligible for $V < V_{FB}$, the current measured under illumination is due to the photocreated carriers tunneling through the barriers. The photocurrent is zero at the flat-band condition, i.e., when $V = V_{FB} = \mu_p/e$, from which we determine the position of μ_p. The photocurrent (PC) response of the $Ga_{1-x}Mn_xAs$ diode exhibits a negative photocurrent at biases below $V_{FB} = 1.410$ V (Fig. 2c). The $I(V)$ curves measured under different excitation powers all intersect at V_{FB} at which the photocurrent is zero. We observe a similar PC ef-

fect in our control sample, but the intersection point occurs at a significantly higher bias, $V_{\rm FB} = 1.514$ V (right insets of Fig. 2c). This corresponds to the hole channel being at an energy $\mu_p = 1.514 \pm 0.005$ eV below the GaAs conduction band edge at the flat-band voltage. This is close to the band gap of pure GaAs at $T = 4.2$ K ($E_g = 1.519$ eV). The corresponding energy for the $Ga_{1-x}Mn_xAs$ diode is considerably smaller, $\mu_p = 1.410 \pm 0.005$ eV. Hence, we deduce that there is an interface barrier of height $U_{\rm h} = E_{\rm v} - \mu_p = 0.11$ eV between holes at up in the $Ga_{1-x}Mn_xAs$ layer and the valence band edge, $E_{\rm v} = 1.519$ eV, in the adjacent GaAs layers. This barrier explains the absence of distinct hole resonant tunneling peaks in the dark $I(V)$ curve of our $Ga_{1-x}Mn_xAs$ diode.

An particulary interesting interesting feature observed in the annealed $Ga_{1-x}Mn_xAs$ RTDs is that they show a significant tunneling current at $V < V_{\rm FB}$ due to Mn_i diffusion from top p-layer of $Ga_{1-x}Mn_xAs$ into i-GaAs layer. This current is very dependent on the annealing temperature, and can be described by a simple Mn_i diffusion model with coefficients experimentally derived for Mn_i out-diffusion from $Ga_{1-x}Mn_xAs$ films [8]. By the careful selection of the annealing conditions we can control the diffusion of Mn_i into the active region of the RTD to create a small number of novel quantum dot, QD, structures in the quantum well. Each of these is formed by a nanocluster of Mn_i ions, which have diffused from the $Ga_{1-x}Mn_xAs$ layer into the active region of the device. At $V < V_{\rm FB}$ we observe electron tunneling into the quantum states of these dots as sharp resonant peaks on $I(V)$ [12]. Magnetotunnelling spectroscopy of these resonances reveals the electronic nature of these QDs. We find that the tunnelling electrons are confined by a deep (~ 0.1 eV) parabolic electrostatic potential created by the charge of the Mn_i ions that make up the nanocluster. Our magnetotunneling measurements [4] provide detailed images in Fourier space of the probability densities of quantum-confined $1s$, $2px$, $2py$, ... electronic eigenstates of these QDs [12]. We also observe additional resonant peaks in the current-voltage characteristics due to electron tunnelling into the $1s$ ground states of the isolated Mn_i donors. The high magnetic field Zeeman spin-splitting of the Mn_i donor ground state indicates an isotropic g-factor, $g = 2$, and a significant spin-spin interaction of the donor electron with the half-filled d-shell of Mn_i [12].

Conclusions

We have studied a p-i-n light-emitting resonant tunneling diode in which the p-type hole emitter is $Ga_{1-x}Mn_xAs$ p-layer with $x = 3\%$. The incorporation of substitutional Mn leads to a significant modification of the electronic band. Photoconductivity measurements as a function of bias provide a means of determining precisely the position of the hole chemical potential in the $Ga_{1-x}Mn_xAs$ layer with respect to the band edges in adjacent GaAs layers. We found, that resonant-tunneling devices with top $Ga_{1-x}Mn_xAs$ layer are very sensitive to the low temperature (150 °C) annealing due to diffusion of interstitial Mn into the tunnel barrier of the device. Magnetotunnelling spectroscopy revealed the quantum-dot origin of the localized energy states created by the Mn interstitials, and provide detailed images in Fourier space of the probability densities of quantum-confined electronic eigenstates. We also observe tunnelling into individual isolated Mn_i donor states showing significant magnetic field Zeeman spin-splitting with an isotropic g-factor, $g = 2$. This information should be of use in the design and study of spintronic devices.

Acknowledgements

This work was performed in collaboration with O. Thomas, L. Eaves, A. Patane, R. P. Campion, K. W. Edmonds, C. T. Foxon, B. L. Gallagher, D. K. Maude, E. E. Vdovin. I also acknowledge a helpful discussion with Prof. T. Jungwirth. This work is supported by EPSRC (UK).

References

[1] Y. Ohno *et al*, *Nature* **402**, 790 (1999).
[2] T. Jungwirth *et al*, *Phys. Rev. B* **72**, 165204 (2005).
[3] T. Jungwirth *et al*, *Rev. Mod. Phys.* **78**, 809 (2006).
[4] O. Thomas *et al*, *Appl. Phys. Lett.* **90**, 082106 (2007).
[5] R. A. Chapman and W. G. Hutchinson, *Phys. Rev. Lett.* **18**, 443 (1967).
[6] K. S. Burch *et al*, *Phys. Rev. Lett.* **97**, 087208 (2006).
[7] T. Tsuruoka *et al*, *Appl. Phys. Lett.* **81**, 2800 (2002).
[8] K. W. Edmonds *et al*, *Phys. Rev. Lett.* **92**, 037201 (2004).
[9] K. Y. Wang *et al*, *J. Appl. Phys.* **95**, 6512 (2004).
[10] P. M. Martin *et al*, *Semicond. Sci. Technol.* **7**, B456 (1992).
[11] A. Patane *et al*, *Phys. Rev. B* **65**, 165308 (2002).
[12] to be published elsewhere.

15th Int. Symp. "Nanostructures: Physics and Technology"
Novosibirsk, Russia, June 25–29, 2007

Inducement and suppression of the Coulomb effects in elastic 2D-2D electron tunnelling in a quantizing magnetic field

V. G. Popov[1], Yu. V. Dubrovskii[1] and J.-C. Portal[2,3]

[1] Institute of Microelectronics Technology of RAS, Chernogolovka 142432, Russia
[2] INSA, F31077 Toulouse Cedex 4, France
[3] Grenoble High Magnetic Field Laboratory, MPI-CNRS, BP166 38042 Grenoble Cedex 9, France

Abstract. Tunnelling between two-dimensional electron systems has been studied in the magnetic field perpendicular to the systems planes. The satellite conductance peaks of the main resonance have been observed due to the electron tunnelling assisted by the elastic scattering on impurities in the barrier layer. These peaks are shown to shift to the higher voltage due to the Coulomb pseudogap in the intermediate fields. In the high magnetic fields the pseudogap shift is disappeared.

Introduction

Coherent 2D-2D tunnelling is well known to have a resonance when subband energies E_{01} and E_{02} coincide in both two-dimensional electron systems (2DESs). Quantizing a lateral motion of electrons a normal magnetic field sharpens the coherent resonance and produces a series of satellite resonances originated from tunnelling between Landau levels (LL) with different numbers assisted the elastic scattering on impurities [1]. The condition of the elastic 2D-2D tunnelling is the following: $E_{01} - E_{02} = k\hbar\omega_c$. Here k is an integer number, ω_c is the cyclotron frequency. In other words in tunnel spectra the nearest satellites are separated by a voltage interval $V_c = \hbar\omega_c/e$. This single particle picture ignores many-body effect such as the Coulomb pseudogap (CP) that provides an additional voltage shift of the coherent resonance [2]. The pseudogap is originated from relaxation processes induced by the tunnelling electrons. In other words the tunnelling electron should have an additional energy to spend it on the relaxation therefore tunnelling is suppressed at low energies. This scenario is valid while the tunnelling time is very short in compare with the relaxation times. The interesting question is what happens if the relaxation will take part in tunnelling of electrons. To clarify the question it is suitable to investigate processes providing peak features in the tunnel spectra. The features of the elastic 2D-2D tunnelling are such kind of features. Here the Coulomb effects is reported to be revealed and studied in elastic 2D-2D electron tunnelling. In particular an inducement and a suppression of the Coulomb effects have been observed in a quantizing magnetic field.

1. Experiment

The investigated tunnel diodes represented columns wet-etched in a single barrier heterostructure of GaAs/$Al_{0.3}Ga_{0.7}As$/GaAs type. The barrier layer was of 20 nm thickness and doped with Si at the middle. Due to the donor ionization the 2DESs accumulate on both side of the tunnel barrier in the undoped spacer layers of 70 nm thickness. The resistance of the spacers was quite low in compare with the barrier one. This provided common Fermi levels in 2DESs and adjacent contact n^+-GaAs regions. The potential profile of the heterostructure is shown in Figure 1. The symmetry of the structure is supposed to be a result of the dopants diffusion during the crystal growth. The conductance-voltage dependencies are shown in Figure 2 at different magnetic fields. At zero field the conductance peaks are the coherent resonant those. In particular the peak at $V_b = 3$ mV corresponds to the 0-0 resonance, i.e. $E_{01} = E_{02}$ and peak at $V_b = -12$ mV takes place when $E_{01} = E_{12}$. The electron concentrations were determined from magneto-oscillations of the tunnel current at low bias voltages and from the voltage position of the current peak at zero magnetic field. They are $n_1 = 3 \times 10^{11}$ cm^{-2} and $n_2 = 5 \times 10^{11}$ cm^{-2} the mobilities can be also estimated as $\mu_{1,2} \approx 50000$ cm^2/Vs [3]. The I-V curves of the tunnel diodes demonstrate a nonmonotonous magnetic dependence of the coherent-resonance position. The voltage dependencies of the tunnel conductance have pronounced satellite resonances or the conductance peaks shown in Figure 2. The satellite peaks also have nonmonotonous magnetic dependencies resembled the coherent resonance one (see Fig. 2).

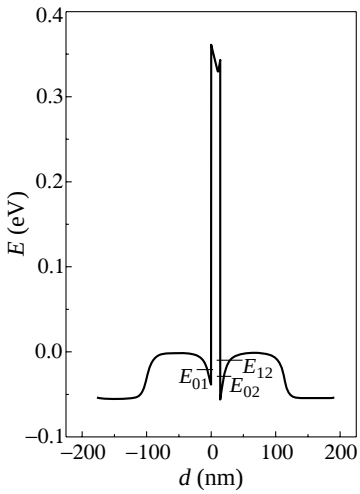

Fig. 1. The potential profile of the conductance-band bottom of the heterostructure under investigation with the quantum levels calculated self-consistently.

2. Discussion

The triangles in Figure 2 follow the coherent peak position. The circles show the expected values for the first satellite peaks separated from coherent one at $V_{\pm s} = \pm\hbar\omega_c/e$. One can see that the expected positions are in quite good agreement with experimental ones at the positive voltage polarity (filled circles in Fig. 2) and in disagreement with those at negative polarity (empty circles in Fig. 2) at least for the magnetic field range

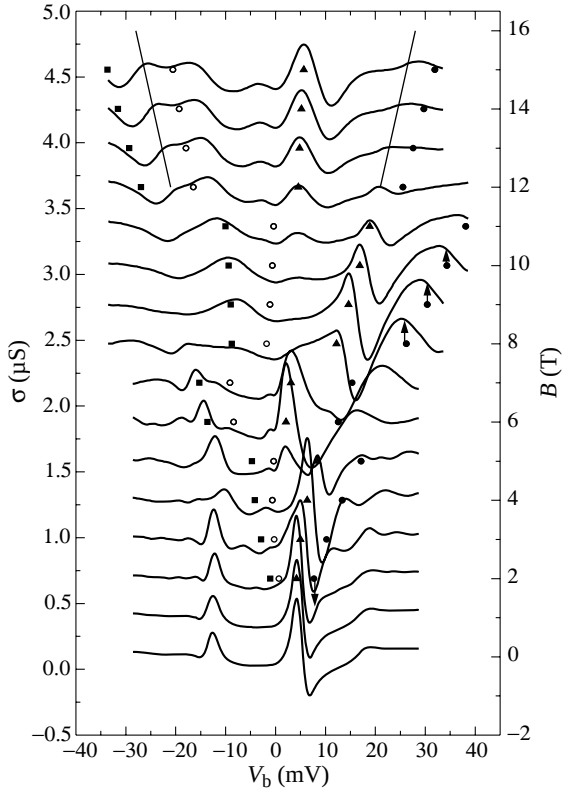

Fig. 2. Tunnel conductance-voltage dependencies at different magnetic fields in combination with the peaks positions magnetic dependencies. The curves are shifted to correspond magnetic field scale B, i.e. with step being proportional to the field that.

$B \in (6\,T; 11\,T)$. It is interesting to note that the deviation can be cancelled with an additional voltage shift depended upon magnetic field. So if one supposes $V_{-s} \approx -1.5\hbar\omega_c/e$ the data coincidence will be better (see. squares at the negative voltage in Fig. 2). Such shift can be explained by the CP. In this case the positive satellite shifts together with the coherent peak and the energetic interval between them remains the same $eV_{+s} = \hbar\omega_c$. As for the negative satellite it is experienced the reverse shift and the energetic distance is increased on the double value of the CP $eV_{-s} = -\hbar\omega_c - 2\Delta_C$. The value of the CP can be estimated from the splitted coherent peak at very high magnetic fields . At these fields both 2DESs have the only one populated LL. Under this ultraquantum limit the resonant voltage should be zero [3]. In this case deviation originates only from the CP. Hence one can easy estimate the CP as a value of the deviation, i.e. $\Delta_C \approx 0.3\hbar\omega_c$. Thus one can justify the large value of V_{-s}. The next interesting feature appears at high magnetic fields $B > 11$ T where both the empty circles and the squares have lack to describe the satellite peaks positions. Moreover each peak has splited on a strongly and a weakly field depended ones. The strongly field-depended peaks follow to the cyclotron lines, i.e. $eV_{\pm p} = \pm\hbar\omega_c$ (see solid lines in Fig. 2). They can be considered as elastic satellites without the CP shift. The weakly depended peaks can be assigned to resonant tunnelling between the ground and the first excited subbands. Thus we can interpret the experimental data as a suppression of the CP effect on elastic peaks. Such suppression can be expected because, when the LL energy exceeds the first excited subband one, the intensive inter-subband scattering can decrease an electron life-time on the LL, i.e. the relaxations becomes faster, and thus decrease the role of the Coulomb effects.

Conclusions

The Coulomb pseudogap has been found to cause an additional voltage shift of the conductance peaks originated from 2D-2D tunnelling assisted by the elastic scattering. The disappearance of the shift has been also observed in the strong field when $\hbar\omega_c > E_{12} - E_{02}$ (see Fig. 1). The appearance of the CP effects means that elastic tunnelling is still quite fast in compare with lateral relaxation. The effect disappearance takes place probably due to the additional relaxation process, i.e. inter-subband scattering, becomes significant.

Acknowledgements

This work has been supported in part by the RFBR (grant 07-02-00487), INTAS (grant YSF 05-109-4786), "Russian Science Support Foundation", and RAS program "Quantum nanostructures".

References

[1] W. Demmerle, J. Smoliner *et al*, *Phys. Rev. B* **44**, 3090 (1991).
[2] J. G. S. Lok, A. K. Geim *et al*, *Phys. Rev. B* **56**, 1053 (1997).
[3] V. G. Popov, Yu. V. Dubrovskii and J. C. Portal, *JETP* **102**, 677 (2006).

15th Int. Symp. "Nanostructures: Physics and Technology"
Novosibirsk, Russia, June 25–29, 2007

Atomic-scale study of the impurity atoms effect on the $1/f^{\alpha}$ noise characteristics of the tunneling current from individual InAs(110) atomic sites

A. I. Oreshkin[1], S. I. Oreshkin[1,2], N. S. Maslova[1], V. N. Mantsevich[1], D. A. Muzychenko[1], S. V. Savinov[1] and V. I. Panov[1]

[1] Moscow State University, Department of Physics, Moscow, 119992, Russia
[2] Sternberg Astronomical Institute, Universitetsky pr., 13, Moscow, 119992, Russia

Abstract. We report the results of UHV STM investigations of tunneling current noise spectra in vicinity of individual impurity atoms on the InAs(110) surface. It was found out that the power law exponent of $1/f^{\alpha}$ noise depends on the presence of impurity atom in the tunneling junction area. This is consistent with proposed theoretical model considering tunneling current through two state impurity complex model system taking into account many-particle interaction.

Introduction

Up to now the typical approach to $1/f^{\alpha}$ noise problem consists of "by hand" introducing of the random relaxation time τ for two-state system with the probability distribution function A/τ_0^{α}. Therefore the averaged over τ_0 noise spectra of two-states system has power law singularity. But the physical nature and the microscopic origin of such probability distribution function in general is unknown. Although the current noise gives a basic limitation for the performance of scanning tunneling microscope, only the limited number of works was devoted to study $1/f^{\alpha}$ noise. Park *et al* [1] and Stoll *et al* [2] have analyzed the STM data obtained above the surface of pyrolytic graphite. The power low exponent α equal to about 1.4 has been determined in [2]. Coulomb blockade as one of the sources of $1/f^{\alpha}$ noise generation is considered in [3]. The other possible mechanism is the process of atomic adsorption/desorption on the sample/tip surface in the region of tunneling contact [4]. In [5] the $1/f^{\alpha}$ tunneling current noise is explained in terms of surface diffusion of molecules adsorbed in the tunneling contact area. To the best of our knowledge tunneling current noise STM measurements were performed only for relatively simple surfaces like gold, graphite etc. Our main goal was to clarify the *microscopic* origin of $1/f^{\alpha}$ noise. The main question in this context is how the different impurity atoms on the surface or subsurface layers and the surface defects are influencing tunneling current noise spectra.

1. Experimental

We have used specially prepared InAs slabs ($2 \times 2 \times 4$ mm^3), which were cleaved *in situ* in UHV conditions. In the first set of experiments the S doped InAs (n-type bulk conductivity) single crystals were investigated. The chemical doping concentration was 1.5×10^{18} cm^{-3}. In the second set of experiments the Mn doped InAs (p-type bulk conductivity) single crystals were investigated. The chemical doping concentration was 1.4×10^{16} cm^{-3}. In all our measurements the tunneling bias voltage was applied to the sample, while the STM tip was virtually grounded. The presented results were obtained with a tungsten STM tips. During the sample cleavage the pressure in the UHV chamber was always lower than 1×10^{-10} torr. To properly select the set point for the STM tunneling current noise measurements we have performed the spatially resolved tunneling spectroscopy experiments. To maintain high signal to noise ratio these experiments were carried out in the current imaging tunneling spectroscopy (CITS) mode.The slice of two-dimensional array of I(V) curves at certain value of bias voltage represents the spatial distribution of tunneling current at fixed tip-sample separation (current image). These current images give information complementary to the information which is contained in normal constant current STM (topography) image.

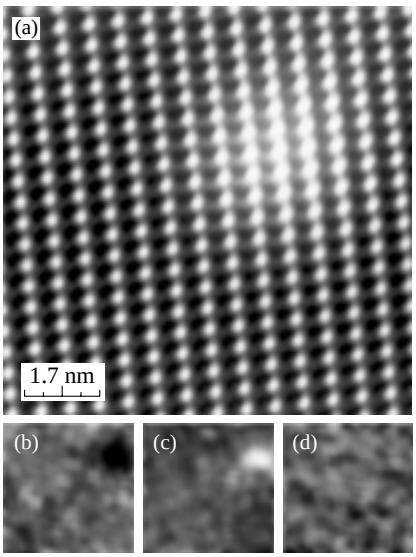

Fig. 1. (a) High-resolution STM topographic image of S-dopant atom on the InAs(110) surface [$V_s = -1.16$ V, $I = 30$ pA]. The current image of S dopant atom on InAs(110) surface at (b) -0.91; (c) -0.20; (d) 0.46 V bias voltage. Scan area is 10×10 nm.

Because we are interested in tunneling current noise characteristics above defect free area as compared to the region of impurity atom we used the following procedure of the bias set point selection. We chose the bias voltage for current noise measurements at which the contribution from dopant atom on current image has its maximum. This means that the spot on current image caused by the presence of dopant atom is the most bright. Interesting to note that in cases of $InAs_s$ and $InAs_{Mn}$ the bright spot on current image is clearly visible in wide bias voltage range approximately corresponding to the band gap range.

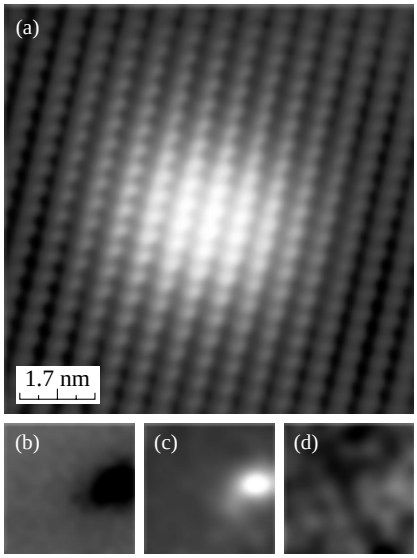

Fig. 2. (a) High-resolution STM topographic image of Mn-dopant atom on the InAs(110) surface [$V_s = 0.77$ V, $I = 30$ pA]. The current image of Mn dopant atom on InAs(110) surface at (b) -1.00, (c) 0.15, (d) 0.48 V bias voltage. Scan area is 12.6×12.6 nm.

The typical high resolution filled states STM images of S and Mn individual impurities on the InAs(110) surface are shown on Fig. 1(a) and Fig. 2(a) correspondingly. Let us note, that both dopant atoms look on the occupied states STM images as round protrusions approximately 1 Å in height. The localization radius can also be estimated from STM images. In both cases it roughly equals to 40 Å providing high residual conductivity of our samples. The current images of S dopant atom on the InAs(110) surface at different values of bias voltage are shown on Fig. 1(b), (c), (d). The most remarkable contribution from dopant atom to the current image occurs at -0.2 V bias voltage (Fig. 1(c)). The behavior of Mn dopant atom on the InAs(110) surface is slightly different from the behavior of S impurity atom partially due to the fact that in our case $InAs_{Mn}$ has p-type of bulk conductivity. The current images of Mn dopant atom on the InAs(110) surface at different values of bias voltage are shown on Fig. 2(b), (c), (d). The most remarkable contribution from dopant atom to the current image occurs at 0.15 V bias voltage (Fig. 2(c)). Based on this analysis the following set points values V_s for tunneling current noise measurements were chosen: $V_s = -0.2$ V for $InAs_s$, $V_s = +0.15$ V for $InAs_{Mn}$. The tunneling current value used for feedback stabilization of the tip-sample gap is equal 30 pA in all cases. It is important to note that input stage of our tunneling current preamplifier built with Burr–Brown OPA602 operational amplifier does not limit the resolution of our measurements. We have found that both for $InAs_s$ and $InAs_{Mn}$ the power law exponent is different for measurements above defect free surface area and above impurity atom. For $InAs_s$ the power law exponent α measured above clean surface is equal to 0.89 whereas above dopant atom it has value 1.16. For $InAs_{Mn}$ the power law exponent α measured above clean surface is equal to 1.04 whereas above dopant atom it has value 0.75. One can see the difference in the behavior of the power law exponent in cases of $InAs_s$ and $InAs_{Mn}$. While moving from the impurity atom to the clean surface α is decreasing for $InAs_s$ sample. The opposite situation was observed for $InAs_{Mn}$ surface. The α is increasing when moving away from dopant atom. The model

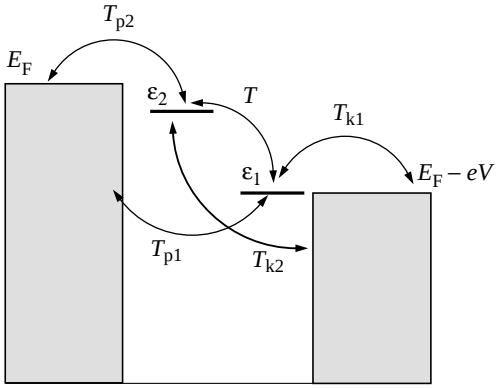

Fig. 3. Schematic diagram of tunneling through states localized on impurity atom and on the STM tip apex.

system (Fig. 3) can be described by hamiltonian $\hat{H}$:

$$\hat{H} = \hat{H}_0 + \hat{H}_T + \hat{H}_{int}\,,$$

$$\begin{aligned}
\hat{H}_0 &= \sum_k (\varepsilon_k - eV) c_k^+ c_k + \sum_p \varepsilon_p c_p^+ c_p + \sum_{i=1,2} \varepsilon_i a_i^+ a_i,\\
\hat{H}_T &= \sum_{k,i} T_{ki} c_k^+ a_i + \sum_{p,i} T_{pi} c_p^+ a_i + T \sum a_1^+ a_2 + \text{h.c.},\\
\hat{H}_{int} &= \sum_{k,k'} W_1 c_k^+ c_{k'} a_1 a_1^+ + W_2 c_k^+ c_{k'} a_2 a_2^+ .
\end{aligned}$$

For clean surface one should put $T_{p2} = 0$, $\varepsilon_2 = 0$, $T = 0$, $W_2 = 0$, $T_{k2} = 0$, $\varepsilon_1 = eV$, if ε_1 is connected with the tip apex state. Re-normalization of T_{k1} due to switching "on" and "of" of W_1, gives the low frequency contribution to $S(\omega)$ above clean surface:

$$S_{clean}(\omega) = \left(\frac{\xi_0}{\omega}\right)^{-W_1\nu}.$$

The low frequency noise spectra above impurity can be estimated as:

$$S_{imp}(\omega) \sim S_1(\omega) S_2(\omega) \sim \left(\frac{\xi_0}{\omega}\right)^{-(W_1+W_2)\nu}.$$

$$\alpha_{imp} = -(W_1 + W_2)\nu\,.$$

This model qualitatively describes the observed experimental results.

Acknowledgement

This work was partially supported by RFBR grants Nos. 06-02-17076-a, 06-02-17179-a, 05-02-19806-MF, 06-02-08306-OFI, president grants for scientific school No. 4599.2006.2 and No. 4464.2006.2.

References

[1] S. Park *et al*, *Appl. Phys. Lett.* **48**, 112 (1986).
[2] E. Stoll *et al*, *Surf. Sci.* **181**, 222 (1987).
[3] K. Maeda *et al*, *J. Vac. Sci. Technol. B* **12** (3), 2140 (1994).
[4] M. Lozanoet *et al*, *Europhys. Lett.* **30** (9), 537 (1995).
[5] G. K. Zyrianov, *Low-voltage electronography* L. (1986).

15th Int. Symp. "Nanostructures: Physics and Technology"
Novosibirsk, Russia, June 25–29, 2007

Anisotropic magnetic field dependence of many-body enhanced electron tunnelling through a quantum dot

E. E. Vdovin[1], Yu. N. Khanin[1], O. Makarovsky[2], A. Patane[2], L. Eaves[2], M. Henini[2] and K.A. Benedict[2]

[1] Institute of Microelectronics Technology RAS, 142432 Chernogolovka, Russia
[2] School of Physics and Astronomy, University of Nottingham, NG7 2RD, UK

Abstract. We investigate the effect of an applied magnetic field on resonant tunneling of electrons through the bound states of self-assembled InAs quantum dots (QDs) embedded within an (AlGa)As tunnel barrier. At low temperatures ($\leq$ 2 K), a magnetic field **B** applied either parallel or perpendicular to the direction of current flow causes a significant enhancement of the tunnel current. For the latter field configuration, we observe a strong angular anisotropy of the enhanced current when **B** is rotated in the plane of the quantum dot layer. We attribute this behavior to the effect of the lowered symmetry of the QD eigenfunctions on the electron-electron interaction.

The Fermi-edge singularity (FES) is a many-body interaction effect, which has been observed in a variety of systems, including X-ray absorption in metals [1] and photoluminescence from semiconductor quantum wells (QWs) [2]. Theoretical work by Matveev and Larkin predicted the existence of an FES for the case when electrons tunnel through a localised state in a potential barrier [3]. An electron tunneling into a localized level generates a scattering potential for the electrons in the contact leads. The change of occupation of the localized level during the tunneling leads to a change in the scattering potential and a power-law singularity in the electron tunneling rate. A strong dependence of the FES on a magnetic field, **B**, applied parallel to the direction of current flow has been observed in quantum dot tunnelling experiments. For electron tunneling into a QD from a low-density two-dimensional electron gas (2DEG), the current was observed to depend in an oscillatory manner on the Landau level filling factor of the 2DEG [4], whereas for the case of tunneling from a three-dimensional (3D) Fermi sea, the current was strongly enhanced at high magnetic field due to the effect of partial spin polarization of the electrons [5].

In this paper, we investigate how the tunnel current through a QD at low temperatures is influenced by magnetic field. We examine not only the **B** $\parallel$ **J** geometry, but also when **B** is perpendicular to **J**. For **B** $\perp$ **J**, we observe an unexpectedly strong angular anisotropy in the FES when **B** is rotated in the plane of the QD layer.

The sample studied was a single-barrier 8 nm GaAs-$Al_{0.4}Ga_{0.6}As$-GaAs heterodiode, grown by molecular-beam epitaxy on (100)-oriented Si doped n-GaAs substrate. InAs quantum dots were grown on the center plane of the barrier using the Stranski–Krastanow growth mode, producing a dot density of 2×10^{11} cm^{-2} with a typical size 10 nm.

Figure 1 shows I(V) curves for a 50 μm diameter mesa measured at $T = 0.5$ K. The peaks labeled A, B, C and D, are observed in forward bias between 8 and 50 mV. We attribute each peak to resonant tunneling of electrons from the emitter Fermi sea into a discrete state of a QD. The peak current increases only slightly with decreasing temperature, indicating that for $B = 0$ the FES is weak even at $T = 0.4$ K. But we observe the anomalous enhancement of the tunneling through quantum dot in a magnetic field both the parallel and the perpendicular to the current attributed to a many-body contribution which arises due to the strong interaction of a tunnelling electron with the Fermi sea in the emitter [6].

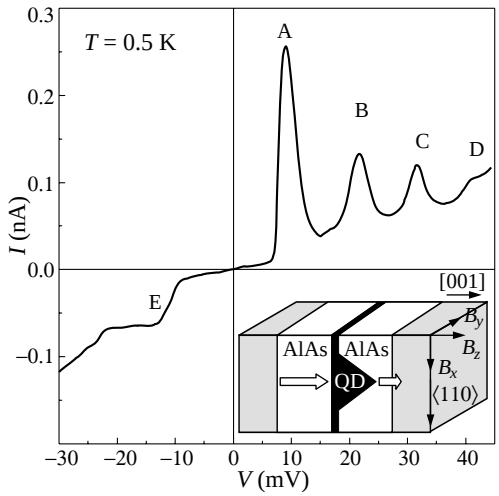

Fig. 1. I(V) curve at $T = 0.5$ K and $B = 0$ T for a mesa diode of diameter 50 μm. The inset shows schematically our coordinate scheme relative to the crystallographic axes and electron tunneling through a QD in forward bias.

We now consider the magnetoanisotropy effects observed for **B** $\perp$ **J**. Figure 2 compares the B-dependence of peak A for two different temperatures, 0.4 K (a) and 4 K (b). The field is applied parallel to one of the $\langle 110 \rangle$ axes in the (001) plane (to within $\pm 5^\circ$). As shown in Figure 2(c), a strong increase of the peak current is observed at $T = 0.4$ K with increasing B up to 6 T. When **B** is increased further, the peak current decreases and is quenched above 10 T. In contrast, at $T = 4$ K the magnetic field leads to an approximately monotonic decrease of the amplitude of the peak current, similar to the behavior observed previously for other QD devices investigated at 4 K [7].

In order to investigate further the nature of the FES for the **B** $\perp$ **J** configuration, we have carried out a series of angular anisotropy measurements for different orientations of **B** relative to the crystalline axes in the plane of the tunnel barriers. The magneto-anisotropy of peak A at 4 K and 0.4 K when **B** is rotated in the (001) plane is plotted in Figure 3. At 0.4 K we observe a two-fold magneto-anisotropy of the FES enhancement of peak A. The striking feature is that the enhancement occurs predominantly when **B** is applied along one of the $\langle 110 \rangle$ directions of the (001) plane. The angular measurements have

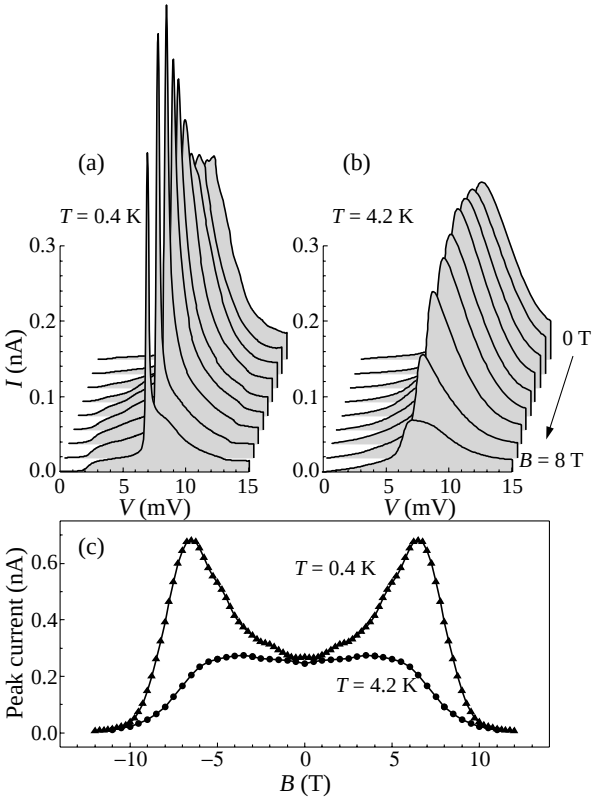

Fig. 2. Magnetic field dependence from 0 to 8 T of peak A in I(V) with $\mathbf{B} \perp \mathbf{J}$ at (a) $T = 0.4$ K (b) and $T = 4.2$ K. **B** is oriented along one of the ⟨110⟩ crystalline axes in the (001) plane. (c) Dependence of peak current on magnetic field **B** applied along ⟨110⟩ at $T = 0.4$ and 4.2 K.

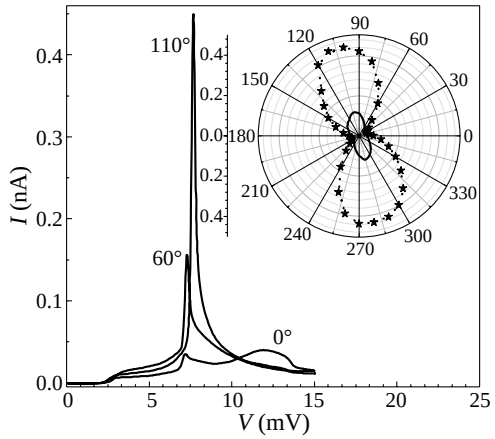

Fig. 3. I(V) characteristic at the perpendicular to the current magnetic field of 8 T at $T = 0.4$ K. Inset: angular dependence of the peak current (stars — at $T = 0.4$ K, solid line — at $T = 4$ K).

allowed us to receive two completely unexpected results, which one could not be forecast within the framework of the existing theories. At first, as it is visible from a Fig. 3, the amplitude FES has very strong angular dependence. Secondly, the anisotropy of FES is reflection of an anisotropy of wave function of the quantum dot. Should be noted that that FES and wave function of the QD demonstrate identical type of the anisotropy, despite of sharp difference of dependences of the peak current from value of magnetic field in high and low temperature cases.

The FES arises from the response of the electrons in the emitter Fermi sea to the change in charge on the dot when an electron tunnels into and out of it. The anisotropy of the FES enhancement indicates that this many-body interaction is strongly influenced by the anisotropic confinement potential of the QDs. In particular, the appearance of a partial $2p_x$-like character in the lower temperature ($T = 0.4$ K) anisotropy plot of peak A in Figure 3 may arise from a virtual tunneling process through the first-excited state ($2p_x$-like) and then down to the ground state ($1s$-like) of the dot, mediated by interactions with electrons in the emitter Fermi sea.

Acknowledgements

The work is partly supported by EPSRC (UK), RFBR 06-02-16556, the Royal Society and the SANDiE Network of Excellence of the European Commission (NMP4-CT-2004-500101). The authors thank A. V. Khaetski and I. V. Larkin for useful discussions, and V. V. Belov for technical assistance.

References

[1] G. D. Mahan, *Phys. Rev.* **163**, 612 (1967).
[2] M. S. Skolnick, J. M. Rorison, K. J. Nash, D. J. Mowbray, P. R. Tapster, S. J. Bass, and A. D. Pitt, *Phys. Rev. Lett.* **58**, 2130 (1987).
[3] K. A. Matveev and A. I. Larkin, *Phys. Rev. B* **46**, 15337 (1992).
[4] A. S. G. Thornton, T. Ihn, P. C. Main, L. Eaves, K. A. Benedict, and M. Henini, *Physica B* **249**, 689 (1998).
[5] I. Hapke-Wurst *et al*, *Phys. Rev. B* **62**, 12621 (2000).
[6] Y. N. Khanin and E. E. Vdovin, *JETP Letters* **81**, 267 (2005).
[7] E. E. Vdovin *et al*, *Science* **290**, 122 (2000).

15th Int. Symp. "Nanostructures: Physics and Technology"
Novosibirsk, Russia, June 25–29, 2007

New MBE fabricated structure for tunneling spectroscopy of 2D electron system in GaAs with near-to-surface δ-layer

I. P. Kazakov[1], I. N. Kotel'nikov[2], Yu. V. Fedorov[3], A. S. Bugaev[3], E. V. Glazyrin[1] and M. N. Feiginov[4]

[1] P. N. Lebedev Physical Institute of RAS, 119991 Moscow, Russia
[2] Institute of Radioengineering and Electronics of RAS, 125009 Moscow, Russia
[3] Institute of UHF Semiconductor Electronics of RAS, 117105 Moscow, Russia
[4] Technische Universität Darmstadt, D-64283 Darmstadt, Merck str. 25, Germany

Abstract. The tunnel structures Al/δ-GaAs with high quality Al/(100)GaAs interface were grown by molecular beam epitaxy under RHEED control. The 2D subbands in GaAs δ-doped layer and many-particles effects were observed in tunneling spectroscopy measurements on Al/δ-GaAs junctions at low temperatures.

Introduction

The experimental information on size-quantized states in semiconductor structures is generally obtained from optical and magnetotransport measurements. During the recent years tunneling spectroscopy method (TSM) [1] is becoming widely recognized. Unlike magnetotransport measurements capable of investigations of occupied states only, TSM allows to study both occupied and empty states. The resolution of TSM is comparable with optical methods. TSM allows to determine the energy level positions of semiconductor structures with the precision of several hundred μV at helium temperatures from tunneling spectra. The Al/δ-GaAs tunnel structure (Fig. 1) is an important object for the TSM investigation of a two-dimensional electron system (2DES). The tunnel barrier of the structure is embedded in GaAs and a quantum well with the confined 2DES originates from δ-doped GaAs layer. A high-quality Al/GaAs interface can be produced by molecular beam epitaxy (MBE) [2–4]. However the possibility of Al/GaAs heterointerface application for tunnel structures was never consistently studied before. In this work we report the growth of Al/δ-GaAs heterostructures by MBE. We study the possibility of GaAs epitaxial layers parameters determination from tunneling measurements. We also show that the structures can be successfully used for many-body effects observations [5–7].

Experimental results and discussion

The Al/δ-GaAs tunnel structures were prepared on semi-insulating (100) substrate by MBE. The near-to-surface Si δ-doped layer was formed at the distance about 20 nm under Al/GaAs interface. The density of the Si atoms in the δ-layer was $(5-9) \times 10^{12}$ cm^{-2}. Epitaxial Al-layer was grown directly in MBE chamber after cooling of the GaAs substrate $<100\,^{\circ}$C under reflection high-energy electron diffraction (RHEED) control [3,4]. Prior to the growth of Al layer Ga-stabilized reconstruction (3×6) was established on GaAs surface. RHEED patterns evidenced island growth mechanism on the initial stages

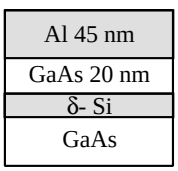

Fig. 1. Schematic model of Al/δ-GaAs tunnel structure.

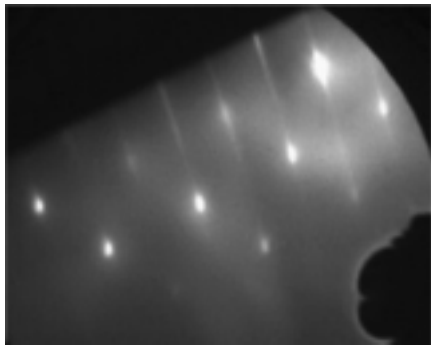

Fig. 2. RHEED pattern of Al surface, $E = 15$ keV, [010] azimuth.

of Al growth with a part of the islands randomly oriented. As the formation of an Al film took place, preferred orientation of Al became evident. The Al-layer showed an orientation of $\{100\}$ on $\{100\}$ GaAs surface with a rotation of 45° about the [100] axis. The Al layer is rotated in order to accommodate the mismatch between Al and GaAs lattices, as Al doubled lattice constant (8,0992 Å) is almost equal to GaAs unit cell diagonal (7,9948 Å). The RHEED pattern in the [010] azimuth is shown on Fig. 2. The pattern is typical for a monocrystalline flat surface. However, the patterns in the principal azimuths showed side reflexes, indicating the presence of misoriented areas.

Atomic force microscopy (AFM) observations (Fig. 3) indicated the presence of preffered orientation observed by RHEED on Al surface. Surface defects obvious on AFM images are supposed to be the regions with other orientations. Despite the presence of the surface defects, the quantum properties of Al/GaAs Schottky barrier were observed on samples with quite large surface area. This fact may prove that Schottky barriers properties do not depend dramatically on Al film orientation.

Al/δ-GaAs tunnel junctions with Al-gate area A from 1 to 0.01 mm^2 were formed and Au-Ge-Ni ohmic contacts to δ-layer were prepared. The 2D electron densities n_{2D} in δ-layer of the junctions were obtained in $(5-20) \times 10^{11}$ cm^{-2} range. The high quality of the tunnel junctions was demonstrated by the measurements of the tunneling spectra (TS) at temperatures range 0.3–4.2 K.

The energy positions of subbands in the δ-layer were measured and many-particles singularities were observed in TS. The tunnel conductance $\sigma = dI/dU$ and TS ($dln\sigma/dU$) are shown on Fig. 4 (for $A = 0.01$ mm^2 and $T = 4.2$ K) where arrows mark the energies E_i of subbands in δ-layer (dips in the

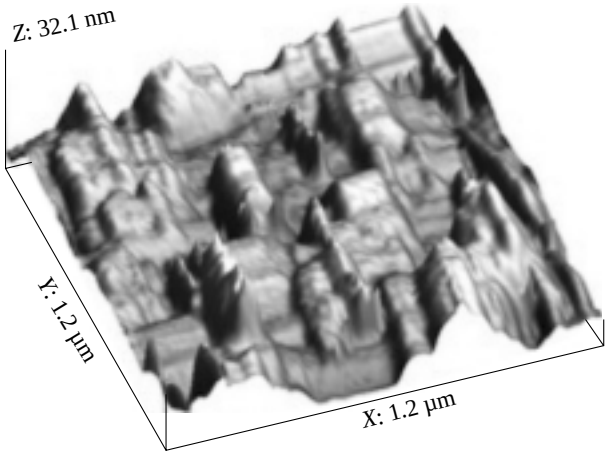

Fig. 3. AFM image of Al surface.

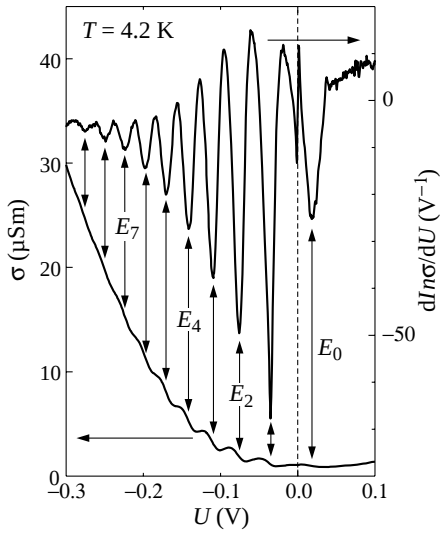

Fig. 4. Tunnel conductance $\sigma = dI/dU$ and tunneling spectrum ($d \ln \sigma / dU$) for Al/δ-GaAs tunnel junction at $T = 4.2$ K.

TS) and bias voltage $U = 0$ is a position of Fermi level E_F in the 2DES.

The occupied level E_0 is situated at $U > 0$ and the subbands from E_1 to E_9 are empty states of the δ-layer ($U < 0$ and electron tunneling to 2DES). The value $E_F - E_0 = 20$ meV ($n_{2D} = 5 \times 10^{11}$ cm^{-2}) for this junction is equal to Fermi energy of the 2DES. The measured subbands energies are in a good agreement with the self-consistent calculations of the TS for the junction [5].

The new effects (the persistent tunneling photoconductivity [5], the reflection of tunneling electrons near LO-phonon emission threshold [6,7] and the intersubband polaron coupling [7]) were found in TS experiments and the effects like negative differential conductance [7] were predicted in the junctions [9]. It was shown that the parameters of tunnelling barrier, of δ-doping layer and of the residual dopant in the epitaxial GaAs, obtained during MBE growth, can be found from the tunneling spectroscopy experiments. The superconducting gap in the tunneling density of states of Al-gate of the junctions was also observed at $T < 1.1$ K in TS [8].

Acknowledgements

The work was supported by the RFBR, the RAS Fundamental researches and Russian Science and Innovations Federal Agency grants.

References

[1] E. L. Wolf, *Principles of Electron Tunneling Spectroscopy*, (Oxford: Oxford Univ. Press), 1985.
[2] S. J. Pilkington and M. Misson, *Journal of Crystal Growth* **196**, 1 (1999).
[3] G. M. Vishnevetskiy, E. V. Glazyrin, I. A. Soubbotin, E. M. Pashaev and I. P. Kazakov, *Proc. of Fundamental and Applied Problems of Modern Physics*, Demidov Forum (Russia, Moscow, 2006), 87.
[4] I. P. Kazakov, V. I. Vdovin, G. M. Vishnevetskiy, E. V. Glazyrin, E. M. Pashaev and I. A. Soubbotin, *Proc. of XII National Conference on Crystal Growth* (Russia, Moscow, 2006), 371.
[5] I. N. Kotel'nikov, S. E. Dizhur, M. N. Feiginov, N. A. Mordovets, *Semiconductors* **40**, 839 (2006).
[6] I. N. Kotel'nikov and S. E. Dizhur, *JETP Lett.* **81**, 458 (2005).
[7] S. E. Dizhur, I. N. Kotel'nikov and E. M. Dizhur, *Journal of Commun. Technology and Electronics* **51**, 588 (2006).
[8] I. N. Kotel'nikov, E. M. Dizhur, A. N. Voronovsky, and S. E. Dizhur, *Proc. of 14th International Symposium "Nanostructures: Physics and Technology"* (St Petersburg, Russia, 2006), 352 (2006).
[9] M. N. Feiginov, *Appl. Phys. Lett.* **81**, 930 (2002).

15th Int. Symp. "Nanostructures: Physics and Technology"
Novosibirsk, Russia, June 25–29, 2007

Enhancement of electron drift velocity by localization of interface phonons in a HEMT channel

J. Požela

Semiconductor Physics Institute, 01108 Vilnius, Lithuania

Abstract. A new approach for the reduction of the scattering rate of electrons by polar optical phonons in the double heterojunction quantum well based on the phonon localization in narrow phonon wells is proposed. The enhancement of electron mobility in the HEMT $Al_{0.2}Ga_{0.8}As/GaAs/Al_{0.2}Ga_{0.8}As$ channel by inserting thin (1 ML) InAs phonon barriers is observed experimentally.

Introduction

In double barrier heterostructures the electron scattering rate by confined polar optical (PO) phonons radically decreases with decreasing a width of a quantum well (QW) [1, 2]. However, this decrease is overcompensated by the strong increase of the electron scattering rate by interface (IF) phonons [3, 4].

In this report, the possibilities of the essential decrease of the IF phonon scattering rate by the localization of the IF phonon potential inside the QW are considered.

1. Localization of interface phonons

Figure 1 shows schematically the 2D double barrier heterostructure, in which electrons are confined in the QW layer of the material A between two barrier layers of the material B. In the case when the bulk longitudinal PO phonon frequencies in the materials A and B are different, the PO phonons are confined as well as electrons in the layer A. The phonon confinement is accompanied by the rise of IF phonons. In narrow QWs, the electron scattering by the IF phonon potential becomes a predominant mechanism.

The IF phonon potential function

$$\varphi_q = F\varphi(z), \tag{1}$$

where F is the phonon amplitude, and $\varphi(z)$ is the dependence of the phonon amplitude on direction z perpendicularly to a layer plane, obtained from the Laplace's equation.

Frequencies of IF phonons are obtained from the border conditions:

$$\varepsilon_A(\omega)\frac{\partial\varphi_q}{\partial z} = \varepsilon_{\rm B}(\omega)\frac{\partial\varphi_q}{\partial z} \quad \text{at} \quad \pm\frac{L_A}{2}, \tag{2}$$

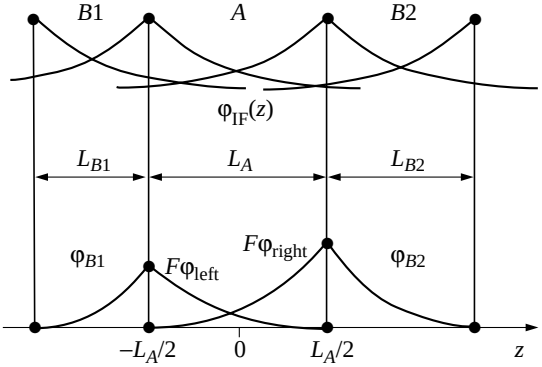

Fig. 1. Schematic view of the IF phonon potentials in the case of localization, $F\varphi_{\rm left}$ and $F\varphi_{\rm right}$, and without localization, $\varphi_{\rm IF}$.

where for binary semiconductors:

$$\begin{aligned}\varepsilon_A(\omega) &= \varepsilon_{\infty A}\frac{\omega^2-\omega_{{\rm L}A}^2}{\omega^2-\omega_{{\rm T}A}^2},\\ \varepsilon_{\rm B}(\omega) &= \varepsilon_{\infty B}\frac{\omega^2-\omega_{{\rm L}B}^2}{\omega^2-\omega_{{\rm T}B}^2},\end{aligned} \tag{3}$$

where $\varepsilon_{\infty A,B}$ are the high-frequency dielectric permittivities, $\omega_{{\rm L}B}$, $\omega_{{\rm T}B}$ and $\omega_{{\rm L}A}$, $\omega_{{\rm T}A}$ are the longitudinal and transverse optical phonon frequencies in the barrier material B and in the QW material A.

The solution of (2) gives two branches of IF phonon frequencies: ω_A and $\omega_{\rm B}$. These frequencies are in the intervals:

$$\omega_{{\rm L}A} > \omega_A > \omega_{{\rm T}A}, \quad \omega_{{\rm L}B} > \omega_{\rm B} > \omega_{{\rm T}B}. \tag{4}$$

This means that

$$\varepsilon_A(\omega_A) < 0, \quad \varepsilon_{\rm B}(\omega_{\rm B}) < 0, \tag{5}$$

and consequently, if the barrier materials B_1 and B_2 are identical, the potential waves with frequencies ω_A and $\omega_{\rm B}$ are fully reflected from the borders A/B. In that case, the IF phonon potential is localized inside the layer A, and for the left interface B_1/A we can obtain:

$$\varphi_{\rm left} = \frac{e^{-qz} - e^{+qz}e^{-q{\rm L}_A}}{e^{+qL_A/2} - e^{-qL_A/2}e^{-qL_A}}, \tag{6}$$

and for the right side interface A/B_2:

$$\varphi_{\rm right} = \frac{e^{+qz} - e^{-qz}e^{-qL_A}}{e^{+qL_A/2} - e^{-qL_A/2}e^{-qL_A}}, \tag{7}$$

where q is the IF phonon wave vector in a QW plane.

The localized IF phonon potential amplitude, according to the dielectric continuum model [4, 5], is equal to:

$$F^2 = \frac{h}{S}F_e, \tag{8}$$

where S is the normalization area in a QW plane,

$$F_e = \left[q\left(\frac{\partial\varepsilon_A}{\partial\omega}\coth\frac{qL_A}{2} + \frac{\partial\varepsilon_{\rm B}}{\partial\omega}\coth\frac{qL_{\rm B}}{2}\right)\right]^{-1}, \tag{9}$$

and depends on the phonon frequency and QW width.

Figure 2 shows the decrease of the localized IF phonon potential amplitude with decreasing the QW width. Note that the

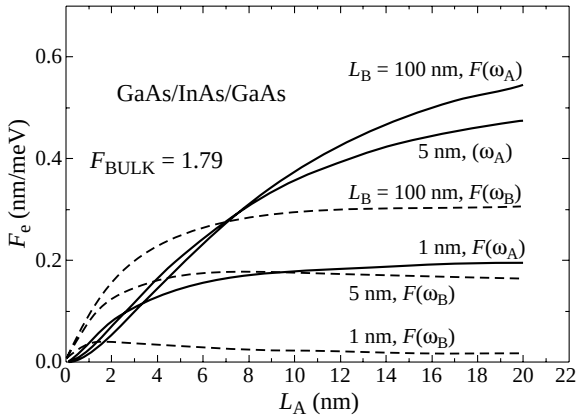

Fig. 2. Dependence of factor F_e on the QW width L_A at different thickness of the barrier layer B for the GaAs/InAs/GaAs structure at $q = \sqrt{2m\omega/h}$.

value of $F_e = 1.79$ for the bulk PO phonon is much larger than for the localized IF phonon. This means that IF phonon localization in a narrow phonon well strongly reduces the electron-phonon scattering rate.

Note that a thin ($L_B \to 0$) phonon barrier does not generate IF phonons (due to $F_e \to 0$).

2. Electron-localized PO phonon scattering rate in AlAs/GaAs/AlAs HEMT channel

We shall characterize the electron-PO phonon scattering rate by [5, 6]

$$W(k_i) = W_0 \left(N_{qv} \pm \frac{1}{2} + \frac{1}{2} \right) \times \int_0^{2\pi} \left| \int_{-L_A/2}^{+L_A/2} \varphi_{ei} \varphi_{ef} \varphi_{qv}(q_0, z) dz \right|^2 d\theta, \quad (10)$$

where

$$W_0 = \frac{me^2}{2\pi h^3}, \quad N_q = \left[\exp\left(\hbar\omega_v / kT\right) - 1 \right]^{-1},$$

φ_{ei} and φ_{ef} are the initial and final states of electron normalized wave functions, respectively, $\varphi_q(q_0, z)$ is the phonon potential function (see Eq. (1)), $q_0(\theta)$ is the emitted (absorbed) phonon wave vector. For simplicity, the electron intrasubband scattering is considered, and is assumed $\varphi_{ei}\varphi_{ef} = 2/L_A \cos^2(\pi z/L_A)$. The confined phonon wave function is assumed to be $\varphi_C \sim \sin(n\pi z/L_A)$.

Figure 3 demonstrates the calculated dependence $W(L_A)$ for the AlAs/GaAs/InAs/GaAs/AlAs double barrier HEMT channel with the inserted thin InAs barrier in the center of GaAs QW and without the barrier.

The electron-localized IF phonon scattering rate weakens in the narrow QW. Because of that, the electron-localized IF phonon scattering rate does not compensate the strong decrease of electron scattering rate by confined phonon. As a result, the total scattering rate in the interval from $L_A = 12$ nm to $L_A = 5$ nm decreases with decreasing QW width.

Especially, the great total scattering rate decrease is arisen when the GaAs QW layer is divided into two narrow phonon wells by thin (1 ML) InAs barrier for phonons.

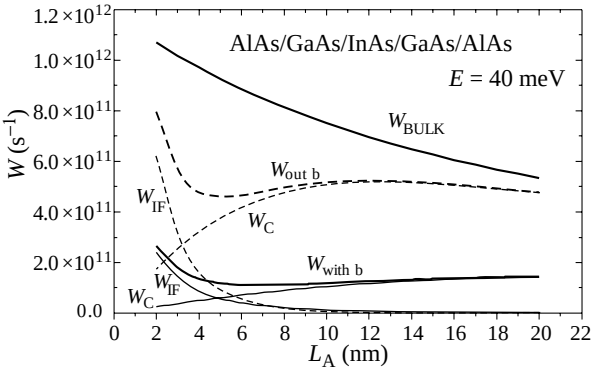

Fig. 3. QW width dependence of electron-PO phonon scattering rate W in GaAs QW with the inserted InAs barrier, $W_{\text{with b}}$, and without it, $W_{\text{out b}}$. W_C , W_{IF}, W_{BULK} are the electron scattering rates by confined, localized IF and bulk phonons, respectively. Electron energy $E = 40$ meV.

Note that the scattering rate calculated using electron scattering by bulk phonon approximation, W_{BULK}, (Fig. 3) significantly exceeds the real scattering rate. The widely used electron-bulk phonon approximation can not be used in narrow QWs.

3. Experiment

The electron mobility in modulation doped (HEMT) $Al_{0.2}Ga_{0.8}As/GaAs/Al_{0.2}Ga_{0.8}As$ structures with a thin GaAs layer of thickness $L = 12$ nm containing three InAs barriers, and without the barriers, was measured experimentally. One of the barriers was inserted into a GaAS QW center and another two — at the GaAs/AlGaAs heterojunctions (Fig. 4).

The mobility measured in the structure with the InAs barriers is 1.1–1.2 times larger than the mobility in the structure without the barriers. (Fig. 5).

The estimation of the electron mobility ($\overline{\mu} = \int \mu f(E) dE$) using approximation

$$\overline{\mu} = \frac{e}{2\pi m} \frac{1}{\overline{W}_{\text{opt}} + \overline{W}_{\text{other}}}, \quad (11)$$

where $\overline{W}_{\text{opt}}$ is the calculated mean values of electron-PO phonon scattering rate, shows that in the experimental structures,

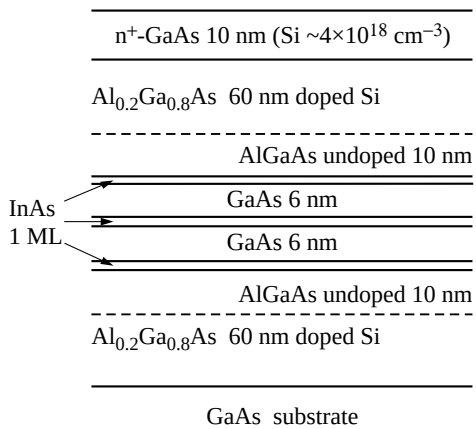

Fig. 4. Schematic view of the experimental structure $Al_{0.2}Ga_{0.8}As/GaAs/Al_{0.2}Ga_{0.8}As$ with inserted thin (1 ML) InAs phonon barriers.

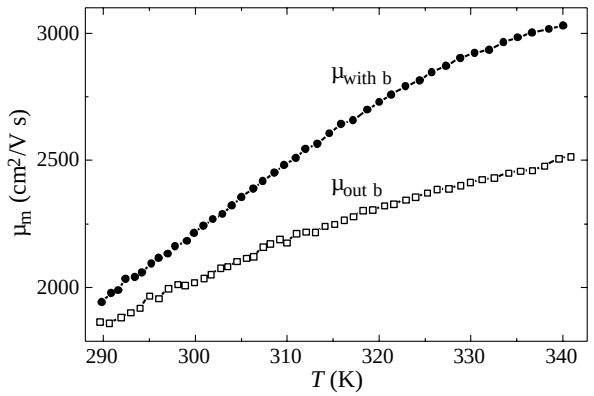

Fig. 5. Temperature dependence of experimentally measured mobility in the $Al_{0.2}Ga_{0.8}As/GaAs/Al_{0.2}Ga_{0.8}As$ structure without the InAs barriers, $\mu_{\text{out}\,b}$, and in the $Al_{0.2}Ga_{0.8}As/InAs/GaAs/InAs/GaAs/InAs/Al_{0.2}Ga_{0.8}As$ structure with the thin 1 ML InAs barriers, $\mu_{\text{with}\,b}$.

the electron-PO phonon scattering is not a dominant scattering mechanism. In the structures without the barriers at $T = 300$ K, the measured mobility $\mu_{\text{exp}} = 2000$ cm^2/Vs. This means that at the calculated $\overline{W}_{\text{opt}}^{\text{out}\,b} = 2 \times 10^{11}$ s^{-1}, the scattering rate by other scattering mechanisms can be estimated as $\overline{W}_{\text{other}} = 8.5 \times 10^{11}$ s^{-1}. Then the estimation for the mobility at $T = 300$ K in the structures with the InAs barriers, using the calculated $W_{\text{opt}}^{\text{with}\,b} = 0.5 \times 10^{11}$ s^{-1} gives the increased mobility $\overline{\mu}_{\text{estim}}^{\text{with}\,b} = 2335$ cm^2/Vs.

Taking into account the increase of $\overline{W}_{\text{opt}}$ with increasing temperature due to the increase of the number of electrons with the energy large than the optical phonon energy, the similar estimation of the mobility in the structure with the barriers at $T = 340$ K gives $\mu_{\text{estim}}^{\text{with}\,b}(340K) = 3100$ cm^2/Vs.

The experimentally measured mobility in the structure with the barriers is less than the estimated value of the mobility taking into account the increase of W_{other}, when InAs barriers are inserted into the QW. But in any cases the mobility in the structures with the barriers is larger than in the structures without the barriers.

The giant enhancement (1.7-times) of electron drift velocity is experimentally observed at high electric fields ($>10^3$ V/cm) in a wide GaAs channel (50 nm) of the $Al_{0.2}Ga_{0.8}As/GaAs/Al_{0.2}Ga_{0.8}As$ structure with the inserted thin InAs barriers (every 6 nm) in a center of the doped (10^{18} cm^{-3}) channel as compared with the structure without the inserted InAs barriers. That confirms the great increase of W_{opt} for the high energy electron, when the strong mechanism with phonon emission dominates over the scattering mechanism W_{other}.

Acknowledgements

I would like to thank V. Evtikhiev and A. Shkolnik (Ioffe Institute) for providing the AlGaAs/GaAs/AlGaAs structures, J. Storasta and A. Mekys (Vilnius University) for help in measurements and my collegues K. Požela and V. Juciene for help in calculations and carrying out some experiments.

References

[1] J. Požela, V. Juciene, *Semiconductors* **29**, 236 (1995).
[2] J. Požela *et al*, *Semicond. Sci. Technol.* **10**, 1555 (1995).
[3] B. K. Ridley *et al*, *Proc. 23rd ICPS*, Berlin, 1807 (1996).
[4] N. Mori, T. Ando, *Phys. Rev. B* **40**, 6175 (1989).
[5] I. Lee *et al*, *Phys. Rev. B* **51**, 7046 (1995).
[6] J. Požela *et al*, *Physica E* **5**, 108 (1999).

15th Int. Symp. "Nanostructures: Physics and Technology"
Novosibirsk, Russia, June 25–29, 2007

Short-wavelength plasmons in low-dimensional structures

A. V. Chaplik[1,2], L. I. Magarill[1,2] and R. Z. Vitlina[1]

[1] Institute of Semiconductor Physics SB RAS, Novosibirsk, 630090, Russia
[2] Novosibirsk State University, Novosibirsk, 630090, Russia

Abstract. Behavior of plasmon spectrum in systems of different dimensionality is discussed. It is shown that unlike 2D and 3D cases in the spectrum of 1D plasmon the termination point is absent.

Introduction

Plasma oscillations in low-dimensional systems attract much attention now, mainly, from the viewpoint of manipulations with teraherz electromagnetic waves. The available experiments with low-dimensional plasmons relate to the long-wavelength limit when the spatial dispersion of the dynamical conductivity can be neglected, and, furthermore, the quasiclassical approximation is valid for calculations of the plasma response function. In this limit (and for zero temperature) the Landau damping of plasmons vanishes. Modern progress in nanotechnology makes the fabrication of structures with typical wavelength of plasmons in nanoscale topical. Correspondingly, it becomes interesting to investigate the dispersion law of plasma waves in the short-wave length regime, especially in the vicinity of the termination point of plasmons spectrum. In the present paper we consider (within RPA method) 1D plasma waves in nanotubes and in a cylindrical quantum wire, 2D plasmons in a single electron sheet beyond the frames of quasiclassical approximation. For the comparison we present also our results for very well known 3D (bulk) plasmons but in the vicinity of their termination point.

1. Plasma waves in nanotubes and quantum wires

Consider first a cylindrical nanotube with the single particle spectrum of semiconductor type

$$\varepsilon_{p_z,l} = \frac{p_z^2}{2m} + Bl^2, \tag{1}$$

where $l = 0, \pm1, \pm2, \ldots$, $B = 1/2mR^2$, m is the effective mass, R is the tube radius and p_z is the electron momentum along the tube axis; we set $\hbar = 1$. The polarization operator reads:

$$\Pi(\omega; q, n) = \frac{1}{4\pi^2 R}\sum_l \int_{-\infty}^{\infty} dp_z \frac{f_{p_z-q,l-n} - f_{p_z,l}}{\varepsilon_{p_z,l} - \varepsilon_{p_z-q,l-n} - \omega - i\delta}, \quad (\delta = +0). \tag{2}$$

Here n and q are the plasmon azimuthal number and its momentum along nanotube, respectively, $f_{p_z,l} \equiv f(\varepsilon_{p_z,l})$ is the Fermi distribution function. After solving the Poisson equation for a hole cylinder one arrives at the equation for plasma waves dispersion relation

$$\Pi(\omega; q, n) I_n(qR) K_n(qR) + \frac{m a_B}{4\pi R} = 0. \tag{3}$$

Here $I_n(t)$, $K_n(t)$ are the modified Bessel functions, $a_B = \kappa/me^2$ is the effective Bohr radius (κ is the dielectric constant).

The exact analytical solution of Eq. (3) is possible for the ultraquantum case, when only the lower subband ($l = 0$) is populated; n and q remain arbitrary:

$$\omega_n^2(q) = \left(\frac{q^2}{2m} + Bn^2\right)^2 + (qv_F)^2 + qv_F\left(2Bn^2 + \frac{q^2}{m}\right)\coth\left(\frac{\pi q a_B}{4I_n(qR)K_n(qR)}\right). \tag{4}$$

In the long wavelength limit ($qR \ll 1$) one obtains from Eq. (4) for $n = 0$ the 1D plasmon dispersion law with logarithmic singularity:

$$\omega_0^2 = \frac{2e^2 N_L q^2}{m\kappa} \ln\frac{\gamma}{kR}, \tag{5}$$

where $N_L = 2p_F/\pi$ is the linear electron concentration, $\gamma = 2/e^C \simeq 1.123$, $C \approx 0.577$ is the Euler's constant.

A remarkable feature of the Eq. (4) is the absence of the termination point of the plasmon spectrum when q tends to infinity. The curve $\omega(q)$ asymptotically "presses" itself to the curve $qv_F + q^2/2m$, which is the boundary of the continuum of single particle excitations, but, in the contrast with 2D and 3D cases (see below) nowhere touches the boundary curve. We interpret this as follows: in the 1D situation the decay of plasmons in the electron-hole pairs is kinematically possible only in the phase space of zero measure because all the three quasiparticles must move along the one straight line.

For a cylindrical quantum wire one can obtain similar results. The spectrum of axial symmetric ($n = 0$) plasmon in the wire with one populated subband reads:

$$\omega_0^2(q) = \frac{q^4}{4m^2} + (qv_F)^2 + \frac{q^3 v_F}{m}\coth\left(\frac{\pi q a_B}{4\mathcal{I}(qR)}\right), \tag{6}$$

where $\mathcal{I}(x)$ is given by

$$\mathcal{I}(x) = 4\int_0^1 dt\, t \frac{J_0^2\left(x_1^{(0)}t\right)}{J_1^4\left(x_1^{(0)}\right)}\left[\int_0^t dt' t' J_0^2\left(x_1^{(0)}t'\right) I_0\left(xt'\right) K_0(xt) + \int_t^1 dt' t' J_0^2\left(x_1^{(0)}t'\right) I_0(xt) K_0\left(xt'\right)\right]. \tag{7}$$

Here $x_1^{(0)} \approx 2.405$ is the first root of the Bessel function $J_0(x)$. At $qR \ll 1$ we again get the formula of type Eq. (5) with another constant under logarithm:

$$\omega_0^2 = \frac{2e^2 N_L q^2}{m\kappa} \ln\frac{\gamma_1}{kR}, \quad \gamma_1 \approx 2.22. \tag{8}$$

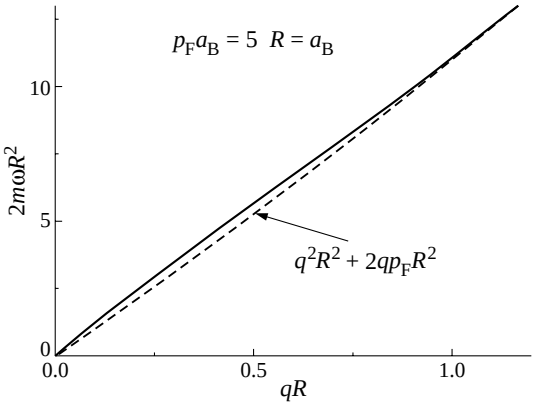

Fig. 1. Spectrum of 1D plasmon in nanotube.

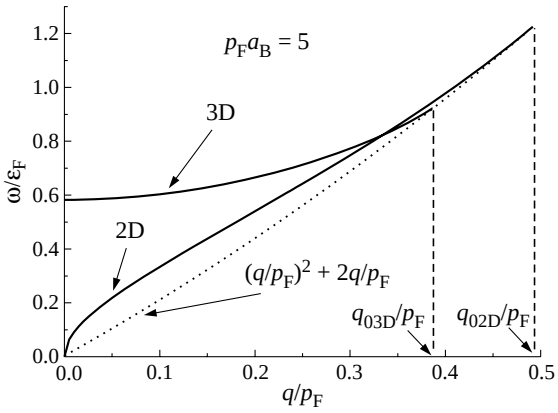

Fig. 2. Behavior of the plasmon spectrum in 2D and 3D systems.

Of course, for $q \geq p_F$ the effects of the Luttinger liquid should be taken into account (see, e.g., [1]). However, the specific feature of the 1D case is the existence of the Landau-damping-free plasmons up to momenta of the order of p_F that is not the case in 2D and 3D systems.

2. 2D electron sheet

Despite of the enormous number of the works devoted to this problem, to our best knowledge the RPA dispersion law of the 2D plasmons applicable for all values of q is not published till now. The corresponding formula reads:

$$\omega^2(q) = \left(qv_F + \frac{q^2}{2m}\right)^2 + \frac{q\left(8p_Fa_B - 4q^2a_B^2 - q^3a_B^3\right)^2}{16a_B^3m^2\left(qa_B + 4\right)}. \tag{9}$$

The formula (9) is valid for $q \leq q_0$, where q_0 is the positive root of the equation:

$$8p_Fa_B - 4q^2a_B^2 - q^3a_B^3 = 0. \tag{10}$$

Eq. (10) determines the termination point of the plasmon spectrum, after which the Landau damping starts. In the "metallic" limit $p_Fa_B \gg 1$ the termination point is $q_0 \simeq 2p_F^{1/3}/a_B^{2/3} \ll p_F$. We emphasize that the plasmons cease to be good quasiparticles (because of the Landau damping) within the quasiclassical domain $q_0 \ll p_F$, when the treatment of the electron plasma as a continual medium is still valid.

From Eq. (9) it is easy to show that $d\omega/dq|_{q=q_0} = q_0/m + v_F$, i.e. the plasmon spectrum touches the bounding parabola $q^2/2m + v_Fq$ at the termination point.

3. Bulk plasmons

Analogous conclusions are true for the bulk plasmons. From the textbook expression for longitudinal dielectric permittivity (see, e.g., [2], page 204) one can write the dispersion equation

$$\frac{1 + \pi a_Bq^2}{2p_F} - g(\omega_+) + g(\omega_-) = 0, \tag{11}$$

where

$$g(\omega) = \frac{m\left(\omega^2 - q^2v_F^2\right)}{2q^3v_F}\ln\left(\frac{\omega + qv_F}{\omega - qv_F}\right),\ \omega_\pm = \omega \pm q^2/2m.$$

The equation (11) is valid when the condition $\omega > q^2/2m + qv_F$ is satisfied. This requirement leads to the following equation for defining the termination point:

$$\left(1 + \frac{q}{2p_F}\right)\ln\left(1 + \frac{2p_F}{q}\right) = 1 + \frac{\pi q^2a_B}{2p_F}. \tag{12}$$

For $p_Fa_B \gg 1$ we get $q_0 \simeq \sqrt{(2p_F/\pi a_B)\ln(\lambda p_Fa_B)}$ (λ is the constant of the order 1) that is again $q_0 \ll p_F$. Hence, the domain of validity of the Goldman asymptotic behavior ([2], page 206) is rather narrow

$$\sqrt{\frac{p_F}{a_B}} \ll q \ll \sqrt{\frac{2p_F}{\pi a_B}\ln(\lambda p_Fa_B)}. \tag{13}$$

By means of implicit derivation of Eq. (11) one can show that the plasmon spectrum approaches the bounding parabola with touch at the termination point, as it occurs in 2D case.

Acknowledgements

This work was supported in part by the grant of RFBR No. 04-02-16398, Program for support of scientific schools of the Russian Federation No. 4500.2006 and INTAS No. 03-51-6453.

References

[1] M. P. A. Fisher, L. I. Glazman, *Transport in a One-Dimensional Luttinger Liquid*, cond-mat/9610037.

[2] E. M. Lifshitz, L. P. Pitaevskii, *Fizicheskaya kinetika*, (Moskva: Nauka) p. 204 (1979).

15th Int. Symp. “Nanostructures: Physics and Technology”
Novosibirsk, Russia, June 25–29, 2007

Effect of DC electric field on longitudinal resistance of two dimensional electrons in a magnetic field

Sergey Vitkalov[1], Jing-qiao Zhang[1], A. A. Bykov[2], A. K. Kalagin[2] and A. K. Bakarov[2]

[1] The City College of New York, New York, NY, USA
[2] Institute of Semiconductor Physics, 630090 Novosibirsk, Russia

Abstract. The effect of a DC electric field on the longitudinal resistance of highly mobile two dimensional electrons in heavily doped GaAs quantum wells is studied at different magnetic fields and temperatures. Strong suppression of the resistance by the electric field is observed in magnetic fields at which the Landau quantization of electron motion occurs. The phenomenon survives at high temperature where Shubnikov de Haas oscillations are absent. The scale of the electric fields essential for the effect is found to be proportional to temperature in the low temperature limit. We suggest that the strong reduction of the longitudinal resistance is the result of a nontrivial change in the distribution function of 2D electrons induced by the DC electric field. Comparison of the data with recent theory yields the inelastic electron-electon scattering time $\tau_{\rm in}$ and the quantum scattering time $\tau_{\rm q}$ of the electrons at high temperatures, a regime where previous methods were not successful.

Introduction

The nonlinear properties of highly mobile two dimensional electrons in AlGaAs/GaAs heterojunctions is a subject of considerable current interest. Strong oscillations of the longitudinal resistance induced by microwave radiation have been found at magnetic fields which satisfy the condition $\omega = n \times \omega_{\rm c}$, where ω is the microwave frequency, $\omega_{\rm c}$ is cyclotron frequency and $n = 1, 2\ldots$ [1,2]. At high levels of the microwave excitations the minima of the oscillations can reach values close to zero [3,4,5,6]. This so-called zero resistance state (ZRS) has stimulated extensive theoretical interest [7,8,9,10]. At higher magnetic field $\omega_{\rm c} > \omega$ a considerable decrease of magnetoresistance with microwave power is found [2,5,6] which has been attributed to intra-Landau-level transitions [11].

Another interesting nonlinear phenomenon has been observed in response to DC electric field [12, 13]. Oscillations of the longitudinal resistance, periodic in inverse magnetic field, have been found at DC biases satisfying the condition $n \times \hbar\omega_{\rm c} = 2R_{\rm c}E_{\rm H}$, where $R_{\rm c}$ is the Larmor radius of electrons at the Fermi level and $E_{\rm H}$ is the Hall electric field induced by the DC bias in the magnetic field. The effect has been attributed to “horizontal” Landau–Zener tunneling between Landau levels, tilted by the Hall electric field $E_{\rm H}$ [12].

In this paper we report a new phenomenon. We have observed a strong reduction of the 2D longitudinal resistance induced by DC electric field $E_{\rm dc}$ that is substantially smaller than that required for the “horizontal” electron transitions between Landau levels [12, 13]. In contrast to the inter Landau level scattering, the observed effect depends strongly on temperature.

1. Experimental

Two samples (GaAs quantum well wiith width 13 nm) were studied with electron density $n_1 = 1.22 \times 10^{16}$ m^{-2}, $n_2 = 0.84\times10^{16}$ m^{-2},and mobility $\mu_1 = 93$ m^2/Vs, $\mu_2 = 68$ m^2/V s at $T = 2.7$ K. The longitudinal resistance was measured using a current of 0.5 μA at a frequency of 77 Hz in the linear regime. Direct electric current (bias) was applied simultaneously with AC excitation through the same current leads (see insert to Fig. 1).

Typical curves of the longitudinal resistance r_{xx} are shown as a function of the DC bias in Fig. 1 at two temperatures. At high DC bias the resistance exhibits maxima that satisfy the condition $n \times \hbar\omega_{\rm c} = 2R_{\rm c}E_{\rm H}$, corresponding to “horizontal” transitions between Landau levels [12, 13]. Another striking feature is the sharp peak at zero DC bias which broadens as the temperature is raised. The reduction of the resistance is observed at high temperatures where no SdH oscillations are present. This is quite different from what one expects for electron heating by the electric field. As shown in the insert to Fig. 1, the resistance increases for higher temperatures, in contrast with the observed decrease with applied electric field.

From a theoretical perspective, nonlinear phenomena in high mobility 2D electron systems can be conveniently separated into: (a) effects of electric field on the electron distribution function [10], and (b) effects of electric field on the kinematics of electron scattering [8,9]. It was recently realized

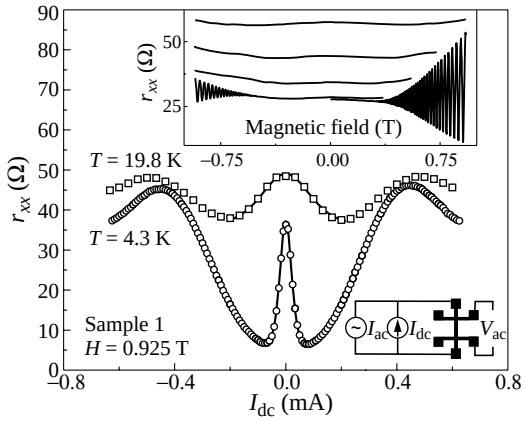

Fig. 1. Dependence of the differential resistance r_{xx} on DC bias at $B = 0.925$ T. Circles correspond to $T = 4.3$ K, squares correspond to $T = 19.8$ K. The solid lines are theoretical curves. The fitting parameters are $I_0 = 0.055$ mA and $\delta = 0.334$ for $T = 4.3$ K and $I_0 = 0.1802$ mA and $\delta = 0.177$ for $T = 19.8$ K. The top inset shows quantum oscillations of the longitudinal resistance at different temperatures $T = 1.9$ K, 4.2 K, 9.9, 19.8 and 35 K (curves in ascending order); $I_{\rm dc} = 0$ A. The experimental set-up is shown at bottom right.

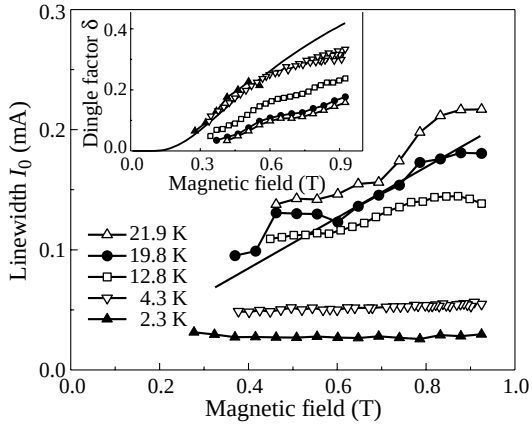

Fig. 2. Dependence of the width of the peak I_0 on magnetic field at different temperatures, as labeled. The solid line represents the linear dependence expected from the theory in the high temperature limit (see Eq. 2). The inset shows the magnetic field dependence of the parameter δ obtained from the fit of the zero bias peak using Eq. 3. The solid line presents the theoretical dependence of the Dingle parameter δ on magnetic field, corresponding to a quantum scattering time $\tau_q = 1.5$ ps.

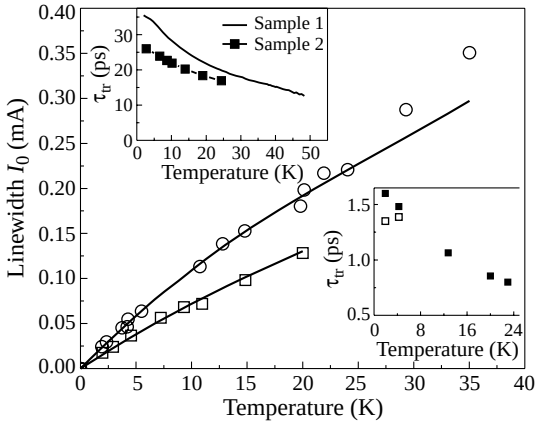

Fig. 3. Dependence of the width of the zero bias peak I_0 on temperature for sample N1 (open cirles) and sample N2 (open squares) at $B = 0.925$ T. The solid lines are the theory. The comparison gives an inelastic scattering time $\tau_{in} = 10/T^2$ $(12/T^2)$ (ns) for sample N1(N2). The top inset shows the transport time τ_{tr} vs temperature at $B = 0$ T. The dependence of the quantum scattering time τ_q on temperature is shown in the bottom insert. Open squares indicate the τ_q determined from the amplidute of the SdH oscillations. Filled squares are determined from the amplitude of the zero bias peak.

that the the first of these should provide the dominant contribution to the nonlinear response in 2D electron systems. Below we will compare our results with this approach [10].

Relative to the Drude conductivity, σ_D, in zero magnetic field, the theory predicts a longitudinal conductivity:

$$\Delta\sigma_{xx}/\sigma_D = 2\delta^2\left[1 - \frac{4Q_{dc}}{1+Q_{dc}}\right], \qquad (1)$$

where $\delta = exp(-\pi/\omega_c\tau_q)$ is the Dingle factor, τ_q is the quantum scattering time and the parameter Q_{dc} is

$$Q_{dc} = \frac{2\tau_{in}}{\tau_{tr}}\left(\frac{eE_{dc}v_F}{\omega_c}\right)^2\left(\frac{\pi}{\hbar\omega_c}\right)^2 = \frac{I_{dc}^2}{I_0^2}. \qquad (2)$$

Here τ_{tr} is the transport scattering time and v_F is the Fermi velocity. To compare with experiment we have expressed the parameter Q_{dc} in terms of DC electrical current I_{dc}.

The dependence of the width of the peak (I_0) on magnetic field is presented in Fig. 2 at different temperatures. At high temperature $kT > \hbar\omega_c$ ($\hbar\omega_c/k = 18$ K at $B = 0.925$ T), the peak width varies considerably with magnetic field. The approximately linear increase of the scale I_0 with magnetic field agrees with the theory.

The temperature dependence of the width of the peak is shown in Fig. 3. At low temperatures the width of the peak is found to be proportional to the temperature T. The solid lines in the figure are theoretical curves plotted in accordance with Eq. 1,2.

Acknowledgements

This work was supported by NSF: DMR 0349049; DOE-FG02-84-ER45153 and RFBR, project No. 04-02-16789 and 06-02-16869.

References

[1] M. A. Zudov *et al*, *Phys. Rev. B* **64**, 201311(R) (2001).
[2] P. D. Ye *et al*, *Appl. Phys. Lett* **79**, 2193 (2001).
[3] R. G. Mani *et al*, *Nature* (London) **420**, 646 (2002).
[4] M. A. Zudov *et al*, *Phys. Rev. Lett* **90** 046807 (2003).
[5] S. I. Dorozhkin, *JETP Lett.* **77**, 577 (2003).
[6] R. L. Willettet *et al*, *Phys. Rev. Lett* **93**, 026804 (2004).
[7] A. V. Andreev *et al*, *Phys. Rev. Lett.* **91**, 056803 (2003).
[8] A. C. Durst *et al*, *Phys. Rev. Lett.* **91**, 086803 (2003).
[9] M. G. Vavilov *et al*, *Phys. Rev. B* **69**, 035303 (2004).
[10] I. A. Dmitriev *et al*, *Phys. Rev. B* **71**, 115316 (2005).
[11] S. I. Dorozhkin *et al*, *Phys. Rev. B* **71**, 201306(R) (2005).
[12] C. L. Yang *et al*, *Phys. Rev. Lett.* **89**, 076801 (2002).
[13] A. A. Bykov *et al*, *Phys. Rev. B* **72**, 245307 (2005).

15th Int. Symp. "Nanostructures: Physics and Technology"
Novosibirsk, Russia, June 25–29, 2007

Piecewise parabolic magnetoresistance of the 2DEG with periodical lattice of scatterers

M. V. Budantsev[1], *A. G. Pogosov*[1] and J.-C. Portal[2,3]

[1] Institute of Semiconductor Physics, Novosibirsk 630090, Russia
[2] GHMF, CNRS/LCMI, BP-166, F-38042, Grenoble, Cedex 9, France
[3] INSA-Physique and Institut Universitaire de France, F-31077, Toulouse, Cedex 4, France

Abstract. An unusual piecewise parabolic manetoresistance has been experimentally found in the two-dimensional electron gas with a periodic triangular lattice of scattering disks — antidots. Transitions between the successive parabolic pieces are abrupt, characterized by narrow intervals of magnetic fields compared to the widths of the parabolic pieces themselves. The observed anomalous magnetoresistance is negative, its respective amplitude is not small, and it has a classical origin. The unexpected piecewise parabolic behavior can be related to percolation properties of two-dimensional lattice or to the classical memory effects. A proper understanding of the observed effect requires further theoretical study.

Introduction

Investigation of electron transport phenomena and scattering in a two-dimensional electron gas (2DEG) attracts great attention of researchers. Recently, this interest is mainly caused by phenomena exceeding the limits of the Drude approach, leading to interesting experimentally observable effects. In the present work we report on the observation of a new effect of this kind found in the 2DEG with periodical lattice of scatters. We have found that the magnetic field dependence of the sample resistance represents itself a piecewise parabolic function. Unfortunately there is a lack of appropriate theory describing such an unusual behavior. Thus our discussion, following the detailed explanation of experimentally obtained results, will be limited by comparative analysis of the closest theoretical models.

Experimental results

Experimental samples were fabricated on the basis of the 2DEG in AlGaAs/GaAs heterostructure with electron mobility $\mu = 300\times10^3$ cm^2/V s and electron density $N_S = 3{-}5\times10^{11}$ cm^{-2} measured at temperature 4.2 K. The two-dimensional lattice of periodically situated circular scatters — antidots — was created using electron lithography method with subsequent anisotropic plasma etching. The lattice of antidots has a triangular symmetry. The period of the lattice is $d = 0.6\,\mu$m and lithographic diameter of antidots $2a = 0.25\,\mu$m. The lattice was placed at the macroscopic Hall bar with dimensions $L\times W = 100\times50\,\mu$m^2.

The resistance was measured using standard lock-in technique at frequency 7 Hz, at ac current 10^{-8} A. Measurements were carried out at temperatures 1.6–4.2 K, in magnetic fields up to 1 T, directed perpendicular to the plane of the 2DEG. The electron density in the sample was changed by LED illumination, which allowed to change the resistance of the sample from 15 kOhms down to 1 kOhm.

A row of magnetoresistance traces $R_{xx}(B)$ for different sample states, measured at temperature 3 K is plotted in Fig. 1(a). We will characterize the state of the sample by its resistance at zero magnetic field $R_0 = R_{xx}(0)$. All the measured dependencies demonstrate negative magnetoresistance (NMR) up to magnetic field values of 0.5−0.8 T. In low magnetic fields in the range $0.05 < |B| < 0.2$ T NMR has characteristic form similar to the linear dependence $R_{xx}(B) \sim -|B|$. Temperature

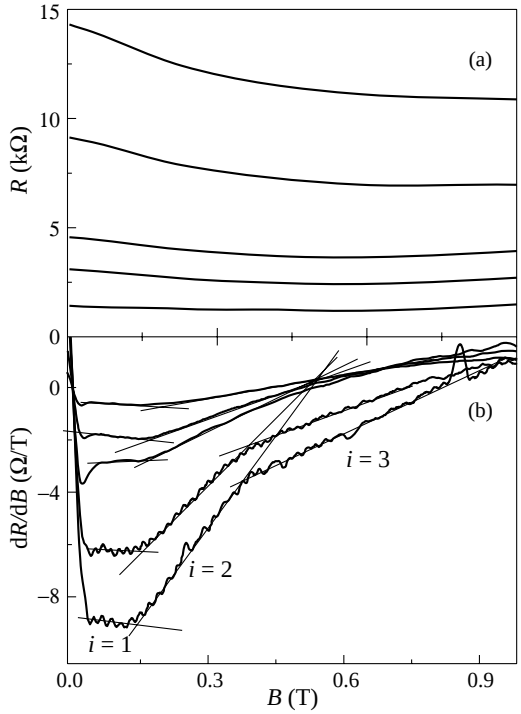

Fig. 1. (a) Magnetoresistance of periodic lattice of antidots experimentally measured for different sample states. (b) Derivative $dR_{xx}(B)/dB$, obtained by numerical differentiation of experimental dependencies. Linear fits of $dR_{xx}(B)/dB$ for different magnetic field regions (i) are shown by solid straight lines.

measurements demonstrate that for all of the sample states the observed NMR has weak temperature dependence only in the small range of very low magnetic fields $B < 0.02$ T. This indicates that the NMR in this range originates from the quantum interference effects (weak localization). This range of magnetic fields is not considered in the present work. In the whole magnetic field range of interest ($0.02 < |B| < 1$ T) the observed NMR is temperature independent, which points to its classical origin (non-weak localization).

For the detailed analysis of the magnetoresistance we have plotted the derivative $dR_{xx}(B)/dB$ (Fig. 1(b)), obtained by numerical differentiation of experimental dependencies. One can see that in a wide region of magnetic fields $|B| > 0.05$ T

for all of the sample states the derivative of the magnetoresistance is a piecewise linear function with very narrow transition regions between the pieces. For low resistance states one can identify two linear regions of dR/dB in the ranges $0.05 < |B| < 0.17$ T and $0.17 < |B| < 0.54$ T, while for high resistive states there is an additional inflection at $B \approx 0.38$ T followed by the third linear region extending up to $B \approx 0.9$ T. It should be also noted that for all of the sample states (both high resistive and low resistive) all the lines extrapolating linear dependencies of $dR(B)/dB$ in the second region intersect at one universal point $B \approx 0.54$ T. Based on the described analysis of the derivative $dR(B)/dB$ we can conclude that the resistance is a piecewise parabolic function of magnetic field, formed by the second order polynomials $R_i(R_0, B) = a_i(R_0) + b_i(R_0)B + c_i(R_0)B^2$, where i corresponds to different magnetic field regions. Moreover, at low magnetic fields ($i = 1$) the derivatives $dR_{xx}(B)/dB$ are almost magnetic field independent ($c_1(R_0) \approx 0$ for all values of R_0), and thus $R(B)$ can be considered as an almost linear function of magnetic field.

A detailed analysis of the dependence $R(B)$ in the vicinity of the point of transition between two pieces of parabolas shows that the width of this transitional region is only 10% of the width of the pieces themselves or even less. Such an abrupt switch of the system response resembles the behavior normally observed at phase transitions.

Discussion

To our knowledge the described piecewise parabolic behavior of the magnetoresistance was not reported for the similar systems before. There is a lack of theory that could explain the observed behavior completely. Let us consider theoretical models which are the closest to the considered case.

Percolation approach

In terms of the percolation theory the conductivity of the considered triangular lattice of antidots can be considered as a bond problem [1]. Namely, the triangular cavities between three neighboring antidots are considered as "sites" while bottlenecks (between two neighboring antidots), connecting adjacent "sites" are considered as resistances ("bonds"). These sites and bonds form a honeycomb lattice. The values of the resistances (bonds) are distributed due to random impurities and technological imperfections. The width of this distribution is large, since the resistance of a narrow bottleneck is highly sensitive to the deviations of electrostatic potential. Finally, to form the problem in terms of the percolation theory assume that the bonds with resistances larger than some typical value r_c are blocked while the rest are open. According to the percolation theory [1], the probability x to find an unblocked bond determines the conductivity $\sigma \sim (x - x_c)^t$, where x_c is the percolation threshold and t is a corresponding critical exponent. For the case of the 2D honeycomb lattice [1] $x_c \approx 0.65$ and $t \approx 1.2$. The bond resistances, and consequently the driving parameter x are affected by the applied magnetic field $x = x(B)$. Critical magnetic field is thus $x(B_c) = x_c$. The dependence $\sigma(x)$ is almost linear ($t = 1.2$), and to obtain the experimentally observed linear dependence $\sigma(B)$ one must assume that $x(B)$ is almost linear function. However, this assumption is too strong. Moreover, the percolation model in this form cannot explain multiple critical points observed in our experiment.

Memory effects

Another theoretical model, that can be also relevant to our case is based on non-Markovian memory effects originating from the anomalous diffusion of electrons along classical trajectories [2]. For the system of 2D electrons scattering on the randomly distributed hard disks it is shown in [2] that memory effects arising in backscattering effects lead to the enhancement of the resistance of the system at zero magnetic field compared to the Drude model. Application of an external magnetic field destroys the anomalous backscattering trajectories leading to the linear negative magnetoresistance at intermediate magnetic fields. The characteristic parameter of the model $\beta_0 = 2na^2$ (gas parameter), where n is the 2D concentration of discs, is compared with dimensionless magnetic field $\beta = \omega_c\tau$ (ω_c is the cyclotron frequency, τ is the scattering time). The authors of ref. [2] taking into account correlations of N-th order found that the function $\delta\rho(\beta)/\rho$ is a parabolic function of β with different parameters for each region $\beta_0^{N+1} < \beta < \beta_0^N$. This behavior is very close to the experimentally observed ones, including the presence of multiple critical magnetic field points $\beta_N = \beta_0^N$. It should be noted that more detailed comparison of the model with our experiment is impossible, since the described theory is developed for the case of small values of gas parameter $\beta_0 \ll 1$, and consequently for $|\delta\rho|/\rho \ll 1$, while in our experiment $\beta_0 \sim 1$ and $|\delta\rho|/\rho \sim 1$. However, we believe that the increase of β_0 can only enhance the role of correlations and the considered effect, and thus, the condition $\beta_0 \ll 1$, taken to simplify the calculations, is in this sense artificial.

A complete explanations of the described piecewise parabolic behavior of the magnetoresistance experimentally found in the present paper requires further theoretical study.

Acknowledgements

The authors are grateful to V. Yu. Kachorovskii for fruitful discussions. The work was supported by RFBR (grant 05-02-17200) and INTAS (grant YS–ID 639).

References

[1] B. I. Shklovskii and A. L. Efros, *Electronic Properties of Doped Semiconductors*, Berlin: Springer-Verlag, 1984.

[2] V. V. Cheianov, A. P. Dmitriev and V. Yu. Kachorovskii, *Phys. Rev. B* **70**, 245307 (1999).

15th Int. Symp. "Nanostructures: Physics and Technology"
Novosibirsk, Russia, June 25–29, 2007

Conductivity of two-dimensional electron systems (soft mode, metal-insulator transition)

E. G. Batyev[1,2]

[1] Institute of Semiconductor Physics, 630090 Novosibirsk, Russia
[2] Novosibirsk State University, 630090 Novosibirsk, Russia

Abstract. A description is proposed for a low-density 2D electron system. In such a system, the correlation effects due to the interaction between the charge carriers can play a significant role. The system is assumed to possess a short-wavelength soft mode, which models the effect of the aforementioned interaction. The conductivity of the system depends not only on the common impurity scattering of carriers, but also on the scattering of the Bose excitations (the soft mode), which leads to an additional dissipation of the momentum of the system. The number of the Bose excitations varies with temperature, which causes a temperature dependence of the conductivity. That is good for sufficiently low disorder (in the metallic phase). But near the metal-insulator transition, the disorder effects become important. The possible way is to consider this one in terms of a percolation theory. In our model, the initial structure is taken to be the skeleton of an infinite cluster. Percolation paths are assumed to have regions where two phases having similar energies, namely, liquid (conducting) and solid (nonconducting) phases, can compete with each other. The ratio of these phases changes as a function of the system parameters and temperature. This behavior generates a change in the infinite cluster and results in the conductor-insulator transition. The obtained temperature dependencies of resistivity agree qualitatively with experiments.

There is the well-known statement that, in disordered 2D systems, all single-particle (electron and hole) states are localized [1]; i.e., the metallic state in such systems is impossible. But experiments show other picture (see, e.g., reviews [2, 3]), namely, the metallic state is possible for high-mobility samples. The above-mentioned statement is correct for non-interacting particles whereas the experiments have dealings with strong-interacting carriers. However, the transition to insulating state takes place as the carrier concentration decreases, apparently, because of reduction of their Coulomb interaction which becomes smaller as compared with the influence of disorder.

In the concerned systems, the Coulomb interaction of carriers is much greater than their kinetic energy (the parameter $r_S \gg 1$). So it is the strong correlated liquid (so-called Wigner liquid) and, under further increase of the r_S, the Wigner crystal is generated. It is natural to expect that just the strong correlations result in substantial increase of resistivity with temperature in metallic phase. This scenario is examined in the Section 1. As regards the metal-insulator transition, this property is essentially connected with disorder and is considered in the Section 2.

1. Soft mode

In the Wigner liquid, there is a short-range order as in the Wigner crystal. As a precursor of the crystallization, an appearance of the so-called soft mode is possible. If that is the case, this one has a minimum at the finite momenta. That looks like the roton minimum in the superfluid ^{4}He. Similar assumption about soft mode was used under construction of the theory of liquid-crystal phase transition in ^{3}He [4].

Thus, our basic assumption is following one: besides the ordinary for Fermi liquid excitations of Fermi type, in the Wigner liquid, there are the Bose-type excitations corresponding to the soft mode [5].

The spectrum $\Omega_{\mathbf{q}}$ of the Bose excitations is proposed in the form

$$\Omega_{\mathbf{q}}^2 = \Omega_0^2 + v_0^2(q - q_0)^2 \,. \qquad (1)$$

Here, apparently, $\Omega_0 < \epsilon_F$, $v_0 \sim v_F$, $q_0 \sim p_F$ (ϵ_F, v_F, p_F are the Fermi energy, velocity, momentum correspondingly). Further the assumption is made that $q_0 > 2p_F$ therefore the Bose excitations are the good, weakly damped ones.

So, the system under study contains two types elementary excitations. Both of them are scattered by the impurities, and the system loses its momentum through these two channels. One can assume that, at low temperatures, as usual, the contribution made by the Fermi excitations is temperature-independent. This is not the case with the Bose excitations because of the dependence of their number $N_{\mathbf{q}}$ on temperature:

$$N_{\mathbf{q}} = \left\{ \exp \frac{\Omega_{\mathbf{q}} + \mathbf{qu}}{T} - 1 \right\}^{-1} \qquad (2)$$

where $\mathbf{u}$ is the velocity of the system.

Let τ_1 be the relaxation time by the Fermi excitations (presumably constant) and τ_2 be the relaxation time by the Bose excitations. For conductivity σ, we use the ordinary formula

$$\sigma = \frac{ne^2\tau}{m} \,, \quad \frac{1}{\tau} = \frac{1}{\tau_1} + \frac{1}{\tau_2} \,.$$

The calculations of τ_2 give the result [5]:

$$\frac{1}{\tau_2} = \frac{n_i}{n} \frac{q_0^2}{\pi m} \left\{ \exp\left(\Omega_0/T\right) - 1 \right\}^{-1} \,,$$

where n_i is the impurity concentration.

The resistivity $\rho = 1/\sigma$ at low temperatures, $T < \Omega_0$, can be represented in the form:

$$\rho \approx \rho_0 + \rho_1 \exp(-\Omega_0/T) \,. \qquad (3)$$

In some experiments [6, 7], it is this type of temperature dependence that is obtained for sufficiently low temperatures. The experiments [6, 7] show that the value of Ω_0 (the T_0 in their designation) decreases as the density of carriers becomes lower, which is quite natural for such a quantity: the role of

the correlation effects increases with decreasing density, and this leads to softening of the soft mode. At high temperatures, it is necessary to take into account a change of the soft mode spectrum [8], and as a result, the saturation of resistivity with temperature is appeared.

2. Metal-insulator transition

For the clean system (without disorder), under decrease of carrier concentration, the liquid-crystal phase transition takes place (the Wigner crystal is generated). The point of absolute instability of the liquid is the point $\Omega_0 = 0$.

For disordered system, apparently when the interaction of carriers with disorder become of order of the Coulomb interaction with each other, the metal-insulator transition happens. (This transition is observed by way of the temperature behavior of resistivity [1,2].) This kind of transition does not occur by uniform manner because of fluctuations in impurity distribution. Therefore, we accept the percolation model to describe the transition [9].

In the model, the main points are as follows: (i) closeness to the percolation threshold, (ii) an infinite (percolation) cluster as the initial object, and (iii) the variation of this cluster with the system parameters and temperature due to the possibility of formation (and competition) of different phases having substantially different kinetic properties (e.g., conducting and insulating phases). This behavior is local (in percolation paths, in the bonds of the infinite cluster), which gives a global conductor-insulator transition (throughout a sample).

We now analyze a bottleneck. Let $\epsilon_{\rm L}$ be the energy of this region in a liquid (conducting) state, and let $\epsilon_{\rm S}$ be the energy of this region in a solid (nonconducting) state. The corresponding probabilities are defined by the conventional expressions

$$W_{\rm L} \sim \eta_{\rm L} \exp(-\epsilon_{\rm L}/T)\,, \quad W_{\rm S} \sim \eta_{\rm S} \exp(-\epsilon_{\rm S}/T)\,,$$

where $\eta_{\rm L,S}$ is the statistical weight of the corresponding phase. The probability $W_{\rm S}(\epsilon)$ of the fact that a bond is blocked (a region is solidified) is

$$W_{\rm S}(\epsilon) = \frac{\eta}{\exp(\epsilon/T)+\eta}\,, \tag{4}$$

$$(\eta = \eta_{\rm S}/\eta_{\rm L}\,, \quad \epsilon = \epsilon_{\rm S} - \epsilon_{\rm L})\,.$$

Naturally, a certain scatter of energies $g(\epsilon)$ is assumed to exist. It is equal to

$$g(\epsilon) = \frac{1}{\Delta\sqrt{\pi}} \exp\left\{-\frac{(\epsilon-\epsilon_0)^2}{\Delta^2}\right\}. \tag{5}$$

Here ϵ_0, Δ, and η are the phenomenological parameters of the theory. The parameter ϵ_0 specifies the transition, since it passes through zero near this transition.

Equations (4) and (5) are related to bonds that can be blocked. Let the fraction of such bonds at a maximum be x_0. Then, at an arbitrary temperature, the fraction of blocked bonds $x_{\rm b}$ is defined by the integral

$$x_{\rm b} = x_0 \int d\epsilon\, \frac{g(\epsilon)\eta}{\exp(\epsilon/T)+\eta}\,. \tag{6}$$

In our model, it may be assumed that conductivity σ is proportional to $(x - x_{\rm c})$, where x is the fraction of open bonds whereas $x_{\rm c}$ is its critical value. So, we have

$$\sigma \sim (x - x_{\rm c}) = (1 - x_{\rm b} - x_{\rm c}) = (1 - x_{\rm c})\left\{1 - \frac{x_0}{1-x_{\rm c}} \int d\epsilon\, \frac{g(\epsilon)\eta}{\exp(\epsilon/T)+\eta}\right\}.$$

At high temperatures ($T \gg |\epsilon_0|, \Delta$), we should obtain a finite conductivity, since this is an experimental fact. This gives a condition for x_0, which can be written as

$$\frac{x_0}{1-x_{\rm c}} = b\,\frac{1+\eta}{\eta}\,, \quad b < 1\,. \tag{7}$$

Finally, for resistivity $\rho = 1/\sigma$, we obtain

$$\rho^*(T) = \frac{\rho(T)}{\rho(\infty)} = (1-b)\left\{1 - b\int d\epsilon\, \frac{g(\epsilon)(1+\eta)}{\exp(\epsilon/T)+\eta}\right\}^{-1}. \tag{8}$$

The quantity $\rho(\infty)$ is the limiting resistivity at high temperatures.

The theory contains certain phenomenological parameters b, η, Δ which, in the vicinity of the metal-insulator transition, could be considered as the constants. As to the ϵ_0, we can expect that $\epsilon_0 \sim n - n_0$ near the transition. Here, n_0 is a certain purity-dependent concentration characteristic of a sample: the higher the sample purity, the smaller the value of n_0.

In the limiting case, $\Delta \to 0$, from Eq. (8), we have:

$$\rho^*(T) = \frac{(1-b)\left[\exp(\epsilon_0/T)+\eta\right]}{\left[\exp(\epsilon_0/T)+\eta\right] - b(1+\eta)}, \quad (b<1)\,.$$

As follows from this expression, a separatrix corresponds to a point $\epsilon_0 = 0$ (at this point, the temperature dependence disappears and the metal-insulator transition takes place). The sign (and value) of ϵ_0 affects the variation of resistivity with temperature, in which connection, the case of $\epsilon_0 > 0$ ($\epsilon_0 < 0$) corresponds to the metallic (insulating) state.

Acknowledgements

This work was supported by the Russian Foundation for Basic Research (project No. 06-02-16923) and by the Council under President of Russian Federation for supporting of leading scientific schools (project No. NSh–4500.2006.2).

References

[1] E. Abrahams, P. W. Anderson, D. C. Licciardello, and T. V. Ramakrishnan, *Phys. Rev. Lett.* **42**, 673 (1979).
[2] E. Abrahams, S. V. Kravchenko, and M. P. Sarachik, *Rev. Mod. Phys.* **73**, 251 (2001).
[3] S. V. Kravchenko and M. P. Sarachik, *Rep. Prog. Phys* **67**, 1 (2004).
[4] E. G. Batyev, *Sov. Phys. JETP* **43**, 300 (1976).
[5] E. G. Batyev, *JETP Letters* **72**, 506 (2000).
[6] Y. Hanein *et al*, *Phys. Rev. Lett.* **80**, 1288 (1998).
[7] S. J. Papadakis and M. Shayegan, *Phys. Rev. B* **57**, R15068 (1998).
[8] E. G. Batyev, *JETP Letters* **73**, 566 (2001); **74**, 231 (2001).
[9] E. G. Batyev, *JETP* **102**, 776 (2006).

15th Int. Symp. “Nanostructures: Physics and Technology”
Novosibirsk, Russia, June 25–29, 2007

The impact of spin-orbit coupling on the quantum Hall quantization law in 2DEG subject to periodic potential: Berry curvature and semiclassical dynamics

V. Ya. Demikhovskii and A. A. Perov
Nizhny Novgorod State University, Gagarin avenue, 23, 603950 Nizhny Novgorod, Russia

Abstract. We evaluate the distribution of Hall conductances of magnetic subbands formed in two-dimensional electron gas with Rashba spin-orbit (SO) coupling placed in a periodic potential and perpendicular magnetic field. In this semiconductor structure the spin-orbit coupling mixes the states of different magnetic subbands and changes the distribution of their Hall conductances in comparison with the case of spinless particles. The calculations were made for semiconductor structures with a weak (AlGaAs/GaAs) and relatively strong (GaAs/InGaAs) SO and Zeeman interactions. The Hall conductances of fully occupied magnetic subbands depend on the system parameters and can be changed when neighboring subbands touch each other.

Introduction

The problem of electron quantum states and quantum Hall quantization law for an electron gas subject to both periodic potential and homogeneous magnetic field remains to be actual for several last decades. There are various approaches and models for periodic potential and different approximations which are used for investigations of these problems (see, Ref. [1]). However, the spin-orbit interaction is usually excluded from the models as well as the Zeeman term. Such approach can be justified as long as the amplitude of the periodic potential is big enough to make the Landau level splitting much greater than the typical spin-orbit coupling energy and the Zeeman term. At the same time, under the realistic experimental conditions with 2D electron gas subject to the potential of lateral superlattice the potential amplitude V_0 can be of the same order as the spin-orbit (SO) Rashba coupling. For example, in recent papers [2] where a pioneering step into experimental observation of 2D magnetic Bloch states has been done, the magnitude of V_0 was around 1–5 meV. In semiconductor structures with large SO coupling [2] the typical splitting energy can be of the same order as V_0.

In this presentation we investigate the quantum Hall effect in 2D electron gas with SO Rashba coupling subject to both periodic potential of a superlattice and a uniform perpendicular magnetic field. The calculations were carried out for two semiconductor systems with weak and quite strong SO interaction. The Zeeman effect for electrons was also taken into account. As was established, the Hall conductance quantization rule depends on the system parameters at fixed magnetic flux per unit cell of the superlattice and changes at the moment when the neighboring magnetic subbands touch each other. As we will see below, in the system with a weak SO coupling when the SO and Zeeman splittings are smaller than Landau level splitting due to the action of periodic potential the neighboring magnetic subbands are overlapped but not degenerated for any quasimomentum $\mathbf{k}$. In that case the Hall conductance quantization rule is the same as for spinless particles [1]. We found that with the decreasing superlattice period the effect of SO coupling rises and the distribution of Hall conductances in magnetic subbands is changed at the moment when neighboring subbands touch each other. In semiconductor structures where SO coupling as well as Zeeman splitting are larger than the splitting by periodic potential, we found a new distribution law for Hall currents of fully occupied magnetic subbands.

1. Theoretical model and magnetic spinor Bloch states

The quantum states of 2D electron gas with SO Rashba coupling subject to potential $V(x, y)$ which is periodic in the (X, Y) plane with the period a, and in a uniform magnetic field $\mathbf{H}$ perpendicular to the plane was evaluated in our previous work [3]. The correspondent Hamiltonian has the following form:

$$\hat{H} = (\hat{\mathbf{p}} - e\mathbf{A}/c)^2/2m^* + \hat{H}_{\mathrm{R}} - g\mu_{\mathrm{B}} H\hat{\sigma}_z + V(x, y),$$

where $\hat{H}_{\mathrm{R}} = \frac{\alpha}{\hbar}\left(\hat{\sigma}_x(\hat{p}_y - eA_y/c) - \hat{\sigma}_y\hat{p}_x\right)$ is the Rashba Hamiltonian of an electron in uniform magnetic field. Here $\hat{p}_{x,y}$ are the momentum operator components, m^* is the electron effective mass, $\hat{\sigma}_i$ $(i = x, y)$ are the Pauli matrices, α is the parameter of the SO coupling, g is the Zeeman factor, and μ_{B} is the Bohr magneton. We use the Landau gauge in which the vector potential has the form $\mathbf{A} = (0, Hx, 0)$ and consider the potential $V(x, y) = V_0(\cos(2\pi x/a) + \cos(2\pi y/a))$. The quantum states structure of the system under consideration depends crucially on the parameter $\Phi/\Phi_0 = p/q = |e|Ha^2/2\pi hc$ (p and

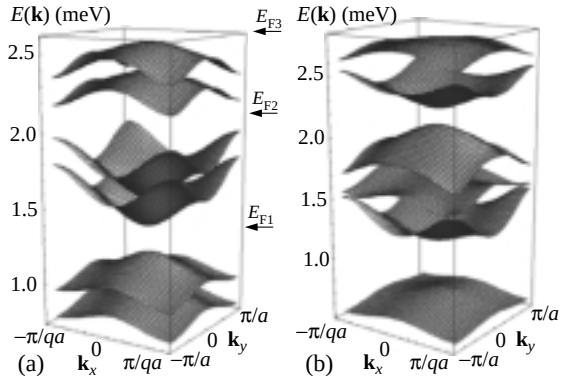

Fig. 1. The dispersion laws in magnetic subbands at $p/q = 3/1$ for: (a) three pairs of overlapped subbands for AlGaAs/GaAs superlattice structure ($m^* = 0.067m_0$, $\alpha = 2.5 \times 10^{-12}$ eV m, $g = -0.44$, $a = 80$ nm, $V_0 = 1$ meV), (b) six separated magnetic subbands in GaAs/InGaAs superlattice structure ($m^* = 0.05m_0$, $\alpha = 2.5 \times 10^{-11}$ eV m, $g = -4.0$, $a = 80$ nm, $V_0 = 1$ meV).

q are prime integers) which is the number of flux quanta per unit cell, and Φ_0 is the flux quanta.

The experimental values of Rashba coupling constant α for different materials range from about 2×10^{-12} eV m to 4×10^{-11} eV m. The calculations of quantum states were carried out for two semiconductor structures with different strength of SO coupling. One of them is 2D electron gas in AlGaAs/GaAs heterojunction with superlattice periodic potential. This structure is characterized by small SO Rashba constant α and relatively small g-factor. The parameters of another system correspond to GaAs/$In_xGa_{1-x}As$ heterostructure where SO coupling parameter and g-factor have large values.

The dispersion laws $E_\mu(\mathbf{k})$ in MBZ are presented in Fig. 1(a), (b) for $p/q = 3/1$ for parameters AlGaAs/GaAs and GaAs/$In_{0.23}Ga_{0.77}As$ structures, respectively. Here we consider the magnetic subbands attached to the lowest pair of unperturbed levels E_0^+ and E_1^- [4].

2. Hall conductance quantization law

The Hall conductances of magnetic subbands were obtained by integration of the Berry curvatures $\Omega_\mu(\mathbf{k})$ (see Fig. 2) over magnetic Brillouin zone [5]. It was found that in real semiconductor superlattice systems subject in uniform magnetic field at the presence of spin-orbit coupling the distribution of Hall conductances in magnetic subbands can differ from another one obtained by Thouless *et al* [1] in the model of spinless particles. Even in the case of relatively weak SO coupling and Zeeman term the distribution of Hall conductances is changed with the decreasing lattice period.

The distribution of Hall conductance in magnetic subbands for AlGaAs/GaAs and GaAs/InGaAs superlattice structures is shown in Figs. 3(a) and (b), respectively. In systems with weak SO coupling when the SO and Zeeman terms are smaller than

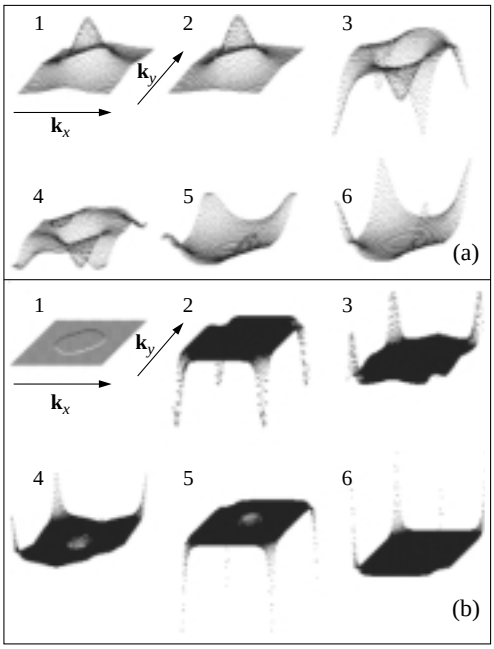

Fig. 2. The Berry curvatures $\Omega_\mu(\mathbf{k})$ (arb. units) for 2D electron gas in (a) AlGaAs/GaAs and (b) GaAs/$In_{0.23}Ga_{0.77}As$ structures with lateral superlattice at $p/q = 3/1$, $a = 80$ nm and $V_0 = 1$ meV. The parameters of the SO and Zeeman interactions are the same as in Fig. 1. The subband indices $\mu = 1, \ldots, 6$ are displayed near each of the surfaces $\Omega_\mu(\mathbf{k})$.

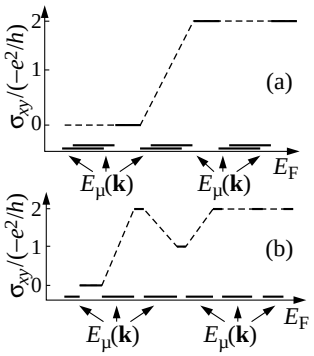

Fig. 3. The Hall conductance quantization laws in six fully occupied magnetic subbands at $p/q = 3/1$ for the same parameters as in Fig. 1: (a) for AlGaAs/GaAs structure, (b) for GaAs/InGaAs structure.

the Landau level broadening produced by the periodic potential, a quant of the Hall current is carried by the middle subband from each group of three subbands (Fig. 3(a)). So, the results of our calculations are in good agreement with Thouless *et al* [1] results. With the decreasing superlattice period the distribution of Hall conductances of magnetic subbands is changed drastically. At the critial value of the period $a = 56$ nm the second and the third subbands contact each other and the dispersion laws $E_\mu(\mathbf{k})$ ($\mu = 2, 3$) are modified. At the same time the correspondent Berry curvatures $\Omega_\mu(\mathbf{k})$ and, therefore, the topological invariants (first Chern numbers) of these subbands defining their Hall conductance are changed dramatically. We found that in AlGaAs/GaAs superlattice structure at $a = 50$ nm the following sequence of Hall conductances in units of $(-e^2/h)$ is realized: 0,2,−1,1,0,0. As a result, in the system which is characterized by a weak Rashba and Zeeman coupling constants at the certain lattice parameters the distribution of Hall conductances can be totally different from another one distribution predicted for spinless particles [1].

If the SO and Zeeman terms are comparable to the Landau level broadening caused by the superlattice periodic potential, the distribution of Hall conductance across six subbands measured in units of $-e^2/h$ follows the same sequence as before: 0, 2, −1, 1, 0, 0 (see Fig. 3(b)). Correspondingly, the Hall current here is carried by the second, the third, and the fourth magnetic subbands. Moreover, we observed that each time when two bands touch each other while the SO or Zeeman coupling parameters are varied, the conductances of these subbands may not be conserved when the bands split again. However, the sum of the Hall conductances remains unchanged.

Acknowledgements

This work was supported by the program of the Russian Ministry of Education and Science "Development of scientific potential of high education" (project 2.1.1.2363), grant of Russian Foundation of Basic Research (No. 06-02-17189) and grant of the President of Russian Federation (No. MK-5165.2006.2).

References

[1] D. J. Thouless *et al*, *Phys. Rev. Lett.* **49**, 405 (1982).
[2] C. Albrecht *et al*, *Phys. Rev. Lett.* **86**, 147 (2001); M. G. Geisler *et al*, *Phys. Rev. Lett.* **92**, 256801 (2004).
[3] V. Ya. Demikhovskii *et al*, *Europhys. Lett.* **76** iss. 3, 477 (2006).
[4] X. F. Wang *et al*, *Phys. Rev. B* **67**, 085313 (2003).
[5] Ming-Che Chang *et al*, *Phys. Rev. B* **53**, 7010 (1996).

15th Int. Symp. "Nanostructures: Physics and Technology"
Novosibirsk, Russia, June 25–29, 2007

Collective response of a 2DEG in a Si/SiGe heterostructure under microwave radiation

S. Sassine[1,2], Yu. Krupko[1], *E. B. Olshanetsky*[3], Z. D. Kvon[3], J.-C. Portal[1,2,4], J. M. Hartmann[5] and J. Zhang[6]

[1] GHMFL, CNRS, BP 166, F-38042, Grenoble Cedex 9, France
[2] INSA, 135 Avenue de Rangueil, F-31077, Toulouse Cedex 4, France
[3] Institute of Semiconductor Physics, Novosibirsk 630090, Russia
[4] Institut Universitaire de France, 103 Bd. St. Michel, F-75005, Paris, France
[5] CEA/LETI, F-38054, Grenoble Cedex 9, France
[6] University College, London WC 15 75, United Kingdom

Abstract. The effect of microwave radiation on the magnetoresistance of a two- dimensional electron gas in Si/SiGe heterostructure is reported for the first time. Application of microwave radiation results in resonant photoconductivity responses at magnetic field values that are consistently lower than expected for the cyclotron resonance (CR) in an infinitely large two-dimensional electron system. This shows that the microwave-induced response in a 2D electron gas in Si/SiGe heterostructure is dominated by plasmon excitations.

Introduction

The study of various resonance effects in a 2D electron system under electro-magnetic radiation can in some cases provide information that it would be difficult to obtain by standard transport measurements. Unlike 3D samples, however, direct absorption or transmission spectroscopy in the case of a 2DES would be problematic due to the low electron densities in single or even multiple quantum wells [1]. Previously, it has been demonstrated that a much higher sensitivity can be obtained if the radiation absorption is detected electrically via a resonant change induced in the sample resistance or magnetoresistance (photoconductivity) [2]. The change in magnetoresistance is the consequence of a resonant increase in the temperature of the 2DES associated with resonant absorption of radiation power. This method has been successfully employed for the study of both the cyclotron and electron spin resonances [3–8]. In the case of the cyclotron resonance there have been two types of experiments that differed by the employed radiation frequency range. The first cyclotron resonance photoconductivity experiments to be carried out were performed on a 2DEG in GaAs/AlGaAs using far-infrared radiation with the wavelength of about 100–200 μm [6,7]. The resonant peaks observed in these experiments were located near the quantum Hall effect maxima in magnetoresistance and were identified as conventional cyclotron resonance corresponding to the frequency $f_c = eB/2\pi m^*$. Later, in an experiment performed similarly on a 2DEG in a GaAs/AlGaAs heterostructure, a microwave radiation of frequency 70–170 GHz has been employed [8]. In this experiment the resonant peaks were observed in relatively weak magnetic fields approximately coinciding with the setting in of Shubnikov–de Hass oscillations. It was found that these resonant peaks in magnetoresistance were systematically shifted to lower magnetic fields with respect to the expected position of a cyclotron resonance peak corresponding to the applied microwave radiation frequency. The analysis of the data has shown that the observed peaks are in fact due to a collective confined 2D plasmon excitation with the confinement length determined by the width W of the samples. As a result the observed 2D plazmon excitations all have the same wavelength $\lambda = 2W$.

1. Experimental

To our knowledge after the Ref. [8] there has been no attempt to carry out a similar study on a different 2D system. In the present work we report the first observation of 2D magnetoplasmon excitations in a 2D electron gas in Si/SiGe heterostructure. For this purpose two Si/SiGe wafers fabricated by different methods have been used. The wafers had the following parameters: Wafer A — a CVD reactor grown wafer with the electron density $N_s = 5.8 \times 10^{11}$ cm^{-2} and the mobility $\mu = 186000$ cm^2/V s ($T = 1.4$ K); Wafer B — an MBE grown wafer with the density of the 2DEG $N_s = 6.6 \times 10^{11}$ cm^{-2} and the mobility $\mu = 66700$ cm^2/Vs. Hall bars with the dimensions 100×50 μm^2 were fabricated on top of each wafer using conventional photolithography technique. The measurements have been performed using MW radiation in the frequency range of 80–120 GHz. The MW radiation was guided to the sample by a brass tube of a circular cross section. The experiments were carried out at a temperature 1.4 K.

2. Discussion

Normalised magnetoresistance curves taken in both samples for several fixed values of MW radiation frequency are shown in Fig. 1. One can see that the well-resolved resonance peaks in both samples shift to higher magnetic field as the radiation frequency increases.

In Fig. 2(a) we plot the resonance MW radiation frequency $f_{\rm res}$ versus the resonance peak position (as marked by arrows in Fig. 1). For comparison we also plot the cyclotron resonance frequency dependence on magnetic field for the case of an infinitely large 2DEG ($f_c = eB/2\pi m^*$, where $m^* = 0.19m_e$, the effective mass of 2D electrons in Si). As is clear from the Fig. 2(a) the $f_{\rm res}(B)$ dependence, which is the same for the two investigated samples, does not coincide with that of cyclotron resonance. In Fig. 2(b) we re-plot the data from Fig. 2(a) as $f_{\rm res}^2$ versus B^2. We find that the resonant positions for both samples follow the relation $f_{\rm res}^2 = f_{\rm res}^2(B = 0) + f_c^2(B)$. Presented in this way the dependence is linear with the slope $\Delta(f_{\rm res}^2)/\Delta(B^2) = (eB/2\pi m^*)^2$, where $m^* = 0.19m_e$. The extrapolation to $B = 0$ gives $f_{\rm res}(B = 0) = 94.3$ GHz.

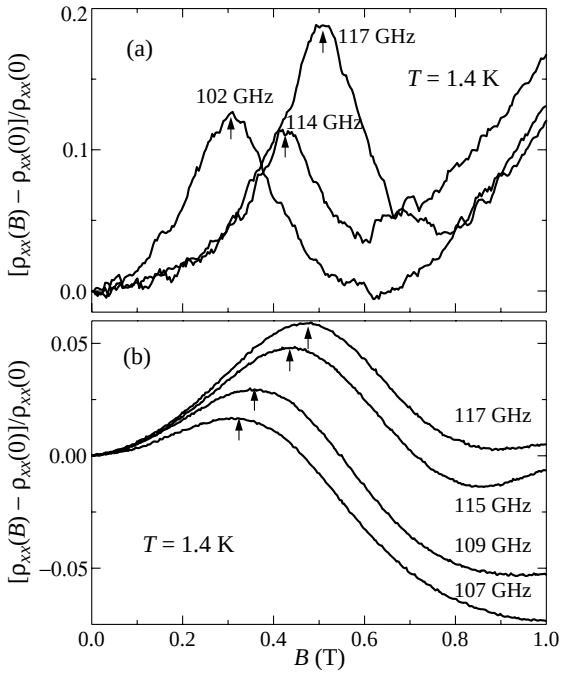

Fig. 1. Photoresponse of samples A — (a) and B — (b) to MW radiation for several fixed MW frequency values; the arrows mark the resonance peaks positions.

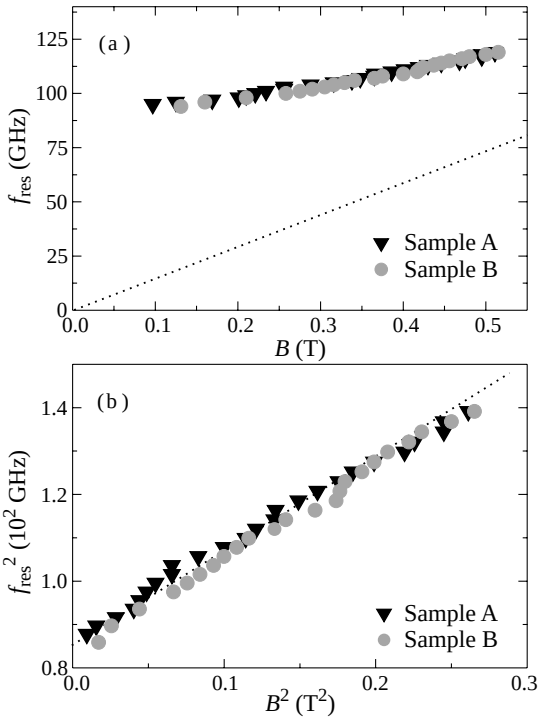

Fig. 2. (a) The triangles and circles mark the experimental resonance frequencies $f_{\rm res}$ versus the magnetic field position $B_{\rm res}$ for sample A and sample B respectively. The dashed line corresponds to the cyclotron frequency $f_{\rm c} = eB/2\pi m^*$ with $m^* = 0.19m_e$; (b) Data from Fig. 3(a) re-plotted on quadratic scale; the dashed line $f_{\rm c}^2(B^2)$ with $m^* = 0.19m_e$ marks the slope of the experimental dependence.

Similar to Ref. [8], from the observed quadratic behavior we conclude that the photoresponse in our samples is determined by collective effects. In an infinitely large 2DEG the frequency of plasmon oscillations is given by [9]:

$$f_{\rm p}^2 = \frac{N_s e^2}{8\pi^2 \varepsilon_{\rm eff}\varepsilon_0 m^*} k, \qquad (1)$$

where k is the plasmon wave vector, N_s the electron density and $\varepsilon_{\rm eff} = 1/2(\varepsilon_{\rm Si} + \varepsilon_{\rm vac})$ the effective dielectric constant, $\varepsilon_{\rm Si} = 11.9$. In the presence of a perpendicular magnetic field plasmons evolve to magnetoplasmons that have the following dispersion relation [10–12]:

$$f_{\rm mp}^2 = f_{\rm p}^2(B=0) + f_{\rm c}^2, \qquad (2)$$

where $f_{\rm c}$ is the cyclotron frequency. As one can see, in an infinitely large 2DEG plasmons have a gapless energy spectrum. For any given value of magnetic field there will be a continuum of excitation frequencies $f_{\rm mp}$ that will exclude the observation of any resonance effect. In our case, however, we have plasmons confined within a rectangular Hall bar. In Ref. [8] for a qualitative explanation of a similar experimental data a simple model was proposed according to which in a rectangular Hall bar sample there will be just a single plasmon mode with $k = \pi/W$, i.e. with one half of the plasmon wavelength fitting into the Hall bar width W. Using this model we obtain for sample A $f_{\rm p}(B=0) = 109.4$ GHz and for sample B $f_{\rm p}(B=0) = 116.7$ GHz. These values agree quite well with the experimental value $f_{\rm res}(B=0) = 94.3$ GHz. Similar to Ref. [8] we find that the calculated values are consistently higher than the experimental one. The experiment shows that the photoresponse is dominated by a single plasmon mode $k = \pi/W$.

In conclusion, we have studied the microwave photoconductivity response in a 2DEG in Si/SiGe heterostructure. Similar to a previous study in AlGaAs/GaAs Ref. [8], we find that the observed resonant photoresponse is dominated by collective plasmon excitations mode with a wavelength equal to a double width of the Hall bar. The photoresponse in two Si/SiGe samples grown by different methods and having different parameters of the 2DEG was found to be qualitatively the same.

Acknowledgements

This work was supported by ANR PNANO MICONANO and RFBR project No. 06-02-16129.

References

[1] N. Nestle *et al*, *Phys. Rev.* **B56**, R4359 (1997).
[2] D. Stein *et al*, *Surf. Sci.* **142**, 406 (1984).
[3] M. Dobers *et al*, *Phys. Rev.* **B38**, 5453 (1988).
[4] M. Dobers *et al*, *Phys. Rev.* **B40**, 8075 (1989).
[5] E. B. Olshanetsky *et al*, *Phys. Rev.* **B67**, 165325 (2003).
[6] J. C. Maan *et al*, *Appl. Phys. Lett.* **40**, 609 (1982).
[7] M. J. Chou *et al*, *Proceed. 18th ICPS*, Stockholm, 1986, p. 437.
[8] E. Vasiliadou *et al*, *Phys. Rev* **B48**, 17145 (1993).
[9] F. Stern, *Phys. Rev. Lett.* **18**, 546 (1967).
[10] A. V. Chaplik, [*Sov. Phys. JETP* **35**, 395 (1972)].
[11] S. J. Allen *et al*, *Phys. Rev. Lett.* **38**, 980 (1977).
[12] D. Heitmann, *Surf. Sci.* **170**, 332 (1986).

15th Int. Symp. "Nanostructures: Physics and Technology"
Novosibirsk, Russia, June 25–29, 2007

Optimization of multilayer AlN/AlGaN/GaN/AlGaN heterostructures with quantum well channel for high power microwave field effect transistors

S. I. Petrov, A. N. Alekseev, S. B Aleksandrov, A. E. Byrnaz, V. P. Chaly, D. M. Krasovitskiy, M. V. Pavlenko, M. Yu. Pogorel'sky, A. P. Shkurko, I. A. Sokolov, M. A. Sokolov, M. V. Stepanov, A. G. Tkachenko, L. E. Velikovskiy and I. E. Velikovskiy

JSC "Svetlana–Rost", St Petersburg, Russia

Abstract. In doubly electron confined AlGaN/GaN/AlGaN heterostructures with 50 Å QW-GaN channel grown on sapphire substrates by ammonia molecular beam epitaxy current densities up to 1.0 A/mm were reached. In test DHFETs, fabricated from such a structures, electron confinement is essentially improved while other DC-mode parameters were competitive to ones obtained on "thicker" HEMT-like devices. Issues of heterostructure design and growth optimization are discussed.

Introduction

Field effect transistors (FET) based on GaN/AlGaN heterostructures (HS) rise above a number of similar microwave devices based on traditional semiconductors. The main peculiarity of nitride HS is that the two-dimensional electron gas (2DEG) formed at GaN/AlGaN interface can reach sheet electron density more than 10^{13} cm^{-2} due to large band offsets and "piezodoping" effect. 2DEG electron mobility depends essentialy on crystal quality of layers in HS: values of cm^2/V s (300 K) have been published [1], while electron motilities in the range of 1000–1500 cm^2/V s are typical for most publications. FETs based on such HS usually show current densities of 0.6–1.2 A/mm and transconductance in 120–200 mSm/mm range. These values together with high breakdown voltages provide in some cases an order of magnitude higher power densities as compared with GaAs. As a result, microwave power densities up to 32 W/mm for GaN-based discrete devices [2] and output power over 150 W for power amplifiers [3] have been demonstrated. The key issue for the development of high power devices is the electron confinement which is directly effects on transistors cut off and leakage [4]. Besides, hot electrons spillover under high gate-source bias takes place and limits maximum current and thus power density. The latter essentially contributes to the so called "RF-current collapse" due to electron trapping in buffer and upper barrier layers. Leakage can be minimized by compensation doping of GaN buffer layer with impurities producing deep levels, such as Fe, C, Mg etc. [5]. To reduce current collapse related to surface traps, various passivation techniques are used, for example silicon nitride based [6]. Nevertheless, above methods can not prevent electron trapping in thick buffer GaN layer, moreover, the problem seems to be accented because an additional traps are produced by compensation doping of buffer layer. Alternatively, better electron confinement without electron trapping can be obviously provided in double heterostructures (DHS), containing wider bandgap semiconductor material underneath an active GaN channel. A number of publications reporting succesful realisation of DHS field effect transistors (DHFETs) based on AlGaN/GaN/AlGaN [7,8] are available, and device parameters are competitive to ones obtained on "classic" HS GaN/AlGaN. We also previously reported on multylayer heterostructures AlN/AlGaN/GaN/AlGaN with GaN channel layer thickness of 140 nm, showing DEG motilities 1000–1350 cm^2/V s at sheet electron densities $1.0-1.6\times10^{13}$ cm^{-2}. DHFETs based on such MHS demonstrated current density up to 1 A/mm in DC-mode [9]. To improve electron confinement and so device performance, GaN thickness should be further decreased. Besides, it seens also technologically attractive due to the distance from AlGaN buffer to surface will be redused too, thus making mesa-isolation etch and gate metallization easer and more reliable. However, mobility drastically decreases in DHS when channel layer is reduced. We also reported on influence of MHS design on mobility and electron sheet concentration and current densities up 0.6 A/mm in MHS with quantum well channel was then demonstrated [10]. Here we discuss further optimization of AlN/AlGaN/GaN/AlGaN MHS design and growth conditions, that allows to reach QW-MHS current densities as high as ones inherent in MHS with "thicker" GaN channel layer. Accordingly, DHFETs based on these new QW-MHSes show an excellent confinement even at high current density of 1.0 A/mm that is matter of interest for high power microwave applications.

1. Experimental

AlN/AlGaN/GaN/AlGaN MHS were grown on (0001) sapphire substrates by ammonia molecular beam epitaxy using specialized nitride MBE system STE3N2 (SemiTeq). The main peculiarities of this system are extremely high (up to 12000 °C) growth temperatures and V/III ratios (up to 1000), combined with with all the traditional MBE opportunities. The main peculiarities of our MHS design is 0.2 μm thick AlN tamplate, grown at 1200 °C directly before heterostructure within the same epitaxy process [9]. Properties of grown samples were studied using atomic-force nicroscopy (AFM), X-ray diffraction (XRD), capasitance-voltage (C-V) and temperature dependent Hall measurements. Test transistors with 1×20 μm gate geometry were fabricated on MHS by planar processing including photolithography, e-beam metallization, rapid thermal annealing and reactive ion etching techniques. At this stage, no surface passivations were used.

2. Results and discussion

Reduction of GaN channel thickness alone, without another changes in AlN/AlGaN/GaN/AlGaN MHS design, deteriorates

2DEG mobility due to following main reasons. First, relaxation above critical thickness may be accompanied by formation of various defects, contributing to an additional carrier scattering; so narrowing the channel to thickness close to this defect region results in mobility degradation. Second, polarization induced bow of GaN channel bandgap is essentially pronounced when channel thickness is narrower. As a result, parasitic hole conductivity appears in some cases near bottom interface AlGaN/GaN (analogous to 2DEG formation near upper GaN/AlGaN interface). It was found in our earlier work, that parasitic hole conductivity is not formed when Al content at bottom interface AlGaN is lower than 15%, however polarization induced distortion band diagram is enough for quantum confinement even at quite low Al content in in AlGaN buffer layer of 10%. Besides, critical thickness of relaxation for Al content in 10–20% range was estimated to be 15–20 nm. So for optimum design of MHS with quantum well channel, buffer layer should be finished by AlGaN with 10% Al content and channel thickness should be 5 nm [10]. In present report we show that optimization of AlN template growth condition, combined with appropriate AlGaN intermediate layers, together allow to substantially increase electron mobility in MHS with quantum well. Because of polarization induced bowing of bandgap makes electron concentration lower, we also optimized Al content in cap layer. Thus, Al mole fraction of 0.4–0.45 instead of commnoly used 0.25–0.35, give an increase from the common values of (0.9–1.1) cm^{-2} up to (1.5–1.7) cm^{-2} while keeping mobility in the range of 1100–1300 $cm^2/V\,s$. In conclusion, modified design and optimized growth conditions together allow to increase current density in MHS with QW-channel up to 1.0 A/mm. Important, that DC I-V characteristics (Fig. 1) of QW-MHS even at high current density demonstrate no hysteresis often seen in 2DEG-heterostructures with "thicker" GaN channels. It clearly confirms efficiency of electron confinement in such a MHS as well as its good prospects to collapse- free high power microwave operation.

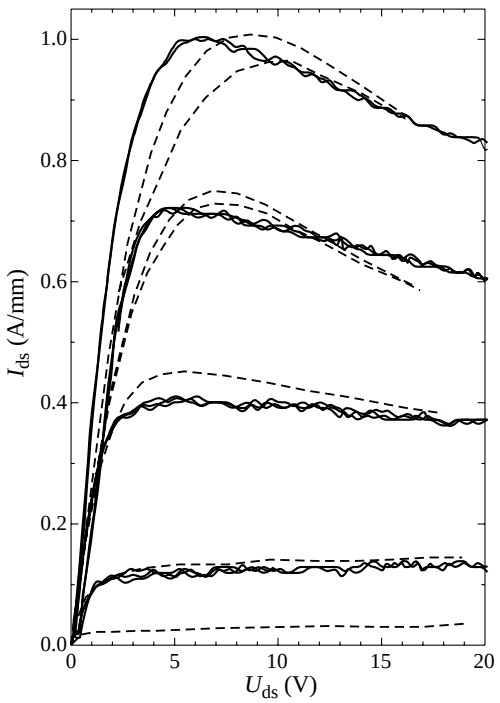

Fig. 1. DC-mode current-voltage characteristics of DHFETs based on MHS with 140 nm (red curves) and 50 Å QW (black curves) GaN channels.

References

[1] R. Gaska *et al*, *Appl. Phys. Lett.* **74**, 287 (1999).
[2] Y. F. Wu *et alIEEE Electron Dev. Lett* **25**, 117 (2004).
[3] T. Kikkawa *et al*, *GaAs MANTECH-2004, New Orleans.* www.gaasmantech.org/Digests/2004/2004Papers/6.1.pdf
[4] Y. K. Su *et al*, *Mat. Sci. Eng.* **B 110**, 172 (2004).
[5] H. Tang *et al*, *Solid-State Electronics* **44**, 2177 (2002).
[6] A. E. Vertiatchikh *et al*, *Elec. Lett.* **38**, 388 (2002).
[7] G. Simin *et al*, *Jpn. J. Appl. Phys.* **40**, L1142 (2001).
[8] C. Q. Chen *et al*, *Appl. Phys. Lett.* **82**, 4593 (2003).
[9] Y. Cordier *et al*, *J. Crystal Growth* **278**, 393 (2005).
[10] A. N. Alekseev *et al*, *Tech. Phys. Lett.* **31**, 846 (2005).

15th Int. Symp. “Nanostructures: Physics and Technology”
Novosibirsk, Russia, June 25–29, 2007

Temperature driven crossover from diffusion to hopping probed by the nonohmic conductivity

A. A. Sherstobitov[1], G. M. Minkov[1], A. V. Germanenko[2], O. E. Rut[2] and B. N. Zvonkov[3]

[1] Institute of Metal Physics RAS, 620041 Ekaterinburg, Russia
[2] Ural State University, 620083 Ekaterinburg, Russia
[3] Physical-Technical Research Institute, University of Nizhni Novgorod, 603600 Nizhni Novgorod, Russia

Abstract. We experimentally study the nonohmic conductivity of two dimensional disordered system at decreasing temperature. The investigations were curried out in wide temperature range 50 mK–4.2 K. This allows us to trace the crossover from diffusive to hopping conductivity at fixed disorder. In our structures this crossover is observed when the low temperature conductivity is about $(10^{-2}-10^{-3})G_0$.

The increase of a disorder (amplitude of long range potential fluctuations δ) or the decrease of the Fermi level (E_F) leads at low temperature to the conductivity mechanism changing: from the diffusion at $E_F/\delta > 1$ to the hopping at $E_F/\delta < 1$. In two dimensional systems there is another reason for localization: localization by quantum interference. This leads to well known property of two dimensional systems: at zero temperature all states are localized. However, at large $k_F l$-value about 20 (where k_F is the Fermi quasimomentum, l is the mean free path) even at 10 mK the magnitude of quantum corrections is about 20% of Drude conductivity ($\sigma_{Dr} = \pi G_0 k_F l$ (where $G_0 = e^2/(2\pi^2\hbar) = 1.23 \times 10^{-5}$ Ohm^{-1})). At not a very large $k_F l \simeq 2-3$, the quantum corrections value can be close to the Drude conductivity, can substantially decrease the low temperature conductivity, and, possibly, lead to the localization at experimentally achievable temperatures. In our previous work [1] we studied this situation at decreasing of σ_{Dr} in limited temperature range from 0.4 K to 4.2 K. This restriction gave no way of tracing of the crossover from diffusive to the hopping conductivity at fixed disorder. In the present work we significantly extend the investigated temperature range down to millikelvins.

Our method of the conductivity mechanism determination is based on the fact that in the diffusive regime the nonohmic conductivity is due to the electron gas heating only and the electron- and lattice-temperature dependence of energy relaxation rate $P(T_e, T_l)$ is of special form. It can be represented as difference of two identical functions, one of them depends on the electron temperature and another one depends on the lattice temperature [2]:

$$P(T_e, T_l) = F(T_e) - F(T_l). \tag{1}$$

It is seen, that the derivative $\partial P(T_e, T_l)/\partial T_e$ does not depend on T_l:

$$\frac{\partial P(T_e, T_l)}{\partial T_e} = \frac{\partial F(T_e)}{\partial T_e}. \tag{2}$$

Let us show, that in this case the derivative $\partial P(\sigma, T_l)/\partial\sigma$ is also independent of T_l. In diffusive case the conductivity σ is a single-valued function of T_e only, and we can use the inverse function $T_e(\sigma)$ to represent the dependence $P(\sigma, T_l)$ as $P(\sigma, T_l) = P(T_e(\sigma), T_l)$. Then:

$$\frac{\partial P(\sigma, T_l)}{\partial\sigma} = \frac{\partial P(T_e, T_l)}{\partial T_e}\frac{\partial T_e(\sigma)}{\partial\sigma}. \tag{3}$$

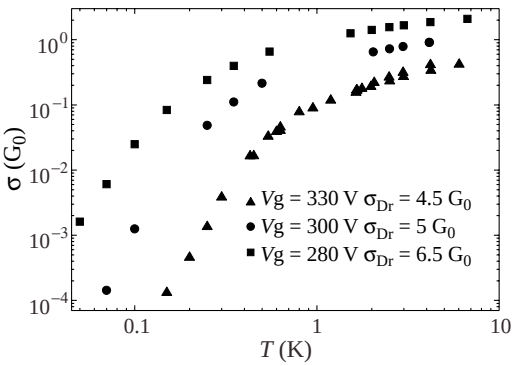

Fig. 1. The temperature dependence of conductivity.

In the right side $\partial T_e/\partial\sigma$ is just the derivative of the inverse temperature dependence. As was shown above the $\partial P(\sigma, T_l)/\partial T_e$ is independent of T_l. Then, $\partial P(\sigma, T_l)/\partial\sigma$ is independent of lattice temperature as well.

Experimentally, we measure $\sigma(Q)$ at fixed lattice temperature T_l, where $Q = I V$ is the Joule power injected in the sample. For steady state the injected power Q is equal to the energy relaxation rate P. In what follows we will not discriminate these functions and will use the symbol P. The function $P(\sigma)$ is the inverse function of $\sigma(P)$. If we measure the derivatives $\partial P(\sigma)/\partial\sigma$ at different lattice temperatures, all the curves must fall on single universal curve.

In the hopping regime the written above is invalid [1]. In this case the derivative $\partial P(\sigma)/\partial\sigma$ will depend on T_l, i.e., curves measured at different T_l will not fall on common curve.

Here, we investigated the nonohmic conductivity for heterostructure with InGaAs single quantum well in GaAs. The structure had a Si δ doping layer in the center of the quantum well. The electron density and mobility were $n = 1.65 \times 10^{16}$ m^{-2} and $\mu = 0.12$ m^2/(V s), respectively. The samples were mesa etched into Hall bars on which basis the field-effect transistors with an Ag gate electrode were fabricated. It was very important to use thick insulator between gate electrode and 2D channel to decrease the influence of voltage drop over the channel. We used the 10 μm organic insulator (polyimid) which was coated on to the cap layer before fabrication of the gate electrode. Applying the gate voltage V_g we varied the concentration in order to reach the value of ultra low temperature conductivity about $10^{-4}G_0$.

In what follows, we will characterize each state of the system by the Drude conductivity value σ_{Dr}. The value of σ_{Dr} was

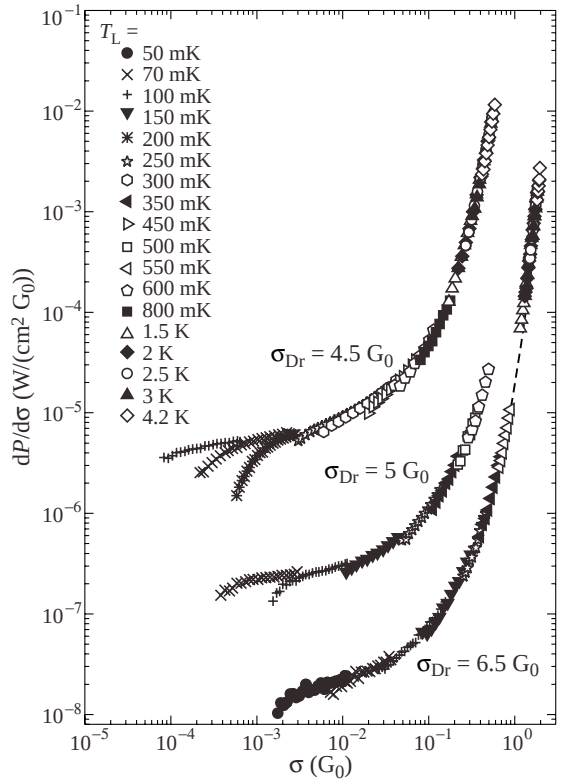

Fig. 2. The $\partial P(\sigma, T_l)/\partial\sigma$ as a function of conductivity. Different symbols denotes different lattice temperatures T_l.

determined from the analysis of the magnetoresistance and Hall effect at high temperature when $\sigma > G_0$, as discussed in [3]. In Figure 1 the temperature dependence of the conductivity for the investigated σ_{Dr} values is presented. It is seen that for the actual σ_{Dr} values the conductivity changes in wide range from $\sigma \simeq 2G_0$, where the conductivity is diffusive, down to $\sigma \sim 10^{-4}G_0$. It should be noted that, the most part of the investigated conductivity range is covered at each σ_{Dr} value (i.e. at fixed disorder). So, we can trace the behavior of the nonohmic conductivity starting from the diffusive conductivity down to very low conductivity values, where the transition to the hopping conductivity mechanism is possible. This allows us to examine the possibility of the conductivity mechanism changing by the quantum interference.

The derivatives $\partial P(\sigma, T_l)/\partial\sigma$ for the investigated σ_{Dr} values are presented in Figure 2. It is seen that the behavior of the derivatives is determined by the low temperature conductivity value, rather than by the Drude conductivity. On this figure the several ranges of conductivity can be marked out. The first range, $\sigma > 1G_0$. It is commonly accepted, that in this range the conductivity mechanism is diffusion. Really, the derivatives in this range perfectly coincide. Second range, the conductivity σ is in the range from $1G_0$ to $\sim 3 \times 10^{-3}G_0$. In this range the derivatives, obtained at different lattice temperatures fall on common curve, as well. The third range σ is less than $3 \times 10^{-3}G_0$. The derivatives do not fall here on common curve. The presence of the lattice temperature dependence of the derivative is evident.

Such behavior of the derivatives shows that down to the low temperature conductivity value of about $3 \times 10^{-3}G_0$ the conductivity mechanism is diffusion over the delocalized states. In this case the temperature dependence is determined by the quantum corrections. This agrees with results of the studies of quantum corrections to the conductivity at decreasing $k_F l$ [3].

Only when the low temperature conductivity becomes lower than $\sim 3 \times 10^{-3}G_0$ the conductivity mechanism is changed to the hopping one. It should be noted that in the investigated structures the conditions of the crossover to the hopping conductivity mechanism weakly depend on the Drude conductivity and they are almost determined by the low temperature conductivity value.

It is clearly seen that at $\sigma_{Dr} = 4.5G_0$ the conductivity mechanism has changed from diffusion to the hopping when σ become lower $3 \times 10^{-3}G_0$. So, we found that at fixed disorder the quantum interference can lead to the conductivity mechanism changing from diffusion to the hoping one.

In summary, we have shown, that at not a very large value of $k_F l$ at the decreasing of the temperature the quantum corrections can substantially decrease the conductivity while it remains diffusive. At the further decreasing of the temperature they can lead to the conductivity mechanism changing, from diffusive to the hopping one, when the low temperature conductivity becomes smaller than $10^{-3}G_0$.

Acknowledgements

We gratefully thanks Prof. M. E. Gershenson for the useful discussion and collaboration, J. Wei for their assistance in the experiment, Dr. A. A. Zhukov for his help in the sample preparation. This work was supported in part by the RFBR (Grants 06-02-16292, 07-02-00528), the CRDF (Grants EK-005-X1 and Y1-P-05-11) and the grant of president of Russia Federation.

References

[1] G. M. Minkov, A. A. Sherstobitov, O. E. Rut, A. V. Germanenko, *Physica E.* **25**, 42 (2004).
[2] P. J. Price, *J. Appl. Phys.* **53**, 6863 (1982).
[3] G. M. Minkov, O. E. Rut, A. V. Germanenko, A. A. Sherstobitov, B. N. Zvonkov, E. A. Uskova, and A. A. Birukov, *Phys. Rev.* **B65**, 235322 (2002).
[4] M. E. Gershenson, Yu. B. Khavin, D. Reuter, P. Schafmeister, and A. D. Wieck, *Phys. Rev. Lett.* **85**, 1718 (2000).

15th Int. Symp. "Nanostructures: Physics and Technology"
Novosibirsk, Russia, June 25–29, 2007

Circular photogalvanic effect caused by the free-carrier absorption. The spinless mechanism

S. A. Tarasenko
Ioffe Physico-Technical Institute, St Petersburg, Russia

Abstract. The free-carrier (Drude) absorption of circularly polarized radiation in quantum well structures is shown to induce an electric current, which reverses its direction upon switching the light helicity. A pure orbital mechanism of such a circular photogalvanic effect is proposed that does not involve spin of the carriers. The developed microscopic theory can provide an explanation for recent experiments on circular photocurrents in n-doped structures.

1. Introduction

The absorption of circularly polarized light in semiconductor structures may lead to generation of an electric current, which reverses its direction upon switching the light polarization from right-handed to left-handed and vice versa. Such a circular photogalvanic effect (CPGE) has attracted considerable attention recently: It has been observed in zinc-blende- and diamond-type quantum wells (QWs) for a variety of optical ranges, including inter-band, inter-subband, and indirect intra-subband (Drude-like) optical transitions in doped QW structures (for a review see [1]).

So far, the microscopic model of CPGE in QW structures has been developed for the direct inter-band or inter-subband optical transitions. It has been shown that the effect originates from the complicated band structure of the semiconductor compounds, mostly, from spin-orbit splitting of the electron or hole states and linear-in-**k** terms in the matrix elements of the optical transitions.

Here we address CPGE caused by the free-carrier absorption of circularly polarized radiation in n-doped QW structures. We show that a pure orbital mechanism of the effect can predominate in this spectral range, which is related to neither spin-orbit coupling nor spin-sensitive selection rules for the optical transitions. This mechanism is based on interference of different pathways contributing to the light absorption [2].

We consider CPGE in (001)-oriented QWs grown from zinc-blende-type semiconductors. Symmetry analysis shows that the helicity dependent photocurrent **j** in such structures can be induced only at oblique incidence of the radiation and is described by two linearly independent constants γ_1 and γ_2 as follows:

$$\begin{aligned} j_x &= [\gamma_2 l_x - \gamma_1 l_y] I P_{\rm circ}, \\ j_y &= [\gamma_1 l_x - \gamma_2 l_y] I P_{\rm circ}, \end{aligned} \qquad (1)$$

where $\mathbf{l} = \mathbf{q}/q$ is the unit vector pointing in the light propagation direction, $\mathbf{q}$ and I are the wave vector and intensity of the light inside the structure, respectively; $P_{\rm circ}$ is the radiation helicity ranging from -1 (for the left-handed circular polarization) to $+1$ (for the right-handed circular polarization); $x \parallel [100]$, $y \parallel [010]$, and $z \parallel [001]$ are the cubic crystallographic axes. Phenomenologically, the constant γ_1 is related to the heterostructure asymmetry, i.e., nonequivalence of the z and $-z$ directions, while the constant γ_2 originates from lack of an inversion center in the host crystal.

In this report we present a microscopic theory for the orbital mechanism of CPGE and show that this mechanism contributes to both γ_1 and γ_2 constants.

2. Misroscopic theory

The light absorption by free carriers is always accompanied by electron scattering from static defects or phonos, because of the need for energy and momentum conservation. Such indirect optical transitions are treated as second-order processes, which involve electron-photon interaction and electron scattering, via virtual intermediate states. The intermediate states can be those within the same quantum subband, $e1$ in our case, or in other conduction or valence subbands. The dominant pathway determining the QW absorbance involve intermediate states within the subband $e1$ (see Fig. 1). These processes can be induced by the in-plane component of the polarization vector **e** only and do not lead to any circular photocurrent.

The helicity dependent photocurrent arises if one takes into account interference of the processes depicted in Fig. 1 and those with virtual intermediate states in other conduction or valence subbands. Such optical transitions with intermediate states in the subband $e2$, which contribute to the free-carrier absorption, are sketched in Fig. 2.

The light absorption is contributed by processes with all possible intermediate states. Under excitation with circularly polarized light the processes depicted in Fig. 1 and Fig. 2 interfere. They are added constructively for transitions to states with a certain wave vector $\mathbf{k}'$ and destructively for transitions to $-\mathbf{k}'$. Thus, the transition rates to the states $\mathbf{k}'$ and $-\mathbf{k}'$ are different, resulting in an imbalance of the photoexcited carries in **k**-space, i.e., in an electric current. The orientation of the wave vector $\mathbf{k}'$, where the transitions via the different subbands are added constructively, is determined by the light helicity. Therefore, the photocurrent reverses its direction by changing the light polarization from right-handed to left-handed.

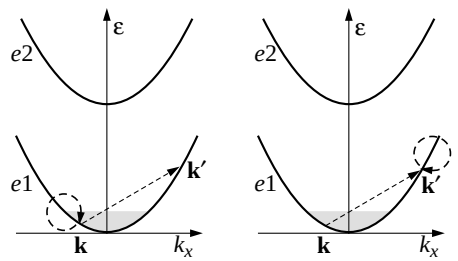

Fig. 1. Intrasubband optical transitions $(e1, \mathbf{k}) \to (e1, \mathbf{k}')$ with intermediate states in the subband $e1$. Dashed circles and dotted lines represent electron-photon interaction and electron scattering, respectively. Panels correspond to possible processes: electron-photon interaction followed by electron scattering and electron scattering followed by electron-photon interaction.

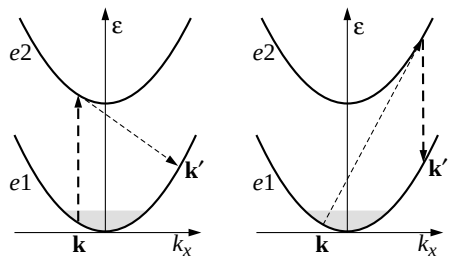

Fig. 2. Intrasubband optical transitions $(e1, \mathbf{k}) \to (e1, \mathbf{k}')$ with intermediate states in the subband $e2$. Dashed and dotted lines represent electron-photon interaction and electron scattering, respectively. Panels correspond to possible processes: electron-photon interaction followed by electron scattering and electron scattering followed by electron-photon interaction.

The detailed microscopic theory of the CPGE is conveniently developed in the framework of the Boltzmann equation. Making allowance for the transitions via the subbands $e1$ and $e2$, one can write for the photocurrent

$$\mathbf{j} = e\frac{4\pi}{\hbar}\sum_{\mathbf{k},\mathbf{k}'}[\tau_{\rm p}(\varepsilon_{\mathbf{k}'})\mathbf{v}_{\mathbf{k}'} - \tau_{\rm p}(\varepsilon_{\mathbf{k}})\mathbf{v}_{\mathbf{k}}] \times \left|M^{(e1)}_{\mathbf{k}'\mathbf{k}} + M^{(e2)}_{\mathbf{k}'\mathbf{k}}\right|^2 (f_{\mathbf{k}} - f_{\mathbf{k}'})\delta(\varepsilon_{\mathbf{k}'} - \varepsilon_{\mathbf{k}} - \hbar\omega)\,, \quad (2)$$

where e is the electron charge, $\mathbf{v}_{\mathbf{k}} = \hbar\mathbf{k}/m^*$ and $\varepsilon_{\mathbf{k}} = \hbar^2k^2/(2m^*)$ are the electron velocity and kinetic energy, $\tau_{\rm p}$ is the momentum relaxation time, $M^{(e1)}_{\mathbf{k}'\mathbf{k}}$ and $M^{(e2)}_{\mathbf{k}'\mathbf{k}}$ are the matrix elements of the optical transitions via the subbands $e1$ and $e2$, respectively, $f_{\mathbf{k}}$ is the function of equilibrium carrier distribution in the subband $e1$, and the factor 4 in Eq. (2) accounts for the spin degeneracy. The square of the matrix element sum in Eq. (2) contains the interference term $2{\rm Re}[M^{(e1)}_{\mathbf{k}'\mathbf{k}} M^{(e2)*}_{\mathbf{k}'\mathbf{k}}]$. This term is odd in the wave vector and proportional to the light helicity $P_{\rm circ}$. It is the term that is responsible for the orbital mechanism of CPGE.

Calculation shows that, for the case of electron scattering by short-range static defects or quasi-elastic scattering by acoustic phonons, the constant γ_1 has the form

$$\gamma_1 = -2e\tau_{\rm p}\frac{\omega z_{21}}{\varepsilon_{21}}\,\xi\eta_{\parallel}\,, \quad (3)$$

where z_{21} is the coordinate matrix element between the envelope functions in the subbands $e1$ and $e2$ [$\varphi_1(z)$ and $\varphi_2(z)$, respectively], $\eta_{\parallel}$ is the QW absorbance for radiation polarized in the QW plane, and ξ is a dimensionless parameter, which depends on the structure design and mechanisms of scattering. The parameter ξ is given by

$$\xi = \int_{-\infty}^{+\infty}\varphi_1^3(z)\varphi_2(z)w(z)dz \Big/ \int_{-\infty}^{+\infty}\varphi_1^4(z)w(z)dz\,, \quad (4)$$

with $w(z)$ being the distribution function of the scatterers along the growth direction [$w(z)$ is a constant for scattering by bulk phonons].

In accordance with general symmetry arguments, the helicity dependent photocurrent corresponding to the phenomenological constant γ_1 is related to inversion asymmetry of the heterostructure. This follows also from Eqs. (3) and (4), which demonstrate that the sign and magnitude of γ_1 is determined by asymmetry of the confinement potential and the doping profile. In particular, $\gamma_1 \equiv 0$ for the absolutely symmetrical structures, where $w(z)$ and $\varphi_1(z)$ are even functions while $\varphi_2(z)$ is an odd function with respect to the QW center.

On the contrary, the constant γ_2 in the phenomenological equation (1) is related to lack of an inversion symmetry in the bulk hosting semiconductor. Thus, γ_2 can be nonzero even in symmetrical QWs grown from zinc-blende-type compounds. To obtain this photocurrent contribution one has to take into account the lattice symmetry of the QW host semiconductor. This can be done considering interference of optical transitions with intermediate states in the subband $e1$ and those via the valence-band states.

Calculation shows that, for the free-carrier absorption assisted by quasi-elastic scattering from acoustic phonons, the constant γ_2 has the form

$$\gamma_2 = -2e\tau_{\rm p}\frac{\Xi_{cv}}{\Xi_c}\frac{\omega P}{E_g^2}\,\zeta\eta_{\parallel}\,, \quad (5)$$

where Ξ_c and Ξ_{cv} are the intra-band and inter-band deformation-potential constants (Ξ_{cv} does not vanish due to the lack of the inversion symmetry in zinc-blende-type semiconductors), E_g is the band gap energy, $P = i(\hbar/m_0)\langle S|p_z|Z\rangle$ is the Kane matrix element, and ζ is a parameter depending on the QW width, the carrier distribution and the photon energy. For a rectangular quantum well with the infinitely high barriers, $\zeta = k_\omega a/12$ if the photon energy is much large than the mean electron energy, where $k_\omega = \sqrt{2m^*\omega/\hbar}$ and a is the QW width.

3. Conclusion. Comparison with experiments

We have shown that the free-carrier absorption of circularly polarized radiation in quantum well structures leads to an electric current, which reverses its direction upon switching the light helicity. The proposed pure orbital mechanism of the circular photogalvanic effect is based on interference of different pathways contributing to the light absorption.

Following Eqs. (1) and (3) we can estimate the magnitude of the circular photocurrent density. It gives $j_{\rm orbit} \sim 10^{-8}$ A/cm for the photon energy $\hbar\omega = 10$ meV, the light intensity $I = 1$ W/cm^2, the carrier density $N_e = 10^{12}$ cm^{-2}, the QW width $a = 150$ Å, the incidence angle corresponding to $l_x = 0.2$, and the structure asymmetry $\xi = 0.2$. The estimated magnitude of the photocurrent corresponds to that measured in experiments on (001)-oriented structures [1].

Acknowledgements

This work was supported by the RFBR, programs of the RAS, President Grant for Young Scientists, and the Russian Science Support Foundation.

References

[1] S. D. Ganichev and W. Prettl, *J. Phys.: Condens. Matter* **15**, R935 (2003).

[2] S. A. Tarasenko, *Pis'ma Zh. Eksp. Teor. Fiz.* **85**, 216 (2007); [*JETP Lett.* **85**, 182 (2007)].

15th Int. Symp. "Nanostructures: Physics and Technology"
Novosibirsk, Russia, June 25–29, 2007

2D electron accumulation layer induced on the n-InGaN surface

G. V. Benemanskaya, S. V. Ivanov, V. N. Jmerik, G. E. Frank-Kamenetskaya and M. N. Lapushkin
Ioffe Physico-Technical Institute, St Petersburg, Russia

Abstract. We report on first observation of an charge accumulation layer (AL) - 2D electron channel created by Cs adsorption on the n-InGaN surface in wide coverage range from 0.1ML to 2ML. Photoemission from Cs/n-InGaN interface has been found by excitation of visible light in the transparency region of InGaN. Under Cs adsorption, sharp decrease in work function up to 1.40 eV is revealed and shown to be due to formation of an 2D electron channel (AL) in the downward conductivity-band-bending region close to the surface. Theoretical investigation is carried out to ascertain energetic parameters of AL. A phenomenon is observed, namely, the appearance of an oscillation structure in spectra of photoyield. A model conception taking into account both the formation of AL and occurrence of multiple-beam interference in parallel-sided InGaN-GaN epilayer is suggested

Introduction

We have experimentally achieved the formation of an 2D electron channel — charge accumulation layer (AL) that is formed in situ by Cs adsorption on InGaN n-type surface. The possibility of creation of similar 2D structure has not yet been examined. Electronic and atomic properties of III-nitride surfaces are still poorly understood and then they give rise controversy despite effective technology progress in growing of high-quality materials and their application to high power electronic, photodetectors and light emitting devices. The GaN(0001) surface and metal/GaN interfaces were studied by conventional Auger electron, core-level, X-ray and ultraviolet photoemission spectroscopies. The ultrathin Cs/n-GaN and Ba/n-GaN interfaces have been now studied [1]. Anomalous behavior of band-bending near the surface and new phenomenon of formation of 2D electron accumulation layers have been revealed. It is noteworthy to point out that accumulation layers were obtained previous to our studies exclusively on clean surfaces (InAs and InN). Here we represent first investigation of the Cs/InGaN interface

1. Experimental results and discussion

Photoemission studies have been performed in situ in a vacuum of $P \sim 5 \times 10^{-11}$ Torr. Prior to studies, sample is annealed in situ at $\sim$ 450 °C. To ascertain Cs coverages, sources are accurate calibrated to dosage using original technique. The Cs overlayers are presented in monolayer (ML) units. Note that the 1 ML is defined as one metal adatom per InGaN(0001) 1×1 surface atom and equal to 9.9×10^{14} atoms cm^{-2}. The technique of photoemission yield spectroscopy (PYS) excitation by the *s*- and *p*- polarized light has been used. Details of PYS can be found elsewhere [1,2].To ascertain Cs coverages, source is accurate calibrated to dosage. The Cs overlayers are presented in monolayer (ML) units. Note that the 1 ML is defined as one metal adatom per GaN(0001) 1×1 surface atom and equal to 9.9×10^{14} atoms cm^{-2}.

The $In_{0.14}Ga_{0.86}N$ layer was grown by plasma-assisted molecular beam epitaxy (PA MBE) on a 3-μm-thick GaN-MOVPE/c-sapphire template coated by a 200-nm-thickGaN PA MBE buffer layer. Details of the PA MBE growth have been reported elsewhere [3]. The GaN buffer layer was grown at the slightly Ga-rich conditions (flux intensity ratio of Ga/N $\leq$ 1.1)

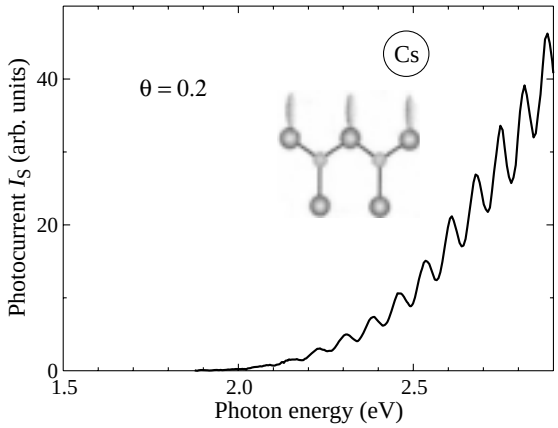

Fig. 1. Spectra of the photoemission current I_S for the 0.2 ML of Cs coverage at the InGaN surface and schema of Cs adsorption.

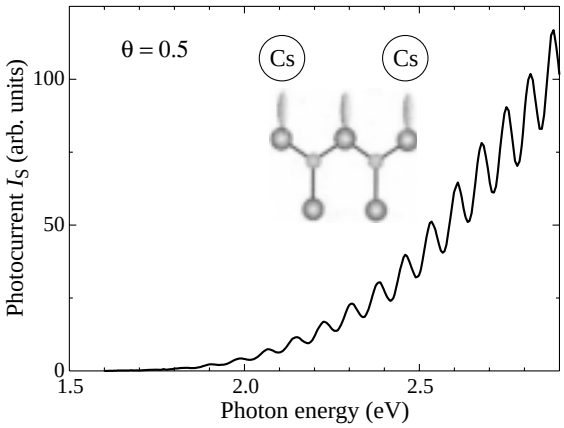

Fig. 2. Spectrum of the photoemission current I_S for the 0.5 ML of Cs coverage at the InGaN surface and schema of Cs adsorption.

at the growth rate 0.36 μm/h, that resulted in the atomically smooth droplet-free surface. The 70-nm-thick InGaN layer was grown at even more metal-rich conditions with the excess of In ((Ga+In)/N = 1.55). Relatively high growth temperature (T_S = 630 °C) enabled one to avoid In micro-droplets on the InGaN surface and obtain by AFM the atomically smooth surface. High structural properties and absence of phase separation in the InGaN layer were confirmed by observation of a single symmetrical peak in the x-ray diffraction scan with

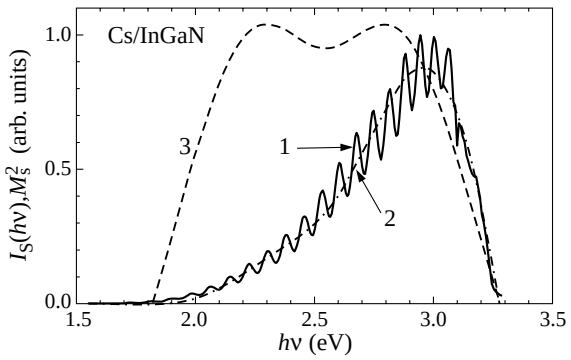

Fig. 3. Experimental (1) and calculated (2) spectra of the photoemission current I_S for 0.4 ML Cs coverage at the InGaN surface. Calculated photoemission matrix element (3).

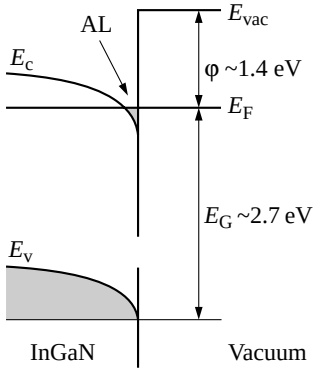

Fig. 4. Energy diagram of downward band-bending and formation of AL at the InGaN surface with Cs adlayer.

relatively narrow FWHM of 218 arcsec and well pronounced interference fringes.

We study the photoemission and electronic properties of $Cs/In_{0.14}Ga_{0.86}N$ interface. Photoemission from accumulation layer is revealed by excitation of visible light in the transparency region of InGaN (Fig. 1–3). The work function minimum is found to reduce up to 1.4 eV. The Cs adsorption is found to induce formation of AL in band-bending region of InGaN (Fig. 4). Therefore, metallic-like accumulation layer is created. Fig. 3. represents experimental and calculated spectra of photoyield $I_S(h\nu)$ for the 0.4 ML Cs coverage. Character of spectra is very unusual. To explain origin of the oscillation structure, a model taking into account both the accumulation layer and constructive interference in parallel-sided plate of InGaN + GaN is suggested.

Acknowledgements

The authors thank V. S. Vikhnin for fruitful discussions. This work was supported by grant 07-02-00510-a of RFBR and by grant 10a of the program P-03 of Presidium of RAS.

References

[1] G. V. Benemanskaya *et al*, *Appl. Phys. Lett.* **85**, 1365 (2004); *JETP Lett.* **77**, 226 (2003); **81**, 519 (2005); *JETP* **103**, 439 (2006).

[2] G. V. Benemanskaya *et al*, *Surf. Sci* **523**, 211 (2001); *Surf. Sci.* **302**, 303 (1996).

[3] S. V. Ivanov, V. N. Jmerik, T. V. Shubina *et al*, to be published, *J. of Crystal Growth* (2007).

15th Int. Symp. "Nanostructures: Physics and Technology"
Novosibirsk, Russia, June 25–29, 2007

Nanostructures for nanoelectronics: No potential for room temperature applications?

D. Bimberg

Institut für Festköperphysik, Technische Universität Berlin, Hardenbergstr. 36, 10623 Berlin, Germany

Two of the major scientific and technological challenges for the next 10–15 years highlighted in the 2005 ITRS roadmap are

— the development of novel nanoscale devices for future generations of memories like DRAM/Flash and
— closing the rapidly increasing memory access bottleneck.

Practical solutions must operate at room temperature.

In this talk, a novel type of memory, the "QD-Flash" based on quantum dots [1] (QDs) is suggested [2]. In actual fact the QD-Flash merges the advantages of classical DRAM and Flash memories. In a first step towards a QD-Flash the carrier retention time in QDs at room temperature has to be increased such that it is beyond the magic DRAM limit of 1 ms [3]. We demonstrate here 1.5 s carrier retention time at room temperature. Further extension by several orders of magnitude by changing the QD and/or matrix material is discussed.

Prototype design e.g. by IBM for a Terabus, potentially closing the memory access bottleneck exists. Wide ranging applicability of such concepts depends on the availability of temperature robust high speed VCSELs. We have recently demonstrated the first VCSELs, operating error free at 20 Gbit/s between 25 and 85 °C with a bit-error-rate below 10^{-12}, based on submonolayer deposition growth mode of InAs. Their peak differential efficiency decreases only from 0.7 W/A at 25 °C to 0.6 W/A at 85 °C [4].

References

[1] D. Bimberg, M. Grundmann, and N. N. Ledentsov, *Quantum Dot Hetero- structures*, J. Wiley, Chichester (1999).
[2] M. Geller, A. Marent, and D. Bimberg, *A non-volatile memory based on semiconductor nanostructures*, CPT Patent application, submitted (2006).
[3] A. Marent, M. Geller, A. P. Vasi'ev, E. S. Semenova, A. E. Zhukov, V. M. Ustinov, and D. Bimberg, *Appl. Phys. Lett.* **89**, 072103 (2006).
[4] F. Hopfer, A. Mutig, G. Fiol, M. Kuntz, S. S. Mikhrin, I. L. Krestnikov, D. A. Livshits, A. R. Kovsh, C. Bornholdt, V. Shchukin, N. N. Ledentsov, V. Gaysler N. D. Zakharov and P. Werner, and D. Bimberg, *Proc. SPIE* **6350**, 635003 (2006).

Author Index